Theoretical Analysis and Experimental Verification of Microwave Radiation Features of Fractured Rock

Shanjun Liu[1], **Zhongyin Xu**[1], **Lixin Wu**[1, 2], **and Bo Tang**[1]

[1]Institute for Geo-informatics & Digital Mine Research, Northeastern University, Shenyang 110819, China
[2]IoT & Perception Mine Research Center, China University of Mining and Technology, Xuzhou, China

Abstract— Some researchers carried out the microwave detecting experiment of loaded rock, and found the microwave radiation changing significantly when the rock fractured, which indicates that the passive microwave is possible to detect the phenomenon of rock fracture and failure, including earthquakes. But it is unclear by now about the patterns and rules of microwave radiation variation in rock fractures, and the theoretical foundation is also unclear. In this paper we first analyze the microwave radiation characteristics and the influence factors of fractured rock based on the microwave radiation theory of layered medium, and the microwave radiation feature is compared with that of intact rock. Then the theoretical analysis results are verified by a series of passive microwave detecting experiment of fractured rocks.

1. INTRODUCTION

Rock fracture and failure is a common phenomenon in nature, many geological disasters including earthquake, landslide, collapse, ground subsidence, slope instability, rock burst, mine earthquake etc. are related to rock fracture and failure. Since the beginning of this century, many strong earthquakes have happened in the world, which caused serious disasters to mankind. In order to explore the abnormal phenomenon before earthquakes, many people analyzed the thermal infrared radiation variation before the earthquake based on the satellite remote sensing data and found some thermal infrared anomalies appearing before violent earthquakes [1–4]. But it is difficult to recognize the anomaly in cloudy conditions due to inability of infrared radiation to pass through clouds and arrive to the satellite. By contrastmicrowave is not only able to pass through clouds even small rain, but also pass through some-depth soil. Therefore microwave can availably explore the anomaly from the thermal and geology structure change due to earthquake action.

In order to validate the correctness of the above thought some microwave radiation observing experiment were carried out in rock loading process, and found that microwave radiation energy of rock significantly changed with the change of rock stress state, and most rock appeared abnormal precursory with sharp increase or decrease before failure of rock, further research also found that the radar wave reflection strength of rock changed with the change of pressure [5, 6]. In 2006, Maki et al. [7] found that rocks appeared microwave signal variation at 300 MHz, 2 GHz, 22 GHz when the rock failure in uniaxial compression loading. Based on the experimental results Takashi et al. [8] presented a data-restructuring algorithm and applied it to analyze the AMSR-E data for the earthquake of Wenchuan earthquake on May 12, 2008, and found definitive microwave signals around the epicenter one day after the main shock. In order to eliminate the stable influence of geography, terrain, cover sphere and seasons, as well as the random influence of weather Liu et al. [9] presented a two-step method to extract the seismic microwave radiation anomaly related with earthquake. Furthermore the two-step method was applied to analyze the anomaly of Wenchuan earthquake based on the data of AMSR-E. The result showed positive radiation anomaly appearing around the epicenter before and after the earthquake.

But it is unclear by now about the patterns and rules of microwave radiation variation in rock fracturing process. In this paper we firstly analyze the microwave radiation characteristics and the influence factors of fractured rock based on the microwave radiation theory of layered medium, and the microwave radiation feature is compared with that of intact rock. Then the theoretical analysis results are verified by a series of passive microwave detecting experiment of fractured rocks.

2. THEORETICAL ANALYSIS ON MICROWAVE RADIATION OF FRACTURED ROCK

Compared with the intact rock, fractured rock exist the non continuous surface in its internal, so the fractured rock has a layered structure. Therefore we can use the microwave radiation theory of layered medium to analyze the microwave radiation characteristics of fractured rock.

In order to understand easily the microwave radiation of layered rock we first calculate the microwave radiation of intact rock.

2.1. Microwave Radiation of Intact Rock

Because the intact rock is equivalent to the monolayer rock, the microwave radiation received by the radiometer is composed of three parts, as shown in Fig. 1. The first part is the radiation of rock itself, expressed by T_S. The second part is the radiation of back environment, expressed by T_{e2}. The third part is the reflection of rock on the front environment radiation, expressed by T_{e1}.

2.1.1. The Calculation of T_S

In Fig. 1, T_s is the any thin layer of rock, its contribution to the radiometer is composed of two parts: one part is the upward radiation T_{s1}, it upward radiates to the above interface of rock with the angle θ_2, then transmits to the radiometer with the angle θ_1 or is reflected repeatedly by the two interface and transmits to the radiometer at last, as shown by the red line of Fig. 1. The other part is the downward radiation T_{s1}. It downward radiate to the lower interface with the angle θ_2, then is reflected by the lower interface and finally transmit to the radiometer with the angle θ_1, as shown by the black line of Fig. 1. According to the microwave radiation theory of layered medium, we can get following formulas,

$$\begin{aligned} T_{s1} &= T_A \cdot (1-\Gamma_1) + T_A \cdot (1-\Gamma_1) \cdot \frac{\Gamma_1 \cdot \Gamma_2}{L^2} + T_A \cdot (1-\Gamma_1) \cdot \left(\frac{\Gamma_1 \cdot \Gamma_2}{L^2}\right)^2 + \ldots \\ &= T_A \cdot (1-\Gamma_1) / \left(1 - \Gamma_1 \cdot \Gamma_2 / L^2\right) \end{aligned} \tag{1}$$

$$\begin{aligned} T_{s2} &= T_A \cdot (1-\Gamma_1) \cdot \frac{\Gamma_2}{L} + T_A \cdot (1-\Gamma_1) \cdot \frac{\Gamma_2}{L} \cdot \frac{\Gamma_1 \cdot \Gamma_2}{L^2} + T_A \cdot (1-\Gamma_1) \cdot \frac{\Gamma_2}{L} \cdot \left(\frac{\Gamma_1 \cdot \Gamma_2}{L^2}\right)^2 + \ldots \\ &= T_A \cdot (1-\Gamma_1) \cdot \Gamma_2 / \left[L \cdot \left(1 - \Gamma_1 \cdot \Gamma_2 / L^2\right)\right] \end{aligned} \tag{2}$$

Γ_1 is the reflectivity of the above interface, Γ_2 is the reflectivity of the lower interface, T_A is the total radiation energy from the rock to the above interface, expressed by following formula:

$$T_A = \int_0^d dT_A(\theta_2, \xi) = T_2 \cdot \left(1 - \frac{1}{L}\right) \quad L = \exp\left(k_e \cdot d \cdot \sec(\theta_2)\right) \tag{3}$$

T_2 is the thermodynamic temperature of the rock, k_e is the extinction coefficient of the rock, d is the thickness of the rock.

2.1.2. The Calculation of T_{e2}

T_{e2} in Fig. 1 is the radiation of the back environment of rock, which can be considered as a semi-infinite medium, and only exist upward radiation, as shown by the green line of the Fig. 1. It firstly transmits into the rock, then is reflected repeatedly by two interface, finally transmit to the radiometer. According to the microwave radiation theory of layered medium we can get following formula,

$$\begin{aligned} T_{e2} = {} & T_3 \cdot \Gamma_e \cdot \frac{(1-\Gamma_2) \cdot (1-\Gamma_1)}{L} + T_3 \cdot \Gamma_e \cdot \frac{(1-\Gamma_2) \cdot (1-\Gamma_1)}{L} \cdot \frac{\Gamma_1 \cdot \Gamma_2}{L^2} + T_3 \cdot \Gamma_e \cdot \frac{(1-\Gamma_2) \cdot (1-\Gamma_1)}{L} \\ & \cdot \left(\frac{\Gamma_1 \cdot \Gamma_2}{L^2}\right)^2 + \ldots = T_3 \cdot \Gamma_e \cdot (1-\Gamma_1) \cdot (1-\Gamma_2) / \left[L \cdot \left(1 - \Gamma_1 \cdot \Gamma_2 / L^2\right)\right] \end{aligned} \tag{4}$$

T_3 is the thermodynamic temperature of back environment. Γ_e is the emissivity of back environment.

2.1.3. The Calculation of T_{e1}

In Fig. 1 T_{e1} expresses the radiation contribution of front environment. It includes two parts: one part is the reflection of rock surface to the radiometer, and the other part firstly transmits into the rock then is reflected by the lower interface to above interface, and finally transmits to the radiometer.

In order to calculate T_{e1}, we first calculate the summary of T_{s1}, T_{s2} and T_{e2},

$$T'_{int} = T_{s1} + T_{s2} + T_{e2} \tag{5}$$

Then the effective reflectivity Γ_{eff} of rock and back environment is obtained,

$$\Gamma_{eff} = 1 - T'_{int} / T_2 \tag{6}$$

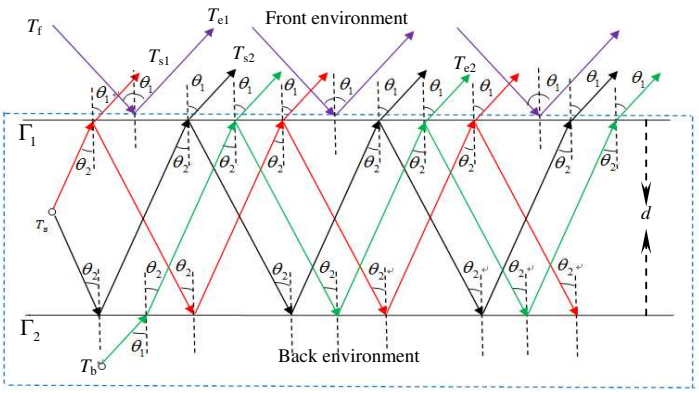

Figure 1: Schematic diagram of microwave radiation of intact rock.

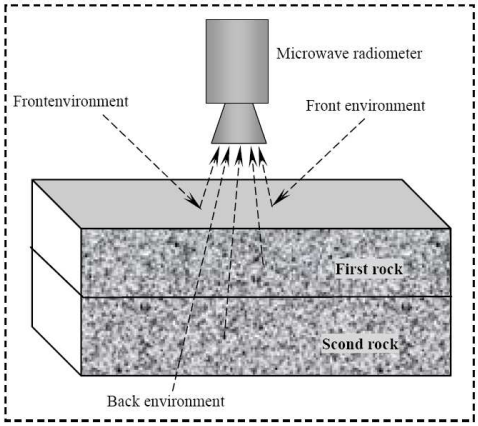

Figure 2: Microwave radiation of two-layer rock.

Therefore, T_{e1} can be calculated by the following formula,

$$T_{e1} = T_f \cdot \Gamma_{eff} \tag{7}$$

T_f is the microwave brightness temperature of front environment. Thus the microwave radiation of intact rock is obtained,

$$T_{lay1} = T_{s1} + T_{s2} + T_{e2} + T_{e1} \tag{8}$$

2.2. Microwave Radiation of Two-layer Rock

When the rock is composed of two layers of medium, the microwave radiation received by the radiometer consists of four parts, as shown in Fig. 2. The first part is the radiation from the first layer of rock; the second part is the radiation form the second layers of rock; the third part is the radiation from the back environment; the fourth part is the reflection of front environment.

2.2.1. Brightness Temperature Contribution of the First Layer of Rock

The brightness temperature contribution of the first layer of rock includes T_{AU1}, T_{AD1} and T_{A12}, as shown in Fig. 3(a). They are calculated by the following formulas:

$$T_{AU1} = T_{A1} \cdot (1 - \Gamma_1)/(1 - \Gamma_1 \cdot \Gamma_2/L_1^2) \tag{9}$$

$$T_{AD1} = T_{A1} \cdot (1 - \Gamma_1) \cdot \Gamma_2/\left[L_1 \cdot \left(1 - \Gamma_1 \cdot \Gamma_2/L_1^2\right)\right] \tag{10}$$

$$T'_{A12} = T_{A1} \cdot (1 - \Gamma_1)/\left(1 - \Gamma_1 \cdot \Gamma_2/L_1^2\right) + T_{A1} \cdot (1 - \Gamma_2) \cdot \Gamma_1/\left[L_1 \cdot \left(1 - \Gamma_1 \cdot \Gamma_2/L_1^2\right)\right] \tag{11}$$

$$T''_{A12} = T'_{A12} \cdot \frac{\Gamma_3}{L_2^2} \cdot (1 - \Gamma_2)^2/\left(1 - \Gamma_2 \cdot \Gamma_3/L_2^2\right)] \tag{12}$$

$$T_{A12} = T''_{A12} \cdot (1 - \Gamma_1) \cdot (1 - \Gamma_2)/\left[L_1 \cdot \left(1 - \Gamma_1 \cdot \Gamma_2/L_2^2\right)\right] \tag{13}$$

Therefore, the radiation B_1 of the firstlayer rock is

$$B_1 = T_{AU1} + T_{AD1} + T_{A12} \tag{14}$$

2.2.2. Brightness Temperature Contribution of the Second Layer of Rock

The calculation of the brightness temperature contribution of the second layer of rock is divided into two steps, as shown in Fig. 3(b). The first step is to calculate the radiation of second layer of rock to the bottom surface of the first layer of rock, which is consists of the upward radiation T_{AU2} and the downward radiation T_{AD2},

$$T_{AU2} = T_{A2} \cdot (1 - \Gamma_2)/(1 - \Gamma_2 \cdot \Gamma_3/L_2^2) \quad T_{AD2} = T_{A2} \cdot (1 - \Gamma_2) \cdot \Gamma_3/\left[L_2 \cdot \left(1 - \Gamma_2 \cdot \Gamma_3/L_2^2\right)\right] \tag{15}$$

So the radiation T'_{A2} of second-layer rock to the bottom surface of the first-layer rock is

$$T'_{A2} = T_{AU2} + T_{AD2} \tag{16}$$

The second step is to calculate the attenuation and reflection of the radiation T'_{A2} when it passes into the first-layer rock, thus B_2 can be obtained,

$$B_2 = T'_{A2} \cdot (1 - \Gamma_2) \cdot (1 - \Gamma_1)/[L_1 \cdot (1 - \Gamma_1 \cdot \Gamma_2/L_1^2)] \tag{17}$$

2.2.3. Brightness Temperature Contribution of the Back Environment

The calculation of the brightness temperature contribution of the back environment can divided into two steps, as shown in Fig. 3(c). The first step is to calculate the radiation attenuation when it passes into the second-layer rock, the second step is to calculate the radiation attenuation when it passes into the first-layer rock.

$$T'_{e2} = T_{e2}\cdot(1-\Gamma_3)\cdot(1-\Gamma_2)/[L_2\cdot(1-\Gamma_2\cdot\Gamma_3/L_2^2)];\quad B_{e2} = T_{e2}\cdot(1-\Gamma_2)\cdot(1-\Gamma_1)/[L_1\cdot(1-\Gamma_1\cdot\Gamma_2/L_1^2)] \tag{18}$$

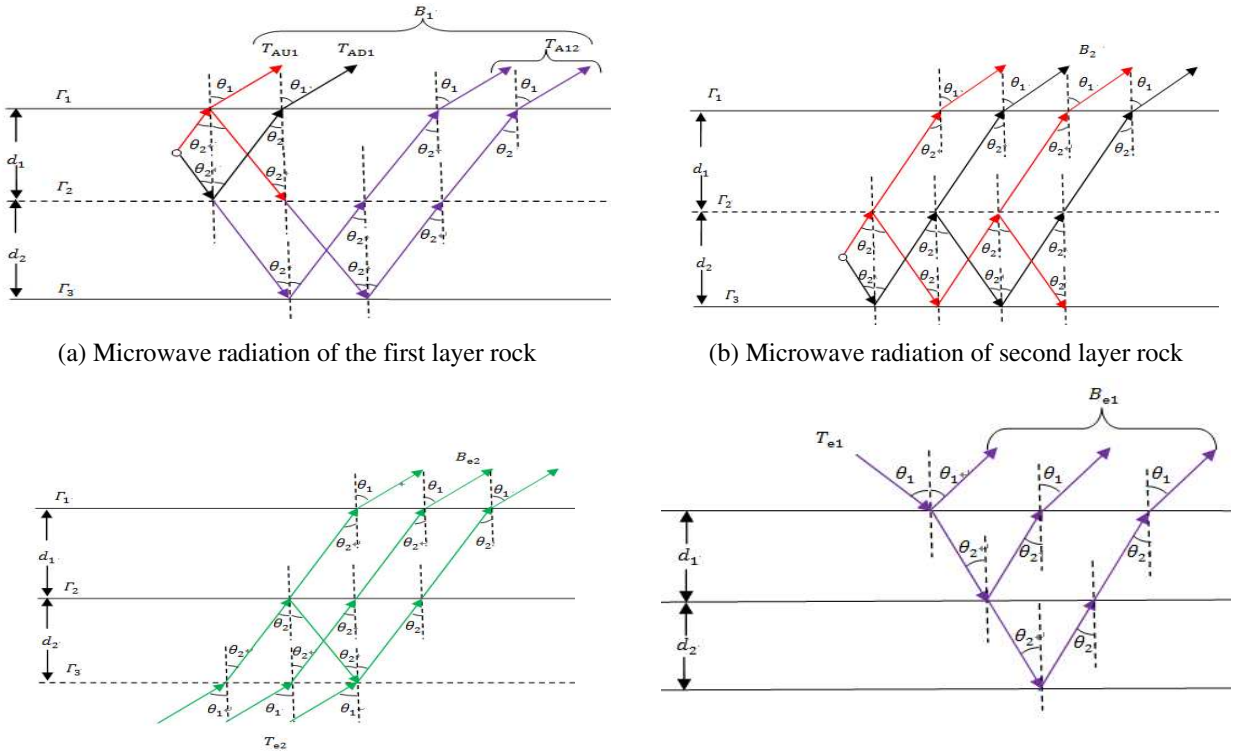

(a) Microwave radiation of the first layer rock

(b) Microwave radiation of second layer rock

(c) Microwave radiation of back environment

(d) Microwave radiation of front environment

Figure 3: Microwave radiation composition of two-layer rock.

2.2.4. Brightness Temperature Contribution of the Front Environment

In order to simplify the process, we can calculate the effective reflectance of rock,

$$\Gamma_{eff} = 1 - (B_1 + B_2 + B_{e2})/T_2 \tag{19}$$

So the brightness temperature contribution B_{e1} can be obtained,

$$B_{e1} = T_{e1}\cdot\Gamma_{eff} \tag{20}$$

Through the above analysis, the total radiation contribution of the two-layer rock to the radiometer is expressed by the following formula:

$$T_{lay2} = B_1 + B_2 + B_{e1} + B_{e2} = B_1 + B_2 + T_{e1}\cdot\left(1 - \frac{B_1 + B_2 + B_{e2}}{T_2}\right) + B_{e2} \tag{21}$$

3. EXPERIMENTAL VERIFICATION OF THE THEORETICAL MODEL

3.1. Microwave Radiation Comparison of Layered Rock and Intact Rock

Assuming the observation is taken under the condition of horizontal polarization and cold sky background. The observation angle is 40°. The thickness of intact rock is 10 cm. The total thickness of two-layer rock is also 10 cm, and the thickness of first layer is 3 cm, the thickness of

second layer is 7 cm. According to the above theory model, the brightness temperature of intact rock can be calculated to be 278 K, but the brightness temperature of two-layer rock is only 262.8 K, which is lower than the intact rock.

Figure 4 shows the microwave observation result of intact rock and fractured rock by a C-band radiometer under cold sky background and horizontal polarization. The rock type and the thickness of intact rock and fractured rock are the same. Fig. 4 shows that the microwave brightness temperature of intact rock is higher than the fractured rock at any observation angles, and the difference between them is 4–8 K, which indicates that when rock is fractured the microwave brightness temperature will decreases.

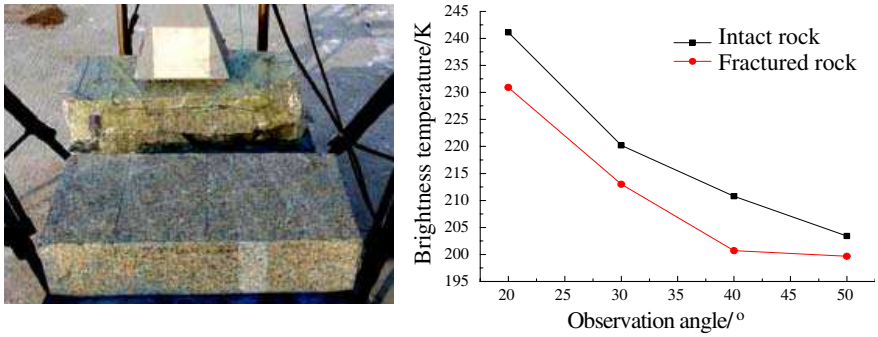

Figure 4: C-band microwave observation of intact rock and fractured rock under cold sky background and horizontal polarization.

3.2. Effect of the Front Environment on the Microwave Observation

Assuming the microwave observation is taken at horizontal polarization, the observation angle is 50°, and the observation frequency 18.7 GHz. The thickness of an intact rock is 15 cm, and the total thickness of a two-layer of rock is also 15 cm. The other observation conditions and parameters are shown in Table 1. Table 2 shows the theoretical calculation results at different front environment.

It can be found from Table 2 that the brightness temperature both intact rock and layered rock increase with the increase of the temperature of the front environment. When the observation is taken in an indoor environment the brightness temperature difference between intact rock and layered rock is very little, only 0.06 K. But when the observation is taken in cold sky background the brightness temperature difference is larger, up to 8.9 K, which indicates the rock fracturing phenomena is easy to be detected. So the microwave observation of the rock fracturing phenomena should be chosen in outdoor and cold sky background.

Table 1: Experimental condition and parameters of microwave observation.

Temperature of rock	Temperature of back environment	Real part of electric constant	Imaginary part of electric constant	Relative permeability	Magnetic susceptibility	Thickness of the first layer	Thickness of second layer
300 K	300 K	2	0.07	1	0.0001	5 cm	10 cm

To verify the influence of the front environment on the microwave radiation, we carried out the microwave observation test respectively in indoor and outdoor environment for intact and fractured rock. The result is shown in Table 3. Table 3 shows the difference of observation in different conditions. The microwave brightness temperature difference between intact and fractured rock is very small in indoor environment, less than 3 K. In contrast, in the cold sky background the difference is up to 10.61 K (C-band, sandstone). The experimental result is similar to the theoretical calculation results, which indicates that the front environment has an important impact on the microwave observation.

3.3. Effect of the Observation Angles on the Microwave Radiation

Assuming the microwave observation is taken at horizontal polarization and cold sky background. The thicknesses of the first layer and second layer of rock are respectively 1.5 cm and 2.5 cm. We analyze the effect of observation angles on the microwave observation. Fig. 5(a) shows the theoretical simulation result. From the diagram we can see the brightness temperature of layered

Table 2: Effect of the front environment on the microwave radiation received by the radiometer.

Temperature of front environment/K	Brightness temperature for intact rock/K	Brightness temperature for layered rock/K	Brightness temperature difference between intact rock and Stratified rock/K
298 K (Indoor)	299.82	299.76	0.06
78 K (Liquid nitrogen background)	280.19	273.38	6.81
10 K (Cold sky background)	274.12	265.22	8.9

Table 3: Microwave brightness temperature contrast for intact and fractured rock at vertical observation and in different environment.

Waveband	Rock type	Cold sky background		Indoor environment	
		Fractured rock	Intact rock	Fractured rock	Intact rock
band C	Granite	264.23	281.31	292.22	292.97
	Sandstone	262.1	272.72	286.16	287.09
Band K	Granite	277.7	287.52	297.15	300.14
	Sandstone	268.88	276.7	292.66	293.87

rock decrease with the increase of the observation angle. Fig. 5(b) and Fig. 5(c) are the experimental observation result of Kband radiometer at horizontal polarization, which is the similar to the theoretical simulation results.

(a) Theoretical simulation result (b) Experimental scene (c) Experimental result

Figure 5: Effect of the observation angles on the microwave radiation.

Assuming the observation is taken at horizontal polarization and frequency 18.7 GHz, the other observation conditions and parameters are shown in the Table 1. Table 4 show the observation result of intact and layered rock under different observation angles. It can be found that the brightness temperature difference of intact rock and layered rock increases gradually with the increase of the observation angles. When the observation angle increases from 35° to 60°, the brightness temperature difference of the intact rock and layered rock increases from 6.14 K to 11.73 K, which indicates that microwave detection on rock fracture phenomenon should choose large observation angle. In practice the observation angle of satellite microwave remote sensing is mostly 55°, which is larger and suitable to detect the crystal rock fracture phenomenon, such as the earthquake.

3.4. Effects of Observation Frequency on Microwave Radiation

Assuming the observation at horizontal polarization and the cold sky background with temperature 10 K, the observation angle is 40° and the other observation conditions and parameters are same as Table 1. Table 5 is the theoretical simulation result of brightness temperature of intact rock and layered rock at different frequencies.

It can be found from Table 5 that the brightness temperature difference of intact rock and layered rock decreases with the increase of frequency. When the frequency increases from 6.6 GHz (band C) to 31.68 GHz (band Ka) the brightness temperature difference of intact rock and layered

Table 4: The microwave observation result of intact and layered rock at different observation angles.

Observation angles/°	Brightness temperature of intact rock/K	Brightness temperature of layered rock/K	Difference of Brightness temperature between intact and layered rock/K
35	285.34	279.20	6.14
40	282.69	275.82	6.87
45	279.08	271.30	7.78
50	274.12	265.22	8.9
55	267.22	257.00	10.22
60	257.54	245.81	11.73

Table 5: Theoretical simulation result of brightness temperature of rocks at different observation frequencies.

Frequencies/GHz	Brightness temperature of intact rock/K	Brightness temperature of layered rock/K	Brightness temperature difference of intact rock and layered rock/K
6.6	281.19	263.83	17.36
13.9	282.59	272.77	9.82
18.7	282.69	275.82	6.87
31.68	282.71	279.92	2.79

rock decreases from 17.36 K to 2.79 K. The experimental results indicated that the low-frequency radiometer is easier to detect the fracture phenomenon of crust rock.

4. CONCLUSION

In this paper, the microwave radiation characteristics and the influence factors of fractured rock is analyzed based on the microwave radiation theory of layered medium, and the microwave radiation feature of fractured rock is compared with that of intact rock. Then some theoretical analysis results are verified by the passive microwave detecting experiment. The main results are: (1) the microwave brightness temperature of layered rock is smaller than that of intact rock under same conditions; (2) the environmental radiation have an important influence to brightness temperature of layered rock, and the brightness temperature increase with the increase of environmental temperature in the front of rock; (3) the brightness temperature of layered rock decrease with the increase of the observing angle; (4) the brightness temperature of layered rock increase with the increase of the microwave frequency.

The experiment results indicated that it is possible to use the microwave remote sensing to monitor the fracturing of rock masses, including earthquakes.

ACKNOWLEDGMENT

This work is supported by the National Important Basic Research Project (No. 2011CB707102), the National Natural Science Foundations of China (No. 41074127) and the Specialized Research Fund for the Doctoral Program of Higher Education (No. 20120042110029).

REFERENCES

1. Gorny, V. I., "The earth outgoing IR radiation as an indicator of seismic activity," *Proc. Acad. Sci. USSR*, Vol. 30, No. 1, 67–69, 1988.
2. Tronin, A. A., "Satellite thermal survey — A new tool for the study of seismoactive regions," *INT. J. Remote Sensing*, Vol. 17, No. 8, 1439–1455, 1996.
3. Qiang, Z. J., X. D. Xu, and C. G. Dian, "Thermal infrared anomaly precursor of impemding earthquake," *Chinese Science Bulletin.*, Vol. 36, No. 4, 319–323, 1991.
4. Tramutoli, V., V. Cuomob, C. Filizzola, et al., "Assessing the potential of thermal infrared satellite surveys for monitoring seismically active areas: The case of Kocaeli earthquake. August 17, 1999," *Remote Sensing of Environment*, Vol. 96, 409–426, 2005.

5. Deng, M. D., Z. F. Fan, C. Y. Cui, et al., "The experimental study for earthquake prediction by passive microwave remote sensing," *J. Infrared Millim. Waves*, Vol. 14, No. 6, 401–406, 1995.
6. Qian, J. D., M. D. Deng, J. Y. Yin, et al., "A basic experimental study of earthquake prediction in terms of radar technology," *Chinese J. Geophys.*, Vol. 48, No. 5, 1103–1109, 2005.
7. Maki, K., T. Takano, and E. Souma, "An experimental study of microwave emissions from compression failure of rocks," *Journal of the Seismological Society of Japan, Second Series*, Vol. 58, No. 4, 375–384, 2006.
8. Maeda, T. and T. Takano, "Detection of microwave signals associated with rock failures in an earthquake from satellite-borne microwave radiometer data," *IEEE International Geoscience and Remote Sensing Symposium*, Cape Town, South Africa, 2009.
9. Liu, S., Y. Ma, and L. Wu, "Microwave radiation anomaly of wenchuan earthquake and its mechanism," *IEEE International Geoscience and Remote Sensing Symposium*, Vancouver, Canada, 2011.

Surface Scattering Characteristics and Snow Accumulating-melting Behaviors from GNSS Reflectometry

Shuanggen Jin and Nasser Najibi
Shanghai Astronomical Observatory, Chinese Academy of Sciences, Shanghai 200030, China

Abstract— GNSS-R (Global Navigation Satellite System-Reflectometry) can remotely sense Earth's surface characteristics and retrieve geophysical parameters, e.g., snow depth and soil moisture. However the surface reflectivity interaction and scattering characteristics from GNSS signals are not clear. In this paper, we model the scattering properties and investigate the surface's reflectivity characteristics interacting with GPS L1 and L2 signals in order to retrieve multipath signals and precisely infer surface characteristics. Furthermore, the effects of snow accumulating and melting together with bare soil and fixed snow depth are studied by GNSS-R. A case study from GPS observations at BAKE site is also presented as well as discussed.

1. INTRODUCTION

The Earth's surface is very complex, particularly the cryosphere, including the frozen hydrosphere (sea ice and river ice) and snowy products (snow-covered surface, permafrost and icy frozen ground) [5]. These areas are normally located far from human inhabitations with very severe climatic conditions, which are difficultly measured their variations using traditional techniques [4]. Moreover, cryospheric variations significantly affect the energy and mass balance exchange between the Earth's surface and the atmosphere [9] as well as environment changes. For example, the melting ice sheets result in the sea level rise, which may unfortunately affect human living conditions and environment. Therefore, it is very necessary to monitor snow changes and investigate the physical processes of snowy surfaces by using possible remote sensing techniques.

Recently, Global Navigation Satellite System (GNSS) reflected signals can be used to remotely sense the Earth's surface [2, 5], such as soil moisture [7] and snow depth [1, 8]. To retrieve the surface properties from ground GNSS-reflected signals, the physical surface reflectivity of the scattered and reflected signals should be taken into account. Furthermore, the chemical surface characteristic for different reflectance polarizations and different grazing angles in interacting with the GNSS signals should be known. However, most past works were focusing on the capabilities and methods of geophysical parameters retrieval (e.g., soil and snow density models), while the interaction of GNSS reflected signals with the surface is not clear. In this paper, the Surface scattering characteristics and effects of snow accumulation and snow melting as well as bare soil and stable snow surface on GPS reflected signals are modeled and investigated using the multipath from free geometrical linear combinations of GPS observations in Northern Canada.

2. THEORY AND METHODOLOGY

Two types of polarized signals from GPS satellite and surfaces are acquired by ground GPS receiver: Right-Hand Circular Polarization (RHCP) and Left-Hand Circular Polarization (LHCP) (Fig. 1). The reflected surface's signals are not only LHCP, but in fact is a combination of RHCP and LHCP signals. Generally, the incident RHCP with the angles of less than the Brewster angle produces mainly a RHCP reflected wave, while the incident RHCP for the angles with greater than the Brewster angle produces a LHCP reflected wave. At the Brewster angle, the reflected signal is linearly polarized.

In order to remotely sense the snow surface characteristics using ground GPS receiver's observations, the physical geometry of GPS reflected signals and the characteristics of surface reflected signals are analyzed. The reflected signals from the ground GPS receiver are carried by a time delay when they arrive at the GPS receiver antenna, which will result in a phase shift on the received GPS signals by the antenna. The phase change $\delta\Phi$ of received signal from the reflected surface is related to the attenuation factor that depends on the reflected surface and the height of GPS antenna as well as the reflected surface characteristics [8]. There are several methods to get reflected signals of GPS observations (code pseudorange, carrier phase and Doppler). Here using the ionospheric free geometrical linear combination is more practical due to eliminating the most effects of the ionosphere on the GPS signals. The GPS ionospheric free geometrical linear combination of carrier

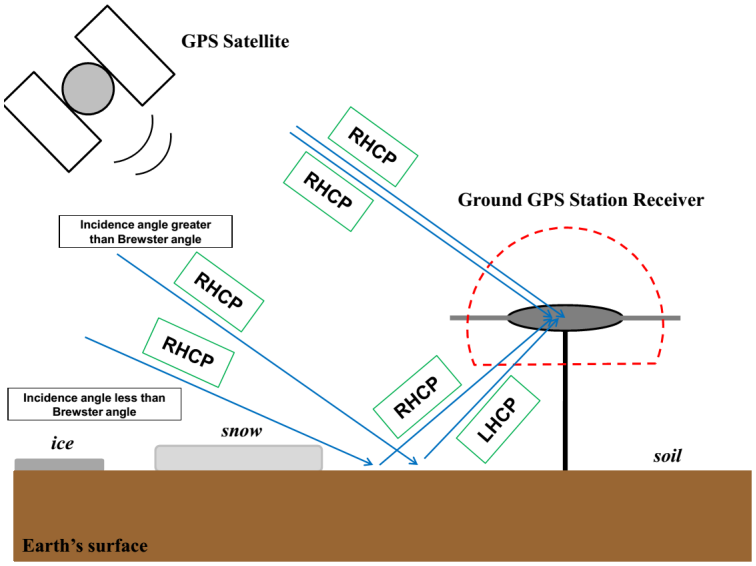

Figure 1: Surface reflectance process in GPS L1 and L2 signals for Right-Hand Circular Polarization (RHCP) and Left-Hand Circular Polarization (LHCP) components and the Brewster angle.

phase signals is expressed as [6]:

$$\text{GPS-L4} = \Phi_{IF} = -\frac{f_1^2}{f_1^2 - f_2^2} \times \Phi_1 + \frac{f_2^2}{f_1^2 - f_2^2} \times \Phi_2 \tag{1}$$

where Φ_{IF} is ionosphere free linear combination (GPS-L4), f_1 and f_2 denote the GPS frequencies ($f_1 = 1575.42\,\text{MHz}$, $f_2 = 1227.60\,\text{MHz}$), and Φ_1 and Φ_2 are the GPS dual-frequency carrier phase signals. Although the geometric information has been cancelled out by taking the difference, Φ_{IF} is geometry-free as well. The variability of reflected phase shift with respect to GPS antenna height variations (H) depends mostly on GPS satellite elevation angle (ε) and H contributes significantly to the physical reflectivity of ground GPS receiver environments The variability of GPS-L4 reflects these changes. In the following section, forward modeling of GPS reflected signals and GPS-L4 as well as their changes from real GPS observations for different snow depth changes scenarios will be

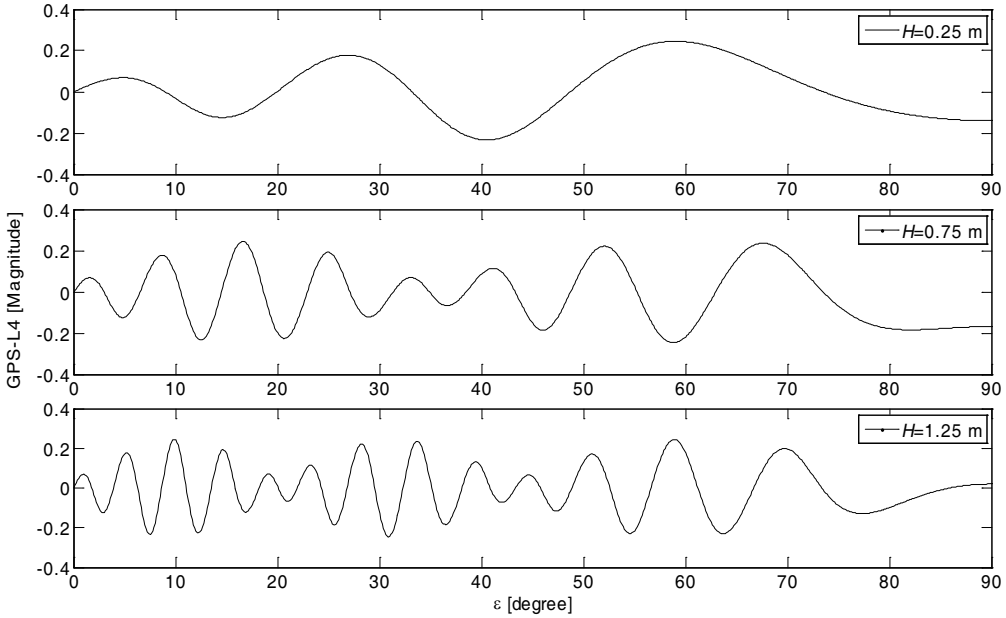

Figure 2: GPS-L4 values for snow surface ($H = 0.25\,\text{m}$), snow depth changes ($H = 0.75\,\text{m}$) and stable snow on the ground ($H = 1.25\,\text{m}$) with satellite elevation angles (ε) (GPS antenna length is assumed to be 1.5 m).

discussed in details.

3. RESULTS AND DISCUSSIONS

The effects of snow accumulation and melting and also fixed Earth surface (bare soil and stable snow surface) on GPS reflected signals are presented in the following. In general, the snow accumulation and snow melting are causing changes of the GPS antenna height with increasing or decreasing. The GPS antenna length is a constant and therefore depends on the existed physical environment around ground GPS receiver.

3.1. Variability of GPS-L4 Values Caused by Snow Depth Changes

The GPS-L4 values in different satellite elevation angles for snow depth variations (e.g., $H = 0.75\,\mathrm{m}$), stable snow on the ground and etc. are modeled as Fig. 2. It is clearly seen that the frequency of GPS-L4 values is increasing while the physical conditions around the GPS receiver is changing through the increase in the GPS antenna height. The amplitude of GPS-L4 value is

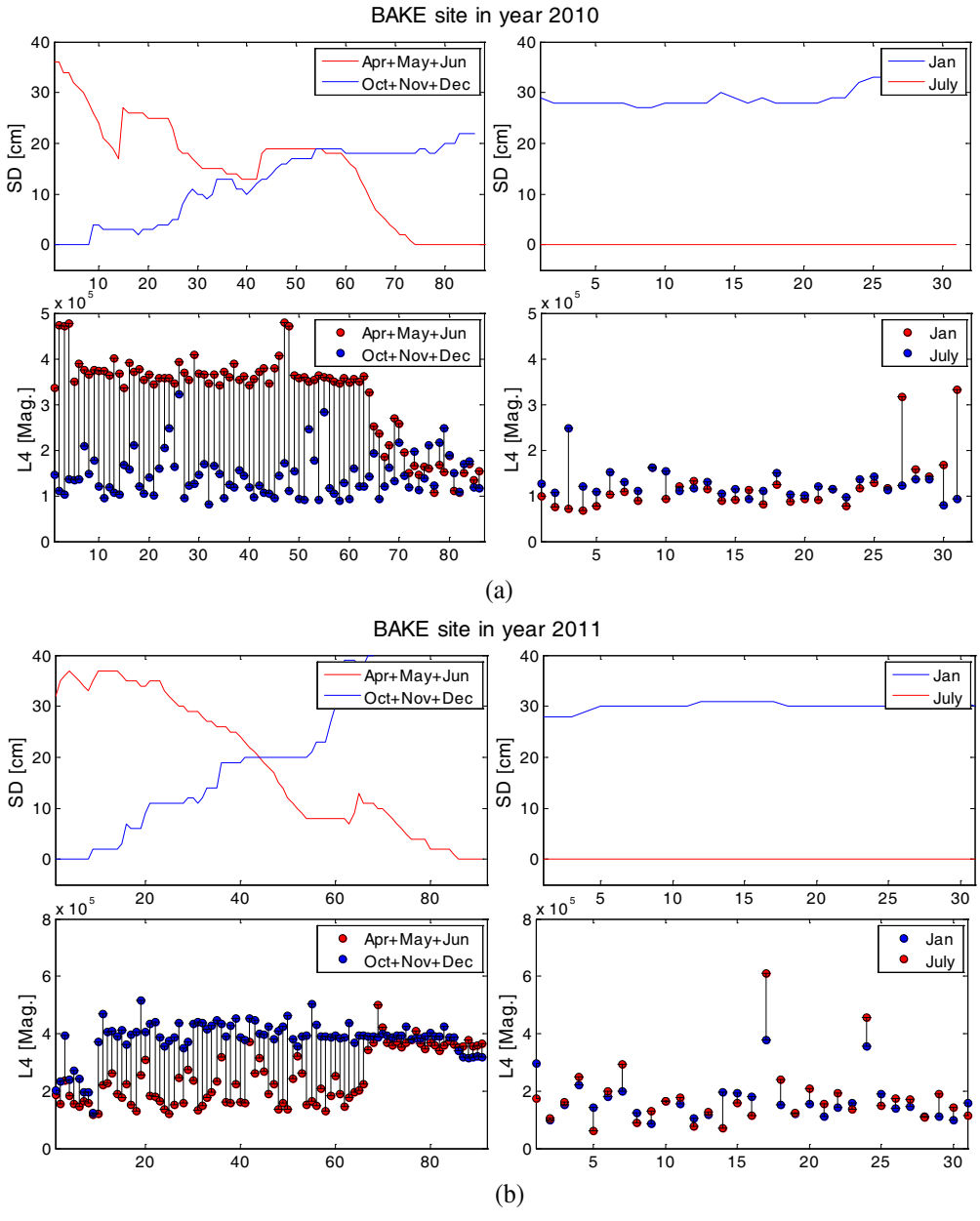

Figure 3: Variability of snow depth (SD) and GPS-L4 values for snow accumulation season (October, November and December) and snow melting season (April, May and June) and stable snow on the ground (January) and stable bare soil (July) at BAKE site in (a) 2010 and (b) 2011.

stable approximately, but is very sensitive to the caused changes on initial situation around GPS receiver. Furthermore, the GPS-L4's amplitude in each case is greater for those higher satellite elevation angles than low ones.

3.2. Changes of Snow States from GPS Observations

The average daily GPS-L4 values based on Eq. (1) for all possible GPS L1 and L2 carrier phase observables are computed for years of 2010 and 2011 at BAKE site in Northern Canada. The daily snow depth (SD) values are from the meteorological center at co-located BAKE GPS station. Fig. 3 shows the variability of SD and GPS-L4 for snow accumulation season (October, November and December) and snow melting season (April, May and June) and fixed snow on the ground (January) and bare soil (July) at BAKE site in 2010 and 2011. The GPS-L4 values as GPS reflected signals from ground GPS receiver show the changes in the GPS antenna height, reflecting the snow accumulating and melting.

4. CONCLUSIONS

The effects of physical reflectivity variability on the ground GPS reflected signals under conditions of snow accumulation and melting as well as bare soil and stable snow are presented and discussed, including the changes in reflected GPS signal phase shift and its variability as well as GPS-L4 values. The modeled snow depth changes are showing the capability of GPS reflected signals to sense the physical variations around the ground GPS receivers. The effect of simulated snow accumulation and snow melting scenarios on the reflected GPS signal phase shift is stable with similar pattern. GPS multipath by L4 reflects the physical situations around the ground GPS receiver and therefore the snow depth changes around the GPS receiver will cause changes of GPS-L4 values. Daily GPS-L4 observations are studied and validated at BAKE GPS station in Northern Canada for snow accumulation months (October, November, December) and snow melting months (March/April, May, June) in 2010 and 2012. The results show that the difference between snow accumulation and melting time series is constant approximately and depends on the caused changes into physical conditions around GPS receiver, while there is a difference in the amplitude of the accumulating and melting. This study presents the effects of snow depth changes on the GPS reflected signals. However, other more factors should be taken into account related to the surface characteristics polarization. Therefore, it needs to further study with considering varied types of snow for more cases in the future.

ACKNOWLEDGMENT

This work was supported by the Main Direction Project of Chinese Academy of Sciences (Grant No. KJCX2-EW-T03), Shanghai Science and Technology Commission Project (Grant No. 12DZ2273 300) and National Natural Science Foundation of China (NSFC) Project (Grant Nos. 11173050 and 11373059). We thank the IGS for providing the GPS data.

REFERENCES

1. Jacobson, M. D., "Inferring snow water equivalent for a snow-covered ground reflector using GPS multipath signals," *Remote Sensing*, Vol. 2, No. 10, 2426–2441, 2010.
2. Jin, S. G. and A. Komjathy, "GNSS reflectometry and remote sensing: New objectives and results," *Adv. Space Res.*, Vol. 46, No. 2, 111–117, 2010, doi:10.1016/j.asr.2010.01.014.
3. Jin, S. G., G. P. Feng, and S. Gleason, "Remote sensing using GNSS signals: Current status and future directions," *Adv. Space Res.*, Vol. 47, No. 10, 1645–1653, 2011, doi:10.1016/j.asr.2011.01.036.
4. Jin, S. G. and G. P. Feng, "Large-scale variations of global groundwater from satellite gravimetry and hydrological models, 2002–2012," *Global Planet. Change*, Vol. 106, 20–30, 2013, doi:10.1016/j.gloplacha.2013.02.008.
5. Jin, S. G., T. van Dam, and S. Wdowinski, "Observing and understanding the Earth system variations from space geodesy," *J. Geodyn.*, Vol. 72, 1–10, 2013, doi:10.1016/j.jog.2013.08.001.
6. Jin, S. G. and N. Najibi, "Sensing snow height and surface temperature variations in greenland from GPS reflected signals," *Adv. Space Res.*, Vol. 53, No. 11, 1623–1633, 2014, doi:10.1016/j.asr.2014.03.005.
7. Larson, K. M., E. E. Small, E. Gutmann, A. Bilich, J. Braun, and V. Zavorotny, "Use of GPS receivers as a soil moisture network for water cycle studies," *Geophys. Res. Lett.*, Vol. 35, L24405, 2008, doi:10.1029/2008GL036013.

8. Najibi, N. and S. G. Jin, "Physical reflectivity and polarization characteristics for snow and ice-covered surfaces interacting with GPS signals," *Remote Sens.*, Vol. 5, No. 8, 4006–4030, 2013, doi:10.3390/rs5084006.
9. Warner, T. A., G. M. Foody, and D. Nellis, *The SAGE Handbook of Remote Sensing*, 397–411, SAGE Publications, 2009.

A Novel Keystone Transform Based Algorithm for Moving Target Imaging with Radon Transform and Fractional Fourier Transform Involved

Jiefang Yang[1, 2] **and Yunhua Zhang**[1]

[1]The Key Laboratory of Microwave Remote Sensing, Chinese Academy of Sciences, China
[2]University of Chinese Academy of Sciences, China

Abstract— In this paper, we propose a novel algorithm for SAR ground moving target imaging (SAR/GMTI) and motion parameters estimation (MPE) in consideration of Doppler ambiguity. This algorithm involves the keystone transform (KT) and the modified second-order keystone transform (MSKT), Radon transform (RT) and Fractional Fourier transform (FrFT). With this algorithm, the fast moving targets can be focused well and the motion parameters can be estimated accurately even in situation of Doppler ambiguity. The effectiveness of the proposed algorithm is demonstrated by processing the simulated airborne SAR data.

1. INTRODUCTION

Synthetic aperture radar ground moving target imaging (SAR/GMTI) is widely used in both civilian and military applications. There are various algorithms proposed for dealing with moving targets [1–3]. The keystone transform (KT) [1] and the second-order KT (SKT) [3] can be used to correct the RCM of moving targets without any prior knowledge required about their motion parameters. However, both KT and SKT suffer from the Doppler ambiguity problem. In real-world situations, Doppler ambiguity usually occurs for SAR imaging of fast moving target due to the limited PRF. In this paper, we propose an algorithm based on KT and Modified SKT (MSKT) for SAR/GMTI and MPE in Doppler ambiguity situation. This algorithm involves Radon transform (RT) [4] and Fractional Fourier transform (FrFT) [2] besides KT and MSKT. With this algorithm, the fast moving targets can be focused well and the motion parameters can be estimated accurately. The effectiveness of the proposed algorithm is demonstrated by processing the simulated airborne SAR data.

The remainder of the paper is organized as follows. In Section 2, we introduce the imaging model of an airborne SAR observing moving target and deduce the signal expression after range compression. In Section 3, we describe the proposed algorithm for moving target imaging and MPE. In Section 4, the simulated data is processed to show the effectiveness of the proposed algorithm. Finally, conclusion is drawn in Section 5.

2. THE IMAGING MODEL AND SPECTRUM ANALYSIS

The geometry of a broadside SAR observing a moving target is shown in Fig. 1. We use the LFM signal as the transmitted signal, so the baseband echo can be expressed as [5]:

$$s(\tau,\ \eta) = \sigma \mathrm{rect}\left[\frac{\tau - 2R(\eta)/c}{T_p}\right] \mathrm{rect}\left(\frac{\eta}{T_a}\right) \exp\left\{-j\frac{4\pi f_c}{c}R(\eta) - j\pi K\left(\tau - \frac{2R(\eta)}{c}\right)^2\right\} \quad (1)$$

where $R(\eta)$ denotes the instantaneous slant range between radar and target, A denotes an arbitrary complex constant, τ and η represent range-time and azimuth-time, respectively. T_p, f_c and K represent the time duration, carrier frequency and slope of the transmitted LFM signal, respectively. T_a denotes the target exposure time in azimuth.

According to Fig. 1, $R(\eta)$ can be expressed as follows:

$$\begin{aligned} R(\eta) =& \sqrt{(y_0 + v_y\eta)^2 + (V - v_x)^2\eta^2 + H_0^2} \approx R_0 + \alpha\eta + \beta\eta^2 + \chi\eta^3 \\ \text{and} \quad & \begin{cases} R_0 = \sqrt{y_0^2 + H_0^2}, \quad \alpha = v_y \sin\vartheta \\ \beta = \frac{(V-v_x)^2 + v_y^2\cos^2\vartheta}{2R_0}, \quad \chi = -\frac{v_y \sin\vartheta \cdot \left[(V-v_x)^2 + v_y^2\cos^2\vartheta\right]}{2R_0^2} \end{cases} \end{aligned} \quad (2)$$

where, V and H_0 denote the velocity and height of the radar platform, v_x and v_y denote the along-track velocity and across-track velocity of the target, respectively, y_0 denotes the ground range of

the moving target perpendicular to projection of the flight track, ϑ denotes the incident angle of SAR antenna, and $\sin\vartheta = y_0/R_0$.

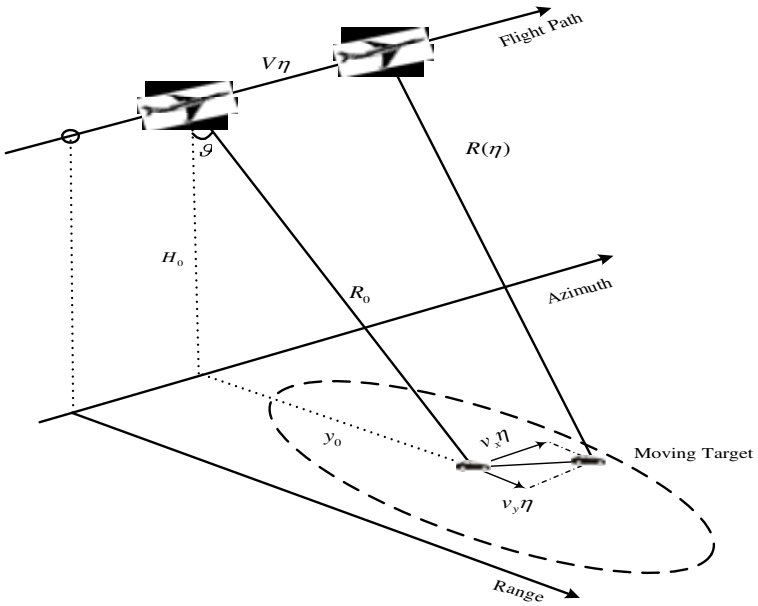

Figure 1: The geometry of SAR observing a moving target.

Suppose $\mu = f_\tau/f_c$ ($\mu \ll 1$, since $f_\tau \ll f_c$ is valid for general SAR), the output of range matched filtering in (f_τ, η) domain is expressed as:

$$S(f_\tau,\eta) = G(f_\tau,\eta)\exp\left\{-j\frac{4\pi f_c}{c}(1+\mu)\alpha\eta\right\}\exp\left\{-j\frac{4\pi f_c}{c}(1+\mu)\beta\eta^2\right\}\exp\left\{-j\frac{4\pi f_c}{c}(1+\mu)\chi\eta^3\right\} \tag{3}$$

where $G(f_\tau,\eta) = \sigma\text{rect}\left(\frac{f_\tau}{KT_p}\right)\text{rect}\left(\frac{\eta}{T_a}\right)\exp\left\{-j\frac{4\pi f_c}{c}(1+\mu)R_0\right\}$.

Suppose $\alpha = \alpha_0 + n\alpha_{prf}$, α_0 corresponds to the ambiguous Doppler centroid, n denotes the PRF fold factor and $\alpha_{prf} = c\text{PRF}/(2f_c)$, then the second term in (3) can be expressed as following:

$$\exp\left\{-j\frac{4\pi f_c}{c}(1+\mu)\alpha\eta\right\} = \exp\left\{-j\frac{4\pi f_c}{c}(1+\mu)\alpha_0\eta\right\}\exp\left\{-j\frac{4\pi f_c}{c}\mu n\cdot\alpha_{prf}\eta\right\} \tag{4}$$

In (4) we omit the phase term $\exp\left\{-j\frac{4\pi f_c}{c}n\alpha_{prf}\eta\right\} = \exp\{-j2\pi n\text{PRF}\eta\} = 1$.

3. THE PROPOSED ALGORITHM

In this section, we will present the proposed algorithm for moving target imaging and MPE. We first conduct KT on (3) to correct the range walk induced by the ambiguous Doppler centroid. KT is substituting the azimuth-time η with the expression $\eta = \left(\frac{f_c}{f_c+f_\tau}\right)\xi = \frac{1}{1+\mu}\xi$ [1]. After KT, the signal in (3) is changed to:

$$\begin{aligned} S_1(f_\tau,\xi) \;=\; & G(f_\tau,\xi)\exp\left\{-j\frac{4\pi f_c}{c}\alpha_0\xi\right\}\exp\left\{-j\frac{4\pi f_c}{c}\frac{\mu}{1+\mu}n\cdot\alpha_{prf}\xi\right\} \\ & \exp\left\{-j\frac{4\pi f_c}{c}\frac{\beta}{1+\mu}\xi^2\right\}\exp\left\{-j\frac{4\pi f_c}{c}\frac{\chi}{(1+\mu)^2}\xi^3\right\} \end{aligned} \tag{5}$$

Next, we will use (6) in the following to correct the range walk induced by the integer PRF ambiguity, and estimate n as done in [6], we will not repeat here.

$$H_1(f_\tau,\xi) = \exp\left(j\frac{4\pi f_c}{c}\frac{\mu}{1+\mu}n\cdot\alpha_{prf}\xi\right) = \exp\left(j2\pi\frac{f_\tau}{f_c+f_\tau}n\cdot PRF\xi\right) \tag{6}$$

By multiplying (5) with (6), the signal is expressed as following:

$$S_2(f_\tau,\xi)=G(f_\tau,\xi)\exp\left\{-j\frac{4\pi f_c}{c}\alpha_0\xi\right\}\exp\left\{-j\frac{4\pi f_c}{c}\frac{\beta}{1+\mu}\xi^2\right\}\exp\left\{-j\frac{4\pi f_c}{c}\frac{\chi}{(1+\mu)^2}\xi^3\right\} \quad (7)$$

In the following, let us conduct MSKT on (7) for range curvature correction, which is substituting ξ with the expression $\xi=\sqrt{1+\mu}\varsigma=\sqrt{1+\frac{f_\tau}{f_c}}\varsigma=\sqrt{\frac{f_c+f_\tau}{f_c}}\varsigma$. After applying the MSKT, the signal becomes as,

$$S_3(f_\tau,\varsigma)=G(f_\tau,\varsigma)\exp\left\{-j\frac{4\pi}{c}\left(f_c+\frac{f_\tau}{2}\right)\alpha_0\varsigma\right\}\exp\left\{-j\frac{4\pi f_c}{c}\beta\varsigma^2\right\}\exp\left\{-j\frac{4\pi}{c}\left(f_c-\frac{f_\tau}{2}\right)\chi\varsigma^3\right\} \quad (8)$$

where the approximations $\sqrt{1+\mu}\approx 1+\mu/2$ and $1/\sqrt{1+\mu}\approx 1-\mu/2$ are applied.

After transforming (8) to (τ,ς) domain through range IFFT, the signal can be expressed as following:

$$\begin{aligned}s_3(\tau,\varsigma) &= A\text{rect}\left(\frac{\varsigma}{T_a}\right)\text{sinc}\left(KT_p\left(\tau-\frac{2R_0}{c}-\frac{\alpha_0}{c}\varsigma+\frac{\chi}{c}\varsigma^3\right)\right)\\ &\quad\exp\left\{-j\frac{4\pi f_c}{c}\alpha_0\varsigma\right\}\exp\left\{-j\frac{4\pi f_c}{c}\beta\varsigma^2\right\}\exp\left\{-j\frac{4\pi f_c}{c}\chi\varsigma^3\right\}\end{aligned} \quad (9)$$

Since $|\chi|\ll|\alpha_0|$ is usually valid, the target trajectory can be treated as an inclined line with a fix slope along the azimuth dimension. We can estimate the slope using RT, and thus obtain the estimation of α_0, denoted by α_0^{est} [4]. At this time, we can obtain the estimation of α as $\alpha^{est}=\alpha_0^{est}+n\cdot\alpha_{prf}$, and construct the correction function for range walk and Doppler shift as following:

$$H_2(f_\tau,\varsigma)=\exp\left\{j\frac{4\pi f_c}{c}\alpha_0^{est}\varsigma+j\frac{2\pi f_\tau}{c}\alpha_0^{est}\varsigma\right\} \quad (10)$$

Let us multiply (8) with (10) and do range IFFT, the signal in (τ,ς) domain is expressed as,

$$s_4(\tau,\varsigma)=A\text{rect}\left(\frac{\varsigma}{T_a}\right)\text{sinc}\left(KT_p\left(\tau-\frac{2R_0}{c}\right)\right)\exp\left\{-j\frac{4\pi f_c}{c}\beta\varsigma^2\right\}\exp\left\{-j\frac{4\pi f_c}{c}\chi\varsigma^3\right\} \quad (11)$$

Eqaution (11) shows that, the energy of the moving target is concentrated in a single range cell. Here, we can extract the moving target azimuthal signal and estimate the Doppler rate through FrFT [2], denoted by K_d^{est}, and then we can obtain the estimation of β as $\beta^{est}=-cK_d^{est}/4f_c$. We should indicate that the third-order phase term is treated as clutter in the implementation of FrFT. In the following, we can calculate the motion parameters as,

$$v_y^{est}=\alpha^{est}/\sin\vartheta,\quad\text{and}\quad v_x^{est}=V-\sqrt{2R_0\beta^{est}-\left(v_y^{est}\cos\vartheta\right)^2} \quad (12)$$

At present, we can construct the azimuth matched filter function $H_a(f_\xi)$ and the third-order phase compensation function $H_4(f_\tau,\xi)$ as follows,

$$H_a(f_\xi)=\exp\left\{j\pi\frac{cf_\xi^2}{4f_c\beta^{est}}\right\},\quad\text{and}\quad H_4(f_\tau,\xi)=\exp\left\{j\frac{4\pi f_c}{c}\left(1-\frac{f_\tau}{2f_c}\right)\chi^{est}\xi^3\right\} \quad (13)$$

After azimuth matched filtering and compensation of the third-order phase to (11), the final image of the moving target in (τ,ξ) domain can be obtained as following:

$$s_{ac}(\tau,\xi)=A\text{sinc}\left[KT_p\left(\tau-\frac{2R_0}{c}\right)\right]\cdot\text{sinc}\left(\frac{4\beta^{est}}{\lambda}T_a\xi\right) \quad (14)$$

4. SIMULATION

In this section, we will conduct simulations to validate the proposed algorithm. In real situations, there exist nonlinear motions for the SAR platform. However, these motion errors can be well compensated by the existing methods [7]. After the motion compensation, the proposed algorithm can be used to deal with the moving targets. Therefore, the motion errors of the SAR platform are not taken into consideration in this simulation. The simulation system parameters are listed in Table 1. There are three moving targets in the scene, T_1 is a slowly moving target without inducing Doppler ambiguity, while T_2 and T_3 are fast moving targets with Doppler ambiguity induced. The true motion parameters of the targets and the estimated motion parameters with the proposed algorithm are listed in Table 2, it is clear that our algorithm can achieve accurate MPE. Fig. 2

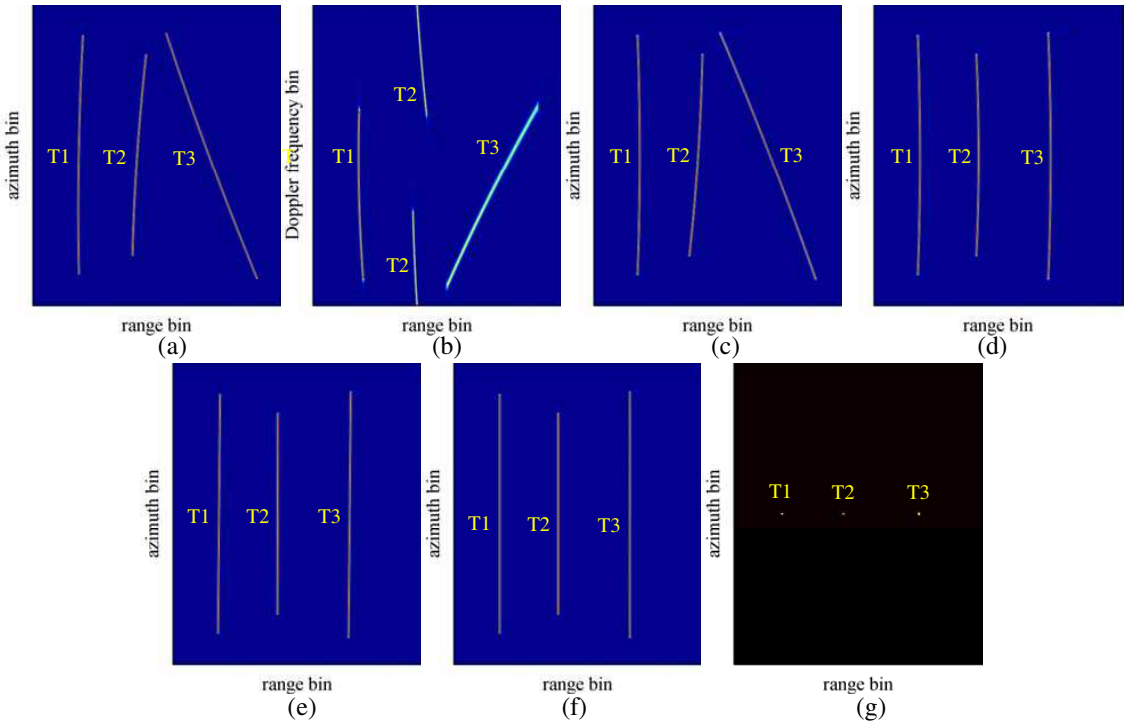

Figure 2: The procedure of the proposed algorithm. (a) The target trajectories after range compression, which shows that the range walk and range curvature for the three targets are different. (b) The Doppler spectrums after range compression, the spectrum of T_2 is split into two parts. (c) The result of KT, which shows that the range walk of T_1 is corrected, while the range walks of T_2 and T_3 still exist due to the integer PRF ambiguity. (d) The result after integer PRF ambiguity compensated for T_2 and T_3, which shows that there are only range curvatures left. (e) The result of applying MSKT, which shows that the range curvatures for each target are corrected. (f) The result of range walks correction after using RT to estimate the slope, which shows that the energy of each target is concentrated in a corresponding range cell. (g) The final focused image after using FrFT to estimate the Doppler rate and then having the azimuthal signals compressed.

Table 1: The simulation system parameters.

carrier frequency f_c	bandwidth B	pulse duration T_p	range sampling rate F_s	incident angle ϑ
14.0 GHz	200 MHz	5 us	250 MHz	45°
azimuth beamwidth	PRF	platform velocity V	platform height H_0	
3°	1000	120m/s	5000m	

Table 2: The simulated targets motion parameters.

Targets	R_0(m)	v_y(m/s)	v_y^{est}(m/s)	Relative error	v_x(m/s)	v_x^{est}(m/s)	Relative error
T_1	7007	2	1.99	0.5%	3	2.97	1%
T_2	7071	8	8.00	0	−20	−19.98	0.1%
T_3	7149	−43	−42.99	0.02%	4	3.60	10%

presents the result of each step of the proposed algorithm until the final image is obtained, obviously, they are very well focused, i.e., the effectiveness of the proposed algorithm is demonstrated.

5. CONCLUSION

In this paper, we propose an algorithm for SAR/GMTI and MPE. In this algorithm, the KT, the MSKT, the RT and the FrFT are utilized. With this algorithm, the fast moving targets can be well focused and their motion parameters can be estimated accurately even with the Doppler ambiguity involved. The effectiveness of the proposed algorithm is validated by processing the simulated airborne SAR data.

REFERENCES

1. Perry, R. P., R. C. DiPietro, and R. L. Fante, "SAR imaging of moving targets," *IEEE Transactions on Aerospace and Electronic Systems*, Vol. 35, No. 1, 188–200, 1999.
2. Sun, H., G. S. Liu, H. Gu, and W. M. Su, "Application of the fractional Fourier transform to moving target detection in airborne SAR," *IEEE Transactions on Aerospace and Electronic Systems*, Vol. 38, No. 4, 1416–1424, 2002.
3. Zhou, F., R. Wu, M. Xing, and Z. Bao, "Approach for single channel SAR ground moving target imaging and motion parameter estimation," *IET Radar Sonar and Navigation*, Vol. 1, No. 1, 59–66, 2007.
4. Warrick, A. L. and P. A. Delaney, "Detection of linear features using a localized radon transform," *Conference Record of the Thirtieth Asilomar Conference on Signals, Systems and Computers*, 1245–1249, 1996.
5. Cumming, I. G. and F. H. Wong, *Digital Signal Processing of Synthetic Aperture Radar Data: Algorithms and Implementation*, Artech House Norwood, 2004.
6. Su, J., M. Xing, G. Wang, and Z. Bao, "High-speed multi-target detection with narrowband radar," *IET Radar Sonar and Navigation*, Vol. 4, No. 4, 595–603, 2010.
7. Carrar, W. G., R. S. Goodman, and R. M. Majewski, *Spotlight Synthetic Aperture Radar-signal Processing Algorithm*, Artech House, Norwood, MA, 1995.

Why Optical Images are Easier to Understand Than Radar Images? — From the Electromagnetic Scattering and Signal Point of View

Yunhua Zhang and Jingshan Jiang
The Key Laboratory of Microwave Remote Sensing
Center for Space Science and Applied Research, Chinese Academy of Sciences
No. 1 Nanertiao, Zhongguancun, Haidian, Beijing 100190, China

Abstract— As the bandwidth of SAR/ISAR system continuously increases as well as the synthetic aperture techniques develop, the spatial resolution of radar image is higher and higher. However, the high resolution of radar image does not mean the resolving ability for targets is high. We may have the same experience that the optical image is much easy to understand than radar image even if it has less resolution. A simple and frank explanation is due to the wavelengths of optical waves are much shorter than that of microwaves at which radars usually work, e.g., in the order of 10^{-5}–10^{-4}. Are there any the deep reasons for this? We will illustrate the inherent reasons in this paper from the aspects of imaging geometry and principle, electromagnetic scattering, signal characteristics, and so on.

1. INTRODUCTION

High spatial resolution radars and optical cameras are two major kinds of sensors for civilian earth observation, and military applications. Their images are quite different from each other and radar images are usually much more difficult to understand [1–3]. This paper will discuss about this issue and show the reasons.

We know that the human eye's vision system is similar to a camera, or in another words, the human eye is indeed a camera. The basic imaging principle of optical camera is "small-hole" imaging, it gets the two dimensional resolutions about the target through angular discrimination, but for SAR/ISARs, they get the range resolution by discriminating the arrived time from target, which is proportional to the signal bandwidth, and thus is inversely proportional to the time duration of compressed pulse signal, while get the azimuthal resolution through aperture synthesis, which is inversely proportional to the coherent integration time. So radar images have unavoidable and severe geometric distortion compared with optical images, e.g., layover and foreshorten, which makes the radar images more difficult to read.

For ordinary optical camera, the signal (light) comes from the sun or other artificial sources, it is wideband, continuous, random and incoherent. When imaging, the signal interacts with the target, where reflections and scattering occur. Due to the short wavelength, which is in the order of several hundreds of nanometers, the scattering exhibits diffusion characteristics and is localized for almost all natural or man-made targets, i.e., the scattered signals from every part (structure) of the target go through the lens and is sensed by different part of CCD matrix to form a pixel. The pixel is formed by incoherently summing the single scattering and multi-scattering signals from the same part of the target, so there is only additive noise, at the same time the scattering center (referred to as the pixel) is very stable and independent on the direction of incident light if the looking direction is fixed. But for SAR/ISAR, the transmitted signals and the scattered signals are both coherent, and the image is reconstructed by coherent processing the echoes, where the pixel position is not stable but dependent on the direction of incident wave, i.e., one may get different radar images for the same target even the looking direction is fixed but the incidences are different. The role of multiple scattering effect is very useful for camera in some degree for increasing the randomness of incident light, so make the image looks more uniform and smooth, but for radar, it is very harmful because it leads to the scattering centers deviated from their geometric position or induces ghost scattering centers. The noise in SAR/ISAR images is composition of additive and multiplicative noises, so it is very hard to remove. For camera, the signals come from the surface scattering of the target, but for radars, the signals come from both the surface scattering and the volume scattering for general nonmetal target, and the volume scattering makes the scattering centers more complicated.

As for the signal point of view, for camera, the light waves are continuous, non-coherent and are of one octave. But for SAR/ISAR, the signals are usually pulsed and coherent. So integration

time for optical image can be much longer than that of radar image, i.e., the signal to noise ratio (SNR) of optical image could be much higher than that of radar image.

Optical images and SAR images are presented and compared to illustrate the similarity and the difference between them.

2. COMPARISON OF IMAGING PRINCIPLES

Generally, SAR works on side-looking mode (the boresight is normal to the moving direction of SAR platform). It get the range resolution by compressing the echo pulse (usually LFM pulse, i.e., chirp signal is used) and the wider the bandwidth of the pulse the fine the range resolution, i.e., the closer the distance between two targets at which they can be resolved. Fig. 1 show the imaging geometries for SAR (range direction) and optical camera. As can be seen, the target A, B and C on the ground plane are transferred to A', B' and C' in the slant plane for SAR, while they are transferred to A'', B'' and C'' in the focal plane for camera. Obviously, the transformation from A, B and C to A', B' and C' are nonlinear and even becomes much complicated if A, B and C are of different height, but it is linear from A, B and C to A'', B'' and C'', and becomes less distorted if the targets are not of the same height.

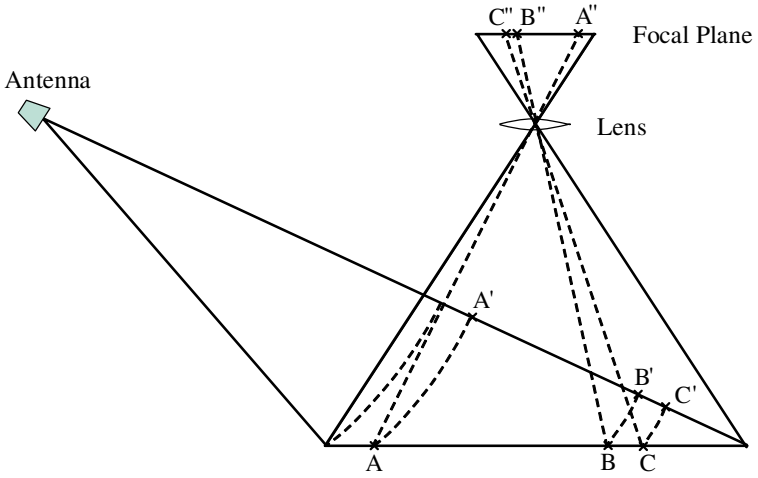

Figure 1: The geometries of SAR and optical camera.

For SAR, The resolvability of B and C depends on the signal bandwidth and the azimuth resolution and range resolution can be different; while for camera it depends on the aperture size of the lens and we do not need to distinguish the azimuth resolution and range resolution, we only need to concern about the angular resolution. When imaging, the SAR obtains the azimuth resolution and range resolution separately, while the camera obtains them simultaneously. It means the imaging process and the correction of geometrical distortion for optical camera is much simpler and easier than that of SAR. Fig. 2 shows the principle explanation for SAR obtaining the azimuthal resolution. Let us assume the SAR moves along a straight line and transmits pulses repeatedly with a period of T when moving, the Doppler frequency changes when the SAR moves at different position with the target still within the radar beam. The azimuth resolution of SAR depends on total change of the Doppler frequencies Δf_d as well as the speed of the SAR movement v.

Once again we should emphasize that the imaging principle of optical camera is exactly the same as human's eye system.

Figure 3 present the SAR image and the optical image (from Google map) of the same ground area, as can be clearly seen, the building marked in the box has been severely distorted in the SAR image due to layover effect.

3. COMPARISON OF EM SCATTERINGS

3.1. Single Scattering and Multiple Scattering

When electromagnetic (EM) waves are incident on a target, currents will be induced on the surface or inside the target, and then scattering electromagnetic waves resulted from the induced current will be generated and some of them back to the radar. The EM scattering problem from a target can be solved by solving the corresponding magnetic field integral equation (MFIE) (or electric

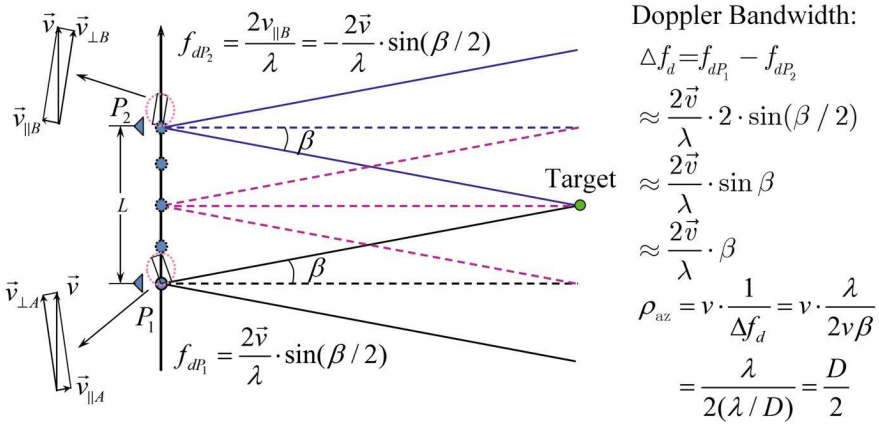

Figure 2: The principle explanation for SAR obtaining the azimuth resolution.

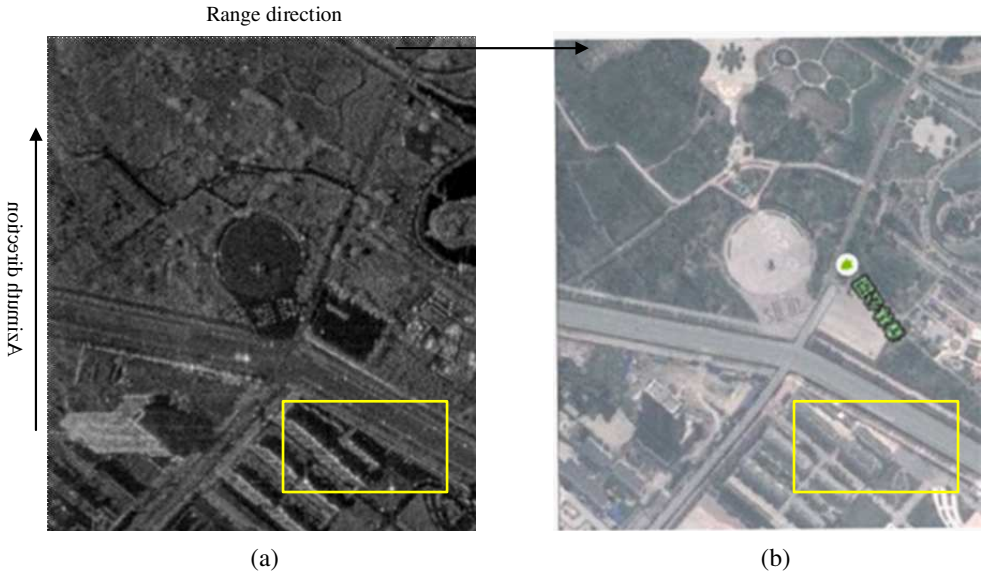

Figure 3: (a) The SAR image and (b) the optical image.

field integral equation, EFIE) as shown by (1). The total induced current by the incident field can be decomposed into two parts, one part is directly resulted from the incident field (1st scattering) as represented by the first part of (2), the other part is resulted from the interactions between different parts of the target (2nd or higher multiple scattering) as represented by the second part of (2).

$$2\hat{n} \times \mathbf{H}^i(\mathbf{r}) = \mathbf{J}_s(\mathbf{r}') - 2\hat{n} \times \int_S [\mathbf{J}_s(\mathbf{r}') \times g + \nabla' g] ds' \tag{1}$$

$$\mathbf{J}_s(\mathbf{r}') = 2\hat{n} \times \mathbf{H}^i(\mathbf{r}) + 2\hat{n} \times \int_S [\mathbf{J}_s(\mathbf{r}') \times g + \nabla' g] ds' \tag{2}$$

$$\mathbf{H}^{\mathrm{s}} = -\frac{jke^{-jkr}}{4\pi r} \int_{\mathrm{S}} \hat{s} \times \mathbf{J}_{\mathrm{s}}(\mathbf{r}') \mathrm{e}^{jk\mathbf{r}' \cdot (\hat{s} - \hat{i})} d\mathbf{r}' \tag{3}$$

The$g$in (1) and (2) is the Green's function. As we know the higher the frequency of the EM wave the weaker the multiple scattering of a target, i.e., the more the g as well as the interaction is localized and thus the stable the equivalent scattering centers may formed.

As for SAR imaging, the pixels are of range information relative to radar, and thus multiple scattering may easily lead to ghost target as shown in Fig. 4 (the dashed target). But for optical

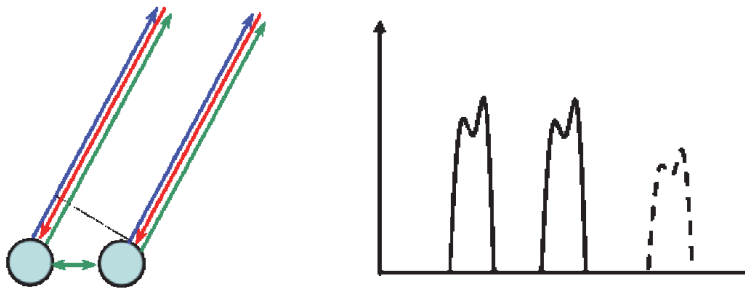

Figure 4: The effect of multiple scattering for radar: Ghost target.

camera the ghost target is relatively hard to produce by multiple scattering.

3.2. Coherent Scattering and Non-Coherent Scattering

As shown in Fig. 2, SAR utilizes the coherent echoes from the same target to form a synthesized large antenna aperture to realize high azimuth resolution, so, the echoes from infinitesimally sub-scattering centers within a resolution cell will superposed in complex domain (with both amplitude and phase taken into account), and thus multiplicative speckle noise (MSN [4, 5] will be generated. The existence of MSN preclude us from understanding SAR images especially for high-resolution SAR images, because they may destroy the inherent texture information [6] of the true target. We have a Chinese proverb to describe coherent scattering's role for SAR imaging: "succeeded because of Xiao He, defeated also because of Xiao He". One of the most difficult things for SAR image processing is just the MSN because we have to sacrifice the spatial resolution in order to get rid of it.

As for optical cameras, only thermal (additive) noise exists in the images because the scattering echoes from the target are non-coherent with each other and they are superposed in real domain. Up to now, there are plenty of effective methods proposed to denoise optical images. Besides, super-resolution algorithms work much better for optical imaging than for radar imaging. The reason is just due to the noise model for optical images is different from that for radar images.

3.3. Mirror Scattering and Diffuse Scattering

The wavelengths of optical waves (hereinafter visible optical waves are assumed) are usually $10^{-5} \sim 10^{-4}$ order of that of radar waves and the facet surfaces of natural targets as well as man-made target are rough for optical waves but they are smooth for radar waves. So diffuse scattering occurs for optical waves but mirror scattering occurs for radar waves. The diffuse scatterings are very helpful for forming localized equivalent scattering centers because no matter what direction of the incident waves, there always have comparable backscatterings with other directions, i.e., the impacting points of incident waves are always visible to the optical camera and thus can be imaged. In this way, the geometrical shape of a target can be very well recorded by an optical camera. As for radars, the mirror scatterings can result in the impacting points not visible to radar (no backscattering back to radar) and also make the scattering centers unstable (slight change of incident angles may lead to position change of scattering centers). Fig. 5 schematically shows how the scattering center changes as the incident wave changes.

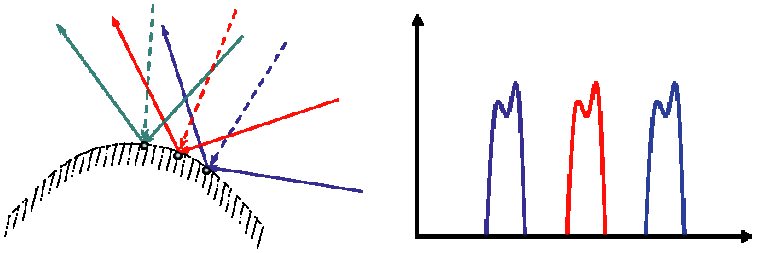

Figure 5: The position of scattering center changes as the incident direction changes.

3.4. Surface Scattering and Volume Scattering

We know that the penetration capability of EM waves into a target relates to the wavelengths, the longer the wavelength the stronger the penetration. Therefore, for general non-metal target, the optical waves mainly scatters on the surface, but for radar waves, not only surface scattering but also volume scattering exist. The volume scattering may further complicate the echoes and deteriorate the imaging process.

4. COMPARISON OF SIGNALS

As introduced above, for SAR imaging, each transmitted pulse has fixed phase relation with other transmitted pulses. The role of the signal bandwidth for SAR imaging is for obtaining high resolution, but it is for enriching the reflection of detailed structures for optical camera imaging. We all have the same experience that the pictures taken inside a room using the artificial light or the flasher, are always not as good as that taken outside under a good weather condition. The reason is that the natural light signal is of high quality compared with artificial lights: they are wideband (with wavelength ranges from 380 nm to 800 nm), continuous and non-coherent.

For SAR, the pulse duration, i.e., the integration time for radar receiver is usually in the order of several to tenths of microseconds, but for optical cameras the integration time is usually in the order of hundreds to thousands of microseconds. It is to say the integration time of an optical camera can be hundreds of times larger than that for a radar receiver. The longer the integration time for a receiver, the better the random noise can be reduced.

In this regard, radar signals always cannot be comparable to natural lights.

5. CONCLUSION

We have shown in this paper that the imaging geometry, the EM scattering and the signal characteristics are the three major reasons which make the SAR images more difficult to understand than optical images. We also mention that the similarity between human's eye system and optical camera is also a reason in this regard. It is also interesting to point out that optical camera is indeed a radar because it is also composed of antenna (lens), transmitter (non-cooperative, the sun or other artificial light source) and receiver (CCD), which are the typical parts of a radar. For SAR, the spatial resolution is usually decoupled into azimuthal resolution and range resolution, and they are decided respectively by the synthesized aperture size and the signal bandwidth, having nothing to do with the distance between the scene and the radar. As for optical camera, the spatial resolution is decided by the angular resolution which is inversely proportional to the lens size, the shortest wavelength of the light, and the distance between the observed scene and the camera, having nothing to do with the bandwidth of light.

REFERENCES

1. Sullivan, R. J., *Microwave Radar Imaging and Advanced Concepts*, Artech House, INC, 2000.
2. Skinner, J. P., et al., "Normalization and interpretation of radar images," *IEEE Transactions on Antennas and Propagation*, Vol. 46, No. 4, 502–506, 1998.
3. Brett, B., "Some issues in inverse synthetic aperture radar image reconstruction," *Inverse Problems*, Vol. 13, 571–584, 1997.
4. Oliver, C. and S. Quegan, *Understanding Synthetic Aperture Radar Images*, SciTech Publishing, INC, 2004.
5. Lee, J.-S. and E. Pottier, *Polarimetric Radar Imaging from Basics to Applications*, Chapter 4, CRC Press, 2009.
6. Ulaby, F. T., et al., "Texture information in SAR images," *IEEE Transactions on Geoscience and Remote Sensing*, Vol. 24, No. 2, 235–245, 1986.

Landslide Displacement Monitoring Using Multi-aperture InSAR and D-InSAR

Liming He[1], **Lixin Wu**[1, 2], **Shanjun Liu**[1], **and Chang Su**[1]

[1]Institute for Geo-informatics & Digital Mine Research
College of Resources and Civil Engineering, Northeastern University, Shenyang 110819, China
[2]IoT & Perception Mine Research Center
China University of Mining and Technology, Xuzhou 221116, China

Abstract— Landslides caused by open-pit mining are one of the most dangerous geological hazards in China. Displacement of landslides are different from the deformation of ground subsidence due to existing horizontal deformation and vertical deformation at the same time. In this paper, we extend the multi-aperture InSAR method to monitor large-scale horizontal deformation of landslides. And then, we integrate the multiple-aperture InSAR and traditional differential SAR interferometry (D-InSAR) to reveal deformation field distribution of landslides caused by open-pit mining. The results demonstrated that the proposed procedure is effective to monitor large-scale horizontal deformation and vertical deformation of landslides, especially for the north-south direction landslides.

1. INTRODUCTION

With the rapid exploitation and over utilization of mineral resources, the open-pit mines around the world have becoming bigger and deeper ever before. The largest open-pit mine in Asia is Fushun west open-pit mine, which located in Fushun city, Liaoning province, Northeast of China. At present, Fushun west open-pit mine has been the formation of 6,600 meters from east to west, 2,200 meters from north to south, with an average depth of about 420–520 meters, covering an area of about 10,870,000 square meters of open-pit mining. It has a long history of more than one hundred years and made important contributions to China's economic development. However, serious geological disasters, especially large-scale landslides, has become a direct threat to the residents and factories in Fushun city due to excessive and long-term coal mining. The direct economic loss has reached as much as 1.5 billion Yuan. Therefore, it is important to investigate the geological disaster situation, determine the location and size of landslides. Compared to traditional methods, for example leveling measurements and global positioning system (GPS) measurements, interferometric synthetic aperture radar (InSAR) has many advantages such as lager coverage and lower cost, and it can work in all-weather conditions to monitor surface deformation [1].

A special feature of landslides at Fushun west open-pit mine is that the main deformation occurred along the north-south direction. However, the conventional differential SAR interferometry (D-InSAR) technique can only measure one-dimensional (1-D) deformation along the line-of-sight (LOS) direction. It means that any component of motion orthogonal to the LOS cannot be detected. In the nearly north-south flight pattern of current commercial SAR satellites, the D-InSAR method are only sensitive to the deformation along the up-down and east-west direction [2]. Therefore, it is almost unable to measure the displacements occurring in the north-south direction at Fushun west open-pit mine with conventional interferometry.

To cope with the problem of deformation monitoring along the north-south direction, Michel et al. proposed a novel method utilizing radar amplitude information to measure azimuthal offsets [3]. However, this method involve sub-pixel correlation of the radar images, and are computationally expensive. Furthermore, the accuracy of the offset-tracking method, depending on the spatial resolution of the SAR data and the precision of the coregistration, is generally very low. In 2006, a significant improvement in measuring along-track deformation was made by Bechor and Zebker with a new approach: multiple-aperture InSAR (MAI) [4]. The MAI method is more accurate than the offset-tracking approach with less computation time, and it is easy to implement using conventional InSAR software. In 2009, Jung et al. further improved the accuracy of MAI method by introducing a step of baseline error correction [5].

In this paper, we aim to extend the MAI method to the large-scale landslides monitoring at Fushun west open-pit mine due to its main displacements along the north-south direction. By integrating multiple-aperture InSAR and traditional D-InSAR, we explore to reveal the 3-D deformation distribution of landslides caused by coal mining.

2. DATA AND METHODOLOGY

SAR data used in this study were acquired from the Phased Array type L-band Synthetic Aperture Radar (PALSAR) sensor onboard Advanced Land Observing Satellite (ALOS). The PALSAR sensor operated in L-band frequency (1.27 GHz), with a ground surface resolution about 7 m in both range and azimuth directions, and a swath width of 70 km. Table 1 lists the detailed information of the used SAR data. The two scenes from the ascending orbit are in fine beam single polarization (FBS, HH-polarization). The perpendicular baseline of the interferometric pair is 76 m and the temporal baseline is 1012 days.

Table 1: Summary of the used ALOS-PALSAR data.

No.	Acquisition Date	Track	Orbit Direction	Beam Mode	Polarization	Temporal baseline (day)	$B_\perp$ (m)
1	13 Apr. 2008	433	Ascending	FBS	HH	1012	76
2	20 Jan. 2011						

The MAI technique firstly divided a pair of full-aperture single-look complex (SLC) images into four sub-aperture SLC images via common band filtering method in the azimuthal direction. The azimuth common band filtering was conducted following Wegmüller et al. [6] in this study. Based on the two new forward-looking and backward-looking SLC pairs, we can produce one forward-looking interferogram and one backward-looking interferogram with the conventional D-InSAR method. And then, a complex-conjugate multiplication of the forward-looking interferogram Φ_f and backward-looking interferogram Φ_b produces the MAI interferogram Φ_{MAI}:

$$\Phi_{MAI} = \Phi_f - \Phi_b \tag{1}$$

The azimuthal displacement can be calculated from the MAI interferometric phase [4]:

$$x_{az} = \frac{l}{4\pi n}\Phi_{MAI} \tag{2}$$

where x_{az} is the surface deformation in the azimuthal direction, l represents the effective antenna length, n represents the fraction of the full-aperture width.

According to the principle of MAI, the forward-looking and backward-looking interferometric phases are differenced, this process reduces some common errors from topographic and tropospheric sources [4]. But residual topographic and flat-earth errors caused by the small difference between the perpendicular baselines of the forward-looking and backward-looking SAR pairs, should be removed before producing azimuth deformation. In this study, the polynomial models were used to simulate and eliminate both phase residuals following the method described by Jung et al. [5].

3. RESULTS

3.1. LOS Deformation from D-InSAR

The two-pass D-InSAR method was utilized to obtain the LOS displacements firstly. As part of the D-InSAR processing, an external digital elevation model (DEM) data from Shuttle Radar Topography Mission-3 (SRTM-3) was used to remove topographic component of interferometric phase. Before unwrapping the phase, it is necessary to reduce phase noise and improve fringe visibility of interferometric phase. For this purpose, an adaptive interferogram filtering algorithm [7] was applied by setting a large rectangular patch sizes and high values of exponential power spectrum filter parameter. In this study, we found that the patch size of 256×256 and the filter parameter of 1.0 improved fringe visibility significantly. Furthermore, to suppress the speckle noise, the interferogram was looked down in range and azimuth by 4 and 6, respectively. After that, the interferogram was unwrapped using the minimum cost flow (MCF) algorithm [8]. The geocoded LOS displacement in WGS84 coordinate system is shown in Figure 1. It can be seen that landslides occurred at the edge of the huge open-pit with large area in the north and south of Fushun west open-pit mine. The largest vertical displacement is estimated by Figure 1 up to 1.10 m.

3.2. Azimuthal Deformation from MAI

The MAI data processing was applied to obtain the azimuthal deformation in this section. Firstly, the forward-looking and backward-looking SLC scenes were produced using common band filtering method. The same processing as D-InSAR described in Section 3.1 are then used to generate

the forward-looking and backward-looking interferograms, however, the unwrapping step can be ignored. Then, conjugate multiplication between the forward-looking and backward-looking interferograms was conducted to obtain the final MAI interferogram. Finally, the polynomial model was used to eliminate the flat-earth and topographic phase residuals. Because the effective antenna length of ALOS-PALSAR is 8.9 m, therefore, a single phase fringe in the MAI interferogram represents 8.9 m surface displacement in the along-track direction. Figure 2 shows that the azimuthal displacement of Fushun west open-pit mine in WGS84 coordinate system. Compared with Figure 1, we can know that the region of horizontal deformation is similar to the area of vertical displacement, and the motion is direct to the bottom of the open-pit mine along the slope direction. The largest horizontal displacement is estimated by Figure 2 up to 1.45 m.

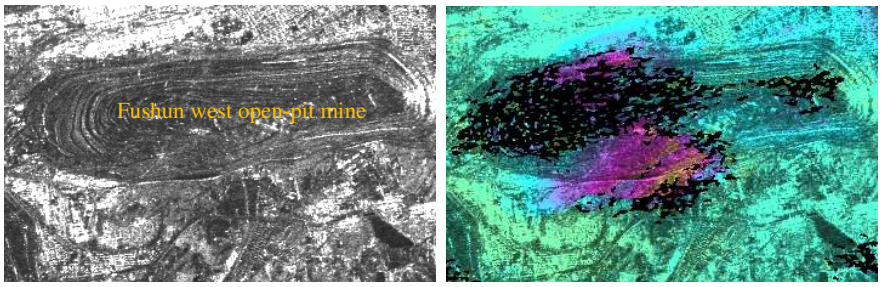

(a) (b)

Figure 1: LOS displacement obtained by D-InSAR. (a) SAR intensity image of Fushun west open-pit mine; (b) LOS deformation in the north and south of Fushun west open-pit mine.

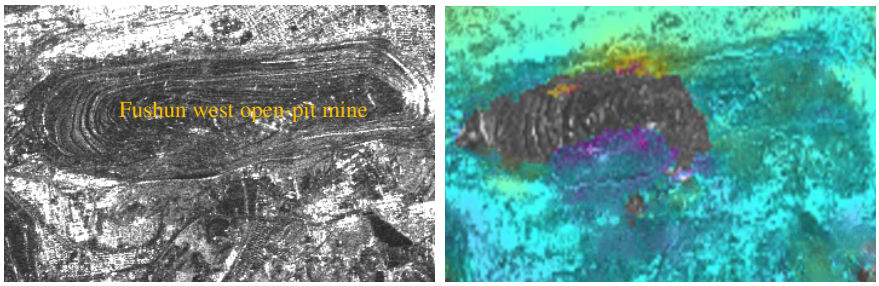

(a) (b)

Figure 2: Azimuthal displacement obtained by MAI. (a) SAR intensity image of Fushun west open-pit mine; (b) Azimuthal deformation in the north and south of Fushun west open-pit mine.

By integrating Figure 1 and Figure 2, we can determine the boundaries and intensity of landslides in the north and south of Fushun west open-pit mine. What is most important, we can obtain the detailed distribution of landslides via only two SAR images.

4. CONCLUSION

A novel technique by integrating the multiple-aperture InSAR and traditional D-InSAR has been utilized to monitor lagre-scale horizontal deformation and vertical deformation of landslides caused by coal mining in Fushun west open-pit mine. The boundaries of landslides revealed by the new method occurred in the north and south of Fushun west open-pit mine are consistent with the results of field investigation. In the future, we plan to extend this method to time-series analysis on the basis of the small baseline subset (SBAS) algorithm to extract long time horizontal displacement and vertical displacement from the overall perspective via multi-temporal SAR data.

ACKNOWLEDGMENT

This research was supported by the National Important Basic Research Project (Grant No. 2011CB707102), the National Natural Science Foundation of China (Grant No. 41104104), and the Fundamental Research Funds for the Central Universities (Grant No. N120801001).

REFERENCES

1. Massonnet, D. and K. L. Feigl, "Radar interferometry and its application to changes in the Earth's surface," *Reviews of Geophysics*, Vol. 36, 441–500, 1998.

2. Wright, T. J., B. E. Parsons, and Z. Lu, "Toward mapping surface deformation in three dimensions using InSAR," *Geophysical Research Letters*, Vol. 31, L01607, 2004.
3. Michel, R., J. P. Avouac, and J. Taboury, "Measuring ground displacements from SAR amplitude images: Application to the Landers earthquake," *Geophysical Research Letters*, Vol. 26, 875–878, 1999.
4. Bechor, N. B. and H. A. Zebker, "Measuring two-dimensional movements using a single InSAR pair," *Geophysical Research Letters*, Vol. 33, L16311, 2006.
5. Jung, H.-S., J.-S. Won, and S.-W. Kim, "An improvement of the performance of multiple-aperture SAR interferometry (MAI)," *IEEE Transactions on Geoscience and Remote Sensing*, Vol. 47, 2859–2869, 2009.
6. Wegmüller, U., C. Werner, M. Santoro, T. Strozzi, and A. Wiesmann, "ERS-ENVISAT TanDEM data over sea and shelf ice," *Proceedings of Fringe 2009 Workshop*, Frascati, Italy, 2009.
7. Goldstein, R. M. and C. L. Werner, "Radar interferogram filtering for geophysical applications," *Geophysical Research Letters*, Vol. 25, 4035–4038, 1998.
8. Costantini, M., "A novel phase unwrapping method based on network programming," *IEEE Transactions on Geoscience and Remote Sensing*, Vol. 36, 813–821, 1998.

A PolSAR Classification Method Based on Scattering Model and Polarization Correlation Coefficient

Jianbo Wang[1, 2], **Chao Wang**[1], **Hong Zhang**[1], **Fan Wu**[1], **and Bo Zhang**[1]

[1]Key Laboratory of Digital Earth Sciences
Institute of Remote Sensing and Digital Earth, CAS, Beijing 100094, China
[2]University of Chinese Academy of Sciences, Beijing 100049, China

Abstract— Recently, many PolSAR image classification methods have been proposed. One commonly used method is based on the scattering model. However, traditional classification based on scattering model usually overestimates the volume scattering contributions, especially in urban areas, resulting in buildings not orthogonal to radar Line-Of-Sight (LOS) misjudged as forests. To solve this problem, an improved PolSAR classification method based on scattering model and polarization correlation coefficient is presented in this paper. By introducing two types of polarization correlation coefficients, circular-pol correlation coefficient (CCC) and normalized circular-pol correlation coefficient (NCCC), the oriented buildings can be effectively extracted from the volume scattering. Since the amplitude values of CCC of forests are very small, while that of buildings orthogonal to radar LOS or with small orientation angles are close to 1. Therefore, the CCC parameter is firstly used to extract some slightly tilted oriented buildings form the initial volume scattering category. Then, the NCCC parameter is introduced to distinguish the buildings with large orientation angles from the remainder volume scattering components. Since these buildings hold strong non-reflection symmetry and larger orientation angles, the values of NCCC of this kind are much larger than that of forests. Finally, the extracted buildings are reclassified into a new oriented buildings category. In order to maintain the dominant scattering mechanism characteristics, the classification method preserving scattering characteristics is utilized to classify the corrected scattering categories. The proposed classification algorithm remedies the defect of traditional scattering-model-based classification method and the experiment result of an E-SAR L-band PolSAR image of Oberpfaffenhofen, Germany demonstrates the effectiveness of the proposed method.

1. INTRODUCTION

Terrain classification has become one of the most important applications for polarimetric synthetic aperture radar (PolSAR) image. Among various classification methods, the method utilizing targets scattering mechanisms model is a hot topic [1]. To maintain targets polarimetric scattering characteristics, Lee et al. [2] developed a classification method comprised of three-component scattering model and wishart classifier. This method preserves the purity of scattering categories in classification procedures, which greatly improves the result of the classification based on scattering model. By now, the scattering-model-based decomposition is the primary approach to get scattering mechanism information of targets. However, a known issue of this decomposition is the overestimation of volume scattering power, especially in urban areas [3]. Traditional scattering-model-based decompositions usually assume that man-made structures corresponds to double-bounce scattering and only volume scattering contributes to the cross-polarization term. As we know, buildings aligned facing the radar look direction satisfy the reflection symmetry and produce high double-bounce scattering power. Nevertheless, the oriented buildings whose walls are not orthogonal to radar LOS do not satisfy the reflection symmetry. These buildings will introduce cross-polarization power, resulting in these buildings misjudged as forest.

In order to eliminate the classification confusion, an improved PolSAR image classification method based on scattering model and polarization correlation coefficient is presented in this paper. It is known that the circular-pol correlation coefficient (CCC) and the normalized circular-pol correlation coefficient (NCCC) contain essential polarimetric information and have good performances on terrain classification and detection of targets. By introducing the two parameters in classification based on scattering model, the oriented buildings can be successfully distinguished from forest areas. A DLR E-SAR L-band quad-polarized SAR image of Oberpfaffenhofen, Germany is used to verify the effectiveness of the proposed method.

2. BACKGROUND AND THEORY

In this section, we give a brief review of the four-component model-based decomposition and two polarization correlation coefficients.

2.1. Four-component Model-based Decomposition

In order to accommodate the decomposition scheme for the more general scattering case, Yamaguchi proposed a four-component scattering model. Based on the Freeman and Durden decomposition, the decomposition model introduces an additional helix scattering corresponding to non-reflection symmetric cases [4]. Four-component decomposition with coherence matrix can be written as

$$\langle [T] \rangle = f_s \langle [T] \rangle_s + f_d \langle [T] \rangle_d + f_v \langle [T] \rangle_v + f_C \langle [T] \rangle_c \tag{1}$$

where f_s, f_d, f_v and f_c are the coefficients to be determined. $\langle [T] \rangle_s$, $\langle [T] \rangle_d$, $\langle [T] \rangle_v$, $\langle [T] \rangle_c$ are expansion matrices corresponding to the surface, double-bounce, volume and helix scattering mechanisms, respectively. According to the decomposition algorithm, the total scattering power can be successfully decomposed into four scattering components, Ps, Pd, Pv and Pc.

2.2. The Circular-pol Correlation Coefficient (CCC)

The circular-pol correlation coefficient can be expressed as

$$\rho_{RR-LL} = \frac{\langle S_{RR} S_{LL}^* \rangle}{\sqrt{\langle S_{RR} S_{RR}^* \rangle \langle S_{LL} S_{LL}^* \rangle}} = \frac{\left\langle 4 |S_{HV}|^2 - |S_{HH} - S_{VV}|^2 \right\rangle - i4Re \langle S_{HV}^* (S_{HH} - S_{VV}) \rangle}{\sqrt{\left\langle |S_{HH} - S_{VV} + i2S_{HV}|^2 \right\rangle \left\langle |S_{HH} - S_{VV} - i2S_{HV}|^2 \right\rangle}} \tag{2}$$

Schuler et al. [5] indicate that $|\rho_{RR-LL}|$ is related to the surface roughness and man-made structures. For low surface roughness bare land, the value is relatively large, while for other natural distributed targets such as forests, $|\rho_{RR-LL}|$ is very low. In addition, when radar illumination direction is orthogonal to the alignment of the buildings, $|\rho_{RR-LL}|$ tends to be unity, whereas for oblique illumination case, it becomes smaller with the increasing of building orientation angle [6]. Therefore, CCC can be utilized to distinguish the slightly tilted oriented buildings.

2.3. The Normalized Circular-pol Correlation Coefficient (NCCC)

In order to reduce the effects of scattering terms that are associated with natural areas and simultaneously to enhance the return from man-made structures, Ainsworth et al. [7] introduce a parameter, the normalized circular-pol correlation coefficient (NCCC), which can be written as

$$\rho'_{RR-LL} = \left| \frac{\rho_{RR-LL}}{\rho_{RR-LL}(0)} \right| = \sqrt{\frac{1 + \tan^2(4\theta)}{1 - \tau^2}} \tag{3}$$

where θ is orientation angle, and τ is helicity indictor. $\rho_{RR-LL}(0)$ is the normalization term, under the reflection symmetry $\langle S_{HV} S_{HH}^* \rangle \approx \langle S_{HV} S_{VV}^* \rangle \approx 0$. And it can be straightforwardly derived from Eq. (2) as

$$\rho_{RR-LL}(0) = \frac{\left\langle 4 |S_{HV}|^2 - |S_{HH} - S_{VV}|^2 \right\rangle}{\left\langle 4 |S_{HV}|^2 + |S_{HH} - S_{VV}|^2 \right\rangle} \tag{4}$$

With the normalization processing, the NCCC will be close to unity for reflection symmetry scatterers and larger than unity for the non-reflection symmetry case. So NCCC is considered as a useful polarimetric indicator for distinguishing oriented buildings with large orientation angles from volume scattering.

3. METHOD

In order to reduce the classification confusion between oriented buildings and the volume scattering category, we propose an improved classification method based on four-component scattering model and the two parameters, CCC and NCCC. The flow chart of the proposed method is shown in Figure 1. Detailed steps are as follows.

3.1. Four-component Decomposition and Initial Classification

Apply four-component decomposition to PolSAR data, then divide pixels into surface, double-bounce and volume scattering categories, based on the maximum power of the three scattering mechanisms (the helix category is ignored).

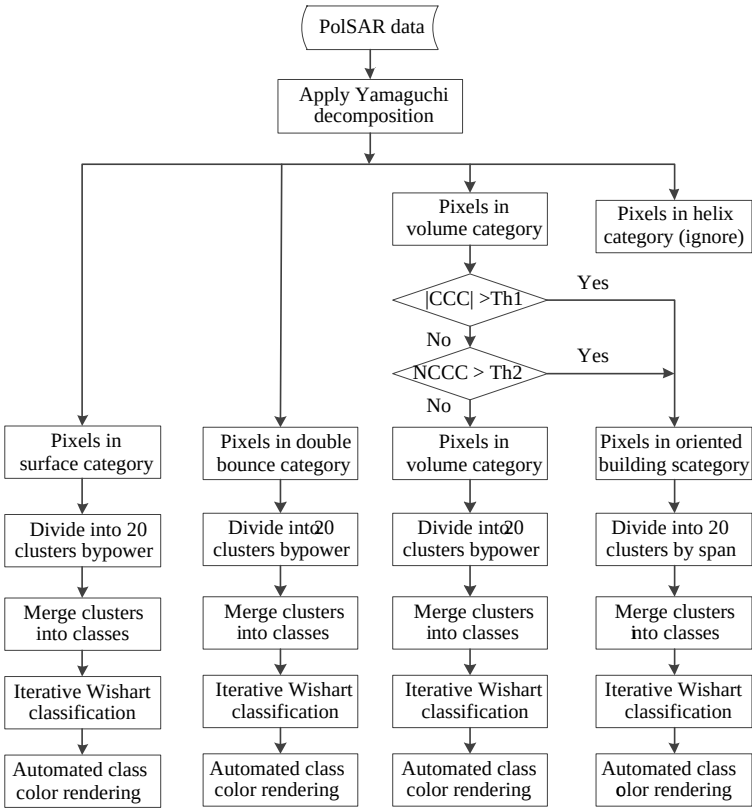

Figure 1: The flow chart of the proposed classification method.

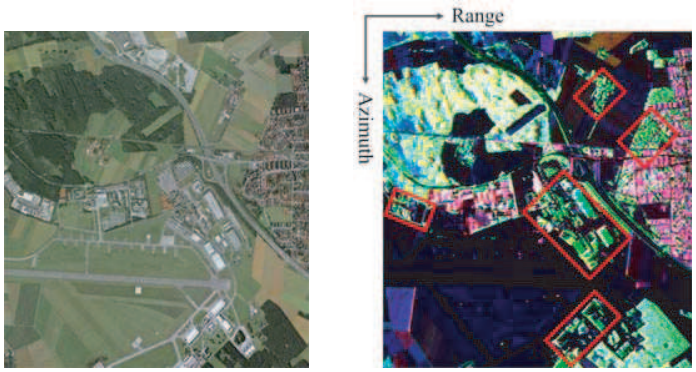

Figure 2: (a) Optical image. (b) Four-component decomposition result.

3.2. Scattering Categories Rectification

Calculate the amplitude of CCC (|CCC|) and NCCC, respectively. In order to distinguish the oriented buildings, set two reasonable corresponding thresholds Th1 and Th2. For each pixel belong to volume scattering category, if the |CCC| is larger than Th1 or less than Th1 but with NCCC larger than Th2, reclassify it into a new oriented buildings category, otherwise remain its volume scattering category unchanged.

3.3. Classification with Wishart Classifier

For the surface, double-bounce and rectified volume categories, they are finely classified into small clusters according to the dominated scattering mechanism powers. While the extracted oriented buildings category is finely classified according to the total scattering power. Then apply the classification method preserving polarimetric scattering characteristics [2]. The procedures mainly include fine clusters partition, cluster merging, iterative Wishart classification and automated color rendering.

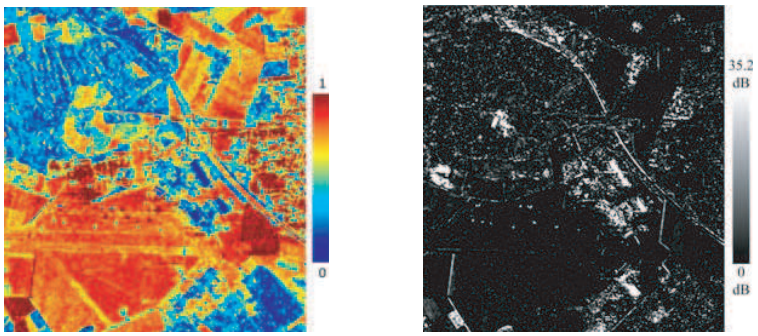

Figure 3: ((a) The amplitude of CCC. (b) The logarithmic graph of NCCC.

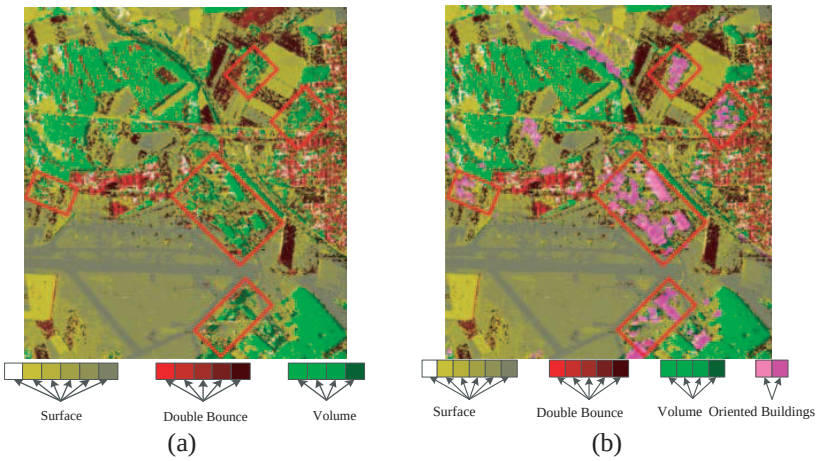

Figure 4: Classification results. (a) Traditional method. (b) The proposed method.

4. RESULTS AND DISCUSSIONS

A DLR E-SAR L-band full polarized image is used to demonstrate the effectiveness of the proposed method. The data is acquired over Oberpfaffenhofen, Germany. The image contains 1300×1200 pixels and its spatial resolution is $3\,\mathrm{m} \times 3\,\mathrm{m}$. The corresponding optical image is shown in Figure 2(a). There exist forest, lawns, farmland, and buildings with different orientation angles in the imagery.

In order to illustrate the influence of building alignment direction, we show in Figure 2(b) a result of the four-component decomposition. Color-code is used for indication of the scattering powers: Red (double-bounce scattering), Green (volume scattering), and Blue (surface scattering), respectively. It can be easily observed that buildings facing the radar look direction present double-bounce scattering characteristic, while the oriented buildings not orthogonal to radar LOS shown in red rectangular regions are dominated by volume scattering mechanism. To analysis the performance of oriented buildings on two polarization correlation coefficients, the amplitude of CCC, |CCC|, and the logarithmic graph of NCCC are shown in Figures 3(a) and (b). It can be seen that some slightly tilted oriented buildings also have relatively large |CCC|, besides the buildings facing the radar look direction. And those buildings with orientation angles around $\pm 45^\circ$ have larger NCCC than forest areas. Therefore, two appropriate thresholds can be set to extract the oriented buildings from the volume scattering. As for the PolSAR data used in this paper, two reasonable thresholds, Th1 and Th2, are set to 0.65 and 0.35 respectively.

Then by applying the proposed classification method, an improved classification result is shown in Figure 4(b). For better comparison, Figure 4(a) presents the traditional classification result. It can be observed that these oriented buildings in the red rectangular regions are effectively distinguished from volume scattering. In addition, surface and double-bounce classes remain their scattering characteristics unchanged, which well preserves the advantage of the traditional classification method for these targets.

5. CONCLUSIONS

This paper proposed an improved PolSAR image classification method based on scattering model and polarization correlation coefficient. In order to solve the classification confusion between oriented buildings and forests, the proposed method introduces two polarization correlation coefficients, circular-pol correlation coefficient and normalized circular-pol correlation coefficient. According to the different performance of oriented buildings and forests on the two parameters, two reasonable thresholds are set to distinguish the two kinds. The proposed method effectively weakens the scattering mechanism ambiguity and remedies the defect of traditional scattering-model-based classification method. The experiment result of an E-SAR L-band PolSAR image of Oberpfaffenhofen, Germany demonstrates the effectiveness of the method for terrain classification.

ACKNOWLEDGMENT

This work was supported in part by the Director Innovation Fund of the Center for Earth Observation and Digital Earth, Chinese Academy of Sciences and in part by the National Natural Science Fund Project of China under Grant 41331176, and Grant 41371413.

REFERENCES

1. Qi, Z., A. G. O. Yeh, X. Li, et al., "A novel algorithm for land use and land cover classification using RADARSAT-2 polarimetric SAR data," *Remote Sens. Environ.*, Vol. 118, 21–39, 2012.
2. Lee, J. S., M. R. Grunes, E. Pottier, et al., "Unsupervised terrain classification preserving polarimetric scattering characteristics," *IEEE Trans. Geosci. Remote Sens.*, Vol. 42, No. 4, 722–731, 2004.
3. Van Zyl, J. J., M. Arii, and Y. Kim, "Model-based decomposition of polarimetric SAR covariance matrices constrained for nonnegative eigenvalues," *IEEE Trans. Geosci. Remote Sens.*, Vol. 49, No. 9, 3452–3459, 2011.
4. Yamaguchi, Y., Y. Yajima, and H. Yamada, "A four-component decomposition of POLSAR images based on the coherency matrix," *IEEE Geosci. Rem. Sens. Lett.*, Vol. 3, No. 3, 292–296, 2006.
5. Schuler, D. L., J. S. Lee, D. Kasilingam, et al., "Surface roughness and slope measurements using polarimetric SAR data," *IEEE Trans. Geosci. Remote Sens.*, Vol. 40, No. 3, 687–698, 2002.
6. Moriyama, T., S. Uratsuka, T. Umehara, et al., "Polarimetric SAR image analysis using model fit for urban structures," *IEICE Transactions on Communications*, Vol. 88, No. 3, 1234–1243, 2005.
7. Ainsworth, T. L., D. L. Schuler, and J. S. Lee, "Polarimetric SAR characterization of man-made structures in urban areas using normalized circular-pol correlation coefficients," *Remote Sensing of Environment*, Vol. 112, No. 6, 2876–2885, 2008.

Analysis of Optimal Panel Geometry for Self-illustration Corner Reflector

C. R. Li[1, 2], **Y. S. Zhou**[1, 2], **and L. L. Ma**[1, 2]

[1]Key Lab of Quantitative Remote Sensing Information Technology, Chinese Academy of Sciences, China
[2]Academy of Opto-Electronics, Chinese Academy of Sciences, China

Abstract— Self-illuminating corner reflector is the corner reflector that all the rays that enter the reflector's cavity experience the triple reflection on the panel and return to the radar. It has the advantage of reducing the unexpected coherent ground interaction and thus improving the accuracy of RCS and benefiting SAR calibration and image quality assessment. The optimal panel geometry is the one that has the minimal edge length for a given panel area in order to alleviate edge diffraction. The panel geometry had been previously designed to be square, pentagon and hexagon. In this paper, the general expressions for the panel area and panel external edge length of arbitrarily self-illuminating corner reflectors were described by parameter equation firstly. Then the edges of reflector panel were assumed as circular arc and further elliptical arc for analysis. Through a numerical approximation approach, the external edge lengths of those self-illuminating trihedral corner reflectors are derived and compared. The results showed that the self-illuminating trihedral corner reflector with circular arc had the minimal edge length and was the optimal panel geometry among the panel geometries under analysis.

1. INTRODUCTION

SAR calibration is becoming more and more important for quantitative earth observation application [1–3]. The mostly widely used corner reflector as radar bright point target is the triangular trihedral corner reflectors. It has the advantage of large radar cross section (RCS), extremely wide RCS pattern, light weight, cheap and simple to manufacture. The panel geometry for trihedral corner reflector has been traditionally chosen as triangular shape [4–6]. However, not all the panel area is the effective area which contributes to the nominal RCS of the reflector. The additional 'tip' reflecting area, if interacting with ground plane, will yield an increase of RCS. This problem will affect SAR radiometric and phase calibration accuracy. The self-illuminating corner reflectors are proposed to solve this problem [7]. All the rays that enter the reflector's cavity experience the triple reflection on the panel and return to the radar. There are many types of self-illuminating corner reflectors, e.g., square, hexagon. Note that the nominal RCS of trihedral corner reflector is calculated by the panel area and radar wavelength, however this is true only when the leg length is very large compared to the radar wavelength. Otherwise, the contribution from edge diffraction becomes an issue. Since edge diffraction is proportional to the panel external edge length, the optimal panel geometry is the one that has the minimal external edge length for the same panel area. In [7], the panel geometry was assumed as polygon and optimum hexagon panel geometry was obtained. Based on the above approach, this paper analyzes more types of self-illuminating corner reflectors. For this purpose, the general expressions for the panel area and panel external edge length of arbitrarily self-illuminating corner reflectors are described by parameter equation firstly. Then the edges of reflector panel are assumed as straight line, circular arc, and elliptical arc. Through a numerical approximation approach, the external edge lengths of those self-illuminating trihedral corner reflectors are derived and compared.

2. TYPES OF SELF-ILLUSTRATION CORNER REFLECTOR AND ITS MATHEMATIC EXPRESSION

2.1. Expression of Self-illustration CR

Figure 1 shows the geometry of a self-illuminating corner reflector. Assuming curve $\mathbf{C}$ has the following form:

$$\mathbf{C}(\tau) = [0, f(\tau), g(\tau)], \quad \tau \in [0, t] \tag{1}$$

where $f(0) = 0$, $f(t) = l$, $g(0) = l$, $g(t) = l$ denote that the curve passes point A and B'. Arbitrary point p on YOZ plane will be mapped onto point p'. According to the mapping relationship, the coordinate of p' could be expressed by coordinate of p as

$$\begin{cases} x_{p'} = z_p \\ y_{p'} = z_p - y_p \end{cases} \tag{2}$$

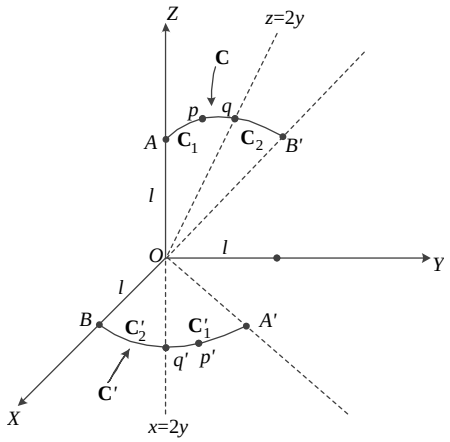

Figure 1: Mapping geometry.

So the curve $\mathbf{C}'$ on XOY plane could be expressed by: $\mathbf{C}' = [g(\tau), g(\tau) - f(\tau), 0], \tau \in [0, t]$. When τ increase from 0 to t, curve $\mathbf{C}$ traces from A to B' and curve $\mathbf{C}'$ traces from A' to B. On the other hand, according to the self-illuminating symmetry requirements, the curve mapped onto XOY must be identical to the curve mapped to YOZ, therefore there is point $t = t_0$, so that

$$\begin{cases} x_{q'} = z_q \\ y_{q'} = y_q \end{cases} \tag{3}$$

Substituting (3) into (2), then

$$y_{q'} = z_q - y_q = y_q \Rightarrow \begin{cases} z_q = 2y_q \\ x_{q'} = 2y_{q'} \end{cases} \tag{4}$$

Equation (4) means that there must be one point q on lines $z = 2y$ for arbitrary self-illuminating corner reflector. According to [7], the edge curve $\mathbf{C}_1$ and $\mathbf{C}_2$ of the self-illuminating corner reflector has the following forms:

$$\mathbf{C}_1(\tau) = [0, f_1(\tau), g_1(\tau)], \quad \tau \in [0, t_0] \tag{5}$$

$$\mathbf{C}_2(\tau) = [0, g_1(\tau), g_1(\tau) - f_1(\tau)], \quad \tau \in [0, t_0] \tag{6}$$

In Section 3, the types of edge curve $\mathbf{C}_1$ (i.e., straight line, circular, elliptical) will be discussed.

2.2. RCS and Edge Length of Self-illustration Corner Reflector

According to area integration formula, one panel area of the trihedral corner reflector could be expressed as

$$S = 2 \cdot \int_0^{t_0} \left(f_1' g_1 - g_1' f_1\right) d\tau \tag{7}$$

where f' denotes partial derivatives of f, and g' denotes partial derivatives of g.

3. ANALYSIS OF THE MINIMAL EDGE LENGTH OF VARIOUS TYPES OF SELF-ILLUSTRATION CORNER REFLECTOR

According to curve integration formula, edge length L of the trihedral corner reflector could be expressed as

$$L = 2 \cdot \int_0^{t_0} \left\{ \sqrt{f'^2_1 + g'^2_1} + \sqrt{(f'_1 - g'_1)^2 + g'^2_1} \right\} d\tau \tag{8}$$

The purpose is to choose f so that it would minimize (8) subject to constraint (7).

3.1. Curve $\mathbf{C}_1$: Straight Line

For simplicity, firstly assume the curve $\mathbf{C}_1$ is a straight line. According to (6), $\mathbf{C}_2$ is also a straight line, and thus the panel geometry is polygon. The shape of the panel geometry is dependent on the position of point q. If q lies on AB', then the panel geometry is square, and edge length of the

panel geometry is $2\sqrt{A}$. If q lies on the position that makes the three points on the same straight line, then the panel geometry is pentagon, and edge length of the panel geometry is $2.1\sqrt{A}$.

In order to obtain the minimal edge length, express the area and edge length of polygon as:

$$S = l^2 + l\,(2y_0 - l) \tag{9}$$

$$L = 2\left(\sqrt{y_0^2 + (2y_0 - l)^2} + \sqrt{(l - y_0)^2 + (2y_0 - l)^2}\right) \tag{10}$$

From (9) and (10), the relation between external edge length L and interior leg length l could be derived, as shown in Figure 3. The minimal edge length is $L_{\min} = 1.9441\sqrt{S}$ when $l = 0.9469\sqrt{S}$. It can be concluded that among polygonous panel geometry, hexagon is the optimal panel geometry.

3.2. Curve $\mathbf{C}_1$: Circular Arc

According to the isoperimetric theorem, the circle has the shortest perimeter among all planar shapes with the same area, so the external edge length of a circular arc panel should be even smaller than that of hexagon panel, theoretically. Assume that the curve $\mathbf{C}_1$ is part of a circle with the center at $(y_0,\, l - x)$, as shown in Figure 4. From Figure 4, radius of the circle is

$$r = \sqrt{y_0^2 + x^2} = x + (2y_0 - l) \tag{11}$$

and the line segment

$$x = \frac{y_0^2 - (2y_0 - l)^2}{2(2y_0 - l)} \tag{12}$$

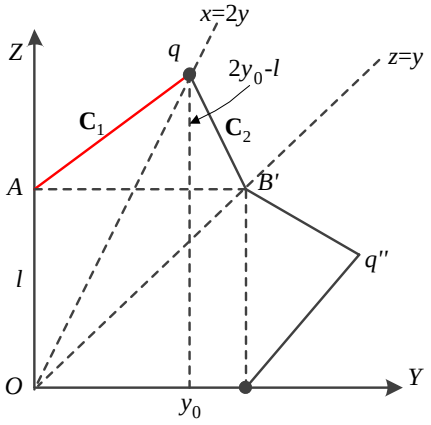

Figure 2: Panel geometry of polygon.

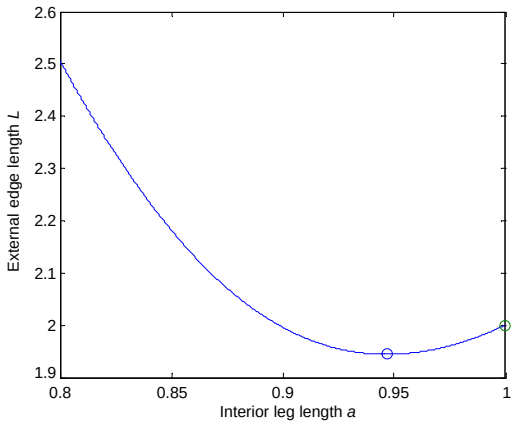

Figure 3: The relation between edge length L with interior edge length l.

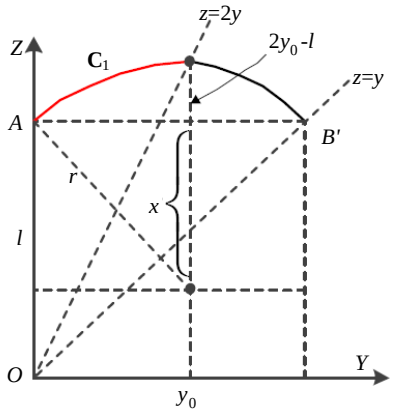

Figure 4: Panel geometry of circular arc.

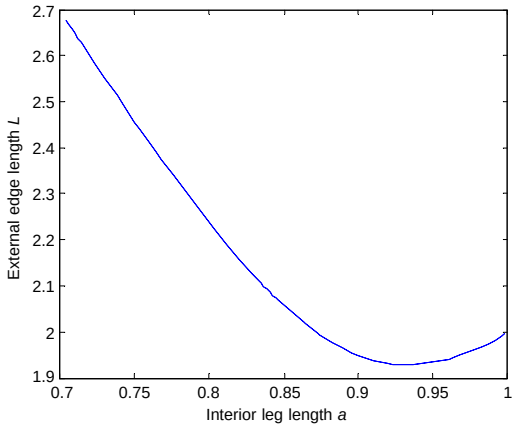

Figure 5: The relation between edge length L with interior edge length l.

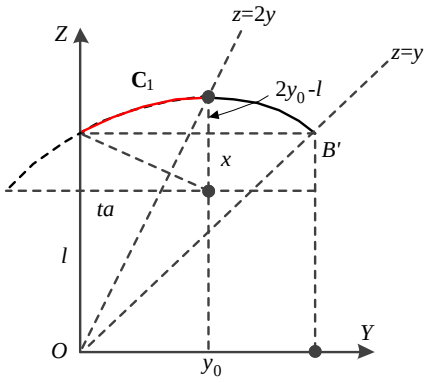

Figure 6: Panel geometry of elliptical arc.

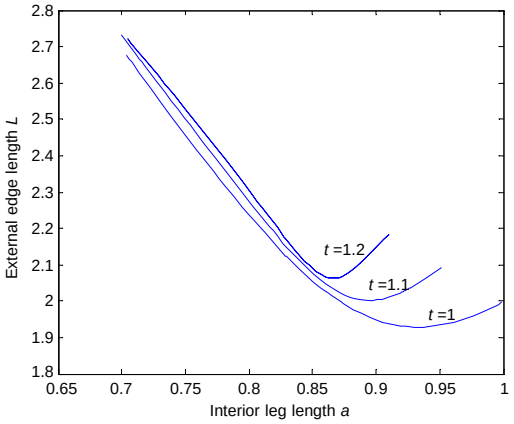

Figure 7: The relation between edge length with interior edge length l at different ratio t.

Table 1: Comparison of the edge lengths of different panel geometries.

Types of CR / Properties	straight line			circular arc	ellipse edge
	square	pentagon	hexagon		
Panel area	S	S	S	S	S
Interior leg length S	$\sqrt{S}$	$0.866\sqrt{S}$	$0.9469\sqrt{S}$	$0.932\sqrt{S}$	$0.932\sqrt{S}$
Minimum of external edge length	$2\sqrt{S}$	$2.1\sqrt{S}$	$1.9441\sqrt{S}$	$1.9282\sqrt{S}$	$1.9282\sqrt{S}$

The parameter equation for the circular arc is:

$$\begin{cases} y = f(\tau) = y_0 + r\cos\tau \\ z = g(\tau) = (l-x) + r\sin\tau \end{cases}, \quad \tau \in \left[\frac{\pi}{2} + \arctan\left(\frac{y_0}{x}\right), \frac{\pi}{2}\right] \tag{13}$$

Using (7), (8) and (11)∼(13), and through a numerical approximation approach [8], the relationship between edge length L with l has been derived and shown in Figure 5. When $l = 0.932\sqrt{S}$, the minimal edge length $L_{\min} = 1.9282\sqrt{S}$, which is smaller than that of the hexagon panel geometry.

3.3. Curve $\mathbf{C_1}$: Ellipse Arc

Now consider the more general case of the ellipse edge. Assume that the curve $\mathbf{C}_1$ is part of an ellipse with the center at $(y_0, l-x)$, semi-major axis $b = ta$ (t is the ratio between semi-major and short axis) and semi-minor axis a as shown in Figure 6. From Figure 6, the line segment

$$x = \frac{-y_0^2/t^2 - 4y_0^2 - l^2 + 4ly_0}{2l - 4y_0} - (2y_0 - l) \tag{14}$$

The parameter equation for the ellipse arc is:

$$\begin{cases} y = f(\tau) = y_0 + b\cos\tau \\ z = g(\tau) = (l-x) + a\sin\tau \end{cases}, \quad \left[\frac{\pi}{2} + \arctan\left(\frac{y_0}{x}\right), \frac{\pi}{2}\right] \tag{15}$$

The relation between edge lengths with interior edge length l at different ratio t are shown in Figure 7. We can see that when $t = 1$ (i.e., the circular arc case), the minimal edge length $L_{\min} = 1.9282\sqrt{S}$ when $l = 0.932\sqrt{S}$. The results showed that the minimal external edge length is obtained when the semi-major axis of the ellipse equals to semi-minor axis, which means that the panel geometry with circular arc has the minimal external edge length.

4. CONCLUSION

This paper analyzed the edge lengths of different types of self-illustration corner reflector. The simplest panel geometry of the self-illustration corner reflector is the polygon, but it would not have

the minimal external edge length according to the isoperimetric theorem. This paper extended the type of panel geometry to the more general case (elliptical arc) for analysis. The results showed that the minimal external edge length is obtained when the semi-major axis of the ellipse equals to semi-minor axis, which means that the panel geometry with circular arc has the minimal external edge length. Its value was smaller than that of the polygon, which verified the assumption derived from the isoperimetric theorem. In the future the RCS accuracy will be validated by simulation and RCS testing the prototype of the circular arc self-illustration corner reflector.

ACKNOWLEDGMENT

This work was supported in part by the National Natural Science Foundation of China (Grant Nos. 41101335, 61331020) and National High Technology Research and Development Program of China (Grant No. 2013AA122903).

REFERENCES

1. Zhou, Y. S., W. Hong, Y. P. Wang, and Y. R. Wu, "Maximal effective baseline for polarimetric interferometric SAR forest height estimation," *Science China Information Sciences*, Vol. 55, No. 4, 867–876, 2012.
2. Freeman, A., "SAR calibration: An overview," *IEEE Transactions on Geoscience and Remote Sensing*, Vol. 30, No. 6, 1107–1121, Nov. 1992.
3. Gonzalez, J. H., M. Bachmann, G. Krieger, and H. Fiedler, "Development of the TanDEM-X calibration concept: Analysis of systematic errors," *IEEE Transactions on Geoscience and Remote Sensing*, Vol. 48, No. 2, 716–726, 2010.
4. Doerry, A. W., "Reflectors for SAR performance testing," Sandia National Laboratories, 2008.
5. Döring, B. J., P. R. Looser, M. Jirousek, and M. Schwerdt, "Reference target correction based on point-target SAR simulation," *IEEE Transactions on Geoscience and Remote Sensing*, Vol. 50, No. 3, 951–959, 2012.
6. Gray, A. L., P. W. Vachon, C. E. Livingstone, and T. I. Lukowski, "Synthetic aperture radar calibration using reference reflectors," *IEEE Transactions on Geoscience and Remote Sensing*, Vol. 28, No. 3, 374–383, 1990.
7. Sarabandi, K. and T. C. Chiu, "Optimum corner reflectors for calibration of imaging radars," *IEEE Transactions on Geoscience and Remote Sensing*, Vol. 10, No. 44, 1348–1361, 1996.
8. Zhou, Y. S., C. R. Li, L. L. Ma, M. Y. Yang, and Q. Liu, "Improved trihedral corner reflector for high-precision SAR calibration and validation," *Proc. 2014 IEEE International Geoscience and Remote Sensing Symposium (IGARSS 2014)*, Québec, Canada, Jul. 13–Jul. 17, 2014.

Coherent Detected Temporal Optical Code Division Multiplexing System with High Spectral Efficiency Using Nyquist Pulse Shaping

Lin Chen, Xuezhi Hong, and Changjian Guo*
ZJU-SCNU Joint Research Center of Photonics
South China Normal University (SCNU), Guangzhou 510006, China

Abstract— We propose a high spectral efficiency temporal coded OCDM system using Nyquist pulse shaping and coherent detection (Nyquist-OCDM). The proposed system is compared with conventional OCDM system in terms of spectral efficiency and error vector magnitude. The system performance under different number of codes and different length of code is investigated by simulation.

1. INTRODUCTION

By employing dedicated orthogonal codes for each channel, optical code division multiplexing (OCDM) system offers several attracting features [1], e.g., asynchronous access, soft-capacity and high security, etc.. However, the spectral efficiency (SE) of OCDM system is decreased in the spectrum spreading process if the number of codes N_c employed is less than the spreading length N_l. In traditional OCDM systems, the spectral efficiency is further limited by the large carrier spacing (> baud rate) in spectral coded systems [2] or non-ideal pulse shaping (not Nyquist) in temporal coded systems [3]. In [4], we have proposed a high SE spectral coded system based on orthogonal frequency multiplexing (OFDM) with carrier spacing equals to baud rate.

In this paper, we present a coherent detected temporal coded OCDM system in which Nyquist pulse shaping is employed to improve the SE. By Nyquist pulse shaping of temporal coded signal, the spread spectrum width of signal can be reduced to chip-rate. Therefore, the SE of proposed system is improved compared with conventional temporal coded OCDM system [3] whose spectrum width could be several times of the encoding/decoding chip rate. Furthermore, the OCDM encoding/decoding and Nyquist pulse shaping are conducted in electrical domain, which can share the existing facilities with other digital signal processing (DSP) functions in the coherent optical communication system.

2. PRINCIPLE AND SIMULATION SETUP

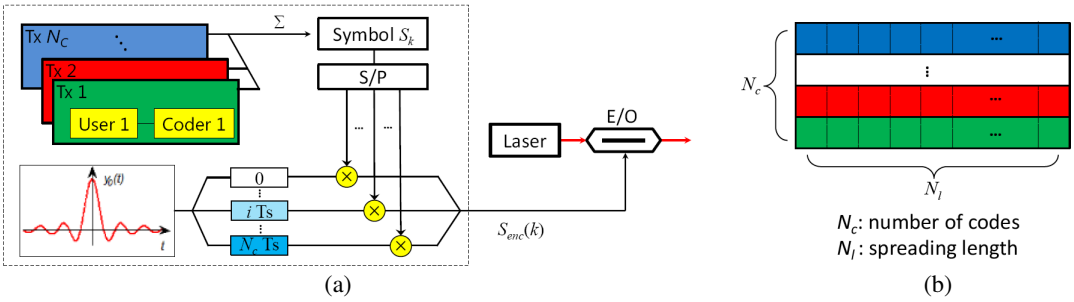

Figure 1: (a) Generation of Nyquist-OCDM signal and (b) the structure of codes.

Figure 1 depicts the generation of Nyquist-OCDM signal. In encoding step, specific code from the same orthogonal code set (e.g., Walsh code) with code length N_l is assigned to one of the N_c user for spreading. The spread signal from all users are then converged. The i_{th} block S_i of the sum of N_c encoded data can be described as:

$$S_i = \{C_{im}\} \quad (m = 1, 2, 3, \ldots, N_l)$$

where C_{im} is the mth chip in ith block. Without loss of generality, all users are assumed to transmit data with identical symbol rate R and modulation format (M bits per symbol). Thus, the chip rate

*Corresponding author: Changjian Guo (changjian.guo@coer-scnu.org).

of temporal encoding is $R_s = RN_l$ The spread signal is then pulse shaped by a Nyquist filter. The Nyquist shaped temporal coded signal is a finite sequence of N temporal symbols S^i_{enc} [5], which can be expressed as:

$$y(t) = \sum_{i=0}^{N-1} S^i_{enc}(t) \quad S^i_{enc}(t) = \sum_k C_{ik} \sin c\left(\frac{t - t_k}{T_s}\right) e^{j2\pi i F_s t} \quad |t_{k+1} - t_k| = T_s = \frac{1}{F_s}$$

By sampling $S^i_{enc}(t)$ with sample rate $R_s = N_l/T_s (iT_s < t < iT_s + T_s)$, the sampled signal is:

$$S^i_{enc}(m) = \sum_k C_{ik} \sin c\left(\frac{mT_s - t_k}{T_s}\right) e^{j2\pi i F_s m T_s} = \sum_k C_{ik} \sin c\,(m-k)\, e^{j2\pi i F_s m T_s} = C_{im}$$

Therefore, the original data can be recovered by decoding the sampled signal ($S^i_{enc}(m) = C_{im}$) at the receiver. Since the bandwidth of Nyquist-shaped baseband signal equals to chip rate R_s when the roll-off factor $\alpha = 0$ [6] the theoretical spectral efficiency of above system is:

$$SE = M\frac{N_c R}{R_s} = M\frac{N_c}{N_l}\,\text{bit/s/Hz}$$

The maximum $SE_{\max}(= M\,\text{bit/s/Hz})$ is achieved when $N_c = N_l$, which is at least two times of SE of the traditional OCDM system [2] and equals to SE of the spectral efficient OFDM-OCDM system [4] The encoded signal is sent to modulator for electrical-optical (E-O) coversion.

Figure 2 shows the simulation setup for the transmission of Nyquist-CDM signal over 400 km standard single mode fiber (SSMF) link with coherent detection. The pseudo-random binary sequences (PRBS) of order 15 is generated at an aggregate bit rate of 40 Gbps. The QPSK mapped data is serial to parallel (S/P) converted to emulate data streams for different users ($N_c = 256$). Data from all users are encoded in parallel using orthogonal Walsh codes ($N_l = 256$). The sum of all encoded signal is filtered by a Nyquist filter to get an inter-symbol-interference (ISI)-free narrow band signal. Then the complex Nyquist shaped temporal coded signal sample is converted to electrical signals by two digital-to-analog converters (DACs) and modulated on optical carrier from the laser (central wavelength = 1552.52 nm, i.e., central frequency = 193.1 THz) with an optical I/Q modulator. The laser power and linewidth are set to 1 mW and 100 kHz, respectively. The optical spectrum of the modulated signal is shown in the inset of Fig. 2 whose bandwidth is equal to chip rate (20 Gchip/s) as the roll-off factor is 0.

The signal is transmitted over four spans, each of which consists of 100 km SSMF and an Erbium Doped Fiber Amplifier (EDFA) with a noise figure of 5 dB. The transmitted optical signals is detected by a coherent receiver. The optical-electrical (O-E) converted signal is sampled and digitalized by two analog-to-digital converters (ADCs). The outputs from ADCs are feed to the DSP blocks for signal recovery. Firstly, the chromatic dispersion is compensated in frequency domain and carrier phase is then estimated using Viterbi-Viterbi algorithm. The phase corrected signal is sent to the CDM decoder. Finally, the decoded signal is sliced and demapped to bits.

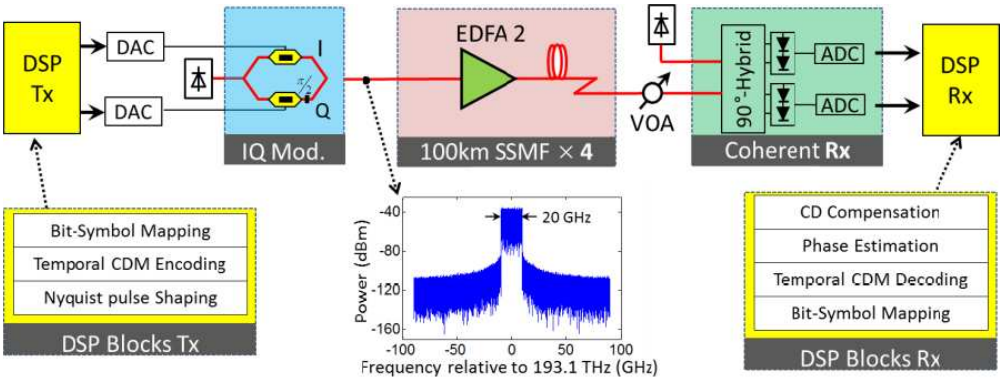

Figure 2: Simulation setup (inset: optical spectrum after Nyquist shaping).

3. RESULTS

Figure 3(a) shows the error vector magnitude (EVM) [7] of proposed Nyquist-OCDM system with respect to received OSNR (green triangle) in the back-to-back configuration The OSNR is measured with a spectral resolution of 0.1 nm. Compared with OCDM only system (red circle), no OSNR penalty is found due to Nyquist pulse shaping, which can be explained by the ISI free feature of Nyquist pulses in time-domain.

For OCDM based optical access networks the maximum number of users is limited by the power loss caused by power splitter in the remote node (RN). To emulate the such attenuation in simulation, a variable optical attenuator (VOA) is used after 400 km fiber but before the optical mixer at the receiver side to adjust the received optical power. The measured EVM versus additional attenuation is shown in Fig. 3(b). The measured EVM is 34.0% when the additional attenuation by VOA is 35 dB. The large link power budget mainly benefits from the coherent detection.

The impact of N_c and N_l is also studied. Three different scenarios: (i) $N_c = N_l = 128$; (ii) $N_c = 256$, $N_l = 128$; (iii) $N_c = 256$, $N_l = 256$ are evaluated. Fig. 4 shows the recovered signal constellations after transmission over 400 km SSMF Corresponding EVM (in percentage) is shown on the top of each constellation. Though orthogonal codes are employed in our system, the system's EVM is still slightly related to N_l and N_c. Although the SE achieves maximum when all orthogonal codes are used for coding ($N_l = N_c$) the system performs worst at the same time With the same code length (N_l) the peak to average power ratio of encoded signal increases for larger N_c, which degrades the system performance by interacting with fiber nonlinearity and component nonlinearity (e.g., nonlinear transfer function of optical modulator). With the same number of users (N_c), longer code length sacrifices the SE but helps to reduce the average power which relieves the fiber nonlinearity impact on the signal. These indicate that a tradeoff between SE and system performance has to be made when choosing N_l and N_c.

Our scheme also provides high secure transmission. The received data can only be recovered when the correct codes are provided for decoding. Furthermore, Nyquist-OCDM can combine with WDM technology to improve transmission capacity.

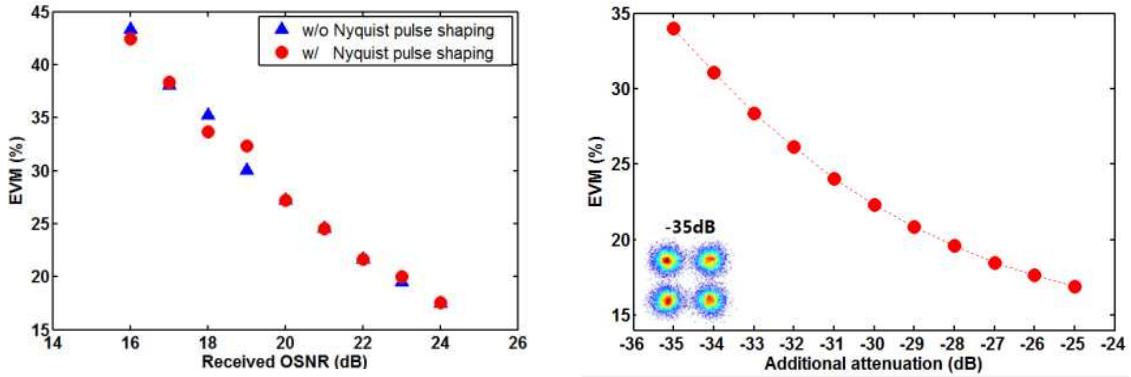

(a) (b)

Figure 3: (a) EVM vs received OSNR for Nyquist-OCDM (red) and OCDM only system (blue). (b) EVM vs link attenuation for Nyquist-OCDM system.

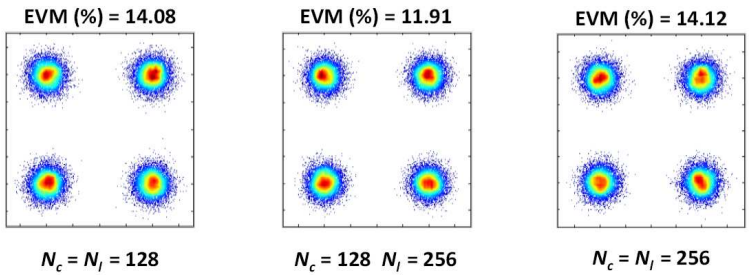

Figure 4: Recovered QPSK signal constellations after 400-km SSMF transmission.

4. CONCLUSION

In this paper, we proposed a high spectral efficiency temporal coded OCDM system using Nyquist pulse shaping and coherent detection. The maximal SE of Nyquist-OCDM system is at least two times of that of the traditional OCDM system. The transmission of Nyquist-OCDM system using Walsh codes over 400 km SSMF is evaluated by simulation. The system performance towards the number of users and code length are investigated, which showed that Nyquist-OCDM is a promising technology for optical access network.

ACKNOWLEDGMENT

This work is supported by the China Postdoctoral Science Foundation (No. 2013M531868), Guangdong Innovative Research Team Program (No. 201001D0104799318), 863 project (Ministry of Science and Technology of China, No. 2012AA012201), and the National Nature Science Foundation of China (No. 61107020).

REFERENCES

1. Ghafouri-Shiraz, H. and M. Massoud Karbassian, *Optical CDMA Networks: Principles, Analysis and Applications*, Wiley, New York, 2012.
2. Toliver, P., et al., "Demonstration of high spectral efficiency coherent OCDM using DQPSK, FEC, and integrated ring resonator-based spectral phase encoder/decoders," *Proceedings of OFC/NFOEC*, PDP 7, 2007.
3. Wang, Z. X., et al., "Secure optical transmission in a point-to-point link with encrypted CDMA codes," *IEEE Photonics Technology Letters*, Vol. 22, No. 19, 1410–1412, 2010.
4. Hong, X., et al., "Coherent detected secure point-to-point optical fiber transmission using ultra-dense optical spectral phase coding (UD-SPC) and multilevel BCJR equalization," *Proc. of Asia Communications and Photonics Conference*, ATh4C.3, 2012.
5. Schmogrow, R., M. Winter, et al., "Real-time Nyquist pulse generation beyond 100 Gbit/s and its relation to OFDM," *Optics Express*, Vol. 19, No. 1, 317–337, 2012.
6. Cartledge, J. C., J. D. Downie, et al., "Pulse shaping for 112 Gbit/s polarization multiplexed 16-QAM signals using a 21 GSa/s DAC," *Optics Express*, Vol. 19, No. 26, B628–B635, 2011.
7. Schmogrow, R., B. Nebendahl, et al., "Error vector magnitude as a performance measure for advanced modulation formats," *IEEE Photonics Technology Letters*, Vol. 24, No. 1, 61–63, 2012.

Sub-symbol Based Carrier Phase Recovery in CO-OFDM System with Linear Interpolation

Xiaojian Hong, Xuezhi Hong, and Sailing He
ZJU-SCNU Joint Research Center of Photonics
South China Normal University (SCNU), Guangzhou 510006, China

Abstract— A novel optical carrier phase recovery algorithm using phase linear interpolation and sub-symbol processing is proposed for CO-OFDM system. Compared with the conventional carrier phase recovery approach, the new algorithm can promote the system's laser linewidth tolerance significantly with increased temporal resolution in tracking the carrier phase.

1. INTRODUCTION

Coherent optical orthogonal frequency division multiplexing (CO-OFDM) has been intensively studied for its high tolerance to chromatic dispersion (CD) and polarization mode dispersion (PMD) [1–3]. However, the performance degradation caused by laser phase noise is more pronounced in CO-OFDM system compared with the single carrier counterpart. In CO-OFDM system, laser phase noise degrades the received signal quality in two ways: the common phase error (CPE) and the inter-carrier-interference (ICI). The former one causes an identical phase rotation for all subcarriers while the latter one induces frequency dependent noise for each subcarrier channel. To suppress these distortions, pilot subcarrier aided (PA) carrier phase recovery technique is widely applied because of its simplicity [2–5]. In PA CPE compensation (CPEC) scheme [2, 3], symbol rotation is corrected while the ICI is left uncompensated as laser phase noise is assumed to be constant in one CO-OFDM symbol. However, for relatively large laser linewidth and/or long symbol duration scenarios, the degradation due to ICI becomes pronounced and need to be compensated. In [4, 5], partial ICI suppression is achieved by temporal linear interpolation (LI) of CPE in the adjacent symbols. In [6], frequency domain orthogonal basis expansion-based method (OBE) has been proposed to suppress both CPE and partial ICI, in which complex matrix inversion operation is needed.

To improve the ICI tolerance of CO-OFDM system, we proposed a carrier phase recovery method based on sub-symbol processing in our former paper [7], in which a full CO-OFDM symbol is temporally partitioned into several blocks (i.e., sub-symbols) to obtain a high temporal resolution of carrier phase recovery. In this paper, we propose a novel carrier phase recovery algorithm based on linear interpolation and sub-symbol processing. By combining the above two ingredients, a better tracking of the carrier phase can be achieved with the new algorithm compared to the former one [7]. The principle and feasibility of our proposal are shown in the following sections. Performance evaluation and key parameter optimization are conducted with Monte-Carlo simulation.

2. PROPOSED CARRIER PHASE RECOVERY SCHEME

2.1. PSystem Model and Notation

The schematic diagram of our proposed algorithm is depicted in Fig. 1. The nth element of the mth vector is denoted by x_n^m/X_n^m in time/frequency domain, respectively. The signal model in the presence of phase noise is studied in [2]. At the nth signal sample of the mth OFDM symbol, laser phase noise introduces a random phase rotation of $e^{j\phi_n^m}$ in the time domain where $\phi_n^m = \phi_{n-1}^m + u$ and $u \sim N\ (0, \sigma_u^2)$. The phase noise variance is $\sigma_u^2 = 2\pi\beta T_s$ where T_s is the CO-OFDM symbol duration, β is the two-side 3-dB bandwidth of the laser phase noise.

After coherent detection, the phase noise of the free-running lasers at the transmitter and the receiver is linearly transferred from optical domain to electrical domain. The O/E converted signal is sampled and digitalized by the analog-to-digital converter (ADC). Several digital signal processing (DSP) functions are then executed to recover the transmitted data. Firstly, the cyclic prefix (CP) of signal is removed and frequency offset is compensated digitally. The signal is then converted to frequency domain by fast Fourier transform (FFT). The effect of phase noise on CO-OFDM system after frequency offset compensation can be expressed as a convolution in the frequency domain.

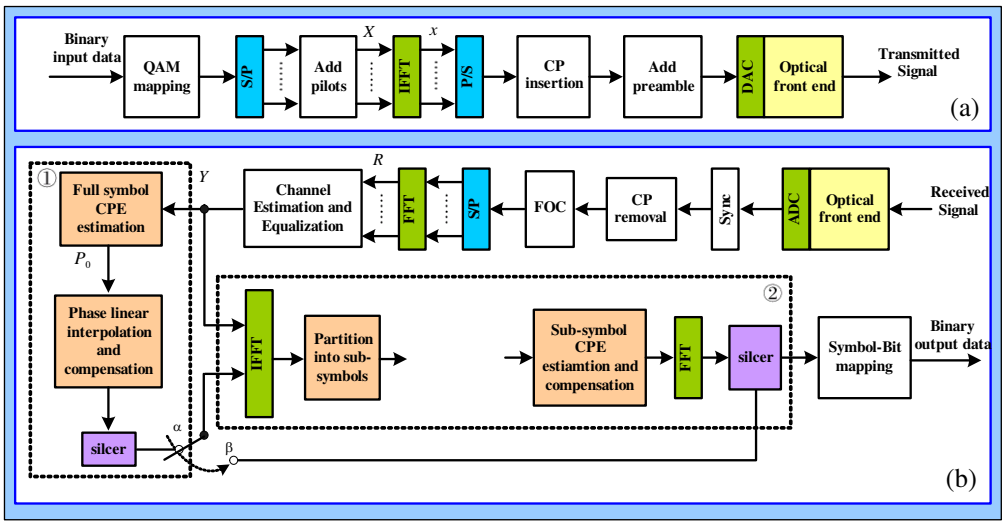

Figure 1: Schematic diagram of CO-OFDM, (a) transmitter and (b) receiver with proposed phase noise suppression algorithm. S/P: serial-to-parallel conversion; P/S: parallel-to-serial conversion; Sync: synchronization. FOC: frequency offset compensation.

Assuming that both timing synchronization and frequency tracking are perfectly performed, the received signal R can be expressed as [5]:

$$R_k^m = \sum_{q=0}^{N-1} P_{\langle k-q\rangle}^m H_q X_q^m + W_k^m = P_0^m H_k X_k^m + \sum_{q=0, q\neq k}^{N-1} P_{\langle k-q\rangle}^m H_q X_q^m + W_k^m : 0 \le k \le N-1 \quad (1)$$

where N is the number of subcarriers, X, P, H and R are the transmitted data symbol, the phase noise spectral components, the channel frequency response and the received data symbol in frequency-domain, respectively. The notation $\langle\cdot\rangle$ denotes the modulo-N operation and W is the additive Gaussian distributed noise with zero mean and variance σ_u^2. The kth phase noise spectral component of the mth symbol P_k^m, can be written as:

$$P_k^m = \frac{1}{N}\sum_{n=0}^{N-1} e^{j\phi_n^m} \exp\left(-\frac{j2\pi nk}{N}\right) : 0 \le k \le N-1. \quad (2)$$

As seen in (1), the first part P_0^m is the common term influencing all subcarriers, therefore, representing the CPE contribution. The second part $\sum_{q=0, q\neq k}^{N-1} P_{\langle k-q\rangle}^m H_q X_q^m$ stands for the contribution of ICI.

2.2. Carrier Phase Recovery Algorithm

After channel estimation and equalization, two types of processes are performed: one is the 'full symbol linearly interpolated carrier phase estimation process' and the other one is the 'sub-symbol phase noise suppression process'. The second process can be executed iteratively until a predetermined number of iteration is completed to obtain a better phase noise suppression effect.

In the first process, the pilot subcarriers are used to estimate the CPE in every full OFDM data symbol. The least-squares (LS) algorithm can be used to estimate CPE as follow:

$$CPE^m = angle(P_0^m) = angle\left\{\frac{\sum_{k\in S_p}(X_k^m)^* Y_k^m}{\sum_{k\in S_p}\left|X_k^m\right|^2}\right\} \quad (3)$$

where S_p is the set of the subcarriers indices corresponding to the pilot subcarriers.

The carrier phase at the middle of the corresponding symbol is set equal to the estimated CPE. The carrier phase of the remaining intermediate temporal sample is obtained by linear interpolating the CPE estimation of the adjacent symbols. As can be seen from Fig. 2, the equalization of the

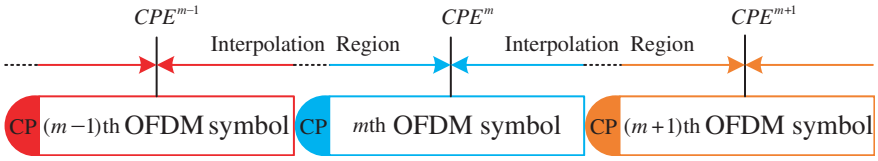

Figure 2: Diagram of phase linear interpolation with three adjacent CO-OFDM symbols.

mth received symbol can be completed only after reception of the $(m+1)$th symbol which results in one symbol latency.

The carrier phase is compensated coarsely using the interpolated estimation. After tentative decision on coarsely compensated samples, the second stage carrier phase recovery is processed. In the second stage, the output from the slicer $\hat{X}$ and channel equalized samples Y are converted back to time domain by using IFFT operation and then partitioned into several sub-symbols. After taking the normalized S-point FFT operation on the sub-symbol samples, sub-symbol CPE estimation is processed by comparing the phase of the "recovered" temporal samples $\hat{X}_k^b$ and the channel equalized temporal samples $\hat{Y}_k^b$ using LS algorithm.

$$\hat{P}_0^b = \frac{\sum_{k=0}^{S-1} (\hat{X}_k^b)^* \hat{Y}_k^b}{\sum_{k=0}^{S-1} \left|\hat{X}_k^b\right|^2} \tag{4}$$

where S is the length of the sub-symbol. The estimated sub-symbol CPE values are then used to update the carrier phase of every sample. Finally, the phase corrected data is decision and mapped from symbol to bits.

3. SIMULATION RESULTS AND DISCUSSIONS

The proposed algorithm is assessed through Monte-Carlo simulation. We use 'LI-SCPEC' to refer to the proposed algorithm. The parameters of simulated CO-OFDM system are as follows. The mapped 16-QAM signal is converted to time domain by 256-point IFFT. 40 guard sub-carriers are added and allocated at both side of the band. 10 pilots are uniformly inserted into each block. The CP length is 32. The sampling rate R_s is 10 GSamples/s. Thus the duration of OFDM symbol is 28.8 ns. Ideal frequency offset compensation and channel equalization are assumed in the simulation to obtain an accurate laser phase noise tolerance measurement.

The bit error rate (BER) versus optical signal to noise ratio (OSNR) curves using different algorithms for 250 kHz laser linewidth are show in Fig. 3(a). At 20 dB OSNR, the BER of LI-SCPEC ($N_B = 1$), LI-SCPEC ($N_B = 2$) and LI-SCPEC ($N_B = 4$) are 4.17e-4, 6.4e-5 and 4.85e-5, respectively, which show that the performance improvement increases as N_B from 1 to 2, 4. When comparing with the full symbol decision-feedback algorithm (DF-CPEC) which have a comparable complexity, the corresponding sub-symbol algorithm offer 2.06 dB ($N_B = 2$) and 2.36 dB ($N_B = 4$) OSNR gain at BER = 1.0e-3.

In Fig. 3(b), we compare the required OSNR at BER = 1.0e-3 as a function of combined laser linewidth. For comparison, the performance of CPEC algorithm in [2], LI algorithm in [5] and previous sub-symbol algorithm SCPEC in [7] are also show in Fig. 3(b). The laser linewidth tolerance is evidently improved by the LI-SCPEC algorithm. For laser linewidth of 250 kHz, the required OSNR of CPEC, LI, DF-CPEC, SCPEC ($N_B = 2$) are 24.1 dB, 20.38 dB, 18.69 dB and 17.57 dB, while 16.63 dB for LI-SCPEC ($N_B = 2$). The advantage of LI-SCPEC method tends to be larger when the laser linewidth increases. For OSNR = 20 dB, the system's laser linewidth tolerance is about 154 kHz (CPEC), 230 kHz (LI), 298 kHz (DF-CPEC), 382 kHz (SCPEC, $N_B = 2$) and 541 kHz (LI-SCPEC, $N_B = 2$). Thus, LI-SCPEC algorithm promotes system tolerance of laser phase noise evidently.

The contour plot of the receiver sensitivity (in OSNR) penalty at BER = 1.0e-3 are depicted in Fig. 4(a) for LI-SCPEC with respect to different laser linewidth ($0 \sim 345$ kHz) and different number of sub-symbols N_B ($1 \leq N_B \leq 6$). The reference is the OSNR at BER = 1.0e-3 in ideal coherent detection with perfect carrier phase recovery. For a certain range ($0 \sim 200$ kHz), there exist an optimal number of sub-symbol. The OSNR penalty drops with increasing number of sub-symbols (≤ 6) if the linewidth > 250 kHz. A few number of sub-symbols (≤ 4) is sufficient to obtain a

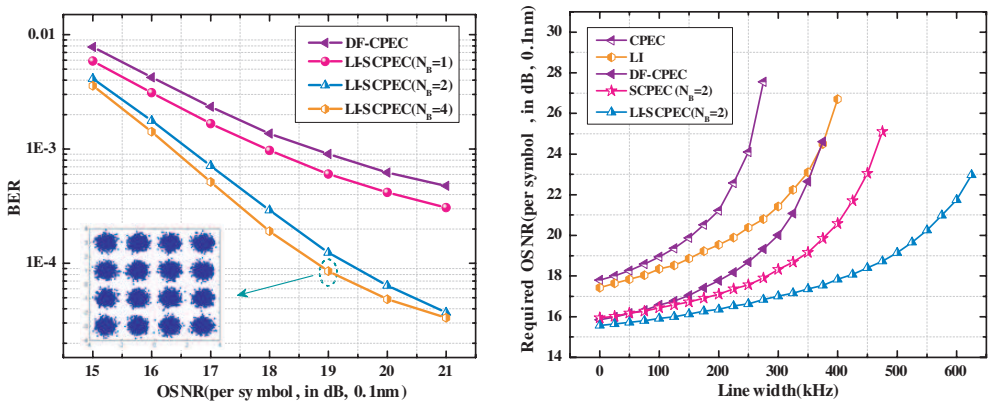

Figure 3: (a) BER performance in B2B case for laser linewidth = 250 kHz, inset shows the corresponding constellation, (b) required OSNR at BER =1.0e-3 with different carrier phase recovery algorithms.

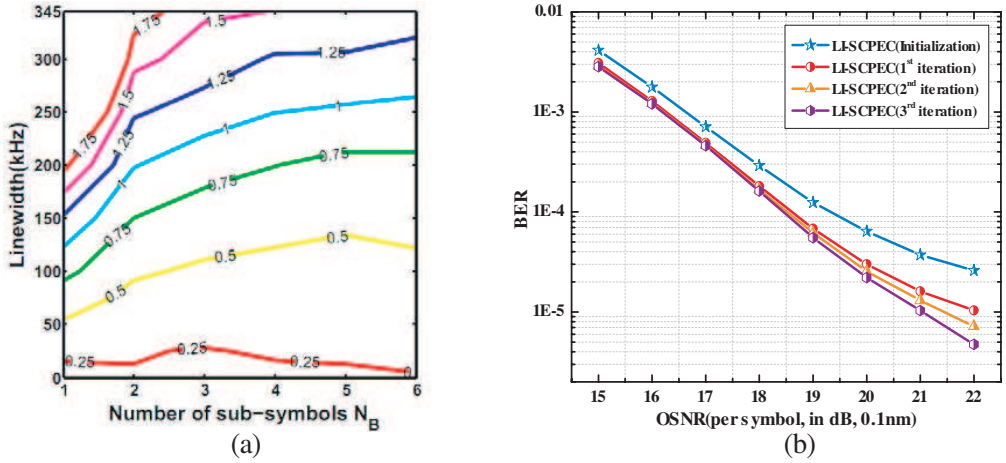

Figure 4: (a) Receiver sensitivity penalty at 1.0e-3 versus the different laser linewidth and different number of sub-symbols NB, (b) BER versus OSNR curves for the proposed carrier phase recovery algorithm after iteration.

moderate OSNR penalty ($\leq$ 1.5 dB) for a large interval of laser linewidth (0 $\sim$ 345 kHz), which relieves the complexity requirement of our algorithm.

The BER performance of proposed algorithm after iteration is shown in Fig. 4(b). The performance of CO-OFDM system (linewidth = 250 kHz, N_B = 2) is improved by iteration. The iteration gain at BER = 1.0e-3 is 0.365 dB, 0.418 dB, 0.431 dB for number of iteration = 1, 2 and 3, respectively. Note that the curves almost converge after the first time of iteration, which implies that the number of iteration = 1 is enough to obtain a reasonable improvement.

4. CONCLUSION

In this paper, we propose a novel carrier phase recovery method based on linear interpolation and sub-symbol processing. The accuracy of sub-symbol carrier phase estimation is improved by linear interpolation. The effectiveness of proposed method is evaluated by simulation which shows that the system's laser linewidth tolerance can be enhanced significantly. The optimized performance of the algorithm can be achieved with a moderate number of sub-symbols and a small number of iteration.

ACKNOWLEDGMENT

This work is supported by the China Postdoctoral Science Foundation (No. 2013M531868), Guangdong Innovative Research Team Program (No. 201001D0104799318) and Young Faculty Research Fund of SCNU (No. 13KJ04).

REFERENCES

1. Shieh, W. and I. Djordjevic, *OFDM for Optical Communications*, ELSEVIER, USA, 2009.
2. Yi, X., W. Shieh and Y. Ma, "Phase noise effect on high spectral efficiency coherent optical OFDM transmission," *IEEE Journal of Lightwave Technology*, Vol. 26, No. 10, 1309–1316, 2008.
3. Yi, X., W. Shieh, and Y. Tang, "Phase estimation for coherent optical OFDM," *IEEE Photonics Technology Letters*, Vol. 19, No. 12, 919–921, 2007.
4. Rabiei, P., W. Namgoong and N. Al-Dhahir, "A non-iterative technique for phase noise ICI mitigation in packet-based OFDM systmes," *IEEE Transactions on Signal Processing*, Vol. 58, No. 11, 5945–5950, 2010.
5. Mousa-Pasandi, M. E. and D. V. Plant, "Non-iterative interpolation-based partial phase noise ICI mitigation for CO-OFDM transport systems," *IEEE Photonics Technology Letters*, Vol. 23, No. 21, 1594–1596, 2011.
6. Fang, X., C. Yang, T. Zhang, and F. Zhang, "Orthogonal basis expansion-based phase noise suppression for PDM CO-OFDM system," *IEEE Photonics Technology Letters*, Vol. 26, No. 4, 376–379, 2014.
7. Hong, X. and S. He, "Sub-frame carrier phase estimation for coherent optical orthogonal frequency multiplexing system," *Progress In Electromagnetics Research Symposium Abstracts*, 314–315, Stockholm, Sweden, August 314-315, 2013.

30×100 GHz Digitally Wavelength Switchable V-coupled-cavity Laser with Cleaved Facets

Yuan Zhuang, Xin Zhang, and Jian-Jun He
State Key Laboratory of Modern Optical Instrumentation, Centre for Integrated Optoelectronics
Department of Optical Engineering, Zhejiang University, Hangzhou 310027, China

Abstract— We present some latest results on the V-coupled-cavity laser (VCCL) with cleaved facets. Over 30 channels with 100 GHz spacing and side-mode-suppression-ratio over 30 dB are achieved with single electrode tuning. The fabrication process is the same as that of a Fabry-Perot laser and the device size is only 500 μm × 300 μm.

1. INTRODUCTION

Widely tunable lasers are of vital importance for the modern optical communication systems. With the development of dense wavelength division multiplexing (DWDM) systems, tunable lasers are required to have large wavelength tuning range, large side-mode-suppression-ratio, low cost and low manufacture complexity. Over the decades, many tunable lasers are invented, such as sampled grating distributed Bragg reflector (SGDBR) laser [1], superstructure grating (SSG) DBR laser [2], distributed feedback (DFB) laser array with micro-electro-mechanical system (MEMS) switches [3], wavelength switchable semiconductor laser based on half-wave coupled Fabry-Pérot and rectangular ring resonators [4], and V-coupled-cavity laser with etched facets [5]. However, the former three kinds of lasers not only require complicated fabrication process for gratings, but also use multiple electrodes to control the wavelength tuning effect, which adds to the overall cost. And the latter two lasers require a deep-etch fabrication step to form the reflection facets.

Coupled-cavity lasers with an etched trench or cleaved-coupled-cavity (C^3) structure have been investigated in the 1980's. While the theory of such a coupled-cavity is well established and fabricating it needs no epitaxial regrowth, the SMSR of coupled-cavity laser is very poor (about 20 dB). Recently we developed a simpler design of V-coupled-cavity laser with cleaved facets, emitting 30 channels wavelength with a side-mode-suppression-ratio (SMSR) around 30 dB. Such a simple, compact and high-performance laser is a promising alternative to the existing tunable lasers and has great potential for wide use in optical networks.

2. DEVICE STRUCTURE AND FABRICATION

The V-coupled-cavity laser comprises a fixed gain cavity and a channel selector cavity with different optical path length and a 2×2 half-wave coupler, as shown in Fig. 1. The 2×2 half-wave coupler is designed to have an optimal coupling coefficient to ensure high side-mode suppression ratio (SMSR). Unlike normal multimode interference (MMI), the cross-coupling coefficient of the half-wave coupler has a relative phase of π with respect to self-coupling coefficient. The length of the fixed gain cavity is designed to be 466 μm, so that the resonance frequency spacing is 100 GHz as defined by ITU. The length of the channel selector cavity is 512 μm, a little longer than that of the fixed gain cavity so that the wavelength tuning range can be magnified by the Vernier effect. Three electrodes are deposited on the top surface, and a ground electrode is deposited on the back side. The wavelength tuning is accomplished by changing the current on the electrode of the channel selector cavity.

The principle of digital wavelength tuning is schematically shown in Fig. 2. Δf stands for the frequency interval of resonant modes in the fixed gain cavity, and $\Delta f'$ stands for the frequency interval of resonant modes in the channel selector cavity. The lasing mode occurs at a resonant frequency f_0. By shifting the resonant frequency comb of the channel selector cavity by $|\Delta f - \Delta f'|$, the lasing mode can be swiched to an adjacent mode of the fixed cavity. As a result, the shift of the laser frequency with the averaged effective refractive index change of the channel selector cavity is amplified by a factor of $\Delta f'/|\Delta f - \Delta f'|$ and only a single electrode is required for the wavelength switching. The distance between two aligned resonant peaks are called the free spectral range (FSR) of the coupled-cavity.

A standard ridge waveguide laser structure with InGaAsP/InP multiple quantum wells (MQW) was used to fabricate the laser. The MQW structure was grown by metal-organic chemical vapor deposition. It consists of 0.2 μm Zn-doped In0.53Ga0.47As cap, 1.5 μm Zn-doped InP cladding,

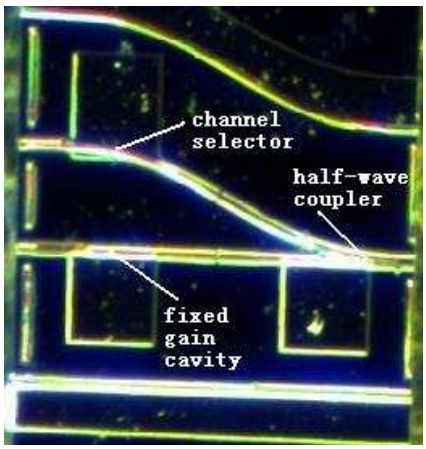

Figure 1: Optical microscope image of the V-coupled-cavity laser.

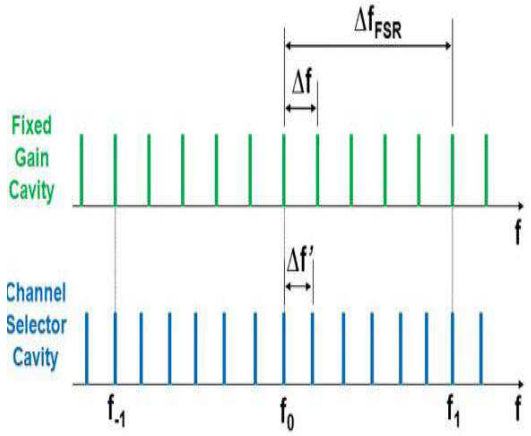

Figure 2: Schematic diagram illustrating the relationships between the resonant frequency combs of the two cavities.

0.004 µm Zn-doped InGaAsP etch-stop layer, 0.15 µm Zn-doped InP cladding, 0.06 µm InGaAsP step-graded index separate confinement layers with the bandgap wavelength λ_g varying from 1.05 µm to 1.25 µm, five repeats of 5.5 nm undoped 1.2% compressively strained InGaAsP quantum well and 10 nm InGaAsP barrier (λ_g = 1.25 µm), 0.06 µm InGaAsP step-graded index separate confinement layers, and 1.5 µm Si-doped InP buffer on n-doped InP substrate. The measured photoluminescence peak wavelength is at about 1.55 µm. It is an all-active device with no grating or ring resonators, and therefore it does not require any epitaxial regrowth. The fabrication process is similar to simple Fabry-Perot lasers and the device length is less than 0.5 mm.

3. MEASUREMENT RESULTS

The fabrication process is the same as that of a Fabry-Perot laser. First, the wafer was cleaved into bars, then the lasers were tested on an aluminum nitride (AlN) with a thermo-electric cooler (TEC) controlled at 20°C. The currents injected on the half-wave coupler and fixed-gain cavity are 50 mA and 30 mA, respectively. Fig. 3 shows the wavelength of the main mode as a function of the tuning current on the channel selector cavity. When the current on the channel selector increases from 18 mA to 145 mA, the wavelength tuning is about 25 nm and the lasing wavelength is switched digitally over 33 consecutive channels.

Figure 4 shows the spectrum of the laser when the current on the channel selector was 30 mA. It shows a single-mode emission spectrum with SMSR of 33 dB. Fig. 5 shows the overlapped spectra for all of the 30 channels. The SMSR are around 30 dB for all the channels. The SMSR can be further improved by design optimization and fabrication improvement.

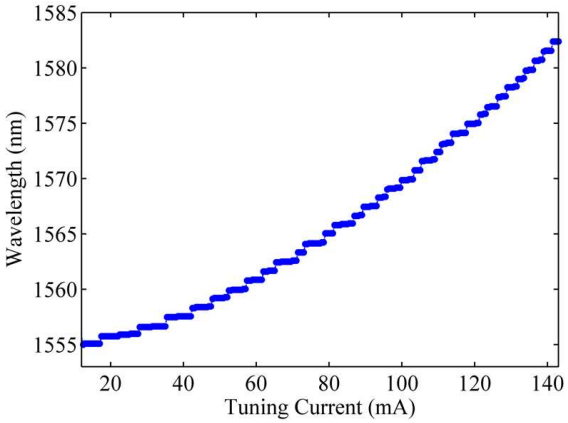

Figure 3: Measured digital wavelength tuning curve.

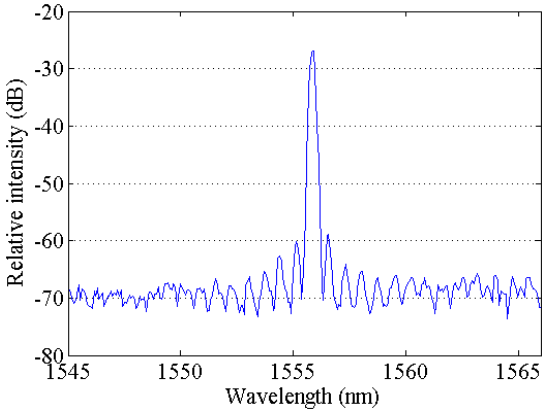

Figure 4: Measured single channel spectrum.

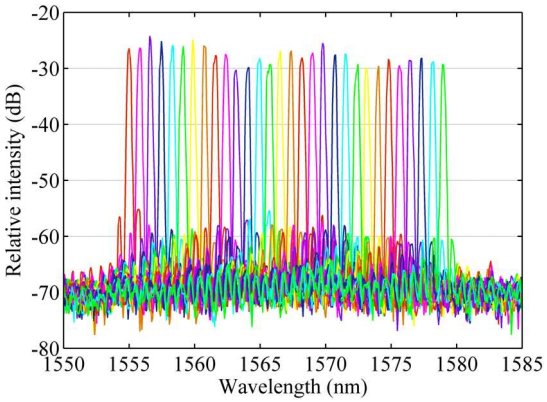

Figure 5: Overlapped 30-channel spectra.

4. CONCLUSIONS

Single-electrode-controlled 30×100 GHz wavelength switchable V-coupled-cavity laser with cleaved facets is demonstrated with a SMSR as high as 30 dB. It is compact, easy to be fabricated, and allows the lasing wavelength to be switched over a wide range with a single electrode control. The fabrication process is exactly the same as that of Fabry-Perot laser, thus it does not require complex gratings, epitaxial regrowth and deep-etched reflection facets. Since the device size is comparable to conventional DFB or Fabry-Perot lasers, it can be easily fit into a small-form-factor package. Because of its advantages, V-coupled-cavity laser with cleaved facets can be used for practical applications in optical networks.

ACKNOWLEDGMENT

This work was funded by the National High-Tech R&D Program of China (grant No. 2013AA014401), and the National Natural Science Foundation of China (grant No. 61377038).

REFERENCES

1. Coldren, L. A., "Monolithic tunable diode lasers," Selected Topics in *Quantum Electronics*, Vol. 6, No. 6, 988–999, 2000.
2. Tohmori, Y., Y. Yoshikuni, H. Ishii, et al., "Broad-range wavelength-tunable superstructure grating (SSG) DBR lasers," *Quantum Electronics*, Vol. 29, No. 6, 1817–1823, 1993.
3. Pezeshki, B., E. Vail, J. Kubicky, et al., "20-mW widely tunable laser module using DFB array and MEMS selection," *Photonics Technology Letters*, Vol. 14, No. 10, 1457–1459, 2002.
4. Wu, L., Y. Wang, T. Yu, et al., "Wavelength switchable semiconductor laser based on half-wave coupled Fabry-Pérot and rectangular ring resonators," *Photonics Technology Letters*, Vol. 24, No. 12, 991–993, 2012.
5. Jin, J., L. Wang, T. Yu, et al., "Widely wavelength switchable V-coupled-cavity semiconductor laser with 40 dB side-mode suppression ratio," *Optics Letters*, Vol. 36, No. 21, 4230–4232, 2011.

Radiation of Inverted Pendulum with Hysteretic Nonlinearity

Mikhail E. Semenov[1, 2, 3], **Peter A. Meleshenko**[1, 2],
Hang T. T. Nguyen[4], **Alexander F. Klinskikh**[2], **and Anton G. Rukavitcyn**[2]

[1]Zhukovsky-Gagarin Air Force Academy, Russia
[2]Voronezh State University, Russia
[3]Voronezh State University of Architecture and Civil Engineering, Russia
[4]Institute of Technology, Vietnam National University — Ho Chi Minh City, Vietnam

Abstract— In this work we investigate the radiation of the charged inverted pendulum with a hysteretic nonlinearity in the form of a backlash in the suspension point. The radiated power is obtained in the frame of dipole approach. Due to the presence of hysteretic nonlinearity there are some interesting peculiarities take place, in particular, our numerical simulation shows that the radiated power turns in to zero during the hysteretic nonlinearity acts. This fact opens a new way for control of the inverted pendulum's dynamics.

1. INTRODUCTION

The problem of the inverted pendulum has a long history [1, 2] and remains relevant even in the present days [3–5]. As well known the model of the inverted pendulum plays the central role in the control theory [6–11]. It is well established benchmark problem that provides many challenging problems to control design. Because of their nonlinear nature pendulums have maintained their usefulness and they are now used to illustrate many of the ideas emerging in the field of nonlinear control [12]. Typical examples are feedback stabilization, variable structure control, passivity based control, back-stepping and forwarding, nonlinear observers, friction compensation, and nonlinear model reduction. The challenges of control made the inverted pendulum systems a classic tools in control laboratories.

In order to make an adequately description of the dynamics of real physical and mechanical systems it is necessary to take into account the effects of hysteretic nature such as "backlashes", "stops", etc. The mathematical models of such nonlinearities according to the classical patterns of Krasnosel'skii and Pokrovskii [13], reduce to operators that are treated as converters in an appropriate function spaces. The dynamics of such converters are described by the relation of "input-state" and "state-output".

As is known, most of the real physical and technical systems contain a various kind of parts that can be represented as a cylinder with a piston. Inevitably, the backlashes appear in such systems during its long operation due to the "aging" of the materials. As was mentioned above such backlashes are of hysteretic nature and the analysis of such nonlinearities is quiet important and actual problem. Also we would like to note that, for our knowledge, the problem of charged inverted pendulum was not considered in the literature. In this way the problem of stabilization of inverted pendulum using, e.g., an electrical field, seems novel and promisingly.

2. INVERTED PENDULUM WITH HYSTERETIC NONLINEARITY IN SUSPENSION: MATHEMATICAL MODEL

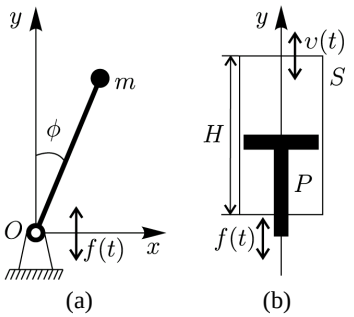

Figure 1: Geometry of the problem. (a) General view of the inverted pendulum. (b) The suspension point (cylinder and piston).

The model of inverted pendulum with oscillating suspension point (see panel a in Fig. 1) was studied in detail by Kapitza [2]. Let us recall that the equation of motion of pendulum has the form:

$$\ddot{\phi} - \frac{1}{l}[g + \ddot{f}(t)]\sin\phi = 0 \tag{1}$$

where ϕ is the angle of vertical deviation of the pendulum, l is the pendulum's length, g is the gravitational acceleration and $f(t)$ is the law of motion of the suspension point (of course, this equation should be considered together with the corresponding initial conditions).

Let us consider a system where the base of the pendulum is a physical system (P, S) formed by a cylinder of length H and the piston P[1]. We determine the piston's position by the coordinate $f(t)$ and the cylinder's position by coordinate $\upsilon(t)$. Let us assume also that the "leading" element in the system (P, S) is a cylinder P. In this assumption the system (P, S) can be considered as a converter Γ with the input signal $f(t)$ (piston's position) and the output signal $\upsilon(t)$ (cylinder's position). Such a converter is called *backlash*. The set of its possible states is $f(t) \le \upsilon(t) \le f(t)+H$ $(-\infty < f(t) < \infty)$. The cylinder's position $\upsilon(t)$ at $t > t_0$ is defined by $\upsilon(t) = \Gamma[t_0, \upsilon(t_0)]f(t)$, where $\Gamma[t_0, \upsilon(t_0)]$ is the operator defined for each $\upsilon_0 = \upsilon(t_0)$ on the set of continuous inputs $f(t)$ $(t > t_0)$ for which $\upsilon_0 - H < f(t) < \upsilon_0$ [13].

We assume that the piston's acceleration periodically changes from $-a\omega^2$ to $a\omega^2$ with the frequency ω. This assumption consists in the fact that the linearized equation of motion of such a pendulum can be written in the form[2]:

$$\begin{aligned} &\ddot{\phi} - \frac{1}{l}[g + a\omega^2 G(t, H)w(t)]\phi = 0, \\ &w(t) = -\mathrm{sign}[\sin(\omega t)], \\ &\phi(0) = \phi_{10},\ \dot{\phi}(0) = \phi_{20}, \end{aligned} \tag{2}$$

where $\mathrm{sign}(z)$ is the usual signum function, $G(t, H)w(t)$ is the acceleration of the suspension point and

$$G(t, H) = \begin{cases} 0, & t \in (t^*, t^* + \Delta t), \\ 1, & t \text{ out of } (t^*, t^* + \Delta t), \end{cases}$$

where t^* are the moments after which the acceleration's sign change takes place, $\Delta t = \sqrt{\frac{2H}{a\omega^2}}$ is the time for which the piston passes through the cylinder.

Let we pass to dimensionless units in (2) using the following change:

$$x \equiv \phi,\ \tau = \omega t,\ k = \frac{g}{l\omega^2},\ s = \frac{a}{l},\ \Delta\tau = \sqrt{\frac{2H}{sl}}.$$

As a result, we obtain an equation similar to Meissner equation, but with the negative coefficients and hysteretic nonlinearity, namely:

$$\begin{aligned} &\ddot{x} - [k - sG(\tau, H)\mathrm{sign}(\sin\tau)]x = 0, \\ &G(\tau, H) = \begin{cases} 0, & \tau \in (\tau^*, \tau^* + \Delta\tau), \\ 1, & \tau \text{ out of } (\tau^*, \tau^* + \Delta\tau), \end{cases} \\ &x(0) = x_{10},\ \dot{x}(0) = x_{20}, \end{aligned} \tag{3}$$

Using the monodromy matrix technique, based on the Floquet results, we can determine the

[1]Both the cylinder and piston are ideal, absolutely rigid and can move along the y-axis in the infinite ranges as it is shown in panel b of the Fig. 1.

[2]It should also be pointed out that such a periodic behavior of the piston's acceleration (namely, the fact that the acceleration of the piston changes from $-a\omega^2$ to $a\omega^2$) is an assumption of the model presented in this paper. Such a model allows us to obtain some analytical results, namely, the explicit conditions for the stability zones. Also, the numerical simulations are most effectively in the frame of this model. Moreover, such a model of the piston's behavior most effectively and adequately describes the dynamics of the parts of real technical devices.

zones of stabilization for the system under consideration (for details see [5]), namely:

$$\Big|\cos(k_2\gamma)\left[2\cosh(2\sqrt{k}\Delta\tau)\cosh(k_1\gamma)+\sinh(2\sqrt{k}\Delta\tau)\sinh(k_1\gamma)\left(\frac{\sqrt{k}}{k_1}+\frac{k_1}{\sqrt{k}}\right)\right]$$
$$+\sin(k_2\gamma)\left[\sinh(2\sqrt{k}\Delta\tau)\cosh(k_1\gamma)\left(\frac{\sqrt{k}}{k_2}-\frac{k_2}{\sqrt{k}}\right)+\cosh^2(\sqrt{k}\Delta\tau)\sinh(k_1\gamma)\left(\frac{k_1}{k_2}-\frac{k_2}{k_1}\right)\right.$$
$$\left.+\sinh^2(\sqrt{k}\Delta\tau)\sinh(k_1\gamma)\left(\frac{k}{k_1k_2}-\frac{k_1k_2}{k}\right)\right]\Big|<2. \tag{4}$$

Here $(k_1)^2=k+s$, $(k_2)^2=s-k$ $(s>k)$, $\gamma=\pi-\Delta\tau$. Thus, the *stability zone* of the system (3) in the space of parameters is defined by the inequality (4).

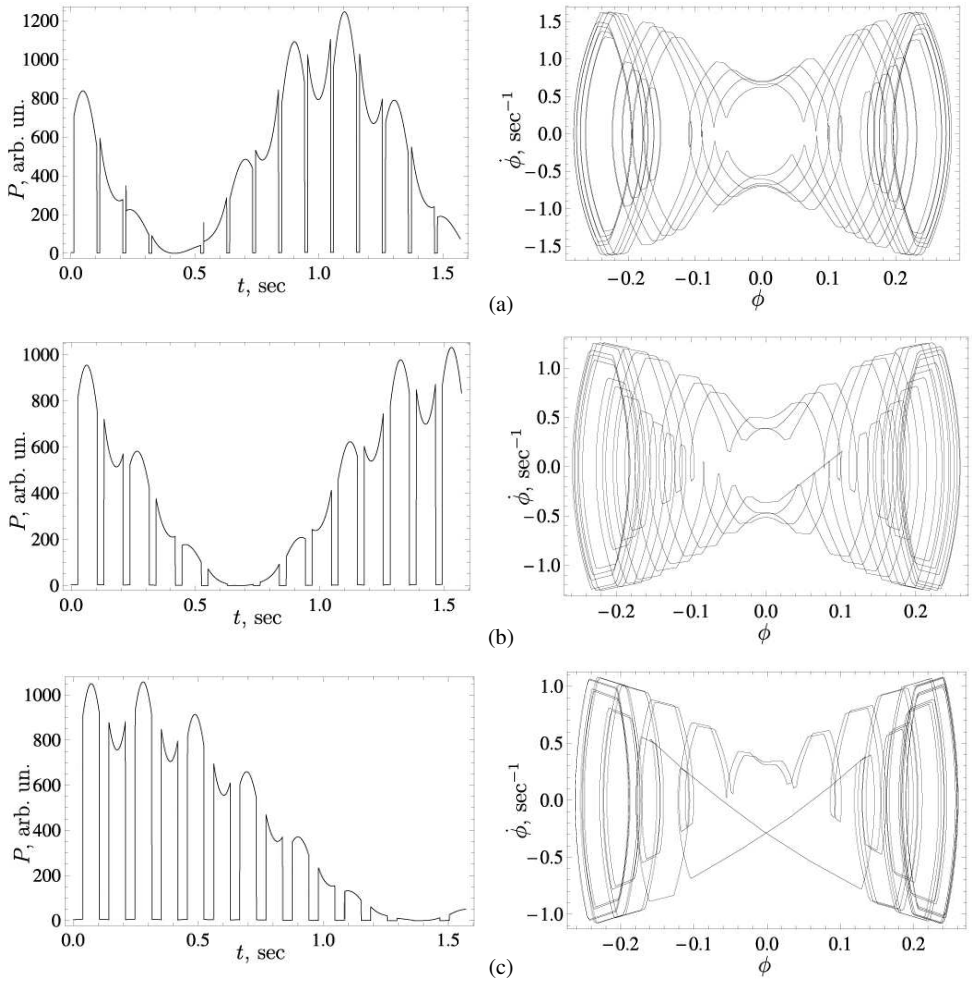

Figure 2: Radiated power P (per arbitrary units) as a function of time and phase portrait of inverted pendulum with the hysteretic nonlinearity in suspension for various values of hysteretic parameter H (another parameters of the system under consideration are presented in the main text). (a): $H=0.01\,\mathrm{m}$; (b): $H=0.05\,\mathrm{m}$; (c): $H=0.1\,\mathrm{m}$.

3. RADIATION OF INVERTED PENDULUM WITH HYSTERETIC NONLINEARITY

Consistent numerical solution of the Equation (3) allows us to determine the law of motion $\phi(t)$. Let us assume also that the pendulum is charged (the charge of a pendulum is q). Following the ideology of classical electrodynamics this fact means that the system under consideration can be considered as a source of electromagnetic radiation (because of non zero acceleration). Namely, the radiated power in the dipole approach can be written in the standard manner [14] (of course, for such a system the dipole momentum is non zero and, as a result, the dipole radiation takes place):

$$P=\frac{2}{3c^3}|\ddot{d}(t)|^2=\frac{2q^2l^2}{3c^3}|\ddot{\phi}(t)|^2, \tag{5}$$

where $d(t) = ql\phi(t)$ is a dipole momentum of a pendulum (as usual, double dot denotes the second derivative), c is the speed of light.

In the Fig. 2, we present the results of numerical simulations for the radiated power (per arbitrary units, namely we present the value of $\frac{3c^3P}{2q^2l^2}$) togeteher with the corresponding phase portrait at various values of hysteretic parameter H. The parameters of pendulum are: $l = 1\,\mathrm{m}$, $g = 9.8\,\mathrm{m}\cdot\mathrm{sec}^{-2}$; the amplitude and frequency of oscillation of the piston are $a = 0.15\,\mathrm{m}$ and $\omega = 30\,\mathrm{sec}^{-1}$, respectively; the initial conditions are $\phi(0) = 0.2$ and $\dot{\phi}(0) = 1\,\mathrm{sec}^{-1}$.

As we can see the presence of the hysteretic nonlinearity leads to the fact that the radiated power turns in to zero at some time moments. These moments exactly correspond to the time intervals during the hysteretic nonlinearity acts. In this way, this fact opens a new way for control of the inverted pendulum's dynamics, e.g., using the electrical field.

4. CONCLUSIONS

In this paper we have considered the problem of inverted pendulum with a hysteretic nonlinearity in the form of a backlash in suspension point. Namely, we have pointed out on the possibility to detecting of the electromagnetic radiation from the charged pendulum. Due to the presence of hysteretic nonlinearity there are some interesting results take place. In particular, our numerical simulations show that the radiated power turns in to zero at the time moments during the hysteretic nonlinearity acts. This fact opens a new way for control of the dynamics of inverted pendulum (e.g., using the electrical field or, in general, the fields with electromagnetic nature). Of course, the problem of stabilization of the inverted pendulum using an electrical field seems novel and promisingly.

REFERENCES

1. Stephenson, A., "On an induced stability," *Phil. Mag.*, Vol. 15, 233, 1908.
2. Kapitza, P. L., "Pendulum with a vibrating suspension," *Usp. Fiz. Nauk*, Vol. 44, 7–15, 1951 (in Russian).
3. Arinstein, A. and M. Gitterman, "Inverted spring pendulum driven by a periodic force: Linear versus nonlinear analysis," *Eur. J. Phys.*, Vol. 29, 385–392, 2008.
4. Butikov, E. I., "Oscillations of a simple pendulum with extremely large amplitudes," *Eur. J. Phys.*, Vol. 33, 1555–1563, 2012.
5. Semenov, M. E., D. V. Shevlyakova, and P. A. Meleshenko, "Inverted pendulum under hysteretic control: Stability zones and periodic solutions," *Nonlinear Dynam.*, Vol. 75, 247–256, 2014.
6. Mikheev, Y. V., Sobolev, V. A. and Fridman, E. M., "Asymptotic analysis of digital control systems," *Automat. Rem. Contr.*, Vol. 49, 1175–1180, 1988.
7. Chernous'ko, F. L. and S. A. Reshmin, "Time-optimal swing-up feedback control of a pendulum," *Nonlinear Dynam.*, Vol. 47, 65–73, 2007.
8. Sazhin, S., Shakked, T., Katoshevski, D. and Sobolev, V., "Particle grouping in oscillating flows," *Eur. J. Mech. B-Fluid.*, Vol. 27, 131–149, 2008.
9. Boubaker, O., "The inverted pendulum: A fundamental benchmark in control theory and robotics," *International Conference on Education and e-Learning Innovations (ICEELI 2012)*, 1–6, 2012.
10. Kim, K. D. and P. Kumar, "Real-time middleware for networked control systems and application to an unstable system," *IEEE Transactions on Control Systems Technology*, Vol. 21, 1898–1906, 2013.
11. Huang, J., et al., "Modeling and velocity control for a novel narrow vehicle based on mobile wheeled inverted pendulum," *IEEE Transactions on Control Systems Technology*, Vol. 21, 1607–1617, 2013.
12. Åström, K. J. and K. Furuta, "Swinging up a pendulum by energy control," *Automatica*, Vol. 36, 287–295, 2000.
13. Krasnosel'skii, M. A. and A. V. Pokrovskii, *Systems with Hysteresis*, Springer Verlag, New York, 1989.
14. Landau, L. D., E. M. Lifshitz, and L. P. Pitaevskii, *Electrodynamics of Continuous Media*, Vol. 8, 2nd Edition, Butterworth-Heinemann, Oxford, 1984.

Aharonov-Bohm Control of Optical Properties in System of Parallel Coupled Quantum Wells

Peter A. Meleshenko[1, 2], Hang T. T. Nguyen[3], and Alexander F. Klinskikh[2]

[1]Zhukovsky-Gagarin Air Force Academy, Voronezh, Russia
[2]Voronezh State University, Voronezh, Russia
[3]Institute of Technology, Vietnam National University — Ho Chi Minh City, Ho Chi Minh City, Vietnam

Abstract— In this paper we consider the system of parallel coupled identical one-dimensional quantum wells (such a system can be presented as a multi-arm quantum ring) with a given properties, namely, a width and a depth. Addition of the Aharonov-Bohm flux at origin of such a "ring of quantum wells" allows to change the distance between the bound states as well as their positions just only by changing the magnetic flux. Thereby, the Aharonov-Bohm flux can be considered as a "strong" driven parameter for the optical properties of the system under consideration.

1. INTRODUCTION

In recent time various one-dimensional (quantum wires, quantum rings [1] etc.) and two-dimensional systems (such as graphene [2]) have particular interest in connection with the development of low-dimensional technologies. In particular, such systems is widely used (or proposed to be used) in different fields, such as optics [3], spintronics [4], quantum interferometry [5] etc.. It should be noted that the charge transport process in such structures is of purely quantum nature. A special kind of such a low-dimensional systems are quantum interference devices (such as quantum graphs and quantum rings). Using these devices it is possible to observe the "delicate" quantum effects that are connected with the changes in the electron's wave function phase.

In this work we consider (our consideration is based on the scattering theory which allow to investigate not only the continuous spectrum of charge carriers, but also the discrete spectrum) the system of parallel coupled identical one-dimensional quantum wells (such a system can be considered as a multi-arm quantum ring). State of an electron in such a system has an interesting properties, namely, if one change the number of parallel coupled quantum wells the new bound states in such a system will not appear (as is known, when the quantum wells are arranged in series, i.e., the width of the resulting quantum well increases, there are many bound states in such a system and addition of new wells leads to increasing of the number of bound states) just only shift to the limiting value which determines by the parameters of a single well. In the case of quantum wells with two bound states we have the same result, however the distance between the bound states (it should be noted that the distance between the bound states corresponds to THz frequencies) decreases when the number of wells in a system increases. As a result, the characteristics of such a system, e.g., the optical properties (namely, the frequencies of laser transitions), can be changed by addition of new wells only. Addition of the Aharonov-Bohm flux at origin of such a "ring of quantum wells" allows to change the distance between the bound states as well as their positions just only by changing the magnetic flux. As a result, the Aharonov-Bohm flux can be considered as a "strong" driven parameter for the optical properties of the system under consideration.

2. MAIN FORMALISM

Most of the problems of one-dimensional quantum mechanics can be formulated in terms of quantum graphs. Moreover, the solution of these problems in the frame of the graphs formalism could be more efficient and "elegant" in comparison with the traditional methods of quantum mechanics. A simple and clear example which demonstrates the "elegancy" of the graphs formalism is the problem of the one-dimensional quantum well.

There are various ways to solve the Schrödinger equation in the graph [6–8]. In the presented work we use the *vertex amplitudes* method [9]. The main idea of this method is to express the parameters of the problem through the values of the wave function at the vertex of graph Ψ_1 and Ψ_2. The considered method allows to solve the scattering problem in the quantum graph, to find the energy spectrum and to construct the wave functions. The classical analog of the *vertex amplitudes* method is the Kirchhoff's nodal potentials method in the theory of electrical circuits.

Let us consider the one-dimensional scattering problem for a quantum graph with the potentials that are placed in the graph's edges. We assume that the quasi-one-dimensional dynamics takes place[1]. The considered quantum graph consists of a compact part connected with the reservoirs of the charge carries by the semi-infinite edges. We denote these edges as the *in, out*-edges. In this edges the asymptotic conditions for the electron wave functions with respect to the compact part of the graph are realized.

The wave functions of an electron in the *in, out*-edges are:

$$\psi_{in} = a_{in}\exp(ikx) + b_{in}\exp(-ikx), \tag{1}$$
$$\psi_{out} = a_{out}\exp(ikx) + b_{out}\exp(-ikx), \tag{2}$$

where k is the electron wave-number. As it follows from (1) and (2) the elastic scattering takes place. This assumption facilitates further mathematics.

In each edges γ_n of length l_{γ_n} the proper coordinates are used $\xi_{\gamma_n} \in [0, l_{\gamma_n}]$. In the *in, out*-edges coordinates are defined in a different way: $\xi_{in} \in (-\infty, 0)$, $\xi_{out} \in (0, \infty)$. These coordinates are just a natural parameter in differential geometry [10]. The electron wave function Ψ in the graph is represented by a set of components $\psi_{\gamma_n}(\xi_{\gamma_n})$, $n = 1, 2, \ldots, M$, where M is the number of edges in graph. Each element $\psi_{\gamma_n}(\xi_{\gamma_n})$ of the set is governed by the Schrödinger equation:

$$\begin{aligned} &H_{\gamma_n}\psi_{\gamma_n}(\xi_{\gamma_n}) = \varepsilon_{\gamma_n}\psi_{\gamma_n}(\xi_{\gamma_n}), \\ &H_{\gamma_n} = \left[-\frac{\hbar^2}{2}\frac{d}{d\xi_{\gamma_n}}\left(\frac{1}{m_{\gamma_n}}\frac{d}{d\xi_{\gamma_n}}\right) + V_{\gamma_n}(\xi_{\gamma_n})\right], \\ &D(H_{\gamma_n}) = \{\psi_{\gamma_n} : \psi_{\gamma_n} \in C_0^{\infty}[\gamma_n]\}, \end{aligned} \tag{3}$$

where m_{γ_n} is an effective mass of an electron in the edge γ_n, V_{γ_n} is the real and locally measurable potential placed in the edge γ_n.

Let us consider the edge γ_n with a potential which is localized somewhere in this edge. The wave function ψ_{γ_n} can be determined by the following pairs of coefficients: $(a_{\gamma_n}, b_{\gamma_n})$ and $(c_{\gamma_n}, d_{\gamma_n})$. They have the following meaning: the wave function in every edge outside the potential can be taken in the form $a\exp(ikx) + b\exp(-ikx)$, thereby, the pair $(a_{\gamma_n}, b_{\gamma_n})$ are the coefficients of ψ_{γ_n} before the potential and the pair $(c_{\gamma_n}, d_{\gamma_n})$ are the coefficients of ψ_{γ_n} beyond the potential.

An application of the continuity and hermiticity conditions leads to the system of linear algebraic equations for the *vertex amplitudes* $\mathbf{\Psi} = (\Psi_{in} \equiv \Psi_1, \Psi_2, \ldots, \Psi_{out} \equiv \Psi_n)^T$. This system contains the coefficients of functions ψ_{γ_n}. Hence to solve the obtained system for $\mathbf{\Psi}$ it is needed to express a_{γ_n}, b_{γ_n}, c_{γ_n} and d_{γ_n} in terms of $(\Psi_1, \Psi_2, \ldots, \Psi_n)$. In order to do this we use the following obvious relations:

$$\begin{pmatrix} a_{\gamma_n} \\ b_{\gamma_n} \end{pmatrix} = \mathbf{\Gamma}^{(1,\gamma_n)} \begin{pmatrix} \Psi_n \\ \Psi_{n+1} \end{pmatrix}, \quad \begin{pmatrix} c_{\gamma_n} \\ d_{\gamma_n} \end{pmatrix} = \mathbf{\Gamma}^{(2,\gamma_n)} \begin{pmatrix} \Psi_n \\ \Psi_{n+1} \end{pmatrix}. \tag{4}$$

The pairs of coefficients $(a_{\gamma_n}, b_{\gamma_n})$ and $(c_{\gamma_n}, d_{\gamma_n})$ are related by the transfer-matrix $\mathbf{M}$ [11]:

$$\begin{pmatrix} a_{\gamma_n} \\ b_{\gamma_n} \end{pmatrix} = \mathbf{M}^{(\gamma_n)} \begin{pmatrix} c_{\gamma_n} \\ d_{\gamma_n} \end{pmatrix}. \tag{5}$$

The elements of the $\mathbf{M}$-matrix are

$$\mathbf{M}^{(\gamma_n)} = \begin{pmatrix} 1/t_{\gamma_n} & r_{\gamma_n}/t_{\gamma_n} \\ r^*_{\gamma_n}/t^*_{\gamma_n} & 1/t^*_{\gamma_n} \end{pmatrix}, \tag{6}$$

$t_{\gamma_n}(r_{\gamma_n})$ is the transmission (reflection) amplitude for the potential placed in the edge γ_n. Using the relations (4), (5) and hermiticity condition one get:

$$\begin{aligned} &\mathbf{\Gamma}^{(1,\gamma_n)} = \frac{1}{\zeta - \zeta^*}\begin{pmatrix} \zeta & -1 \\ -\zeta^* & 1 \end{pmatrix}, \\ &\text{where} \quad \zeta = \exp(-ik\xi_{v_{n+1}})\mathrm{M}^{(\gamma_n)}_{11} - \exp(ik\xi_{v_{n+1}})\mathrm{M}^{(\gamma_n)}_{12}. \end{aligned} \tag{7}$$

[1]Let us note, that the quasi-one-dimensional dynamics may be realized in the lowest sub-band of a very narrow quantum wire. The wire width in the real experiments can not be infinitely narrow. But, for the quantum wire under low temperature the electron dynamics is quasi-one-dimensional because the higher transverse levels can not be excited.

From (4), (5) it follows

$$\mathbf{\Gamma}^{(2,\gamma_n)} = \left[\mathbf{M}^{(\gamma_n)}\right]^{-1} \mathbf{\Gamma}^{(1,\gamma_n)}. \tag{8}$$

Finally, (4), (7), (8) together with the hermiticity condition lead to the system of linear equation for unknown vector $\mathbf{\Psi}$. Finding the $\mathbf{\Psi}$ solves the transport problem for graph because the wave functions ψ_{in}, ψ_{out} satisfy the following conditions at the *in,out*-vertices:

$$1 + r(k) = \Psi_{in}, \quad t(k) = \Psi_{out}. \tag{9}$$

3. PARALLEL COUPLED QUANTUM WELLS UNDER AHARONOV-BOHM EFFECT

Using the presented technique, let us consider the interesting system of n parallel coupled quantum wells (for details see [9]). It is interesting to note that if one change the number of quantum wells in such a system the new bound states will not appear (as is known, when the quantum wells are arranged in series, i.e., the width of the resulting quantum well increases, there are many bound states in such a system and addition of new wells leads to the fact that the number of bound states increases) just only shift to the limiting value which determined by the parameters of single well (in the case of identical wells). The problem becomes more complicated if at the center of such a ring-like system there is an infinitely thin solenoid carrying finite magnetic flux Φ (see the Fig. 1). At the same time it is a standard situation in the quantum transport [12].

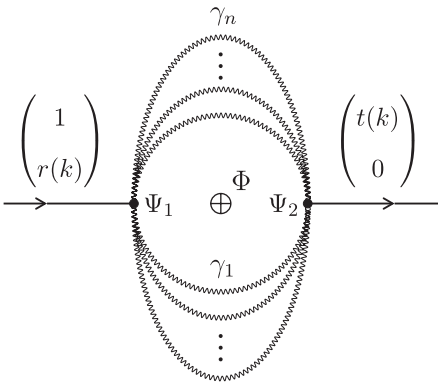

Figure 1: Graph that corresponds to the scattering problem in the system of n parallel coupled quantum wells with the AB flux Φ. The wavy lines represent the potential (in the considered case the potential is the rectangular quantum well).

The magnetic flux modifies the phase of the wave function in the ring[2] while the *in, out*-wave functions are still the same, namely:

$$\begin{aligned} \psi_{in} &= \exp(ikx) + r(k)\exp(-ikx), \\ \psi_{out} &= t(k)\exp(ikx), \\ \psi_{\gamma_1} &= a_{\gamma_1}\exp(ik^- x) + b_{\gamma_1}\exp(-ik^+ x), \\ \psi_{\gamma_2} &= a_{\gamma_2}\exp(ik^+ x) + b_{\gamma_2}\exp(-ik^- x), \end{aligned} \tag{10}$$

where $k^- = k - \alpha$, $k^+ = k + \alpha$, $\alpha = \Phi/(\Phi_0 L)$, Φ is the magnetic flux through the loop section area, $\Phi_0 = 2\pi\hbar c/e$ and L is the ring's length.

The explicit expression for the transmission amplitude (in the case of identical wells) can be obtained in the following form[3] (using the technique of graphs [9]):

$$t_n(k) = \frac{4inkq\sin(ql)\cos\left(\frac{\alpha}{2n}\right)}{(2nq)^2\cos^2\left(\frac{\alpha}{2n}\right) + k^2\sin^2(ql)\left(1 + 2inq\cot(ql)\right)^2},$$

where $q = \sqrt{k^2 - V}$, $V = 2m_e U/\hbar^2$, U is the well's depth and l is the well's width, n is a number of quantum wells in a system, α is a dimensionless AB flux. As is known the energies of bound

[2]Equation (10) is presented for the case of two-arm ring, for the multi-arm ring the result can be obtained by a similar way.

[3]Here we would like to note that the graph ideology allows to obtain the transmission coefficient not only in the case of identical wells, but in this case only numerical results take place.

states correspond to simple poles of the transmission amplitude. In order to determine the bound states energies $E_{bound} = -\hbar^2\kappa^2/2m_e$ we construct the analytic continuation of the transmission amplitude $t(i\kappa)$.

In the Fig. 2, we present the results of numerical simulations for the logarithm of the transmission coefficient $\ln|t(i\kappa)|^2$ which determines the bound states positions in the system under consideration.

We see that the presence of the AB flux leads to the fact that the bound state position in such a system becomes dependent on the value of AB flux. As a result also the optical properties that determined by the bound states positions become dependent on the AB flux. Namely for some values of the AB flux the bound state in such a system will not appear due to interference effects. In this paper we present the results for the case when the single well contains single bound state. In the case when the quantum well contains two bound states the positions of these states together with the distance between them depends not only on the number of wells in the system, but also on the value of AB flux (it should be noted also that the distance between the bound states corresponds to THz frequency domain, so the considered system seems promisingly and perspective in connection with development of modern low-dimensional optics). We can conclude that the number of wells in such a system together with the AB flux can be considered as driven parameters for the bound states positions as well as for the distance between the bound states. These facts open a new way for control of the optical properties of ring-like structures by addition of extra wells in the system, as well as by changing of the magnetic flux through the system.

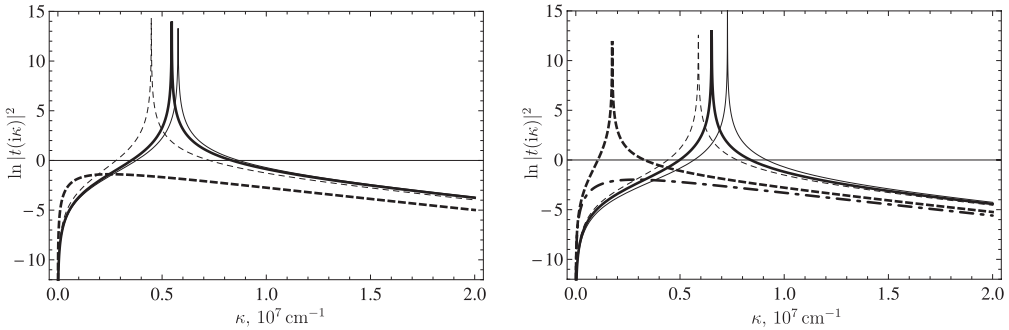

Figure 2: Logarithm of the transmission coefficient $\ln|t(i\kappa)|^2$ for various AB fluxes α in the case of two coupled wells ((a) $n = 2$) and four coupled wells ((b) $n = 4$) as a function of the wave number κ ($k = i\kappa$). (a) Thin solid line is $\alpha = 0$, thick solid line is $\alpha = 0.5$, thin dashed line is $\alpha = 1$, thick dashed line is $\alpha = 2$; (b) Thin solid line is $\alpha = 0$, thick solid line is $\alpha = 1.5$, thin dashed line is $\alpha = 2$, thick dashed line is $\alpha = 3.5$, thick dot dashed line is $\alpha = 4$. The parameters of wells are $U = -0.5\,\mathrm{eV}$ and $l = 10^{-7}\,\mathrm{cm}$.

4. CONCLUSIONS

In this paper we have considered a system of parallel coupled quantum wells with the AB flux at origin of such a system. In the case of similar quantum wells the explicit analytic expression for the transmission amplitude is observed and numerically analyzed. In particular, it is shown numerically that changing of wells number in the system (in the the case of identical wells) does not lead to appearance of a new bound states. However, the addition of new wells leads to the fact that the bound states positions in such a system shift to some limiting value determined by the characteristics of a single well. Addition of the AB flux at origin of such a system leads to the fact that the bound states position become dependent on its values. Moreover, for some values of the AB flux the bound states in such a system will not appear due to quantum interference effects. Thus, we can conclude that the number of quantum wells in the system under consideration together with the AB flux can be considered as driven parameters for the bound states positions as well as for the distance between the bound states. As a result, the optical properties of such a system (frequencies of laser transitions) depend on the number of well as well as on the AB flux. These facts open a new way for control of the optical properties of ring-like structures with quantum wells by addition of extra wells in the system, as well as by changing of the magnetic flux through the system.

REFERENCES

1. Fuhrer, A., S. Lüsher, T. Ihn, et al., "Energy spectra of quantum rings," *Nature*, Vol. 413, 822–825, 2001.
2. Castro Neto, A. H., F. Guinea, N. M. R. Peres, et al., "The electronic properties of graphene," *Rev. Mod. Phys.*, Vol. 81, 109–162, 2009.
3. Suarez, M., T. Grosjean, D. Charraut, et al., "Nanoring as a magnetic or electric field sensitive nano-antenna for near-field optics applications," *Opt. Commun.*, Vol. 270, 447–454, 2007.
4. Cohen, G., O. Hod, and E. Rabani, "Constructing spin interference devices from nanometric rings," *Phys. Rev. B.*, Vol. 76, 235120, 2007.
5. Liu, D.-Y., J.-B. Xia, and Y.-C. Chang, "One-dimensional quantum waveguide theory of Rashba electrons," *J. Appl. Phys.*, Vol. 106, 093705, 2009.
6. Xia, J., "Quantum waveguide theory for mesoscopic structures," *Phys. Rev. B*, Vol. 45, 3593–3599, 1992.
7. Texier, C. and G. Montambaux, "Scattering theory on graphs," *J. Phys. A: Math. Gen.*, Vol. 34, 10307–10326, 2001.
8. Akkermans, E., A. Comtet, J. Desbois, et al., "Spectral determinant on quantum graphs," *Ann. Phys.*, Vol. 284, 10–51, 2000.
9. Klinskikh, A. F., A. V. Dolgikh, P. A. Meleshenko, and S. A. Sviridov, "On the electron scattering on the one-dimensional complexes: The vertex amplitudes method," 1–14, Arxiv preprint arXiv:1012.3634v2, 2011.
10. Dubrovin, B. A., A. T. Fomenko, and S. P. Novikov, *Modern Geometry — Methods and Applications: Part I: The Geometry of Surfaces, Transformation Groups, and Fields* , Springer-Verlag, New-York, 1992.
11. Klinskikh, A. F., D. A. Chechin, and A. V. Dolgikh, "Modified transfer matrix method for quantum cascade lasers," *J. Phys. B: At. Mol. Opt.*, Vol. 41, 161001, 2008.
12. Bulgakov, E. N., K. N. Pichugin, A. F. Sadreev, and I. Rotter, "Bound states in the continuum in open Aharonov-Bohm rings," *JETP Lett.*, Vol. 84, 430–435, 2006.

S-band Circular Polarization Patch Antenna Design for the Large Curvature Conformal Structure

Yuan Yuan and Zhi Xu
Aviation Key Laboratory of Science and Technology on AISSS
China Leihua Electronic Technology Research Institute, Wuxi, China

Abstract— A circular polarization patch antenna operating at S-band is proposed which is complaint with a large curvature column structure. The coupling effects between the conformed antenna and the based structure are considered accurately in the refined simulation models and impedance performance has been illustrated in the paper. The designed maximal gain in the normal direction of the antenna aperture reaches 7 dBi possessing the polarization axial ratio from 0.3 dB to 3.2 dB within $\pm 45^\circ$ scanning volume.

1. INTRODUCTION

Conformal antennas are growing considerably in their adaptabilities for the applications in which the impacts of the aerodynamic shapes are essential to be concerned [1, 2]. Generally, microstrip patches are selected in the conformal antenna designs due to the low profile characteristic and abilities for the resemblance with the exterior shapes, especially for the aircraft shells.

Recently, the increasing requirements of the low radar cross section (RCS) and wide scan angles boost the further developments of conformal phased array systems [3]. Adequate achievements have been done almost following the same speculation that the array consists of tiny planar antenna elements ranged in certain radius and is approximately identical structure with the carrier. A typical conformal array antenna has been shown in Figure 1 as radar seeker for missile-borne requirement [4].

However, the missile-borne applications, such as communication and remote metering, are gradually operating at S-band [5]. The conformal patch antenna also needs to be circular polarization and pasted on the surface not in common with radar indicator antenna. In some case, the patch dimension is nearly equivalent to the missile radius. Accordingly, the approximate planar theory is disabled and the new investigation is put forward to optimize the patch traits giving attention to conformal circular polarization design.

In this paper, a conformal patch antenna working at S-band with circular polarization is designed on a column in large curvature, namely, the column radius is nearly equivalent to the patch dimension. An optimized model with the reasonable parameters is framed. Then, the effective calculated results are obtained simultaneously. The simulated maximal gain in the normal direction of the antenna reaches 7 dBi with the polarization axial ratio from 0.3 dB to 3.2 dB in the direction of $\pm 45^\circ$ scanning scope.

Figure 1: Conformal array antenna for missile-borne.

2. BASE ANTENNA CONFIGURATION

The traditional patch antenna is designed with circular polarization characteristic firstly. It is basically to compute the patch obeying classical theory and design the feeding structure using strip lines. The dimensions of the patch can be calculated according to the operating frequency, dielectric constant and the thick of the material, meanwhile the feed line is carried out in the same way. Arlon DiClad880 is selected to as the substrate material. Its dielectric constant is 2.2. The thicknesses of the two substrates are 1.016 mm. The structure of the planar antenna is given in

Figure 2. As shown, the element is composed of an upper patch, a feed-line in medium, a ground plane and two substrate layers.

In Figure 3, W_a is the length of the square radiation patch. The active termination of the feed-line is W_0 in wide and the width of the transmission part is W_1. In order to obtain the circular polarization, the feed-line differ between the input and two feed points is reasonable designed as the length which is equally 90° phase postponed to decide the vortical direction of the circular polarization.

In this paper, a right-handed circular polarization is simulated by HFSS. Calculated parameters are: $W\_a = 43\,\text{mm}$, $W_0 = 6.2\,\text{mm}$, $W_1 = 4\,\text{mm}$ and the length differ is 20.49 mm. The simulated results are revealed in Figure 4. The simulated polarization axial ratio is below 3 dB between ±80° and below 1.4 dB in the direction of ±45° scanning space with HFSS software. A maximal gain is obtained about 8 dBi in normal direction. The VSWR of input port is 1.69 at 2.25 GHz.

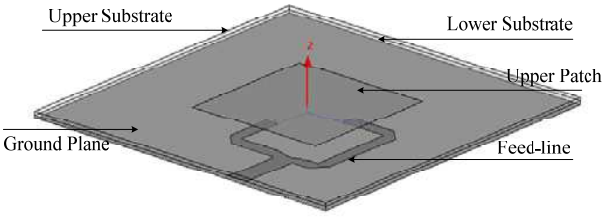

Figure 2: Geometry of the planar antenna.

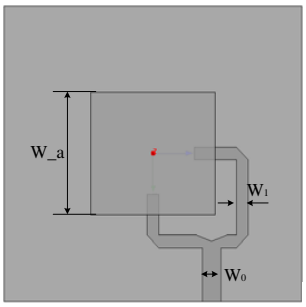

Figure 3: Parameters of the planar antenna.

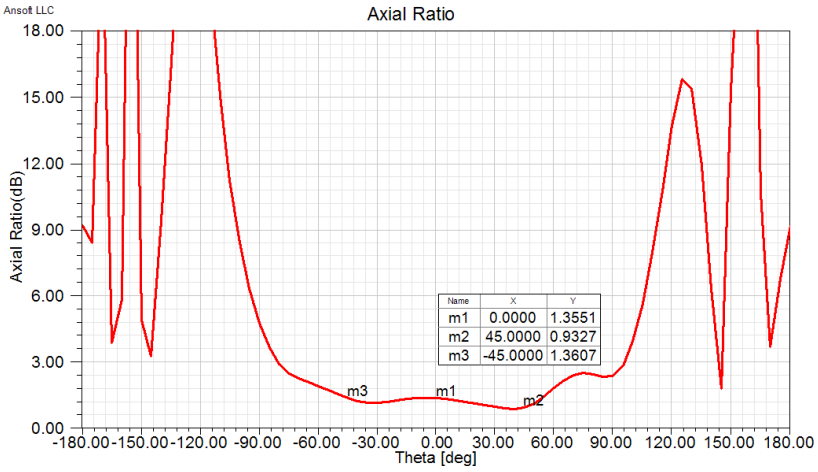

Figure 4: Axial ratio of the planar antenna at 2.25 GHz.

3. CONFORMAL ANTENNA DESIGN AND RESULTS

A circular polarization patch antenna working at 2.25 GHz is designed which is conformal on a column in large curvature. The conformal antenna model is composed of an exterior patch, a feed-line in middle, an inner ground plane and two substrate layers. It is also used the substrate material Arlon DiClad880 with the same dielectric constant 2.2 and the thicknesses of the two substrates 1.016 mm. The structure of the conformal antenna model is given in Figure 5.

As illustrated in Figure 5, the pillar radius r is equal to 50 mm and nearly equivalent to patch dimension. W_b is the length of the exterior square patch. W_3 is the width of the active termination of the feed-line and W_4 is the size of the transmission part. Accordingly, the approximate planar theory is disabled and the application is put forward to optimize the patch characteristics giving attention to conformal circular polarization design.

At first, a model is simulated in which the parameters are identical to the planar antenna model with $W\_b = W\_a = 42\,\text{mm}$, $W_3 = W_0 = 6.2\,\text{mm}$, $W_4 = W_1 = 4\,\text{mm}$ and the path differ 20.49 mm.

The calculated result is shown in Figure 6. The polarization axial ratio is all above 16.7 dB between ±45°. The circular polarization characteristic is destroyed completely. Due to this phenomenon, it is significant to optimize the parameters in the next model by changing the sizes.

According to the requirement of the right-handed circular polarization, the path differ of two feed-lines between the input and two feed points is considerably optimized to produce 90° phase delay, which is vital factor to the conformal antenna achieving circular polarization. Once the planar antenna is conformal on a pillar, the characteristic of the patch and feed-line would be changed, especially in the changing of equivalent length of the transmission part in path differ.

The second model is built and simulated by optimizing parameters of the conformal antenna. After tuning the W_b, W_3, W_4 and path differ, the preferable results are accomplished as shown in

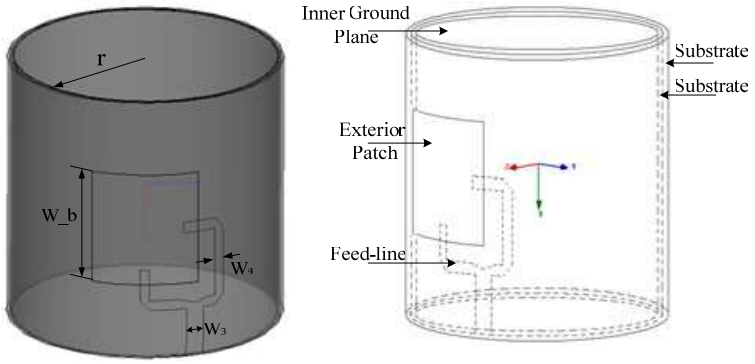

Figure 5: Geometry of the conformal antenna.

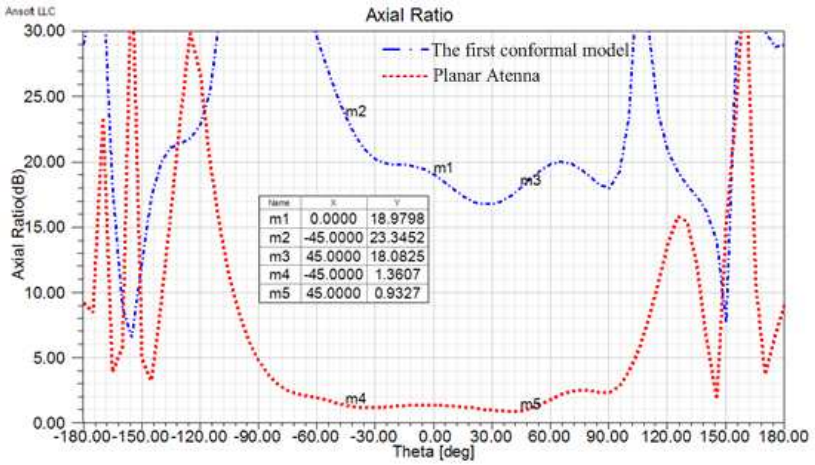

Figure 6: Axial ratio of the planar antenna and the first conformal model at 2.25 GHz.

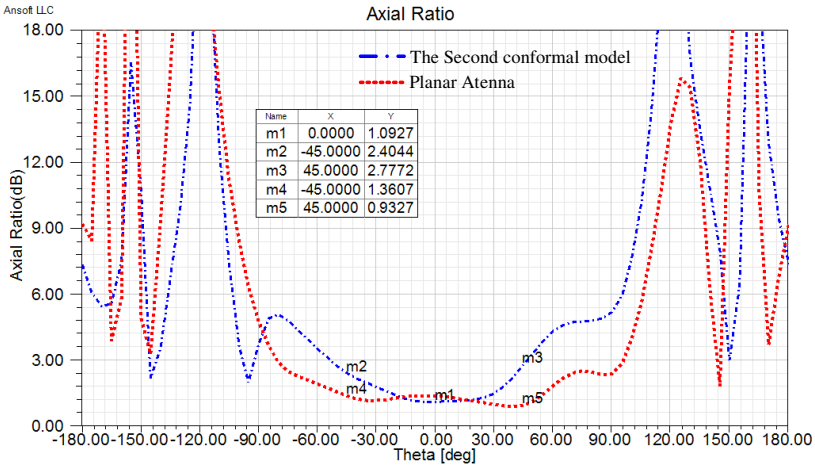

Figure 7: Axial ratio of the planar antenna and the second conformal model at 2.25 GHz.

Figure 7. The optimized results by HFSS show a maximal gain of 7 dBi in normal direction with the polarization axial ratio from 0.3 dB to 3.2 dB in the direction of $\pm 45^\circ$ scanning scope.

In this condition, $W\_b = 43$ mm, $W_3 = 6.5$ mm, $W_4 = 4$ mm, and the path differ changed to 20.07 mm. The most improvement is the path differ which determines the phase relationship mostly.

4. CONCLUSIONS

This paper designs a typical circular polarization patch antenna working at S-band which is conformal on a column with large curvature. An optimized model with the reasonable parameters is constructed and the simulated results are obtained simultaneously. The optimized results show a maximal gain of 7 dBi in normal direction and the polarization axial ratio from 0.3 dB to 3.2 dB in the direction of $\pm 45^\circ$ scanning scope.

In practical application, the path differ of double feed-points is the most important factor to control the phase relationship. It must be calculated carefully to obtain the anticipant results.

REFERENCES

1. Wu, C., M. Zhang, R. Wu, and H. Zhang, "Simulation and optimization of missile-conformal seeker antenna," 2009.
2. Xiao, Y. and Y. Li, "Conformal antenna applied to the anti-radiation missile," *Shipboard Electronic Counter Measure*, Vol. 31, No. 2, 2008.
3. Mailloux, R. J., *Phased Array Antenna Handbook*, 2nd Edition, 185, Artech House, Boston, MA, 2005.
4. Zhu, S., "Development of conformal antenna and electronic warfare applications," *Journal of Chinese Electronic Research Institute*, Vol. 2, No. 6, 2007.
5. Wang, L. and H. Peng, "Study on missile borne conformal antenna," *Western Electric*, Vol. 5, 34–38, June 1994.

Application of Artificial Magnetic Conductor in Aperture-coupled Microstrip Antenna

Chao Fang and Guizhen Lu
Communication University of China, China

Abstract— A new technology of the slot waveguide transmission line has been concerned. The application of this technology in aperture of coupled microstrip antenna is studied in this paper. The dispersion characteristics are analyzed in the communication bands. The design and analysis of aperture-coupled microstrip antenna adding Artificial Magnetic Conductor (AMC) has been done. The numerical results show that the antenna structure is well to achieve the expected design requirements.

1. INTRODUCTION

In the millimeter-wave technology, in order to overcome the problem of transmission loss of traditional transmission lines, a new technique has been widespread concern. The new technique is slot waveguide transmission line. Quasi-TEM waves can be transmitted in this transmission line over a wide bandwidth. Slot waveguide technology was first proposed as the range of 30 GHz to THz transmission line in the literature [1]. Application of traditional transmission line is limited by the transmission performance, device integration and cost in this frequency range. Slot waveguide transmission line is used to solve this problem.

The first planar waveguide is constituted by two parallel plates. Electromagnetic wave that perpendicular to the plane of the waveguide can be propagated in this waveguide. If one of the conductors in the planar waveguide is replaced by magnetic conductor, electromagnetic wave can't be propagated when the distance between the planar waveguide is less than the 1/4 wavelength. Conductor transmission line is added between the perfect conductor and the perfect magnetic conductor. This conductor transmission line just likes a slot in the perfect conductor plane. This slot can be used to propagate Quasi-TEM waves.

Electromagnetic characteristics of Artificial Magnetic Conductor (AMC) can be changed by artificially [2]. The formula about the surface impedance of AMC was proposed in literature [3]. Literature [4] studied the dispersion characteristics of the slot waveguide. Literature [5] studied the impedance characteristics of the slot waveguide. Application of the slot waveguide in millimeter-wave devices was studied in literature [6]. Application of package in monolithic microwave integrated circuit (MMIC) was proposed in literature [6].

Aperture-coupled microstrip antenna was used very widely in wireless communication. But this antenna has radiation effects on the back. This drawback limits the application of this antenna in communication. In order to overcome the back radiation effects, the traditional method is to add a reflective plate or cavity on the back. However, the reflective plate tends to produce unwanted effects of radiation. And cavity produces high order mode of electromagnetic radiation. This paper studies the application of AMC in aperture-coupled microstrip antenna. AMC is added on back of antenna. The radiation effect on the back can be reduced.

2. STRUCTURE OF WAVEGUIDE

Planar waveguide consists of two parallel metal planes. When the spacing between two parallel metal planes is less than 1/2 wavelength, TEM electromagnetic waves can propagate perpendicular to the surface. If the planar waveguide be made by a metallic conductor and a magnetic conductor. When the spacing between two parallel planes is less than 1/4 wavelength, the electromagnetic wave can't propagate in such a planar waveguide.

Development of meta-material technology provides a new method to achieve AMC. The dispersion characteristics of the planar waveguide which made by a metallic conductor and AMC were discussed in literature [4]. AMC is made by periodic array of metal wires. Effective permittivity is shown in Formula (1).

$$\vec{\varepsilon}(\omega, k_z) = \varepsilon_0 \varepsilon_h \left[\hat{x}\hat{x} + \hat{y}\hat{y} + \varepsilon_{zz}\left(\omega k_z\right)\hat{z}\hat{z}\right] \tag{1}$$

where,

$$\varepsilon_{zz}(\omega k_z) = 1 - \frac{k_p^2}{k_h^2 - k_z^2}, \quad k_h = \sqrt{\varepsilon} k \tag{2}$$

$$k_p = \frac{1}{a}\sqrt{\frac{2\pi}{\ln(a/2\pi b) + 0.5275}} \tag{3}$$

a is the period of the array, b is the radius of the wire. When the height of the wire is 1/4 wavelength, the wire array and the air interface can be considered as a magnetic conductor. Electromagnetic waves can't propagate in this waveguide from 10 GHz to 20 GHz [4]. In this paper, aperture of coupled microstrip antenna operates at 2.3 GHz. The structure of the planar waveguide must be re-designed so that electromagnetic waves can't propagate in waveguide at 2.3 GHz. The radius of the wire is 2 mm. The height of the wire is 31.25 mm.

Dispersion analysis of wave propagation is calculated using the model shown in Figure 1. X direction and Y direction are the periodic boundary conditions. Z direction is perfect boundary conditions for the conductor.

Figure 2 gives the dispersion curve. Electromagnetic waves don't have propagation modes from 1.9 GHz to 4.36 GHz.

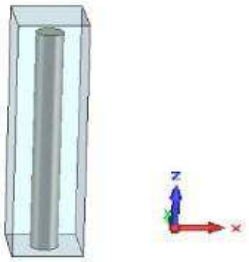

Figure 1: Periodic structural unit.

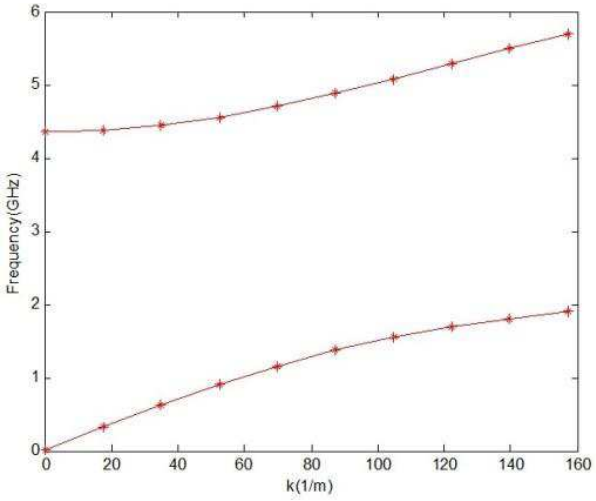

Figure 2: Dispersion curve.

3. APERTURE-COUPLED MICROSTRIP ANTENNA

Feeder and microstrip antenna are electrically isolated by technology of aperture-coupled microstrip antenna. They are coupled through a slot on the ground plane. Therefore, feeder and antenna elements can be optimized separately. Coupling aperture is $0.141\lambda \times 0.019\lambda$. An aperture-coupled microstrip antenna working at 2.3 GHz is shown in Figure 3. There is AMC at back of the antenna. AMC and the metal surface form a planar waveguide structure. According to Section 2, electromagnetic waves can't propagate in this structure at 2.3 GHz. So back radiation effects are reduced. The size of the microstrip patch is 30 mm $*$ 40 mm. The size of coupling slot is 14mm $*$ 1.55 mm. Permittivity of the dielectric substrate is 2.2. The distance between the microstrip antenna and the metal ground is 1.6 mm. The distance between the feeder and the metal ground is 1.6 mm.

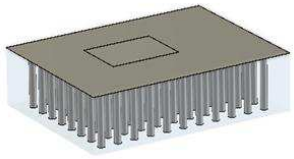

Figure 3: Aperture-coupled microstrip antenna with AMC.

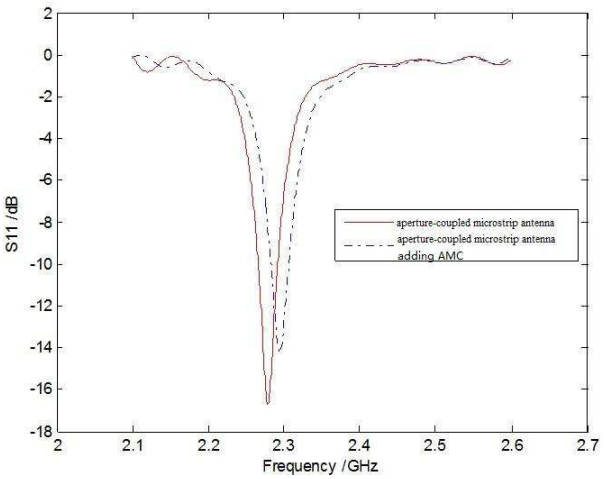

Figure 4: S_{11}.

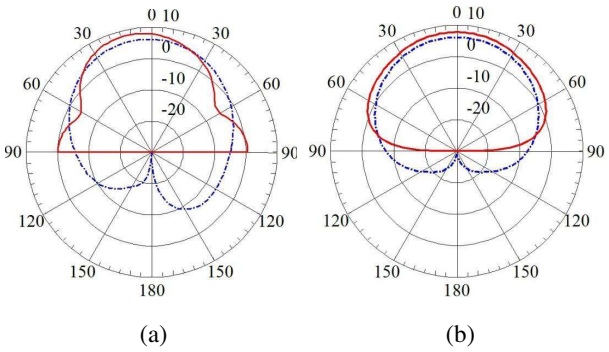

Figure 5: (a) X-Z antenna gain. (b) Y-Z antenna gain.

4. CONCLUSION

An aperture-coupled microstrip antenna is shown in Figure 3. Since the number of unknown variables is large, I simulated this structure by finite difference time domain (FDTD). The simulation results are shown in Figures 4 and 5.

S_{11} don't change a lot with AMC from Figure 4. Both of them have the same variation. Just the best match frequency shift position slightly. The reason is some parasitic reactance component by adding AMC. The size of the periodic array can be adjusted to improve the result of antenna.

The solid line is the gain curve with AMC. The dotted line is the gain curve without AMC. The gain has a small increase by adding AMC. The back radiation is greatly reduced at the same time.

REFERENCES

1. Kildal, P. S., et al., "Local metamaterial based waveguides in gaps between parallel metal plates," *IEEE Antennas Wireless Propagat. Letters*, Vol. 8, 84–87, 2009.
2. Lu, G., H. Yin, Y. Li, and X. Wei, "Multiscale analysis of metamaterials," *Chinese Journal of Radio Science*, Vol. 27, No. 6, 1124–1127, 2012.
3. Silveirinha, M. G., et al., "Electromagnetic characterization of textured surfaces formed by metallic pins," *IEEE Transactions on Antennas and Propagation*, Vol. 56, No. 2, 405–415, 2008.
4. Polemi, A., et al., "Dispersion characteristics of a metamaterial-based parallel-plate ridge gap waveguide realized by bed of nails," *IEEE Transactions on Antennas and Propagation*, Vol. 59, No. 3, 904–913, 2011.
5. Kildal, P.-S., et al., "Design and experimental verification of ridge gap waveguide in bed of nails for parallel plate mode suppression," *IET Microwaves, Antennas and Propagation*, 1, 2009.
6. Alfonso, E., et al., "Gap waveguide components for millimeter-wave systems: Couplers, filters, antennas, MMIC packageing," *ISAP*, 243, Nagoya, Japan, 2012.

Design of Broadband Vector Modulator Based on HMC500LP3 Chip

Qian Xu, Jungang Miao, and Chen Chen
Electromagnetics Laboratory, Beihang University, China

Abstract— Vector modulator technology in active phased array antenna has been used as a replacement of conventional digital phase shifter and digital attenuator. In this paper, vector modulator is realized by a vector modulation HMC500LP3 chip from Hittite company using Agilent ADS software. The HMC500LP3 is a Vector Modulator RFIC with high dynamic range and differential input. As a demonstration of the vector modulator's flexibility, the HMC500LP3 chip has been fabricated and characterized by means of S-parameter measurements. What's more, this paper systematically presents the vector modulator measurement step which uses Agilent USB/GPIB control module 82357B to have logic control of vector network analyzer and DC Power Analyzer by MATLAB software. The DEEMBDING calculation for SMA connector is completed by the MATLAB software. Finally, the measurement results show that the chip of the HMC500LP3 vector modulator can realize a continuously controlled 360° phase shifting range and a range of (−9 dB)–(−41 dB) for the amplitude over the 1.8 GHz–2.2 GHz band. Measured S_{11} and S_{22} are below −17 dB and −15 dB.

1. INTRODUCTION

Active phased array antenna system has recently attracted considerable interest in the antenna technology research. The problem of improving the precision of phase shifting has not been addressed until M.Tuckman proposed the concept module of the vector modulator in 1988 [1]. The complexity of designing a digital phase shifter increases with the operating frequency and poor uniformity of digital attenuators, while the application of vector modulator can largely decrease hardware complexity, reduce the size of the component, lower cost, and improve the flexibility of amplitude modulation and phase modulation [2].

Figure 1 shows the schematic and principle of the vector modulator presented. A 3-dB Lange coupler splits the input signal into two orthogonal portions: in-phase and quadrature-phase. These two portions are attenuated by two bi-phase amplitude modulators, which are controlled by two bias voltages I and Q respectively. Combining these two modulated portions with a Wilkinson coupler completes the modulating function [3].

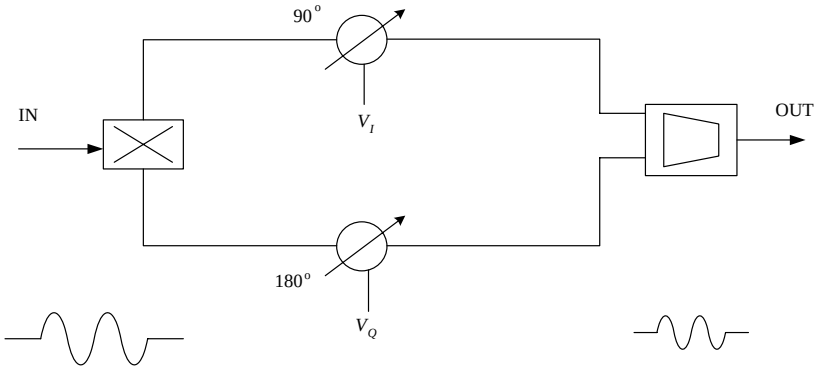

Figure 1: Typical schematic diagram of the vector modulator.

2. CIRCUIT DESIGN

2.1. Features of the HMC500LP3 Chip

Figure 2 shows the schematic of the HMC500LP3 chip. According to the datasheet, I & Q ports of the HMC500LP3 can be used to continuously vary the phase and amplitude of RF signals by up to 360 degrees and 40 dB respectively. The chip supports a 3 dB modulation bandwidth of 150 MHz. The input IP3/noise floor ratio is 185 dB with an input IP3 of +33 dBm and input noise floor of −152 dBm/Hz. These parameters can meet the demand of the vector modulator design.

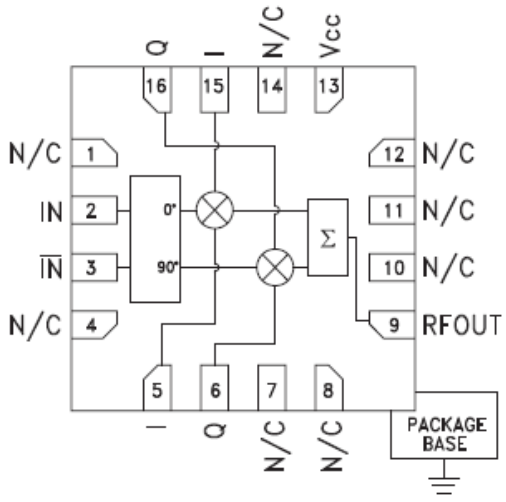

Figure 2: Schematic of the HMC500LP3.

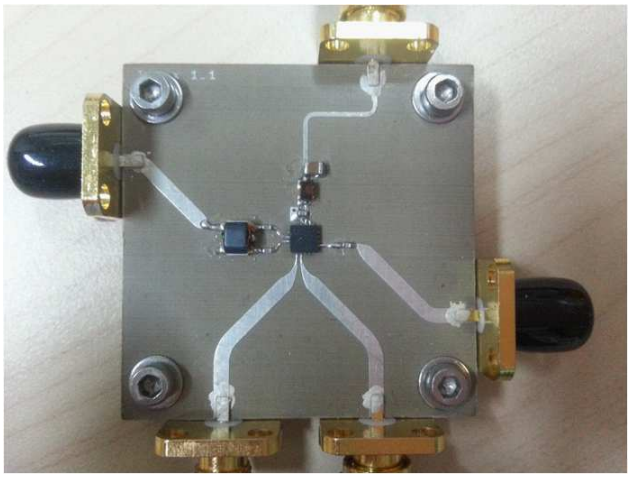

Figure 3: A photograph of HMC500LP3.

A photograph of the vector modulator chip and its peripheral circuit is shown in Figure 3. The chip is bonded on a test substrate. The required chip area is only 4 cm × 4 cm.

The thickness of the board is confirmed to 30 mil based on the TC350 substrate. According to the properties of the board, the width of 50 ohm microstrip line is 1.6712 mm calculated by the ADS software. For optimum performance, the input should be AC coupled and driven through a Balun BD1631J50100AF with an approximately 100 Ω differential impedance. Similarly, the output should be DC blocked.

The I-Q input promises to be a vital component for the realization of vector modulator, with pin 5 chosen as I voltage input pin 6 as Q voltage input. For the feed circuit, the nominal voltage supply for the HMC500LP3 is 7.6 V and is applied to the pin 13. All the pins are gradually connected so that reflection and parasitic capacitance can be reduced. Because the power supply circuit noise at the work frequency may have a bad effect on the chip, each of the supply pins is connected with a capacitor in 0402 package and a inductor in 0805 package to provide high frequency bypass near the operating frequency.

Solder The exposed paddle on the underside of the package is soldered to a low thermal and electrical ground plane. These layers should be stitched together with 5 vias under the exposed paddle, because the rise of the chip's temperature can lead to the decrease of chip life, even make the chip burned down.

3. PRODURES OF THE TESTING

Taking precision and verifiability into consideration, closed loop calibration method is adopted in this paper. Figure 4 and Table 1 show the general characterization bench setups used extensively for the HMC500LP3. The whole system is composed of vector network analyzer, DC power analyzer and control computer with each instrument being connected by GPIB Bus. An automated VISA program is used to control the R&S ZVA24 vector network analyzer and the Agilent DC power analyzer model N6705 is connected by GPIB. DC power analyzer can provide 3 independent voltage and current outputs, so we set CH1 for the vector modulator module power supply channels and CH2/CH3 for in phase/orthogonal control signal respectively.

Table 1: Input return loss vs I voltage and Q voltage.

DC power analyzer model N6705	CH1 for network analyzer
	CH2 for in phase control signals
	CH3 for orthogonal control signal
R&S ZVA24 Vector network analyzer	Measure HMC500LP3 S parameters
GPIB Address	5: DC power analyzer N6705 20: Vector network analyzer

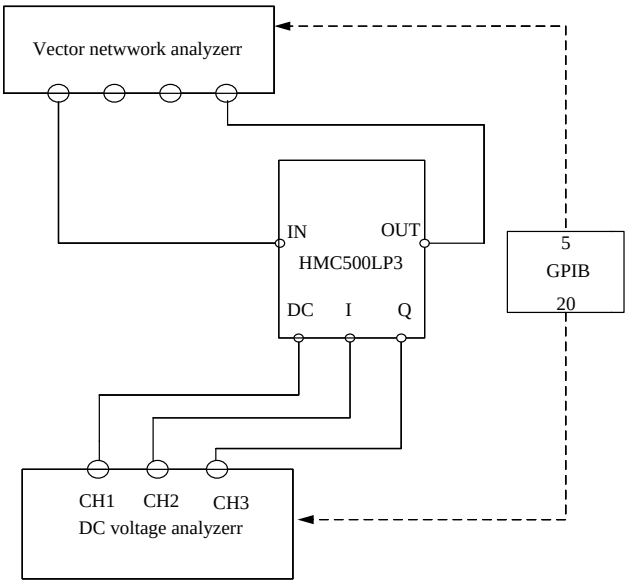

Figure 4: S parameter measurement setup.

After insuring the instrument having been installed well, we set 0 V as the initial value of power supply module and increase it through three different ways: from 0 V to 1 V at intervals of 0.1 V, from 1 to 7 V at intervals of 0.5 V, from 7 V to 7.4 V at intervals of 0.1 V. I control voltage is increased from 0 V to 0.5 V at intervals of 0.1 V, the same as Q control voltage.

Five different voltage values, 7.5 V, 7.75 V, 8 V, 8.25 V, 8.5 V, are set up in the DC voltage supply. Under the different DC voltage supply, I/Q control voltage are respectively set up 11 points which is swept from 0.5 V to 2.5 V at the intervals of 0.2 V. S-parameters are measured under the above

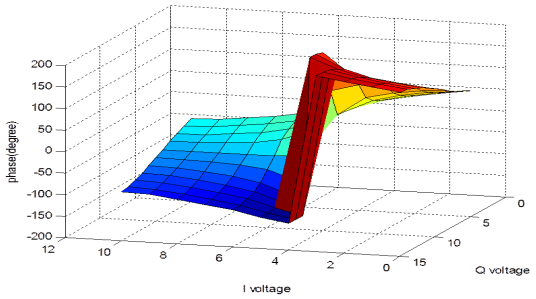

Figure 5: Phase vs I/Q voltage at the 7.75 V DC su]

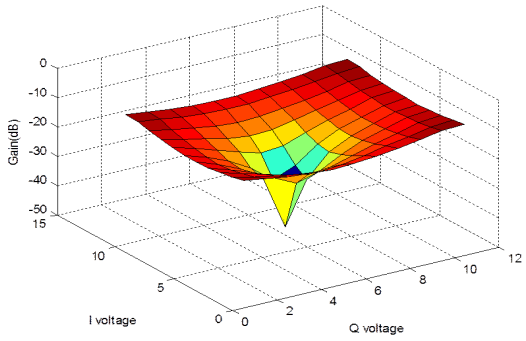

Figure 6: Gain vs I/Q voltage at the 7.7 5V DC su]

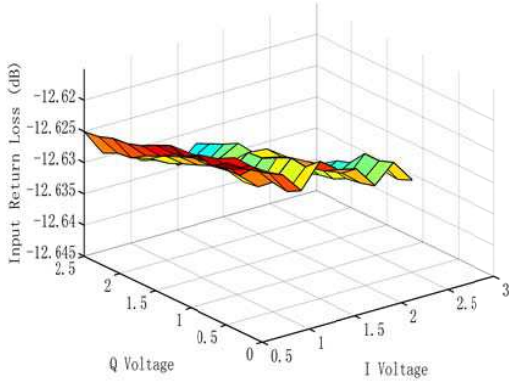

Figure 7: Input return loss vs I voltage and Q voltage.

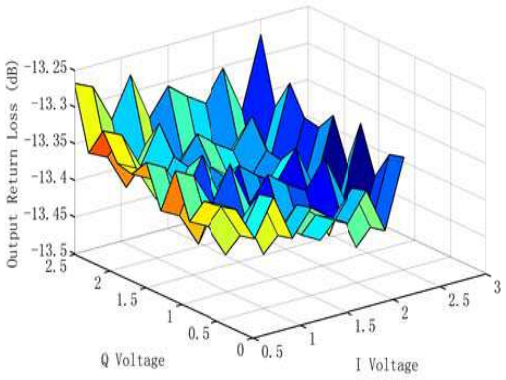

Figure 8: Output return loss vs I voltage and Q voltage.

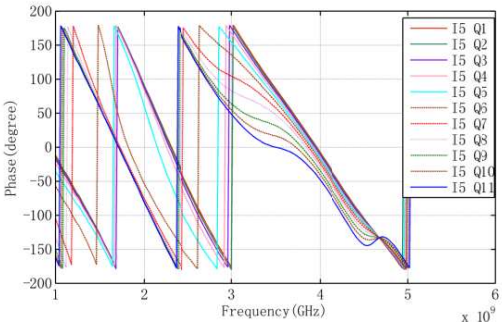

Figure 9: Phase vs Frequency and Q voltage values at 2.5v of I voltage.

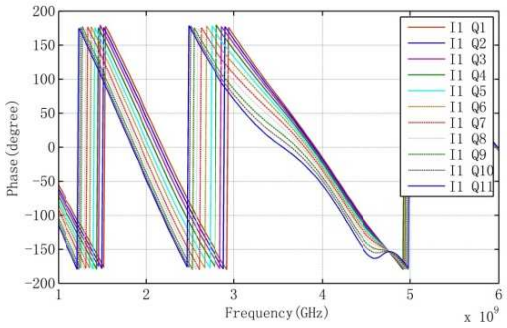

Figure 10: Phase vs Frequency and Q voltage values values at 0.5v of I voltage.

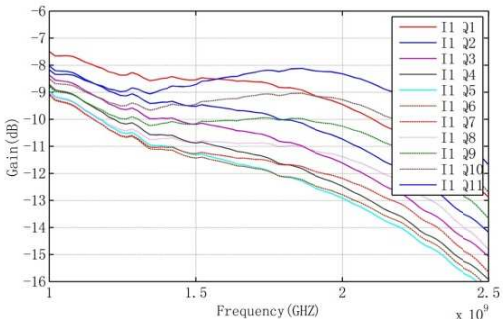

Figure 11: Frequency vs Gain and different Q voltage values under the I voltage value is 0.5 V.

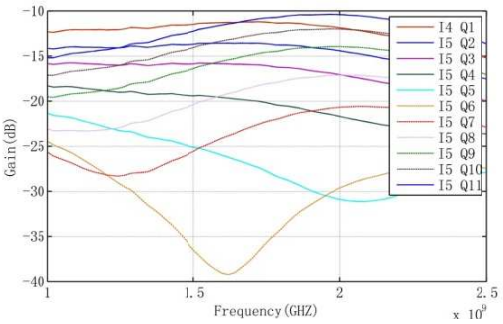

Figure 12: Frequency vs Gain and different Q voltage values under the I voltage is 2.5 V.

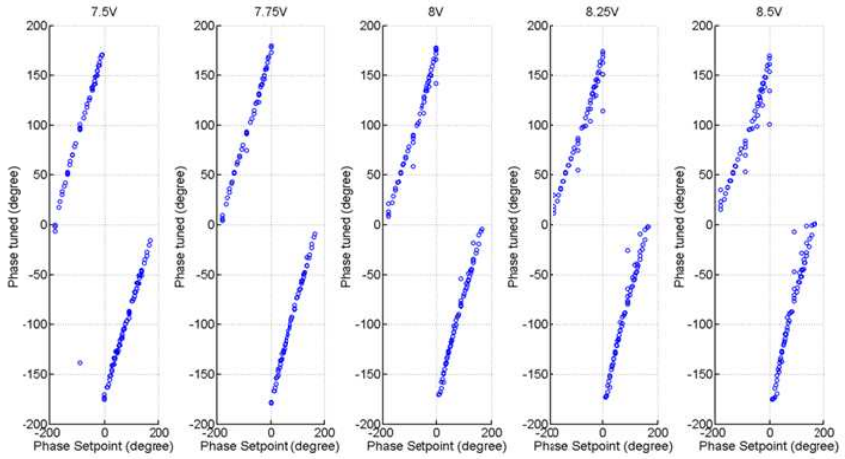

Figure 13: Phase setting vs phase and DC supply @$F = 2$ GHz.

voltage supply from 0 GHz to 6 GHz. The total number of points is 605.

All the bias voltages and I/Q supply voltages of vector modulators are programmed by control computer. At the same time, control computer reads the measured S parameters by VNA. Finally, for all the measurements of the HMC500LP3, the loss of the Balun, which is used to drive the input port, is de-embedded from these measurements. After completing the measurements, the module should be returned to the initial state and closed.

4. THE RESULT OF THE TEST

As Figure 5 and Figure 6 show, the HMC500LP3 can be used to continuously change the phase and amplitude of RF signals by up to 360 degrees and realize a range of -9 dB–(-41 dB) for the amplitude under the different voltage values of the I and Q.

Figure 7 and Figure 8 illustrate the input return loss and output return loss performance of the

different I/Q voltage values. The HMC500LP3 can achieve the input return loss greater than 17 dB and the output return loss greater than 15 dB over a broad frequency range. The chip modulator has excellent input and output matching performance.

As is shown in the Figure 9 and Figure 10, a linear correlation is found between the phase shifting degree and frequency. What is more, the slope of the lines is constant no matter what I voltage and Q voltage are. The chip model shows excellent phase linearity for various I and Q voltage values. Different I and Q voltage values can get different initial phases.

Figure 11 and Figure 12 show the Gain vs Frequency under the different I voltage values at the operating frequency. The gain flatness at 0.5 V of I voltage is much better than that at 2.5 V from 1.8 to 2.2 GHz.

Figure 13 illustrates excellent linear performance of phase setting for various DC supply. Any phase can be achieved through the vector modulator.

5. CONCLUSION

In this paper, the HMC500LP3 chip is introduced and applied into vector modulator. The outstanding measured results show that vector modulator can cover a phase shifting of 360° and are able to provide gain over 40 dB. This chip can be applied to realize active phased array antenna. Incident wave phase difference through phased array antenna is associated with the frequency and the incident angle. Given the good linear correlation between the phase shifting degree and frequency. By HMC500LP3 chip phase difference of incident wave can be compensated with a certain range.

REFERENCES

1. Tuckman, M., "*I-Q* vector modulator — The ideal control component," *Microwave System News*, 105–115, May 1988.
2. McPherson, D. S., "Vector modulator for W-band software radar techniques," *IEEE Transactions on Microwave Theory and Techniques*, Vol. 49, No. 8, 1451–1461, S. Lucyszyn, Microwave & Syst. Res. Group, Surrey Univ., Guildford, UK, Aug. 2001.
3. Han, K., L. Wu, Y. Sun, T. Tian, and X. Sun, "The development of an Ka band 8×8 active phased array antenna base on modulation technology," *2011 International Workshop on Antenna Technology (iWAT)*, 453–456, Mar. 2011, Doi: 10.1109/IWAT.2011.5752356.
4. Chow, P. S., J. M. Cioffi, and J. A. C. Bingham, "A practical discrete multitone transceiver loading algorithm for data transmission over spectrally shaped channels," *IEEE Transactions on Communications*, Vol. 43, 234–773, 1995.
5. Fischer, R. F. H. and J. B. Huber, "A new loading algorithm for discrete multitone transmission," *IEEE Proc. Globecomm.*, Vol. 1, 724–728, 1996.
6. Joonsuk, K. and J. M. Cioffi, "Spatial multiuser access OFDM with antenna diversity and power control," *52nd Vehicular Technology Conference, IEEE-VTS Fall VTC 2000*, 273–279, Boston, MA, USA, 2000.
7. Tarokh, V., N. Seahachi, and A. R. Calderbank, "Space-time codes for high data rate wireless communications performance analysis and code construction," *IEEE Trans. Inform. Theory*, Vol. 45, 1456–1467, 1999.

A Novel Substrate Integrated Waveguide Back-cavity Antenna with Bow-tie Shaped Slot

Chuang-Ming Tong[1, 2], **Weijian Pang**[1], **Xiong Zou**[1], **and Tong Wang**[1]

[1]School of Air and Missile Defense, Air Force Engineering University, Xi'an 710051, China
[2]State Key Lab. of Millimeter Waves, Nanjing, Jiangsu 210096, China

Abstract— As substrate integrated waveguide cavity-backed antenna with narrow rectangular slot always be narrow banded, a novel cavity-backed antenna with bow-tie shaped slot is proposed. Bow-tie shaped slot is integrated on the SIW cavity to wide the bandwidth. Design and simulation process are also given in this paper, the key parameters affecting the performance of antenna is studied, and test sample is fabricated and tested. Test results show that 3.96% relative bandwidth and 4.9 dBi gain are obtained at the antenna center frequency 5.3 GHz. The simulation results coincide well with simulated results, verify the validity of the designing.

1. INTRODUCTION

The development of communication system has led designers to pursue light, low profile, easy manufactured and integrated antennas [1]. Thus, the technology of printed patch antenna is favored and admired. But, the traditional printed patch antenna has great transmission loss. In recent years, substrate integrated waveguide (SIW) is developed and has became a research hotspot, and these researches springing up [2–6].

SIW is a new type of guided wave structure as a good alternate when the antenna being designed required light and easy integrated as traditional metal waveguide is no longer suitable. As a new and good wave transmission structure, SIW is especially suitable to form slot antenna, and a lot articles about this is published [7–10], using SIW structure to form a backed-cavity is also a research hotspot in recent years [11, 12]. Backed-cavity slot antenna based on SIW formed a resonant cavity behind the antenna makes it can filter the interference signal out of work frequency band, this nature greatly improve the performance of the receiver and reduce the size of circuit.

Reference [11] proposed a backed-cavity antenna with narrow gap, and has obtained the good radiation effect, but the working frequency band is limited, only 1.32% relative bandwidth.

In this letter, in order to design a low profile narrowband omni-directional antenna using in short range wireless communication system, a novel SIW backed-cavity antenna with bow-tie shaped slot is proposed and analyzed. The backed-cavity structure is formed by SIW theory to filter out unwanted frequencies and bow-tie shaped slot is used to produce the omnidirectional pattern. Compared to the reference [11], the proposed antenna bandwidth reached 3.96%. The detailed design and simulation process are given in this paper, key parameters affecting the performance of antenna is studied, and the test results is also given and analyzed.

2. DESIGN AND SIMULATION

The topology of the antenna proposed is shown in Fig. 1. Antenna is designed using ARLON substrate ($\varepsilon_r = 2.2$ and 1 mm thickness). Cavity is designed based on the classic theory of rectangular waveguide cavity and it is formed by a series of mental through-hole with 0.3 mm radius and 1 mm distance, the radius and distance value satisfy the rule of SIW structure design [13]. The cavity works at its first TE_{101} mode. A cavity works at TE_{mnl} can be determined by following formulas:

$$a = \frac{c}{f_c \times 2 \times \varepsilon_r} \tag{1}$$

$$\beta_{mn} = \sqrt{k^2 - \left(\frac{m\pi}{a}\right)^2 - \left(\frac{n\pi}{h}\right)^2} \tag{2}$$

$$k = \omega\sqrt{\mu\varepsilon} \tag{3}$$

$$\lambda_g = \frac{2\pi}{\beta_{mn}} \tag{4}$$

$$b = l\frac{\lambda_g}{2} \tag{5}$$

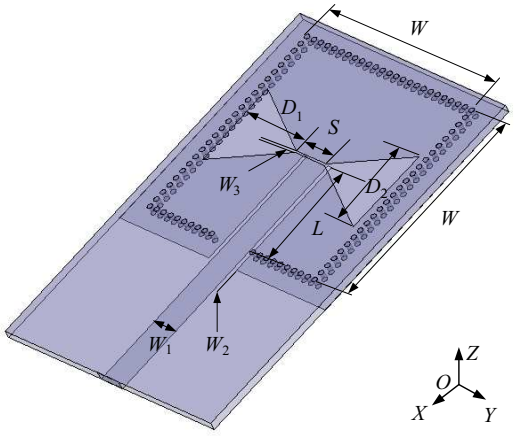

Figure 1: Topology of the antenna.

In the formulas, a, b, h represent the width, length, and height of cavity, respectively.

The coplanar waveguide (CPW) transition structure is used to improve the coupling degree between the external micro-strip and the cavity. The radiation slot is formed by a pair of symmetrical triangles connected by a narrow gap; the narrow gap is overlapped with the end of CPW structure end which is helpful to improve the radiation performance of the bow-tie slot.

The center frequency of the antenna is general decided by the size of cavity, but the shape of the triangle is an important factor of the radiation performance of antenna, tuning the value of D_1 and D_2 can change the center frequency of the antenna and get best radiation performance.

Using HFSS 11 to modeling and simulate. Fig. 2 and Fig. 3 show the affection characteristics according to the variation of D_1 and D_2, respectively. The value of D_1 and D_2 show direct ratio with the center frequency of antenna. Based on the character, micro-tuning of the center frequency in engineering is realized, which makes design much easier.

In order to test the radiation performance of the antenna proposed, a test piece with center frequency 5.29 GHz is researched. The dimensions of antenna are shown in Table 1.

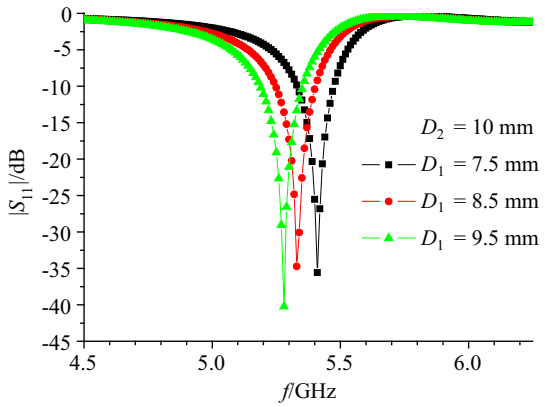

Figure 2: Matching characteristics according to the variation of D_1.

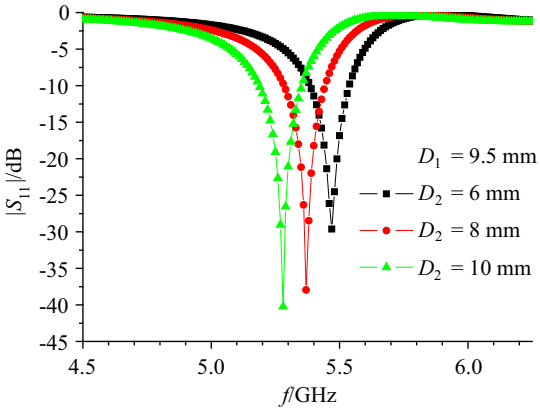

Figure 3: Matching characteristics according to the variation of D_2.

Table 1: Dimensions of antenna.

W	W_1	W_2	W_3
24 mm	3.1 mm	0.5 mm	0.2 mm
S	D_1	D_2	L
1 mm	1 mm	22 mm	12.5 mm

3. EXPERIMENT RESULTS AND ANALYSIS

Figure 4 shows the manufactured antenna, (a) is the top photography and (b) is the bottom photography. SMA is utilized in connecting the antenna under test with the experiment equipment. The return loss curves are shown in Fig. 5 It is shown in the figure that the return loss is more than 10 dB in the frequency scope of 5.16 GHz–5.37 GHz.

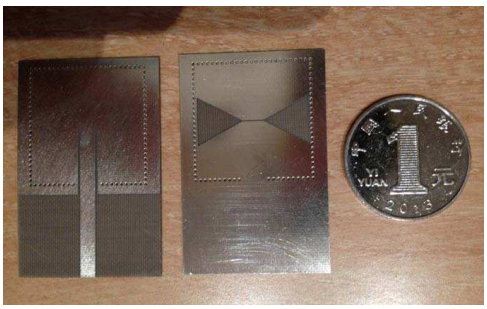

Figure 4: Test structure of antenna.

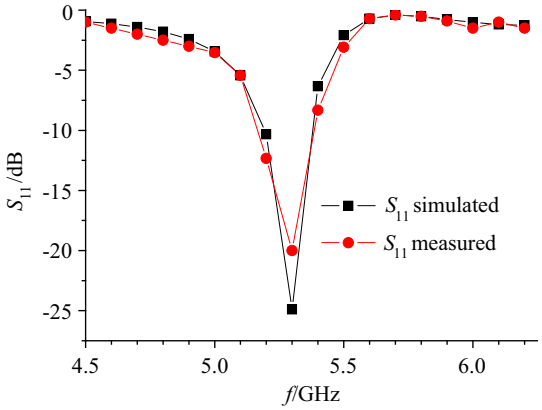

Figure 5: Simulated and measured return loss of antenna.

Simulated and measured far-filed antenna radiation patterns are shown in Fig. 6. Fig. 6(a) for E-plane, where 4.9 dBi Gain and 84° half-power beam width is obtained, the cross-polarization is lower than −48 dB. Fig. 6(b) shows the measurement results of H-plane, where also a 4.9 dBi best Gain is obtained, and cross-polarization radiation is not so good as E-plane, lower than −19 dB. The measured results show good agreement with simulated ones.

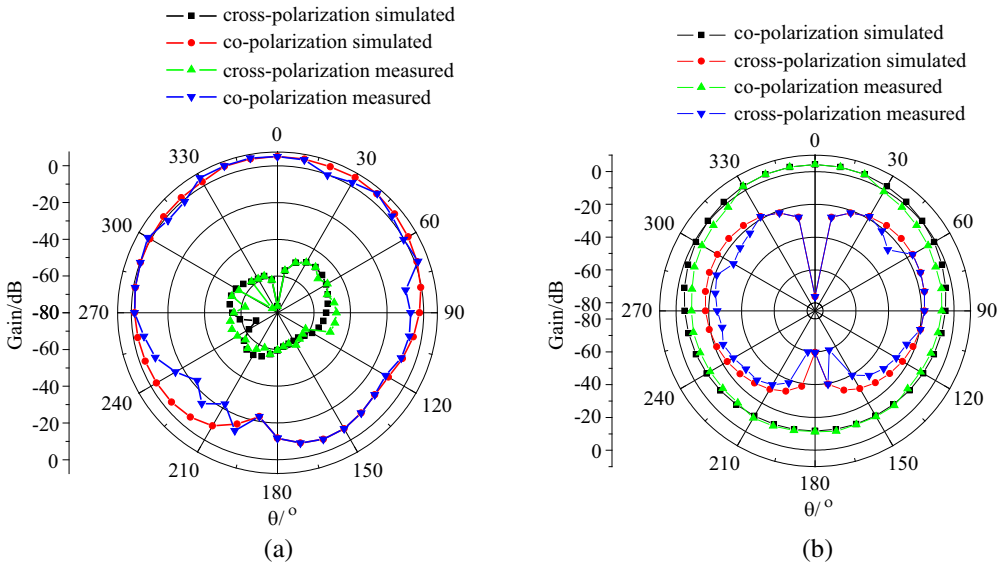

Figure 6: Measured and simulated directivity diagram. (a) E-plane. (b) H-plane.

4. CONCLUSION

In this paper, a SIW backed-cavity antenna with bow-tie shaped aperture is proposed and designed, key parameters of the antenna are studied. By integrating bow-tie shaped aperture, the antenna obtain wider bandwidth than the narrow rectangular slot antenna, but the radiation pattern of the antenna is reduced, thus the antenna is suitable for the communication system which require covering wider scope. Finally, the antenna is fabricated and tested. The measured results and simulation results are in good agreement, verify the validity of the design.

ACKNOWLEDGMENT

This work was supported by the National Key Laboratory of Millimeter Waves at Southeast University in China (No. K201201); the Natural Science Foundation of China (No. F010603).

REFERENCES

1. Luo, G. Q., Z. F. Hu, et al., "Planar slot antenna backed by substrate integrated waveguide cavity," *IEEE Antennas and Wireless Propagation Letters*, Vol. 7, 236–239, 2008.
2. Hong, W., et al., "Integrated SIW and HMSIW microwave and millimeter wave antennas," *IEEE IWAT'2007*, 69–72, Cambridge, England, 2007.
3. Awida, M. H. and A. E. Fathy, "Substrate integrated waveguide Ku-band cavity-backed 2×2 microstrip patch array antenna," *IEEE Antennas and Wireless Propagation Letters*, Vol. 8, 1054–1056, 2009.
4. Zhang, Q. and Y. Lu, "45° linearly polarized substrate integrated waveguide-fed slot array antennas," *ICMMT 2008*, 2008.
5. Dong, Y. and T. Itoh, "Substrate integrated composite right-/left-handed leaky-wave structure for polarization-flexible antenna application," *IEEE Transactions on Antennas and Propagation*, Vol. 60, No. 2, 760–771, 2012.
6. Cassivi, Y., L. Perregrini, P. Arcioni, et al., "Dispersion characteristics of substrate integrated rectangular waveguide," *IEEE Microwave and Wireless Components Letters*, Vol. 12, 333–335, 2002.
7. Xu, J., Z. N. Chen, X. Qing, and W. Hong, "140-GHz planar broadband LTCC SIW slot antenna array," *IEEE Transactions on Antennas and Propagation*, Vol. 60, No. 6, 2012.
8. Liu, J., D. R. Jackson, and Y. Long, "Substrate integrated waveguide (SIW) leaky-wave antenna with transverse slots," *IEEE Transactions on Antennas and Propagation*, Vol. 60, No. 1, 20–29, 2012.
9. Wang, X., Z. Weng, et al., "Design and implementation on miniaturized waveguide slot array antenna at Ku-band," *Journal of Microwaves*, Vol. 24, No. 3, 33–35, 2008.
10. Xu, J. F., Z.-Q. Kuai, and P. Chen, "W band multi-beam substrate integrated waveguide (SIW) slot array antenna," *Journal of Microwaves*, Vol. 25, No. 2, 1–5, 2009.
11. Bohórquez, J. C., H. A. F. Pedraza, I. C. H. Pinzón, et al., "Planar substrate integrated waveguide cavity-backed antenna," *IEEE Antennas and Wireless Propagation Letters*, Vol. 8, 1139–1142, 2009.
12. Wu, W., "Design of SIW cavity-backed circular-polarized antennas using two different feeding," *IEEE Transactions on Antennas and Propagation*, Vol. 59, No. 4, 1398–1403, 2011.
13. Li, Y. and W. Hong, "Investigations on the propagation characteristics of the substrate integrated waveguide based on the method of lines," *IEEE Proceedings Microwaves, Antennas and Propagation*, Vol. 152, No. 1, 35–42, 2005.

A Novel UWB Antenna with Dual-band Notched Characteristics

Yongfan Lin, Jiangang Liang, Zimu Yang, Zhiyong Xu, and Rui Wu
Air Force Engineering University, Xi'an, Shanxi 710051, China

Abstract— A novel omnidirectional ultra-wide band (UWB) antenna with dual band-notched characteristics are designed in this paper. To obtain extended impedance band-width, a small rectangular-shaped defected ground structure is used. The antenna has a good performance on impedance characteristics with the bandwidth from 2.0 GHz to 13.7 GHz. A U-shaped defected patch structure as well as a $\prod$-shaped defected patch structure are applied to obtain a dual band-notched characteristics at bandwidth of 5.29 GHz $\sim$ 6.608 GHz and 3.30 GHz $\sim$ 3.87 GHz, covering WIFI (5.470 GHz $\sim$ 5.725 GHz) and WIMAX (3.3 GHz–3.8 GHz) working frequency bandwidth. The problem of interference among spectrum can be solved effectively using this antenna.

1. INTRODUCTION

In 2002, the Federal Communications Commission approved rules for the commercial use for the ultra-wideband (UWB) with a frequency range of 3.1 GHz–10.6 GHz for commercial purposes, and then UWB technology has been widely used in various radars and it play an important role in the communication system [1, 2], because of the narrowband system of the UWB technology has incomparable advantage just like low cost, high speed and anti-multipath effect. However, the working bandwidth for UWB antenna will cause interference with existing narrowband wireless communication systems, for example WIFI (5.470 GHz–5.725 GHz) and WiMAX (3.3 GHz–3.8 GHz). Therefore, in order to prevent the interference between the spectrum and improve the utilization rate and independence of spectrum, it is particularly important to research UWB antenna with the stopband characteristics [3, 4].

UWB antenna with band-notched characteristics has many different kinds of structure. Generally, they always develop from two basic structures, one is 'strip' and the other one is 'slot'. Recently, to obtain the frequency band-notch function, modified planar monopoles with the slots on the patch of the antenna is proposed [5–7]. Modified planar monopoles with the strip structure is proposed to get double band-notched characteristics [8]. Multiple fractal-shaped slots-based UWB antenna is proposed to get triple band-notched functionality [9]. In this paper, a novel dual band-notched UWB antenna is proposed with the $\prod$-shaped and U-shaped slots in the patch. Obvious band-notched characteristics and good performance on omnidirectional radiation characteristics on the whole frequency band are realized by this simple structure. In aspect of implementing spectrum coexistence the antenna will gets better application.

2. ANTENNA DESIGN

$\prod$-shaped and U-shaped are designed in the patch of the UWB antenna. According to the theory of resonance, the formula used to calculate the size of the slot is $W = \lambda_{re}/2$, $\lambda_{re} = \lambda_0/\sqrt{\varepsilon_{re}}$, λ_0 is the wavelength of the center frequency of the notch band. So the band-notched characteristics for different working bandwidths can be realized by improving the size of the slots.

When the size of slot is $W = \lambda_{re}/2$, current resonance will occur around slot, the surface current distribution of the antenna at 5.5 GHz and 3.5 GHz are shown in Figure 1. As it is shown, current resonance occurs around U-styled slot and current distributes mostly around U-styled slot at 5.5 GHz. Band-notched function is created at 5.5 GHz because of the energy radiated by the antenna is few. The same situation occurs at 3.5 GHz around $\prod$-styled slot. So two distinct band-notched functions are got by the new structure.

The geometry of the presented antenna is illustrated in Figure 2. The dimensions of the optimized antenna are depicted in Table 1. The antenna is fabricated on a substrate of 50 mm $\times$ 40 mm $\times$ 0.8 mm with dielectric constant of 4.5, the loss tangent of 0.0035. The antenna consists of a circle radiation patch connected to a 50-Ω microstrip line on the front side and a partial ground plane on the back side.

3. RESULTS AND DISCUSSION

The band-notched characteristics produced by different slots are illustrated, simulated VSWR of the antenna with different slots shown in Figure 3. As it is shown, because of the different sizes

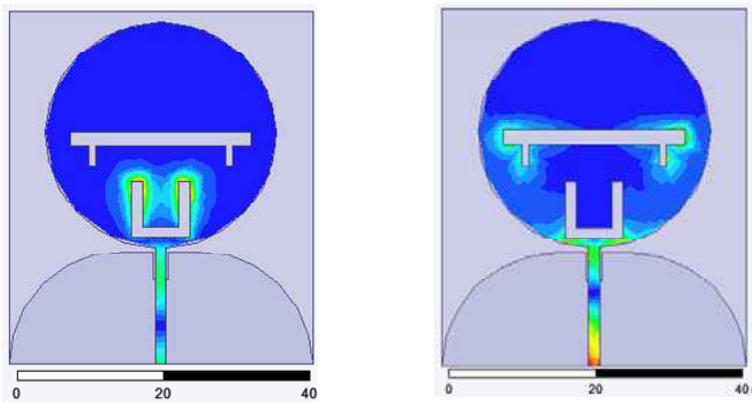

5.5 GHz 3.5 GHz

Figure 1: Surface current distribution on the proposed antenna at 5.5 GHz and 3.5 GHz.

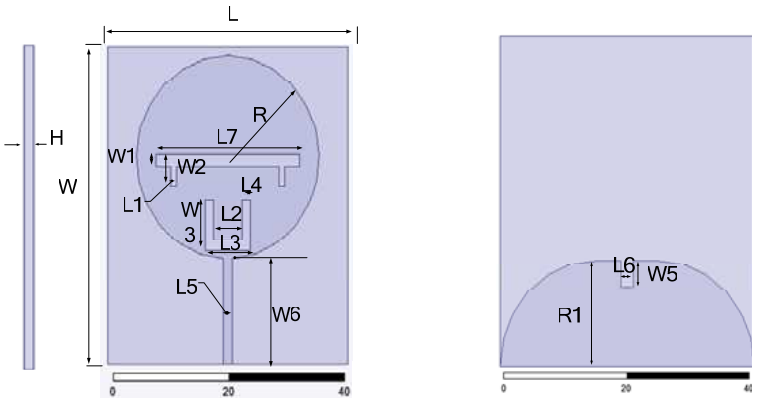

Figure 2: Geometry of the proposed antenna.

Table 1: Optimized antenna parameters (units: mm).

W	$W1$	$W2$	$W3$	$W4$	$W5$	$W6$	$L1$	$L2$	$L3$	$L4$	$L5$	$L6$	$L7$
50	2	5	8	1.5	4	16.8	1	5	8	1.5	1.6	2.1	24

of the $\prod$-shaped and U-shaped slots, the antenna has different band-notched characteristics. Two independent stopbands from 3.30 GHz–3.87 GHz and 5.29 GHz–6.608 GHz are created distinctly. The band-notched characteristic near 3.5 GHz mainly affected by the size of $\prod$-shaped slot, while the band-notched characteristic near 5.5 GHz mainly affected by the U-shaped slot. Meanwhile, the simulated result of a reference antennas with only one slot are also depicted as comparison.

Figure 4 illustrates simulated VSWR for the proposed antenna with different $L3$ and $L7$. It

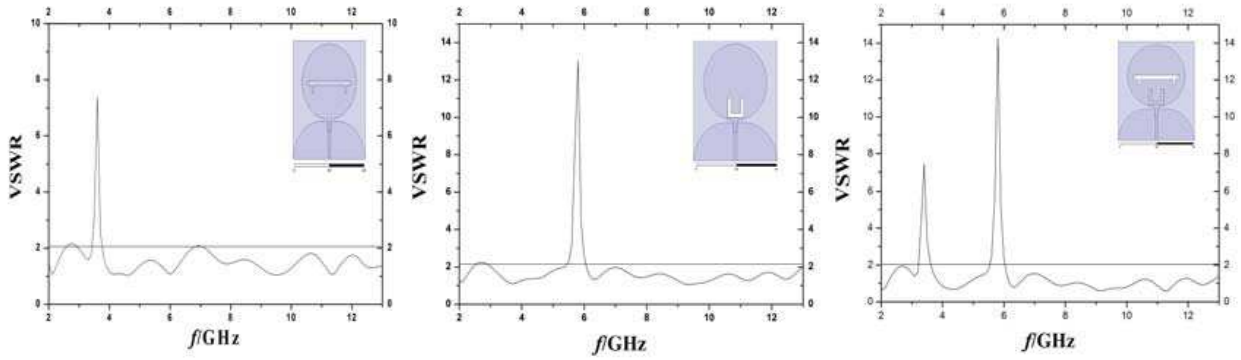

(a) (b) (c)

Figure 3: Simulated S_{11} for different slots.

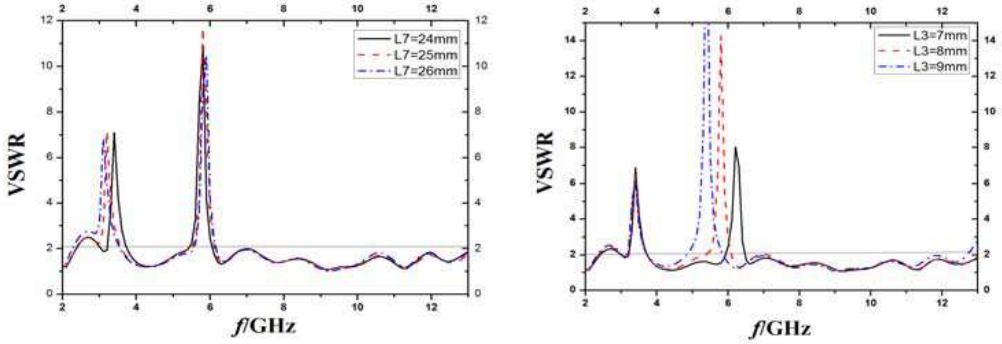

Figure 4: Simulated S_{11} for different sizes of $L7$ and $L3$.

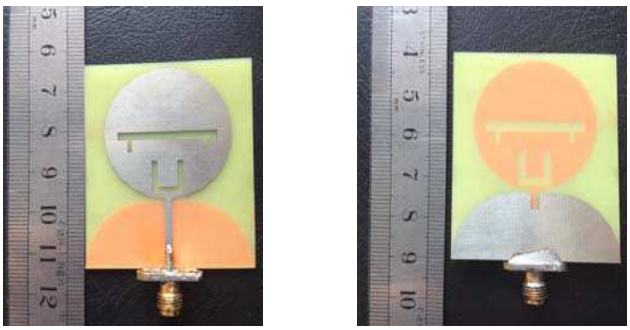

Figure 5: Photograph of the fabricated antenna.

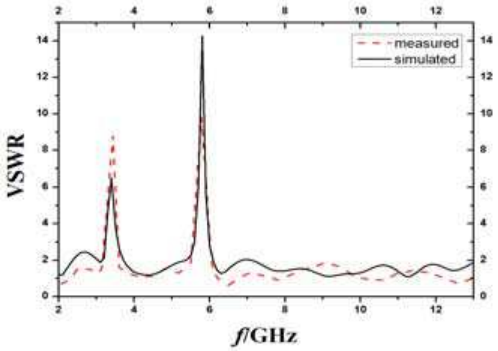

Figure 6: Simulated and measured VSWR.

exhibits the effect of the size of U-shaped and $\prod$-shaped slots, actually the center of the notch band is associated with the size of the slots. The parametric study shows that as the length of the segment $L3$ changes, the band produced by U-shaped slot is shifted significantly without affecting the other notched band. On the contrary, when the $\prod$-shaped slot size $L7$ shifts, the lower notched band shifts significantly without affecting the higher notched band. And we can see that the bigger the $L3$ and $L7$ the lower the notch frequency turns to be. The working frequency band of WIFI (5.470 GHz–5.725 GHz) and WIMAX (3.3 GHz–3.8 GHz) can be covered by shifting the size of $L3$ and $L7$.

The photograph of the antenna is shown in Figure 5. The simulated and measured VSWR of the proposed antenna are shown in Figure 6. It is shown that the simulated and measured results exhibit a good consistency.

The simulated radiation patterns at 2 GHz, 5 GHz, 7 GHz, 9 GHz are depicted in Figure 7. It can be seen that the antenna has a nearly omnidirectional radiation pattern in the H-plane and a radiation pattern in the E-plane. The presented antenna exhibits a good radiation performance.

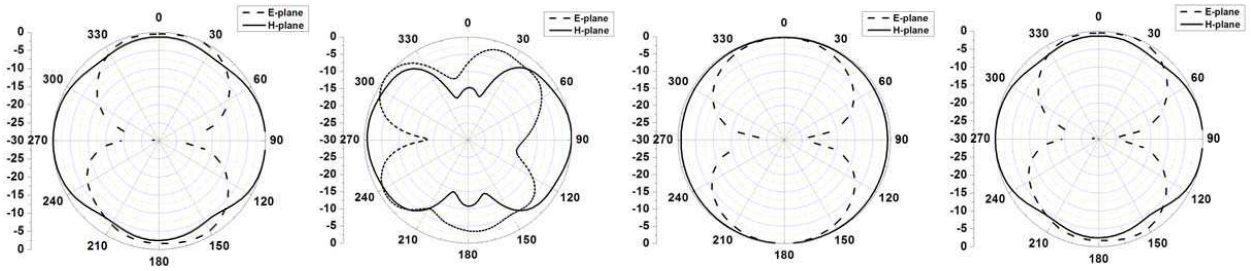

(a) 7 GHz (b) 9 GHz (c) 2 GHz (d) 5 GHz

Figure 7: Radiation patterns of the antenna at (a) 5 GHz and (b) 7 GHz.

4. CONCLUSION

A novel compact UWB planar antenna with dual-notched bands has been presented and discussed. The wide impedance band-width (2.0 GHz–13.7 GHz) is realized by a rectangle-shaped defected ground structure (DGS). The presented antenna exhibits a broad bandwidth and omnidirectional radiation performance. In addition, the dual band-notched characteristics are realized by a U-shaped as well as a $\prod$-shaped slot. Simulated and measured results show that the working band-width of WIFI (5.470 GHz–5.725 GHz) and WIMAX (3.3 GHz–3.8 GHz) are covered by the two band notches. The problems of spectrum coexistence and interference among spectrum can be solved effectively.

REFERENCES

1. Zhan, K., Q. Guo, and K. Huang, "A miniature planar antenna for Bluetooth and UWB applications," *Journal of Electromagnetic Waves and Applications*, Vol. 24, No. 6, 2299–2308, 2010.
2. Reza, Z. and A. Abdolali, "A very compact ultra wide band printed omnidirectional monopole antenna," *IEEE Antennas and Wireless Propagation Letters*, Vol. 9, 471–473, 2010.
3. Yuan, G., J. Lin, and B. Li, "Design of a UWB printed antenna with triple-band notched characteristic," *Elictronic. Sci. & Tech.*, 71–73, 2013.
4. Song, Y. I-C., J. Ding, and C.-J. Guo, "Research on a printed monopole UWB antenna with dual band-rejection characterisitc," *Journal of Microwaves*, Vol. 29, 65–69, Feb. 2013.
5. Saada, A. A. R., M. M. M. Ali, and E. E. M. Khaled, "An integrated 3G/Bluetooth and UWB antenna with a band-notched feature," *Journal of Electromagnetic Waves and Applications*, Vol. 27, No. 18, 2430–2441, 2013.
6. Cheng, S. and A. Rydberg, "Printed slot planar inverted cone antenna for ultra wide band applications," *IEEE Antennas and Wireless Propagation Letters*, Vol. 7, 18–21, 2008.
7. Akbari, M., S. Zarbakhsh, and M. M. Young, "A novel UWB antenna with dual-stop band characteristics," *Microwave and Optical Technology Letters*, Vol. 55, No. 11, 2741–2745, 2013.
8. Goraia, A., A. Karmakar, M. Pal, and R. Ghatak, "Multiple fractal-shaped slots-based UWB antenna with triple-band notch functionality," *Journal of Electromagnetic Waves and Applications*, Vol. 27, No. 18, 2407–2415, 2013.
9. Xie, M., Q. Guo, and Y. Wu, "Design of a miniaturized UWB antenna with band-notched and high frequency rejection capability," *Journal of Electromagnetic Waves and Applications*, Vol. 25, Nos. 8–9, 1103–1112, 2011.

Spurious Modes Reduction in a Patch Antenna Using a Novel DP-EBG Structure

Zhi-Yong Xu, Hou Zhang, Rui Wu, and Yong-Fan Lin
School of Air and Missile Defense, Air Force Engineering University, Xi'an, Shaanxi 710051, China

Abstract— A novel dual planar electromagnetic bandgap (DP-EBG) microstrip structure with wide stopband and flat passband is presented. It is demonstrated that the proposed structure achieves a Ultra-Wide stopband and excellent passband performance within a compact circuit area. And the DP-EBG structure is employed in the feed line of patch antenna with the aim of suppressing harmonics and other spurious modes. Simulated and measured results indicate that the application of this DP-EBG structure not only drastically diminishes spurious radiations of 2nd $\sim$ 6th harmonics in a broad frequency band, but also overcome some shortages of other EBG microstrip antennas introduced in previous research.

1. INTRODUCTION

The active integrated antennas play an important role in the framework of modern wireless communication systems [1]. The evolution of communication systems, demand antennas with specific operational features and create the necessity to develop advanced new methods to design them in order to fulfill the imposed technical requirements. So more and more new technologies are utilized in the modern antennas. One of them, being choice for many antenna engineers, is the EBG (Electromagnetic Band Gap) technology [2].

The electromagnetic band-gap (EBG) structure exhibits a bandstop behavior over a certain frequency range, in which the propagation of electromagnetic waves is prohibited [3]. Recently, some papers have proposed the employment of EBG structures for the improvement of the antennas' radiating features. For example, the EBG structure has been developed to reduce the spurious harmonic radiation of the patch antenna. For microstrip patch antenna with proximity coupled feeding line, the second and third harmonics are eliminated by adjusting the length of feed line and introducing one resonant cell [4]. A CPW-fed circular slot antenna with an arc-shaped slot inserted on the ground conductor was designed for achieving four-frequency band notch characteristic in the range of $2 \sim 10$ GHz [5].

In this paper, a novel dual planar electromagnetic bandgap (DP-EBG) microstrip structure is proposed. Wide stopband and compact size are realized with asymmetric defected ground structure (ADGS). Furthermore the new structure is utilized to suppress harmonics and other spurious modes of the patch antenna. Both simulated and measured results demonstrate that the patch antenna which adopt the new structure obtains better performance than that of other designs in previous references in view of harmonic signal suppression and radiation patterns.

2. NOVEL DP-EBG STRUCTURE DESIGN AND ANALYSIS

As shown in Fig. 1, the novel dual planar electromagnetic bandgap (DP-EBG) microstrip structure is achieved with a combination of two one-dimensional (1-D) EBG structures, namely the asymmetric defected ground structure (ADGS) and the microstrip line type electromagnetic bandgap (ML-EBG) structure. According to [6], The ADGS circuit not only provides deeper stopband but also decreases the physical dimensions when compared with the microstrip line type EBG structure due to its highly-resonant characteristics. Hence, if we superpose the microstrip line type EBG structure and the ADGS section into a double-plane configuration, this assembled configuration may be expected to realize better stopband and low-pass band performance than that of any other single type EBG structure.

Based on this idea, we propose a novel compact dual planar electromagnetic bandgap (DP-EBG) microstrip structure as shown in Fig. 1, in order to achieve minimization, only one unit cell are etched underneath the adjacent EBG square patches. In addition, the proposed DP-EBG microstrip structure using a FR4 substrate with 0.8 mm thick and a dielectric constant of 2.65. The line width w for all models is chosen to be 2.2 mm (equal to the width of microstrip 50 ohm line). And other correlative structural dimensions are calculated and shown in Table 1.

Figure 2 shows S-parameters of the proposed DP-EBG microstrip structure. Regarding Fig. 2, the most important feature of the proposed DP-EBG microstrip structure is about -20 dB stopband

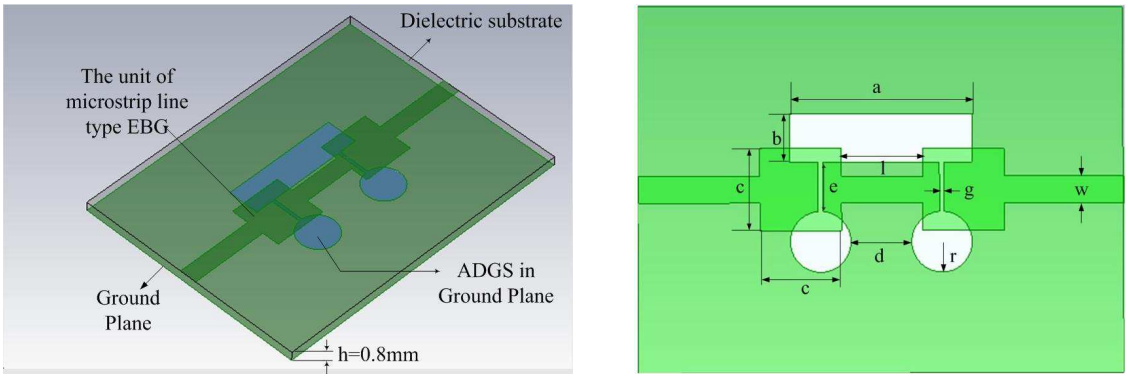

Figure 1: Schematic of the novel DP-EBG microstrip structure. (a) 3-D view. (b) Top view.

Table 1: Structural dimensions.

Parameters	d	a	b	c	r	g	e
Value (mm)	4	14	4	6.7	2.5	0.4	4.5

from 3.5 GHz to 13 GHz (In other words, the relative bandwidth is over than 115%) in addition to the negligible insertion loss which is less than 0.3 dB throughout the passband. These favorable results are profit from the fact that the longitudinal resonant modes of the microstrip line type EBG structure and the transverse resonant modes of the ADGS are strongly coupled through the DGS gap fields so that the passband and stopband characteristics are effectively improved by these multiple resonant modes. By virtue of the highly resonant mechanism, this novel DP-EBG structure has relatively wider stopband characteristics and smaller required circuit size than that of the new EBG structure proposed in [7, 8] which satisfies the Bragg reflection condition.

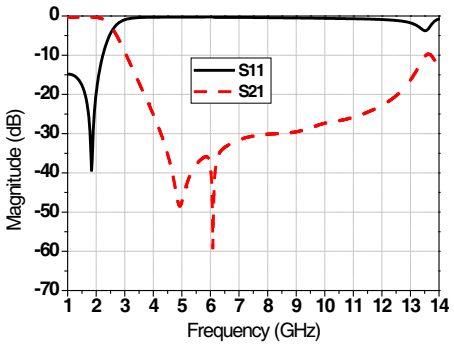

Figure 2: S-parameters of the proposed DP-EBG microstrip structure.

3. APPLICATION OF THE NOVEL DP-EBG STRUCTURE IN MICROSTRIP ANTENNA

3.1. The Novel EBG Microstrip Antenna Design

In order to validate the validity of the novel DP-EBG structure in the usage of suppressing spurious radiations of patch antenna, a normal microstrip patch antenna that serves as the reference antenna and operates at 1.83 GHz is designed firstly. Fig. 3(a) shows the configuration of the reference antenna. A $50 \times 50\,\mathrm{mm}^2$ square patch is fabricated on the FR4 substrate with the physical size of $118 \times 91 \times 0.8\,\mathrm{mm}^3$ and the relative permittivity of $\varepsilon_r = 2.65$. A 50 ohm microstrip feed line is used for antenna excitation. Inset cut with the length (L_{gap}) of 18.8 mm and the width (W_{gap}) of 1.2 mm is also adopted for a good impedance design for the reference antenna. Additionally, other structural parameters are evaluated and shown in Fig. 3(a).

Then, the proposed DP-EBG structure shown in Fig. 1 was constructed in the feed line of the microstrip patch antenna, and it is apparent from the schematics shown in Fig. 3(b) that this

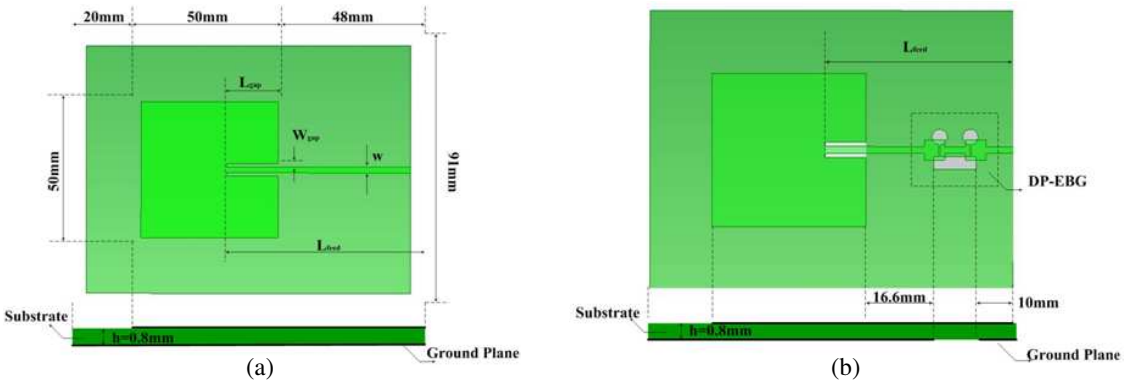

Figure 3: Sketch of the printed antennas. (a) The reference patch antenna. (b) The proposed EBG patch antenna.

novel EBG microstrip antenna has the same dimensions as that of the reference antenna except a modulated microstrip line on top of a perturbed ground plane etched with ADGS.

The above models are fabricated and measured experimentally to confirm the theoretical analysis with respect to the reflection coefficients and radiation properties. All the simulation is carried out by HFSS. The reflection or transmission coefficients of all the fabricated prototypes are measured using an Anritsu ME7808A vector network analyzer while the radiation patterns are measured inside an anechoic chamber with an AV3635 antenna measurement system.

4. SIMULATION AND EXPERIMENTAL RESULTS

It is shown in Fig. 4 that the simulation and measurement return loss of the two antennas has been depicted. Reasonable agreement is observed between the measurements and the simulated data over the entire frequency span. The difference in the value of input return loss could be due to the number of sampling points taken while the slight shift in frequency could be attributed to the variation of the actual dielectric constant and the machining error. From the measured result shown in Fig. 4(a), the dominant resonant frequency of the reference antenna is 1.85 GHz, slightly shifting from the simulated one and its -10 dB bandwidth is about 16 MHz. The reference antenna also resonates at many harmonic frequencies along with other surface wave modes. However, for the EBG antenna, these harmonic resonances as well as other surface wave modes are totally suppressed within a wide frequency band except the fundamental as shown in Fig. 4(b). It is also easily found by comparing the measured S_{11} of both antennas that the proposed EBG antenna has the same fundamental frequency (i.e., 1.85 GHz) as that of the reference antenna, and the bandwidth and the reflection coefficient roughly remain unchanged. Therefore, the proposed EBG antenna obtains a number of attractive features, which include the following.

I. The operating frequency is not shifted away from the original resonance of the reference antenna, even though the patch size of the EBG antenna remain unchanged. Unlike other designs introduced in the references [4, 9–11], where the fundamental frequencies of EBG antenna were always shifted more or less if they have the same patch size as that of the normal one. This character can be attributed to two reasons. Firstly, the low-pass characteristics of the feed line constructed with the proposed DP-EBG structure is so well that the propagation loss is small and can be comparable to that of a conventional microstrip line. On the other hand, the distance between the patch's bottom edge and the DP-EBG structure's top side is enough long (i.e., 16.6 mm, which is longer than $\lambda_g/10$, where λ_g is the wavelength under the substrate corresponding to 1.85 GHz), so the electromagnetic field in the vicinity around the patch is not disturbed by the DP-EBG structure, making the fundamental frequency of the EBG antenna be stable. So, the method in this letter can be utilized to design an EBG patch antenna operating on any required fundamental frequency and reducing spurious modes over a wide band even though the patch size is calculated by using the conventional procedure applied to the normal microstrip patch antenna.

II. The proposed EBG antenna achieves the goal of notably diminishing resonances of 2nd $\sim$ 6th harmonics and other surface wave modes over a wide frequency range extending from 2 GHz up to 9 GHz, so this proposed EBG antenna obtains better performance than that of other designs in references [4, 5, 9–11] with regard to the frequency bandwidth of harmonic suppression. Moreover, the total length of the two EBG units is about 21.4 mm, less than 1/7 of the free space wavelength at

1.85 GHz. There is no increase in the size of the antenna while the other features are not degraded.

In addition, the radiation patterns at the fundamental frequency are simulated and measured for both antennas as depicted in Fig. 5 and Fig. 6. These power levels are normalized by the maximum level of the reference antenna at the dominant resonant frequency. The experimental co-polarization patterns agree well with simulated ones except some discrepancies which can be attribute to the fabrication inaccuracy. It is easily seen from the measured results that both antennas have almost identical and quite stable co-polarization pattern characteristics in both plane at the fundamental frequency. The EBG antenna radiates broadside, and maintains a cross-polarization level similar to that of the reference one, which is not presented here and remain below -20 dB in the E-plane and H-plane respectively. The realized gain of the EBG antenna is similar to that of the reference antenna (the reference antenna: 6.0 dB; the EBG antenna: 6.0 dB), satisfying the requirements for engineering applications. And there is no energy leaking in our designed EBG antenna, which can be studied from the Fig. 6 that the front-to-back ratio is only a little lower than that of the reference one because the DP-EBG structure constructed in the feed line cannot resonate effectively as an antenna and results in a negligible radiation loss at the operating frequency. Besides that, there is also no beam squint in the fundamental radiation pattern, which is different from the case presented in [9] where the DGS operating with some energy letting out is so close to the patch's bottom edge that its radiation disturbs the antenna's main radiation pattern. Therefore, this proposed EBG antenna in this paper obtains better radiation performance at the fundamental frequency in comparison with some designs in former references.

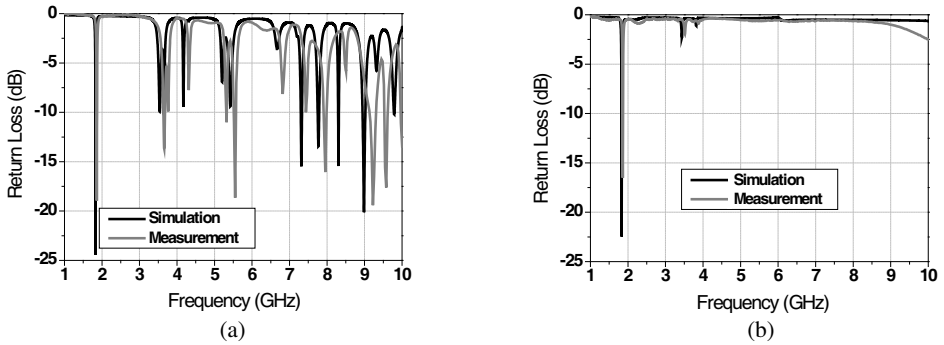

Figure 4: (a) Calculated and measured return losses for the normal antenna and (b) the proposed EBG antenna.

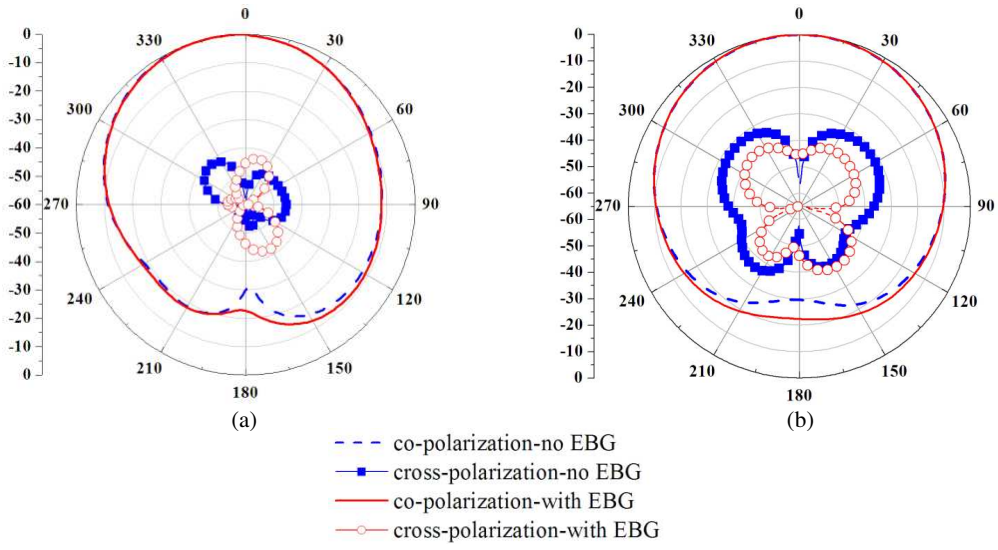

Figure 5: Simulated radiation patterns for the reference antenna and the EBG antenna. (a) E-plane. (b) H-plane.

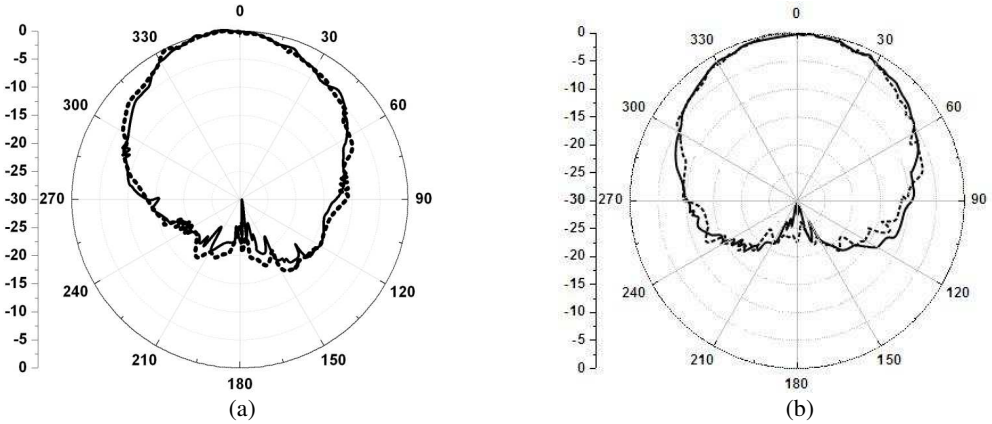

Figure 6: Measured co-polarization radiation patterns for the reference antenna (rigid line) and the EBG antenna (broken line) at the dominant resonant frequency. (a) E-plane. (b) H-plane.

5. CONCLUSIONS

A patch antenna with a novel DP-EBG structure constructed in the feeding network has been studied in this letter. It is demonstrated that the usage of the novel DP-EBG microstrip structure in the patch antenna leads to a perfect removal of multiple harmonics and other spurious resonances over a wide frequency range, while improvements in radiations at the fundamental frequency is more significant as compared to other designs given in the previous research. By modulating the separation between DP-EBG structure inserted in the feed line and the patch's bottom edge at a moderate distance (i.e., longer than $\lambda_g/10$), we realize the goal of making the fundamental frequency of the EBG antenna unchanged when compared with the normal one even though the patch sizes of two antennas are identical. Therefore, the design of the EBG patch antenna operating at any certain frequency and reducing spurious modes over a wide band can be simplified by using the method proposed in this paper since the patch sizes can be calculated through the conventional evaluating procedure. Further more, due to the small dimension of the DP-EBG structure, compact feed network is achieved. Therefore, the proposed EBG antenna in this letter is quite effective for the suppression of spurious signals, and may find applications in compact active circuit system and modern wireless communication realm.

REFERENCES

1. Mourtzios, C. and K. Siakavara, "Novel antenna configurations with non-uniform EBG lattices for wireless communication networks," *The 7th European Conference on Antennas and Propagation (EUCAP)*, 2748–2752, 2013.
2. Ikeuchi, R. and A. Hirata, "Dipole antenna above EBG substrate for local SAR reduction," *IEEE Antennas and Wireless Propagation Letters*, Vol. 10, 904–906, 2011.
3. Zhu, H. and J. Mao, "Miniaturized tapered EBG structure with wide stopband and flat passband," *IEEE Antennnas and Wireless Prppagation Letters*, Vol. 11, 314–317, 2012.
4. Inclán-Sánchez, L., J. Vázquez-Roy, and E. Rajo-Iglesias, "Proximity coupled microstrip patch antenna with reduced harmonic radiation," *IEEE Transactions on Antennas and Propagation*, Vol. 57, No. 1, 27–32, 2009.
5. Yeo, J. and D. Kim, "Harmonic supperssion characteristic of a CPW-FED circular slot antenna using single slot on a ground conductor," *Progress In Electromagnetics Research Letters*, Vol. 11, 11–19, 2009.
6. Parui, S. K. and S. Das, "A novel asymmetric defected ground structure for implementation of elliptic filters," *IEEE MTT-S International Microwave and Optoelectronics Conference*, 946–949, Brazil, 2007.
7. Zhu, H. and J. Mao, "Miniaturized tapered EBG structure with wide stopband and flat passband," *IEEE Antennas and Wireless Propagation Letters*, Vol. 11, 314–317, 2012.
8. Wang, C. and T. Wu, "Model and mechanism of miniaturized and stopband-enhanced interleaved EBG structure for power/ground noise suppression," *IEEE Transactions on Electromagnetic Compatibility*, Vol. 55, 159–167, 2013.

9. Sung, Y. J. and Y.-S. Kim, "An improved design of microstrip patch antennas using photonic bandgap structure," *IEEE Transactions on Antennas and Propagation*, Vol. 53, No. 5, 1799–1804, 2005.
10. Lee, J.-G. and J.-H. Lee, "Suppression of spurious radiations of patch antennas using split-ring resonators (SRRs)," *Microwave and Optical Technology Letters*, Vol. 48, No. 2, 284–287, 2006.
11. Mandal, M. K., P. Mondal, S. Sanyal, and A. Chakrabarty, "An improved design of harmonic suppression for microstrip patch antennas," *Microwave and Optical Technology Letters*, Vol. 49, No. 1, 103–105, 2007.

A Novel DP-EBG Structure for Low-pass Filter of Wide Stopband

Hou Zhang, **Zhi Yong Xu**, **Yong Fan Lin**, **and Rui Wu**
School of Air and Missile Defense, Air Force Engineering University, Xi'an, Shan'xi 710051, China

Abstract— In this letter, a novel dual planar electromagnetic bandgap (DP-EBG) microstrip low-pass filter structure is investigated. The presented structure is realized by superposing two different one-dimensional (1-D) electromagnetic bandgap (EBG) structures which have different center frequency of the stopband into a coupled dual-plane configuration. Both simulation and experimental results have verified that only two cells of the proposed structure are enough for the measured −20 dB stopband from 3.7 GHz to 14 GHz with a excellent low-pass performance in a small circuit area. Since this novel design demonstrates superior low-pass filtering functionality, we expect this novel structure is widely used for wideband monolithic circuit applications.

1. INTRODUCTION

The electromagnetic bandgap (EBG) structure is a frequency-selective structure capable of restricting the electromagnetic waves along one or more directions within a certain frequency band. Due to the bandgap that can filter out the unwanted signals, the EBG structures have been widely used in antennas, filters, couplers, high-speed circuits, etc. [1–4]. Therefore, the investigation of EBG structures have attracted much attention recently.

In modern telecommunication systems, high-performance microwave circuits with compact size, low insertion loss, steep rejection, and wide stopband are widely required. In [5], a compact tapered planar EBG structure is proposed for achieving wide stopband and flat passband, in comparison with traditional planar EBG structure, the new structure obtained a relative fractional bandwidth of 93.7% in the stopband below −20 dB. In [6], An interleaved electromagnetic bandgap (EBG) structure is investigated to be with a compact size and wide stop-band bandwidth for suppressing power/ground noise in power distribution networks, the interleaved EBG structure achieve substantial improvements on the bandwidth of 51.1% compared with the conventional EBG structure. Several researchers have focused on achieving compact design and wide frequency stopband using multilayered planar techniques, such as [7–10]. For example, T. Akalin [7] has proposed a dual-planar EBG microstrip low-pass filter, but this require large size and has a limitation in compact microstrip circuit applications.

In this paper, we introduce a novel dual planar electromagnetic bandgap (DP-EBG) structure which is achieved with a combination of two one-dimensional (1-D) EBG structures having different center frequencies of the stopband, namely the elliptical dumbbell defected ground structure (ED-DGS) and the microstrip line type electromagnetic bandgap (ML-EBG) structure. A low-pass filter using two cells of the proposed DP-EBG structure demonstrate a rejection of below −20 dB in the range from 3.7 GHz to 14 GHz and negligible insertion loss in the passband. As compared to previous research on EBG low-pass filters, the proposed structure achieves better performance with a ultra-wide stopband and a significant reduction in physical size.

2. NOVEL DP-EBG MICROSTRIP LOW-PASS FILTER STRUCTURE

The ordinary filters can be achieved with the microstrip line type electromagnetic bandgap (ML-EBG) structure which consists of the conductor ground plane and periodic patches inserted in the microstrip line on the top plane, as shown in Fig. 1. Since it is designed to satisfy the Bragg reflection condition [11], the period d equals half of guided wavelength at center frequency of the stopband.

It is simple to use the ML-EBG structure for the design of the microstrip filters, but this structure is not compact in physical size for low-frequency band applications since it is designed to satisfy the Bragg reflection condition. In order to provide more evident stopband characteristic and decreese the circuit layout size, a rectangular dumbbell defected ground structure (DGS) unit was proposed in [12]. The DGS filters not only provide deeper stopband but also decrease the physical dimensions when compared with a conventional ML-EBG filter due to its highly-resonant characteristics [12]. However, it is experimentally found that the passband performance of the DGS with only one or a few unit lattices is not good [13]. Hence, if we superpose the ML-EBG structure and the DGS section into a double-plane configuration, in which two types of EBG cells are too

strongly coupled to probably remove above mentioned shortages, this compact configuration may be expected to realize better stopband and low-pass performance than that of any single type EBG structure and could be used as a new good low-pass filter.

Based on this idea, we propose a novel compact dual planar electromagnetic bandgap (DP-EBG) microstrip filter as shown in Fig. 2, in which a ML-EBG structure is overlapped on a elliptical dumbbell defected ground structure (ED-DGS). In Fig. 2, each rectangular patch etched on the microstrip line together with its underlying ED-DGS located on the ground plane can be treated as a unit cell, so this novel DP-EBG filter consists of two cells. we simulated a ML-EBG unit cell on a common ground and a common microstrip on a ED-DGS unit cell in addition to the proposed filter structure shown in Fig. 2 using a F4B substrate with 0.8-mm thick and a dielectric constant of 2.65 by Anosoft HFSS. The linewidth w for all models is chosen to be the characteristic impedance of 50 Ω microstrip line.The ED-DGS cell in the proposed DP-EBG filter is designed for 5.42 GHz resonant frequency, and the ML-EBG structure is designed for 7 GHz Bragg condition so the period of the lattice (d) is set as 13.4 mm. Also, other structural dimensions are calculated and shown in Table 1.

Then, in order to characterize the proposed DP-EBG microstrip filter experimentally, we fabricated this structure and its S-parameters were measured to validate the simulation results. Fig. 3 shows the fabricated structure, which has a F4B substrate ($2.65\varepsilon_r$ and 0.8 mm thickness).

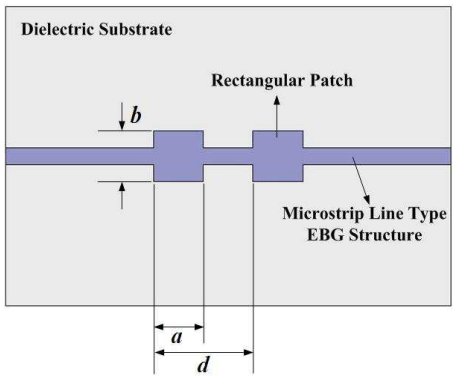

Figure 1: Front view of the ordinary filter using ML-EBG structure which is built up on the microstrip line.

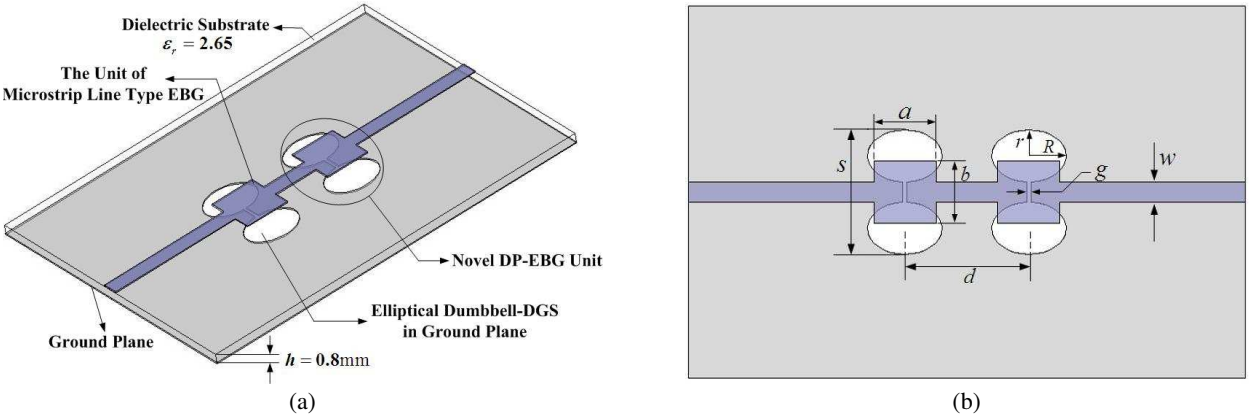

Figure 2: Schematic of the novel DP-EBG microstrip structure. (a) 3-D view. (b) Top view.

Table 1: Novel DP-EBG microstrip structure specifications, where the axial ratio: R/r is assigned to be 10/7.

Parameters	w	a	b	R	r	g	s
Value (mm)	2.2	6.7	5	4	2.8	0.5	15.4

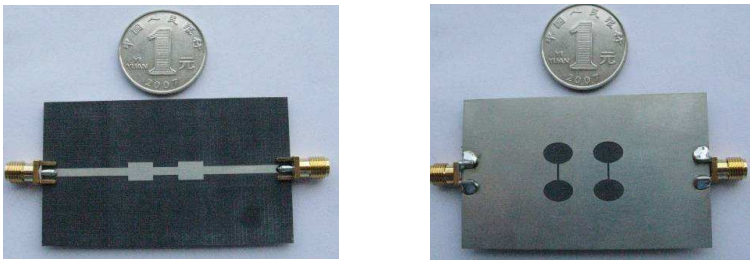

(a) (b)

Figure 3: Manufactured prototype of the novel DP-EBG microstrip structure. (a) Top view. (b) Bottom view.

3. NUMERICAL AND MEASUREMENT RESULTS

Figure 4 shows the calculated data of the single ML-EBG cell and the single ED-DGS cell. The single ML-EBG cell shows flat transmission characteristics and very low insertion loss without ripples in the passband while the single ED-DGS cell shows a attenuation pole location in the stopband which is wider than that of a single ML-EBG cell, indicating there is a highly-resonant behavior in the ED-DGS. It can be concluded from results shown in Fig. 4 that the DGS unit provide evident stopband characteristics while the ML-EBG cell shows good low-pass performance.

Figure 5 shows S-parameters of the proposed DP-EBG microstrip structure consisting of one cell and two cells, It can be seen from the Fig. 5 that the return loss in the lowpass band for the one-unit microstrip structure is not always below -10 dB and its corresponding insertion loss is also a little higher than that of the DP-EBG structure including two cells. In Fig. 5(b), the measured data agree well with the simulation results except the difference occurring in the high frequency band which could be attributed to the variation of the actual dielectric constant and the loss tangent. Also, it has been assumed infinite conductivity for the metallic strip and the ground plane in the simulation. The Fig. 5(b) also show that the most important feature of the proposed DP-EBG microstrip filter is about -20 dB stopband from 3.7 GHz $\sim$ 14 GHz (In other words, the relative bandwidth is over than 116%) in addition to the negligible insertion loss which is less than 0.5 dB throughout the passband (0 GHz $\sim$ 2 GHz). It is also noted that there are some attenuation pole locations in the stopband which are more deeper than that shown in Fig. 4(b), meaning the resonant behavior of it is more intense than that of the single ED-DGS cell. These favorable results for the proposed DP-EBG filter structure can be explained by the theory introduced in [8] that the longitudinal resonant modes of the ML-EBG structure and the transverse resonant modes of the ED-DGS are strongly coupled through the ED-DGS gap fields so that the passband and stopband characteristics are effectively improved by these multiple resonant modes. Further more, by virtue of the highly-resonant mechanism, this novel DP-EBG filter has relatively wider stopband characteristics and smaller required circuit size than that of other dual planar EBG filters proposed in [9, 10] which satisfies the Bragg reflection condition. Also, this new DP-EBG structure, having only one substrate, is much simpler to be fabricated than that of the EBG filter introduced in [6] which consists of dual attached slabs while the relative stopband bandwidth is also wider. Therefore, it is testified from the experimental results that the DP-EBG microstrip structure proposed in this letter is a new compact low-pass filter with ultra-wide stopband.

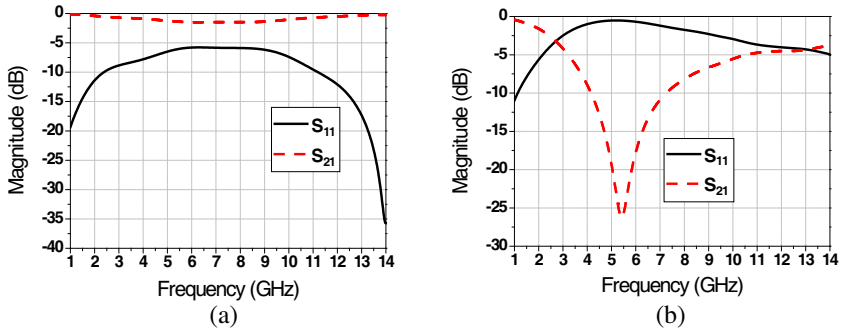

Figure 4: Simulated results of EBG cells, (a) single ML-EBG cell and (b) single ED-DGS cell.

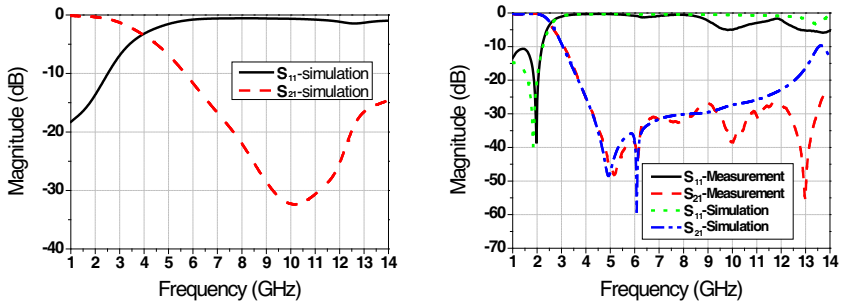

Figure 5: S-parameters of the proposed DP-EBG microstrip structure, (a) simulated results of one DP-EBG cell and (b) simulated and measured results of two DP-EBG cells.

4. CONCLUSIONS

A novel low-pass filter structure using the DP-EBG configuration is designed and implemented in this paper. Due to the dual planar arrangement of two different EBG structures as well as their unique characteristics, this proposed EBG filter structure obtains a relative fractional bandwidth of more than 116% in the stopband below −20 dB and excellent low-pass performance in a compact physical size. The structure was fabricated and the measured results are in good agreement with the simulation results, verifying the good performance of the proposed structure. Since this novel filter structure is easy to fabricate and shows superior passband and stopband characteristics in a small circuit area, it will be widely applied in various monolithic circuits.

REFERENCES

1. Mosallaei, H. and K. Sarabandi, "A compact wide-band EBG structure utilizing embedded resonator circuits," *IEEE Antennas and Wireless Propagation Letters*, Vol. 4, 5–8, 2005.
2. Ikeuchi, R. and A. Hirata, "Dipole antenna above EBG substrate for local SAR reduction," *IEEE Antennas and Wireless Propagation Letters*, Vol. 10, 904–906, 2011.
3. Elsheakh, D. N., H. A. Elsadek, E. A. Abdallah, H. Elhenawy, and M. F. Iskander, "Enhancement of microstrip monopole antenna bandwidth by using EBG structures," *IEEE Antennas and Wireless Propagation Letters*, Vol. 8, 959–962, 2009.
4. Liang, H. C. and Q. H. Liu, "Novel array EBG structures for ultra-wideband simultaneous switching noise suppression," *IEEE Antennas and Wireless Propagation Letters*, Vol. 10, 588–591, 2011.
5. Zhu, H. and J. Mao, "Miniaturized tapered EBG structure with wide stopband and flat passband," *IEEE Antennas and Wireless Propagation Letters*, Vol. 11, 314–317, 2012.
6. Wang, C. and T. Wu, "Model and mechanism of miniaturized and stopband-enhanced interleaved EBG structure for power/ground noise suppression," *IEEE Transactions on Electromagnetic Compatibility*, Vol. 55, 159–167, 2013.
7. Akalin, T., M. A. G. Laso, E. Delos, T. Lopetegi, O. Vanbesien, M. Sorolla, and D. Lippens, "High performance double-sided microstrip PBG filter," *Microwave Opt. Technol. Lett.*, Vol. 35, No. 2, 90–93, Oct. 2002.
8. Kim, J. and H. Lee, "Wideband and compact bandstop filter structure using double-plane superposition," *IEEE Microwave and Wireless Components Letters*, Vol. 13, No. 7, 279–280. 2003.
9. Huang, S. Y. and Y. H. Lee, "Tapered dual-plane compact electromagnetic bandgap microstrip filter structure," *IEEE Trans. Microw. Theory Tech.*, Vol. 53, No. 9, 2656–2664, Sep. 2005.
10. Huang, S. Y. and Y. H. Lee, "Compact U-shaped dual planar EBG microstrip low-pass filter," *IEEE Transactions on Microwave Theory and Techniques*, Vol. 53, No. 12, 3799–3805, 2005.
11. Lopetegi, T., "Design of improved 2-D photonic bandgap microstrip structures," *The 23rd International Conference on Infrared and Millimeter Waves*, 197–198, 1998.
12. Ahn, D., J.-S. Park, C.-S. Kim, et al., "A design of the low-pass filter using the novel microstrip defected ground structure," *IEEE Transactions on Microwave Theory and Techniques*, Vol. 49, No. 1, 86–93, 2001.
13. Lim, J., C. Kim, J. Park, et al., "Design of 10 dB 90° branch line coupler using microstrip line with defected ground structure," *Electronics Letters*, Vol. 36, No. 21, 1784–1785, 2000.

A Novel Method for Sparse Array Antenna Through-the-wall Imaging Radar Wall Clutter Elimination Using Independent Component Analysis

Chi Zhang, **Yue-Li Li**, **and Zhi-Min Zhou**
College of Electronic Science and Engineering
National University of Defense Technology, Changsha, Hunan 410073, China

Abstract— A wall clutter elimination method for the through-the-wall imaging radar (TWIR) with sparse array antenna is presented in this paper. Unlike the synthetic aperture radar (SAR) processing techniques, we scan the elements of the array periodically to create a range profile (RP) matrix for each transmit/receive antenna pair. Then, based on analysis of the weak fluctuation among RP signals, we apply independent component analysis (ICA) on each RP matrix to decompose the signal components and remove the wall clutter. The experimental results show that the proposed method can separate targets and wall clutter components, and improve the signal-to-clutter ratio (SCR) of final image effectively.

1. INTRODUCTION

Through-the-wall imaging radar (TWIR) emits electromagnetic waves to image and localise objects or people behind walls, which can assist actions in many area such as military, antiterrorism and rescues [1]. However, the serious interference caused by the reflections from walls is the main difficulty against revealing a scene [2]. To mitigate the wall clutter, a direct approach is to subtract the background from the measured data. But sometimes the empty room data is unavailable in the real scenarios. The statistical techniques like singular value decomposition (SVD) and principal component analysis (PCA) can project the echo into targets and clutters subspaces and abandon the latter according to the magnitude of the singular value or eigenvalue without other priori information [3, 4]. However, when the reflections of targets are weak, the characteristic of targets subspace is unobvious. In contrast, based on the hypothesis that the observed signal is a linear combination of independent components, i.e., source signals which are statistically independent from each other, the independent component analysis (ICA) algorithm can separate target signals and clutters more effectively.

ICA method has been reported to process a B-scan matrix which is formed through the movement of monostatic radar alone the crossrange in synthetic aperture radar (SAR) imaging approach [3, 4]. While the single-output multiple-input or multiple-input multiple-output processing techniques are suitable for multistatic system using an array antenna. In this case, a B-scan-like two-dimensional matrix can be formed by scanning the elements of the array one antenna pair at a time [5]. But sometimes, the sparsity of array elements limits the number of range profiles (RP), i.e., observed signals obtained in one single scanning. This will hinder the effectiveness of ICA method. To overcome the issue, a multiple scanning based ICA method is proposed based on the analysis of the weak fluctuation among RP signals in different periods, which implements multiple scanning of the array antenna, then applies ICA to a RP matrix for each transmit/receive antenna pair and remove the wall clutter components.

The formation of RP is briefly introduced in Section 2, as well as ICA model. Then the multiple scanning based ICA method for sparse array antenna is discussed in Section 3. To examine the feasibility of the proposed method, a four-element fixed array antenna is employed to detect two trihedrals in a room in Section 4 The experimental results show that the proposed method can separate target and wall clutter components effectively. The signal-to-clutter ratio (SCR) is promoted in final image after removing the wall clutter components.

2. SIGNAL REPRESENTATION

For a one-dimensional fixed array, RP is obtained for each antenna pair by scanning the elements of array. The wideband signal waveform is synthesized by stepped-frequency continuous wave (SFCW) with a finite number K of frequency points, be denoted as $f_k = f_0 + (k-1)\,\Delta f$, $k = 0, 1, \ldots, K-1$, where f_0 denotes the start frequency and Δf represents the frequency step size. Inverse discrete

Fourier transform is implemented to generate the time-domain signal given by

$$r_n^l = \sum_{k=0}^{N-1} u_k^l \exp\left(j\frac{2\pi n}{N}k\right), \quad 0 \le n \le N-1 \tag{1}$$

where u_k^l is the frequency-domain data at f_k, n denotes the range cell index. Let $\mathbf{R}^l = [r_0^l, r_1^l, \ldots, r_{N-1}^l]$ represents the RP in the field of view of lth antenna pair in matrix notation, $l \in \{1, 2, \ldots, L\}$.

In [3], a few statistical techniques for wall clutter elimination are reported based on monostatic system using SAR imaging approach. Among them, the ICA algorithm is attractive due to its relatively good signal decomposition performance. ICA models the observed signal as a linear combination of independent source signals as follows [6]

$$\mathbf{X} = \mathbf{AS} \tag{2}$$

here $\mathbf{X} = [x_1, x_2, \ldots, x_M]^T$ is the observed signals matrix in rows of N samples, $\mathbf{A}$ denotes a $M \times P$ constant mixing matrix which has full column rank, and $\mathbf{S} = [s_1, s_2, \ldots, s_P]^T$ is the matrix of independent source signals. Both $\mathbf{A}$ and $\mathbf{S}$ are unknown. The task of ICA is to determine a full rank separating matrix $\mathbf{W}$ to estimate the source signals as

$$\mathbf{S} = \mathbf{WX} \tag{3}$$

In SAR mode, the observed signal represents the RP obtained at antenna position m. Then $\mathbf{X}$ is equivalent to the so called B-scan matrix.

3. MULTIPLE SCANNING BASED ICA

Naturally, a similar representation of observed signal can be introduced into the multistatic system with array antenna, but here$m$ denotes the transmit/receive antenna pair index, i.e., l. For an array antenna with Q elements where all of the antennas are used to both transmit and receive, one can obtain $L = Q \times (Q-1)$ combinations of antenna pair at most. If the element is sparsely distributed, which means that Q is small, the number of observed signals M will be limited. On the other hand, from Equations (2), (3) and properties of rank of matrix, the following relationship can be derived

$$\min(M, N) \ge rank(X) = rank(S) = P \tag{4}$$

Usually the number of discrete sample points is greater than the antenna pair index. So, this is equivalent to $M \ge P$. That means ICA needs more (at least equal) observed signals than the latent sources to make the estimation feasible. Consider the large amount of latent sources in real senarios, the condition may not be satisfied.

To overcome this issue, we scan the array antenna periodically and observe the RP obtained in every scanning. Let $\mathbf{R}_m^l$ represents the RP obtained in mth scanning of lth antenna pair, which is shown in Figure 1. Ideally, if the target is stationary, $\mathbf{R}_m^l$ will not change with m. However, in practice, the RP exists weak fluctuation due to issues involving multipath, slight change of enviroment, and unstability of TWIR system. Figure 2 shows the mean removal magnitde samples of $\mathbf{R}_m^l$ at different range cells n in 50 scanning.

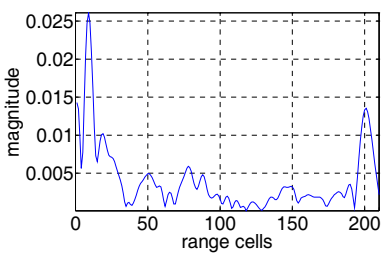

Figure 1: The RP of one antenna pair.

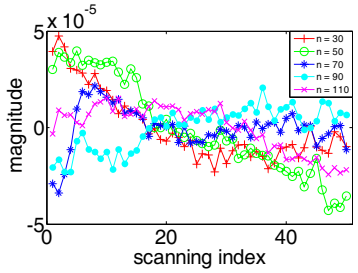

Figure 2: The fluctuation of RP in practical.

As seen, $\mathbf{R}_m^l$ always has a random variation (about 0.1% of the mean) at different range cells with m. So $\mathbf{R}_m^l$ can be used as the observed signal and rewrite the ICA model as follows

$$\mathbf{x}_m^l = \sum_{p=1}^{P} a_{m,p}^l \mathbf{s}_p^l \tag{5}$$

here m denotes the scanning index, $\mathbf{x}_m^l$ represents $\mathbf{R}_m^l$, $\mathbf{s}_p^l$ is the pth source signal of the lth antenna pair, and $a_{m,p}^l$is the corresponding mixing coefficient which also relates to l. This means we apply ICA to a RP matrix, $\mathbf{X}^l = \left[\mathbf{R}_1^l, \mathbf{R}_2^l, \ldots, \mathbf{R}_M^l\right]^T$, for each antenna pair l individually, $l = 1, 2, \ldots, L$. In this way, the lack of observed signals can be overcomed by implementing multiple scanning of the array antenna such that the condition $M \geq P$is satisfied. After decomposition, the wall clutter related signal components which are parts of terms in the sum on the left side of (5) can be removed. The sum of remaining components that contain target information is keeped, which is denoted as $\mathbf{x}_{tar,m}^l$. After $\mathbf{x}_{tar,m}^l$ is obtained for every antenna pair, a two-dimensional matrix represented by $\mathbf{B}_m = \left[\mathbf{x}_{tar,m}^1, \mathbf{x}_{tar,m}^2, \ldots, \mathbf{x}_{tar,m}^L\right]$ is formed for beamforming.

4. EXPERIMENTAL RESULTS

To examine the feasibility of the multiple scanning based ICA approach, experimental data is collected with a four-element Vivaldi array antenna placed parallel to the wall, as shown in Figure 3. The array is 3 m long with an inter-element spacing of 1m and located at a distance of 6.6 m from the exterior wall at the height of 1 m. A 3.2 m × 7 m room surrounded by brick wall with 0.35 m thickness is used for imaging. Two trihedrals of different size are located at same height as that of the array. The one of size 30 cm is located at (−1.4 m, 8.7 m), the other of size 20 cm is located at (1.2 m, 8.1 m). The middle of array is defined as coordinate origin. Wideband signal waveform is synthesized by SFCW which starts from 317 MHz and ends at 1815MHz with steps of size 2 MHz.

First of all, the empty room data is collected which is used as background. Then, the scene is scanned 50 times with the array in the presence of targets such that a 50 × 200 RP (the part of RP outside the imaging field is truncated) matrix, $\mathbf{X}^l$, is formed for each antenna pair. The ICA algorithm is applied to each $\mathbf{X}^l$. Take the 9th pair (antenna 3 transmits, antenna 4 receives) as an example, Figure 4 shows parts of the signal components of $\mathbf{x}_{25}^9$ after decomposition. The background-subtracted RP is indicated by the magenta lines marked with asterisk in Figures 4(b), (c). Notice that the first two peaks which represent trihedral 2 and 1 coinside with component 2 and 3 (the solide blue lines) respectively. Besides, reflections of the exterior and interior walls contribute to component 1 and 4 respectively. This can be verified by observing original RP of the 9th antenna pair which has been shown in Figure 1. The wall clutter related components like component 1 and 4 can be removed according to their peak position.

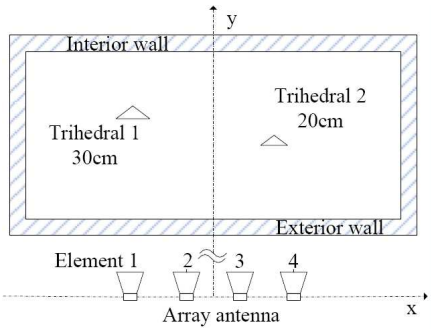

Figure 3: The experimental scene.

As raised above, a two-dimensional matrix represented by $\mathbf{B}_{25}$ is formed for beamforming. Here, the backprojection (BP) algorithm is implemented. Figure 5(a) shows the original BP image without clutter elimination. The heavy wall reflection makes the targets totally invisible. In contrast, using the proposed method, wall clutters are eliminated efficiently and two targets can be observed in Figure 5(b). As mentioned at the beginning of Section 3, we also use the RP of every antenna pair collected in one scanning to form a 12 × 200 B-scan-like matrix. Then implement ICA

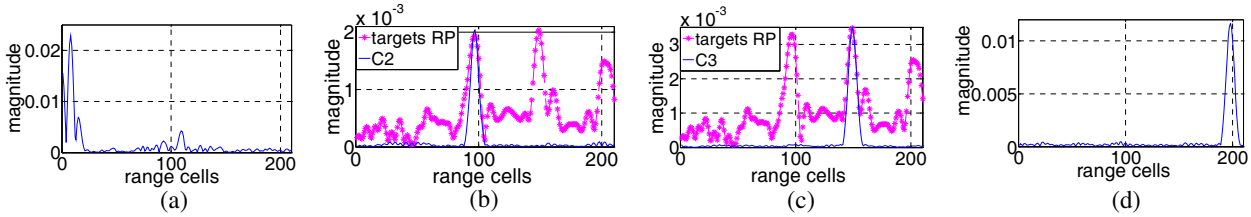

Figure 4: Parts of signal components of observed signal. (a) Component 1. (b) Component 2 (C2). (c) Component 3 (C3). (d) Component 4.

to decompose it and remove the wall clutter related portion. However, as shown in Figure 5(c), the target portion is still invisible in the final beamforming result. The performance of different methods is further compared by calculating the SCR of BP images as follows [7]

$$SCR = N_2 \sum_{(i,j)\in\{A_1,A_2\}} \|I_{ij}\| \Big/ N_1 \sum_{(i,j)\in A_3} \|I_{ij}\| - 1 \tag{6}$$

where N_1 is the number of pixels defining two $0.5\,\mathrm{m} \times 0.3\,\mathrm{m}$ rectangular areas A_1, A_2 around the targets, N_2 is the number of pixels of the entire image area A_3, $\|I_{ij}\|$ denotes the intensity of pixels in corresponding area. It is observed that the BP image processed by multiple scanning based ICA has better SCR performance, as shown in Table 1. However, as shown in Figure 5(b), there are still some ghost targets due to the multipath effects in the scenario.

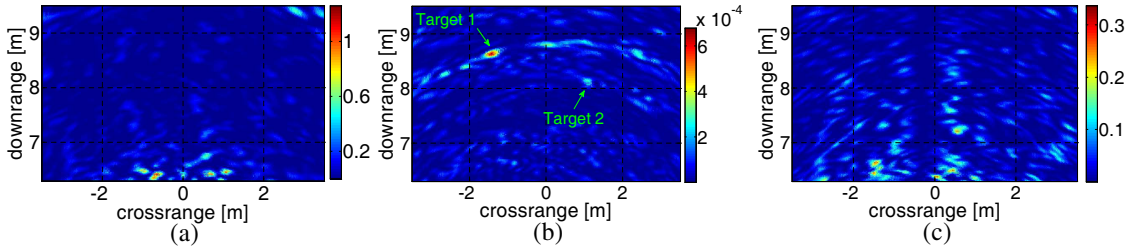

Figure 5: BP image. (a) Original image. (b) Multiple scanning based ICA. (c) Single scanning based ICA.

Table 1: SCR of different BP images.

	Original image	Multiple scanning based ICA	Single scanning based ICA
SCR	0.304	1.93	0.871

5. CONCLUSION

In this paper, we propose a multiple scanning based ICA method for TWIR wall clutter elimination. It can overcome the issue associated with the lack of observed signals for system with sparse array antenna. Experimental results show that the proposed method can separate target and wall clutter components effectively, and the SCR is promoted after removing the latter in final imaging result. Further, the multipath propagation effects should be studied to remove ghost targets in the image.

REFERENCES

1. Baranoski, E. J., "Through-wall imaging: Historical perspective and future directions," *Journal of the Franklin Institute*, Vol. 345, No. 6, 556–569, 2008.
2. Tivive, F. H. C., M. G. Amin, and A. Bouzerdoum, "Wall clutter mitigation based on eigen-analysis in through-the-wall radar imaging," *2011 17th International Conference on Digital Signal Processing (DSP)*, IEEE, 2011.
3. Verma, P. K., A. N. Gaikwad, D. Singh, and M. J. Nigam, "Analysis of clutter reduction techniques for through wall imaging in UWB range," *Progress In Electromagnetics Research B*, Vol. 17, 29–48, 2009.

4. Karlsen, B., et al., "Independent component analysis for clutter reduction in ground penetrating radar data," *International Society for Optics and Photonics, AeroSense 2002*, 2002.
5. Hunt, A. R., "A wideband imaging radar for through-the-wall surveillance," *International Society for Optics and Photonics Defense and Security*, 2004.
6. Bingham, E. and H. Aapo, "A fast fixed-point algorithm for independent component analysis of complex valued signals," *International Journal of Neural Systems*, Vol. 10, No. 1, 1–8, 2000.
7. Brunzell, H., "Detection of shallowly buried objects using impulse radar," *IEEE Transactions on Geoscience and Remote Sensing*, Vol. 37, No. 2, 875–886, 1999.

A Dual Band U-shaped Slot Antenna for WLAN and WiMAX Applications

Zimu Yang[1], **Hou Zhang**[1], **Ning Zhou**[2], **and Biao Wu**[2]

[1]Air Force Engineering University, China
[2]Electronic Systems Engineering Corporation of China (ESECC), China

Abstract— A compact dual band antenna with two U-shaped slots is presented. The antenna structure consists of rectangular patch and a ground plane at the same side. By using two U-shaped slots, the dual band characteristics are successfully obtained. Utilizing a CPW (Coplanar Waveguide) feeding line, the overall dimension of the antenna is 34.5 mm × 40 mm, which printed on an FR4 substrate with a dielectric constant of 2.95 and a substrate thickness of 0.8 mm. Simulation and measurement results show that the antenna impedance bandwidth covers the frequency range of 2.15 to 3.72 GHz. With almost omni-directional radiation pattern, the proposed antenna configuration can be applied to WLAN and WiMAX devices.

1. INTRODUCTION

Rapid development of wireless applications has promoted the printed antenna with characteristics of low cost, miniaturization and profiles reduction. Increasing attentions have been attached to wide dual-band and multi-band antennas vary with area or country [1]. Numerous types of popular antennas have been proposed and published for wireless local area network (WLAN) and World wide Inter operability for Microwave Access (WiMAX) applications [2, 3]. Many of them belong to categories such as the circular slot antennas, slot monopole antennas and slot antennas with triangular SRR terminated feedline [4–6]. To enhance the impedance bandwidth, the monopole and the slots with different shapes is used [7, 8]. With outstanding features, CPW-fed antennas have lower radiation losses and less dispersion than microstrip lines [9].

In this letter, a novel CPW-fed dual-band antenna with U-shaped slots is proposed, simple and well suited for WLAN and WiMAX operation. Owing to the two U-shaped slots, dual band resonant modes are brought in. The proposed antenna employs two L-shaped slots in the ground plane to broaden the impedance bandwidth which can easily cover the WLAN and WiMAX bands [10]. The antenna has promising features, including good impedance matching performance over the whole operating frequency band and stable radiation patterns. Good agreement between the measurement and simulation is achieved.

2. ANTENNA DESIGN

Figure 1 shows the configuration of CPW-fed dual-band slot antenna as well as the coordinate axis. The antenna is printed on a FR4 substrate with thickness of 0.8 mm, relative permittivity of 4.3 and loss tangent of 0.02, respectively. A 50-Ω CPW transmission line of a signal strip is used for feeding the antenna. Two U-shaped slots in the rectangular radiating patch generate two resonant modes and L-shape slots help to enhance the impedance bandwidth. Simulation and optimization of the antenna have been conducted with high-frequency structure simulator (HFSS) which is based on the finite element method. As shown in Table 1, the optimal parameters for proposed configuration are obtained.

Table 1: Value of the optimized parameters (unit: mm).

W	L	S	W_1	W_2	W_3	W_4	W_5	W_6
34.5	40.0	0.3	33.6	18.9	16.4	14.9	14.7	16.0
W_7	W_8	L_1	L_2	L_3	L_4	L_5	S_1	h
14.9	1.5	10.5	2.6	6.5	26.7	2.0	0.5	0.8

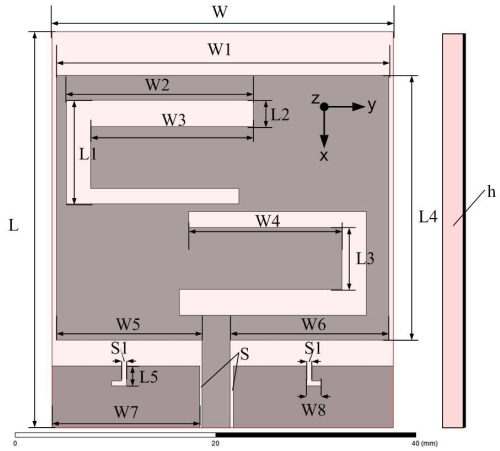

Figure 1: Configuration of the proposed antenna.

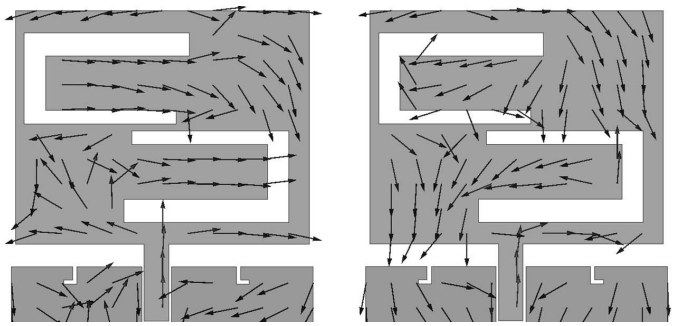

(a) 2.45 GHz (b) 3.44GHz

Figure 2: Surface current distributions of the proposed antenna.

3. SIMULATION AND MEASUREMENT

Figures 2(a) and 2(b) plot the current distributions of the proposed dual-band slot antenna at the central frequencies of the first and second resonant bands, respectively. As shown in Figure 2, the U-shaped slots increase the current routes to achieve two resonant bands.

Figure 3 plots the measured and simulated S_{11} curves against frequency. The antenna has two operating bandwidths with the central frequencies of 2.45 GHz and 3.44 GHz and the simulated results agree excellently with measurements.

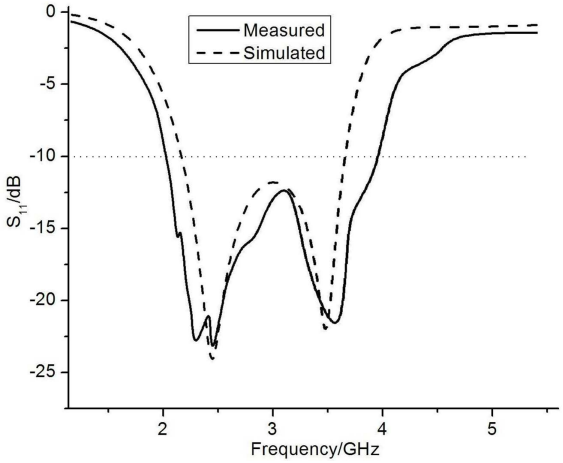

Figure 3: Measured and simulated S_{11} of the prototypes.

Figure 4 demonstrates the measured radiation pattern at 2.45 and 3.44 GHz. At low band, a figure-eight radiation pattern is obtained in the E-plane, and a nearly omni-directional radiation pattern in the H-plane. Although the obtained patterns are not as good as a conventional simple monopole antenna, they are close to the monopole-like patterns.

In Figure 5, the measured gain at low band varies in a range of $3.44 \sim 5.23$ dBi and varies in a range of about $3.12 \sim 4.09$ dBi at the high band. For bandwidth frequencies associated with dual impedance, acceptable broadside radiation patterns and favorable cross-polarization characteristics are obtained. However, the gain variations reach more than 1.0 dBi across the operating bandwidths from 2.40 to 2.60 GHz. As the antenna gain is a function of its electrical dimensions relative to the wavelength of interest, current distribution, and radiation pattern, the proposed antenna has larger gain in the lower band. Photograph of the fabricated antenna is shown in Figure 6.

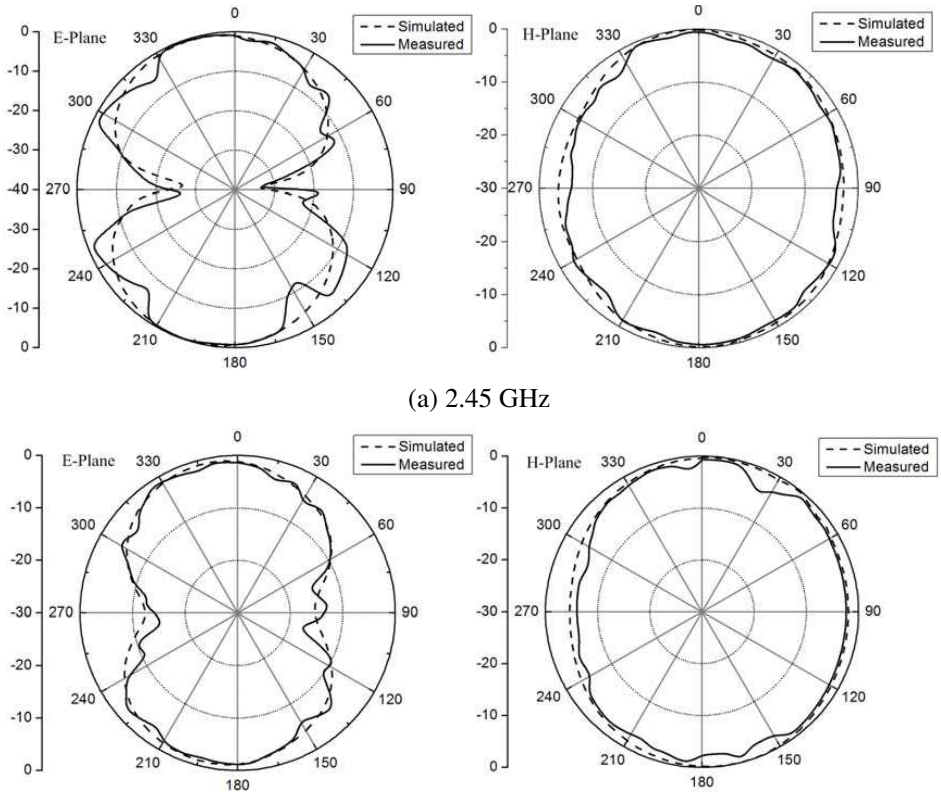

(a) 2.45 GHz

(b) 3.44 GHz

Figure 4: Radiation patterns of the presented antenna.

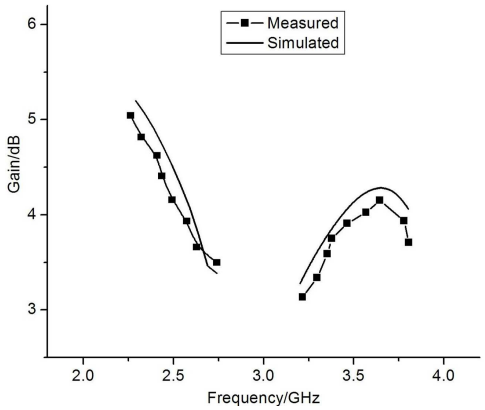

Figure 5: Simulated and measured gain against frequency for the proposed antenna.

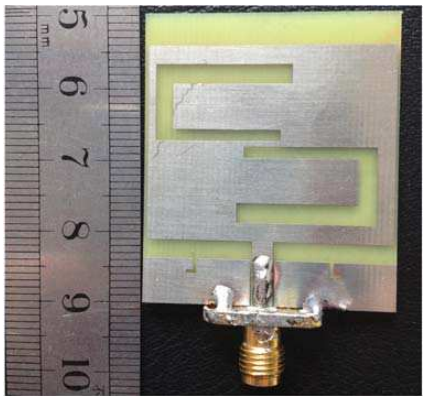

Figure 6: Photograph of the fabricated antenna.

4. CONCLUSION

A novel CPW-fed U-shaped slot antenna is proposed for WLAN and WiMAX applications. Two resonant operating bands are introduced by the U-shaped slots. Owing to the L-shaped DGS, the bandwidths of the proposed antenna are enhanced. Simulations and measurements have indicated that the proposed antenna can be effectively used for WLAN and WiMAX applications.

ACKNOWLEDGMENT

This research was financially supported by the grant from National Science and Technology Major Project (No. 2012ZX03006003).

REFERENCES

1. John, G., D. Kraus, and R. J. Marhefka, *Antennas for All Applications*, McGraw-Hill, New York, 2002.
2. Malik, J. and M. V. Kartikeyan, "Stacked equilateral triangular patch antenna with Sierpinski gasket fractal for WLAN applications," *Progress In Electromagnetics Research Letters*, Vol. 22, 71–81, 2011.
3. Malik, J. and M. V. Kartikeyan, "Metamaterial inspired patch antenna with L-shape slot loaded ground plane for dual band (WiMAX/WLAN) applications," *Progress In Electromagnetics Research Letters*, Vol. 31, 35–43, 2012.
4. Chiang, M. J., T. F. Hung, and S. S. Bor, "Dual-band circular slot antenna design for circularly and linearly polarized operations," *Microwave Opt. Technol. Lett.*, Vol. 52, 2717–2721, 2010.
5. Huang, C.-Y. and E.-Z. Yu, "A slot-monopole antenna for dual-band WLAN applications," *IEEE Antennas Wireless Propag. Lett.*, Vol. 10, 500–502, 2011.
6. Yang, K., H. Wang, Z. Lei, Y. Xie, and H. Lai, "CPW-fed slot antenna with triangular SRR terminated feedline for WLAN/WiMAX applications," *Electron. Lett.*, Vol. 46, Jun. 2011.
7. Badhai, R. K. and N. Gupta, "Reduced size bow-tie slot monopole antenna for landmine detection," *Microwave Opt. Technol. Lett.*, Vol. 52, 123–125, Jan. 2010.
8. Thomas, K. G. and M. Sreenivasan, "Compact CPW-fed dual-band antenna," *Electron. Lett.*, Vol. 46, 13–14, 2010.
9. Tan, Y. M., et al., "A novel wideband antenna for dual band WLAN application," *IEEE Int. Conf. Communication Systems (ICCS)*, 97–100, 2010.
10. Zhang, T., G. Fu, Z.-Y. Zhang, X. Chen, and Z. Mei, "Design of a printed sleeve antenna with broadband," *Journal of Microwaves*, Vol. 4, 197–199, 2010.

Two Miniaturized Microstrip Patch Antenna for Chinese Compass Navigation Satellite System Based on High-permittivity Substrate

Hangying Yuan, Shaobo Qu, Jieqiu Zhang,
Jiafu Wang, Hua Ma, Lin Zheng, and Mingbao Yan
College of Science, Air Force Engineering University, Xi'an 710051, China

Abstract— With the rapid development of navigation satellite systems, China is accelerating the pace of development of its own Compass Navigation Satellite System (CNSS for short). In CNSS system, miniaturized antennas are more attractive. However, conventional CNSS antennas work at low operation frequency (L band, 1.616 ± 5 MHz and S Band, 2492 ± 5 MHz) which lead to large scale by using low-permittivity ceramic substrate. Consequently, in this paper, we present two miniaturized CNSS microstrip antennas based on high-permittivity ($\varepsilon_r = 16$) ceramic substrate. One is corner-cut-patch structure, and the other is two-pair-slot-patch structure. They work at S Band (2492 ± 5 MHz, right-handed circular polarization, RHCP) to receive position information. An experiment was carried out to verify our design. For corner-cut structure, numerical results show that impedance bandwidth ($S_{11} < -10$ dB), 3 dB axial ratio bandwidth and gain are about 62 MHz, 15 MHz, and 3.48 dB, and measured results shows that impedance bandwidth ($S_{11} < -10$ dB) and 3 dB axial ratio bandwidth are about 66 MHz, 12 MHz, respectively. Meanwhile, for slot structure, numerical results show that impedance bandwidth ($S_{11} < -10$ dB), 3 dB axial ratio bandwidth and gain are about 94 MHz, 23 MHz, and 3.96 dB, and measured results shows that impedance bandwidth ($S_{11} < -10$ dB) is about 132 MHz and 3 dB axial ratio bandwidth is much larger than 22 MHz, respectively. Obviously, the characteristics of slot-patch structure are better than the characteristics of corner-cut structure. Measured results fit well with the simulation results. The two antennas can fully meet the requirement of CNSS. Meanwhile, comparing with the conventional low-permittivity substrate antennas, the two antennas remain their well performances with a reduced size by 75% to 80%. Such advantages make it proper to practical applications.

1. INTRODUCTION

Microstrip patch antennas (MPAs) has been widely used in modern communication and weapon systems for their irreplaceable advantages such as low profile, light weight, and easily to be implemented and integrated characteristics [1–3]. With the rapid development of Chinese Compass Navigation Satellite system (CNSS for short), the demand for CNSS terminal microstrip antennas is quite urgent [4–6]. In CNSS system, antennas work at low operation frequency (L band, 1.616 ± 5 MHz and S Band, 2492 ± 5 MHz) which lead to large scale by using low-permittivity substrate. The reason is shown in equation $L = c/2f\sqrt{\varepsilon_r}$, where L is the size of the square radiation patch, c is the velocity of light, f is the central frequency of the antenna, ε_r is the relative permittivity of the substrate. It is obviously that using high-permittivity substrate is an effective way to achieve minimized antennas.

In communication systems, circularly polarized antennas are more attractive. Linear polarized antenna can only receive part or none of the signal, which significantly lowers the antenna's efficiency. The common methods to achieve a circularly polarized microstrip patch antenna are to truncate corners or slots on the radiation patches [7, 8]. In this paper, two miniaturized CNSS microstrip patch antennas are present. One is corner-cut-patch structure, and the other is two-pair-slot-patch structure. By using high-permittivity ceramic ($\varepsilon_r = 16$) as the substrate, the antennas keep their performances with a reduced size by 75% to 80% comparing with the conventional ones using low-permittivity substrate. The proposed antennas and results are presented and discussed as follows. In Section 2, the geometries of the proposed antennas are presented. Simulated and measured results including S_{11}, axial ratio and radiation pattern are given in Section 3. Conclusion is provided in Section 4.

2. ANTENNA DESIGN

The geometry of the corner-cut-patch structure antenna at S band is shown in Figure 1. A low-cost substrate with $\varepsilon_r = 16$, $\tan\delta = 0.001$ and $h = 4$ mm was chosen. A parametric study was carried out using High Frequency Structure Simulator (HFSS) to achieve optimal performances,

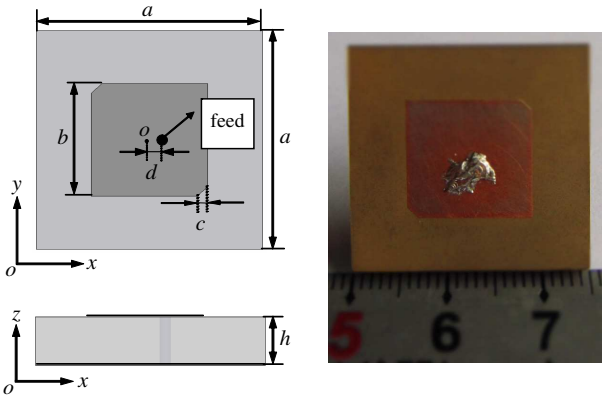

Figure 1: The geometry of the corner-cut-patch structure antenna. (a) The designed antenna. (b) The fabricated antenna.

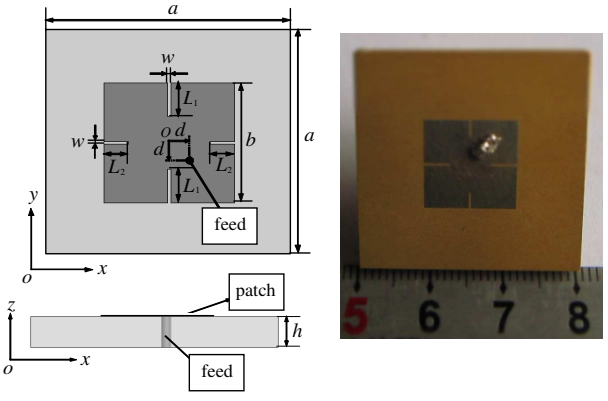

Figure 2: The geometry of the two-pair-slot-patch structure antenna. (a) The designed antenna. (b) The fabricated antenna.

and the geometric dimensions of the proposed antenna are as follows: $a = 25\,\text{mm}$, $b = 12.85\,\text{mm}$, $c = 1.15\,\text{mm}$, $d = 1.6\,\text{mm}$.

The geometry of the two-pair-slot-patch structure antenna at S band is shown in Figure 2. It is composed of two pairs of slots, and the slots are etched on the patches to realize right handed circularly polarizations (RHCP) or left handed circularly polarizations (LHCP) states. Such differences lie on the length ratio of the slot in x- and y-directions. A low-cost substrate with $\varepsilon_r = 16$, $\tan\delta = 0.001$ and $h = 4\,\text{mm}$ was chosen. By the optimization, the geometric dimensions of the proposed antenna are as follows: $a = 30\,\text{mm}$, $b = 12.12\,\text{mm}$, $L_1 = 3.4\,\text{mm}$, $L_2 = 2.28\,\text{mm}$, $w = 0.3\,\text{mm}$, $d = 1.4\,\text{mm}$.

3. SIMULATED AND MEASURED RESULTS

We used the full wave simulation software High Frequency Structure Simulator (HFSS) version 12.0 to calculate its performances, and use Vector Network Analyzer (VNA) to measure its performance. The reflection coefficient is closely related to the transmission coefficient. Meanwhile, in general, when the axial ratio is lower than 3 dB, we can consider that this antenna achieved excellent circularly polarized performance.

Figure 3 shows the simulated and measured S_{11} and Axial Ratio (AR) results of the corner-cut-patch structure antenna, the real line is the simulated results curve and the dashed line is the measured results curve. From Figure 3, we can see that the simulated and measured impedance bandwidth ($S_{11} < -10\,\text{dB}$) are 62 MHz and 66 MHz, the simulated and measured 3 dB axial ratio bandwidth are 15 MHz and 12 MHz.

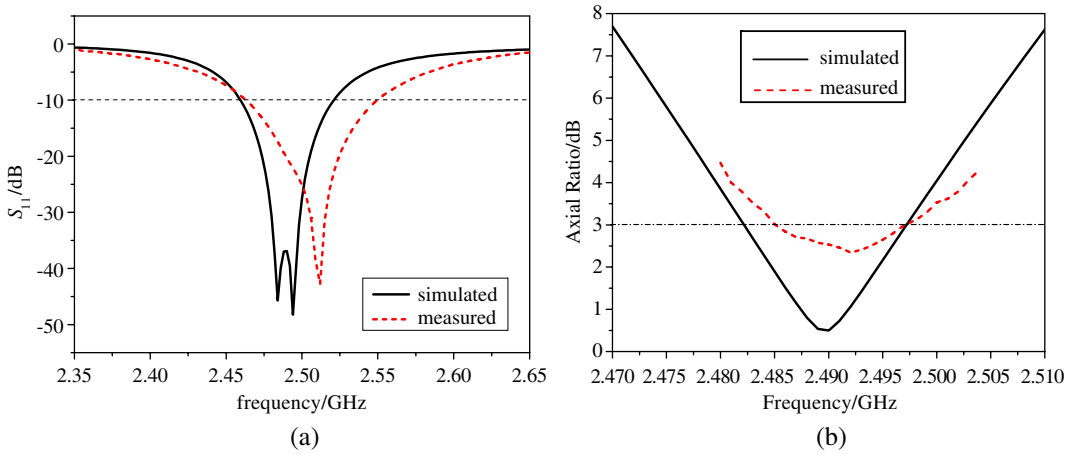

Figure 3: The simulated and measured S_{11} and Axial Ratio (AR) results of the corner-cut-patch structure antenna. (a) The S_{11}. (b) The Axial Ratio (AR).

Figure 4 shows the simulated and measured normalized radiation pattern at 2.492 GHz, the real line is the simulated results curve and the dashed line is the measured results curve. Due to the lack of normative horn antennas at S band, it is difficult for us to measure the gain of this antenna. The simulated gain at S band is 3.48 dB.

Figure 5 shows the simulated and measured S_{11} and Axial Ratio (AR) results of the two-pair-slot-patch structure antenna, the real line is the simulated results curve and the dashed line is the measured results curve. The simulated and measured impedance bandwidth ($S_{11} < -10$ dB) are 94 MHz and 132 MHz, the simulated and measured 3 dB axial ratio bandwidth are 23 MHz and

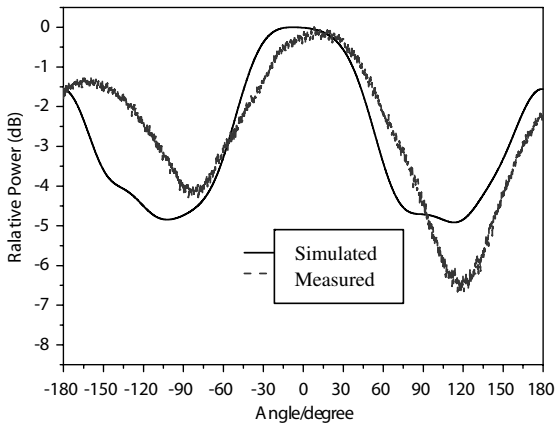

Figure 4: The simulated and measured normalized radiation pattern at 2.492 GHz.

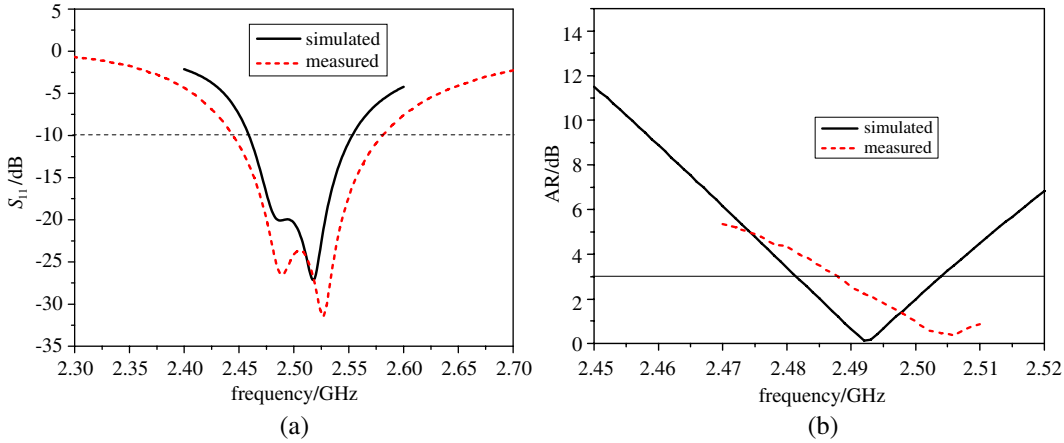

Figure 5: The simulated and measured S_{11} and Axial Ratio (AR) results of the two-pair-slot-patch structure antenna. (a) The S_{11}. (b) The Axial Ratio (AR).

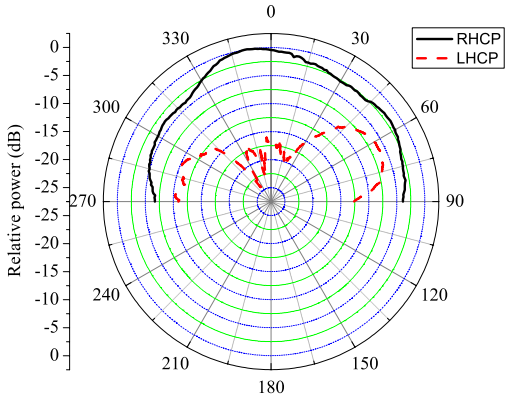

Figure 6: The simulated and measured normalized radiation pattern at 2.492 GHz.

larger than 22 MHz.

Figure 6 shows the simulated and measured normalized radiation pattern at 2.492 GHz, the real line is the simulated results curve and the dashed line is the measured results curve. The simulated gain is 3.96 dB.

4. CONCLUSION

In this paper, we present two minimized RHCP microstrip antennas at S band for CNSS. The measured results agree well with the simulated ones. Meanwhile, the characteristics of slot-patch structure are better than the characteristics of corner-cut structure. Comparing with the conventional low-permittivity substrate antennas, the two antennas remain well performances with a reduced size by 75% to 80%. Such advantages make it proper to practical applications.

ACKNOWLEDGMENT

This work was supported in part by the National Science Foundation for Post-doctoral Scientists of China under Grant Nos. 2013M532131, 2013M532221, and in part by National Natural Science Foundation of China under Grants No. 61302023.

REFERENCES

1. Nakamura, T. and T. Fukusako, "Broadband design of circularly polarized microstrip patch antenna using artificial ground structure with rectangular unit cells," *IEEE Transactions on Antennas and Propagation*, Vol. 59, No. 6, 2103–2110, 2011.
2. Roy, A., P. K. Choudhary, S. Anand, and P. P. Sarkar, "A novel approach on miniaturization of microstrip patch antenna with loaded strips," *ICECI Proceeding*, 2014.
3. Sun, D., W. Dou, and L. You, "A broadband proximity-coupled stacked microstrip antenna with cavity-backed configuration," *IEEE Antennas and Wireless Propagation Letters*, Vol. 10, 1055–1058, 2011.
4. Tian, X. Q., S. B. Liu, Y. S. Wei, and X. Y. Zhang, "Circularly polarized microstrip antenna with slots for Beidou (COMPASS) navigation system," *ISSSE Proceeding*, 2010.
5. Li, B., Y. Guan, Y. Jiang, and A. Zhang, "Compact dual band and circularly polarized microstrip antenna for CNSS," *Cross Strait Quad-Regional Radio Science and Wireless Technology Conference*, 2011.
6. Yuan, H., J. Zhang, S. Qu, H. Zhou, J. Wang, H. Ma, and Z. Xu, "Dual-band dual-polarized microstrip antenna for compass navigation satellite system," *Progress In Electromagnetics Research C*, Vol. 30, 213–223, 2012.
7. Tiang, J.-J., M. T. Islam, N. Misran, and M. Singh, "Circular microstrip slot antenna for dual-frequency FRID application," *Progress In Electromagnetics Research*, Vol. 120, 499–512, 2011.
8. Yang, S. S., K.-F. Lee, A. A. Kishk, and K.-M. Luk, "Design and study of wideband single feed circularly polarized microstrip antennas," *Progress In Electromagnetics Research*, Vol. 80, 45–61, 2008.

Investigating the Dual-passbands Frequency Selective Surface with Complementary Structure

Lin Zheng, Shaobo Qu, Jieqiu Zhang, Jiafu Wang, Hang Zhou, Mingbao Yan, Zhiyuan Zhang, Hangying Yuan, Yongfeng Li, and Yongqiang Pang
College of Science, Air Force Engineering University, Xi'an 710051, China

Abstract— A dual-band frequency selective surface (FSS) is presented. The complementary hexagonal loop resonators are used in each FSS unit cell to obtain this ability. We designed three styles FSS composed of circle loop squared loop and hexagonal loop arranged in a 2-D periodic lattice. These FSSs are engineered a hybrid of three layers closely coupled FSS. The outer layers of elements and a middle layer of complementary elements are etched either side of a dielectric substrate. The proposed FSS structure is independent of incident polarization and angle because of centrosymmetric of the unit cell. We investigate the frequency responses of such periodic structures induced field distribution. It is demonstrated that transmission zeros occur in passbands formed by the mode of aperture resonance and aperture coupled patch resonance. By simulating their transmission and reflection coefficients under normal and oblique TE and TM incidences, show that it has a stable frequency response at different oblique incident angles and the advantages of high selectivity.

1. INTRODUCTION

The frequency selective surface (FSS) has found widespread applications, such as antennas and radomes for aircraft and communication fields [1, 2]. With the development of radome's performance and the improvement of communication devices, the requirements of multi-frequency communication become more and more significant. For those applications, the multi-band FSS have been used especially when multiple independent transmission bands are required. Therefore the multi-band FSS designs have been investigated extensively [3, 4]. In the past, several techniques have been used to design multi-band FSS, include cascading multi-layer different unit cell to obtain multi-resonance [5] and single-layer FSS with the fractal structures [6]. Recently, in substrate-integrated waveguide technology, dual-band FSS was constructed to obtain a large band separation, band-reject response [7–12].

In this letter, we present a complementary structure of FSS, comprising loop elements with complementary loop elements connected via two layers dielectric, as shown in Figure 1. The field distribution is shown to analyse the resonant frequencies. In the end, we obtained dual-passbands frequency selective surface with excellent performances. These FSSs have advantages to high selectivity, stable performance, compact volume and easy to be fabricated by print circuit board technology.

2. DESIGN AND ANALYSIS

In this Section, we present the results of numerical simulation of the FSS models shown in Figure 1. These FSSs have a substrate with relative permittivity of $\varepsilon_r = 2.65$, loss tangent of 0.01 and

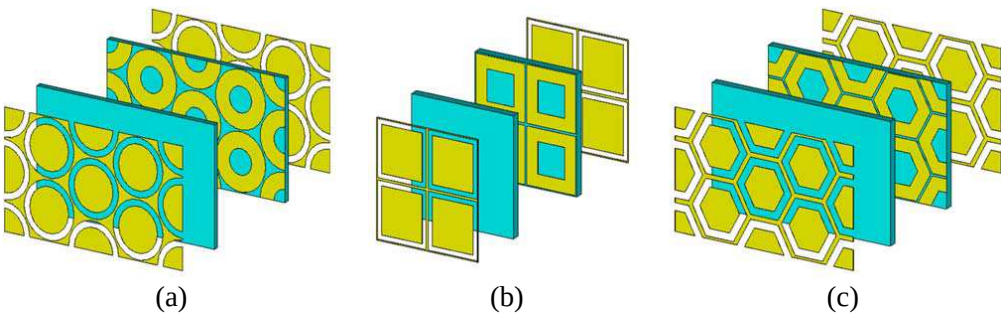

Figure 1: Geometry of 3D FSS element. (a) Circle element view. (b) Square element view. (c) Hexagonal element view.

thickness of $h_{sub} = 1\,\text{mm}$. Finite element method (FEM) was used to calculate its reflection and transmission characteristics. Assume that these FSSs is an infinite periodic structure. The four side of the unit cell are set to be periodic boundary and these FSSs are excited by the TE and TM polarizations. The S parameters of this FSS under normal incident are presented in Figure 2. It is found that the transmission property has dual-band performance.

The magnetic field distribution at first transmission zeroes are plotted in Figure 3(a). It is found that the first transmission zeroes (under TE normal incidence Circle at 5.712 GHz, Square at 5.824 GHz, Hexagonal at 6.24 GHz, respectively) corresponds to the aperture resonance, whereas the second transmission zeroes of these elements (also under TE normal incidence Circle at 11.664 GHz, Square at 12.944 GHz, Hexagonal at 15.248 GHz, respectively) exhibit the opposite direction of currents arise in top layer and middle layer were shown in Figure 3(b). So we can affirm that it is a patch-aperture resonance mode.

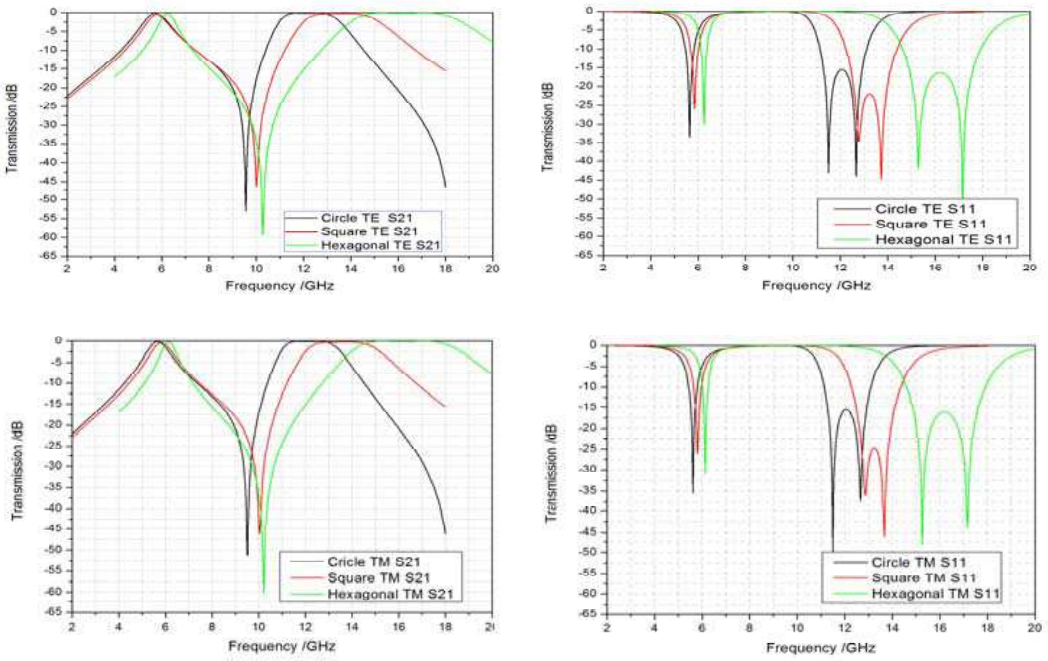

Figure 2: Frequency responses under normal incidence.

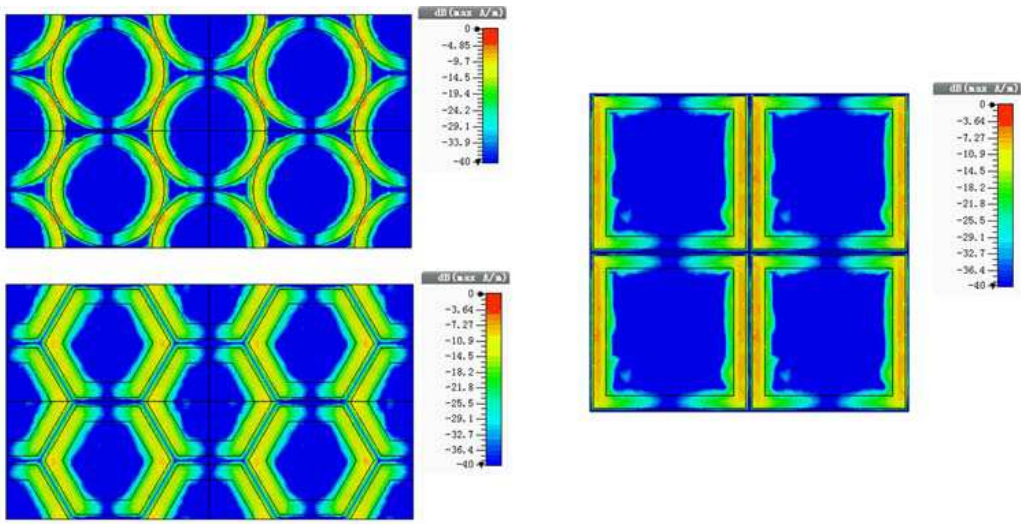

(a)

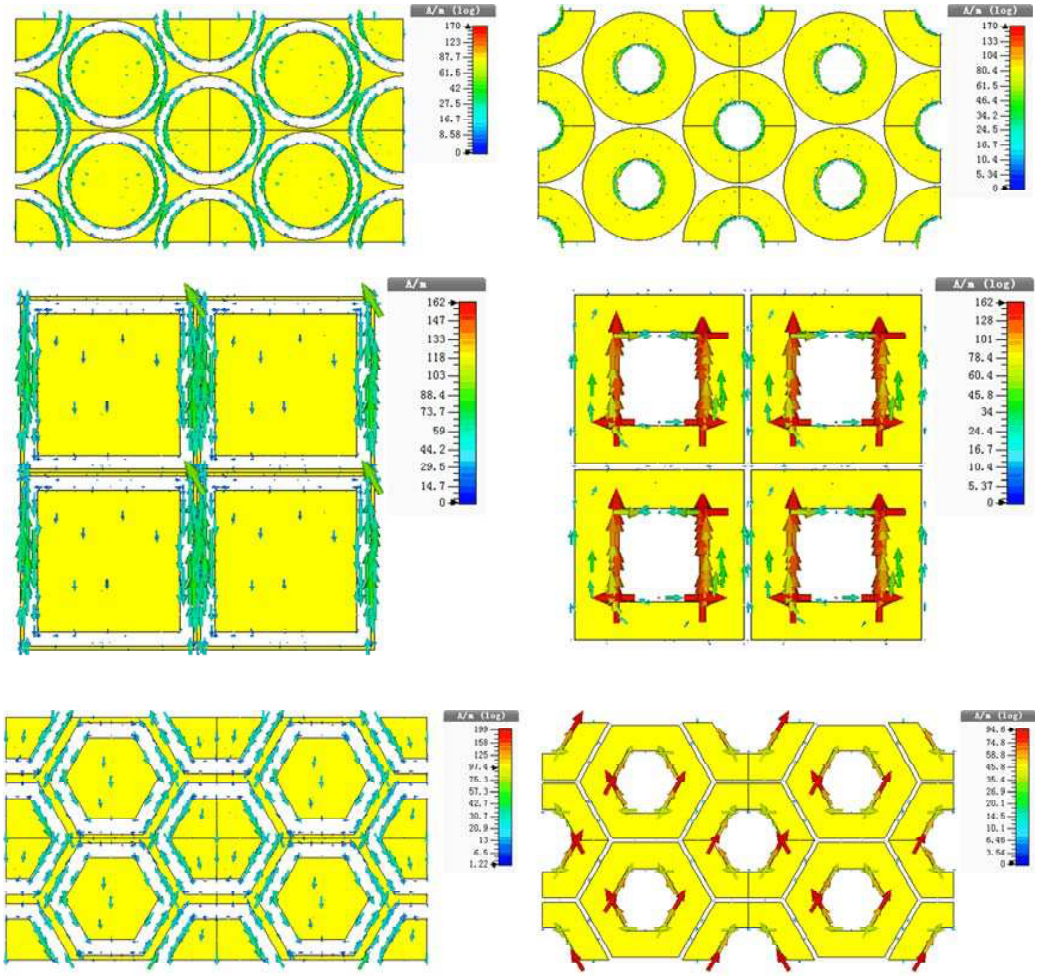

(b)

Figure 3: Current distribution at two zeroes of transmission response. (a) At first transmission zeroes. (b) At second transmission zeroes

3. STABLE PERFORMANCE ANALYSIS

The excellent frequency selective surface would provide stable performance under different incidence angles and polarizations. Usually, dual-passbands FSS should have large band separation and flat passbands. A high rejection edge is also a good benefit.

Figure 4 gives these frequency selective surfaces under different incidence angles and polarizations. These frequency selective surfaces is stable under oblique incidence angles from 0° to 30° for both TE and TM polarization, its transmission is obviously dual-passbands performance. The first passband bandwidth of −3 dB reaches (circle: 1 GHz, square: 900 MHz, hexagonal: 800 MHz, respectively), and second passband relative bandwidth of −3 dB reaches (circle: 2.8 GHz, square: 3.2 GHz, hexagonal: 4.8 GHz, respectively).

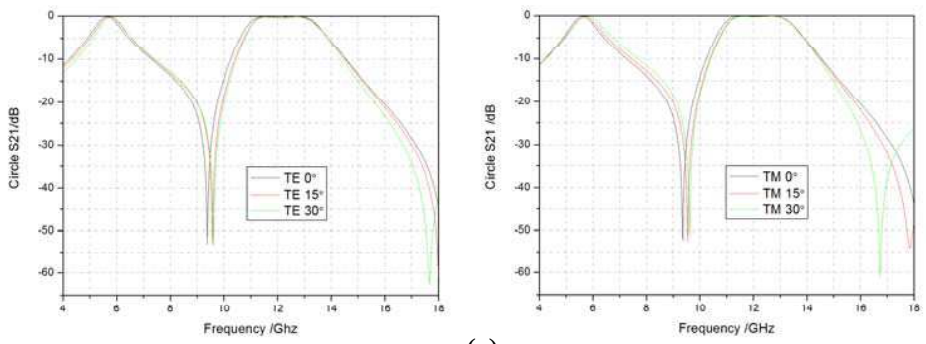

(a)

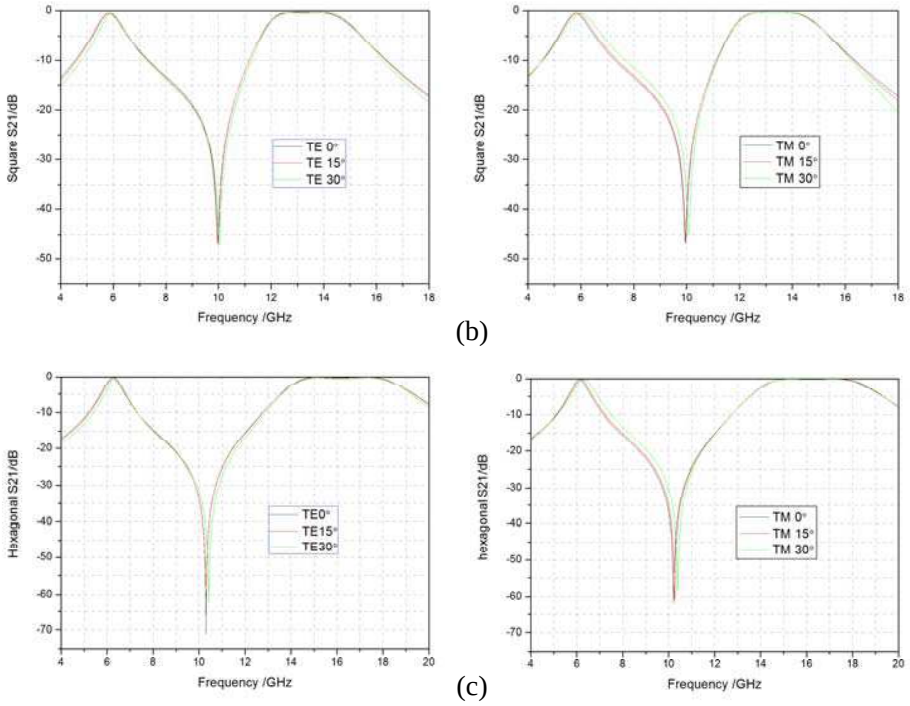

Figure 4: Frequency response of these FSS under incidence angles from0° to 30° for both TE and TM polarization. (a) Circle element. (b) Square element. (c) Hexagonal element

4. CONCLUSION AND DISCUSSION

In this paper, we proposed a dual-passbands frequency selective surface with stable performances. The complementary struct was designed for obtain advantages. The each passband has stable performance various incident angles and TE/TM polarizations. The dual-passbands frequency selective surface has advantages of high selectivity, large band separation. Such a frequency selective surface can provide practical applications in communications filed, etc.

ACKNOWLEDGMENT

The authors are grateful to the supports from the National Natural Science Foundation of China under Grant Nos. 61331005, 11204378, 11274389, 11304393, 61302023, the Aviation Science Foundation of China under Grant Nos. 20132796018, 20123196015, the National Science Foundation for Post-doctoral Scientists of China under Grant Nos. 2013M532131, 2013M532221, the Natural Science Foundation of Shaanxi Province under Grant No. 2013JM6005, and the Special Funds for Authors of Annual Excellent Doctoral Degree Dissertations of China under Grant No. 201242.

REFERENCES

1. Munk, B. A., *Frequency Selective Surface: Theory and Design*, Wiley, New York, 2000.
2. Wu, T. K., *Frequency Selective Surfaces and Grid Arrays,* Wiley, New York, 1995.
3. Wang, X.-Z., J.-S. Gao, and N.-X. Xu, "Design and study of the dual-band frequency-selective surface operation at Ku/Ka-band," *Acta Phys. Sin.*, Vol. 62, No. 16, 167307, 2013.
4. Park, J. H and H. K. Choi, "Design of bouble frequency selective surfaces using multiresonant ring patch elements of four differert sizes for four bands," *Microwave and Optical Technology Letters*, Vol. 56, No. 3, 547–552, 2014.
5. Cimen, S., "Novel closely spaced planar dual-band frequency-selective surface," *IET Microw. Antennas Propag.*, Vol. 7, No. 11, 894–899, 2013.
6. Wang, S.-S., J.-S. Gao, X.-G. Feng, and J.-L. Zhao, "Design methods of Y apertures fractal FSS," *Optics and Precision Engineering*, Vol. 19, No. 5, 959–966, 2011.
7. Luo, G., Q. W. Hong, Z. C. Hao, B. Liu, W. D. Li, et al., "Theory and experiment of novel frequency selective surface based on substrate integrated waveguide technology," *IEEE Trans. Antennas Propag.*, Vol. 53, No. 12, 4035–4043, Dec. 2005.

8. Luo, G. Q., W. Hong, Q. H. Lai, K. Wu, and L. L. Sun, "Design and experimental verification of compact frequency selective surface with quasi-elliptic bandpass response," *IEEE Trans. Micro. Theory Tech.*, Vol. 55, No. 12, 2481–2487, 2007.
9. Luo, G. Q., W. Hong, H. J. Tang, J. X. Chen, et al., "Filtenna consisting of horn antenna and substrate integrated waveguide cavity FSS," *IEEE Trans. Antennas Propag.*, Vol. 55, No. 1, 92–98, 2007.
10. Luo, G. Q., W. Hong, H. J. Tang, J. X. Chen, and L. L. Sun, "Triband frequency selective surface with periodic cell perturbation," *IEEE Micron. Wireless Compon. Lett.*, Vol. 17, No. 6, 436–438, 2007.
11. Zhou, H., S.-B. Qu, et al., "Dual-band frequency selective surface with quasi-elliptic bandpass response," *Chin. Phys. B*, Vol. 21, No. 3, 030301, 2012.
12. Zhou, H., S.-B. Qu, et al., "Dual-band frequency selective surface with large band separation and stable performance," *Chin. Phys. B*, Vol. 21, No. 5, 054101, 2012.

An Ultra Wideband Printed Helical Antenna with Low Profile

Xihui Tang[1], **Ruirui Li**[2], **Jihong Pei**[2], **and Yunliang Long**[3]

[1]Shenzhen Key Lab of Advanced Communications and Information Processing
College of Information Engineering, Shenzhen University, China
[2]College of Information Engineering, Shenzhen University, Shenzhen, China
[3]Department of Electronics and Communication Engineering
Sun Yat-Sen University, Guangzhou, China

Abstract— This paper presents a compact ultra-wideband strip helical antenna with circular polarization. In order to achieve circular polarization and impedance matching with helix of 1.1 turns, the helix is made of uniform metallic strip instead of traditional metallic wire. Considering the convenience in manufacture, the uniform metallic strip is firstly printed on a substrate with $\varepsilon_r = 2.2$, $h = 0.5\,\text{mm}$, then the substrate is rolled into the shape of cylinder such that a helix is formed. A $50\,\Omega$ coaxial cable is directly connected to the helix without an impedance matching section. The ground plane, which is printed on another substrate with $\varepsilon_r = 2.2$, $h = 3\,\text{mm}$, is placed under the helix. To demonstrate this method, a 1.1-turns helical antenna is fabricated, measured and analyzed. Measured results show that the proposed antenna has an impedance bandwidth ($S_{11} \leq -10\,\text{dB}$) of more than 70%, and an axial ratio (AR) bandwidth ($\text{AR} \leq 3\,\text{dB}$) of 55%. These wideband circular polarized (CP) characteristics indicate that the proposed antenna has a potential application in wide-band/multi-band wireless communications.

1. INTRODUCTION

The conventional cylindrical axial-mode helical antenna [1] is a good candidate for circle polarization applications due to its advantages such as high gain and wideband AR bandwidth. However, its large profile limits its applications in wireless communication terminals. A series of small and low profile cylindrical helical antennas are presented by H. Nakano [2, 3]. But these types of antennas have a narrow AR bandwidth and are difficult to impedance match with $50\,\Omega$ coaxial feed. In the last twenty years, H. T. Hui and his group introduce a type of hemispherical helical antenna [4–6]. Comparing with the conventional cylindrical helical antenna, the hemispherical helical antennas have much wider beamwidth for circular polarization. Nevertheless, their AR bandwidths are less than 15% and disable to satisfy the high data rate information transmission. Recently, a wideband hemispherical helical antenna has been reported [7]. Using a tapered metallic strip instead of wire, the hemispherical helical antenna in [7] has an AR bandwidth of 24%. However, it needs a section of impedance matching thus the antenna structure is complicated and difficult to be fabricated.

In this paper, a new type of cylindrical strip helical antenna with low profile and broadband operation for circular polarization is presented. Instead of traditional metallic wire, the proposed strip helical antenna is made of uniform metallic strip. As a result, a wideband AR bandwidth of 55% is obtained when the strip helix is only 1.1 turns. Moreover, an impedance bandwidth of 77%, which can completely cover the AR bandwidth, is achieved without an impedance matching section. To verify these good CP features, a prototype of the proposed strip helical antenna is fabricated and analyzed both numerically and experimentally. Simulated results are obtained using commercial software 'HFSS'.

2. ANTENNA STRUCTURE

The structure of the strip helical antenna is illustrated as in Fig. 1. It consists of a cylindrical helix and a circular ground plane. The cylindrical helix is made of metallic strip with uniform width (w). For convenience to fabrication, it is printed on Substrate A with ($\varepsilon_{r1} = 2.2$, $h_1 = 0.5\,\text{mm}$). Then Substrate A is rolled into a hollow cylinder thus a strip helix is formed. The detail dimensions of the helix are as follows: D is the diameter of the helix, S is the spacing between turns (center-to-center), α is the pitch angle ($\alpha = \arctan(S/\pi D)$), L is the length of one turn, and n is the number of turns. The circular ground plane, which is printed on the bottom layer of substrate B ($\varepsilon_{r2} = 2.2$, $h_2 = 3\,\text{mm}$), is placed below the helix for axial-mode operation. A $50\,\Omega$ SMA (diameter of 1 mm) is attached to the bottom of the strip helix.

The proposed helix is made of uniform metallic strip, which is different from the conventional wire helix. This change offers advantages to both input impedance and radiation characteristics

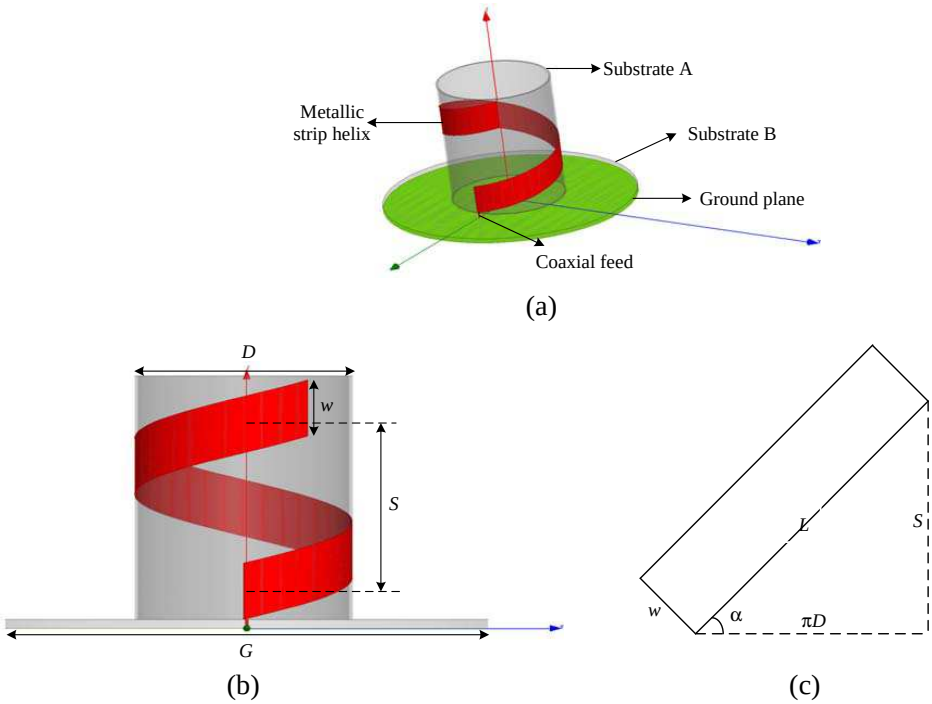

Figure 1: Geometry of the proposed antenna. (a) 3D view. (b) Side view. (c) Unrolled strip helix of one turn.

of the antenna. As is well known, a strip monopole has much more operation bandwidth than a wire monopole. Similarly, a strip helical antenna has much better impedance matching than a wire helical antenna. Particularly, the input impedance of the strip helical antenna almost keeps stable over an ultra wide frequency range. Thus, by tuning the width of the metallic strip, the strip helical antenna can reach a broadband impedance width. On the other hand, it is found that the strip helical antenna just needs around 1.1 turns to achieve axial radiation mode with circular polarization, while the conventional wire helical antenna needs at least 3 turns. Consequently, The strip helix can reduce the axial height of the antenna significantly.

3. SIMULATED AND MEASURED RESULTS

In order to demonstrate the good performance of the proposed strip helical antenna, a prototype is fabricated. The detail dimensions of the strip helix are as follows: $D = 72\,\text{mm}$, $w = 22\,\text{mm}$, $S = 65\,\text{mm}$, $\alpha = 16°$, $L = 235\,\text{mm}$, $n = 1.1$. The diameter of the circular ground plane (G) is 160 mm. Measurement is with the aid of the E5071C Network Analyzer and the Near Field Antenna Measurement System, Satimo. Measured results for reflect coefficient (S_{11}), axial ratio, gain, and radiation patterns are presented and compared with the corresponding simulated results.

The reflect coefficient (S_{11}) of the proposed strip helical antenna are depicted in Figure 2. Since the input impedance of the proposed strip helical antenna is stable and matching with 50 Ω across a large frequency range, ultra wideband impedance bandwidths are obtained. The simulated impedance bandwidths ($S_{11} \leq -10\,\text{dB}$) is more than 85% from 1.18 GHz to 3 GHz and beyond (we tested only between 1–3 GHz), while the measured impedance bandwidths is about 77% from 1.22 GHz to 2.76 GHz).

Figure 3 exhibits both the simulated and measured results for AR and gain in the axial direction of the helix. There is a good agreement between the simulated and measured results. From the AR curves, it is observed that the proposed strip helical antenna has simulated and measured AR bandwidths (AR $\leq$ 3 dB) are 56% (1.23–2.19 GHz) and 55% (1.25–2.2 GHz), respectively. The measured center operation frequency is 1.725 GHz. During the AR bandwidth, the simulated and measured peak gain is 8.5 dBic and 8 dBic, respectively. From 1.8 GHz to 2.2 GHz, both the simulated and measured gain decrease. It is because that the direction of maximum radiation is offset the axial direction with tilt angle τ in higher frequency band.

Figure 4 shows the simulated and measured radiation patterns at 1.725 GHz (radiation patterns at 1.25 GHz and 2.2 GHz are not shown for brevity). The proposed strip helical antenna is of right-

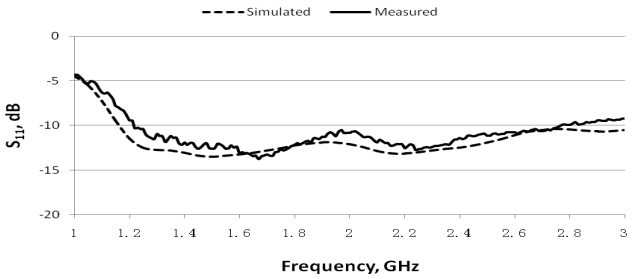

Figure 2: Reflection coefficient (S_{11}) against frequency of the proposed antenna.

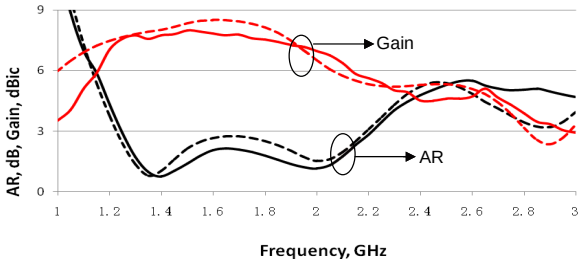

Figure 3: Axial ratio and gain against frequency of the proposed antenna. Solid line: measured data, dash line: simulated data.

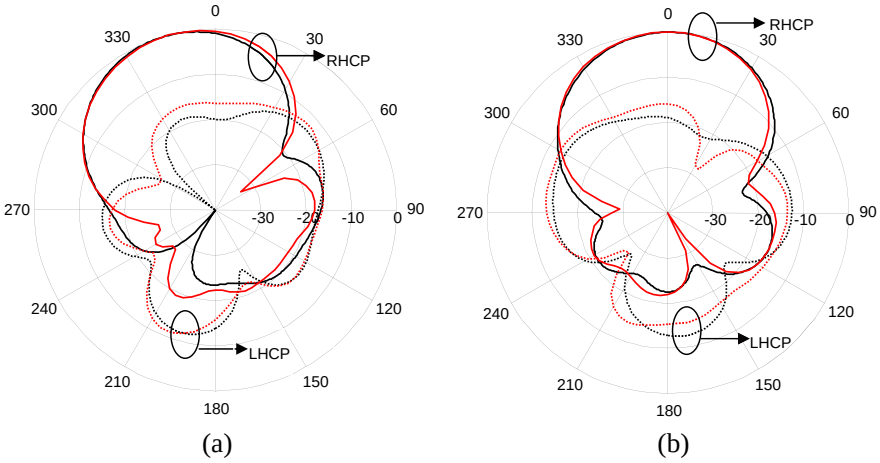

Figure 4: Radiation patterns of the proposed antenna at 1.725 GHz. (a) $\phi = 0°$ plane, (b) $\phi = 90°$ plane. Red line: measured data, black line: simulated data..

hand circular polarization (RHCP). The radiation patterns are symmetric about the axial direction at $\phi = 90°$ plane. While the maximum radiation is offset the axial direction with tilt angle $\tau = -16°$ at $\phi = 0°$ plane. In fact, in both the simulation and measurement, the radiation patterns are very symmetric in lower cutoff frequency, 1.25 GHz. As the operation frequency increases, the radiation patterns become more and more asymmetric. Since the pitch angle α is equal to 16° and not small, the asymmetry of the proposed antenna structure can not be neglected, especially in higher frequency band.

4. CONCLUSION

A new type of helical antenna with the use of uniform metallic strip is proposed for wideband circular polarization. Comparing with the conventional cylindrical helical antenna, the proposed strip helical antenna needs less turns helix to achieve broadband CP bandwidth of 55%. Furthermore, Its AR bandwidth is covered by a large impedance bandwidth, which reaches 77%. Due to these advantages, the proposed antenna has a potential application in high data rate wireless communication systems.

ACKNOWLEDGMENT

This work is supported by the Natural Science Foundation of China (61301075) and the Shenzhen Fundamental Research Project (JCYJ20120613165052982).

REFERENCES

1. Kraus, J. D., "The helical antenna," *Proceedings of the IRE*, 263–272, 1949.
2. Nakano, H., Y. Samada, and J. Yamauchi, "Axial mode helical antennas," *IEEE Trans. Antennas Propag.*, Vol. 34, No. 9, 1143–1148, 1986.
3. Nakano, H., H. Takeda, T. Honma, H. mimaki, and J. Yamauchi, "Extremely low-profile helix radiating a circularly polarized wave," *IEEE Trans. Antennas Propag.*, Vol. 39, No. 6, 754–757, 1991.

4. Hui, H. T., K. Y. Chan, E. K. N. Yung, and X. Q. Shing, "Coaxial-feed axial mode hemispherical helical antenna," *Electron. Lett.*, Vol. 35, No. 23, 1982–1983, 1999.
5. Hui, H. T., K. Y. Chan, and E. K. N. Yung, "The input impedance and the antenna gain of the spherical helical antenna," *IEEE Trans. Antennas Propag.*, Vol. 49, No. 8, 1235–1237, 2001.
6. Hui, H. T., K. Y. Chan, and E. K. N. Yung, "The low-profile hemispherical helical antenna with circular polarization radiation over a wide angular range," *IEEE Trans. Antennas Propag.*, Vol. 51, No. 6, 1415–1418, 2003.
7. Alsawaha, H. W. and A. Safaai-Jazi, "Ultrawideband hemispherical helical antennas," *IEEE Trans. Antennas Propag.*, Vol. 58, No. 10, 3175–3181, 2010.

Discussions on the FSS Transmitted Beam Shift in Quasi-optic Instruments

M. Jin, Y. Bai, and C. Gao
Science and Technology on Electromagnetic Scattering Laboratory, Beijing 100854, China

Abstract— The Frequency Selective Surface is the key component in the Quasi-Optic instrument for feeding large reflector antennas, because of that beams from horns in different frequency band can be combined on a sharing feeding aperture. The aberration to the transmitted beam through FSS is an important problem in fabricating a multi-band QO feed, and must be evaluated in the design stage. Recently, an efficient anticipation method was reported, which can be used to predict the tangential beam shift caused by the FSS and one FSS design is considered. In this paper, we will further discuss the longitude transmitted beam shift anticipation, and consider another FSS structure to show that method can be universal to different FSS structural types.

1. INTRODUCTION

The Quasi-Optical (QO) and beam waveguide (BWG) instruments have found to be with high transmission efficiency and low dispersion, and have become popular in the reflector antenna systems [1–3]. The frequency selective surface (FSS) is the key component in the multi-band QO and BWG, as one can use it to combine beams in different frequency bands onto a shared feed aperture [4, 5]. To be more specifically, a beam in the stop band can be reflected by the FSS, while that in the pass band can be transmitted through it. For the transmitted beam, the FSS structure will introduces both degradation (beam deforming) and shifting effects, which bring difficulties in fabricating a multi-band QO or BWG instrument and must be evaluated [1–3, 6]. The degradation effect due to the FSS has been intensively studied. In most of the reports, methods based on plane-wave spectrum (PWS) formulations have been proposed and verified to be accurate in finding the transmitted field distributions [6–9]. In those methods, the incident and transmitted beams are expanded in the plane wave spectrum and the influence on each PW component by FSS can be included in the analysis. Consequently, results of a 2-D angular sweeping of simulations under periodic boundary conditions (PBC) are required to implement the PWS method [6–10].

In a multiband QO instrument, the FSS is deployed among a serial of components in each beam path, where systematic design has to be performed [1–4]. In this case, an even more efficient method to investigate the transmitted beam aberrations would help in the early design stage. Recently, we reported a anticipation method for the transmitted beam shift caused by FSS [11]. That method is based on the phase analysis of the plane-wave transmission functions of FSS within a range of incident angles, and only the results of a 1-D sweeping of PBC simulations is required. In the reported work, the anticipation method for tangential beam shift was validated by the PWS algorithms. In this work, we are to discuss the longitudinal transmitted beam shift, and address another FSS structure to show the university of that Method.

2. ANALYTIC MODEL AND VERFICATION METHOD

2.1. Analytic Model

In Fig. 1, the analytic model for anticipating the transmitted beam shift through FSS is presented, along with the beam transmission through free-space as the reference. The difference between the analytic model in this work and that in [11] is the consideration of longitudinal beam shift Δl. As the detailed derivations for the beam shift anticipation can be found in [11], related formulations would not be included in this paper for brevity. Further, the formulations related to the Δl which has not been included in [11] will be presented in this work.

In Fig. 1, the transmitted aperture TA is shifted from RA (reference aperture) with tangential beam shift of Δt and Δl, so that the transmitted beam on TA in the FSS transmitted system is most approximated to that on RA in the Free-space transmission system. Considering the plane wave transmission function in the Free-space system to be $h(\theta, \varphi)$, that in the FSS system from IA to TA to be $\arg(h^t_{\xi\xi}(\theta, \varphi, \Delta t, \Delta l)$, and that from IA to RA to be $h^{t0}_{\xi\xi}(\theta, \varphi)$. We have:

$$h^t_{\xi\xi}(\theta, \varphi, \Delta t, \Delta l) = h^{t0}_{\xi\xi}(\theta, \varphi) \cdot e^{-j\left[\begin{array}{l}(-\Delta t \cdot \cos\alpha + \Delta l \cdot \sin\alpha) \cdot k_x \\ +(\Delta t \cdot \sin\alpha + \Delta l \cdot \cos\alpha) \cdot k_z\end{array}\right]} \quad (1)$$

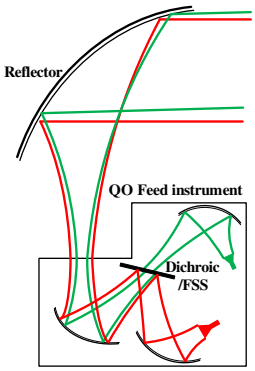

Figure 1: Configuration of an FSS in an QO feed for reflector antenna (not to scale), the beam shift effect by FSS is also demonstrated.

Actually, the beam shift cause by the FSS is due to the difference between the phase distributions of $h^{t0}_{\xi\xi}(\theta,\varphi)$ and $h(\theta,\varphi)$. If proper Δt and Δl can be introduced as in Fig. 2, so that $\arg(h^{t}_{\xi\xi}(\theta,\varphi,\Delta t,\Delta l)$ approximates to $\arg(h(\theta,\varphi))+\mathbf{Cons}$, then the FSS transmitted system with corresponding Δt and Δl can be regarded as the shift-corrected one for beam transmission. Here, **Cons** stands for a constant number.

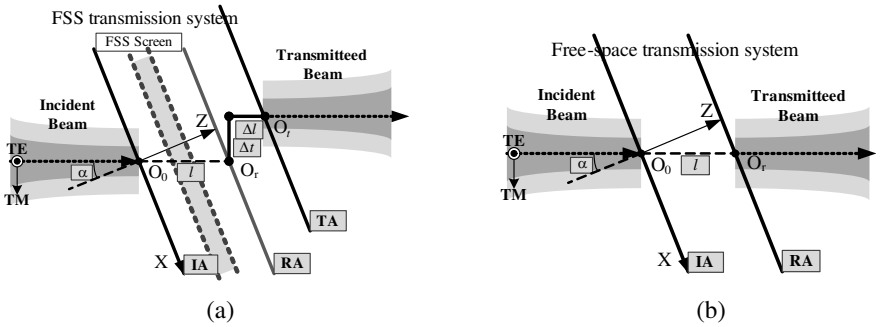

Figure 2: Configuration of beam propagation systems with a FSS screen and without a FSS screen (Free-space).

We are to do the phase analysis in the XOZ plane. The first step is conducting an 1-D θ sweeping ($\varphi=0°$) of PBC-simulations for the FSS structure, using commercial software [12] to obtain the $h^{t0}_{\xi\xi}(\theta,0°)$. Then, a phase difference function is defined as:

$$p^{d}_{\xi}(\theta,\Delta t,\Delta l)=\arg(h(\theta,0°))-\arg\left(h^{t}_{\xi\xi}\left(\theta,0°,\Delta t,\Delta l\right)\right) \tag{2}$$

Now we can perform the beam shift anticipation by doing:

(1) Tangential shift correction: Adjusting Δt to have $p^{d}(\theta,\Delta t,\Delta l=0)$ reach its extremum at $\theta=\alpha$, that also means $\arg(h^{t}_{\xi\xi}(\theta,0°,\Delta t,0))$ reaches its extremum at $\theta=\alpha$ as $\arg(h(\theta,0°))$ does. The founded Δt is named as Δt_a.

(2) Longitudinal shift correction: Adjusting Δl to make the absolute value of $p^{d}(\theta,\Delta t_a,\Delta l)$ as small as possible within the region of θ we care. The founded Δl is called by Δl_a.

In this paper, the scheme to find Δt_a and Δl_a is called the ***Phase Correction*** scheme.

2.2. Verification Method

To validate the anticipated beam shift, Δt_a and Δl_a, a direct way is to compare the FSS transmitted fields on **TA** with the free-space transmitted fields on **RA**. The PWS method can be used in accurately finding the transmitted fields through FSS, as has been proven in a number of references [6–10]. The incident is the same as in [11]. For the TM or TE incident, we set the incident field distributions on **IA** to be with only E_x(E_z also exists but is not needed to be considered in the calculation) or E_y component respectively.

Further evaluation of the beam shift Δt and Δl basing on the PWS simulation results can be done via the coupling coefficients. The free-space transmitted fields on **RA** are considered as the reference, to be compared with the FSS transmitted fields on **TA** with Δt and Δl as variables. Then coupling coefficients $C(\Delta t,\ \Delta l)$, between the free-space transmitted fields E_ξ^{Free} and FSS transmitted fields $E_\xi^{FSS}(\Delta t, \Delta l)$, is defined as:

$$C^{POL}(\Delta t, \Delta l) = \left| \frac{\left\langle E_\xi^{Free} | E_\xi^{FSS}(\Delta t, \Delta l) \right\rangle}{\left\langle E_\xi^{Free} | E_\xi^{Free} \right\rangle^{0.5} \cdot \left\langle E_\xi^{FSS}(\Delta t, \Delta l) | E_\xi^{FSS}(\Delta t, \Delta l) \right\rangle^{0.5}} \right| \tag{3}$$

where: $\langle f|g\rangle = \iint f(x,y) \cdot g^*(x,y)dxdy$, and POL stands for TM or TE, when ξ stands for x or y respectively. Clearly, when $C(\Delta t, \Delta l)$ reaches its maximum value, the corresponding $\Delta t_{\max}$ and $\Delta l_{\max}$ is the correct shift compensation for $\mathbf{O}_t$ as in Fig. 2.

3. RESULTS AND DISCUSSIONS

First, the same FSS structure studied in [11] is considered in this work, which is design for TE and TM beam transmission around 90 GHz at oblique incident of ($\theta = \alpha = 30°$, $\varphi = 0°$). At 90 GHz, the $p^d(\theta)$ curves for TE and TM beam shift anticipation is presented in Fig. 4. Then those anticipated Δt_a and Δl_a are verified by the coupling coefficient results based on the PWS calculated field distributions, as in Fig. 5. As can be seen, the Δt_a can be accurately anticipated as stated in [11]. However, the anticipated Δl_a is near to but not at, the positions where the maximum of coupling coefficient $C(\Delta t_{\max},\ \Delta l)$ stand. This fact implies the information that $\arg(h^t_{\xi\xi}(\theta, 0°))$ offers is not sufficient for the accurate Δl determination. On the other hand, results shows that coupling coefficients $C(\Delta t, \Delta l)$ varies much more severely versus Δt than versus Δl. And this fact agrees with the common sense that the tangential beam shift Δt caused by FSS is much more

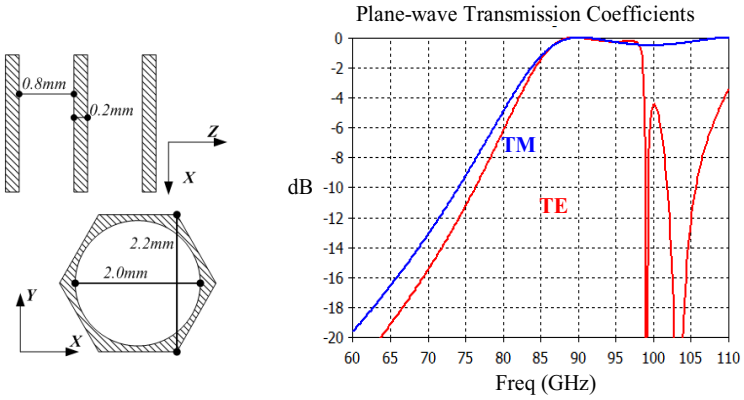

Figure 3: 3-layer FSS structure and its transmission coefficients at the design angle ($\theta = 30°$ and $\varphi = 0°$).

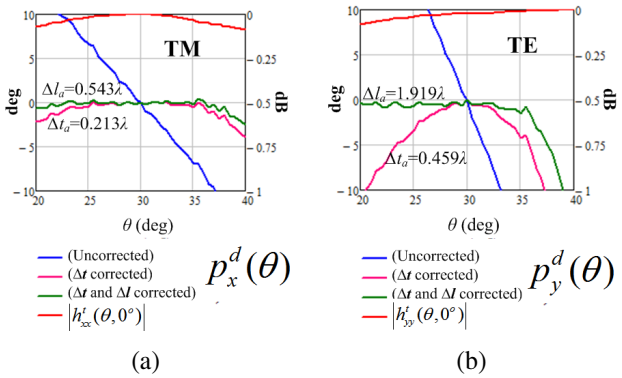

(a) (b)

Figure 4: The $p^d(\theta)$ curves in different stages of phase correction scheme, at 90 GHz, in cases of (a) TM and (b) TE incident.

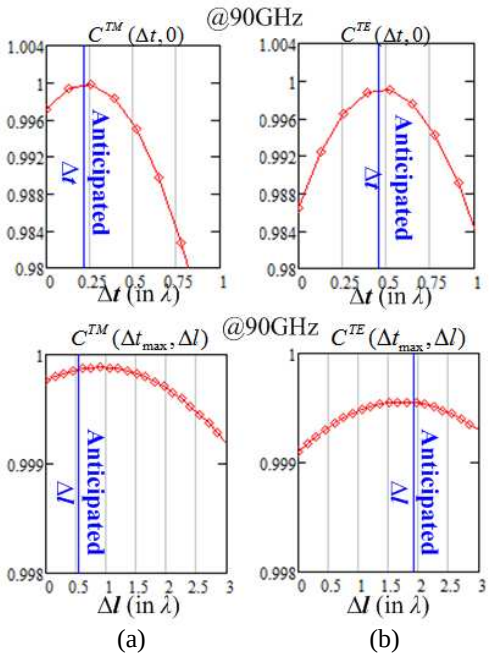

Figure 5: Curves of calculated coupling coefficients between Free-space transmitted fields on **RA** and FSS (the first one) transmitted fields on **TA** as in Fig. 2, along Δt (first row) and Δl (second row), at 90 GHz, in the cases of (a) TM and (b) TE incident; the positions of anticipated Δt_a and Δl_a by the proposed method are also marked.

worthy of attentions than the longitudinal shift Δl, for the sake of transmission efficiency in the design of an QO feed.

Another FSS design considered in this work, is a two-layer ring slot structure supported by a dielectric plate. The purpose to study such a FSS design is to show that the method can be utilized regardless of FSS structure types. The plane-wave transmission coefficients at the design angle ($\theta = \alpha = 30°$, $\varphi = 0°$) are shown in Fig. 6. The anticipated Δt_a from 85 GHz to 100 GHz by the phase correction scheme, and the corresponding $C^{TE}(\Delta t, \Delta l = 0)$ and $C^{TM}(\Delta t, \Delta l = 0)$ distributions based on the PWS simulation results, are presented in Fig. 7. In both the cases of TE and TM incident, the corresponding anticipated Δt_a walk along the maximum $C(\Delta t)$ positions which are near to $\Delta t = 0$, that means the tangential shift anticipations were accurate within the pass band. Meanwhile, the fact that the maximum of $C(\Delta t)$ approaches to 1 (> 0.999) from 85 GHz to 100 GHz in both the cases of TE and TM incident, shows that the degradation effects by the FSS are weak.

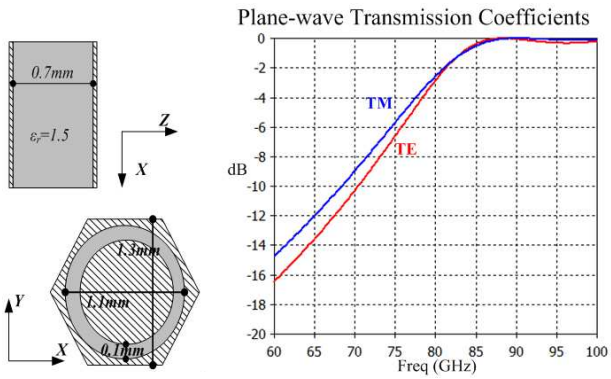

Figure 6: 2-layer FSS structure and its transmission coefficients at design angle ($\theta = 30°$ and $\varphi = 0°$).

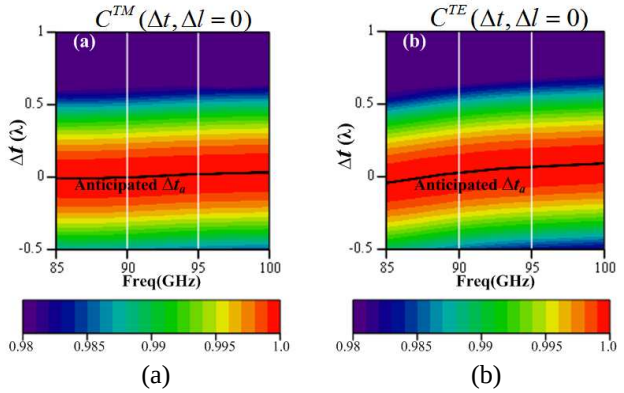

Figure 7: Distribution of calculated coupling coefficients $C(\Delta t, \Delta l = 0)$, between free-space transmitted fields on **RA** and FSS (the second one) transmitted fields on **TA** as in Fig. 2, from 85 to 100 GHz, in cases of (a) TM and (b) TE incident; the positions of anticipated Δt_as by the proposed method at varying frequencies, are also marked.

4. CONCLUSION

In this paper, we further discussed the beam transmission shift through FSS based on the method reported in [11]. The longitudinal beam shift is discussed, which is found to be with a smaller effect on the transmitted beams through FSS. We also considered another FSS structure to perform the tangential beam shift anticipation, and accurate results were obtained. That means the tangential shift anticipation method in [11] can be utilized regardless of FSS structure types.

REFERENCES

1. Foster, L. P. R. and R. J. Wylde, "The effect of quasi-optical errors on reflector antenna performance," *IEEE Trans. on Microwave Theory Technique*, Vol. 40, No. 6, 1318–1322, 1992.
2. Costes, L., C. Bushell, M. J. Buckley, and G. Mason, "Microwave humidity sounder (MHS) antenna," *Proc. SPIE*, Vol. 3870, Florence, Italy, Dec. 1999.
3. Jorgensen, R., G. Padovan, P. de Maagt, D. Lamarre, and L. Costes, "A 5-frequency milimeter wave antenna for a spaceborne limb sounding instrument," *IEEE Trans. on Antennas Propagat.*, Vol. 49, No. 5, 2001.
4. Goldsmith, P. F., *Quasioptical Systems: Gaussian Beam Quasioptical Propogation and Applications*, Wiley-IEEE Press, New York, 1998.
5. Dickie, R., R. Cahill, H. S. Gamble, V. F. Fusco, A. G. Schuchinsky, and N. Grant, "Spatial demultiplexing in the sub-millimeter wave band using multilayer free-standing frequency selective surfaces," *IEEE Trans. on Antennas Propagat.*, Vol. 5, No. 6, 1904–1911, 2005.
6. Pasian, M., M. Bozzi, and L. Perregrini, "Accurate modeling of dichroic mirrors in beam-waveguide antennas," *IEEE Trans. on Antennas Propagat.*, Vol. 61, No. 4, 1931–1938, 2013.
7. Donnan, R. S. and A. Yamsiri, "Accurate modeling of dichroic mirrors in beam-waveguide antennas," *EuCAP 2007*, Nov. 2007.
8. Prakash, V., N. T. Huang, and R. Mittra, "Accurate analysis of interaction between microwave antennas and frequency selective surface (FSS) radomes," *ICAP 2003*, Vol. 1, 401–404, 2003.
9. Jin, M., M. Bai, N. Ou, and J. Miao, "The plane-wave spectrum approach for beam transmission through planar FSS structures," *IEEE ICMMT 2012*, 2012.
10. Bai, M., M. Jin, N. Ou, and J. Miao, "On scattering from an array of absorptive material coated cones by the PWS approach," *IEEE Trans. on Antennas Propagat.*, Vol. 61, No. 6, 3216–3224, 2013.
11. Jin, M. and M. Bai, "On the transmitted beam shift through FSS structure by phase analysis," *IEEE Antenna Wireless Propagat. Lett.*, Pre-published online.
12. https://www.cst.com/Products/CSTMWS.

Retrieval of Bare-surface Soil Moisture from Simulated Brightness Temperature Using Least Squares Support Vector Machines Technique

Fei Xu, Qinghe Zhang, and Qiyuan Zou
School of Science, Three Gorges University, Yichang, Hubei 443002, China

Abstract— Soil moisture is an important parameter for hydrological and climatic investigations. It also plays a critical role in the prediction of erosion, flood or drought. In this paper, we explore the use of the support vector machine technique for modeling soil moisture inversion. LS-SVM is improved by the standard SVM and has more attractive properties. Experimental tests are carried by using the different set of training and test data. The methodologies have been applied to two sets of data to retrieve soil moisture and obtained the root mean squared error (RMSE) and the determination coefficient (R^2). The emissivity model (Q/H model) is applied to acquire the brightness temperature. The frequencies of interest include 1.4 GHz (L-band) of the soil moisture and ocean salinity (SMOS) sensor at two incidence angles and 6.9 GHz (C-band) of the advanced microwave scanning radiometer (AMSR) viewing angle of 55 deg. The effectiveness is assessed by considering various combinations of the input features. This study demonstrates the great potential of LS-SVM in the retrial of soil moisture from passive microwave remotely sensed data.

1. INTRODUCTION

The soil moisture of the bare-surface soil plays a key role of seasonal climate evolution and prediction because that it is a critical parameter in the mass and energy transfer between the soil and atmosphere [1]. The retrieval of surface soil moisture based on land surface hydrology models is of great important in myriad applications, including agriculture, water resource management to numerical weather foresting, climate change, and monitoring events (e.g., floods and droughts) [2].

Passive microwave remote sensing is a viable method in the research on land surface parameters. Recently, much effort has been devoted to effective approaches to estimate soil moisture and other surface parameters. Generally, there are two types of approaches to be used: physical modeling and semiempirical [3] in recent years. The traditional theories: the small perturbation (SPM), Kirchhoff approximation (KA). Moreover, the integral equation model (IEM) has demonstrated a much wider applicable scope for surface roughness conditions [4]. The empirically adopted IEM (EA-IEM) fit a wide range of soil dielectric constants, incidence angles [5]. For the semiempirical models, the Q/H model presented by Wang and Choudhury [6, 7], is a function of the surface roughness and dielectric properties and widely used in the remote sensing community. Now, many studies and methods have been undertaken in radar sensing research to retrieve the soil moisture and surface roughness [8–11]. Combined experimental or a model-based data, several papers applied the artificial neural network (ANN) and support vector regression. LS-SVM were introduced [12, 13] as reformulations to standard SVM which simplify the training process of SVM in a great extent by replacing the inequality constraints with equality ones. LS-SVM has been applied to forecasting in many areas of engineering.

Therefore, in this study, the goal is to approach the soil moisture of the inversion problem by using LS-SVM combined with Q/H model, and manage to enhance the accuracy of the retrieval process.

2. MICROWAVE SOIL MOISTURE RETRIEVAL APPROACH

2.1. Surface Roughness Model

In many studies, the Q/H model was the most commonly used to describe roughness surface radiation [6, 7]. The measurements of electromagnetic radiation emitted or reflected by soil surface, which can monitor the soil moisture. The expression of surface of the brightness temperature is given below

$$T_B = e \cdot T_S \tag{1}$$

where T_B is the brightness temperature, T_S is the soil surface temperature and e is the soil emission. This equation descripts the fact that both surface temperature and emission decide soil surface

brightness temperature. Besides, soil brightness temperatures have linear relation with emission at the fixed soil surface temperature according to Eq. (1). e is decided by the characteristic of target object and related to the reflectivity r by reciprocity: $e = 1 - r$. Relate to smooth surface reflectivity, rough surface reflectivity can expressed as

$$r_{sp} = [(1 - Q)r_{op} + Qr_{oq}] \exp(-h) \tag{2}$$

where, r_{sp} is the rough surface reflectivity, the subscript p and q denote either V or H polarization. For a homogeneous soil with a smooth surface, the reflectivity at V and H polarization r_{ov} and r_{oh} are given by the Fresnel expression

$$r_{oh} = \left| \left(\cos\theta - \sqrt{\varepsilon_r - \sin^2\theta} \right) \Big/ \left(\cos\theta + \sqrt{\varepsilon_r - \sin^2\theta} \right) \right|^2 \tag{3}$$

$$r_{ov} = \left| \left(\varepsilon_r \cos\theta - \sqrt{\varepsilon_r - \sin^2\theta} \right) \Big/ \left(\varepsilon_r \cos\theta + \sqrt{\varepsilon_r - \sin^2\theta} \right) \right|^2 \tag{4}$$

where θ is the incidence angle and ε_r is the complex dielectric constant of the soil that depends primarily on the soil moisture content. In Q/H model, Q is a mixing parameter between polarizations V and H, and can be discarded sometimes. In theorythe parameter $h = (4\pi\sigma\cos\theta/\lambda)^2$ is used for surface roughness correction.

2.2. Least Square Support Machines Regression

LS-SVM are reformulations, the result in a set of linear equations instead of a quadratic programming problem for SVM. The x_i and y_i are the input and the output of the ith example, l presents the number of samples, consider a given training set: $\{(x_i, y_i)|x_i \in R^l, y_i \in R\}_{i=1,2,\ldots,l}$. The goal of the support vector method is to construct a regression of the following form

$$y = \omega^T \phi(x) + b \tag{5}$$

where $\phi(\cdot)$ is the nonlinear map mapping the input space to a usually high dimensional feature space, $\omega \in R^l$ is coefficient vector and $b \in R$ is bias term. These unknown parameters ω and b can be obtained [12, 13]

$$\min J(\omega, \xi) = \frac{1}{2}\omega^T\omega + \frac{1}{2}\gamma \sum_{i=1}^{l} \xi_i^2 \quad s.t. \quad y_i \left[\omega^T \phi(x) + b\right] = 1 - \xi_i, \quad \xi_i \geq 0, \quad i = 1, 2, \ldots, l \tag{6}$$

The Lagrange corresponding to Eq. (6) can be defined as follows:

$$L(\omega, \xi, \alpha) = \frac{1}{2}\omega^T\omega + \frac{1}{2}\gamma \sum_{i=1}^{l} \xi_i^2 - \sum_{i=1}^{l} \alpha_i \left(\omega^T \phi(x_i) + b + \xi_i - y_i\right) \tag{7}$$

where α_i $(i = 1, 2, \ldots, N)$ are the Lagrange multipliers. The value of ω and ξ are obtained from the solution, and the Kuhn-Tucker conditions can be expressed by

$$\begin{bmatrix} 0 & \vec{1}^T \\ \vec{1} & z^T z + \gamma^{-1} I \end{bmatrix} \begin{bmatrix} b \\ \alpha \end{bmatrix} = \begin{bmatrix} 0 \\ y \end{bmatrix} \tag{8}$$

where I is the identity matrix, $z = [\phi(x_1), \ldots, \phi(x_l)]$; $y = [y_1, \ldots, y_l]^T$; $\vec{1} = [1, \ldots, 1]^T$; $\alpha = [\alpha_1, \ldots, \alpha_l]^T$.

The solution of αa nd b can be obtained by solving Eq. (8) and substitute to Eq. (5). According to the Mercer rule, the Kernel function $K(x_i, y_j) = \phi(x_i)^T \phi(y_j)$ Eq. (5) is presented as:

$$y(x) = \sum_{i=1}^{l} \alpha_i K(x_i, x) + b \tag{9}$$

3. DATA SET AND DESIGN OF EXPERIMENTS

In order to evaluate and characterize the effect of roughness on surface emission. Meanwhile, SM is sensitive to low-frequency ban at bare or low vegetated soils. We generated a simulated surface emission data based for two specific frequencies 1.4 GHz of the SMOS sensor and 6.9 GHz of the AMSR, respectively. Some initial specific parameters are related in the process of SM simulation, e.g., the soil surface temperature, the structure of the surface soil texture, soil bulk density (p_s), surface roughness etc.. According to the some reference, we designed the study area SM simulation input data sets, which were listed in Table 1.

The training of the LS-SVM data have been simulated in terms of the soil surface emissivity dual-polarization from Eq. (1). We set the soil moisture content (MV) from 2%–42%, and σ in the range of 0.1–1.6 cm. For simulated data sets, we converted into soil dielectric constant model [18], and generated MV and brightness temperature more than 900 samples. The inputs are the brightness temperature, the outputs is the MV as well. Considering the input parameters affect the estimation, various combinations are taken in account, the following design of experiments:

(1) three 1-D modes: a) two L-band 1-D modes: emissivity polarization H and V at 1.4 GHz and incidence angles 20 and 40 deg respectively; b) one C-band 1-D mode: emissivity dual-polarization at 6.9 GHz at an angle of 55 deg.

(2) one L-band 2-D mode: combine two angles of incidence that correspond to one L-band 2-D mode, i.e., dual-polarization at 1.4 GHz at angles of 20 and 40 deg.

(3) three integrated C- and L-band modes: at C-band combined with the front two steps to become integrated C- and L-band multiple dimensional emissivity modes.

Table 1: Data sets of soil moisture simulated.

Parameters	Temperature	Sand (g/g)	Clay (g/g)	p_s (g/cm^3)	Frequency	Incidence angle
value	23°	42%	18%	1.4	1.4, 6.9 GHz	20, 40, 55 deg

Table 2: The R^2 and RMSE of SM by the LS-SVM and BPNN method.

EXPERIMENTS		LS-SVM		BPNN	
		R^2	RMSE (%)	R^2	RMSE(%)
L-band 1-D mode	1.4 GHz/20 deg	1.0	0.0016	0.997172	0.8838
	1.4 GHz/40 deg	1.0	0.0002	0.999435	0.5780
AMSR mode	6.9 GHz/55 deg	0.990461	1.595	0.98775	1.8105
L-band 2-D mode	1.4 GHz/20 + 40 deg	1.0	0.0023	0.997296	0.8489
combined 6.9 GHz and L-band 1-D mode	6.9 GHz/55 deg, 1.4 GHz/20 deg	0.999548	0.3696	0.997590	0.9651
	6.9 GHz/55 deg, 1.4 GHz/40 deg	0.999961	0.1216	0.998976	0.6049
3-D mode	6.9 GHz/55 deg, 1.4 GHz/20,40 deg	0.999968	0.11	0.998793	0.6414

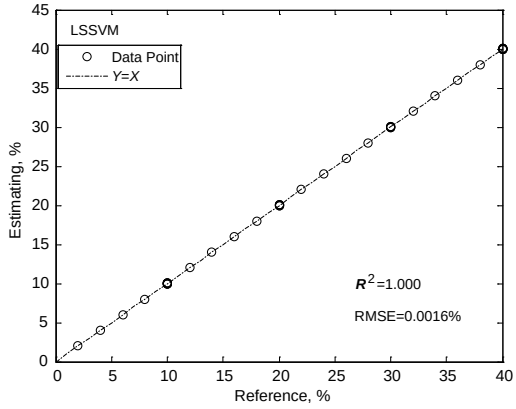

Figure 1: Retrieved SM 1-D mode (L-, H and V, 20 deg).

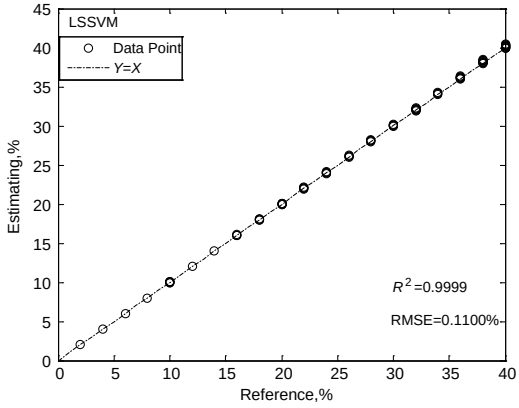

Figure 2: Retrieved SM combined 6.9 GHz with L-2-D modes.

4. RESULTS AND COMPARISON

Through the brightness temperature simulation and numerical experiments, we obtained the retrieval results for the soil moisture, the R^2 between the retrieved SM and the reference, and the RMSE in SM are also given in the Table 2.

As were shown in the figures (part of the results) and Table 2, obviously, we can get the following main conclusions: L-band result is better than C-band in different wavelengths; the result of large angle is better than the small angle within a limited range; the inversion of SM at C-band combined with L-band displayed that 3-D mode is better than 2-D modes. In Table 2, both of those two methods result sound, evidently, LS-SVM method has an advantage over BPNN method.

5. CONCLUSION

In this study, we had come up with the LS-SVM to retrieve the SM from simulated brightness temperature. The result of the design is based on the simulations of Q/H model that is a promising approach to further investigate the sensing of the SM by space-based microwave radiometers such as the AMSR and SMOS.

ACKNOWLEDGMENT

This work was supported by the National Natural Science Foundation of China (No. 61179025) and the Natural Science Foundation of Hubei Provincial Department of Education (No. D20111201).

REFERENCES

1. "Implementation plan for the global observing system for climate in support of the UNFCCC," Tech. Rep. 1244, World Meteorological Organization, Intergovernmental Oceanographic Commission, United Nations Environment Programme, International Council Science, Geneva, Switzerland, 2010.
2. Douville, H. and F. Chauvin, "Relevance of soil moisture for seasonal climate predictions: A preliminary study," *Climate Dyynamics*, Vol. 16, Nos. 10–11, 719–736, Oct. 2000.
3. Ulaby, F. T., R. K. Moore, and A. K. Fung, "Radar remote sensing and surface scattering and emission theory," *Microwave Remote Sensing: Active and Passive*, Vol. 2, Adision-Wesley, Reading, MA, 1982.
4. Fung, A. K., *Microwave Scattering and Emission Models and Their Applications,* Artech House, Norwood, MA, 1994.
5. Song, K., X. Zhou, and Y. Fan, "Empirically adopted IEM for retrieval of soil moisture from radar backscattering coefficients," *IEEE Trans. Geosci. Remote Sens.*, Vol. 47, No. 6, 1662–1672, Jun. 2009.
6. Wang, J. R. and B. J. Choudhury," Passive microwave radiation from soil: Examples of emission model and observation," *Passive Microwave Remote Sensing of Land-atmosphere Interactions*, VSP, Zeist, The Netherlands, 1995.
7. Wang, J. R. and B. J. Choudhury, "Remote sensing of soil moisture content over bare fields at 1.4 GHz frequency," *J. Geophys. Res.*, Vol. 86, 5277–5282, 1981.
8. Liou, Y. A., Y. C. Tzeng, and K. S. Chen, "A neural network approach to radiometric sensing of land-surface parameters," *IEEE Trans. Geosci. Remote Sens.*, Vol. 37, 2718–2724, 1999.
9. Liu, S. F., Y. A. Liou, W. J. Wang, J. P. Wigneron, and J. B. Lee, "Retrieval of crop biomass and soil moisture from measured 1.4 and 10.65 GHz brightness temperatures," *IEEE Trans. Geosci. Remote Sens.*, Vol. 40, No. 8, 1260–1268, 2002.
10. Atluri, V., H. Chih-Cheng, and T. L. Coleman, "An neural network for classifying and predicting soil mo isture and temperature using Levenberg-Marquardt algorithm," *IEEE Southeastcon'99 Proceedings*, 1999.
11. Pasolli, L., C. Notarnicola, and L. Bruzzone, "Estimating soil moisture with the support vector regression technique," *IEEE Trans. Geosci. Remote Sens. Letters*, Vol. 8, No. 6, 1080–1084, Nov. 2011.
12. Suykens, J. A. K. and J. Vandewalle, "Least squares support vector machine classifiers," *Neural Processing Letters*, Vol. 9, No. 3, 293–300, Jun. 1999.
13. Suykens, J. A. K. and J. Vandewalle, "Recurrent least squares support vector machines classifiers," *IEEE Transactions on Circuits and Systems-I*, Vol. 47, No. 7, 1109–1114, Jul. 2000.

14. Dobson, M. C., F. T. Ulaby, M. T. Hallikainen, and M. A. EI-Rayes, "Microwave dielectric behavior of wet soil — Part II: Dielectric mixing models," *IEEE Trans. Geosci. Remote Sens.*, Vol. 23, 35–46, 1985.

A Method of Two-dimensional MIMO Planar Array Design Based on Sub-array Segmentation for Through-wall Imaging

Pengfei Liu, Biying Lu, and Xin Sun
College of Electronic Science and Engineering
National University of Defense Technology, Changsha 410073, China

Abstract— In three-dimensional (3-D) through-wall imaging (TWI) applications, imaging performance is directly affected by the configuration of the arrays. In this paper, the concept of equivalent array is introduced to design the 2-D MIMO array. A method named sub-array segmentation is used to circumvent the de-convolution process between the equivalent array and MIMO array. To get the optimum array among the results after the de-convolution, a concept of comprehensive size is used to evaluate the physical size of the MIMO array by using the information of sub-array segmentation, which is inspired by the split transmit virtual aperture (STVA) that has the shortest physical size given the virtual aperture. Finally, a 2-D UWB-MIMO array is designed for TWI as an example to validate the proposed method.

1. INTRODUCTION

Recent years, radar imaging technology has made a great progress with the introduction of various new concepts. To meet the needs of anti-terrorism in the cities, street fighting, as well as the personnel rescue buried in the ruins, ultra-wideband TWI technology has been widely studied. To solve the problem of the shadow effect and space ambiguity phenomena in 2-D imaging, getting the 3-D information of target scene by 2-D spatial distribution of antennas becomes an urgent need.

In order to overcome the disadvantages of time costing of synthetic aperture imaging system and the prohibitive cost of real aperture imaging in 3-D TWI, MIMO imaging [1], which uses the virtual array concept to get a larger virtual imaging aperture while using much lesser actual number of array elements, are widely used. Equivalent array, such as virtual aperture [2–4], which makes the bistatic pattern of MIMO array equivalent to the monostatic pattern, provides an important tool for the analysis and design of MIMO array.

In [5] Lockwood proposed a framework for designing the 2-D sparse array by selecting different element spacing within the transmit/receive elements, Smith obtained Several typical configurations of 2-D array under far-field condition using Fast Fourier transform methods in [6], X. D. Zhuge in [7] extended the method of separable aperture functions for designing an uniform linear array to an uniform rectilinear array. As the bistatic-to-monostatic equivalence condition is valid only at a small range of angle, in most cases, the size of the designed MIMO array is expected to be as small as possible to keep the similar illumination geometry with the equivalent array. Refer to the STVA given by Lu Biying in [2], a method based on the sub-array segmentation is introduced to solve the problem of de-convolution, and a best choice for the smallest physical size of the MIMO array is made among the results after the de-convolution according to the criterion of comprehensive size. An example of 2-D planar array is made to validate the proposed method in the end.

2. VIRTUAL APERTURE

Virtual aperture [2–4] is based on the equivalence between the two-way bistatic array and the two-way monostatic array, using the principle of Phase Center Approximation (PCA). Consider the 2-D MIMO array composed of M transmit and N receive elements located on the xz plane, in which the location of mth transmit element is $\mathbf{r}_{t,m} = (x_{t,m}, 0, z_{t,m})$, $m = 0, 1, 2, \ldots, M-1$, and the location of nth receive element is $\mathbf{r}_{r,n} = (x_{r,n}, 0, z_{r,n})$, $n = 0, 1, 2, \ldots, N-1$. The virtual aperture element $\mathbf{r}_{v,i}$, come from $\mathbf{r}_{t,m}$ and $\mathbf{r}_{r,n}$, may be expressed as

$$\mathbf{r}_{v,i} = (x_{v,i}, 0, z_{v,i}) = ((x_{t,m} + x_{r,n})/2, 0, (z_{t,m} + z_{r,n})/2) \tag{1}$$

where $i = (m+1)(n+1) - 1$, $m = 0, 1, 2, \ldots, M-1$, $n = 0, 1, 2, \ldots, N-1$.

3. 2-D MIMO ARRAY DESIGN

As known that the equivalent virtual array can be regarded as the space convolution between the transmit and receive elements of MIMO array, got as

$$D_e(r) = D_t(r) * D_r(r) \tag{2}$$

where $D_e(r)$ is the distribution function of the equivalent array, $D_t(r)$ and $D_r(r)$ are the distribution functions of the transmit and receive array, "$*$" represents the space convolution operation.

Due to the nature of convolution, the equivalent array can be seen as a combination of receive array copies, when the number of transmit elements is given. Thus, in some cases, the de-convolution of the equivalent array can be simplified to the segmentation of the equivalent array with the same structure of sub-arrays.

For a 2-D planar array, assume that the 2-D uniform plane array composed with $N \times M$ equivalent virtual elements is considered. The intervals between the elements along the x-label and the z-label are respectively d_x and d_z. The distribution function of the equivalent virtual array can be expressed as

$$D_e(r) = \left\{ (r, w_e(r)) \middle| \begin{array}{l} r(x) = x_m,\ m = 1, 2 \ldots, M \\ r(z) = z_n,\ n = 1, 2 \ldots, N \end{array} ,\ w_e(r) = 1 \right\} \tag{3}$$

The center position of the equivalent array is

$$O(x_0, z_0) = ((x_1 + x_M)/2, (z_1 + z_N)/2) \tag{4}$$

Given the number of transmit elements T, which is a divisor of $N \times M$, then the number of receive elements can be determined by $R = N \times M/T$. Factor R, and let N_R represents the number of factorizations. For the ath factorization $R = R_{ax} \times R_{az}$, factor R_{ax} and R_{az} respectively, the number of factorizations N_{ax} and N_{az} can be got. If R_{ax} is not a divisor of M or R_{az} is not a divisor of N, N_{ax} or N_{az} should be set to null. If R_{ax} equals to M or R_{az} equals to N, N_{ax} or N_{az} should be set to unity. Note that the pth factorization of R_{ax} is $R_{ax} = R_{apr} \times R_{aps}$, and the qth of R_{az} is $R_{ax} = R_{apr} \times R_{aps}$. The number of sub-array segmentations for the equivalent array can be formulated as

$$N_E = \sum_{a=1}^{N_R} N_{ax} \times N_{az} \tag{5}$$

Take any kind of the sub-array segmentation from N_E, a structure of sub-array can be obtained. Thus, a copy of the receive array can be expressed as follows

$$\begin{aligned} D_{r0}(r) \ = \ & \left\{ (r, w_{r0}(r)) \middle| \begin{array}{l} r(x) = x_m,\ m = (R_x - 1) \times M/R_{aps} + 1, 2 \ldots, R_{aps},\ R_x = 1, \ldots, R_{apr}; \\ r(z) = z_n,\ n = (R_z - 1) \times N/R_{aqs} + 1, 2 \ldots, R_{aqs},\ R_z = 1, \ldots, R_{aqr}; \end{array} \right. \\ & \left. w_{r0}(r) = 1 \right\} \end{aligned} \tag{6}$$

The center position of the receive array copy is

$$\begin{aligned} & O(x_0', z_0') = ((x_1 + x_{m0})/2, (z_1 + z_{n0})/2), \\ & m0 = (R_{apr} - 1) \times M/R_{aps} + R_{aps},\ n0 = (R_{aqr} - 1) \times N/R_{aqs} + R_{aqs} \end{aligned} \tag{7}$$

Then, the distribution function of the receive array can be expressed as

$$\begin{aligned} D_r(r) = & \left\{ (r, w_r(r)) \middle| \begin{array}{l} r(x) = 2(x_m + x_0 - x_0'),\ m = (R_x - 1) \times M/R_{aps} + 1, \ldots, R_{aps},\ R_x = 1, \ldots, R_{apr} \\ r(z) = 2(z_n + z_0 - z_0'),\ n = (R_z - 1) \times N/R_{aqs} + 1, \ldots, R_{aqs},\ R_z = 1, \ldots, R_{aqr} \end{array} \right. , \\ & \left. w_r(r) = 1 \right\} \end{aligned} \tag{8}$$

Combine Eq. (3), Eq. (8) and the positional relationship of the equivalent virtual array given in Eq. (1), the distribution function of the transmit array is

$$D_t(r) = \left\{ (r, w_t(r)) \middle| \begin{array}{l} r(x) = [2(i-1) - (M/R_{ax} - 1)] \times M/R_{aps} d_x + x_0,\ i = 1, 2 \ldots, M/R_{ax} \\ r(z) = [2(j-1) - (N/R_{az} - 1)] \times N/R_{aqs} d_z + z_0,\ j = 1, 2 \ldots, N/R_{az} \end{array} , w_t(r) = 1 \right\} \tag{9}$$

It is easy to find that different segmentations lead to different results of the de-convolution MIMO arrays, when given the same equivalent array. Refer to the STVA, which has the shortest physical size when given the effective aperture, a concept of comprehensive size, which use the information of sub-array segmentation to evaluate the truly physical size of the MIMO array, is introduced as follows

$$S_e = S_{r0} \cup d_{tx} d_{tz} (N_{tx} - 1)(N_{tz} - 1)) \tag{10}$$

where S_e represents the comprehensive size or the final physical size of the MIMO array, S_{r0} represents the size of sub-array, N_{tx} and N_{tz} represent the number of sub arrays along the x-label and z-label direction, d_{tx} and d_{tz} represent the intervals between sub-arrays along the x-label and z-label direction, "$\cup$" means to take the union.

According to the projection slice theory [8], the pattern of the planar array at a certain direction is determined by the projection of array elements onto a rotated axis at that particular angle within the array plane. If the beam patterns along two orthogonal directions are only concerned, a 2-D planar array can be designed as a composition with two basic one-dimensional linear arrays designed with the performance requirements previously.

Thus, the 2-D MIMO array can be designed as the following steps:

(1) Design two basic one-dimensional linear arrays meeting with the performance requirements of the azimuth, elevation direction [2];

$$D_1(r) = \{(r, w_1(r))|r(x) = x_m,\ m = 1, 2 \ldots, M,\ w_1(r) = 1\} \tag{11}$$

$$D_2(r) = \{(r, w_2(r))|r(z) = z_n,\ n = 1, 2 \ldots, N,\ w_2(r) = 1\} \tag{12}$$

(2) Compose the two basic one-dimensional linear arrays designed above into a 2-D uniform planar array, as shown in Eq. (3);

(3) For the given number of transmit elements, segment the 2-D uniform planar array according to Eq. (5) to obtain a copy of receive array as shown in Eq. (6), and then select the smallest comprehensive size among the receive array copies after segmentation according to Eq. (10).

(4) Obtain the receive array from the copy of receive array based on Eq. (8), and get the transmit array as shown in Eq. (9).

4. AN EXAMPLE AND SIMULATION RESULTS

Array Requirements: Design a 2-D UWB-MIMO array, with resolutions of 0.3 m in both the azimuth and elevation direction at a distance of 5m. The side lobe levels should be below -18 dB. The number of transmit elements is 9, and the physical size of the MIMO array should be as small as possible.

To meet the UWB imaging requirements, a stepped frequency signal is emitted, the center frequency is 1.5 GHz, the bandwidth is 2 GHz, the frequency step is 4 MHz. In accordance with the design steps described above and paper [2], the length of one-dimensional uniform linear array and the number of elements should satisfy

$$\sigma = 0.886\lambda_c/4 \left(\frac{L/2}{\sqrt{(L/2)^2 + R^2}} \right) \tag{13}$$

$$N = \text{int}_{up}(\max(1/RL, f_H/(B \cdot GL))) \tag{14}$$

where $\text{int}_{up}(\cdot)$ is the top integral function.

From Eq. (13) and Eq. (14), the length of one-dimensional uniform linear array $L = 1.5$ m and the number of elements $N = 12$ can be obtained. Thus, a two-dimensional uniform array of $12 \times 12(1.5\,\text{m} \times 1.5\,\text{m})$ would be got from the two basic one-dimensional uniform linear arrays with the interval $d = 0.1364$ m between the elements. Given the number of transmit elements as $T = 9$, the square equivalent array could be segmented into 9 kinds of 16-sub-arrays with same structure as shown in Figure 1 according to the Eq. (5).

According to Eq. (10), the comprehensive apertures of the segmentations shown in Figure 1 can be calculated in Table 1. From Table 1, array 5 acquires the smallest comprehensive size and the corresponding smallest physical size of the MIMO array. The resulted MIMO array following the design steps is shown in Figure 2.

Table 1: Comprehensive sizes for the 9 different segmentations illustrated in Figure 1.

N	1	2	3	4	5	6	7	8	9
S_e	64	56	72	56	49	63	72	63	81

To validate the performance of the designed equivalent array and MIMO array, a simulation is taken and the resulted PSF is shown in Figure 3. It can be found that both the designed equivalent array and MIMO array well meet the design requirements and the PSFs keep almost identified, which has verified the accuracy of the method to use equivalent array to design the MIMO array and the effectiveness of the method to use the sub-array segmentation to circumvent the de-convolution process between the equivalent array and the MIMO array.

Adopt the designed 2-D MIMO array into the 3-D TWI application with a simulation. Assume that the MIMO array locates at 3 m far away from the wall, the thickness of the wall is 0.2 m and the dielectric constant is 4.2, two point targets distributed along the elevation direction locate at 2 m after the wall, the interval between the targets is 0.4 m. The illumination geometry and the result imaging are shown schematically in Figure 4. It can be found from the simulation results

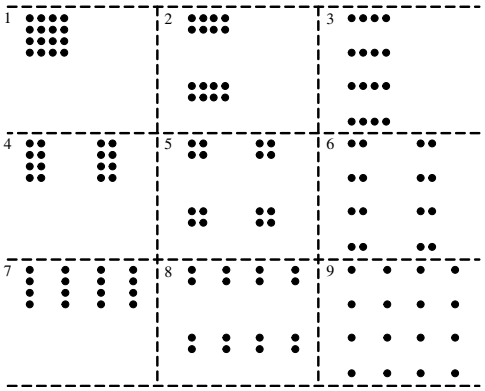

Figure 1: 9 kinds of structures for the 16-element sub-array.

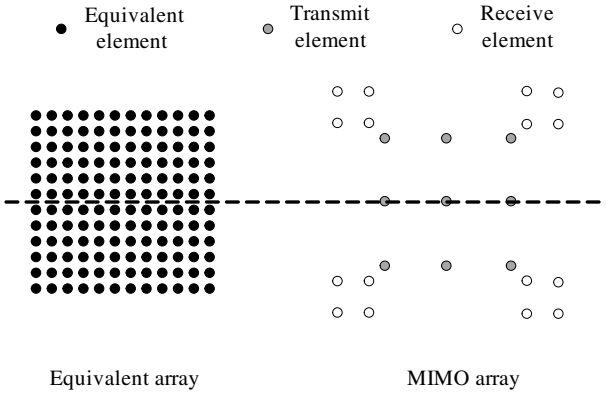

Figure 2: 2-D equivalent array and MIMO array

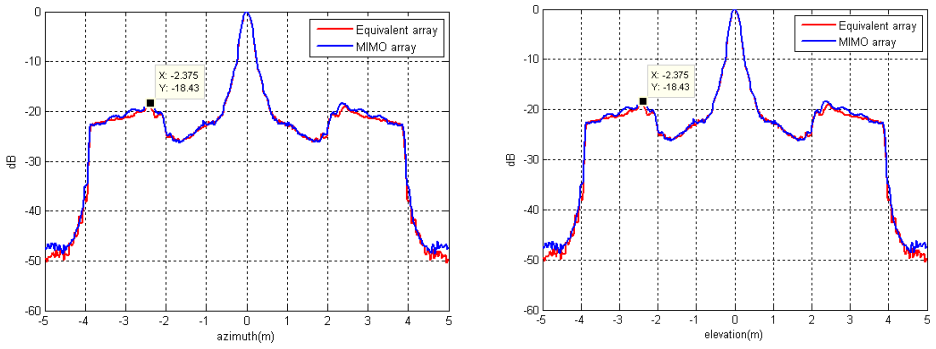

(a) (b)

Figure 3: The PSFs of the equivalent array and MIMO array in azimuth and elevation directions. (a) PSFs in azimuth direction. (b) PSFs in azimuth direction.

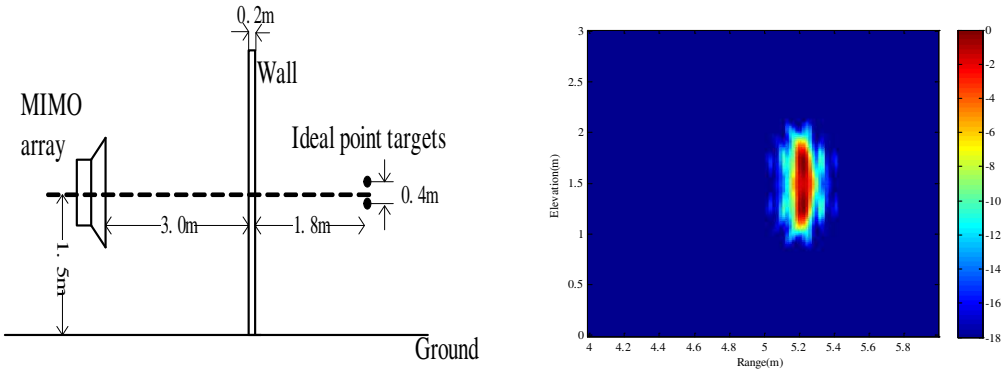

(a) (b)

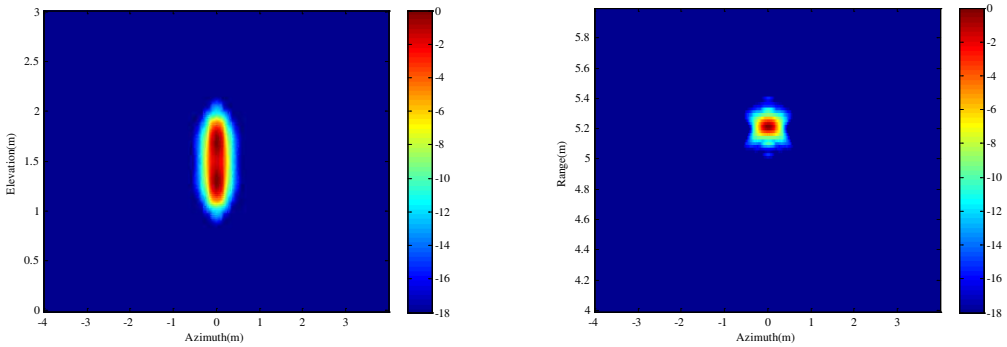

(c) (d)

Figure 4: The illumination geometry and the result imaging for 3-D TWI. (a) The illumination geometry. (b) The slice of range-elevation plane. (c) The slice of azimuth-elevation plane. (d) The slice of azimuth-range direction.

that the designed 2-D MIMO array behave a perfect performance in the 3-D TWI.

5. CONCLUSIONS

In this paper, the concept of equivalent array is introduced to analyze and design the 2-D MIMO array. The principle of the shortest physical size for the one-dimensional STVA array is extended to the 2-D MIMO array with the concept of comprehensive size and the method of sub-array segmentation is used to circumvent the de-convolution process between the equivalent array and the MIMO array. At last, an example is taken to design a 2-D UWB-MIMO array, and the simulation gives a perfect result.

ACKNOWLEDGMENT

This work was supported in part by the National Natural Science Foundation of China under Grant 61372161 and 61271441.

REFERENCES

1. Fishler, E., A. M. Haimovich, and R. S. Blum, "MIMO radar: An idea whose time has come," *IEEE Radar Conference*, 71–78, Philadelphia, PA, 2004.
2. Lu, B. Y., Y. Zhao, X. Sun, and Z. M. Zhou, "Design and analysis of ultra wide band split transmit virtual aperture array for trough the wall imaging," *International Journal of Antennas and Propagation*, Vol. 2013, 2013.
3. Wang, W. Q., "Virtual antenna array analysis for MIMO synthetic aperture radars," *International Journal of Antennas and Propagation*, Article ID 587276, 1–10, 2012.
4. Bradley, C., P. Collins, and D. Falconer, "Evaluation of a near-field monostatic-to-bistatic equivalence theorem," *IEEE Trans. Geosci. Remote Sens. E*, Vol. 46, No. 2, 449–457, Feb. 2008.
5. Lockwood, G. R. and F. S. Foster, "Optimizing the radiation pattern of sparse periodic two-dimensional arrays," *IEEE Trans. Ultrason., Ferroelectr. Freq. Control*, Vol. 43, 15–19, Jan. 1996.
6. Smith, S. W. and H. G. Pavy, "High-speed ultrasound volumetric imaging system-part I: Transducer design and beam steering," *IEEE Trans. Ultrason., Ferroelectr. Freq. Control*, Vol. 38, 100–108, Mar. 1991.
7. Zhuge, X. D. and A. G. Yarovoy, "Near field ultra-wideband imaging with two dimensional sparse MIMO array," *Proc. The Fourth European Conference on Antennas and Propagation (EuCAP)*, 1–4, Barcelona, Spain, April 1–4, 2010.
8. Steinberg, B. D. and H. M. Subbaram, *Microwave Imaging Technique*, Wiley, New York, 1991.

Analysis of the Low Intensity Terahertz Radiation Influence on Lymphocyte Early Activation Markers

M. V. Duka (Tsurkan)[1], **M. K. Serebriakova**[2, 4], **I. V. Kudryavtsev**[2, 3], **A. S. Trulioff**[2, 4], **and O. A. Smolyankaya**[1]

[1]ITMO University, Russia
[2]Institute of Experimental Medicine of the NorthWest Branch of the Russian Academy of Medical Sciences, Russia
[3]Far Eastern Federal University, Russia
[4]Saint-Petersburg State University, Russia

Abstract— According to the literary data, terahertz radiation has some effects on different blood cells. Our study focuses on the determining the level of some cell surface antigens of lymphocytes when exposed to broadband terahertz range of 0.05–1.70 THz. These data indicate that terahertz radiation with power density of 9.55, 0.63 and 0.03 mW/cm^2 for 1 minute does not alter the functional activity of lymphocytes.

1. INTRODUCTION

To date, literature sources contain a number of studies on the influence of terahertz (THz) radiation on the functional activity of human blood cells. At various times, the objects of the study were erythrocytes or platelets [1], leukocytes [2], as well as lymphocytes. In the case of the latter, the emphasis was on the role of THz radiation of varying power in regulation of advancing of cells in the cell cycle [3, 4], violation of integrity of the genetic material of cells and DNA stability [4, 5]. However, to evaluate the functional state of cells correctly, one can use a somewhat different approach, based on determining the level of surface antigens that characterize the functional state of cells, i.e., cell activation markers. Lymphocyte activation markers spectrum is very broad. They are traditionally divided into several groups depending on the time of appearance on lymphocyte surface after its activation. During the study, we have selected two antigens — CD38 and CD69, increasing the level of surface expression of which allows to assess the functional state of cells in culture conditions in vitro.

Molecule CD38 — is a transmembrane protein, which is an enzyme that regulates the cytoplasmic calcium concentration — the main mediator in signal transmission from the surface receptors to the cell nucleus. In addition, this enzyme has a number of other properties and can exhibit the activity of adenosine diphosphate-ribosyl cyclase, cyclic adenosine diphosphate ribosyl hydrolase, and NAD-glycohydrolase [6]. CD38 acts as a receptor modulating cell-to-cell cooperation, and can play a role in signal transmission from extracellular space into the cytoplasm of cells. This molecule is widely represented on activated blood cells, which include T-, B-, NK-cells and some other types of cells, and determining the level of expression of this molecule is of important prognostic value while managing the patients with different pathologies [7]. As for the second activation marker selected for our research, CD69 molecule refers to integral membrane proteins. It is believed that CD69 is involved in proliferation of leukocytes, because the level of its expression correlates with an increase in proliferative activity of cells, however, the expression level of this molecule is extremely low on the "resting" — not activated lymphocytes (typically, T- and B-cells) [8].

2. EXPERIMENTAL SETUP

The generation effect of THz radiation is that the laser beam of femtosecond interval creates free charge carriers on semiconductor surface, the motion of which in the magnetic field generates THz radiation. This principle is called a photoconductive antenna generation. In the present research we developed an optical design of the experiment as shown in Fig. 1. Detailed description of the scheme is given in [9].

The generated THz radiation had the frequency band of 0.05–1.7 THz with a maximum signal at 0.5 THz, and the THz pulse duration was 2.5 ps. The samples were irradiated for 1 min. The power of the THz radiation was varied by means of filters, and, allowing for absorption by the plate, was 30, 2 and 0.1 μW. The irradiation area was 3.14 cm^2. The power density was accordingly 9.55, 0.63, and 0.03 μW/cm^2. The experiments were carried out at the temperature of 20°C. Each

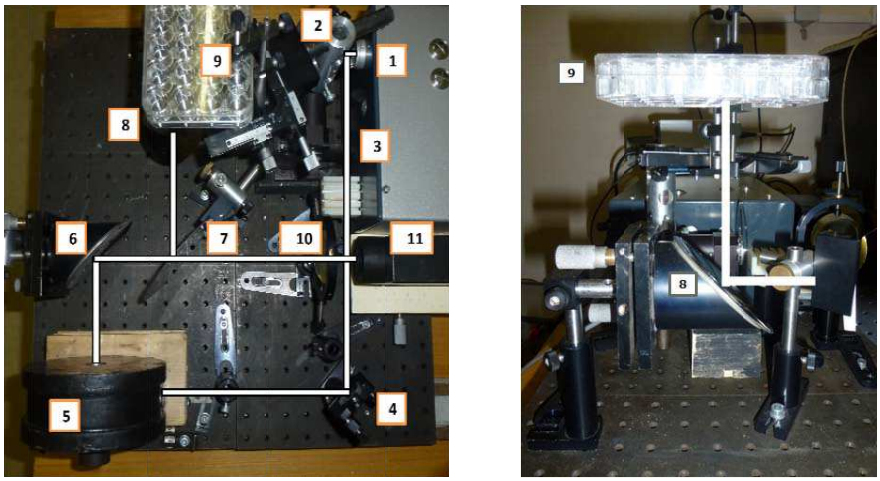

(a) (b)

Figure 1: Scheme of terahertz photometer: (a) top view; elements 8 and (b) 9 — a side view: 1 — femtosecond laser (Yb: KYW, 1040 nm, 120 fs, 75 MHz, 1 W); 2, 4 — mirrors; 3 — mechanical modulator; 5 — InAs crystal placed inside a magnet (angle of incidence was 45°); 6, 8 — the parabolic mirror; 7 — beam splitter plate; 9 — an object placed in the wells; 10 — lens; 11 — opto-acoustic detector.

power irradiated by one sample from each donor (18 donors). 18 control wells were not subjected to irradiation.

3. MATERIALS AND METHODS

Venous blood sampling from clinically healthy donors was carried out with heparinized (10 IU/ml) test tubes. The blood was mixed with sterile phosphate-buffered saline (PBS) in the ratio of 1 : 2, and lamination by the density gradient of 1.077 g/mL of Histopaque-1077 (Sigma-Aldrich, USA), and then subject to centrifugation for 30 min at 400 g and at 18–22°C. Upon the completion of centrifugation, the mononuclear cell layer was collected, formed at the phase interface. The resulting cell suspension was washed twice with the complete culture medium (CCM), prepared based on RPMI-1640 ("Biolot", St. Petersburg) with addition of 10% heat-inactivated fetal bovine serum (FBS, "Biolot", St. Petersburg), 50 g/ml gentamicin ("Biolot", St. Petersburg) and 2 mM L-glutamine ("Biolot", St. Petersburg), for 7 minutes while accelerating at 300 g. Then the number of the obtained cells was determined using a hemocytometer. For experimental set up, the wells of 24-well plates ("Sarstedt", Germany) were filled with 200 µl of cell suspension (5×10^6 cells/ml) poured to CCM. After radiation treatment, lymphocytes cultures were added with 250 µl of CCM and incubated at 37°C under 5% CO_2 for 24 hours. Upon completion of incubation, the cells were mixed with cooled PBS containing 2% of FBS, transferred into centrifuge tubes, and washed twice with PBS (300 g for 8 min). The resulting cell suspension was used for performing the experiments described below.

Upon completion of incubation, the lymphocyte suspension was washed twice with PBS at the above described conditions, and then mixed with 100 µl of fresh PBS. To identify the major cell populations the following antibodies were used: to identify the population of T-lymphocytes — CD3-PC7 (Cat. No. 737657), to identify B-lymphocytes — CD19-ECD (A07770), to identify a population of natural killer cells — CD56-PC5.5 (A79388). Antibodies against CD69 (IM1934U) and CD38 (A07778), PE labeled (phycoerythrin) and FITC (fluorescein isothiocyanate-dextran), respectively, were used as activation markers. To correctly identify the lymphocyte population the pan-leucocyte APC labeled (alofikotsianin) marker CD45 (IM2473) was used. Staining with antibodies against surface antigens was carried out in accordance with the manufacturer's recommendations; to assess the level of expression of activation markers the isotype controls were used. At least 20000 lymphocytes were analyzed for each sample by flow cytometer Navios ("Beckman Coulter", USA). Analysis of the results was performed using Kaluza software ("Beckman Coulter", USA).

4. RESULTS AND DISCUSSION

Results were expressed as percentage of cells bearing either one of activation markers (CD38+CD69− and CD38−CD69+), both markers simultaneously (CD38+CD69+), or bearing no of them (CD38−CD69−). These markers were examined for populations of T-lymphocytes (responsible for implementation of cell responses of the acquired immunity), B-lymphocytes (the main function of which is to participate in humoral responses of the acquired immunity), as well as natural killer (NK) cells, and NKT-cells — peripheral blood lymphocyte populations involved in antiviral and antitumor body responses. Processing of the results was performed using PASW Statistics 18 software package (IBM, USA). The results are summarized in the Table 1.

Table 1: The percentage distribution of the cells by the presence of these activation markers ($X \pm s$, $n = 18$, X — average, s — error, n — number of observations for one point).

Power density, $\mu W/cm^2$	T-lymphocytes, %				B-lymphocytes, %			
	CD69+ CD38−	CD69+ CD38+	CD69− CD38+	CD69− CD38−	CD69+ CD38−	CD69+ CD38+	CD69− CD38+	CD69− CD38−
control	5.0 ± 0.8	8.8 ± 1.4	52.2 ± 2.9	34.0 ± 2.6	9.6 ± 1.0	27.7 ± 1.8	49.5 ± 2.0	13.1 ± 2.2
0.03	5.0 ± 0.7	9.1 ± 1.9	52.9 ± 2.9	33.0 ± 2.5	9.5 ± 1.2	29.0 ± 2.0	49.2 ± 2.2	12.2 ± 1.8
0.63	5.2 ± 0.7	9.3 ± 1.6	52.1 ± 2.8	33.5 ± 2.6	9.8 ± 1.2	29.9 ± 1.7	48.6 ± 2.0	11.7 ± 1.7
9.55	5.1 ± 0.5	9.1 ± 1.5	52.2 ± 2.6	33.6 ± 2.7	9.4 ± 1.0	29.0 ± 1.7	49.6 ± 1.8	12.1 ± 1.7
Power density, $\mu W/cm^2$	NK, %				NKT, %			
	CD69+ CD38−	CD69+ CD38+	CD69− CD38+	CD69− CD38−	CD69+ CD38−	CD69+ CD38+	CD69− CD38+	CD69− CD38−
control	1.5 ± 0.3	72.7 ± 5.0	23.5 ± 4.8	2.3 ± 0.5	18.2 ± 2.6	15.6 ± 0.7	32.5 ± 3.9	33.7 ± 3.2
0.03	1.8 ± 0.4	72.0 ± 4.7	23.8 ± 4.5	2.4 ± 0.6	18.7 ± 2.9	16.6 ± 1.5	32.2 ± 3.9	32.5 ± 3.5
0.63	1.7 ± 0.3	72.4 ± 4.7	23.8 ± 4.5	2.1 ± 0.5	18.7 ± 2.6	16.7 ± 1.3	32.8 ± 3.9	31.8 ± 3.3
9.55	1.8 ± 0.3	72.2 ± 4.6	23.8 ± 4.3	2.2 ± 0.5	19.6 ± 2.7	16.7 ± 1.5	32.2 ± 3.5	31.4 ± 2.9

In the course of this study, no increase in the level of surface expression of CD38 on any of the cell types studied, which include T-, B-, NK- and NKT-cells, was noted. However, literature study indicates that the significant increase in CD38 level is reported in culture conditions of lymphocytes in vitro in response to the introduction of standard immunological stimulants such as phorbol myristyl acetate, as well as IL-4 and anti-CD3 or M surface immunoglobulins, respectively [10]. When using terahertz radiation with the power density of 9.55, 0.63 and 0.03 mcW/cm^2 no activation of any of the above cell populations was the case. Similar results were obtained when assessing the level of expression of CD69 of major lymphocyte populations, changes in the expression level of which may be associated with proliferative activity of lymphocytes. As mentioned above, this molecule is nearly absent on inactivated cells (T- and B-lymphocytes in particular). However, during the transfer of lymphocytes to the activated state on RNA level — using polymerase chain reaction — a significant increase in CD69 gene expression is observed 3–4 hours after the activation of cells in vitro [11]. This is precisely why the CD69 marker is traditionally treated as "early" lymphocyte activation marker. As for the populations of cytotoxic cells (NK- and NKT-cells), the expression level of CD69 on them is continuously higher. Whereas additional stimulation of cells is accompanied by an additional increase in the level of both CD69, and CD38 [7, 12]. It's worth mentioning that the latter antigen — CD38− in case of B-lymphocytes and natural killer cells — is treated by most researchers as a "differentiation" or maturation marker characterized by the "maturity degree" of cells, rather than their activation status.

Literature analysis showed that there is no effect on the kinetics of the cell cycle, micronucleus formation, proliferation index and the induction of micronuclei cells with cytogenesis block when irradiating human peripheral blood lymphocytes with free-electron laser at 0.12 and 0.13 THz for 20 min, and average power of 1 mW and 0.6 mW, respectively [3].

In work [4] it was shown that using the radiation of 0.13 THz (20 min) in the power range of 0.15–5.00 mW/cm^2, other researchers have also confirmed no effect on cell cycle kinetics of lymphocytes. They also noted that the THz radiation causes no chromosome damage (MN-analysis).

Impact of THz radiation (0.1 THz, 31 mW/cm^2) lasting for 60, 120 and 1440 min causes genome instability in lymphocytes [5]. However, according to G. J. Wilmink, these results should be treated

with caution [13].

All the above studies used continuous radiation sources. Also, power density of THz radiation and duration of irradiation of the above works is significantly higher than those used in our experiment (9.55, 0.63 and 0.03 mW/cm^2, for 1 minute). Only work [5] is comparable to ours in regard to power density (31 mW/cm^2). However, a large number of publications concerning the effects of weak fields show that a low-intensity radiation can cause biological effects, which are not observed during the radiation of a greater power. So the main possible mechanisms regarding the millimeter and submillimeter wave (terahertz) range are presented in [14]. We should also note that our earlier experiments on nerve cells [15] showed that the reduction of broadband terahertz radiation power density leads to stimulation of cell growth. Based on the above, we have chosen the power density data.

Due to the fact that the main practical interest of the use of THz radiation in medicine today is aimed to develop diagnostic terahertz instruments, to diagnose using these instruments it makes sense, to our opinion, to define the duration of exposure based on the duration of the study procedure. Since the scanning takes a few minutes, then the exposure duration at this stage was chosen as 1 min.

In our study, terahertz radiation with the power density of 9.55; 0.63 and 0.03 mW/cm^2 for 1 minute did not alter the functional activity of lymphocytes. It is possible that an increase in exposure duration may affect the activation of cells. Variation of irradiation parameters will be the next stage of our research.

5. CONCLUSION

Analysis of the level of expression of cell activation markers (CD38 and CD69) lymphocytes (T-lymphocytes, B-lymphocytes, natural killer cells and NKT-cells) showed that the terahertz pulse irradiation with the frequency range of 0.05–1.7 THz and power density of 9.55; 0.63; 0.03 mW/cm^2 for 1 minute does not result in the reliable increase in number of lymphocytes containing these markers.

ACKNOWLEDGMENT

This work was financially supported by Government of Russian Federation, Grant 074-U01.

REFERENCES

1. Kirichuk, V. F., E. V. Andronov, O. N. Antipov, A. N. Ivanov, A. P. Krenitsky, J. A. Krylov, S. V. Suhova, and A. Tsymbal, "Influence of electromagnetic terahertz waves on living systems," *Bulletin of Medical Internet Conferences*, Vol. 2, No. 6, 421–425, 2012 (in Russian).
2. Zeni, O., G. P. Gallerano, A. Perrotta, M. Romanò, A. Sannino, M. Sarti, M. D'Arienzo, A. Doria, E. Giovenale, A. Lai, G. Messina, and M. R. Scarfì, "Cytogenetic observations in human peripheral blood leukocytes following in vitro exposure to THz radiation: A pilot study," *Health Phys.*, Vol. 92, No. 4, 349–357, 2007.
3. Scarfi, M. R., M. Romano, R. Di Pietro, O. Zeni, A. Doria, G. P. Gallerano, E. Giovenale, G. Messina, A. Lai, G. Campurra, D. Coniglio, and M. D'Arienzo, "THz exposure of whole blood for the study of biological effects on human lymphocytes," *Journal of Biological Physics*, Vol. 29, 171–177, 2003.
4. Doria, A., G. P. Gallerano, E. Giovenale, G. Messina, A. Lai, A. Ramundo-Orlando, V. Sposato, M. D'Arienzo, A. Perrotta, M. Romano, M. Sarti, M. R. Scarfi, I. Spassovsky, and O. Zeni, "THz radiation studies on biological systems at the ENEA FEL facility," *Infrared Physics & Technology*, Vol. 45, 339–347, 2004.
5. Korenstein-Ilan, A., A. Barbul, P. Hasin, A. Eliran, A. Gover, and R. Korenstein, "Terahertz radiation increases genomic instability in human lymphocytes," *Radiation Research*, Vol. 170, No. 2, 224–234, 2008.
6. Dos Santos, D. C., P. C. Neves, E. L. Azeredo, M. Pelajo-Machado, J. M. Martinho, L. F. Pacheco-Moreira, C. C. Araujo, O. G. Cruz, J. M. de Oliveira, and M. A. Pinto, "Activated lymphocytes and high liver expression of IFN-γ are associated with fulminant hepatic failure in patients," *Liver Int.*, Vol. 32, No. 1, 147–157, 2012.
7. Slyker, J. A., B. Lohman-Payne, G. C. John-Stewart, T. Dong, D. Mbori-Ngacha, K. Tapia, A. Atzberger, S. Taylor, S. L. Rowland-Jones, and C. A. Blish, "The impact of HIV-1 infection and exposure on natural killer (NK) cell phenotype in Kenyan infants during the first year of life," *Front Immunol.*, Vol. 3, 399–406, 2012.

8. Caruso, A., S. Licenziati, M. Corulli, A. D. Canaris, M. A. De Francesco, S. Fiorentini, L. Peroni, F. Fallacara, F. Dima, A. Balsari, and A. Turano, "Flow cytometric analysis of activation markers on stimulated T cells and their correlation with cell proliferation," *Cytometry*, Vol. 27. No. 1, 71–76, 1997.
9. Duka (Tsurkan), M. V., Y. S. Nesgovorova, O. A. Smolyanskaya, V. G. Bespalov, I. V. Kudryavtsev, A. V. Polevshchikov, M. K. Serebryakova, I. V. Nazarova, and A. S. Trulev, "Study of the action of broad-band terahertz radiation on the functional activity of cells," *Journal of Optical Technology*, Vol. 80, No. 11, 655–660, 2013.
10. Deterre, P., V. Berthelier, B. Bauvois, A. Dalloul, F. Schuber, and F. Lund, "CD38 in T- and B-cell functions," *Chem. Immunol.*, Vol. 75, 146–168, 2000.
11. Reddy, M., E. Eirikis, C. Davis, H. M. Davis, and U. Prabhakar, "Comparative analysis of lymphocyte activation marker expression and cytokine secretion profile in stimulated human peripheral blood mononuclear cell cultures: An in vitro model to monitor cellular immune function," *J. Immunol. Meth.*, Vol. 293, Nos. 1–2, 127–142, 2004.
12. Montoya, C. J., J. C. Catano, Z. Ramirez, M. T. Rugeles, S. B. Wilson, and A. L. Landay, "Invariant NKT cells from HIV-1 or mycobacterium tuberculosis-infected patients express an activated phenotype," *Clin. Immunol.*, Vol. 127, 1–6, 2008.
13. Wilmink, G. J. and J. E. Grundt, "Invited review article: Current state of research on biological effects of terahertz radiation," *J. Infrared Milli. Terahz. Waves*, Vol. 32, 1074–1122, 2011.
14. Betsky, O. V., N. D. Deviatkov, and V. V. Kislov, "Lowintensity MM-waves in biology and medicine," *Biomedical Radioelectronics*, Vol. 10, 13–29, 1998.
15. Tsurkan, M. V. and O. A. Smolyanskaya, "Impact of terahertz radiation on cells," *Microwave Conference Proceedings (APMC)*, 630–632, 2013.

Influence of Terahertz Radiation with a Frequency 0.05 ÷ 1.7 THz on Mitochondrial Membrane Potential of Tumor Cells

M. V. Duka (Tsurkan)[1], **M. K. Serebriakova**[2, 4], **I. V. Kudryavtsev**[2, 3], **A. S. Trulioff**[2, 4], **A. S. Nazarova**[4], **and O. A. Smolyankaya**[1]

[1]ITMO University, Russia
[2]Institute of Experimental Medicine of the North-West Branch of the Russian Academy of Medical Sciences, Russia
[3]Far Eastern Federal University, Russia
[4]Saint-Petersburg State University, Russia

Abstract— In order to ensure safety in the use of terahertz radiation for medical problems, impact assessment of broadband terahertz radiation in the frequency range of 0.05–1.7 THz was made to investigate functional activity of tumor cells in vitro. According to the results of flow cytometry we can speculate that pulsed terahertz radiation with a power density of up to near 10 mW/cm^2 and duration of 1 minute does not change functional activity of tumor cells.

1. INTRODUCTION

In recent years, application of sources of terahertz (THz) radiation is rapidly growing. It is estimated that it can be used in medical diagnosis of skin diseases and skin cancer [1, 2]. However, the divergent data on the effects of THz radiation are questioning the safety of its use. To assess the effects of THz radiation at the cellular level, the mitochondrial membrane potential and the permeability of the cell membrane of certain cells of transplanted crops were investigated after exposure by flow cytometry.

Let us consider the works devoted to the change in membrane potential of cell and membrane permeability when exposed to THz radiation. Thus, radiation at of 2.5 THz results in damage of membrane morphology and intracellular structures, and the fall in the membrane potential of neurons [3], and radiation at a frequency of about 2.31 THz can cause reversible damage of the barrier properties of neuron' membrane [4]. However, other researchers have proved, that using the same object under the radiation of 0.60 and 0.75 THz, all the changes are solely due to the temperature increase [5].

Effect of increasing the permeability of the cell membrane was obtained when exposed to THz radiation with the frequency of 2.52 THz and the power density of 227 mW/cm^2 for over 12 seconds and the decrease was observed when decreasing the duration of exposure [6].

Lipid bilayer demonstrated an increase in membrane permeability when using a pulsed source (0.13 THz, 7 Hz, 7.7 mW/cm^2 for 2 minutes) and lack of any effects from continuous radiation source [7].

Investigators observed both blocking and increased neuronal activity upon the exposure to radiation of 0.06 THz for 1 min under low power density (0.07, 0.28, 0.56 and 0.74 m/cm^2) [11]. These authors have also demonstrated that radiation frequency of about 0.05 THz (15 mW/cm^2, 2 min) induces the opening of ion channels during the exposure, and their sealing 3 minutes after the exposure [8].

Thus, these studies indicate that the terahertz radiation increases the permeability of the membrane and results in changes in membrane potential. However, most of these data were obtained using continuous radiation sources, and the issue concerning the impact of broadband pulse THz radiation remains open. And the relevance of our ongoing work is this is due to this fact.

2. EXPERIMENTAL SETUP

Experimental setup. In the layout of the apparatus, the radiation of femtosecond laser with an Yb : KYW active medium (wavelength 1040 nm, pulse width 120 fs, pulse-repetition rate 75 MHz, mean power 1 W) was modulated by a mechanical modulator and was then fed to an InAs crystal located in a special system with magnetic induction $B = 2.2$ T. THz radiation generated in the InAs crystal was collimated by an off-axis parabolic mirror to a beam splitter plate. The femtosecond radiation reflected from the crystal was absorbed in a fluoroplastic filter. Next, the part of the

radiation transmitted through the beam splitter plate was focused by a lens onto a GC-1P optoacoustic detector, another part of the radiation was directed by parabolic mirror toward the object. The loss of THz radiation on the plate in which the cells are held was 20%. The generated THz radiation had a frequency band of 0.05–1.70 THz with a maximum signal at 0.50 THz, and the THz pulse was 2.5 ps wide, exposure time was 1 min. The irradiation area was 3.14 cm^2. The power density was 9.55, 0.63 and 0.03 $\mu W/cm^2$. Three series of experiments were carried out for each cell culture. The irradiation was done three times in each series at each power. As a control, wells in the plate that were not subjected to the action of the irradiation were used for each of the powers.

Objects. Cell cultures of the following lines were chosen as objects of study: adherent cultures A-549 (carcinoma cells of human lung), BT-20 (adenocarcinoma cells of the mammary gland); suspension cultures U937 (a cell line of leukosis of human histocytes), HL-60 (cells of human promyeloid leukemia).

Evaluation of mitochondrial membrane potential and cellular membrane permeability with flow cytometry. Assay principle. This method is based on using two fluorescent dyes-3,3'-dihexyl carbocyanine iodide ($DiOC_6(3)$) and propidium iodide (PI). $DiOC_6(3)$ belongs to the group of cationic lipophilic dyes, which have been named in literature as "mitochondrial probes", as they are used to study the mitochondrial membrane potential of cells [9]. Due to its lipophilic properties $DiOC_6(3)$ is able to freely penetrate through the lipid bilayer cell membranes (surface membrane of a cell, as well as the inner and outer mitochondrial membrane) and, thanks to the cationic properties, this dye accumulates in the areas with a high concentration of protons, i.e., under the inner membrane of mitochondria. This effect is accompanied by changes in fluorescence intensity of cells in the green subspectrum, and that is recorded during the flow cytometer analysis [10]. If the concentration of protons is reduced, as is the case during the initial stages of the physiological cell death-apoptosis, then the dye will accumulate inside them less effectively, and, as a result, the intensity of its fluorescence will be reduced. Hence, it is possible to distinguish the living cells with effectively functioning mitochondria (and, consequently, of high fluorescence intensity) from dead or dying cells with damaged mitochondrial function. As a result, these cells possess reduced fluorescence intensity. If mitochondrial depolarization is treated as an "early" event when at apoptosis start, the integrity damage of the membrane surface (i.e., its fragmentation) is usually typical for the cells at the terminal stages of their death. In this regard, to identify the different stages of apoptosis, aside from $DiOC_6(3)$, the cells are further stained with PI-dye capable of interacting with nucleic acids of cells. PI can't diffuse through bilayer lipid membranes and, consequently, can't bind with cellular DNA. However, as far as the fragmentation of cytoplasmic and nuclear membranes takes place, the dye enters the cell and interacts with RNA and DNA. This interaction results in accumulation of the dye in cytoplasm and nucleus, and the cell acquires fluorescence in the red subspectrum.

Thus, the living cells will have a bright fluorescence in the channel intended for detecting $DiOC_6(3)$, but won't accumulate propidium iodide (phenotype $DiOC_6(3)^{bright}PI^-$). Cells in the early stages of apoptosis (reduced mitochondrial potential, but plasma membrane still keeps its integrity and impermeability to propidium iodide) will be of phenotype $DiOC_6(3)^{dim\text{-}to\text{-}neg}PI^-$). However, the cells in the late stage of apoptosis or the ones that have already died (necrosis), will not efficiently accumulate $DiOC_6(3)$, but will be stained with P-$DiOC_6$ phenotype $(3)^{dim\text{-}to\text{-}neg}PI^+$.

Staining procedure. To assess the mitochondrial membrane potential the 100 µl of cell suspension ($2–3 \times 10^6$ cells/ml) was added with 20-fold working solution $DiOC_6(3)$ ("Invitrogen", USA) to yield a final dye concentration of 20 nM [11]. The working solution was prepared extempete, adding 10 µl of stock solution (stock −1 mg/ml of dimethylsulfoxide (DMSO), pipetted by 10 µl and stored before use at −20°C), 4900 µl of PBS After adding the dye, the samples were thoroughly mixed and incubated at 37°C under 5% CO_2 atmosphere in a dark place for 20 min. Upon completing the incubation, the samples were washed with PBS containing 2% FBS (8 min at 300 g). Then, the supernatant was removed and the cell pellet was transferred to 100 µl of fresh PBS. The resulting cell suspension was added with 10 µl of propidium iodide solution ("Sigma-Aldrich", USA) to get a final concentration of PI of 1 ug/ml. Further, the samples were incubated for 10 min at room temperature, protected from light. Upon completion of incubation, the samples were added with 200 µl of PBS, and the cytometric measurement was performed. At least 50,000 single cells were analyzed for each sample. To distinguish single cells from sticking together (aggregates), and subsequently discriminate aggregates from the assay, the following combinations of signals on forward (a value proportional to the cell size) and side (a value characterizing the cell structure) scattering-peak intensity against the intensity of the integral signals of FS or SS, as well as the flight time against

the intensity of the integral signals of FS or SS. Analysis of results was performed using Kaluza software ("Beckman Coulter", USA).

3. RESULTS

To analyze the results of flow cytometry the histograms of fluorescence intensity of $DIOC_6(3)$ have been plotted, the increase in fluorescence intensity of which depends on mitochondrial membrane potential. Fig. 1 demonstrates one typical example of such histogram for each cell culture used

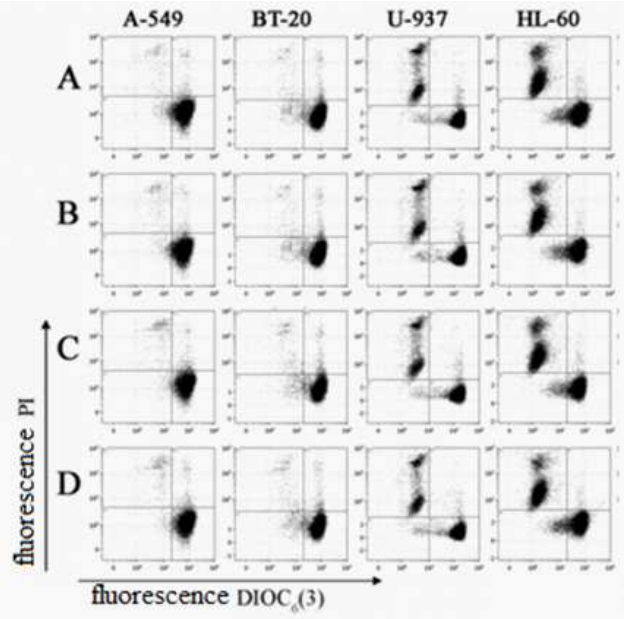

Figure 1: Examination of mitochondrial membrane potential using fluorescent dye $DIOC_6(3)$. X-direction: $DIOC_6$ fluorescence intensity (3); Y-direction: propidium iodide fluorescence intensity. Left to right — different cell lines. Downwards are the examples of histograms of cell distribution in control wells and in radiation-exposed wells with the power of 0.1; 2 and 30 mW (series of histograms A, B, C and D, respectively).

Table 1: The evaluation results the mitochondrial membrane potential and the permeability of the cell membrane using flow cytometry ($X \pm s$, $n \geq 4$ for each culture).

Cell culture	Radiation power, mW	Living cells, %	Early stage of apoptosis, %	Late stage of apoptosis/necrosis, %
A-549	Control	95.9 ± 0.5	1.2 ± 0.7	2.8 ± 0.3
	0.1	96.2 ± 0.3	1.2 ± 0.4	2.6 ± 0.3
	2	96.3 ± 0.4	0.7 ± 0.2	3.0 ± 0.3
	30	96.4 ± 0.4	0.7 ± 0.2	2.9 ± 0.2
BT-20	Control	93.3 ± 0.2	2.6 ± 0.5	4.1 ± 0.4
	0.1	93.1 ± 0.2	2.5 ± 0.4	4.4 ± 0.6
	2	93.3 ± 0.3	2.4 ± 0.5	4.3 ± 0.3
	30	93.2 ± 0.3	2.7 ± 0.5	4.1 ± 0.2
HL-60	Control	65.2 ± 7.7	4.1 ± 1.2	30.7 ± 8.4
	0.1	66.4 ± 7.7	4.3 ± 1.4	29.3 ± 8.7
	2	66.6 ± 8.5	3.9 ± 1.3	29.6 ± 9.5
	30	67.7 ± 7.3	4.0 ± 1.2	28.4 ± 8.1
U-937	Control	56.3 ± 8.6	2.4 ± 0.3	41.3 ± 6.5
	0.1	55.9 ± 6.4	2.5 ± 0.3	41.6 ± 6.5
	2	56.4 ± 6.7	2.8 ± 0.3	40.8 ± 6.5
	30	58.1 ± 6.5	2.3 ± 0.3	39.7 ± 6.6

during the experiment.

The obtained histogram data have been processed and presented in Table 1 showing the percentage of living cells and cells that are at the early and late stages of apoptosis.

4. CONCLUSION

Thus, on various tumor cell cultures such as adherent cultures (carcinoma cells of the human lung, adenocarcinoma cells of the mammary gland) and suspension cultures (a cell line of leukosis of human histocytes, and cells of human promyeloid leukemia) using flow cytometry it is shown that the action of pulsed broadband terahertz radiation in the frequency range of 0.1–1.7 THz with the power of 30, 2, and 0.1 μW has no significant effect on the change in the functional activity of cells mitochondria, as well as does not damage the integrity of their lipid bilayer surface membranes.

However, the lack of effect may be due to the fact that the cells are in an aqueous medium, which is absorbed greatly in terahertz spectral range. Despite the fact that this assumption does not explain the absence of any effect on adhesive culture monolayer cells such as A-549 and BT-20 which are tightly adjacent to the substrate surface. Based on this fact, additional researches with cell cultures are needed, involving various duration and power of irradiation.

ACKNOWLEDGMENT

This work was financially supported by Government of Russian Federation, Grant 074-U01.

REFERENCES

1. Panwar, A. K., et al., "Terahertz imaging system for biomedical applications: Current status," *Int. J. Eng. Technol.*, Vol. 13, No. 2, 33–39, 2013.
2. Yin, X., B. W.-H. Ng, and D. Abbott, "Terahertz imaging for biomedical applications," *Pattern Recognition and Tomographic Reconstruction*, 316, 2012.
3. Olshevskaya, J. S., A. S. Ratushnyak, A. K. Petrov, A. S. Kozlov, and T. A. Zapara, "Effect of terahertz electromagnetic waves on neurons systems," *IEEE Region 8 International Conference on Computational Technologies in Electrical and Electronics Engineering, SIBIRCON 2008*, 210–211, 2008.
4. Olshevskaya, J. S., A. S. Kozlov, A. K. Petrov, T. A. Zapara, and A. S. Ratushnyak, "Cell membrane permeability under the influence of terahertz (submillimeter) laser radiation," *International Symposium — Terahertz Radiation: Generation and Applications*, Vol. 5, No. 4, 177–181, Vestnik Novosibirsk State University, 2010.
5. Alekseev, S. I. and M. C. Ziskin, "Effects of millimeter waves on ionic currents of Lymnaea neurons," *Bioelectromagnetics*, Vol. 20, No. 1, 24–33, 1999.
6. Wilmink, G. J., B. D. Rivest, B. L. Ibey, C. L. Roth, J. Bernhard, and W. P. Roach, "Quantitative investigation of the bioeffects associated with terahertz radiation," *Proc. SPIE*, Vol. 7562, 75620L-1–75620L-10, 2010.
7. Ramundo Orlando, A. and G. P. Gallerano, "Terahertz radiation effects and biological applications," *J. Infrared Millimeter and Terahertz Waves*, Vol. 30, 1308–1318, 2009.
8. Siegel, P. H. and V. Pikov, "Can neurons sense millimeter waves?," *SPIE Photonics West*, 7562-17, BiOS, 2010.
9. Siegel, P. H. and V. Pikov, "Impact of low intensity millimeter-waves on cell membrane permeability," *34th International Conference on Infrared, Millimeter, and Terahertz Waves, IRMMW-THz 2009*, Vol. 1, No. 1, 21–25, 2009.
10. Cottet-Rousselle, C., X. Ronot, X. Leverve, and J. F. Mayol, "Cytometric assessment of mitochondria using fluorescent probes," *Cytometry A*, Vol. 79, No. 6, 405–425, 2011.
11. Wlodkowic, D., W. Telford, J. Skommer, and Z. Darzynkiewicz, "Apoptosis and beyond: Cytometry in studies of programmed cell death," *Methods Cell Biol.*, Vol. 103, 55–98, 2011.
12. Castedo, M., K. Ferri, T. Roumier, D. Metivier, N. Zamzami, and G. Kroemer, "Quantitation of mitochondrial alterations associated with apoptosis," *J. Immunol. Methods*, Vol. 265, Nos. 1–2, 39–47, 2002.

The Baroque Music's Influence on Learning Efficiency Based on the Research of Brain Cognition

Rong Gu, **Jie Zhang**, **Junhe Zhou**, **and M. S. Tong**
Department of Electronic Science and Technology
Tongji University, 4800 Cao'an Road, Shanghai 201804, China

Abstract— To let the brain be in the best condition for learning is the task faced to teachers for improving the students' abilities of memory, attention, thinking and so on, which is also a work of great significance for improving the teaching quality. This article discusses the influence of the Baroque music on learning state from the perspective of electroencephalogram analysis. First electroencephalogram (EEG) data of the n-back experiments are collected before and after listening to the Baroque music. Then its frequency, the energy, α wave distribution, scalp, event related potential and other components are compared. Specially, the brain's memory and attention are analyzed and estimated by extracting useful EEG information in time-domain, frequency-domain and spatial distribution. The experimental results show that Baroque music has a positive influence on improving learning efficiency. So that teachers can use Baroque music to assist teaching as reform means, which will provide an effective way to improve the learning efficiency and teaching quality.

1. INTRODUCTION

Brain is the organ of learning. Human intelligence activities are closely related to the states of human brain. Only by following the brain activity patterns, the learning efficiency could be promoted and the brain function could be further developed. In recent years, by the technologies such as EEG and fMRI, the brain's memory, thinking, learning, emotional and other advanced features are in-depth studied, which confirms that the brain science is bound up with education and has important guiding value to educational practice. The research on brain science is widely used in the field of education, as the important basis of reforming the traditional teaching methods. Therefore, the rational use of the human brain cognitive rules can help improve students' learning efficiency. For the past few years, the research on close integration of brain science and education has been carried out and become a hot spot. The scientists of many countries are researching it.

In this paper, by using high-resolution 64-channel EEG technology, the EEG data extracted before and after the n-back experiments are analyzed to explore the impact of the Baroque music on learning efficiency.

2. EFFECT OF SOUND WAVES ON THE BRAIN

Music is also an acoustic wave, any sonic vibrations stimulate the auditory systemby the process of converting from mechanical energy of sound source vibrations to neural signals, chemical signals, electrical signals. These signals, interact with each other to form auditory perception, along the neural pathway: the brainstem, the hypothalamus and the brain cortex. For example, musical instruments produce sound. This mechanical energy can cause vibrations in the cochlea, then the hair cells arranged on the base film are stimulated to produce receptor potential, projecting to the neurons nucleus through the auditory nerve fibers. However, we just hear the sound, not knowing what kind of instrument sounds. It needs for various types of cells in the nucleus to make judgments by sound frequency, intensity, and other features. Because there is a gap between the cells, there is no direct electrical coupling, nerve signals can not pass. Fortunately, there is a specific communication joint between neurons, called synapses. Presynaptic neurons by releasing a neurotransmitter convert chemical signals to electrical signals, and then the neurotransmitter carrying music information act on the postsynaptic membrane, then the chemical signals into electrical signals. The music propagation in the auditory system is realized.

There are dozens of brain neurotransmitters, each of which has a special physiological function. By changing the function of neurons, bringing the biological functional effects can produce an effect on mental activity, emotional reactions, learning and memory, and so on. The vibration in different parts of the base film is caused by acoustic wave of different frequencies. Bioelectrical activity of auditory nerve fibers, on behalf of acoustic wave of different frequencies, likes tides ups and downs, forms brain waves. Low frequency components of the brain waves are related to the activities

of neurotransmitters. Various neurotransmitters have their unique ultra-slow-wave frequencies. The amplitude variation of brain waves corresponds with the strength of the neurotransmitter. That is, the frequency stimulation of the acoustic wave changes the original EEG rhythm. So music stimulation is changing the brain wave rhythm, while also changing the brain physiological functions.

Baroque music in line with 50 to 70 beats/minute is ideal for rapid enhancing learning efficiency. "Baroque" came from the Portuguese barroco, meaning less rounded pearls. Baroque music is the music generated within the period of 1600–1750. Its effect on learning efficiency is mainly reflected in the impact on the brain α-wave. For a more precise understanding of the effect of Baroque music on learning efficiency, we designed the n-back experiment to test memory. The subjects' EEG data are obtained before and after the music during the experiments. Then the effects of Baroque music on wave frequency, amplitude, and energy distribution are detailed analyzed. Thereby the stimulation of Baroque music on memory and attention during the learning process is clarified.

3. ANALYSIS OF EEG-BASED LEARNING EFFICIENCY

How to determine whether the student's learning state is optimum or not? There are many ways in which EEG is an effective method of analysis. EEG is the most commonly used and most objective physical signs of studying of the human brain. When the person's attention, memory, etc. change, EEG signal recorded will change accordingly. Thus, the degree of students' memory or attention can be estimated by recording and analyzing their EEG signals. This is an effective method to determine whether the brain is in the best learning state or not. The human brain is a very complex nonlinear dynamic systems. EEG is the weak potential difference measured from the scalp, when a considerable number of neurons in the brain neural network are discharging synchronously. Now many laboratory instruments can be used to detect the potential difference, then electroencephalogram can be obtained. In this article, the brain's memory and attention are analyzed and estimated by extracting useful EEG information from the time domain, frequency domain and the spatial distribution.

Time domain information is usually composed of a number of event-related potentials (ERP) composition. ERP is referred to the bio-electric response detected in the corresponding parts of the brain, which is generated with a relatively fixed time interval and the specific phase from the stimulation, when a particular part of the nervous system is given corresponding stimulation. ERP reflects activities of neurons in brain. In all ERP components, P300 is the most classic, first discovered and most extensively studied one. P300 is the positive peak of brain waves around 300 ms after stimulation, which is induced by the endogenous event. The waveform is most obvious near the midline of the parietal lobe, mainly reflecting the brain's cognitive processes to external information. The frequency domain information is the use of power spectrum analysis, obtained the frequency variation of brain waves associated with brain activities. When a person's state of consciousness varies, the frequency of the brainwave is different. According to the frequency from low to high, the brain waves can be divided into δ waves (0.5–4 Hz), θ waves (4–8 Hz), α wave (8–13 Hz), β wave (13–25 Hz), γ wave (> 25 Hz). If the dominant brainwave is α wave, the person could have the feeling of comfort and concentration, achieve extraordinary memory, highly focused and unusual creativity. In particular, high-amplitude α waves can lead to high learning efficiency. Spatial information is focused on the spatial distribution of the EEG signals on surface of the scalp. By recording the EEG signals, we can analyze the activities of different brain regions. This spatial distribution of EEG can also be used as the characteristic information to analyze brain activities.

4. EXPERIMENTS AND DATA ACQUISITION

4.1. n-back experiments

The tasks of n-back experiments are a series of continuous implementation, which are widely used to stimulate the brain activities in nerve imaging experiments. It is proposed by Wayne Kirchner in 1958. n-back task is a series of stimulus, the paradigm requires subjects to response when the current stimulus matches the one appeared n times before. Load factor n may be adjusted to vary the difficulty of the task. When $n = 1$, the subjects were asked to compare the current stimulus with the stimulus immediately preceding it; when $n = 2$, then compare the current one with the one two times before; when $n = 3$, compare the current one with the one three times before, and so on, with changing the difficulty of the task.

The position matching task is programmed by using E-prime software. displayed on a computer screen in different positions on white background. The black "+" sign of different position is

displayed with white background on the computer screen, the position of "+" sign is random for subjects. each "+" sign appears for a second. The subjects are asked to remember its position and make the appropriate choice by entering the judgment of their vertical position through the computer keyboard. Because the 3-back task is too difficult, this experiment is reduced to 1-back task and 2-back task. When $n = 1$, the subjects are asked to compare the relative vertical position of the current "+" sign and the one previous it, and then press the appropriate key. There are forty "+" signs in all in 1-back task. When $n = 2$, it need to compare the relative vertical position of current "+" sign and the interval one preceding it. There are forty "+" signs in 2-back task too. Two parts are proceeding continuously. They will be carried out before and after Baroque music, which last three to four minutes.

4.2. Experimental Process and EEG Acquisition

In the trials, EEG data of the subjects are collected by NeuroScan's EEG/ERP recorder and the corresponding acquisition system. 20 healthy undergraduate and graduate students as subjects participate voluntarily in the experiment. For the one-dimensional spatial position of visual stimulus ("+" sign), the subjects perform on the memory, judgment and choice. During the experiments, the subjects' EEG data are collected before and after Baroque music. Then the data are comparatively analyzed to study whether Baroque music can affect the improvement of the learning efficiency on some appropriate variables. In the experiment, Vivaldi's "Four Seasons" is used as Baroque music. First, n-back experiment is carried out before the music. Next, subjects listen to the Baroque music, which lasts 30 minutes. And then, n-back experiment is carried out again after the music for the same subjects. EEG data are collected during the experiments.

5. EXPERIMENTS AND DATA ACQUISITION

5.1. Data Processing Method

The reaction time and the correct rate about the location matching task are recorded by E-prime software in the experiment. These can be used as basis of assessing the impact of Baroque music on the learning efficiency.

In the analysis of EEG data, you must preprocess the data firstly. By using Curry 7 software, the collected raw EEG data are preprocessed. It includes filtering, baseline correction, the DC drift premovement, bad channel re-movement, EOG interference exclusion, down sampling, etc.. Since four basic brainwaves frequency ranges from 0.5 to 30 Hz approximately, and δ wave in our research is not considered, so the brain wave information is left only from 1 to 30 Hz by band pass filtering. The EEG data above 30 Hz and below 1 Hz are removed. By comparing the VEO (EOG) waveforms, EOG interference is excluded. The filter range is plus or minus 200 microvolts. While ensuring appropriate data details, the data file is compressed. It can reduce the computer's running burden in the subsequent operation, speed up the data processing and save the storage space.

Analyzed data is from 0 ms to 2000 ms when stimulus appears. After removing artifacts such as unreliable data, ensure that in each test mode, the data superposition averaging are more than 30 segments. Then observe the amplitude of ERP waveform and contrast of energy distribution, especially P300 component, which reflects the brain's cognitive processes to external information.

By the power spectrum analysis, different waves' energy and the distribution of various brain regions are extracted. The excitation of Baroque music is investigated on the α wave.

5.2. Results Discussion

The experimental data are obtained through averaging. The experimental results are shown in Table 1. It can be seen, in both the 1-back and 2-back experiments, the reaction times are decreased after Baroque music. The accuracy of the two tasks are both improved. While the increase of accuracy is not obvious, but the reaction time is shortened more obviously in 2-back compared with the 1-back. It is thus clear that, when task difficulty or memory load increases, the Baroque music is more effective for improving the memory.

Figure 1 shows the power spectral distribution of all channels before and after music. The left is the data before music, right for after the music. We can see after the music. There is an evident energy fluctuation on the rise within α wave band (about 10 Hz). It indicates that α brain waves are excited evidently after stimulation of Baroque music for 30 minutes. So the Baroque music is verified having an effect on stimulating α brain waves.

The two diagrams of Figure 2 show the Event-Related Potentials (ERP) of all channels before and after music. All the data segments (trails) are superimposed on the average in the experiments. After the music, there is an evident P300 waveform close to 239 ms latency. Obviously, by contrast

Table 1: Parameters of analytical pdfs fitted to the empirical data.

average		Reaction time	accuracy
1-back task	**Before music**	594.22 ms	90.10%
	After music	513.61 ms	92.70%
2-back task	**Before music**	928.36 ms	72.30%
	After music	752.57 ms	86.70%

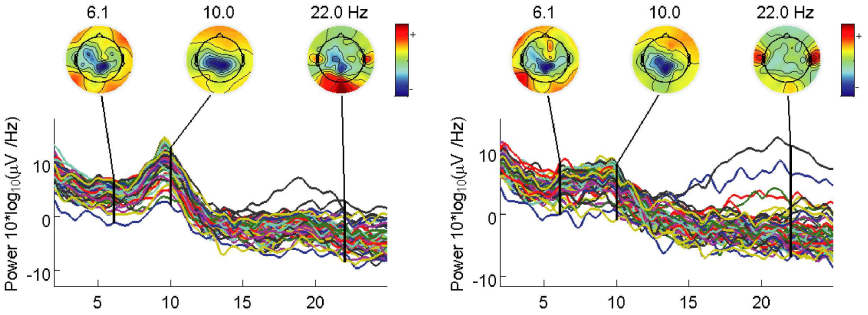

Figure 1: The power spectrum distribution before and after Baroque music.

of EEG data, the amplitude of P300 component has been greatly improved after music. The P300 has great relationship with human activities of identification, discovery, perception and memory. The increase of P300 amplitude, just from the microscopic point of view, verify that Baroque music has positive influence on improving memory and attention.

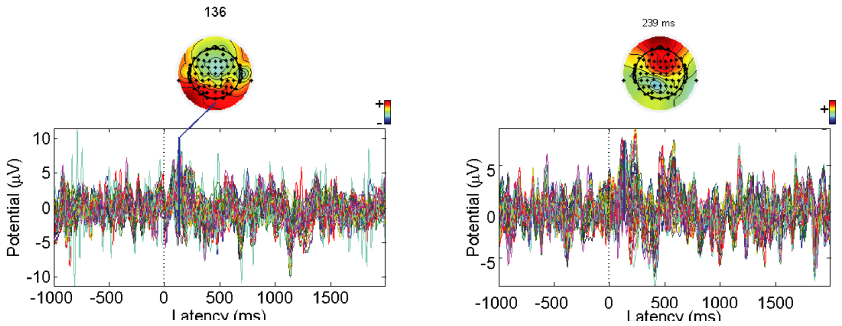

Figure 2: The event-related potentials (ERP) of all channels before and after Baroque music.

In addition, to verify the stimulation effect of Baroque music on α brain waves, the subjects are instructed to do deep breathing exercises with background music — 'The Four Seasons' by Antonio Vivaldi. Within 25 minutes, from drowsy to awake, the changes in the power spectrum of the subjects' alpha brainwave ($8 \sim 13$ Hz) were extracted. Figure 3 shows the changes in the power spectrum of EEG at 10 Hz. It can be seen that the power spectral density of EEG at 10 Hz ascends gradually as the level of vigilance changes. The power spectral density at other frequencies in α band has similar variation. However, it is most obvious around 10 Hz. As time goes on, with

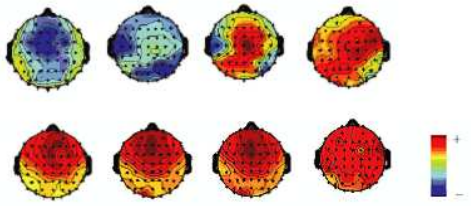

Figure 3: The average energy variations of EEG at around 10Hz. Each sub graph represents.

the stimulation of Baroque music, the power spectral density of α wave changes significantly in 20 minutes. Alpha brainwave gradually became dominant, proving that the subjects have been into the state of relaxed alertness from being sleepy. This experiment has verified the effect of musical stimulation on α wave. the EEG power distribution on the strength at a certain moment.

6. CONCLUSION

This paper explores the optimum learning state from the perspective of brain cognition and EEG-based analysis method is proposed from time domain, frequency domain, spatial distribution. N-back experiments are designed to study the subjects' attention and memory. The results show that Baroque music is beneficial to enhance learning efficiency. It can quickly and effectively stimulate α brain waves, increase the amplitude of ERP, shorten the reaction time, improve the response accuracy, and improve the memory and attention of brains. Baroque music can really make a person to be in a balanced, stable, calm state of mind, and improve their learning efficiency. Therefore, teachers can use Baroque music as teaching reform methods to assist instruction and enhance the students' learning effects. With the deepening of research on the brain's learning mechanisms, our understanding of the teaching process is constantly changing. Brain science's contribution continues to increase its impact on education, which will provide the correct and effective way to improve the quality of teaching.

REFERENCES

1. Boksem, M. A., T. F. Meijman, and M. M. Lorist, "Effects of mental fatigue on attention: An ERP study," *Cogn. Brain Res.*, Vol. 25, No. 1, 107–116, 2005.
2. Fuller, R., "Towards a general theory of driver behavior," *Accident Analysis and Prevention*, Vol. 37, No. 6, 461–472, 2005.
3. Jansson, A., E. Olsson, and M. Erlandsson, "Bridging the gap between analysis and design: Improving existing driver interfaces with tools from the framework of cognitive work analysis," *Cognition, Technology & Work*, Vol. 8, No. 1, 41–49, Springer, London, 2006.
4. Vossen, H., G. Van Breukelen, et al., "More potential in statistical analyses of event-related potentials: A mixed regression approach," *International Journal of Methods in Psychiatric Research*, Vol. 20, No. 3, 56–68, 2011.
5. Ghani, F., M. Jilani, M. Raghav, O. Farooq, and Y. U. Khan, "Development of brain computer interface for elbow movement detection," *JNIT*, Vol. 3, No. 3, 66–74, 2012.
6. Dzitac, I., T. Vesselenyi, and R. C. Tarca, "Identification of ERD using fuzzy inference system for brain-computer interface," *International Journal of Communications & Control*, Vol. 6, No. 3, 403–417, 2011.
7. Jones, A., "Music and the cognitive process — Student perceptions," *Polyglossia*, Vol. 19, 143–150, 2010.
8. Reinhard, S., G. Wilfried, and S. Irene, "EEG-mapping during music stimulation," *Psychomusicology*, 159–170, 2011.

Analysis of Spectral Characteristics of the Human Cornea Obtained in the Terahertz Frequency Range

M. I. Sulatsky[1], **E. A. Strepitov**[1], **O. A. Smolyanskaya**[1], **M. K. Khodzitskiy**[1], **I. V. Prozheev**[1], **E. L. Odlyanitskiy**[1], **A. G. Zabolotniy**[2], **and I. A. Geyko**[2]

[1]ITMO University, Saint-Petersburg, Russia
[2]Krasnodar Branch of "S. N. Fyodorov Eye Microsurgery Complex", Krasnodar, Russia

Abstract— The spectral characteristics of the human cornea in vitro were analyzed in this work. Correct identification of the reflection spectra peaks allows using the terahertz radiation as the new diagnostics method of eye diseases.

1. INTRODUCTION

Today there is quite a number of corneal diseases that lead to impairment or loss of sight. For example, dry eye syndrome leads to drying of a cornea. Another example keratitis characterized by the so-called corneal syndrome (lacrimation, photophobia, blepharospasm), results in an irritation of sensory nerves of a cornea [1]. Last years the investigations of various degenerative processes in a cornea are of considerable interest for ophthalmic diagnostics. It is worth saying that the diagnostics of eye diseases is a very important step to carry out preventive and therapeutic measurements. Currently an eye examination with a slit lamp (biomicroscopy the eye) is used for research of a cornea state (transparency, sphericity, gloss) in low vision clinics [2]. There are most of the vibrational-rotational spectral lines of water and many organic macromolecules, such as proteins, nucleic acids, DNA, as well as the frequencies of intermolecular interactions spectral lines in the terahertz (THz) frequency range [3]. It should be noted that the characteristic feature of THz radiation is strong absorption of radiation by water, and the absorption intensity is much higher than in the millimeter wavelength range. It is well known that there are no blood vessels but many nerve endings in a cornea. Human cornea contains $75 \div 80\%$ of water [4]. Above mentioned diseases affect on a cornea composition, particularly on the quantity of water content. Therefore the visible differences in reflection spectrum of pathological cornea compared with reflection spectrum of healthy ones may be observed. At the present time the different scientific works are devoted to the research of the possible methods of parameters monitoring of a cornea state using THz radiation. In particular, the article [5] presents the application of THz technology to visualize the hydration content in ex vivo porcine corneas. In this article the pulsed reflective THz spectroscopy system was developed specifically for hydration sensing. The point of maximum reflection was found to be coincident with the center of cornea. The reflection decreased from the center to the cornea edges, suggesting that the cornea center was more hydrated than the edges.

In this work, we obtained the spectral characteristics of the human cornea using the THz pulsed spectrometer in the reflection mode.

2. EXPERIMENTAL SETUP

The reflection spectra were obtained by the THz time domain (TD) spectrometer [6]. The characteristics of the spectrometer are following: the spectral resolution of 15 GHz, the sensitivity of lock-in amplifier of 1 mV, the lock-in amplifier time constant of 1 s. The THz broadband pulsed radiation had the following parameters: the spectral range of 0.1–2.0 THz, the pulse duration of 2.7 ps, the average power of 30 mW.

THz radiation was generated by femtosecond laser (Yb:KYW) irradiation of undoped indium arsenide crystal. The femtosecond laser parameters are following: the wavelength of 1040 nm, the pulse duration of 120 fs, the pulse repetition rate of 75 MHz, the power of 1 W. The spectra in frequency domain were obtained by the Fourier transform of the measured time domain waveforms of the reference sample and the biological object.

3. OBJECT UNDER THE STUDY

In this paper, two different human corneas in-vitro, respectively, were studied. Corneoscleral surgical specimens were obtained by cutting out the eyes, which were preserved in the Borzenka-Moroz medium at the temperature of +4°C. The canned samples were stored during 5 days from the

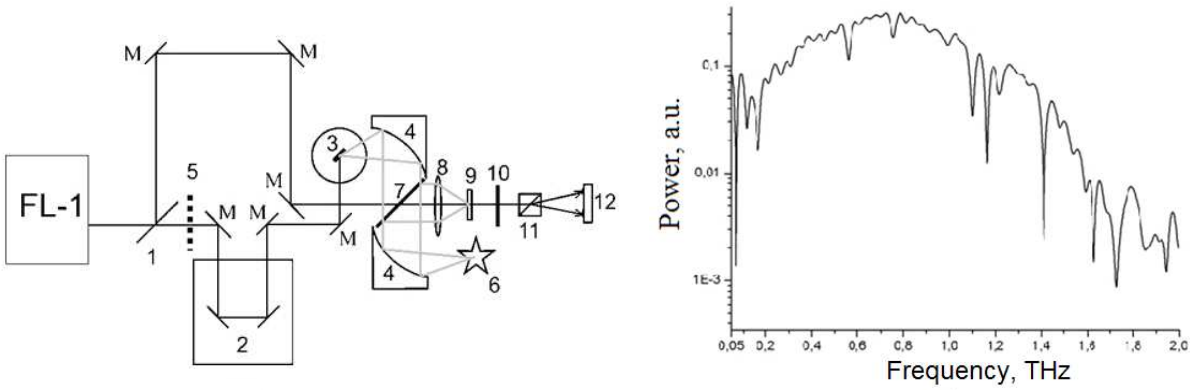

(a) (b)

Figure 1: Scheme of (a) the THz pulsed broadband spectrometer in the reflection mode and (b) the reference THz pulse frequency spectrum. FL-1 — infrared laser; M — mirrors; 1 — beam splitter; 2 — optical delay line; 3 — THz radiation generator: crystal of InAs in a magnetic system; 4 — parabolic mirrors; 5 — chopper; 6 — biological object; 7 — THz radiation beam splitter on the basis of high-resistivity silicon wafer; 8 — TPX polymer lens; 9 — electro optical crystal of CdTe; 10 — achromatic quarter-wave plate; 11 — Wollaston prism; 12 — balanced photodiodes.

operation moment until the experiment. The corneoscleral discs were cut out of the eyes in vitro. The sparing technique based on microsurgical approach allows preserving native, architectonic and endothelial cell density of corneas in-vitro during their hypothermic preservation in the cultural environment. The domestic environment for hypothermic preservation of the viable corneas in vitro had high barrier properties and it stabilized cell membranes, safety and stability of endothelial cell density during the cold storage process. The typical microphotography of human cornea is presented in the Figure 2.

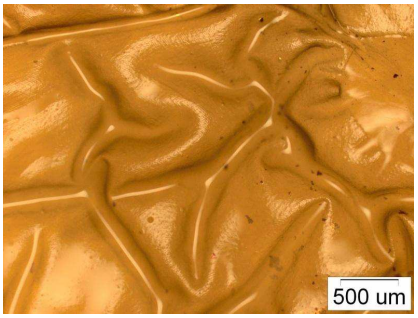

Figure 2: Microphotography of object under study (microscope OLYMPUS STM6).

The location of the sample in the THz spectrometer scheme is shown in the Figure 3. The reflection time domain waveforms were recorded sequentially for the following structures: mirror, object + mirror, dielectric, dielectric + object.

4. RESULTS AND DISCUSSION

In our work, we obtained the spectral characteristics of two different human corneas in vitro. Averaging was made by five measurements of each sample of cornea. The average reflection spectrum of the first sample of the normal human cornea in vitro is shown in the Figure 4. The pronounced peak in the reflection spectrum at the frequency of 0.9 THz and the faint peak at 1 THz are observed.

The average reflection spectrum of the second sample of the normal human cornea in vitro is shown in the Figure 5. The pronounced peak in the reflection spectrum at the frequency of 0.9 THz and the faint peaks near 1.3, 1.8 THz are observed.

The visible differences in the characteristic spectral lines in the reflection spectra of two samples of the normal human corneas can be explained by various composition and water content.

THz absorption spectrum of water is illustrated in the Figure 6 [7]. Comparing the our results with the absorption spectrum of water, it can be assumed that in our spectra the reflection peaks

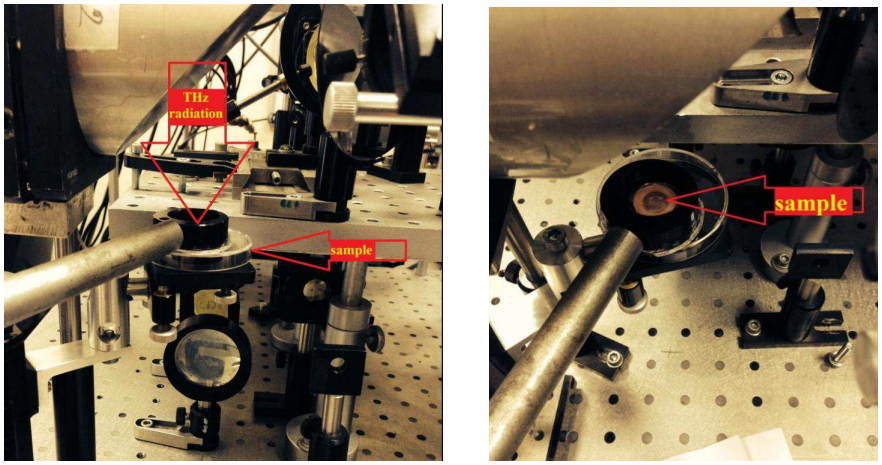

Figure 3: Photo of the irradiation human cornea using the pulsed THz spectrometer in the reflection mode.

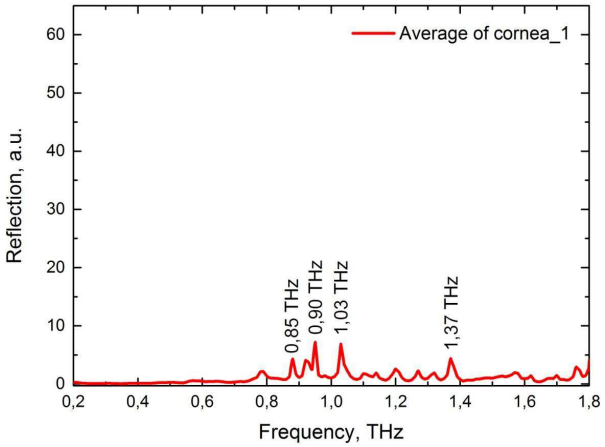

Figure 4: The average reflection spectrum of the first sample of the normal human cornea in vitro.

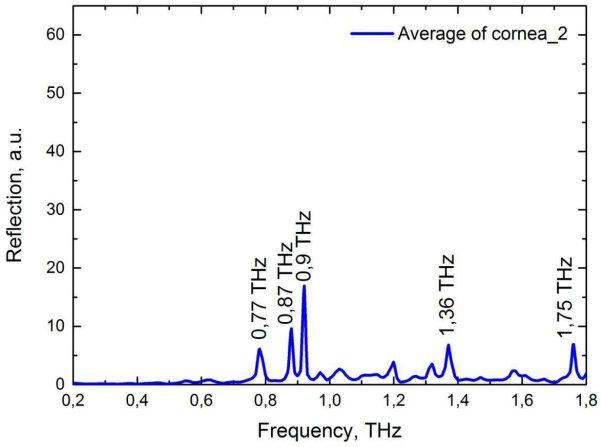

Figure 5: The average reflection spectrum of the second sample of normal human cornea in-vitro.

near 1.00 THz and 1.70 THz are associated with the absorption of radiation by water.

The manifestation and correct identification of the characteristic peaks of the reflection spectra, which are specific to the certain diseases (such as different types of keratitis) in the reflection spectra of the human cornea, it can be seen as new non-invasive diagnostics method of the human cornea state.

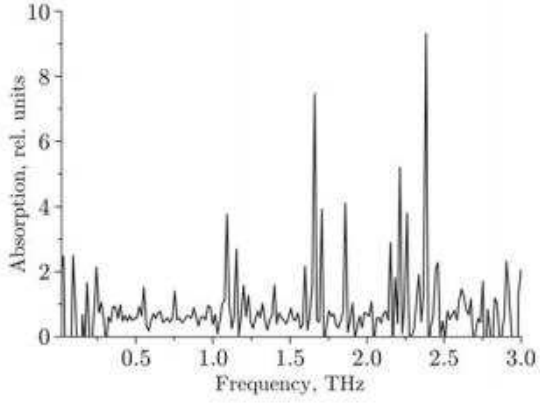

Figure 6: The absorption spectrum of water [7].

Finally, in this paper we proposed the possible option of development of the new non-invasive diagnostics of the cornea state by the identification of the reflection spectrum peaks.

5. CONCLUSIONS

The spectral characteristics of the human cornea were analyzed for the development of the non-invasive methods of cornea diagnostics for the frequency range of 0.1–2.0 THz.

ACKNOWLEDGMENT

This work was financially supported by Government of Russian Federation, Grant 074-U01. The authors are grateful to Ms. Balya V. K for the photographing of specimens.

REFERENCES

1. Tang, A., M. E. Marquart, J. D. Fratkin, C. C. McCormick, A. R. Caballero, H. P. Gatlin, and R. J. O'Callaghan, "Properties of PASP: A pseudomonas protease capable of mediating corneal erosions," *Invest. Ophthalmol. Vis. Sci.*, Vol. 50, No. 8, 3794–3801, 2009.
2. Birich, T. A., L. A. Marchenko, and A. Chekina, *Ophtalmology*, 978-985-06-1298-4, 2007.
3. Nazarov, M. M., A. P. Shkurinov, V. V. Tuchin, and X.-C. Zhang, *Terahertz Tissue Spectroscopy and Imaging in Handbook of Photonics for Biomedical Science*, 97, 2010.
4. Perederiy, V. A., "Eye diseases," *The Complete Reference — M*, 704, Penguin Books, 2008.
5. Singh, R., P. Tewari, J. Bourges, J. Hubschman, D. Bennett, Z. Taylor, H. Lee, E. Brown, W. Grundfest, and M. Culjat, "Terahertz sensing of corneal hydration," *32nd Annual International Conference of the IEEE EMBS Buenos Aires*, 978-1-4244-4124-2/10, Argentina, Aug. 31–Sep. 4, 2010.
6. Bespalov, V. G., A. A. Gorodetskiy, I. Y. Denisyuk, S. A. Kozlov, and V. N. Krylov, "Methods of generating superbroadband terahertz pulses with femtosecond lasers," *Journal of Optical Technology*, Vol. 75, No. 10, 636–642, 2008.
7. Antsygin, V. D., A. A. Mamrashev, N. A. Nikolaev, and O. I. Potaturkin, "Small-size terahertz spectrometer using the second harmonic of a femtosecond fiber laser," *Optoelectronics, Instrumentation and Data Processing*, Vol. 46, No. 3, 294–300, Jun. 2010.

Study of Penetration Depth Dispersion of THz Radiation in Human Pathological Tissues

I. V. Prozheev, **O. A. Smolyanskaya**, **M. V. Duka**, **A. A. Ezerskaya**, **V. V. Orlov**, **E. A. Strepitov**, **N. S. Balbekin**, **and M. K. Khodzitsky**
ITMO University, Saint Petersburg, Russia

Abstract— The dispersion of penetration depth of terahertz radiation in various human pathological tissues were obtained and analyzed for development of subcutaneous diseases diagnostics in terahertz frequency range.

1. INTRODUCTION

The terahertz (THz) radiation is an electromagnetic radiation in the wavelength range of 3 mm–30 mkm (the frequency range of 0.1–10 THz). Terahertz radiation is perspective for applications in spectroscopy and medicine. Actual use of THz radiation is to diagnose skin pathologies, such as chemical and thermal burns, mechanical damage, skin cancer and other morphological changes [1]. Diagnosis of skin cancer in the early stages becomes a complex process that requires to know how deep the radiation passes into the skin. It is necessary not to miss early cancer when examining the patient [2]. This paper is devoted to investigation of penetration depth of radiation in normal and pathological human skin tissues, for development of subcutaneous diseases diagnostics in the frequency range of 0.1–2 THz.

2. MATERIALS

We investigated in vivo several samples of human tissues: normal skin tissue, thermal burn skin tissue, chemical burn skin tissue, skin covered by ointment containing glycerin. All measurements were carried out at room temperature. Five measurements were made for each tissue sample. In one set of measurements we used an ointment in case to increase penetration depth of radiation. The ointment contained 39% of glycerin, cetearyl alcohol, stearic acid, palmitic acid, sodium cetearyl sulfate.

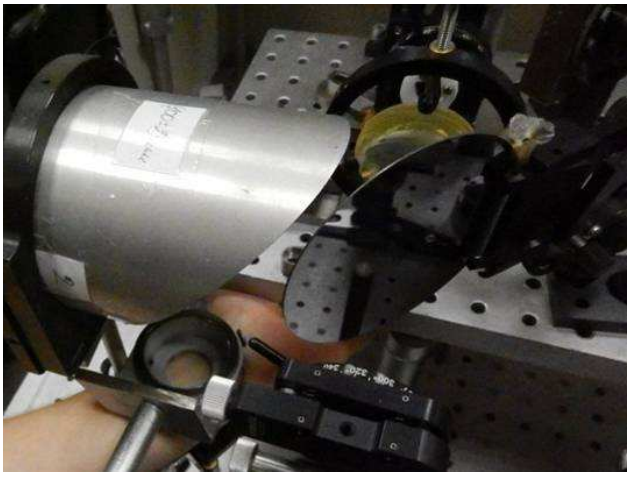

Figure 1: Sample of normal male human tissue in measurement window of terahertz time domain spectrometer.

3. EXPERIMENTAL SETUP

The reflection spectra were obtained by THz time domain reflection spectroscopy, utilizing ultra short electromagnetic pulses generated from an InAs semiconductor in magnetic system driven by femtosecond laser pulses. The THz spectrometer has the following characteristics: the average power of 30 μW; the frequency range of $0.1 \div 2.0$ THz, THz pulse duration of 3 ps, the spectral resolution about of 15 GHz [3]. The signals measured by the spectroscopy system are time domain

waveforms that are directly proportional to the terahertz electric field. The frequency domain spectra were obtained from time domain waveforms using Fast Fourier Transform (FFT). Thus, it is possible to recover both phase and amplitude information, which provides a direct measure of the frequency-dependent refractive index of the tissue sample, absorption coefficient and penetration depth.

4. METHOD

In experiment we obtain THz pulses reflected from the interfaces of polystyrene window/skin sample. THz pulse reflected from the sample contains the first pulse reflected from the front of polystyrene window (reference pulse) and the second delayed pulse from the polystyrene — skin interface (sample pulse) [4]. The Happ-Genzel apodization function was applied to Fourier trans-

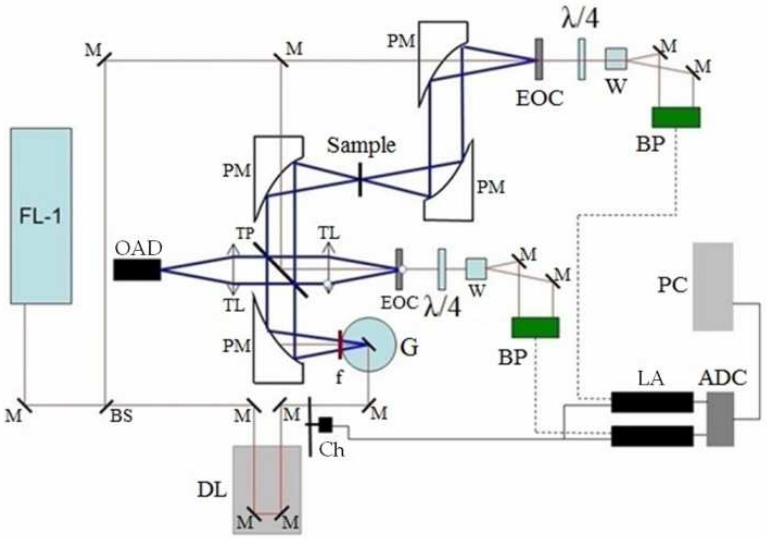

Figure 2: Scheme of the universal pulsed broadband THz spectrometer. FL-1 — laser of femtosecond pulses, M — mirrors, BS — beam splitter, DL — optical delay line, G — generator of THz radiation based on the crystal InAs, PM — parabolic mirrors, TL — lenses for THz radiation, f — teflon filter, TP — translucent silicon plate, Ch — chopper, EOC — electro optical crystal of CdTe, W — Wollaston prism, BP — balanced photodiodes, LA — lock-in amplifier, ADC — analog-to-digital converter, PC — personal computer, OAD — opto-acoustic detector (Golay cell).

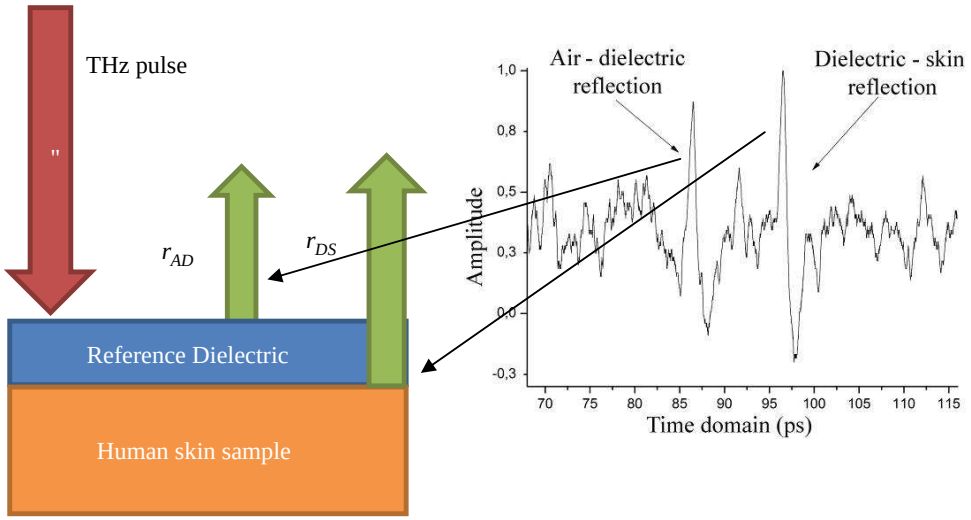

Figure 3: Scheme of the experiment. The first pulse indicates reflection from air-dielectric interface. The second pulse appears from dielectric-skin interface reflection.

form integration to reduce the ripples for each pulses (r_{AD}, r_{DS}). The Happ-Genzel function is often used to achieve a good balance between ripple size and resolution. The ratio of the Fourier transform of the reference pulse $\hat{E}_R(\upsilon)$ and the sample pulse $\hat{E}_S(\upsilon)$, is

$$\frac{\hat{E}_S(\upsilon)}{\hat{E}_R(\upsilon)} = \frac{t_{AD} r_{DS} t_{DA}}{r_{AD}} \exp\left(i \frac{4\pi n_D d_D \upsilon}{c}\right) \tag{1}$$

where t_{AD}, r_{AD}, t_{DA}, $\hat{r}_{DS}$ are Fresnel coefficients at normal incidence for the amplitude transmission t, and reflection r. The subscripts indicate the interfaces: air (A), polystyrene (D), skin (S). The Fresnel coefficients for the air-polystyrene interfaces are real because dry air and polystyrene have no absorption. The phase shift is represented in exponential factor, where n_D is the refraction index of polystyrene and d_D is the thickness of used window. From the Equation (1) we may obtain real and imaginary parts of refractive index and absorption coefficient of skin: $\hat{n}_S = n'_S - jn''_S$, where

$$n'_S = \frac{n_D\left(1 - R^2\right)}{1 + R^2 + 2R\cos\theta}, \tag{2}$$

$$n''_S = n_D \frac{-2R\sin\theta}{1 + R^2 + 2R\cos\theta}, \tag{3}$$

$$\alpha_S = \frac{4\pi\upsilon n_D}{c} \frac{-2R\sin\theta}{1 + R^2 + 2R\cos\theta}. \tag{4}$$

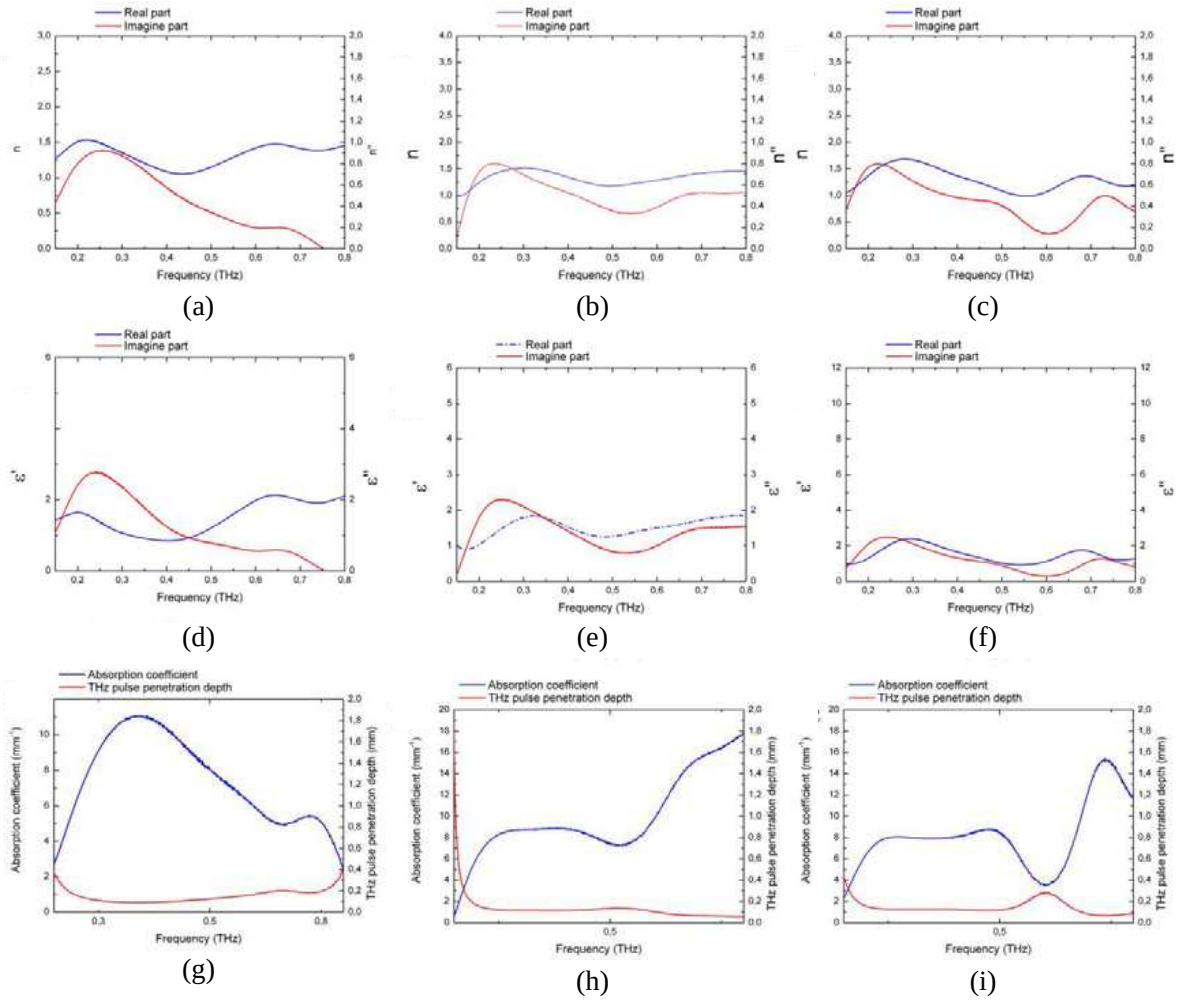

Figure 4: (a), (b), (c) Both real and imagine parts of refractive index, (d), (e), (f) dielectric permittivity, (g), (h), (i) absorption coefficient and penetration depth, (a), (d), (g) healthy skin, (b), (e), (h) skin with chemical burn, (c), (f), (i) skin with thermal burn.

If both thickness and refractive index of reference dielectric are known then amplitude R and phase angle θ can be obtained experimentally. Penetration depth can be calculated as $\sigma = \frac{1}{\alpha}$ [5]. Real and imagine parts of skin permittivity ($\hat{\varepsilon} = \varepsilon' + i\varepsilon''$) are calculated from the relation $\hat{\varepsilon} = \hat{n}^2$.

5. RESULTS

The results of the measured time domain waveforms processing are presented in Fig. 4. It is clearly seen that the explicit increase of the imaginary part of refraction index (as well as the absorption coefficient) of pathological skin (chemical burn and thermal burn) in comparison with healthy skin is observed in the frequency range of 0.6–0.8 THz (Figs. 4(a)–(c)). The effect results in the dramatically decrease of THz pulse penetration depth from 0.1 mm till 0.05 mm for skin with chemical burn and from 0.3 mm till 0.1 mm for skin with thermal burn in this frequency range (Figs. 4(g)–(i)). This fact worsens the possibility of THz diagnostics of subcutaneous diseases of burned tissue in the frequency range of 0.6–0.8 THz.

6. CONCLUSIONS

We experimentally obtained THz reflection spectra of normal human skin and human skin with thermal and chemical burns in the range 0.15–1.0 THz. Both real and imagine parts of refractive index, dielectric permittivity, absorption coefficient and penetration depth were derived by analysis of reflection spectra.

ACKNOWLEDGMENT

This work was financially supported by Government of Russian Federation, Grant 074-U01.

REFERENCES

1. Ezerskaya, A. A., E. A. Strepitov, I. V. Prozheev, and O. A. Smolyanskaya, "Research of specific peculiarities of THz reflection spectra of abnormal human tissues," *15th International Conference Laser Optics*, 433–434, Jun. 25–29, 2012.
2. Nazarov, M. M., A. P. Shkurinov, Y. A. Kuleshov, and V. V. Tuchin, "Terahertz impulse spectroscopy of biological tissues," *Quantum Electronics*, Vol. 38, No. 7, 647–654, 2008.
3. Bespalov, V. G., et al., "Methods of generating superbroadband terahertz pulses with femtosecond lasers," *Journal of Optical Technology*, Vol. 75, No. 10, 636–642, 2008.
4. Roenne, C., L. Thrane, P. O. Astrand, A. Wallqvist, K. V. Mikkelsen, and S. R. Keiding, "Investigation of the temperature dependence of dielectric relaxation in liquid water by THz reflection spectroscopy and molecular dynamics simulation," *J. Chem. Phys.*, Vol. 107, 5319–5331, 1997.
5. Wilmink, G. J., B. L. Ibey, et al., "Development of compact terahertz time-domain spectrometer for the measurement of the optical properties of biological tissues," *Journal of Biomedical Optics*, Vol. 16, No. 4, Apr. 2011.

A Comparative Study of Analytical and Numerical Analysis for Coaxial Probe Aperture in a Dissipative Media

K. Y. You[1], **C. Y. Lee**[2], **and C. W. Lee**[1]

[1]Department Communication Engineering, Faculty of Electrical Engineering
Universiti Teknologi Malaysia (UTM), Johor 81310, Malaysia
[2]Faculty of Bioscience and Medical Engineering
Universiti Teknologi Malaysia (UTM), Johor 81310, Malaysia

Abstract— This paper presents an analysis of the coaxial probe aperture immersed in a dissipative medium using Levine's integral calculation and Nevels's MoM routines. The analytical integration and MoM are programmed with MATLAB code. The comparison between simplicity and accuracy of both methods has been discussed in detail. This paper intends to enhance the compatibility study of analytical and numerical methods for coaxial probe, since literature on this study for coaxial probe is less compared to linear monopole.

1. INTRODUCTION

Analytical and numerical modeling is a tool that cannot be lacked in the current communication educational, research and engineering world. Communication devices can be designed and modified in a short time based on the modeling calculated results without building an actual prototype and repeatedly testing its performance by using measurement method. Directly, the cost and time in the design of communication devices, such as antenna, filter and directional coupler can be saved. However, the main purpose of this study is for new researchers involved in the communication to better understand the development background and concepts of numerical modeling other than use only. In additional, a good understanding of the mathematical principles of wave propagation and radiation is an essential requirement for undergraduate in communication engineering, especially for student who prepares to further their postgraduate study. Although, relevant information in this regard can be found in many textbooks, mostly are on the modeling of a linear monopole (or dipole), very little information on the open-ended coaxial probe. Hence, in this paper, a brief review of analytical and method of moment (MoM) based numerical modeling are particularly focused on a coaxial probe.

There are close relationship between the analytical and numerical modeling, due to the fact that MoM cannot be used if problems have no established analytical integral equation as a governing function. Moreover, the accuracy of the MoM method is dependent on the rigors of the integral equation. Fortunately, there are several rigorous quasi-static integrals have been derived, such as Levine's [1] and Nevels's [4] admittance integral formulations. The MoM, a technique that is suitable to be used to solve the unbounded scattering wave problems, and requires no special boundary treatment, since those integral equations are expressed in terms of Green's functions, which are naturally satisfied the radiated fields. In fact, the difference between the analytical and numerical modeling are the complexity of the solutions. In engineering field, the analytical solutions require various assumptions in the theoretical equation. For instance, the difference in the voltages between the coaxial gap (at $a < \rho < b$) at aperture surface (at $z = 0$) is assumed to be 1 V (or 1/2 V) for analytical solution as shown in Figure 1(a). However, in numerical solution, the difference voltage is an unknown parameter. For instance, the MoM routines may divide the aperture surface into small element areas and the unknown difference voltages at each area are solved one by one [3, 4] as shown in Figure 1(b). Thus, the distribution of voltage difference at the aperture surface can be virtualized obviously. The more detail procedures description for the MoM methods for open-ended coaxial probe was available in following section.

2. ANALYTICAL METHOD

In this work, the derivations of analytical formulations are not shown explicitly, since that information was available in the literatures [1–5]. For coaxial probe, the scattering aperture analysis was widely referred to axisymmetric transverse magnetic (TM) formulation as [2, 4]:

$$H_{\phi}^{+} = \frac{j\omega\varepsilon_o\varepsilon_r}{\pi}\int_a^b\int_0^{\pi} E_o \frac{\exp(-jkr)}{r}\cos\phi'\rho' d\phi' d\rho' \tag{1}$$

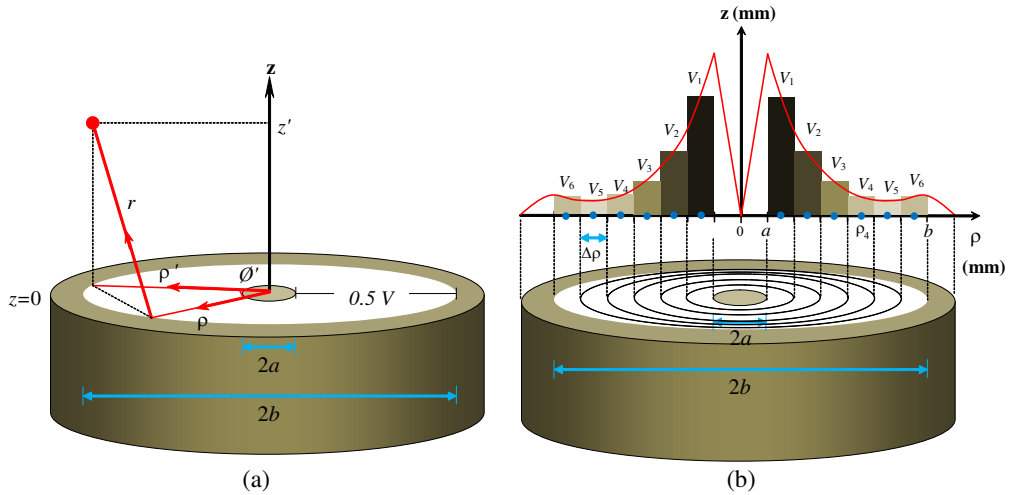

Figure 1: (a) Cylindrical coordinates used in evaluating the aperture probe radiation field analytically. (b) Vector voltage V_n for each grid positions at surface of the aperture probe.

where E_o is the magnitude of radial electric field. The distance between two points, r, at exterior region as shown in Figure 1(a) is written as:

$$r = \sqrt{\rho^2 + \rho'^2 - 2\rho\rho' \cos(\phi' - \phi) + (z - z')^2} \tag{2}$$

The ω and k are the angular frequency and propagation constant for the external medium at exterior region (at $z' \geq 0$), respectively. Symbols of ε_o and ε_r are the permittivity of free space and relative permittivity of the external medium (at $z' \geq 0$), respectively. At discontinuity aperture, $z = z' = 0$, the magnitude of radial electric field, E_o in (1) is given as:

$$E_o = \frac{V_o}{\rho' \ln(b/a)} \tag{3}$$

where V_o is the voltage between the inner and outer conductors ($a < \rho < b$) at the aperture. For the $V_o = 1/2\,\mathrm{V}$ excitation, the (1) is re-written as [2]:

$$H_\phi^+ = \frac{j\omega\varepsilon_o\varepsilon_r}{2\pi \ln(b/a)} \int_a^b \int_0^\pi \frac{\exp(-jkr)}{r} \cos\phi' d\phi' d\rho' \tag{4}$$

From (4), the integral formulation for E_ρ component at exterior medium ($z' > 0$) is given as [2]:

$$E_\rho = \frac{-1}{j\omega\varepsilon_o\varepsilon_r} \frac{\partial H_\phi}{\partial z} = \frac{-1}{2\pi \ln(b/a)} \int_a^b \int_0^\pi \frac{\exp(-jkr)}{r} \cos\phi' \left(jk + \frac{1}{r}\right)(z - z')\, d\phi' d\rho' \tag{5}$$

The aperture admittance integral equations for open-ended coaxial radiator can be derived by matching the field components, $H_\phi^- = \frac{I}{2\pi\rho}$ (inner region, $z \leq 0$) and (4) (exterior region, z $\geq$ 0), since those tangential fields are continuous across the interface aperture ($z = z' = 0$):

$$H_\phi^- = H_\phi^+ \tag{6a}$$

$$\frac{I}{2\pi\rho} = \frac{j\omega\varepsilon_o\varepsilon_r}{\pi} \int_a^b \int_0^\pi E_o \frac{\exp(-jkr)}{r} \cos\phi' \rho' d\phi' d\rho' \tag{6b}$$

The current, I in (6b) are substituted by the following relationship: $I = VY$ and $V = \int_a^b E_o\, d\rho$, yields

$$\frac{Y}{2\pi\rho} \int_a^b E_o\, d\rho = \frac{j\omega\varepsilon_o\varepsilon_r}{\pi} \int_a^b \int_0^\pi E_o \frac{\exp(-jkr)}{r} \cos\phi' \rho' d\phi' d\rho' \tag{7}$$

where Y is the input admittance on surface, $z = z' = 0$. After some mathematical operation work, the input admittance, Y, which is normalized by characteristic admittance, Y_o, of coaxial line can be formulated. There are several expression form of normalized admittance, $\tilde{Y}_{in}$ are tabulated in Table 1.

Table 1: Various types of input admittance formulations of open-ended coaxial probe available in literatures.

Normalized Admittance Formulations of Open-Ended Coaxial Probe (only TEM mode)	
$\tilde{Y}_{in} = \frac{jk\varepsilon_r}{\sqrt{\varepsilon_c}\ln(b/a)} \int_0^\infty \frac{d\zeta}{\zeta(\zeta^2-k^2)^{1/2}} \left\lvert J_o(\zeta a) - J_o(\zeta b)\right\rvert^2$ [1]	(8)
$\tilde{Y}_{in} = \frac{jk\varepsilon_r}{\pi\sqrt{\varepsilon_c}\ln(b/a)} \int_a^b \int_a^b \int_0^\pi \frac{\exp(-jkr)}{r} \cos\phi' d\phi' d\rho' d\rho$ [5]	(9)
$\tilde{Y}_{in} = \frac{1}{\eta_c \ln(b/a)} \int_a^b \frac{1}{\rho'} d\rho' + \frac{j\omega\varepsilon_o\varepsilon_r\rho}{2\pi} \int_a^b \int_{-\pi}^\pi \frac{\exp(-jkr)}{r} \cos\phi' \rho' d\phi' d\rho'$ [4]	(10)
$\tilde{Y}_{in} = \frac{2V_o}{\int_a^b E_\rho d\rho'} - 1$ [4]	(11)

3. NUMERICAL METHOD (MOMENT OF METHOD)

In method of moment (MoM) solution, the analytical integrals in Section 2 have been discretized and expressed it in matrix form. In fact, the MoM basically involves 3 main steps:

1. Derive an unknown parameter in the algebraic equations using Ohm's law ($V = IZ$ or $VY = I$) and analytical integral (The unknown parameter normally either is vector current, I or vector voltage, V).
2. Solve the unknown parameter using matrix routine (such as Gaussian elimination method).
3. Interpret the results in desired domains. (In H field domain, E field domain, input impedance, Z_{in} or input admittance, Y_{in}).

For coaxial probe case, the vector voltage, V_n at the aperture probe surface is assumed as the unknown parameter and the algebraic equations to be solved which is written in matrix form as [4]:

$$[Y_{mn}][V_n] = [I_m] \tag{12}$$

where Y_{mn} and I_m are the admittance and the vector current at surface of the aperture probe ($z = z' = 0$), respectively [4]:

$$Y_{mn} = \frac{\ln\left(\frac{\rho_n+\Delta\rho/2}{\rho_n-\Delta\rho/2}\right)}{\eta_c \ln(b/a)} + \frac{j\omega\varepsilon_o\varepsilon_r\rho_m}{2\pi} \int_{\rho_n-\Delta\rho/2}^{\rho_n+\Delta\rho/2} \int_{-\pi}^{\pi} \cos\phi' \frac{\exp\left(-jk\sqrt{\rho_m^2+\rho'^2-2\rho_m\rho'\cos\phi'}\right)}{\sqrt{\rho_m^2+\rho'^2-2\rho_m\rho'\cos\phi'}} d\phi' d\rho' \tag{13}$$

and

$$I_m = \frac{2V_o}{\eta_c \ln(b/a)} \tag{14}$$

where η_c is the intrinsic impedance of the coaxial line. The ε_o and ε_r are the permittivity of free space and the relative permittivity of the exterior medium, respectively. The unknown vector voltages, $[V_n]$ on aperture probe are determined by inverting the admittance matrix, $[Y_{mn}]$ and multiplying with the, $[I_m]$. The radial electric field, $E_{\rho n}$ at n match point position on surface aperture, can be found by substituting the set values of $[V_n]$ into (15):

$$E_{\rho n} = \begin{cases} \frac{V_n}{\rho} & \text{for } \left(\rho_n - \frac{\Delta\rho}{2}\right) < \rho < \left(\rho_n + \frac{\Delta\rho}{2}\right) \\ 0 & \text{other} \end{cases} \tag{15}$$

Once the electric field, $E_{\rho n}$ on each match point positions has been determined, the (1) can be re-exam by replacing (15) into (1) as:

$$H_\phi^+ = \frac{j\omega\varepsilon_o\varepsilon_r}{\pi} \sum_{n=1}^{N} V_n \int_{\rho_n-\Delta\rho/2}^{\rho_n+\Delta\rho/2} \int_0^\pi \frac{\exp(-jkr)}{r} \cos\phi' d\phi' d\rho' \tag{16}$$

Besides that, from the total value of electric field, $\sum V_n$, the input admittance, $\tilde{Y}_{in}$ of the entire surface aperture can be calculated by discretizing the integral electric field term in (11) with $V_0 = 1\,\mathrm{V}$, yields:

$$\tilde{Y}_{in} = \left(\frac{2V_o}{\sum_{n=1}^{N} V_n \ln\left(\frac{\rho_n + \Delta\rho/2}{\rho_n - \Delta\rho/2}\right)} - 1 \right) \tag{17}$$

4. RESULTS AND DISCUSSION

In this work, the vector voltage, V_n on surface of aperture coaxial probe was simulated using $N = 10$ match points along the radius, ρ as depicted in Figure 2(a). The calculations assumed that the section of coaxial line ($a < \rho < b$) is filled with Teflon ($\varepsilon_c = 2.06$) and the value ratio of $b/a = 3.298$ with $a = 0.4545\,\mathrm{mm}$. In addition, the external dissipative medium at exterior region ($z' > 0$) was assumed to be methanol liquid and its dispersive properties obtained from Cole-Cole model with $\varepsilon_s = 33.7$, $\varepsilon_\infty = 4.35$, $\tau = 49.64\,\mathrm{ps}$ and $\alpha = 0.0426$.

From Figure 2(b), the radial electric field decay exponentially as expected with the radial distance ($E_\rho \propto 1/\rho$). The comparison between analytical and numerical results for the magnetic field, $H_\emptyset$ and electric field, E_ρ at 3 GHz are shown in Figures 3(a) and (b), respectively. The absolute values of $H_\emptyset$ and E_ρ were normalized with its own maximum values ($H_{\emptyset\,\max}$ and $E_{\rho\,\max}$) to facilitate the comparison. The calculation for $H_\emptyset$ and E_ρ using (4) and (5), respectively, were conducted by a 12×12-order Gaussian double integral method. Figure 3(a) shows the limitation of analytical calculation using (4) at aperture probe ($z = z' = 0$) and poor agreement with the numerical calcu-

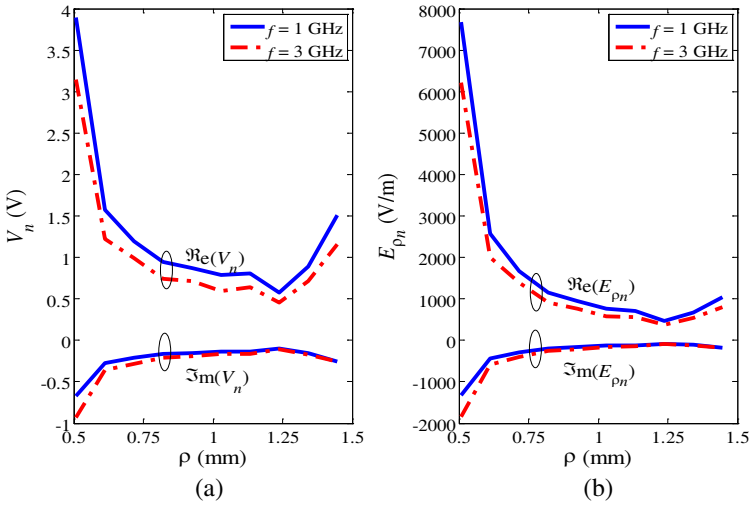

Figure 2: (a) The vector voltage, V_n and (b) vector electric field, $E_{\rho n}$ along the radius, ρ axis on surface aperture ($z = z' = 0$).

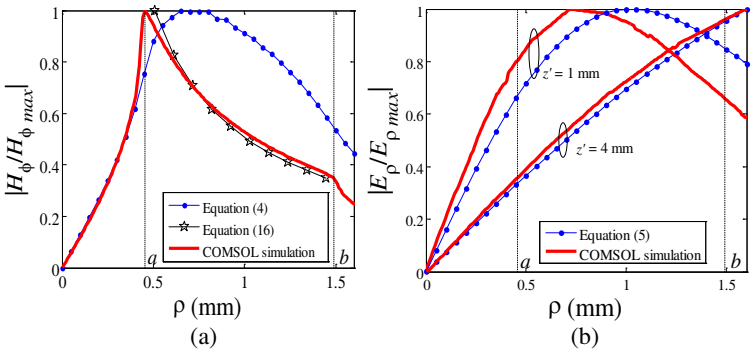

Figure 3: (a) The normalized absolute magnetic field versus radius, ρ axis on surface aperture ($z' = 0$). (b) The normalized absolute electric field versus radius, ρ on $z' = 1\,\mathrm{mm}$ plane and $z' = 4\,\mathrm{mm}$ plane (above the surface aperture).

lations [Equation (16) and COMSOL simulation]. From Figure 3(b), the analytical calculation of E_ρ using (5) was closed to the COMSOL simulation results when the observation plane moves far away from the aperture. It deduced that the Equation (5) is only suitable for far field observation.

The normalized input admittance, $\tilde{Y}_{in}$, is a complex number which can be separated into normalized values of conductance, $G(0)/Y_o$ and susceptance, $B(0)/Y_o$ as $\tilde{Y}_{in} = G(0)/Y_o + jB(0)/Y_o$. The comparison of calculated $G(0)/Y_o$ and $B(0)/Y_o$ using models [(8), (9), (17), and COMSOL simulation], and the simulation results for methanol are showed in Figures 4(a) and (b), respectively. The calculation for admittance in Equation (9) was conducted by a $5 \times 5 \times 7$-order Gaussian triple integral method, while Equation (8) was solved by the series expansion method with 9 terms of series [6]. Figures 4(a) and (b) clearly show good agreement for the $G(0)/Y_o$ and $B(0)/Y_o$ results which are obtained from Equation (17) and COMSOL simulation. The ignoring of TM_{0n} modes in (8) and (9) causes low accuracy of the analytical calculation results; however, it leads to a relatively simple mathematical solution.

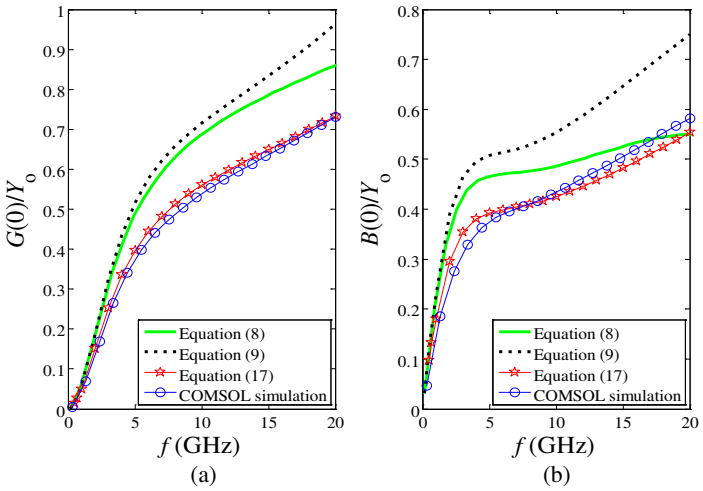

Figure 4: The calculated (a) normalized conductance, $G(0)/Y_o$ and (b) normalized suscepatnce $B(0)/Y_o$ for methanol at 25°C by considering size of probe with $b/a = 3.298$ and $a = 0.4545$ mm.

5. CONCLUSION

In this work, the coaxial probe has been used as an example of the electromagnetic field analysis, in order to link the analytical formulations with numerical solutions. The restrictions and limitations of analytical models for coaxial probe have been studied and the reasons for replacement of analytical method by a numerical method have been briefly discussed.

ACKNOWLEDGMENT

This study was supported by the Universiti Teknologi Malaysia and Ministry of Higher Education (MOHE) Malaysia under project number Q.J130000.2523.04H77.

REFERENCES

1. Levine, H. and C. H. Papas, "Theory of the circular diffraction antenna," *J. Appl. Phys.*, Vol. 22, 29–43, 1951.
2. Tsai, L. L., "A numerical solution for the near and far fields of an annular ring of magnetic current," *IEEE Trans. Antennas Propagat.*, Vol. 20, 569–576, 1972.
3. Harrington, R. F., "Matrix methods for field problems," *Proceedings of the IEEE.*, Vol. 55, 136–149, 1967.
4. Nevels, R. D., C. M. Butler, and W. Yablon, "The annular slot antenna in a lossy biological medium," *IEEE Trans. Microwave Theory Tech.*, Vol. 33, 314–319, 1985.
5. Misra, D., "A quasi-static analysis of open-ended coaxial lines," *IEEE Trans. Microwave Theory Tech.*, Vol. 35, 925–928, 1987.
6. You, K. Y., J. Salleh, M. F. A. Malek, A. Zulkifly, E. M. Cheng, and K. Y. Lee, "Modeling of coaxial slot waveguides using analytical and numerical approaches: Revisited," *International Journal of Antennas and Propagation.*, Vol. 2012, 1–12, 2012.

Time-frequency Spectrum and Path Loss by Wind Turbine Forward Scattering

M. B. Raza and T. Fickenscher
Helmut Schmidt University, Hamburg, Germany

Abstract— Diffraction loss and deviation of the Doppler spectrum caused by a wind turbine (WT) rotor is analyzed by using a one-dimensional Fresnel diffraction approach applied to the forward scattered signal. To characterize performance degradation of radar and communication systems by a WT, forward scatter path loss and the relative phase shift of the received signal are investigated. Theoretical results are verified by comparison with Uniform Theory of Diffraction (UTD) simulations obtained by FEKO. A joint time-frequency analysis is performed using Short Time Fourier Transform (STFT) to obtain localized time-dependent frequency information about the Doppler deviation.

1. INTRODUCTION

Serious concerns have been raised in recent years about the effects of the growing number of wind turbines on existing radio communication systems [1]. The performance of radar and communication systems can be significantly deteriorated owing to the interference caused by scattering, diffraction and near-filed effects of a nearby WT. Moreover, the rotating blades of the electrically large WT introduce a time variant deviation of the Doppler return, which can cause serious radar clutter problems. Most of the efforts to characterize the signal degradation caused by a WT have focused on the backscatter region [2], while the WT forward scatter investigations have concentrated mainly on the shadowing and range effects in the context of interference with radio and TV broadcast stations as well as with navigation systems and weather radars [3, 4].

In this paper we present an approximation for the calculation of the time variant diffraction induced path loss and phase modulation in the forward scatter region, if the line-of-sight path is obstructed by the rotor swept area of a WT. This scenario is particularly true for weather radars. A one-dimensional Fresnel diffraction approach is applied to a WT rotor in specular direction (head-on view along rotor axis). The rotor blades are assumed to be opaque. The time variant diffraction induced path loss and phase modulation are determined. These calculated values are then used for a time frequency analysis based on STFT to obtain the time variant deviation of the Doppler spectrum along with time-varying motion dynamic features of the received signal. For a radar system, the signal is diffracted twice at the WT blades. To account for the round trip, the one way path loss and phase modulation is multiplied by a factor of 2.

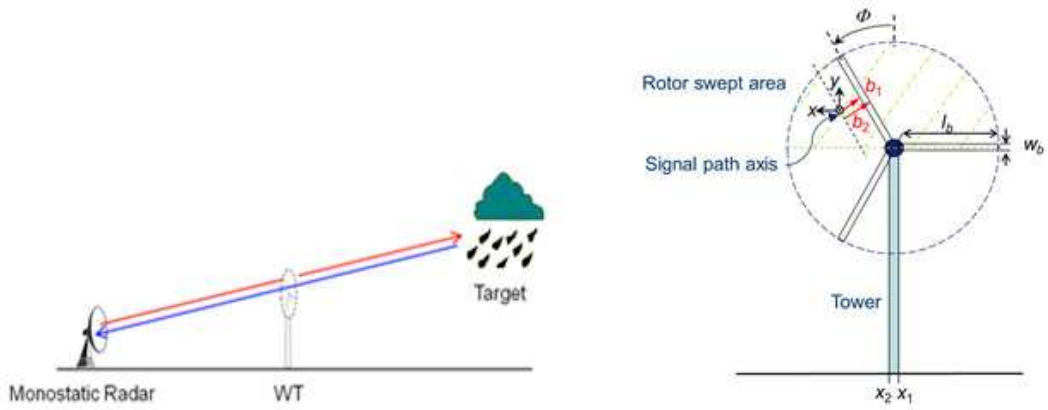

Figure 1: (a) WT obstructing a weather radar. (b) Plane of obstruction — WT in specular direction (head-on view along rotor axis. Shaded part represents the obstruction zone.

2. PATH LOSS AND TIME FREQUENCY SPECTRUM DETERMINATION

Figure 1(a) shows a WT obstructing a radio link. We assume the simplest interference scenario of a signal path cutting the plane of obstruction inside the upper half of rotor swept area (above nacelle) [5]. The signal is periodically obstructed by the rotating blades and hence a time variant Doppler deviation of the received signal is observed. The impact of the static WT tower is neglected. For the simplification of calculations, the blades are assumed to be of rectangular shape in the plane of obstruction. Furthermore, only a single blade with infinite length is considered for the aforementioned simplest interference scenario. We use a one dimensional Fresnel diffraction approximation along a horizontal axis perpendicular to the line-of-sight path (Figure 1(b), origin of x-and y-coordinate aligned with the axis of the signal path in the plane of obstruction) [6].

The amplitude of the electric field at a target located on the axis of the signal path is given by

$$E_p = \frac{E_u}{\sqrt{2}} \left\{ [C(\nu) - jS(\nu)]_{\nu_{b2}}^{+\infty} + [C(\nu) - jS(\nu)]_{-\infty}^{\nu_{b1}} \right\} \tag{1}$$

where E_u is the electric field amplitude at the target in the absence of the obstruction. C and S are the well-known Fresnel integrals. ν is a dimensionless aperture coordinate given as

$$\nu_{x1/2} = \left[-\sqrt{x_0^2 + y_0^2} \cdot \sin\left(\phi + \arctan \frac{x_0}{y_0} \right) \pm \frac{w_b}{2} \right] + \sqrt{\frac{2}{\lambda} \left(\frac{1}{d_1} + \frac{1}{d_2} \right)} \tag{2}$$

where d_1 is the distance between the radar site and the WT, d_2 is the distance between the WT and the target, λ is the wavelength of the radar signal, x_o and y_o are the coordinates at the rotor axis and w_b is the blade width. The + sign is applicable for v_1 and the − sign for v_2. A detailed description of this approach can be found in [7]. The results obtained are verified with 3D field solver using Uniform Theory of Diffraction (UTD) method and software package FEKO. The time frequency spectrum is obtained by the short time fourier transform (STFT) of the received time domain signal.

3. RESULTS AND DISCUSSION

The diffraction path loss is calculated at a frequency of 1.30 GHz, which is typically used for weather radars. The WT model used for this investigation has three blades, each with a length of 64 m. The width of the blade at the point where the signal path cuts through the plane of obstruction is assumed to be $w_b = 1.5$ m. A blade rotation speed of 15 rpm is assumed. The signal path is set to be 60 m above the rotor axis (close to the tip of the blade). The WT is at $d_1 = 500$ m away from the transmitter and the receiver is located at 8000 m ($d_2 = 7500$). The one way diffraction induced loss ($\Delta\alpha d$) and the phase shift ($\Delta\beta d$) at 1.3 GHz vs rotation angle Φ are shown in Figures 2(a) and (b). For a radar system, these values have to be multiplied by a factor of 2. For $\Phi = 0$ the upper blade is oriented vertically. At $\Phi = 60°$ this blade is as far from the axis of the signal path

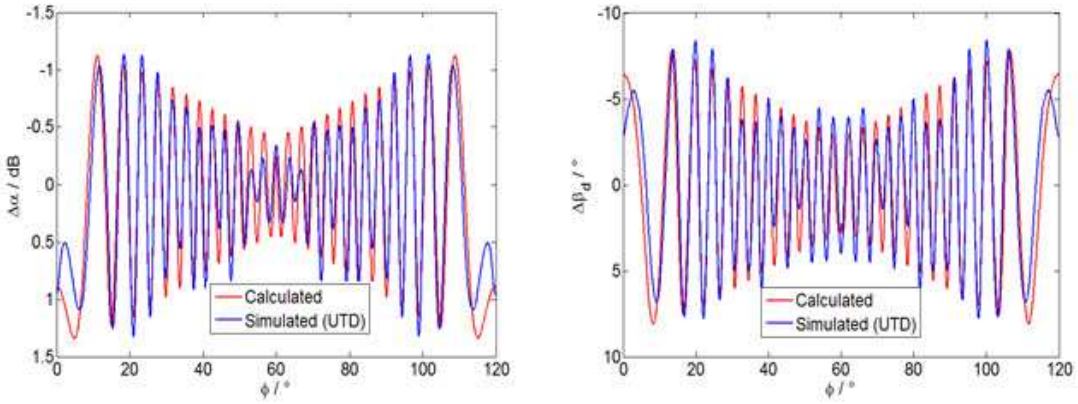

Figure 2: Impact of 3-blade rotor vs rotor angle Φ at 1.3 GHz: diffraction induced one way (a) loss and (b) phase shift for $d_1 = 500$ m and $d_2 = 7500$ m.

as the next blade following in clockwise direction. Thus, all graphs show an even symmetry along Φ for every 60°. The calculated values are verified by comparison with UTD simulation results obtained by software package FEKO.

The comparison in Figure 2 shows a slight disagreement between the calculated and simulated curves. This can be attributed to the scattering at the edges of the blade, which is not considered in our theoretical approach. Moreover, FEKO simulations are carried out with three rotor blades, whereas, the theoretical model only considers a single infinite long blade. At values of Φ around 60°, the next blade which is not considered in the theoretical model is approaching the line of sight and hence diffraction effects of both the blades appear to be significant rather than just the one accounted for. However, for most values of Φ, the two results agree with each other.

Figure 3 shows the maximum value of $\Delta\alpha_d$ for values of d_1 ranging from 500 m to 7500 m. The distance of the WT from the tranmistter (d_1) is varied keeping the overall link distance constant at $d_1 + d_2 = 8$ km. The lowest value of diffraction loss is observed when the WT is located midway between the transmitter and the receiver ($d_1 = d_2 = 4000$ m). As the location of the WT is moved closer to either the transmitter or the receiver, the diffraction loss starts to increase. Due to symmetry, d_1 and d_2 can be interchanged. This underlines the importance of keeping the WT considerably far from a communication system.

The Doppler deviation introduced by the rotating blades can be characterized by the time frequency spectrum of the received signal. A Hamming window of 256 samples for a sampling frequency of 1 kHz is used to obtain the STFT of the received time domain signal. Figure 4 shows the spectrum of the received signal ($d_1 = 500$ m, $d_2 = 7500$ m). For a rotational speed of 15 RPM, a single rotation of one blade is completed in 4 seconds. Noticeable sinusoidal tracks are visible. At low values of Φ, one blade is in close proximity to the line of sight, obstructing the first few Fresnel zones. This gives rise to a strong low frequency component. As the blade rotates, its distance from the signal axis increases and it is cutting through a higher order Fresnel zones at a given time span, introducing higher frequency components with a peak ocurring at $\Phi = 60°$. Beyond this angle, the next blade starts approaching the line of sight, moving towards Fresnel zones of larger sizes (lower order Fresnel zones) thus introducing more components of lower frequencies. Overall, a significant

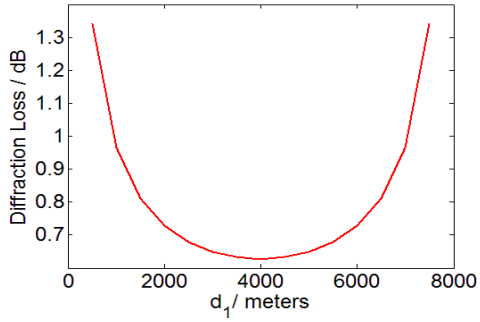

Figure 3: Variation of maximum one-way diffraction loss with changing values of d_1.

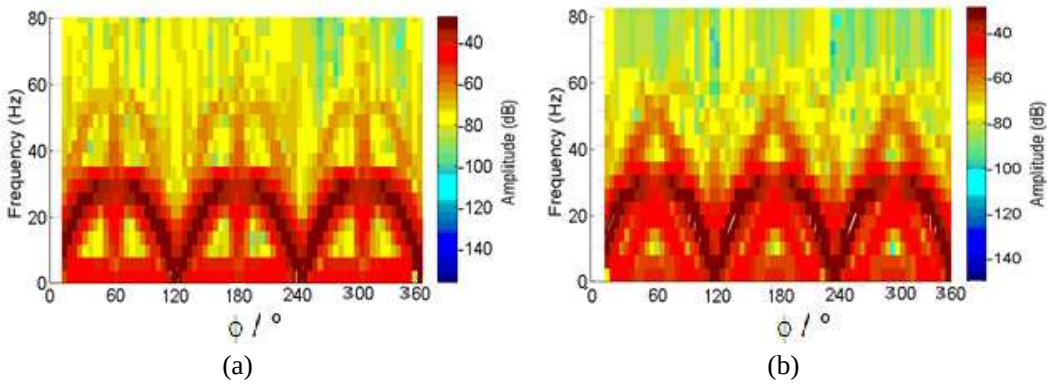

Figure 4: Two-Way Normalized time-frequency spectrum at 1.3 GHz for $d_1 = 500$ m and $d_2 = 7500$ m. (a) Calculated. (b) Simulated.

Doppler deviation of up to 55 Hz is observed. For a Doppler radar, this corresponds to a target velocity of 6.3 m/s. A weather radar, like all Doppler radars, relies on Doppler-shifted radar returns for the estimation of wind speed. Doppler deviation caused by WT blades will therefore lead to inaccurate wind measurements.

The investigations presented in this paper so far have ignored the ground plane effects. 3D radars like weather radars are less susceptible to the ground plane reflections, owing to their extremely narrow beams. However, the ground plane effects become significant for 2D radar systems and fixed radio links and hence must be taken into account. Figures 5(a) and (b) compare $\Delta\alpha_d$ and $\Delta\beta_d$ with and without the presence of a ground plane, for the same set of parameters described earlier. These values are obtained by UTD simulations. Higher values of $\Delta\alpha_d$ and $\Delta\beta_d$ are observed if the ground plane is accounted for. This results in an even stronger Doppler deviation compared to the case where the ground plane is neglected.

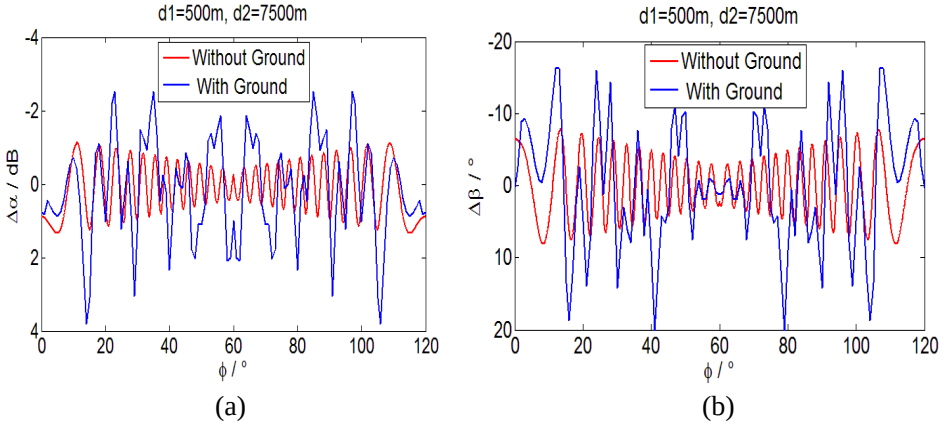

Figure 5: Impact of 3-blade rotor vs rotor angle Φ at 1.3 GHz, with and without ground plane: simulated diffraction induced (a) loss and (b) phase shift for $d_1 = 500$ m and $d_2 = 7500$ m.

4. CONCLUSIONS

One-dimensional Fresnel diffraction approach has been applied to calculate the impact of diffraction on the amplitude and phase of the WT forward scattered signal. Furthermore, deviation of the Doppler spectrum caused by the time variant amplitude and phase modulation of the two-way signal is presented. A joint time-frequency analysis of the diffracted signal has been performed using STFT to highlight the motion dynamic Doppler features. It has been demonstrated that a Doppler deviation of up to 55 Hz will occur in the forward scatter region for radars operating at 1.3 GHz. For the characterization of the WT forward scatter in the presence of a ground plane, a thorough investigation needs to be carried out by placing the WT at different locations along the radio link. Different transmitter and receiver orientations for varying antenna height and signal path also need to be considered for outlining the worst case scenario of WT interference. Moreover, the impact of multiple wind turbines has to be further investigated. An extension of the presented study has to be investigated.

REFERENCES

1. Poupart, J. M., "Wind farms impact on radar aviation interests final report," DTI PUB URN 03/1294, 2003.
2. Brenner, M., "Wind farms and radar," JSR-08-126, Prepared by the Mitre Corporation, Jan. 2008.
3. Chisholm, D., A. Tommy, and P. Curtis, "Project Hayes: Compatibility with radio services," Broadcast Communication Limited, Jul. 2006.
4. Randhawa, B. S. and R. Rudd, "RF measurement assessment of potential wind farm interference to fixed links and scanning telemetry devices," ERA Report No. 2008-0568 (Issue 3), Mar. 2009.
5. Fickenscher, T. and M. B. Raza, "Diffraction loss and phase modulation of terrestrial radio-link by wind turbine," *International Workshop on Antenna Technology 2014*, Sydney, Mar. 4–6, 2014.

6. Raza, M. B. and T. Fickenscher, "Radar Doppler deviation by wind turbine," *International Radar Symposium IRS 2014*, Gdansk, Jun. 16–18, 2014, in Press.
7. Pedrotti, F. L., L. M. Pedrotti, and L. S. Pedrotti, *Introduction to Optics,* 3rd Edition, PTR Prentice Hall Inc., New Jersy, USA, 2006.

Experimental the Microwave Absorption of Rice Husk/Ash Mixture

Y. S. Lee[1], **F. Malek**[2], **E. M. Cheng**[3],
Wei-Wen Liu[4], **N. A. C. Ali**[3], **F. H. Wee**[1],
M. N. Iqbal[1], **L. Zahid**[1], **F. S. Abdullah**[2], **and M. Othman**[2]

[1]School of Computer and Communication Engineering, Pauh Putra Campus
Universiti Malaysia Perlis (UniMAP), Arau, Perlis 02600, Malaysia
[2]School of Electrical Systems Engineering, Pauh Putra Campus
Universiti Malaysia Perlis (UniMAP), Arau, Perlis 02600, Malaysia
[3]School of Mechatronic Engineering, Pauh Putra Campus
Universiti Malaysia Perlis (UniMAP), Arau, Perlis 02600, Malaysia
[4]Institute of Nano Electronic Engineering (INEE)
Universiti Malaysia Perlis (UniMAP), Kangar, Perlis 01000, Malaysia

Abstract— This paper is to study the performance of rice husk and rice husk ash (RH-RHA) mixture material as a microwave absorber. The microwave absorption and dielectric properties, ε of RH-RHA mixture with different ratio were investigated in microwave frequency region 8.2 to 12.4 GHz (X-band). A waveguide transmission line method (Nicholson-Ross-Weir) was used to measure the complex permittivity of RH-RHA with different weight ratio mixture. The RH-RHA microwave absorbers were designed and simulated in CST-MWS. The various ratio RH-RHA mixtures show the different dielectric properties and the microwave absorption was investigated. The 60%RH-40%RHA microwave absorber has the best microwave absorption 46–76%.

1. INTRODUCTION

Rice is producing the crop in the form of rice husk (RH), where the rice husk ash (RHA) is the byproduct of RH that is obtained after burning rice husks in furnace or open air. Open air burning the RH at the paddy field causes environment pollution. The RH can be reused and applied in microwave absorber application [1–3]. The RH and RHA are lossy material due to their unique dielectric properties. The dielectric constant, ε_r' is the ability of a material to store electromagnetic wave [4–6]. The loss factor, ε_r'' is the ability of the material convert the electromagnetic wave into heat and dissipated [7, 8]. The dielectric properties of a material are important in microwave absorption. In this work, the RHA have been investigated as the material for the microwave absorbers. The microwave absorption of the rice husk and rice husk ash mixture (RHA) was investigated in various ratio mixtures.

2. EXPERIMENTAL

The raw RH and RHA were mixed with polyester and methyl-ketone-polymer. The RH and RHA were composites with different ratio. Table 1 shows the ratio of the RH and RHA composites. The RH was composite with difference amount of RHA from 20% to 60% of weight ratio.

Table 1: Rice husk/rice husk ash ratio (%total weight).

Sample code	Rice Husk (%)	Rice Husk Ash (%)
RA82	80	20
RA64	60	40
RA46	40	60

The fabricated samples were fabricated in a rectangular shape with 5 mm thickness which fit into the samples holder. Figure 1 shows the Fabricated samples and sample holder. The complex relative permittivity or dielectric properties ($\varepsilon_r = \varepsilon_r' - j\varepsilon_r''$) of RH-RHA composites were measured using rectangular waveguide and Agilent 85071E software over 8.2–12.4 GHz frequency range.

3. SIMULATION

The dielectric properties of the absorbing materials are the basic parameters. The results of different RH-RHA samples are simulated using Computer Simulation Technology (CST) Microwave Studio

(a) (b)

Figure 1: (a) Fabricated samples and (b) sample holder with sample.

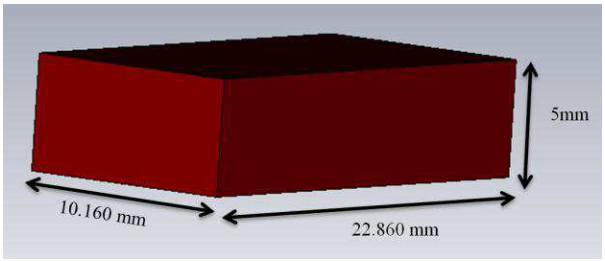

Figure 2: Samples dimension in CST.

software. Before simulate the result, the sample must be defined the dielectric constant and loss factor in CST-MWS over 8.2 GHz–12.4 GHz frequency range. In this simulation, the RH-RHA samples were simulated with metal backed plate. The RH-RHA microwave absorber has been designed and simulated in CST-MWS. The various ratio RH-RHA mixtures show the different dielectric properties and the microwave absorption. The microwave absorption was calculated by Equation (1) [9, 10];

$$A(\%) = \left[1 - (S_{11})^2\right] \cdot 100\% \tag{1}$$

where $A(\%)$ and S_{11} are the percentage of absorption loss and reflection loss. The microwave absorbers do not absorb any microwave the entire signal if the microwave absorber unable to absorb microwave and the $A \cong 0\%$. The performance of RH-RHA samples can obtained using CST microwave studio [11]. Figure 2 shows the sample dimension designed in CST microwave studio.

4. RESULTS AND DISCUSSION

4.1. Dielectric Propeties

The dielectric constant and loss factor result are shown in Figures 1(a) and (b). The various ratio RH-RHA mixtures show the different dielectric properties of RA82, RA64, and RA46. From Figures 1(a) and (b), the dielectric constant and loss factor were increased by increasing the ratio of RHA in the composition. For samples RA82, the values of dielectric constant and loss factor are 3.6–3.7 and 0.43–0.57 respectively. The dielectric constant and loss factor of samples RA64 is 3.7–4.2 and 0.57–0.65 respectively. The sample RA46 has the highest dielectric constant values 4.1–4.7 and 0.65–0.79 over 8.2–12.4 GHz frequency range.

When the ratio of RHA increase from 20% to 60%, the dielectric constant and loss factor

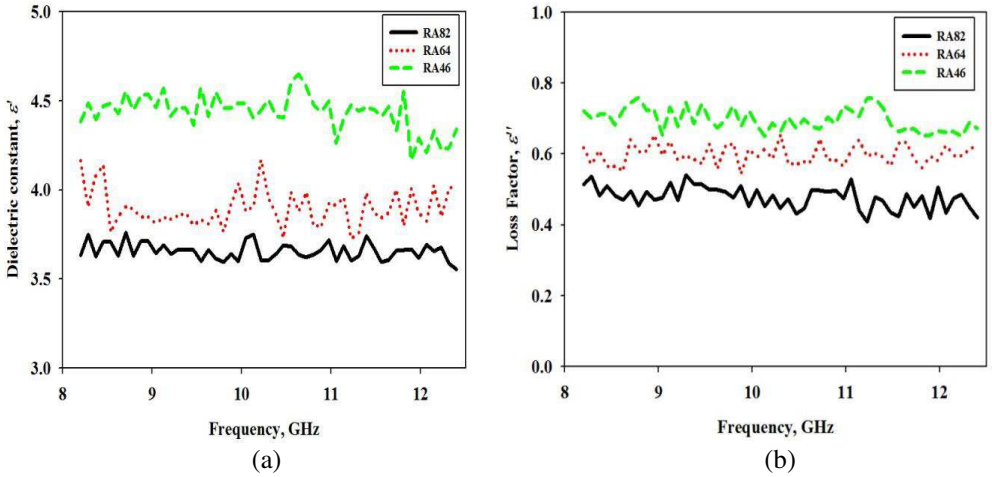

(a) (b)

Figure 3: (a) Dielectric constant and (b) loss factor of samples RA82, RA64, and RA46.

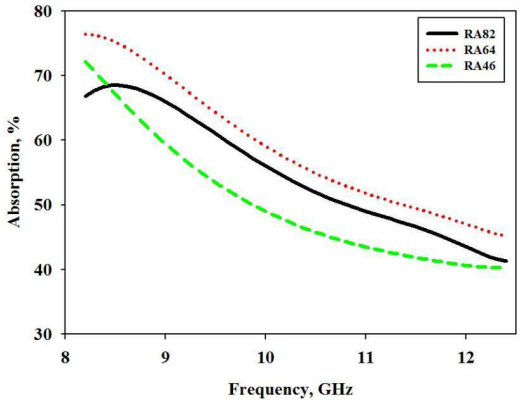

Figure 4: Percentage microwave absorption of RH-RHA samples.

increase from 3.6 to 4.7 and 0.43 to 0.79. The different ratio of RH-RHA samples has various values of dielectric properties.

4.2. Microwave Absorption

The RH-RHA samples was simulate in CST microwave studio to obtain the reflection loss (S_{11}). Then microwave absorption was calculated using Equation (1). Figure 4 shows the microwave absorption of RH-RHA samples.

The microwave absorption of RH-RHA samples were decreased with increasing the frequency. The RA82 sample microwave absorption 40–70% over 8.2–12.4 GHz frequency region. The microwave absorption of RA64 and RA46 are 40–73% and 46–76% respectively. The RA64 has the highest microwave absorption compare to RA82 and RA46. The highest absorption point of RA64 sample at 8.2 GHz with 76% microwave absorption. The average microwave absorption values of RA82, RA64, and RA46 are 54.92%, 58.74%, and 50.15% respectively over frequency region.

5. CONCLUSIONS

The various ratio RH-RHA composites have the different dielectric properties. The dielectric properties of RH-RHA samples were increased with the RHA amount increased in the composites ratio. The microwave absorption of RH-RHA samples with 5 mm thickness was decreasing with increasing the frequency. The RA64 microwave absorber has the best microwave absorption in 8.2–12.4 GHz frequency range.

ACKNOWLEDGMENT

The authors acknowledge the University Malaysia Perlis and the Malaysian Ministry of Higher Education for providing the Fundamental Research Grant Scheme (FRGS Grant No.: 9011-00011), which enabled the publication of this article.

REFERENCES

1. Iqbal, M. N., et al., "A study of the anechoic performance of rice husk-based, geometrically tapered, hollow absorbers," *International Journal of Antennas and Propagation*, Vol. 2014, 2014.
2. Nornikman, H., M. F. B. A. Malek, M. Ahmed, F. H. Wee, P. J. Soh, A. A. A.-H. Azremi, S. A. Ghani, A. Hasnain, and M. N. Taib, "Setup and results of pyramidal microwave absorbers using rice husks," *Progress In Electromagnetics Research*, Vol. 111, 141–161, 2011.
3. Nornikman, H., M. F. B. A. Malek, P. J. Soh, A. A. A.-H. Azremi, F. H. Wee, and A. Hasnain, "Parametric study of pyramidal microwave absorber using rice husk," *Progress In Electromagnetics Research*, Vol. 104, 145–166, 2010.
4. Du, Y., et al., "Pure carbon microwave absorbers from anion-exchange resin pyrolysis," *Synthetic Metals*, Vol. 160, 2191–2196, 2010.
5. Liao, Z., et al., "Absorption enhancement of fractal frequency selective surface absorbers by using microwave absorbing material based substrates," *Photonics and Nanostructures — Fundamentals and Applications*, Vol. 9, 287–294, 2011.

6. Chojnacki, E., et al., "Microwave absorption properties of carbon nanotubes dispersed in alumina ceramic," *Nuclear Instruments and Methods in Physics Research Section A: Accelerators, Spectrometers, Detectors and Associated Equipment*, Vol. 659, 49–54, 2011.
7. Sabouroux, P. and D. Ba, "Epsimu, a tool for dielectric properties measurement of porous media: Application in wet granular materials characterization," *Progress In Electromagnetics Research B*, Vol. 29, 191–207, 2011.
8. Lee, Y. S., M. F. B. A. Malek, E. M. Cheng, W. W. Liu, K. Y. You, M. N. Iqbal, F. H. Wee, S. F. Khor, L. Zahid, and M. F. B. Haji Abd Malek, "Experimental determination of the performance of rice husk-carbon nanotube composites for absorbing microwave signals in the frequency range of 12.4–18 GHz," *Progress In Electromagnetics Research*, Vol. 140, 795–812, 2013.
9. Bian, B.-R., et al., "A new triple-band polarization-insensitive wide-angle microwave metamaterial absorber," *Session 1PK*, 416, 2013.
10. Kung, P. and S. Kim, "Terahertz metamaterial absorbers for sensing and imaging," *Session 2A1. Manipulating Wave with Metamaterials and Photonic Crystal*, 148, 2013.
11. Lee, Y., et al., "An experimental thickness of microwave absorber effect absorption in Ku-band frequency," *2013 IEEE Symposium on Wireless Technology and Applications (ISWTA)*, 172–175, 2013.

The Performances of Sugarcane Bagasse (SCB) — Rubber Tire Dust Composite as Microwave Absorber in X-Band Frequency

Liyana Zahid[1], **Mohd Fareq Abd Malek**[2], **Ee Meng Cheng**[3], **Wei Wen Liu**[4], **Seng Yeng Lee**[1], **Muhammad Nadeem Iqbal**[1], **and Supri A. Ghani**[5]

[1]School of Computer and Communication Engineering, Pauh Putra Campus
Universiti Malaysia Perlis, Arau, Perlis 02600, Malaysia
[2]School of Electrical Systems Engineering, Pauh Putra Campus
Universiti Malaysia Perlis, Arau, Perlis 02600, Malaysia
[3]School of Mechatronic, Pauh Putra Campus
Universiti Malaysia Perlis, Arau, Perlis 02600, Malaysia
[4]Institute of Nano Electronic Engineering (INEE), Pauh Putra Campus
Universiti Malaysia Perlis, Arau, Perlis 02600, Malaysia
[5]School of Material Engineering, Pauh Putra Campus
Universiti Malaysia Perlis, Arau, Perlis 02600, Malaysia

Abstract— In this work, the performances which are the reflection loss and absorption for composite of sugarcane bagasse (SCB) and rubber tire dust as microwave absorber were investigated in the range frequency of 8.2–12.4 GHz (X-Band). Sugarcane bagasse (SCB) is one of the major agricultural wastes. This residue agricultural waste material has potential to be used as an alternative material for microwave absorber in Radio Frequency (RF) anechoic chamber. Rubber tire dust is one of the residues from tire wear. This paper shows the method about how the sample which is the composite of sugarcane bagasse with rubber tire dust was fabricated and the measurement to get the reflection loss (S_{11}) and transmission coefficient (S_{21}). The thickness of the sample is 5 mm. The methodologies included in this work are defining the dielectric properties and measurement of the samples using transmission line technique (waveguide). The dielectric constant, ε' from the transmission line measurement of the composite of sugarcane bagasse-rubber tire dust is 3.35. The S_{11} results showed that the SCB-rubber tire dust composite absorber was found to be better which means lower than -10 dB. The results proved that SCB-rubber tire dust was a good alternative to be used as microwave absorber. The goal of this investigation is to have the better electromagnetic reflection (S_{11}) which is less that -10 dB with the usage of the new agricultural waste such as sugarcane bagasse (SCB) and rubber tire dust. These can help save the nature and environmental friendly.

1. INTRODUCTION

Sugarcane bagasse, SCB is the byproduct from the production and processing of sugar cane (*Saccarhumofficinarum*) to produce sugar. In the SEM-EDS results for determination of carbon and silica content in sugarcane bagasse, it showed that sugarcane bagasse contained 9.78% of silica and 90.22% of carbon [1]. Carbon is one of the elements in a microwave absorber to absorb the unwanted microwave signal [2]. A radio frequency anechoic chamber is a shielded room whose walls have been covered with a material that can scatter and absorb the incident energy that can simulate free space. Recent innovations such as the used of ferrite tiles have greatly enhanced the performance of anechoic chamber [3]. So, this work which is the composite of sugarcane bagasse with rubber tire dust is one of the innovation to improve the performance of microwave absorber. Absorbers are the main components in anechoic chamber. They were functioning in eliminating the reflected signals [4]. Rubber tire dust is tire wear that are commonly composed of natural and/orsynthetic rubbers, carbon black, and extender oils, respectively, accounting for 40–60%, $\sim 30\%$, and 10–20% by mass [5].

2. METHODOLOGY

The methodology included in this work are fabricating the sample which is the composite of sugarcane bagasse with rubber tire dust, defining the dielectric properties consist of dielectric constant and loss factor and measurement of the samples using transmission line technique (waveguide technique). Before fabricating the samples, the sugarcane bagasses needed to be processed first. Then, the sugarcane bagasse will be mixed with rubber tire dust and turn them into composite form using mould. For two-port reflection/transmission measurement, the sample is placed between two

waveguides. In this work, the dielectric properties have been determined using Agilent 85071E Software. The measured reflection and transmission coefficients, S_{11} and S_{21} of samples were obtained from this transmission line technique measurement [6].

3. RESULT AND DISCUSSION

The electric permittivity and magnetic permeability are important factor in characterizing the microwave absorbers. The permittivity is a measure of the material's effect on the electric field in the electromagnetic wave. The quantity ε' is sometimes called the dielectric constant which is something of a misnomer when applied to absorbers as ε' can vary significantly with frequency. The quantity ε'' is a measure of the attenuation of the electric field cause by the material. So, the dielectric constant of materials such as sugarcane bagasse and rubber tire dust needed to be defined first. In this work, the transmission line technique has been used. In order to measure the reflection coefficient (S_{11}) and transmission coefficient (S_{21}), a section and part of the waveguide was filled in with the material sample [7–11]. Adequate sample thickness must be used in order to obtain an accurate measurement result.

3.1. Dielectric Constant and Loss Factor

Table 1 below shows the dielectric constant and loss factor of the two materials which are sugarcane bagasse and rubber tire dust in the range frequency of 8.2 to 12.4 GHz.

Table 1: Dielectric constant of sugarcane bagasse and rubber tire dust.

Material	Dielectric Constant, ε'	Loss Factor ε''
	8.2–12.4 GHz	
Sugarcane Bagasse (SCB)	2.66	0.29
Rubber Tire Dust	4.12	0.18

The overall dielectric constant for the rubber tire-dust sample for the entire X-Band frequency spectrum (8.2–12.4 GHz) was in the range of 3.4 to 4.2 which was greater than the range for the sugarcane bagasse material which is in the range of 2.6 to 2.9. This was due to the presence of the high dielectric constant material, that is, rubber, which is the major component in the tire dust. The higher value of the dielectric constant of the tire dust indicated that the signal was propagated at a slow speed due to the large refractive index of the medium [12]. Based on the result, the composite of sugarcane bagasse has high loss factor than other composite. In consideration of microwave absorption, the dissipation of energy in material is related to the imaginary part (ε'') [13].

3.2. Measurement of the Samples Using Transmission Line Technique

Figures 1(a) & (b) below showed the S_{11} and S_{21} for pure sugarcane bagasse and composite of SCB and RTD in range frequency of 8.2–12.4 GHz. Table 2 showed the average reflection loss and percentage of the microwave signal absorption.

In this work, the average reflection loss of sugarcane bagasse sample is 14.06 and the absorption is about 41.51%. Then, the next sample is fabricated in composite of sugarcane bagasse and rubber tire dust. The composition of sugarcane bagasse-rubber tire dust is 50 : 50 respectively. The average reflection loss for composite of SCB and RTD is 11.73. From the result, it shows

Table 2: Average reflection loss and absorption of sugarcane bagasse and composite of sugarcane bagasse with rubber tire dust.

Frequencies (GHz)	Pure Sugarcane Bagasse (SCB)		Composite of sugarcane bagasse with rubber tire dust	
	Average Reflection Loss (dB)	Absorption (%)	Average Reflection Loss (dB)	Absorption (%)
8.2–10.0	−15.00	34.47	−9.97	45.6
10.0–12.4	−13.35	46.04	−13.07	55.23
8.2–12.4	−14.06	41.51	−11.73	51.62

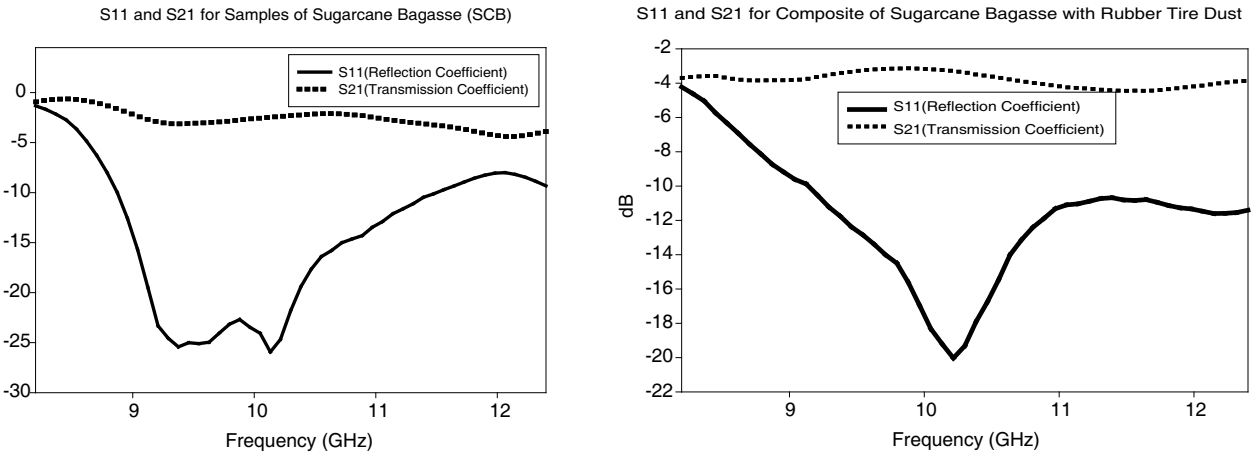

Figure 1: S_{11} and S_{21} for samples of sugarcane bagasse and composite of sugarcane bagasse with rubber tire dust.

that when sugarcane bagasse was added with rubber tire dust, it enhances the performance of the absorber which is 51.62% of absorption compare to pure sugarcane bagasse which is 41.51%. So, rubber tire dust can be a potential material to be added to sugarcane bagasse in fabricating the pyramidal microwave absorber.

4. CONCLUSION

Based on the reflection loss performance from the measurement using the transmission line technique, the sugarcane bagasse-rubber tire dust has the potential to be used as the alternative material in fabricating the microwave absorber. The main objectives of this research are to design, develop, fabricate and measure an efficient, environmental friendly and low cost pyramidal microwave absorber using agricultural waste such as sugarcane bagasse and rubber tire dust. By using the sugarcane bagasse, they can reduce the landfill waste and reduce the cost of production of the microwave absorber compared to use the existing expensive material such as polyurethane and polystyrene. The fabricated microwave absorber can operate successfully in the microwave range frequency 8.2 to 12.4 GHz.

REFERENCES

1. Daud, S., S. S. Salleh, M. N. Salleh, F. H. Kasim, and S. A. Saad, "Analysis of chemical composition in sugarcane bagasse and rice straw for their suitability using in paper production," *ICoSM*, 291–292, May 2007.
2. Ibrahim, I. M., N. M. Yaakob, M. N. Husain, S. M. Se, A. Shaaban, P. Pos, and D. Tunggal, "The effect of the carbon to the S_{11} measurement on the pyramidal microwave absorbers," *IEEE Symposium on Wireless Technology and Applications (ISWTA)*, Vol. 3, 141–145, 2011.
3. Dash, G. and A. LLC, "How RF anechoic work," alum.mit.edu, 1999.
4. Emerson and Cumming, "Data sheet of eccosorb VHP NRL pyramidal microwave absorber," 2008.
5. Kumata, H., "Evaluation of hydrogenated resin acids as molecular markers for tire-wear debris in urban environments," *Environ. Sci. Technol.*, Vol. 45, 9990–9997, 2011.
6. Agilent, Technologies Inc, "Agilent basics of measuring the dielectric properties of materials," 2006.
7. Al-Moayed, N. N., M. N. Afsar, U. A. Khan, S. McCooey, and M. Obol, "Nano ferrites microwave complex permeability and permittivity measurements by T/R technique in waveguide," *IEEE Transactions on Magnetics*, Vol. 44, No. 7, 1768–1772, 2008, doi:10.1109/TMAG.2008.920846.
8. Chung, B.-K., "Dielectric constant measurement for thin material at microwave frequencies," *Progress In Electromagnetics Research*, Vol. 75, 239–252, 2007.
9. Chung, B. K., "Aconvenient method for complex permittivity measurement of thin materials at microwave frequencies," *Journal of Physics D: Applied Physics*, Vol. 39, 1926–1931, 2006.

10. Iatrou, C. T. and M. Cavenago, "Field analysis of rectangular waveguide open junction," *IEEE Transactions on Microwave Theory and Techniques*, Vol. 45, No. 2, 165–172, 1997, doi:10.1109/22.557596
11. Sarabandi, K. and F. T. Ulaby, "Technique for measuring the dielectric constant of thin materials," *IEEE Transactions on Instrumentation and Measurement*, Vol. 37, No. 4, 631–636, 1988.
12. Lesurf, J., "Warp factor ε!," University of St. Andrews, 2006, http://www.st-andrews.ac.uk/∼www_pa/Scots_Guide/info/comp/passive/capacity/dielec/di_const/dicon.html.
13. NadeemIqbal, M., M. F. Malek, Y. Lee, L. Zahid, and M. S. Mezan, "A study of the anechoic performance of rice husk based, geometrically tapered, hollow absorbers," *International Journal of Antennas and Propagation*, Vol. 2014, 2014.

Study on the Relationship between the Size of Resin Sprue on GIS and Intensity of UHF Electromagnetic Waves Radiated from Partial Discharge

Xingwang Li[1], **Siyang Wu**[2], **Qizheng Ye**[2], **and Chu Yang**[2]

[1]Electric Power Research Institute of Guangdong Power Grid Corporation, Guangzhou 510600, China
[2]State Key Laboratory of Advanced Electromagnetic Engineering and Technology
Huazhong University of Science and Technology, Wuhan 430074, China

Abstract— Gas insulated switchgear (GIS) of different manufacturers have different sizes of resin sprues and the size of resin sprue has direct effects on the ultra high frequency (UHF) electromagnetic waves motivated by partial discharge (PD), which brings about many difficulties in accurate estimate of the severity of PD. On the platform of a 252 kV GIS, we used UHF sensors which were mounted on resin sprues of different sizes that had been set up in advance to detect electromagnetic wave signals emitted by a needle-plane PD model in GIS and found that with an increment of the length of resin sprue's long edge, the signal intensity enhances first and weakens later and reaches its maximum at 75 mm. Another simulation experiment which used pulse signal generator to provide excitation source for the transmitting antenna in GIS to simulate PD and detected signals in the same way to the former also found the same conclusion. This conclusion offers important references for the options of the optimal size of resin sprue and development of external UHF sensor.

1. INTRODUCTION

Gas insulated switchgears (GIS) are widely used as main switching equipment in the power system. Partial discharge (PD) reflects the insulation performance of GIS, which is not only the precursor of GIS internal defects but also leads to gradual insulation deterioration and eventual breakdown. As PD detection can discover the early defects in GIS, which provides a chance to take effective measures to prevent its development, it is remain the most important tool in dielectric detection and diagnosis for GIS equipment. In recent years, the ultra high frequency (UHF) method is becoming more and more popular for on-site PD detection of GIS, because of its features such as high sensitivity high S/N ratio and capacity of defect location and identification.

To make GIS enclosure reliable grounding and prevent the insulation material from chemical corrosion, most basin-type insulators of GIS are overlaid by metal ring. In this situation the UHF electromagnetic waves can only radiate from a rectangular hole on the metal ring, which is called the resin sprue since it is used to inject epoxy resin into basin-type insulator when it being manufactured. However, GIS of different manufacturers have different sizes of resin sprues and the size of resin sprue has direct effects on the UHF electromagnetic waves motivated by PD, which brings about many difficulties in accurate estimate of the severity of PD. So it is very necessary and urgent to study the effects of resin sprue and determine the optimal size for it.

Currently, some scholars have done some research into the issue of resin sprue and they derived some meaningful conclusions such as the propagation mode of UHF electromagnetic waves passing through the hole, the structure of electric filed on the surface of the hole and so on. However, there are few papers concentrating on the effects of resin sprue's size on the UHF electromagnetic waves.

On the platform of a 252 kV GIS, the authors accumulated a great number of data through a lot of experiments. On this basis, combining experiment results and simulation calculation, we focused our study on the relationship between the size of resin sprue and the intensity of UHF electromagnetic waves radiated form the hole. Then we drew a conclusion that offers important references for the options of the optimal size of resin sprue and development of external UHF sensor.

2. STRUCTURE OF RESIN SPRUE

GIS has fully enclosed metal structure and every basin-type insulator connects two adjacent gas tanks. Currently most basin-type insulators have their surfaces covered by metal rings, which are safely grounded and provide effective prevention from erosion and radiation. There is a small hole on each metal ring, as shown in Fig. 1. It's called the resin sprue since it is used to inject epoxy resin into the basin-type insulator when it being manufactured. The cross-section of the basin

sprue is rectangle with rounded corners and its size is different due to the different manufactures and voltage levels. For now the common sizes of the resin sprue are: depth: 25 mm, length of the long edge: 45 mm, length of the short edge: 20 mm.

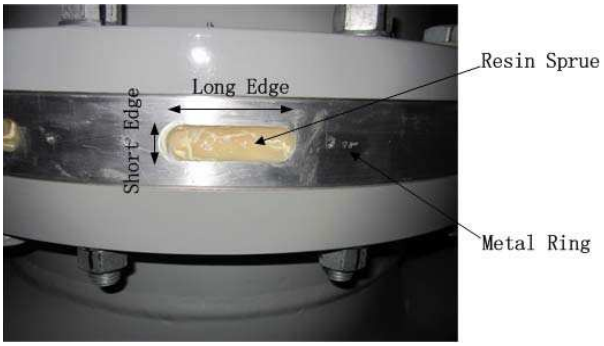

Figure 1: Rein sprue in the metal ring.

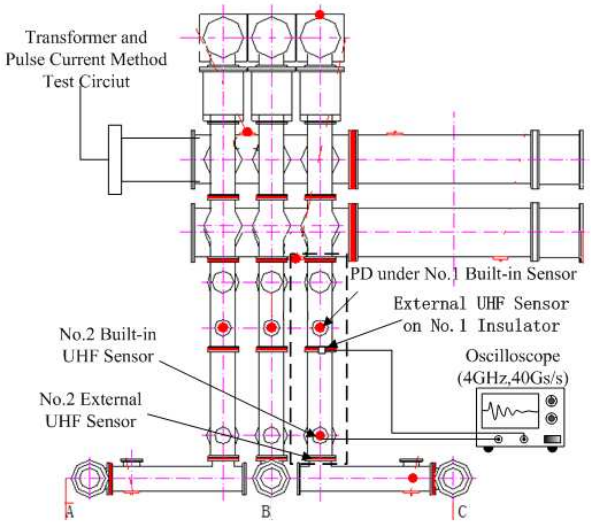

Figure 2: 252 kV GIS experiment platform (top view).

3. EXPERIMENTAL SETUP

The authors built up a 252 kV PD detection platform of UHF sensors, as shown in Fig. 2. The experiment was mainly carried out in two of the gas tanks in phase C of the GIS, which is in the box of dotted line in Fig. 2. Each of the basin-type insulator in phase C has 4 resin sprues of different sizes distributed along the circumference of it and the size of them were respectively 15 mm × 45 mm, 15 mm × 55 mm, 15 mm × 75 mm and 15 mm × 85 mm.

Given that the PD can't be very stable, which means even under the same voltage level PDs of same discharge quantity may excite UHF signals of different amplitude. In order to minimize the this factor's unfavorable effects, the experiment was taken as follows: the external sensor connected to an oscilloscope (4 GHz, 20 GS/s) through a power amplifier (Gain 20 dB) was fixed on the 4 resin sprues of different sizes on No. 1 basin-type insulator successively. Simultaneously the No. 2 built-in sensor was used as a reference sensor directly connected to the oscilloscope to check the results. Under a relative stable discharge quantity (with the voltage unchanged), the external sensor on each resin sprue and the built-in sensor collected at least 200 sets of data respectively. Then we averaged the data to reduce noises and divided the signal amplitude (that had been averaged) collected from the external sensors by signal amplitude (that had been averaged) collected from No. 2 built-in sensor to characterize the intensity of the UHF signals passing through the resin sprues. The external sensors we used were produced by DMS.

Figure 3: Needle-plane discharge model.

We applied power frequency voltage step by step at a needle-plane PD model set in the gas tank filled up with SF_6 gas (0.4 Mpa) to generate PD through a 550 kV gas-insulated transformer. The PD model, of which the PD quantities is under 30 pC, was mounted on the center conductor beneath No. 1 built-in sensor, as shown in Fig. 3.

4. EXPERIMENT RESULTS

4.1. Experiment Results Based on PD Model

After processing the experiment data according to the method mentioned early, we got the results shown in Fig. 5.

As is shown in Fig. 4, we can see that with the length of resin sprue's long edge increasing, the signal intensity enhances first and weakens later and reaches its maximum at 75 mm. The trend of the variation is independent of discharge quantity and the amplitude of UHF electromagnetic waves.

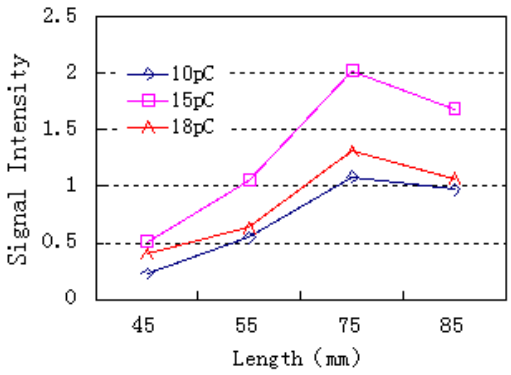

Figure 4: Signal intensity produced by the PD model for the different lengths of the long edge.

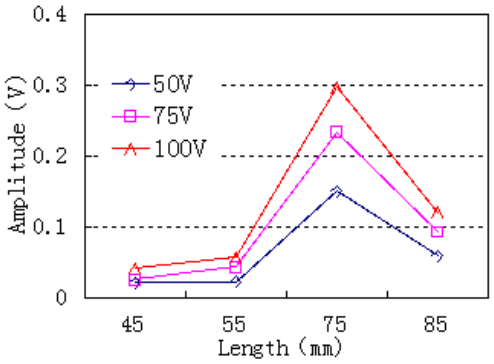

Figure 5: Signal intensity produced by the pulse injection for the different lengths of the long edge.

4.2. Experiment Results Based on Pulse Injection

In order to validate the accuracy of the experiment results, we conducted another set of experiments which used a pulse signal generator to provide excitation source for the transmitting antenna in GIS to simulate PD. As the pulse signals generated in this way is stable, we can minimize the accidental error and random interference to a great extent, which is more beneficial to study on the propagation characteristic of UHF electromagnetic waves passing through the resin sprue.

The rise time of the pulse was less than 0.3 ns and the output amplitude had three values which are 50 V, 75 V and 100 V. No. 1 built-in sensor was used as the transmitting antenna and two same external sensors — one was fixed on No. 1 basin-type insulator, the other on No. 2 basin-type insulator were used to collect UHF signals radiated from the resin sprues of different sizes. Under each output amplitude, each sensor collected at least 200 sets of data respectively. Then we averaged the data to reduce noises and the final results are shown in Fig. 5.

As is shown in Fig. 5, we can see that with the length of resin sprue's long edge increasing, the signal intensity enhances first and weakens later and reaches its maximum at 75 mm. The trend of the variation is independent of the output amplitude of the pulse and the distance between the excitation source and resin sprues.

The experiment results based on PD model and that based on pulse injection are consistent.

5. CONCLUSION

From this paper we could obtain a conclusion that with the length of the resin sprue's long edge increasing, the UHF signal intensity enhances first and weakens later and reaches its maximum at 75 mm.

For reason of the limited equipment condition, the resin sprues used in the experiment have only 4 sizes, thus leading to fewer points in the curves of the figure, which to some extent might affect

the accuracy of the curves and the reliability of the results. This is what should be improved and overcame in the future work.

REFERENCES

1. Kreuger, F. H., "Partial discharge detection in high-voltage equipment," 1989.
2. Pearson, J. S., O. Farish, B. F. Hampton, et al., "Partial discharge diagnostics for gas insulated substations," *IEEE Trans. on Dielectrics and Electrical Insulation*, Vol. 2, No. 5, 893–905, 1995.
3. Judd, M. D., O. Farish, and B. F. Hampton, "The excitation of UHF signals by partial discharges in GIS," *IEEE Trans. on Dielectrics and Electrical Insulation*, Vol. 3, No. 2, 213–228, 1996.
4. Cleary, G. P. and M. D. Judd, "UHF and current pulse measurements of partial discharge activity in mineral oil," *IEE Proceedings — Science, Measurement and Technology*, Vol. 153, No. 2, 47–54, 2006.
5. Meijer, S. and J. J. Smit, "UHF defect evaluation in gas insulated equipment," *IEEE Trans. on Dielectrics and Electrical Insulation*, Vol. 12, No. 2, 285–296, 2005.
6. Okabe, S., T. Yamagiwa, and H. Okubo, "Detection of harmful metallic particles inside gas insulated switchgear using UHF sensor," *IEEE Trans. on Dielectrics and Electrical Insulation*, Vol. 15, No. 3, 701–709, 2008.
7. Kurrer, R. and K. Feser, "The application of ultra-high-frequency partial discharge measurements to gas-insulated substations," *IEEE Transactions on Power Delivery*, Vol. 13, No. 3, 777–782, 1998.
8. Judd, M. D. and O. Farish, "A pulsed GTEM system for UHF sensor calibration," *IEEE Transactions on Instrumentation and Measurement*, Vol. 47, No. 4, 875–880, 1998.
9. Tang, J., Z. Xu, X. Zhang, et al., "GIS partial discharge quantitative measurements using UHF microstrip antenna sensors," *IEEE Annual Report-Conference on Electrical Insulation and Dielectric Phenomena, 2007, CEIDP 2007*, 116–119, 2007.
10. Tang, J., G. Wei, C. Sui, et al., "Research on the dipole antenna sensor with broadband for partial discharge detection in GIS," *High Voltage Engineering*, Vol. 30, No. 3, 29–31, 2004 (in Chinese).
11. Yan T., H. Zhan, S. Zheng, et al., "Study on the propagation characteristics of partial discharge electromagnetic waves in 252 kV GIS," *2012 IEEE International Conference on Condition Monitoring and Diagnosis (CMD)*, 685–689, 2012.
12. Lu, Q., S. Zheng, and X. Li, "Study on propagation characteristics of UHF signal via hole of GIS metal flange and development of external radiating antenna," *Power System Technology*, Vol. 37, No. 8, 2303–2309, 2013.
13. Wang, L., S. Zheng, C. Li, et al., "Distribution of electric field strength and spectral characteristic of UHF signal of partial discharge inside GIS at resin sprue of metal ring," *Power System Technology*, Vol. 1, 2014.
14. Pearson, J. S., "Partial discharge diagnostics for gas-insulated substations," *IEEE Trans. on D & EI*, Vol. 2, No. 5, 893–905, 1995.
15. Sellars, G., B. F. Hampton, and O. Farish, "Identifying the streamerleader transition in SF_6 using the UHF technique," *Proceedings of the 8th ISH*, 279–282, Yokohama, Japan, 1993.
16. Hampton, B. F. and R. J. Meats, "Diagnostic measurements at UHF in gas insulated substations," *IEEE Proceedings*, Vol. 135, No. 2, 137–145, 1988.
17. Judd, M. D. and O. Farish, "Transfer functions for UHF partial discharge signals in GIS," *11th-ISH. [S.l.]*, Vol. 5, 74–77, 1999.
18. Celozzi, S., G. Lovat, and R. Araneo, *Electromagnetic Shielding*, 35–36, John Wiley & Sons, Inc., 2008.

Printed Inverted-F MIMO Antenna for TD-LTE Mobile Terminal

Hui Liu[1, 2], **Youhuan Guo**[1], **Te Pan**[2], **Zhibin He**[2], **and Sailing He**[2, 3]

[1]Computer Science and Engineering Department, Guangdong Peizheng College, Guangzhou, China
[2]Centre for Optical and Electromagnetic Research, Academy of Advanced Optoelectronics
South China Normal University, Guangzhou, China
[3]The Royal Institute of Technology, Stockholm, Sweden

Abstract— With the rapid growth and development of the mobile communication technologies in recent years, many mobile communication technologies appeared one after another, of particular concern is 3GPP long term evolution (LTE). TD-LTE is growing rapidly in China and is also widely considered in the forth generation (4G) mobile communication now. MIMO technology, which utilizes multiple antenna to improve spectrum efficiency and increase the system channel capacity, is one of the 4G key technologies.

In this paper a MIMO antenna, operating on TD-LTE frequency band for TD-LTE mobile terminal is designed. The proposed MIMO antenna consists of two modified IFA structures has the advantage of compact structure and multiband for 4G handheld devices. The antenna designed to cover the TD-LTE frequency band of 1880 −1900 MHz and 2575–2635 MHz for China Mobile. The simulated and test results show that the isolation and S_{11} parameters of the proposed MIMO antenna can meet TD-LTE mobile communication requirements.

1. INTRODUCTION

The 4th generation in the wireless evolution is called the Long Term Evolution (LTE) which will provide higher peak data rates, higher spectral efficiency and lower latency taking advantage of the latest enabling technologies such as Orthogonal Frequency Division Multiple Access (OFDMA), Adaptive modulation and coding (AMC) and Multiple-Input Multiple-Output (MIMO) technologies.

The 1.8 GHz and 2.6 GHz band is used for China Mobile's LTE systems in mainland China. Due to the small size of LTE mobile terminal, the design of Multiple-Input Multiple-Output (MIMO) antenna with broadband or multiband on small handsets is a real challenge. And due to the integration of multiple antennas on a single portable device with very limited space, mutual coupling between multiple antennas is severe, and the MIMO antenna for mobile terminal systems with high isolation is of great importance to bring 4G capabilities to reality.

Many printed MIMO antennas have been discussed in literature recently. In [1], a compact planar MIMO antenna system of four elements is proposed for the whole 2.4-GHz WLAN band. Two types of antenna elements printed on different sides of the substrate are used in the structure for better isolation performance. In addition, a series of slits etched in the ground plane is proposed to improve the mutual coupling. In [2], a modified PIFA antenna by adding a proper chip capacitor was designed to enhance the lower band and by adding a shorted strip or forming a coupled section to enhance the upper band. In [3], by adding the two parasitic monopoles, the mutual coupling is greatly improved, meanwhile, the bandwidth increases somewhat. In [4], a penta-band CRLH-based antenna was designed and integrated into a cellular handset. The measured results demonstrated that the proposed CRLH-based antenna had superior performance and smaller size compared to other conventional antenna designs.

In this article, we proposed a modified IFA antenna printed on one top layer of a 0.6 mm thick with the FR4 substrate and the dielectric constant of 4.5. The antenna was designed to cover the low band and upper band of TD-LTE for mobile terminals.

2. ANTENNA DESIGN

The basic antenna element has the shape of English character F, and hence it is called inverted-F antenna. The print IFA is a new different antenna based on the basis of monopole antenna with a short-circuit line, so the transmission line theory of the original model must be modified [5–9]. The print IFA can be similar to a transmission line which is shorted in one end and which is opened in a nother. It can be modeled by the equivalent circuit method.

The geometry and photo of the proposed MIMO antenna for mobile terminals is shown in Fig. 1. The antenna consisted of two elements were placed in the right and left corners of a PCB with a volume of 69 mm ∗ 69 mm ∗ 0.6 mm.

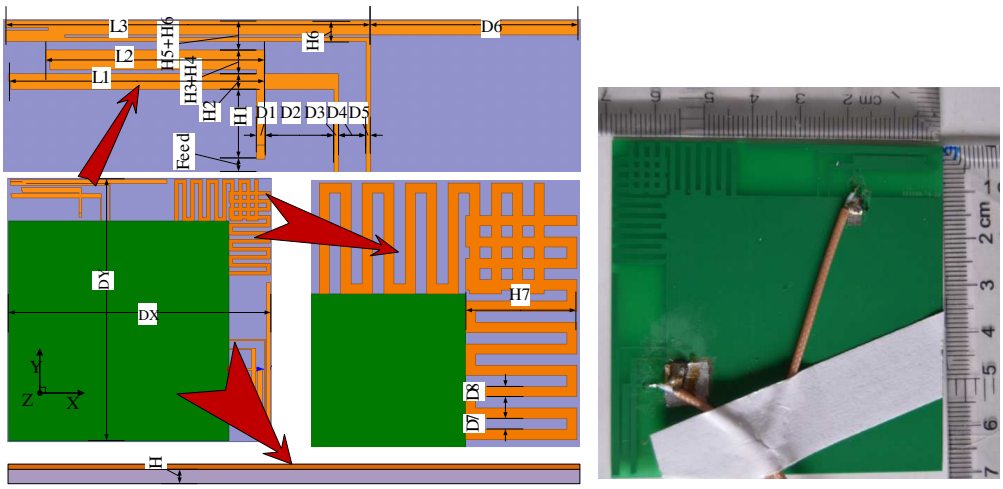

Figure 1: (a) MIMO antenna model. (b) Photo of MIMO antenna.

The traditional inverted-F antenna covers only one frequency band and it should be modified to have multiband frequency band-with. In order to get the dual band performance of each MIMO antenna element, a branch with the length of $L2$ was used to get another band. The modified inverted-F antenna with two radiation arm can provide two resonating path, but it is difficult to get a wide upper band (2.6 GHz) of TD-LTE. To deal with this problem, a parasitic element with a length of $L3$ was introduced to increase the upper band-with. The dimensions of the basic antenna element are (in millimiters) shown in Table 1.

Table 1: Comparison between the perfusion coefficient (B) for the different tissues.

$D1$	$D2$	$D3$	$D4$	$D5$	$D6$	$D7$	$H1$	$H2$	$H3$	$H4$
0.6	5	0.3	2	0.3	15	1	5	1.1	0.3	1.4
$H5$	$H6$	$H7$	$L1$	$L2$	$L3$	F	H	DX	DY	
0.6	1.5	1.9	17.7	14.9	26	1	0.6	69	69	

For the design of a compact MIMO antenna, coupling among antenna elements can no longer be neglected because antenna elements are closely spaced in a limited room, and the displacement between antennas will be influenced both in space diversity and in induced pattern diversity. We proposed two methods to reduce the mutual coupling of the MIMO antenna. The firs method is the use of ground elements. The second method is layout of two antenna element with different places.

3. RESULTS AND DISCUSSION

The commercial software HFSS and CST was used for the simulation of the MIMO antenna model. The simulated and measured S-parameters are showed in Fig. 2. As shown in Fig. 2, we can see that both of simulation and measured results are in agreement.

The simulated of 3D farfeild radiation patterns are shown in Fig. 3, antenna 1 with lumport 1 is shown in the up corner of the model, antenna 2 with lumport 2 is shown in the low corner.

The correlation coefficient (ρ) is a measure that describes how much the communication channels are isolated or correlated with each other. This metric considers the radiation pattern of the antenna system, and how much the patterns affect one another when operated simultaneously. The square of the correlation coefficient is known as the envelop correlation coefficient. The envelop correlation

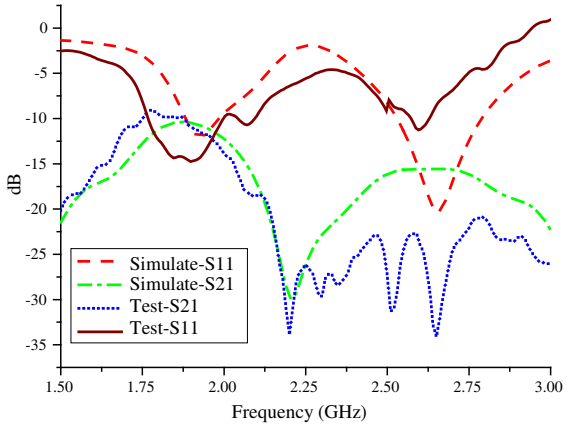

Figure 2: S-parameters.

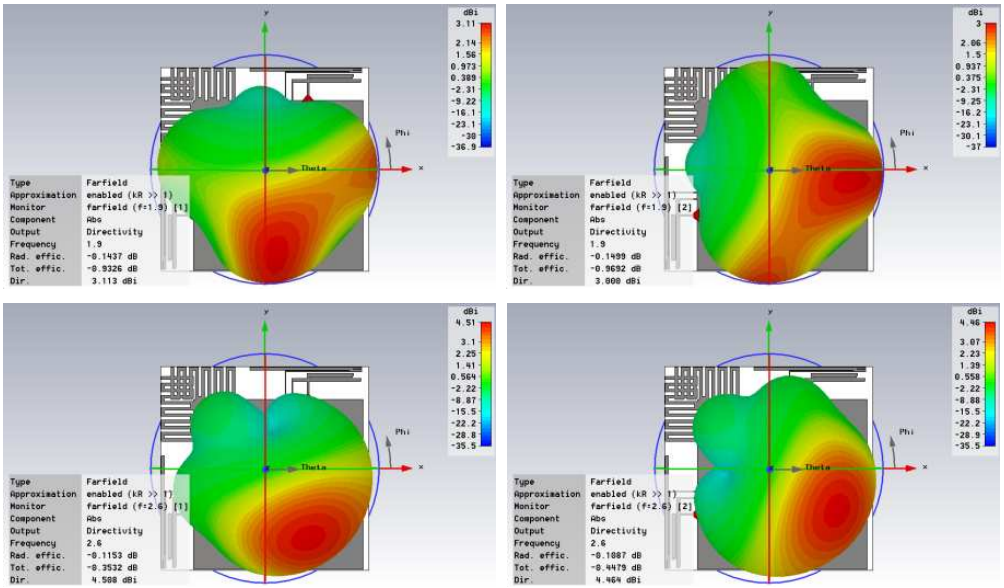

Figure 3: 3D radiation patterns.

coefficient (ρ_e) can be calculated using the following formula [10].

$$\rho_e = \frac{\left|\iint_{4\pi}\left[\vec{F}_1(\theta,\varphi) * \vec{F}_2(\theta,\varphi)\right] d\Omega\right|^2}{\iint_{4\pi}\left|\vec{F}_1(\theta,\varphi)\right|^2 d\Omega \iint_{4\pi}\left|\vec{F}_2(\theta,\varphi)\right|^2 d\Omega}, \tag{1}$$

where $\vec{F}_i(\theta,\varphi)$ is the three-dimensional field radiation pattern of the antenna when the i port is excited, and Ω is the solid angle. The asterisk is the Hermitian product operator. This is a complicated expression that requires three-dimensional radiation-pattern measurements and numerical integration.

The correlation coefficient can be calculated using the S parameters for simple in [11, 12] when a lossless and single-mode antenna is considered. The formula with S parameters only is given by

$$\rho_{eij} = |\rho_{ij}|^2$$

where

$$\rho_{ij} = \frac{S_{ii}^* S_{ij} + S_{ji}^* S_{jj}}{\sqrt{\left(1 - |S_{ii}|^2 - |S_{ji}|^2\right)\left(1 - |S_{jj}|^2 - |S_{ij}|^2\right)}} \tag{2}$$

As shown in Fig. 4, the radiation-pattern-based ECC of the proposed MIMO antenna has the ECC of below 0.05 in both lower and higher frequency bands. The modified inverted-F antenna with

compact size and dual band frequency is suitable to be an antenna element of MIMO antenna for TD-LTE.

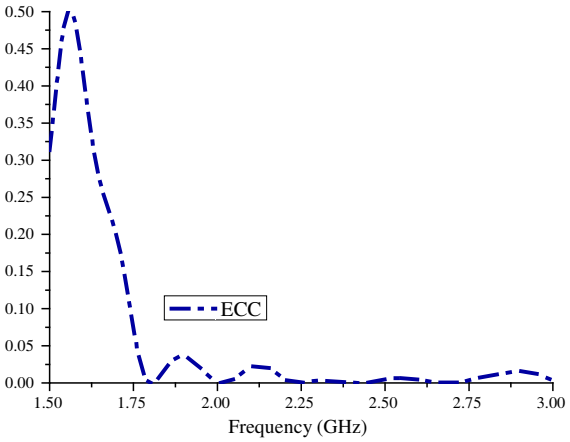

Figure 4: ECC.

4. CONCLUSION

The small printed inverted-F antenna (IFA) for LTE system, near the band-with 1800 MHz and 2.6 GHz, has been studied in this paper. The small antenna can be used in other frequency band wireless communication system such as 3G. It is very convenient and quickly to design this kind of antenna, more over, this kind of antenna designed in the experiment can be easily mass-fabricated with low production cost.

ACKNOWLEDGMENT

This work was supported by the Guangdong Peizheng College Key Research Program (No. 14pzxmy b013 and No. 14pzxmzd02), the partial support of Guangdong Innovative Research Team Program (No. 201001-D0104799318), the National High Technology Research and Development Program (863 Program) of China (No. 2012AA030402).

REFERENCES

1. Li, H., J. Xiong, and S. He, "A compact planar MIMO antenna system of four elements with similar radiation characteristics and isolation structure," *IEEE Antennas and Wireless Propagation Letters*, Vol. 8, 1107–1110, 2009.
2. Wong, K.-L., H.-J. Jiang, and T.-W. Weng, "Small-size planar LTE/WWAN antenna and antenna array formed by the same for tablet computer application," *Microwave and Optical Technology Letters*, Vol. 55, No. 8, 1928–1933, Aug. 2013.
3. Li, Z., Z. Du, and M. Takahashi, "Reducing mutual coupling of MIMO antennas with parasitic elements for mobile terminals," *IEEE Transactions on Antennas and Propagation*, Vol. 60, No. 2, 473–481, Feb. 2012.
4. Lee, C.-J., W. Huang, A. Gummalla, and M. Achour, "Small antennas based on CRLH structures: Concept, design, and applications," *IEEE Antennas and Propagation Magazine*, Vol. 53, No. 2, 11–25, Apr. 2011.
5. Zhu, Q., K. Fu, and Y. Li, "The analysis of planar inverted-F antennas with equivalent models," *Journal of University of Science and Technology of China*, Vol. 35, No. 2, 144–147, Apr. 2005.
6. Gallo, M., O. Losito, V. Dimiccoli, D. Barletta, and M. Bozzetti, "Design of an inverted F antenna by using a transmission line model," *Proc. Proceedings of the 5th European Conference on Antennas and Propagation, (EUCAP)*, 635–637, Apr. 2011.
7. Jung, J., H. Lee, and Y. Lim, "Modified meander line monopole antenna for broadband operation," *Electronics Letters*, Vol. 43, No. 22, 508–510, 2007.
8. Misman, D., I. A. Salamat, M. F. Abdul, et al., "The effect of conductor line to meander line antenna design," *Proc. Antennas and Propagation Conference, (LAPC)*, 17–18, Mar. 2008.
9. Khaleghi, A., "Dual band meander line antenna for wireless LAN communication," *IEEE Transactions on Antennas and Propagation*, Vol. 55, No. 3, 1004–1009, 2007.

10. Sharawi, M. S., "Printed multi-band MIMO antenna systems and their performance metrics," *IEEE Antennas and Propagation Magazine*, Vol. 55, No. 5, 218–232, Oct. 2013.
11. Blanch, S., J. Romeu, and I. Corbella, "Exact representation of antenna system diversity performance from input parameter description," *IET Electronic Letters*, Vol. 39, No. 9, 705–707, May 2003.
12. Hallbjorner, P., "The significance of efficiencies when using S-parameters to calculate the received signal correlation from two antennas," *IEEE Antennas and Wireless Propagation Letters*, Vol. 4, 97–99, 2005.

Compact Circularly Polarized RFID Tag Antenna with an Embedded U-shaped Feedline for Metallic Surfaces

Te Pan[1], **Shuai Zhang**[2], **Zhibin He**[1], **Hui Liu**[1], **and Sailing He**[1, 2]

[1]Centre for Optical and Electromagnetic Research
Academy of Advanced Optoelectronics, South China Normal University, Guangzhou, China
[2]The Royal Institute of Technology, Stockholm, Sweden

Abstract— A passive radio frequency identification (RFID) tag antenna with circular polarization (CP) radiation is proposed to operate at 902–928 MHz and mount on metallic surfaces. A U-shaped terminal short-circuited feedline welded to a tag-chip is embedded in a rectangular slot to achieve a coupled feeding and a good impedance matching. By employing two truncated corners and two L-shaped slots with unequal length on the patch, a good left-hand circular polarization (LHCP) and compact size are obtained. The measured impedance bandwidth of the antenna is 85 MHz (875–960 MHz), while the simulated 3-dB CP bandwidth is 6 MHz (912–918 MHz). The proposed tag antenna shows reasonable read ranges when mounted on the metal plate in the following experiment.

1. INTRODUCTION

In commercial applications of UHF band RFID, most reader antennas are design as circular polarization (CP) for increasing the diversity of orientation, while the majority of tag antennas are designed as linear polarization (LP) [1, 2]. Under this circumstance, the mismatch of polarization will happen and cause unwanted loss of power transmission between reader and tag. Owing to the tag-chip is designed with capacitive input impedance, the conjugate impedance matching should be acquired between the chip and tag antenna to achieve the maximum read range of the tag. Nowadays, lots of commercial sectors also demand the tag antenna with the ability to mount on metallic surface [3]. In general, it is a challenge to design a metal-mountable tag antenna with CP, in the meanwhile, has a simple method to fulfill the complex impedance matching.

Up to now, some works [4–6] are proposed to overcome the mentioned challenges. In [4–6], they all introduce a good technique to attain the CP, impedance matching and an excellent performance when the tag antenna is mounted on metallic plates. But their feedlines occupy some redundant area outside the radiator and cause asymmetries in these antenna structures. This will bring an increase of the overall size (the size of antenna top layer metallization) and a reduction of the antenna gain in the boresight direction.

To reduce the overall size and achieve a good impedance matching, we propose a compact CP RFID tag antenna with a U-shaped terminal grounded feedline embedded in a rectangular slot for application of metal-mountable. The 3-dB CP bandwidth of 6 MHz is accomplished by etching on the patch with two truncated corners and two L-shaped slots of unequal lengths. By tuning the diagonal truncations and the two L-shaped slots, a good CP is realized. The rectangular slot and the L-shaped slot also help to obtain a compact patch size. The tag shows a good performance of read range when it is mounted on metals.

2. ANTENNA STRUCTURE AND DESIGN

The geometry is shown in Fig. 1. The substrate we used is FR4 (relative permittivity of 4.4, loss tangent of 0.02) with a thickness of $h = 1.6$ mm. The two L-shaped slotswith the same width of 1.5 mm, length of S_1, S_2 respectively and the truncated corners are etched on the $60 \times 60\,\text{mm}^2$ radiating patch to produce CP. The ground plane size is $85 \times 85\,\text{mm}^2$ and the operating frequency band is set to 902–928 MHz. A terminal grounded U-shaped feedine, with a width equal to 1.7 mm and a coupling distance of $D = 1$ mm, is embedded in the rectangular slot ($S_W = 30$ mm, $S_L = 15$ mm) to capacitively excite the patch. The impedance of the welded Monza4 tag chip ($11 + j143\,\Omega$ at 915 MHz, threshold power $Pth = -17.4$ dBm) is also matched by the feedine. In the view of the theory of short-circuited transmission line from [7], the total length of the feedline should be set to 27.9 mm to get reactance of 143 jΩ by applying the following formula (1):

$$143 = Z_0 \tan\left[\frac{2\pi}{\lambda}(L_1 + L_2)\right] \tag{1}$$

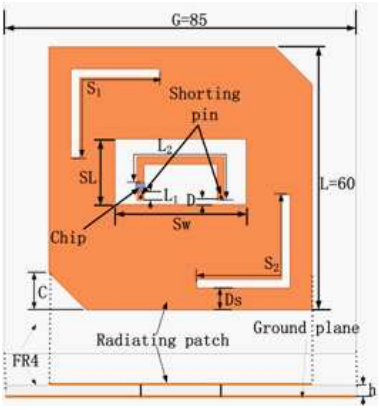

Figure 1: The geometry of the proposed circularly polarized patch tag antenna (unit: mm).

In the formula, the feedline width of 1.7 mm determines the characteristic impedance Z_0, and λ means the guided wavelength at 915 MHz. Considering the electromagnetic coupling effect [8], the feed line length should be slightly tuned to 37.7 mm to ensure the antenna impedance be close to $11 + 143j\Omega$ at 915 MHz. Table 1 shows the detailed dimensions of the designed antenna.

Table 1: Optimized design parameters of the antenna (Unit: mm).

D_s	L_1	L_2
15.1	18	3
C	S_1	S_2
8.5	33.6	35.6

3. RESULTS AND DISCUSSIONS

In this paper, the ANSYS HFSS is applied to accomplish the work of simulation and optimization. The impedance bandwidth of our RFID tag antenna is defined by the power reflection coefficient (PRC) $\Gamma < -3$ dB [9]. The input impedances are successfully measured by using the method of [10], with a four-port VNA (Agilent N5247A) and a test fixture. Fig. 2 shows the input impedances from measuring and simulating and the corresponding PRC chart respectively. As the condition of impedance matching is mainly decided by the reactance matching, so the measured results are actually fitting well with the simulated ones. In fact, as compared with the simulation, the measured 3 dB PRC shows a better bandwidth of 85 MHz (from 875 to 960 MHz), which completely cover the 902–928 MHz band. The difference between the measurement and the simulation may be caused by the test fixture placed above the antenna and the deviation of the antenna fabrication process.

In the following, the analysis of realizing a good CP by adding the truncated corners and the two unequal L-shaped slots is discussed. Firstly, the satisfactory CP is not able to realize only with the truncated corners under the current feeding condition. So we introduce the two L-shaped slots with unequal length to further enhance the CP performance. As the simulated amplitude ($|E_x|$, $|E_y|$),

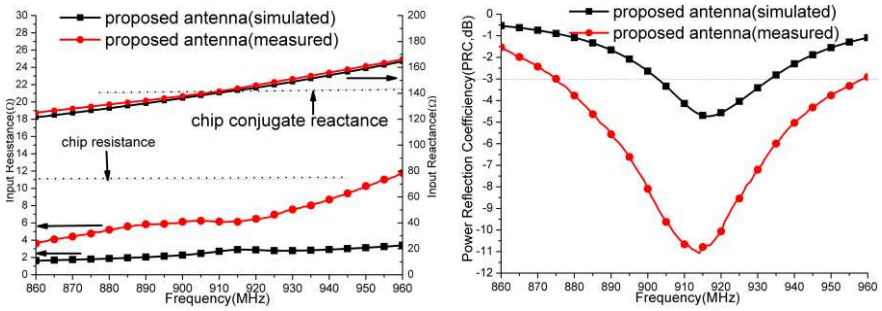

Figure 2: Measured and simulated input impedances, power reflection coefficient of the proposed tag antenna.

the relevant phase difference ($\Phi_y - \Phi_x$), and the corresponding AR bandwidth diagram exhibited in Fig. 3, we can see that the amplitude will be equal around 91 5MHz regardless of the L-shaped slots, but the phase difference will move to the lower frequency when the L slots are added. So the L-shaped slots can be uesed to tune the phase difference to achieve a good and pure CP radiation and reduce radiator size at the same time.

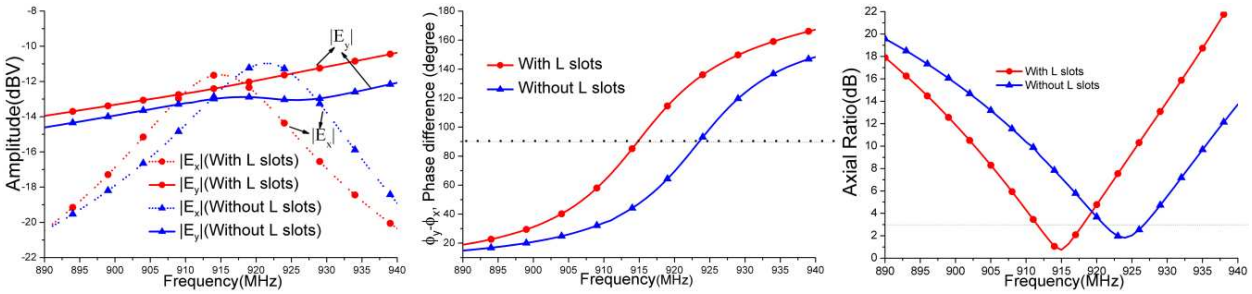

Figure 3: Simulated amplitude and phase difference diagrams of E_x and E_y, axial ratio in the boresight direction.

Under the current technical constrain, the radiation patterns of the RFID tag antenna is difficult to measure, so Fig. 4 only presents the simulated CP radiation patterns at 915 MHz. In Fig. 4, the 3-dB beamwidth is about 75° and a good front-to-back radiation ratio of 50 dB in both the x-z and y-z planes is revealed. This indicates an excellent and pure left hand circular polarization (LHCP) radiation of our antenna when it is placed in free space. Fig. 4 also shows the simulated gains of our tag antenna in different placement environments (free space, as well as mounted on metal plates of various sizes) and the corresponding AR diagram. In fact, the antenna gain will be about −8.5 dBi and the minimum point of AR will stay around 915 MHz when size of the mounted metal is more than $100 \times 100\,\text{mm}^2$. The antenna gain will promote about 1 dB when installed on the metal rather than in free space. As the figure presents, the proposed antenna will maintain a reliable gain and a good CP whether it is in free space or mounted on metals.

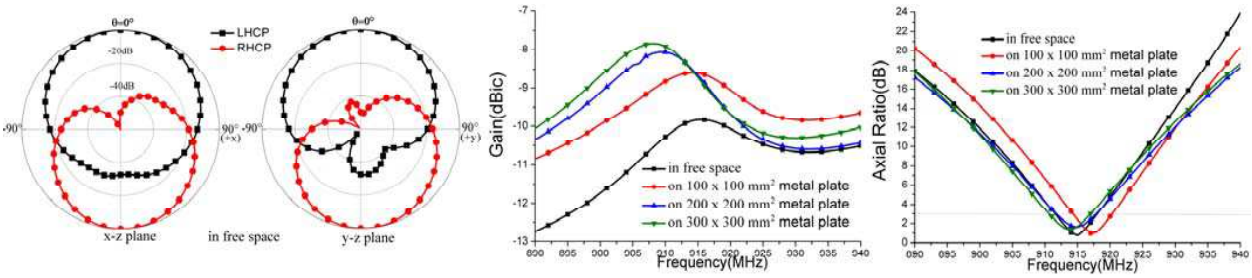

Figure 4: Simulated normalized CP gain radiation patterns at 915 MHz, antenna gains and axial ratio.

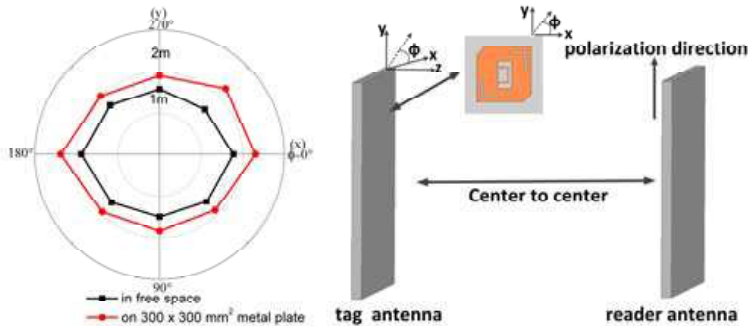

Figure 5: Measured reading distances when the tag antenna is rotated along the φ direction with a fixed reader antenna.

Table 2: Comparison between measured and calculated maximum reading distances of the proposed CP tag using LP reader antenna and CP reader antenna with the same output power (3.98 W) at the operating frequency.

Conditions	Simulated Gain (G_r)	Reading Distance by LP Reader Antenna (m)		Reading Distance by CP Reader Antenna (m)	
		Meas.	Cal.	Meas.	Cal.
Free Space	−9.8 dBic	1.88	2.26	2.74	3.2
$300 \times 300\,\text{mm}^2$ metal plate	−8.7 dBic	2.38	2.56	3.27	3.62

The read range measurement of our tag antenna is shown in Fig. 5 and Table 2. An RFID reader module (IPJ R420) with operating frequencies of 902–928 MHz, a LP reader antenna (Laird-E9012PLNF, gain of 12 dBi) and a CP reader antenna (Laird A9028, gain of 8 dBi) are applied to do the read range measurement. The overall output power of the read antenna system is set to 3.98 W in each case. As shown in Fig. 5, the tag antenna is rotated along the φ direction and the LP reader antenna is fixed to measure the maximal reading distances, under the conditions of in free space and on metal plates with two different areas ($100 \times 100\,\text{mm}^2$, $300 \times 300\,\text{mm}^2$). In free-space, the read range presents similar distances around 1.7 m at all angles of φ. In addition, when mounted on $300 \times 300\,\text{mm}^2$ metal plates, it shows a stable read range changes between 1.9 to 2.4 m with φ varying. Therefore, it means a good performance of CP radiation and a reliable and practical on-metal reading distance of the proposed antenna. Within the local equivalent isotropic radiated power (EIRP) [11], all the measured and simulated reading distances are given in Table 2. The Friis transmission formula [6] is utilized to calculate the theoretical reading distance.

4. CONCLUSIONS

A compact RFID CP tag antenna has been designed and tested. An AR bandwidth of 6 MHz and compact radiator size of $60 \times 60\,\text{mm}^2$ are obtained by employing the slot-embedded feeding network with good impedance matching. Thanks to the compact and symmetrical radiator, our antenna exhibits a good performance in practice. Later simulations and experiments indicate a good performance of our antenna when mounted on metallic surfaces. Therefore, when it comes to the application of mounting on metallic surfaces, the proposed UHF RFID tag antenna can be a good candidate. The next step of research is to achieve a better impedance matching condition and a broader AR bandwidth.

ACKNOWLEDGMENT

The partial support of Guangdong Innovative Research Team Program (No. 201001D0104799318), the National High Technology Research and Development Program (863 Program) of China (No. 201 2AA030402), the Swedish VR grant (# 621-2011-4620) is also gratefully acknowledged.

REFERENCES

1. Marrocco, G., "The art of UHF RFID antenna design impedance-matching and size-reduction techniques," *IEEE Antennas Propag. Mag.*, Vol. 50, No. 1, 66–79, Feb. 2008.
2. Yang, P. H., Y. Li, L. Jiang, W. C. Chew, and T. T. Ye, "Compact metallic RFID tag antennas with a loop-fed method," *IEEE Trans. Antennas Propag.*, Vol. 59, No. 12, 4454–4462, Dec. 2011.
3. Lin, K. H., S. L. Chen, and R. Mittra, "A looped-bowtie RFID tag antenna design for metallic objects," *IEEE Trans. Antennas Propag.*, Vol. 61, No. 2, 499–505, Feb. 2013.
4. Tseng, Y. M., S. H. Kuo, H. D. Chen, and C. Y. D. Sim, "Circularly polarized circular microstrip RFID tag antenna," *2012 Proceedings of APMC*, 1142–1144, Kaohsiung, Taiwan, Dec. 2012.
5. Chen, H. D., S. H. Kuo, and J. L. Jheng, "Design of compact circularly polarized radio frequency identification tag antenna for metallic object application," *Microw. Opt. Technol. Lett.*, Vol. 55, No. 7, 1481–1485, Jul. 2013.
6. Chen, H. D., S. H. Kuo, C. Y. D. Sim, and C. H. Tsai, "Coupling-feed circularly polarized RFID tag antenna mountable on metallic surface," *IEEE Trans. Antennas Propag.*, Vol. 60, No. 5, 2166–2174, May 2012.

7. Pozar, D. M., *Microwave Engineering*, 3rd Edition, Wiley, New York, 2005.
8. Son, H. W. and C. S. Pyo, "Design of RFID tag antennas using an inductively coupled feed," *Electron. Lett.,* Vol. 41, No. 18, 994–996, Sep. 2005.
9. Nikitin, P. V., K. V. S. Rao, S. F. Lam, V. Pillai, R. Martinez, and H. Heinrich, "Power reflection coefficient analysis for complex impedances in RFID tag design," *IEEE Trans. Microw. Theory Tech.*, Vol. 53, No. 9, 2721–2725, Sep. 2005.
10. Qing, X., C. K. Goh, and Z. N. Chen, "Impedance characterization of RFID tag antennas and application in tag co-design," *IEEE Trans. Microw. Theory Tech.*, Vol. 57, No. 5, 1268–1274, May 2009.
11. "Regulatory status for using RFID in the UHF spectrum," Jan. 20, 2008 Available: www.epcglobalinc.org.

The Research and Application of Array Antenna Element Detecting System

Wentao Zhu, Feng Gao, Zhiyuan Song, and Kai He
China Mobile Group Design Institute Co., Ltd., China

Abstract— This paper analyzes the change of VSWR and radiation performance when the smart antenna element doesn't work. From the analysis, it is found that the damage of the antenna element has great influence on the broadcast beam, and it's not enough to just depend on the detection of VSWR. Traditional detection methods of base station antenna are studied, on the basis of above, a detecting system for array antenna element was researched and established.

1. INTRODUCTION

Array antenna is commonly used in wireless communication base station, which can form a higher gain and specific shaped electromagnetic beam Nowadays, base station antenna with more elements has become the mainstream and tendency especially in the TD-SCDMA system and LTE MIMO system [1, 5]. The arrangement of array is applied not only in one direction (e.g., vertical line array), but also in the orthogonal direction to form planar antenna array [2].

Array antenna has many elements, while one antenna element does not work properly for some reason (such as rosin joint, short circuit, destroy of mechanical structure), the reflection coefficient of the main port does not deteriorate badly, and thus the antenna will not give out a warning of the VSWR. But the array pattern will be significantly affected at this moment, such as asymmetrical antenna pattern, poor sidelobe suppression, decrease of antenna gain, etc..

The existing detection techniques only detect the VSWR [4] of the base station antenna and give out different levels of warning, and thus the abnormal situation of the internal element can't be detected. This paper proposes an antenna element detection system, which was composed of electromagnetic induction sensor and detection circuit.

2. THE INFLUENCE ANALYSIS OF DAMAGED ELEMENT

2.1. The Influence of Damaged Element on VSWR

Figure 1 shows one Vertical line array and feeding network of TD-SCDMA smart antenna. The influence of antenna element on VSWR was tested, the test chose three cases: 1. The antenna elements are in working order; 2. element 1# is damaged; 3. element 1# and element 2# are damaged. The test result is shown in Table 1.

According to test results, the VSWR is 1.21 when the antenna elements are in working order, the VSWR is 1.26 when the antenna element 1# is damaged, and the VSWR is 1.49 when the antenna element 1# and element 2# are damaged. In the three cases, the VSWR can meet the requirement (VSWR < 1.5). The test shows that it's not enough to just depend on VSWR detection in the process of finding element problems.

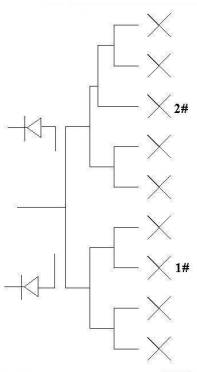

Figure 1: Vertical line array and feeding network of TD-SCDMA antenna.

Table 1: Test result of VSWR.

case	frequency band (GHz)	VSWR
the antenna elements are in working order	$1.88 \sim 2.025$	1.21
element 1# is damaged	$1.88 \sim 2.025$	1.26
element 1# and element 2# are damaged	$1.88 \sim 2.025$	1.49

2.2. The Influence of Damaged Element on Radiation Performance

The Influence of damaged element on radiation performance of broadcast beam is tested, and the results are shown in Fig. 2 and Fig. 3. The results showed that the E-plane pattern of broadcast beam changed obviously in two typical frequency points of F and A frequency band. The upper sidelobe level increase, the lower first null isn't filled, HPBW is unaltered, and front-to-rear ratio changed obviously; the H-plane pattern of broadcast beam changed obviously toward normal elements in two typical frequency points of F and A frequency band, HPBW became narrow obviously, the radiation level decreased more than 15 dB in 60-degree direction, and the pattern is significant different from the normal situation. The test results showed that the damaged element has great influence on radiation performance of broadcast beam, it is very necessary to detect the antenna element.

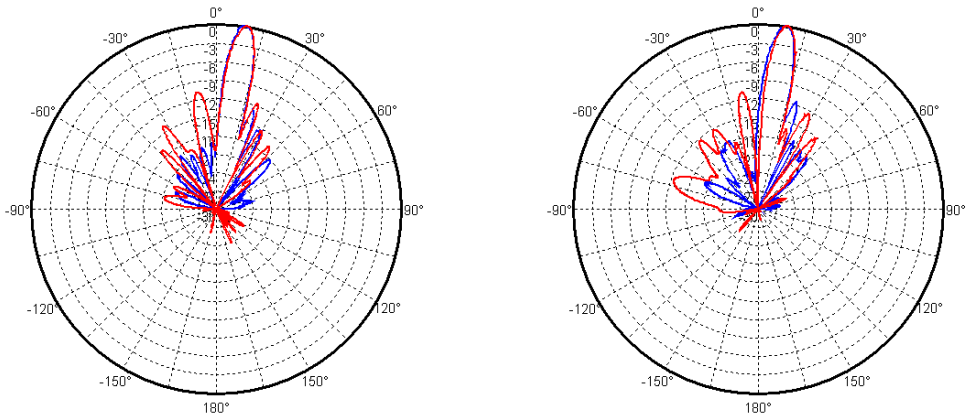

Figure 2: comparison on the E-plane pattern between normal situation and damaged situation of element 1#, 2# (blue line represent normal situation, red line represent damaged situation). (a) 1900 MHz. (b) 2018 MHz.

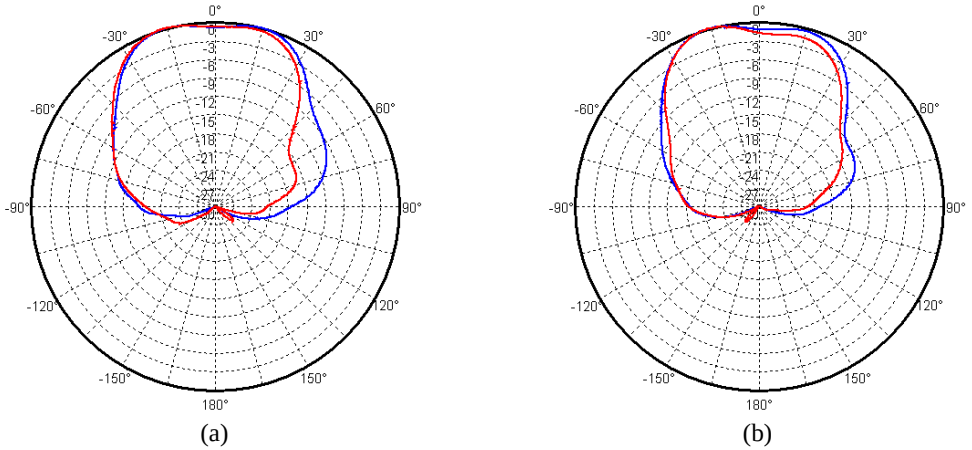

Figure 3: Comparison on the H-plane pattern between normal situation and damaged situation of element 1#, 2# (blue line represent normal situation, red line represent damaged situation). (a) 1900 MHz. (b) 2018 MHz.

3. DETECTION METHODS OF ANTENNA ELEMENT

3.1. Traditional Detection Methods of Antenna and Cable Systems

The failure of antenna and cable system occurs mainly on the antenna, cables and connectors. The detection of antenna and cable system is implemented by measuring the standing wave ratio (VSWR) or the value of return loss and isolation; we can determine the equipping quality and operation state from the detection results. The VSWR alarm of base station antenna is usually set to 1.5, and different types of base stations have different requirements on isolation between antennas.

There are mainly three types of instrument for antenna detection: spectrum analyzer, TDR, and Site Master. When the spectrum analyzer is used to detect the VSWR, the return loss is obtained after the test of the forward and reverse power, and the VSWR is obtained by checking the comparison table of return loss and VSWR; TDR can only roughly observe the waveform of antenna and cable system to determine the problem position; The VSWR and antenna isolation can be measured directly by Site Master, and the fault location is rapid.

3.2. Detection Methods of Antenna Element

Chapter 3.1 shows that the existing antenna detection technology just tests the VSWR and gives different levels of alarm signal, and thus cannot detect the abnormal situation of the internal element of the antenna array However, Chapter 2 of this paper shows that the antenna element testing is necessary; therefore this paper proposes an antenna element detection system, which was composed of electromagnetic induction sensor and detection circuit, this system can realize the detection of smart antenna element.

Figure 4 is a schematic diagram of the antenna element detection system The detection circuit has independent power supply (12 V), which is similar to the RCU (Remote control unit). The signal collected by the detection circuit is transmitted to the base station server by AISG cable [3]; the adapter is mainly used to implement the connection between RS485 and RS232 RS485 has a smaller transmission loss, and it is easy to realize long-distance signal transmission. RS232 interface can be easily connected with PC to facilitate the control of this system.

Based on the comparison of the coupling signal and the reference standard signal, you can achieve the detection of antenna element station.

As shown in Figure 5 the coupling signal acquisition process can be explained by an ordinary 2×8 dual-polarized planar array The antenna has 2 columns, each column has eight elements, and each element has two cross-feed ports to support dual-polarized mode, so that each column has four main ports. The primary port is divided into two sub-ports; the power of two sub-ports is further distributed to the four ports, and different polarization element of eight antenna element is feeded separately.

The coupled signal 1 represents sub-port of the left upper column, once one or some elements does not work the reflection coefficient of port 1 is inevitably abnormal, and the output RF signal of port A must change. The control unit indicates the working status of the element by checking the variation of the coupling signal of port 1 in a similar way, 8 channel signals of ports 1, 2, ..., 8 can be collected to detect the element status of the 16 antenna elements.

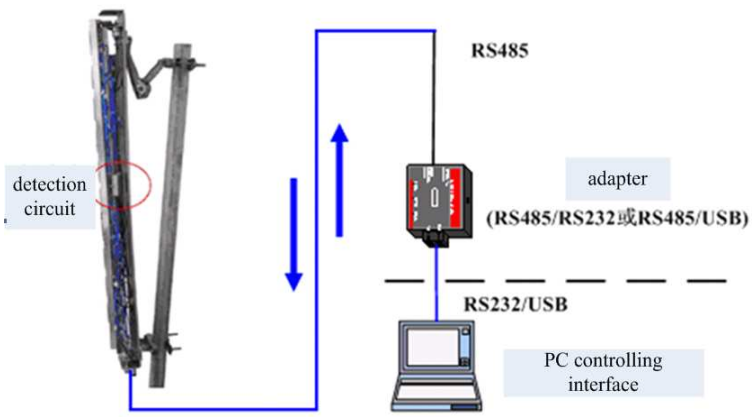

Figure 4: Antenna element detection system schematic.

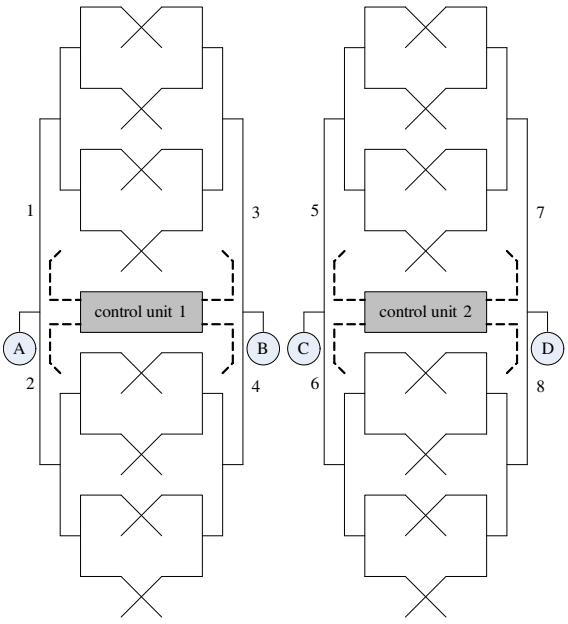

Figure 5: Collection of the coupling signal.

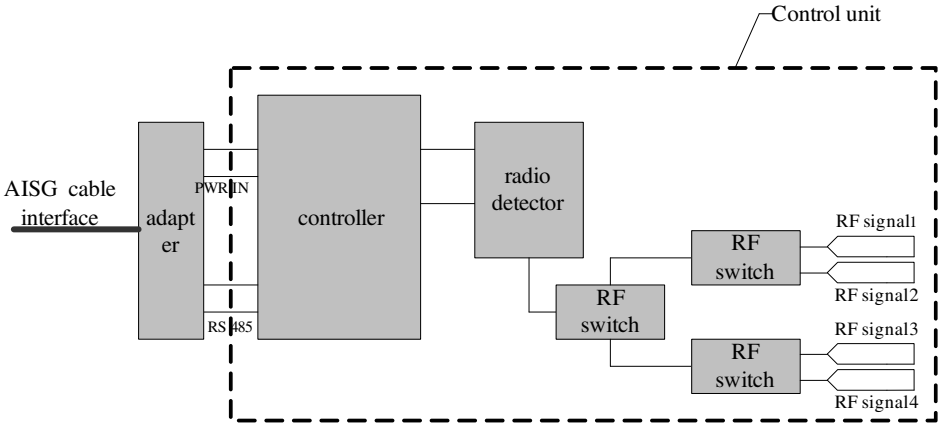

Figure 6: The principle block diagram of the detection circuit.

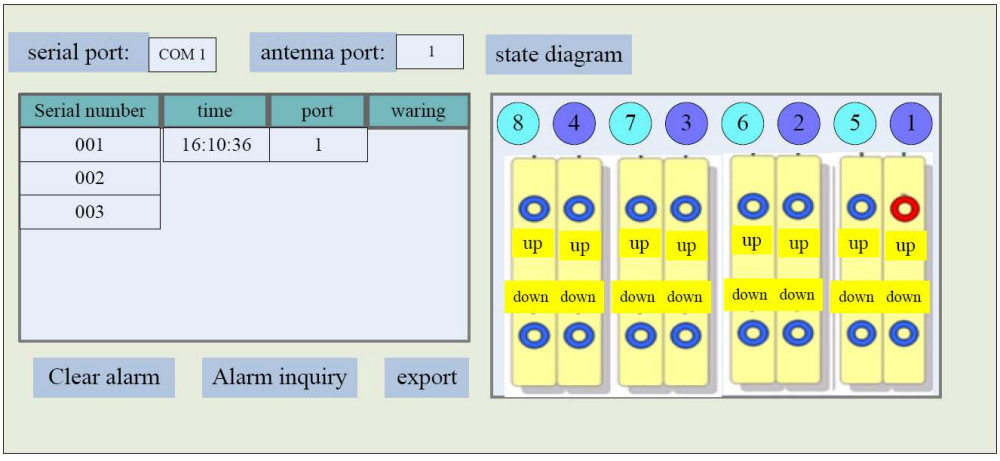

Figure 7: PC controlling interface.

Figure 6 shows the principle block diagram of the detection circuit, the four RF signals can be detected by the RF switch; the radio detector is used to convert radio frequency (RF) signal to the corresponding DC voltage. The DC voltage is converted to digital information by the A/D module

of the controller and then the antenna working condition can be obtained by comparing the digital information with the reference value.

The antenna working condition is monitored by PC controlling interface. Fig. 7 shows the interface of the antenna element condition, the blue light indicates that the elements are normal, and the red light indicates that the elements are failure.

4. SUMMARY

Array antenna has many elements, while some antenna elements don't work properly, the antenna will not often give out a warning of the VSWR. But the array pattern will be significantly affected at this moment. Therefore this paper proposes an antenna element detection system, and the next step is to improve the accuracy of antenna element detection system.

REFERENCES

1. 3G Americas Whitepaper, "MIMO and smart antennas for 3G and 4G wireless systems practical aspects and deployment considerations," May 2010
2. Kraus, J. D. and R. J. Marthefka, *Antennas: For All Applications*, 3rd Edition, McGraw-Hill, 2003.
3. AISG v2.0H, HUhttp://www.aisg.org.uk/U.
4. "Test methods for Base station antenna and cable system," http://www.cnii.com.cn/2006-0529/ca355376.htm.
5. Wang, Y. and S. Sun, *TD-LTE Principles and System Design*, The Posts and Telecommunications Press, June 2010.
6. Gross, F., *Smart Antennas for Wireless Communications*, McGraw-Hill, 2005.

Theoretical Analysis and Test of EMF in TDFI Bus

Wentao Zhu, Feng Gao, Zhiyuan Song, and Kai He
China Mobile Group Design Institute Co., Ltd., China

Abstract— There are growing concerns of electromagnetic radiation, and we performed some tests and theoretical analysis to provide some insight for RF exposure assessment of TDFI equipment. The result of EMF testing in TDFI bus shows that the EMF level generated by TDFI equipment is much less than international standard and people can use it safely.

1. INTRODUCTION

The fourth generation of mobile communications is expected to deliver multimedia services anywhere, anytime, with global support and integrated wireless solutions. TDFI is equipment which transform TD-SCDMA/TD-LTE network signal into WIFI signal, Using TDFI solution, people riding in buses can experience rapid and stable LTE TDD data services using WIFI-enabled smart phones.

Meanwhile, the electromagnetic radiation generated by TDFI is drawing the public's increasing attention. Although the radiation power of TDFI is little, it has both TDS/TDL antenna and WIFI antenna; passengers and drivers are likely to locate in the strong electromagnetic radiation field when riding in buses. For the above reason, we performed some tests and theoretical analysis to provide some insight for RF exposure assessment of TDFI equipment.

In this paper, the bus, which has been installed the TDFI equipment, is named TDFI bus. The result of EMF testing in TDFI bus shows that the EMF level generated by TDFI equipment is less than 0.5 $\mu W/cm^2$, which is much less than international standard (20 $\mu W/cm^2$) [1].

2. BRIEF DESCRIPTIONS OF TDFI

TDFI is Mobile/WIFI Integration equipment. There are two modules in TDFI: one WLAN module is used for Wireless Access, the other TD-SCDMA/TD-LTE module is used for Wireless backhaul instead of a Wired Network. The TD-SCDMA/TD-LTE module receives signals from the Macro network and then relays them towards the end users using WIFI.

TDFI can be deployed in places without IP backhaul network, we use TDFI equipment to solve WLAN backhaul problems and increase usage of TD-SCDMA/TD-LTE networks. With TDFI, end users can access TD-SCDMA/TD-LTE networks with any WIFI-enabled devices to enjoy high-speed mobile data services.

Figure 1 shows the comparison of Traditional WLAN and TDFI, traditional WIFI networks utilize wired transmissions, which causes a lack of transmission resources and a lengthy deployment process. The TDFI solution adopts wireless backhaul instead of wired backhaul to solve the last-mile problem of WLAN deployment. Compared to traditional WIFI networks, the TDFI solution helps operators achieve rapid, low-cost deployment and supports WIFI user authentication and billing.

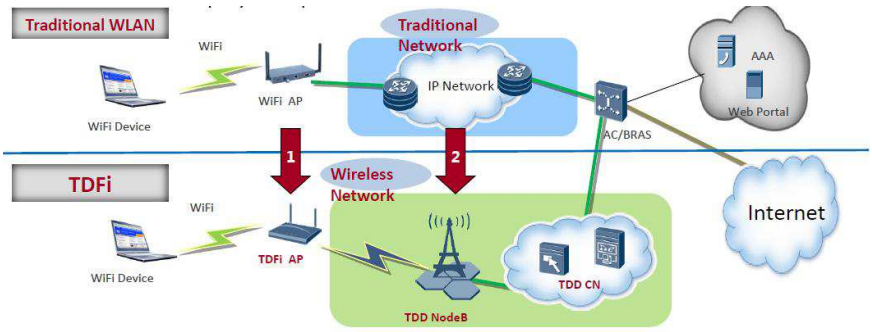

Figure 1: Traditional WLAN and TDFI.

TDFI are mainly deployed in buses, passengers can use the high speed service when the bus is moving. WIFI service on buses has been launched in 1,800 buses on 60 routes in Beijing by March

2013, including No. 1, 52, 57 and 300. It is expected more than 10,000 buses will install Wi-Fi by the end of the 2013.

3. THEORETICAL ANALYSIS AND TEST OF EMF IN TDFI BUS

3.1. Theoretical Analysis

TDFI has both TDS/TDL antenna and WIFI antenna, parameters of TDS/TDL antenna and WIFI antenna are shown in Table 1, TDS/TDL module has 2 elements, average output power of each element is 23 dBm (200 mW). Frame structure of Up/down collocation is DSUUDDSUUD, so the duty ratio is 0.4.

Table 1: Parameters of TDS/TDL antenna and WIFI antenna [2].

TDS/TDL Antenna	Built-in omnidirectional antenna, 3 dBi
WIFI Antenna	8 dBi directional antenna
TDS/TDL Power	2*(23±2 dBm)
WIFI Power	IEEE 802.11b: 15±2 dBm; IEEE 802.11g: 13±2 dBm; IEEE 802.11n: 11±2 dBm
WLAN	2.4G 802.11b/g/n
Size	200 mm × 240 mm × 61 mm (3L)

For propagation distances d much larger than the antenna size, transmit antenna modeled as a point source, the power density S at distance d from a transmitter with power P and antenna gain G is:

$$S = \frac{P_t G_t}{4\pi d^2} \tag{1}$$

In the TDFI bus, the received power S is the sum of TDS/TDL antenna and WIFI antenna radiation energy. There are four parameters, P_1, P_2, G_1, G_2, which represent the TDS/TDL Power, WIFI Power, TDS/TDL Antenna Gain, WIFI Antenna Gain.

$$S = \frac{P_1 G_1 * 0.4}{4\pi d^2} + \frac{P_2 G_2}{4\pi d^2} \tag{2}$$

As the propagation distance increases, the radiated energy is spread over the surface of a sphere of radius d, the path loss PL between two antennas can be expressed as follows, where the loss is found in dB.

$$PL = 32.44 + 20\log d\ (\text{km}) + 20\log f_c(\text{MHz}) \tag{3}$$

The 307 bus, which has two coaches, is 18 meters long, 2.5 meters wide and 3.5 meters high, and the TDFI is installed behind the driver. We choose 8 points for EMF analysis and testing.

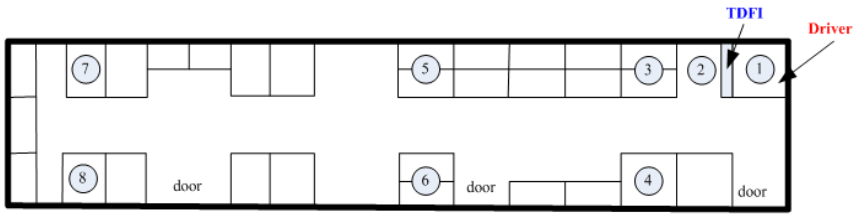

Figure 2: Sampling points of TDFI bus.

The WIFI works in 2400 MHz. Energy contribution of WIFI antenna in point 1 is ignored as it is 8 dBi directional antenna and front-to-back ratio of WIFI antenna is about 12 dB, using the average of TDS/TDL Power and WIFI Power, the theoretical calculation result is shown in Table 2.

Table 2: Theoretical calculation result.

Point	Distance (m)	Theoretical calculation result			
		S (V/m)	S (μW/cm^2)	PL (dB)	WIFI signal strength (dBm)
1	0.5 (driver position)	6.18	10.14	34.02	−33.02
2	0.5	7.30	14.15	34.02	−21.02
3	1.5	2.43	1.57	43.57	−30.57
4	2.5	1.46	0.57	48.00	−35.00
5	8	0.46	0.06	58.11	−45.11
6	8.5	0.43	0.05	58.63	−45.63
7	16	0.23	0.01	64.13	−51.13
8	16.5	0.22	0.01	64.39	−51.39

3.2. EMF Test in TDFI Bus

Two tools were used to test the EMF in the 307 TDFI bus, as shown in Figure 3, one is broadband field meter NBM 550, and anther is Wi-Fi Analytics app in mobile phone. The Amped Wireless Wi-Fi Analytics Tool analyzes the Wi-Fi networks. It provides advanced signal strength graphs of Wi-Fi network.

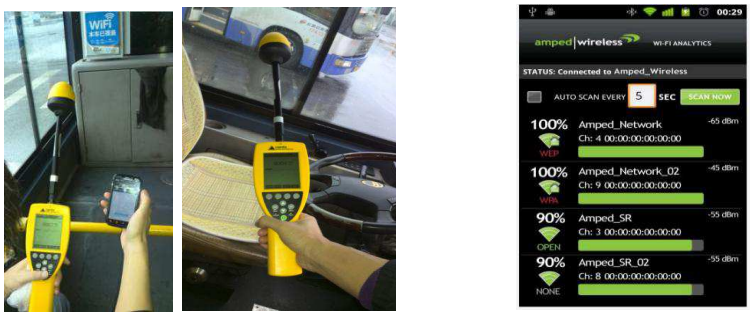

(a) (b)

Figure 3: Test tools ((a) NBM550, (b) Wi-Fi Analytics app).

Record the measured values three times and take the average, the test result is shown in Table 3.

Table 3: Testing result.

Point	Distance (m)	Measured value (average)	
		NBM 550 (μW/cm^2)	Wi-Fi Analytics (dBm)
1	0.5 (driver position)	0.4	−39
2	0.5	0.7	−35
3	1.5	0.3	−37
4	2.5	0.2	−43
5	8	0.1	−45
6	8.5	0.1	−47
7	16	0.1	−50
8	16.5	0.1	−51

Take no account of point 1, theoretical analysis result and testing result of electromagnetic radiation (EMR) intensity in TDFI bus is compared in Figure 6, and theoretical analysis result and testing result of WIFI signal intensity in TDFI bus is compared in Figure 7.

Figure 4: The appearance and inside of 307 TDFI bus.

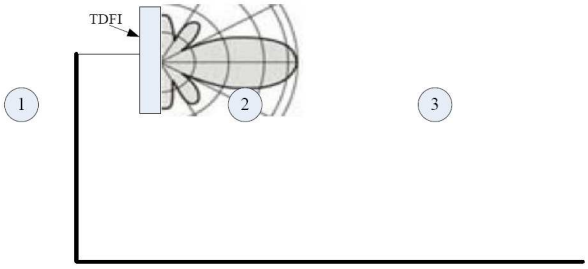

Figure 5: Side view of test point.

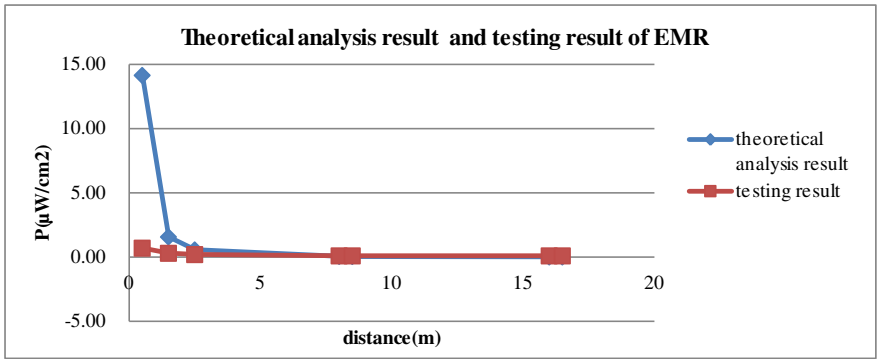

Figure 6: Theoretical analysis result and testing result of EMR in TDFI bus.

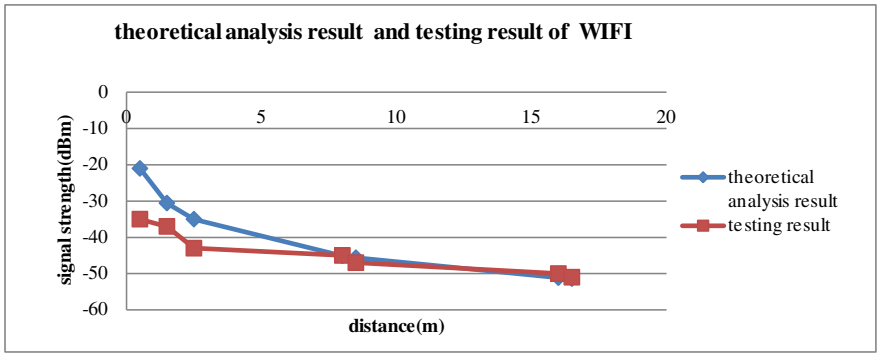

Figure 7: Theoretical analysis result and testing result of WIFI in TDFI bus.

Measured value is identical with the theoretical value while the distance is about 8 m. When the distance is below 8 m, the measured point is not at the main beam direction of the antenna, so the measured value is less than the theoretical value. When the distance is above 8 m, the measured point is affected by the reflection wave, so the measured value is not identical with the theoretical value.

4. CONCLUSIONS

Although passengers and driver is likely to locate in the strong electromagnetic radiation field when riding in buses, theoretical analysis and test of EMR in TDFI bus showed that the EMF level generated by TDFI equipment is less than $0.5\,\mu W/cm^2$, which is much less than international standard ($20\,\mu W/cm^2$).

TDFI can realize hotspot coverage on buses, which will enable further green transportation development. In the near future, the TDFI solution will enable LTE TDD to enrich people's mobile communications in medical care, information sharing, mobile video and community management among others.

REFERENCES

1. GB 8702-88, "Regulations for electromagnetic radiation protection,".
2. TDFi700 product overview v1.0, Huawei Technology Co., Ltd.

Optimal Waveform Design in Through-the-wall Application Based on the Information Theory

Xin Sun, **Bi-Ying Lu**, **Peng-Fei Liu**, **and Zhi-Min Zhou**
College of Electronic Science and Engineering
National University of Defense Technology, Changsha, Hunan 410073, China

Abstract— In this paper, the information theory is introduced to design the optimal waveform for through-the-wall application. Furthermore, the signal model and the target response are analyzed. By comparing the designed signal and the LFM signal, it is shown that the designed waveform achieves a significant improvement than the LFM signal in the aspect of obtaining mutual information of the target response.

1. INTRODUCTION

UWB through-the-wall-radar (TWR) uses the penetrable character of the low-frequency electromagnetic wave to image, detect and locate the human and targets behind the wall. As one of the hot research points, it has great significance in the military and civilian use. With the adaptive radar technology developing, waveform design is becoming one of the most important research directions.

In recent years, the waveform design methods have largely developed. The typical contributions are the method based on maximal SINR principle and the method based on the condition mutual information theory At present, the maximum SINR based method has been applied in TWI waveform design [1–3]. In these papers, the authors processed the research under the single-antenna monostatic operation and multi-antenna multistate operation, respectively. The output SINR has efficiently improved, which is very helpful for the target detection [1–3]. However, these optimize waveforms concentrate most of the energy in one or two narrow frequency bands, corresponding to the target resonant frequency or to those of highest frequency response [2]. However, such a narrow band waveform hardly provides a reasonable ability to resolve the range-to-target. As a result, more work should be done to meet this kind requirement in TWR application.

The paper is organized as follows. In Section 2 the principle of mutual information waveform design is introduced and analyzed. In Section 3, we consider the information waveform design method in TWR application based on the signal model and real requirements. In Section 4, the simulations and the comparison results are presented. Conclusions end this paper.

2. THE WAVEFORM DESIGN IN TWR APPLICATION BASED ON INFORMATION THEORY

According to the real requirements, the duration T and the total energy E_x of the transmission waveform should be finite. The transmission waveform is confined to the symmetric time interval $[-T/2\ T/2]$ and that only negligible energy resides outside the frequency interval $W = [f_0\ f_0 + W]$ for meeting the frequency needs. The mutual information waveform design method is to maximize the condition mutual information between the target response and the received signals (refer to [4]). To simplify the computation and convenience the derivation, we emphasize on the study for the single-antenna monostatic operation.

2.1. The Signal Model

The variable $x(t)$ denotes the transmission signal; the variable $w(t)$ denotes the wall impulse response; the variable $q(t)$ denotes the target impulse response; the variable $w_c(t)$ denotes the color clutter depending on the transmission waveform; the variable $c(t)$ denotes the clutter signals; the variable $n(t)$ denotes the additive Gauss noise; the variable $y(t)$ denotes the output signals. Then we get the signal model [2] in Figure 1.

So we can get the variable $s(t)$, the colored clutter $c(t)$ and the output signal $y(t)$ expression, respectively.

$$s(t) = x(t) * w(t) * q(t) * w(-t) \tag{1}$$

$$c(t) = x(t) * w_c(t) \tag{2}$$

$$y(t) = s(t) + c(t) + n(t) \tag{3}$$

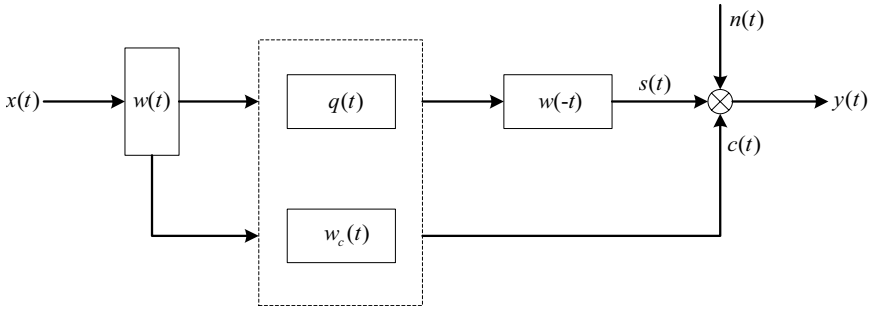

Figure 1: The signal model of TWR.

What we considered is to get more information of the targets behind the wall in TWR. So in the information aspect, it is to make the transmission waveform $x(t)$ maximize the mutual information between the receive signals $y(t)$ and the target response $q(t)$, namely maximizing the variable $I(y(t); q(t)|x(t))$. It is very difficult to get the expression. For convenience in mathematical reasoning, here we resort to a lemma in [4] to proof that the mutual information between the receive signals $y(t)$ and the target response $q(t)$ equals the mutual information between the receive signals $y(t)$ and the "wall-target" total response $g(t)$, namely

$$I(y(t); g(t)|x(t)) = I(y(t); q(t)|x(t)) \tag{4}$$

Proof:

[Lemma 1] Let $a(t)$ and $b(t)$ be finite-energy random processes and let D be a reversible transformation of $a(t)$ to a finite-energy random process $c(r)$ (where r is a new independent variable, but r could equal t). Then

$$I(a(t); b(t)) = I(c(r); b(t)) \tag{5}$$

Here, we define the variable D as follow expression,

$$D: \ q(t) \rightarrow w(t) * q(t) * w(-t) \tag{6}$$

It is obvious that the variable D is a reversible transmission, then define the following expression.

$$g(t) = w(t) * q(t) * w(-t) \tag{7}$$

So we can conclude that the mutual information between the receive signal $y(t)$ and the target response $q(t)$ equals the mutual information between the receive signal $y(t)$ and the "wall-target" total response $g(t)$, namely

$$I(y(t); g(t)|x(t)) = I(y(t); q(t)|x(t)) \tag{8}$$

Thus, according to the lemma, we determine the principle of the TWR application is to maximize the mutual information between the receive signal $y(t)$ and the "wall-target" total response $g(t)$. Then get the expression of the mutual information between the receive signal $y(t)$ and the "wall-target" response $g(t)$ via the above method.

$$I(y(t); g(t)|x(t)) = T \int_W \ln \left[1 + \frac{2|X(f)|^2 \sigma_G^2(f)}{TP_{nn}(f) + 2|X(f)|^2 \sigma_C^2(f)} \right] df \tag{9}$$

where, $|X(f)|^2$ is the optimal waveform magnitude squared spectrum with $\int_W |X(f)|^2 df = E_x$. $\sigma_G^2(f)$ is the "wall-target" response spectrum variance, and the variable $\sigma_c^2(f)$ is the colored clutter spectrum variance.

Resolving for the $|X(f)|^2$ by Lagrange method, get the expression of the variable $|X(f)|^2$, for details expression reasoning resort to [5].

$$|X(f)|^2 = \max \left[0, -R(f) + \sqrt{R2(f) + S(f)(A - D(f))} \right] \tag{10}$$

where,

$$D(f) = TP_{nn}(f)/\left(2\sigma_G^2(f)\right) \tag{11}$$

$$R(f) = \frac{TP_{nn}(f)\left(2\sigma_C^2(f)+\sigma_G^2(f)\right)}{4\sigma_G^2(f)\left(\sigma_C^2(f)+\sigma_G^2(f)\right)} \tag{12}$$

$$S(f) = \frac{TP_{nn}(f)\sigma_G^2(f)}{2\sigma_G^2(f)\left(\sigma_C^2(f)+\sigma_G^2(f)\right)} \tag{13}$$

Here $P_{nn}(f)$ is the power density of the Gaussian noise $n(t)$. The constant A is determined by the following expression.

$$E_x = \int_W \max\left[0, -R(f)+\sqrt{R2(f)+S(f)(A-D(f))}\right]df \tag{14}$$

2.2. The Wall Impulse Response

Once the scattered field is calculated, an approximation of the impulse response of the wall can be obtained according to the convolution relationship between the incident and the response. The matrix-vector expressions are given for the convenience of mathematical reasoning [2].

$$\mathbf{ZW} = \mathbf{S} \tag{15}$$

where, the variable $\mathbf{Z}$ is the M-by-N convolution matrix denotes to the incident waveform; $\mathbf{W}$ is the unknown wall's impulse response and the variable $\mathbf{S}$ is the scatter field vector. The subscript M and N denote the length of the incident waveform and the scatter field, respectively. Let $\mathbf{Z}$ be decomposed using the SVD, we get the expression

$$\mathbf{Z} = \mathbf{U\Sigma V^T} \tag{16}$$

where $\mathbf{U}$ and $\mathbf{V}$ are $M \times M$ orthogonal matrices and $\mathbf{\Sigma}$ is an $M \times M$ diagonal matrix whose entries $(\mathbf{\Sigma})_{ij} = \sigma_i$, $\sigma_i \geq \sigma_{i+1}$ are called the "singular values" of $\mathbf{Z}$. By introducing the vector $\boldsymbol{\eta}$ with the entries

$$\boldsymbol{\eta}_i = \left(\mathbf{U^T s}\right)_i/\sigma_i \tag{17}$$

Then, we can get the matrix-vector expression of the wall impulse response.

$$\mathbf{W} = \mathbf{V}\boldsymbol{\eta} \tag{18}$$

It is mentioned that, some methods or techniques, such as regularization and iterative, are using in the above calculation for resolve the ill-conditioned problem of the expression (15).

2.3. Spectrum Variance Estimate

Some simplification should be done for getting the estimation of the spectrum variance. Assuming the transmission wall illuminating the wall vertically, then the wall response $h(t)$ can be divided into two parts, the forward response and the back response, according to the angle between the receive signal and the wall.

$$h(t) = \sum_{\phi_1}^{h_1(t,\phi_1)} + \sum_{\phi_2}^{h_2(t,\phi_2)} \tag{19}$$

where, the variable h_1 denotes the forward response and the variable h_2 denotes the backward response. Their values depend on the angle ϕ_1 and ϕ_2. It is inevitable that the problem of the direct wave and multipath components are presence in the receive signals. While, there are some techniques and methods can remove these components, such as the time-gating method. So in this paper, we don't consider these problems. It can be concluded that we choose the forward response of the wall in this paper.

$$w(t) = h_1(t, \phi_1) \tag{20}$$

In the single-antenna monostatic operation, the simplest scene is the line which connects the antenna and the target vertical to the wall. At this situation, we choose the right forward response as the wall response.

$$w(t) = h_1(t, 0) \tag{21}$$

Then, we get the expression of the variable $g(t)$.

$$g(t) = h_1(t,0) * q(t) * h_2(t,\pi) \tag{22}$$

For symmetric walls such as homogeneous ones, $h_1(t,0) = h_2(t,\pi)$. A substitution of this expression into (22) yields the variable $g(t)$ and makes the Fourier transform.

$$G(\omega) = H_1(\omega,\pi) \cdot Q(\omega) \cdot H_1(\omega,\pi) = [H_1(\omega,\pi)]^2 \cdot Q(\omega) \tag{23}$$

Attributing to the randomicity of the targets presence, a common way to deal with the targets spectrum variance $\sigma_Q^2(\omega)$ is assumed to obey the gauss distribution. Assuming the target response $Q(\omega)$ also obeys the gauss distribution in the fixed frequency, because $[H_1(\omega,\pi)]^2$ is a fixed coefficient in a certain fixed frequency, then we can get spectrum variance of the "wall-target" response.

$$\sigma_G^2(\omega) = |H_1(\omega,\pi)|^4 \sigma_Q^2(\omega) \tag{24}$$

There are some other methods to estimate the spectrum variance, for example, the Monte Carlo analysis method [6]. It estimates the target spectrum variance via the probability and statistical theories after doing much Monte Carlo simulation. Using this method, the spectrum variance express is,

$$\sigma_Q^2(\omega) = \sum_{i=1}^{m} P_i |Q_i(\omega)|^2 - \left| \sum_{i=1}^{n} P_i Q_i(\omega) \right|^2 \tag{25}$$

where, the targets response q_i is a random variable and the variable p_i is the probability of respective response.

3. SIMULATION

Considering the real requirement in the TWR application, we determine the ultra-wild-band waveform's parameters as follows. The frequency range is 1G $\sim$ 2G, and the waveform duration is 1 µs. The power is 15 mw. Construct the electromagnetic model via CST 2008 software. In this model, the thick of the wall is 20 cm, the conductance of the wall is 0.03 S/m and dielectric permittivity is 4.2.

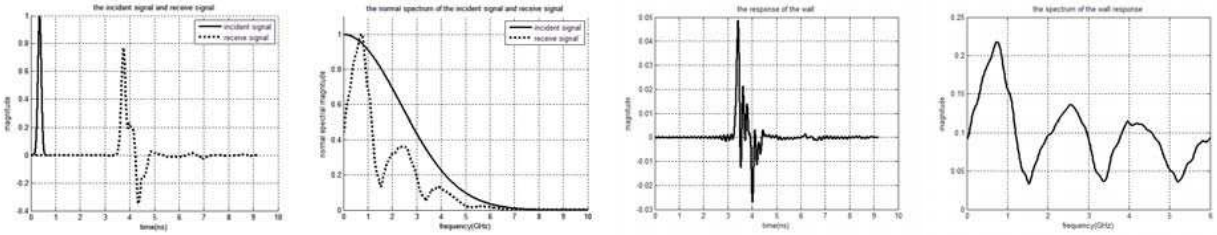

(a) (b) (c) (d)

Figure 2: (a) Time dimension of the incident and forward received signals. (b) Spectrum of the incident and forward received signals. (c) Right forward response. (d) Spectrum of the right forward response.

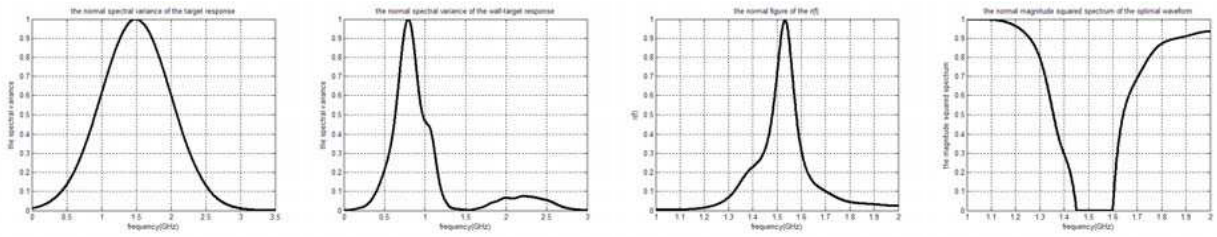

(a) (b) (c) (d)

Figure 3: (a) Normal spectrum variance of the target response. (b) Normal spectrum variance of the "wall-target" response. (c) Normal figure of the middle variable $r(f)$. (d) Normal magnitude squared spectrum of the optimal waveform.

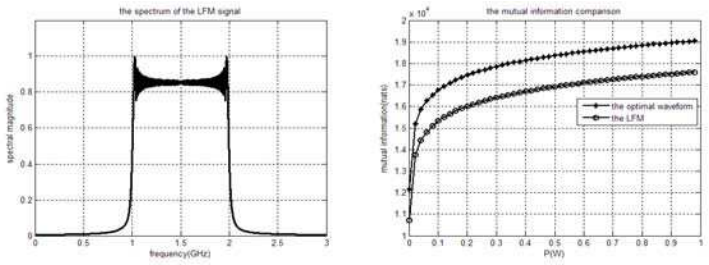

(a) (b)

Figure 4: (a) LFM signal spectrum. (b) Mutual information comparison of the two signals.

The incident waveform is the Gauss signal. Figures 2(a) and (b) are the time dimension and spectral of the incident signal and received signal. Using the expression (22) and FFT transform, we get the time dimension and frequency dimension results of the right forward, shown in Figures 2(c) and 2(d). Assume the spectrum variance of the target as the Figure 3(a) showing, and calculate the spectrum of the "wall-target" response in Figure 3(b). Using the above analysis, we get the magnitude squared spectrum of the optimal waveform, shown in Figure 3(d). By analyzing the results of Figures 3(b) and 5(d), we can get the conclusion that, the optimal waveform is to concentrate most of the energy in the frequency bands, corresponding to the large value of the whole spectrum variance. It doesn't concentrate most of the energy in one or some narrow frequency bands as the maximum SINR method does, which is one of the differences and advantages of this method. The reason why appearing the phenomenon can be explained by the entropy theory. Because the larger of the variance, the more of the entropy value. And larger entropy value includes more information of the target. The advantage is shown in Figure 4(b) by comparing with the LFM signals whose result is in accord on the above analysis.

4. CONCLUSION

From the above theory analysis and simulation comparison, we can conclude that the information waveform design method can be fully applied into the TWR application and get the satisfied result according to signal model and the real requirement. The optimal waveform can be propitious to get more information of the target, which is very important in further process. And this method concentrates most of the energy into the frequency band, corresponding to the large value of the whole spectrum variance, rather than some narrow band. So it eliminates the narrow-band problem of the maximal SINR method at a certain extent. Furthermore, the comparison between the optimal waveform and the LFM waveform shows that the mutual information by the optimal waveform is obviously better than the LFM signal, which has the same duration, frequency interval and energy as the optimal waveform.

It is noted that the more perfect we get the target spectrum variance, the more accurate optimal waveform can be designed and the more target information can be got. Aiming at the problem, we resort to the [4] and adapt the Gauss spectrum variance. And we can also via the Monte Carlo simulation method in [6] to get the spectrum variance. So in the further research, lots of measurements should be done to summarize the spectrum variance in the real scene for getting more perfect result.

ACKNOWLEDGMENT

This work was supported in part by the National Natural Science Foundation of China under Grant 61372161 and 61271441.

REFERENCES

1. Estephan, H., M. Amin, K. Yemelyanov, and A. Hoorfar, "Waveform design for through-the-wall radar imaging application," *Sensors, and Command, Control, Communications, and Intelligence (C3I) Technologies for Homeland Security and Homeland Defense VII*, 2008.
2. Estephan, H., M. Amin, and K. Yemelyanov, "Optimal waveform design for improved indoor target detection in sensing through-the-wall application," *IEEE Transactions on Geoscience and Remote Sensing*, Vol. 48, No. 7, 2930–2941, 2010.

3. Ahmad, F., M. Amin, and H. Estephan, "Multistatic waveform design for seeing through the wall," *International WD&D Conference*, 2009.
4. Bell, M. R., "Information theory and radar waveform design," *IEEE Transaction on Information Theory*, Vol. 39, No. 5, 1578–1597, 1993.
5. Romero, R. and N. A. Goodman, "Information-theoretic matched waveform in signal dependent interference," *IEEE Radar Conference, 2008, RADAR'08*, 2008.
6. Goodman, N. A., P. R. Venkata, and M. A. Neifeld, "Adaptive waveform design and sequential hypothesis testing for target recognition with active sensors," *IEEE Journal of Selected Topics in Signal Processing*, Vol. 1, No. 1, 105–113, 2007.

Analysis of EMF and Interference in the Wireless Charging Robot System

Jung-Ick Moon, In-Kui Cho, Seong-Min Kim, Jae-Hun Yun, and Woo-Jin Byun
Radio Technology Research Department
Electronics and Telecommunications Research Institute (ETRI), Korea

Abstract— In this paper, the analysis of EMF and interference in the service robot with the wireless charging system is presented. The magnetic resonance was used to transfer the high power energy into the service robot. The resonance frequency and transfer distance is about 1.80 MHz and 20 cm, respectively. The wireless charging system is composed of the spiral type resonators, transceiver with communication module, and Pb-battery. Both resonators are made of litz wires to decrease the loss and have two layers to increase inductance.

For the analysis of EMF and interference, the uniform body model defined in IEC 62369-11 and the near-field analysis of the resonators was used. Finally, the strength of the electromagnetic field and SAR (Specific Absorption Ratio) nearby the service robot was obtained.

1. INTRODUCTION

Many researchers have developed the wireless charging system since the magnetic resonance technology was presented from MIT in 2007 [1]. Especially, the wireless power company consortiums such as WPC, A4Wp, and PMA have been developing the standard. As a result, many kinds of the wireless power charging devices for mobile phones are presented in the market and the high-power technology is being applied to charge the electric vehicles [2, 3].

Even though the middle-power solutions are needed to charge the home applications and small robot, EMF (Electro and Magnetic Field) on the energy transfer path, interference with nearby electric devices and SAR (Specific Absorption Ratio) should be considered before use [4]. In this paper, the simulated EM analysis for the wireless charging robot system using middle power is demonstrated and the comparison results according to the presents of the EM shielding are also shown.

2. THE WIRELESS CHARGING ROBOT SYSTEM FOR ROBOT

As shown in Fig. 1, to transfer the high power energy into the service robot, the wireless power transmission technology using magnetic resonance was used. The resonance frequency and transfer distance to obtain more than 70% transfer efficiency is about 1.80 MHz and 20 cm, respectively. And the maximum transmitting power level is 100 W. The wireless charging system is composed of the spiral type resonators, transceiver with communication module, and Pb-battery. Both resonators

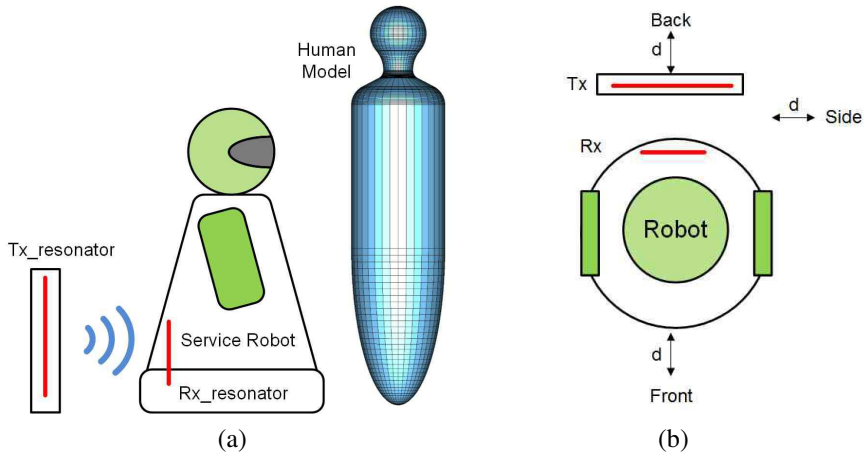

Figure 1: Wireless Charging Robot model. (a) Side view. (b) Top view.

are made of litz wires to decrease the loss and have two layers to increase inductance. The diameters of tx and rx resonator is 40 cm, 30 cm, respectively [5].

For the analysis of EMF and interference, thee uniform body model composed of muscle and defined in IEC 62369-11 was used [6]. The cover contained receiver module, the frame of robot and battery was considered as metal having electric loss. And the other part of robot was done as ABS (acrylonitrile-butadien-styrene resin) material. Three observation points denoted as front, side and back were selected. The distance (d) is from 5 cm to 100 cm and the height of points for averaging the results is 30 cm, 60 cm, and 90 cm, respectively. Finally, the ferrite sheet and rectangular metal plate were located on the back of each resonator to confirm the shielding effect.

3. THE EM ANALYSIS OF WIRELESS CHARGING SYSTEM

Figure 2 shows the EMF strength SAR nearby robot. As shown in figure, the maximum value is calculated on the back of tx-resonator and the minimum is done on the front of robot. Especially, the maximum value is more than 10 times stronger than ICNIRP guidelines (electric field 64.8 V/m, magnetic field 405 mA/m at 1.8 MHz). These results can influence human and electronic devices within the certain zone. Therefore the ferrite sheet and rectangular metal plate were applied to the system for reducing the EMF and the comparison results were shown in figure.

As results, the electric field is decreased to a tenth part of the original value and the magnetic field is done to a fifth part of that. Considering the more suitable shape and location of ferrite sheet and metal plate, significant reduction in EMF could be obtained. And the reasonable power level to satisfy the guide line and the power control function are required on this system. For SAR, very low values were simulated due to the high permittivity of the Body on the low resonant frequency. This means that and low frequency has an advantage in SAR when wireless power transfer technique is applied to high power solutions.

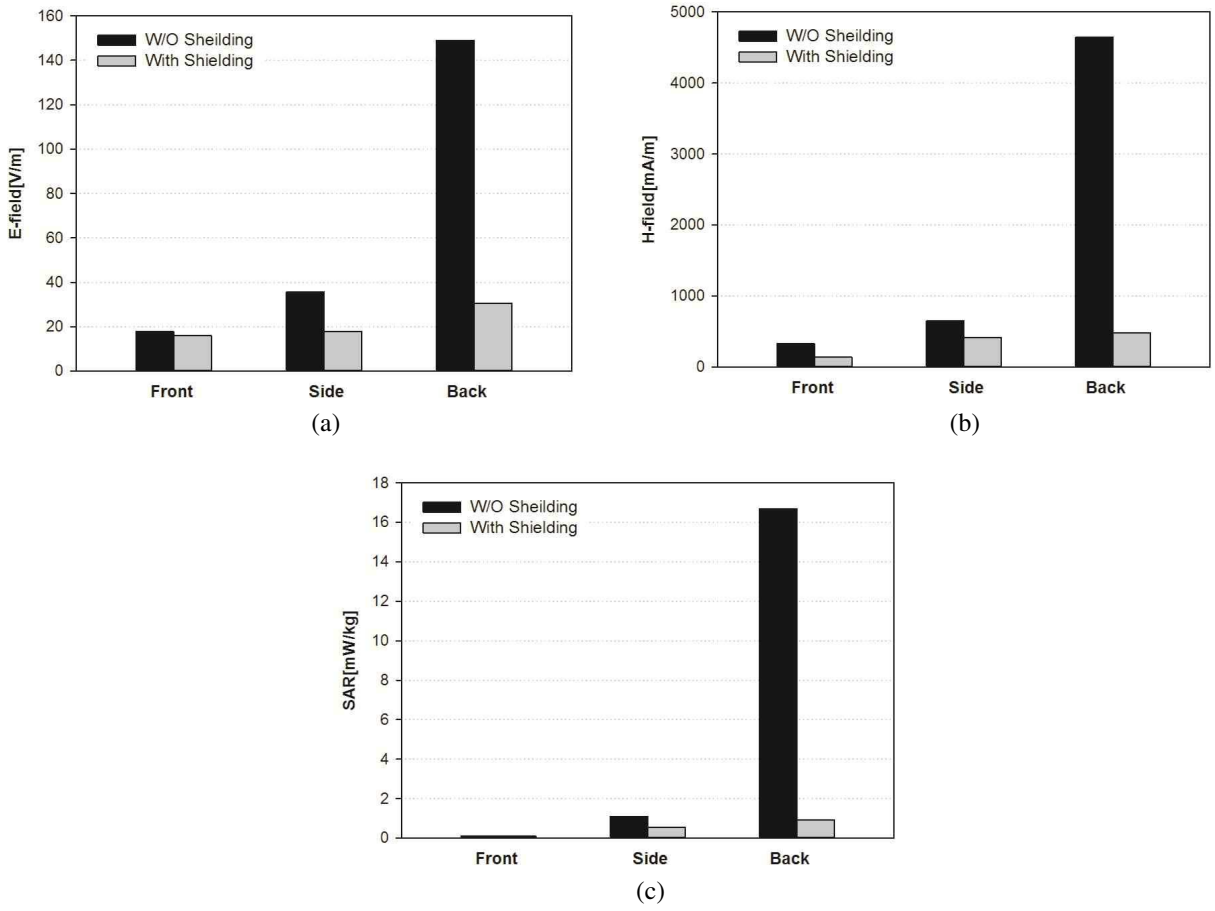

Figure 2: The comparison results of EMF and SAR. (a) E-field, (b) H-field, (c) SAR.

4. CONCLUSIONS

This paper presented the analysis of EMF and interference in the service robot with the wireless charging system is presented. The magnetic resonance was used to transfer the high power energy into the service robot. For the analysis of EMF and interference, the uniform body model defined in IEC 62369-11 and the near-field analysis of the resonators was used. Finally, the strength of the electromagnetic field and SAR (Specific Absorption Ratio) nearby the service robot was obtained and the guided level of the transfer power is suggested.

ACKNOWLEDGMENT

This research was funded by the MSIP (Ministry of Science, ICT & Future Planning), Korea in the ICT R&D Program 2014.

REFERENCES

1. Cheon, S., et al., "Wireless energy transfer system with multiple coils via coupled magnetic resonances," *ETRI Journal*, Vol. 34, 2012.
2. http://www.wirelesspowerconsortium.com/.
3. http://www.rezence.com/.
4. ICNIRP Guidelines, "For limiting guideline to time-varying electric, magnetic and electromagnetic fields (up to 300 GHz)," *Health Physics*, 1998.
5. Kim, S.-M., I. K. Cho, J. I. Moon, et al., "System level power control algorithm in wireless power transmission for reducing EMF," *IEEE WPTC*, May 2014.
6. http://niremf.ifac.cnr.it.

Design of TFOSC Compatible Polarimeter for Polarimetric Observations

S. Helhel[1,2], G. Kahya[1,2], I. Khamitov[1], and C. Bayar[1]

[1]TUBITAK National Observatory (TUG), Akdeniz University Campus, Antalya, Turkey
[2]E.E.E. Department, Engineering Faculty, Akdeniz University, Campus, Antalya, Turkey

Abstract— This study proposes a design steps of a TFOSC focal plane instrument compatible optical polarimeter in order to investigate the physical parameters of targets (such as albedo, diameter, taxonomy of asteroids, porosity) based on the polarization properties of light. Images captured with Polarimeter will be reduced for the atmospheric effect and device errors. The light impinging on WeDoWo prism is divided into four different images which is polarized at 0, 45, 90, 135 degrees and used to determine Stokes' parameters of electromagnetic waves. WeDoWo prism has been designed by using commercial optical design software named ZEMAX, it is 40 mm in diameter and has a thickness of 20 mm.

1. INTRODUCTION

Aim of this study is to design a TFOSC (TUBITAK National Observatory "TUG" Faint Object Spectrograph and Camera) focal plane instrument compatible polarimeter and investigate the physical parameters of targeted asteroids (such as albedo, diameter, taxonomy of asteroids, porosity) based on the polarization properties of light by using this polarimeter which will be designed.

Polarized light can provide additional information about the scene that cannot be obtained directly from the intensity or spectral images. Rather than treating the optical field as scalar, polarization images seek to obtain the vector nature of the optical field from the scene [1].

Instrumental base of 1.5 m Russian-Turkish telescope RTT150 makes it possible to carry out practically whole kind of astrophysical observations in the visible range. Until recently the observational complex included light detectors for high positional and photometric CCD observations, fast photometry, and for obtaining low and high resolution spectra. During the last observation campaign of PHA Apophis close approach, we are faced with lack of spectroscopic observations to determine the taxonomy class of asteroids with visual magnitude fainter than 16 m, due to the requirement of extremely long observational time. In addition to spectroscopic method for taxonomy determination, polarimetric method should also be employed. We present design of a polarimeter for RTT150 for simultaneous imaging of celestial sources on polarization planes on the base of WeDoWo (Wedge Double Wollaston) [2]. The accuracy and magnitude limits are discussed. The designed polarimeter may be used for not only asteroid observations but also for astrophysical sources like SN (Super Nova), AGN (Active Galactic Nuclei) and so on. Thus, the polarimeter integration to the RTT150 telescope increases its capabilities in ground-based observational support of present and future astrophysical space missions (GAIA "Global Astrometric Interferometer for Astrophysics", SRG "Spectrum-Rontgen-Gamma").

In this paper, we propose a Wollaston-based optical prism design principles, and images will be gathered by means of CCD. First measurement results will be presented in the conference.

2. WEDGE DOUBLE WOLLASTON (WEDOWO) PRISM

WeDoWo prism is one of the methods used for determining the celestial body originated light polarization rate throughout the world wide observatories. The light impinging on WeDoWo prism is divided into four different images which is polarized at 0, 45, 90, 135 degrees and used to determine Stokes' parameters of electromagnetic waves. First three elements of Stokes' vector can be determined without needing neither simultaneously obtained light component that have $\lambda/2$ variation nor other moving components [2]. To evaluate optical performance of WeDoWo prism parameters, a commercial optical design software called ZEMAX was used [4]. A space between collimator and camera allows integrating our new polarimeter to the system without any distortion, and by this way it allows to investigate asteroids whose taxonomy class faint less than 16th magnitude and diameter of 300 m.

Since images will be captured simultaneously with this Polarimeter, the atmospheric effect and device errors will be reduced. TFOSC which is a multi-functional device allows both photometry

and spectroscopy at the moments. After designed Polarimeter is integrated to TFOSC, the transition between the three methods will take place fast and optionally according to the observing sources.

3. THEORY OF POLARIZATION

A light is an electromagnetic wave whose polarization characteristics can be completely represented by its Stokes vector (I, Q, U, V) [3]. The Stokes parameters are a set of values that describe the polarization state of electromagnetic radiation. They were defined by George Gabriel Stokes in 1852, as a mathematically convenient alternative to the more common description of incoherent or partially polarized radiation in terms of its total intensity (I), (fractional) degree of polarization (p), and the shape parameters of the polarization ellipse.

The Stokes parameters are linear with intensity, so the link between each pixel of the images and Stokes parameters can expresses with a matrix. If the images are perfectly 0, 45, 90, 135 degrees polarization, the Stokes parameters (in Eq. (1)) can be easily deduced [5]. $I^2 = Q^2 + U^2 + V^2$ (This only holds for 100% polarized waves). I is the total intensity, Q and U are linear polarization and V is circular polarization. V value for linear polarization is zero. The degree of linear polarization of such a light beam is defined as P_L in Eq. (2) and ϕ_L is defined in Eq. (3).

$$\vec{S} = \begin{bmatrix} I \\ Q \\ U \end{bmatrix} = \begin{bmatrix} I_{0^\circ} + I_{90^\circ} \; veya \; I_{45^\circ} + I_{135^\circ} \\ I_{0^\circ} - I_{90^\circ} \\ I_{45^\circ} - I_{135^\circ} \end{bmatrix} \tag{1}$$

I_{0°: the linearly polarized component along the horizontal axis,
I_{90°: the linearly polarized component along the vertical axis,
I_{45°: the linearly polarized component at 45°,
I_{135°: the linearly polarized component at −45°.

$$P_L = \frac{\sqrt{Q^2 + U^2}}{I} \tag{2}$$

$$\phi_L = \frac{1}{2} \arctan \frac{U}{Q} \tag{3}$$

As $P = 1$, the wave is totally polarized.
As $P = 0$, the wave is totally non-polarized.
If $0 < P < 1$, P represents the amount of beam polarization.

Figure 1 represents the WeDoWo schematics. Figure 1(a) is the schematic representation of WeDoWo device and ray-tracing. To prevent vignetting at the prisms interface the wedge angle is chosen to ensure that all rays (including those from the field edges) always travel above/below the optical axis. Middle one is the illustration of how this device creates four polarized images (at 0, 90, 45 and 135 degrees) of a stellar field. Right one is the illustration of how the WeDoWo creates four long slit polarized spectra (at 0, 90, 45 and 135 degrees) of two stars [2].

$$\left(\frac{\theta}{derece}\right) = 2.78 \left(\frac{\theta_{sky}}{100}\right) \left(\frac{D_{Tel}}{1\,\mathrm{m}}\right) \left(\frac{D_p}{1\,\mathrm{cm}}\right)^{-1} \tag{4}$$

θ_{sky} (sky projected angles) is the slit length, D_{tel} is the telescope diameter and D_p is the diameter of the pupil image in Eq. (4). This values for RTT150, as indicated in Eq. (5).

$$\theta_{sky} = 60'', \quad D_{Tel} = 1.5\,\mathrm{m}, \quad D_p = 54\,\mathrm{mm} \tag{5}$$

Combined with Eqs. (1), (2) and [2] we have obtained Eq. (6);

$$\begin{aligned} \alpha &= 18.853 \\ \beta_1 &= 3.591 \\ \beta_2 &= 1.89 \end{aligned} \tag{6}$$

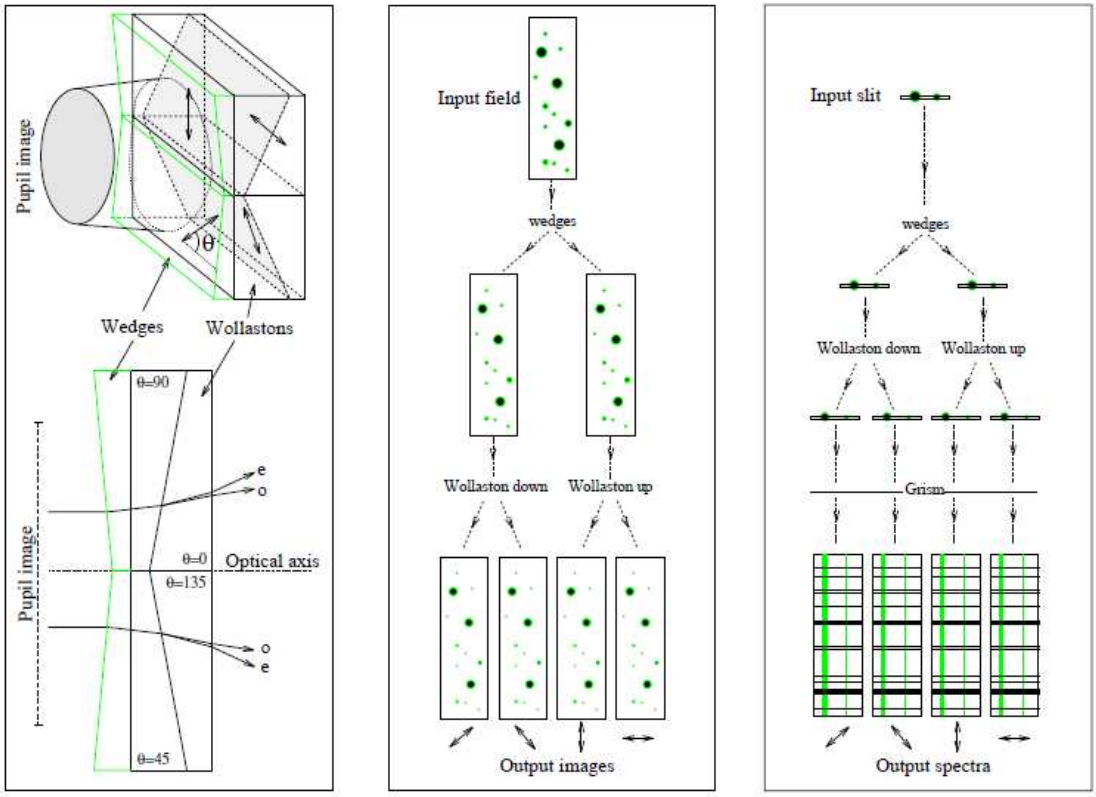

Figure 1: WeDoWo schematics [2].

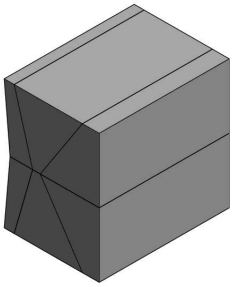

Figure 2: WeDoWo.

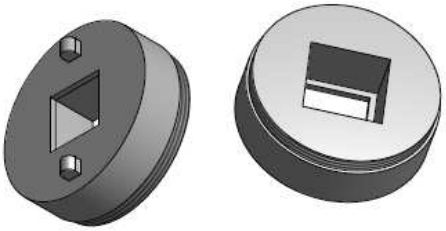

Figure 3: Mouth.

Figure 4: WeDoWo with mouth.

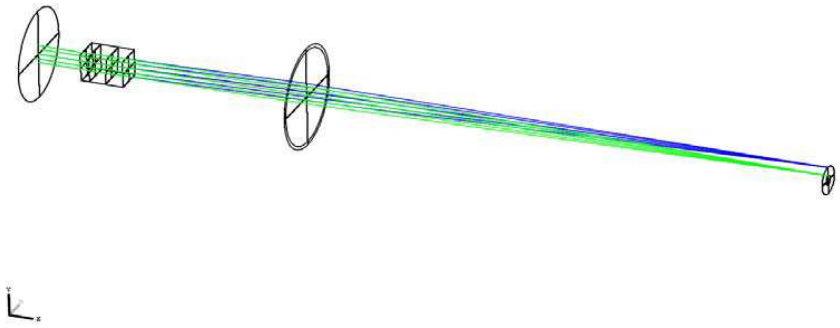

Figure 5: Wollaston birefringent sample with $CaCO_3$ material.

4. NEW OPTICAL DESIGN

We designed new WeDoWo polarimeter prism by using optical design software ZEMAX. The most convenient (and probably the cheapest) material for our design is $CaCO_3$ in visible wave length. A consequence of this choice is that the output images suffer by different lateral chromatism and the outer spectra are much more distorted than the inner one's [2]. Figure 2 shows designed wedged double Wollaston prism, Figure 3 shows its holder, and Figure 4 simulates the held WeDoWo. Figure 5 demonstrates the Wollaston briefringent sample with $CaCO_3$ material. These prisms were produced in St. Petersburg according to our design.

5. CONCLUSION

Designed optical polarimeter integrated to TUBITAK National Observatory TFOSC System will allow polarimetric observations with RTT150 telescope. Optical polarimeter design capability of Turkish scientists has increased by this study, and it is expected that there will be new designs for other aims for near future.

After fine tuning of system, it will be used by astronomers to observe asteroids as well as AGN, SN, pulsars, and so on.

ACKNOWLEDGMENT

This project is supported by TUBITAK (Grand No. 113F263).

REFERENCES

1. Meng, L. and J. P. Kerekes, "Analytical modeing of optical polarimetric imaging systems," Chester F. Carlson Center for Imaging Science, Rochester Institute of Technology, 54 Lomb Memorial Drive, Rochester, 14623, USA, 2011.
2. Oliva, E., "Wedged double Wollaston, a device for single shot polarimetric measurements," *Astronomy & Astrophysics Supplement Series*, Vol. 123, 589–592, 1997.
3. Goldstein, D., *Polarized Light*, 2nd Edition, Revised and Expanded, Marcel Dekker, New York, Basel, 2003.
4. Pernechele, C., L. Abe, P. Bendjoya, J. P. Rivet, A. Cellino, G. Massone, and P. Tanga, "A single-shot optical linear polarimeter for asteroid studies," *Ground-based and Airborne Instrumentation for Astronomy IV, Proceedings of the SPIE*, Vol. 8446, 6, 2012.
5. Lefaudeux, N., N. Lechocınskı, S. Breugnot, and P. Clemenceau, *Compact and Robust Linear Stokes Polarization Camera,* Bossa Nova Technologies, 2008.

Numerical Investigation of a Novel Two-stage Spectral Compression Structure Employing a Logarithmic DIF Cascading with a HNLF-NOLM

Fan Yang[1], **Ying Chen**[1, 2], **Xiaojun Zhou**[1], **Zhiyao Zhang**[1], **Xiangning Chen**[1], **and Yong Liu**[1]

[1]State Key Laboratory of Electronic Thin Films and Integrated Devices
School of Optoelectronic Information
University of Electronic Science and Technology of China, Chengdu 610054, China
[2]Department of Optoelectronics, Academy of Equipment, Beijing 101416, China

Abstract— A novel all-optical spectral compression structure is proposed, which employs a logarithmic dispersion increasing fiber cascading with a highly nonlinear linear fiber-nonlinear optical loop mirror. Numerical simulation is carried out by solving the generalized nonlinear Schrödinger equation using split-step Fouier method, where the soliton number is in the range of $0.5 \leq N \leq 1.4$. The results show that the spectra are well compressed, and the maximal spectral compression ratio can reach 10.93 with a little of pedestal when $N = 1.4$.

1. INTRODUCTION

All-optical analog-to-digital conversion (ADC) has been investigated as a vital technology to overcome the "electronic bottleneck" existed in the traditional electronic ADC. Recent tremendous growth in optical communication and digital signal processing has encouraged the research on the all-optical ADC with high speed and high resolution [1]. The process of the all-optical ADC includes sampling, quantization and coding. In the last several decades, several groups have proposed some schemes for the photonic quantization process [2–4], and one of them is the soliton-self-frequency shift (SSFS) [4]. The main method to improve the resolution of SSFS is to compress the spectral width after SSFS. Up to date, the general scheme is that the pre-negative-chip pulses suffer self-phase modulation (SPM) in fiber [5], the other ones include the schemes of transmitting through dispersion increasing fiber (DIF) [6] and anomalous dispersion fiber [7, 8].

In this paper, a novel two-stage all-optical spectral compression scheme using a logarithmic DIF cascading with a highly nonlinear linear fiber-nonlinear optical loop mirror [9] (HNLF-NOLM) is proposed. The nonlinear propagation of the chirp-free femtosecond pulse at 1550 nm is solved by the split-step Fourier method in the range of $0.5 \leq N \leq 1.4$. The simulation results show that the spectrum, which is compressed by the DIF, can be re-compressed when pulses propagate through the HNLF-NOLM. The spectral compression ratio (SCR) is defined as the ratio of the FWHM (full-width at half maximum) of the input spectrum to that of the compressed one. It is found that the SCR increases with the power of the pulses, and the maximal SCR is 10.93 when $N = 1.4$.

2. OPERATION PRINCIPLE

The scheme of the two-stage spectral compression is shown in Figure 1, which includes DIF for the first stage of spectral compression, and HNLF-NOLM for the second one. The sub-picosecond pulse, whose peak power satisfies the range of $0.5 \leq N \leq 1.4$, is injected into the DIF to generate spectral compression and some negative chirp. Then the pulse enters the HNLF-NOLM. Firstly the negative chirp of the pulse is enhanced in the single mode fiber (SSMF); and then the pulse is divided into the clockwise and counter-clockwise ones in the 2×2 optical power coupler (coupling

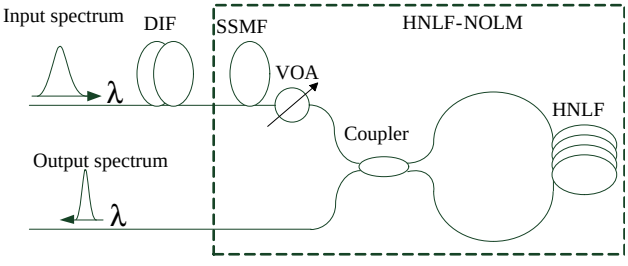

Figure 1: Schematic diagram of the two-stage spectral compression.

ratio is $\alpha : 1-\alpha$, where $\alpha \neq 0.5$) of the HNLF-NOLM, where the spectra of the both pulses are compressed because of the offset between the negative chirp in the pulses and the positive chirp generated by SPM effect in HNLF. When the pulses meet each other again in the coupler, their phase is different because of the SPM effect for different peak power of the pulses in the HNLF. As a result, the two pulses' pedestal can be decreased by interference only if the pulse which enters the NOLM possesses an appropriate power, at the same time, the spectrum of the output pulse is compressed effectively.

3. SIMULATION

In the simulation, the input pulse width is $T_{\mathrm{FWHM}} = 200\,\mathrm{fs}$ with the central wavelength 1550 nm. The dispersion of the DIF increases with the transmission distance of z which is given by the following

$$\beta_2(z) = -\ln\left(e + \frac{z}{L}\left(e^{-\beta_2(L)} - e\right)\right)\ \mathrm{ps}^2/\mathrm{km} \tag{1}$$

where L is the length of the DIF, $\beta_2(z)$ and $\beta_2(L)$ are the GVD parameter of the fiber at z and L, respectively. The parameters of the DIF are shown in Table 1. A 20 m-long SSMF with the dispersion of 15 ps/nm/km is connected with the DIF. In the HNLF-NOLM, the coupler ratio is 60 : 40, and the loss, dispersion, dispersion slope, nonlinearity coefficient of HNLF are 0.939 dB/km, 2.187 ps/nm/km, 0.022 ps/nm^2/km, 27 W^{-1}km^{-1}, respectively. The generalized nonlinear Schrödinger equation which describes the propagation of the pulses in the fibers is solved numerically using split-step Fourier method. In our simulation, the peak power of the input pulse of $P_{\mathrm{peak}} = 10\,\mathrm{W}$, 40 W and 80 W (correspond to $N = 0.5$, 1, 1.4 respectively for the DIF) are used, different SCRs are obtained by controlling the variable optical attenuator (VOA), which is located between the SSMF and coupler.

Figures 2, 3 and 4 illustrate the simulating results of the two-stage spectral compression scheme at $N = 0.5$, 1 and 1.4 respectively. Through the DIF, the spectra of the pulses are compressed from 12.6 nm to 11.96 nm, 9.86 nm, 6.66 nm, respectively, corresponding to the SCR of 1.05, 1.28 and 1.89. This working principle is the reverse operation of the well-adopted soliton temporal compression (spectral broadening) in a dispersion decreasing fiber [10]. In the case of $N = 0.5$, as shown in Figure 2, the minimum spectral width of the output is 8.56 nm which corresponds to the total SCR = 1.47. Figure 3 and Figure 4 represent the variation of the spectra when changing the attenuation of the VOA. It is obviously found that the spectra become narrower with increasing the power injected into the HNLF-NOLM. This behavior can be understood by noting that the initial chirp of the pulses launched into the HNLF-NOLM and the chirp due to the SPM effect are of opposite signs over the central portion of the pulses, and the pulses become less and less chirped with increasing the power launched into the HNLF-NOLM. Moreover, the minimum spectral width of 3.66 nm (total SCR = 3.44) and 1.15 nm (total SCR = 10.93) are obtained, respectively, at $N = 1$

Table 1: Parameters of DIF.

Loss α (m^{-1})	GVD parameter β_2 (ps^2/km)	TOD parameter β_3 (ps^3/km)	Length (m)	nonlinearity coefficient γ (W^{-1}km^{-1})
0.002	$-1\sim-11$	0.02	100	1.96

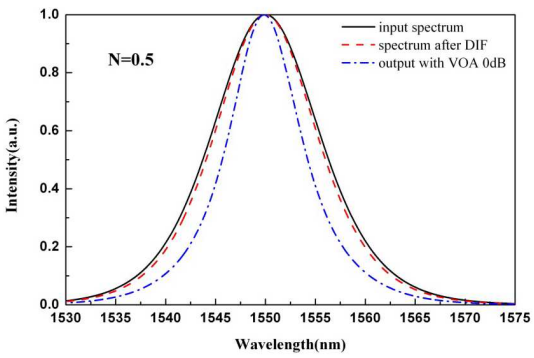

Figure 2: spectra of pulses at $N = 0.5$.

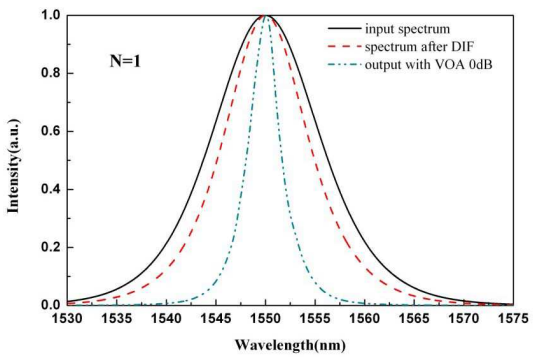

Figure 3: spectra of pulses at $N = 1$.

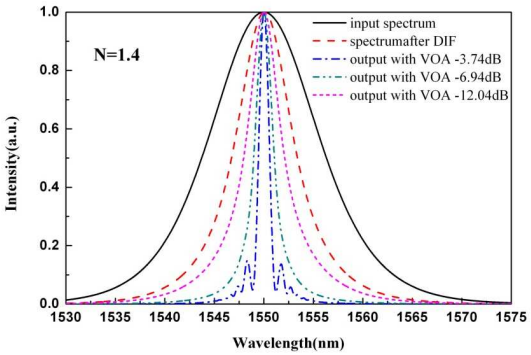

Figure 4: Spectra of pulses at $N = 1.4$.

and $N = 1.4$. However, a pedestal appears clearly, as shown in Figure 4, when the attenuation of the VOA is 3.74 dB for the insufficient compensation of the nonlinear chirp near the pulse edges. Comparing the three figures, the greater N is, the narrower the minimum spectral width gets in the range of $0.5 \leq N \leq 1.4$. Besides, because the Raman term of the GNLS has little effect in the cases of $N \leq 1.4$, there is almost no Raman soliton self-frequency shift which is vital to the resolution improvement of the all-optical quantization based on SSFS.

4. CONCLUSION

A novel two-stage spectral compression structure employing a logarithmic DIF cascading with a HNLF-NOLM is proposed. The numerically results show that the designed scheme works well on the spectral compression in the range of $0.5 \leq N \leq 1.4$ at 1550 nm. The higher peak power of the pulse launched into the HNLF-NOLM, the narrower spectral width is obtained. With little center-wavelength shift, the maximal spectral compression ratio can reach 10.93, at $P_{\text{peak}} = 80$ W.

ACKNOWLEDGMENT

This work is partially supported by Chinese 973 Program under Grant No. 2012CB315701, National Nature Science Foundation of China (No. 61205109), Science and Technology Innovation Team of Sichuan Province (No. 2011JTD0001).

REFERENCES

1. Shoop, B. L., *Photonic Analog-to-digital Conversion,* Springer-Verlag, Berlin, 2001.
2. Oda, S., A. Maurta, and K. Kitaymam, "All-optical quantization scheme based on fiber nonlinearity," *IEEE Photon. Technol. Lett.*, Vol. 16, No. 2, 587–589, 2004.
3. Oda, S. and A. Maurta, "A novel quantization scheme by slicing supercontinuum spectrum for all-optical conversion," *IEEE Photon. Technol. Lett.*, Vol. 17, No. 2, 465–467, 2005.
4. Konishi, T., K. Tanimura, and K. Asano, "All-optical analog-to-digital converter by use of self-frequency shifting in fiber and a pulse-shaping technique," *J. Opt. Soc. Am. B*, Vol. 19, No. 11, 2817–2823, 2002.
5. Washburn, B. R., J. A. Buck, and S. E. Ralph, "Transform-limited spectral compression due to self-phase modulation in fibers," *Opt. Lett.*, Vol. 25, No. 7, 445–447, 2000.
6. Xu, C. and X. Liu, "Photonic analog-to-digital converter using soliton self-frequency shift and interleaving spectral filters," *Opt. Lett.*, Vol. 28, No. 12, 986–988, 2003.
7. Sidorov-Biryukov, D. A., A. Fernandez, and L. Zhu, "Spectral narrowing of chirp-free light pulses in anomalously dispersive, highly nonlinear photonic-crystal fibers," *Opt. Express*, Vol. 16, No. 4, 2502–2507, 2008.
8. Li, H. P., X. J. Zhang, and J. K. Liao, "Spectral compression of femtosecond pulses in photonic crystal fiber with anomalous dispersion," *Proc. of SPIE*, Vol. 7630, 1–6, 2009.
9. Doran, N. J. and D. Wood, "Nonlinear-optical loop mirror," *Opt. Lett.*, Vol. 13, No. 1, 56–58, 1989.
10. Tamura, K. R. and M. Nkakzawa, "54-fs, 10-GHz soliton generation from a polarization-maintaining dispersion-flattened dispersion-decreasing fiber pulse compressor," *Opt. Lett.*, Vol. 26, No. 11, 762–764, 2001.

Design and Performance Evaluation of Single Antenna SSD (Simultaneous Single Band Duplex) System Using Turbo Equalizer

Changyoung An[1], **Hongsik Keum**[2], **and Heung-Gyoon Ryu**[1]

[1]Department of Electronic Engineering, Chungbuk National University, South Korea
[2]Electromagnetic Wave Technology Institute, Rapa, South Korea

Abstract— In this paper, we propose a single antenna SSD (simultaneous single band duplex) system using turbo equalizer. The proposed system communicates simultaneously on single band. That is the proposed system is full-duplex system. The proposed system uses balanced feed network circuit to improve isolation in single antenna structure. Also, the proposed system uses RF cancellation and digital cancellation to cancel self-interference. Additionally, the proposed system uses turbo equalizer to equalize ISI by harsh multipath fading and to collect bit errors by residual self-interference signals. By using turbo equalizer, the proposed system guarantees more QoS (quality of service). In this paper, we uses Simulink simulation program to analyze performance of the proposed system. The simulation results confirm that proposed system can communicate simultaneously by using balanced feed network, RF cancellation, digital cancellation and turbo equalizer in harsh multipath channel on single band.

1. INTRODUCTION

Recently, the use of small wireless terminal device is suddenly increasing. These wireless communication devices use duplex to exchange information. The duplex is a communication system to exchange information with each other while transmission and reception between devices. There are frequency-division duplex (FDD) and time-division duplex (TDD) in these duplex system [1, 2]. TDD is a system for transmission and reception by dividing time-domain. FDD is a system for transmission and reception by dividing frequency-domain. However, TDD requires guard interval that is a period that does not any transmission and reception. Further, it is impossible to use frequency band specified for complete transmit or complete receive. In FDD, there is a drawback that double frequency band is required in order to communicate duplex. Recently, research on SSD system that to solve the drawback of TDD and FDD is performing [3, 4].

SSD system improves the spectrum efficiency because SSD system uses single frequency band for transmission and reception simultaneously. But, SSD system that has these advantages causes self-interference because SSD system communicates simultaneously in the single band. That is, transmission signal of own station is received in receiver of own station. Power of self-interference by transmission signal of own station is larger than power of desired signal from distant station in SSD system. Therefore, the desired signal can be distorted completely by self-interference. If desired signal is distorted by self-interference, then it is impossible to receive information of distant station. Therefore, SSD system requires additional self-interference cancellation technic to cancel huge self-interference.

Generally, well known self-interference cancellation methods are RF cancellation and digital cancellation [5, 6]. RF cancellation is performed for self-interference cancellation in RF stage. RF cancellation cancels direct self-interference that moves directly from transmitter of own station to receiver of own station. Antiphase signal for self-interference cancellation is made by using transmission signal of own station in RF cancellation. Digital cancellation is performed for self-interference cancellation in digital stage after ADC. Digital cancellation cancels multipath self-interference and residual direct self-interference that is self-interference signal after RF cancellation. In these SSD system using RF cancellation and digital cancellation, in order to design RF cancellation circuit, amplitude and phase of self-interference is measured. And then attenuator and phase shifter are designed by using the measured amplitude and phase data. But, this RF cancellation method can be incorrect by change of antenna position and design. If RF cancellation circuit design is not satisfied with condition of same amplitude and antiphase, then performance of RF cancellation is degraded highly. Also, even though this SSD system cancels self-interference effectively by RF cancellation and digital cancellation, performance of SSD system can be degraded by multipath fading from distant station.

Therefore, in this paper, in order to solve this drawback of SSD system using two antennas, we design SSD system using single antenna and balanced feed network. And we propose and analyze single antenna SSD system using turbo equalizer to overcome performance degradation by harsh multipath fading.

2. SYSTEM MODEL

The SSD system is a system for simultaneous transmission and reception on the single band. In this paper, the proposed system is single antenna SSD system using turbo equalizer. In this paper, we use RF cancellation and digital cancellation for SSD communication. And then, we combine SSD system and turbo equalizer to overcome harsh multi-path channel.

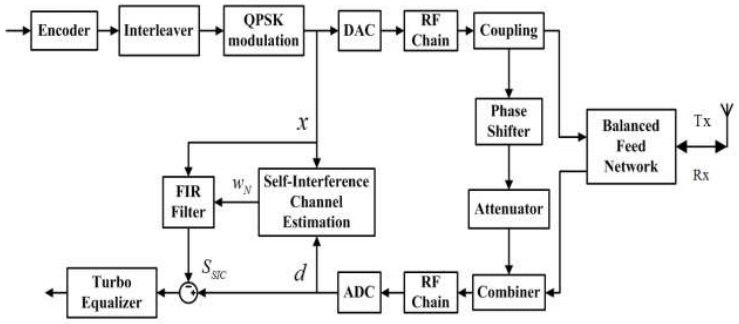

Figure 1: Block diagram of the proposed SSD system.

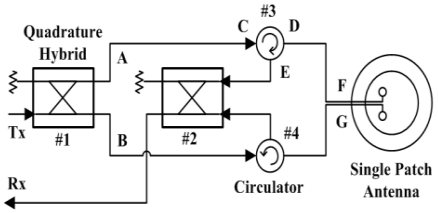

Figure 2: Block diagram of balanced feed network.

Figure 1 shows block diagram of the proposed SSD system using turbo equalizer. In signal flow of the proposed system, In this paper, the proposed system uses RF cancellation to cancel the leakage signal of balanced feed network. But, even though RF cancellation circuit cancels the leakage signal, residual leakage signal exists. Therefore, it is difficult to receive desired signal from distant station because this residual leakage signal and returned signal by multi-path is larger than desired signal from distant station. For this reason, the proposed system needs self-interference cancellation of digital-stage. In this paper, we use digital cancellation with LMS algorithm to cancel residual self-interference.

In this paper, the proposed system model of Fig. 1, it is possible to use the mobile terminal and a base station. The proposed system can increase spectral efficiency in the base station and the mobile terminal.

3. SELF-INTERFERENCE CANCELLATION AND TURBO EQUALIZER

3.1. Balanced Feed Network

Figure 2 shows block diagram of balanced feed network. In this paper, the proposed system uses single patch antenna. It is important to isolate transmit signal and receive signal in a transceiver with single antenna. In general, the transceiver with single antenna uses a circulator to isolate transmit signal and receive signal. Transmit signal from RF chain move to antenna and receive signal from antenna move to receiver by circulator. That is, the circulator prevents the leakage signal to receiver from transmitter. But, using the circulator, it is difficult to completely isolate transmit signal and receive signal. This leakage signal is larger than desired signal from distant station. Therefore, the leakage signal must be cancelled to receive the desired signal. In this paper, the proposed system uses balanced feed network circuit for efficient cancellation of transmit signal by leakage [7].

The balanced feed network isolates transmit signal that leaks to receiver by 40 dB [7]. The self-interference by the transmit leakage signal is $80 \sim 90$ dB larger than the desired signal. Therefore, even though the self-interference is cancelled 40 dB by the balanced feed network, a residual self-interference is larger than the desired signal. If the residual self-interference distorts the desired signal, then it is impossible to decode the desired signal. To solve this drawback, additional self-interference cancellation method is required.

3.2. RF Cancellation

In this paper, the proposed system uses a RF cancellation to cancel the residual self-interference from the balanced feed network. The RF cancellation uses principle that signals which has phase difference of 180 degrees and same amplitude is cancelled by combination each other. In this paper, the proposed system should generate a signal which has phase difference of 180 degrees and same amplitude with the residual self-interference. To generate the cancelling signal, a transmit signal after RF chain in own transmitter go through attenuator and phase shifter.

3.3. Digital Cancellation

Even though the proposed system cancels the self-interference by the balanced feed network and RF cancellation, a portion of the self-interference is remained. Therefore, the proposed system uses a digital cancellation to cancel this residual self-interference.

The digital cancellation is a self-interference cancellation method that estimates a coefficient of self-interference and cancels self-interference by using estimated coefficient in the digital stage. In this paper, the proposed system uses adaptive algorithm for self-interference estimation. In this paper, we use a LMS (least mean square) algorithm as adaptive algorithm. The LMS algorithm is to minimize an error of a desired signal and output signal of FIR filter. That is, the LMS algorithm updates coefficients of FIR filter to minimize the error continuously [8]. In the LMS algorithm, the error of input desired signal and output signal of FIR filter is given by

$$e_k = d_k - W_k^H X_k \tag{1}$$

where d_k is the desired signal, X_k is input signal. W_k^H is estimated coefficient that apply to FIR filter. Therefore, $W_k^H X_k$ is the output signal of FIR filter. The error is calculated by subtracting the output signal of FIR filter from the desired signal. In Equation (1), the desired signal is a receive signal that is combined with self-interference after ADC. The input signal is transmit signal of digital stage before DAC. An equation to update the coefficient of FIR filter is given by [8]

$$W_{k+1} = W_k + 2\mu e_k X_k \tag{2}$$

where μ is step size. Firstly, LMS algorithm estimates coefficient to minimize the error by using Equation (2). Next, the estimated coefficient is applied to a FIR filter. Next, the transmit signal pass through the FIR filter, thereby output of the FIR filter becomes similar to the self-interference. Finally, the self-interference is cancelled by subtracting the output signal of FIR filter from the receive signal in digital stage.

3.4. Turbo Equalizer

In this paper, we use a turbo equalizer to equalize ISI channel and correct bit error by the residual self-interference. The turbo equalizer increases a performance of communication system by combining with equalizer and decoder and by iterating LLR value [9].

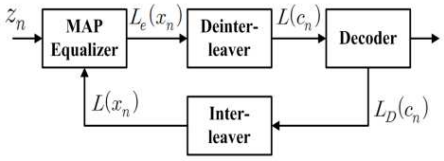

Figure 3: Block diagram of turbo equalizer.

Figure 3 shows block diagram of turbo equalizer. The turbo equalizer consists of MAP equalizer, deinterleaver, decoder and interleaver. The MAP equalizer shows to perform best. The deinterleaver restores mixed bit sequence by the interleaver. The decoder corrects bit error of encoded bit stream. Output of the MAP equalizer is given by [9]

$$L_e(x_n) \cong \ln \frac{P(x_n = +1|z_1, \ldots, z_{K_c})}{P(x_n = -1|z_1, \ldots, z_{K_c})} - \log \frac{P(x_n = +1)}{P(x_n = -1)} \tag{3}$$

where Output of the MAP equalizer is calculated by subtracting a prior probability LLR value from a posterior probability LLR value. z_n, $n = 1, 2, \ldots, K_c$ is receive symbol. The prior probability

$L(x_n)$ that is output of the interleaver shows prior information by generation probability of x_n. $L(x_n)$ is calculated by the decoder. In initial equalization step, $L(x_n) = 0$ because there is a prior information. In the decoder, a posterior probability $P(c_n = x|L(c_1), \ldots, L(c_{K_c}))$, $x \in B$ is calculated by using $L(c_n)$. Output of the MAP decoder is given by [9]

$$L_D(c_n) = \ln \frac{P(c_n = +1|L(c_1), \ldots, L(c_{K_c}))}{P(c_n = -1|L(c_1), \ldots, L(c_{K_c}))} - \ln \frac{P(c_n = +1)}{P(c_n = -1)} \tag{4}$$

where $L(c_n)$ is output of the MAP equalizer. And $L(c_n)$ is calculated by passing $L_e(x_n)$ through the deinterleaver. Output of the MAP decoder feed back to the MAP equalizer through the interleaver. In the MAP equalizer, output of the MAP decoder is used as a prior probability. The turbo equalizer improves the equalization performance by iterating this mechanism. Finally, the MAP decoder decides data bits. Decision equation of data bits is given by [9]

$$\widehat{b}_i = \arg\max_{b\in\{0,1\}} P(b_i = b|L(c_1), \ldots, L(c_{K_c})) \tag{5}$$

4. SIMULATION RESULTS AND ANALYSIS

In this paper, we use the Simulink simulation program to analysis performance of the proposed SSD system using turbo equalizer. In this paper, we consider that power of transmit signal is 20 dB. And, we consider that power of self-interference by multi-path fading is −40 dB. We consider that balanced feed network that isolates transmit path and receive path has phase shift error of 0.5 degrees. In this paper, for digital cancellation, we use a LMS algorithm which has 32 taps. A step size of the LMS algorithm is 0.001. In this paper, we consider that power of transmit signal is 20 dB. We consider that power of receive signal from distant station is −70 dB.

Table 1: Simulation parameters.

Parameters	**Values**
Modulation	QPSK
Adaptive algorithm	LMS
Number of taps	32
Step size	0.001
Channel	Proakis A, Proakis B, Proakis C
Channel coding	Convolution code
Code rate	3/4
Equalizer	Turbo Equalizer
Number of iteration	0, 1, 2, 3, 4

Table 1 shows simulation parameters.

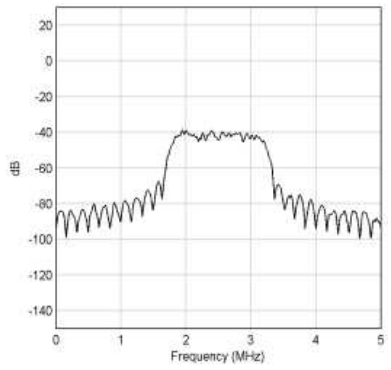

Figure 4: Spectrum of multipath self-interference signal.

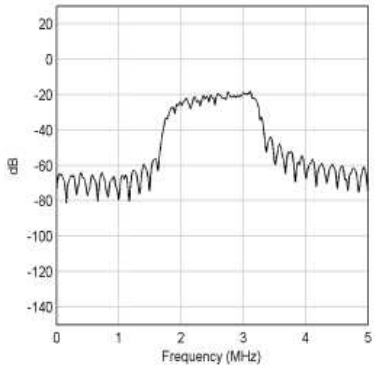

Figure 5: Spectrum of receive signal after balanced feed network.

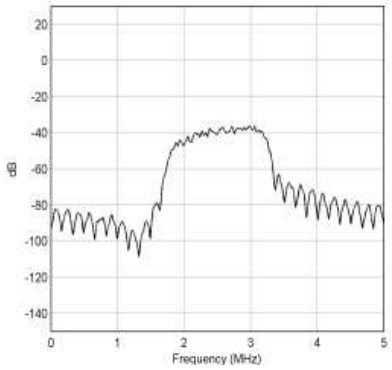

Figure 6: Spectrum of signal after RF cancellation.

Figure 4 shows spectrum of self-interference by multi-path fading. In this paper, we consider that power of self-interference by multi-path fading is −40 dB.

Figure 5 shows spectrum of a receive signal after it has passed through balanced feed network. We can confirm that power of the receive signal after balanced feed network. This signal consists of desired signal, self-interference by multi-path fading and leakage signal of transmit signal from balanced feed network. In receiver path, leakage signal of transmit signal after balanced feed network is larger than desired signal from distant station. Therefore it is impossible to decode desired signal information in receive signal. Therefore, for decode desired signal information, the proposed system requires additional self-interference cancellation method.

Figure 6 shows spectrum after RF cancellation. RF cancellation cancels leaked self-interference signal from balanced feed network. In Fig. 6, we can confirm that self-interference of 20 dB is additionally cancelled by RF cancellation. But, self-interference signal after RF cancellation is larger than desired signal which has power of −70 dB. Therefore, it is impossible to decode desired signal information in receive signal. Therefore, for decode desired signal information, the proposed system requires additional self-interference cancellation method.

Figure 7 shows spectrum of signal after and before digital cancellation. We can confirm that power of signal before digital cancellation is −25 dB ∼ −30 dB. We can confirm that power of signal after digital cancellation is −60 dB ∼ −65 dB. We can confirm that self-interference is cancelled 30 dB ∼ 35 dB additionally.

Figure 8(a) shows performance of the proposed system according to iteration of turbo equalizer in Proakis A. Multi-path fading of Proakis A channel is worse than multi-path fading of Proakis B and Proakis C channel. In Proakis A channel, when the number of iterations of turbo equalizer is 1, performance of the proposed system is saturated. In this paper, we can confirm that performance of the proposed system is 2×10^{-5} at 10 dB when the number of iterations of turbo equalizer is 1 in Proakis A channel.

Figure 8(b) shows performance of the proposed system according to iteration of turbo equalizer in

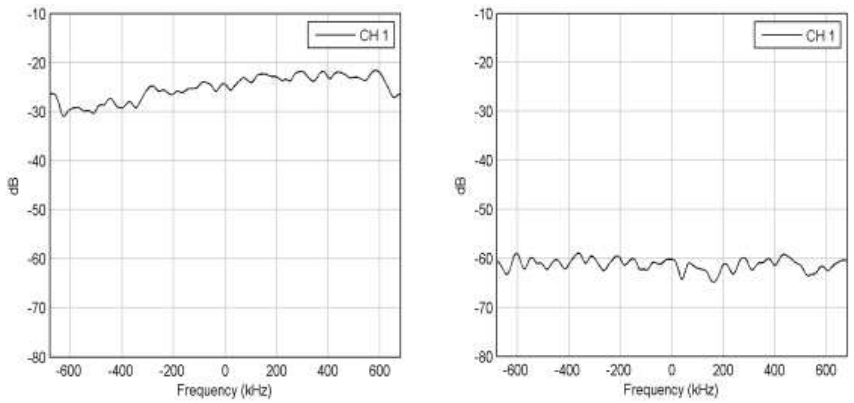

Figure 7: Spectrum of signal after digital cancellation, (a) before (b) after.

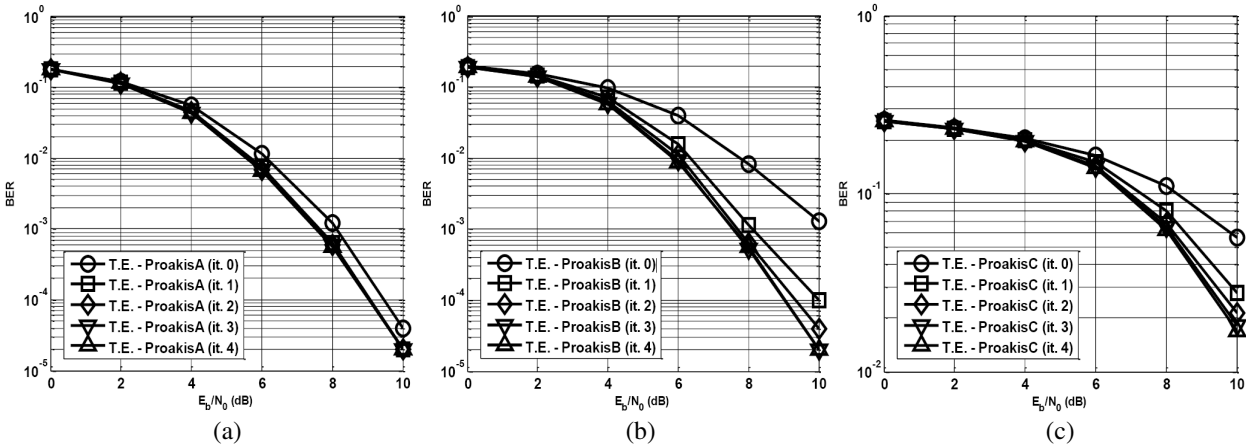

Figure 8: BER performance of proposed system according to global iteration in Proakis A, Proakis B and Proakis C channel. (a) Proakis A channel. (b) Proakis B channel. (c) Proakis C channel.

Proakis B. In Proakis B channel, when the number of iterations of turbo equalizer is 3, performance of the proposed system is saturated. In this paper, we can confirm that performance of the proposed system is 2×10^{-5} at 10 dB when the number of iterations of turbo equalizer is 3 in Proakis B channel.

Figure 8(c) shows performance of the proposed system according to iteration of turbo equalizer in Proakis C. Proakis C channel is harsh multi-path fading channel. In this paper, we can confirm that performance of the proposed system is 2×10^{-5} at 10 dB when the number of iterations of turbo equalizer is 4 in Proakis C channel.

5. CONCLUSION

In this paper, we propose the SSD system using turbo equalizer. In the proposed system, self-interference is cancelled 40 dB by balanced feed network, and self-interference is cancelled 20 dB by RF cancellation. Finally, self-interference is cancelled 30 dB $\sim$ 35 dB by digital cancellation. Totally, performance of self-interference cancellation of the proposed system is 90 dB $\sim$ 95 dB. That is, we can confirm that it is possible to decode desired signal through turbo equalizer in the proposed system. In the proposed system, self-interference is cancelled 90 dB totally in Proakis A, Proakis B and Proakis C channel.

ACKNOWLEDGMENT

This research was supported by Basic Science Research Program through the National Research Foundation of Korea (NRF) funded by the Ministry of Education, Science and Technology (No. 2013-R1A2A2A01005849).

REFERENCES

1. Esmailzadeh, R., M. Nakagawa, and E. A. Sourour, "Time-division duplex CDMA communications," *IEEE Personal Communications*, Vol. 4, No. 2, 51–56, Apr. 1997.
2. Dong, L., "Open-loop beamforming for frequency-division duplex mobile wireless access," *IEEE Transactions on Vehicular Technology*, Vol. 56, No. 4, 1845–1849, Jul. 2007.
3. Choi, J. I., M. Jain, K. Srinivasan, P. Levis, and S. Katti, "Achieving single channel, full duplex wireless communication," *Proc. 16th Annu. Int. Conf. Mobile Comput. Networking (Mobicom'10)*, 1–12, Chicago, USA, Sep. 2010.
4. Duarte, M., C. Dick, and A. Sabharwal, "Experiment-driven characterization of full-duplex wireless systems," *IEEE Trans. Wireless Commun.*, Vol. 11, No. 12, 4296–4307, Dec. 2012.
5. Li, N., W. Zhu, and H. Han, "Digital interference cancellation in single channel, full duplex wireless communication," *8th International Conference on Wireless Communications, Networking and Mobile Computing (WiCOM)*, 1–4, Sep. 21–23, 2012.
6. Riihonen, T. and R. Wichman, "Analog and digital self-interference cancellation in full-duplex MIMO-OFDM transceivers with limited resolution in A/D conversion," *Conference Record of the Forty Sixth Asilomar Conference on Signals, Systems and Computers (ASILOMAR)*, 45–49, Nov. 4–7, 2012.
7. Knox, M. E., "Single antenna full duplex communications using a common carrier," *IEEE 13th Annual Wireless and Microwave Technology Conference (WAMICON)*, 1–6, Apr. 15–17, 2012.
8. Jeong, Y.-H., "A adaptive blind equalization algorithm with a double step size LMS using the decision-directed error," *J. Korean Inst. Commun. Inform. Sci. (KICS)*, Vol. 37, No. 2, 55–60, Korea, Dec. 2012.
9. Tüchler, M., R. Koetter, and A. C. Singer, "Turbo equalization: principles and new results," *IEEE Transactions on Communications*, Vol. 50, No. 5, 754–767, May 2002.

Preparation Technique of AlN Piezoelectric Thin Film

Guanbo Yin[1, 2], S. Imran[3], and Yungui Ma[2]

[1]Department of Materials Science and Engineering
Nanjing University of Science and Technology, Nanjing, China
[2]State Key Lab of Modern Optical Instrumentation
Department of Optical Engineering, Zhejiang University, Hangzhou, China
[3]South China Academy of Advanced Optoelectronics
South China Normal University, Guangzhou, China

Abstract— AlN piezoelectric thin films were prepared by DC magnetron reactive sputtering. A good *c*-axis orientation is essential for obtaining high piezoelectric coefficients. Therefore, the experiments were designed about the four parameters of the sputtering power, volume ratio of N_2 and Ar, gas pressure, and substrate temperature, in order to make sure the deposition parameters of the *c*-axis orientation AlN film. The crystal structure and full width at half maximum (FWHM) of the thin films were analyzed by X-ray diffraction (XRD). The results show that the optimal process parameters were the sputtering power of 200 W, volume ratio of N_2 and Ar of 2 : 8, gas pressure of 3.75 mT. The results provide the experiment evidence and process base for the next study.

1. INTRODUCTION

Aluminum nitride (AlN) is a wide band gap III-V Piezoelectric material with high CMOS compatibility. AlN piezoelectric thin films have excellent properties of physical and chemical, such as good chemical stability, high piezoelectric coefficient, high band gap, and high dielectric constant and so on which led to widespread concern [1–3]. AlN materials are widely used in the ultraviolet range of the light-emitting diode (LED), short-wavelength detectors, field emission displays, and integrated circuit packaging, dielectric isolation and insulation, and other fields.

The lattice orientation of AlN films has great influence on the center frequency and electromechanical coupling coefficient of acoustic wave devices. Control piezoelectric film growth direction along the *c*-axis is very important (002), because only when propagate along the surface of AlN thin films that have high lattice *c*-axis orientation, the surface acoustic wave will have fastest phase speed, meanwhile the film can shows the most excellent piezoelectric properties, so as to achieve a higher electromechanical coupling coefficients [4, 5]. Thus control piezoelectric film growth direction along the *c*-axis (002) is very important. In order to obtain high-quality AlN films, we need to understand the impact factors of the thin films growth and control the behavior of thin films.

Almost all of the deposition techniques, including reactive sputtering [6, 7], chemical vapor deposition [8] and molecular beam epitaxial [9], have been used to deposit aluminum nitride film. In these techniques, the magnetic reactive sputtering has advantages of a simple operation, low equipment cost, low deposition temperature and deposition rate. thus it is the most common method.

2. EXPERIMENT PROCEDURES

There are many methods to prepare AlN films; in this paper we choose DC magnetron reactive sputtering method. Reactive magnetron sputtering has advantages of a simple operation, low equipment cost, low deposition temperature and deposition rate. The aluminum nitride thin films with a typical thickness of about 200 nm were deposited on Pt-covered Si (100) substrate, and using nitrogen as a reaction gas by a chemical reaction. And substrate temperature set 300 degree. Prior to deposition the wafers were cleaned with acetone and deionised water. The deposition chamber was filled with a gas composition consisting of a mixture of N_2 and Ar. The aluminum target, with a purity of 99.999% had a diameter of 50.8 mm. After evacuation of the deposition chamber below 5×10^{-6} mbar, argon gas was introduced to pre-sputter the target for 10 min prior to each film deposition for purification purposes.

3. RESULTS AND DISCUSSION

X-ray diffraction (XRD) technique was used for phase analysis. Figure 1 shows the XRD patterns of samples deposited with different sputtering powers. As can be seen from Figure 1, when sputtering

power are 100 W, 150 W and 250 W, films growth orientation is (110), and films growth orientation is (002) only when sputtering power is 200 W. Table 1 lists FWHM of the (002) peak for the AlN films deposited at various sputtering powers. From Figure 1 and Table 1, Summed up that 200 W is the best sputtering power to the preparation of high c-axis orientation of AlN films.

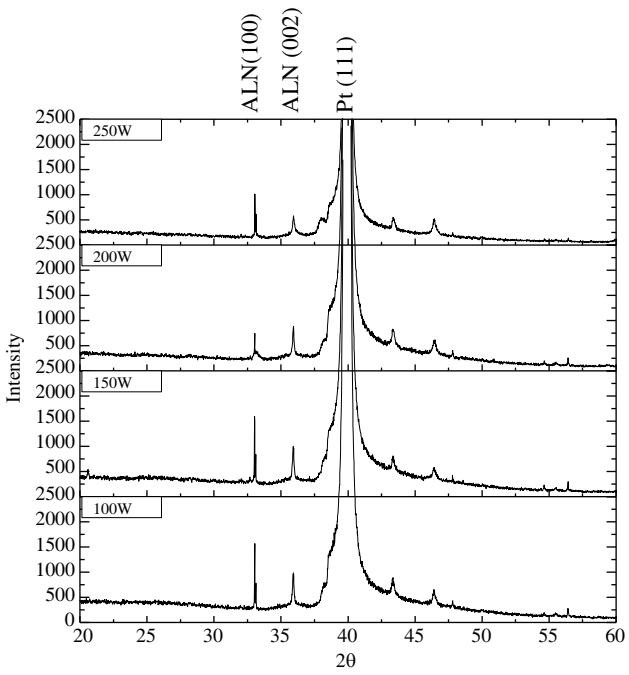

Figure 1: XRD patterns of samples deposited with different sputtering powers.

Table 1: FWHM of the (002) peak for the AlN films deposited at various sputtering powers.

Sputtering power	**FWHM**
100 W	0.15290
150 W	0.15484
200 W	0.15325
250 W	0.23614

Figure 2 show the XRD patterns of samples deposited with different volume ratio of N_2 and Ar. As can be seen from Figure 1, only when volume ratio of N_2 and Ar is 3 : 7, films growth orientation is (002). Table 1 lists FWHM of the (002) peak for the AlN films deposited at volume ratio of N_2 and Ar. The FWHM is smaller, the lattice orientation of films is better. As a result, when volume ratio of N_2 and Ar is 3 : 7, high c-axis orientation of AlN films can be obtained.

Table 2: FWHM of the (002) peak for the AlN films deposited at volume ratio of N_2 and Ar.

volume ratio of N_2 and Ar	**FWHM**
3 : 7	0.12575
4 : 6	0.1388
5 : 5	0.14638
6 : 4	0.14644
7 : 3	0.19923

Figure 3 shows the XRD patterns of samples deposited with different gas pressure. As can be seen from Figure 3, the intensity of the (002) peak more than the (100) peak when gas pressure is 3.75 mT. And FWHM is lowest when gas pressure is 3.75 mT. So 3.73 mT is the best pressure to obtain high c-axis orientation of AlN films.

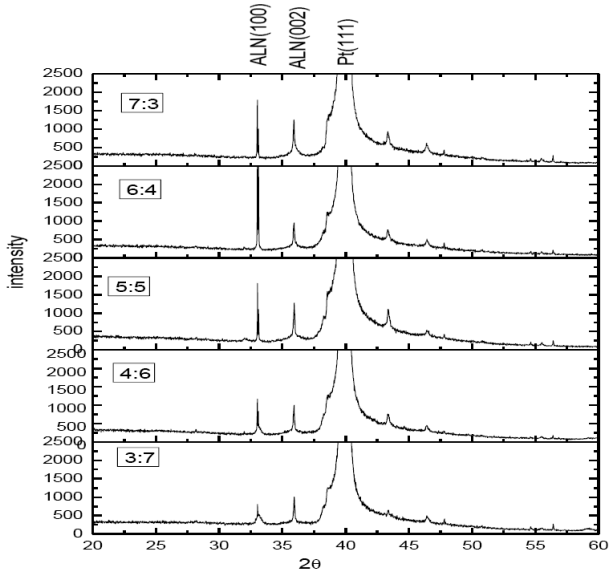

Figure 2: XRD patterns of samples deposited with different volume ratio of N_2 and Ar.

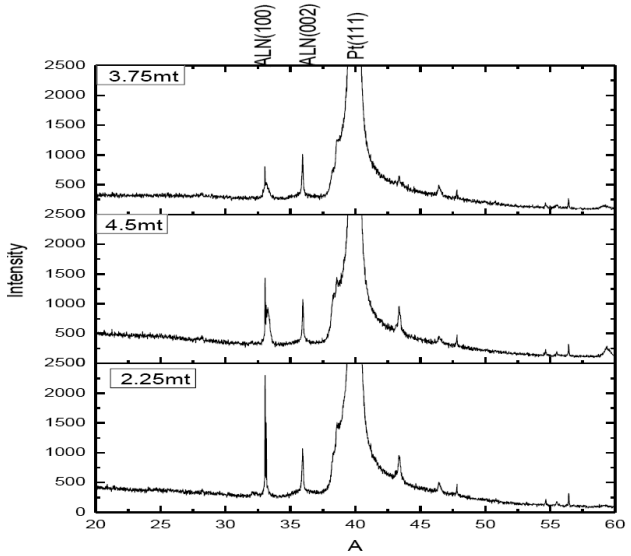

Figure 3: XRD patterns of samples deposited with different gas pressure.

Table 3: FWHM of the (002) peak for the AlN films deposited at various gas pressure.

gas pressure	**FWHM**
2.25 mT	0.14581
3.75 mT	0.12923
4.5 mT	0.12923

4. CONCLUSIONS

In this work, the film samples were prepared under different conditions for performance testing. According to the results of XRD patterns and FWHM of samples, AlN thin films with a high *c*-axis orientation can be obtained well when the sputtering power of 200 W, volume ratio of N_2 and Ar of 2 : 8 and gas pressure of 3.75 mT.

ACKNOWLEDGMENT

This project is partially supported by the National High Technology Research and Development Program (863) of China (No. 2012AA030402).

REFERENCES

1. Morosanu, C., T. A. Stoica, T. F. Stoica, et al., "Optical electrical and structural properties of AlN thin films," *Proceedings of CAS95 Semiconductor Conference*, 183–186, Sinaia, Romania, 1995.
2. Hirose, Y., T. Goto, J. Shiraishi, et al., "Development of AlN substrate for high frequency devices," *Proceedings of the 18th IEEE/CPMT International Electronic Manufacturing Technology Symposium*, 240–243, Omiya, Japan, 1995.
3. Chen, Y. H., Y. Gao, S. W. Xi, et al., "Effect of Ar/O_2 gas ratio and annealing temperature on the structure and properties of ZnO film," *Proceedings of the 10th International Conference on Electronic Measurement & Instruments*, 54–57, Chengdu, China, 2011.
4. Shiosaki, T., T. Yamamoto, T. Oda, et al., "Low-temperature growth of piezoelectric AlN film by rf reactive planar magnetron sputtering," *Appl. Phys. Lett.*, Vol. 36, No. 8, 643–645, 1980.
5. Xu, C. K. and X. L. Meng, *Acoustic Surface Wave Apparatus and Its Application*, 99–108, Science Press, Beijing, 1984.
6. Wang, B., M. Wang, R. Wang, et al., "The growth of AlN films composed of silkworm-shape grains and the orientation mechanism," *Mater. Lett.*, Vol. 53, 367–370, 2002.
7. Cho, J. W., *Pulsed DC Reactive Magnetron Sputtering of Aluminum Nitride Thin Films*, North Carolina State University, Raleigh, 2002.
8. Huang, A. P., G. J. Wang, S. L. Xu, et al., "Oriented AlN films prepared with solid $AlCl_3$ source by bias assisted Cat-CVD," *Mater. Sci. Eng. B*, Vol. 107, No. 2, 161–165, 2004.
9. Cheng, C., Y. Chen, and H. Wang, "Low-temperature growth of aluminum nitride thin films on silicon by reactive radio frequency magnetron sputtering," *J. Vac. Sci. Technol. A*, Vol. 14, No. 4, 2238–2242, 1996.

Research on the Magnetic Field Space-time Distribution in the Air-core Pulse Transformer

Xiao Yang, Jianhua Yang, Xinbing Cheng, Jiajin Lin, and Lin Lian
College of Optoelectronic Science and Engineering
National University of Defence Technology, Changsha 410073, China

Abstract— In the large-scale pulsed power device, the transient strong magnetic field, which is caused by transient high current, may have effects on the insulation property of the whole system. Therefore, in order to investigate the magnetic field space-time distribution and the influence generated by the axial magnetic field on the insulation performance in the pulsed power device, circuit simulation and transient magnetic field simulation are utilized. It can be found that the coupling coefficient makes much influence on the phase difference between the magnetic field and the load voltage. As the coupling coefficient reduces appropriately, the magnetic field in the vicinity of the peak load voltage increases greatly. The magnetic field distribution in the space is much related to the structure of transformers. In the air core of the transformer, the magnetic field is uniform along the radial, but a little higher near the rim. Besides, the magnetic field decreases relatively faster along the axial when it approaches the edge of the coils. Finally, an air-core pulse transformer with a coupling coefficient of 0.8 is constructed, and the magnetic field space-time distributions in the air core and the area between primary and secondary coils are measured. The experimental results correspond with the theoretical simulation results. The conclusions in the paper are favorable to use the transient strong magnetic field reasonably and to improve the insulation property in this type of transformer.

1. INTRODUCTION

The air-core pulse transformer has been applied generally in the pulsed power system. As there isn't any magnetic cores in air-core pulse transformer, it has great advantages, such as light weight and no magnetic saturation effect [1, 2]. Besides, the internal space of the transformer can be used to place other devices, which makes the pulsed power system compact. However, there is a high-intensity transient magnetic field in the region, and it may have effect on the insulation property. Especially in vacuum, the insulation strength of high voltage transformer can be improved with the high-intensity magnetic field [3], and the magnetic field can also be used to restrain the vacuum creepage flashover [4]. Therefore it is necessary to analyse and measure the magnetic field space-time distribution in the air-core pulse transformer if the internal space of the transformer is to be used. In this paper a simulation method of analyzing the magnetic field space-time distribution in the air-core pulse transformer is presented, and the phase relation between the magnetic field and the load voltage is discussed. Finally, the simulation result and the measurement result of the magnetic field space-time distribution in an air-core pulse transformer with coupling coefficient of 0.8 are given.

2. SIMPLIFIED MODEL OF THE AIR-CORE PULSE TRANSFORMER

The schematic of air-cored pulse transformer is given in Figure 1. The primary winding is in single turn, and the cone secondary winding of 300 turns is placed in the primary winding. The radial width of the transformer is 360 mm, and the axial length is 400 mm. In Figure 1 the transformer consists of three regions, the region I is the air core of the transformer, and region II is the space between the primary winding and the secondary winding, and region III is the external of the transformer. The discharge circuit of pulse transformer is given in Figure 2, the circuit parameters are as follows: primary capacitance $C_1 = 1680\,\mu\text{F}$, primary loop equivalent resistance $R_1 = 0.005\,\Omega$ equivalent inductance $L_1 = 0.05\,\mu\text{H}$, primary winding inductance $Lp = 0.3\,\mu\text{H}$. In the secondary circuit capacitance $C_2 = 10\,\text{nF}$, secondary winding equivalent resistance $R_2 = 30\,\Omega$, secondary winding inductance $Ls = 20\,\text{mH}$.

3. SIMULATION OF THE PHASE RELATION OF CURRENT AND LOAD VOLTAGE

The magnetic field generated by the primary winding current and secondary winding current in the transformer are both approximately axial, so the primary winding current and secondary winding current can be added to estimate the combining magnetic field. With the combining current, the phase relation between the magnetic field and the load voltage can be compared.

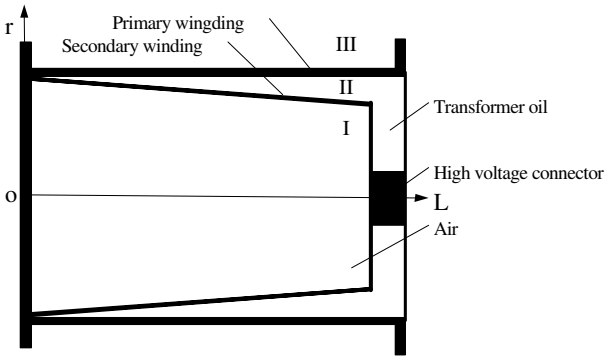

Figure 1: Schematic of air-cored pulse transformer.

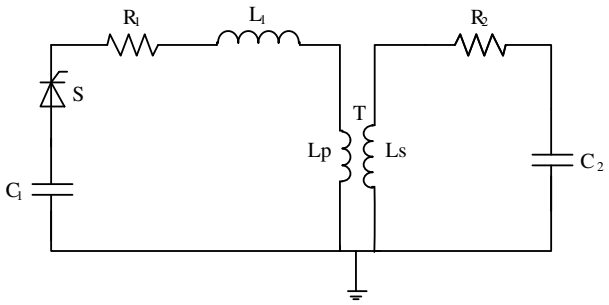

Figure 2: The discharge circuit of pulse transformer.

In the current simulation it can be found that the primary and secondary winding current is in the opposite direction, and the magnetic field in region I is mostly counteracted when the coupling coefficient is nearly 1. Besides, it exists 90° phase difference between the peak of load voltage and the peak of the magnetic field. The result is that the magnetic field nearly disappears when the load voltage approaches its peak. Thus, the transformer with high coupling coefficient can be influenced little by the magnetic field. However, it is different in the transformer with low coupling coefficient such as the air-core pulse transformer. The phase relation among the primary and secondary winding current and the load voltage will change with different coupling coefficient, and those results in the change of the magnetic field. Besides, other parameters like capacitance and inductance have effect on the frequency of the magnetic field, and the resistance and the charging voltage have effect on the size of the magnetic field, but all of them have little effect on the phase difference. Therefore the coupling coefficient is the key factor of changing the time distribution of the magnetic field.

Figure 3 shows the waveform of the primary and secondary current with different coupling coefficients. Ip is the primary winding current, and Is is the secondary winding current. The secondary winding current is multiplied by -300. As Fig. 3 shows, both of the current amplitude decreases with the reducing of coupling coefficient, and Ip decreases more in the forward direction and less in the reverse direction. Especially in the transformer with the coupling coefficient of 0.8, the primary and secondary current are in the same direction at some moments. At the same time, the phase difference between Ip and Is increases when the coupling coefficient falls. That means the Is can't weaken the magnetic field in time. As a result, the magnetic field can reach a rather high level.

The net current I_0 is defined to estimate the magnetic field: $I_0 = Ip + 300 \times Is$. And in order to analyze the magnetic field characteristic in the vicinity of the peak load voltage, the net current and the load voltage with different coupling coefficient are presented in Fig. 4.

As shown in Fig. 4 the net current is incremental before the load voltage reaches its peak. That means the magnetic field increases with the load voltage going up. If the magnetic field is strong enough, such magnetic field time distribution is useful to improve the insulation property. Besides, the net current increases obviously when the coupling coefficient decreases, also the peak of the

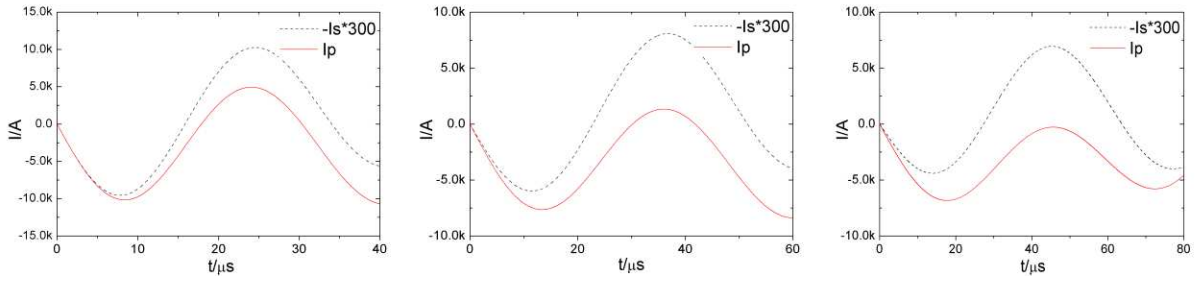

Figure 3: Simulated result of primary and secondary current with different coupling coefficient. (a) Coupling coefficient of 1. (b) Coupling coefficient of 0.9. (c) Coupling coefficient of 0.8.

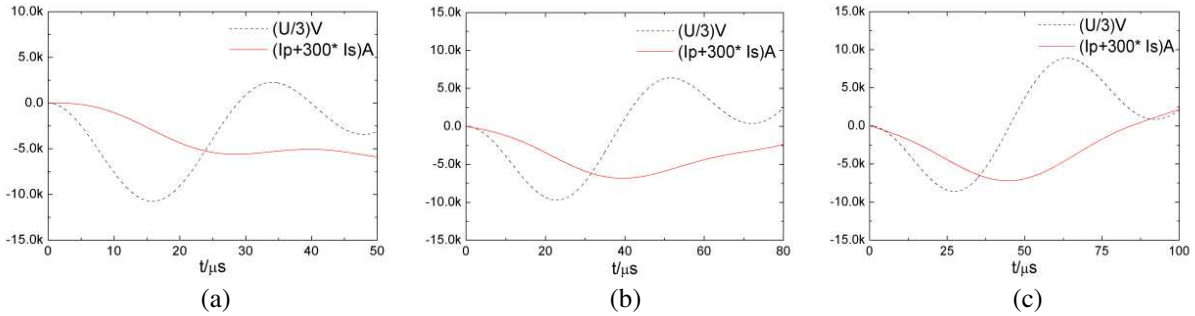

Figure 4: Simulated result of net current and load voltage with different coupling coefficient. (a) Coupling coefficient of 1. (b) Coupling coefficient of 0.9. (c) Coupling coefficient of 0.8.

Table 1: Net current with different coupling coefficient at $0.9U_m$.

Coupling coefficient	1	0.9	0.8	0.7
$0.9U_m$/kV	29.035	26.252	23.211	20.170
Net current/kA	1.82	2.98	3.77	4.30

net current and the load voltage gets closer. The net current with different coupling coefficient at $0.9U_m$ are compared as shown in Table 1, and it indicates that the magnetic field distribution generated by the transformers with low coupling coefficient is more likely to be used.

4. COMPARISON OF SIMULATION AND EXPERIMENT

According to the analysis above, the transformers with low coupling coefficient can get more advantaged magnetic field distribution. Here the magnetic field in a transformer with coupling coefficient of 0.8 was simulated and measured.

The waveform comparison of magnetic field B_y and the net current I_0 is shown in Fig. 5, and they are similar in the time distribution on the whole. It proves the rationality of the analysis method above. And in Fig. 6 three moments are chosen to compare the magnetic field strength in region I and region II before the magnetic field reaches its first peak. And the three moments are $t = 45\,\mu s$ when the magnetic field B_y reaches its peak, $t = 26\,\mu s$ when the load voltage U reaches its peak, and $t = 20\,\mu s$ when the load voltage $U = 0.8U_m$. It can be found that the magnetic field in the region I and region II may reach 0.015 T, however in different moment. But both the magnetic field in the region I and region II can reach 0.01 T at the same time when $U = U_m$. That means the magnetic field strength in the transformer can reach a high level when the system is under high voltage.

Referring to Fig. 7, the magnetic field space distribution in an air-core transformer is simulated as shown in (a)–(c) and measured as shown in (d)–(f). The experiment result practically accords with the simulation. The magnetic field in region I is uniform along the radial, while a little higher

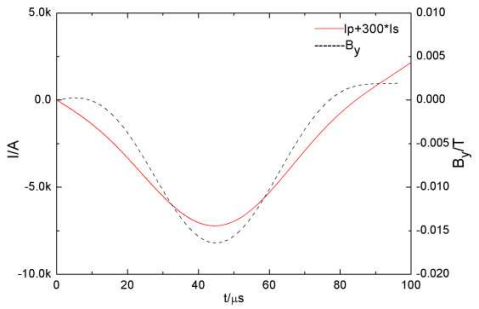

Figure 5: Contrast of net current and B_y waveform.

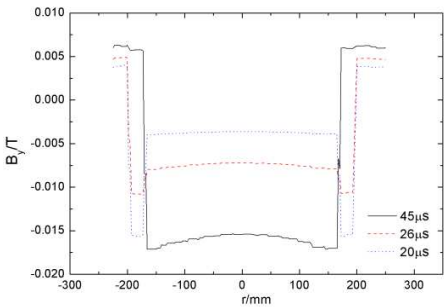

Figure 6: Radial distribution of B_y at different moment.

near the rim. It is also uniform along the axial but decreases fast relatively when it approaches the edge of the coils. The magnetic field distribution in region II is similar.

As shown in Fig. 8, the experimental magnetic field waveform is almost the same with the simulated prediction magnetic field waveform. And the difference in (b) is mainly caused by the nonuniform distribution of the current in the primary winding.

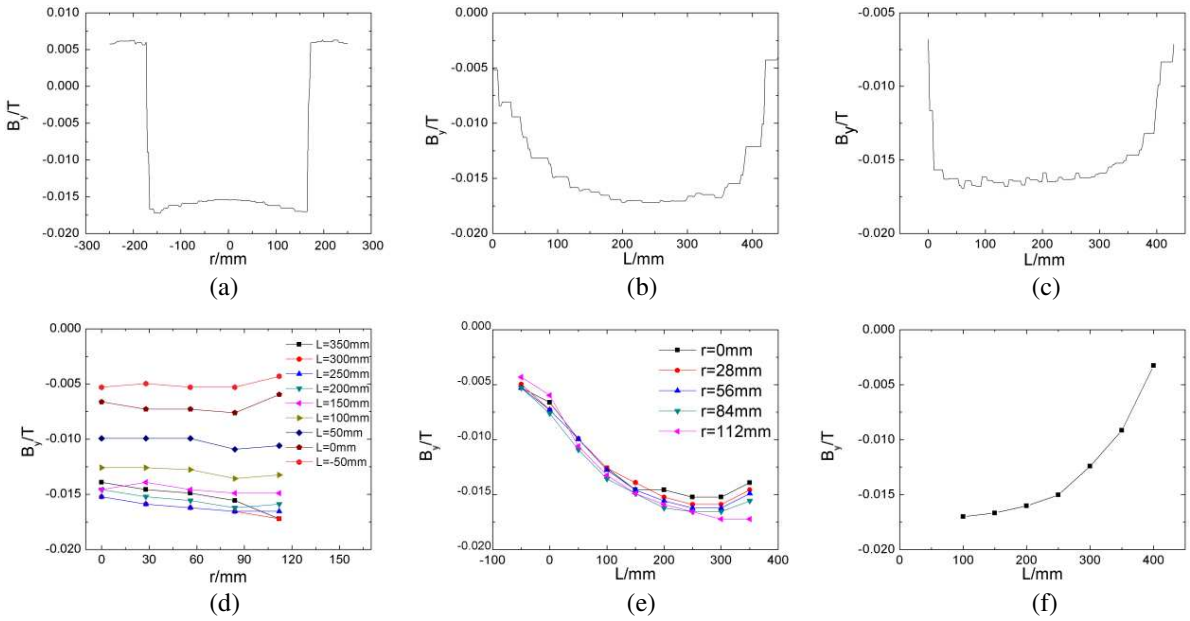

Figure 7: Comparison of simulated and experimental magnetic field space distribution. (a) Simulated radial distribution in I. (b) Simulated axial distribution in I. (c) Simulated axial distribution in II. (d) Experimental radial distribution in I. (e) Experimental axial distribution in I. (f) Experimental axial distribution in II.

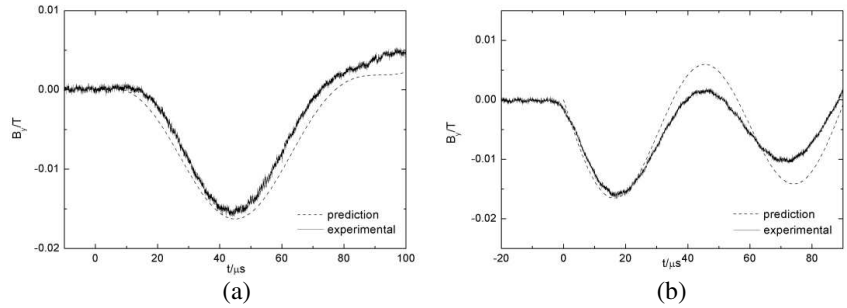

Figure 8: Comparison of simulated and experimental magnetic field time distribution. (a) Magnetic field waveform in region I. (b) Magnetic field waveform in region II.

5. CONCLUSIONS

An approximate method of analyzing the magnetic field space-time distribution in the air-core pulse transformer is presented in this paper. And the coupling coefficient is found to be the key factor influencing the time distribution of the magnetic field, which will determine the phase relation between the transient high voltage and magnetic field. With the coupling coefficient decreasing, the magnetic field increases obviously. The magnetic field space-time distribution in an air-core pulse transformer with a coupling coefficient of 0.8 is simulated and measured, and the experimental results correspond with the simulation result. The magnetic field space distribution is uniform, and it is lower as it's near the top and bottom. The magnetic field strength in the two regions of transformers can reach a high level at the same moment.

REFERENCES

1. Baum, C. E., W. L. Baker, and W. D. Prather, "A highly directive, very intensive, impulse-like radiator," *Proceedings of IEEE*, Vol. 92, No. 7, 1096–1109, 2004.
2. Sarkar, P., S. W. Braidwood, and I. R. Smith, "A compact battery-powered 500 kV pulse generator for UWB radiation," *15th IEEE Internanional Pulsed Power Conference*, 1306–1309, 2005.
3. Istenič, M., B. M. Novac, J. Luo, R. Kumar, and I. R. Smith, "A 0.5 MV magnetically self-insulated pulsed transformer," *J. Phys. D, Appl. Phys.*, Vol. 39, No. 21, 4529–4535, 2006.
4. Bergeron, K. D., "Magnetic inhibition of surface flashover of insulators in vacuum," *J. Appl. Phys.*, Vol. 29, No. 9, 534–536, 1976.

A Compact Relativistic Magnetron with a TE_{10} Output Mode

Di-Fu Shi, Bao-Liang Qian, Wei Li, Hong-Gang Wang, and Lin Lian
College of Optoelectronic Science and Engineering
National University of Defense Technology, Changsha, Hunan 410073, China

Abstract— An S-band compact A6 relativistic magnetron which operates in the π-mode is proposed, and its radiation can be extracted as a TE_{10} mode axially through a rectangular waveguide which is designed to match radially with the anode. Compared with the magnetron with diffraction output (MDO), the magnetron of this structure can reduce the dimension of the output port of the magnetron, and therefore reduce the volume of the coil of the applied magnetic field, and also reduce the distance between the electron dump and the anode block so that both the diameter and the axial length of the magnetron can be minimized. In addition, as a result of the limit to the dimension of the output waveguide, such a simple converter of the magnetron can provide a much purer radiated mode. The softwares of high-frequency field analysis and CHIPIC particle-in-cell (PIC) simulation have been used to analyze and optimize the operating performance of the magnetron proposed in this paper. Simulation results show that under the condition of the applied voltage of 360 kV, the input power of 1.87 GW and the applied magnetic field of 0.4 T, the output microwave power is 409.2 MW and the power conversion efficiency can reach 21.9%, while the resonant frequency of π-mode is 2.5 GHz and the radiated mode is TE_{10} in the rectangular waveguide.

1. INTRODUCTION

The relativistic magnetron, for the reasons of its simple structure, high-power capability, suitable application for long pulse, and high pulse repetition rate, as well as its tunability, has become one of the most promising devices of all high power microwave sources [1]. In recent years, it was explored extensively, including transparent cathode [2–4], electric or magnetic priming [5–9], axial diffraction output [10–13], compactness [14–16], and so on. A compact relativistic magnetron radiating with the lowest order mode is usually required for commercial and military applications. The magnetron with diffraction output (MDO) in which the anode vanes and cavities are tapered radially outward at an optimal angle in the form of a conical horn antenna can be used for mode conversion from the operating π-mode to different TE modes [10]. And modified magnetic field distribution makes the MDO more compact in axial dimension, however, at the expense of increased radial dimension [13]. Recently, a compact A6 relativistic magnetron is proposed which operates in the π-mode and whose radiation is extracted axially as a TE_{11} mode through a cylindrical waveguide with the same cross section as that of the anode block, although with reduced efficiency [14].

In this paper, we describe an S-band compact A6 relativistic magnetron which operates in the π-mode, and its radiation can be extracted as a TE_{10} mode axially through a rectangular waveguide which is designed to match radially with the anode.

This configuration has several advantages: the magnetron of this structure can reduce the dimension of the output port of the magnetron, and therefore reduce the volume of the coil of the applied magnetic field, and also reduce the distance between the electron dump and the anode block so that both the diameter and the axial length of the magnetron can be minimized. In addition, as a result of the limit to the dimension of the output waveguide, such a simple converter of the magnetron can provide a much purer radiated mode.

2. SIMULATION SETUP

The three-dimensional fully electromagnetic and particle-in-cell (PIC) code CHIPIC [17] is used to investigate the performance of the compact relativistic magnetron with TE_{10} output mode. The structure of the well-known A6 magnetron [18] is adopted in this study. Fig. 1(a) shows the schematic diagram of the horizontal cross section of the A6 magnetron with three protrusions alternating with three recessions. Fig. 1(b) shows the 3D view of the converter connecting the A6 magnetron with the rectangular waveguide.

As shown in Fig. 1(a), the structure of the magnetron consists of 6 sectorial ($\theta = 20°$) cavities with height $H_m = 7.2$ cm. The radii of the cathode, the anode, and the cavities are $R_c = 10.0$ mm, $R_a = 21.0$ mm, and $R_v = 42.1$ mm, respectively. In order to improve the output power and reduce the startup time, protrusions and recessions on the inner surface of anode vanes are utilized in

the simulations. The angular width of the protrusions and recessions are $\theta_p = 5°$, and $\theta_r = 5°$, respectively. The protrusion and recession radii are $(R_a - \Delta r) = 20.0\,\text{mm}$ and $(R_a + \Delta r) = 22.0\,\text{mm}$, respectively, where the radial variation $\Delta r = 1\,\text{mm}$ is same for protrusion and recession.

As shown in Fig. 1(b), at the end of the A6 magnetron, two diametrically opposite cavities and the interaction space of the magnetron are converted axially to a rectangular waveguide. And the other cavities are tapered radially inward at an optimal angle ($\alpha = 68.8°$). The length and width

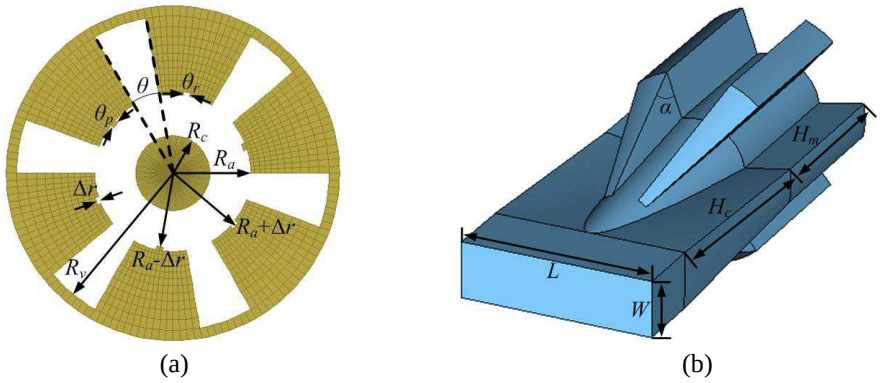

Figure 1: (a) Schematic diagram of the horizontal cross section of the A6 magnetron with three protrusions alternating with three recessions. (b) 3D view of the converter connecting the A6 magnetron with the rectangular waveguide.

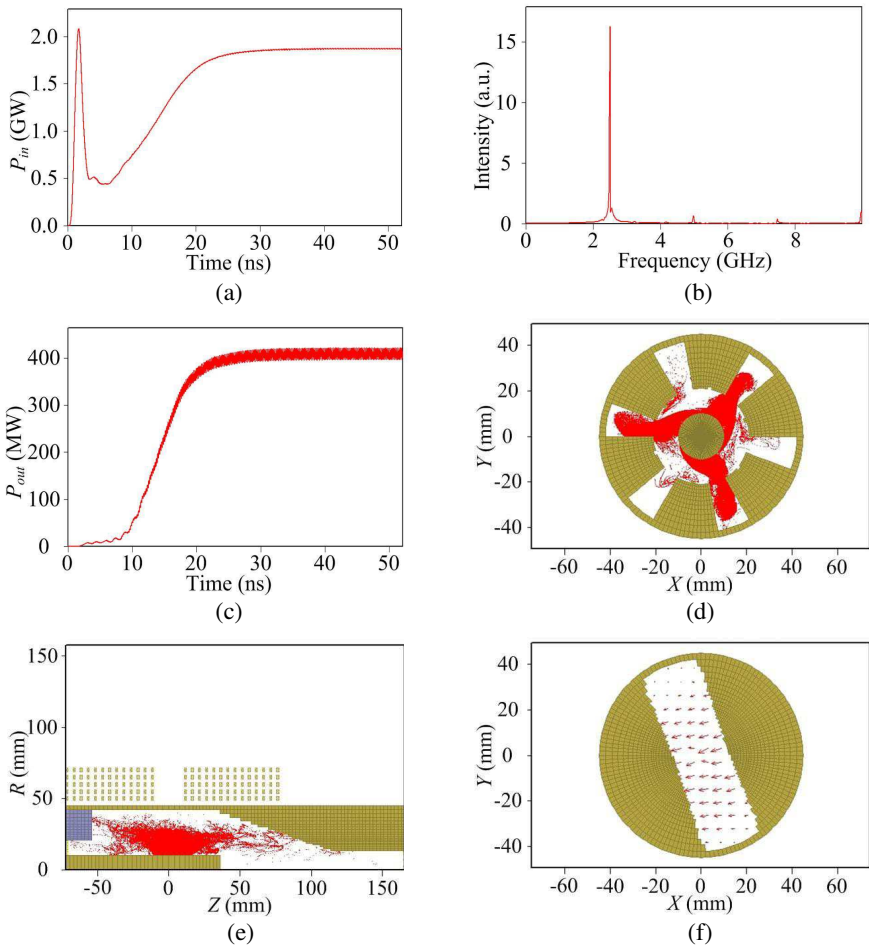

Figure 2: (a) Input power versus time. (b) Spectrum of electric field in resonant cavity. (c) Output power versus time. (d) Electron spokes in the magnetron in the r_θ plane. (e) Particle plot of the electron flow in the magnetron in the r_z plane. (f) Radiated mode of output port.

of the rectangular waveguide are $L = 84.2\,\text{mm}$, $W = 24.0\,\text{mm}$, respectively. The distance between the A6 magnetron and the rectangular waveguide is $H_c = 100.0\,\text{mm}$.

In our simulations, the applied voltage has a rise time of 3 ns after which it maintained a constant amplitude of 360 kV for a duration of 50 ns, and the applied axial magnetic field for interaction space is 0.4 T.

3. SIMULATION RESULTS

According to the simulation setup described in Section 2, the compact magnetron model is investigated by 3D PIC, CHIPIC. And Fig. 2 gives the simulation results.

Figure 2(a) indicates that the input power maintain a constant amplitude of 1.87 GW after 25 ns. Fig. 2(b) indicates that the spectrum of the electric field in resonant cavity is very pure, and the resonant frequency is 2.5 GHz, which is greater than the cutoff frequency for the rectangular waveguide. Fig. 2(c) indicates that the output power of 409.2 MW reaches to saturation at 25 ns, corresponding to the power conversion efficiency of 21.9%. And we believe that further design and optimization could reduce the startup time and increase the power conversion efficiency. Fig. 2(d) shows the electron spokes in the magnetron in the r_θ plane at 30 ns, and it indicates that the magnetron operates at π mode.

Figure 2(e) shows the particle plot of the electron flow in the magnetron in the r_z plane at 30 ns, and it indicates that most leakage electrons from the interaction space can be captured by the converter before the microwave window. Compared with the magnetron with diffraction output (MDO), as shown in Fig. 3, the magnetron of this structure can reduce the dimension of the output port of the magnetron, and therefore reduce the volume of the coil of the applied magnetic field, and also reduce the distance between the electron dump and the anode block so that both the diameter and the axial length of the magnetron can be minimized.

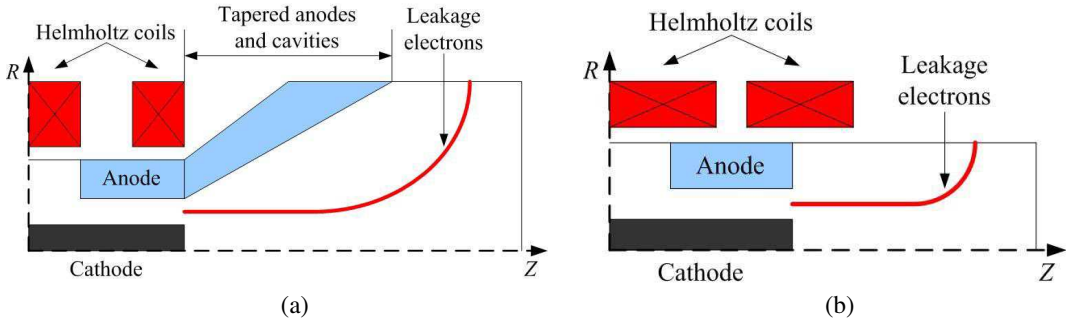

Figure 3: (a) Schematic diagram of the MDO. (b) Schematic diagram of the compact magnetron.

Figure 2(f) indicates that the radiated mode of output port is TE_{10} mode, which is the lowest order mode in the rectangular waveguide. As a result of the limit to the dimension of the rectangular waveguide, only TE_{10} mode can propagate in the rectangular waveguide, so that a pure radiated mode can be obtained.

4. CONCLUSION

In conclusion, a compact relativistic magnetron with TE_{10} output mode is proposed in this paper. The magnetron operates in the π-mode, and its radiation can be extracted as a TE_{10} mode axially through a rectangular waveguide which is designed to match radially with the anode. This design not only makes both the diameter and the axial length of the magnetron minimized, but also provides a much purer radiated mode in the output waveguide, and the magnetron can operate with acceptable efficiency (about 21.9%), although we believe that the further design and optimization of the magnetron may lead to higher efficiency, such as using transparent cathode to increase the efficiency and reduce the startup time, using strap to promote stable generation of the π mode, and using cathode endcap to reduce the leakage electrons from the interaction space.

REFERENCES

1. Benford, J., J. Swegle, and E. Schamiloglu, *High-power Microwaves*, 2nd Edition, Chapter 7, 259–320, Artech House, Norwood, MA, 2006.

2. Fuks, M., S. Prasad, and E. Schamiloglu, "Increased efficiency and faster turn-on in magnetrons using the transparent cathode," *Proc. Int. Conf. CAVMAG*, 76–81, 2010.
3. Schamiloglu, E. and M. I. Fuks, "The transparent cathode: Rejuvenator of magnetrons and inspiration for new RF sources," *Proc. IET Conf. High Power RF Technol.*, 1–5, 2009.
4. Fuks, M. I. and E. Schamiloglu, "70% efficient relativistic magnetron with axial extraction of radiation through a horn antenna," *IEEE Trans. Plasma Sci.*, Vol. 38, No. 6, 1302–1312, Jun. 2010.
5. Kim, J. I., J. H. Won, and G. S. Park, "Electron prebunching in microwave magnetron by electric priming using anode shape modification," *Appl. Phys. Lett.*, Vol. 86, No. 17, 171501-1–171501-3, Apr. 2005.
6. Baiburin, V. B. and K. V. Kaminskii, "Effect of an azimuthally varying magnetic field on the noise level in a multicavity magnetron," *Tech. Phys. Lett.*, Vol. 35, No. 6, 582–584, Jun. 2009.
7. Neculaes, V. B., M. C. Jones, R. M. Gilgenbach, Y. Y. Lau, J. W. Luginsland, B. W. Hoff, W. M. White, N. M. Jordan, P. Pengvanich, Y. Hidaka, and H. L. Bosman, "Magnetic priming effects on noise, startup, and mode competition in magnetrons," *IEEE Trans. Plasma Sci.*, Vol. 33, No. 1, 94–101, Feb. 2005.
8. Hoff, B. W., R. M. Gilgenbach, N. M. Jordan, Y. Y. Lau, E. J. Cruz, D. M. French, M. R. Gomez, J. C. Zier, T. A. Spencer, and D. Price, "Magnetic priming at the cathode of a relativistic magnetron," *IEEE Trans. Plasma Sci.*, Vol. 36, No. 3, 710–717, Jun. 2008.
9. Maurya, S., V. V. P. Singh, and P. K. Jain, "Three-dimensional particle-in-cell simulation of fast oscillation startup and efficiency improvement in a relativistic magnetron with electric priming," *IEEE Trans. Plasma Sci.*, Vol. 40, No. 10, 2686–2692, Oct. 2012.
10. Fuks, M. I., N. F. Kovalev, A. D. Andreev, and E. Schamiloglu, "Mode conversion in a magnetron with axial extraction of radiation," *IEEE Trans. Plasma Sci.*, Vol. 34, No. 3, 620–626, Jun. 2006.
11. Daimon, M., K. Itoh, G. Imada, and W. Jiang, "Experimental demonstration of relativistic magnetron with modified output configuration," *Appl. Phys. Lett.*, Vol. 92, No. 19, 191504-1–191504-3, May 2008.
12. Li, W. and Y.-G. Liu, "An efficient mode conversion configuration in relativistic magnetron with axial diffraction output," *J. Appl. Phys.*, Vol. 106, No. 5, 053303-1–053303-3, Sep. 2009.
13. Li, W., Y.-G. Liu, J. Zhang, D.-F. Shi, and W.-Q. Zhang, "Experimental investigations on the relations between configurations and radiation patterns of a relativistic magnetron with diffraction output," *J. Appl. Phys.*, Vol. 113, No. 2, 023304-1–023304-4, Jan. 2013.
14. Leach, C., S. Prasad, M. Fuks, and E. Schamiloglu, "Compact relativistic magnetron with Gaussian radiation pattern," *IEEE Trans. Plasma Sci.*, Vol. 40, No. 11, 3116–3120, Nov. 2012.
15. Li, W., Y.-G. Liu, T. Shu, H.-W. Yang, Y.-W. Fan, et al., "Experimental demonstration of a compact high efficient relativistic magnetron with directly axial radiation," *Phys. Plasmas*, Vol. 19, No. 1, 013105-1–013105-4, Jan. 2012.
16. Li, W. and Y. G. Liu, "Modified magnetic field distribution in relativistic magnetron with diffraction output for compact operation," *Phys. Plasmas*, Vol. 18, No. 2, 023103-1–023103-4, Feb. 2011.
17. Zhou, J., D. Liu, C. Liao, and Z. Li, "CHIPIC: An efficient code for electromagnetic PIC modeling and simulation," *IEEE Trans. Plasma Sci.*, Vol. 37, No. 10, 2002–2011, Oct. 2009.
18. Palevsky, A. and G. Bekefi, "Microwave emission from pulsed, relativistic e-beam diodes. II. The multiresonator magnetron," *Phys. Fluids*, Vol. 22, No. 5, 986–996, May 1979.

Kind of Dual-band Horn Antenna with Coaxial Feed Structure for High Power Microwave Applications

Qiang Zhang, Sheng-Ren Peng, Cheng-Wei Yuan, Yi-Ming Yang, and Jing Liu
College of Optoelectronic Science and Engineering
National University of Defense Technology, Changsha 410073, China

Abstract— A new kind of dual-band horn antenna for S/X band radiation with high power handling capacity is proposed, which consists of coaxial feed structure flare angle horn and a polyethylene cover. Low band microwave is fed by TE_{11} coaxial waveguide mode, and high band microwave is fed by TE_{11} circular waveguide mode. Based on the specific structure of the horn antenna, mode matching method is utilized to determine scatter matrix of each discontinuity in cross section. To obtain the overall scatter matrix of the antenna, it is necessary to progressively cascade the scatter matrixes, and the overall scatter matrix determines the propagation properties of the horn antenna. Far field radiation pattern of the dual-band antenna can easily get by using mode expansion technology. Furthermore, a dual-band antenna at 3.6 GHz and 9.5 GHz is designed, and theoretical and numerical simulations agree well with each other. It reveals that the dual-band antenna has high power handling capacity with GWs level, and good farfield radiation pattern at each band has been achieved. The theoretical and numerical simulation investigations show that it is a promising method for realizing multi-channel multi-band HPM integrative radiation, which is significant for HPM in some special applications.

1. INTRODUCTION

With the development of high power microwave (HPM) technologies, great efforts have been made on increasing the output power levels and the frequency spectrum of the HPM systems [1]. An interesting direction for HPM development is to investigate devices capable of producing HPM with two stable and separate frequencies [2]. Therefore, extremely dual-band radiation systems [3] with high power-handling capacity are often required for many current applications. As one of the most important sectors in the HPM system, radiation system mainly determines the whole structure of the HPM system. On the other hand, narrow-band HPM source usually operates at single band and has limited output power at present. An alternative method for enhancing the output capacity of HPM system is taking advantage of waveguide-based power combining technologies, not only for increasing the output power levels, but also for the frequency spectrum of the HPM systems [4].

In this paper, a corrugated horn antenna for S/X band with special input port consisting of coaxial feed structure and a small flare angle horn is designed, and this antenna is utilized to radiate HPM in good far-field radiation at each band with high power handing capacity. The optimization has been achieved by mode matching method, and the results are confirmed by numerical simulations.

2. STRUCTURE OF THE ANTENNA

In order to radiate microwaves at each band with high power handing capacity, the designed antenna is shown in Fig. 1. The whole structure of the antenna is divided into three parts: First, the input port consists of a coaxial waveguide working at S-band and a small flare angle horn working at X-band, which realizes that microwaves at each band input through different feeding structure. Second, a circular waveguide with vertical corrugations plays an important part in the dual-band feed, insuring that E-plane and H-plane patterns of the antenna are almost equal to each other in the illuminated area at each band. Third, a plano-convex polyethylene lens cover is utilized to air proof the large flare angle horn, which increases the gain of the antenna to some extent, then the antenna can be pumped into high vacuum state and the electric breakdown threshold is higher than the one in atmosphere [1]. In some special application, this antenna can works as the feed of the near-field Cassegrain antenna.

3. ANALYSIS OF THE ANTENNA

In consideration of the azimuthally symmetric structure of the antenna, it can be regarded as consisting of a battery of discontinuities in cross section and short lengths of waveguides in isolation. Mode matching theory is an effective approach to obtain the overall scatter matrix from which

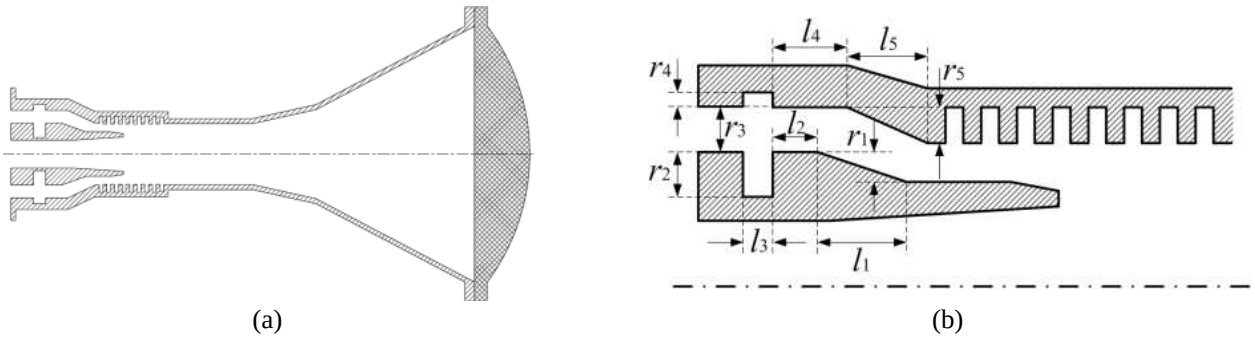

Figure 1: (a) Structure of the antenna. (b) Cross section of the coaxial feeding structure.

to determine the propagation properties of the antenna, which is extensively utilized to design overmoded mode converter and horn antenna [5, 6].

Concretely, we employ mode matching theory to get the scatter matrix of each discontinuity, which is progressively cascaded to obtain the overall scatter matric of the antenna. Using mode expansion technology in the aperture of the antenna, we can get the far-field radiation pattern of the horn antenna at last [7]. In general, the typical components of the antenna shown in Fig. 1 can be listed as follows in Fig. 2. The detail analysis process will be presented in another paper.

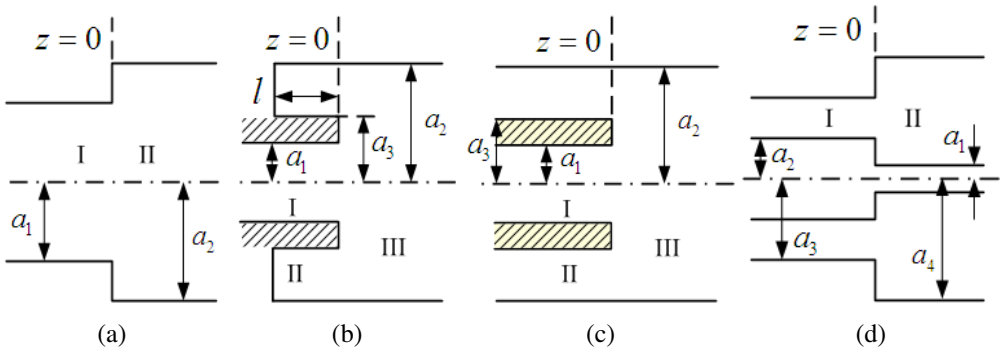

Figure 2: Typical components of the antenna.

Base on the propagation properties of the whole antenna, mode expansion technology is usually utilized to get the far-field radiation pattern of the antenna, by which we could analyse the contribution of each mode generated at the discontinuities makes to the far-field radiation pattern. In order to avoid radio-frequency (RF) electric breakdown occurring in atmosphere side near the outside of the cover, the aperture of the horn should be large enough to own high power handing capacity. We can not only employ aperture field theory to get the far-field radiation pattern of each mode at the aperture of the horn, but also decrease the calculation error generated by ignoring the surface current on the outside of the horn on the calculated far-field radiation pattern [7].

The radiation pattern of the antenna obtained by mode expansion technology can be written as

$$\begin{aligned} F(\theta,\phi) \;=\; & -\frac{C_{TE_{nm}} j^n kan}{\sqrt{\pi(u_{nm}^{*2}-n^2)}}\sqrt{\frac{\omega\mu}{\beta_{nm}^*}}\frac{e^{-jkR}}{R}\cos n\phi[1+t\eta\cos\theta+\Gamma(1-t\eta\cos\theta)]\frac{J_n(ka\sin\theta)}{ka\sin\theta} \\ & +\frac{C_{TE_{nm}} j^n ka}{\sqrt{\pi(u_{nm}^{*2}-n^2)}}\sqrt{\frac{\omega\mu}{\beta_{nm}^*}}\frac{e^{-jkR}}{R}\sin n\phi[\cos\theta+t\eta+\Gamma(\cos\theta-t\eta)]\frac{J_n'(ka\sin\theta)}{1-(\frac{ka\sin\theta}{u_{nm}^*})^2} \\ & -\frac{C_{TM_{nm}} j^n ka}{\sqrt{\pi[(\frac{\chi_{nm}a}{ka\sin\theta})^2-1]}}\sqrt{\frac{\beta_{nm}}{\omega\varepsilon}}\frac{e^{-jkR}}{R}\cos n\phi[(1+t\eta\cos\theta)+\Gamma(1-t\eta\cos\theta)]\frac{J_n(ka\sin\theta)}{ka\sin\theta} \quad (1) \end{aligned}$$

where, $u_{nm}=\chi_{nm}a$, $J_n(u_{nm})=0$, $u_{nm}^*=\chi_{nm}^*a$, $J_n'(u_{nm}^*)=0$, a is the aperture radius, β_{nm} and β_{nm}^* denote propagation constant of TE_{1m} mode and TM_{1n} mode at the aperture, C_{TEnm} and C_{TMnm} denote complex coefficients of TE_{1m} mode and TM_{1n} mode respectively. By employing Eq. (1), one can obtain E-plane and H-plane radiation pattern under the condition of $\varphi=0^\circ$ and $\varphi=90^\circ$, respectively.

4. DESIGN AND NUMERICAL INVESTIGATION OF THE ANTENNA

4.1. Design of the Feeding Port with a Vertical Corrugations Structure

As shown in Fig. 3, the lens-horn antenna is fed by a coaxial waveguide working at S-band and an inner circular waveguide working at X-band, which is the basic component of the antenna. This structure provides the design possibilities to obtain good radiation characteristics at each band with a reasonable size capable of high power handing. The coaxial and circular waveguides are excited by the dominant TE_{11} mode and connected to the corrugated section. Considering its special structure, TE_{1n} and TM_{1n} modes can be excited at each discontinuity in the feed. Employing the optimization tools of CST software, dozens of different geometries have been analysed to reach the final design for the 3.60 and 9.50 GHz central frequency, with the dimensions as follows, $r_1 = 13.63\,\text{mm}$, $r_2 = 22.59\,\text{mm}$, $r_3 = 20\,\text{mm}$, $r_4 = 9.44\,\text{mm}$, $r_5 = 20.13\,\text{mm}$, $l_1 = 38.28\,\text{mm}$, $l_2 = 25.13\,\text{mm}$, $l_3 = 19.31\,\text{mm}$, $l_4 = 35.35\,\text{mm}$, $l_5 = 43.06\,\text{mm}$, and simulated results given in Fig. 4 to Fig. 5. The reflection of feeding port is quite small around the central frequency at each band, indicating the good transmission property of the feed. When the feeding port is fed with 1.0 W microwave, the maximum electric field strength is less than 702 V/m and 852 V/m, respectively. Generally, the feeding port is pumped into high vacuum state for HPM applications, in which the RF electric field breakdown threshold is greater than 1.0 MV/cm [9, 10]. Assuming the RF electric breakdown strength is 700 kV/cm, which has been confirmed in our recently HPM experiments [11], we can infer the maximum allowed input power for this feeding port is about 9.9 GW and 6.7 GW at S-band, X-band, respectively.

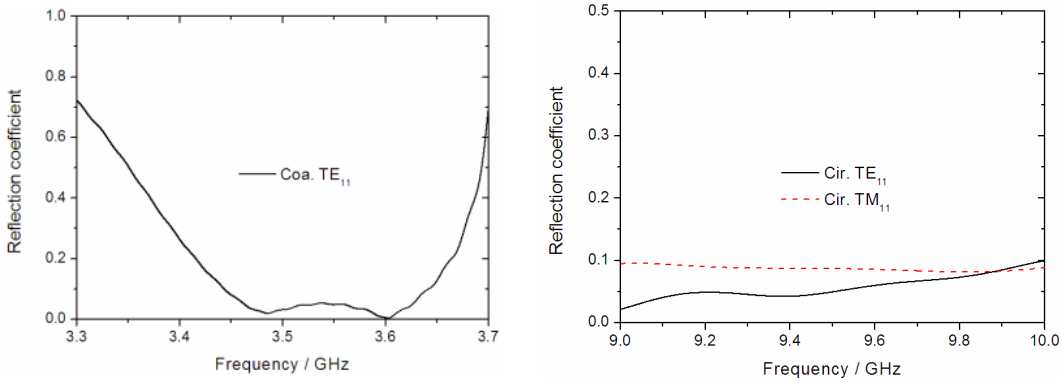

(a) S-band (3.60 GHz) (b) X-band (9.50 GHz)

Figure 3: Reflection coefficients versus frequency at each band.

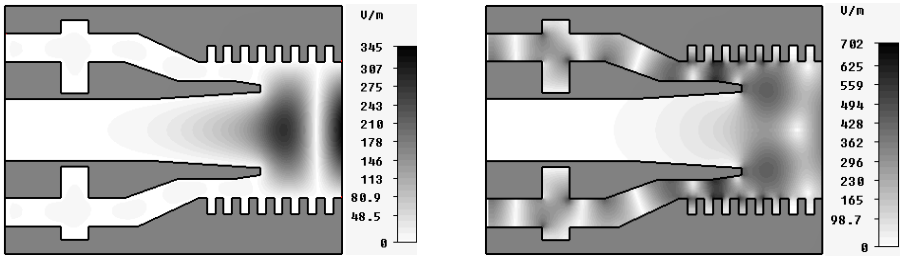

(a) S-band (3.60 GHz, *E*-plane) (b) X-band (9.50 GHz, *E*-plane)

Figure 4: Electric field distribution at each band.

4.2. Design of the Flare Angle Dielectric Lens-horn Antenna

The structure of flare angle antenna is optimized mainly by mode matching technology. In Section 4.1, the feeding port has reached the goal of good transmission property in dual-band, the remained works focus on the optimizing of the radiation property by elaborate design of the circular waveguide with vertical corrugations connected to the flare angle horn antenna. Fig. 6 shows the far-field radiation patterns of the horn antenna without dielectric cover, the theoretical results are

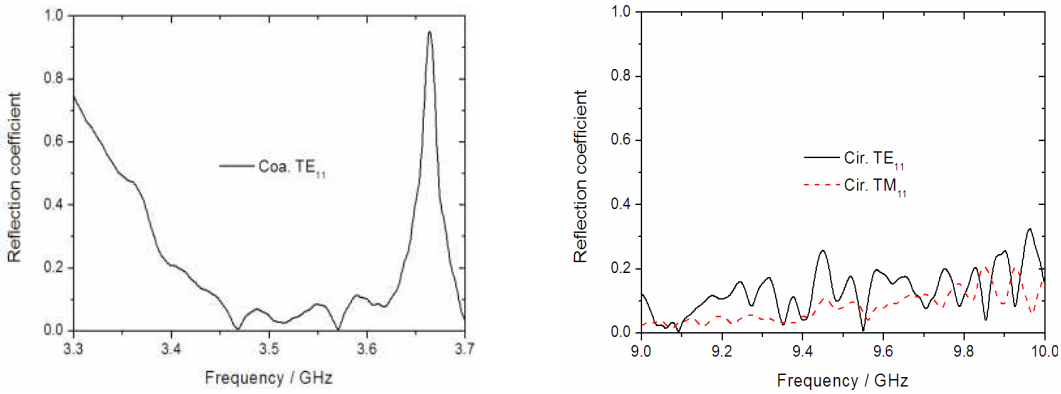

(a) S-band (3.60 GHz) (b) X-band (9.50 GHz)

Figure 5: Reflection coefficients of the antenna at each band.

almost equal to the simulated noes. There is a little difference between the two results mainly for the reason that the surface current on the outside of the horn antenna is neglected in the calculation of the radiation pattern. From the simulated results, we can draw a conclusion that microwaves in dual-band are successfully radiated from the horn antenna, and the radiation patterns have the good performance of azimuthal symmetry, low side lobes, which lays the foundation of adding the dielectric lens cover to airproof the horn antenna.

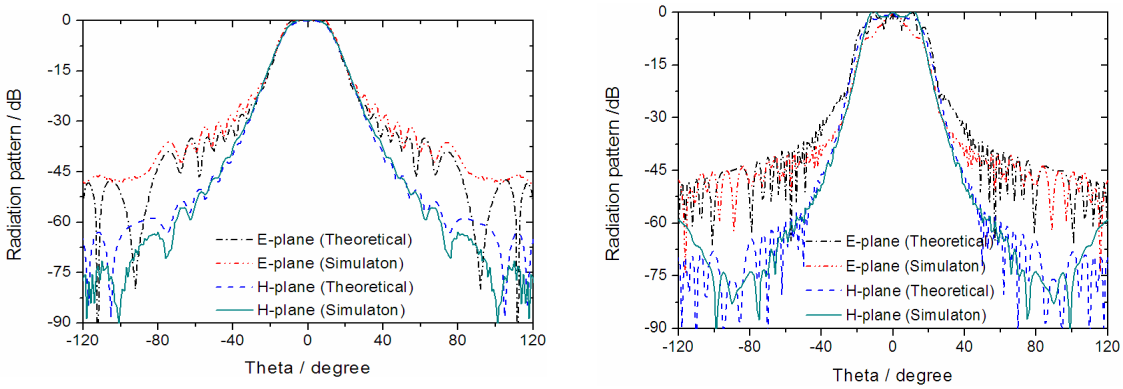

(a) S-band (3.60 GHz) (b) X-band (9.50 GHz)

Figure 6: Radiation patterns of horn antenna without cover.

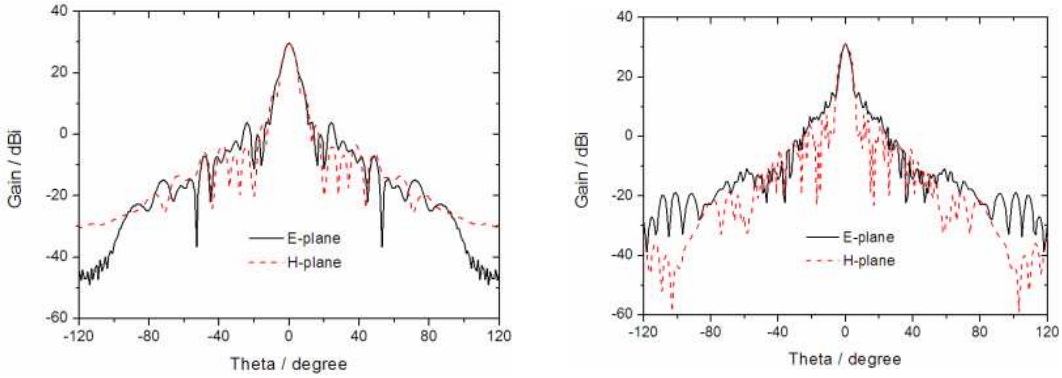

(a) S-band (3.60 GHz) (b) X-band (9.50 GHz)

Figure 7: Far-field radiation pattern of the antenna at each band.

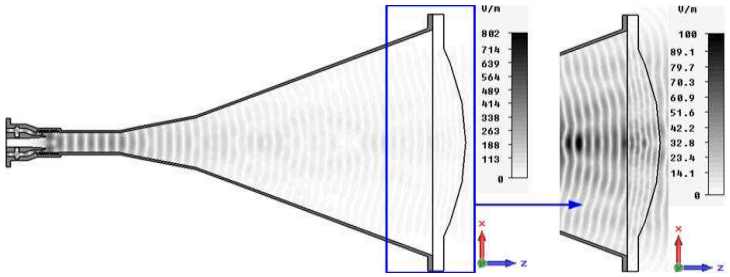

(a) S-band (3.60 GHz), *E*-plane

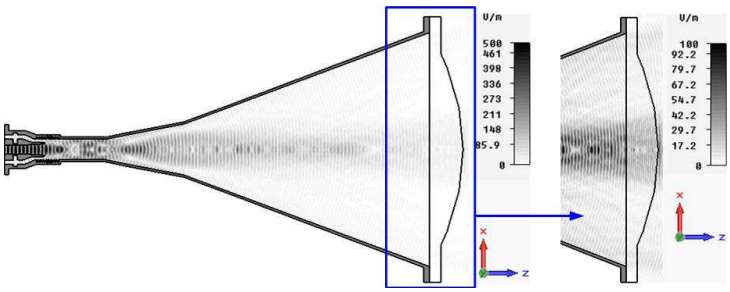

(b) X-band (9.50 GHz), *E*-plane

Figure 8: Electric field distribution of the lens-horn antenna.

Dielectric lens is widely used in the design of the antenna in the traditional communication field [12–14]. On the one hand, the horn antenna covered by dielectric lens can be pump into high vacuum state, and the RF breakdown threshold in the horn antenna is higher than the one in atmosphere. On the other hand, the quasi sphere wave in the horn is transformed to plane wave when it gets through the cover, which enhancing the gain of the horn antenna. Yuan has done plenty investigations about lens cover for high power microwave application and obtained a lot of valuable results [15]. A wide bandwidth plano-convex dielectric lens cover is investigated to airproof the dual-band horn antenna designed above.

To verify the feasibility of the whole antenna, the dual-band dielectric lens-horn antenna connected feeding port is simulated by the numbers. A small reflection caused by the cover has little influence on the good propagation property of the horn antenna. Fig. 7 presents the favourable radiation patterns of the lens-horn antenna. It is obvious that *E*-plane and *H*-plane patterns of the antenna are almost equal to each other in the illuminated area.

The electric field distributions in the horn and outside the cover are shown in the Fig. 8. The quasi sphere wave propagate in the horn, then transformed to plane wave by the cover, which makes the field distribution almost uniform in the aperture of the antenna. The maximum electric field lies in the feeding port, which limits the power handing capacity of the whole antenna. In the practical application, we can optimize the structure of the feeding port to increase the power handing capacity if it is needed.

According to the simulation, the input power is 1.0 Watt, the electric field distribution of the antenna is shown in Fig. 8. Outside the lens cover, the electric field strength is less than 0.43 V/cm at 3.60 GHz and 0.65 V/cm at 9.50 GHz, respectively. Assume the breakdown threshold in atmosphere under the condition of short microwave duration is about 3×10^4 V/cm, so the power breakdown threshold in this area is about $(3 \times 10^4/0.65)2 = 2.3$ GW. As the maximum allowed input power mentioned above for this feeding port is about 9.9 GW and 6.7 GW at S-band, X-band, respectively it means that the electric breakdown will take place in the near field outside the cover of the antenna. As a result, we estimate that the power-handling capacity of the dual-band horn antenna is about 2.3 GW.

5. CONCLUSION

This paper has presented a general study of the dual-band horn antenna with coaxial feed structure. The antenna's far-field radiation patterns belonging to each band have been confirmed by

simulation. In addition, the radiation system is large enough for high power handling capacity, and experimental research is planned for the next step in order to make sure the sufficient power handling capacity.

REFERENCES

1. Benford, J., J. A. Swegle, and E. Schamiloglu, *High Power Microwaves*, 2nd Edition, Taylor & Francis, New York, 2007.
2. Fan, Y. W., et al., "A double-band high-power microwave source," *J. Appl. Phys.*, Vol. 102, No. 10, 303–304, 2007.
3. Imbriale, W. A., "An alternative feed design for the MRO antenna," *Proc. IEEE Antennas Propag. Soc. Int. Symp.*, Vol. 3A, 761–764, 2005.
4. Zhang, Q., C. W. Yuan, and L. Liu, "Design of a dual-band power combining architecture for high-power microwave applications," *Laser and Particle Beams*, Vol. 28, 377–385, 2010.
5. James, G. L., "Analysis and design of TE_{11}-to-HE_{11} corrugated cylindrical waveguide mode converters," *IEEE Trans. Microw. Theory and Techni.*, Vol. 29, No. 10, 1059–1066, 1981.
6. James, G. L., "On the problem of applying mode-matching techniques in analyzing conical waveguide discontinuities," *IEEE Trans. Microw. Theory and Techni.*, Vol. 31, No. 9, 718–723, 1983.
7. Ren, L., *Theory Foundation of Antenna*, Posts & Telecom Press, Beijing, 1980.
8. Cooper, D. N., "Complex propagation coefficients and the step discontinuity in corrugated cylindrical waveguides," *Electron. Lett.*, Vol. 7, 135–136, 1971.
9. Robert, J. B. and S. Edl, *High-power Microwave Sources and Technologies*, IEEE Press, Piscataway, NJ, 2001.
10. Xiao, R. Z., C. H. Chen, W. Song, et al., "A high-power high-efficiency klystronlike relativistic backward wave oscillator with a dual-cavity extractor," *Appl. Phys. Lett.*, Vol. 98, No. 10, 101502, 2011.
11. Zhang, J., Z. X. Jin, J. H. Yang, et al., "Recent advance in long-pulse HPM sources with repetitive operation in S-, C-, and X-bands," *IEEE Trans. Plasma*, Vol. 39, No. 6, 1438–1445, 2011.
12. Rozenfeld, P., "The electromagnetic theory of three-dimensional inhomogeneous lenses," *IEEE Trans. Antennas Propag.*, 366–370, 1975.
13. Fernandes, C. A., "Shaped dielecyric lenses for wireless millimeter-wave communicatioins," *IEEE Trans. Antennas Propag.*, Vol. 41, No. 5, 356–365, 1999.
14. Min, S., H. Jung, G. Park, et al., "Mode conversion of high-power electro- magnetic microwave using coaxial-beam rotating antenna in relativistic backward-wave oscillator," *IEEE Trans. Plasma Sci.*, Vol. 38, No. 6, 1391–1397, 2010.
15. Yuan, C. W., "Investigations of novel coaxial mode converters and mode-transducing antennas for high-power microwave," National University of Defense Technology, 2006.

Comparison of B_1^+ Field and Specific Absorption Rate (SAR) between Birdcage, Transverse Electromagnetic and Microstrip Coil for Ultra High Field MRI at 9.4 Tesla

J. Slim, B. Abu Suheil, D. Hoelscher, and D. Heberling
Institute of High Frequency Technology, RWTH Aachen University, Germany

Abstract— The RF coil is an essential part of MRI systems. In ultra-high field (UHF) MRI, the design of RF coils is a challenging task. The RF coil should resonate at a particular frequency (the Larmor Frequency) and must provide a highly homogeneous B_1^+ field as well. It must be safe to use by maintaining a low specific absorption rate (SAR) value. Homogeneity of the B_1^+ is a supremely important factor in MRI systems. A homogenous B_1^+ allows the spin in different mediums having different electromagnetic properties to see the same B_1^+ field value. When the field-tissue interaction takes place, the spin interacts differently in a unique manner making it possible for materials to be imaged. Generally speaking, this allows higher resolutions images with high contrast increasing therefore the sensitivity of the MRI system. The specific absorption rate is a safety indicator. It is an indicator that reflects how much electromagnetic energy is absorbed in the biological tissue. SAR value must be kept as low as possible. The task of this paper is to provide a quantitative comparison between three common volume RF coils at 9.4 Tesla. The comparison is held in terms of the homogeneity of the B_1^+ both in the loaded and unloaded cases and also as a function of the SAR. Additionally, a comparison with the performance of 7 Tesla published earlier to quantify the gain of increasing the frequency. Before comparing the coils, the coils must be built first. A novel design for each type of coils is shown. Before comparing the coils, the coils must be first built. A novel design for each type of coils is shown. The S-parameter as a clue of resonance at the Larmor frequency is presented accompanied with a comparison with measurements performed. A quantitative approach to assess the interaction between the electromagnetic fields and phantoms is provided and discussed in the context of dielectric resonance. Additional visual clues are provided. A detailed statistical study of the local homogeneity/inhomogeneity is performed. This makes it possible to conduct local field corrections, increasing therefore the homogeneity and consequently the sensitivity of the MRI system.

1. INTRODUCTION

High signal to noise ratio (SNR) and high contrast mechanism are very attractive features of UHF MRI systems [2]. On the other hand, the homogeneity (heterogeneity) of the B_1^+ field and the safety issues remains to be of major concern at high frequencies [5]. The complex structure of the human head leads to highly inhomogeneous current distribution on the coils forming therefore nonuniform B_1^+ field [8]. Consequently, different coils structures tend to have different B_1^+ field homogeneities. Another important quantity is the specific absorption rate (SAR) which has to be maintained as low as possible [1].

In this paper, a comparison in terms of B_1^+ field homogeneity and SAR is drawn between three-well known types of volume coils namely the birdcage, transverse electromagnetic TEM and microstrip coils at 9.4 Tesla; an extension to a previous work conducted at 7 Tesla [3]. The target is to establish a systematic knowledge about these types of coils as a function of field homogeneity and safety.

2. MATERIALS AND METHODS

At 9.4 Tesla the corresponding resonance of the RF coils is exactly 399.69 MHz which is the Larmor frequency [1]. Each type of the RF coils must therefore resonate at this particular frequency.

The Birdcage RF coil consists of two parallel end rings and a number of conductive rungs [2]. 16 legs with 10 mm width and 200 mm length are chosen. The end-rings are made of cooper with 10 mm width. The legs as well as the end-rings are 1 mm thick. 32 capacitors are located on each of the end-rings. With such setup resonance is possible at 400 MHz as can be seen in Figure 1. Two excitations are required and are placed perpendicularly to each other between the RF shield and the end ring. This means a 90° phase shift is required to achieve a circular polarized magnetic field. The TEM and the microstrip RF coils have totally different working principle as compared

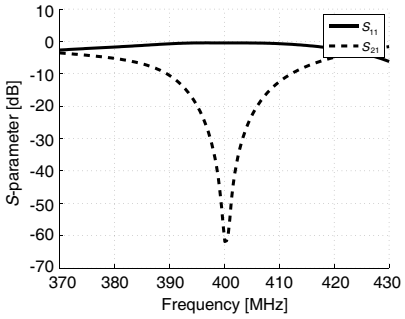

Figure 1: Resonance of the birdcage coil.

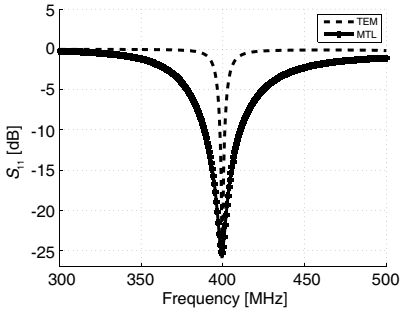

Figure 2: Resonnace of the TEM and the MTL coils.

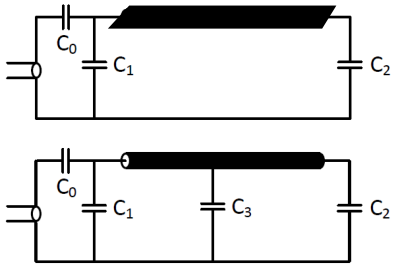

Figure 3: Equivalent circuits of the MTL (top) and TEM (bottom) coils.

to the birdcage coils. The MTL and the TEM are multi-channel RF coils [2]. The coil structure consists of a number of resonators (Figure 3) each of which is excited individually. Such structures provide in general low SAR values and allow better control over the B_1^+ field, making them very attractive for the MRI community.

The transverse electromagnetic (TEM) coil is formed of 16 cylindrical rods of copper each with 5 mm radius and 201 mm length. On each rod, an RC circuit in mounted at the end side with a resistor of 20 Ω and a capacitor of 1.95 pF. An "L-type" matching circuit is used with two capacitors of 2.2 pF and 2 pF respectively.

The microstrip transmission line (MTL) coil is composed of 16 curved strips with 180 mm length, 0.36 mm thickness and arc perimeter of 25.5254 mm placed on a cylindrical Plexiglas holder with a radius of 135 mm and 5 mm thickness. Performing the matching and the resonance was difficult. The capacitances as well as the inductances are not solely determined by the lumped elements but also with by the geometrical setup of the structure. For instance, the gap between the strips and the ground in the TEM structure is in fact a capacitor. Computing the partial inductance/capacitance for such geometry is a supremely difficult task [7]. The problem has been solved by using lumped inductors in series with the capacitors responsible for resonance. As a consequence, an RLC circuit is placed at the end side with a resistance of 50 Ω an inductor with 278.75 pH and a capacitor of 1.8 pF. An "L-type" matching circuit is used with two capacitors each with 2.45 pF. As 16 elements are used, 22.5° phase shift between the elements is required to achieve a circular polarized magnetic field. The resonances of the TEM and the MTL coils are shown in Figure 2. An 8-channels prototype for the MTL coil is shown in Figure 4. A comparison between the S_{11} parameter between the prototype and the simulated model is provided in Figure 5. A good agreement between the measurement and the simulation results is shown. The resonance for the prototype occurred at 403.84 MHz. At 400 MHz, the prototype has an attenuation of 12.7 dB.

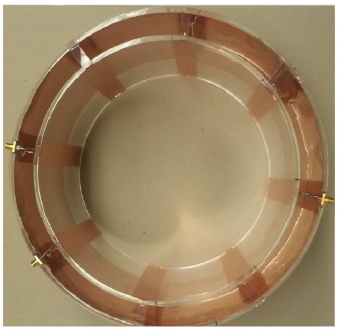

Figure 4: Eight-channels MTL RF coil prototype.

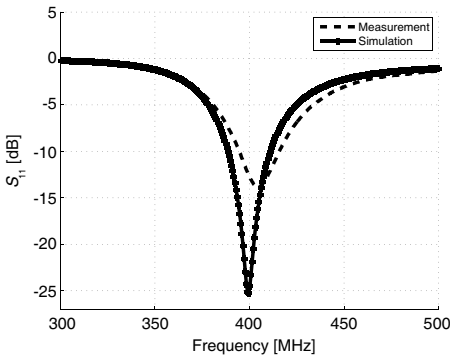

Figure 5: Comparison between simulated and measures S_{11} parameter.

3. RESULTS AND DISCUSSION

The B_1^+ field is the component of the magnetic field that rotates in a plane perpendicular to the static magnetic field in the MRI system [2, 6] and is defined as [2]:

$$B_1^+ = \frac{B_{1x} + jB_{1y}}{2}$$

To produce the desired circular polarized magnetic field, all coils are excited simultaneously with the corresponding phase shift mentioned above. Then by applying Equation (1), the 3D B_1^+ is calculated. A 2-D transversal cut of the 3-D B_1^+ field shows that indeed good levels of homogeneity are achieved, as can be observed in Figure 6. Figure 6 parts ((a), (b) and (c)) represent the unloaded case and the lower parts ((d), (e) and (f)) correspond to the loaded one. In the birdcage and the MTL coils, very strong peak appeared at the center of the phantom while for the TEM coil, the edges of the phantom shares good amount of electromagnetic energy with the center. To make the comparison clearer, the field is evaluated on a line located in the transversal plane perpendicular to the coil direction [3] with a length of 19.2 cm. The B_1^+ field is normalized over the field value at the center as suggested in [3], which is also the maximum field value. In the unloaded case, high levels of homogeneity are expected. Figure 7 provides a closer look. For the unloaded case in the birdcage, the field variation over the whole line is 3.24%. In the TEM coil, this variation reads 6.1%. In the MTL coil, the field does not change more than 11.18%.

The comparison between the field homogeneity of the three types of coils presented here (i.e., at 9.4 Tesla) are in agreement with the results for the 7 Tesla RF coils published in [3]. The birdcage coil is not only able to provide better homogeneity but also to score the highest field value of about 7.0212 Tesla. For the comparison reasons, all the B_1^+ fields calculated are normalized to 1 kW of stimulated power as referred in [2]. These results are summarized in Table 1.

Table 1: Variation of the B_1^+ field amplitude.

	9.4 Tesla		7 Tesla (Ref. [3])
Coil Type	Field Variation [%]	Maximum Value [μT]	Field variation [%]
Birdcage	3.24	7.02	15
TEM	6.12	4.50	23
MTL	11.18	4.10	38

Now, the coils are loaded with water phantoms with a diameter of 19.2 cm. The permittivity, permeability and the conductivity are maintained constant providing therefore a homogeneous medium $\epsilon_r = 81$, $\mu_r = 0.9991$ and $\sigma_e = 0.957\,(\mathrm{S/m})$. The electromagnetic field must interact with the phantom placed in the coils and consequently dielectric resonance is observed [4–6]. This results in strong maxima and minima [4, 5]. The B_1^+ field becomes locally inhomogeneous [6]. The remaining level of homogeneity is now evaluated on a local basis. Numerical electromagnetic simulators discretize Maxwell's Equations. The inherent discrete structure of the solution permits statistical

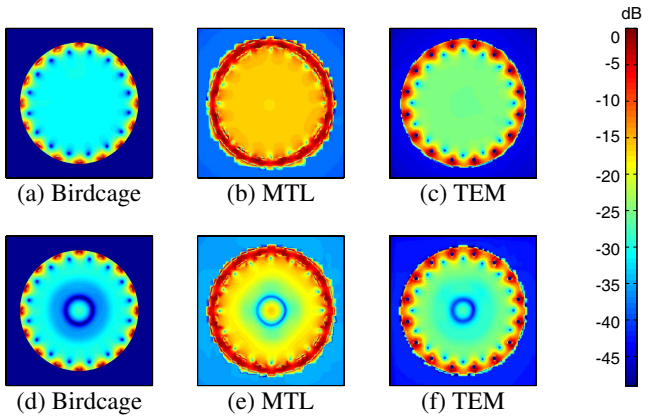

Figure 6: 2-D B_1^+ field distribution (top: unloaded, bottom: loaded).

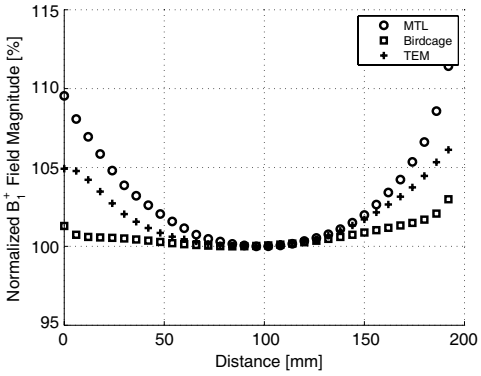

Figure 7: B_1^+ field distribution for the transversal direction for the unloaded coils.

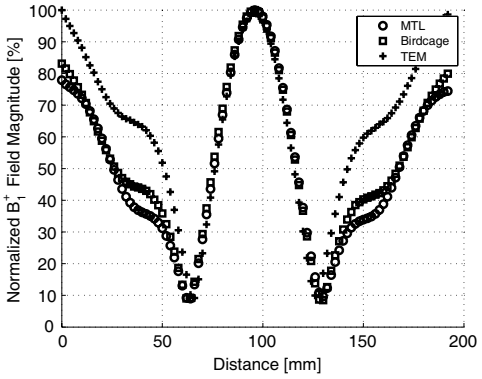

Figure 8: B_1^+ field distribution for the transversal direction for the loaded coils.

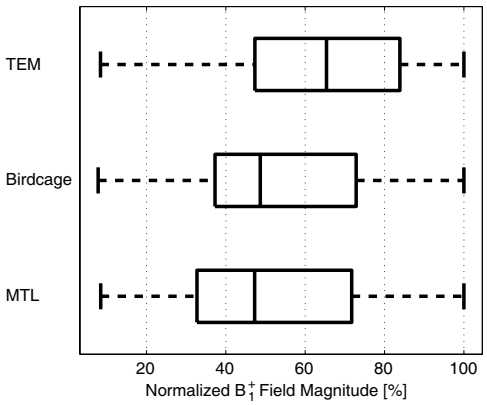

Figure 9: Statistical B_1^+ field distribution for the transversal direction for loaded coils.

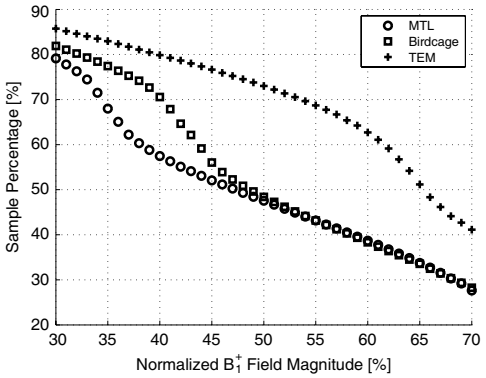

Figure 10: Performance analysis of the coils as a function of B_1^+ field homogeneity.

analysis. When a field is evaluated on a curve, it is actually sampled over this line. For statistical analysis, better induction is drawn if the number of samples is high enough. In this case, 19202 samples are considered for each coil. The distribution of the B_1^+ field amplitude as a function of the number of samples is better represented in a box plot. The birdcage and the MTL behaved similarly despite the high level of homogeneity of the birdcage in the unloaded case. This can be seen in Figures 8 and 9. The percentages of the samples having the same normalized field values share similar portion in the boxplot for the birdcage and the MTL. The birdcage is slightly better. The 75th percentile for the birdcage and the MTL are similar. So does the 25th percentile, the median and the lowest values. The TEM shows to be better in distributing the value of the B_1^+ field amplitude; the edges still have high field values. A performance analysis graph is shown in Figure 10. The idea here is simple; the x-axis shows the preserved value of the normalized B_1^+ field amplitude and the y-axis shows the percentages of the samples that were able to preserves a particular field value. Higher values mean better performance. One can see clearly that the TEM coil has the best performance followed by the birdcage and finally by the MTL coil. The TEM coil was slightly better in the low field values and much better at high field values (i.e., higher than 45% of the maximum field values). The Birdcage up to 45% of the maximum field value was better than the MTL coil. One interesting conclusion is that designing a coil with high B_1^+ field homogeneity in the unloaded cases does not necessarily imply high homogeneity in the loaded case.

The specific absorption rate or SAR is defined as the rate over which the energy is absorbed by the human body when exposed to an RF electromagnetic field. It is calculated by taking the time derivative of the incremental energy dW absorbed by an incremental mass dm contained in a volume element dV of a given mass density ρ using the following formula: $\mathrm{SAR} = \frac{d}{dt}\frac{dW}{dm} = \frac{d}{dt}\frac{dW}{\rho dV}$. A fully featured, highly detailed 'Voxel Model' with 5 mm voxel resolution is used as a phantom because the SAR is related to safety and requires as accurate modeling as possible. 50 W (rms) are fed into the coils as stimulated power. Different coils have different power acceptance capabilities giving rise

to various power loss densities inside the tissues. It has been observed that the SAR value is highest close to the surface of the phantom facing the incident wave. The birdcage has the highest SAR followed by the TEM and the MTL. The Birdcage is a fully coupled structure. The electromagnetic energy is highly concentrated in spots also called 'hot spots'. As the SAR is proportional to the electric field, coils must de-emphasize the electric field for the sake of the magnetic field. The TEM coil acting as a transmission line, appears to have uncontrolled interference of the electric field implying therefore the ability to form hot spots in the phantom. This can be seen in Figure 11. The birdcage forms multiple hot spots and so does the MTL. The red spots appear only at the surface of the phantom in the MTL case. The maximum SAR for the birdcage coil is 6.499 W/kg for 50 W excitation averaged over 10 g. For the same excitation power, the maximum SAR for the MTL coil is 2.627 W/kg and for the TEM coil is 4.646 W/kg. All the SAR calculations have been performed according to the IEEE/IEC 62704-1 standard. In terms of SAR, the MTL has the best performance which is in accordance with [3].

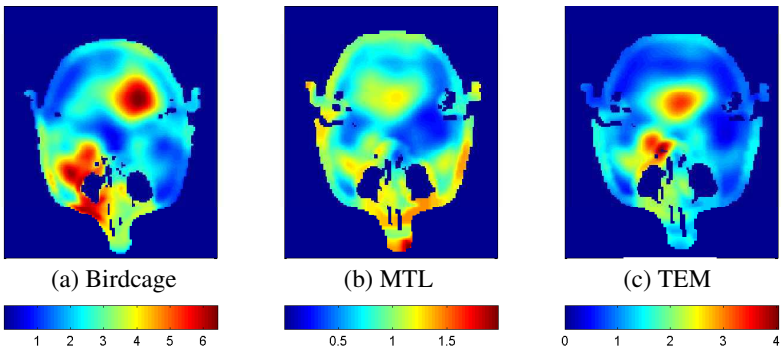

Figure 11: Transversal cut of the SAR in [W/kg].

4. CONCLUSION

The B_1^+ field homogeneity and SAR has been evaluated for the birdcage, TEM, and MTL volume coils. The results were compared to a previous work performed at 7 T. According to the simulation results, the birdcage coil has the best unloaded B_1^+ field homogeneity and the TEM has the best loaded B_1^+ field homogeneity exactly as concluded in [3]. In terms of the SAR, the MTL has the lowest SAR values and therefore it is the safest to use.

REFERENCES

1. Jin, J., *Electromagnetic Analysis and Design in Magnetic Resonance Imaging*, 1st Edition, CRC Press, 1998.
2. Robitaille, P. M. and L. Berliner, *Ultra High Field Magnetic Resonance Imaging*, Springer, 2007.
3. Wang, C. and G. X. Shen, "$B1$ field, SAR, and SNR comparisons for birdcage, TEM, and microstrip coils at 7 T," *J. Magn. Reson. Imaging*, Vol. 24, No. 2, 439–443, 2006.
4. Ibrahim, T. S. and L. Tang, "Insight into RF power requirements and $B1$ field homogeneity for human MRI via rigorous FDTD approach," *J. Magn. Reson. Imaging*, Vol. 25, No. 6, 1235–1247, 2007.
5. Ibrahim, T. S., R. Lee, A. M. Abduljalil, B. A. Baertlein, and P. M. Robitaille, "Dielectric resonances and $B(1)$ field inhomogeneity in UHFMRI: Computational analysis and experimental findings," *J. Magn. Reson. Imaging*, Vol. 19, No. 2, 219–226, 2001.
6. Jin, J. M., J. Chen, W. C. Chew, H. Gan, R. L. Magin, and P. J. Dimbylow, "Computation of electromagnetic fields for high-frequency magnetic resonance imaging applications," *J. Phys. Med. Biol.*, Vol. 41, No. 12, 2719–2738, 1996.
7. Paul, C. R., *Inductance: Loop and Partial*, Wiley, 2001.
8. Yoo, H., J. Lee, C. E. Akgum, A. Gopinah, and J. T. Vaughan, "B_1 field comparisionfor RF coils in ultra-high-field MRI," *Electronics Letters*, Vol. 49, No. 25, 1601–1603, 2013.

A Scaled Simulated Method of Sea Clutter Based on Non-metal Materials

Yajun Wu, Zichang Liang, Li Li, Xiaobing Wang, and Jun Gu
Science and Technology on Electromagnetic Scattering Laboratory, Shanghai, China

Abstract— A new method of the simulated sea clutter in laboratory was proposed in this paper. By employing the scaled measurement technology, we can obtain the electromagnetic scattering characteristics of different sea states. According to the dielectric properties of non-metallic materials construction technique, a new kind of composite material has been constructed by epoxy mixing metal powder and material' reflectivity and complex permittivity meet the electromagnetic character of scaled simulated seawater. The material's permittivity can be controlled over a broad range. According to the geometric similarity conditions of scaled principle, the digital data of the different sea states' surface scaled model is generated basing on the classic sea spectrum model proposed by the oceanographer. The sea surface waveform of the scaled material is processed by CNC machine. We have measured the reflectivity and RCS with the incident angle of scaled PM (Pierson-Moskowitz) spectrum sea surface model made of the composite material proposed, and compared the results with theoretical simulation. The compared results verify the feasibility of the scaled simulated sea surface based on non-metal materials.

1. INTRODUCTION

Foreign military powers attach importance to the electromagnetic scattering measurement technique of the sea clutter in laboratory. While taking advantage of the wave pool simulated sea environment in the United States, the sea scale simulated material has been investigated using to measure the composite scattering characteristics between the ships on the sea at different sea states and analyze the effect of multipath. This method can provide a more accurate calibration data for the electromagnetic scattering theoretical model of the ships on the sea surface and improve measurement efficiency.

At present the scaled measurement technology of the sea clutter and scaled ship on a rough sea surface were investigated less in china. The scaled method of the sea clutter (especially high sea conditions simulation) is a key technology. According to the sea clutter scaled theory and the dielectric properties of non-metallic materials construction technique. A new kind of method that can easily be used to simulate sea clutter in laboratory was proposed in this paper. We used epoxy mixing metal powder to construct a new kind of composite material, and its reflectivity and complex permittivity meet the electromagnetic character of scaled simulated seawater. According to the geometric similarity conditions of scaled principle the data of scaled sea surface model at different sea states is produced. Then the surface of the scaled material is processed by CNC machine. we have measured the reflectivity and RCS at the incident angle of PM spectrum sea surface scaled model made of the composite material proposed, and compared the results with theoretical simulation. The compared results verify the feasibility of method proposed basing on scaled simulated sea clutter.

2. CONSTRUCTION TECHNIQUE OF THE SCALED SIMULATED MATERIALS OF SEA ENVIRONMENT

2.1. Electromagnetic Scaled Theory of Non-metallic Targets

Based on the electromagnetic scaled theory, if the parameters such as the geometry of the target, the working wavelength, the electric field and magnetic field strength are scaled in proportion, accordingly the electromagnetic scattering characteristics of the prototype system and the scaled system are the uniform. Clearly, the electromagnetic scaled measurement must ensure that the various elements of the scaled model (including geometric and physical elements) and the corresponding elements of the real system are proportional. For an perfect conductor or electromagnetic system composed of the lossless medium the similarity condition between scaled simulation and prototype is well known. When the prototype system includes lossy non-metallic materials. The scaled physical condition of the perfect conductor is not sufficient to describe all the similar relationship between the prototype and simulation system. But for the non-metallic dielectric materials, the similarity conditions can be derived from Maxwell's equations theoretically. The formula (1) shows

that the real and imaginary parts of the permeability, and the real and imaginary parts of the permittivity of the scaled and prototype lossy dielectric material are the same, just are invariant to a change in scale factor, then the electromagnetic scattering characteristics of the prototype system and the scaled system are invariant.

$$\begin{cases} p_{\mu r} = \frac{\tilde{\mu}_r}{\mu_r} = 1 \\ p_{\mu i} = \frac{\tilde{\mu}_i}{\mu_i} = 1 \\ p_{\varepsilon r} = \frac{\tilde{\varepsilon}_{1r}}{\varepsilon_{1r}} = \frac{\tilde{\varepsilon}_r}{\varepsilon_r} = 1 \\ p_{\varepsilon i} = \frac{\tilde{\varepsilon}_{1i}}{\varepsilon_{1i}} = \frac{\tilde{\varepsilon}_i + \tilde{\gamma}/\tilde{\omega}}{\varepsilon_i + \gamma/\omega} = 1 \end{cases} \tag{1}$$

Sea environment is non-metallic targets. According to the scaled measurement physical similarity theory, the complex permittivitys of the seawater at the prototype and the scaled frequency should be the same. The complex permittivitys of seawater is expressed as

$$\tilde{\varepsilon} = \varepsilon_r - j\frac{\gamma}{\omega} \tag{2}$$

where, ε_r is the dielectric constant of the medium, γ is the conductivity of the medium, ω is the angular frequency.

According to the scaled measurement similarity conditions, the complex permittivitys of the sea scaled material can be expressed as

$$\bar{\tilde{\varepsilon}} = \bar{\varepsilon}_r - j\frac{\bar{\gamma}}{\bar{\omega}} = \varepsilon_r - j\frac{p\gamma}{p\omega} = \varepsilon_r - j\frac{\gamma}{\omega} \tag{3}$$

where, $\bar{\varepsilon}_r$ is the dielectric constant of the sea scaled material, $\frac{\bar{\gamma}}{\bar{\omega}}$ is the loss of the sea scaled material, p is the scale factor which is the ratio between the size of the scale and full-scale targets.

By comparison of the formulas (2) and (3), the complex permittivitys of the scale and full-scale material must be equal at sea scaled measurement.

For the scaled sea surface, in accordance with the principle of geometric similarity, the wave height and length of scaled sea model should be decreased in scale factor.

2.2. Construction Method of the Seawater Scaled Material

2.2.1. Complex Permittivitys Scaling Simulation

To seawater with 20‰ salinity at 2 GHz as a prototype target the complex permittivity and reflectivity at 2 GHz, are listed in Table 1.

Table 1: Complex dielectric constant and reflectivity of the seawater at 2 GHz.

prototype target	salinity	radar frequency	dielectric constant	reflectivity
seawater	20‰	2 GHz	74.6 + i34	0.8

According to the physical similarity principle, the complex permittivitys of the seawater at scale and full-scale frequency must be equal. The scaled conditions are very harsh, and in laboratory the scaled simulation of sea clutter can not be strictly met, so firstly we developed theoretical simulation to investigate the RCS with the changes of the real part of the seawater' permittivity, imaginary part of the seawater' permittivity, and absolute value of the seawater' permittivity. By theoretical simulation we can select a reasonable simulation range of the seawater' complex permittivity to ensure the accuracy of certain engineering simulation

Using FEKO simulation software, the RCS of the flat made of the non-metallic materials to simulate seawater with the azimuth have been calculated at 10 GHz that non-metallic materials' permittivity is changed with the center of 74.6 + i34. The results show that when the relative error of the permittivity' real and imaginary part are less than 50%, the maximum error of the RCS is less than 1.5 dB.

Using two-scale method to calculate backscattering coefficient of the rough sea surface with the changes of the real part of the seawater' permittivity, imaginary part of the seawater' permittivity,

and absolute value of the seawater' permittivity, the results is shown in Figure 1 and Figure 2 that are the mean value of 30 random samples for vertical polarization. Because the seawater' permittivity are larger, the change of the real part of the seawater' permittivity or imaginary part of the seawater' permittivity alone has little effect to the sea surface' backscattering coefficient, especially change of the imaginary part separately affects smaller to sea surface' scattering. The change of permittivity' absolute value has obvious effect to the backscattering coefficient. When the amount of change in permittivity' absolute value is 50%, the error of the sea surface' backscattering coefficient is approximately 1.5 dB. When the amount of change in permittivity' absolute value is 60%, the error of the sea surface' backscattering coefficient is approximately 2.0 dB. When the amount of change in permittivity' absolute value is 80%, the error of the sea surface' backscattering coefficient is approximately 3.8 dB.

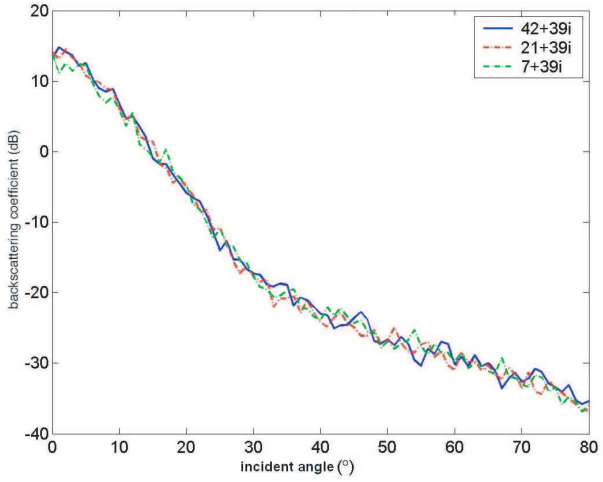

Figure 1: Backscattering coefficient vs. the incident angle plot at the various permittivity' real part.

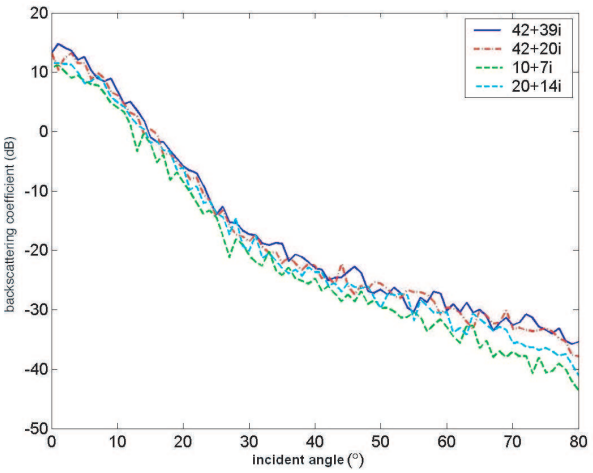

Figure 2: Backscattering coefficient vs. incident angle plot at the various permittivity.

From the above analysis of simulation results, the change of permittivity' absolute value has obvious effect to the backscattering coefficient. Investigating scaled simulated method of sea clutter based on non-metal materials, we can mainly consider the simulation accuracy of the absolute value of the permittivity according to the error demand.

2.2.2. Seawater Scaled Material Construction

We use the known permittivity epoxy mixing metal powder to construct a new composite material that its reflectivity and complex permittivity meet the electromagnetic character of scaled simulated seawater. The metal powder is the filler and the epoxy is the binder. The complex permittivity is determined by the microstructure of each component in the composite material [1]. According to Bruggeman [2] effective medium expression, the complex permittivity of the composite material is be calculated. In the course of constructing composite material, we adjust the percentage of metal powder and epoxy in the composite material repeatedly, measure the complex permittivity and electromagnetic scattering characteristics of the composite materials repeatedly, until the composite material is constructed that matches the permittivity of scaled simulated seawater. Considering the scaled conditions of the simulated seawater and simulation accuracy of the complex permittivity, the composite material has been constructed that its permittivity can be controlled over a broad range while the volume ratio of metal powder and epoxy changes. Figure 3 shows the scaled simulated composite material samples of the seawater. The reflectivity and complex permittivity have been measured at X, Ka band. Table 2 shows the reflectivity results of the composite materials that meet the reflectivity of scaled simulated seawater.

Using short circuit line method and resonant cavity method to measure the complex permittivity of the composite materials that meet the reflectivity of scaled simulated seawater, the real part of composite material permittivity is approximately 61 and the imaginary part is approximately 18 at X band. Relative error of the real part of the permittivity is approximately 18% relative error of the imaginary part of the permittivity is approximately 47% and relative error of permittivity' absolute value is approximately 22%. The real part of composite material permittivity is between 45 and 100 at Ka band and the relative error of the permittivity is less than 40%.

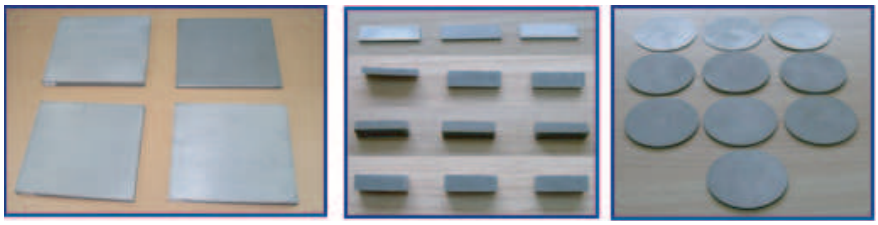

Figure 3: The scaled simulated composite material samples of the seawater.

Table 2: The reflectivity results of the composite materials.

prototype target	full-scale frequency	permittivity	reflectivity	scaled composite material	scale band	reflectivity	reflectivity relative error
seawater	2 GHz	74.6 + i34	0.8	epoxy + metal powder	X	0.794	0.8%
				epoxy + metal powder	Ka	0.79	1.3%

3. PM SPECTRUM SEA SURFACE SCALED MODEL TAILOR AND VERIFICATION

3.1. Digital Data Technique of the PM Spectrum Scaled Sea Surface Models

Basing on the classic sea spectrum model proposed by the oceanographer, the digital data of sea surface models at different sea states are produced. Then according to the geometric similarity conditions of scaled principle the digital data of the sea surface scaled model is calculated and converted into a three-dimensional model. At last the sea surface waveform of the scaled material is processed by CNC machine.

Sea environment is mainly described by the PM spectrum model

$$S(k) = \begin{cases} S_1(k) = \frac{0.00405}{k^3}\exp\left(\frac{-0.74g^2}{k^2u^4}\right) & 0 < k < K_1 \\ S_2(k) = 0.00405K_1^{-1/2}k^{-5/2} & K_1 < k < K_2 = 0.359 \\ S_3(k) = S_4(K_3)(k/K_3)^q & K_2 < k < K_3 = 0.942 \\ S_4(k) = 0.875(2\pi)^{p-1}\frac{g+3gk^2/13.177}{(gk+gk^3/13.177)^{(p+1)/2}} & K_3 < k \end{cases} \tag{4a}$$

$$p = 5.0 - \log_{10}(u_*), \quad q = \log_{10}[S_2(k)/S_4(k)]/\log_{10}(K_2/K_3) \tag{4b}$$

where, $S(k)$ is one dimension sea spectrum ($S_1(k)$ is PM sea spectrum), $k = 2\pi/\lambda$ is wave number of a sine wave component in the sea spectrum, λ is wavelength $g = 980\,\mathrm{cm/s^2}$ and $K_1 = K_2u_{*m}^2/u_*^2$, Friction wind speed $u_* > u_{*m} = 12\,\mathrm{cm/s}$, u is calculated by the formula (5) and is the wind speed at the height of the sea surface.

$$u = \frac{u_*}{40}\ln\frac{19.5}{z_0}\,\mathrm{m/s}, \quad z_0 = 0.684/u_* + 0.0000428u_*^2 - 0.0443\,\mathrm{cm} \tag{5}$$

Formula (6) gives the two dimension sea spectrum calculation formula:

$$S(k,\phi) = \frac{1}{(2\pi)^2k}S(k)\left[1 + a_1\left(1 - e^{-bk^2}\right)\cos(2\phi)\right] \tag{6a}$$

$$a_1 = 2(1-R)/[(1-B)(1+R)] \tag{6b}$$

$$B = \frac{1}{S_t^2}\int_0^\infty k^2S(k)e^{-bk^2}dk \tag{6c}$$

$$R = \frac{S_{ct}^2}{S_{ut}^2}, \quad S_t^2 = S_{ct}^2 + S_{st}^2 \tag{6d}$$

where, ϕ is propagation direction for a sine wave component, $b \approx 1.5\,\mathrm{cm}^2$, S_t^2, S_{st}^2 and S_{ct}^2 are separately the total average gradient' square, the average gradient' square against the wind direction, and the average gradient' square at the crosswind direction, Cox and Munk give a simplified formula:

$$S_{ct}^2 = 0.003 + 0.00192u \tag{7a}$$

$$S_{ut}^2 = 0.00316u \tag{7b}$$

To tailor sea surface scaled model, firstly the wave number and propagation direction of sine wave components in the sea spectrum need to be discrete, and according to the measurement electromagnetic band to confirm the maximum of wave number or the minimum wavelength of the sine wave components that should be less than the minimum electromagnetic wavelength. Secondly the amplitude of each discrete sine wave components at a sea surface wind speed is calculated by the formula (8):

$$A_n = \sqrt{2k_n S(k_n, \phi_n)\Delta k \Delta \phi} \tag{8}$$

According to the geometric similarity conditions of scaled principle, the height of the sea surface model is calculated:

$$z = \frac{1}{p}\sum_{n=1}^{N} A_n \sin\left[pk_n\left(x\cos\phi_n + y\sin\phi_n\right) + \varphi_n\right] \tag{9}$$

where, p is scale factor, k_n is discrete sine wave number A_n is the amplitude of discrete sine wave, ϕ_n is the propagation direction of discrete sine wave, φ_n is the random phase, N is the number of discrete sine wave.

Finally the digital data of the sea surface scaled model is converted into a three-dimensional model and the sea surface waveform of the scaled material is processed by CNC machine.

The depth of the true sea is big enough, and the size of scaled sea model is limited. The thickness of the scaled sea model will affect measurement accuracy. Because the seawater is lossy medium, when the transmission of electromagnetic waves in the sea, the intensity gradually decreases. The penetration depth of electromagnetic wave can be calculated according to the electromagnetic wave attenuation characteristics. The thickness of scaled sea model can only simulate the penetration depth of the true sea.

3.2. Feasibility Measurement and Verification

The PM spectrum sea surface scaled models are tailored using of non-metallic composite materials that meet the complex permittivity and reflectivity of scaled simulated seawate at 2 GHz. Figure 4 is the PM sea surface scaled model of the sea states 2, and scale factor is 1/20. The backscattering coefficient with the incident angle of this model has been measured at 40 GHz, and compared with theoretical simulation result. Figure 5 shows the measurement and simulation RCS with the incident angle, the scale frequency is 40 GHz, and the full-scale frequency is 2 GHz. The solid line curve is the measurement result and the dashed line curve is a simulation result in Figure 5. Within a certain range of the incident angle the measurement and simulation results are basically consistent. The root mean square error that the measurement result is compared with the simulation value of

Figure 4: The PM sea surface scaled model of the sea states 2.

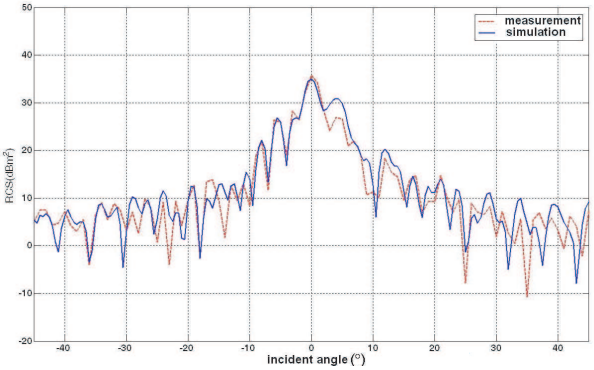

Figure 5: The measurement and simulation RCS plot with the incident angle.

the PM sea spectrum model is 0.29 dB. The research illustrates the sea surface scaled models have feasibility. If the size of the PM spectrum sea surface scaled model is larger, the incident angle range of simulated sea surface backscattering is larger.

4. CONCLUSION

A new method used to simulate sea clutter in laboratory was proposed in this paper. Base on employing the the electromagnetic scaled engineering condition of the sea clutter and the dielectric properties of non-metallic materials construction technique, the composite material to simulate seawater was been constructed by the epoxy mixing metal powder. According to the digital data of the PM spectrum sea surface scaled models. The sea surface waveform of the scaled material was processed by CNC machine. The PM spectrum sea surface scaled model of the sea states 2 was been tailored the backscattering coefficient with the incident angle was been measured and compared the results with theoretical simulation. The compared results verify the feasibility of method proposed basing on scaled simulated sea clutter.

REFERENCES

1. Yang, H., Y. Xia, D. Wen, and S. Lu, "High frequency electromagnetic properties of metal particle-dielectric composites," *Central China Normal Universit Transaction (Natural Science),* Vol. 40, No. 2 177–180, 2006.
2. Bruggeman, D. A. G., "Effective mediummodel for the optical prop-erties of composite materials," *Ann. Phys. Leipzig*, Vol. 24, 636–642, 1935.

RCS Measurement of Large Target in Non-cooperative Near Field Environments

Xiuli Xu, Guangde Tong, Li Li, Kun Cai, Xiaobing Wang, and Chao Wang
Science and Technology on Electromagnetic Scattering Laboratory, China

Abstract— Generally speaking, Radar Cross Section (RCS), which is an important indicator to value the electromagnetic scattering characteristic of a target, has been paid more attention as time goes by since WWI. As we know, when RCS measurement is carried out, the accuracy of RCS measurement results always depends on the testing site and the system, and if the target is too large or the frequency is too high, a cooperative and vast measuring area or a costly compact range facility will be needed. As the testing site sometimes is not large enough for some cases, so the radiation pattern of the transmitting-receiving antenna can't be dealt as the far filed pattern. To solve these problems, this paper presents a new method of RCS measurement basing on SAR imaging by a scanner in near field. And also we employ a new SAR imaging method instead of the traditional ISAR imaging method to transform the electromagnetic scattering near field data of target to the far field RCS. That's saying, the near field data is collected by a portable 1-D scanner SAR imaging system, with the new method, we can obtain the far field by the transformation. Furthermore, in order to get the accurate far-field RCS data of the target, we use a new method to correct the effects of transmitting-receiving antenna's radiation pattern and the difference of the distance from scattering center of the antenna to target in near-field imaging measurement, which we usually call corrected-imaging method. The compared results of theoretical simulation and experimental data show that RCS obtained by the proposed method is satisfied the condition and can be used widely.

1. INTRODUCTION

RCS is an important gist to assess the electromagnetic scattering characteristic of the target, and is traditionally obtained by measurement in a far-field range requiring a long distance between target and antennas, or with a compact range facility requiring a high-quality reflector and suffering from edge diffraction which limits the size of the quite zone. Therefore, the transformation method is used to obtain target's RCS which is based on ISAR-Imaging in near field. ISAR-Imaging measurement needs a turntable, and the position precision of the turntable will be very high if the target is too large or the frequency is too high.

To overcome these problems, a new transformation method between the near-field and the far-field scattering data is introduced in this paper which is based on SAR-Imaging.

2. THEORY

The new method that target's RCS is obtained by SAR-Imaging near-field consists of four steps: Firstly, back-scattering echo of target is obtained with the Spotlight-SAR Imaging measurement system; Secondly, target's accurate scattering-data in near-field is obtained with the filter-process; Thirdly, target scattering-image (or target scattering-center distribution) is obtained with the FBP (filter back-projection) imaging algorithm; Lastly, target's RCS is obtained by vector sum of the target scattering-centers with the radar equation.

2.1. Spotlight-SAR Imaging Measurement

SAR Imaging of the target is based on Spotlight-SAR theory which is illustrated in Figure 1.

That high cross-resolution is obtained with the synthetic-aperture which is made by the transmit-receive antenna moving along the line-rail from the position-A to position-B, and the azimuth angle of the antenna beam is steered continuously to illuminate the target during the antenna's moving. High range-resolution is obtained by transmitting wide-band sweeping signal, and then we can obtain the two-dimensional high resolution image of target.

Two-dimensional high resolution can be expressed as

$$\begin{cases} \delta_y = \frac{\lambda R}{2L_e} \\ \delta_x = \frac{C}{2B} \end{cases} \tag{1}$$

where δ_x is range-resolution, δ_y is cross-resolution, C is wave propagation speed, λ is the radar wavelength, L_e is the synthetic-aperture length, R is the distance between the antenna and terrain scattering-center, B is the sweeping-band.

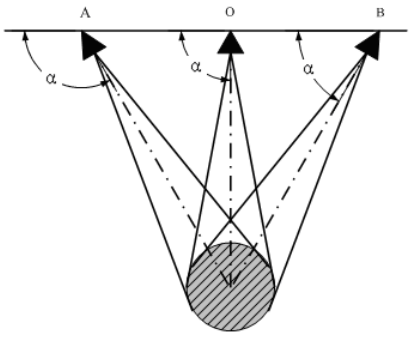

Figure 1: Spotlight-SAR Imaging theory sketch map.

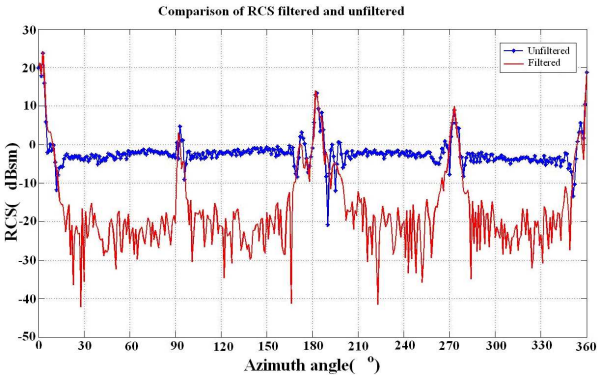

Figure 2: Comparison of RCS filtered and unfiltered.

2.2. Filter-process

Echo received by the antenna includes not only the target's signal but also clutter signal such as coupling signal between the transmitting and receiving antennas, multipath signal between the target and the ground, the background signal, and so on.

RCS measurement accuracy can be improved by opting time domain RCS measurement method based on the sweep, using windowed processing to eliminate those clutter signals. Figure 2 shows the comparison of a special trapezoid composite RCS filtered and unfiltered which shows RCS dynamic is increased after filter-process

2.3. FBP Imaging Process

According to the Spotlight-SAR Imaging measurement theory introduced in Section 2.1, target echo received by the antenna is expressed as

$$F(k, y') = \iint_{x\ y} f(x, y) \exp(-j2\pi kR) \mathrm{d}x\mathrm{d}y \tag{2}$$

where (x, y) is the coordinate of the target scattering-center, (x', y') is the coordinate of the antenna.

Two-dimensional high resolution image of target can be obtained by 2-D FFT transformation with the far-field measurement condition satisfied, the far-field measurement condition is expressed as

$$R = \frac{2D^2}{\lambda} \tag{3}$$

where R is the least far-field measurement distance, D is the maximum wide length of the target. For example, the target with the wide length of two meter is measured at 16 GHz, the least far-field measurement distance (R) will be larger than 400 meters which our measurement-condition can't satisfy, so the really target imaging measurement is usually carried out in near-field. We usually use horn-antenna to finish the target imaging measurement, and the horn-antenna's irradiation to the target is figured as Figure 3.

From Figure 3, we can see firstly that the radiation intensity is different with the radiation angle, and the difference will cause the terrain image's scattering-intensity distortion. Secondly, for a large target measurement in near-field, the distance from the target scattering-centers to the antenna is different, and the difference may be one time which will cause 15 times terrain image's

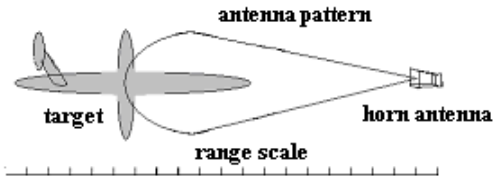

Figure 3: Horn-antenna's irradiation to the target.

scattering-intensity distortion. Therefore, we must correct the effects of antenna radiation pattern and distance factor in near-field measurement.

FBP (filter back-projection) algorithm in near-field can correct the difference of the radiation intensity via importing the antenna radiation pattern, and can correct the difference of the distance from the target scattering-centers to the antenna via importing the distance factor, and the algorithm is expressed as

$$\begin{cases} P_l(l_s) = \int\limits_0^{k_B} (k+k_{\min}) F(k+k_{\min}, y') \exp(\mathrm{j}2\pi k l_s)\,\mathrm{d}k \\ \hat{f}(x,y) = \int\limits_{-Le/2}^{Le/2} P_l(l_s) \exp(\mathrm{j}2\pi k_{\min} l_s) \frac{1}{RG(\varphi)} \frac{R^2}{R_0^2}\mathrm{d}l \\ R = \sqrt{(R_0-x)^2 + (y'-y)^2} \\ l_s = R - R_0, \quad k_B = \frac{2B}{C} \\ \varphi = \mathrm{a}\cos\left|\frac{R^2+R_0^2+y'^2-(x^2+y^2)}{2R\sqrt{R_0^2+y'^2}}\right| \end{cases} \tag{4}$$

where (x, y) is the coordinate of the target scattering-center, (x', y') is the coordinate of the antenna, R_0 is the distance form the antenna to the target center, R is the real distance form the antenna to the target scattering-centers, $F(k + k_{\min}, y')$ is the echo signal of the target after filter-process, $\hat{f}(x, y)$ is the scattering-intensity of the target scattering-center, φ is the angle between the target scattering-center and the antenna-center, $G(\varphi)$ is the antenna pattern.

2.4. Far-field RCS Obtained

The real scattering-intensity or the distribution of target scattering-centers is obtained by FBP process. Once the scattering-image is available, a natural definition of scattering-centers is a discrete set of point scatters, each with position (x_n, y_n) and amplitude A_n, and we will use CLEAN algorithm to find the dominant scattering-centers from the image.

CLEAN algorithm is a robust iterative procedure which successively picks out the highest point in the image, assumes it is a scattering center with the corresponding strength, and subtracts the point spread function $h(x_n, y_n)$ of the scattering center from the image. At the nth iteration, if A_n is the intensity of the highest point in the image with location (x_n, y_n), then the residual image is expressed as

$$(\text{Residual Image})_{n+1} = (\text{Residual Image})_n - A_n \cdot h(x_n, y_n) \tag{5}$$

Target scattering center model can be obtained by CLEAN process. Therefore, target RCS in far-field or at random range in near-field can be obtained by vector sum of the target scattering-centers with the radar equation, and the RCS can be expressed as

$$\sqrt{\sigma} = \sum_{n=1}^{N} \hat{f}(x_n, y_n) \exp\left(-\mathrm{j}\frac{4\pi R_n}{\lambda}\right) \frac{R_0^2}{R_n^2} G(\varphi_n) \tag{6}$$

where is $\sqrt{\sigma}$ the vector RCS of the target, $\hat{f}(x_n, y_n)$ is the nth scattering center's scattering-intensity, R_n is the distance between the antenna center and the target scattering center, R_0 is the distance between the antenna center and the target center, φ_n is the angle between the nth target scattering-center and the antenna-center.

3. MEASUREMENT

To validate the correctness and feasibility of the technology, theoretical simulation and test measurement are made.

3.1. Theoretical Simulation Measurement

In the theoretical simulation measurement, we obtain the special metal plate (1 m × 0.2 m) SAR Imaging data in near-field and the RCS data in far-field with simulation software, and the detailed imaging parameter is

1) R_n (the measurement distance in near-field): 3 m
2) R_f (the measurement distance in far-field): 3 km

3) Scanning scope: $(-3 \sim 3)$ m
4) Sweeping scope: $(8 \sim 12)$ GHz

With the transformation method introduced in this paper, we can obtain the far-field RCS. Figure 4 is the comparison of RCS obtained by simulation and extrapolation, and its average error is less than 1 dB.

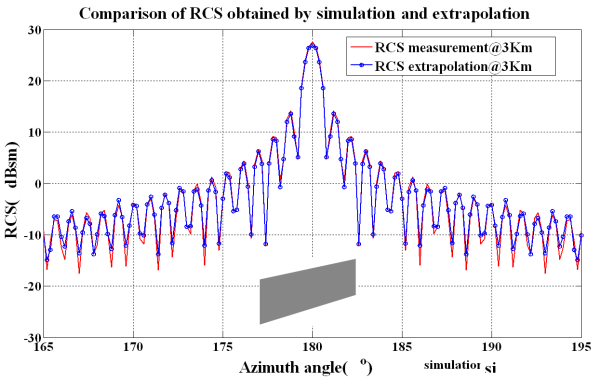

Figure 4: Comparison of RCS simulation and extrapolation.

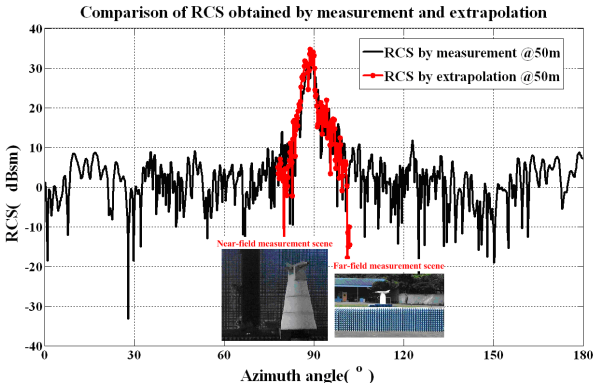

Figure 5: Comparison of RCS measurement and extrapolation.

3.2. Test Measurement

In the test measurement, we obtain the scaled plane model's (2 m×2 m) near-field SAR Imaging data with scanner-SAR Imaging system in the darkroom, and obtain the far-field RCS data with ISAR Imaging system in non-cooperative outdoor environments, and the detailed imaging parameter is

1) R_n (the measurement distance in near-field): 5 m
2) R_f (the measurement distance in far-field): 50 m
3) Scanning scope: $(-2.25 \sim 2.25)$ m
4) Sweeping scope: $(8 \sim 12)$ GHz

With the transformation method introduced in this paper, we can obtain the far-field RCS. Figure 5 is the comparison of obtained by measurement and extrapolation, and its average error is less than 2.5 dB.

4. CONCLUSION

Both the theoretical simulation and test measurement results validate the correctness and feasibility of the technology that target's far-field RCS can be obtained with SAR imaging in non-cooperative near-field environments.

REFERENCES

1. Osipov, A. and H. Kobayashi, "An improved image-based near-field-to-far-field transformation," *Proceedings of Asia-Pacific Microwave Conference*, 1693–1696, 2010.
2. Vaupel, T. and T. F. Eibert, "Comparison and application of near-field ISAR imaging techniques for far-field radar cross section determination," *IEEE Transactions on Antennas and Propagation*, Vol. 54, No. 1, 144–151, 2006.
3. LaHaie, I. J., "Overview of an image-based technique for predicting far-field radar cross section from near-field measurements," *IEEE Antennas and Propagation Magazine*, Vol. 45, No. 6, 159–169, 2003.

Scattering Analysis of Reflectarray Antennas Illuminated by a Point Source for Near Field Focus Applications

Shih-Chung Tuan[1] and Hsi-Tseng Chou[2]

[1]Department of Communications Engineering, Oriental Institute of Technology, Pan-Chiao, Taiwan
[2]Department of Communications Engineering, Yuan Ze University, Chung-Li, Taiwan

Abstract— The scattering and diffraction mechanisms of reflecting and transmitting arrays illuminated by the radiation of a point source for a general near-field focus problem are summarized. In particular, the phenomena are interpreted by the ray decompositions of Floquet waves and result in the solutions, analogous to the ordinary UTD-type formulations for the phased array antennas with a proper parameter mapping. In this approach, the radiations of periodically located current sources are first decomposed into Floquet modes, in which every mode is equivalent to the radiation of continuous current sources with additional linear phase impressions. Fast convergence in the radiation computation can be achieved because relatively few modes will propagate to the target zone with the rest being evanescent. The ray decomposition is performed by asymptotically evaluating the radiation integral of each Floquet mode and interprets the total fields in terms of rays directly radiated from the aperture and diffracted from aperture truncations.

1. INTRODUCTION

Reflectarray and transmitting array antennas are planar structures popularly used to replace the reflector and lens antennas, respectively with an advantage of low profile for easy installment. In comparison with the competing candidate of planar phased array antennas, they are also superior in simplifying the beam forming networks by using the radiation of a feeding antenna to illuminate the arrays. In the past, the majority of the researches in the literature focus on design and implementation methodologies for their applications in the far-field radiations. The radiation mechanisms have not been well developed. In addition, recent interests in the applications of near-field communications have further driven the need to analyze and explore the radiation mechanisms with handful interpretation methodologies, in which ray decompositions based on uniform geometrical theory of diffractions (UTD) has been well recognized to be very effective. The UTD-type ray decomposition has been successfully employed to analyze the radiation mechanisms of phased array antennas. In this approach, the radiations of periodically located current sources are first decomposed into Floquet modes, in which every mode is equivalent to the radiation of continuous current sources with additional linear phase impressions. Fast convergence in the radiation computation can be achieved because relatively few modes will propagate to the target zone with the rest being evanescent. The ray decomposition is performed by asymptotically evaluating the radiation integral of each Floquet mode and interprets the total fields in terms of rays directly radiated from the aperture and diffracted from aperture truncations. More recently we have developed a general solution for the radiation of finite array antennas excited to focus the radiation in the near zone, which accommodate the needs of analysis for the general applications of phased array antennas in both the far- and near-zones. This paper is organized in the following format. Section 2. describes the formulation for the radiation from an one-dimensional (1-D) semi-infinite to (2-D) NSA array. The characteristics are investigated in Subsections 2.1–2.4. In particular, the study focuses on the truncation diffraction mechanism as a compensation to the shortage of Floquet mode phenomena in [1–5], which examine only the radiation mechanisms of infinite array of antennas. Numerical examples are presented in Section 3 for demonstration and validation. Finally a short discussion is presented in Section 4 as a conclusion.

2. 2-D FINITE ARRAY RADIATION PROBLEM

2.1. Composition of 2-D Radiation from a 1-D Array

The semi-infinite, linear array of line sources is illustrated in Figure 1, whose elements are indexed by $n = -\infty \sim N$ and located at $\bar{r}'_n = (nd_x, 0)$ on the x-axis with a period d_x. The line source is

located at $\bar{\rho}_f = (x_f, z_f)$ and radiates fields by

$$u_f(\bar{\rho}) = \frac{1}{4j} I_0 H_0^{(2)}\left(k|\bar{\rho} - \bar{\rho}_f|\right) \cong \frac{e^{-j\pi/4} I_0}{4} \sqrt{\frac{2}{\pi k|\bar{\rho} - \bar{\rho}_f|}} e^{-jk|\bar{\rho} - \bar{\rho}_f|} \tag{1}$$

which will excite the reflecting or transmitting elements in Figures 1(a) and (b), respectively. In (1), $k = 2\pi/\lambda$ is the wave number with λ being the wavelength in free space, and I_0 is used as the reference amplitude of line source. The fields scattered from the array can be found from the radiation of equivalent current, $I(\bar{\rho}')$, on the closed surface enclosing the array structure as illustrated in Figure 1. To the degree of accuracy in the Kirchhoff approximation, the induced current is assumed to be found from the infinite array structure illuminated by the same incident field. Thus it can be approximately expressed as

$$I(\bar{\rho}') = u_f(\bar{\rho}_i) Q(\bar{\rho}') e^{j\phi(\bar{\rho}')} \tag{2}$$

where $\bar{\rho}_i$ and $\bar{\rho}'$ are the position vectors on the closed surface. The function, Q, is related to the reflection and transmission coefficients for the cases of Figure 1, with ϕ being the phase. In the current investigation, one is interested in the scattering field in the $+z$ space, thus only the current on S_t is considered with the others omitted for simplification. The scattering field can be expressed as

$$u_s(\bar{\rho}) = \frac{1}{4j} \int_{x_a}^{x_b} u_f(\bar{\rho}_i) Q(\bar{\rho}') e^{j\phi(\bar{\rho}')} H_0^{(2)}(k|\bar{\rho} - \bar{\rho}'|) dx' \tag{3}$$

where $x_a \to -\infty$ and $x_b = N d_x$ in the current development.

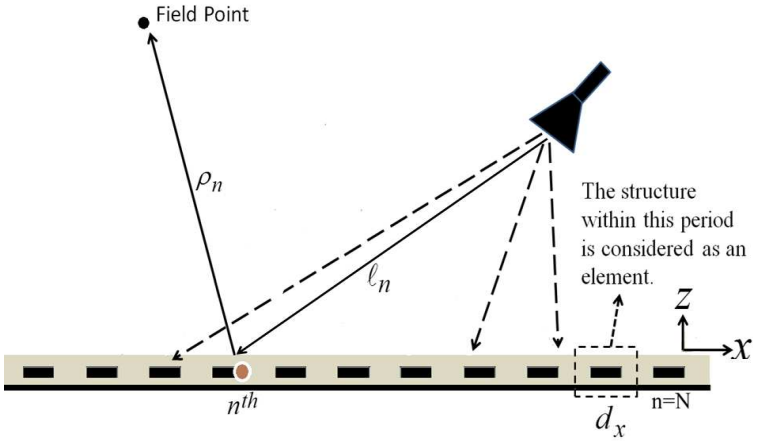

Figure 1: Illustration of 2-D reflectarray radiation problems, where the fields are focused in the near zone.

2.2. Composition of Uniform Asymptotic Formulations

The Floquet waves are obtained by using the following Poisson sum formula:

$$\sum_{n=-\infty}^{N} f(n) = -\frac{f(N^+)}{2} + \sum_{p=-\infty}^{\infty} \int_{-\infty}^{N^+} f(v) e^{-j2\pi pv} dv \tag{4}$$

The evaluation of (3) can be performed asymptotically by employing the spectrum representation of Hankel functions to decompose the radiating fields into components of diffraction mechanisms. Within the UTD framework, the asymptotic evaluation of (3) can be formulated into the following format:

$$A_{net}^p(\bar{r}) = A_{dir}^p(\bar{r}) \cdot U(\mathrm{Re}(x_e - x_s)) + A_{end}^p(\bar{r}) F(ka) \tag{5}$$

where $U(\cdot)$ is the Heaviside step function and $F(\cdot)$ is a transition function to assure the uniform field distribution. In (5), $A_{dir}^p(\bar{r})$ is the asymptotic solution of radiation when the array is extended to a infinity while $A_{end}^p(\bar{r})$ accounts for the effects of truncation. Both components arise from a

radiation point, x_s, on the array aperture, and a diffraction point, x_e, on the edge. This formulation remains valid as the radiation point is close to the diffraction point, i.e., $x_s \to x_e$. However, as mentioned in [?], it exists two radiation points in a general NSA problem. The solution in (5) becomes singular as these two radiation points coincide near the diffraction point at the edge. The characteristics of these terms are addressed in the following subsections.

2.3. The Asymptotic Solution of Direct Radiation from a Non-truncated Array, $A^p_{dir}(\bar{r})$

In (5), $A^p_{dir}(\bar{r})$ is identical to the solution of radiation for an infinite array, whose characteristics have been investigated. The formulation is summarized in the following by

$$A^p_{dir}(\vec{r}) = \frac{jI_oQ}{2dxk^s_z}\sqrt{\frac{-\rho_c}{\rho^s_v-\rho_c}}\frac{1}{\sqrt{\ell^s_v}}e^{-jk(\rho^s_v-\rho^s_{vo})}e^{-j\beta_p x_i} \tag{6}$$

where $x_s = v_s d_x$ with v_s being the contributing saddle point. Here the saddle point, $x_i = x_s$, satisfies the following relation by

$$\frac{k^s_x}{k} = \frac{k^i_x}{k} + \frac{p\lambda}{d_x}; \quad \left(k^s_x, k^i_x\right) = k\left(\frac{x-x_s}{\rho^s_v}, \frac{x_s-x_f}{l^s_v}\right) \tag{7}$$

2.4. The Asymptotic Solution of Edge Point Contribution from a Truncated Array, $A^p_{end}(\vec{r})$

The asymptotic edge point contribution in (5) is developed and summarized in the following formulation:

$$A^p_{end}(\vec{r}) \cong \frac{jI_oQ}{2dx\sqrt{\ell_e}\sqrt{\rho_e}}\left[\frac{-e^{-j\frac{\pi}{4}}}{\sqrt{2\pi k}[(k^e_{xo}-k^e_x)+\beta_p]}\right]e^{-jk(\rho_e-\rho_{eo})}e^{-j\beta_p x_e} \tag{8}$$

3. NUMERICAL EXAMPLES

One first considers the case of scattering characteristic for an 2-D semi-infinite reflectarray, and examines the fundamental mode ($p = 0$) and higher order modes ($p = -1$), whose results are shown in Figures 2(a), (b). The parameters as shown: feed point located at $(-20\lambda, 90\lambda)$, focused point at $(0, 40\lambda)$, number of array element $(-\infty \sim N_x)$, $N_x = 20$ and operation frequency at 10 GHz.

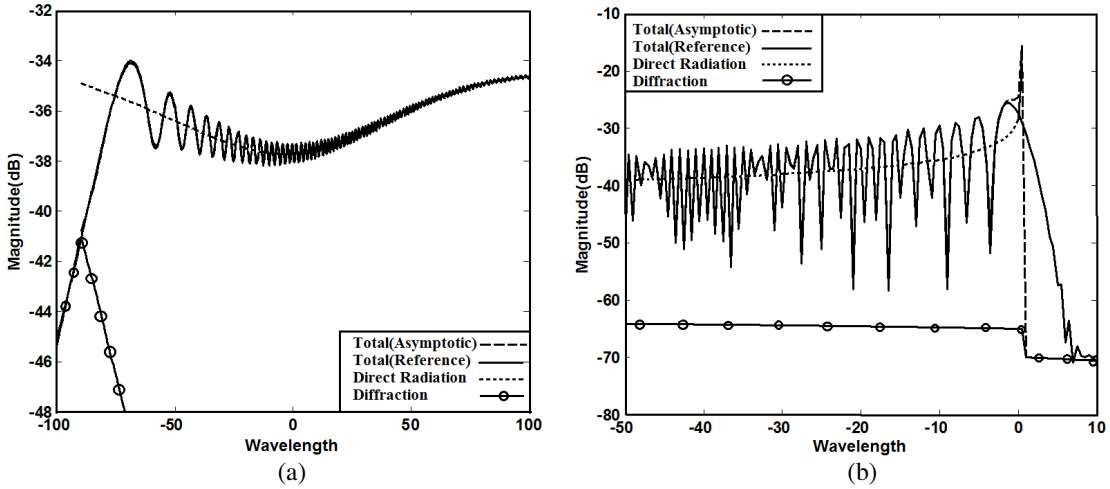

Figure 2: The scattering analysis of semi-reflectarray for dominant mode and higher order mode. (a) $p = 0$ mode. (b) $p = -1$ mode.

4. CONCLUSIONS

An uniform formulation of EM radiation from a semi-infinite, periodic reflectarray is presented in this paper. It decomposes the radiation mechanism with respect to the fundamental concept of UTD, and can be applied to interpret the wave propagation phenomena in a general radiation problem of focused field. In particular, the diffraction mechanisms from the array truncation are investigated with numerical example demonstrations. This formulation remains valid as the

radiation point approaches to the diffraction point on the truncation edge of array. As discussed in [1], there are two radiation points on the array aperture when the radiation focuses in the near-zone. The coincidence of these two radiation point occurs in the case that the field points are on the caustic curves in each Floquet mode. The presented formulation becomes singular as the diffraction point is near the coincident point of these two radiation points. These phenomena will be investigated in the future phase of this work.

REFERENCES

1. Chou, H.-T., "Floquet mode phenomena of infinite phased array antennas in near-field focus applications," *IEEE Transactions on Antennas and Propagation*, Vol. 61, No. 6, 3060–3068, June 2013.
2. Puggelli, F., P. Pathak, M. Albani, and P. Janpugdee, "A hybrid numerical-composite UTD ray analysis of the radiation by large locally convex conformal arrays on large platforms," *Proceedings of 2013 URSI International Symposium on Electromagnetic Theory (EMTS)*, 1064, 1065, May 20–24, 2013.
3. Tuan, S.-C. and H.-T. Chou, "Analytic analysis of transient radiation from phased array antennas in the near- and far-field focus applications," *IEEE Transactions on Antennas and Propagation*, Vol. 61, No. 5, 2519, 2531, May 2013.
4. Pathak, P. H., R. J. Burkholder, J.-F. Lee, and P. Janpugdee, "An efficient hybrid numerical-ray based subaperture formulation for the analysis of large convex conformal antenna arrays on large platforms," *3rd European Conference on Antennas and Propagation, EuCAP*, 2977, 2979, March 23–27, 2009.

Non Destructive Method for Detection Wood-destroying Insects

P. Fiala[1], **M. Friedl**[1], **M. Cap**[1], **P. Konas**[1], **P. Smira**[2], **and A. Naswettrova**[2]

[1]Department of Theoretical and Experimental Electrical Engineering
Brno University of Technology, Technicka 3082/12, Brno 616 00, Czech Republic
[2]Thermo Sanace s.r.o., Chamradova 475/23, Ostrava, Kuncicky 718 00, Czech Republic

Abstract— The problem of finding a suitable diagnostic procedure for the examination of structural elements has been closely analyzed in recent years. In this connection, the main material of interest is wood as a sort of heterogeneous matter, and the diagnostic procedure is directed towards enabling industrial application in the future. A new diagnostic method based on X-ray imaging and acoustic electromagnetic wave; the X-ray technique utilizes the reduction of imaging information into 2D planar projection and acoustic recording system allows to find out activity of the wood-destroying pests. After researching activities and localization of wood-destroying pests, there are two methods for its disposal-thermal sanitation and microwave system.

X-ray method is known as nondestructive diagnostic methods in the medical or veterinary practice. This X-ray mobile system was designed for evaluate of the wood quality and presence of wood-boring insects and wood-destroying fungi. Special software are single parts of the X-ray system and enable automatic/semi-automatic diagnostic of the level of damage wood and localization of wood-destroying pests.

Field X-ray monitoring of vital activity of wood-destroying insects is very robust and ineffective in comparison with the acoustic method, which seems like a much better solution. Therefore was designed acoustic system for the initial detection of wood-destroying insects in building construction.

1. INTRODUCTION

Currently, the protection of structural elements made of wood against decay fungi and wood-destroying insects is widely realized through the thermal treatment technique, which has been known and used in Germany since 1930. The principle of this method consists in heating the related wooden structures, by means of hot air whose temperature does not exceed 120°C, for a period of 4–10 hours. Heat is accumulated inside wooden components of the structure under treatment, and the temperature of these components may reach as high as 60°C within the cross-section, Fig. 1. At the temperature of 55°C, all viable forms (including the ova, worm, nymph, and beetle) of wood-destroying insects perish; this temperature is the boundary value for the coagulation of proteins that nurture wood-destroying insects such as old-house borer (*Hylotrupes bajulus* L.), common house borer (*Anobium punctatum*), the death watch beetle (*Xestobium rufovillosum*), or the powder post beetle (*Lyctus brunneus*).

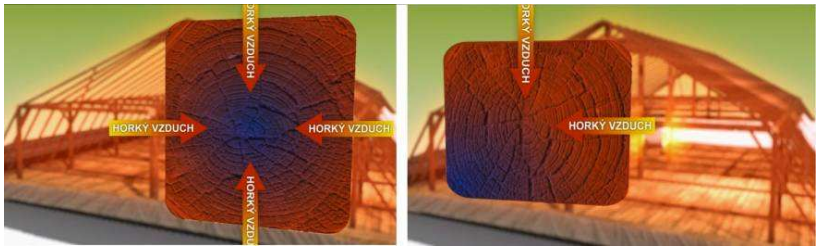

Figure 1: Heat propagation and detection in a non-homogeneous material: wood.

A necessary precondition for any sensible application of the method (Fig. 2) consists in diagnostics performed on damaged portions of structural elements. The diagnostics can be realized by means of non-destructive techniques or, alternatively, through destructive methods resulting in partial disruption of the examined element. This contribution contains the proposal and analysis of a mobile non-destructive diagnostic method (X-Ray monitoring and acoustic system) suitable for use with a damaged or disrupted structural element (Fig. 3). In connection with non-destructive diagnostics, the thermal treatment method constitutes a well-suited approach to be applied in artifacts and buildings of great historic value [1].

Figure 2: The removal and treatment of wood invaded by wood-destroying insects and fungi.

Figure 3: Examples of wood invaded by decay-fungi and wood-destroying insects.

The group of basic treatment methods includes the liquidation of insect foetus, fungus, or rot through the use of hot air or chemical preparations. In all application cases, these techniques are further modified or combined, and the extent of their use is usually determined from the diagnostic results.

2. NON-DESTRUCTIVE DIAGNOSTIC METHODS

The group of non-destructive methods classifying the rate and extent of damage or inhomogeneity in wood includes various techniques that utilize, as a source of the active system, an electromagnetic wave with a wavelength shorter than 3 mm. Thus, wood treatment processes may involve the use of antenna systems applied in the diagnostics of breast carcinoma [2] or utilization of the X-ray diagnostic method known in the fields of human medicine. With this technique, however, there occurs certain difficulty related to the evaluation of damage to the material volume. In spite of the fact, a cycle of tests using damaged material samples (Fig. 3) has led to an alternative approach; this solution is based on the evaluation of the obtained shot image through a transparent X-ray method having a high rate of image resolution. Field X-ray monitoring of vital activity of wood-destroying insects is but relatively robust and ineffective in comparison with the acoustic method, which seems like a much better solution. Therefore was designed acoustic system for the initial detection of wood-destroying insects in building construction.

2.1. X-ray Diagnostic Method

The X-ray method is well-known as a nondestructive diagnostic method used in the medical or veterinary practice. The mobile system shown in Fig. 4 was designed at the DTEEE to evaluate wood quality and detect the presence of wood-boring insects and wood-destroying fungi. The designed diagnostic system is mobile and meets the requirements for accuracy of image resolution evaluation.

Figure 4: X-ray diagnostic system for monitoring building elements.

This system can monitor and evaluate the condition of wooden elements. It is possible to evaluate the level of damage, as shown in Fig. 5 the condition and the presence of Old-house borer

(*Hylotrupes bajulus* L.), a wood-destroying insect. The wood-destroying insect localization has been tested on laboratory samples in a defined manner which were attacked by germs of *Hylotrupes bajulus* L..

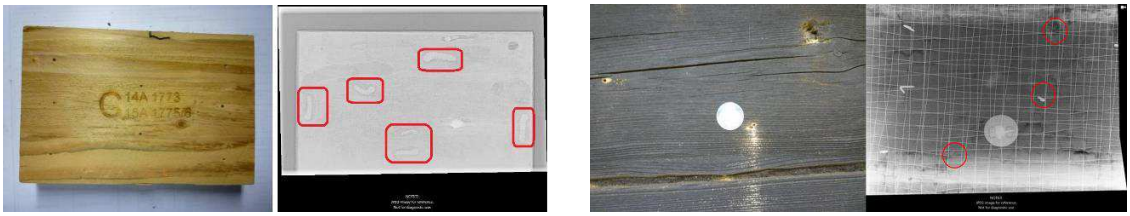

(a) (b)

Figure 5: Attacked wooden elements (the larva is marked). (a) Laboratory sample. (b) Building element combined with plaster and metal mesh; Measured on 1 June 2012, Mlýn, Kozlovice, Czech Republic.

A vital part the X-ray system consists in a special type of software, which enables automatic or semi-automatic diagnostics of the level of damage caused by the insects (Fig. 6). The software also facilitates the localization of wood-destroying pests [4–9].

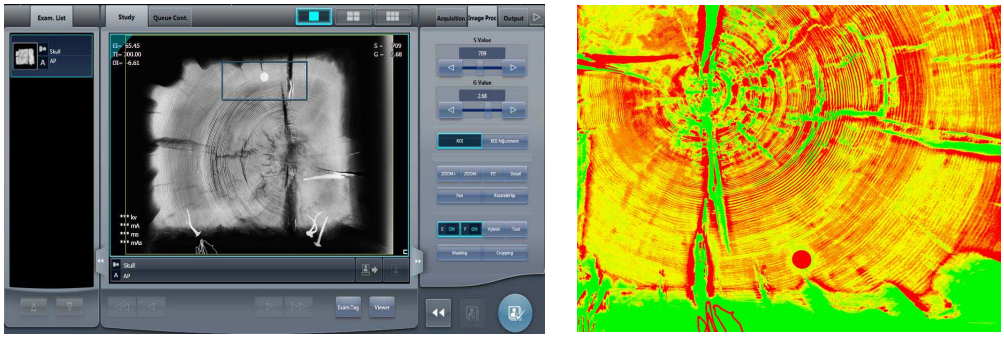

(a) (b)

Figure 6: Special software for processing wood-destroying material. (a) X-ray image of the real sample. (b) Demonstration of the wood damage calculation software.

2.2. Acoustic Diagnostic Method

Wood-destroying insect activity detection is possible due to the sound that issued larvae especially during the creation of feeding damage. The UTEE was developed acoustic device — ACOUSTIC PACK (Fig. 7(a)) for the detection of wood-destroying pests in building elements and verification laboratory and terrain measurements. The acoustic system enables us to record up to 8 audio tracks in real time. Importantly, the system also facilitates the subsequent semi-automatic (automatic) analysis of the tracks and ensures the evaluation of the state of the sample (Fig. 8). The audio signals are recorded by individual sensors (Fig. 7(b)), in which a low-noise preamplifier is integrated [10].

(a) (b)

Figure 7: The realized acoustic diagnostic system. (a) Terrain workplace. (b) Detail of the acoustic sensor.

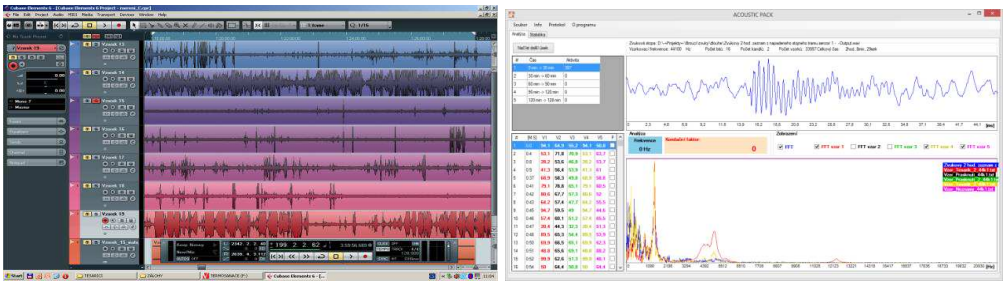

(a) (b)

Figure 8: (a) Special software for recording of the acoustic signals. (b) Designed statistic software for processing and evaluation acoustic data.

The amplified signal is then processed by an A/D converter which sends the data to a PC USB interface; after that, the above-mentioned analysis of the level of damage to the sample is performed. The recording can be continuously run on all eight channels for several days, the resulting state of the sample using the software and displayed graphically. For these purposes special software (Fig. 8(b)) has been programmed that allows you to statistically process the data obtained and protocol indicating the level of attack element of building wood-destroying pest is its output. The system also allows independent on-line listening all the individual audio channels using two headphone outputs. This is advantageous for fast detection and location of the wood-destroying pest, consequently on the basis of this listening is possible strategically locate sensors and start recording for more detailed analysis wood-destroying pest attack.

3. CONCLUSION

We designed and tested new X-ray diagnostic methods (Fig. 4) for 2-D imaging. The parameters were set in such a manner as to enable the imaging of shot sections showing the rate of damage to the heterogeneous structure building. Because this X-ray monitoring of the vital activity of wood-destroying insects is very robust and ineffective, the acoustic method (Fig. 7) was designed. This method allows us to record up to 8 audio tracks in real time; these tracks can be subsequently analyzed on a semi-automatic (automatic) basis, and the evaluation of the state of the sample can be performed. Diagnostic tests of quality (damage) of wooden bearing and structural elements were carried out on real building elements.

Currently, the protection of structural elements made of wood against decay fungi and wood-destroying insects is widely realized through the mainly thermal treatment technique described in the text above. The thermosanitation is using based on the diagnosis rate of infection structures for disposal of wood-destroying pests. These approaches are thermal sanitation (Fig. 1, Fig. 2), which consists in heating the related wooden structures by means of hot air (below 120°C).

ACKNOWLEDGMENT

The research described in the paper was financially supported by the project of the BUT Grant Agency FEKT-S-14-2545/2014, project from Education for Competitiveness Operative Programme CZ.1.07.2.3.00.20.0175 (Electro-researcher) and Thermosanace company Czech Republic. This paper also benefited from the use of the Insight Segmentation and Registration Toolkit (ITK), and pen source software developed as an initiative of the U.S. National Library of Medicine.

REFERENCES

1. Šmíra, P., A. Nasswettrová, J. Štěpánek, and J. Pařílková, "Sanace dřevěných konstrukcí horkým vzduchem," *Dřevostavby 2013, Sborník Přednášek z Odborného Semináře se Zahraniční Účastí 2013, VOŠ Volyně,* 75–84, 2013, ISBN 978-80-86837-51-2.
2. O'Halloran, M., M. Glavin, and E. Jones, "Channel-ranked beamformer for the early detection of breast cancer," *Progress In Electromagnetics Research*, Vol. 103, 153–168, 2010.
3. FOMEI: divize RTG, Mar. 8, 2012, Dostupnéz: http://radiodiagnostika.fomei.com/.
4. Friedl, M., M. Kubásek, P. Šmíra, P. Koňas, and P. Fiala, "X-ray diagnostics of wood invaded by insect," *Measurement 2013*, 303–306, Slovak Academy of Sciences, Bratislava, 2013, ISBN: 9788096967254.

5. Ibáñez, L., W. Schroeder, L. Ng, and J. Cates, "The ITK software guide — Second edition updated for ITK version 2.4," 804, Kitware, Inc., ISBN 1-930934-15-72005.
6. Koňas, P., M. Rybníček, and T. Kolář, "Statistical processing and usage of incomplete tree-ring series," *Proceedings of Abstracts of TRACE 2011*, 44, 2011.
7. Trcala, M. and P. Koňas, "Modelling of coupled moisture and heat transfer during wood drtiny," *Wood Research*, Vol. 57, No. 1, 2012, ISSN 1336-4561.
8. Mikulka, J., E. Gescheidtova, and K. Bartušek, "Evaluation of errors in manual image processing," *PIERS Proceedings*, 84–86, Suzhou, China, September 12–16, 2011.
9. Mikulka, J. and K. Bartušek, "3D reconstruction in magnetic resonance imaging," *PIERS Proceedings*, 1043–1046, Cambridge, USA, July 5–8, 2010.
10. Fiala, P., P. Koňas, M. Friedl, P. Šmíra, P. Dohnal, M. Hanzelka, and A. Nasswettrová, "Combined X-ray diagnostics of heterogeneous biological material," *PIERS Proceedings*, 61–65, Taipei, March 25–28, 2013.

A Novel Miniaturized Frequency Selective Surface with Stable Performances

Rui Wu, Hou Zhang, Zhiyong Xu, Zimu Yang, and Yongfan Lin
School of Air and Missile Defense, Air Force Engineering University, China

Abstract— A novel stable miniaturized band-reject frequency selective surface (FSS) is proposed in this paper. Compared to previous miniaturized structures, the dimension of the proposed FSS unit cell is only $0.050\lambda_0 \times 0.050\lambda_0$ where λ_0 represents the wavelength of the resonant frequency. And characteristics of the new structure are stable with respect to waves with different polarizations and incident angles. Simulation of structure with different parameters is also taken, and the results demonstrate the claimed performance and the possibility of better miniaturization by changing the parameters of the structure. Thus, the proposed structure is suitable for practical application in limited space.

1. INTRODUCTION

Frequency selective surfaces (FSS) which can be widely used as shielding, antenna reflectors, spatial filters, radomes and electromagnetic absorbers, are usually formed by two-dimensional array of metallic patterns printed on a dielectric substrate or etched out of a conductive layer [1]. The array is usually considered to be unlimited in dimension when it is analyzed and simulated. However, the dimension of array is usually limited in dimension in practical measurements and applications. So the enough minituration of FSS that can make the finite FSS perform the characteristics of the original infinite one is very meaningful [2].

Recently, different methods have been used to design the miniaturized FSSs which are much smaller than the wavelength of the resonant frequency. Substrate integrated waveguide (SIW) technology is used to realize a low frequency miniaturized dual-band FSS with close band spacing in [3]. Lumped reactive components can provide a new methodology for miniaturized FSS [4]. Furthermore, utilizing new structures in single-layer and multi-layer FSSs is still an important method for miniaturization of FSS such as the new structure proposed in [5].

In this letter, a new type of miniaturized FSS is proposed, which is composed of a pattern of Y-type metallic spiral strips and a dielectric substrate. Compared with traditional Y-type FSS, it has better miniaturation and better stability with respect to different polarizations and incident angles. The effects of varying the distances between strips, the widths of strips and the relative dielectric constant of the dielectric substrate are analyzed. The results demonstrate good performance of the proposed miniaturized FSS. Moreover, the miniaturization can be further improved by adjusting the parameters.

2. FSS STRUCTURE AND ITS PERFORMANCES

2.1. FSS Structure and Its Transmittances

The structure of the unit cell is presented in Fig. 1 and the FSS array is shown in Fig. 2. The spiral structure can increase the equivalent inductance and capacitance which means the resonant frequency will decrease. Parameters of the structure are defined as follows: length of the metal strips of the first rank $D = 3.7\,\text{mm}$ with the width $y = 0.2\,\text{mm}$, gap for the metal strips on the dielectric substrate $w = w_1 = w_2 = w_3 = w_4 = w_5 = w_6 = 0.2\,\text{mm}$ and $w_7 = 0.1\,\text{mm}$, gaps between each strip $g = 0.02\,\text{mm}$, dielectric substrate height $h = 1.6\,\text{mm}$, relative dielectric constant $\varepsilon_r = 2.65$ and loss tangent $\tan\delta = 0.025$.

It can be observed from the Fig. 3 that the transmission coefficients are almost same for perpendicularly incident waves of different polarization and the resonant frequency is 2.44 GHz. So the dimension of the equal area square unit is $0.050\lambda_0 \times 0.050\lambda_0$ where λ_0 represents the wavelength of the resonant frequency. The results also show the great stability of incident waves with different polarizations.

2.2. Angle Stability and Polarization Stability

Practical application of the FSS usually requires the stability of the FSS with respect to waves of different incident angles. Transmission results under different incident angles of both polarizations are simulated and results are shown in Fig. 4. It can be observed that there is no resonant frequency

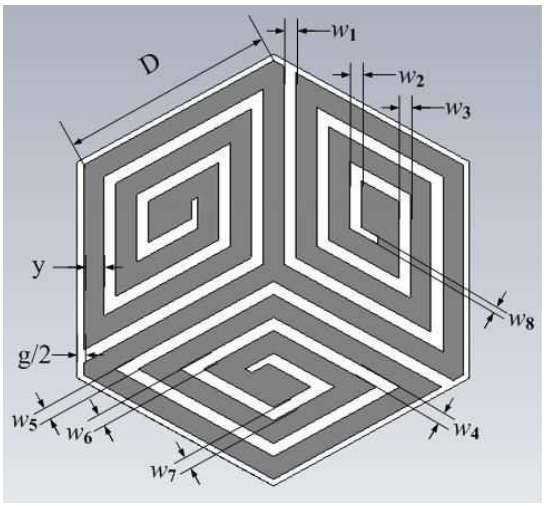

Figure 1: Structure of a unit cell.

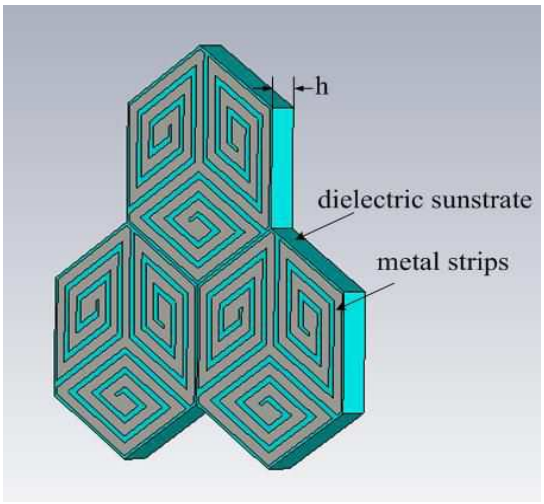

Figure 2: Structure of the FSS array.

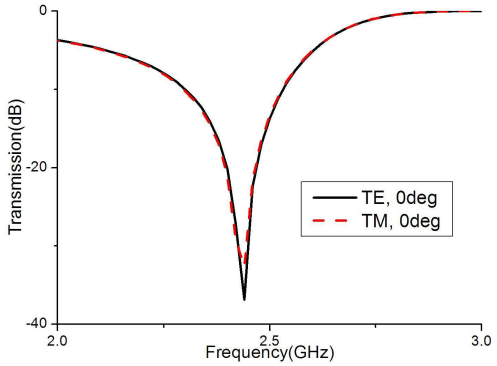

Figure 3: Transmission of the FSS for normal incident waves.

deviation when the incident angle is less than 60° for both polarizations. Therefore the proposed FSS performs excellent polarization and angle stability. It can be applied in the shielding wall to prohibit the transmission of the WiFi, BlueTooth and one of the WLAN band.

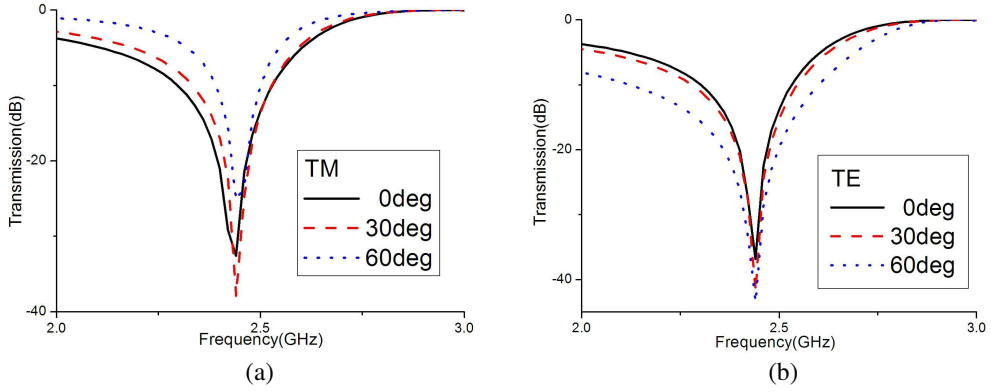

Figure 4: Transmission coefficients of the FSS of different incident angles. (a) *TE*-polarized. (b) *TM*-polarized.

2.3. Effects of Parameters

1) Width of strips: Transmission coefficients of different widths of metal strips are presented in Fig. 5(a). It can be observed that the resonant frequency varies significantly due to the change of metal strips width value. In this paper, y is taken as 0.3 mm to satisfy the requirement for the

bandwidth.

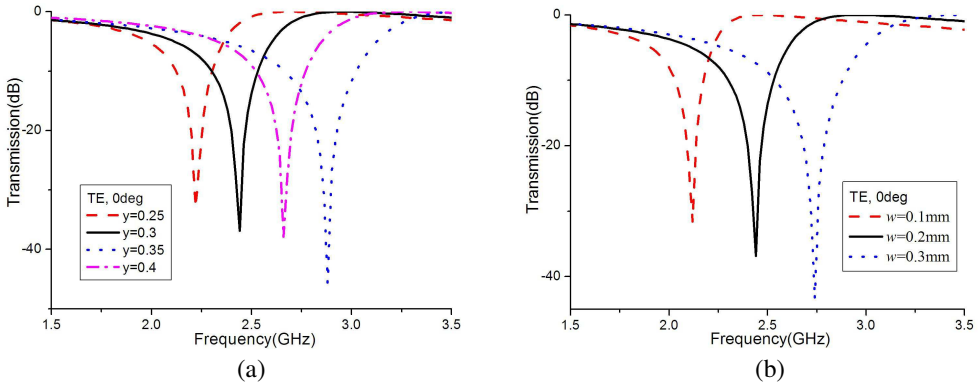

Figure 5: Transmission coefficients of the FSSs with different parameters for normal TE-polarized waves. (a) Widths of strips for normal TE-polarized waves. (b) Distances between strips.

2) Distance between strips: Distance between strips can not only affect equivalent capacitance of a unit cell but also affect equivalent inductance by changing the total length of the strips while other conditions are fixed. Simulations for the proposed structures with different distances between strips are done and the results are presented in Fig. 5(b). It can be seen that with the decrease of distance between strips, values of the resonant frequency decrease significantly. However, as the distance gets smaller the bandwidth also gets smaller. So, when it is utilized in a practical situation, the distance between strips should be controlled so that requirements of both miniaturization and bandwidth can be satisfied.

3) Relative dielectric constant: The dielectric substrate can help improve the miniaturization performance. Resonance of stop-band shifts to lower frequency with the increase of the relative dielectric constant. So the structure proposed in this paper can be further miniaturized. However, it can also be seen in the Fig. 6 that the insertion loss will also raise due to the increase of the

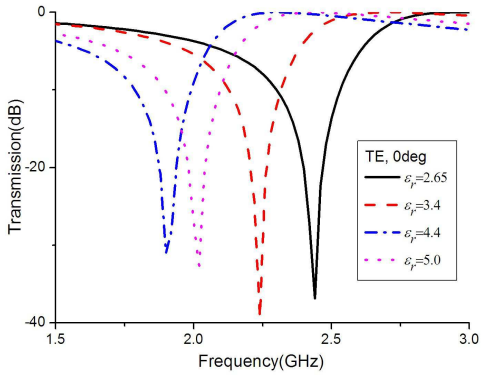

Figure 6: Transmission coefficients of the FSSs of different material permittivity.

Table 1: Results of comparison to other FSSs.

ε_r	FSS structure	Unit cell size
2.65	structure in [5]	$0.077\lambda_0 \times 0.077\lambda_0$
	structure proposed	$0.050\lambda_0 \times 0.050\lambda_0$
3.4	structure in [6]	$0.086\lambda_0 \times 0.086\lambda_0$
	structure proposed	$0.046\lambda_0 \times 0.046\lambda_0$
4.4	structure in [7]	$0.063\lambda_0 \times 0.063\lambda_0$
	structure proposed	$0.041\lambda_0 \times 0.041\lambda_0$
5	structure in [8]	$0.088\lambda_0 \times 0.088\lambda_0$
	structure proposed	$0.039\lambda_0 \times 0.039\lambda_0$

relative dielectric constant.

To prove the excellent miniaturization of the proposed structure, comparison of different structures proposed in previous papers is carried out and the results are presented in Table 1. From the Table 1, it can be observed that the proposed FSS exhibits better miniaturization characteristic.

3. CONCLUSION

A novel miniaturized band-reject FSS is proposed in this paper. This novel miniaturized structure not only shows the great miniaturization with the dimension of the unit cell which is only $0.050\lambda_0 \times 0.050\lambda_0$, but also presents excellent stability with respect to different polarizations and incident angles. It can prohibit the transmission of the WiFi, BlueTooth and one of the WLAN band. Moreover, effects of varying width and length of strips, distance between strips and the relative dielectric constant of the dielectric substrate are analyzed. The results prove great characteristics of the structure. Thus, the proposed FSS is suitable for piratical applications, especially in limited space.

REFERENCES

1. Wu, T. K., *Frequency Selective Surface and Grid Array*, Wiley, New York, 1995.
2. Munk, B. A., *Frequency Selective Surfaces: Theory and Design*, Wiley, New York, 2000.
3. Xu, R.-R., Z.-Y. Zong, and W. Wu, "Low-frequency miniaturized dual-band frequency selective surfaces with close band spacing," *Microw. Opt. Technol. Lett.*, Vol. 51, No. 5, 1238–1240, May 2009.
4. Liu, H. L., K. L. Ford, and R. J. Langley, "Design methodology for a miniaturized frequency selective surface using lumped reactive components," *IEEE Trans. Antennas Propag.*, Vol. 57, No. 9, 2732–2738, Sep. 2009.
5. Yang, G.-H., T. Zhang, W.-I. Li, and Q. Wu, "A novel stable miniaturized frequency selective surface," *IEEE Antennas Wireless Propagation Letters*, Vol. 9, 1018–1021, 2010.
6. Hu, X.-D., X.-L. Zhou, L.-S. Wu, L. Zhou, and W.-Y. Yin, "A miniaturized dual-band frequency selective surface (FSS) with closed loop and its complementary pattern," *IEEE Antennas Wireless Propagation Letters*, Vol. 18, 1374–1377, 2009.
7. Chiu, C.-N. and K.-P. Chang, "A novel miniaturized-element frequency selective surface having a stable resonance," *IEEE Antennas Wireless Propagation Letters*, Vol. 8, 1175–1177, 2009.
8. Xu, Z.-Y., H. Zhang, X. Yin, and Y.-T. Jiang, "The design of a novel miniaturized frequency selective surface," *Nation Conference of Antanna*, 2013.
9. Yang, H.-Y., S.-X. Gong, P.-F. Zhang, F. -T. Zha, and J. Ling, "A novel miniaturized frequency selective surface with excellent center frequency stability," *Microwave Optical Technology Letters*, Vol. 51, 2513–2516, 2009.

Metamaterials-based High-gain Antenna with Wide Viewing Angle

Yang Cao[1, 2] and Xiaobing Wang[1, 2]

[1]Shanghai Radio Equipment Institute, Shanghai 200090, China
[2]Shanghai Key Laboratory of Electromagnetic Environmental Effects for Aerospace Vehicle
Shanghai 200090, China

Abstract— Metamaterials (MMs) refer to a class of artificially engineered structures comprised of electric/magnetic resonant building blocks much smaller than the operating wavelength. The extraordinary electromagnetic responses of MMs, not available for naturally occurring materials, have attracted intensive investigations on the underlying physics as well as related applications. In recent years, MMs-based antennas are widely studied and proved to have great potential in improving the radiation performance. In this paper, a MMs-based Febry-Perot cavity antenna with wide viewing angle is proposed about 14 GHz. The antenna consists of a high-impedance surface which works as an artificial magnetic conductor (AMC) at resonance frequency and a partially reflective surface (PRS). The AMC loading contributes to the low-profile and high-gain property of the antenna, as the AMC ground plane gives a near-zero phase shift in contrast to conventional metal sheet ground plane. The lateral size of the antenna is only about $3\lambda \times 0.6\lambda$; and the thickness is about $\lambda/5$. Metal walls surrounding the limited aperture are introduced to prevent the leakage of cavity mode and improve the radiation pattern, which also protects the antenna from external electromagnetic environment. The MMs-based high-gain antenna has a broad beam width in H-plane, which may be applied in ETC and RFID system.

1. INTRODUCTION

Metamaterials (MMs) [1, 2], a class of man-made materials constructed with artificial electromagnetic atoms/molecules, exhibit many nontrivial properties and novel functionalities, including negative refraction [3], subwavelength imaging [4], invisible cloaking [5–7], etc.. In recent years, MMs are proved to have great potential in antenna applications. They are utilized for antenna miniaturization [8, 9], side-lobe suppression [10], as well as achieving low-profile and high-gain antennas [11–15]. In 1999, D. F. Sievenpiper et al. proposed a subwavelength metal-dielectric-metal structure which can provide zero reflection phase shift at resonance frequencies [16]. It does not change phase of the electric field, but reverses that of the magnetic field, which works as a magnetic mirror and is usually referred to as artificial magnetic conductor (AMC) [17]. AMC loading in a Febry-Perot (F-P) cavity antenna helps significantly reduce the thickness of the antenna while maintaining high directivity [18, 19]. The cavity thickness can be reduced to $\lambda/60$ or even thinner [20].

In this paper, we focus on the design of a F-P cavity antenna with wide viewing angle. The maximum realized gain is 10.9 dB at 14.1 GHz in simulation. And it has a broad beam width of 76° in H-plane for spatial coverage, which may be applied in ETC and RFID system. The proposed antenna is fabricated with printed circuit board (PCB) technique and measured in the microwave chamber. The experimental results are in well agreement with simulations.

2. STRUCTURE DESIGN AND SIMULATIONS

The proposed antenna is schematically shown in Fig. 1. It is comprised of an AMC sheet and a partially reflective surface (PRS), and is fully filled with dielectric substrate. The feeding dipole antenna is centered in the cavity with a length of 18 mm. The AMC sheet has a thickness of $h_1 = 1.6$ mm. Its upper surface is presented in Fig. 1(b). The square patch array has a period of $p = 3.5$ mm and a width of $a = 2.9$ mm. The PRS as shown in Fig. 1(c) shares the same period with the patch array. The wire width is $w = 0.2$ mm. The cavity has a thickness of $h_2 = 3.2$ mm, giving rise to a whole antenna thickness of $h_1 + h_2 = 4.8$ mm, about $\lambda/5$ at 14.1 GHz. The substrate has a dielectric constant of $\varepsilon_r = 2.2$ with a loss tangent of $\tan\delta = 0.0009$. The antenna has 20 periods in x-direction and 4 periods in y-direction, giving rise to a lateral size of 70 mm × 14 mm, about $3\lambda \times 0.6\lambda$. The antenna is surrounded by four metal sheets to suppress mode leakage and improve the directivity of the radiation pattern. As the antenna has a relatively small aperture and strong field concentration, the metal walls also protect the cavity mode from external electromagnetic environment.

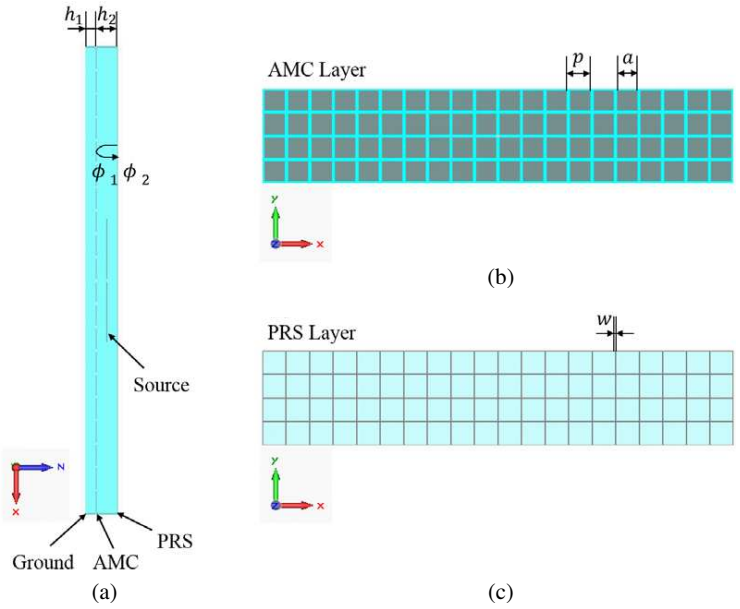

Figure 1: (a) Schematic of the proposed antenna. (b) The AMC layer. (c) The PRS layer.

The cavity mode is excited when the resonant condition is satisfied,

$$-4\pi f n h_2/c_0 + \phi_1 + \phi_2 = 2m\pi \quad (m = 0, \pm 1, \pm 2, \ldots),$$

where f is the operating frequency, c_0 is the light velocity in vacuum, n is the refractive index of the dielectric filling the cavity, h_2 is the cavity thickness [see Fig. 1(a)]. While the PRS gives a phase shift of $\phi_2 \approx \pi$ as metals and high-index dielectric surfaces with $n > 1$, the AMC sheet can provide a phase shift of ϕ_1 which changes from π to $-\pi$ and crosses through zero at the resonance frequency. This property of AMC facilitates the reduction in cavity thickness.

We perform FDTD simulations to determine the property of the antenna system. The cavity mode is excited around 14 GHz, exhibiting high directivity. Fig. 2 presents the radiation pattern in E-plane and H-plane at 14.1 GHz where the realized gain reaches a maximum of 10.9 dB. It can be seen that the proposed antenna has a narrow beam width of 14° in E-plane, while the beam width in H-plane is broad (about 76°), forming a fan-like radiation pattern.

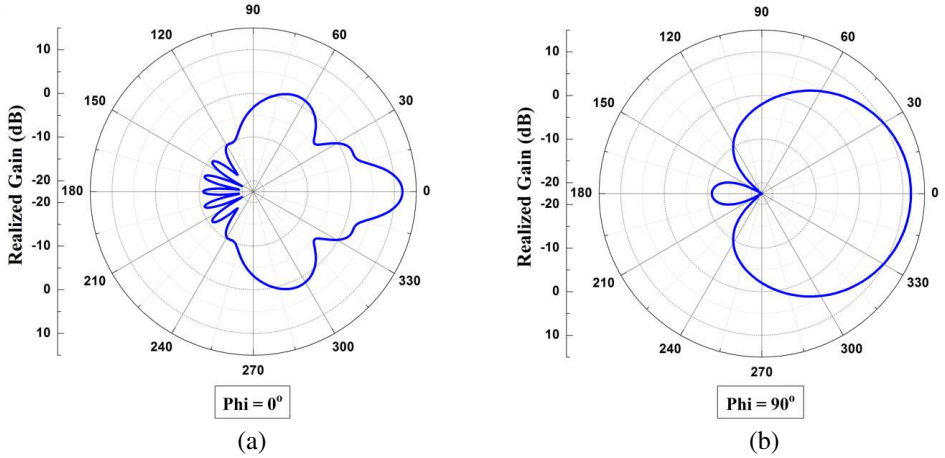

Figure 2: Numerically calculated gain of the antenna in (a) E-plane and (b) H-plane.

3. MEASUREMENTS AND RESULTS

The antenna is fabricated by three pieces of 1.575-mm thick Taconic TLY-5 substrate. A mesh array is etched onto the first layer, working as the PRS. The second layer is an additional dielectric spacer. And the third layer forms the AMC sheet, with a square patch array etched on one side and a ground plane on the other side. Then the three PCBs are assembled in order. Fig. 3 shows the photos of the antenna before and after assembling. The dipole source is fixed between the first and the second layer and fed by a 50 Ω coaxial cable. The whole antenna is surrounded by electro-conductive films as modeled in the simulation.

Measurements of the fabricated antenna are taken in the microwave chamber with a directive horn antennas working at 12.4–18 GHz with a gain factor of 24 dB. The antenna is positioned on a rotary table in the chamber. The rotary table, driven by a computer, provides a finest angular resolution of 0.1°. The far-field pattern is normalized to the gain of standard horn antenna. Fig. 4 shows the radiation pattern in E-plane and H-plane at 14.5 GHz. The half-power bandwidths are

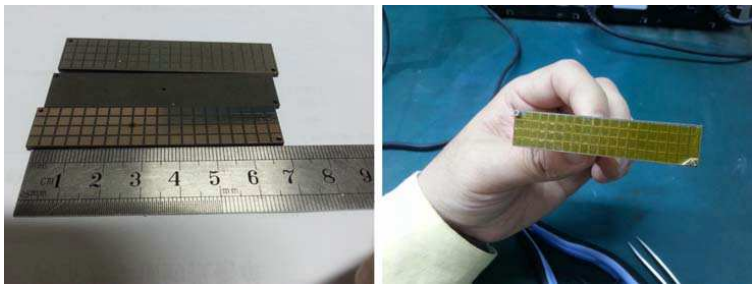

Figure 3: Photos of the fabricated antenna.

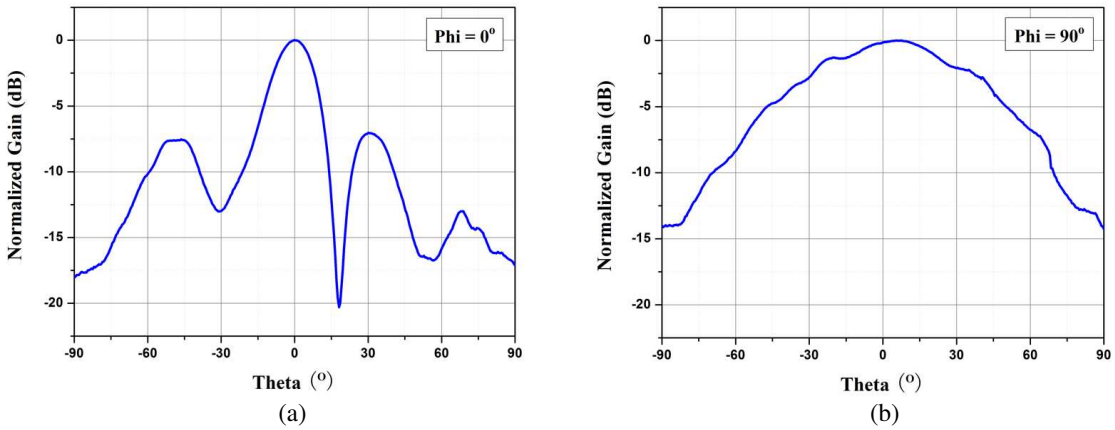

Figure 4: Measured radiation pattern in (a) E-plane and (b) H-plane.

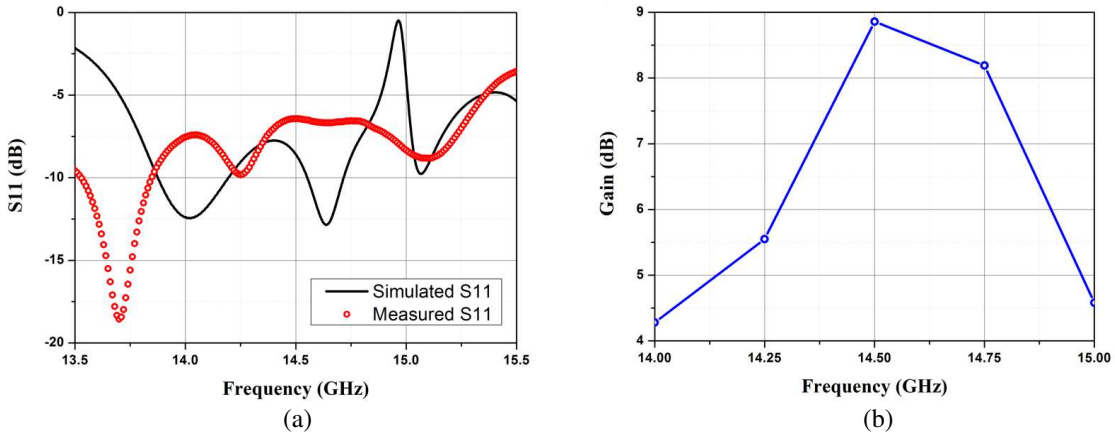

Figure 5: (a) Simulated and measured return loss S_{11}. (b) Measured gain of the antenna.

18° in E-plane and 73° in H-plane, which are in good agreement with the simulation as shown in Fig. 3. Fig. 5(a) presents the simulated and measured return loss S_{11} as a function of frequency. It shows that the return loss is below −6 dB at the working frequency 14.5 GHz, which implies that the cavity mode is well matched to the dipole excitation. The measured gain of the antenna is plotted in Fig. 5(b). It can be seen that there is a peak of 8.9 dB near 14.5 GHz, which indicates the existence of a resonance mode.

4. CONCLUSION

A metamaterials-based high-gain antenna with wide viewing angle is modeled and fabricated. The antenna working around 14 GHz has a overall volume of 70 mm × 14 mm × 4.8 mm. It has a narrow beam width in E-plane, while the beam width in H-plane is broad, forming a fan-like radiation pattern. It is a compact and low-profile design, which has great potential in related applications.

REFERENCES

1. Engheta, N. and R. W. Ziolkowski, *Metamaterials: Physics and Engineering Explorations*, Wiley & Sons, 2006.
2. Cai, W. and V. M. Shalaev, *Optical Metamaterials: Fundamentals and Applications*, Springer, New York, 2009.
3. Shelby, R. A., D. R. Smith, and S. Schultz, "Experimental verification of a negative index of refraction," *Science*, Vol. 292, 77, 2001.
4. Pendry, J. B., "Negative refraction makes a perfect lens," *Phys. Rev. Lett.*, Vol. 85, 3966, 2000.
5. Leonhardt, U., "Optical conformal mapping," *Science*, Vol. 312, 1777, 2006.
6. Pendry, J. B., D. Schurig, and D. R. Smith, "Controlling electromagnetic fields," *Science*, Vol. 312, 1780, 2006.
7. Lai, Y., J. Ng, H. Y. Chen, et al., "Illusion optics: The optical transformation of an object into another object," *Phys. Rev. Lett.*, Vol. 102, 253902, 2009.
8. Yuandan, D., H. Toyao, and T. Itoh, "Compact circularly-polarized patch antenna loaded with metamaterial structures," *IEEE Transactions on Antennas and Propagation*, Vol. 59, 2011.
9. Ouedraogo, R. O., E. J. Rothwell, A. R. Diaz, et al., "Miniaturization of patch antennas using a metamaterial-inspired technique," *IEEE Transactions on Antennas and Propagation*, Vol. 60, 2012.
10. Fan, Y. and Y. Rahmat-Samii, "Reflection phase characterizations of the EBG ground plane for low profile wire antenna applications," *IEEE Transactions on Antennas and Propagation*, Vol. 51, 2003.
11. Feresidis, A. P. and J. C. Vardaxoglou, "High gain planar antenna using optimised partially reflective surfaces," *IEE Proc. — Microwaves Antennas Propag.*, Vol. 148, 2001.
12. Akalin, T., J. Danglot, O. Vanbesien, et al., "A highly directive dipole antenna embedded in a Fabry-Perot type cavity," *IEEE Microw. Wirel. Co.*, Vol. 12, 2002.
13. Feresidis, A. P., G. Goussetis, W. Shenhong, et al., "Artificial magnetic conductor surfaces and their application to low-profile high-gain planar antennas," *IEEE Transactions on Antennas and Propagation*, Vol. 53, 2005.
14. Kuo, H., F. Jiahui, W. Qun, et al., "The design and simulation of a metamaterial and sub-wavelength cavity-based antenna," *Cross Strait Quad-Regional Radio Science and Wireless Technology Conference (CSQRWC)*, 545–548, 2011.
15. Chen, Z.-N., S. Yong, Nasimuddin, et al., "Metamaterials-based high-gain planar antennas (invited paper)," *International Conference on Microwave and Millimeter Wave Technology (ICMMT)*, 1–4, 2012.
16. Sievenpiper, D., L. J. Zhang, R. F. J. Broas, et al., "High-impedance electromagnetic surfaces with a forbidden frequency band," *IEEE Trans. Microw. Theory*, Vol. 47, 1999.
17. Fedotov, V. A., A. V. Rogacheva, N. I. Zheludev, et al., "Mirror that does not change the phase of reflected waves," *Appl. Phys. Lett.*, Vol. 88, 2006.
18. Zhou, L., H. Q. Li, Y. Q. Qin, et al., "Directive emissions from subwavelength metamaterial-based cavities," *Appl. Phys. Lett.*, Vol. 86, 2005.
19. Li, H. Q., J. M. Hao, L. Zhou, et al., "All-dimensional subwavelength cavities made with metamaterials," *Appl. Phys. Lett.*, Vol. 89, 2006.
20. Ourir, A., A. De Lustrac, and J. M. Lourtioz, "All-metamaterial-based subwavelength cavities lambda/60 for ultrathin directive antennas," *Appl. Phys. Lett.*, Vol. 88, 2006.

Design of 90°-switched-line Phase Shifter with Constant Phase Shift Using CRLH TL

Jun Zhang[1] and S. W. Cheung[2]

[1]Tongyu Communication Inc., Zhongshan, Guangdong, China
[2]Department of Electrical and Electronic Engineering, The University of Hong Kong, Hong Kong, China

Abstract— The design of a 90°-switched-line phase shifter using composite right/left handed transmission line (CRLH TL) is presented in this paper. To achieve a relatively constant phase shift over a large bandwidth, a CRLH TL implemented using lumped elements and a right-handed transmission line (RH TL) are used as the reference and delay arms, respectively, of the phase shifter. Computer simulation is used to study and design the phase shifter. The phase shifter is also fabricated and measured to verify the simulation results. For comparison, a conventional 90°-switched-line phase shifter is also designed and simulated. Simulation and measurement results show that, the proposed phase shifter has a constant phase shift, a high return loss and a low insertion loss across the operating frequency band.

1. INTRODUCTION

Phase shifter is an essential component in the designs of in the radar and phased array systems. Insertion loss, operating bandwidth and constant phase shift within the bandwidth are the major concerns in the design of phase shifters. In a switched-line phase shifter, the phase shift is usually obtained by switching between two transmission lines (TL) of different lengths [1]. To achieve a wide operating bandwidth, the characteristic impedances of the two arms should be designed to match the port impedance in both states. Moreover, the slopes of the phase response versus frequency of the two TLs must be the same. However, this is very difficult to achieve, so it is difficult to have a constant phase shift within the operating frequency band.

The concept of metamaterials, commonely known as left-handed materials (LHMs), was first investigated by Veselago in 1968 [2]. LHMs have negative permittivity and permeability which are not commonly found in nature. Although the properties of LMHs promised for a large diversity of novel applications and devices, LMHs did not attract much attention until it was found that the materials could be realized using a general TL approach [3]. Practical left-handed TL (LH TL) also have the right-handed effects, so LHMs realized using TL are called composite right/left handed transmission line (CRLH TL). CRLH TL can be used to design many different microwave components such as phase shifters, delay lines and bandpass filters, etc..

In this paper, we propose to use CRLH TL to design an 90°-switched-line phase shifter with constant phase shift. The constant phase shift is achieved using CRLH TL as the reference arm and a RH TL as the delay arm. The CRLH TL is implemented using lumped elements. For comparison, a conventional 90°-switched-line phase shifter is also designed and simulated. Simulation and measurement results show that our proposed phase shifter can provide a relatively constant phase shift within the operating bandwidth compared with the conventional switched-line phase shifter.

2. THEORY

A conventional transmission lines (TL), in which the phase and group velocity are codirectional, has a positive phase constant β and is referred as a right-hand transmission line (RH TL). The phase response $\mathrm{Ang}(S_{21})$ of a RH TL is negative and linearly relating to frequency. The slope of the phase response versus frequency varies the length of the TL. A CRLH TL has a negative phase constant β and a positive phase response $\mathrm{Ang}(S_{21})$ in the LH region of the dispersion diagram [4]. The phase response $\mathrm{Ang}(S_{21})$ is not linearly relating to frequency, so the slope of the response versus frequency is not constant but varying with frequency. Thus it is possible to design a RH TL and a CRLH TL to have their phase responses quite parallel to each other across the operating bandwidth.

In a switched-line phase shifter, the difference of phase responses in the arms is the phase shift.

$$\theta = (\mathrm{Ang}(S_{21}))_{\text{reference arm}} - (\mathrm{Ang}(S_{21}))_{\text{delay arm}}$$

Thus if the RH TL and CRLH TL are used in the two arms of a switched-line phase shifter, the phase shift could be constant. This idea is used in the design of a 90°-phase shifter in this paper.

In the design, we select the parameters of the CRLH TL and the length of the RH TL to satisfy as much as possible the following two criterions:

1) the phase responses of the RH TL and CRLH TL are in parallel, and
2) the difference of the phase responses at the operating band is 90°.

3. DESIGN OF PHASE SHIFTER

The design of our proposed 90°-switched-line phase shifter is shown in Fig. 1(a). Two singlepole doublethrow (SPDT) switches are used at the input and output of the phase shifter. A CRLH TL implemented using lumped elements is used as the reference arm and a meander RH TL is used as the delay arm of the phase shifter. The SPDT switches are from SKYWORKS Co. Ltd. Each of the SPDT switches has 2 inputs, V_1 and V_2, which are used to select either the reference arm or delay arm. The reference arm can be selected by setting $V_1 = 0\,\mathrm{V}$ and $V_2 = 4\,\mathrm{V}$, while the delay arm can be selected by setting $V_1 = 4\,\mathrm{V}$ and $V_2 = 0\,\mathrm{V}$. The capacitors are from SAMSUNG Co. Ltd. and the inductors are from MURATA Co. Ltd. The phase shifter has an overall area of $40 \times 12.2\,\mathrm{mm}^2$. The CRLH TL and the meander RH TL together are designed manually using computer simulation to achieve a constant phase shift of 90°. The values in the final design are $C_1 = 10\,\mathrm{pF}$, $C_2 = 5\,\mathrm{pF}$ and $L = 12.1\,\mathrm{nH}$. For comparison, a conventional 90°-switched-line phase shifter using RH TLs for both the reference arm and delay arm as shown in Fig. 1(b) is also designed. A Rogers RO4350B substrate with a relative dielectric constant of 3.48, thickness of 0.762 and a loss tangent of 0.003 is used as the substrate in the designs of the two phase shifters. Fig. 2 shows the proposed prototyped 90°-switched-line phase shifter.

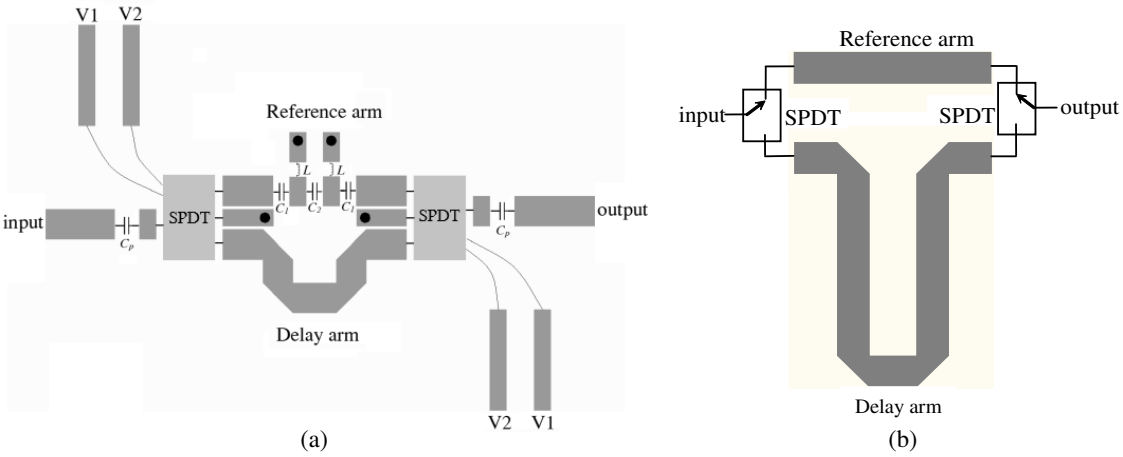

Figure 1: Layouts of (a) proposed and (b) conventional 90°-switched-line phase shifters.

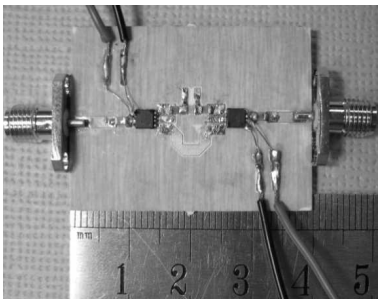

Figure 2: Proposed prototyped 90°-switched-line phase shifter.

4. RESULTS AND DISCUSSIONS

Computer simulation and measurements have been carried out to study the performances of the 90°-switched-line phase shifters. The simulated and measured return losses (RLs), insertion losses (Ils), phase responses and phase shifts are shown in Fig. 3, which show good agreements.

The measured results in Fig. 3(a) show that, with the reference arm switched on, the phase shifter has a operating bandwidth of 0.58–2.7 GHz with RL > 10 dB and IL < 2 dB. When the delay arm is switched on, Fig. 3(b) shows that the phase shifter has a bandwidth of 0.3–2.7 GHz with RL > 20 dB and IL < 2 dB. The differences between the simulated and measured ILs when the

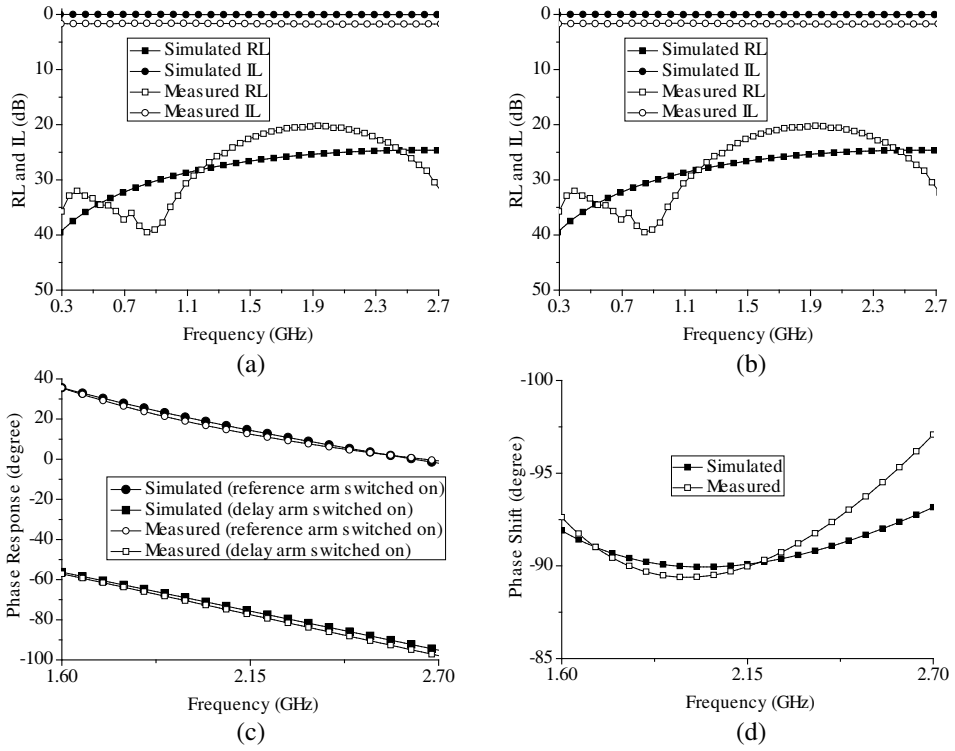

Figure 3: Simulated and measured (a) RLs and ILs with reference arm switched on, (b) RLs and ILs with delay arm switched on, (c) phase responses, and (d) phase shifts of proposed phase shifter.

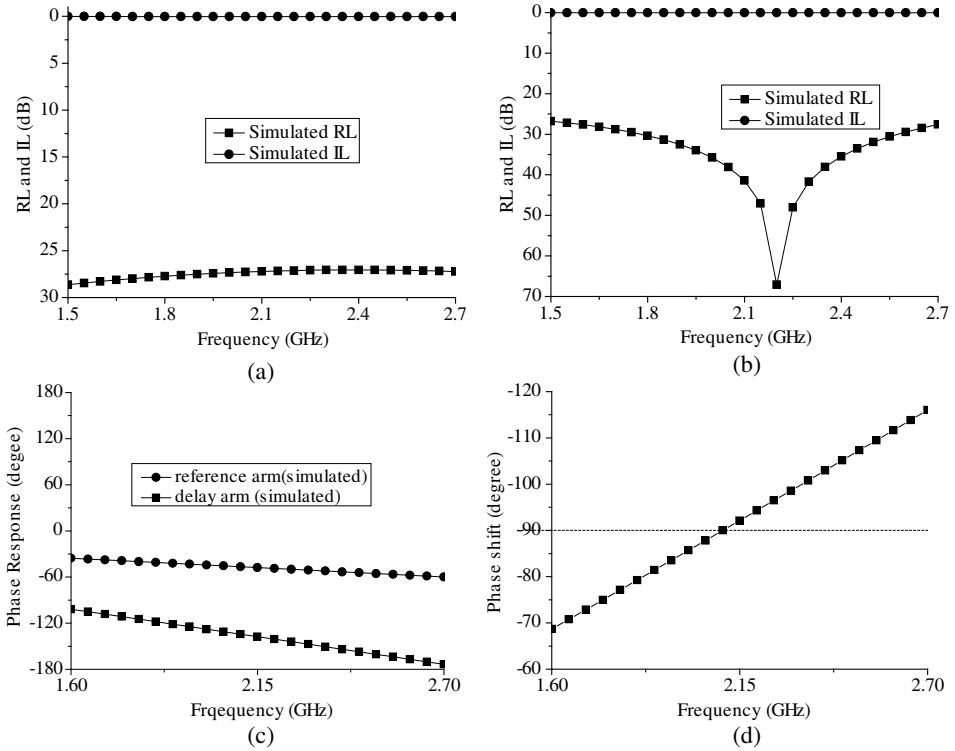

Figure 4: Simulated (a) RL and IL with reference arm switched on, (b) RL and IL with delay arm switched on, (c) phase response, and (d) phase shift of the conventional phase shifter.

reference arm or delay arm is switched on are about 1.6 dB as can be seen in Figs. 3(a) and 3(b). These differences are caused by the IL of the two SPDT switches used in the designs. Fig. 3(c) shows that the simulated and measured phase responses when the reference arm or delay arm is switched on are quite in parallel. Fig. 3(d) shows that the measured phase shift is about $-90°$ with a variation range of $-7°$ to $+0.6°$ in the bandwidth of 1.6–2.7 GHz.

For comparison, the simulated RL, IL, phase response and phase shift of the conventional 90°-switched-line phase shifter in Fig. 1(b) are shown in Fig. 4. Figs. 4(a) and 4(b) show that when the reference arm or delay arm is switched on, good impendence matching in the frequency band of 1.5–2.7 GHz with RL $>$ 20 dB and IL $<$ 1 dB can be achieved. However, the simulated phase responses when the reference arm or delay arm is switched on are not in parallel as shown in Fig. 4(c). The phase shift in the bandwidth of 1.6–2.7 GHz shown in Fig. 4(d) is $-90°$, indicating a large variation range of $-21.3°$ to $+26°$.

5. CONCLUSION

In this paper, a 90°-switched-line phase shifter with constant phase shift using CRLH TL has been designed, fabricated and measured. Results have shown that the proposed phase shifter can provide quite a constant phase shift of $-90°$ with a small variation range of $-7°$ to $+0.6°$. It has a wide operating bandwidth of 1.6–2.7 GHz, a high return loss of more than 10 dB, and a low insertion loss of less than 2 dB.

REFERENCES

1. Keul, S. and B. Bhat, *Microwave and Millimeter Wave Phase Shifters*, Artech house, MA, 1991.
2. Veselago, "The electrodynamics of substances with simultaneously negative values of ε and μ," *Soviet Physics Uspekhi*, Vol. 10, 509–514, 1968.
3. Lai, A., T. Itoh, and C. Caloz, "Composite right/left-handed transmission line metamaterials," *IEEE Microwave Magazine*, Vol. 5, 34–50, Sep. 2004.
4. Zhang, J., "Designs of true-time-delay lines and digital phase shifters using composite right/left-handed transmission lines," S. W. Cheung and T. I. Yuk, The University of Hong Kong, Feb. 2013.

Design of Oscillator Using Zeroth-order Resonator Based on Composite Right/left-handed Transmission Line

Juanjuan Gao and Guizhen Lu
Communication University of China, China

Abstract— The application of novel zeroth-order resonator in RF circuit is investigated in this paper. The zeroth-order resonator is composed by composite right/left handed transmission lines, full-wave simulations with 1-cell and 4-cell resonators are carried out, respectively. Microwave oscillators used zeroth-order resonators, which performed as tuning network, are proposed. The zeroth-order resonators in oscillators determine the frequency. The simulation frequencies of oscillators are 10.5 GHz of 1-cell resonator and 10.1 GHz of 4-cell resonator, respectively.

1. INTRODUCTION

The composite right/left-handed (CRLH) transmission line (TL) is the practical implementation of left-handed metamaterials based on transmission line theory [1]. The CRLH TL structure is composed of unit cells with a series capacitance C_L and a shunt inductance L_L as well as a series inductance L_R and a shunt capacitance C_R. A typical microwave CRLH TL constituted by interdigital capacitors and stub inductors shorted to the ground plane by a via, which was first introduced by Caloz and subsequently used in various applications [2]. In this structure interdigital capacitors and stub inductors provide C_L and L_L, performing left-handed (LH) nature as dominant mode, whereas the parasitic reactances (parasitic capacitance is due to development of voltage gradients, and parasitic inductance is due to current flow along the metallization) provide C_R and L_R performing right-handed (RH) nature at higher frequencies.

Transmission-line resonators, usually open or short circuited, have been developed and practically used in microwave and millimeter-wave circuits. Generally, the resonant frequencies of transmission-line resonators are determined by the length of the lines. Because of the unique feature of CRLH metamaterials that a β of zero can be achieved, zeroth-order resonators have been proposed and developed. Zeroth-order resonator has the advantage that resonant frequency is not related to the physical length of the TL, therefore it can be realized, theoretically, arbitrarily small [3, 4]. Zeroth-order resonators can be exited in open- and short-ended case, as well as variable reactance loads at both ends [5]. By changing load impedance at the terminals the resonant condition of the zeroth-order resonator can be controlled. Researches on zeroth-order resonator are popular in recent years; however the applications in RF circuit, such as oscillator, are not very much.

In this paper, zeroth-order resonators with one terminal open-ended and the other terminal capacitive are developed. Full-wave simulations of resonators, $N = 1$ and $N = 4$, (N is the number of the unit cells in resonator.) are carried out. In addition, oscillators using these resonators as tuning network are proposed.

2. THEORY

AS shown in Fig. 1(a), the unit of a typical equivalent-circuit model for transmission-line resonator based on CRLH TLs is composed of a series branch and a shunt branch. Figs. 1(b) and (c) show the T-type and Π-type unit cell, respectively.

In the open-ended case, shunt resonance in shunt branch is dominant. The shunt admittance is given by

$$Y_{sh} = j\omega C_R + \frac{1}{j\omega L_L} = j\omega C_R \left\{1 - \left(\frac{\omega_{sh}}{\omega}\right)^2\right\} \tag{1}$$

where $\omega_{sh} = 1/\sqrt{L_L C_R}$, which is the shunt frequency. In contrast, in the short-ended case, series resonance in series branch is dominant, The series impedance is given by

$$Z_{sh} = j\omega L_R + \frac{1}{j\omega C_L} = j\omega L_R \left\{1 - \left(\frac{\omega_{se}}{\omega}\right)^2\right\} \tag{2}$$

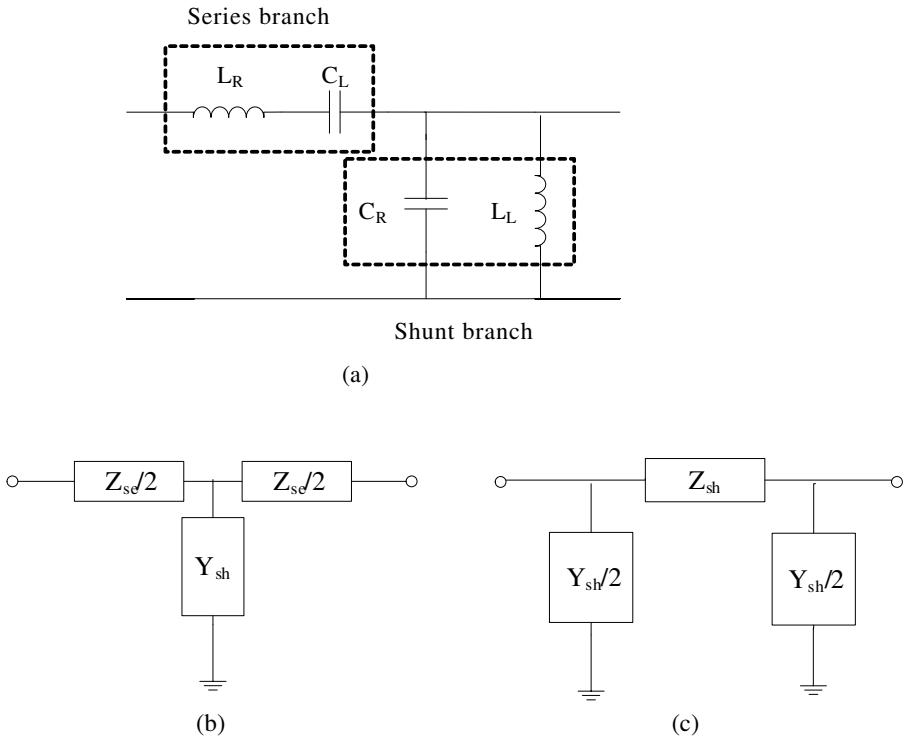

Figure 1: (a) Unit fell of equivalent circuit model. (b) T-type unit cell. (c) Π-type unit cell.

where $\omega_{se} = 1/\sqrt{L_R C_L}$, which is the series resonant frequency. In the particular case of balanced resonances, when $\omega_0^{balanced} = \omega_{se} = \omega_{sh}$, the zeroth-order resonance occurs for both the open-ended and short-ended resonators.

Resonators used in two ports oscillators perform as tuning network, which determine the frequencies of oscillators, shown in Fig. 2. In order to act in oscillator, resonator should obtain good frequency selectivity in oscillator frequency, phase condition also should be satisfied. The phase relation holds:

$$\Delta\varphi = 2m\pi \tag{3}$$

with $m = 0, \pm 1, \ldots, \pm\infty$. CRLH TLs and terminals of zeroth-order oscillator both contribute to $\Delta\varphi$.

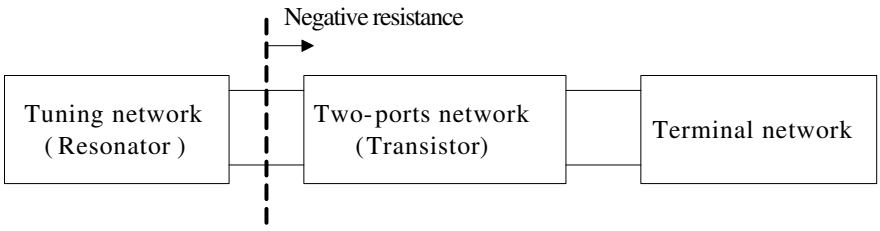

Figure 2: Two ports oscillator circuit.

3. DESIGN AND SIMULATION

The geometries of the designed resonators are shown in Figs. 3(a) and (b), which are 1-cell resonator and 4-cell resonator, respectively. The resonators are constituted by interdigital capacitors, stub inductors and a transmission line, and the transmission line is used to satisfy the phase relation. Parameter extraction was based on the resonators of Fig. 3 with $l_{tl} = 5\,\text{mm}$, $w_{tl} = 1.1\,\text{mm}$, $l_c = 0.8\,\text{mm}$, $l_s = 3\,\text{mm}$, $w_s = 0.5\,\text{mm}$. The number of electrode pairs is 3, and the width of the electrode and the gap between the electrodes are 0.2 mm and 0.15 mm, respectively. The thickness and dielectric constant of the dielectric substrate are 0.51 mm and 3.66.

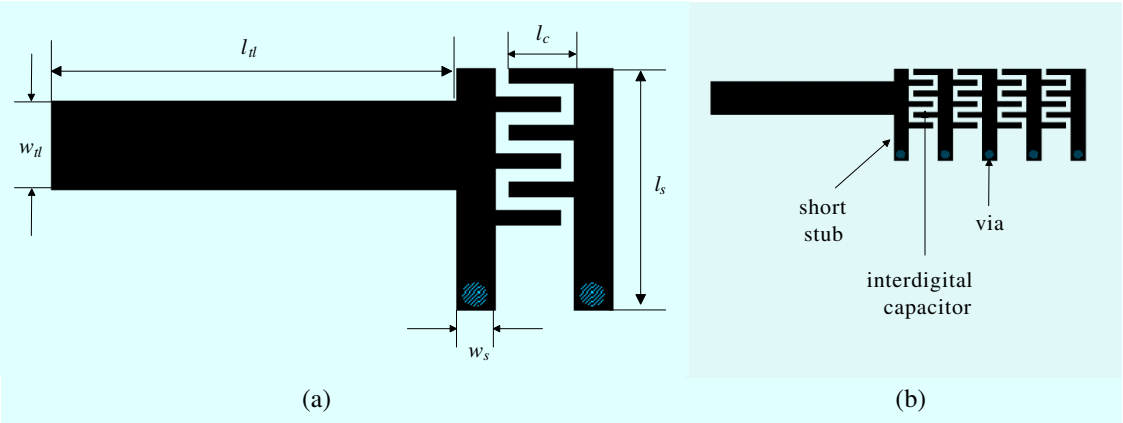

Figure 3: Geometry of zeroth-order resonator. (a) 1-cell resonator. (b) 4-cell resonator.

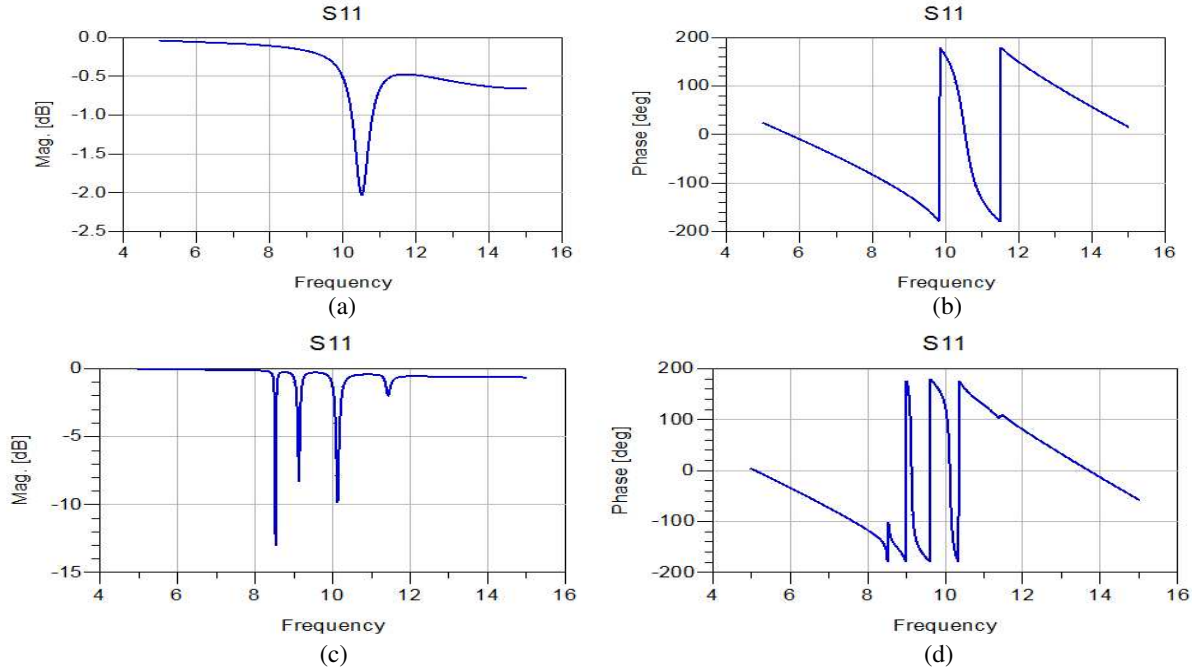

Figure 4: Simulation results of resonator. (a) S_{11} magnitude of 1-cell resonator. (b) S_{11} phase of 1-cell resonator. (c) S_{11} magnitude of 4-cell resonator. (d) S_{11} phase of 4-cell resonator.

In Fig. 4, the full-wave (MOM) simulated S_{11} for proposed resonators are shown. The selective frequency of 1-cell resonator is 10.5 GHz. In resonant frequency, the magnitude of S_{11} is about -2 dB and phase is 0.4 resonances of 4-cell are obtained. Only the second and the third resonances satisfy the phase relation. The simulation results also show that the frequency selectivity of 4-cell resonator is better than that of 1-cell resonator. It is noted that the physical length of zeroth-order resonator is smaller than traditional transmission line resonator.

Oscillator circuit, which is in a common gate configuration, using zeroth-order resonator is shown in Fig. 5. The inductor in series with gate is utilized to increase the instability of transistor. Zeroth-order resonator in series with drain determines the frequency of oscillator. An appropriate terminal network is design to match to a 50 Ω load Z_L.

Transient simulation results of oscillator are shown in Fig. 6. In the Fig. 6(a), oscillator frequency using 1-cell resonator is 10.7 GHz, which is a little higher than the resonant frequency of 1-cell resonator. This is also occurred in 4-cell resonator case. In order to observe oscillogram clearly the plots present only 0.5 ns from 50 to 50.5 ns, shown in Figs. 6(b) and (d). Figs. 6(c) and (f) give the phase noises of oscillator using 1-cell resonator and oscillator using 4-cell resonator, respectively.

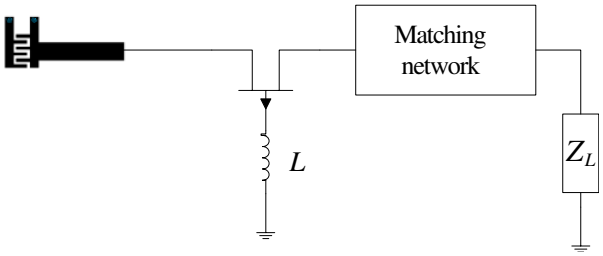

Figure 5: Oscillator circuit using zeroth-order resonator.

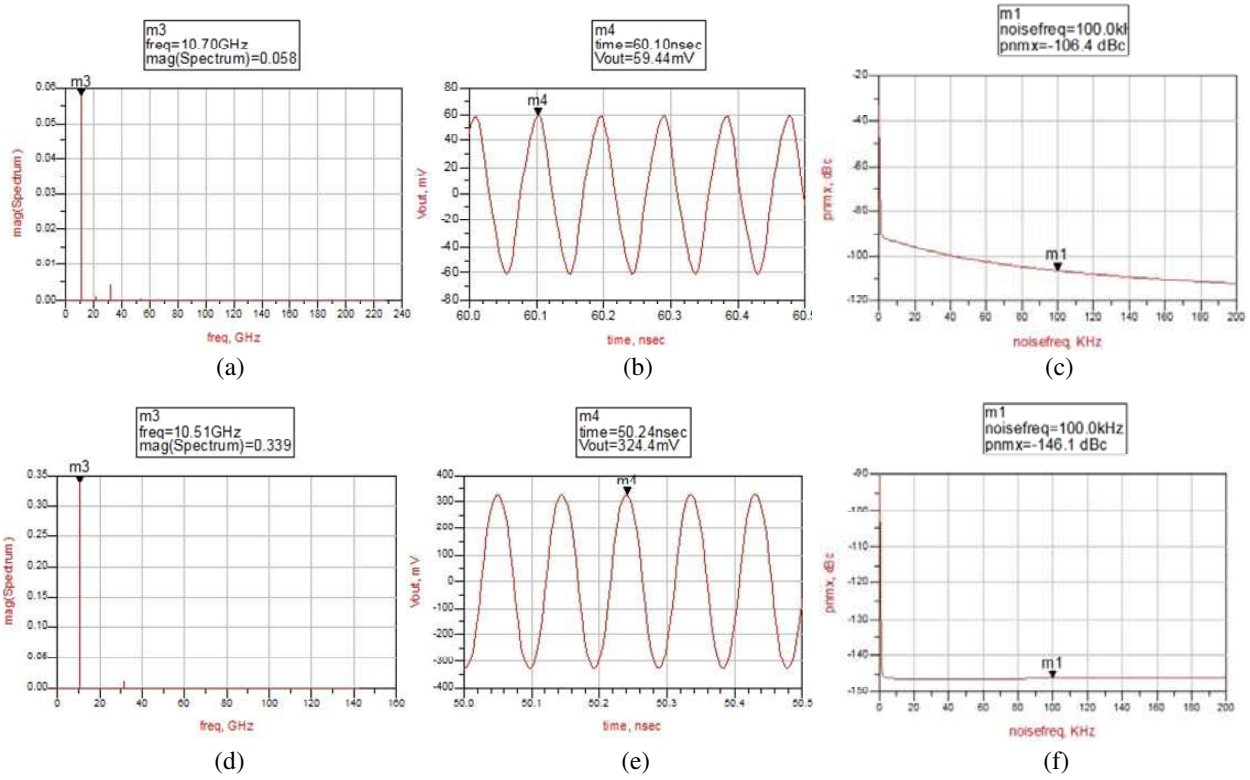

Figure 6: Simulation result of oscillator. (a) Frequency of oscillator using 1-cell resonator. (b) Oscillogram of oscillator using 1-cell resonator. (c) Phase noise of oscillator using 1-cell resonator. (d) Frequency of oscillator using 4-cell resonator. (e) Oscillogram of oscillator using 4-cell resonator. (f) Phase noise of oscillator using 4-cell resonator.

Comparing the results of the two oscillators, we can see the performance of oscillator using 4-cell resonator is better. This indicates that increasing the number of CRLH unit could improve the performances of resonator and oscillator. Above simulations demonstrate that zeroth-order resonator can be applied in RF oscillator.

4. CONCLUSION

Zeroth-order resonators constituted by interdigital capacitors, stub inductors and a transmission line are presented. Full-wave simulations of resonators, with 1-cell case and 4-cell case, are carried out. In addition, oscillators using zeroth-order resonators are designed, which certify the zeroth-order resonators can be applied in RF circuits. Because of the better frequency selectivity of 4-cell resonator, oscillator using 4-cell resonator has better performance at the magnitude of output signal and phase noise. The research we have carried out indicates that increasing the number of CRLH unit could improve the performances of resonator and oscillator.

REFERENCES

1. Caloz, C., H. Okabe, T. Iwai, and T. Itoh, "Transmission line approach of left-handed (LH) materials," *2002 USNC/URSI National Radio Science Meeting*, Vol. 1, 39, San Antonio, TX, Jun. 2002.
2. Lai, A., T. Itoh, and C. Caloz, "Composite right/left-handed transmission line metamaterials," *IEEE Microwave Magazine*, Vol. 5, 34–50, 2004.
3. Sanada, A., C. Caloz, and T. Itoh, "Zeroth-order resonance in composite right/left handed transmission line resonators," *Proc. Asia-Pacific Microw. Conf.*, 1588–1592, 2003.
4. Caloz, C. and T. Itoh, *Electromagnetic Metamaterials: Transmission Line Theory and Microwave Applications*, Wiley, Hoboken, NJ, 2006.
5. Ueda, T., G. Haida, and T. Itoh, "Zeroth-order resonators with variable reactance loads at both ends," *IEEE Transactions on Microwave Theory and Techniques*, Vol. 59, 612–618, 2011.

Transponder Impact on Power and Spectral Efficiencies in WDM Links Based on 10–40–100 Gbps Mixed-line Rates

Vjaceslavs Bobrovs, Peteris Gavars, Girts Ivanovs, Ilja Trifonovs, and Aleksejs Udalcovs
Institute of Telecommunications, Riga Technical University, Riga, Latvia

Abstract— It has been proved that Mixed-Line Rate (MLR) could in a cost-efficient manner scope with heterogeneity of constantly increasing traffic demands in core networks. In the same time, the energy efficiency of a Wavelength Division Multiplexing (WDM) transmission system of a MLR solution depends on the number factors (such as energy efficiency of transponders and regenerators, spectral efficiency, length of transmission distance etc.) and number of wavelengths operating with the particular bitrate and modulation format is one of them. Hence, this papers aims at exploring the power efficient 10 Gbps, 40 Gbps and 100 Gbps wavelength assignment strategy as well as the minimum optical bandwidth required to allocate all wavelengths.

1. INTRODUCTION

During the planning of wavelength division multiplexing (WDM) transport network as well as on its operation pace one of the major constraints is the overall power consumption and power costs per transmitted bps, i.e., energy efficiency [1]. The Mixed-Line Rate (MLR) solutions have proved themselves as a cost efficient solution to deal with the heterogeneity of traffic demands [1, 2]. However, the energy efficiency of such WDM solution depends on the number of parameters such as (*i*) number of wavelengths operating with the particular bitrate and modulation format; *(ii)* energy efficiency of transponder; *(iii)* spectral efficiency which will define the transparent optical reach and, hence, the number of 3R (re-timing, re-shaping, re-amplification) regenerations; *(iv)* distance between two network nodes between whom an end-to-end connection should be provisioned; and (*v*) signal quality need to be guaranteed at the receiving node. In this paper, we focus on MLR solution which employs three different bitrates — 10 Gbps using the non-return-to-zero (NRZ) on-off keying (OOK), 40 Gbps using the NRZ differential phase-shift keying (NRZ-DPSK) and 100 Gbps realized with the dual polarization quadrature phase-shift keying (DP-QPSK). Furthermore, about MLR with such modulation format and bitrate selection have been reported in [3].

In [4–6] authors explores the trade-off between power costs per each transmitted bps, spectral efficiency and the point-to-point transmission distance for the number of Single-Line Rate (SLR) and MLR solutions but none of these papers do not explore the wavelength assignment scheme that must be used to guarantee the lowest overall transponder power consumption regardless to the capacity that need to be transmitted with defined signal quality. Hence, this papers aims at exploring the power efficient 10 Gbps, 40 Gbps and 100 Gbps wavelength assignment approach as well as the minimum optical bandwidth required to allocate these wavelengths in an end-to-end WDM link where the signal quality ($Q \geq 6$) is mainly limited by a linear crosstalk. In addition, in this paper we: (*i*) report about power consumption values for different transponder and 3R types; *(ii)* reveal the minimum allowable frequency intervals between collocated wavelengths; *(iii)* compare the power efficiency of proposed MLR solution with the SLR ones; and *(iv)* analyze the gained transponder load as a function of average aggregated traffic.

2. BACKGROUND AND INITIAL PARAMETERS

In previous research papers, e.g., [4, 5, 7] it has been revealed (*i*) the minimum acceptable frequency intervals (see Table 1) between collocated wavelengths that allows detect signals with $Q \geq 6$ after the transmission over one span of transmission fiber and dispersion compensation module (DCM); *(ii)* transponders and 3Rs power consumption values for the considered modulation formats and bitrates (see Table 2). These parameters will be used further in this research papers.

Comparing these values must be reported that for the transmission capacity higher than 80 Gbps, it is more energy efficiently to use the 100 Gbps DP-QPSK transponders. As for the 3Rs, the situation changes and 40 Gbps NRZ-DPSK ensures lower costs per each transmitted bps.

3. RESULTS AND DISCUSSION

In this section, the impact of transponder power consumption on the width of required frequency band is evaluated. For this reason, firstly we describe an approach that must be used to choose

Table 1: The minimum tolerable channel spacing and Q-factor in the worst system channel.

Wavelengths	**Δ Fmin, [GHz]**	***Q*-factor, [dB]**
10 Gbps–10 Gbps	18.75	16.09
40 Gbps–40 Gbps	112.50	15.56
100 Gbps–100 Gbps	37.50	15.75
10 Gbps–40 Gbps	62.50	23.88
10 Gbps–100 Gbps	31.25	17.08
40 Gbps–100 Gbps	75.00	16.90

Table 2: Power consumption [W] of transponders and 3Rs.

Bitrate and modulation format	**Equipment**	**Power, [W]**
10 Gbps NRZ-OOK	TSP/3R	22.4/20.8
40 Gbps NRZ-DPSK	TSP/3R	69.8/43.6
100 Gbps DP-QPSK	TSP/3R	132.1/158.5

which wavelength to use for data transmission to ensure the lowest possible overall transponder power consumption. Secondly, the overall power consumption of transponder for the SLR scenarios is compared with energy efficient MLR scenario, where number of each wavelength is chosen based on the proposed scheme. The width of frequency band required for transmission as a function of average aggregated traffic also is given. And, finally, transponder load is calculated and compared with the SLR scenarios.

3.1. Energy Efficient Approach to Choose a Number and Type of Required Transponders

As it is mentioned above, the power costs per transmitted bps (i.e., W/bps) or energy efficiency (in J/bit) in MLR transmission systems strongly depends on the number of particular wavelengths used to transmit the particular amount of accumulated traffic. Clear that in the MLR case, the same capacity could be transmitted with different numbers of 10, 40 and 100 Gbps wavelengths. Hence, the overall power consumption of required number of transponders could vary in wide range. But since the transponder power consumption will mainly define the energy efficiency of transmission system (power consumption of inline optical amplifiers is a constant value is inherent to the type modulation format used for data transmission), it is important to choose the combination of 10, 40 and 100 Gbps wavelengths that ensure the lowest overall transponder power consumption for each amount of aggregated traffic. Such algorithm is described in Fig. 1. It is based on the fact that 100 Gbps DP-QPSK transponder has the highest energy efficiency comparing to the 10 Gbps NRZ-OOK and 40 Gbps NRZ-DPSK.

Figure 2 shows that the lowest possible overall power consumption of transponders is secured when not more than three 10 Gbps NRZ-OOK and not more than one 40 Gbps NRZ-DPSK transponders are used for the transmission. In the same time, the number of 100 Gbps DP-QPSK transponders must be increased together with the transmitting capacity (see Fig. 2(c)). This is explained with the highest energy efficiency of 100 Gbps transponders.

If the number of 10, 40 and 100 Gbps wavelengths is chosen based on this proposed algorithm, the overall power consumption required to ensure data transmission over one span of fiber-optical link is: (*i*) the same as it would be in case on 10 Gbps SLR solution, if the transmitting capacity is lower than 30 Gbps; *(ii)* lower than it would be in case of any other number of 10, 40 and 100 Gbps wavelength, if 30 Gbps $< C <$ 60 Gbps; *(iii)* not higher than it would be in pure 100 Gbps SLR solution (see Fig. 3). In addition, it should be noted that curves in Figs. 2–4 have a stepwise form due to the number of transponders which is a discrete and not a continuous variable. For example, 140 Gbps capacity between two nodes should be transmitted by utilizing (*i*) fourteen 10 Gbps, *(ii)* four 40 Gbps or even *(iii)* two 100 Gbps transponders.

The number of particular wavelengths has a strong impact not only on the energy efficiency of transmission but also on the average utilization of WDM system equipment, transponders particularly. From the telecom operator point of view, the installed equipment should be utilized as much as it is possible. Therefore, we also calculated the average utilization of transponders in energy efficient scenario of MLR transmission system, i.e., MLR system where number of 10, 40 and

```
for each amount of aggregated traffic C
    required number of 100G transponders: N_100G = floor(C/100G)
    traffic amount transmitted only with 100G TSP: C_100G = N_100G·100G
    traffic amount that should be transmitted with 40G and/or 10G TSPs: C_40G/10G = C - C_100G
    required number of 40G TSP: N_40G = floor(C_40G/10G/40G)
    traffic transmitted only with 40G TSP: C_40G = N_40G·40G
    traffic amount left only for 10G TSP: C_10G = C_40G/10G - C_40G
    number of 10G TSP: N_10G = ceil(C_10G/10G)
        if power consumption of 100G TSP P_100G < (power consumption of 40G TSP P_40G)·N_40G + (power consumption of 10G TSP P_10G)·N_10G then
            use 40G and/or 10G TSPs
        else
            use 100G TSP
            if P_40G < P_10G·N_10G then
                use 40G TSP
            else
                use 10G TSPs
            end
        end
end
```

Figure 1: Structure of algorithm used to identify the required number of each type of transponders.

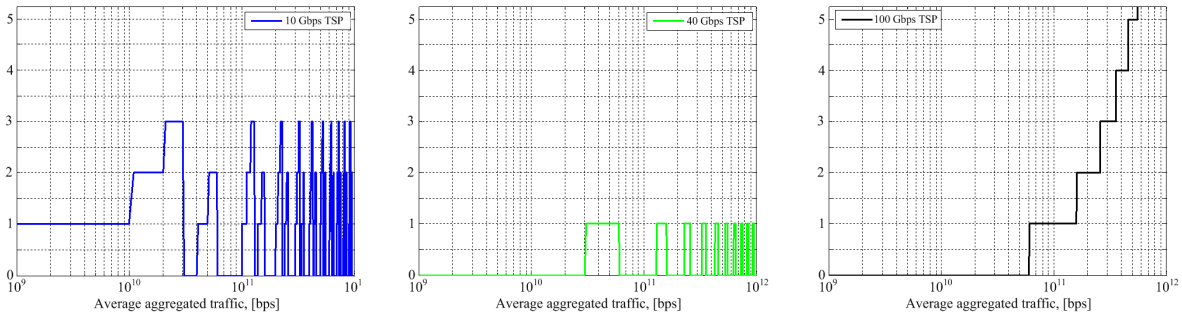

(a) (b) (c)

Figure 2: Number of a different type of transponders: (a) 10 Gbps, (b) 40 Gbps and (c) 100 Gbps required to accumulate traffic in considered scenario of a power efficient MLR-based WDM network.

100 Gbps wavelengths is chosen based on the proposed algorithm. Fig. 4 shows that the average transponder load in case of proposed MLR solution is sufficiently higher comparing to the 100 Gbps SLR. Of course, the use of lower bitrate (e.g., 10 Gbps) ensures very high transponder utilization but in the same time, 10 Gbps transponders cannot secure the lowest overall power consumption of transponder. Hence, we will gain something in terms of transponder load but will definitely lose a lot in terms of power consumption, if 10 Gbps wavelength will be selected for the transmission of large amount of traffic between two network nodes.

3.2. Width of the Frequency Band Required for Transmission

Using the values of frequency intervals summarized in Table 1, the width of optical frequency band that must be used to place 10 Gbps, 40 Gbps and 100 Gbps wavelengths in appropriate sub-bands can be calculated for the considered power efficient solution of MLR transmission system. Fig. 5 shows how changes the width of required frequency band with the average aggregated traffic, if proposed algorithm for the estimation of 10 Gbps, 40 Gbps and 100 Gbps wavelengths is used. The width of total required band is marked with broken red line, while the widths of 10, 40 and 100 Gbps sub-bands are colored in blue, green and black, respectively.

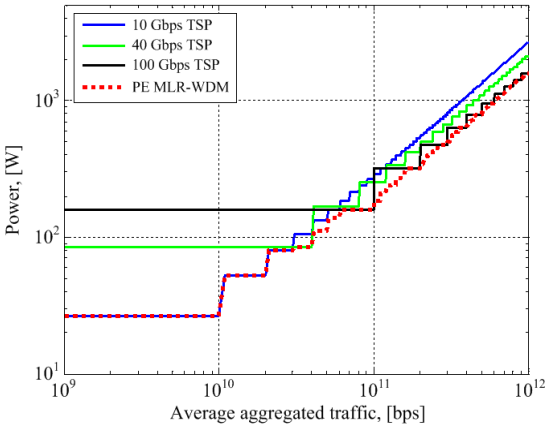

Figure 3: Total power consumption of different TSPs as a function of average aggregated traffic.

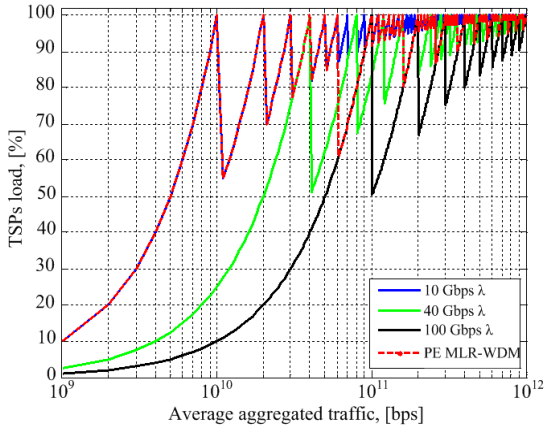

Figure 4: TSPs load in a considered scenario of power efficient MLR-based WDM network as a function of average aggregated traffic.

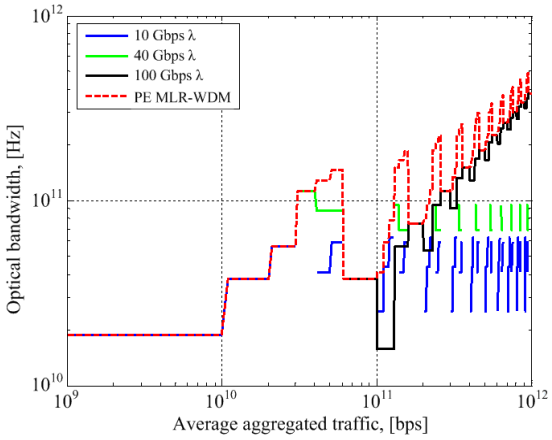

Figure 5: Optical bandwidth required to allocate 10 Gbps, 40 Gbps and 100 Gbps wavelengths as a function of aggregated traffic.

Width of 10 Gbps and 40 Gbps sub-bands is a discrete variable because for some capacities, it is more efficiently from power consumption point of view not to use 10 Gbps and/or 40 Gbps wavelengths at all (see Fig. 2). It also should be noted that for the $C \leq 30$ Gbps, lines colored in red (i.e., total width of required band) and blue (i.e., width of 10 Gbps sub-band) overlap. For the 30 Gbps $\leq C \leq$ 40 Gbps, lines colored in red and green (i.e., width of 40 Gbps sub-band) also overlap. Therefore, it must be concluded that data transmission in power efficient solution of 10–40–100 Gbps MLR system mainly is based on 100 Gbps wavelengths. Such configuration of WDM transmission system secures the lowest transponder power consumption per transmitted bps and gives a flexibility to operate with lower bitrate if necessary.

4. CONCLUSIONS

This paper focuses on a 10 Gbps, 40 Gbps and 100 Gbps wavelength assignment approach that ensures the lowest overall transponder power consumption per 1 bps transmitted over one span of fiber-optical link that consists from 40 km of standard single mode fiber and chromatic dispersion post-compensation module. Wavelengths are placed in optical spectrum using obtained frequency intervals that secure signal detection on the receiver side with Q-factor not lower than 6.

It is revealed that the lowest overall transponder power consumption is secured when not more than there 10 Gbps wavelengths are used to transmit the data and not more than one 40 Gbps wavelength is used regardless to the total capacity need to be transmitted, while the number of 100 Gbps wavelength should be increased as average aggregated traffic grows. This is explained with

the highest energy efficiency of 100 Gbps transponders comparing to the 10 Gbps and 40 Gbps. If the number of each wavelength is selected using this proposed algorithm then the total power consumption required to ensure data transmission over one section of transmission line is: (*i*) the same as it would be for the 10 Gbps SLR solution and the capacity less than 30 Gbps; *(ii)* the lowest one for the traffic between 30 and 60 Gbps; *(iii)* not higher as it would be for 100 Gbps SLR solution.

ACKNOWLEDGMENT

This work has been supported by the European Social Fund within the project Nr. 2013/0012/1DP /1.1.1.2.0/13/APIA/VIAA/051.

REFERENCES

1. Vizcaino, J. L., Y. Ye, and I. T. Monroy, "Energy efficiency analysis for flexible-grid OFDM-based optical networks," *The Int. J. of Comp. and Telecomm. Netw.*, Vol. 56, No. 10, 2400–2419, Jul. 2012.
2. Chowdhury, P., M. Tornatore, A. Nag, E. Ip, T. Wang, and B. Mukherjee, "On the design of energy-efficient mixed-line-rate (MLR) optical networks," *Journal of Lightwave Technology*, Vol. 30, No. 1, 130–139, Jan. 2012.
3. Rival, O. and A. Morea, "Resource requirements in mixed-line rate and elastic dynamic optical networks," *OFC/NFOEC*, 1–3, 2012.
4. Udalcovs, A., P. Monti, V. Bobrovs, R. Schatz, and L. Wosinska, "Power efficiency of WDM networks using various modulation formats with spectral efficiency liminted by linear crosstalk," *Optics Communications*, No. 318, 31–36, 2014.
5. Udalcovs, A., P. Monti, V. Bobrovs, R. Schatz, L. Wosinska, and G. Ivanovs, "Spectral and energy efficiency considerations in mixed-line rate WDM networks with signal quality guarantee," *ICTON 2013*, Tu.D1.3, 1–6, 2013.
6. Bobrovs, V., A. Udalcovs, and G. Ivanovs, "Power efficiency vs. spectral efficiency and transmission distance in 2.5–10–40 Gbps backbone optical networks," *Int. Symp. on Communications, Control and Signal Processing 2014*, 1–4, 2014, to be published.
7. Udalcovs, A., V. Bobrovs, and G. Ivanovs, "Comparison between power efficiency of mixed-line rate over single line rate in spectral efficient WDM networks with signal quality guarantee," *LatinCom 2013*, 1–6, 2013.

Demonstration of Polarization Muiltiplexed Signals Division Using a Fiber Optical Parametric Amplifier

S. Olonkins, I. Lyashuk, and J. Porins
Institute of Telecommunications, Riga Technical University, Azenes st. 16, Riga LV-1048, Latvia

Abstract— The main goal of this paper is to demonstrate the ability of a single pump parametric amplifier with linearly polarized pumping radiation to divide orthogonally polarized optical signals, by emphasizing a signal with certain state of polarization from a combination of orthogonally polarized signals. In the implemented solution two orthogonally polarized optical signals are placed on the same wavelength, and, after being highly attenuated, processed by the parametric amplifier in such a way, that only a signal with a certain state of polarization is amplified. Such additional application of parametric amplifiers has not been demonstrated so far.

1. INTRODUCTION

Due to development of high non-linearity fibers (HNLF) and efficient stimulated Brillouin scattering (SBS) suppression techniques, in recent years fiber optical parametric amplifiers (FOPAs) have received increased attention [1]. Due to the variety of potential applications parametric amplification is positioned as the future leading technique for ultrafast all-optical signal processing in optical communication systems [1, 2]. Additionally to providing optical signal amplification, FOPAs also offer a number of applications for all-optical signal processing, such as: wavelength conversion, 2R and 3R optical signal regeneration, tunable dispersion compensation, and also binary polarization shift keying (2PolSK) to intensity on-off keying (OOK) modulation format conversion [3–5].

The ability to ensure 2PolSK to OOK modulation format conversion is based on the high polarization dependency of the FOPA provided gain. This application requires to use linearly polarized pumping radiation, the state of polarization (SOP) of which should coincide with the SOP of the logical "1" component of the binary PolSK signal. In this case the logical "1" component will receive maximal amplification, and the orthogonally polarized logical "0" will not get amplified [5]. This feature of parametric amplifiers can also be used to ensure one more additional application: division of polarization multiplexed optical signals. Such additional application of parametric amplifiers can be very promising, as potentially it can lead to doubling of spectral efficiency in systems, where FOPAs are used for optical signal amplification.

The main goal of this article is to investigate the ability of FOPAs with linearly polarized pumping radiation to ensure division of two polarization multiplexed signals, placed on the same wavelength, by emphasizing the signal with a certain state of polarization from the overall optical flow.

2. SIMULATION MODEL

For investigation of the ability of the FOPA to emphasize a signal with a certain state of polarization, a simulation model of a 9.953 Gbit/s two channel optical transmission system with non-return to zero (NRZ) encoding technique and OOK modulation format was introduced. This simulation model is shown in Fig. 1. OptSim 5.3 simulation software was chosen as the experimental environment. Previous studies show that results obtained using OptSim simulation software have high correlation with results obtained in a real life experiment [6].

In the transmitter block the radiation of the continuous wave (CW) optical laser is externally modulated via a Mach-Zehnder Modulator, which in its turn is driven by a sequence of NRZ coded electrical pulses that are produced by a tandem of a logical data source and an NRZ coder. For each channel the optical power of the CW laser is 1 mW (0 dBm). Both channels were placed on the same carrier frequency: 196.5 THz (wavelength: 1554.537 nm), corresponding to the wavelength of the S optical band. To ensure that the channels are orthogonally polarized, at each channel the produced NRZ-OOK optical signal passes through an optical polarizer with the same state of polarization, and afterwards the polarized signal from the 2nd channel is processed by a polarization rotator. The state of polarization of the 2nd channel is turned in such a way obtaining such SOP that is orthogonal to the SOP of the signal in the 1st channel.

Afterwards both signals are combined and processed through an optical attenuator with optical signal attenuation of 36 dB. This optical attenuator is used to represent a 150 km long standard

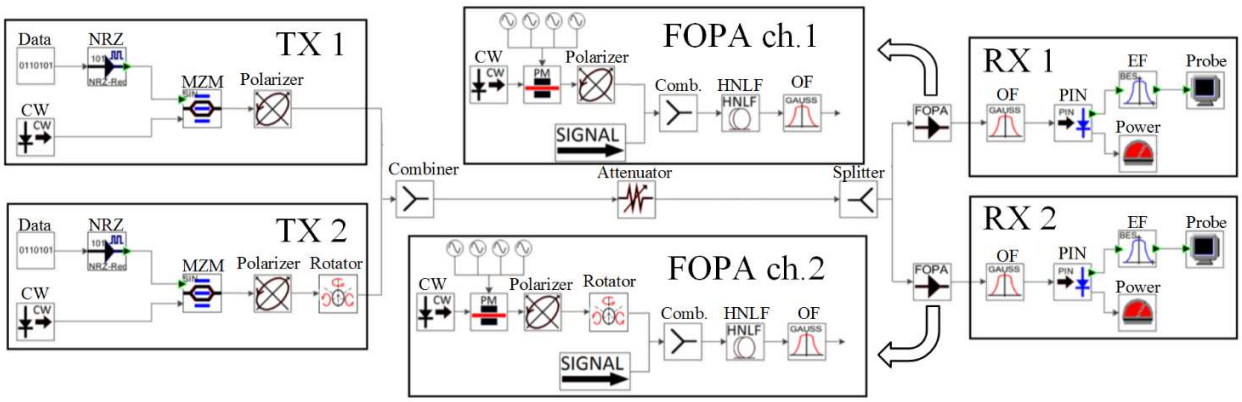

Figure 1: Simulation model of the two channel optical transmission system with FOPA for division and amplification of polarization multiplexed signals.

single mode fiber with attenuation of 0.2 dB/km, and to allocate a 6 dB margin, as it is advised to do during the design process of optical transmission systems [7]. Afterwards the signal is divided among two branches of the transmission system. Each branch represents a receiver block, containing a parametric preamplifier and two receivers: one for the signal at carrier frequency, and one for detection of the generated idler spectral component.

In each branch the FOPA consists of the following mainelements: an optical combiner (to combine the signal with the pump), a 1 kilometer long HNLF (the medium where amplification takes place), and a powerful CW optical laser, that represents the source of the pumping radiation. Parameters of the HNLF can be observed in Table 1.

Table 1: HNLF parameters [8].

Attenuation at 1550 nm, dB/km	0.96
Zero dispersion wavelength, nm	1553.35
Fiber non-linearity coefficient, $(W \cdot km)^{-1}$	15
Core effective area, μm^2	10

The pumping radiation, produced by the CW laser is phase modulated, to broaden its spectrum, and therefore suppress the unwanted impact of stimulated Brillouin scattering; and processed via an optical polarizer, to ensure that the SOP of the pump coincides with the SOP of the corresponding channel. For the same reason, in the case of the 2nd channel the polarized pumping radiation is also sent through a polarization rotator. The power and the wavelength was configured in a way to obtain such configuration of the amplifier that would ensure bit error rate (BER) below $1 \cdot 10^{-12}$ mark, using as less pumping power as possible. To do so it was required for the peak of the gain spectrum to coincide with the frequency of the amplified channel.

At the output of the FOPA the combination of the amplified signal, the pump and the generated idler spectral component is divided among 2 via an optical splitter. At the input of each receiver this combination is processed via a cascade of two bandpass optical filters. It was required to implement double filtering because the extinction ratio of real life optical filters is not enough to filter out the powerful pumping radiation.

3. RESULTS AND DISCUSSIONS

The aim of this section is to analyze the results obtained while configuring the parameters of the amplifier for each of the two receiver blocks, and implement such amplifier configuration that would efficiently emphasize optical signal with a certain state of polarization from the overall optical flow, simultaneously ensuring the required quality of the emphasized signal.

To meet the proposed requirement for efficient division of polarization multiplexed signals using as low pumping power as possible, simultaneously maintaining BER values below the 10^{-12} mark, it was required to configure the amplifier in such a way, that the peak of the gain spectrum would coincide with the frequency of the channel to be amplified. Due to the fact that the process of

parametric amplification is highly dependent on the phase mismatch between the interacting optical fields, it is required to take into account not only the linear phase mismatch that occurs due to fiber dispersion, but also the non-linear phase mismatch that occurs as the consequence of such nonlinear effects as self-phase modulation (SPM) and cross-phase modulation (XPM). Therefore, while adjusting the power of the pumping radiation one must also simultaneously shift the wavelength of the pump in order to maintain the peak of the provided gain spectrum at the desired frequency.

But before seeking for the exact power and wavelength of the pumping radiation, it was required to configure the phase modulation of the pump in order to mitigate the unwanted impact of SBS. The first estimation Pump power and wavelength were chosen to be 550 mW and 1554.1 nm respectively. It was found that the highest optical gain and least amplified signal discrepancies were observed when the pump was phase modulated by four radio frequency tones of 0.13 GHz, 0.42 GHz, 1.087 GHz and 1.94 GHz.

On one hand the usage of phase modulation has decreased the power of the pumping radiation at the input of the HNLF, but on the other hand, this has significantly increased the maximal power of the pump, that could be launched into the HNLF without causing dramatic degradation of amplified signal quality. Eye diagrams of the detected signal and optical spectrum at the output of the FOPA with and without phase modulation of the pump are shown in Fig. 2. As can be seen in Fig. 2(a) and Fig. 2(b) when no action is performed for SBS mitigation even at low amplified signal power the amount of SBS produced signal discrepancies (the elevation of optical spectrum in Fig. 2(b) and Fig. 2(c) is enough to increase BER by at least two orders. If the pump power was 550 mW at the input of the HNLF (without the 3 dB attenuation, caused by phase modulation) even a -1.31 dBm optical signal isn't enough to insure BER below the 10^{-12} mark. It is clear that the peak of amplification is shifted from the desired value (elevation of spectrum in Fig. 2(c) and the obtained level of amplification is not high enough (BER value in Fig. 2(a), so the amplifier needs to be reconfigured. Therefore it was required to obtain the values of the power and wavelength of the pumping radiation, which would match the condition, mentioned at the beginning of this section. For this purpose the dependence of BER values of detected signal on the power of the pumping radiation was obtained (see Fig. 3(a).

In Fig. 3(a) it can be seen that for channel 2 BER values below 10^{-12} mark can be obtained at a slightly lower pump power than for channel 1. This might be related to polarization mode dispersion (PMD) that occurred in the HNLF. PMD caused additional phase mismatch between signal in channel 1 and the pump, therefore the level of amplification was slightly decreased.

Based on the results shown in Fig. 3 it was decided that 530 mW 1553.9 nm pumping radiation should be used. Eye diagrams of the detected signal at carrier frequencies in both receiver blocks

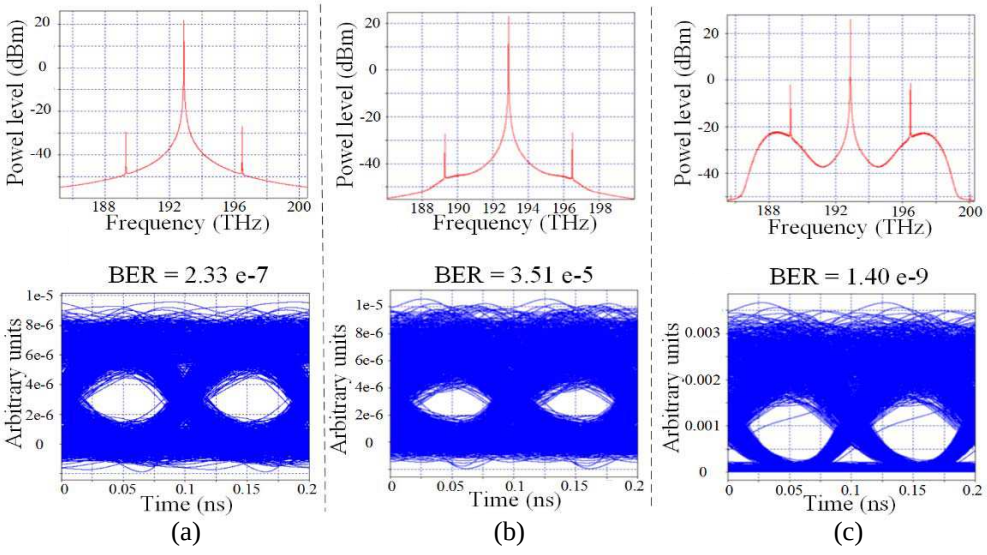

Figure 2: Optical spectrum at the output of the FOPA (to the left) and eye diagram of the detected signal in channel 2 at carrier frequency in the system (a) with pump phase modulation, (b) without pump phase modulation but with the same pump power at the input of the HNLF, (c) and without phase modulation with 550 mW pump power.

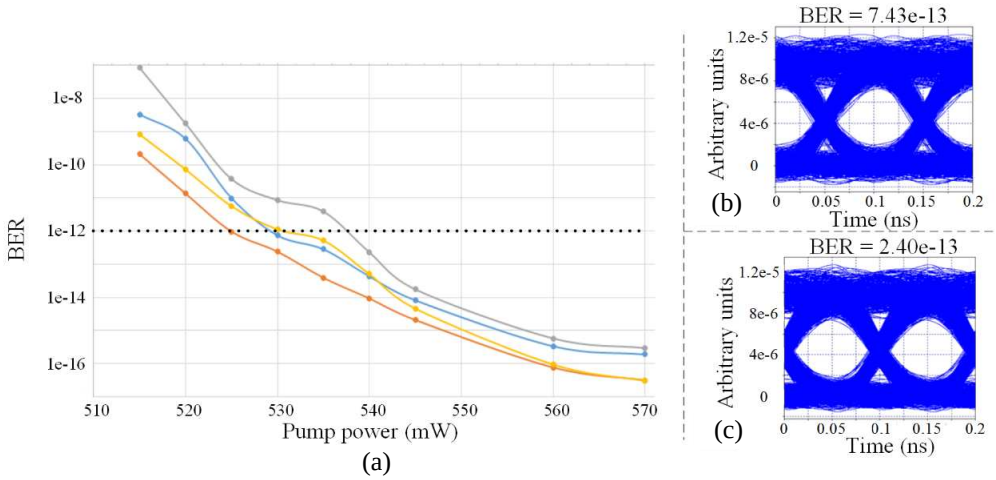

Figure 3: Dependence of BER values of the detected signal on the (a) pumping power of the amplifier at carrier frequencies in the 1st channel (blue), in the 2nd channel (red) and idler frequencies in the 1st channel (grey) and in the second channel (yellow); (b) and eye diagrams of the detected signal at carrier frequency at 530 mW pumping power in the 1st channel and (c) in the 2nd channel.

of the system with the chosen configuration are available in Fig. 3(b) and Fig. 3(c). Fig. 3(b) and Fig. 3(c) also show that even though the signal covered only 1 km of HNLF fiber, the transactions between the logical "1" and the logical "0" were broadened. This, in the absence of high amount of cumulated dispersion, clearly indicates that the signal was influenced by SPM and XPM. Gain spectrum that is provided by the chosen FOPA configuration can be observed in Fig. 4. Due to the fact that gain spectra in both branches were very alike, it was decided to show only the gain spectrum for the 1st channel.

It can be seen from Fig. 4 that the peak of amplification directly coincides with the frequency of the signal to be amplified. On-off gain of 19.95 dB and 20.05 dB was obtained for the 1st and the 2nd channel respectively. The power level of the idler spectral components at the output of the FOPA was about 0.7 dB lover than at carrier frequency. This explains why higher pumping power was required to ensure the desired quality of the signal at idler frequencies (Fig. 3(a)). To assess the produced signal distortions that occurred during the process of amplification, the power of the amplified signal that was required to ensure a certain BER value was compared to an ideal single channel NRZ-OOK system where no amplification is used. The obtained results are shown in Fig. 5.

Figure 5 shows that there is 0.75 dB of power penalty between the signal at carrier frequency and the ideal system. However, for the idler channel this penalty is just under 0.5 dB. This can

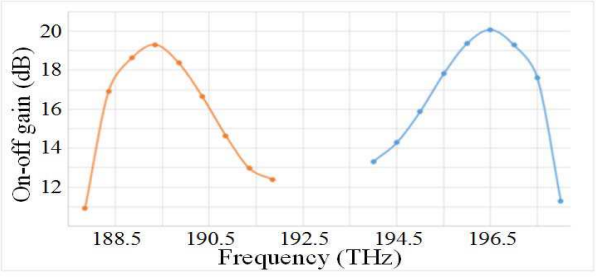

Figure 4: FOPA provided on-off gain at carrier (blue) and idler (orange) frequencies.

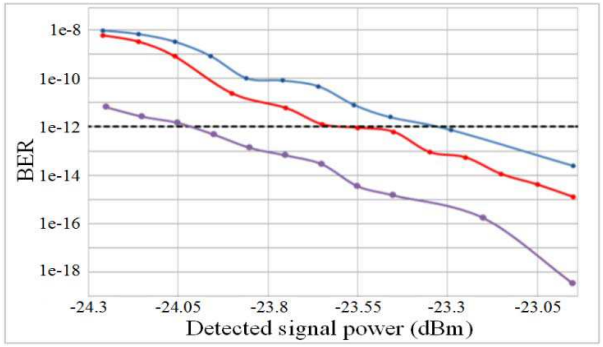

Figure 5: BER value dependence on the power of the detected signal in the ideal OOK system (violet) and in the 1st channel of the system with the chosen FOPA configuration at carrier (blue) and idler (red) frequencies in the system with modulation format conversion.

be explained by the fact that for each channel the orthogonally polarized spectral component was not involved in the process of parametric amplification and wavelength conversion, and, therefore, was not replicated in the idler. But this orthogonal spectral component, which in this case is interpreted as noise, still exists at carrier frequency, and therefore slightly influences the BER value of the detected signal.

4. CONCLUSIONS

In this article the authors have demonstrated the ability of FOPAs to efficiently emphasize a signal with a certain state of polarization, and, therefore, can be successfully used for division of polarization multiplexed signals. It was also shown that phase modulation of the pumping radiation can be successfully implemented to mitigate SBS also in cases where the pump of the FOPA is linearly polarized. In our case this has helped to gain about 2 orders of BER, even though at that time the configuration of the amplifier was not optimal.

It was found that even though signals in both channels were exactly in the same conditions, the difference in amplification has reached 0.1 dB. This can be related to fiber PMD that produced slight phase mismatch between the signal in channel 1 and the pump and, therefore, has caused slight decrease of amplification in comparison with channel 2. Due to the broadened transactions between the logical "1" and logical "0 levels", it was concluded that the emphasized signal has experienced influence of SMP and XPM. The thick logical "1" level in eye diagrams of the detected signal shows that optical noise also was produced during the process of amplification. The increase of the amount of this noise and the growing impact of SPM and XPM have decreased the progress of lowering BER values while increasing the pump power in Fig. 3(a).

It was found that power penalty of 0.75 dB exists between the provided solution and an ideal NRZ-OOK system. For the idler this penalty was by 0.25 dB lower, due to the fact that the orthogonally polarized component was not involved in the process of parametric amplification and, therefore, was not transferred to the idler spectral component.

ACKNOWLEDGMENT

This research has been supported by the European Social Fund within the project No. 2013/0008/1DP/1.1.1.2.0/13/APIA/VIAA/016.

REFERENCES

1. Sylvestre, T., A. Mussot, A. Vedadi, L. Provivo, E. Lantz, and H. Maillotte, "System performance of fiber optical amplifiers," *Fiber and Integrated Optics*, Vol. 27, No. 6, 516–531, 2008.
2. Jopson, R. M. and A. H. Gnauck, "Recent progress in fiber-based optical parametric amplifiers," *2012 17th Opto-electronics and Communications Conference (OECC)*, 59–60, 2012.
3. Karasek, M., P. Honzatko, J. Vojtech, and J. Radil, "Multi-wavelength conversion at 10 Gb/s and 40 Gb/s based on 2 pumps FOPA," *13th International Conference on Transparent Optical Networks (ICTON 2011)*, 1–4, 2011.
4. Wang, J., J. Yu, T. Meng, W. Miao, B. Sun, W. Wang, and E. Yang, "Simultaneous 3R regeneration of $4 * 40$-Gbit/s WDM signals in a single fiber," *IEEE Photonics Journal*, Vol. 4, No. 5, 1816–1822, 2012.
5. Olonkins, S., O. Ozolins, V. Bobrovs, J. Porins, and G. Ivanovs, "Binary PolSK to OOK modulation format conversion in single-pump FOPA for optical access networks," *2013 4th International Workshop Fiber Optics in Access Network (FOAN)*, 15–20, 2013.
6. Trifonovs, I., V. Bobrovs, and G. Ivanovs, "Optimization of a standard bidirectional DWDM solution," *Electronics and Electrical Engineering*, Vol. 115, No. 9, 37–40, 2011.
7. Scemelevs, A. and J. Porins, "BER Performance of a lumped single-pump fiber optical parametric amplifier in a 10 Gbit/s 4-channel S-band DWDM system," *Electronics and Electrical Engineering*, Vol. 93, No. 5, 11–14, 2009.
8. Chen, D. and B. Sun, "Multi-wavelength fiber optical parametric oscillator based on a highly nonlinear fiber and a sagnac loop filter," *Progress In Electromagnetics Research*, Vol. 106, 163–176, 2010.

The Analysis of Receiving Sensitivity Degradation of WLAN Performance due to EMI Noise from SSD Module

Han-Nien Lin[1], **Po-Yu Chiang**[1], **Wang-Chwen Tsai**[1], **and Cheng-Chang Chen**[2]

[1]Department of Communications Engineering, Feng-Chia University
100 Wen-Hua Rd., Taichung 40724, Taiwan, R.O.C.
[2]Section of EMC, Bureau of Standards, Metrology and Inspection, M.O.E.A., Taipei, Taiwan, R.O.C.

Abstract— The Solid State Drive (SSD) is nowadays commonly installed in mobile devices or Ultrabook owing to its compact size and fast processing speed. However, due to ever shrinking space on edge of lid, the WLAN antennas are now usually located at base of Ultrabook computer and thus suffers EMI noise power generated from high speed SSD. Therefore the broadband EMI noise resulted from SSD operation would usually invade the RF communication channel, and thus degrades the receiving sensitivity of the system. In addition, when WiFi tethering is used for cloud applications with the 3G/4G WWAN network through smart phone, the EMI noise from SSD would also affect the file down-loading of mobile phone. Because when Internet accesses with WWAN network, the users always place the mobile phones by side of notebook computer with built-in EMI aggressive SSD. Since the receiving sensitivity of wireless system is the key issue for cloud applications as required by CTIA and related organization, this study investigates the EMI noise coupling mechanism from SSD to antenna and also analyzes the effect on WLAN performance. The coupling mechanism of EMI noise between SSD and RF modules can be categorized as antenna coupling, circuitry coupling, and cavity coupling. With the help of near-field EMC analysis for closely located RF and digital modules in this study, we can identify the root cause of receiving sensitivity degradation and benefit the manufacturers for proper SSD integration with mobile device or Ultrabook computer from compact form design limitation. We also evaluated the noise limit and frequency range for platform noise of wireless communications, and hope to apply the noise budget concept and IC-EMI measurement techniques on the component level to help SSD-related manufacturers and wireless communications system manufacturers to improve the integrating design to meet the performance and EMC requirement in the future study.

1. INTRODUCTION

Owing to its compact size and fast processing speed, the Solid State Drive (SSD) is commonly found been installed in Ultrabook and similar devices. However, such high speed digital module has malignant impact on RF performance of wireless communications. For instance, the SSD usually radiates RF noise power which affects the receiving performance of the WLAN antennas located at base of Ultrabook PC. In addition, when using the WiFi tethering, that is, the users can use the Ultrabook to surf the Internet by the 3G/4G WWAN network via mobile phone, the SSD also radiates the RF noise power which has degraded the reception of mobile phone placed beside the notebook with built-in SSD. When mobile phone is put beside the SSD for WiFi connection as shown in Fig. 1, the EMI signal of another externally connected SSD might also cause the interference on wireless communications.

Figure 1: Scenario of WiFi tethering with mobile phone and external SSD.

2. EMI NOISE EFFECT AND COUPLING MECHANISM ANALYSIS

To quantify the impact of SSD noise power on WLAN performance via embedded antennas, which usually located on the upper left and right corners of the LCD panel for traditional notebook PC as an example, we conduct the throughput rate measurement inside anechoic chamber and show the results with the test setup below in Fig. 2.

Figure 2: Impact of SSD on throughput rate measurement and results.

From the Fig. 2 shown above for the throughput rate measurement, the blue, yellow, and pink lines represent the WLAN throughput rate when the notebook PC is equipped with HDD, shielded SSD, and SSD, respectively. We here also show in Fig. 3 the possible noise coupling configurations and reason for the degradation of WLAN throughput rate. Compared to HDD case, it is found that the SSD noise power dominates the effect. In addition, it also shows the relative position for WLAN antennas with their cable routing, SSD, and WLAN/WWAN module for this throughput rate measurement.

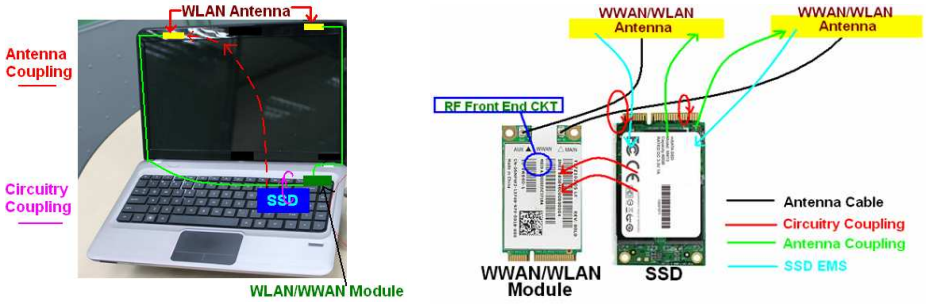

Figure 3: WLAN antennas and cabling configuration with SSD module.

From the analysis of measurement results, the main reason for the degradation of receiving sensitivity is circuitry coupling. The circuitry coupling here means that the SSD noise couples to the mini-coaxial cable connecting WLAN antennas and WLAN module. If the WLAN antennas are further moved down to PC base due to the shrinking lid form limitation of the Ultrabook design, then the SSD EMI noise will even couple directly to the WLAN antennas which is so-called "Antenna Coupling." The coupling mechanism between WLAN antenna and SSD module is illustrated in Fig. 4 for detail.

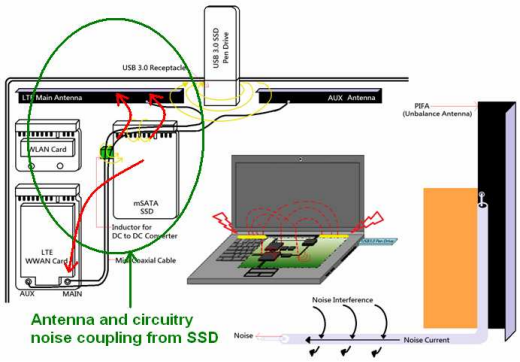

Figure 4: Detailed coupling mechanism between WLAN antenna and SSD module.

We also found out that even the SSD is moved far away from the wireless antenna, as shown below in Fig. 5, RF noise power still couples to antenna from SSD module. Since the chassis of Ultrabook is made of Al-Mg alloy, we therefore call such phenomenon as "cavity resonance" [2] coupling. From the possible coupling mechanism mentioned above, it would be the optimal solution for RFI problems by modifying the components placement layout for better isolation and improving SSD design to mitigate the radiated noise power.

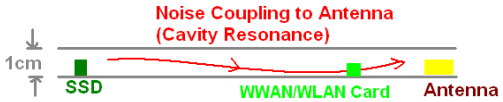

Figure 5: Cavity resonance coupling between WLAN antenna and SSD module.

3. MEASUREMENT SETUP AND PROCEDURES

To help the wireless communications manufacturers and SSD manufacturers identify the root cause of SSD EMI problems on RF receiving performance, we here provide the SSD EMI diagnosis procedures for RF design solutions.

a. Measure the SSD noise power received by the embedded WLAN antennas using the SSD test fixture (Antenna Coupling) as shown in Fig. 6. From the setup shown, the SSD module can be placed in the yellow area of the text fixture and then measure the noise power (generated from SSD) received by WLAN antennas.

   The measurement result is shown in Fig. 7, which shows the noise map in WLAN band (2.4 GHz∼2.5 GHz) and the corresponding noise level of the whole SSD. The corresponding spectrum (from 2415.5 MHz to 2474.4 MHz) for the noise map is shown in the left figure, and the spectrum for the point with the highest noise level in noise map is shown in the right figure. In the Fig. 7, the left one also represents the highest noise level at each frequency point in WLAN band of scanned area.

b. For some critical WLAN channels interfered by SSD found in step 1, we then utilize the PNS [1] (Platform Noise Scanner) for near field noise scanning to locate the EMI noise distribution generated from SSD (Circuitry Coupling & Cavity Resonance [2]) as shown in Fig. 8.

   The current distribution of EMI noise on the victim WLAN antenna from the PNS scanning is shown in Fig. 9 to verify the coupling effect.

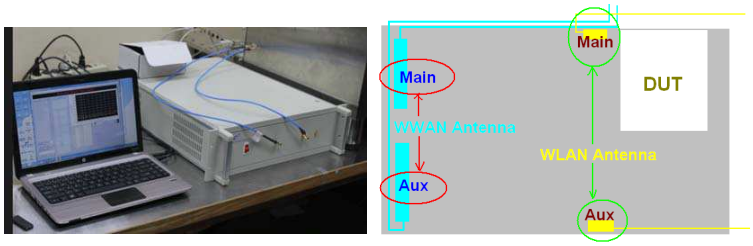

Figure 6: Antenna coupling measurement.

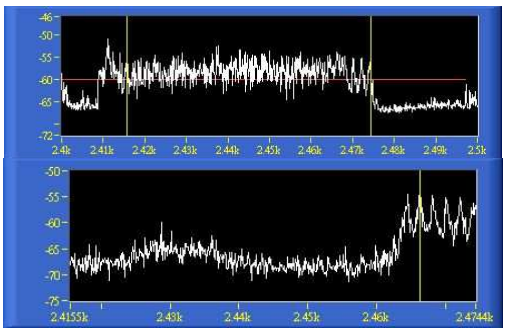

Figure 7: SSD noise map in WLAN band.

Figure 8: Circuitry and cavity resonance coupling measurement.

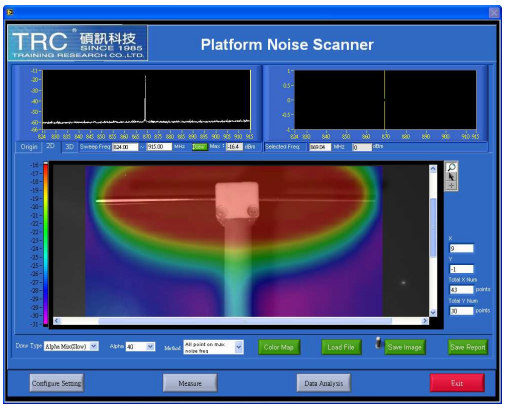

Figure 9: Current distribution on victim antenna.

4. NOISE LIMIT AND FREQUENCY RANGE PLANNING

From the measurement and test plan mentioned for RFI noise evaluation in the previous section, we here suggest that the noise limit of high speed digital component can be determined with the following formula.

$$\text{NLimit}\,(\text{dBm}) = \text{SM}\,(\text{dBm}) + \text{GA}\,(\text{dBi}) - \text{SNR}\,(\text{dB}) \tag{1}$$

For example, if a WLAN device requires $-103\,\text{dBm}$ receiving sensitivity with $2.14\,\text{dBi}$ antenna gain, then the noise limit could be determined as follows.

$$\text{NLimit} = -103\,(\text{dBm}) + -2.14\,(\text{dBi}) - 7\,(\text{dB}) \approx -108(\text{dBm}) \tag{2}$$

Since the coupling coefficient is a transfer function of distance, the separation between SSD module and WLAN antennas should also be taken into consideration when enacting the RF noise limit for each communication band.

Once the SSD RFI noise limit is determined for wireless communications manufacturers, they can control the noise budget for SSD together with the corresponding test fixture shown previously to improve RF receiving performance. With the designated noise limit, the SSD noise level in each band should be further suppressed and validated by IEC 61967 [3] IC-EMI measurement series. From the step 2 test item shown in previous section, the SSD noise level in hot spot image of surface scan is better not exceed $-60\,\text{dBm}/30\,\text{kHz}$ in each communication band. Otherwise, the potential risk for RF de-sensitivity will increase if the antenna cable is routed across the SSD module.

5. NOISE RESULTS OF SSD NEAR FIELD EMI TEST

To illustrate the SSD EMI noise effect on WLAN receiving performance, we have shown in Fig. 10 for antenna receiving EMI power comparison of the SSDs from two different manufacturers S1 and S2. In the left hand side, it shows that the WLAN antennas (both main and auxiliary antenna) receive more noise power from S1 manufacturer's SDD than from S2's. When we utilized the platform noise scanner to scan the SSD's noise current distribution in WLAN band, the result is shown in the right hand side. It can thus be realized that the S1 SSD imposes greater potential risk than S2 SSD for those WLAN communication band.

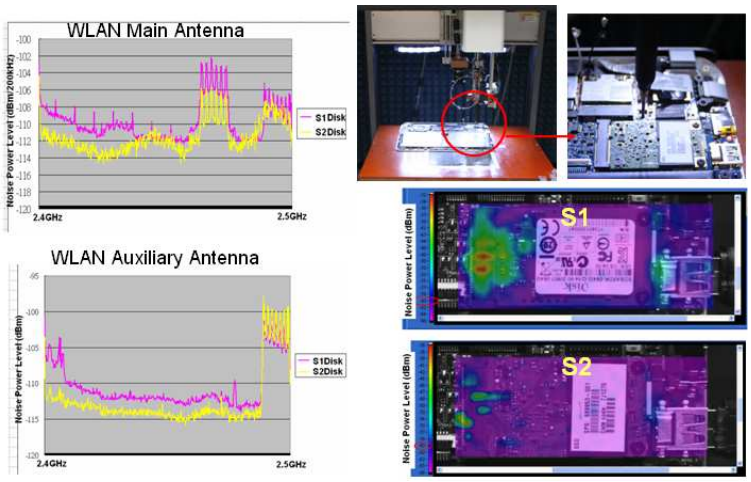

Figure 10: EMI comparison of the SSDs from two different manufacturers.

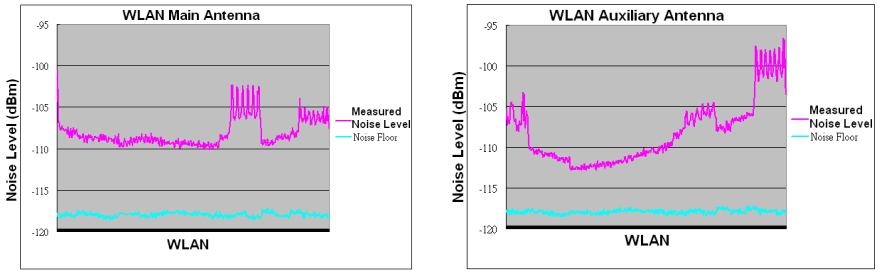

Figure 11: EMI noise power received by main and auxiliary antennas from S3's SSD.

Finally we implemented the SSD made by S3 manufacturer on Ultrabook PC, then we also measured the EMI noise power received by main and auxiliary antennas of WLAN respectively as shown below in Fig. 11. It obviously shows that the noise level of RF module raises drastically, and thus will inevitably degrade the RF receiving performance despite the good RF design practice.

6. CONCLUSION

The SSD EMI noise measurement is conducted to evaluate the noise level and isolation requirement needed for SSD integrated with RF module. For the Ultrabook and notebook PC manufacturers, they can benefit the SSD noise impact on WLAN system and further utilize the mitigation techniques to suppress the noise coupling with compact design limitation from this study. As to the SSD related manufacturers, they can also benefit from understanding the noise current distribution to improve their SSD design to meet the system manufacturers' requirement for platform noise consideration.

ACKNOWLEDGMENT

The authors would like to thank TRC (Training and Research Company) Taiwan for technical support, measurement assistance and test fixture for this study. We would also like to sincerely express appreciation to BSMI (Bureau of Standards, Metrology and Inspection) and NSC (National Science Council) for their financial grants support to this study. The original research work presented in this paper was made possible in part by the BSMI under Contract grant from BSMI Taiwan.

REFERENCES

1. Lin, H.-N., C.-H. Lin, M.-C. Chang, and Y.-Y. Shih, "Analysis ofplatformnoiseeffect on WWAN performance," 719–722, April 2010.
2. Murakami, A., K. Kawashima, and K. Atsuki, "Quantum electronics," *IEEE Journal*, Vol. 39, No. 10, 1196–1204, 1892.
3. Ostermann, T. and B. Deutschmann, "Characterization of the EME of integrated circuits with the help of the IEC standard 61967," Test Workshop, 2003; *The Eighth IEEE European Proceedings*, Academic, New York, 1963; 132–137, May 25–28, 2003.

Research in Modeling and Dynamic Simulation of Linear Eddy Current Braking Force of High-speed Train

X. R. Zhang, Q. Y. Guo, J. Zhang, and M. S. Tong
School of Electronic and Information Engineering, Tongji University, Shanghai 200092, China

Abstract— In this paper, we introduce the principle of high speed train eddy current braking, and establish a complete mathematical model for solving eddy current force definite solution problem. The eddy current braking process is a dynamic process. The air gap distance between the magnetic pole and guide rail induction plate is constantly changing, and the change of air gap and the eddy current brake force are mutually coupled. Obviously, the dynamic coupling process of eddy current braking force with air gap cannot be characterized by static analytical expressions. We propose a method to calculate the dynamic simulation of eddy current braking force considering the change of air gap. First, the finite element method is used to establish the 2-dimensional (2D) model, and then the ANSYS software is applied to simulate the calculation. Finally, the results of eddy current brake force (i.e., horizontal braking force) and the normal force change with speed are obtained. We did the analysis on the simulation results, which were further compared with the experimental data. The reasons of the error were analyzed too. This paper provides a reference for the design of high speed train eddy current device.

1. INTRODUCTION

At present in China, the motor car of high speed multiple units uses the regenerative brake and disc friction brake, while the trailer only uses the disk friction brake. As the braking power of more than 300 km/h level train is very big, the brake disc will be under high heat load. Therefore the design of materials and structure is a challenge. Using eddy current brake can shorten the emergency braking distance and improve the safety of trains. The eddy current brake can also play a role in the normal braking. Using eddy current brake and regenerative brake for high speed scenarios, and using disc friction brake supplement in low speed scenarios, we can greatly reduce the wear of the brake disc and the brake pad.

2. THE PRINCIPLE OF THE LINEAR EDDY CURRENT BRAKING

As shown in Fig. 1, the magnet poles are alternately arranged in accordance with N S maintaining a certain air gap on the conductor. When the exciting coil is energized, the conductor and the electromagnet are not in relative motion ($v = 0$). The main magnetic flux is constant and the magnetic field is symmetric. The suction force is generated between the magnetic and the conductor.

When the electromagnet and the conductor are in relative motion ($v > 0$), the conductor cuts magnetic lines, generating eddy current, deflecting magnetic field lines, thus the tangential component is generated, which is the brake force.

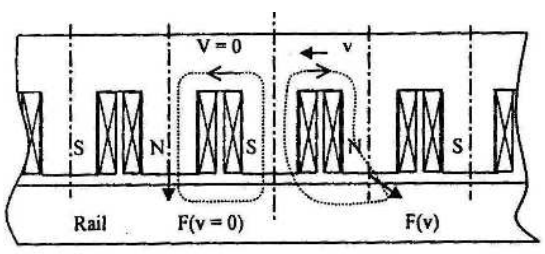

Figure 1: The structural drawing of the eddy current brake.

3. THE MATHEMATICAL EQUATIONS OF LINEAR EDDY CURRENT BRAKE ELECTROMAGNETIC FIELD

For general time-varying electromagnetic fields, Maxwell's equations in differential forms can be written as

$$\begin{cases} \nabla \times \vec{H} = \vec{J} + \dfrac{\partial \vec{D}}{\partial t} \\ \nabla \times \vec{E} = -\dfrac{\partial \vec{B}}{\partial t} + \nabla \times \left(\vec{V} \times \vec{B}\right) \\ \nabla \cdot \vec{B} = 0 \\ \nabla \cdot \vec{D} = \rho \end{cases} \quad \text{Among them} \quad \begin{cases} \vec{D} = \varepsilon \vec{E} \\ \vec{B} = \mu \vec{H} \\ \vec{J} = \sigma \vec{E} \end{cases} \tag{1}$$

where ε, μ and σ, are the permittivity, magnetic permeability and electrical resistivity respectively, ρ is the electrical space charge density.

The eddy current field has the following characteristics:

1. We can ignore the effect of displacement current on the magnetic field.

2. After considering the relative motion of the magnetic field, we can think of the magnetic field is time invariant field.

3. There is no free charge in the field, so the electrical space charge density is 0, $\nabla \cdot \vec{D} = 0$.

In a pair of magnetic poles, for example, the study area is divided into three parts:

the excitation coil region, including the air gap and iron core, and the magnetic yoke region, as well as the induction plate region.

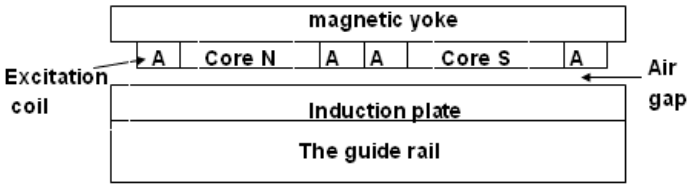

Figure 2: The cross section schematic of eddy current brake.

We divided the above fields into the eddy current region (induction plate) and the non-eddy current region (core, coil and air gap). In the eddy current region we use magnetic vector potential $\vec{A}$ and electric scalar potentials ϕ as unknown functions, and in the non-eddy region we only use $\vec{A}$ as the unknown function. We define

$$\vec{B} = \nabla \times \vec{A} \tag{2}$$

$$\vec{E} = \vec{V} \times \vec{B} - \nabla\phi = \vec{V} \times \nabla \times \vec{A} - \nabla\phi \tag{3}$$

Obviously $\nabla \cdot \vec{B} = 0$ and $\nabla \times \vec{E} = \nabla \times (\vec{V} \times \vec{B})$ are established. The ν is reluctivity (without considering the magnetic saturation, can be considered to be constant), and

$$\vec{H} = \nu \vec{B}. \tag{4}$$

In order to ensure the uniqueness of the magnetic vector potential, the Coulomb gauge condition is introduced in the study area

$$\nabla \cdot \vec{A} = 0 \tag{5}$$

On the outer boundary we define

$$\vec{n} \times \vec{A} = 0 \tag{6}$$

At the same time, a penalty term $-\nabla(\nu \nabla \cdot \vec{A})$ is introduced in the control equations. Due to the addition of this term, the irrotationality of the electric field intensity $\vec{E}$ cannot be hidden, for which

we need to list the explicit formulation. Finally the complete equations for electromagnetic field of eddy current brake are obtained.

$$\left.\begin{aligned}\nabla\times\left(\nu\nabla\times\vec{A}\right)-\nabla\left(\nu\nabla\cdot\vec{A}\right)-\sigma\left(\vec{V}\times\nabla\times\vec{A}-\nabla\phi\right)=0\\ \nabla\cdot\left(\sigma\vec{V}\times\nabla\times\vec{A}+\sigma\nabla\phi\right)=0\end{aligned}\right\}\text{ in the eddy current region}\quad(7)$$

$$\nabla\times(\nu\nabla\times\vec{A})-\nabla\left(\nu\nabla\cdot\vec{A}\right)=\vec{J}_s\text{ in the non-eddy current region}\quad(8)$$

$$\left.\begin{aligned}\left(\nabla\times\vec{A}_1\right)\cdot\vec{n}_{12}=\left(\nabla\times\vec{A}_2\right)\cdot\vec{n}_{12}\\ \left(\nu_1\nabla\times\vec{A}_1\right)\times\vec{n}_{12}=\left(\nu_2\nabla\times\vec{A}_2\right)\times\vec{n}_{12}\\ \nu_1\nabla\cdot\vec{A}_1=\nu_2\nabla\cdot\vec{A}_2\\ \vec{n}\cdot\left(\sigma\vec{V}\times\nabla\times\vec{A}+\sigma\nabla\phi\right)=0\end{aligned}\right\}\text{ on the internal boundary}\quad(9)$$

$$\left.\begin{aligned}\left(\nabla\times\vec{A}\right)\cdot\vec{n}=0\\ \vec{n}\times\vec{A}=0\\ \nu\nabla\cdot\vec{A}=0\end{aligned}\right\}\text{ on the outer boundary}\quad(10)$$

4. DYNAMIC SIMULATION OF LINEAR EDDY CURRENT BRAKE FORCE

In the process of eddy current brake, the air gap distance between the magnetic pole and guide rail induction plate is constantly changing. The change of air gap and the eddy current brake force are mutually coupled, and therefore the eddy current braking process is a dynamic process. Considering the change of air gap, we simulate the dynamics of eddy current brake force using the ANSYS software.

Since the eddy current brake pole is symmetric in the direction of the rail height direction, we established a two-dimensional model to calculate the eddy current field. The parameters of the Maglev Train TR08 are computed by using our program. Eddy current brake force (horizontal brake force) was obtained from the power of the eddy current loss and speed as

$$\overrightarrow{F}=\frac{P}{\overrightarrow{V}}\quad(11)$$

Normal force was calculated by Maxwell stress method

$$\vec{F}=\oiint_S\left[\frac{1}{\mu_0}\left(\vec{n}\cdot\vec{B}\right)\vec{B}-\frac{1}{2\mu_0}B^2\cdot\vec{n}\right]ds\quad(12)$$

5. THE SIMULATION RESULTS

By calculation, we obtained 7×21 sets of data, excitation current varying from 25 A to 55 A, the speed from 100 to 0 m/s (respectively 5 A, 5 m/s as a step). Fig. 3 depicts the eddy current brake force (horizontal brake force) and the normal force changes versus the speed (with the excitation current set to be 45 A).

From Fig. 3, we can see that the eddy current brake force increases rapidly along with the speed in the $0\sim50$ km/h speed region, while in the $50\sim100$ km/h region the brake force changes very little. It roughly reaches a maximum value at 80 km/h. Further more we observe that the normal force is of great value in the low speed region. This force can make the wear plate against the rail and produce the friction braking force. It can supplement the deficiency of the eddy current brake force in the low speed region. With the increasing of speed, the normal force decreases and is negligible in high speed region.

Our experimental data is shown in Fig. 4, where eddy current brake test bench is adopted.

Comparison of Fig. 3 and Fig. 4, we find that the eddy current brake force calculated theoretically is consistent with the actual experimental values, although there is some error in the numerical value. The errors existing in the numerical calculation are caused by the following two reasons.

1.When we built the mathematical model, the boundary conditions were calculated approximately.

2. The air gap of the eddy current brake bench adopted in experiments involves certain errors.

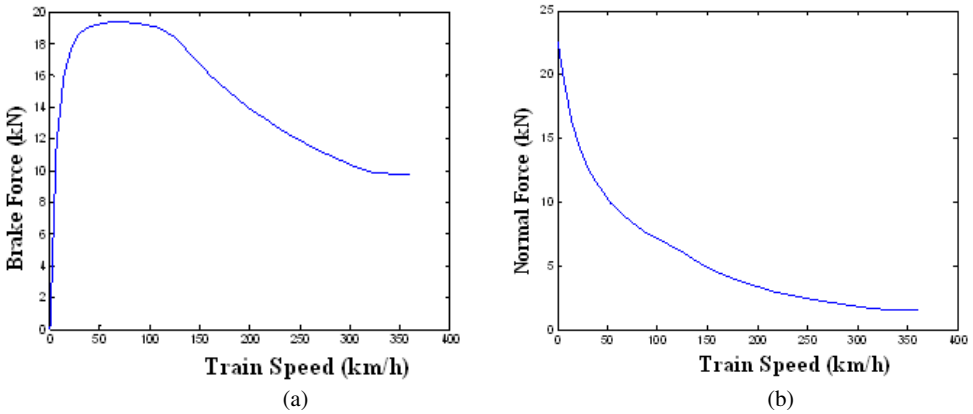

Figure 3: Horizontal brake force, normal force varies with speed (excitation current 45 A).

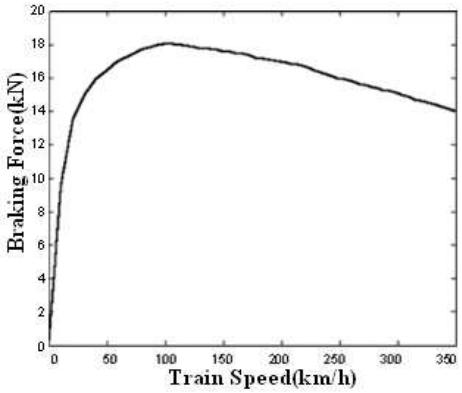

Figure 4: The test results of eddy current brake force.

6. CONCLUSION

In this paper, we proposed a method to calculate the dynamic simulation of eddy current braking force by taking into account the change of air gap. The results of eddy current brake force (i.e., horizontal braking force) and the normal force change with speed are obtained. The simulation results were observed to be consistent with the experimental data. This paper provides a reference for the design of high speed train eddy current devices.

REFERENCES

1. Wang, M.-X., W.-X. Zhou, J. Tang, and X. Guo, "Research on an eddy current braking system applied in a high-speed train model for dynamic test," *Railway Locomotive & Car*, Vol. 33, No. 4, 27–29, 2013.
2. Gu, L.-L., B.-J. Lv, and F.-Y. Ding, "Analysis of the research methods of rail eddy current brake," *Railway Locomotive & Car*, Vol. 33, No. 1, 5–8, 2013.
3. Li, H.-P. and H.-T. Lin, "A study on the design of fundamental brake system for high-speed train," *China Railway Science*, Vol. 24, No. 2, 8–13, 2003.
4. Jiang, D.-Q., C. Yang, W.-B. Ni, X.-M. Wang, and F. Li, "Magnetic field analysis of permanent magnet eddy current brake based on ANSYS," *Railway Locomotive & Car*, Vol. 29, No. 5, 8–10, 2009.

Enhance the Magnetic Properties of Fe-Si-Al-Cr Flaky Particles by Annealing

Nan Zhang, Xin Wang, Peiheng Zhou, Jiangliang Xie, and Longjiang Deng
National Engineering Research Center of Electromagnetic Radiation Control Materials
State Key Laboratory of Electronic Thin Film and Integrated Devices
University of Electronic Science and Technology of China, Chengdu 610054, China

Abstract— Fe-Si-Al-Cr flaky particles were used as microwave absorbing material. Iron-Silicon-Aluminum-Chromium ingots with nominal compositions $Fe_{73}Si_{15}Al_{10}Cr_2$ were produced by alloying the pure elements in an induction melting furnace under argon atmosphere at 0.03 MPa, and then the ingots were crushed into irregular shaped particles. As-crushed alloy had been milled by planetary miller for 32 h. In order to increase the effective permeability, the material was annealed under different conditions. The morphology of the powders was characterized by scanning electron microscope (SEM). The phases of powders were estimated by X-ray diffract ometer (XRD). The microwave permeability dispersion spectra of annealed powders within a frequency range of 0.5–8 GHz was measured. The SEM results showed that particles had been successfully transformed into the flaky shape. The average diameter of flakes is about 43 μm. The average aspect ratio (width/thickness) of flakes is about 28. The XRD results showed that the DO3 ordered phase coexisted with α-Fe(Si,Al,Cr) matrix phase by annealing above 500°C. When the annealing temperature increased from room temperature to 800°C, the grain size grown from 10.4 nm to its maximum 29.8 nm and part of α-Fe(Si,Al,Cr) matrix phase translated into DO3. The imaginary part of the effective permeability increased with the annealing temperature, and decreased when the temperature was above 500°C. The resonance frequency decreased with the annealing temperature, and increased when the temperature was above 400°C. The effective permeability of the powders, obtained by 500°C annealing, had a maximum value of 6.0 at 2.5 GHz.

1. INTRODUCTION

Electromagnetic wave absorbers in the gigahertz range for mobile communications have become widely used. Soft magnetic metal powders, such as Fe-Si-Al alloysor nanocrystalline metal alloys, have attracted considerable attention for shielding against electromagnetic interference (EMI) radiation.

In order to increase the bandwidth of electromagnetic wave absorption andre duce the thickness of an absorber, high permeability values are required, especially high imaginary parts of permeability [1]. The microwave permeability of milled Fe-Si-Al flaky particles has been found to be much larger than those of unmilled particles with irregular shape [2]. It has been proven that magnetic particles with flaky shapes can effectively improve the absorption properties [3]. Tianyu Ma et al. have fabricated thin $Fe_{85.8}Si_{9.6}Al_{5.6}$ (wt.%) nanocrystalline flakes from melt-spun ribbons by a high-energy planetary ball-milling method. They found that the D03 superlattice recovered after annealing for 30 min at 300°C and over, accompanied by modest crystalline growth, causing a clear enhancement in magnetic properties [4]. It has been proven that the addition of Cr in the alloys can improve the effectively permeability of materials [5]. But they did not consider the effect of annealing on the microwave magnetic properties of Fe-Si-Al-Cr flaky particles. Therefore, in this paper, $Fe_{73}Si_{15}Al_{10}Cr_2$ precursor was prepared by ball-milled and then annealed under different temperature. The effects of annealing temperature on the microstructure and magnetic properties of the as-prepared powders were investigated.

2. EXPERIMENTAL PROCEDURES

Stoichiometric $Fe_{73}Si_{15}Al_{10}Cr_2$ compounds were prepared by induction melting under argon atmosphere, the constituting elements with a purity higher than 99.9%. The ingots were crushed into irregular shaped particles with the diameter was hundreds of microns. As-crushed alloy had been milled by planetary miller for 32 h. The as-prepared flakes were annealed in vacuum furnace at different treatment temperatures (from 300°C to 800°C) for 1 hour.

The morphology of the powders was characterized by scanning electron microscope (SEM, JEOL TSM-7600F). The phases of powders were estimated by X-ray diffractometer (XRD, SHIMADZU XRD-7000) with Cu K-radiation. Complex permittivity and complex permeability measurements,

in the frequency range between 0.5 and 18 GHz, were carried out by to roidal samples (mass ratio of powders and paraffin was 4 : 1) of Ø7 mm × Ø3.04 mm × 2.5 mm using microwave vector network analyzer (Agilent 8720ET).

3. RESULTS AND DISCUSSION

After these particles have been milled for 32 h, they have been successfully transformed into the flaky shape, as shown in Figure 1. The average diameter of flakes is about 43 µm. The average aspect ratio (width/thickness) of flakes is about 28.

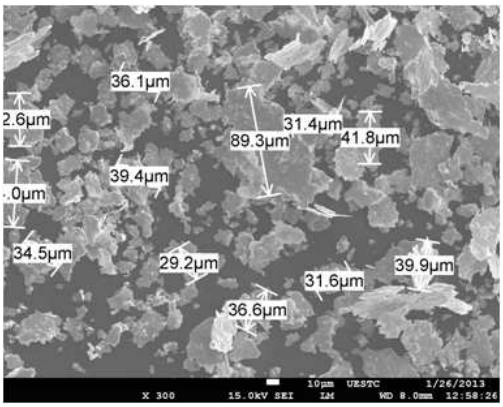

Figure 1: SEM micrographics of various powders milled for 32 h FeSiAlCr.

Figure 2 shows the XRD patterns of different samples. $Fe_{75}Si_{13}Al_{10}Cr_2$ has two kinds of crystal structures with ferromagnetic properties: The ordered DO3 (superlattice) structure and the disordered α-Fe(Si,Al,Cr) structure. Three prominent diffraction peaks in all samples are associated with the (200), (400) and (422) planes of α-Fe(Si,Al,Cr) solid-solution. Two additional peaks at angle about 28° and 31° observed in the ingot sample correspond to a DO3 ordered phase. For the α-Fe(Si,Al,Cr) phase with B. C. Clattice structure, Fe, Si, Al and Cr atoms occupy the lattice sites randomly in the way of continuous substitutional solid solutions. For the DO3 phase, Al and Si atoms dominantly occupy the body-centered site of its unit cell (i.e., superlattice), which is composed of eight B.C.C unit cells. After milling for 32 h, the diffraction peaks of DO3 phase fully disappears, XRD of original powder shows the disordered α-Fe(Si,Al,Cr) structure. The XRD results showed that the DO3 ordered phase coexisted with α-Fe(Si,Al,Cr) matrix phase by annealing above 500°C. When the annealing temperature increased from room temperature to 800°C, three prominent peaks are relatively narrow, attributing to the variation of average grain size and internal strain which can be estimated by Williamson-Hall method [6], as shown in Table 1.

Figure 3 reflects the effective permeability and permittivity of the alloy powders annealed un-

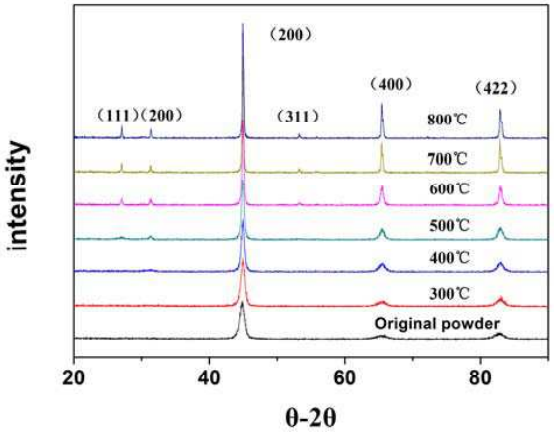

Figure 2: XRD patterns of the ingot simple, the powders milled for 32 h, and then annealed in vacuum furnace at 300°C, 400°C, 500°C, 600°C, 700°C, 800°C.

Table 1: Grain size D (nm), internal strain ε (%) with different annealed temperature.

Annealed temperature (°C)	D (nm)	ε(%)
as-milled	10.4	0.501
300	12.2	0.478
400	16.6	0.461
500	19.6	0.345
600	27.6	0.166
700	28.7	0.108
800	29.8	0.068

der different temperature. Both the real part and imaginary part decreases during the annealing temperature increased from room temperature to 800°C. After annealed, the real part of the permeability of the sample with an increasing temperature first increases, then descending. The real part of the permeability of the powders obtained by 500°C annealing has a maximum value of 9.0 at 1.05 GHz. The imaginary part of the effective permeability also presents a first increase and then decreasing trend. The imaginary part of the effective permeability increased with the annealing temperature, and decreased when the temperature was above 500°C. The effective permeability of the powders, obtained by 500°C annealing, had a maximum value of 6.0 at 2.5 GHz. First, the resonance frequency moves to the low frequency with the annealing temperature, the minimum value of resonance frequency is 1.2 GHz, obtained by 400°C annealing. Then the resonance frequency increased when the temperature was above 400°C.

For cubic crystal ($K_1 > 0$), we can get the resonance frequency f_r by the following formula: $f_r = \gamma H_{eff}$. H_{eff} is magnetic anisotropy field, γ is gyromagnetic ratio. Average grain size grown up from 10.4 nm to 29.8 nm, leading to an increase magnetic anisotropy H_{eff}. Internal strain has an decrease from 0.501% to 0.068%, leading to an decrease of H_{eff}. When the temperature is under 500°C, the decrease of internal strain contribute more to the change of H_{eff} than the grown up of grain size; When the teperature is above 500°C, it is opposite. As a result, f_r presents a first decrease and then increasing trend when the annealing temperature increased from room temperature to 800°C. Similar to H_{eff}, M_s the also presents a first decrease and then increasing

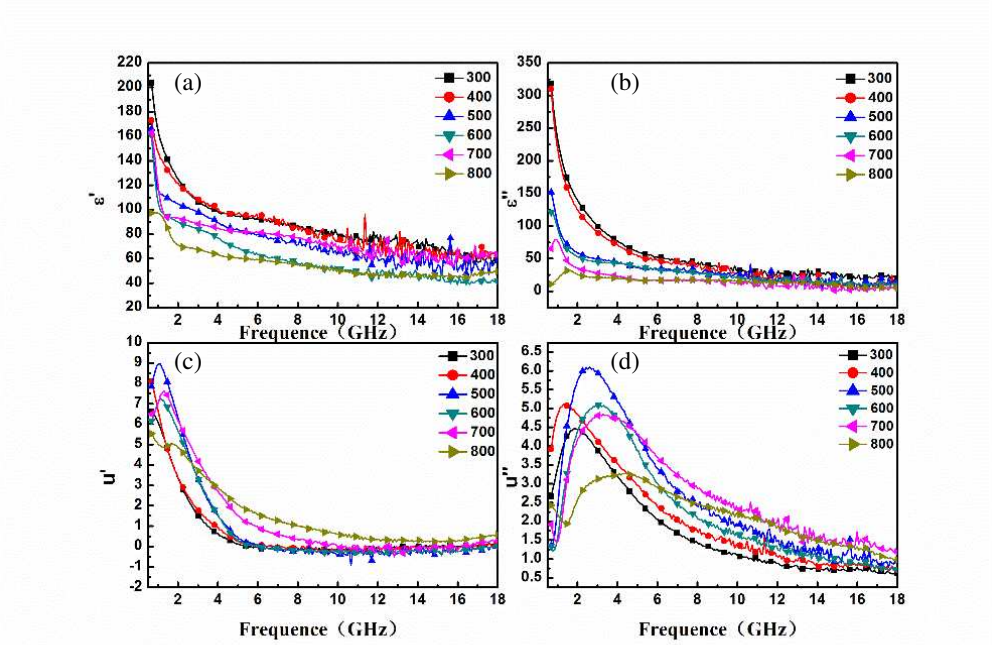

Figure 3: Effect of different components on the microwave permeability and permittivity. (a) The real part of permittivity; (b) The imaginary part of permittivity; (c) Thereal part of permeability; (d) The imaginary part of permeability.

trend.

Permeability values of traditional microwave magneticmaterials are small in quasimicrowave frequencies of gigahertz due to Snoek's limit:

$$(\mu_r - 1)f_r = 2/3\gamma M_s \tag{1}$$

Fe-Si-Al-Cr flaky particles were annealed under different temperature. The shape-dependent Snoek's law as given below indicates that higher permeability can be obtained in flaky particles:

$$(\mu_r - 1)f_r^2 = (\gamma/2\pi)^2 4\pi M_s(H_k + 4\pi M_s D_z) \tag{2}$$

where D_z is the demagnetization factor of the direction normal to the particle plane. D_z value does not change after annealing. According to the change of M_s and f_r, μ_r presents a first decrease and then increasing trend. μ' had a maximum value of 9.0 at 1 GHz, μ'' had a maximum value of 6.0 at 2.5 GHz, obtained by 500°C annealing.

4. CONCLUSION

Flake-shaped particles were annealed under different temperature. The XRD results show that there are two major phases exist: the ordered phase (DO3) and the disordered α-Fe(Si,Al,Cr) structure. When the annealing temperature increased from room temperature to 800°C, the grain size grown from 10.4 nm to its maximum 29.8 nm, the internal strain increases from 0.079% to 0.485%, part of α-Fe(Si,Al,Cr) matrix phase translated into DO3. The effective permeability of the powders, obtained by 500°C annealing, had a maximum value, $\mu' = 9.0$ at 1.2 GHz and $\mu'' = 6.0$ at 2.5 GHz.

REFERENCES

1. Rozanov, K. N., "Ultimate thickness to bandwidth ratio of radar absorbers," *IEEE Transactions on Antennas and Propagation*, Vol. 48, No. 8, 1230–1234, 2000.
2. Han, M. and L. Deng, "Understanding the enhanced microwave permeability of Fe-Si-Al particles by Mössbauer spectroscopy," *Journal of Magnetism and Magnetic Materials*, Vol. 337, 70–73, 2013.
3. Li, Z. W., Z. H. Yang, and L. B. Kong, "Enhanced microwave magnetic and attenuation properties for Z-type barium ferrite composites with flaky fillers," *Journal of Applied Physics*, Vol. 110, No. 6, 063907, 2011.
4. Ma, T., M. Yan, and W. Wang, "The evolution of microstructure and magnetic properties of Fe-Si-Al powders prepared through melt-spinning," *Scripta Materialia*, Vol. 58, 243–246, 2008.
5. Zou, B. F., T. D. Zhou, and J. Hu, "Effect of amorphous evolution on structure and absorption properties of FeSiCr alloy powders," *Journal of Magnetism and Magnetic Materials*, Vol. 335, 17–20, 2013.
6. Williamson, G. K. and W. H. Hall, *Acta Metall.*, Vol. 1, 2, 1953.

Design of Controlling Edge Scattering Based on Tapered Periodic Surfaces Loading

Li-Juan Lu, **Hai-Yan Chen**, **Pei-Heng Zhou**, **Di-Fei Liang**, **and Long-Jiang Deng**
National Engineering Research Center of Electromagnetic Radiation Control Materials
State Key Laboratory of Electronic Thin Film and Integrated Devices
University of Electronic Science and Technology of China, Chengdu 610054, China

Abstract— In this paper, a novel method for controlling trailing edge scattering is proposed based on tapered periodic surfaces (TPS) loading. The TPS is realized by periodic square metallic patches with tapered dimensions at the direction perpendicular to the considered edge but keeping its period unchanged. The backscattering properties from the trailing edge with the proposed TPS loading are analyzed and compared with that of original trailing edge for various frequencies. It is observed that wide angular radar cross section (RCS) reduction can be achieved and the maximum reduction of mono-static RCS is 25 dB. Furthermore, it is found that the proposed TPS loading can more effectively suppress edge backscattering for a wide range of azimuth angles than the popular trailing-edge serration method.

1. INTRODUCTION

With the rapid development of detecting technology, radar cross section (RCS) reduction becomes very important for stealth techniques for military aircrafts or ships [1]. Basic techniques used for RCS reduction involve appropriate shaping, use of radar absorbing materials, and passive and active cancellation of scattered field. Experimental evidence indicates that edges are a major potential scattering source of stealth objects after typical sources such as specular reflection, cavity or ducting scattering and angular scattering are effectively controlled [2]. Edge diffraction can be interpreted by the scattering from discontinuous electromagnetic property between edges and its surrounding. In the region of low RCS, edge scattering should be significantly reduced. Resistive strip is widely used in electromagnetic scattering suppression, especially for surface discontinuities [3–6]. It can break up a single strong echo into many weak ones. Serration is a geometric treatment and also be widely applied to the trailing edges of wings. Obvious examples are the B-2 and F-117A aircraft [7]. It can avoid reflection in the direction of the incoming wave so as to reduce the backscattering from the edges. Therefore, resistive loading and serrated edge are two main methods for suppression of edge scattering.

In this paper, a novel method for trailing edge scattering control using tapered periodic surfaces (TPS) loading is presented. The TPS is realized by periodic square metallic patches with tapered dimensions at the direction perpendicular to the considered edge but keeping its period unchanged. The mono-static RCS is simulated for various frequencies in VV-polarization. The VV-polarization is defined that the electric field vector is perpendicular to the considered edge. To further demonstrate that the method of TPS loading is feasible, the mono-static RCS of the trailing-edge serration, a popular design method, is proposed for comparison.

2. DESIGN AND RESULT

The basic unit cell structure of TPS is shown in Figure 1(a) which consists of metallic square patch printed on a grounded lossless dielectric substrate. By changing the size of patch arrays but keeping its period unchanged, the structure of TPS is realized. The periodicity of square patch arrays is p, the length of the patch is a, the thickness and relative dielectric constant of the substrate are d and ε_r, respectively. Figure 1(b) shows the geometry of TPS loading applied to the square metallic plate with a certain thickness. The length and thickness of the plate are $L = 600\,\text{mm}$ and $t = 2\,\text{mm}$, respectively. For TPS, the length of the patches reduces along the negative x-direction gradually. And the thickness of the substrate is equal to the thickness of the target. The plate lies in the x-y plane with plane wave incident at angle $0^\circ \le \theta \le 90^\circ$ and $\varphi = 0^\circ$, where θ is defined as the pitching angle, and φ represents the azimuth angle. Considered that strong trailing edge scattering occurs for VV-polarization [8], in the following discussion, the analysis is limited electromagnetic scattering properties at VV-polarization.

The abrupt termination of the conducting edge gives rise to a very strong scattering field. The TPS can provide a gradual transition from the considered edge to free space to eliminate the abrupt

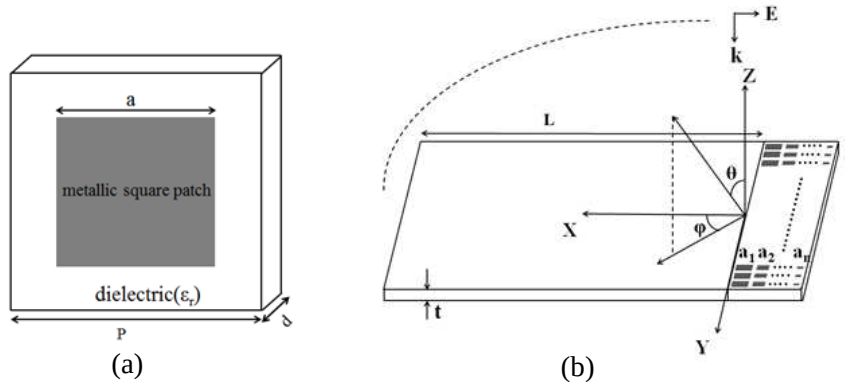

Figure 1: (a) Geometry of a unit cell of uniform periodic square patches printed on a grounded substrate. (b) Geometry of the tapered periodic surfaces loading.

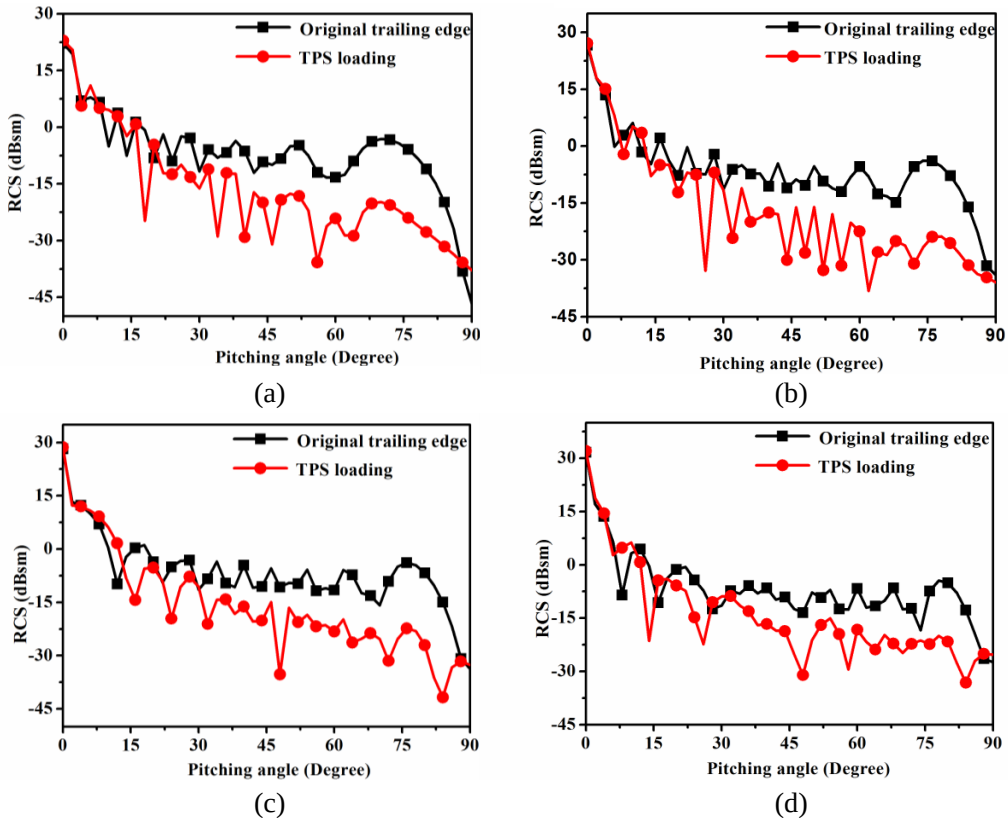

Figure 2: Mono-static RCS from a square plate with original edge and TPS loading for various frequencies: (a) $f = 3\,\text{GHz}$, (b) $f = 5\,\text{GHz}$, (c) $f = 6\,\text{GHz}$, (d) $f = 9\,\text{GHz}$.

edge. Figure 2 shows mono-static RCS pattern for original trailing edge and TPS loading trailing edge at 3 GHz, 5 GHz, 6 GHz and 9 GHz, respectively. For 3 GHz, after the element period and the size patches of TPS are optimized by genetic algorithm, the element period is selected as $P = 25\,\text{mm}$ and the side lengths are selected as $a_1 = 23.6\,\text{mm}$, $a_2 = 21.4\,\text{mm}$, $a_3 = 18.5\,\text{mm}$, $a_4 = 18.5\,\text{mm}$, and $a_5 = 18.5\,\text{mm}$. Similarly, for 5 GHz, $P = 15\,\text{mm}$, $a_1 = 14\,\text{mm}$, $a_2 = 12.5\,\text{mm}$, $a_3 = 11\,\text{mm}$, $a_4 = 9.5\,\text{mm}$, $a_5 = 8\,\text{mm}$, $a_6 = 6.5\,\text{mm}$. For 6 GHz, $P = 12.5\,\text{mm}$, $a_1 = 11.8\,\text{mm}$, $a_2 = 10.7\,\text{mm}$, $a_3 = 9.25\,\text{mm}$, $a_4 = 7.7\,\text{mm}$, $a_5 = 6.3\,\text{mm}$, $a_6 = 5.1\,\text{mm}$. For 9 GHz, $P = 8.33\,\text{mm}$, $a_1 = 7.98\,\text{mm}$, $a_2 = 7.38\,\text{mm}$, $a_3 = 6.43\,\text{mm}$, $a_4 = 5.38\,\text{mm}$, $a_5 = 4.43\,\text{mm}$, $a_6 = 3.58\,\text{mm}$. The parameters of lossless dielectric substrate are fixed as $\varepsilon_r = 2.2$ for various frequencies. Obviously, the TPS loading can effectively suppress the backscattering from trailing edges by the optimal design. The mono-static RCS is reduced up to 20 dB when the pitching angular θ is between 60° and 80°, and the maximum reduction exceeds 25 dB.

To identify the validity of TPS loading, the trailing-edge serration and the TPS loading to reduce

mono-static RCS are compared. Serration is widely applied to the trailing edges of wings, which can avoid reflection in the direction of the incoming wave so as to reduce the backscattering from the edges. In this paper, the angle of serration is selected as 114° based on [9]. The element period and the size patches of TPS are selected as $P = 15\,\text{mm}$, $a_1 = 14\,\text{mm}$, $a_2 = 12.5\,\text{mm}$, $a_3 = 11\,\text{mm}$, $a_4 = 9.5\,\text{mm}$, $a_5 = 8\,\text{mm}$, $a_6 = 6.5\,\text{mm}$, and the lossless dielectric substrate is fixed as $\varepsilon_r = 2.2$. Serrated edge and TPS loading applied to the triangle metallic plate with a certain thickness are

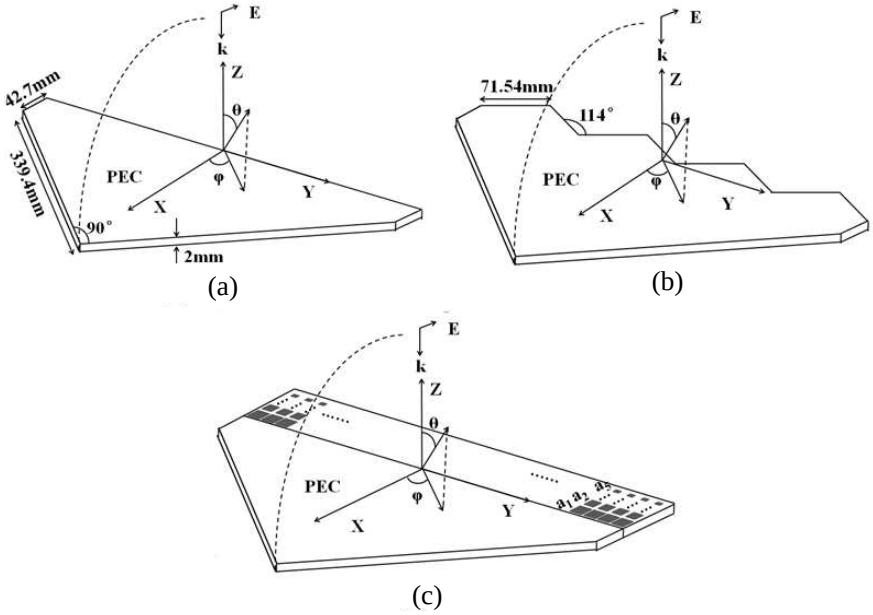

Figure 3: Models for various edge treatments. (a) Original trailing edge. (b) Serrated edge. (c) TPS loading.

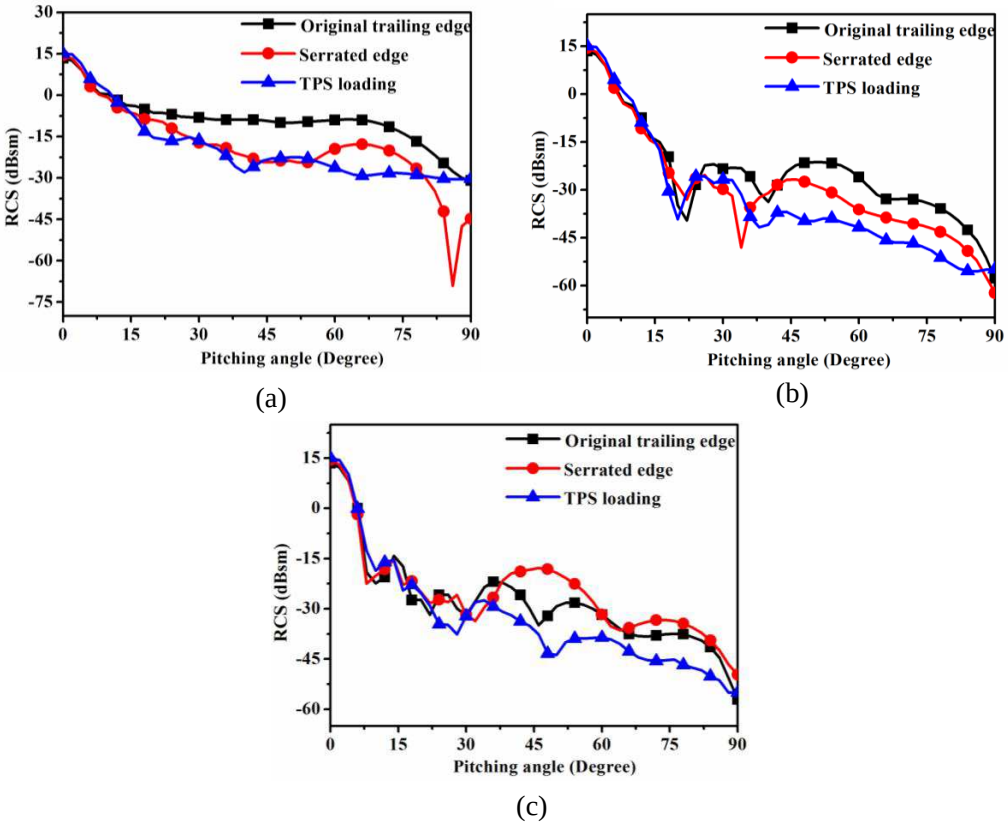

Figure 4: Mono-static RCS from a triangle plate with original trailing edge, serrated edge and TPS loading for various azimuth angles: (a) $\varphi = 0°$, (b) $\varphi = 10°$, (c) $\varphi = 20°$.

shown in Figure 3.

Figure 4 shows electromagnetic scattering patterns for original trailing, serrated edge and TPS loading cases at 5 GHz for the azimuth angle $\varphi = 0°$, 10° and 20°, respectively. Obviously, when the azimuth angle is 0°, the serrated edge and TPS loading can effectively suppress edge backscattering and the average reduction of mono-static RCS exceeds 10 dB. When the azimuth angle is 10°, the TPS loading is more effective for the suppression of trailing scattering than serrated edge. When the azimuth angle is 20°, the mono-static RCS of serrated edge surpasses to the original trailing edge, but the mono-static RCS can still be reduced up to 7∼8 dB at pitching angle $20° < \theta < 90°$ by the TPS loading. Therefore, the TPS loading can effectively suppress edge backscattering for various azimuth angles. However, when the azimuth angle deviates from 0°, the serrated edge does not work well for edge scattering suppression.

3. CONCLUSION

In this paper, it is shown that tapered periodic surfaces loading can reduce the mono-static RCS of trailing edge. By TPS loading, the average value of RCS reduction up to 20 dB can be achieved in a wide angle range for various frequencies. The trailing-edge serration is a popular and effective method for wide angular RCS reduction of a simple target edge. To identify the validity of TPS loading, the trailing-edge serration and the TPS loading to reduce mono-static RCS are compared. With the azimuth angle deviating from 0°, the serrated edge is increasingly close to and even surpasses to the original edge. However, for the TPS loading case proposed in this paper, the RCS reduction is rather considerable for a wide range of azimuth angles.

ACKNOWLEDGMENT

This research is partially supported by the National Natural Science Foundation of China (Grant No. 51025208, and Grant No. 51301031) and the fundamental research funds (Project No. ZYGX201-3J029).

REFERENCES

1. Mallahzadeh, A. R., M. Soleimani, and J. Rashed-Mohassel, "RCS computation of airplane using parabolic equation," *Asia-Pacific Conference Proceedings Microwave Conference Proceedings, APMC 2005*, Vol. 4, Dec. 4–7, 2005.
2. Ivrissimtzis, L. P. and R. J. Marhefka, "Edge-wave diffraction for flat-plate structures," *IEE Proceedings — Microwaves, Antennas and Propagation*, Vol. 141, No. 1, 30–36, 1994.
3. Chen, H. Y., L. J. Deng, and P. H. Zhou, "Suppression of surface wave from finite conducting surfaces with impedance loading at margins," *Journal of Electromagnetic Waves and Applications*, Vol. 24, Nos. 14–15, 1977–1989, 2010.
4. Chen, H. Y., L. J. Deng, P. H. Zhou, et al., "Tapered impedance loading for suppression of edge scattering," *IET Microwaves, Antennas & Propagation*, Vol. 5, No. 14, 1744–1749, 2011.
5. Knott, E. F., "Suppression of edge scattering with impedance strings," *IEEE Transactions on Antennas and Propagation*, Vol. 45, No. 12, 1768–1773, 1997.
6. Chen, H. Y, Z. W. Zhu, L. J. Lu, et al., "Design and implementation of the tapered resistive sheets to control edge scattering," *Journal of Applied Physics*, Vol. 115, No. 16, 164906, 2014.
7. Jenn, D. C., *Radar and Laser Cross Section Engineering*, American Institute of Aeronautics and Astronautics, 2005.
8. Knott, E. F., J. Shaeffer, and M. Tuley, *Radar Cross Section,* SciTech Publishing, 2004.
9. Liu, Z. H., P. L. Huang, Z. Wu, and X. Gao, "Analysis of scattering from serrated edge plate on aircraft with MLFMA," *Journal of Beijing University of Aeronautics and Astronautics*, Vol. 34, No. 05, 499–502, 2008 (in Chinese).

Shock Wave Dynamics in the Cleaning of Container Surfaces

M. Janíček, R. Kadlec, and P. Fiala
Department of Theoretical and Experimental Electrical Engineering
Brno University of Technology, Technická 12, Brno 616 00, Czech Republic

Abstract— Lockable containers are commonly applied in both long-term and short-term storage of materials, substances and commodities. In repeatedly used containers, however, cleaning is a crucial problem: traces of previously stored materials have to be removed quickly and effectively, especially in the case of biological compounds or toxic, radioactive, and otherwise hazardous substances. The chemical-mechanical methods for the elimination of dirt can be excessively complicated or costly (also due to the use of special equipment), and in some materials the cleaning procedure is difficult to control

1. INTRODUCTION

In the field of material and component storage, the operators are faced with the problem of ensuring safe and repeated use of the containers. As indicated within references [1, 2], the situation is even more pressing in the context of specialised physical and chemical laboratories or plants, which apply various cleaning procedures depending on the concrete type of substance.

The authors of this paper propose a single (albeit somewhat limited) cleaning method suitable for universal application both in vessels holding nanomaterial particles and in large-sized containers with hazardous chemical or biological content. The outlined solution utilises shock wave dynamics, which — depending on the circumstances — can be obtained through a controlled electric charge or via detonation produced by a regulated chemical reaction.

2. NUMERICAL MODEL AND ITS FORMULATION

The actual creation of the numerical model is based on the laws of hydrodynamics, or the behaviour of compressible or incompressible fluids. In the given instance, the exciting detonation wave travels through the air, which (in the assumed conditions) acts as a compressible fluid; the interference of the waves at the boundary, or the container wall, nevertheless significantly changes the propagation speed of the superposed wave through the air, and this environment can be interpreted in the outlined situation as an incompressible fluid. For the definition of the model, we assume the equilibrium state, and this description forms the basis of the numerical model design. The model of the assumed task is restricted to the closed area Ω_F according to Fig. 1(a). We then have

$$\Omega_F = \bigcup_{i=1}^{4} \Omega_i \text{ a } \bigcup_{i=1}^{4} \Gamma_{\Omega i} = \Gamma_F. \tag{1}$$

From the state of the dynamic equilibrium of the system in the area Ω_F, it is possible to observe (in a simplified manner) at the boundary Γ_1 the conditions for the undamped process of an incompressible environment as the formula for the stress tensor $\overleftrightarrow{T}$

$$\mathrm{div}\overleftrightarrow{T} + \mathbf{f}_s = 0 \quad \text{in the area } \Omega_1. \tag{2}$$

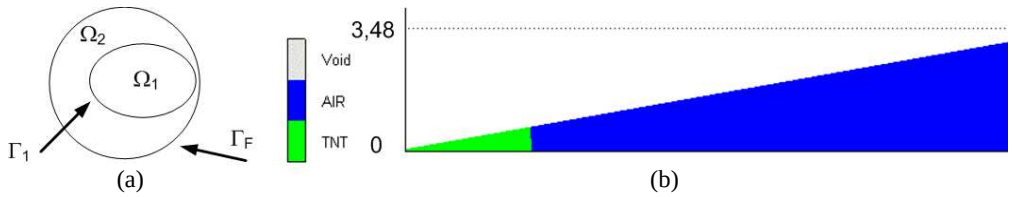

Figure 1: (a) The general distribution of areas and boundaries in the numerical model; (b) the distribution of material in the charges and the environment.

The vector of the specific force $\mathbf{f}_s$ is described by the formula

$$\mathbf{f}_s = \mathbf{f}_0 + \mathbf{f} + \rho \frac{\partial^2 \mathbf{s}}{\partial t^2}, \quad \forall t \geq 0, \tag{3}$$

where ρ is the specific density, $\mathbf{s}$ is the position vector, $t$is the time. The specific force $\mathbf{f}$ is expressed for the presence of plasma, with the magnetic flux density $\mathbf{B}$ and the current density $\mathbf{J}$, as

$$\mathbf{f} = \mathbf{J} \times \mathbf{B}. \tag{4}$$

The stress tensor from Formula (2) can be written as

$$\overleftrightarrow{T} = \overleftrightarrow{D}_F \cdot \overleftrightarrow{e} \tag{5}$$

The tensor of specific deformations is expressed as

$$\overleftrightarrow{e} = \begin{bmatrix} \frac{\partial s_x}{\partial x} & \frac{\partial s_x}{\partial y} - \frac{\partial s_y}{\partial x} & \frac{\partial s_x}{\partial z} - \frac{\partial s_z}{\partial x} \\ \frac{\partial s_x}{\partial y} - \frac{\partial s_y}{\partial x} & \frac{\partial s_y}{\partial y} & \frac{\partial s_y}{\partial z} - \frac{\partial s_z}{\partial y} \\ \frac{\partial s_x}{\partial z} - \frac{\partial s_z}{\partial x} & \frac{\partial s_y}{\partial z} - \frac{\partial s_z}{\partial y} & \frac{\partial s_z}{\partial z} \end{bmatrix}. \tag{6}$$

By substituting the stress tensor (5) and the specific force (4) in the Formula (2) and through extension, we obtain the equation

$$(\lambda_1 + \lambda_2)\,\mathrm{graddiv}\,\mathbf{s} + \lambda_2 \nabla^2 \mathbf{s} + \mathbf{f}_s = 0, \tag{7}$$

in which the Lamé constants λ_1, λ_2 are expressed for the isotropic material as

$$\lambda_1 = \frac{E_u \sigma}{(1+\sigma)\,(1-2\sigma)}, \quad \lambda_2 = \frac{E_u}{2\,(1+\sigma)}. \tag{8}$$

For the Poisson's constant σ, we have $\sigma \neq -1 \wedge \sigma \neq 0.5$, and E_u is Young's elastic modulus. This model, however, is not suitable for use in the area Ω_F, namely for the dynamics of compressible fluids with speeds over $v > 10\,\mathrm{m/s}$. The solution is unstable, and it is not of converging character in the application of either the FEM or the FVM. The physical model for the part of the area Ω_1 with an incompressible fluid from the distribution of velocities (pressures) is determined on the basis of the dynamic condition

$$\mathrm{div}\,\mathbf{v} = 0, \tag{9}$$

in the state of steady flow and considering the known distribution of the specific mass ρ

$$\mathrm{div}\,\rho\,\mathbf{v} = 0. \tag{10}$$

The fluid flow can also be described as eddy, and we then have

$$\mathrm{rot}\,\mathbf{v} = 2\omega, \tag{11}$$

where ω is the angular speed of fluid. By applying Stoke's and Helmholtz's theorems for the moving particle and the continuity equation, we formulate from the balance of forces the Navier-Stokes equation [3] for the fluid element

$$\frac{\partial \mathbf{v}}{\partial t} + \mathbf{v} \cdot \mathrm{grad}\,\mathbf{v} = \mathbf{A} - \frac{1}{\rho}\mathrm{grad}\,p + \boldsymbol{\upsilon} \cdot \Delta \mathbf{v}, \tag{12}$$

where $\mathbf{A}$ is the external acceleration, p is the pressure, $\boldsymbol{\upsilon}$ is the kinetic viscosity. In the above Equation (12), the pressure loss can be superseded by the function

$$\begin{aligned} \mathrm{grad}\,p = &- \left(K_x \rho \mathbf{v}_x \left|\mathbf{v}\right| + \frac{f_r}{D_h} \rho\, \mathbf{v}_x \left|\mathbf{v}\right| + C_x \mu_p \mathbf{v}_x \right) \mathbf{u}_x - \left(K_y \rho\, \mathbf{v}_y \left|\mathbf{v}\right| + \frac{f_r}{D_h} \rho \mathbf{v}_y \left|\mathbf{v}\right| + C_y \mu_p \mathbf{v}_y \right) \mathbf{u}_y \\ &- \left(K_z \rho\, \mathbf{v}_z \left|\mathbf{v}\right| + \frac{f_r}{D_h} \rho\, \mathbf{v}_z \left|\mathbf{v}\right| + C_z \mu_p \mathbf{v}_z \right) \mathbf{u}_z \end{aligned} \tag{13}$$

where K represents the locally restricted pressure forces, f_r is the drag coefficient, D_h is the hydraulic radius, C is the transmissivity of the system, μ_p is the fluid dynamic viscosity, $\mathbf{u}_x$, $\mathbf{u}_y$, $\mathbf{u}_z$ are the unit vectors of the Carthesian coordinate system. The drag coefficient can be substituted with a function from the Blasi formula

$$f_r = aR_e^{-b}, \tag{14}$$

in which the coefficients a, b are determined according to reference [4], and R_e is the Reynolds number. The above-described model can be further solved using again the finite element or the finite volume methods (FEM; FVO). Their main limitation can be identified in the necessity to correctly formulate the dependence of instantaneous values of velocity $\mathbf{v}$ (x, y, z, t) on time and space, and their major advantage consists in the evaluation accuracy and solution stability in the time domain. In the search for the convergent system, we tested various approaches based on ANSYS, SFX and DYNA [6]. For the FVM, it is possible to expect here a converging solution up to the mean velocity having the maximum of 150 m/s, as previously obtained from the CFX program. The ANSYS tool uses, at speeds of $Ma > 3$ for the compressible environment at the boundary between the wall and the fluid, the Van Driest transformation

$$U_{com,x,y,z} = \frac{u_\tau}{\kappa} \ln\left(\frac{y^* y}{\upsilon}\right) + C \tag{15}$$

where $U_{com,x,y,z}$ is the logarithmically expressed speed of the compressible medium wave, u_τ is the velocity in the transverse direction, κ is the constant, y is the distance from the wall, υ is the specific volume, C is the constant. Another option consists in applying the shock load method [5], which is known from its use with solid states and compressible fluids. Major attention has to be paid to the model of the material, considering the following aspects:

1. elastic deformation (v_d — the speed of incidence; D — the load intensity), $v_d \approx 1$ m/s, $D \approx 10^{-5}$.
2. beginning of plastic deformation, $v_d \approx 10$ m/s, $D \approx 10^{-3}$.
3. plastic deformation, $v_d \approx 100$ m/s, $D \approx 10^{-1}$.
4. intensive plastic deformation, $v_d \approx 1000$ m/s, $D \approx 10^{+1}$.
5. phase and chemical variations in the material, $v_d \approx 10000$ m/s, $D \approx 10^{+3}$.

To facilitate successful creation and solution of the model, a higher number of stability conditions have to be applied during the formulation of the physical model. Thus, it is convenient to use the law of conservation of mass, the law of conservation of momentum, and the law of conservation of energy. These physical models are then converted to a mathematical model in the form

$$[M_F]\left\{\ddot{S}\right\} + [C_F]\left\{\dot{S}\right\} + [K_{F1} - K_{F2}]\{S\} = \begin{bmatrix} 0 & 0 & 0 & 0 \\ 0 & 0 & 0 & 0 \\ 0 & 0 & 0 & 0 \\ -K_{F5} & K_{F4} & -K_{F3} & K_{Fe} \end{bmatrix} \begin{Bmatrix} F \\ p_\sigma \\ p_n \\ E_{Te} \end{Bmatrix}, \tag{16}$$

where M_F, C_F, K_{F1}, K_{F2}, K_{F3}, K_{F4}, K_{F5}, K_{Fe} are the coefficients of the systems of equations of the LS Dyna module (the ANSYS tool) [6], S is the discrete nodal values of the displacement vectors. The entire solution is carried out via the explicit method for transient analysis, whose closer description can be found in reference [6]. The model of the physical approach is best described within source [7] as a dynamic model of viscous fluids. This model is based on dynamic stability of the system and complemented with the laws of conservation of mass, momentum, and energy; the formulation is known as the dynamic equilibrium equation, and its structure can be obtained via combining the Equations (2) and (3).

$$\rho\frac{dv}{dt} = f_s + div\vec{\vec{T}} \quad \text{in the area } \Omega_F. \tag{17}$$

3. ANALYSIS AND EVALUATION OF THE NUMERICAL MODELS

The geometry and distribution of the materials are shown in Fig. 1(b). The unlimited model representing the propagation of the detonation and the pressure wave was analysed as a 1D task. For the model of the explosive, we used the TNT agent in an elongated charge having the diameter of 8 mm. The air was included up to the distance of 200 mm. Subsequently, the resulting pressure

wave was transferred to a 2D model, which was carried out using the AUTODYN 2D tool; the results of the analysis are presented in Fig. 2 for the time interval of 0–200 µs from the beginning of the detonation. Here, the interpreted analysis of the pressure field distribution is presented. At the moment the wave front reflects from the walls of the container, the interference of the waves and the wave propagation on the surface of the container wall will occur.

When designing a system for the cleaning of small-size containers whose dimensions range between 0 µs and 10 cm, we can act on the container walls by utilising the properties of an electric discharge and creating a detonation wave through a controlled process. This method is characterised by several advantageous aspects, above all repeatability and safe formation or shaping of the detonation wave via electronic circuits. Thus, the described technique is suitable for use in demanding applications, for example the removal of nanoelements, which may stick to the container wall and are difficult to identify. In the given context, the proposed approach can also be suitably utilised to eliminate materials chemically unsafe of consisting of multiple biological structures. In containers with dimensions ranging between 100 cm and 10 m, it is possible to exploit the chemical reactive and formation processes related to detonation. An example of such technology consists in solidifying towers. To describe solidification as a waste material conversion process, let us refer to the object in Fig. 3, in which the flue ash obtained after the first stage of combustion product cleaning is mixed with the output of the second stage of purification; water and cement are used as the binding agents.

At present, solidifying towers are cleaned either mechanically (Fig. 3(b) or chemically. In Fig. 3(c), we present the use of blasting technics for the decontamination of solidifying towers. The intensity of the shock wave I is directly proportional to the initial energy ΔE and indirectly proportional to the propagation plane S, considering a spherical plane. $I = \Delta E/S$, where $S = 4\pi \cdot l_2$,

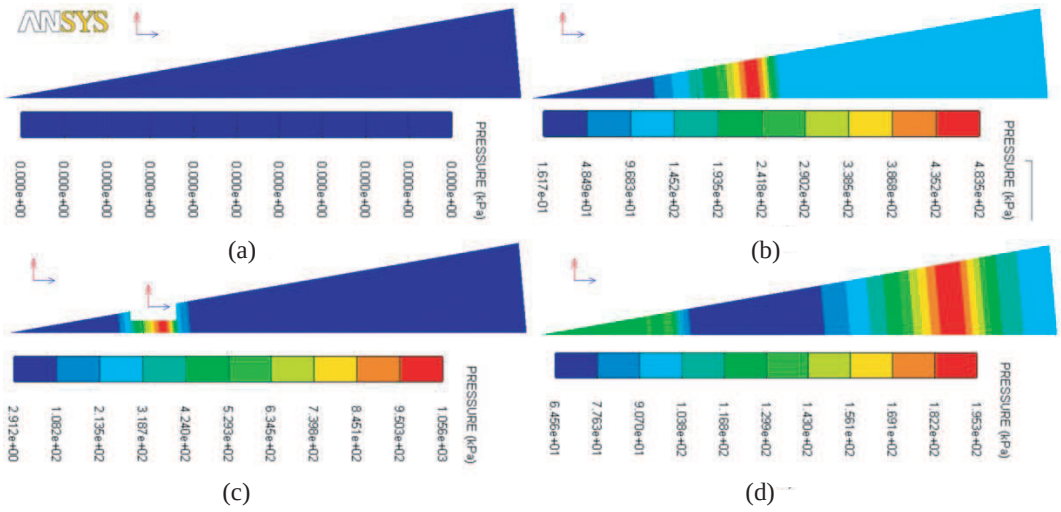

Figure 2: (a) The initial pressure state $p(t)$, $t = 0$. (b) The pressure distribution $p(t)$, $t = 30$ µs. (c) $p(t)$, $t = 60$ µs. (d) $p(t)$, $t = 195$ µs.

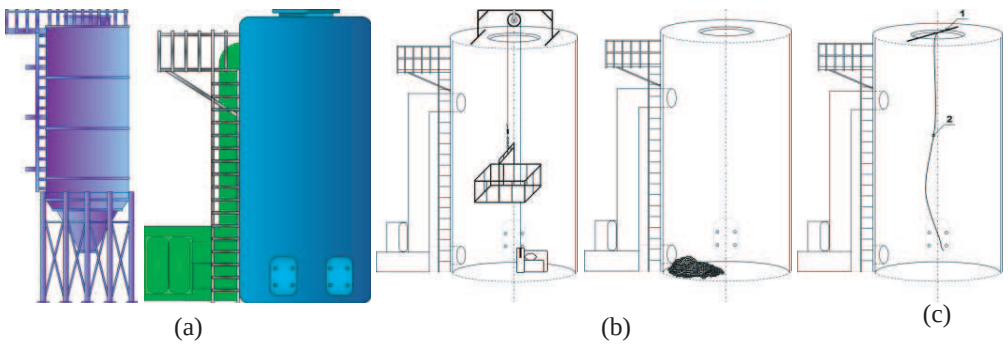

Figure 3: (a) A solidifying tower. (b) Mechanical cleaning of a solidifying tower. (c) Cleaning process using an elongated charge.

in which l_2 is the distance of the direct detonation line 1 from the location of the detonation origin. The actual cleaning process exploits the energy of a shock wave. The shock wave induced by the blast of an explosive charge acts both on obstacles in its path and on the environment through increased pressure and via the related dynamic forces. This reaction can be utilised in reducing the unfavourable effects upon the container wall during the interference of shock waves generated by smaller charges.

The interference of two circular or spherical waves, Fig. 4, occurs as a product of the burning of two charges located at an ample distance from each other. An interfered wave develops within this process, and the resulting split waves propagate from both sources simultaneously against one another. Here, the aim is to acquire identical waveforms of the waves in time; in this state, the waves oscillate with the same phase. The obtained superposed wave will create a reflected component, Fig. 4, which propagates in the opposite direction at a speed up to 26-fold higher. Such a speed value constitutes the double of the value of the reflexive pressures.

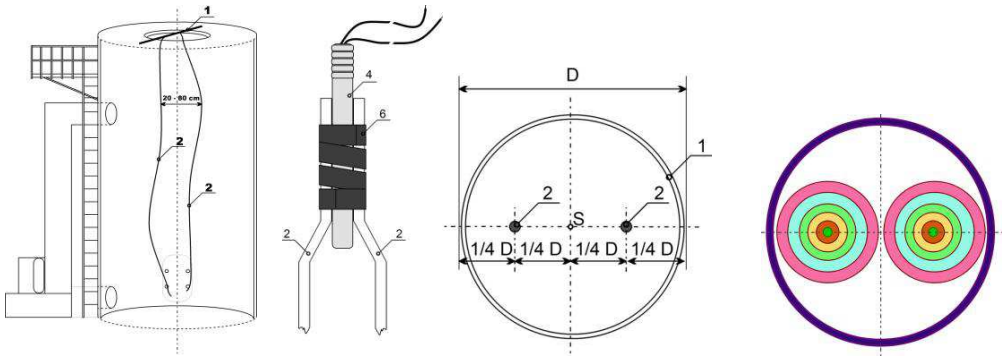

Figure 4: The arrangement of two elongated charges and the shock wave propagation.

4. CONCLUSION

The described technique of shock wave generation ensures a higher efficiency rate in the cleaning of container surfaces. In small-sized containers, the desired detonation waves can be obtained via various physical processes or phenomena, for example through controlled electric charges in the air or another applicable gas.

ACKNOWLEDGMENT

The research described in the paper was financially supported by Czech Science Foundation (GA 13-09086S), a project of the BUT science fund, No. FEKT-S-14-2545/2014, and a project from the Education for Competitiveness Operative Programme, No. CZ.1.07.2.3.00.20.0175 (Electro-researcher).

REFERENCES

1. Foerster, C. L., C. Lanni, R. Lee, G. Mitchell, and W. Quade, "Tests of an environmental and personnel safe cleaning process for Brookhaven National Laboratory accelerator and storage ring components," *J. Vac. Sci. Technol. A*, Vol. 15, No. 3, 731–735, May/Jun. 1997.
2. Mathewson, G., J.-P. Bacher, K. Booth, R. S. Calder, G. Dominichini, A. Grillot, N. Hilleret, D. Latorre, F. Le Normand, and W. Unterlerchner, "Comparison of chemical cleaning methods of aluminum alloy vacuum chambers for electron storage rings," *J. Vac. Sci. Technol. A*, Vol. 7, No. 1, 77–82, Jan./Feb. 1989.
3. Fleischner, P., "Hydromechanika," 186 s, Skripta VUT FS, VUT, Brno, 1990 (Hydromechanics), ISBN 80-214-0266-1.
4. Černoch, S., "Strojně technická příručka," 12, přepracované vydání, 386 s, SNTL Praha, 1968 (in Czech).
5. Buchar, J. and J. Voldřich "Terminální balistika," ACADEMIA, AV ČR Praha, Praha, 2003
6. "Manuály ANSYS v12.0," Huston, USA, 2009 (ANSYS Manuals).
7. Brdička, M, L. Samek, and S. Brnuno, "Mechanika kontinua," ACADEMIA, No. CV 2000, sv. 481, CS AV Praha, 2000 (Continuum Mechanics).

Elimination of a Fire through Shock Wave Interference: The Numerical Model and Application Scenarios

M. Janicek, P. Fiala, and R. Kadlec
Department of Theoretical and Experimental Electrical Engineering
Faculty of Electrical Engineering and Communication
Brno University of Technology, Technicka 12, Brno 616 00, Czech Republic

Abstract— The authors present a non-traditional approach to the elimination of large-scale fire events, for example road and railway tanker accidents. The proposed solution consists in utilising the interference of shock waves generated by highly explosive substances. Within the analysis, the authors introduce the results obtained via the numerical modelling of the dynamical system behaviour and include the basic verification of the solution, which is carried out by means of the related experimental model.

1. INTRODUCTION

The energy of a shock wave can be utilised to stop the propagation of a land or forest fire [1]. If the use of concentrated charges is assumed, then these charges (weighing between 6 and 12 kilograms each) are to be distributed in a row at the distance of 1 m from one another, connected via a detonating cord, and detonated simultaneously just before the arrival of the fire front to approximately 10 meters from the explosive setup (Fig. 1).

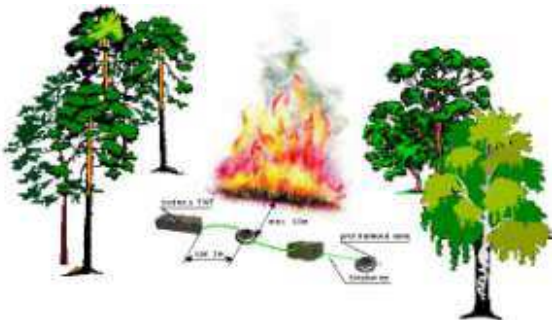

Figure 1: The use of concentrated charges arranged in a row to generate a shock wave suppressing the propagation of a surface fire.

Generally, it is possible to extinguish a fire by means of elongated charges containing suitable blasting agents [2]. The propagation of a surface fire can be effectively stopped by the initiation of charges configured in two rows or a circle; in this case, the energy released by two or more interfering shock waves constitutes a powerful fire-eliminating instrument, as indicated in source [2].

2. NUMERICAL MODEL AND ITS FORMULATION

The actual creation of the numerical model is based on the laws of hydrodynamics, or the behaviour of compressible and incompressible fluids; see references [2]. In the given instance, the exciting detonation wave travels through the air, which (in the assumed conditions) acts as a compressible fluid; the interference of the waves, however, significantly changes the superposed wave propagation speed in the air, and this environment can be interpreted in the indicated situation as an incompressible fluid. For the definition of the model, we assume the equilibrium state, and this description constitutes the basis of the numerical model design. The model of the assumed task is restricted to closed area Ω_F according to Fig. 2. We then have

$$\Omega_F = \bigcup_{i=1}^{4} \Omega_i \text{ a } \bigcup_{i=1}^{4} \Gamma_{\Omega i} = \Gamma_F. \tag{1}$$

From the state of the dynamic equilibrium of the system in the area Ω_F, it is possible to observe (in a simplified manner) at the boundary Γ_1 the conditions for the undamped process of an incompressible environment.

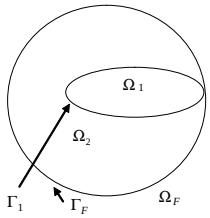

Figure 2: The general distribution of areas and boundaries in the numerical model.

To facilitate successful creation and solution of the model, a higher number of stability conditions have to be applied during the formulation of the physical model; thus, the designed mathematical model becomes more stable. For the given purpose, we can conveniently utilise the following formulas: The law of conservation of mass

$$\rho_0 U_s = \rho_1 (U_s - v_p) \quad \text{in the area } \Omega_F, \tag{2}$$

where ρ_0 is the volume density in the initial state (or in an uncompressed space), U_s is the wave speed in the uncompressed space, v_p is the shock wave speed, ρ_1 is the volume density in the compressed space. Then, for the law of conservation of momentum, we can write the equation

$$p_1 - p_0 = \rho_0 U_s v_p \quad \text{in the area } \Omega_F, \tag{3}$$

where p_1 is the instantaneous value of pressure in the compressed region, and p_0 is the instantaneous value of pressure in the uncompressed region. The law of conservation of energy is expressed as

$$\vec{e}_{Te1} - \vec{e}_{Te0} = \frac{1}{2}(p_1 + p_0)(V_0 - V_1) \quad \text{in the area } \Omega_F, \tag{4}$$

where $\vec{e}_{Te1}$, $\vec{e}_{Te0}$ are the specific deformation tensors in the compressed (index 1) and uncompressed space (index 0), V_0 is the specific volume of the uncompressed region, V_1 is the specific volume of the compressed region. The above-discussed models are formed using ANSYS tools, such as LS Dyna or Autodyn [4]. As both the burning and the pressure wave propagation are dynamical processes, it is suitable to complete the model with the parameter of the state of oxygen balance during the burning [3].

Figure 3: The distribution of the pressure state $p(t)$, (a) $t = 0.0\,\mu s$, (b) $t = 203.0\,\mu s$, (c) $t = 318.0\,\mu s$ in elongated charges.

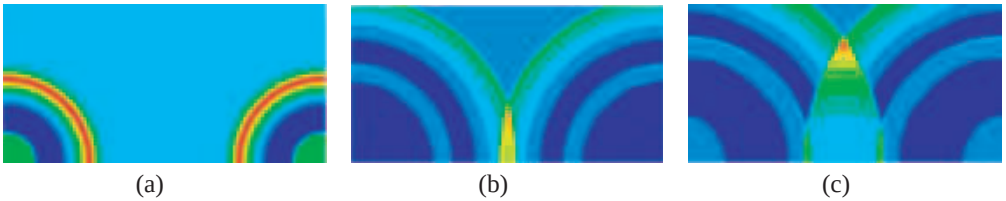

Figure 4: The initial pressure condition $p(t)$, (a) $t = 11.0\,\mu s$, (b) $t = 350.0\,\mu s$, (c) $t = 500.0\,\mu s$ in the circular configuration of elongated charges.

The distribution of the state of instantaneous oxygen balance in a fluid (or the air) can be determined according to several models [10], from which the Jones-Wilkins-Lee model appears to be the most convenient option for the purposes of the research described herein. The instantaneous

oxygen distribution has to be considered during the actual creation and processing of the model. The model can be expressed by the formula

$$p(\rho, W) = A\left[1 - \frac{\omega\rho}{R_1\rho_0}\right] e^{\left(-\frac{R_1\rho_0}{\rho}\right)} + B\left[1 - \frac{\omega\rho}{R_2\rho_0}\right] e^{\left(-\frac{R_2\rho_0}{\rho}\right)} + \omega\rho\,(W - W_0)\,, \tag{5}$$

where A, B, R_1, R_2, ω are the constants for the given blast, and W_0 is the reference internal energy in the uncompressed state. Examples of the representation of pressure development analysis for both the standard arrangement of elongated charges and their circular configuration are shown in Figs. 3 and 4, respectively.

3. DESIGN OF A FIRE ELIMINATION METHOD UTILISING A CONTROLLED EXPLOSION

Tanker fires on railway tracks or roads are often poorly accessible for fire-fighting trucks and other heavy equipment, and this condition constitutes a significant problem as classical fire extinguishing methods frequently have to be used. In this context, the main disadvantage of the classical techniques consists in two aspects, namely the use of high-pressure hoses and limited access to water sources. Owing to these drawbacks, it is often necessary to carry out a very demanding transfer of fire-fighters and the related bulk of technical equipment to suppress a mere local fire, which is nevertheless situated in difficult terrain [7, 8]. In such conditions, considerable damage to property may arise in addition to personal health risks. Another important factor is the actual length of the fire suppression process; with long quenching of burning liquid fuel, there is a high probability that the fire will eventually produce a detonation and spread itself in the surrounding areas, Figs. 5 and 6. The above-described drawbacks and limitations of known fire-extinguishing methods related to flammable liquids transported by road or railway tankers can be substantially reduced by the proposed novel technique of eliminating such liquid substance fires [9]; more concretely, the discussed method is a procedure utilizing the interference of shock waves induced by the explosion of blasting agent charges. The principle of the technique consists in creating a direct or concave operational line formed by a homogeneous detonating system [2] (Fig. 5) or, alternatively, by individual detonating elements; these elements are then interconnected by means of a quick match string (Fig. 8) that carries the detonation pulse. The total detonating potential of the operational line corresponds to a speed of 4200 to 6700 $\mathrm{m \cdot s^{-1}}$. If we use a new version of electronic detonators, then each detonator can be placed separately in the individual detonating elements; subsequently, the relevant programming is carried out. Thus, we may eliminate the process of interconnecting the individual charges (detonating elements) by means of the quick match string that carries the detonation pulse (the detonating fuse/cord). The exact distance between this line for centralised detonation launch and the actual burning object depends on the fire intensity. The explosion of a charge in the air or a compressible fluid is accompanied by the propagation of a shock wave from the point of detonation, and this wave then progressively loses its energy until it converts itself into an acoustic wave, whose speed is identical with the speed of sound propagation. If the shock wave collides with a solid barrier, it reflects from this barrier and acts on it with a reflective pressure (whose value may reach as high as thirty six times the pressure on the shock wave front). These characteristics determine the eventual destructive force of the shock wave. However, the reflective pressure value in acoustic waves constitutes merely a double of the pressure on the shock wave front. It is possible to prevent the propagation of fire by means of exploding charges arranged in two rows (or in a circle); this arrangement enables us to utilise the interference energy of the impact and the reflection related to two (or several) shock waves. The interference of two circular (or spherical) waves occurs, for example, during the explosion of two charges which are placed within a sufficient distance from each other (Fig. 4). Thus, undulations are generated that propagate simultaneously against one another from the direction of both sources. If two charges of the same explosive having an identical weight are blasted at the same moment of t_0, they oscillate in identical phases. The resulting interfered wave is then given by the superposition of both travelling waves. If both the charges are blasted at the same moment of t_0, the wave fronts travel against each other and, after colliding at the speed of v_0, they induce a backward wave; this wave, however, has a speed of v_0 that may be up to 64-fold higher, which constitutes a double (the sum) of both reflective pressures. If we allow simultaneous induction of waves from two elongated charges arranged in a parallel way, with the fire area located between the charges, we obtain a situation when both the blast waves collide and reflect at a multiple speed in the middle of the fire area. The effect is multiply more intensive in comparison with the application of only one detonating wave, and the advantage of the

Figure 5: The photo documentation of a tanker railway collision.

Figure 6: The photo documentation of a tanker highway collision.

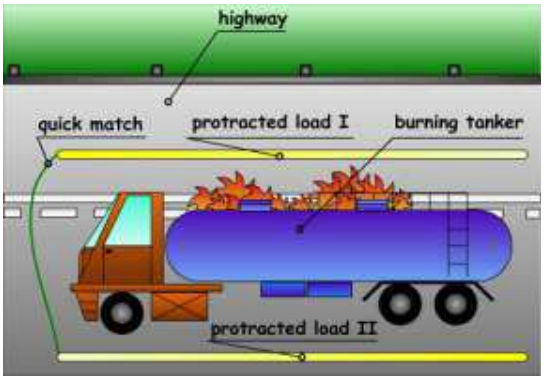

Figure 7: Elongated charges positioned to extinguish a burning tanker.

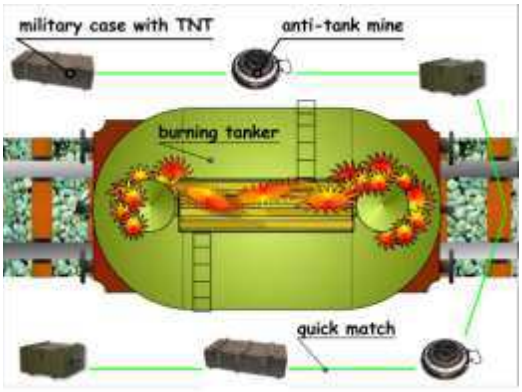

Figure 8: The arrangement of concentrated charges extinguishing the fire of a railway tanker.

solution consists in the fact that elongated charges can be located at a greater distance from the fire.

A homogeneous detonating system can be formed advantageously using a continuous elongated charge. A heterogeneous fire-quenching (operational) line usually consists of individual detonating elements; these elements can be set up by the help of concentrated charges (Fig. 8), partial elongated charges, anti-tank or anti-personnel mines, and explosive boxes (containers). In order to transfer the related detonation pulse, we can utilise instruments such as a detonating fuse or a new electronic detonator specially developed for the discussed purpose [2]. Depending on the applied initiators and detonation pulse transfer instruments [3], the detonation process is then started by means of fire initiation, electric ignition, or remote control.

4. CONCLUSION

The main advantages of the proposed method for local surface (ground) fire elimination using blasting technics consist in its simplicity, effectivity, and application characteristics. The last of these points primarily refers to possible utilisation of the method in emergencies where only a small number of people (rescuers) are involved or where water is available only with considerable difficulty. These aspects of the discussed method are further demonstrated on the reduced experimental models. Significantly, this fire extinguishing technique does not require the use of heavy or special machines, and it obviates the problems connected with the transportation of such machines or related fire-fighting persons. Thus, we may control and progressively extinguish even very complicated fires, which are often difficult to eliminate by means of currently available technologies. Above all, however, the proposed quenching method provides a higher degree of protection regarding the engaged fire-fighters and their costly equipment.

ACKNOWLEDGMENT

The research described in the paper was financially supported by a grant of the BUT science fund, No. FEKT-S-14-2545/201, and the authors also received assistance from projects within the Education for Competitiveness Operative Programme, Nos. CZ.1.07.2.3.00.20.0175 and CZ.1.07/2.3.00/3-0.0005.

REFERENCES

1. Government Decree No. 172/2001 Coll., "Laying down the rule of procedure for the act on fire prevention,".
2. Janíčk, M., *Dizertační práce: Využití trhací techniky při mimoř'adných událostech,* ev. č'ıslo: 28900220103001, Žilinská univerzita v Žilině, Fakulta špeciálného inžinierstva, Žilina, 2010, (Dissertation: *Application of Blasting Technics in Emergencies*, Reg. No. 28900220103001, Žilinská univerzita v Žiline, Faculty of Special Engineering).
3. Chitrin, L. I., *Fizika Gorenija i Vzyryva*, 437 s, GLAVPOLIGRAFPROM, USSR, Moscow, 1957.
4. Manuály ANSYS v12.0, Houston, USA 2009 (ANSYS manuals).

High Gain Electromagnetically Coupled Stacked Circular Disk Patch Antenna for Wideband Application

N. P. Yadav, W. Wu, and D. G. Fang
School of Optoelectronic, Nanjing University of Science and Technology, China

Abstract— Bandwidth enhancement behavior of an electromagnetically coupled stacked circular disk patch antenna is presented theoretically. The effects of feed point locations, radius of parasitic disk, and air gap-spacing are analyzed to achieve optimum conditions for wideband operation. The antenna shows a bandwidth as large as twelve times of that of a single circular patch antenna. The radiation patterns of the antenna are similar to those of the single disk antenna. The theoretical results are in reasonable agreement with the simulated ones from IE3D.

1. INTRODUCTION

A microstrip patch antenna has practical advantages such as low profile, light weight, low cost, and easy integration with printed circuits. One of the principal limitations of such antenna is its inherent narrow bandwidth which is of the order of few percent. It has been realized that bandwidth enhancement can be achieved by increasing effective volume of the patch antenna and introducing parasitic elements. The technique of stacking patches is one of the most popular ways to achieve broadband characteristic [1–3]. The present endeavor, therefore, is concerned with theoretical investigations in which bandwidth enhancement is achieved using two-layer electromagnetically coupled circular patch antenna. The theoretical investigations are carried out using cavity model and circuit theory concept. The theoretical results are compared with simulated results of the MoM based IE3D [4]. The details of investigations are given in the following sections.

2. THEORETICAL CONSIDERATIONS

The geometrical configuration of the two layered electromagnetically coupled stacked circular patch antenna is shown in Fig. 1. It consists of a driven circular patch of radius $a = 13.233\,\text{mm}$ and a parasitic circular patch of radius $b = 13.365\,\text{mm}$. The driven patch is printed on a substrate material-I of relative permittivity $\varepsilon_{rd} = 2.45$ and thickness $h_d = 1.522\,\text{mm}$. A coaxial probe of radius 0.564 mm excites the driven patch in TM_{11} mode of frequency 4.09 GHz. The probe feed is located at distance $a_f = 7.94\,\text{mm}$ from the center of the lower disk.

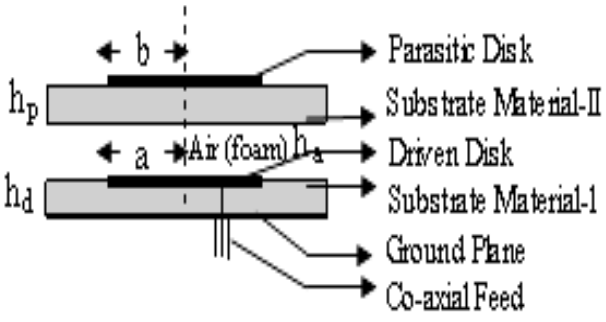

Figure 1: Geometrical configuration of the stacked antenna.

The parasitic patch is printed on a substrate material-II of thickness $h_p = 0.7609\,\text{mm}$ and dielectric constant $\varepsilon_{rp} = 2.45$. A foam material of relative permittivity $\varepsilon_{ra} = 1.22$ and thickness $h_a = 4.764\,\text{mm}$ is sandwiched between the two disks.

Under the assumptions of the cavity model, the stacked antenna can be considered to be consisting of two coupled cavity resonators, namely, lower cavity resonator and upper cavity resonator. The lower cavity resonator resembles a microstrip disk antenna covered with dielectric materials (foam and substrate material-II). Here, the effect of material of the upper patch may be neglected because fields are concentrated in the region between the lower patch and the ground plane. The

upper cavity resonator consists of uncovered upper disk patch and the lower disk patch. The resonance frequencies of each resonator of the stacked disk antenna can be calculated using an approach similar to that of single microstrip disk antenna. Also, when a microstrip disk is covered by dielectric materials, the resonance behavior and the impedance characteristics are changed with relative permittivity, loss tangent, and thickness of the substrate material.

Being covered with super-substrate, the effective relative permittivity of substrate materials for lower disk resonator is given as [5]

$$\varepsilon_{ef} = \varepsilon_{ra} q_1 + \varepsilon_{req} \frac{(1-q_1)^2}{\varepsilon_{req}(1-q_1-q_2)+q_2} \tag{1}$$

where q_1 and q_2 are the filling factors defined for $a/h > 1$ [5]. Also, ε_{req} is the equivalent relative permittivity of the substrate materials above the lower disk and it is given as [6].

$$\varepsilon_{req} = \frac{\varepsilon_{ra}\varepsilon_{rp}(h_a+h_p)(1-\tan\delta_a\tan\delta_p)}{\varepsilon_{rd}h_a + \varepsilon_{ra}h_d} \tag{2}$$

The resonance frequency of TM_{11} mode for the lower disk resonator is given as

$$f_{rd} = \frac{\alpha_{11}c}{2\pi a_{eff}\sqrt{\varepsilon_{ef}}} \tag{3}$$

where $\alpha_{11} = k_{11}a$ is defined by $J'(k_{11}a) = 0$. Also, c is the velocity of light in free space and a_{eff} is the effective radius of lower disk, given as [7]

$$a_{eff} = a\left[1 + \frac{2h_d}{\pi a\varepsilon_{ef}}\left(\ln\frac{\pi a}{2h_d} + 1.7726\right)\right]^{1/2}; \quad \text{For } a/h \gg 1. \tag{4}$$

Based on the cavity model, the input impedance of a microstrip disk antenna may be computed by modeling the microstrip antenna as a parallel resonant LCR circuit. Therefore, the equivalent circuit of lower disk resonator may be represented as shown in Fig. 2(a). The circuit parameters of this resonator can be calculated as [8]

$$R_d = \frac{h_d^2 E_0^2 J_1^2(k_{11}a_f)}{2P_T} \tag{5}$$

$$C_d = \frac{\pi a^2 \varepsilon_0 \varepsilon_{ef}}{h}\left\{1 + \frac{2h_d}{\pi a\varepsilon_{ef}}\left[\ln\frac{a}{2h_d} + 1.41\varepsilon_{ef} + 1.77 + \frac{h_d}{a}(0.268\varepsilon_{ef}+1.65)\right]\right\} \tag{6}$$

$$L_d = \frac{1}{4\pi^2 f_{rd}^2 C_d} \tag{7}$$

Here, E_0 is the electric field intensity at the feed point and P_T is the total power lost that includes the power radiated and the power attenuated in the disk resonators owing to the finite conductivity of the disk conductor and imperfect dielectric substrate. Thus, from Fig. 2(a), the input impedance of the lower disk resonator can be derived as

$$Z_d = \frac{j\omega R_d L_d}{R_d - \omega^2 R_d L_d C_d + j\omega L_d} \tag{8}$$

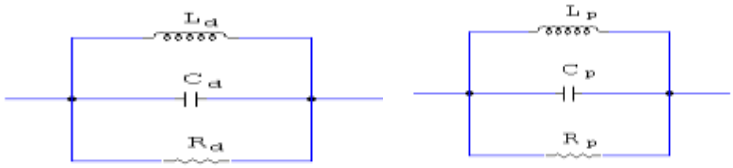

(a) (b)

Figure 2: Equivalent circuits of (a) driven disk, (b) parasitic disk.

As the upper parasitic patch is responsible for the upper disk resonator formed between the two disks, its resonance frequency can be given as

$$f_{rp} = \frac{\chi_{11} c}{2\pi b_{eff} \sqrt{\varepsilon_{req}}} \tag{9}$$

where $\chi_{11} = k_{11} b$ is defined by $J'(k_{11} b) = 0$ and b_{eff} is the effective radius of upper disk that can be computed using Equation (4) and replacing a, h_d, and ε_{ef} by b, $(h_p + h_a)$, and ε_{req} respectively. In addition, the equivalent circuit of the upper disk resonator is shown in Fig. 2(b), from which its impedance can be derived as

$$Z_p = \frac{j\omega R_p L_p}{R_p - \omega^2 R_p L_p C_p + j\omega L_p} \tag{10}$$

where, R_p, L_p, and C_p are the resonant resistance, inductance, and capacitance of the upper resonators. These parameters may be calculated using formulas (5)–(7) (Equations (5)–(7)) and replacing a, h_d, ε_{ef}, and f_{rd} by b, $(h_p + h_a)$, ε_{req}, and f_{rd} respectively.

Figures 3(a) & (b) show the current distributions on the lower driven disk patch and upper parasitic patch. Current flows on the lower patch due to coaxial feeding but the current on the upper parasitic patch is due to electromagnetic coupling between the two resonators.

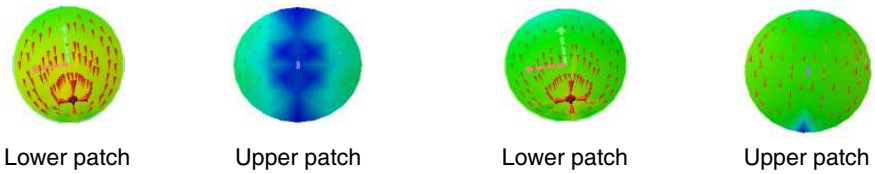

Figure 3: Current distributions on the patches at frequencies (a) 3.76 GHz and (b) 4.51 GHz.

The strength of current on the parasitic patch is dependent on the coupling coefficient. If L_m and C_m are the mutual inductance and mutual capacitance, the equivalent circuit showing electromagnetic coupling between two patches, may be represented as shown in Fig. 4(a). From the simplified equivalent circuit, shown in Fig. 4(b), the input impedance of the proposed stacked antenna can be derived as

$$Z_{in} = \frac{Z_d \left(Z_c + Z_p\right)}{Z_d + Z_c + Z_p} \tag{11}$$

Here, Z_c is the impedance due to inductive and capacitive coupling given as

$$Z_c = \frac{j\left(\omega^2 L_m C_m - 1\right)}{\omega C_m} \tag{12}$$

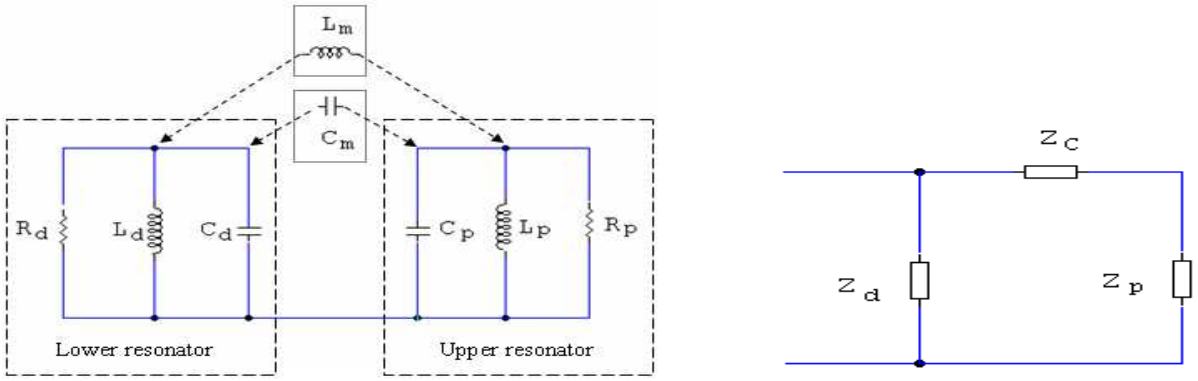

Figure 4: Equivalent circuits of proposed antenna (a) showing electromagnetic coupling and (b) after simplification.

The return loss value of the stacked antenna can calculated as

$$RL = -20\log\frac{1+\Gamma}{1-\Gamma} \tag{13}$$

where $\Gamma = \frac{Z_{in}-Z_0}{Z_{in}+Z_0}$ and Z_0 is the characteristic impedance of the coaxial feed (50 ohms).

The bandwidth of the antenna can be evaluated as

$$BW = \frac{f_2 - f_1}{f_c} \times 100 \tag{14}$$

where f_1 and f_2 are the lower and upper frequency band-edges for return loss value ≤ -10 dB and f_c is the center frequency.

For dominant mode TM_{11}, the E-plane and H-plane radiation patterns of the antenna can be calculated by adding together the contributions of the fields due to lower and upper patches. Thus the radiation fields of the antenna can be given as [8]

$$E_\theta = -j^n \begin{bmatrix} \frac{Va_{eff}k_0}{2}\frac{e^{-jk_0r}}{r}\cdot\cos\phi\cdot J_n'(k_0a\sin\theta) + K_c \\ \frac{Vb_{eff}k_0}{2}\frac{e^{-jk_0r}}{r}\cdot\cos\phi\cdot J_n'(k_0b\sin\theta) \end{bmatrix} \tag{15}$$

$$E_\phi = nj^n \begin{bmatrix} \frac{Va_{eff}k_0}{2}\frac{e^{-jk_0r}}{r}\cdot\sin\phi\cos\theta\cdot\frac{J_n(k_0a\sin\theta)}{k_0a\sin\theta} + K_c\frac{Vb_{eff}k_0}{2}\frac{e^{-jk_0r}}{r} \\ \cdot\sin\phi\cos\theta\cdot\frac{J_n(k_0b\sin\theta)}{k_0b\sin\theta} \end{bmatrix} \tag{16}$$

where V is the radiating edge voltage, and r is the distance of an arbitrary far-field point, k_0 is the propagation constant in free space in TM_{11} mode, and K_c in coupling coefficient of the two resonators.

3. DISCUSSION OF RESULTS

The effect of feed location (a_f) on the antenna performance is shown in Fig. 5. It is observed that a_f has crucial effect in decreasing the mismatching of the antenna. It also affects the operational frequency band of the antenna and gives maximum frequency. Fig. 6 shows the effect of air gap-spacing (h_a) on the antenna performance. It is found that h_a plays a crucial role in controlling the resonance frequencies of the antenna and its matching as well. For low value of h_a, matching at lower resonance frequency improves, while at a higher resonance frequency the case is otherwise. Similarly, at higher value of h_a matching at higher resonance frequency improves and degrades at lower resonance frequency. The best matching at both resonance frequencies is achieved at $h_a = 4.76$ mm. The variation of return loss with frequency at different values of radius (b) of the

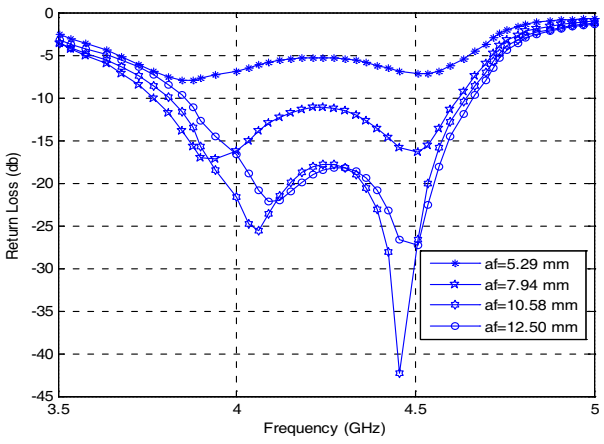

Figure 5: Return loss vs. frequency at different feed locations (a_f) for $a = 13.233$ mm, $b = 1.01a$, $\varepsilon_{rd} = \varepsilon_{rp} = 2.45$, $\varepsilon_{ra} = 1.22$, $h_d = 1.522$ mm, $h_a = 4.764$ mm, and $h_p = 0.7609$ mm, band for $a_f = 7.94$ mm.

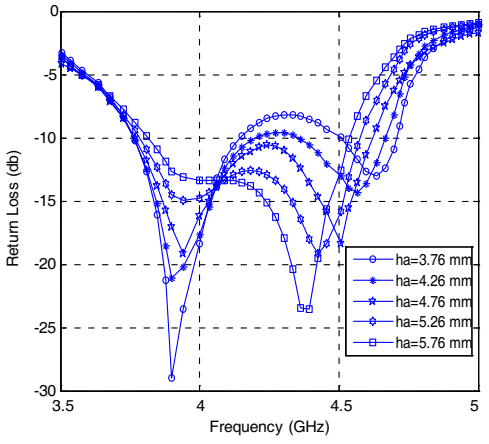

Figure 6: Return loss vs. frequency at different air gap-spacing (h_a) for $a = 13.233$ mm, $b = 1.01a$, $a_f = 7.94$ mm, $\varepsilon_{rd} = \varepsilon_{rp} = 2.45$, $\varepsilon_{ra} = 1.22$, $h_d = 1.522$ mm, and $h_p = 0.7609$ mm.

parasitic disk is shown in Fig. 7. It is observed that increase in b causes slight decrease in both the resonance frequencies but considerable decrease in frequency band. Also, it controls the matching effect of the antenna.

The optimum return loss curve at the optimum design parameters of the antenna is shown in Fig. 8, with a comparison between theoretical and simulated results. Theoretically, the antenna resonates at frequencies $f_1 = 3.9407\,\text{GHz}$ and $f_2 = 4.5085\,\text{GHz}$. On the other hand, simulated results show resonances at $f_1 = 3.9696\,\text{GHz}$ and $f_2 = 4.4848\,\text{GHz}$. From this figure it is noted that the antenna can operate with bandwidth of 19.79%, which is approximately twelve times the 1.66% bandwidth of single disk patch antenna.

The E- and H-plane radiation patterns of the optimized antenna at frequency 4.515 GHz are shown in Figs. 9 & 10. It is found that the 3-dB beam width of the antenna is 87.4° and 73° for E- and H-plane patterns respectively. They are 83.2° and 70° for simulated E-and H-plane patterns at the same frequency. The comparison shows good agreement between the theoretical and simulated results that justify the veracity of the proposed method.

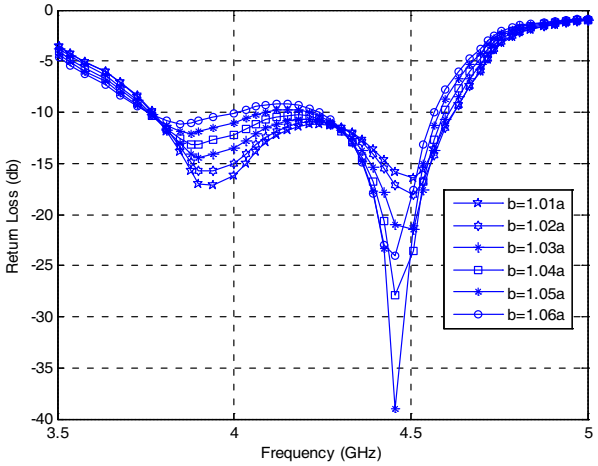

Figure 7: Return loss vs. frequency at different radius of parasitic disk (b) for $a = 13.233\,\text{mm}$, $a_f = 7.94\,\text{mm}$, $\varepsilon_{rd} = \varepsilon_{rp} = 2.45$, $\varepsilon_{ra} = 1.22$, $h_d = 1.522\,\text{mm}$, $h_a = 4.764\,\text{mm}$, and $h_p = 0.7609\,\text{mm}$.

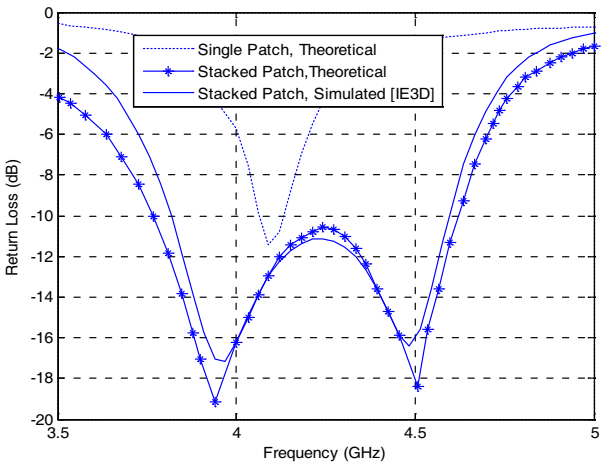

Figure 8: Optimum return loss curve for optimum design parameters: $a = 13.233\,\text{mm}$, $b = 1.01a$, $a_f = 7.94\,\text{mm}$, $\varepsilon_{rd} = \varepsilon_{rp} = 2.45$, $\varepsilon_{ra} = 1.22$, $h_d = 1.522\,\text{mm}$, $h_a = 4.764\,\text{mm}$, and $h_p = 0.7609\,\text{mm}$.

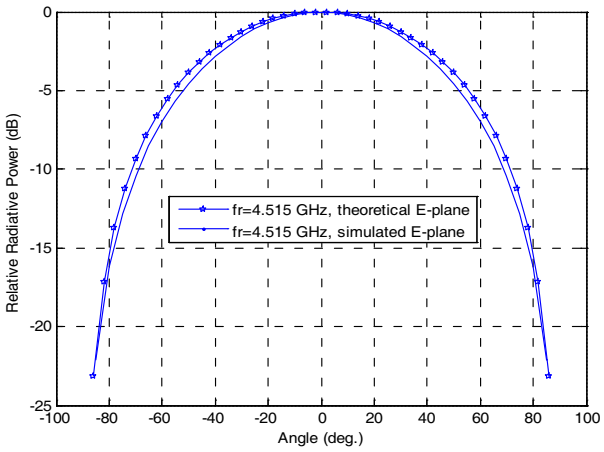

Figure 9: E-plane radiation patterns.

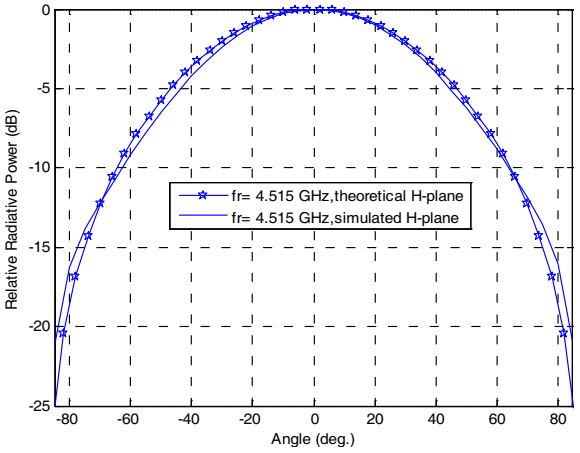

Figure 10: H-plane radiation patterns.

4. CONCLUSIONS

It may be concluded that due to dual resonance nature the antenna shows a broadband characteristics. Feed point location, radius of the parasitic disk, and air gap-spacing has profound effects on

the antenna performance. It is also concluded that the bandwidth of the antenna may be broadened to as high as 19.79% with proper combination of interspacing of the patches. The radiation patterns are reasonably good for the use in both linear and planar arrays.

REFERENCES

1. Ansari, J. A., P. Singh, and N. P. Yadav, "Analysis of wideband multilayer patch antenna with two parasitic elements," *Microwave and Optical Technology Letters,* Vol. 51, 1397–1401, 2009.
2. Ansari, J. A., N. P. Yadav, and P. Singh, "Analysis of disk patch antenna with parasitic elements in single and multilayer structures," *Microwave and Optical Technology Letters*, Vol. 52, No. 4, 865–870, Apr. 2010.
3. Bhatnagar, P. S., J. P. Daniel, K. Mohdjoubi, and C. Terret, "Experimental study on stacked triangular microstrip antennas," *Electron. Lett.*, Vol. 22, 864–865, 1986.
4. IE3D Zeland software Inc., USA, version 14.05, 2008.
5. Zhong, S. S., G. Liu, and G. Qasim, "Closed form expressions for resonant frequency of rectangular patch antennas with multidielectric layers," *IEEE Trans. Antenna Propagat.* Vol. 42, 1360–1363, 1994.
6. Ribero, J. M., J. P. Damiano, and R. Staraj, "Accurate analysis and synthesis of annular microstrip antennas," *IEEE Proc. Microw. Antenna Propag.,* Vol. 144, 341–346, 1997.
7. Derneryd, A. G., "Analysis of the microstrip disc antenna element," *IEEE Trans. Antenna Propagat.,* Vol. 27, 660–664, 1979.
8. Garg, R., P. Bhartia, I. Bahl, and A. Ittipiboon, *Microstrip Antenna Design Handbook*, 339–354, Artech House, Norwood, MA, 2001.

Analysis of Spectral Characteristics of Normal Fibroblasts and Fibroblasts Cultured with Cancer Cells in Terahertz Frequency Range

E. A. Strepitov[1], **I. V. Prozheev**[1], **N. S. Balbekin**[1], **M. I. Sulatsky**[1], **M. K. Khodzitsky**[1], **O. A. Smolyanskaya**[1], **A. S. Trulioff**[2],**and M. K. Serebryakova**[2]

[1]ITMO University, Saint-Petersburg, Russia
[2]Saint-Petersburg State University, Saint-Petersburg, Russia

Abstract— We propose a new method of cancer diagnostics based on identification of characteristic cancer spectral lines in the frequency range of 0.1–2 THz. Using terahertz spectral database of normal and pathological human tissues we could monitor the slightest changes caused by the appearance of cancer at the early stages.

1. INTRODUCTION

Nowadays despite the decreasing impact of cancer diseases [1], this problem remains relevant and it is still necessary to perform accurate diagnostics of cancer tumors at the early stages with high reliability. Invasive methods such as biopsy are predominant among various methods of cancer diagnostics [2, 3]. It means that a piece of human tissue with suspected tumor is removed, and if cancer cells are not found in this piece, the procedure should be repeated. Invasive methods are gradually being replaced by non-invasive terahertz (THz) imaging and tomography methods, which are more reliable, but do not allow unique identification of malignant tumor, and the results must be confirmed by invasive methods. Therefore it is essential to develop an independent and accurate methodology for cellular composition analysis of malignant tumors using a vast variety of heterogeneous cell cultures.

In our research we use non-invasive terahertz pulsed spectroscopy method, which has great advantages in comparison with other methods, including short time of excitation (it takes about 3–5 minutes to analyze a section of the sample) and other characteristics associated with the properties of THz radiation. There is no doubt about the statement that THz radiation is nowadays the most promising technique and favorably compares with other types of radiation. It should be mentioned that unlike microwave radiation THz radiation is not ionizing but it has sufficient penetration depth [4].

2. EXPERIMENTAL SETUP

The group of experiments was carried out using the reflection and transmission modes of the universal pulsed broadband THz spectrometer [5]. The generator of THz radiation is based on the InAs crystal in the magnetic system, bombarded with pulses of femtosecond laser FL-1. Following the passage through a teflon filter THz radiation hits the sample, which is fixed at the focal plane perpendicularly to the beam by a triaxial object table. The setup of THz spectrometer is characterized by the following parameters: the pulse power of 1 W, the pulse duration of 2.7 ps, the chopper frequency of 670 Hz, the spectral range from 0.2 to 2.0 THz, the average THz radiation power of 30 mW.

3. OBJECT UNDER THE STUDY

The research was conducted on the following cell cultures: primary human fibroblasts, transplantable lines A549 (human lung carcinoma cells) and COLO 320 HSR (sigmoid colon carcinoma cells); cell cultivation was carried out according to the recommendations of the "Bank of cell cultures" Institute of Cytology RAS. To perform the experiments cells were subcultured into wells of a 6 well flat-bottomed polystyrene plate ("Sarstedt", Germany) and incubated until a confluent monolayer was formed. To investigate the spectral characteristics of heterogeneous cell cultures two different cell types were added to one of the plate's well. Immediately prior to the measurement the biological medium was completely removed. All types of cell cultures were presented in four repeats.

The following Figure 3 demonstrates the sizes of normal fibroblasts in three dimensions.

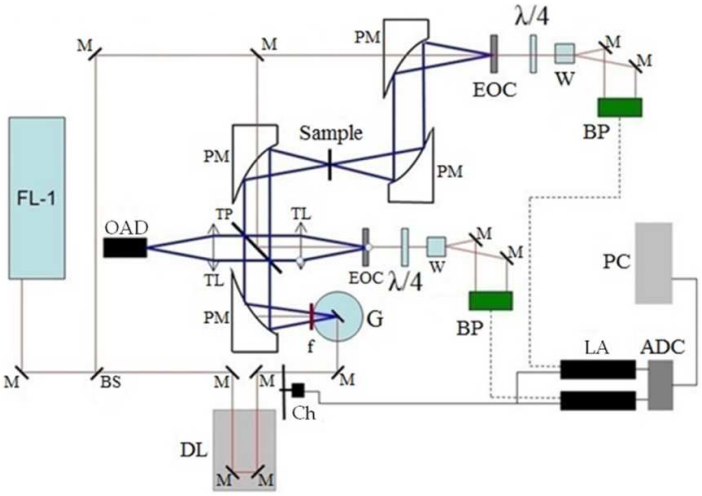

Figure 1: Scheme of the universal pulsed broadband THz spectrometer. FL-1 — infrared laser, M — mirrors, BS — beam splitter, DL — optical delay line, G — generator of THz radiation based on the crystal InAs, PM — parabolic mirrors, TL — lenses for THz radiation, f — teflon filter, TP — translucent silicon plate, Ch — chopper, EOC — electro optical crystal of CdTe, W — Wollaston prism, BP — balanced photodiodes, LA — lock-in amplifier, ADC — analog-to-digital converter, PC — personal computer, OAD — opto-acoustic detector (Golay cell).

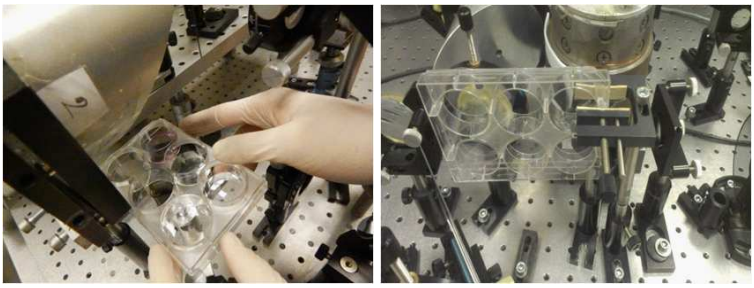

(a) (b)

Figure 2: Photo of (a) reflection mode and (b) transmission mode of the universal pulsed broadband THz spectrometer.

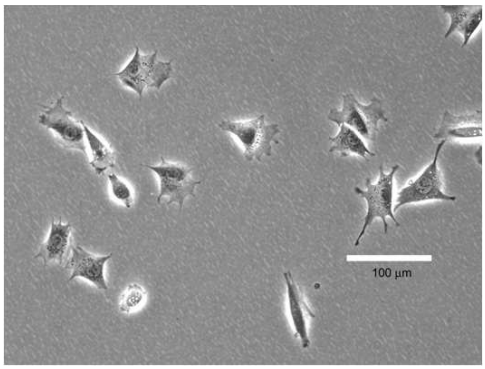

Figure 3: Normal fibroblast cells in-vivo [6].

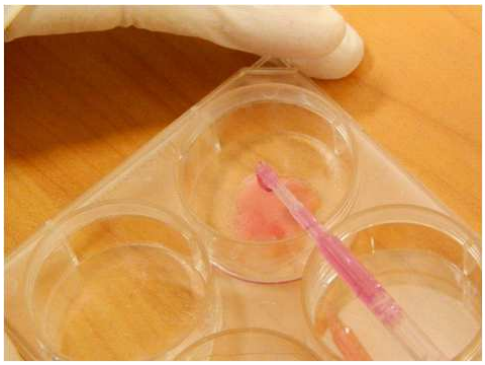

Figure 4: Sample preparation before the experiment.

As per this image the length and width seem to be $\sim$ 30–50 µm (the area should be roughly around 900 μm^2). The third dimension (thickness) can be assumed to be around 3–7 µm [6].

The following Figure 4 illustrates the process of samples preparation before the experiments: Physiological fluid which supports cultured cells must be removed using a special instrument to avoid the absorption of THz radiation by water. The duration of the experiment should not exceed 5 minutes due to the cells death in the absence of liquid.

4. RESULTS AND CONCLUSIONS

Based on the intensity of the reflection and transmission peaks we could make a conclusion about normal/abnormal state of the test cells.

Before conducting the main research the spectrum of the polystyrene material was obtained and analyzed in order to normalize the spectra of investigated samples (Figure 5).

The reflection and transmission spectra of normal fibroblasts, cancer cells, and fibroblasts cultured with pathological cells (A549, COLO 320 HSR) were obtained using standard THz pulsed spectroscopy technique in the frequency range of 0.2–2 THz.

The normalized and averaged reflection spectra of fibroblasts are presented in the Figure 6. It should be mentioned that spectra averaging was performed for the measurements of two groups of identical cells. In case of the fibroblasts with A549 cells one high intensity reflection peak at the frequency of 1.43 THz remains unchanged, the peaks at the frequencies of 1.69 and 1.77 decrease, the peaks at other frequencies are suppressed. In case of the fibroblasts with COLO 320 HSR cells the intensity of reflection peaks at the frequencies of 1.11, 1.33 and 1.43 THz decreases and one case of increase was registered at 1.77 THz.

The transmission spectra of fibroblasts were obtained and processed in a similar manner, and are presented in the Figure 7. In this part of the study we examine the case when fibroblasts were cultured with cancer cells A549. As was expected in this case two transmission peaks appear at the frequencies of 0.92 and 1.93 THz, the high intensity peak at the frequency of 1.52 THz disappears.

The key aspect of non-invasive diagnostics of human integumentary tissues diseases is a possibility to determine different cell types in the examined area. This is especially important in the diagnostics of tumors of various genesis. Appearance of the characteristic peaks, which are specific to certain cells, in the reflection and transmission spectra of the skin samples can be an early marker of malignant transformation.

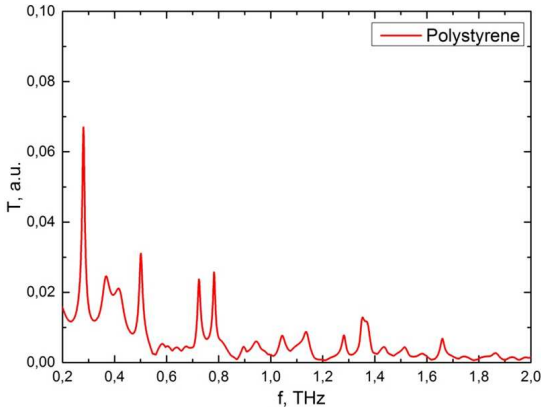

Figure 5: Transmission spectrum of polystyrene substrate without any cells.

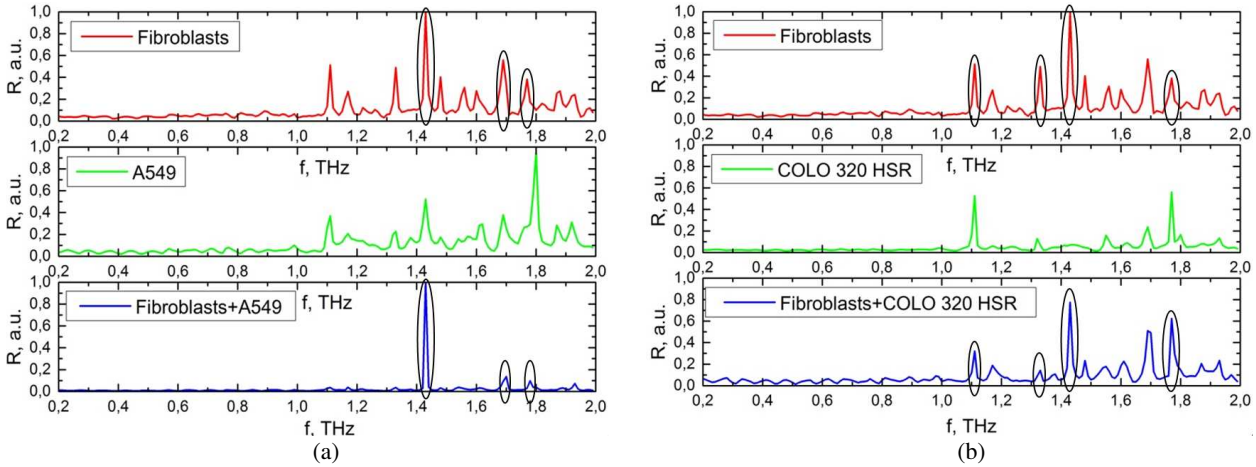

Figure 6: Reflection spectra of normal fibroblasts and fibroblasts cultured together with (a) A549 cancer cells, (b) COLO 320 HSR cancer cells.

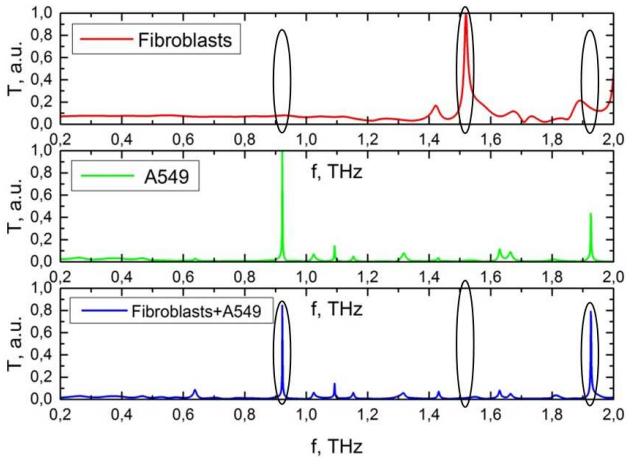

Figure 7: Transmission spectra of normal fibroblasts and fibroblasts cultured together with A549 cancer cells.

Thus, in this paper we propose a new method of diagnostics based on identification of characteristic cancer spectral lines, which allows monitoring of the appearance of cancer at the early stages.

ACKNOWLEDGMENT

This work was financially supported by Government of Russian Federation, Grant 074-U01.

REFERENCES

1. Siegel, R., J. Ma, Z. Zou, and A. Jemal, "Cancer statistics," *CA: A Cancer Journal for Clinicians*, Vol. 64, No. 1, 9–29, 2014.
2. Travis, W. D., et al., "Pathologic diagnosis of advanced lung cancer based on small biopsies and cytology: A paradigm shift," *Journal of Thoracic Oncology*, Vol. 5, No. 4, 411–415, 2010.
3. Cooperman, A. M., V. Katz, D. Zimmon, and G. Botero, "Laparoscopic colon resection: A case report," *Journal of Laparoendoscopic Surgery*, Vol. 1, No. 4, 221–224, 1991.
4. Nazarov, M. M., A. P. Shkurinov, E. A. Kuleshov, and V. V. Tuchin, "Terahertz pulse spectroscopy of biological tissues," *Quantum Electronics*, No. 7, 647–654, 2008.
5. Bespalov, V. G., et al., "Methods of generating superbroadband terahertz pulses with femtosecond lasers," *Journal of Optical Technology*, Vol. 75, No. 10, 636–642, 2008.
6. http://biology.stackexchange.com/questions/8994/fibroblast-cells-and-fibers.

Fully Monolithic Photonic Integrated Circuits for Microwave and Millimeter Wave Signal Generation

G. Carpintero[1], K. Balakier[2], C. Gordón[1,3], G. Kervella[4], R. Guzmán[1], A. Jiménez[1], M. J. Fice[2], M. Chitoui[4], F. Van Dijk[4], and X. Leijtens[5]

[1]Universidad Carlos III de Madrid, Madrid 28911, Spain
[2]Department of Electronic and Electrical Engineering, University College London
Torrington Place, WC1E 7JE, UK
[3]National Secretary of Science, Technology and Innovation, Senescyt, Quito, Ecuador
[4]III-V Lab, Palaiseau Cedex 91767, France
[5]COBRA Research Institute, Eindhoven University of Technology
Den Dolech 2, Eindhoven 5612AZ, The Netherlands
(*Invited Paper*)

Abstract— We present two different photonic integrated circuits aimed to generate electrical signals within the microwave and millimeter wave range with two different techniques. The first approach uses the heterodyne technique, implementing a monolithic dual wavelength source by integrating on a single chip two distributed feedback (DFB) lasers together with the high speed photodiode. The second approach, using mode locked lasers, describes a novel device structure based on multimode interference reflectors (MIR).

1. INTRODUCTION

Recent technology roadmaps point to the need of increasing the data rates used in wireless communication systems into the multi-gigabit-per-second to cope with the future needs based in current trends of the demand [1]. A current cost effective solution is to increase the carrier wave frequency into the millimeter wave region, moving to the E-band — 60 to 90 GHz — and beyond [2]. The difficulties to generate, amplify and modulate signals at these frequencies have been overcome by combining electronic with photonic techniques. Currently, most if not all of the reported wireless communication links operating above 100 GHz employ photonic generation of the carrier frequency. There are many different photonic techniques available to generate continuous-wave (CW) frequencies, such as optical heterodyning using two frequency-tunable laser diodes, optical heterodyning using two modes filtered from a multi-wavelength source, combining a CW laser with external modulator and using mode-locked lasers [3].

On several of these approaches, fiber optic components were needed in the photonic system to generate the signal. It has been demonstrated that slight integration efforts lead to significant improvement in the generated millimeter wave signal quality, highlighting the importance of monolithic integration [4]. Currently, InP generic foundry models offer active-passive integration technology to fabricate Photonic Integrated Circuits (PIC) on Multi-Project Wafer (MPW) runs. Complex functionalities can be integrated on a single chip combining a small number of standardized basic building blocks (BB) with high performance [5]. In addition, because generic integration technologies can serve a large market, this allows approaching costs provided by economy of scale. In this work, we demonstrate recent advances in the development of PICs for microwave and millimeter wave signal generation, ranging from the monolithic integration of dual distributed feedback (dual-DFB) lasers to fully monolithic Mode locked laser diodes (MLLD).

On the first approach, described in Section 2, we show a fully monolithic millimeter-wave wireless transmitter, including two DFB lasers and optical combiners for the dual wavelength generation, electro-optic modulators (EOM) for data modulation, and, crucially, integrated high-speed photodiodes (PD) to generate the millimeter electrical signal. Semiconductor optical amplifiers (SOA) are also included to compensate the optical losses. This approach, which has the great advantage of continuous tuning of the wavelength spacing, requires a dedicated fabrication process flow to develop all these components in the same chip.

Finally, Section 3 reports a novel monolithic mode-locked approach, showing a novel cavity structure using multimode interference mirrors (MIR) that is fully integrated in the PIC, without need of cleaved facets. This is a step forward since in a MLLD, the length of the resonator defines the repetition rate. With this approach we have a lithographic control of the cavity length. Also,

we address the drawback of using cleaved facets that prevents its integration with other optical components into a PIC.

2. PHOTONIC INTEGRATED HETERODYNE SOURCES

Dual wavelength photonic integrated circuits have commonly been developed through monolithic integration of at least two single wavelength semiconductor lasers and combining the two wavelengths on-chip. Several approaches have been already demonstrated, using as single wavelength semiconductor laser either a Distributed Bragg Reflector (DBR) [6] or a Distributed Feedback Lasers (DFB) [7]. We have recently produced a significant advance, developing a photonic integrated circuits that includes two DFB lasers, both having a phase shift written in the middle of the Bragg grating to guarantee single mode operation, together with a 2×2 multimode interference (MMI) coupler to combine the two wavelengths, bent SOAs to boost the optical power within the waveguides, and monolithically integrated Uni-Traveling Carrier photodiodes (UTC-PD). Between each MMI output and the UTC-PD, the light passes through another bent SOA (to boost the optical signal after passing through the combiner), an electro-optical modulator (to introduce the data modulation on-chip) and a straight SOA (to boost the signal entering the photodiode). The chip also provides an optical output combining the two wavelengths through a 2×1 MMI coupler. This combiner has been included in order to allow phase noise reduction through optical injection locking. The whole device is 4.4 mm long and 0.7 mm wide.

One of the main technological achievements of this approach has been the development of a fabrication process flow that allows the growth of the different components, in particular the high-speed photodiodes, in the single PIC. The layers were grown on a semi-insulating InP wafer in order to reduce the parasitic capacitance and get a sufficiently large detection bandwidth of the photodiodes. Active/passive integration is achieved using a butt-joint process. The active layers consist of 6 InGaAsP quantum wells. DFB lasers, SOAs and modulation sections contain the same quantum well stack. The Bragg grating is formed in an InGaAsP layer placed above the quantum wells and defined by e-beam lithography. The UTC layers are similar to the ones used in [8], are grown above the passive waveguide, to implement two $3 \times 15\,\mu$m UTC-PD. The fabrication required 3 epitaxial growth steps. After wafer thinning and back metal deposition a first set of measurements were performed directly on the wafer. After these first measurements, chips were cleaved and mounted on AlN submounts.

Using the left-hand side optical output of the device shown in Fig. 1, we have been able to measure simultaneously the spectrum of the optical signal generated by the chip and the generated high frequency electrical signal from the monolithically integrated UTC photodiodes when the DFB lasers were electrically tuned and some of the SOAs biased. For the measurements showing the tuning range of the two wavelengths, one of the DFB lasers was biased with a current varying from 50 mA to 86 mA while the other was biased with a current varying within a 50 to 198 mA range. Within these bias ranges, the UTC photocurrent varied between 1.12 and 6.27 mA. During operation, the photodiode is reversed biased at 2.5 V. Dark current of $< 10\,\mu$A was measured at this bias point. The measured optical spectra are presented in Fig. 2, where for the shown sample a continuous tuning of the optical frequency difference between the two DFB tones from 5 to 110 GHz is observed. The wavelength tuning is thermal through changes in the DFB bias current. Also, as the two lasers are close to each other, we observe thermal cross-talk between the two lasers.

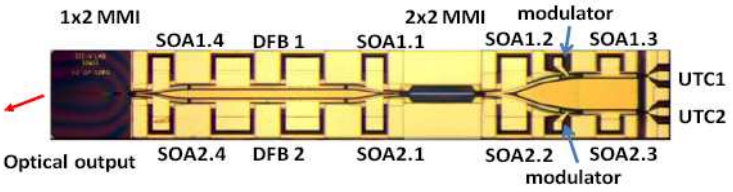

Figure 1: Microscope view of the dual DFB dual wavelength source.

Figure 3 shows the electrical spectra corresponding to the different bias conditions shown in Fig. 2, measured using a Rohde & Schwarz FSU67 electrical spectrum analyzer, with a FS-Z110 external mixer for measurements above 65 GHz. As the electrical spectrum shows, we observe the heterodyne signal without noticeable effects of the additional optical tones, although may have a negative effect generating a photocurrent and potentially limiting the maximum generated electrical power. In order to measure the maximum electrical power, we biased the two DFB lasers at 95 mA,

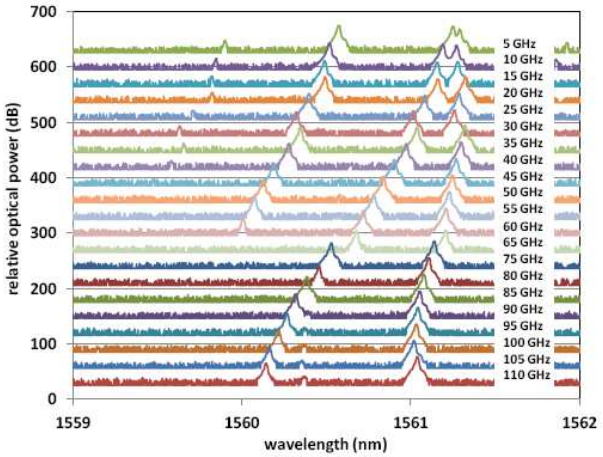

Figure 2: Optical spectrum at the optical output varying the current injected on the two DFB.

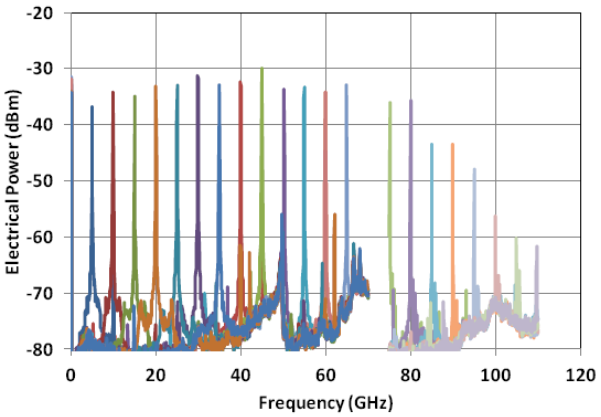

Figure 3: Electrical spectrum at the output pads of the monolithic UTC photodiode.

generating a wavelength spacing of 95.7 GHz. We measured −12 dBm detected power on an Agilent E4418B EPM series power meter with a W8486A power sensor a maximum when the photodiode was reversed biased to −2.5 V with 8.76 mA generated photocurrent. The losses due to RF probe and signal free space propagation path (< 3 cm) between antenna on the probe and power meter are not corrected.

3. PHOTONIC INTEGRATED MODE LOCKED SOURCES

Several wireless communication links that have been reported, operating above 100 GHz, employed pulsed sources to generate the carrier frequency. The pulsed system output ∼ 7 dB more power at the same P_{opt}, than heterodyne ones, suggesting that the conversion process depends more on the peak than the mean optical power. The drawback is that most mode-locked laser diodes (MLLD) usually require cleaved facets to create the cavity. We present here an alternative to mode locked ring lasers, in which the mirrors are defined by Multimode Interference Reflectors (MIR) [10], creating a novel mode locking structure shown in Fig. 4. The rectangular metal contacts upwards are the SOA sections. The downward contact is the saturable absorber section, and the extremes are 2×0 MIR reflectors, with 50% reflectance, providing the other 50% at the output on both ends. The device was fabricated in a Multi-Project Wafer (MPW) run for InP-based Photonic Integrated Circuits (PICs). The total length of the cavity is 2210 µm, which defines a frequency spacing of 18.67 GHz. The use of MIR reflectors gives full flexibility on the location of the device within the Photonic Integrated Circuit chip, except for the extremes, which are now of finite length, and in a passive epilayer. Thus we have located the SA along the active epilayer region, at the midpoint ($L/2$) of the cavity, to achieve a repetition rate at the second harmonic, 37.34 GHz by colliding pulse mode locking. Other locations for the SA are shown in the microscope photograph of the device in Fig. 4.

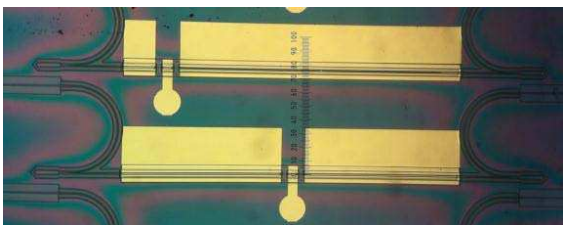

Figure 4: Microscope view of the monolithic mode-locked laser diode (mMLLD).

The device was characterized on a copper chuck stabilized in temperature to 17°C. The light outputs the chip through angled facets which are AR-coated. The optical spectrum, shown in Fig. 5, was observed collecting the light with an anti-reflection lensed fiber followed by a Yokogawa AQ6370B optical spectrum analyzer. The mode locking of the laser was studied observing the RF spectra, recorded on an Anritsu MS2668C Electrical Spectrum Analyzer and a XPDV2120R U2T photodiode with 50 GHz bandwidth. The mode beating spectrum with $I_{\text{SOA}} = 90$ mA and $V_{\text{SA}} = -2.5$ V is shown in Fig. 6(a), showing the fundamental frequency peak at 46.49 dB over the

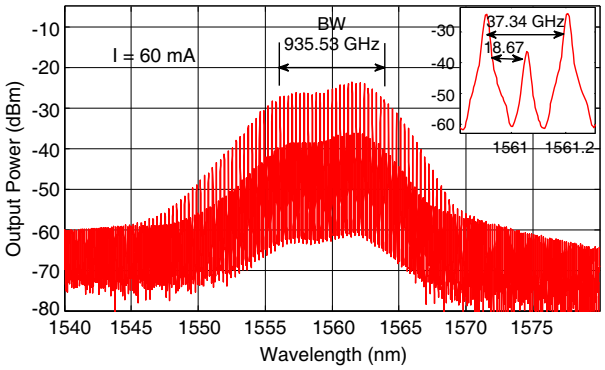

Figure 5: Optical spectrum at the optical output of the mMLLD.

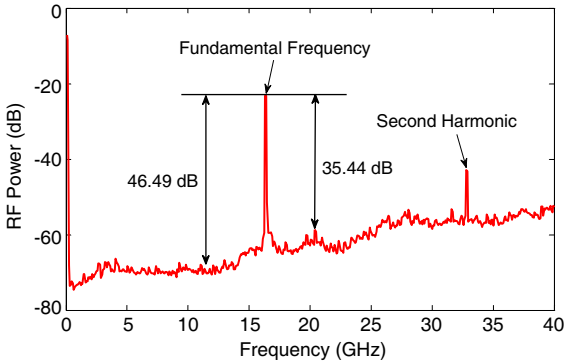

Figure 6: Electrical spectrum of the mMLLD.

noise floor at $f_{\text{rep}} \sim 16.7\,\text{GHz}$. The FWHM linewidth of the beating RF spectrum, when fitted to a Lorentzian lineshape is 91.90 kHz.

4. CONCLUSIONS

We have presented two different photonic integrated circuit approaches to generate carrier waves within the millimeter-wave frequency range. The approach using two monolithically integrated DFB lasers has the main advantage of the frequency tuning range, covering from 5 GHz to 110 GHz in a single device. We also report for the first time a new class of mode locked sources based on monolithic MIR reflectors, which can be integrated within a chip.

ACKNOWLEDGMENT

This work was supported by the European Commission and carried out within the framework of the European STREP project iPHOS (www.iphos-project.eu) under Grant agreement No. 257539.

REFERENCES

1. Ericsson Mobility Report, Nov. 2013.
2. Stohr, A., "Photonic millimeter-wave generation and its applications in high data rate wireless access," *IEEE Top. Meeting on Microwave Photonics (MWP)*, Oct. 5–9, 2010.
3. Nagatsuma, T., "Radio spectral evolution with photonics," *Int. Top. Meeting on Microwave Photonics*, Sep. 9–Oct. 3, 2008.
4. Nagatsuma, T., H. Ito, and K. Iwatsuki, "Generation of low-phase noise and frequency-tunable millimeter-/terahertz-waves using optical heterodyning techniques with uni-traveling carrier photodiodes," *36th European Microwave Conference*, Sep. 10–15, 2006.
5. Smit, M., X. Leijtens, E. Bente, J. van der Tol, H. Ambrosius, D. Robbins, M. Wale, N. Grote, and M. Schell, "Generic foundry model for InP-based photonics," *IET Optoelectronics*, Vol. 5, No. 5, 187–194, Oct. 2011.
6. Ponnampalam, L., M. Fice, F. Pozzi, C. Renaud, D. Rogers, I. F. Lealman, D. G. Moodie, P. J. Cannard, C. Lynch, L. Johnston, M. J. Robertson, R. Cronin, L. Pavlovic, L. Naglic, M. Vidmar, and A. Seeds, "Monolithically integrated photonic heterodyne system," *J. Light. Technol.*, Vol. 29, No. 15, 2229–2234, Aug. 2011.
7. Van-Dijk, F., A. Accard, A. Enard, O. Drisse, D. Make, and F. Lelarge, "Monolithic dual wavelength DFB lasers for narrow linewidth heterodyne beat-note generation," *Int. Topical Meeting on Microwave Photonics*, 73–76, Oct. 18–21, 2011.
8. Rouvalis, E., M. Chtioui, M. Tran, F. Lelarge, F. van Dijk, M. J. Fice, C. C. Renaud, G. Carpintero, and A. J. Seeds, "High-speed photodiodes for InP-based photonic integrated circuits," *Opt. Express*, Vol. 20, 9172–9177, 2012.
9. Moeller, L., A. Shen, C. Caillaud, and M. Achouche, "Enhanced THz generation for wireless communications using short optical pulses," *38th Int. Conference on Infrared, Millimeter, and Terahertz Waves (IRMMW-THz)*, 1–3, Sep. 1–6, 2013.
10. Kleijn, E., M. K. Smit, and X. J. M. Leijtens, "Multimode interference reflectors: A new class of components for photonic integrated circuits," *J. Light. Technol.*, Vol. 31, 3055, 2013.

Strong Confinement of Flexible Graphene Plasmons and Its Application

J. Wang, W. B. Lu, X. B. Li, J. Hu, and X. F. Gu
State Key Laboratory of Millimeter Waves, School of Information Science and Engineering
Southeast University, China

Abstract— The intrinsic strong confinement of flexible graphene plasmons (FGPs) is investigated in this paper, such unique property is interpreted by the ultra small thickness and metal like effective dielectric constant from the perspective of classical electromagnetic analysis. Utilizing this advantage, signals and energy can naturally propagate along curved surfaces with little curve-induced radiation loss and acceptable intrinsic propagation loss. Meanwhile, the metal plasmons (MPs) and graphene plasmons (GPs) on curved waveguides are simulated to illustrate the different property. At last, a stereo resonator is proposed as an application for the FGPs based devices.

1. INTRODUCTION

Metal plasmons (MPs), the collective oscillations of electron plasma generated by the interaction between photons and charge carriers, which can make light signals be localized and guided along the metal surfaces beyond the diffraction limit, opens the door of next generation highly compact devices [1–3]. And more specifically, when signals are expected to be manipulated at curved surfaces in many plasmonic circuits (e.g., ring resonators [4, 5]), the curve-induced radiation loss leads a considerable influence of the propagation efficiency [7–11]. Studies focusing the reduction of such radiation loss mainly include dielectric cladding [6, 12] and transformation optics [5], which greatly promotes the progress of the flexible metal plasmons (FMPs). In addition, new methods and materials are still being exploited to satisfy various application requirements, such as new property and different frequencies.

In the past few years, a new two dimensional (2D) material named graphene has been found to be able to support plasmons in the Terahertz (THz) and infrared (IR) regimes [13], which is similar with the conventional noble metals (e.g., gold and silver) in optical regime because they both exhibit a negative real part of permittivity. Graphene plasmons (GPs) are proved to be a promising alternative to the MPs with their unique tunability [13–15], which has been utilized to design reconfigurable components for various plasmonic devices. Among them, the "black hole" [16], planar lens [17, 18], four-status switch [19] and so on are proposed.

On the other hand, GPs are found to be able to confine on the curved surfaces [20] and sharp bends [21] naturally with little SIL. Therefore, such strong confinement of flexible graphene plasmons (FGPs) provides a more simple solution to adaptive plasmonic systems [22] than FMPs. In this context, this paper investigated the strong confinement of FGPs, which is by means of classical electromagnetic analysis. The lateral confinement and the propagation properties are exploited in detail. And for a better understanding of the comparison between the FMPs and FGPs, the thin metal film is discussed together with the graphene sheet.

2. THE INTRINSIC CONFINEMENT OF FGPS

2.1. The Effective Medium Model of Graphene

Compared with the complex explanation of electron behavior when the metal is irradiated by the light, the plasmonic waves can be acquired through a more simple way by using the Maxwell's equations and the boundary conditions [1]. In fact, the graphene plasmonic properties can be described through the classical electromagnetic theory which has a good agreement with the first principle calculations except its size goes down to quantum scale [23]. Here, only the bulk GPs is considered, and the graphene is modeled as an effective medium with an dielectric constant $\varepsilon_g = 1 + i\sigma/(t_g\varepsilon_0\omega)$ [24], where $t_g = 1\,\text{nm}$ is the effective thickness of single layer graphene, and the conductivity σ is calculated using the local random phase approximation (RPA) formula [25], which is related with the temperature T, Fermi level E_F, and the intrinsic relaxation time τ of carriers.

$$\sigma(\omega) = \frac{2e^2\omega_T}{\pi\hbar}\frac{i}{\omega + i\tau^{-1}}\log\left[2\cosh\left(\frac{\omega_F}{2\omega_T}\right)\right] + \frac{e^2}{4\hbar}\left[H\left(\frac{\omega}{2}\right) + i\frac{2\omega}{\pi}\int_0^\infty \frac{H\left(\frac{\omega'}{2}\right) - H\left(\frac{\omega}{2}\right)}{\omega^2 - \omega'^2}d\omega'\right] \quad (1)$$

where where $H(\omega) = \sinh(\omega/\omega_T)/[\cosh(\omega_F/\omega_T) + \cosh(\omega/\omega_T)]$, $\omega_F = E_F/\hbar$, $\omega_T = k_B/\hbar$, k_B is the Boltzmann constant and $\hbar$ is the reduced Planck constant. The first and second terms of Eq. (1) mean the intraband and interband responses respectively. Fig. 1 shows the dispersion relation of ε_g at the condition of $T = 300\,\mathrm{K}$, $E_F = 0.4,\ 0.6,\ 0.8\,\mathrm{eV}$ and $\tau = 3.0e^{-13}\,\mathrm{s}$.

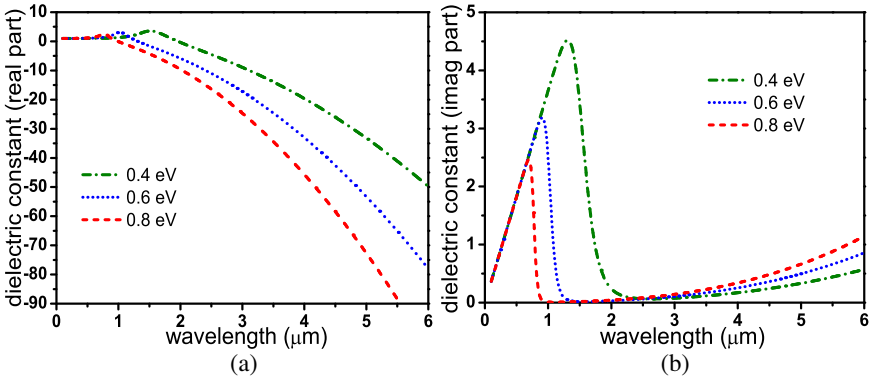

Figure 1: The dispersion relation of ε_g, (a) real part and (b) image part.

From Fig. 1, we can see that ε_g has a negative real part in the Terahertz (THz) and infrared (IR) regimes, which makes the graphene support transverse-magnetic (TM) mode waves. Moreover, on the optical regime, the the value of ε_g is positive, thus the graphene behaves a dielectric property. On the other hand, the image part of ε_g that influences the decay property of plasmonics ranges rapidly in the IR regime and slowly in THz regime, and we can find a frequency regime according to small image part of ε_g for the propagation of plasmonics at different Fermi levels.

2.2. Comparison of Graphene and Conventional Noble Metal Films

For the sake of comparison, a gold film with a finite thickness t_m and a dielectric constant ε_g calculated by the Drude model (the plasma frequency $\omega_p = 9.02\,\mathrm{eV}$ and the collision frequency $\omega_c = 0.0269\,\mathrm{eV}$) [26] is embedded in two dielectric media characterized by ε_1 and ε_2, as Fig. 2 displays.

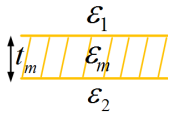

Figure 2: Gold film embedded in two media.

The characteristic equation of plasmons for the above metal film can be expressed as [27, 28]:

$$\tanh(\alpha_m t_m)(\varepsilon_1\varepsilon_2\alpha_m^2 + \varepsilon_m^2\alpha_1\alpha_2) + [\alpha_m(\varepsilon_1\alpha_2 + \varepsilon_2\alpha_1)\varepsilon_m] = 0 \tag{2}$$

where we have introduced $\alpha_j^2{=}\beta^2 - \varepsilon_j k_0^2$ with $j = \{1, 2, m\}$. The transcendental set of Eq. (1) contains symmetric and antisymmetric modes, resulting two branches of the dispersion relation curves. The case of $\varepsilon_1 = 1$ and $\varepsilon_2 = 1$ corresponds to the suspended gold film, which is considered in this paper. Fig. 3 presents the normalized propagation constant with different thicknesses at $0.63\,\mu\mathrm{m}$.

We can see from Fig. 3 that as the thickness decreases, the propagation constant divides into two modes, one is symmetric and the other is antisymmetric. It can be indicated from Fig. 3(a) that when the thickness becomes smaller, the symmetric mode plasmonic wave and free space light overlap, as a result, only the antisymmetric mode left. Simultaneously, the effective refractive index n_{eff} raises rapidly as the decrease of thickness. However, the propagation length $\ell_p = 0.5\mathrm{Im}(\beta^{-1})$ has an inverse relationship with the image part of the propagation constant, we can learn from Fig. 3(b) that the antisymmetric mode has shorter ℓ_p than symmetric mode. In short, the preliminary prediction is that the ultra thin graphene film has a large n_{eff} and a relatively small ℓ_p .

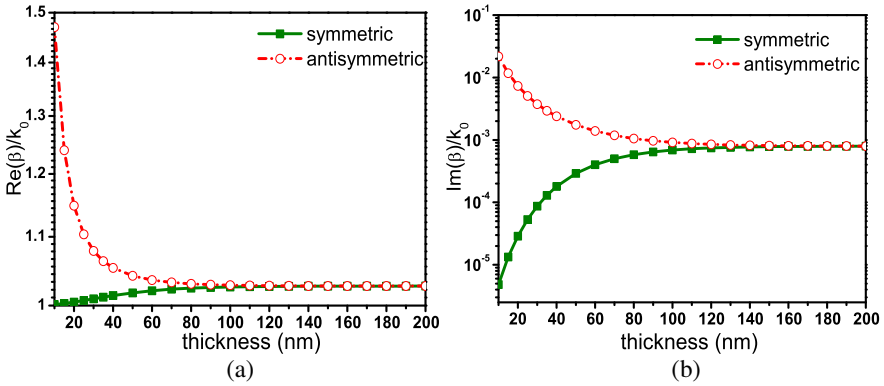

Figure 3: The relation between the (a) real part and (b) image part of the normalized propagation constant and thickness.

Next we analysis the propagation dispersion property of graphene. The propagation constant can be expressed in a simple form as [24]:

$$\beta = k_0\sqrt{1-\left(\frac{2}{\sigma\eta_0}\right)^2} \tag{3}$$

where σ is the conductivity of graphene, and η_0 is the impedance of free space. And the confinement is characterized by the lateral decay length, which is defined as $\ell = 1/\mathrm{Re}[\sqrt{\beta^2 - k_0^2}]$ [29]. Fig. 4 exhibits the propagation length (a) and lateral decay length (b) of graphene and a 40 nm gold film.

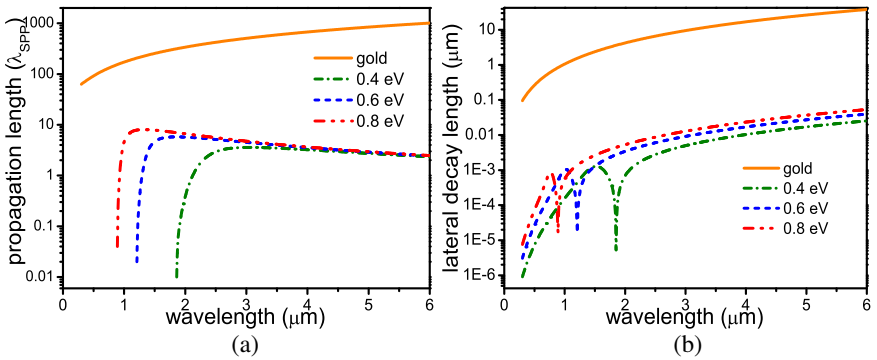

Figure 4: The (a) propagation length and (b) lateral decay length of the gold film (solid line) and the graphene (dash lines corresponding to 0.4, 0.6 and 0.8 eV).

From Fig. 4(a), we can see that the propagation length of gold film is better than graphene, and the best propagation length of graphene is approximately $8\lambda_{SPP}$, which occurs at about 1.33 μm. However, the lateral decay length of graphene is very small and times smaller than gold film, showing good confinement. Owing to the high confinement, the energy trends to propagate along bended or curved surface with little SIL.

Another parameter closely related to the confinement is the critical curvature radius for GPs. Actually, energy can be considered no longer confined when the real part of β is reduced below k_0. From this point, the critical curvature radius can be written as [20]:

$$r^* = \frac{k_0}{\mathrm{Re}[\sqrt{\beta^2 - k_0^2}](\beta - k_0)} \tag{4}$$

where we have assumed the propagation constant on the curved surface approximates to that on flat surface. With Eq. (4), the critical curvature radii in the case of 1 μm incident light for 0.8 eV doped graphene and 40nm gold film are $0.001\lambda_{SPP}$ and $95\lambda_{SPP}$ respectively, which proves further that the intrinsic confinement of graphene is better than conventional metal, and makes it easily being designed unusual shaped plasmonic devices.

3. NUMERICAL EXPERIMENT AND APPLICATION FOR FGPS

To demonstrate the difference of MPs and GPs in further, three waveguides corresponding to different curvatures are modeled, and the curve-induced radiation loss can be learned from the change of field distributions on the surface. Fig. 5 shows H_x distributions at 500 THz for 40 nm gold film based waveguide and 50 THz for graphene waveguide which is simulated by CST Microwave Studio.

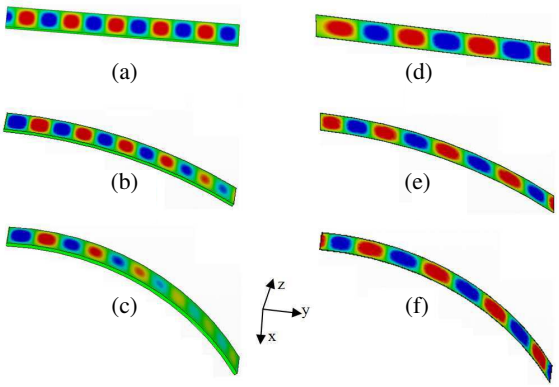

Figure 5: The propagation property of plasmonics on a)–(c) gold film (and (d)–(f) graphene waveguides corresponding to different curvatures (a), (d) infinite (the straight waveguide), (b), (e) 30 degrees, and (c), (f) 60 degrees.

From Fig. 5(a)–Fig. 5(c) we can see that few waves of MPs can propagate along the curved surface, which indicates that the MPs cannot be well supported by curved surfaces. At the same time, Fig. 5(d)–Fig. 5(f) tells us that the GPs can be well confined on curved surface.

Based on the above analysis and simulation, we increase the curvature further to 360 degrees, which forms a stereo ring resonator with the inner radius R and width W. In order to couple energy to this ring and make it work, a straight waveguide with the same width is placed near the ring, the gap between them is G, and the graphene sheet is deposited on the substrate (Al_2O_3), the scheme is illustrated as Fig. 6(a). We can see that the structure is simple and fully open (i.e., without cladding and transformation optics design).

The transmission spectrum is shown as Fig. 6(b) with the following parameters: $R = 60$ nm, $W = 40$ nm, $G = 10$ nm and $E_F = 0.6$ eV. We can see from Fig. 6(a) that there are 3 resonances from 5 to 25 THz. What's more, the field distribution on the YOZ plane corresponding to the 3rd resonance is presented as the inset of Fig. 6(b). It can be clearly found that there are three well confined plasmonic waves on the ring, and few fields at the output, which performs as the "band-stop" function. In fact, the resonator is tunable in addition to its flexibility, the resonance mode N is the same with the number of plasmonic waves on the ring, in other words,

$$2\pi R = N\lambda_{SPP} = Nc/(f_r n_{eff}) \tag{5}$$

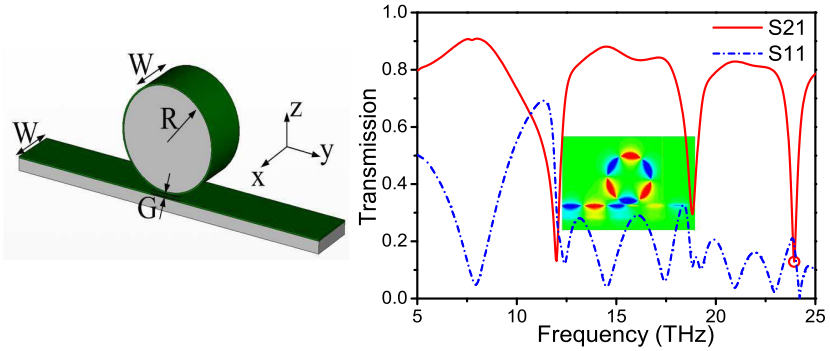

Figure 6: The scheme of the (a) stereo ring and (b) its transmission spectrum, the field distribution on YOZ plane is also provided in the inset of (b).

where c is the free space light speed, f_r is the resonance frequency. We can learn that f_r can be tuned both by the geometric size (to change R) of the ring and the doping level of graphene (to change n_{eff}).

4. CONCLUSION

In conclusion, we have investigated the FGPs from the perspective of classical electromagnetic theory. Distinguished with the conventional noble metal, the graphene can strongly confine plasmons on the surface. This feature allows us to manipulate the energy flow along the curved surface, which is proved by several demonstrations. At last, a stereo resonator is designed as the application example of FGPs. Various graphene based flexible plasmonic devices are expected to be proposed in the future.

ACKNOWLEDGMENT

This work was supported by the National Natural Science Foundation of China (Grant Nos. 61271057, 61071045), the Doctoral Fund of Ministry of Education of China (No. 20110092110009), the Fundamental Research Funds for the Central Universities and the Innovation Program for Graduate Education of Jiangsu Province (Grant No. CXLX13_092).

REFERENCES

1. Dragoman, M. and D. Dragoman, "Plasmonics: Applications to nanoscale terahertz and optical devices," *Progress in Quantum Electronics*, Vol. 32, No. 1, 1–41, 2008.
2. Gramotnev, D. K. and S. I. Bozhevolnyi, "Plasmonics beyond the diffraction limit," *Nature Photonics*, Vol. 4, No. 2, 83–91, 2010.
3. Ozbay, E., "Plasmonics: Merging photonics and electronics at nanoscale dimensions," *Science*, Vol. 311, No. 5758, 189–193, 2006.
4. Diniz, L. O., E. Marega, Jr., F. D. Nunes, and B.-H. V. Borges, "A long-range surface plasmon-polariton waveguide ring resonator as a platform for (bio) sensor applications," *Journal of Optics*, Vol. 13, No. 11, 115001, 2011.
5. Xu, H., X. Wang, T. Yu, H. Sun, and B. Zhang, "Radiation-suppressed plasmonic open resonators designed by nonmagnetic transformation optics," *Scientific Reports*, Vol. 2, 115001, 2012.
6. Berini, P. and J. Lu, "Curved long-range surface plasmon-polariton waveguides," *Optics Express*, Vol. 14, No. 11, 115001, 2011.
7. Wang, W., Q. Yang, F. Fan, H. Xu, and Z. L. Wang, "Light propagation in curved silver nanowire plasmonic waveguides," *Nano Letters*, Vol. 11, No. 4, 1603–1608, 2011.
8. Dikken, D. J., M. Spasenovic, E. Verhagen, D. van Oosten, and L. K. Kuipers, "Characterization of bending losses for curved plasmonic nanowire waveguides," *Optics Express*, Vol. 18, No. 15, 16112–16119, 2010.
9. Hasegawa, K., J. U. Nockel, and M. Deutsch, "Surface plasmon polariton propagation around bends at a metalCdielectric interface," *Applied Physics Letters*, Vol. 84, No. 11, 1835–1837, 2004.
10. Hasegawa, K., J. U. Nockel, and M. Deutsch, "Curvature-induced radiation of surface plasmon polaritons propagating around bends," *Physical Review A*, Vol. 75, No. 6, 063816, 2007.
11. Liaw, J.-W. and P.-T. Wu, "Dispersion relation of surface plasmon wave propagating along a curved metal-dielectric interface," *Optics Express*, Vol. 16, No. 7, 4945–4951, 2008.
12. Holmgaard, T., Z. Chen, S. I. Bozhevolnyi, L. Markey, A. Dereux, A. V. Krasavin, and A. V. Zayats, "Bend-and splitting loss of dielectric-loaded surface plasmon-polariton waveguides," *Optics Express*, Vol. 16, No. 18, 13585–13592, 2008.
13. Jablan, M., H. Buljan, and M. Soljacic, "Plasmonics in graphene at infrared frequencies," *Physical Review B*, Vol. 80, No. 24, 245435, 2009.
14. Ju, L., B. Geng, J. Horng, C. Girit, M. Martin, Z. Hao, H. A. Bechtel, X. Liang, A. Zettl, and Y. R. Shen, "Plasmonics in graphene at infrared frequencies," *Nature Nanotechnology*, Vol. 6, No. 10, 630-634, 2011.
15. Fei, Z., A. Rodin, G. Andreev, W. Bao, A. McLeod, M. Wagner, L. Zhang, Z. Zhao, M. Thiemens, and G. Dominguez, "Gate-tuning of graphene plasmons revealed by infrared nano-imaging," *Nature*, Vol. 487, 82–85, 2012.

16. Jiang, Y., W. B. Lu, H. J. Xu, Z. G. Dong, and T. J. Cui, "A planar electromagnetic "black hole" based on graphene," *Physics Letters A*, Vol. 376, No. 17, 1468–1471, 2012.
17. Xu, H. J., W. B. Lu, Y. Jiang, and Z. G. Dong, "Plasmonics in graphene at infrared frequencies," *Applied Physics Letters*, Vol. 100, No. 5, 051903, 2012.
18. Xu, H. J., W. Bing Lu, W. Zhu, Z. G. Dong, and T. J. Cui, "Efficient manipulation of surface plasmon polariton waves in graphene," *Applied Physics Letters*, Vol. 100, No. 24, 243110, 2012.
19. Wang, J., W. B. Lu, X. B. Li, Z. H. Ni, and T. Qiu, "Graphene plasmon guided along a nanoribbon coupled with a nanoring," *Journal of Physics D: Applied Physics*, Vol. 47, No. 13, 245435, 2014.
20. Lu, W. B., W. Zhu, H. J. Xu, Z. H. Ni, Z. G. Dong, and T. J. Cui, "Flexible transformation plasmonics using graphene," *Optics Express*, Vol. 80, No. 24, 245435, 2009.
21. Zhu, X., W. Yan, N. A. Mortensen, and S. Xiao, "Bends and splitters in graphene nanoribbon waveguides," *Optics Express*, Vol. 21, No. 3, 3486–3491, 2013.
22. Aksu, S., M. Huang, A. Artar, A. A. Yanik, S. Selvarasah, M. R. Dokmeci, and H. Altug, "Flexible plasmonics on unconventional and nonplanar substrates," *Advanced Materials*, Vol. 23, No. 38, 4422–4430, 2011.
23. Thongrattanasiri, S., A. Manjavacas, and F. J. G. de Abajo, "Quantum finite-size effects in graphene plasmons," *ACS nano*, Vol. 6, No. 2, 1766–1775, 2012.
24. Vakil, A. and N. Engheta,, "Transformation optics using graphene," *Science*, Vol. 332, No. 6035, 1291–1294, 2011.
25. Emani, N. K., T. F. Chung, X. Ni, A. V. Kildishev, Y. P. Chen, and A. Boltasseva, "Electrically tunable damping of plasmonic resonances with graphene," *Nano Letters*, Vol. 12, No. 10, 5202–5206, 2012.
26. Ordal, M., L. Long, R. Bell, S. Bell, R. Bell, R. Alexander., Jr., and C. Ward, "Optical properties of the metals Al, Co, Cu, Au, Fe, Pb, Ni, Pd, Pt, Ag, Ti, and W in the infrared and far infrared," *Applied Optics*, Vol. 22, No. 7, 1099–1119, 1983.
27. Burke, J., G. Stegeman, and T. Tamir, "Surface-polariton-like waves guided by thin, lossy metal films," *Physical Review B*, Vol. 44, No. 11, 5855, 1991.
28. Tassin, P., T. Koschny, M. Kafesaki, and C. M. Soukoulis, "A comparison of graphene, superconductors and metals as conductors for metamaterials and plasmonics," *Physical Review B*, Vol. 6, No. 4, 259–264, 2012.

Transmission Analysis of a Ternary Diversity Reception Based on OFDM FSO System over Correlated Log-normal Fading Channel

Yuwei Su, **Fan Bai**, **and Mitsuji Matsumoto**
Global Information and Telecommunication Studies, Waseda University, Japan

Abstract— With the increasing requirements for larger bandwidth and higher data rate transfer of information, free space optical (FSO) communication has received growing attention in recent years. Atmospheric turbulence factors may give the most serious influence to the performance of the FSO system. In this paper, orthogonal frequency division multiplexing (OFDM) is chosen for the purpose of against channel dispersion and time varying environment. Spatial diversity is another efficient way to mitigate the effects of scintillation. We investigate the performance of OFDM FSO system of a ternary receiver with EGC reception combining scheme in log-normal distribution atmospheric turbulence channel. We analyze the probability distribution function (PDF) of the received light intensity in ternary diversity reception. Based on the simulation results, we present a comparison of the transmission performance among ternary receiver, dual receiver and single receiver system over correlated log-normal weak turbulence fading channel. The results would be useful for design and evaluation of optical wireless communication system.

1. INTRODUCTION

Free space optics (FSO) communication has received increasing attention in recent years, since it fulfill the requirement of higher transmission speed and wider bandwidth in modern communication system. Compared with the RF communication system, the FSO communication system has lighter, smaller and more energy efficient devices. In some special area, where the optical fiber networks are not available to be established, the FSO system can be a suitable alternative option [1, 3].

The atmospheric turbulence situation has a great influence on the performance of FSO communication system. As atmospheric channel changes randomly, the laser irradiance in receiving plane would have a spatial and temporal fluctuation known as scintillation. The optical scintillation could cause an unacceptable channel fading in FSO communication [2]. Classical studies of atmospheric turbulence were focus on fluctuations in the velocity field of a viscous fluid, which can be simplified as a stochastic field model. Log-normal distribution perform excellent match in describing the weak atmospheric turbulence [3].

Orthogonal frequency division multiplexing (OFDM) is a kind of multi-carrier modulation which the data information is carried over many lower rate subcarriers. It has been widely used in wireless communication and adopted in a lot of high speed communication standards: ITU-T G. hn; IEEE 802.11a, g, n, ac; IEEE 802.15.3a; IEEE 802.16e; IEEE 802.20 and so on. One of the advantages of OFDM is that it is a suitable technology against channel dispersion and time varying environment [1].

Spatial diversity is another way to mitigate the channel fading of FSO communication system. With the larger size of the reception, the system performance would get better [3, 8]. However, the increasing lens radius would lead to the cost and the weight of the reception terminal increase exponentially. It is kind of a trend to replace one big lens to several smaller receivers [4]. Most of the previous research on FSO communication system with multiple receivers concerned each reception being independent with others, which meant the distance between two individuals was long enough [5]. It would make serious difficulties in the design of FSO system [2].

In this paper, a ternary reception OFDM FSO system is proposed to mitigate the channel fading over log-normal distribution atmospheric turbulence. In order to have an insight into the performance of the system, we compare the ternary reception system with single reception and dual reception systems on the average bit-error-ratio (BER), average signal-to-noise ratio (SNR) and outage probability (OP).

The remainder of this paper organized as follows, in Section 2, we give a brief introduction of the ternary reception OFDM FSO system. In Section 3, we analyze the received light intensity probability distribution function (PDF) over log-normal distribution atmospheric turbulence. In Section 4, we investigate the transmission performance of the system. In Section 5, we present the conclusion.

2. TERNARY RECEPTION SYSTEM ARCHITECTURE

In order to mitigate the light intensity fluctuation in FSO communication, increasing the diameter of the aperture known as Aperture Average is a feasible solution [8]. But the increasing size of lens would lead to a sharp increasing of the cost. Hence we consider replacing one big lens to several small lenses is more efficient.

In this paper, we consider a ternary receiver. As showed in Fig. 1, D is the diameter of each lens. Consider two separate lenses lens_i and lens_j, d_{ij} presents the central distance between lens_i and lens_j. Fig. 2 shows a brief architecture of ternary diversity reception OFDM FSO system. The electrical signal is modulated by OFDM Modulator and converted to optical signal by laser-diode. The optical signal propagates through turbulence and would be received by the ternary receiver. After converted back electrical signal, the signals from three detectors would be demodulated by OFDM Demodulator and combined under equal gain combining (EGC) scheme.

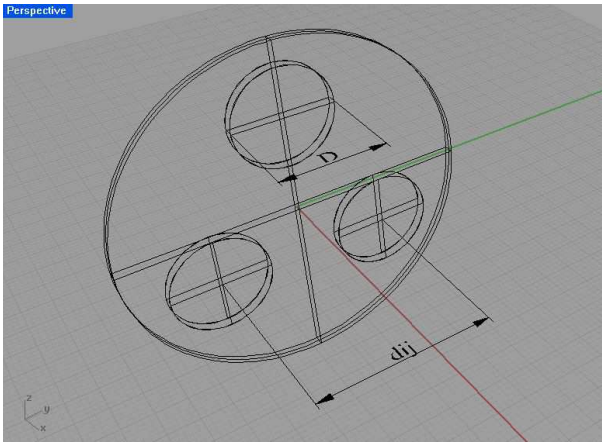

Figure 1. Ternary receiver.

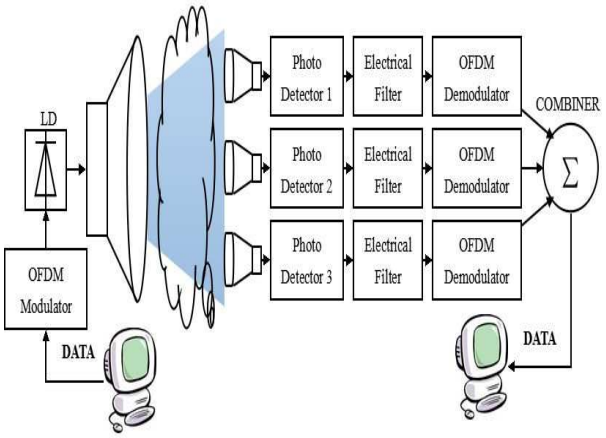

Figure 2. System architecture.

3. LIGHT INTENSITY PROBABILITY DISTRIBUTION

In the theory used to derive the atmospheric turbulence, optical field propagation can be seen as a random process. The received light intensity of lens_i and lens_j have average value I_i and I_j. Correlation coefficient γ_{ij} of lens_i to lens_j is presented by function (1):

$$\gamma_{ij}(d_{ij}, D) = \frac{B_{I,ij}(I_i, I_j, d_{ij}, D)}{\sqrt{\sigma_i^2 \sigma_j^2}} \tag{1}$$

$B_{I,ij}(I_i, I_j, d_{ij}, D)$ is covariance of lens_i to lens_j, which is presented by function (2). The σ_i^2 and σ_j^2 are the variances of lens_i and lens_j, which can be calculated by function (3) [3].

$$B_{I,ij}(I_i, I_j, d_{ij}, D) = \frac{\langle I_i I_j \rangle}{\langle I_i \rangle \langle I_j \rangle} - 1 \tag{2}$$

$$\sigma_i^2(D) = B_{I,ij}(I_i, 0, D) = \frac{\langle I_i^2 \rangle}{\langle I_i \rangle^2} - 1 \tag{3}$$

The symbol $\langle \cdot \rangle$ stands for the ensemble average value. Based on Rytov Theory, I_i, I_j, σ_i^2 and σ_j^2 are the variables versus atmospheric turbulence situation, which can be described by Rytov Variance σ_R^2. Hence the correlation coefficient is a function of the receivers setting and turbulence condition, as showed in Fig. 3. We can see that with increasing of the central distance d_{ij}, correlation coefficient γ_{ij} is drawing close to 0. And when turbulence is getting stronger, γ_{ij} is getting higher.

According to the extended Rytov theory, we can use the log-amplitude X to indicate the light intensity I by the function $I = I_0 \exp(2X - 2X_0)$. As the optical field propagation through atmospheric turbulence is random process, the received light intensity should be presented by a probability distribution function (PDF) [6, 7].

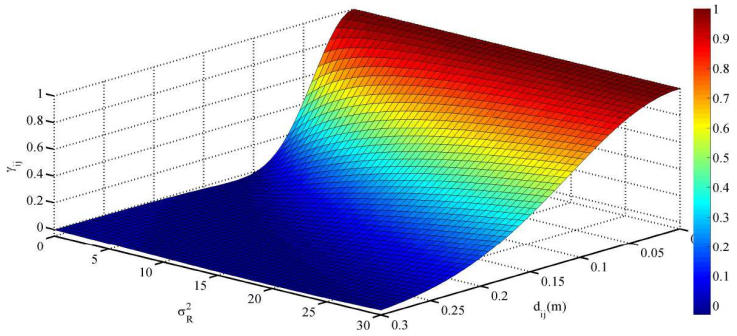

Figure 3. Channel correlation coefficient under different separation distance and turbulence condition.

Log-normal distribution is widely used in describing the turbulence situation. A single receiver log-normal PDF of received light intensity is:

$$f_1(I) = \frac{1}{2I}\frac{1}{\sqrt{2\pi\sigma_X^2}}\exp\left\{-\frac{[\ln(I)-\ln(I_0)]^2}{8\sigma_X^2}\right\} \tag{4}$$

where I_0 denotes the ensemble average received light intensity and σ_X^2 denotes the variance of X. In this paper, we consider the situation of weak turbulence ($\sigma_R^2 = 0.14$) and the three receivers setting as an equilateral triangle with same diameters. We can extend PDF to the situation of ternary reception as function (5):

$$f_{3I}(I) = \frac{1}{16\pi I^3}\cdot\frac{1}{\sqrt{2\pi\sigma_X^6(1-3\gamma^2+2\gamma^3)}}\cdot\exp\left\{-\frac{1}{8(1-3\gamma^2+2\gamma^3)}\cdot\left[3\sigma_X^4(1-2\gamma+\gamma^2)\ln^2\left(\frac{I}{I_0}\right)\right]\right\} \tag{5}$$

4. PERFORMANCE OF TERNARY RECEPTION OFDM FSO SYSTEM

In this paper, we use OFDM signal for its advantages against channel dispersion and time varying environment. The OFDM signal with N subcarriers, after up-conversion can be written as below, where ω_n is the nth subcarrier angular frequency, φ_n is the nth subcarrier initial phase, A_n is nth subcarrier complex data symbol.

$$S_{OFDM}(t) = \sum_0^{N-1} S_n(t) = \sum_0^{N-1} A_n \exp(j\omega_n t + \varphi_n), \quad 0 \le t \le T_s \tag{6}$$

We assumed the total noise power is a sum of thermal noise, shot noise and relative intensity noise process:

$$N_0(I_1,I_2,I_3) = \frac{4K_B T_{abs} F}{R_L}B_e + 2qI_{ph}(I_1,I_2,I_3)B_e + (RIN)I_{ph}^2(I_1,I_2,I_3)B_e \tag{7}$$

I_{ph} is DC of total received current, K_B is Boltzmann's constant, T_{abs} is absolute temperature, F is the noise figure of the receiver electronics, R_L is PD load resistor, q is electron charge and B_e is the Electrical filter bandwidth. The ensemble average SNR and ensemble average BER can be calculated as:

$$\langle SNR\rangle = \int_0^\infty\int_0^\infty\int_0^\infty SNR(I_1,I_2,I_3)\cdot f_I(I_1,I_2,I_3)dI_1dI_2dI_3 \tag{8}$$

$$\langle BER\rangle = \int_0^\infty\int_0^\infty\int_0^\infty BER(I_1,I_2,I_3)\cdot f_I(I_1,I_2,I_3)dI_1dI_2dI_3 \tag{9}$$

In Fig. 4, we set the lens diameters of single, dual and ternary reception are 12 cm, 8.49 cm and 6.93 cm, so that the total reception area of three schemes are the same. We can see that ternary reception system with low correlation coefficient ($\gamma = 0$) perform better.

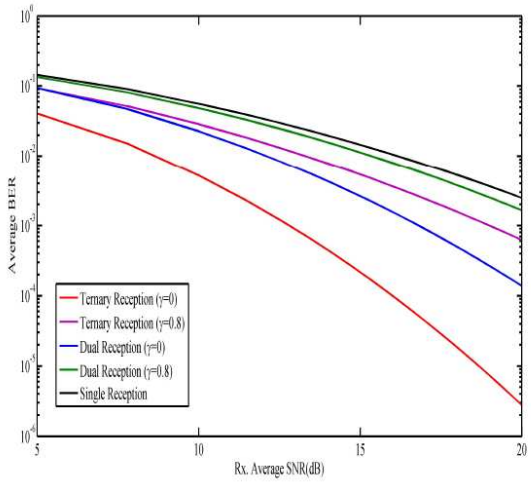

Figure 4. Under different reception.

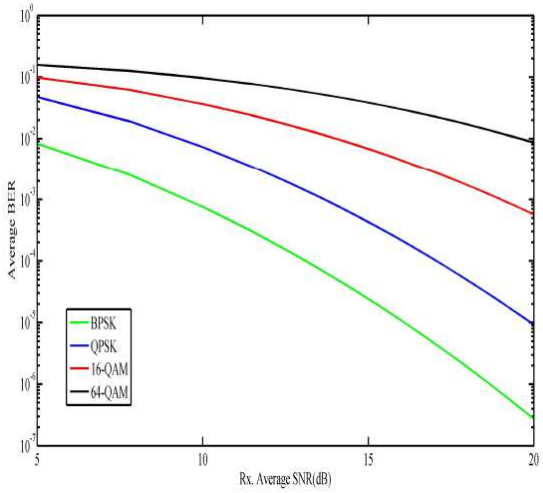

Figure 5. Under different modulation.

Figure 5 shows the transmission performance of ternary reception system with different modulation schemes. It is clear that the higher constellation size modulation require more received powers to reduce BER of the system. Consider a threshold SNR_{th}. Only when the SNR of the system is better than the SNR_{th}, the quality of communication is acceptable. Otherwise, we can see the communication is failed. Define the probability of the SNR falling worse than the SNR_{th} as the outage probability P_{outage}. It can be written as:

$$P_{outage}(SNR_{th}) = P[SNR < SNR_{th}] \tag{10}$$

Figure 6 shows that, in certain threshold SNR_{th}, ternary reception system has lower outage probability.

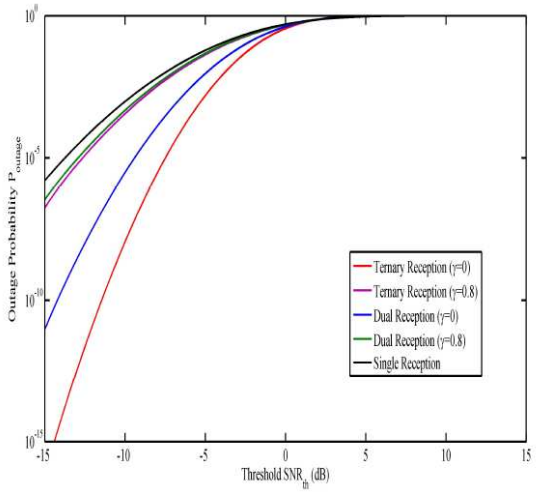

Figure 6. Outage probability.

Parameter	Value
Operating wavelength (λ)	1550 nm
Relative intensity noise (RIN)	-130 dB/Hz
PD load resistor (R_L)	50 Ω
Absolute temperature (T_{abs})	300 K
Transmission distance (L)	2 km
Electron charge (q)	1.602×10^{-19}C
Noise figure (F)	2 dB
Electrical filter bandwidth (B_e)	2 GHz
Number of carrier (N_s)	256
Optical modulation index (m_n)	1%

Table 1.

5. CONCLUSION

In this paper, we propose a ternary diversity reception OFDM FSO system. Considering the effects of correlation coefficient, we analyze the probability distribution function of received light intensity and investigate the transmission performance of the system in log-normal distribution atmospheric

turbulence. In terms of the numerical results about comparisons with other reception schemes (single reception, dual reception) on average SNR, average BER and outage probability, we can see that ternary diversity reception OFDM FSO system has an apparent advantage on mitigating atmospheric turbulence channel fading.

REFERENCES

1. Bekkali, A., "Transmission analysis of OFDM-based wireless services over turbulent radio-on-FSO links modeled by gamma-gamma distribution," *IEEE Photonics Journal*, Vol. 2, No. 3, Jun. 2010.
2. Armstrong, J., "OFDM for optical communications," *IEEE/OSA J. Lightwave Technol.*, Vol. 27, 189–204, Feb. 2009.
3. Andrews, L. C. and R. L. Phillips, *Laser Beam Propagation through Random Media*, 2nd Edition, SPIE, Bellingham, WA, 2005.
4. Chen, Z., "Channel correlation in aperture receiver diversity systems for free-space optical communication," *Journal of Optics*, Nov. 2012.
5. Mohammad Navidpour, S., "BER performance of free-space optical transmission with spatial diversity," *IEEE Transactions on Wireless Communications*, Vol. 6, No. 8, Aug. 2007.
6. Zhu, X. and J. M. Kahn, "Free-space optical communication through atmospheric turbulence channels," *IEEE Trans. Commun.*, Vol. 50, No. 8, 1293–1300, Aug. 2002.
7. Skraparlis, D., "On the effect of correlation on the performance of dual diversity receivers in lognormal fading," *IEEE Communications Letters*, Vol. 14, No. 11, Nov. 2010.
8. Khalighi, M.-A., "Fading reduction by aperture average and spatial diversity in optical wireless system," *J. Opt. Commun. Netw.*, Vol. 1, No. 6, Nov. 2009.

The Principle of the Technology and Design of the Parabolic Strip Telescope

J. Červený, V. Kosejk, and G. Chadzitaskos
Department of Physics, Faculty of Nuclear Sciences and Physical Engineering
Czech Technical University, Břehová 7, CZ-115 19, Prague

Abstract— Contribution of this paper is a proposal of the new special type of telescope with a parabolic strip as a primary element for astronomical observations or for measurements with good angular resolution in one direction. The observed objects are displayed as lines in the image plane of a length equal to the width of the mirror strip. If we observe a sufficiently bright object, the observation allows us to distinguish fine detail or fine movements on the sky. Each line segment corresponds to the integral intensity of the incident light from the observed object in the direction perpendicular to the mirror strip. For the reconstruction of the whole image with good resolution we need a parabolic mirror strip to rotate around the optical axis, and a series of sequential snaps with a special camera. Different algorithms for reconstruction of the image are used. The main advantage of this rotating telescope is mechanical and manufacturing technological simplicity and an innovative design. Nothing comparable has yet been made. Currently constructed large telescopes are made up of segments, using adaptive optics, and generally it is technologically challenging. Systems of interfering telescopes are built (the effective diameter of 30 m to the get better resolution. The proposed telescope can be made of a 50-m long tape without any technological problems. We created two prototypes of telescopes: a small one, with a 0.3-m long mirror strip, and a bigger one, with a 1.4-m long mirror strip. Both telescopes are supported by parallactic mountings, and both are equipped with special cameras with optics, electronics, computer with special controlling software, special servo stepper motors fitted with mechanical transmission, construction of lightweight alloys, plastics and composites.

1. INTRODUCTION

This new type of a telescope with a parabolic strip fulfilling the function of an objective is the most fundamental modification of a telescope since the time when first patent was granted to the Dutch optician Hans Lippershey, and the times of those who followed in the footsteps of famous scientists such as Galileo Galilea, Johannes Kepler, and Isaac Newton. The first reflector, a telescope using a mirror as an objective, was designed by Isaac Newton who thus solved the problem of a chromatic aberration caused by different refraction indices for different wavelengths of light in an objective lens. Types of telescope constructions:

- Refracting telescopes

A telescope objective contains a lens or a system of lenses. The optical size of an objective is determined by the lens speed, focal length and the maximum possible magnification.

- Reflecting telescopes

The objective of a reflector is a concave spherical primary mirror, which may be parabolic or hyperbolic. The surface area of the mirror determines the lens speed of a telescope. An image of an object is reflected by a secondary mirror and subsequently observed through an eyepiece. In this telescope type, light is reflected by mirrors and so its tube is only half size, and a heavy mirror is located on the side of an observer, not on the external end of a tube as is the case with a refractor objective.

- Combined refraction/reflection systems

A telescope is composed of two or more mirrors and an objective with a system of lenses. Optically, the secondary mirror is located in front of the primary mirror. Thus, light rays are first reflected from the primary mirror into the secondary mirror, falling on the lens system of an objective. Therefore, these telescopes usually have smaller diameters and their lens speed is also smaller.

Figure 1: A new type of a parabolic strip telescope.

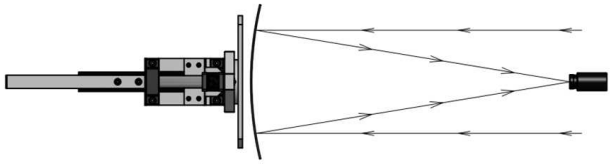

Figure 2: The diagram of a parabolic strip telescope.

1.1. The Principle of a Parabolic Strip Telescope

Observed objects are displayed as line segments in the image plane. Every line segment the length of which equals to the width of a strip corresponds to the integral intensity of the incident light falling from the observed objects in the direction perpendicular to a parabolic strip. Through subsequent rotation of the whole telescope or just its strip around the optical axis (the axis perpendicular to the strip centre in the apex of a parabola) and application of the Radon inversion transformation, we may reconstruct the image of an observed object with a good resolving power. It is also possible to reconstruct an image from one snap without any rotation; in this case the angular resolution in the two mutually perpendicular directions will be of different orders. This fact can be utilized for example for the observing of fine movements of brighter objects in the direction of travel. Software processing reconstructs an image according to specific needs and possibilities to make use of the properties of a telescope.

2. THE CONSTRUCTION PRINCIPLES FOR A PARABOLIC STRIP TELESCOPE

A distinctive feature of the proposed project of a construction of the new type of a telescope with a parabolic strip fulfilling the function of an objective is that it enables observations or astronomical measurements with a good resolving power in one direction and a worse in the perpendicular direction. The angular resolving power is given by the ratio of the wavelength to the length of the projection of a parabolic strip to the plane tangential to the apex of the parabolic stripe. When observing objects that are sufficiently bright, this observation enables to resolve fine details or catch sight of fine movements in this direction. Observed objects are displayed as line segments in the image plane of a length equal to the strip width. Each of the line segments corresponds to the integral intensity of the incident light from the observed objects in the direction perpendicular to the strip. So that the whole image could be reconstructed with the same good resolving power, the whole telescope or just its parabolic strip can be subsequently rotated around the optical axis (the axis perpendicular to the strip centre in the apex of a parabola) while taking a series of snaps, and apply the Radon inversion transformation as in the case of computed tomography. This means that when we have enough incident light (which is determined by the surface area of a strip), we can resolve fine details. A great technological advantage is that it is incomparably cheaper and easier to manufacture a strip than a paraboloid. It is sufficient to manufacture only parabolic holders and a mirror strip made of an elastic material; the tension in the material which a strip is made of will ensure that the shape will be stable and accurate. In addition, the construction is significantly lighter than that of a paraboloid. Nowadays, very big telescopes composed of segments, or systems of interfering telescopes are constructed at exorbitant costs to achieve fine resolution. Among other

things, the system designed by us has more mechanical advantages. Thanks to its low price, it would be possible to deploy a system of telescopes with a tilt angle of for example 15° and install them all over the Earth in different terrestrial longitudes so that they would cover the whole sky. The mechanical construction will be simplified, gravitational impacts will be relatively small and the observation possibilities will be multiplied — it is possible to make simultaneous observations in every angle. Deployment on satellites will also be cheaper thanks to a smaller weight. The resolution power of a telescope fitted with a 120-cm long strip should be similar to the resolution power of a parabolic with a diameter of 150 cm.

2.1. The Structural Design and Production of a Prototype of a Parabolic Strip Telescope

A parabolic strip telescope is composed of four main parts:

- A multi-axis astronomical stand with an automatic rotation system following the stellar drift
- A fixed static holder of a telescope with a step-by-step actuating mechanism
- A rotating part of a telescope with a parabolic strip and optics
- A control and evaluation unit

Fixed static holder of a telescope with a step-by-step actuating mechanism The static part of a telescope is composed of a load bearing structure (a weldment from aluminium sections) and two locks with bearings. The rotational movement is secured by a step-by-step actuating mechanism with a step of 0.9° and a timing pulley gear with a ratio of gearing of 1/5.

The control unit controlling the movements of the rotating part of a telescope and the control unit of the camera that records a series of snaps are installed on the opposite end of the load-bearing structure.

2.2. The Rotating Part of a Telescope with a Parabolic Strip and Optics

The rotating part of a telescope is designed and composed of the following components: the main load-bearing part made of aluminium sections which is machined on a CNC milling machine (4) and a lathe (5). A timing pulley with a shaft made of aluminium alloy is accurately fixed to this main load-bearing structure by means of assembling components. The following most important components of a telescope are located on the opposite side of the main part: A flexible parabolic mirror strip which is inserted between two plexy appliances with an exact slot cut out by a CNC jig wirecutter. The welded solid construction of a camera holder made of aluminium alloy that ensures exact adjusting of the scanning chip of a camera into the focal point of the incidence of the rays reflected from the parabolic mirror strip.

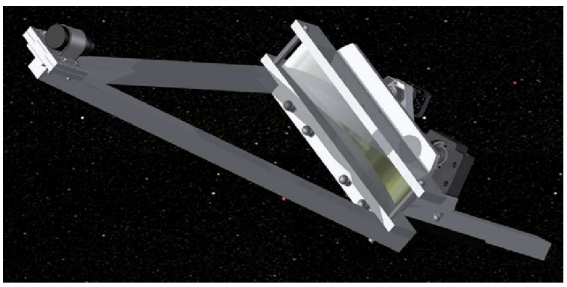

Figure 3: Parabolic strip telescope.

3. THE TECHNOLOGY HAS SEVERAL ADVANTAGES

- A good resolution power of a telescope in one direction.
- The manufacturing is many times cheaper than the production of common parabolic strip telescopes.
- Utilization of such a device for example for the tracking of movement and identification of small asteroids in the vicinity of the Earth.

It would be advisable to develop a network of telescopes with a long strip that would be used to monitor the sky and deployed along the meridian according to our proposal (parabolic strips long tens of meters). For objects emitting sufficient light, it may be quite cheap to obtain knowledge

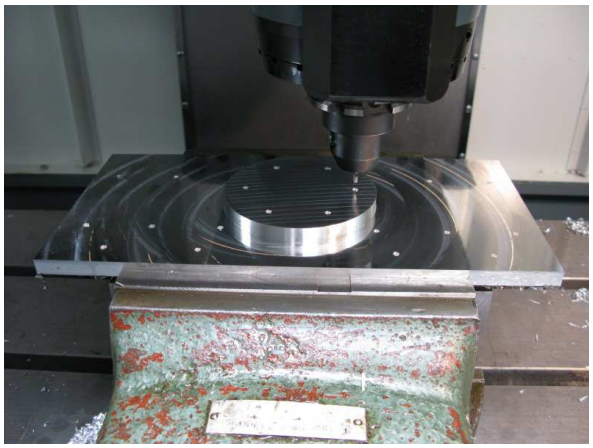

Figure 4: The milling of the surface areas of the main load-bearing part of a telescope.

Figure 5: Lathe-turning of the main load-bearing structure of a telescope.

of minor details. The market seems to be limited only to astronomical observations and remote research of the Earth. Taking into account the technological simplicity and a smaller weight of the telescope, the possibility of its utilization on the Earths orbit and in the cosmic space remains open.

4. ADVANTAGES

- high mounting not being necessary,
- low wind influence,
- low gravitational influence.

ACKNOWLEDGMENT

The support by the Ministry of Education of the Czech Republic pre-seed project has been acknowledged.

REFERENCES

1. Chadzitaskos, G., "Parabolic strip telescope," arXiv: astro-ph/1304.6530, 2013.
2. King, H. C., *The History of the Telescope*, Dover Publication, New York, 2003.
3. ESO 2012, "The very large telescope," https://www.eso.org/public/teles-instr/vlt.html.
4. Chadzitaskos, G. and J. Tolar, CZ Patent 298313, 2007.
5. Chadzitaskos, G. and J. Tolar, *Proc. SPIE. 5487, Optical, Infrared, and Millimeter Space Telescopes*, 1137, doi: 10.1117/12.5546007(arXiv: astro-ph/0310064), 2004.
6. Beylkin, G., *IEEE Transaction on Acoustics, Speech, and Signal Processing*, Vol. 35, No. 2, 162, 1987.

Detection Loophole-free Entanglement Verification

Xiao Yuan[1], **Ping Xu**[2, 3], **Luo-Kan Chen**[2, 3], **He Lu**[2, 3], **Xing-Can Yao**[2, 3], **Xiongfeng Ma**[1], **Yu-Ao Chen**[2, 3], **and Jian-Wei Pan**[2, 3]

[1]Center for Quantum Information, Institute for Interdisciplinary Information Sciences
Tsinghua University, Beijing 100084, China
[2]Hefei National Laboratory for Physical Sciences at Microscale, Department of Modern Physics
University of Science and Technology of China, Hefei, Anhui 230026, China
[3]Shanghai Branch, CAS Center for Excellence and Synergetic Innovation Center in Quantum Information
Quantum Physics University of Science and Technology of China, Shanghai 201315, China

Abstract— Quantum entanglement is an essential resource in quantum information processing, which needs to be verified in many tasks such as quantum cryptography and computation. Due to imperfect detection devices when implementing measurements, the conventional entanglement witness method could wrongly conclude a separable state to be entangled. Inspired by the attacks in quantum key distribution, we construct and experimentally realize a time-shift attack on the conventional entanglement witness process. We demonstrate that any separable state can be falsely identified to be entangled. In order to close detection loopholes, we design and experimentally realize a measurement-device-independent entanglement witness for various two-qubit states. We demonstrate that an entanglement witness can be realized without detection loopholes.

1. INTRODUCTION

It has been widely recognized that quantum entanglement plays an important role in the quantum information processing such as quantum computation [1], quantum teleportation [2] and quantum cryptography [3, 4]. Being the key resource for these tasks, quantum entanglement need to be verified in many circumstances. Entanglement witness (EW) is a conventional way to detect entanglement, which gives one of two outcomes: Yes or No, corresponding to the conclusive result that the state is entangled or to failure to draw a conclusion, respectively. Mathematically, for a given entangled quantum state ρ, a Hermitian operator W is called a witness if $tr[W\rho] < 0$ (output of 'Yes') and $tr[W\sigma] \geq 0$ (output of 'No') for any separable state σ. It is strictly forbidden when we identify a separable state to be entangled. Note that there could also exist entangled state ρ' such that $tr[W\rho'] \geq 0$ (output of 'No'), thus it is OK to fail identifying an entangled state.

In the experiment, one can realize the conventional EW with only local measurements by decomposing W into a linear combination of product Hermitian operators. Then one can do measurements locally on each part and gather measurement outcomes to decide whether the state is entangled or not. A faithful conclusion of such witness relies on the correctness of the experimental implementation, imperfections of detection devices could wrongly conclude a separable state to be entangled. In the practical case, we can regard such imperfection as possible attacks from an adversary, Eve. For example, if the measurement devices used by the witnessers might possibly be manufactured by some untrusted party, who could collaborate with Eve and deliberately fabricate devices to make the real implementation $W' = W + \delta W$ be deviated from W, such that W' is not a witness any more,

$$tr[W'\sigma] < 0 < tr[W\sigma]. \tag{1}$$

That is, with the deviated witness W', a separable state σ could be identified as an entangled one, which is more likely to happen when $tr[W\sigma]$ is near zero.

In quantum key distribution (QKD), the security could be guaranteed by proving the presence of entanglement in a secure QKD channel where an entanglement-breaking channel would cause insecurity [5]. Thus there exist strong correlation between the security of QKD and the success of EW. For the varieties of attacks in QKD, such as time-shift attack [6] and fake-state attack [7], one may also find similar detection loopholes in the conventional EW process. Originated from this analogy, we construct a time-shift attack that manipulates the efficiency mismatch between detectors used in an EW process. Under this attack, any state could be witnessed to be entangled, even if the input state is separable. By this example, we demonstrate that there do exist loopholes in the conventional EW procedure.

Recently, Lo et al. [8] proposed an measurement-device-independent (MDI) QKD method, which closed all possible attacks of detectors. As the aforementioned similarity between QKD and EW, one would also expect that there exist EW schemes without detection loopholes. Meanwhile, a nonlocal game is proposed to distinguish any entangled state from all separable states [9]. Inspired by this game, Branciard et al. [10] proposed an MDIEW method, where they proved that there always exists an MDIEW for any entangled state with untrusted measurement apparatuses.

In this paper, we first design a time-shift attack to the conventional EW such that every separable state would be witnessed to be entangled. Then based on the proposal in Ref. [10], we design and experimentally realize an MDIEW scheme to close such detection loopholes. We thus practically show a way to witness entanglement without assuming detectors be perfect.

2. MAIN RESULT

2.1. Time-Shift Attack

In the following, we will focus on the bipartite scenario involving two parties Alice and Bob. Consider a type of bipartite quantum states in the form of

$$\rho_{AB}^{v} = (1-v)\left|\Psi^{-}\right\rangle\left\langle\Psi^{-}\right| + \frac{v}{2}(|00\rangle\langle 00| + |11\rangle\langle 11|), \tag{2}$$

with $v \in [0,1]$ and $|\Psi^{-}\rangle = (|01\rangle - |10\rangle)/\sqrt{2}$. The state is entangled if $v < 1/2$, which can be witnessed by a conventional EW,

$$W = \frac{1}{2}I - |\Psi^{-}\rangle\langle\Psi^{-}|, \tag{3}$$

with result $tr[W\rho_{AB}^{v}] = (2v-1)/2$.

The idea of time-shift attack is originated from quantum cryptography [6] and takes advantage of efficiency mismatches existing in measurement devices. Inspired by this idea, we construct a time-shift attack for the conventional witness defined in Eq. (3). Define $\sigma_0 = I$ and σ_1, σ_2, σ_3 be the Pauli matrices σ_x, σ_y, and σ_z, correspondingly. Then we can decompose W to

$$W = \frac{1}{4}\left(\sum_{i=0}^{3}\sigma_i \otimes \sigma_i\right), \tag{4}$$

and the EW can be realized by local measurements,

$$Tr\left[W\rho_{AB}\right] = \frac{1}{4}\left(1 + \langle\sigma_x\sigma_x\rangle + \langle\sigma_y\sigma_y\rangle + \langle\sigma_z\sigma_z\rangle\right). \tag{5}$$

As shown in Fig. 1, we exploit the time mismatch of the two single-photon-detectors such that one detector is more efficient than the other. In this case, the real implementation (W') is deviated from the original design witness W. In the attack Eve can suppress the positive contributes of the witness result $Tr[W\rho_{AB}]$ to let the witness result $Tr[W'\rho_{AB}]$ be negative by adjusting the time mismatch. For example, when measuring $\sigma_x\sigma_x$, Alice and Bob will project the input state to the

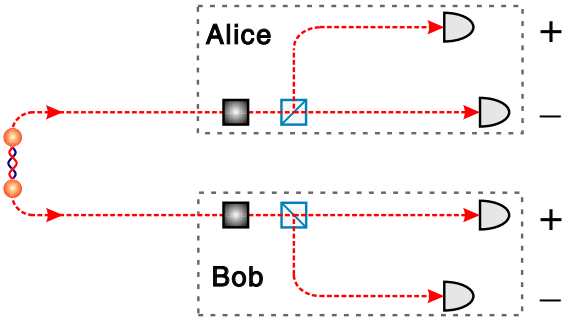

Figure 1: Time-shift attack on the conventional EW. Built-in delay lines enable Eve to control the efficiency of coincidence detection between Alice's and Bob's outcomes.

eigenstates of σ_x, that is σ_x^+ and σ_x^-, corresponding to positive and negative eigenvalue respectively, and obtain probabilities $\langle\sigma_x^\pm\sigma_x^\pm\rangle$. Then the value of $\langle\sigma_x\sigma_x\rangle$ is defined as

$$\langle\sigma_x\sigma_x\rangle = \langle\sigma_x^+\sigma_x^+\rangle + \langle\sigma_x^-\sigma_x^-\rangle - \langle\sigma_x^+\sigma_x^-\rangle - \langle\sigma_x^-\sigma_x^+\rangle. \tag{6}$$

The probabilities $\langle\sigma_x^\pm\sigma_x^\pm\rangle$ is measured from coincidence counts $N_A^\pm N_B^\pm$ of detectors, that is

$$\langle\sigma_x^\pm\sigma_x^\pm\rangle = \frac{N_A^\pm N_B^\pm}{\sum N_A^\pm N_B^\pm}. \tag{7}$$

If the positive coincidence counts are all suppressed, that is $N_A^+N_B^+ = N_A^-N_B^- = 0$, then the outcome of $\langle\sigma_x\sigma_x\rangle$ is

$$\langle\sigma_x\sigma_x\rangle = -\langle\sigma_x^+\sigma_x^-\rangle - \langle\sigma_x^-\sigma_x^+\rangle = -\frac{N_A^+N_B^-}{\sum N_A^\pm N_B^\pm} - \frac{N_A^-N_B^+}{\sum N_A^\pm N_B^\pm} = -1. \tag{8}$$

Similarly, the all the other local measurements $\langle\sigma_y\sigma_y\rangle$ and $\langle\sigma_z\sigma_z\rangle$ become -1 by suppressing positive coincidence counts, which gives a witness result of

$$Tr[W'\rho_{AB}] = -\frac{1}{2} \tag{9}$$

for any state ρ_{AB}.

In our experiment demonstration, we only suppress the positive coincidence counts to 10.9(1)% instead of neglecting all of them. Under this attack, any state could be witnessed to be entangled, even if the input state is separable. By this example, we demonstrate that there do exist loopholes in the conventional EW procedure.

2.2. Counter-Measure: MDIEW

The MDIEW method in Ref. [10] is capable to close all detection loopholes, such as the time shift attack we showed in the last paragraph. As shown in Fig. 2, MDIEW requires Alice (Bob) to prepare another ancillary state τ_s (ω_t) and perform Bell-state measurements (BSMs) on the to be witnessed state and the ancillary state.

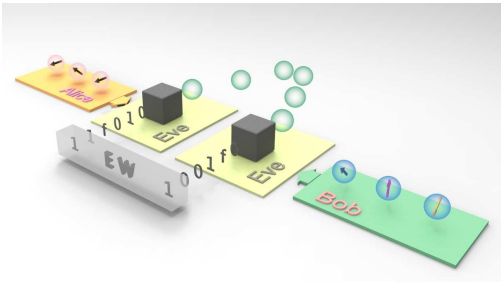

Figure 2: Measurement device independent entanglement witness.

Conditioned on the measurement outcomes, a and b, MDIEW is defined as

$$J(\rho_{AB}) = \sum_{s,t} \beta_{s,t}^{a,b} p(a,b|\tau_s,\omega_t), \tag{10}$$

where the choice of the ancillary states are labeled by s and t. That is, ρ_{AB} is entangled while $J(\rho_{AB}) < 0$ and for any separable state σ_{AB}, we have $J(\sigma_{AB}) \geq 0$. Here the probabilities $p(a,b|\tau_s,\omega_t)$ are obtained from performing two BSMs on the to be witnessed state ρ_{AB} and the ancillary states τ_s and ω_t. That is,

$$p(a,b|\tau_s,\omega_t) = Tr[(M_a \otimes M_b)(\tau_s \otimes \rho_{AB} \otimes \omega_s)], \tag{11}$$

where M_a and M_b represent BSMs performed by Alice and Bob with outcome a and b, respectively.

The MDIEW is capable to witness any entangled state, because it can be constructed from the conventional EW such that $J = tr[W\rho]/4$. Here the coefficient $\beta_{s,t}^{a,b}$ is determined by the choice

of ancillary states, measurement outcomes and the conventional witness W. In the experiment, as only two $|\Phi^+\rangle = (|00\rangle + |11\rangle)/\sqrt{2}$ and $|\Phi^-\rangle = (|00\rangle - |11\rangle)/\sqrt{2}$ out of four BSM outcomes are recorded, we consider the outcomes of a and b to be $+$ and $-$, which refer to $|\Phi^+\rangle$ and $|\Phi^-\rangle$, respectively. Thus, there are four kinds of $\beta_{s,t}^{a,b}$, depending on different values of a and b. By doing this, we improve the efficiency of experiments by four times comparing to the original proposal [10].

$$J = \frac{1}{4}\sum_{s,t}\left(\beta_{s,t}^{++}p(+,+|\tau_s,\omega_t) + \beta_{s,t}^{+-}p(+,-|\tau_s,\omega_t) + \beta_{s,t}^{-+}p(-,+|\tau_s,\omega_t) + \beta_{s,t}^{--}p(-,-|\tau_s,\omega_t)\right) \quad (12)$$

To witness entanglement for the bipartite states defined in Eq. (2) with MDIEW defined in Eq. (12), in total eight different ancillary state pairs should be prepared, and the results are summarized in Table 1.

Table 1: Our MDIEW in the form of Eq. (12) for the bipartite states defined in Eq. (2).

τ_s	ω_t	β_{st}^{++}	$p(+,+\|\tau_s,\omega_t)$	β_{st}^{+-}	$p(+,-\|\tau_s,\omega_t)$
$I/2$	$I/2$	$2\sqrt{3}-2$	$1/16$	$2\sqrt{3}+2$	$1/16$
$\frac{I+\sigma_x}{2}$	$\frac{I+\sigma_x}{2}$	1	$(1-v)/16$	-1	$(1+v)/16$
$\frac{I+\sigma_y}{2}$	$\frac{I+\sigma_y}{2}$	1	$(1-v)/16$	-1	$(1+v)/16$
$\frac{I+\sigma_z}{2}$	$\frac{I+\sigma_z}{2}$	1	$(1-v)/8$	1	$(1-v)/8$
$I/2$	$\frac{I+(\sigma_x+\sigma_y+\sigma_z)/\sqrt{3}}{2}$	$-\sqrt{3}$	$1/16$	0	-
$\frac{I+(\sigma_x+\sigma_y+\sigma_z)/\sqrt{3}}{2}$	$I/2$	$-\sqrt{3}$	$1/16$	0	-
$I/2$	$\frac{I+(-\sigma_x-\sigma_y+\sigma_z)/\sqrt{3}}{2}$	0	-	$-\sqrt{3}$	$1/16$
$\frac{I+(-\sigma_x-\sigma_y+\sigma_z)/\sqrt{3}}{2}$	$I/2$	0	-	$-\sqrt{3}$	$1/16$

Based on this proposal, we design and implement the MDIEW for the bipartite scenario, which is immune to all detection loopholes [11].

2.3. Experiment Results

In the experiment, eight ancillary state pairs $\{\tau_s, \omega_t\}$ are prepared. The states are encoded by tunable waveplates (one HWP sandwiched by two QWPs), which can realize arbitrary single-qubit unitary transformation. Different from directly polarization measurement in the conventional EW, the analysis of MDIEW is completed by BSMs on $\rho_3^v \otimes |\tau_s\rangle\langle\tau_s|_2$ and $\rho_4^v \otimes |\omega_t\rangle\langle\omega_t|_5$, with two, $|\Phi^\pm\rangle = (|HH\rangle \pm |VV\rangle)/\sqrt{2}$, out of four outcomes been collected, where ρ_3^v (ρ_4^v) is the experimentally to-be-witnessed state sent to Alice (Bob).

3. CONCLUSION

In this work, by proposing and realizing the time shift attack to the conventional EW methods, we claim that there do exist severe loopholes in the conventional EW procedure. Meanwhile, as a counter-measure, we design and realize the recently proposed MDIEW methods with six photon entanglement. The experimental results show that the MDIEW is practical for real-life implementation. We further expect that such MDI strategy can be applied to other fields, such as quantum key distribution and quantum secret sharing.

ACKNOWLEDGMENT

This work has been supported by the National Basic Research Program of China Grants No. 2011CB A00300, No. 2011CBA00301, No. 2011CB921300, and No. 2013CB336800, the National Natural Science Foundation of China Grants, and the Chinese Academy of Sciences.

REFERENCES

1. Bennett, C. H. and S. J. Wiesner, "Communication via one-and two-particle operators on Einstein-Podolsky-Rosen states," *Phys. Rev. Lett.*, Vol. 69, No. 20, 2881, 1992.
2. Bennett, C. H., et al., "Teleporting an unknown quantum state via dual classical and Einstein-Podolsky-Rosen channels," *Phys. Rev. Lett.*, Vol. 70, No. 13, 1895, 1993.

3. Bennett, C. H. and G. Brassard, "Quantum cryptography: Public key distribution and coin tossing," *Proceedings of IEEE International Conference on Computers, Systems and Signal Processing*, Vol. 175, No. 150, 1984.
4. Ekert, A. K., "Quantum cryptography based on Bell's theorem," *Phys. Rev. Lett.*, Vol. 67, No. 6, 661–663, 1991.
5. Curty, M., M. Lewenstein, and N. Ltkenhaus, "Entanglement as a precondition for secure quantum key distribution," *Phys. Rev. Lett.*, Vol. 92, No. 21, 217903, 2004.
6. Qi, B., C. H. F. Fung, H. K. Lo, et al., "Time-shift attack in practical quantum cryptosystems," *Quantum Inf. Comput.*, Vol. 7, No. 073, 2007.
7. Makarov, V., A. Anisimov, and J. Skaar, "Effects of detector efficiency mismatch on security of quantum cryptosystems," *Phys. Rev. A*, Vol. 74, No. 2, 022313, 2006.
8. Lo, H. K., M. Curty, and B. Qi, "Measurement-device-independent quantum key distribution," *Phys. Rev. Lett.*, Vol. 108, No. 13, 130503, 2012.
9. Buscemi, F., "All entangled quantum states are nonlocal," *Phys. Rev. Lett.*, Vol. 108, No. 20, 200401, 2012.
10. Branciard, C., D. Rosset, Y. C. Liang, et al., "Measurement-device-independent entanglement witnesses for all entangled quantum states," *Phys. Rev. Lett.*, Vol. 110, No. 6, 060405, 2013.
11. Xu, P., X. Yuan, L. K. Chen, et al., "Implementation of a measurement-device-independent entanglement witness," *Phys. Rev. Lett.*, Vol. 112, No. 14, 140506, 2014.

Graphene-based Transparent Nano-heater for Thermally-tuning Silicon Nanophotonic Integrated Devices

Longhai Yu, Sailing He, Jiajiu Zheng, and Daoxin Dai
State Key Laboratory for Modern Optical Instrumentation
Centre for Optical and Electromagnetic Research
Zhejiang Provincial Key Laboratory for Sensing Technologies
Zhejiang University, Zijingang Campus, Hangzhou 310058, China

Abstract— For the traditional metal heaters used for SOI (silicon-on-insulator)-nanowire devices, a thick SiO_2 upper-cladding layer is usually needed between the metal heater and the silicon core to isolate metal absorption, which makes the thermal tuning be with low response speed, low heating efficiency, and low maximal temperature. In this paper, we propose and demonstrate a graphene-based transparent nano-heater for SOI nanowires. The present transparent graphene nano-heater is designed to contact directly with the silicon core of an SOI nanowire by utilizing the transparency of graphene. The lack of the thick SiO_2 upper-cladding layer between the heater and the core region helps make fast thermally-tuning nanophotonic integrated devices. It is also beneficial to improve the heating efficiency because the heating volume is shrunk significantly. The graphene nano-heater is designed optimally to avoid any significant excess loss for the guided modes in the SOI nanowires. For example, the theoretical propagation losses of TE- and TM-polarization modes of a 600 nm-wide SOI nanowire with a 100 nm-wide graphene nano-heater are as low as $\sim 0.005\,\mathrm{dB/\mu m}$ and $\sim 0.013\,\mathrm{dB/\mu m}$ respectively. With this graphene-based transparent nano-heater, we present a thermally-tuning silicon Mach-Zehnder interferometer (MZI). The power consumption to have π phase-shift is $\sim 5.2\,\mathrm{mW}$ and $\sim 5.7\,\mathrm{mW}$ for TE- and TM-polarization modes, respectively. The theoretical response time is $\sim 4.4\,\mu\mathrm{s}$, which is about twice faster than that for the case of using a traditional metal heater. In addition, the temperature of the silicon core is almost the same as that of graphene nano-heaters. In contrast, for the case of traditional metal heaters, the silicon core has much lower temperature than the metal heater while the metal heater has a limited maximal operation-temperature. This indicates that one can achieve higher achievable temperature for the silicon core with the present graphene nano-heater than the traditional metal heater. Graphene can also be used as a heat conductor (other than heater) by utilizing its high thermal conductivity of up to 5300 W/mK. The excellent thermal properties of graphene make it very useful to enable efficient thermally-tuning nanophotonic integrated devices including optical switches, optical filters, etc..

1. INTRODUCTION

Silicon photonics has been regarded as one of the most promising technologies to realize low-cost large-scale photonic integrated circuits (PICs) because of the ability for ultra-small bending and the compatibility with CMOS fabrication processes [1]. It is well known that silicon has a large heat conductivity and a large thermo-optical (TO) coefficient ($\sim 1.8 \times 10^{-4}$/K at the wavelength of 1.55 μm), which are beneficial to realize efficient thermally-tuning nanophotonic integrated devices [2]. Traditional metal heaters used for SOI nanowires usually require a thick SiO_2 upper-cladding layer between the metal heater and the silicon core to isolate metal absorption. However, this will introduce some disadvantages, e.g., low response speed, low heating efficiency, and low maximal temperature.

Graphene has attracted strong interest for both fundamental studies and applications since the two-dimensional sheet was first exfoliated in 2004 [3]. Due to its unique structure, graphene has many extraordinary mechanical, electronic, photonic, and thermal properties [4]. A single-layer graphene is only 0.34 nm-thick, and it only absorbs $\sim 2.3\%$ of the vertically incident light. Thermal conductivity of up to 5300 W/mK is observed in graphene at room temperature [5, 6]. Graphene is also suggested to have a high value of optical damage threshold and excellent mechanical stability [5].

In this paper, we propose and demonstrate a graphene-based transparent nano-heater on SOI nanowires for the first time. The graphene nano-heater is designed to contact directly with the silicon core and there is no significant excess loss for the light propagating along the SOI nanowire because of the graphene transparency. By removing a thick SiO_2 upper-cladding layer (needed for a traditional metal heater), the graphene nano-heater has improved heating efficiency, response

speed and maximal operation-temperature. Based on the graphene nano-heater, a thermally-tuning silicon Mach-Zehnder interferometer (MZI) is also presented. The excellent thermal properties of graphene make it very useful to enable efficient thermally-tuning nanophotonic integrated devices including optical switches, optical filters, etc..

2. STRUCTURE AND DESIGN

The cross-section view of an SOI nanowire is shown in Figure 1(a). We choose an SOI wafer with a 250 nm-thick top silicon layer ($h_{Si} = 250\,\text{nm}$) and a 3 µm-thick SiO_2 box layer. Graphene is transferred directly to the core of the SOI nanowire and is then patterned to a nanoribbon [7], which is located at the edge of the SOI nanowire. The propagation losses for TE- and TM-polarization modes (see Figure 1(b)) are mainly due to the absorption of graphene [7, 8], and thus they are significantly dependent on the widths (w_{Si}, w_G) of the SOI nanowire and the graphene nanoribbon. A finite element simulation (FEM) mode-solver is used to evaluate the propagation losses of SOI nanowires with graphene nano-heaters and the waveguide parameters are optimized to reduce the excess loss for the guided modes.

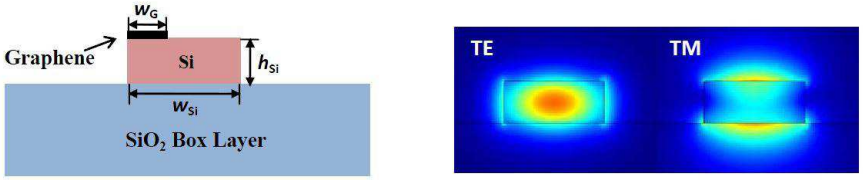

Figure 1: (a) Cross-section view of an SOI nanowire and a graphene nano-heater. (b) TE- (left) and TM- (right) polarization modes of an SOI nanowire.

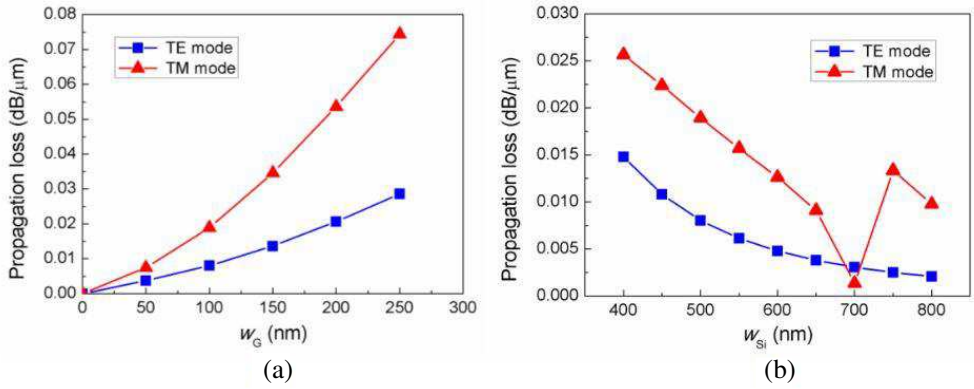

Figure 2: Propagation losses for TE- (blue squares) and TM- (red triangles) polarization modes (a) as w_G varies when $w_{Si} = 500\,\text{nm}$ and (b) as w_{Si} varies when $w_G = 100\,\text{nm}$.

Figure 2(a) shows the calculated propagation losses for TE- and TM-polarization modes as the width w_G of the graphene nanoribbon varies when $w_{Si} = 500\,\text{nm}$. With the increase of w_G, the propagation loss for both polarization modes gets an increase as well. Therefore it is desired to have a narrow graphene nanoribbon. Here we choose $w_G = 100\,\text{nm}$ regarding the fabrication process. In Figure 2(b), we show the calculated propagation losses for the case of $w_G = 100\,\text{nm}$ as the width w_{Si} of the SOI nanowire varies. It can be seen that the propagation losses get a significant decrease for both TE- and TM-polarization modes when w_{Si} increases from 400 nm to 600 nm. When $w_{Si} =\sim 700\,\text{nm}$, the TM polarization mode is hybridized, which makes the absorption loss reduced significantly (see Figure 2(b)). Regarding the single-mode condition, we choose $w_{Si} = 600\,\text{nm}$. Then the corresponding propagation losses are only $\sim 0.005\,\text{dB/µm}$ for TE polarization mode and $\sim 0.013\,\text{dB/µm}$ for TM polarization mode, which are much smaller than those of previous graphene-silicon hybrid SOI nanowires [7, 8]. And a graphene transparent nano-heater is achieved.

3. CHARACTERIZATION OF GRAPHENE TRANSPARENT NANO-HEATER

The thermal behaviors of the present graphene transparent nano-heater are modeled by using Poisson equation with FEM tools (similar to that in Reference [9]. The input power per unit length is 0.2 mW/μm, and the room temperature is 300 K. Figure 3 shows the results for 250 nm × 600 nm SOI nanowires with a 100 nm-wide graphene nano-heater, as well as a traditional metal heater (for which the metal is 1 μm-wide and the SiO_2 upper-cladding layer is 1 μm-thick).

From Figure 3, it can be seen that the temperatures in the silicon core are $T =\sim 449.8$ K and $T =\sim 376.9$ K when using a graphene nano-heater and a traditional metal heater, respectively. The power consumption for a nanowire in unit length to increase temperature by 1 K is ~ 0.00134 mW/ μmK and ~ 0.00260 mW/μmK, respectively. The power consumption of a graphene nano-heater is 50% smaller than that of a traditional metal heater. The improved heating efficiency of graphene nano-heaters results from the lack of the thick SiO_2 upper-cladding layer between the heater and the silicon core region, which reduces the heating volume significantly. Figure 3 also indicates that the temperature of the silicon core is almost as same as that of the heater for the case of using a graphene nano-heater. In contrast, when using a traditional metal heater, the temperature of the silicon core is much lower than that of the heater (e.g., $\Delta T =\sim 73$ K in the present case). Therefore, graphene nano-heaters are beneficial to achieve a higher operation-temperature and a larger tunable range in thermally-tuning nanophotonic devices.

Temporal responses of temperature for SOI nanowires with a graphene nano-heater and a metal heater are also calculated and compared as shown in Figure 4. The 90% rise time, which is defined as the time it takes for the change of temperature to reach 90% of the maximum value from zero, is

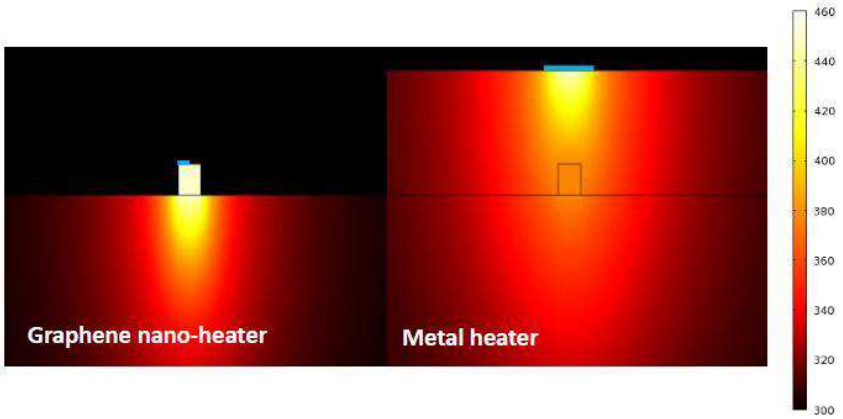

Figure 3: Temperature distribution of a 250 nm × 600 nm SOI nanowire. Left, using a 100 nm-wide graphene transparent nano-heater. Position of graphene is shown in blue line. Right, using a traditional 1 μm-wide metal heater with a 1 μm-thick SiO_2 up-cladding layer. Position of metal is shown in blue line.

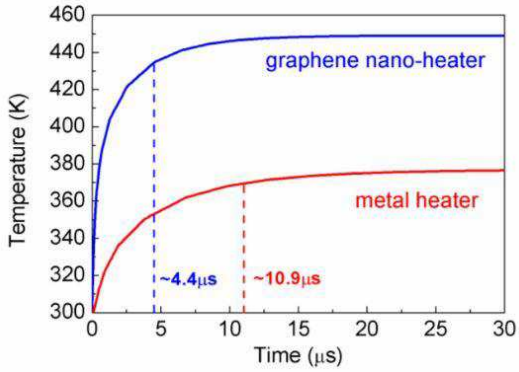

Figure 4: Temporal responses of temperature for SOI nanowires with a graphene nano-heater and a traditional metal heater. The 90% rising times are ~ 4.4 μs and ~ 10.9 μs respectively.

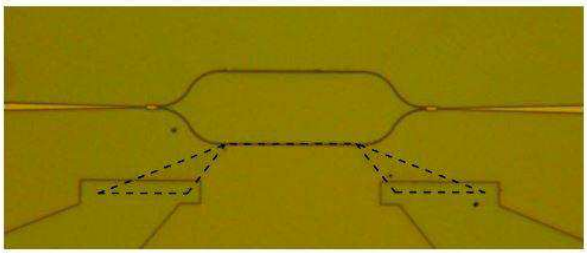

Figure 5: Microscopy picture of a Mach-Zehnder interferometer (MZI). One arm is heated by a graphene transparent nano-heater (dash line).

$\sim 4.4\,\mu s$ for graphene nano-heaters and $\sim 10.9\,\mu s$ for traditional metal heaters. This is because the SiO_2 upper-cladding region has poor thermal conductivity. For traditional metal heaters, it will take some time to transport heat from the heater to the silicon core, while for graphene nano-heaters, this problem is removed since graphene nano-heaters contact the silicon core directly.

The present graphene transparent nano-heater is then used to realize a thermally-tuning silicon Mach-Zehnder interferometer (MZI). As shown in Figure 5, one of the two MZI arms is heated and a phase difference $\Delta\varphi$ between the two arms is introduced. It indicates that the power consumption for $\Delta\varphi = \pi$ is $\sim 5.2\,mW$ and $\sim 5.7\,mW$ for TE- and TM- polarization modes respectively, which is half of that by using traditional metal heaters.

4. CONCLUSION

We have demonstrated a graphene-based transparent nano-heater for thermally-tuning silicon nanophotonic devices. The excess loss of graphene nano-heaters are minimized by optimizing the structure design. The theoretical calculation has shown that the present graphene nano-heaters have better performance than traditional metal heaters in terms of heating efficiency, response speed and maximal operation-temperature. It will help to enable efficient and fast thermally-tuning nanophotonic integrated devices, such as optical switches, optical filters, and so on. Based on the high thermal conductivity of graphene and the structure design, graphene can also be used as a heat conductor instead of a heater in the future.

REFERENCES

1. Soref, R., "The past, present, and future of silicon photonics," *IEEE Journal of Selected Topics in Quantum Electronics*, Vol. 12, No. 6, 1678–1687, 2006.
2. Espinola, R. L., M. C. Tsai, J. T. Yardley, and R. M. Osgood, "Fast and low-power thermooptic switch on thin silicon-on-insulator," *IEEE Photonics Technology Letters,* Vol. 15, No. 10, 1366–1368, 2003.
3. Novoselov, K. S., A. K. Geim, S. V. Morozov, D. Jiang, Y. Zhang, S. V. Dubonos, I. V. Grigorieva, and A. A. Firsov,"Electric field effect in atomically thin carbon films," *Science,* Vol. 306, No. 5696, 666–669, 2004.
4. Bonaccorso, F., Z. Sun, T. Hasan, and A. C. Ferrari, "Graphene photonics and optoelectronics," *Nature Photonics,* Vol. 4, No. 9, 611–622, 2010.
5. Bao, Q. L. and K. P. Loh, "Graphene photonics, plasmonics, and broadband optoelectronic devices," *Acs. Nano.*, Vol. 6, No. 5, 3677–3694, 2012.
6. Balandin, A. A., S. Ghosh, W. Z. Bao, I. Calizo, D. Teweldebrhan, F. Miao, and C. N. Lau, "Superior thermal conductivity of single-layer graphene," *Nano Letters,* Vol. 8, No. 3, 902–907, 2008.
7. Yu, L., J. Zheng, D. Dai, and S. He, "Observation of optically induced transparency effect in silicon nanophotonic wires with graphene," *SPIE OPTO*, 89890C-89890C–8, San Francisco, California, USA, Feb. 1–6, 2014.
8. Yu, L., Y. Xu, Y. Shi, and D. Dai, "Linear and nonlinear optical absorption of on-chip silicon-on-insulator nanowires with graphene," *Asia Communications and Photonics Conference*, AS1B.3, Guangzhou, China, Nov. 7–10, 2012.
9. Yang, L., D. X. Dai, and S. L. He, "Thermal analysis for a photonic Si ridge wire with a submicron metal heater," *Optics Communications,* Vol. 281, No. 9, 2467–2471, 2008.

On an Application of the Hypothesis for the Identity of the $L_2(c, \rho, n)$ and $\hat{L}_2(\hat{c}, \hat{\rho}, \hat{n})$ Numbers

Mariana Nikolova Georgieva-Grosse[1] and Georgi Nikolov Georgiev[2]

[1]Consulting and Researcher in Physics and Computer Sciences, D-70839 Gerlingen, Germany
[2]Faculty of Mathematics and Informatics
University of Veliko Tirnovo "St. St. Cyril and Methodius", BG-5000 Veliko Tirnovo, Bulgaria

Abstract— The theory of waveguides is pointed out as a field of application of the mathematical hypothesis, asserting that the finite real positive numbers $L_2(c, \rho, n)$ and $\hat{L}_2(\hat{c}, \hat{\rho}, \hat{n})$, advanced through some positive purely imaginary, resp. real zeros in x, resp. in $\hat{x}$ of a special function, constructed by two complex $\Phi(a, c; x)$ and $\Phi(a, c; \rho x)$, resp. real $\hat{\Phi}(\hat{a}, \hat{c}; \hat{x})$ and $\hat{\Phi}(\hat{a}, \hat{c}; \hat{\rho}\hat{x})$ Kummer, and two complex $\Psi(a, c; x)$ and $\Psi(a, c; \rho x)$, resp. real $\hat{\Psi}(\hat{a}, \hat{c}; \hat{x})$ and $\hat{\Psi}(\hat{a}, \hat{c}; \hat{\rho}\hat{x})$ Tricomi confluent hypergeometric ones of appropriately picked out parameters and variable, are identical, provided it is fulfilled: $c = \hat{c}$, $\rho = \hat{\rho}$ and $n = \hat{n}$, (a — complex; $\hat{a}$, c, $\hat{c}$, $\hat{x}$, ρ and $\hat{\rho}$ — real; ρ and $\hat{\rho}$ — positive, less than unity; x — positive purely imaginary; n — natural and $\hat{n}$ — positive integer; n and $\hat{n}$ — numbers of the zeros). It is indicated that the truthfulness of statement formulated entails the coincidence in case $c = \hat{c} = 3$ of certain (envelope) curves in the phase diagrams of the normal TE_{0n} and of the one of the two possible slow $\hat{TE}_{0\hat{n}}$ modes — the $\hat{TE}^{(1)}_{0\hat{n}}$ wave ($n = \hat{n}$) in the coaxial waveguide with ferrite, magnetized azimuthally in negative (clockwise) direction of equations, written in terms of the quantities $L_2(c, \rho, n)$, resp. $\hat{L}_2(\hat{c}, \hat{\rho}, \hat{n})$. The curves mentioned restrict the areas of propagation of the first (second) mode from the side of higher (lower) frequencies. Besides, the physical sense ascribed to parameter ρ ($\hat{\rho}$) is a relative thickness of the central conductor of the structure and to n ($\hat{n}$) — an order of the propagating mode.

1. INTRODUCTION

Recently, it has been established that if the limited arbitrary real numbers c and $\hat{c}$, the real positive ones ρ and $\hat{\rho}$, ($0 < \rho < 1$ and $0 < \hat{\rho} < 1$), and the natural number n and the positive integer $\hat{n}$ are equal, the same holds for the finite real positive numbers $L_2(c, \rho, n)$ and $\hat{L}_2(\hat{c}, \hat{\rho}, \hat{n})$, defined like the attained under certain conditions common limits of some infnite sequences of real numbers, as well. The terms of the latter are proportional to the positive purely imaginary, resp. real zeros of a complex, resp. real transcendental function, involving four complex, resp. real Kummer and Tricomi confluent hypergeometric functions $\Phi(a, c; x)$ and $\Psi(a, c; x)$ [8] of appropriately chosen parameters and variable [17]. (Hats "ˆ" are put above the symbols, relevant to the second class of numbers [2, 4]. In view of this, the quantities c and $\hat{c}$ are the second parameters of confluent functions, ρ and $\hat{\rho}$ are parameters, multiplying the independent variable of functions $\hat{x}$, resp. $\hat{x}$, while n and $\hat{n}$ are the numbers of the zeros in question of the general function. This assumption has been called Hypothesisi for the identity of $L_2(c, \rho, n)$ and $\hat{L}_2(\hat{c}, \hat{\rho}, \hat{n})$ numbers [1].

In this investigation an application of the above statement in the theory of azimuthally magnetized coaxial ferrite waveguides [3–5], is considered. It has been found out earlier that there are $En_{1-} - (\hat{E}n_{1-}-)$ envelope curves in the the $\bar{\beta}(\bar{r}_0) - [\bar{\hat{\beta}}^{(1)}(\bar{\hat{r}}^{(1)}_0)-]$ phase diagram of the normal TE_{0n} [3–5] (of the the $\hat{TE}^{(1)}_{0\hat{n}}$ wave which is the one of the two possible slow $\hat{TE}_{0\hat{n}}$ [4]) modes of equation $\bar{\beta}_{en-} = \bar{\beta}_{en-}(\bar{r}_{0en-})[\bar{\hat{\beta}}^{(1)}_{en-} = \bar{\hat{\beta}}^{(1)}_{en-}(\bar{\hat{r}}^{(1)}_{0en-})]$, written in parametric form as: $\bar{r}_{0en-} = L(c, \rho, n)/[|\alpha_{en-}|(1 - \alpha^2_{en-})^{1/2}]$, $\bar{\beta}_{en-} = (1 - \alpha^2_{en-})^{1/2}(\bar{\hat{r}}^{(1)}_{0en-} = \hat{L}_2(\hat{c}, \hat{\rho}, \hat{n})/\{|\hat{\alpha}^{(1)}_{en-}|[1 - (\hat{\alpha}^{(1)}_{en-})^2]^{1/2}\}$, $\bar{\hat{\beta}}^{(1)}_{en-} = [1 - (\hat{\alpha}^{(1)}_{en-})^2]^{1/2})$ with $c = \hat{c} = 3$ [3–5]. Here $\bar{\beta}$ and $\bar{r}_0$ ($\bar{\hat{\beta}}^{(1)}$ and $\bar{\hat{r}}^{(1)}_0$) are the normalized in a special way phase constant and guide radius, $\rho(\hat{\rho})$ is the relative thickness of the central switching conductor of the structure, $\alpha(\hat{\alpha})$ is the off-diagonal ferrite Polder permeability tensor, $n(\hat{n})$ — order of the mode. All quantities without (with) hats relate to the normal (slow) modes, those with the superscripts (1) — to the slow $\hat{TE}^{(1)}_{0\hat{n}}$ waves and the ones with the subsript "$en-$" — to the envelopes. (Note that both α and $\hat{\alpha}^{(1)}$ are less than unity.) The $En_{1-} - (\hat{E}n_{1-}-)$ line for specific $n(\hat{n})$ restricts from above (below) the phase characteristics for negative (clockwise) ferrite magnetization. It follows from the Hypothesis for identity of numbers that if $\rho = \hat{\rho}$ and $n = \hat{n}$, the

envelopes in question for a TE_{0n} and a $\hat{TE}^{(1)}_{0\hat{n}}$ mode of the same order in two waveguides of the same relative thickness of the inner wire (or in given configuration) coincide. Accordingly, it could be regarded as a line at which the normal mode is transformed to a slow one when the normalized radius (i.e., frequency) grows. Graphical results for different parameters $\rho(\hat{\rho})$ are presented and juxtaposed, assuming $n = \hat{n} = 1$.

2. HYPOTHESIS FOR THE IDENTITY OF THE $L_2(c, \rho, n)$ AND $\hat{L}_2(\hat{c}, \hat{\rho}, \hat{n})$ NUMBERS

Definition 1: *The $L_2(c, \rho, n)$ numbers in which c is a restricted arbitrary real, positive, negative or zero, ρ is real, positive, $0 < \rho < 1$ and n is a natural number, are finite real positive ones, specified in the following way:*

i) In case $c \neq l$, $l = 0, -1, -2, \ldots$:

$$L_2(c, \rho, n) = \lim_{k_- \to -\infty} K_{2-}(c, \rho, n, k_-) = \lim_{k_- \to -\infty} M_{2-}(c, \rho, n, k_-), \tag{1}$$

where $K_{2-}(c, \rho, n, k_-) = |k_-| \chi^{(c)}_{k_-,n}(\rho)$, $M_{2-}(c, \rho, n, k_-) = |a_-| \chi^{(c)}_{k_-,n}(\rho)$ and $\chi^{(c)}_{k_-,n}(\rho)$ is the nth positive purely imaginary zero of the function $F_2(a, c; x, \rho) = \Phi(a, c; x)\Psi(a, c; \rho x) - \Phi(a, c; \rho x)\Psi(a, c; x)$ in x, $(n = 1, 2, 3, \ldots)$ in which $\Phi(a, c; x)$ and $\Psi(a, c; x)$ are the Kummer and Tricomi confluent hypergeometric functions with $a = a_-$ $a_- = c/2 - jk_-$ — complex, $c = 2\mathrm{Re}a$ $(c = 2\mathrm{Re}a_-)$, $x = jz$ — positive purely imaginary, z — real, positive, k_- — real, negative, $-\infty < k_- < 0$, ρ — real, positive, (c, n — fixed).

ii) On the understanding that $c = l$ and ε is an infinitesimal positive real number:

$$L_2(c, \rho, n) = \lim_{\varepsilon \to 0} L_2(l - \varepsilon, \rho, n) = \lim_{\varepsilon \to 0} L_2(l + \varepsilon, \rho, n) = L_2(2 - l, \rho, n), \tag{2}$$

where $L_2(l - \varepsilon, \rho, n)$ and $L_2(l + \varepsilon, \rho, n)$ are finite real positive quantities, determined in the sense of point i).

iii) When $c = g$, $g = 2 - l (g = 2, 3, 4, \ldots)$:

$$L_2(g, \rho, n) = \lim_{\varepsilon \to 0} L_2(g - \varepsilon, \rho, n) = \lim_{\varepsilon \to 0} L_2(g + \varepsilon, \rho, n). \tag{3}$$

[$L_2(g - \varepsilon, \rho, n)$, $\lim_{\varepsilon \to 0} L_2(g + \varepsilon, \rho, n)$ *and ε are specified like in the previous item.*]

Besides it is carried out too:

$$L_2(c, \rho, n) = L_2(2 - c, \rho, n), \quad c \neq l, \tag{4}$$

$$L_2(1 + h, \rho, n) = L_2(1 - h, \rho, n), \quad h \neq l, \tag{5}$$

$$L_2(1 + l, \rho, n) = L_2(1 - l, \rho, n), \tag{6}$$

h — real number.

Definition 2: *The $\hat{L}_2(\hat{c}, \hat{\rho}, \hat{n})$ numbers in which $\hat{c}$ is a restricted arbitrary real positive, negative or zero, $\hat{\rho}$ is real, positive, $0 < \hat{\rho} < 1$ and $\hat{n}$ is a natural number are finite positive real ones determined by means of* **Definition 1** *provided:*

i) The meaning of notations is unchanged;

ii) The form of equalities is preserved the same;

iii) Hats are put above all symbols;

iv) All quantities are assumed real;

v) In point i) $\hat{\chi}^{(\hat{c})}_{\hat{k}_-,\hat{n}}(\hat{\rho})$ is the $\hat{n}$th real positive zero of the function $\hat{F}_2(\hat{a}, \hat{c}; \hat{x}, \hat{\rho}) = \hat{\Phi}(\hat{a}, \hat{c}; \hat{x})\hat{\Psi}(\hat{a}, \hat{c}; \hat{\rho}\hat{x}) - \hat{\Phi}(\hat{a}, \hat{c}; \hat{\rho}\hat{x})\hat{\Psi}(\hat{a}, \hat{c}; \hat{x})$ in $\hat{x}$ in which $\hat{\Phi}(\hat{a}, \hat{c}; \hat{x})$ and $\hat{\Psi}(\hat{a}, \hat{c}; \hat{x})$ are the Kummer and Tricomi confluent hypergeometric functions with $\hat{a} = \hat{c}/2 + \hat{k}_-$ — real, negative, $(\hat{a} \neq -\hat{m}, \hat{m} = 1, 2, 3, \ldots)$, $\hat{c} > 0$ or $\hat{c} < 0$ (in both cases $\hat{a} < \hat{c}$), $\hat{x}$ — real, positive, $\hat{k}_- = \hat{a} - \hat{c}/2$ — real, negative, $\hat{n} = 1, 2, \ldots, \hat{t}$, $\hat{t}$ — finite positive integer, whose numerical equivalent is determined by the parameters of $\hat{F}_2$ $(\hat{a}_- \equiv \hat{a})$, $(\hat{c}, \hat{n}$ — fixed).

vi) Item iii) might be dropped.

Hypothesis 1: *On condition that* $c = \hat{c}$, $\rho = \hat{\rho}$ *and* $n = \hat{n}$, *where* c *and* $\hat{c}$ *are restricted arbitrary real,* ρ *and* $\hat{\rho}$ *are real, positive, less than unity,* n *is a natural number and* $\hat{n}$ *— a positive integer (*n *and* $\hat{n}$ *— restricted), the* $L_2(c,\rho,n)$ *numbers in the sense of* **Definition 1** *and the* $\hat{L}_2(\hat{c},\hat{\rho},\hat{n})$ *ones in that of* **Definition 2**, *are identical. Accordingly, it is fulfilled:*

$$L_2(c,\rho,n) \equiv \hat{L}_2(\hat{c},\hat{\rho},\hat{n}). \tag{7}$$

If beside the above assumptions it holds also that $c = \hat{c} \neq l$ $(l = \hat{l})$, $c = g$, $g = 2 - l$ $(g = 2,3,4,\ldots)$, $k_- = \hat{k}_-$ is large negative and $\varepsilon = \hat{\varepsilon}$ is an infinitesimal positive real number, it is true:

$$\chi^{(c)}_{k_-,n}(\rho) \approx \hat{\chi}^{(\hat{c})}_{\hat{k}_-,\hat{n}}(\hat{\rho}), \tag{8}$$

$$K_{2-}(c,n,\rho,k_-)\,M_{2-}(c,n,\rho,k_-) \approx \hat{K}_{2-}\left(\hat{c},\hat{n},\hat{\rho},\hat{k}_-\right) \approx \hat{M}_{2-}\left(\hat{c},\hat{n},\hat{\rho},\hat{k}_-\right). \tag{9}$$

(The meaning of all tokens is as in **Definitions 1** and **2**.).

3. APPLICATION IN THE THEORY OF WAVEGUIDES

The propagation of normal TE_{0n} (slow $\hat{TE}_{0\hat{n}}$) modes of phase constant $\beta(\hat{\beta})$ in the coaxial waveguide of outer and inner conductor radii r_0 and r_1, resp., uniformly filled with azimuthally magnetized lossless remanent ferrite, described by a Polder permeability tensor $\vec{\vec{\mu}} = \mu_0[\mu_{ij}]$, $i,j = 1,2,3$, $\mu_{12} = \mu_{21} = \mu_{23} = \mu_{32} = 0$, $\mu_{ii} = 1$, $\mu_{13} = -\mu_{31} = -j\alpha$, $\alpha = \gamma M_r/\omega$, ($\gamma$ — gyromagnetic ratio, M_r — remanent magnetization, ω — angular frequency of the wave), and a scalar permittivity $\varepsilon = \varepsilon_0\varepsilon_r$, is governed by the equations:

$$\Phi(a,c;x_0)/\Psi(a,c;x_0) = \Phi(a,c;\rho x_0)/\Psi(a,c;\rho x_0), \tag{10}$$

$$\hat{\Phi}(\hat{a},\hat{c};\hat{x}_0)/\hat{\Psi}(\hat{a},\hat{c};\hat{x}_0) = \hat{\Phi}(\hat{a},\hat{c};\hat{\rho}\hat{x}_0)/\hat{\Psi}(\hat{a},\hat{c};\hat{\rho}\hat{x}_0). \tag{11}$$

In Eq. (10) $a = c/2 - jk$, $c = 3$, $x_0 = jz_0$, $k = \alpha\bar{\beta}/\left(2\bar{\beta}_2\right)$, $z_0 = 2\bar{\beta}_2\bar{r}_0$, $\rho = \bar{r}_0/\bar{r}_1$ (k, z_0, ρ — real, $-\infty < k < +\infty$, $0 < |\alpha| < 1$, $z_0 > 0$, $0 < \rho < 1$). It is satisfied, if $\bar{\beta}_2 = \chi^{(c)}_{k,n}(\rho)/(2\bar{r}_0)$ that determines the eigenvalue spectrum of the fields studied. The barred (normalized) quantities are introduced through the relations: $\bar{\beta} = \beta/\left(\beta_0\sqrt{\varepsilon_r}\right)$, $\bar{\beta}_2 = \beta_2/\left(\beta_0\sqrt{\varepsilon_r}\right)$, $\bar{r}_0 = \beta_0 r_0\sqrt{\varepsilon_r}$, $\bar{r}_1 = \beta_0 r_1\sqrt{\varepsilon_r}$, resp. where $\beta_0 = \omega\sqrt{\varepsilon_0\mu_0}$, $\{\bar{\beta}_2 = \left[\omega^2\varepsilon_0\mu_0\varepsilon_r\left(1-\alpha^2\right) - \beta^2\right]^{1/2}$ — radial wavenumber$\}$. Figs. 1(a)–(c) and 2(a)–(c) portray the region (featured by light green) in which the normal TE_{01} wave may be sustained for positive ($\alpha_+ > 0$) and negative ($\alpha_- < 0$) ferrite magnetization in case $\rho = 0$, 0.05 and 0.1, resp. The relevant normalized $\bar{\beta}(\bar{r}_0)$ — phase characteristics with α as parameter, counted, employing the scheme, worked out earlier [1], are also shown in these pictures by solid and dashed lines, resp. In case $\alpha_+ > 0$, the aforesaid region is bounded from the side of lower frequencies by the $\alpha = 0$ solid curve, concurring to a dielectric-loading and is termless beyond the frequency range above. When $\alpha_- < 0$, however, it is bilaterally limited. Its lower border is more complex and as an upper one serves the En_{1-} — envelope dotted line of equation of equation $\bar{\beta}_{en-} = \bar{\beta}_{en-}(\bar{r}_{0en-})$, written in parametric form as: $\bar{r}_{0en-} = L_2(c,\rho,n)/[|\alpha_{en-}|(1-\alpha^2_{en-})^{1/2}]$, $\bar{\beta}_{en-} = (1-\alpha^2_{en-})^{1/2}$ (α_{en-} is a parameter).

In Eq. (11) $\hat{a} = \hat{c}/2 + \hat{k}$, $\hat{c} = 3$, $\hat{x}_0 = 2\hat{\beta}_2\hat{r}_0$, $\hat{k} = \hat{\alpha}\bar{\hat{\beta}}/(2\bar{\hat{\beta}}_2)$, $\hat{\rho} = \bar{\hat{r}}_0/\bar{\hat{r}}_1$, $\bar{\hat{\beta}} = \hat{\beta}/(\beta_0\sqrt{\varepsilon_r})$, $\bar{\hat{\beta}}_2 = \hat{\beta}_2/(\beta_0\sqrt{\varepsilon_r})$, $\bar{\hat{r}}_0 = \beta_0\hat{r}_0\sqrt{\varepsilon_r}$ and $\bar{\hat{r}}_1 = \beta_0\hat{r}_1\sqrt{\varepsilon_r}$, $\{\hat{\beta}_2 = [\hat{\beta}^2 - \omega^2\varepsilon_0\mu_0\varepsilon_r(1-\hat{\alpha}^2)]^{1/2}$ — radial wavenumber$\}$. All quantities relevant to the slow waves are real and are distinguished by hats "ˆ". They are transmitted, provided $\bar{\hat{\beta}}_2 = \hat{\chi}^{(\hat{c})}_{\hat{k}_-,\hat{n}}(\hat{\rho})/(2\bar{\hat{r}}_0)$, assuming $\hat{k}_- < \hat{k}_{-th}(\hat{\rho})$, where $\hat{k}_{-th}(\hat{\rho}) < 0$ is certain threshold value of parameter $\hat{k}_-$, depending on $\hat{\rho}$, i.e., for $\hat{\alpha}_- < 0$ only [5]. The $\bar{\hat{\beta}}^{(1)}(\bar{\hat{r}}^{(1)}_0)$ — dashed phase curves of the $\hat{TE}^{(1)}_{0\hat{n}}$ mode (the one of the two possible $\hat{TE}_{0\hat{n}}$ waves — $\hat{TE}^{(1)}_{0\hat{n}}$ and $\hat{TE}^{(2)}_{0\hat{n}}$ [4]), supported for $|\hat{\alpha}^{(1)}_-| < 1$ are depicted in Figs. 2(a)–(c). They have a lower limit — the $\hat{En}_{1-}$ — envelope of equation $\bar{\hat{\beta}}^{(1)}_{en-} = \bar{\hat{\beta}}^{(1)}_{en-}(\bar{\hat{r}}^{(1)}_{0en-})]$, presented parametrically like: $\bar{\hat{r}}^{(1)}_{0en-} = \hat{L}_2(\hat{c},\hat{\rho},\hat{n})/\{|\hat{\alpha}^{(1)}_{en-}|[1-(\hat{\alpha}^{(1)}_{en-})^2]^{1/2}\}$, $\bar{\hat{\beta}}^{(1)}_{en-} = [1-(\hat{\alpha}^{(1)}_{en-})^2]^{1/2}$ ($\hat{\alpha}^{(1)}_{en-}$ is a parameter). The domain in that the slow wave in question might get excited (presented by dark green) is restricted from below and unlimited from above. (Throughout the paper the subscripts "+" ("−") and "$en-$"

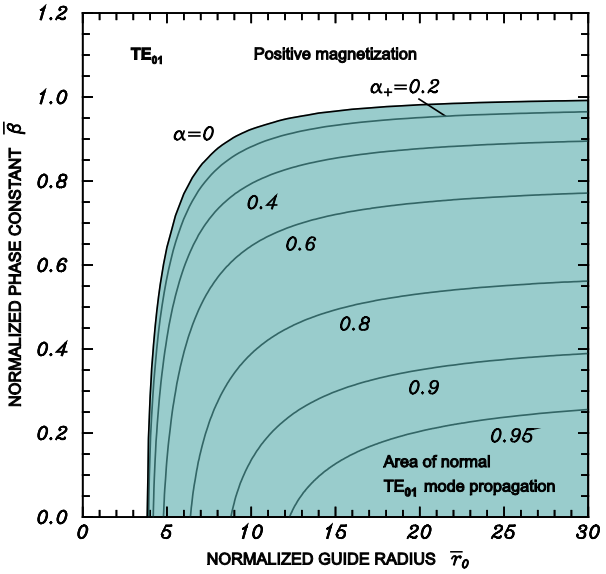

Figure 1: Area of normal TE_{01} mode propagation in case of positive magnetization of the azimuthally magnetized circular ferrite waveguide.

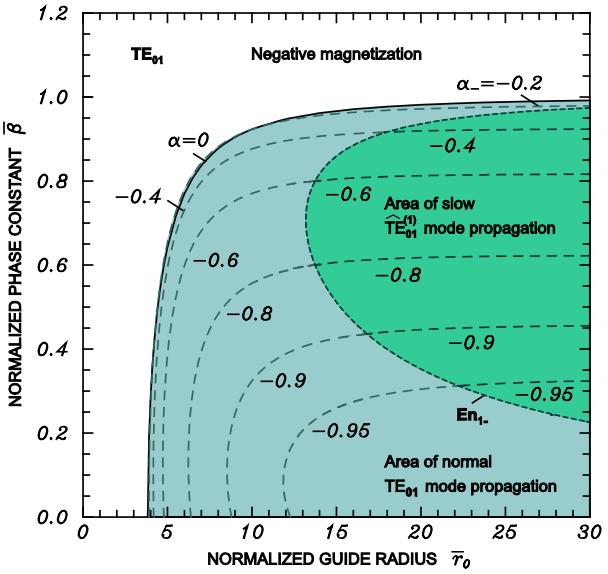

Figure 2: Areas of normal TE_{01} and slow $\hat{TE}_{01}^{(1)}$ mode propagation in case of negative magnetization of the azimuthally magnetized circular ferrite waveguide.

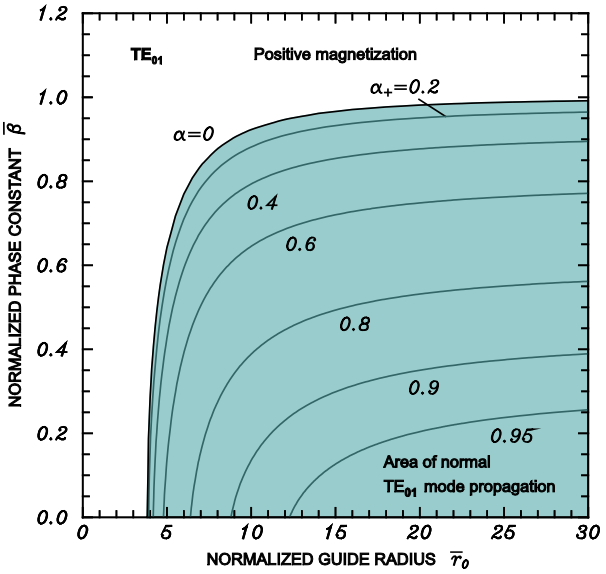

Figure 3: Area of normal TE_{01} mode propagation in case of positive magnetization of the azimuthally magnetized coaxial ferrite waveguide, $\rho = 0.05$.

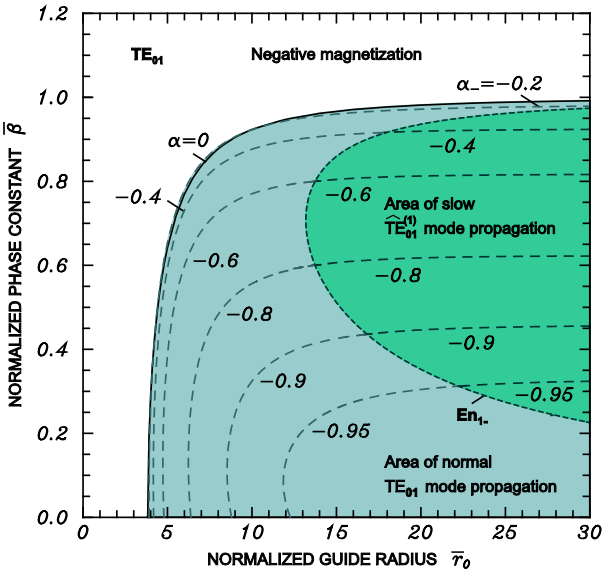

Figure 4: Areas of normal TE_{01} and slow $\hat{TE}_{01}^{(1)}$ mode propagation in case of negative magnetization of the azimuthally magnetized coaxial ferrite waveguide, $\rho = 0.05$.

distinguish the quantities, relevant to positive (negative) magnetization, resp. to the envelopes and the superscript (1) — marks those, having reference to the $\hat{TE}_{0\hat{n}}^{(1)}$ mode.). Since $c = \hat{c} = 3$, with regard to Hypothesis 1 (Eq. (7)), it follows that if $\alpha_{en-} \equiv \hat{\alpha}_{en-}^{(1)}$ and $n = \hat{n}$, then $\bar{r}_{0en-} \equiv \bar{\hat{r}}_{0en-}^{(1)}$ and $\bar{\beta}_{en-} \equiv \bar{\hat{\beta}}_{en-}^{(1)}$, i.e., the $En_{1-}-$ and $\hat{E}n_{1-}-$ curves coincide. Thus, in case of negative magnetization the $En_{1-} - (\hat{E}n_{1-}-)$ line separates the zone of propagation in two sub-domains: left (light green) and right (dark green) in which a normal TE_{0n} and slow $\hat{TE}_{0\hat{n}}^{(1)}$ mode, resp. might be observed. Besides, it is connected with the upper boundary of the region of phase shifter operation of the confguration for the first set of fields [5].

As seen the increase of ρ shifts the envelope(s) to the right. Thus, the area of normal TE_{0n}

mode propagation expands (of the slow $\hat{TE}_{0\hat{n}}^{(1)}$ waves shrinks). Thus, the first (second) ones might be transmitted (might get excited) at higher frequencies when the central conductor becomes thicker.

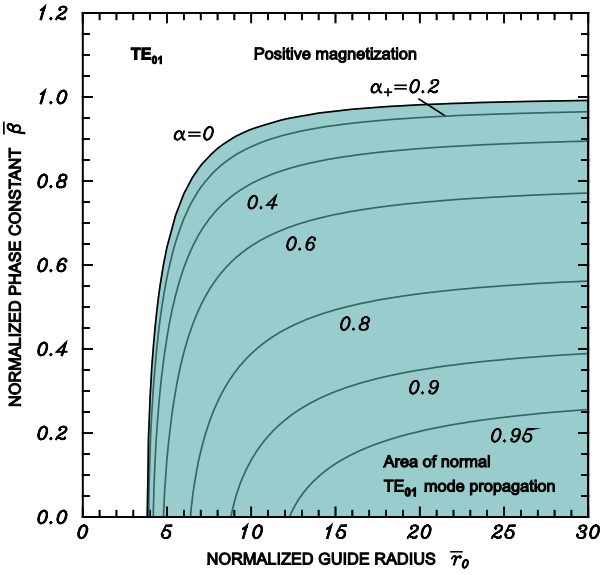

Figure 5: Area of normal TE_{01} mode propagation in case of positive magnetization of the azimuthally magnetized coaxial ferrite waveguide, $\rho = 0.1$.

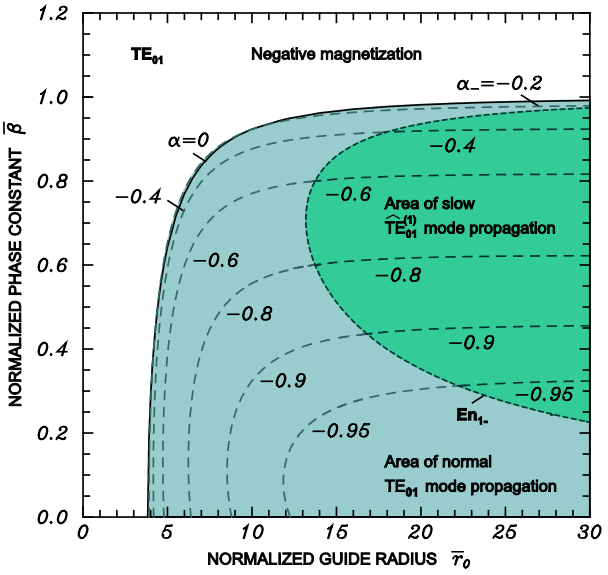

Figure 6: Areas of normal TE_{01} and slow $\hat{TE}_{01}^{(1)}$ mode propagation in case of negative magnetization of the azimuthally magnetized coaxial ferrite waveguide, $\rho = 0.1$.

4. THEOREM FOR THE IDENTITY OF THE $L_2(c, \rho, n)$ AND $\hat{L}_2(\hat{c}, \hat{\rho}, \hat{n})$ NUMBERS

In case $\rho = 0$ (circular waveguide, entirely filled with azimuthally magnetized ferrite) the relevant $En_{1-}-$ and $\hat{E}n_{1-}-$ curves of parametric equations of the form: $\bar{r}_{0en-} = L(c,n)/[|\alpha_{en-}|(1-\alpha_{en-}^2)^{1/2}]$, $\bar{\beta}_{en-} = (1-\alpha_{en-}^2)^{1/2}$ and $\bar{\hat{r}}_{0en-}^{(1)} = \hat{L}(\hat{c},\hat{n})/\{|\hat{\alpha}_{en-}^{(1)}|[1-(\hat{\alpha}_{en-}^{(1)})^2]^{1/2}\}$, $\bar{\hat{\beta}}_{en-}^{(1)} = [1-(\hat{\alpha}_{en-}^{(1)})^2]^{1/2}$, resp are completely indistinguishable. This is a corollary of Theorem 1 [3] for the identity of $L(c,n)$ and $\hat{L}(\hat{c},\hat{n})$ numbers (denoted recently also as $L_1(c,n)$ and $\hat{L}_1(\hat{c},\hat{n})$ ones [5]).

The exact numerical analysis has shown that for some values of parameters $c = \hat{c}$, $\rho = \hat{\rho}$ and $n = \hat{n}$ there is a slight deviation between the calculated outcomes for $L_2(c,\rho,n)$ and $\hat{L}_2(\hat{c},\hat{\rho},\hat{n})$. In particular this is observed in case $c = \hat{c} = 3$, corresponding to the propagation problem considered [5]. Accordingly, the resulting $En_{1-}-$ and $\hat{E}n_{1-}-$ curves should not coincide completely.

This would lead to the appearance of a gap between the existence areas of the normal and slow waves in which no propagation at all is possible or to the springing up of a region in which the areas in question would overlap, i.e., in which a simultaneous propagation of slow and normal wave could be observed for in the same band.

Such effects, however, are not observed in the circular waveguide ($\rho = 0$) which is a partial case of the coaxial structure ($\rho > 0$). There are no physical reasons which could lead to their appearance when the finite central conductor is inserted. Thus, the deviation from the exact coincidence of mathematical outcomes of statement (7) should be ascribed to computational reasons only.

This could be accepted as a physical substantiation of the truthfulness of relation (7). Therefore the Hypothesis for identity of $L_2(c,\rho,n)$ and $\hat{L}_2(\hat{c},\hat{\rho},\hat{n})$ numbers could be reformulated as a Theorem for the identity of $L_2(c,\rho,n)$ and $\hat{L}_2(\hat{c},\hat{\rho},\hat{n})$ numbers.

5. CONCLUSION

It is demonstrated numerically that the positive real numbers $L(c;n)$ and $\hat{L}(\hat{c};\hat{n})$ (the limits of specially constructed sequences of numbers with terms, involving the zeros of certain complex, resp. real Kummer functions) concur, if their parameters c and $\hat{c}$ (arbitrary real), and n and $\hat{n}$ (restricted natural numbers), are the same. It is shown that the peculiarities of the rotationally symmetric TE modes transmission in the circular waveguide, entirely filled with azimuthally magnetized ferrite

are directly linked with this mathematical outcome. From a physical point of view its validity when $c = \hat{c} = 3$ for each $n = \hat{n}$ means existence of a curve in the phase portrait of geometry for negative magnetization of the load at which the propagating mode is transformed from normal to slow.

ACKNOWLEDGMENT

We express our gratitude to our mother Trifonka Romanova Popnikolova and to our late father Nikola Georgiev Popnikolov for their self-denial and for their tremendous efforts to support all our undertakings.

REFERENCES

1. Georgiev, G. N. and M. N. Georgieva-Grosse, "Hypothesis for the identity of the $L_2(c, \rho, n)$ and $\hat{L}_2(\hat{c}, \hat{\rho}, \hat{n})$ numbers and its application in the theory of waveguides," *Progress In Electromagnetics Research Symposium Abstracts*, 805–806, Stockholm, Sweden, Aug. 12–15, 2013; *PIERS Proceedings*, 940–945, Stockholm, Sweden, Aug. 12–15, 2013.
2. Tricomi, F. G., *Funzioni Ipergeometriche Confluenti*, Edizioni Cremonese, Rome, Italy, 1954.
3. Georgiev, G. N. and M. N. Georgieva-Grosse, "New elements in the theory of the coaxial waveguide with azimuthally magnetized ferrite," *Proc. Int. Sem. Days Diffr., 2005, DD'05*, 81–93, in Abstracts, 29, St. Petersburg, Russia, Jun. 28–Jul. 1, 2005.
4. Georgiev, G. N. and M. N. Georgieva-Grosse, "A property of the $L(c, \rho, n)$ numbers and its application to waveguide propagation," *Proc. XXIX URSI General Assembly*, BK.6(120), CDROM, Chicago, IL, USA, Aug. 7–16, 2008.
5. Georgieva-Grosse, M. N. and G. N. Georgiev, "Transmission properties of the circular waveguide completely or partially filled with azimuthally magnetized ferrite: Review of recent results," *Proc. 1st IEEE-APS Topical Conf. Antennas Propagat. Wireless Commun., IEEE APWC'11*, 865–868, Turin, Italy, Sep. 12–16, 2011, (*Invited Paper* in the Special Session "Advances in wireless communications and their applications" organized by M. N. Georgieva-Grosse and G. N. Georgiev).

Solving Nonlinear Helmholtz Equation via Fourier Series

M. S. Sautbekova and S. S. Sautbekov
Eurasian National University, Kazakhstan

Abstract— In recent work, we represent a new way of solving non-linear Helmholtz equation. Undefined solution Helmholtz equation is reduced to the system of non-linear algebraic equations by spreading it in a Fourier series, in which we find Fourier coefficients. Later on, by these coefficients we can define our unknown function.

1. INTRODUCTION

Non-linear phenomena accompany many physical processes investigated in optics, acoustics, fluid dynamics, plasma physics and other fields of physics. Abstracting from specific, defined physical properties of mechanisms of processes in each of these areas, it is possible to establish general laws and regularities non-linearity manifestations, regardless of their physical content. This suggests that the theory of non-linear wave processes of physical self-discipline is quite extensive and dynamic. Confirming its widest possibilities is the fact that the methods and results of the theory of non-linear waves have been successfully applied in other fields of knowledge, not only in the natural sciences, but also economic and humanitarian. Significant place in the theory of non-linear waves occupy weakly non-linear wave processes, and increasing interest in them is stimulated by practical needs of optoelectronics, fiber optics and non-linear acoustics [3, 4]. From a physical standpoint weakly non-linear processes distinguished by the condition that the amplitude of the wave field are large enough so that you can not neglect the effects of non-linearity, but they can be seen as complementary to the linear wave background process. Influence of strong non-linearity results in a change of a qualitative nature of the wave process in comparison with the linear case. Analytical description of weak non-linearity requires the development of special methods of asymptotic solutions of the model equations.

In recent work we consider the non-linear Helmholtz equation, modelling weakly non-linear evolution of the beam.

2. THE STATEMENT OF PROBLEM

Consider non-linear Helmholtz equation of next view:

$$\left(k_0^2 + \Delta\right) U = -\alpha |U|^2 U, \tag{1}$$

where $\alpha \ll 1$, k_0 are constants.

Define Fourier series in complex form

$$U \sim \sum_{n=-\infty}^{+\infty} C_n e^{ixn\frac{2\pi}{l}},$$

where C_n is Fourier coefficients.

Replacing function U by it's Fourier series, we get Helmholtz equation in next form:

$$k_0^2 \sum_{n=-\infty}^{+\infty} C_n e^{ixn\frac{2\pi}{l}} - \left(\frac{2\pi}{l}\right)^2 \sum_{n=-\infty}^{+\infty} C_n e^{ixn\frac{2\pi}{l}} n^2 = -\alpha \left| \sum_{k=-\infty}^{+\infty} C_k e^{ixk\frac{2\pi}{l}} \right|^2 \sum_{n=-\infty}^{+\infty} C_n e^{ixn\frac{2\pi}{l}} \tag{2}$$

For further convenience we replace Fourier series by it's partial sums $\sum_{n=-M}^{M} C_n e^{ixn\frac{2\pi}{l}}$, where M is integer and further denote $\frac{2\pi}{l}$ as p.

$$k_0^2 \sum_{n=-M}^{M} C_n e^{ixnp} - p^2 \sum_{n=-M}^{M} C_n e^{ixnp} n^2 = -\alpha \left| \sum_{k=-M}^{M} C_k e^{ixkp} \right|^2 \sum_{n=-M}^{M} C_n e^{ixnp} \tag{3}$$

By using mathematical induction to (3), for $M = 1, 2, 3, \ldots$, we obtain formula of Equation (1) for general case:

$$k_0^2 \sum_{n=-M}^{M} C_n e^{ixnp} - p^2 \sum_{n=-M}^{M} C_n e^{ixnp} n^2 = -\alpha \sum_{n=-M}^{M} e^{ipnx} \sum_{s,k=-M}^{M} \bar{C}_{s+k-n} C_s C_k, \tag{4}$$

where $M \to \infty$, $\bar{C}_n$ is conjugate value to C_n.

By using orthonormality

$$\int_0^l e^{impx} e^{-inpx} dx = \delta_{mn}$$

and taking scalar product from both sides of (4), we obtain infinite system of non-linear algebraic equations, which we reduce by M:

$$C_n \left(k_0^2 - p^2 n^2\right) = -\alpha \sum_{s=-M}^{M} \sum_{k=-M}^{M} \bar{C}_{s+k-n} C_s C_k \tag{5}$$

Also get a system of non-linear algebraic equations for conjugate coefficients:

$$\bar{C}_n \left(k_0^2 - p^2 n^2\right) = -\alpha \sum_{s,k=-M}^{M} C_{s+k-n} \bar{C}_s \bar{C}_k \tag{6}$$

Thus the problem is reduced to an infinite system of algebraic Equations (5), (6) for $M \to \infty$.

3. SOLVING A SYSTEM OF NON-LINEAR ALGEBRAIC EQUATIONS

In this part we describe analytical way of solving non-linear system by structured algorithm.

Consider our obtained double size system of non-linear equations with conjugate part. And for convenience we reduce it so, that the number of undefined values coincide with the number of equations.

$$\begin{cases} C_0 k_0^2 = -\alpha \left(\bar{C}_0 C_0^2 + \bar{C}_1 C_0 C_1 + \bar{C}_{-1} C_0 C_{-1} + \ldots\right) \\ C_1 \left(k_0^2 - p^2\right) = -\alpha \left(\bar{C}_{-1} C_0^2 + \bar{C}_0 C_0 C_1 + \bar{C}_{-2} C_0 C_{-1} + \ldots\right) \\ \ldots \\ C_n \left(k_0^2 - p^2 n^2\right) = -\alpha \sum_{s=-M}^{M} \sum_{k=-M}^{M} \bar{C}_{s+k-n} C_s C_k \\ \ldots \\ \bar{C}_1 \left(k_0^2 - p^2\right) = -\alpha \left(C_{-1} C_0^2 + C_0 \bar{C}_0 \bar{C}_1 + C_{-2} \bar{C}_0 \bar{C}_{-1} + \ldots\right) \\ \ldots \\ \bar{C}_n \left(k_0^2 - p^2 n^2\right) = -\alpha \sum_{s,k=-M}^{M} C_{s+k-n} \bar{C}_s \bar{C}_k \end{cases} \tag{7}$$

where $n = \pm 1, \pm 2, \ldots, \pm M$, M is any integer.

Consider iteration method for system. First, we lead (7) to the next form

$$\begin{cases} f_1 \left(C_0, \ldots, C_n, \bar{C}_0, \ldots, \bar{C}_n\right) = 0 \\ f_2 \left(C_0, \ldots, C_n, \bar{C}_0, \ldots, \bar{C}_n\right) = 0 \\ \ldots \\ f_N \left(C_0, \ldots, C_n, \bar{C}_0, \ldots, \bar{C}_n\right) = 0, \end{cases} \tag{8}$$

where $f_j(C_0, \ldots, C_n, \bar{C}_0, \ldots, \bar{C}_k) : \mathbb{R}^n \to \mathbb{C}$ are non-linear functions, $j = \overline{1, N}$.

1. Set the initial approximation $C^{(0)} = (C_{10}, C_{20}, \ldots, C_{n0})$ and very small value $\varepsilon > 0$, let $k = 0$.
2. Calculate $C^{(k+1)}$ by the formula

$$C^{(k+1)} = \Phi(C^{(k)}),$$

where $\Phi(C) = C + \Lambda F(C)$, $F(C) = (f_1(C), \ldots f_N(C))$, $\Lambda = -W^{-1}(C^{(0)})$ if $\det W(C^{(0)}) \neq 0$,

$$W(C) = \begin{pmatrix} \frac{\partial f_1(C)}{\partial C_0} & \cdots & \frac{\partial f_1(C)}{\partial C_n} & \cdots & \frac{\partial f_1(\bar{C})}{\partial \bar{C}_0} & \cdots & \frac{\partial f_1(\bar{C})}{\partial \bar{C}_n} \\ & \vdots & & \ddots & & \vdots & \\ \frac{\partial f_N(C)}{\partial C_0} & \cdots & \frac{\partial f_N(C)}{\partial C_n} & \cdots & \frac{\partial f_N(\bar{C})}{\partial \bar{C}_0} & \cdots & \frac{\partial f_N(\bar{C})}{\partial \bar{C}_n} \end{pmatrix} \quad - \quad \text{Jacoby matrix of } N \times N$$

where we take $N = 2n + 2$, $C = (C_0, \ldots, C_n, \bar{C}_0, \ldots, \bar{C}_n)$. In case if $\det W(C^{(0)}) = 0$, then another initial value should be chosen.

3. If $\Delta^{(k+1)} = \max |C_j^{(k+1)} - C_j^{(k)}| \leq \varepsilon$, then process is ended and solution $C^* \cong C^{(k+1)}$. If $\Delta^{(k+1)} > \varepsilon$, then assuming $k = k + 1$ and go to 2.

Denote the right hand side of system (7) respectively $\varphi_1, \varphi_2, \ldots, \varphi_N$.

Theorem 1. (Sufficient condition of convergence of iteration method)
Let functions $\varphi_j(C)$ and $\varphi'_j(C)$ are continuous in G domain, $j = \overline{1, N}$ and the next inequality holds

$$\max_{C \in G} \max_j \sum_{k=0}^{n} \left| \frac{\partial \varphi_j}{\partial C_k} \right| \leq q < 1,$$

where q is constant. If the successive approximations $C^{(k+1)} = \Phi(C^{(k)})$, $k = 0, 1, 2, \ldots$, do not go out of G, then the process of successive approximations converges: $C^* = \lim\limits_{k \to \infty} C^{(k)}$ and C^* is the unique solution of the system (8) in G.

4. SOME PROPERTY OF SOLUTION OF HELMHOLTZ EQUATION

In this section we led some property of solution of non-linear Helmholtz equation.

Since at least 60 years it is well-known that Nikol'skij-Besov spaces represent a useful notion of regularity not only in the context of approximation theory but also in other branches of mathematics. In fact, for us the scale of Lizorkin-Triebel-Morrey and Nikol'skij-Besov-Morrey spaces will be more important.

Theorem 2. *Let $1 < p$, $q < \infty$, $s > 0$ and $0 \leq \lambda < 1/p$. A function $U \in M_p^\lambda(\mathbb{T})$ belongs to $\mathcal{E}^s_{\lambda,p,q}(\mathbb{T})$ if, and only if,*

$$\| U \,|\mathcal{E}^s_{\lambda,p,q}\|^{\#} := \left\| S_1 U \,|M_p^\lambda(\mathbb{T})\right\| + \left\| \left(\sum_{N=1}^{\infty} N^{(s-1/q)q} \,| U - S_N U \,|^q \right)^{1/q} \left| M_p^\lambda(\mathbb{T}) \right\| < \infty \,. \tag{9}$$

Furthermore, the quantities $\| \cdot \,|\mathcal{E}^s_{\lambda,p,q}\|^{\#}$ and $\| \cdot \,|\mathcal{E}^s_{\lambda,p,q}\|$ are equivalent on $M_p^\lambda(\mathbb{T})$, i.e., there exist two positive constants A, B s.t.

$$A \,\| U \,|\mathcal{E}^s_{\lambda,p,q}\|^{\#} \leq \| U \,|\mathcal{E}^s_{\lambda,p,q}\| \leq B \,\| f \,|\mathcal{E}^s_{\lambda,p,q}\|^{\#}$$

holds for all $U \in M_p^\lambda(\mathbb{T})$.

Remark 1. Of course, Thm. 2 solves problems (i) and (ii) stated at the beginning of the Introduction in [5] with $E = M_p^\lambda(\mathbb{T})$ (under the given restrictions).

Theorem 3. *Let $1 < p < \infty$, $1 \leq q \leq \infty$, $s > 0$ and $0 \leq \lambda < 1/p$. A function $U \in M_p^\lambda(\mathbb{T})$ belongs to $\mathcal{N}^s_{\lambda,p,q}(\mathbb{T})$ if, and only if,*

$$\| U \,|\mathcal{N}^s_{\lambda,p,q}\|^{\#} := \left\| S_1 U \,|M_p^\lambda(\mathbb{T})\right\| + \left(\sum_{N=1}^{\infty} N^{(s-1/q)q} \left\| U - S_N U \,|M_p^\lambda(\mathbb{T})\right\|^q \right)^{1/q} < \infty \,. \tag{10}$$

Furthermore, the quantities $\| \cdot \,|\mathcal{N}^s_{\lambda,p,q}\|^{\#}$ and $\| \cdot \,|\mathcal{N}^s_{\lambda,p,q}\|$ are equivalent on $M_p^\lambda(\mathbb{T})$, i.e., there exist two positive constants A, B s.t.

$$A \,\| U \,|\mathcal{N}^s_{\lambda,p,q}\|^{\#} \leq \| U \,|\mathcal{N}^s_{\lambda,p,q}\| \leq B \,\left\| U \,|\mathcal{N}^s_{\lambda,p,q}\right\|^{\#}$$

holds for all $U \in M_p^\lambda(\mathbb{T})$.

Remark 2. (i) We shall call the spaces $\mathcal{E}^s_{\lambda,p,q}(\mathbb{T})$ periodic Lizorkin-Triebel-Morrey spaces. They represent the Lizorkin-Triebel scale built on the Morrey space $M^\lambda_p(\mathbb{T})$ [5].
(iii) The spaces $\mathcal{N}^s_{\lambda,p,q}(\mathbb{T})$ will be called periodic Nikol'skij-Besov-Morrey spaces. They represent the Nikol'skij-Besov scale built on the Morrey space $M^\lambda_p(\mathbb{T})$ [5].
(iv) We would like to mention that there exist some further scales of smoothness spaces related to Morrey spaces, namely Nikol'skij-Besov-type spaces $B^{s,\tau}_{p,q}(\mathbb{R}^n)$ as well as Lizorkin-Triebel-type spaces $F^{s,\tau}_{p,q}(\mathbb{R}^n)$. (More you may see in [5]).

5. CONCLUSION

We considered non-linear Helmholtz equation, solution is defined via Fourier series and analytical way of solving is represented. Also shortly some properties of solution are led in field of Function spaces and approximation theory.

REFERENCES

1. Vladimirov, V. S., *Equations of Mathematical Physics*, Nauka, Moscow, 1981 (in Russian).
2. Schwartz, L., *Mathematics for the Physical Sciences*, Mir, Moscow, 1965 (in Russian).
3. Ferreira, A. C., M. B. C. Costa, A. G. Colho, Jr., C. S. Sobrinho, J. L. S. Lima, J. W. M. Menezes, M. L. Lyra, A. S. B. Sombra, C. Xu, J. Weng, H. Li, and W. Xiong, "Analysis of the nonlinear optical switching in a Sagnac interferometer with non-instantaneous Kerr effect," *Optics Communications*, No. 5, 23–38; Vol. 285, No. 6, 1408–1417, 2012.
4. Mukherjee, P. K., "Pretransitional Kerr effect and nonlinear dielectric effect in the isotropic phase of the isotropic to smectic-E phase transition," *Journal of Molecular Liquids*, Vol. 175, 1–3, 2012.
5. Sautbekova, M. and W. Sickel, "Strong summability of Fourier series and Morrey spaces," *Analysis Mathematica*, Vol. 40, 31–62, 2014.

Synthesis of the Sparse Conformal Arrays with Convex Optimal Method

Xiaowen Zhao[1, 2], **Qingshan Yang**[1], **and Yunhua Zhang**[1]

[1]Key Laboratory of Microwave Remote Sensing
Center for Space Science and Applied Research, Chinese Academy of Sciences, Beijing 100190, China
[2]University of Chinese Academy of Sciences, Beijing 100049, China

Abstract— In this paper, the convex optimal technique is applied to synthesis of sparse conformal arrays for fitting the predefined patterns using as few elements as possible. The original synthesis problem can be formulated by minimizing the number of active elements subjected to the constraints on the pattern requirements. Unfortunately, it needs to solve a NP-hard problem since the objective function of the related problem is nonconvex. The minimization of the l_1-norm is presented to relax the above constraint into a convex way. Towards this end, the proposed method can determine both the corresponding locations and amplitudes of the sparse elements based on l_1-norm of the sparsest excitation set. The method for conformal array optimization addressed in this paper is easy to be implemented and has low computational load. Numerical simulations validate the effectiveness and high accuracy of the proposed synthesis method.

1. INTRODUCTION

Conformal antenna arrays with low profile have been widely used in the fields of space-borne, air-borne and missile-borne radar, space vehicles and sonar due to its low Radar Cross-Section (RCS) and no extra aerodynamic drag [1]. In the case of conformal array, the well-known Fourier transform relationships between element excitations and far field pattern breaks down, and on the other hand, array factor theory does not hold any more since each element pattern depends on its respective orientation, which make the corresponding synthesis problem significantly difficult. Up to now, iterative least square techniques [2] and stochastic optimization such as genetic algorithms (GA) [3], simulated annealing (SA) [4], particle swarm (PS) [5] and differential evolution algorithm (DEA) [6] have been widely applied to the synthesis of conformal array. However, few methods have been proposed to thin out the conformal array matching the desired pattern.

Recently, an effective and robust technique, convex optimal method, has been proposed to design the maximally sparse linear arrays fitting the desired patterns [7]. This method can find the minimum number of active elements and their corresponding positions and excitations by using the reference pattern samples. In this paper, we will extend this method to the sparse conformal array. Notably, the convex optimal method must be carefully described in the case of conformal array due to the complexity of synthesis dimensions and the definition of each element pattern in the synthesis processing. Therefore, in Section 2, the addressed synthesis problem is formulated based on convex optimal method in detail. Numerical tests are presented in Section 3. Finally, some conclusions are drawn in Section 4.

2. PROBLEM FORMULATION

For a conformal array consisting of N elements with arbitrary geometry distribution, the far-field beam pattern in the generic direction (θ, φ) can be expressed as

$$F(\theta,\varphi) = \sum_{n=0}^{N-1} \omega_n g_n(\theta,\varphi)\, e^{j\frac{2\pi}{\lambda}(x_n \sin\theta\cos\varphi + y_n \sin\theta\sin\varphi + z_n\cos\theta)} \tag{1}$$

in which θ and φ are the elevation and azimuth angles, ω_n is the corresponding excitation of the n-th element at (x_n, y_n, z_n) in global Cartesian coordinate system, $g_n(\theta, \varphi)$ is the element pattern in the global coordinate system, where $n = 0, 1, \ldots, N-1$, λ is the wavelength. The position vector of the n-th element is

$$\vec{r}_n = (x_n, y_n, z_n) \tag{2}$$

while the unit vector in direction (θ, φ) is

$$\vec{r} = (\sin\theta\cos\varphi, \sin\theta\sin\varphi, \cos\theta) \tag{3}$$

Thus, Equation (1) can be further written in a matrix form as

$$\mathbf{F}(\theta,\varphi) = \mathbf{V}(\theta,\varphi)\,\mathbf{W} \tag{4}$$

where

$$\mathbf{V}(\theta,\varphi) = \left(g_0(\theta,\varphi)\,e^{j\frac{2\pi}{\lambda}\vec{r_0}\cdot\vec{r}}, g_1(\theta,\varphi)\,e^{j\frac{2\pi}{\lambda}\vec{r_1}\cdot\vec{r}}, \ldots, g_{N-1}(\theta,\varphi)\,e^{j\frac{2\pi}{\lambda}\vec{r_{N-1}}\cdot\vec{r}}\right) \tag{5}$$

$$\mathbf{W} = [\omega_0, \omega_1, \ldots, \omega_{N-1}]^T \tag{6}$$

and $\mathbf{W}$ is the weighting vector, $\mathbf{V}(\theta, \varphi)$ is the steering vector, T denotes the transpose. It must be pointed out that the element pattern $g_n(\theta_n, \varphi_n)$ in the local coordinate system need to be transformed to $g_n(\theta, \varphi)$ in the global coordinate system before calculating the far-field pattern [1]. Since the elements in conformal array generally direct their radiation beams toward different directions.

Let us define the aperture of the conformal array as S and the reference pattern as $F_{ref}(\theta, \varphi)$, respectively. Firstly, K measurements will be obtained by sampling on the reference pattern, the sampling directions are as [8]

$$\theta = \pi\frac{\mathrm{mod}(k, K_\theta)}{K_\theta - 1} \qquad \varphi = 2\pi\frac{\lfloor k/K_\theta \rfloor}{K_\varphi - 1} \tag{7}$$

where $k = [0, 1, \ldots, K]$, $K = K_\theta \times K_\varphi$. Meanwhile, the column vector consisting of the aforementioned samplings is denoted as $\mathbf{F}_{ref}$. Moreover, let us assume that a P-element conformal array can approximately radiate the reference pattern with a matching error of ε. The P elements are selected from N predefined candidate locations within the aperture S. In order to achieve the minimum number of active element P, the related sparse conformal array synthesis is formulated mathematically as

$$\min \|\mathbf{W}\|_{l_0} \quad s.t. \quad \|\mathbf{F}_{ref} - \mathbf{V}\mathbf{W}\|_{l2} \le \varepsilon \tag{8}$$

where $\|\mathbf{W}\|_{l0}$ denotes the number of nonzero elements of the vector $\mathbf{W}$. As we know, the objective function in (8) is nonconvex. It is worth noting that l_0-norm should be replaced with its convex approximation, i.e., l_1-norm, to avoid the NP-hard problem [7]. Towards to this end, the synthesized problem is relaxed to a convex problem as following

$$\min \|\mathbf{W}\|_{l_1} \quad s.t. \quad \|\mathbf{F}_{ref} - \mathbf{V}\mathbf{W}\|_{l2} \le \varepsilon \tag{9}$$

An iterative weighted l_1-norm algorithm as shown in [7] is also herein applied to enhancing the sparsity of the solution $\mathbf{W}$ (see [7] for the details). In addition, the iterative convex optimization problem is convenient to solve optimally because useful software, such as CVX is readily available with only a few iterations (less than 5 for the synthesis problem as following).

3. NUMERICAL EXAMPLES

In this section, two numerical simulations are carried out to verify the effectiveness and accuracy of the aforementioned method for sparse conformal array synthesis. In order to describe the approximation degree of the synthesized pattern to the reference pattern, the matching error is defined as

$$\varepsilon = \frac{\int_0^{2\pi}\int_0^{\pi} |F_{ref}(\theta,\varphi) - F(\theta,\varphi)|^2\, d\theta d\varphi}{\int_0^{2\pi}\int_0^{\pi} |F_{ref}(\theta,\varphi)|^2\, d\theta d\varphi} \tag{10}$$

As the first example, the target pattern is from a uniform circular array composed of 30 isotropic elements with the radius $R = 15\lambda/2\pi$. The elements are equally spaced with $\lambda/2$ along the periphery of the circle. By using the proposed method, a sparse array with only 22 elements conformal to the herein circle is achieved, i.e., 8 elements are saved. The sparse array layout and excitations are shown in Fig. 1. The minimum inter-element spacing is 0.63λ and the maximum inter-element spacing is 0.72λ in the synthesized sparse array. The synthesized pattern, as shown in Fig. 2(a), has a total matching error of 1.862×10^{-4} in 3-D form as compared to the target (see Fig. 2(b)). The comparison between the synthesized pattern and the target pattern is also presented by the

plots in the planes $\varphi = 0°$ (Fig. 3(a)) and $\varphi = 90°$ (Fig. 3(b)). It is clear that the pattern matching error is negligible.

Next, our method is applied to synthesizing a cylindrical array so as to further test the sparse performance. The target pattern is from a 4-by-24 element array uniformly spaced by 0.5λ and located on a cylindrical surface of radius $R = 15\lambda$, as presented in [9]. The excitation in the 24-element direction is Chebyshev amplitude distribution while uniform excitation in the 4-element direction is used. The corresponding n-th element pattern in the global coordinate system is

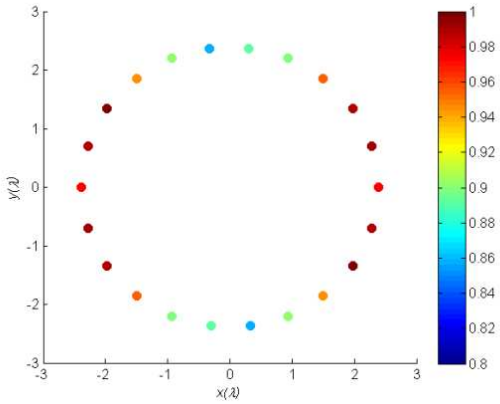

Figure 1: The layout and excitations of the synthesized arrays.

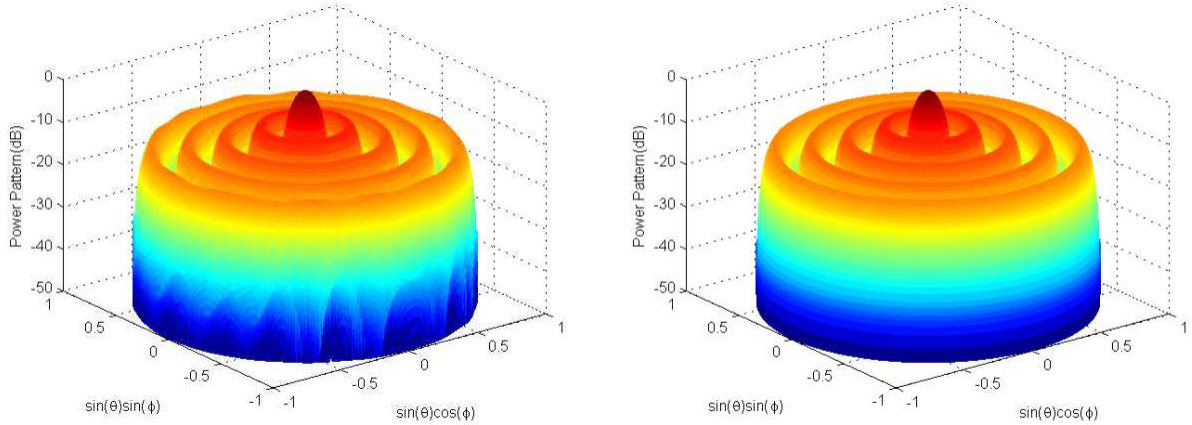

Figure 2: The comparison between the synthesized pattern and the target in 3-D. (a) The reconstructed pattern by sparse array, (b) the target pattern by the uniform circular array.

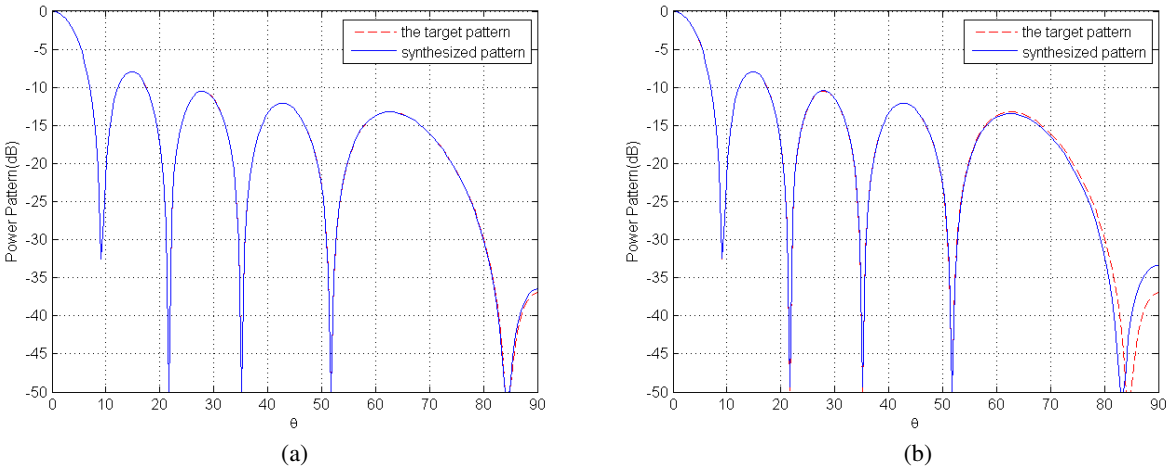

Figure 3: The synthesized pattern as compared to the target. (a) $\varphi = 0°$ plane, (b) $\varphi = 90°$ plane.

expressed as following

$$g_n(\theta,\varphi) = \sin\theta\cos(\varphi-\varphi_n) \tag{11}$$

where φ_n is the corresponding element's azimuthal position. The aperture of the herein cylindrical array is discretized only along the arc as

$$\begin{cases} x_n = R\cos\left(-\dfrac{11}{90}\pi + \dfrac{22}{90}\dfrac{\mathrm{mod}(n,n_{xy})}{n_{xy}-1}\right) \\ y_n = R\sin\left(-\dfrac{11}{90}\pi + \dfrac{22}{90}\dfrac{\mathrm{mod}(n,n_{xy})}{n_{xy}-1}\right) \\ z_n = -\dfrac{3}{4}\lambda + \dfrac{3}{2}\lambda\dfrac{\lfloor n/n_{xy}\rfloor}{n_z-1} \end{cases}, \quad n = 0,\ldots,N-1 \tag{12}$$

where $N = n_{xy} \times n_z$, n_{xy} is defined as the element number along the azimuthal direction, n_z denotes the elements number along the axial direction. As expected, a sparse cylindrical array consisted of 79 elements (Fig. 4(a)) is obtained to reproduce the target pattern with the matching error $\varepsilon = 1.047 \times 10^{-2}$, i.e., 18% of the total elements are saved as compared to the reference array presented in [9]. It means the cost can be further reduced and the feeding network can be further simplified in practical applications by the proposed method. The comparison between the synthesized pattern and the target in the plane $\theta = 90°$ (Fig. 4(b)) clearly indicate that the sparse

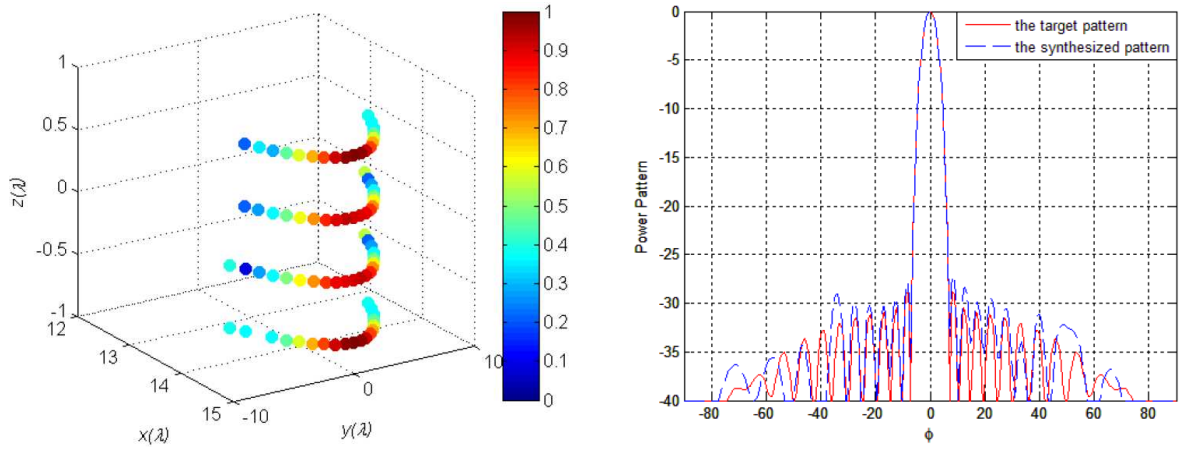

Figure 4: (a) The layout and excitations of the synthesized cylindrical conformal array, (b) the synthesized pattern along with the target in plane $\theta = 90°$.

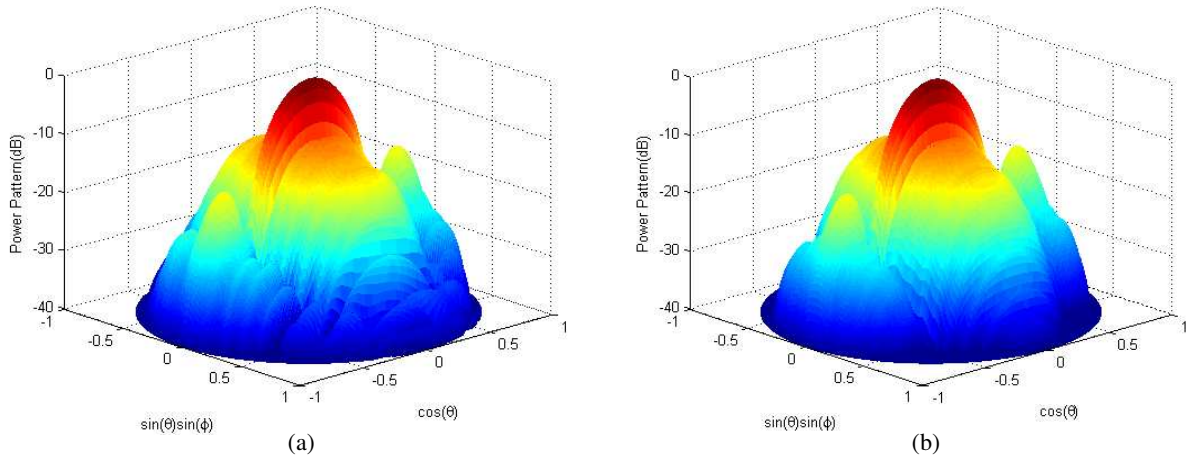

Figure 5: The comparison between the synthesized pattern and the target in 3-D. (a) The reconstructed pattern, (b) the target pattern.

conformal solution realizes an accurate reconstruction of the target main-beam while with only some minor mismatching in low side-lobes. The related 3-D radiation patterns are shown in Fig. 5. Moreover, the reconstructed array would be sparser if we discrete the cylindrical aperture in axial direction further.

4. CONCLUSION

In this paper, the convex optimal method has been introduced to design sparse conformal arrays in match of the reference patterns. The synthesis problem can be formulated by minimizing the number of active elements subjected to the constraints on the pattern requirements. To form the optimization problem, much dense elements are first assigned to equally spaced dense positions, which compose the conformal array aperture. The convex optimal method is aimed to find the active elements from the predefined candidate positions within the conformal array. In addition, this method can derive the element positions and weights simultaneously. Compared with the stochastic algorithms, the proposed method is very simple and easy to carry out, the computational burden is acceptable. Numerical experiments are conducted to validate the effectiveness and flexibility of the proposed method.

REFERENCES

1. Josefsson, L. and P. Persson, *Conformal Array Antenna Theory and Design*, IEEE Press, Piscataway, NJ, USA, 2006.
2. Vaskelainen, L. I., "Iterative least-squares synthesis methods for conformal array antennas with optimized polarization and frequency properties," *IEEE Transactions on Antennas and Propagation*, Vol. 45, 1179–1185, 1997.
3. Xu, Z., H. Li, Q.-Z. Liu, and J.-Y. Li, "Pattern synthesis of conformal antenna array by the hybrid genetic algorithm," *Progress In Electromagnetics Research*, Vol. 79, 75–90, 2008.
4. Ferreira, J. and F. Ares, "Pattern synthesis of conformal arrays by the simulated annealing technique," *Electronics Letters*, Vol. 33, 1187–1189, 1997.
5. Lu, Z.-B., A. Zhang, and X.-Y. Hou, "Pattern synthesis of cylindrical conformal array by the modified particle swarm optimization algorithm," *Progress In Electromagnetics Research*, Vol. 79, 415–426, 2008.
6. Guo, J.-L. and J.-Y. Li, "Pattern synthesis of conformal array antenna in the presence of platform using differential evolution algorithm," *IEEE Transactions on Antennas and Propagation*, Vol. 57, 2615–2621, 2009.
7. Zhao, X., Q. Yang, and Y. Zhang, "Compressed sensing approach for pattern synthesis of maximally sparse non-uniform linear array," *Microwaves, Antennas & Propagation, IET*, Vol. 8, 301–307, 2014.
8. Viani, F., G. Oliveri, and A. Massa, "Compressive sensing pattern matching techniques for synthesizing planar sparse arrays," *IEEE Transactions on Antennas and Propagation*, Vol. 61, 4577–4587, 2013.
9. Lu, Z.-B., A. Zhang, and X.-Y. Hou, "Pattern synthesis of cylindrical conformal array by the modified particle swarm optimization algorithm," *Progress In Electromagnetics Research*, Vol. 79, 415–426, 2008.

EM Scattering Computation of Electric-large Lossy Dielectric Target Based on Ray Tracing

Hao Zheng and Hongxia Ye
Key Lab of Wave Scattering & Remote Sensing Information, Fudan University, China

Abstract— The high frequency (HF) PO/GO computation based on ray tracing approach is presented to fast compute the EM scattering from arbitrary dielectric target with electric-large size. For lossy medium, the generalized Snell-Descartes and Fresnel laws are introduced to determine the propagation direction of equi-phase and equi-amplitude plane of reflection and refraction wave, which is the main difference from the classical ray tracing approach. The GO reflection and refraction rays are traced according to the propagation direction of equi-phase surface step by step. Accompany with the wave propagation, the phase delay is computed along the normal direction of equi-phase, and the energy attenuation is computed along the normal direction of equi-amplitude. On the exiting surface, the PO integration of surface field is considered for outgoing field computation. For lossy dielectric surface, the PO surface field is inhomogeneous, and this paper derives an analytical integral formula for arbitrary triangular patch to avoid the numerical integral on the dense meshing of 1/8 wavelength. In numerical simulation, the target is constructed with triangular dielectric patches according to its geometry CAD model, not need to mesh according to the electric wavelength. Several models, such as multi-layer dielectric plate, dielectric coating plate, lossy dielectric cubic, et al., are used for validation and comparison with FEKO software, taking the requirements of memory and CPU time into consideration. The numerical simulation indicates that the new HF method is valid and efficient for electric-large target with arbitrary dielectric medium.

1. INTRODUCTION

MoM and FDTD [2] are both numerical methods which are widely used for RCS calculation of radar objectives. However, they're not suitable for electric-large complex objects for the large requirement in both computer storages and computing time. Much more effective approaches are high-frequency methods, especially for PO [3] and GO [4]. Xu and Jin [5] put forward a novel method called bi-directional analytic ray tracing (BART). In BART, objects are composed of many triangle facets based on its CAD model and they are traced by rays which are expressed as triangular beams through triangle operations. The consumption of storages and time only depends on the ray tracing orders and shapes of objects without the influences of frequencies. However, the BART has not been applied to lossy dielectric materials [6]. When the BART is applied to lossy materials, the properties of lossy materials should be considered. When electromagnetic wave impinges on lossy interfaces, complex refracted angles are yielded by the complex Snell Descartes [7, 8] law, which means the equal-phase surface and the equal-amplitude surface won't coincide.

In this paper, the BART [5] is extended for electric-large lossy object. The complex Snell-Descartes law is used for determining the transmitting direction of both equal-phase plane and equal-amplitude plane and a novel computing method is deduced. Some examples such as lossy object or multiple layered plates are also computed and E-BART is compared with numerical method.

2. E-BART FOR DIELECTRIC LOSSY TARGET

BART was originally proposed for RCS calculation of electric-large PEC object. The core conception of this method is to trace two rays from forward direction in transmitter and backward direction in receiver based on Fresnel law step by step. If two rays impinge on a same facet, then a scattering path is formed. The whole scattering contribution is calculated by 1-order PO and multi-order GO. To extend it to lossy dielectric objects, complex Snell-Descartes laws [7, 8] and novel computing method are introduced in E-BART.

2.1. PO/GO

When an EM wave $\mathbf{E}_i(\mathbf{r}) = \hat{\mathbf{e}}_i E_0 e^{i\mathbf{k}_i\cdot\mathbf{r}}$ impinges on the surface of a lossy media, the equal-phase surface and equal-amplitude surface won't coincide. The wave vector can be decomposed of transmitting vector of equal-phase $\hat{\mathbf{o}}$ and the attenuation vector of equal-amplitude $\hat{\mathbf{f}}$. The wave vector $\mathbf{k}$ is expressed as $\mathbf{k} = k_0(N\hat{\mathbf{o}} + iK\hat{\mathbf{f}})$.

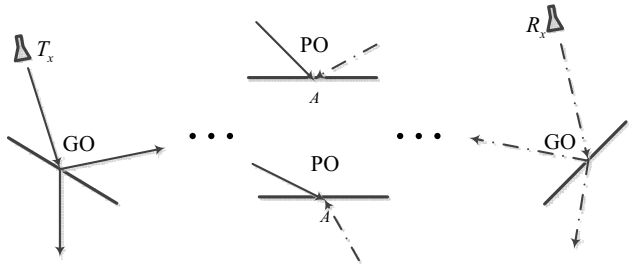

Figure 1: Ray tracing paths of E-BART.

Define $\hat{\mathbf{n}}$ as the normal vector of interface of two different materials. θ demonstrates the included angle between $\hat{\mathbf{n}}$ and $\hat{\mathbf{o}}$, γ demonstrates the included angle between $\hat{\mathbf{n}}$ and $\hat{\mathbf{f}}$.

Define $n = \sqrt{\varepsilon_r} = n' + in''$, complex cosine $\cos\tilde{\alpha}$ and complex sine $\sin\tilde{\alpha}$ can be expressed as follows:

$$\cos\tilde{\alpha} = \frac{N\cos\theta + iK\cos\gamma}{n' + in''} \sin\tilde{\alpha} = \frac{N\sin\theta + iK\sin\gamma}{n' + in''} \tag{1}$$

Then the Fresnel reflection and refraction coefficients are as follows:

$$\begin{aligned} R_h &= \frac{\eta_2\cos\tilde{\alpha}_1 - \eta_1\cos\tilde{\alpha}_2}{\eta_2\cos\tilde{\alpha}_1 + \eta_1\cos\tilde{\alpha}_2}, \quad T_h = \frac{2\eta_2\cos\tilde{\alpha}_1}{\eta_2\cos\tilde{\alpha}_1 + \eta_1\cos\tilde{\alpha}_2} \\ R_v &= \frac{\eta_1\cos\tilde{\alpha}_1 - \eta_2\cos\tilde{\alpha}_2}{\eta_1\cos\tilde{\alpha}_1 + \eta_2\cos\tilde{\alpha}_2}, \quad T_v = \frac{2\eta_2\cos\tilde{\alpha}_1}{\eta_1\cos\tilde{\alpha}_1 + \eta_2\cos\tilde{\alpha}_2} \end{aligned} \tag{2}$$

Then the PO matrix can be expressed according to [5–9]. When $k \to \infty$, GO matrix is deduced as follows, $\hat{\mathbf{q}}$ and $\hat{\mathbf{p}}$ are vectors of vertical and horizontal polarizations.

$$\begin{aligned} \tilde{\mathbf{R}} &= \begin{bmatrix} \left(\hat{\mathbf{q}}_i \times \hat{\mathbf{k}}_r\right)\cdot\hat{\mathbf{e}}_{sv} & \hat{\mathbf{q}}_i\cdot\hat{\mathbf{e}}_{sv} \\ \left(\hat{\mathbf{q}}_i \times \hat{\mathbf{k}}_r\right)\cdot\hat{\mathbf{e}}_{sh} & \hat{\mathbf{q}}_i\cdot\hat{\mathbf{e}}_{sh} \end{bmatrix} \begin{bmatrix} R_v & 0 \\ 0 & R_h \end{bmatrix} \begin{bmatrix} \hat{\mathbf{e}}_{iv}\cdot\hat{\mathbf{p}}_i & \hat{\mathbf{e}}_{ih}\cdot\hat{\mathbf{p}}_i \\ \hat{\mathbf{e}}_{iv}\cdot\hat{\mathbf{q}}_i & \hat{\mathbf{e}}_{ih}\cdot\hat{\mathbf{q}}_i \end{bmatrix} \\ \tilde{\mathbf{T}} &= \begin{bmatrix} \left(\hat{\mathbf{q}}_i \times \hat{\mathbf{k}}_t\right)\cdot\hat{\mathbf{e}}_{sv} & \hat{\mathbf{q}}_i\cdot\hat{\mathbf{e}}_{sv} \\ \left(\hat{\mathbf{q}}_i \times \hat{\mathbf{k}}_t\right)\cdot\hat{\mathbf{e}}_{sh} & \hat{\mathbf{q}}_i\cdot\hat{\mathbf{e}}_{sh} \end{bmatrix} \begin{bmatrix} T_v & 0 \\ 0 & T_h \end{bmatrix} \begin{bmatrix} \hat{\mathbf{e}}_{iv}\cdot\hat{\mathbf{p}}_i & \hat{\mathbf{e}}_{ih}\cdot\hat{\mathbf{p}}_i \\ \hat{\mathbf{e}}_{iv}\cdot\hat{\mathbf{q}}_i & \hat{\mathbf{e}}_{ih}\cdot\hat{\mathbf{q}}_i \end{bmatrix} \end{aligned} \tag{3}$$

2.2. Field Computation of a Single Tracing Path

According to BART, the total RCS contribution of a certain path can be expressed as

$$\mathbf{E}_s = \frac{e^{ik_0 r}}{r} \left\{ \prod_{b=m}^{1} \overline{\mathbf{G}}_b e^{i\mathbf{k}_b\cdot\mathbf{r}_b} \cdot \overline{\mathbf{P}} \cdot \prod_{f=1}^{n} \overline{\mathbf{G}}_f e^{i\mathbf{k}_f\cdot\mathbf{r}_f} \right\} \cdot \mathbf{E}_i \tag{4}$$

$\overline{\mathbf{G}}$ is the GO matrix of a certain dielectric interface. $\overline{\mathbf{P}}$ is the PO matrix of the facet A. This computation formula is applied to PEC objects, but it is not suitable for lossy dielectric objects.

As the scattering field is contributed by the induced electric and magnetic surface currents exposed to the outer free space, the integrated PO facet should not be inside the tracing object and the PO position should be replaced by the last hitting facet, which is exposed to the free space. The contribution of original PO facet is expressed as a transformed GO matrix and the contribution of last hitting facet is expressed as a transformed PO matrix.

The transformed GO matrix relies on the PO integration I_0. When the geometrical reflection or geometrical refraction occurs, I_0 reaches the maximum value A_0, which is the intersected area of facet A. Then the transformed GO matrix $\overline{\mathbf{G}'}_P$ can be approximately derived as $\overline{\mathbf{G}'}_P = (I_0/A_0)\overline{\mathbf{G}}_0$. The matrix $\mathbf{G}_0$ shares the same formula of Eq. (3). The transformed PO matrix $\overline{\mathbf{P}'}_G$ is demonstrated according to [5–9]. Substituting $\mathbf{k} = k_0(N\hat{\mathbf{o}} + iK\hat{\mathbf{f}})$, $\mathbf{r} = \hat{\mathbf{o}}l$, $\overline{\mathbf{G}'}_P$ and $\overline{\mathbf{P}'}_G$ into Eq. (4), we can get

$$\mathbf{E}_s = \frac{e^{ik_0 r}}{r}\frac{I_0}{A_0} \left\{ \overline{\mathbf{P}'}_G \cdot \prod_{b=m}^{2} \overline{\mathbf{G}}_b e^{ik_0 N_b l_b} e^{-k_0 K_b\left(\hat{\mathbf{f}}_b\cdot\hat{\mathbf{o}}_b\right)l_b} \cdot \overline{\mathbf{G}}_0 \cdot \prod_{f=1}^{n} \overline{\mathbf{G}}_f e^{ik_0 N_f l_f} e^{-k_0 K_f\left(\hat{\mathbf{f}}_f\cdot\hat{\mathbf{o}}_f\right)l_f} \right\} \mathbf{E}_i \tag{5}$$

3. NUMERICAL SIMULATION

In this section, some numerical examples are presented for E-BART validation. Firstly a two-layer plate's presented here. The dielectric constant of upper layer and lower layer is $\varepsilon_{r1} = 3 + i3$ and $\varepsilon_{r2} = 4 + i4$, respectively. The sizes of the two layers are both $1\,\mathrm{m} \times 1\,\mathrm{m} \times 0.01\,\mathrm{m}$. Assuming electromagnetic wave ($\theta_i = 30°$, $\varphi_i = 0$, $f = 1.26\,\mathrm{GHz}$) impinges on the plates. From Figure 2, we can see that E-BART matches with FEKO well, except at some low grazing angles. In FEKO, about 2.45 GBytes and 15 mins are needed, while only about 50 Mbytes and 25 s are needed in E-BART.

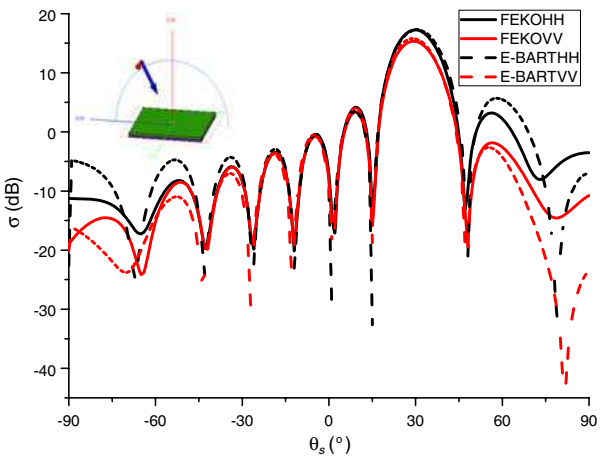

Figure 2: Comparisons of E-BART and FEKO.

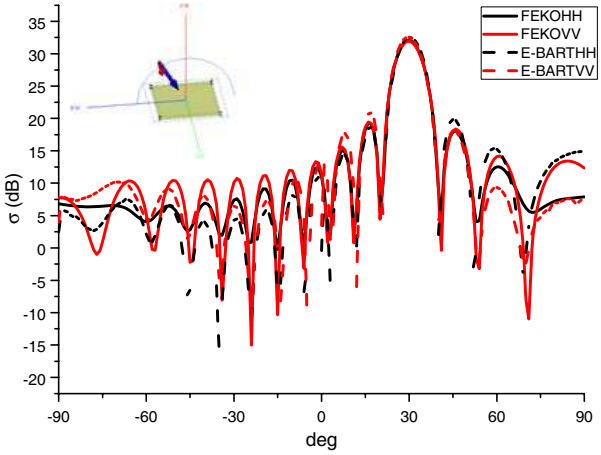

Figure 3: RCS of a coated PEC plate.

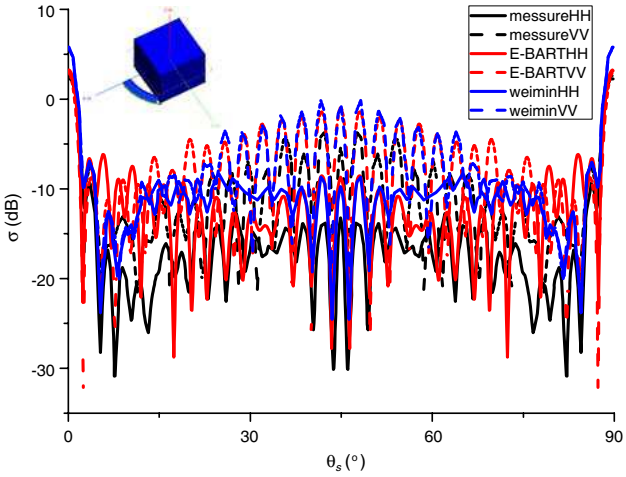

Figure 4: Comparison of different methods for PVC-cube RCS.

Now consider a coated plate consisted of an interior PEC plate ($2\,\mathrm{m} \times 2\,\mathrm{m} \times 0.1\,\mathrm{m}$) and an exterior lossy dielectric plate ($2.1\,\mathrm{m} \times 2.1\,\mathrm{m} \times 0.12\,\mathrm{m}$, $\varepsilon_r = 2 - 0.02i$). The electromagnetic wave ($f = 1\,\mathrm{GHz}$) propagates from $\theta_i = 30°$, $\varphi_i = 0$ and the RCS in $\theta_s = -90° \sim 90°$, $\varphi_s = 180°$ is computed. It can be seen that E-BART also matches well with coated PEC objects, except at some low grazing angles. In FEKO, about 4.5 GBytes is needed and about 1 h will be cost. While in E-BART, only 40 Mbytes and 1min are consumed.

Another example of lossy PVC-cube is tested here to validate E-BART. The side length of the cube is $sl = 12\,\mathrm{cm}$ and dielectric constant is $\varepsilon_r = 2.7 + i0.01$. The following figure compares E-BART with the method of Weinmann. It's proved that within $\theta_s \in (20° \sim 45°)$, E-BART yield a better result. But the result still deviates from the measured results especially for HH polarization because of the non-edge diffraction in the extended E-BART.

4. CONCLUSION

The E-BART method utilizes the complex Snell-Descartes laws to determine the propagation paths and the novel analytical computing method to get the RCS of complex lossy objects. According to the comparisons of numerical methods, E-BART is effectively for the RCS of complex lossy objects.

REFERENCES

1. Harrington, R. F., *Field Computation by Moment Methods*, McMillan, New York, 1968.
2. Taflove, A. and S. Hagness, *Computational Electrodynamics: The Finite-difference Time-domain Method*, Artech House, Boston, MA, 2000.
3. Franceschetti, G., A. Iodice, and D. Riccio, "A canonical problem in electromagnetic backscattering from buildings," *IEEE Transaction on Geoscience and Remote Sensing*, Vol. 40, No. 8, 1787–1801, Aug. 2002.
4. Kouyoumjian, R. G., "Asymptotic high frequency methods," *Proceedings of the IEEE*, Vol. 53, No. 8, 864–876, Aug. 1965.
5. Xu, F. and Y. Q. Jin, "Bidirectional analytic ray tracing for fast computation of composite scattering from electric-large target over a randomly rough surface," *IEEE Transactions on Antennas and Propagation*, Vol. 57, No. 5, 1495–1505, May 2009.
6. Weinmann, F., "PO/PTD ray tracing for arbitrary metallic and dielectric objects," *IEEE Transactions on Antennas and Propagation*, Vol. 54, No. 6, 1797–1806, Jun. 2006.
7. Dupertuis, M. A., M. Proctor, and B. Acklin, "Generalization of complex Snell-Descartes and Fresnel laws," *Journal of the Optical Society America A*, 1159–1166, Nov. 1994.
8. Chang, P. C. Y., J. G. Walker, and K. I. Hopcraft, "Ray tracing in absorbing media," *Journal of Quantitative Spectroscopy and Radiative Transfer*, Vol. 96, No. 3, 327–341, 2005.
9. Tsang, L. and J. A. Kong, *Scattering of Electromagnetic Waves: Advanced Topics*, Vol. 3, 413 pages, Wiley Interscience, 2001.

Effect of a Linear Frequency Modulation on the Nonlinear Dynamics of an Electromagnetic Pulse in a Graded-index Waveguide

I. M. Oreshnikov and M. A. Bisyarin
Faculty of Physics, Saint-Petersburg University, Saint-Petersburg, Russia

Abstract— The present paper is aimed at a consistent analytical description of a combined interplay of linear frequency modulation of the high-frequency carrier, nonlinearity, and inhomogeneity of an optical fiber on the propagation of an arbitrary mode feasible in the fiber, with vortex modes included. Formal asymptotic procedure is applied to the problem of wave propagation and equations for the mode structure and the envelope of the chirped pulse are derived. Lagrangian is proposed enabling to reformulate the envelope equation as a variational problem which is then solved for the case of travelling pulse of an arbitrary shape. Explicit expressions for the pulse parameters are derived via characteristics of the gradient optical fiber and the structure of propagating mode.

1. INTRODUCTION

Since the prediction of bright and dark optical solitons in media with proper dispersive characteristics [1] and the experimental observation of soliton formation in optical fibers [2] a great progress has been achieved in sophistication and application of nonlinear localized optical waves in various artificial structures [3]. Optical fibers turned out to be a very favourable and common medium due to a low threshold of nonlinear effects excitation [4] and feasibility of waveguiding devices with stable geometry. Various types of optical fibers are now being produced commercially — mono- and multimode, stepwise and graded-index etc. — with each of them having its utilization area. Design of specific refractive index profiles enables to control the dispersive characteristics of optical waveguides. Use of a linear frequency modulation can partly mitigate the dispersive broadening, so far as, with the proper sign of the linear frequency modulation being chosen, the modulation overplays the dispersion, which leads to pulse compression up to a certain propagation distance, and only on passing this distance the pulse dispersive spreading becomes irreversible. An analytical account of nonlinearity in propagation of a pulse with a quadratic phase modulation in a graded-index optical fiber has been recently attained by means of an asymptotic procedure [5] with respect to the pulse amplitude assumed to be a small parameter. Stated in [5] is the necessity to discern between pulses with modulation depth of different orders of magnitude, and the nonlinear Schrödinger equation for the pulse envelope is generalized onto the case where phase modulation and longitudinal inhomogeneity of the waveguide are taken into account.

So far as the information capacity of any transmission system is limited with a finite bandwidth and noise [6], a point is once attained at which only novel physical ideas or technologies could provide a further growth in the information transmission rate. Recent developments in fiber optics communications are now toughly coming at the "capacity crunch" conditioned by approaching the fundamental limits due to signal-to-noise ratio and nonlinearity of available optical fibers [7]. A possible way to provide a principal capacity growth consists in utilization of the mode division multiplexing in fibers, and involvement of the modes with orbital angular momentum [8]. Reported in [9] is a phase diffractive optical element and algorithm forming an informative set of optical vortices in a laser beam in the fiber. The present paper is aimed at a consistent analytical description of a combined interplay of linear frequency modulation of the high-frequency carrier, nonlinearity, and inhomogeneity, either transverse and longitudinal, of the fiber, on the propagation of an arbitrary mode feasible in the fiber, with vortex modes included. A variational approach stemming from Whitham's principle [10] is used in the analysis of the equation derived for the pulse envelope, this succeeded in determination of practical characteristics of the short optical pulse.

2. NONLINEAR WAVE EQUATION AND ANSATZ

The short pulse propagation in a graded-index waveguide is expedient to be treated as a weak-nonlinear process thus enabling to combine modal structure of the pulse and its nonlinear evolution along the waveguide axis. Thus a small parameter δ which should be introduced for asymptotic analysis is chosen as an order of magnitude of the pulse amplitude. Henceforth dimensionless variables are used: ρ — radial coordinate multiplied by the wavenumber *in vacuo*, s — longitudinal

coordinate multiplied by the wavenumber *in vacuo* and δ^2 (i.e., squeezed proportionally to δ^2), t — time multiplied by the angular frequency, thus the nonlinear wave equation is written down as follows

$$\Delta f - \left(\beta^2(\rho,s) + \frac{1}{2}\alpha^2(\rho,s)\,|f|^2\right)\frac{\partial^2 f}{\partial t^2} = 0 \tag{1}$$

α, the Kerr coefficient, characterizes the nonlinear properties of the medium, β defines the refractive index profile within the cross-section in the linear regime of propagation, accounting for a longitudinal inhomogeneity via dependence on s. The solution to Equation (1) is sought for as

$$f(\rho,\varphi,s,t) = \delta F(\rho,\varphi,s,\theta)\exp\left[i\left(R(s)/\delta^2 - t - \delta^3\mu(s)t^2\right)\right] + \text{c.c.} \tag{2}$$

$$\theta(s,t) = \frac{1}{\delta}Q(s) - \delta t \qquad R(s) = \int\limits_0^s r(s')\mathrm{d}s' \qquad Q(s) = \int\limits_0^s q(s')\mathrm{d}s'$$

the linear frequency modulation depth is taken as $\delta^3\mu(s)$ admitting its dependence along the propagation path and assuming its order of magnitude corresponding to ordinary modulation [5]. An essential feature of the Ansatz (2) consists in introduction of the envelope phase θ, so the instantaneous wavenumbers $r(s)$ of the high-frequency carrier and $q(s)$ of the envelope are supposed to be different functions on s. The complex amplitude is represented as a series $F(\rho,\phi,s,\theta) = \sum_{j=0}^{\infty}\delta^j F_j(\rho,\phi,s,\theta)$ in powers of the small parameter. We'll require that the complex amplitude vanishes with distancing from the waveguide axis.

3. MODE STRUCTURE AND ENVELOPE OF THE CHIRPED PULSE

The main order complex amplitude obeys the equation

$$\frac{\partial^2 F}{\partial\rho^2} + \frac{1}{\rho}\frac{\partial F}{\partial\rho} + \frac{1}{\rho^2}\frac{\partial^2 F}{\partial\varphi^2} + \left(\beta^2(\rho,s) - r^2(s)\right)F = 0 \tag{3}$$

and must be 2π-periodic with respect to φ, bounded at the axis $\rho = 0$, and vanish for $\rho \to \infty$. The azimuthal dependence could be chosen via either $\{\cos m\phi,\ \sin m\phi\}$ or $\{e^{\pm im\phi}\}$, the latter corresponds to a vortex mode with a screw-like wave front. The structure of the problem in (3) implies the possibility to present a vortex mode as a product $F(\rho,\phi,s,\theta) = V(\rho,s)U(s,\theta)e^{im\phi}$, where $V(\rho,s)$ the normalized eigenfunction of the Sturm-Liouville problem reduced from (3) by extracting the azimuthal dependence ($r(s)$ is the eigenvalue) and $U(s,\theta)$ characterizes the dynamics of the pulse envelope. Further approximations to the complex amplitude F are determined from inhomogeneous equations with left-hand side analogous to that in (3) and with right-hand side calculated in previous steps of the asymptotic procedure. In order to obey the boundary conditions for F_j one has to impose conditions of compatibility onto the right-hand sides, which leads to an additional series of equations. So the problem on F_1 allows to obtain an expression

$$q(s) = r(s) + \frac{1}{r(s)}\int\limits_0^\infty \rho\left(\frac{\partial V}{\partial\rho}\right)^2\mathrm{d}\rho + \frac{m^2}{r(s)}\int\limits_0^\infty \frac{V^2}{\rho}\mathrm{d}\rho \tag{4}$$

which, according to (2), determines the phase of the pulse envelope, depending on the order of vorticity m. Another inference consists in stating the relationship

$$\mu(s)Q^2(s) = \mu_0 Q_0^2 = \text{const} \tag{5}$$

meaning that the carrier modulation depth evolution is strictly bound to the envelope phase. The compatibility condition for the problem on F_2 results in a nonlinear equation describing the dynamics of the pulse envelope

$$2ir(s)\frac{\partial U}{\partial s} + g(s)\frac{\partial^2 U}{\partial\theta^2} + ij(s)\frac{\partial U}{\partial\theta} + ir'(s)U + 4\theta\mu(s)r(s)q(s)U + d(s)U + h(s)\,|U|^2\,U = 0 \tag{6}$$

The pulse envelope U is a function of the envelope phase θ defined by (2) and longitudinal coordinate s, $r(s)$ is defined as well by (2), and $r'(s)$ is the derivative. Formulae for coefficients $g(s)$, $j(s)$,

$d(s)$ and $h(s)$ are derived quite analogously to those in [5], their dependence on s is caused by the longitudinal inhomogeneity of the waveguide. It should be emphasized that these coefficients are specific for a mode chosen in solving (3), henceforth Equation (6) is valid for any radial, azimuthal or vortex mode. Explicit formulae can be readily obtained for a quadratic dependence of the refractive index on the radial coordinate.

4. VARIATIONAL APPROACH TO ENVELOPE ANALYSIS

The equation for the pulse's envelope (6) can be analyzed by means of variational approach [11, 12] which had been substantiated in [13] for generalized nonlinear Schrödinger equation with additional terms of some special kind. Note first of all that Equation (6) turns out to be an Euler equation for the following Lagrangian density

$$\begin{aligned}\mathcal{L}(s,\theta) &= ir(s)\left(\frac{\partial U}{\partial s}U^* - U\frac{\partial U^*}{\partial s}\right) - g(s)\frac{\partial U}{\partial \theta}\frac{\partial U^*}{\partial \theta} + d(s)UU^* \\ &\quad + \frac{1}{2}ij(s)\left(\frac{\partial U}{\partial \theta}U^* - U\frac{\partial U^*}{\partial \theta}\right) + 4\theta\mu(s)r(s)q(s)UU^* + \frac{1}{2}h(s)\left(UU^*\right)^2 \end{aligned} \tag{7}$$

One can try to find a solution in the form of a travelling wave of unknown shape $P(x)$ with the variable amplitude $A(s)$, phase $\Phi(s)$, instant envelope frequency $\Omega(s)$, width $\sigma(s)$ and the envelope shift $\Delta(s)$

$$U(s,\theta) = A(s)P(x)e^{i\Omega(s)\theta + i\Phi(s)} \qquad x(s,\theta) \equiv \frac{\theta - \Delta(s)}{\sigma(s)} \tag{8}$$

$$U(0,\theta) = A_0 P(x_0)e^{i\Omega_0\theta + i\Phi_0} \qquad x_0 \equiv \frac{\theta - \Delta_0}{\sigma_0} \tag{9}$$

Substituting these into the Lagrangian density (7) we come to

$$\mathcal{L}_P(s,\theta) = -2r\left(\frac{\mathrm{d}\Omega}{\mathrm{d}s}\theta + \frac{\mathrm{d}\Phi}{\mathrm{d}s}\right)A^2P^2 - \frac{g}{\sigma^2}A^2\left(\frac{\mathrm{d}P}{\mathrm{d}x}\right)^2 + \frac{1}{2}hA^4P^4 - \left(g\Omega^2 + j\Omega - d\right)A^2P^2 + 4\theta\mu rqA^2P^2$$

We can now integrate the Lagrangian density $\mathcal{L}_P$ over the phase variable θ resulting in the reduced Lagrangian

$$\begin{aligned}\langle\mathcal{L}_P\rangle(s) &\equiv \int_{-\infty}^{+\infty}\mathcal{L}_P(s,\theta)\mathrm{d}\theta = -\frac{\sigma(s)}{c(s)}\int_{-\infty}^{+\infty}\mathcal{L}_P(s,x)\mathrm{d}x \\ &= -2r\sigma\Delta\left(\frac{\mathrm{d}\Omega}{\mathrm{d}s} - 2\mu q\right)AI_0 - 2r\sigma^2\left(\frac{\mathrm{d}\Omega}{\mathrm{d}s} - 2\mu q\right)AI_1 - 2r\sigma\frac{\mathrm{d}\Phi}{\mathrm{d}s}A^2I_0 \\ &\quad -2\frac{g}{\sigma}AI_2 - \sigma(g\Omega^2 + j\Omega - d)AI_0 + \frac{1}{2}h\sigma A^4I_3 \end{aligned} \tag{10}$$

where the following integrals are introduced

$$I_0 = \int_{-\infty}^{+\infty}P^2(x)\mathrm{d}x \qquad I_1 = \int_{-\infty}^{+\infty}xP^2(x)\mathrm{d}x \qquad I_2 = \int_{-\infty}^{+\infty}\left(\frac{\mathrm{d}P}{\mathrm{d}x}\right)^2\mathrm{d}x \qquad I_3 = \int_{-\infty}^{+\infty}P^4(x)\mathrm{d}x$$

For the reduced Lagrangian (10) then follows the principle of the least action $\delta\int\langle\mathcal{L}_P\rangle\,\mathrm{d}s = 0$. It allows us to determine the optimal functional dependencies for the pulse parameters. By taking functional derivatives with respect to the pulse parameters A, σ, Δ, Ω and Φ one can, after some manipulations, obtain the following explicit expressions

$$A^2(s) = \frac{D^2}{4}\frac{I_3}{I_2}\frac{h}{gr^2} \tag{11}$$

$$\Omega(s) = \Omega_\infty - 2\frac{\mu_0 Q_0^2}{Q(s)} \tag{12}$$

$$\sigma(s) = \frac{4}{D}\frac{I_2}{I_3}\frac{g(s)r(s)}{h(s)} \tag{13}$$

where $D \equiv r(0)\sigma_0 A_0^2$ and $\Omega_\infty \equiv \Omega_0 + 2\mu_0 Q_0$. The envelope shift $\Delta(s)$ and envelope phase $\Phi(s)$ in (8), (9) are expressed as follows

$$\Delta(s) = \Delta_0 + \Omega_\infty \int_0^s \frac{g(s')}{r(s')} \mathrm{d}s' + \frac{I_1}{I_0}\left(\sigma_0 - \sigma(s)\right)$$

$$\Phi(s) = \Phi_0 + \int_0^s \left[\frac{3D}{8}\frac{h(s')}{r^2(s')} - \frac{1}{2r(s')}\left(\Omega_\infty^2 g(s') - 4\frac{\mu_0\Omega_0^2}{Q^4(s')}g(s') - d(s')\right)\right] \mathrm{d}s'$$

To illustrate the results of this analysis one can look at the simple case of pulse propagation in an optical fiber with a refractive index profile that remains constant along the fiber's length. In this case the Equations (5), (11), (12), and (13) can be simplified leading to following explicit expressions

$$A^2(s) = A_0^2 \tag{14}$$

$$\sigma(s) = \sigma_0 \tag{15}$$

$$\mu(s) = \frac{\mu_0 Q_0^2}{(Q_0 + qs)^2} \tag{16}$$

$$\Omega(s) = \Omega_\infty - 2\frac{\mu_0 Q_0^2}{(Q_0 + qs)} \tag{17}$$

From (14) and (15) it follows, that amplitude and width of the pulse remain constant along the fiber's length. Qualitatively dependencies (16) and (17) are sketched in the Figure 1. It can be seen that while the pulse propagates the phase modulation depth $\mu(s)$ slowly decays to zero, thus leveling the instant carrier frequencies of the front and the rear ends of the pulse. This effect is accompanied by the envelope frequency $\Omega(s)$ asymptotically approaching it's final value of Ω_∞ that is either greater or less than initial frequency Ω_0 depending on the sign of the μ_0.

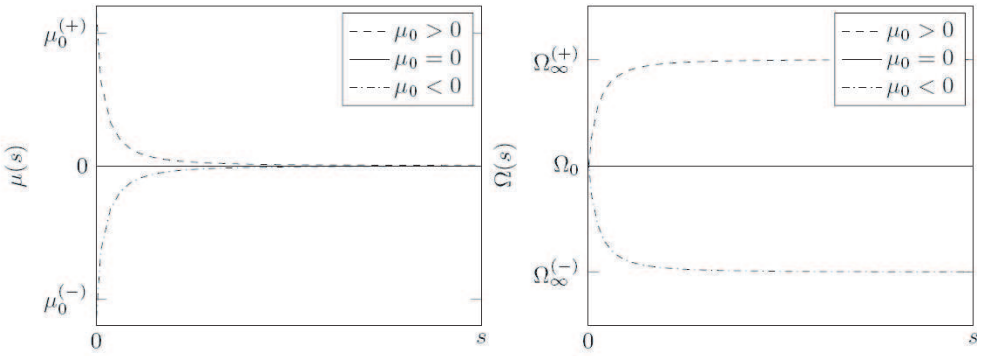

(a) (b)

Figure 1: Qualitative asymptotic behaviour of the (a) chirp depth $\mu(s)$ and (b) envelope frequency $\Omega(s)$ in a fiber with a profile independent on s. Constants $\mu_0^{(-)}$ and $\Omega_0^{(-)}$ correspond to the case of $\mu_0 < 0$. Constants $\mu_0^{(+)}$ and $\Omega_0^{(+)}$ correspond to the opposite case of $\mu_0 > 0$.

5. CONCLUSION

An outline has been presented for the asymptotic procedure needed to describe propagation of an arbitrary, vortex included, mode with linear frequency modulation of the carrier in a nonlinear graded-index optical fiber with slowly-varying longitude inhomogeneity. The Lagrangian density for the envelope equation was guessed and the problem was analyzed by means of a variational approach. The explicit expressions for the pulse amplitude, width, phase shift, envelope shift and envelope frequency were obtained for an arbitrary propagating mode. The modulation depth is found to be decaying along the fiber's length, while the envelope frequency tends asymptotically to some specific value that depends on the initial modulation frequency and depth.

ACKNOWLEDGMENT

The authors acknowledge Saint-Petersburg State University for a research grant 11.0.61.2010. The work was also partly supported by the Russian Foundation for Basic Research under grant No. 13-02-00212.

REFERENCES

1. Hasegawa, A. and F. Tappert, "Transmission of stationary nonlinear optical pulses in dispersive dielectric fibers," *Appl. Phys. Lett.*, Vol. 23, 142, 171, 1973.
2. Mollenauer, L. F., R. H. Stolen, and J. P. Gordon, "Experimental observation picosecond pulse narrowing and solitons in optical fibers," *Phys. Rev. Lett.*, Vol. 45, 1095, 1980.
3. Kivshar, Yu. and G. Agrawal, *Optical Solitons. From Fibers to Photonic Crystals*, Academic Press, 2003.
4. Stolen, R. H., "Nonlinearity in fiber transmission," *Proc. IEEE*, Vol. 68, 1232, 1980.
5. Bisyarin, M. A., "Nonlinear chirped pulses in graded-index optical fibers with longitudinal inhomogeneity," *Proc. SPIE*, Vol. 6614, 661406, 2007.
6. Schwartz, M., *Information Transmission, Modulation, and Noise*, McGraw-Hill Book Company Inc., 1959.
7. Ellis, A., J. Zhao, and D. Cotter, "Approaching the non-linear Shannon limit," *J. Lightwave Tech.*, Vol. 28, 423, 2010.
8. Bozinovic, N., et al., "Terabit-scale orbital angular momentum mode division multiplexing in fibers," *Science*, Vol. 340, 1545, 2013.
9. Kirilenko, M. S. and S. N. Khonina, "Information transmission using optical vortices," *Optical Memory and Neural Networks*, Vol. 22, 81, 2013.
10. Whitham G. B., *Linear and Nonlinear Waves*, John Wiley & Sons, 1974.
11. Anderson D., "Variational approach to nonlinear pulse propagation in optical fibers," *Phys. Rev. A*, Vol. 27, 3135, 1983.
12. Kath, W. L. and N. F. Smyth, "Soliton evolution and radiation loss for the nonlinear Schrödinger equation," *Phys. Rev. E*, Vol. 51, 2, 1995.
13. Bergé, L. and A. Couairon, "A variational method for extended nonlinear Schrödinger systems," *Physica D*, Vol. 152–153, 752, 2001.

Three-dimensional Loaded Dipoles for Applications in Frequency Selective Structures

A. K. Rashid[1, 2], **S. Ullah**[3], **and S. A. Nauroze**[2]

[1]Namal College Mianwali, Pakistan
[2]National University of Computer and Emerging Sciences, Pakistan
[3]National University of Science and Technology, Pakistan

(*Invited Paper*)

Abstract— A three-dimensional (3-D) frequency selective structure (FSS) is proposed, which consists of a two-dimensional (2-D) periodic arrays of loaded strip dipoles. These strip dipoles are loaded along the thickness of the FSS, which leads to certain advantages compared to the conventional 2-D loading. Unit-cell period is greatly reduced, and a relatively stable frequency response is achieved under even a large variation of the angle of incidence

1. INTRODUCTION

Conventional frequency selective surfaces consist of two-dimensional (2-D) unit-cell shapes like dipoles, loops, etc. [1, 2]. A number of variations to earlier simple shapes have been proposed over the last three decades, which lead to an advantage in certain applications [3–5]. This quest for finding the best shape continues till date, and more recently, a few three-dimensional unit-cell shapes have also been considered [6, 7]. Freedom of variation in third dimension actually offers more flexibility in designing innovative unit-cell geometries. It appears prudent to efficiently use the third dimension (thickness) of a frequency selective structure (FSS) in order to obtain improved performance of certain parameters. Based on that, it may be useful to reconsider the conventional FSS shapes, and modify them to utilize the freedom of third dimension. This may lead to better and interesting FSS designs, which may also be easy to analyze and fabricate with the present computational and manufacturing technology.

Dipole constitutes one of the earliest shapes used in FSS designs [1]. It has been a preferred choice for application in linearly polarized FSSs. A number of other FSS shapes have actually been derived from a dipole unit-cell, and they include loaded-dipoles [3], meander-lines [4], crossed-dipoles [8], Jerusalem cross [9], tri-poles [10], etc.. These modified forms basically lead to more compact shapes, which can also be applied in dual-polarized FSS.

We study an FSS consisting of a 2-D periodic array of strip dipoles, which have been loaded along the third dimension (thickness) of FSS. This scheme leads to a compact unit-cell geometry, which is actually desirable to improve the angular performance of an FSS [1, 2]. The proposed structure is easy to fabricate on a two-layer printed circuit board (PCB).

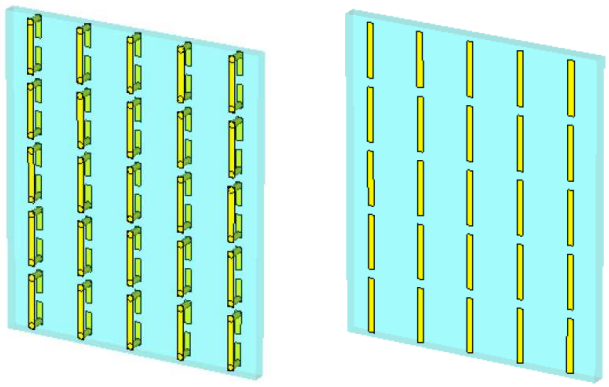

Figure 1: (a) Conventional 2-D array of printed dipoles, (b) proposed array of three-dimensional loaded dipoles.

2. DESCRIPTION OF THE STRUCTURE

A perspective view of the proposed structure is shown in Fig. 1(a). A conventional FSS consisting of 2-D unloaded strip dipoles is also given as Fig. 1(b). Our proposed dipole consists of strips and two conducting cylinders. The two cylinders represent the two via-holes, which connect the opposite sides of a printed circuit board (PCB) where strips are printed. Fig. 2 shows detailed views of a unit-cell of this structure. Vertical period and horizontal periods are denoted by p_y and p_x, respectively. Length of the dipole as seen in the top view is represented by a. Width of the strips and the diameter of the via-hole are kept identical, and they are given by w. Strips are printed on a substrate of height d, dielectric constant ε_r. Gap between strips on the back side of the PCB is denoted by g.

The perspective view of a unit-cell (Fig. 2) shows a case of normal incidence when the incident electric field is parallel to the printed strip. However, we also study this structure under oblique incidence under both parallel (transverse electric) and perpendicular (transverse magnetic) polarizations, following the convention given in [1]. Based on that, the incident angle θ is defined with respect to the positive z-axis.

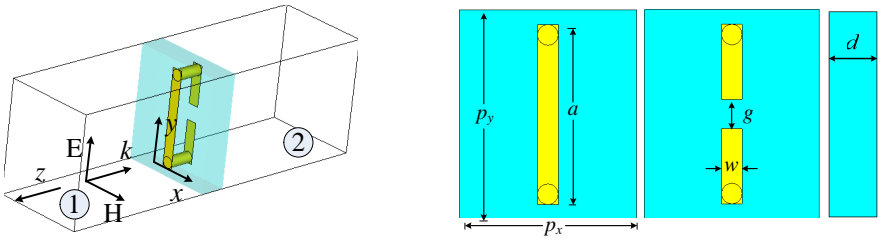

Figure 2: Different views of a unit-cell of the proposed structure.

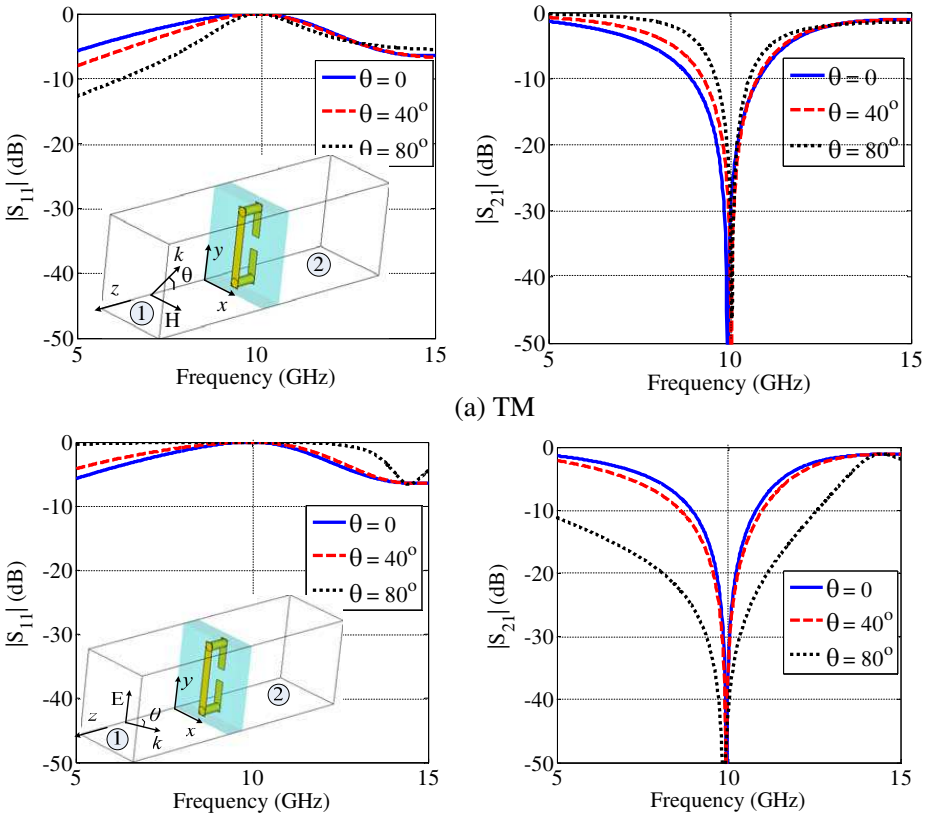

Figure 3: Scattering parameters of the proposed structure under oblique (a) TE and (b) TM incidence ($p_x = 6\,\text{mm}$, $w = 0.7\,\text{mm}$, $d = 1.6\,\text{mm}$, $\varepsilon_r = 2.2$, $p_y = 7.1\,\text{mm}$, $a = 6.1\,\text{mm}$, $g = 1\,\text{mm}$).

3. RESULTS

Figure 3 presents a design example of the proposed structure operating at 10 GHz. Horizontal and vertical periods are set as 6 mm and 7.1 mm, respectively. Since these periods are much smaller than the operating wavelength at 10 GHz, an excellent angular stability of scattering parameters is seen, as expected. For the purpose of fair comparison, we have designed another FSS based on conventional printed dipoles shown in Fig. 1(b). Results of this design example are given in Fig. 4. Horizontal periods of the two designs have been kept identical. Similarly, the gap between two adjacent shapes along the vertical direction ($p_y - a$) has also been set as the same for the two designs. Both are fabricated using on identical substrates. For resonance at 10 GHz, the vertical period of the conventional design turns out to be 14 mm, which is almost twice as large as that of the proposed three-dimensional dipole. For this reason, a relatively poor angular performance of the 2-D FSS is expected, and it is verified from the results of TM incidence shown in Fig. 4(a). Comparison of Fig. 3(a) and Fig. 4(a) is easily understandable from the theory of conventional frequency selective surfaces [1, 2].

Figures 3(b) and 4(b) show the scattering parameters response under TE incidence. It is again seen that the proposed 3-D structure performs superior to the conventional 2-D FSS. Based on these comparisons, it appears clear that 3-D dipole forms an attractive candidate for FSS applications, especially those where high degree of angular stability is required.

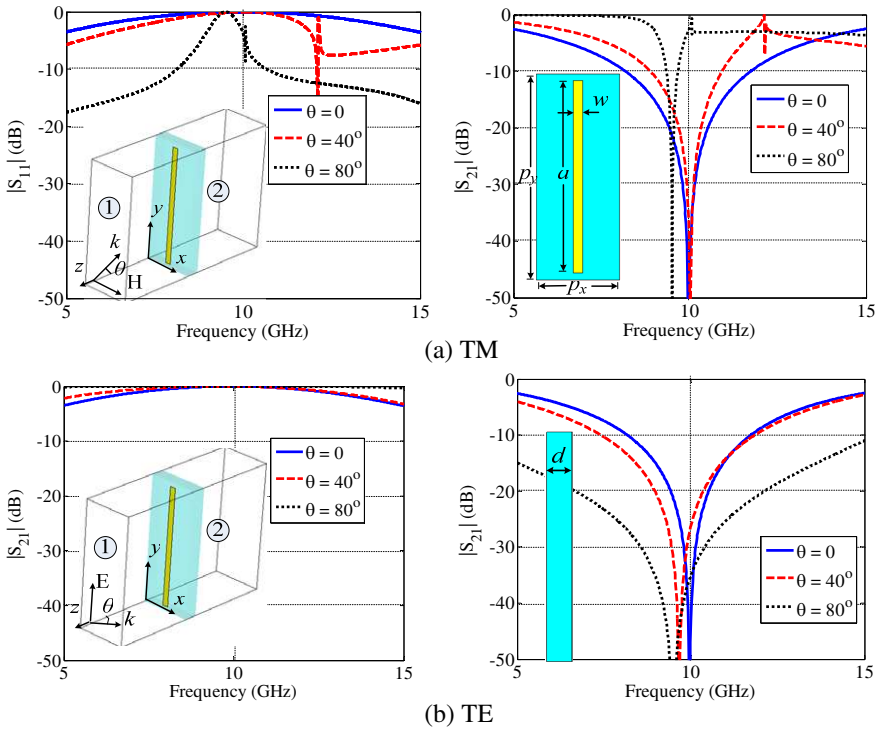

Figure 4: Scattering parameters of a conventional 2-D array of printed dipoles under (a) TM and (b) TE incidence ($p_x = 6$ mm, $w = 0.7$ mm, $d = 1.6$ mm, $\varepsilon_r = 2.2$, $p_y = 15$ mm, $a = 14$ mm).

4. CONCLUSIONS

A new 3-D FSS has been proposed, which consists of a 2-D periodic array of folded/loaded strip dipoles. The proposed structure exhibits stable frequency response even under a large variation of the angle of incidence. It is expected that this new 3-D FSS may find many useful practical applications, especially where 2-D strip dipoles were previously used.

REFERENCES

1. Munk, B. A., *Frequency Selective Surfaces: Theory and Design*, John Wiley & Sons Inc., 2000.
2. Wu, T. K., *Frequency Selective Surface and Grid Array*, John Wiley & Sons Inc., 1995.
3. Munk, B. A., R. G. Kouyoumjian, and L. Peters, "Reflection properties of periodic surfaces of loaded dipoles," *IEEE Trans. on Antennas and Propag.*, Vol. 19, No. 5, 612–617, Sep. 1971.

4. Parker, E. A. and A. N. A. El-Sheikh, "Convoluted array elements and reduced size unit cells for frequency selective surfaces," *IEE Proc. Microwaves, Antennas and Propag.*, Vol. 138, No. 1, 19–22, Feb. 1991.
5. Zheng, S. F., Y. Z. Yin, H. L. Zheng, Z. Y. Liu, and A. F. Sun, "Convoluted and interdigitated hexagon loop unit cells for frequency selective surfaces," *Electron. Lett.*, Vol. 47, No. 4, 233–235, Feb. 2011.
6. Luo, G. Q., W. Hong, Q. H. Lai, K. Wu, and L. L. Sun, "Design and experimental verification of compact frequency-selective surface with quasi-elliptic bandpass response," *IEEE Trans. on Microwave Theory and Tech.,* Vol. 55, No. 12, 2481–2487, Dec. 2007.
7. Rashid, A. K., Z. Shen, and B. Li, "An elliptical bandpass frequency selective structure based on microstrip lines," *IEEE Trans. on Antennas and Propag.*, Vol. 60, No. 10, 4661–4669, Oct. 2012.
8. Hamdy, S. M. A. and E. A. Parker, "Influence of lattice geometry on transmission of electromagnetic waves through arrays of crossed dipoles," *IEE Proc. Microwaves, Antennas and Propag.*, Vol. 129, No. 1, 7–10, Feb. 1982.
9. Anderson, I., "On the theory of self-resonant grids," *The Bell System Technical Journal,* Vol. 54, No. 10, 1725–1731, 1975.
10. Pelton, E. L. and B. A. Munk, "Periodic antenna surface of triple slot elements," United States Patent 3,975,738, Aug. 17, 1976.

Semi Analytical Model for Non-Resonant Layered Frequency Selective Surfaces (FSS)

Poojali Jayaprakash and Kavitha Arunachalam
Department of Engineering Design, Indian Institute of Technology Madras, 600036, India

Abstract— The proposed approach employs transmission line theory to model electromagnetic wave propagation through FSS comprising of non-resonant metal grids and patches. The equivalent reactance of the individual metal layers is initially estimated by minimizing the error between scattering parameters obtained from 3D full wave simulations and $ABCD$ matrix of the free standing structure. With the knowledge of the individual metal layer's reactance, a simple analytical model is adopted to predict the frequency response of multi-layered FSS for different configurations without the need for 3D full wave simulations. Performance of this semi-analytical approach is studied for varying unit cell size, D ($\lambda/5$–$\lambda/15$), metallization dimensions, and number of FSS layers in X-band (8–12 GHz). The frequency response of the semi-analytical model is in good agreement with 3D full wave simulations suggesting that the proposed approach is faster and simpler for design of multi-layered non-resonant FSS.

1. INTRODUCTION

Miniaturized FSS are periodic metallic structures comprising of non-resonant inductive grids and capacitive patches stacked on thin low loss dielectric substrate. These are widely used in satellite communication and remote sensing systems for selective reception or rejection of a band of frequencies [1]. In non-resonant FSS, the size, D of an unit cell, i.e., building block of the periodic structure is typically smaller compared to the operating wavelength (λ) [2]. Equivalent circuit models provide a quick and easy means to predict and understand the frequency response of layered non-resonant unit cells [2, 4, 5]. In [2], a transmission line model was introduced to explain the frequency response of non-resonant FSS comprising of inductive grids and capacitive patches. Analytical expressions for inductance (L) and capacitance (C) in [2] which were based on [3] do not hold good for design and analysis of layered FSS. Hence, a generalized equivalent circuit method was presented in [4]. However, this method requires further numerical simulations for parameter optimization. Furthermore, it models the dielectric layer in the FSS as a LC circuit instead of a delay line. In this work, we propose a computationally simple and realistic model for design of multi-layered non-resonant FSS. Section 2 presents the analytical model, L and C parameter estimation for the individual metal layers and model validation for layered non-resonant FSS. The performance of the proposed model is validated using a finite element method based EM simulation software, HFSS® for varying unit cell size, D ($\lambda/5$–$\lambda/15$), metallization dimensions and FSS layers (1–3) in the X band (8–12 GHz). Results and discussion are presented in Section 3 followed by conclusion.

2. METHODOLOGY

2.1. Analytical Model

Figure 1 shows the generalized cascaded transmission line representation of a multi-layered FSS, where M_i refers to the ith non-resonant metal layer and D_i is the ith low loss dielectric substrate, d_i is the thickness of ith dielectric substrate and and $i = 1, 2, \ldots, n$. The cascaded transmission line is terminated by ports 1 and 2 with free space impedance (Z_0). The measurement plane for the input (port 1) and output (port 2) ports is the defined at a distance, d_0 from the layered FSS as in the

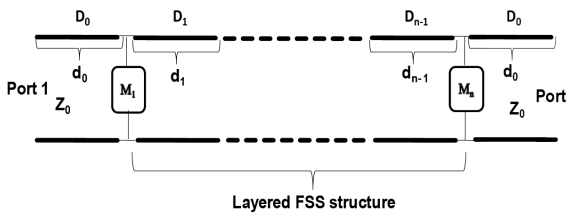

Figure 1: Generalized Transmission line model approach for Non-resonant FSS structures.

3D full wave simulations. It should be noted that the metal layers are modeled as either inductive or capacitive elements depending on the unit cell's physical structure, and dielectric substrates are modeled as delay lines. The $ABCD$ parameters of the cascaded structure is given by [6],

$$\begin{bmatrix} A^C & B^C \\ C^C & D^C \end{bmatrix}_{cascaded} = \begin{bmatrix} A & B \\ C & D \end{bmatrix}_{Air} \begin{bmatrix} A & B \\ C & D \end{bmatrix}_{FSS} \begin{bmatrix} A & B \\ C & D \end{bmatrix}_{Air}, \tag{1}$$

where,

$$\begin{bmatrix} A & B \\ C & D \end{bmatrix}_{FSS} = \prod_{i=1}^{n} \begin{bmatrix} A & B \\ C & D \end{bmatrix}_{M_i} \begin{bmatrix} A & B \\ C & D \end{bmatrix}_{D_i}; \quad \begin{bmatrix} A & B \\ C & D \end{bmatrix}_{Air} = \begin{bmatrix} \cos(\beta_0 d_0) & jZ_0 \sin\beta_0 d_0 \\ \frac{j\sin(\beta_0 d_0)}{Z_0} & \cos(\beta_0 d_0) \end{bmatrix} \tag{2a}$$

$$\begin{bmatrix} A & B \\ C & D \end{bmatrix}_{D_i} = \begin{bmatrix} \cos(\beta_i d_i) & jZ_0 \sin\beta_i d_i \\ \frac{j\sin(\beta_i d_i)}{Z_0} & \cos(\beta_i d_i) \end{bmatrix}; \quad \begin{bmatrix} A & B \\ C & D \end{bmatrix}_{M_i} = \begin{bmatrix} 1 & 0 \\ Y_i & 1 \end{bmatrix}; \quad i = 1, 2, 3, \ldots, n \tag{2b}$$

In Eq. (2), $\beta_0 = \frac{2\pi}{\lambda_0}$, is free space propagation constant, $\beta_i = \frac{2\pi}{\lambda_i}$, is propagation constant in the dielectric substrate and $Y_i = jwL_i$ or $1/(jwC_i)$ depending on the type of metal layer. A simpler estimate for L_i and C_i based on the theory of infinite wire grids and metal patches given by [3],

$$C_i = \varepsilon_0 \varepsilon_{eff}(2D/\pi)\log[csc(\pi s/2D)]; \quad L_i = \mu_0(D/2\pi)\log[csc(\pi w/2D)] \tag{3}$$

was adopted in [2, 4, 5] for equivalent circuit representation of non-resonant FSS. In Eq. (3), D is unit cell size, s is gap between patches, w is width of the wire grid, ε_{eff} is effective permittivity of the medium and ε_0, μ_0 are free space permittivity and permeability respectively. Using Eqs. (1)–(2), transmission (S_{21}^C) and reflection (S_{11}^C) scattering parameters of the cascaded system in Figure 1 can be written as [6],

$$S_{11}^C = \frac{A^C + \frac{B^C}{Z_0} - C^C Z_0 - D^C}{\left(A^C + \frac{B^C}{Z_0} + C^C Z_0 + D^C\right)}; \quad S_{21}^C = \frac{2}{\left(A^C + \frac{B^C}{Z_0} + C^C Z_0 + D^C\right)} \tag{4}$$

For a given estimate of the circuit parameters, L_i and C_i for the ith metal layer, Eqs. (1), (2), (4) were used to calculate the scattering parameters of the layered non-resonant FSS.

2.2. 3D EM Simulation

Scattering parameters of the individual metal layers in free space were obtained using 3D EM simulation software, HFSS®. Due to the periodicity of the unit cell, 3D EM wave simulations were studied for the FSS unit cell by enforcing periodic boundary conditions. Scattering parameters were calculated for a free standing non-resonant unit cell of size, D for an incident plane wave with TM polarization and metal thickness of 17 microns. Simulations were carried out for varying cell size (D), patch gap (s) and grid width (w) summarized in Table 1 for signal transmission in the X band (8–12 GHz). Transmission parameter, obtained for the inductive and capacitive unit cell FSS models in Table 1 were used to estimate the equivalent inductance (L) and capacitance (C) respectively based on the model presented in Section 2.1.

2.3. Circuit Parameter Estimation

The equivalent circuit parameter of the free standing single layers in Table 1 was estimated by solving the following minimization problem,

$$\min\left(\left\|S_{21}^M - S_{21}^C(y)\right\|^2\right), \quad y \in R^1 \tag{5}$$

Table 1: Single layer inductive grids and capacitive patches simulated in HFSS®.

Unit cell	D (mm)	s (mm)	w (mm)
1	2	0.25	0.25
2	3	0.5	0.5
3	4	0.3	0.3
4	5	0.5	0.5
5	7	1.0	1.0

where S_{21}^{M} and S_{21}^{c} are complex one dimensional vectors of size $N \times 1$ representing frequency domain transmission parameters obtained using 3D EM simulations and Eq. (4) respectively over 8–12 GHz (X band) and, y is the real valued circuit parameter which is either L or C depending on the metal layer. This optimization problem was solved using golden section algorithm which is one of the efficient methods for single variable optimization [7]. It should be noted that the complex transmission vectors, S_{21} in Eq. (4) are represented as real valued vectors of size $2N \times 1$ in the optimization routine. The search space was bounded between $y_{\min}$ and $y_{\max}$ estimated based on Eq. (3) and the search was continued until the cost function in Eq. (5) was below a predetermined threshold, δ.

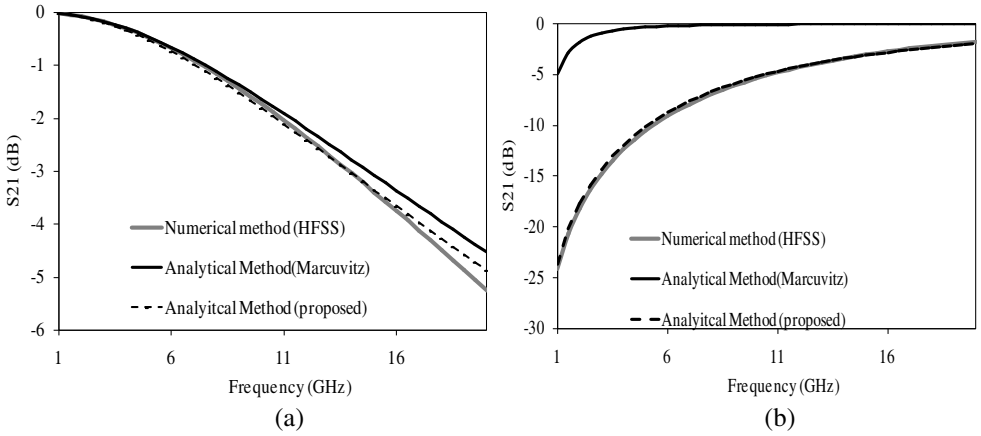

Figure 2: Comparison of the transmission parameter obtained for a free standing FSS metal layer using analytical approach Eq. (3) and the proposed semi-analytical model with 3D EM simulations; (a) patches and (b) wire grids for unit cell #5 in Table 1.

2.4. Multilayered FSS Design

Agreement between the proposed semi-analytical model and 3D EM simulation was studied for a second order X band (8–12 GHz) FSS. For this study, unit cell model 1 was chosen since the idea was to create a miniaturized layered FSS structure. The second order FSS unit cell consisted of the following layers: patch, dielectric, grid, dielectric and a patch. The physical dimensions of multi-layered FSS were $D = 2\,\text{mm}$ ($\lambda/15$ at 10 GHz), $d_1 = 0.64\,\text{mm}$, $d_2 = 1.28\,\text{mm}$, $s_1 = 0.1\,\text{mm}$, $s_2 = 0.35\,\text{mm}$ and $w = 0.35\,\text{mm}$. The dielectric material chosen was RO3010 with dielectric constant $\varepsilon_r = 10.2$ and loss tangent, 0.0035. The scattering parameters of the multi-layered FSS were calculated using the cascaded 3-layer FSS $ABCD$ matrix (Eq. (1)) where the $ABCD$ matrices of the metallic grid and patches were determined following the approach in Section 2.3.

3. RESULTS AND DISCUSSION

3.1. Equivalent Circuit Model for Single FSS Layer

3D EM simulations were carried out for the unit cell models in Table 1 using HFSS and estimation of the equivalent circuit parameters for the free standing metal layers were carried out in MATLAB. Figure 2 shows signal transmission parameter, S_{21} calculated for unit cell #5 for both inductive grid and capacitive patch models using 3D EM simulations, and estimated L and C values of the proposed equivalent circuit approach. Equivalent circuit approach based on Eq. (3) is also shown in Figure 2 for comparison. It should be noted that the frequency response exhibits low pass behavior for capacitive patches and high pass behavior for inductive grids for both analytical models as explained in [2, 3]. However, the proposed approach yields a better approximation for the 3D EM simulations over the entire frequency band. This enables us to extend the model prediction for design and analysis of multi-layered FSS structures comprising of repetitive capacitive and inductive grids. Table 2 summarizes the equivalent circuit parameters estimated using the proposed semi-analytical model for the single layer FSS unit cells listed in Table 1. Circuit parameters based on Marcuvitz model (Eq. (3)) is also listed in Table 2 for comparison. Interestingly, a comparison between the circuit parameters estimated using the proposed semi-analytical model and Marcuvitz's analytical model indicates an average correction factor of 0.3π for capacitance and 0.03π for inductance to Eq. (3).

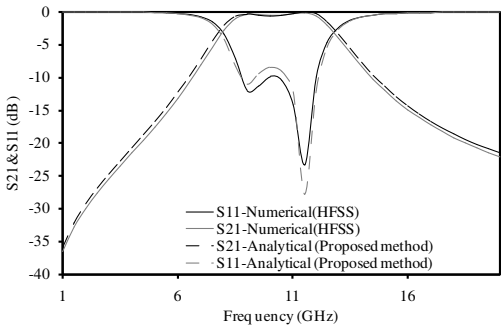

Figure 3: Comparison of the scattering parameters obtained for the second order FSS using the proposed semi-analytical approach with 3D EM simulations.

Table 2: Summary of the equivalent circuit parameters estimated by the proposed model and comparison with analytical Eq. (3) proposed in [2] for free standing inductive and capacitive metal layer of Table 1.

Unit cell	L-Marcuvitz (nH)	L-optimized (nH)	C-Marcuvitz (fF)	C-optimized (fF)
1	6.45	0.56	18	19
2	8.00	0.71	22	23
3	16.91	1.59	47	49
4	18.31	1.73	50	54
5	20.76	1.98	57	59

Table 3: Comparison of proposed method with [2].

SI. No.	**Frequency (GHz)**	**Transmission Loss, S_{21} (dB)**		
		HFSS	**Proposed Method**	**Ref. [2]**
1	8.7	−0.6	−0.8	−4.4
2	9.0	−0.5	−0.7	4.8
3	9.5	−0.4	−0.7	−5.3
4	10.0	−0.5	−0.7	−5.8
5	10.5	−0.4	−0.4	−6.3
6	11.0	−0.2	−0.1	−6.7
7	11.5	−0.1	−0.04	−7.5

3.2. Model Validation for Multi-layered FSS

Figure 3 shows the comparison between the scattering parameters obtained for the second order FSS using the proposed semi-analytical model with 3D EM simulations. It can be observed that the proposed semi-analytical model compares very well with 3D simulations of the cascaded multi-layered FSS. Table 3 summarizes the performance of the proposed equivalent circuit model for the second order FSS with 8–12 GHz transmission window. It should be noted that the semi-analytical model indicated a constant correction factors to the analytical Eq. (3) depending on whether the metal layer comprised of grids or patches. Substitution of the analytical Eq. (3) with the correction factors for L and C in the cascaded transmission line model given by Eqs. (1) and (2) yielded very good results with the full wave simulations. Thus, the proposed semi-analytical model could be used as a quick and easy means to predict the frequency response of multi-layered non-resonant FSS.

4. CONCLUSION

A cascaded transmission line model is proposed for design and analysis of multi-layered non-resonant FSS comprising of metallic grids and patches. The equivalent circuit parameters estimated for the free standing metal layers based on the proposed semi-analytical approach were found to differ from the analytical equations by a constant correction factor. The performance of the proposed cascaded transmission line model obtained using the estimated equivalent circuit parameters for the

individual metal layers agreed very well with 3D simulations. Application of the correction factor to the classical model in [3] was shown to work for both single and multi-layered miniaturized FSS. The proposed methods is a quick and easy means to design multi-layered FSS configurations without the need to run time consuming 3D EM simulations for the cascaded structure.

REFERENCES

1. Munk, B. A., *Frequency Selective Surfaces: Theory and Design*, Wiley-Interscience, New York, 2000.
2. Sarabandi, K. and N. Behdad, "A frequency selective surface with miniaturized elements," *IEEE Trans. Antennas Propag.*, Vol. 55, No. 5, 1239–1245, May 2007.
3. Marcuvitz, N., *Waveguide Handbook*, Boston Technical Publishers, Lexington, MA, 1964.
4. Al-Joumayly, M. A. and N. Behdad, "A generalized method for synthesizing low-profile, bandpass frequency selective surfaces with non-resonant constituting elements," *IEEE Trans. Antennas Propag.*, Vol. 58, No. 5, Dec. 2010.
5. Al-Joumayly, M. and N. Behdad, "A new technique for design of low-profile, second-order, bandpass frequencyselective surfaces," *IEEE Trans. Antennas Propag.*, Vol. 57, No. 2, 452–459, Feb. 2009.
6. Ludwig, R. and G. Bogdanov, *RF Circuit Design Theory and Applications*, 2nd Edition, Pearson, 2012.
7. Deb, K., *Optimization for Engineering Design*, PHI Learning Private Limited, 2010.

Patch Antenna with Electrically Tunable Ferrite-ferroelectric Bilayer

Kaida Xu[1], **Ronald J. Spiegel**[2], **Yonghong Zhang**[1], **William T. Joines**[2], **and Qing Huo Liu**[2]

[1]EHF Key Lab of Science, University of Electronic Science and Technology of China, Chengdu, China
[2]Department of Electrical and Computer Engineering, Duke University, Durham, NC, USA

Abstract— A coaxial-fed patch antenna with a ferrite-ferroelectric bilayer above a regular alumina substrate has been designed and analyzed. The ferrite-ferroelectric bilayer, multiferroic heterostructure, consists of a near-single-crystal ferrite yttrium iron garnet (YIG) film layer and a ferroelectric ceramic barium strontium titanate (BST) film layer with thicknesses of 1 μm and 0.5 μm, respectively. When the electric field applied across the BST layer changes from 2.5 V/um to 15 V/um, its permittivity will be tuned, thus the operating frequency of the antenna will shift as well. We also analyze the influence of the static magnetic field variation to the operating frequency of the antenna.

1. INTRODUCTION

Planar patch antennas are widely used because of their low cost, easy design, and suitability for integration with other printed circuits. In order to lower the operating frequency or miniaturize the overall size of the antenna, metamaterials with embedded metallic periodic structures have been used as antenna substrate for achieving relative permeability larger than unit [1], but it is so complicated to design and fabricate. Recently, the electric-field-tunable ferrite-ferroelectric bilayer structures [2, 3] with high permittivity and permeability but low loss have been demonstrated. In this paper, we apply this multiferroic heterostructure bilayer YIG and BST into the patch antenna to make the operating frequency electrically tunable. The interactions among the parameters of YIG and BST are also explored and analyzed.

2. FERRITE-FERROELECTRIC MATERIAL ANALYSIS

For the ferrite media, the permeability tensor of a gyromagnetic ferrite substrate, depending on the excitation frequency and applied DC bias magnetic field, has the following Hermitian form [4]:

$$\bar{\bar{\mu}} = \begin{bmatrix} \mu & -j\kappa & 0 \\ j\kappa & \mu & 0 \\ 0 & 0 & 1 \end{bmatrix} \tag{1}$$

where μ and κ are given by [4]

$$\mu = \mu_+ + \mu_- \tag{2}$$

$$\kappa = \mu_+ - \mu_- \tag{3}$$

$$\mu_\pm = \mu'_\pm - j\mu''_\pm \tag{4}$$

$$\mu_0(1-\mu'_\pm) = \frac{\gamma Ms(\omega_0 \pm \omega)T^2}{1+(\omega_0 \pm \omega)^2T^2} \tag{5}$$

$$\mu_0\mu''_\pm = \frac{\gamma MsT^2}{1+(\omega_0 \pm \omega)^2T^2} \tag{6}$$

The definition of parameters in above equations can be found in Table 1, where $\omega_0 = \gamma H_0$, $T = 2/(\gamma\Delta H)$. All the above parameters are in cgs unit. The relative permeability can be expressed by $\mu_r = (\mu^2 - \kappa^2)/\mu$. Here we use the ferrite layer with $\gamma = 2.8$ MHz/Oe, $Ms = 3000$ G, $\Delta H = 350$ Oe, and $H_0 = 2800$ Oe, and the variation of relative permeability μ_r has been illustrated in Fig. 1. The relative permeability is constant with the value of 2 except the range from around 1.1 to 1.4 GHz.

For the ferroelectric layer, the tunable electric field applied across the BST layer can change its permittivity [3]. In reality, in some range of the static magnetic field operated on the ferrite media YIG, there are interactions between the permittivity of BST and permeability of YIG. For instance, the gyromagnetic ratio of YIG is taken $\gamma = 6.15$ MHz/Oe while the other parameters Ms, ΔH and H_0 are the same as the aforementioned values. When electric field value $E = 2.5$ V/um,

Table 1.

γ	Gyromagnetic ratio	T	Relaxation time period	Ms	Saturation magnetization
H_0	Bias magnetic field	ΔH	Magnetic line width	ω	Angular excitation frequency

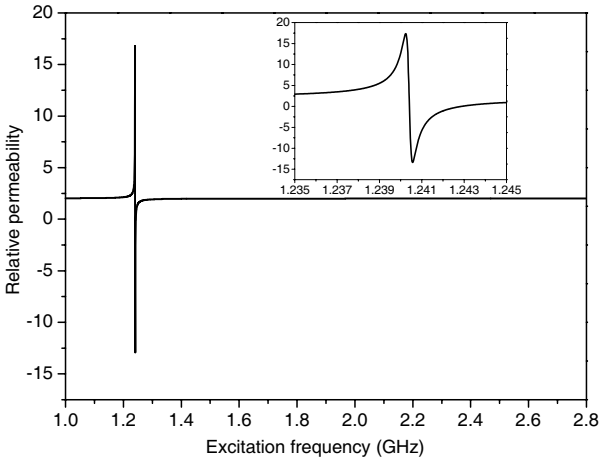

Figure 1. Variation of relative permeability at different excitation frequencies. The inset is the zoomed plot from 1.235 to 1.245 GHz.

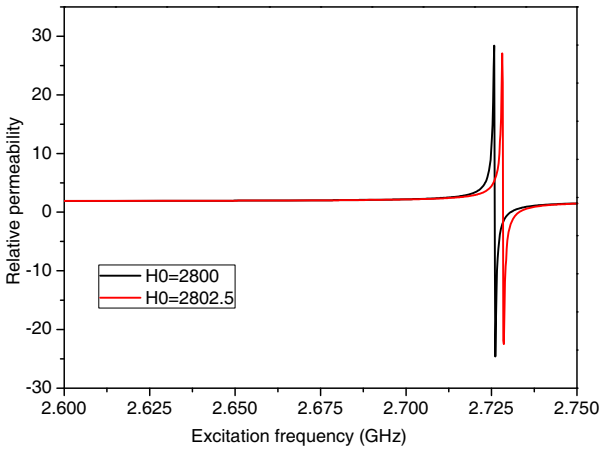

Figure 2. Variation of relative permeability at different bias magnetic field.

where the corresponding relative permittivity of BST is about 850 obtained from [3], is tuned to $E = 15.0\,\mathrm{V/um}$, i.e., $\varepsilon_r = 570$, the static field H_0 will be increased by around 2.5 Oe. Fig. 2 illustrates the variation of relative permeability at two different bias magnetic fields. At frequency 2716 MHz, the relative permeability will reduce from 15 to 3 as H_0 shifts from 2800 to 2802.5 Oe.

3. ANTENNA CONFIGURATION AND RESULTS

The proposed coaxial-fed patch antenna is comprised of a regular alumina substrate (relative permittivity $\varepsilon_r = 9.9$, thickness $h = 2\,\mathrm{mm}$), a ferrite-ferroelectric bilayer, a copper patch and a ground plane, which can be seen in Fig. 3. The ferrite-ferroelectric bilayer consists of a near-single-crystal ferrite yttrium iron garnet (YIG) film layer and a ferroelectric ceramic barium strontium titanate (BST) film layer with thicknesses of 1 µm and 0.5 µm, respectively. The two thin electrodes deposited on both surfaces of the BST and electromagnet for biasing the YIG can be neglected in the simulation model of the antenna. When we use the ferrite YIG layer with $\gamma = 2.8\,\mathrm{MHz/Oe}$, $Ms = 3000\,\mathrm{G}$ and $\Delta H = 350\,\mathrm{Oe}$, and apply bias magnetic field $H_0 = 2800\,\mathrm{Oe}$, the parameters (i.e., $\varepsilon_r = 14.78$ and $\mu_r = 2$) of the ferrite YIG layer can be almost unchanged if the operating frequency is not at $1.235 \sim 1.245\,\mathrm{GHz}$. Thus, when the electric field applied across the BST layer changes from 2.5 V/um to 15 V/um, the operating frequency of the antenna will be shifted from 2615 MHz up to 2716 MHz as shown in Fig. 4.

However, if we use the ferrite YIG layer with $\gamma = 5.92\,\mathrm{MHz/Oe}$, $Ms = 3000\,\mathrm{G}$ and $\Delta H = 350\,\mathrm{Oe}$, and still apply bias magnetic field $H_0 = 2800\,\mathrm{Oe}$, the relative permeability at 2.5 V/um (i.e., 2615 MHz) will not vary as shown in Fig. 2, while the relative permeability at 15 V/um will be

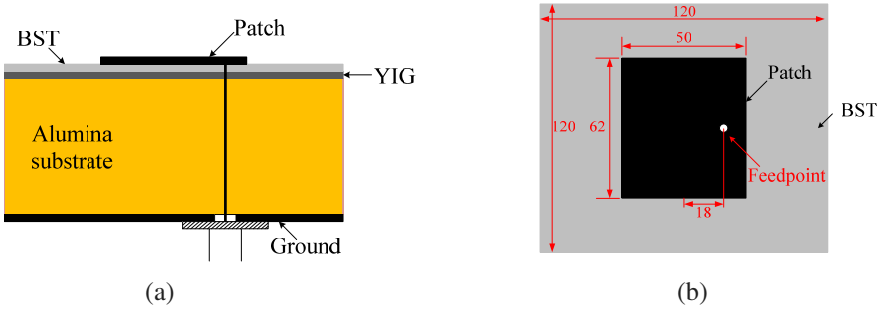

(a) (b)

Figure 3. The proposed patch antenna. (a) Side view, and (b) top view (units: mm).

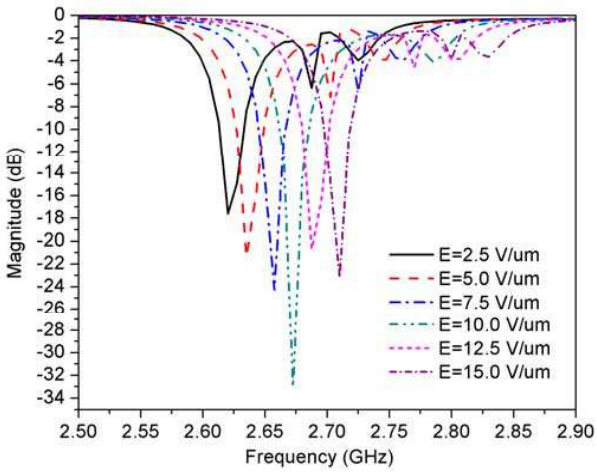

Figure 4. S_{11} of the antenna with tunable E-field across the BST layer.

reduced from 15 to 3, which makes the resonant frequency increase from 2716 MHz to 2760 MHz through the simulation. Using this method, the operating frequency tunability can be larger (the width range from 101 to 145 MHz) under the confined tunable electrical field.

4. CONCLUSION

A coaxial-fed patch antenna with electrically tunable ferrite-ferroelectric bilayer has been designed. The interactions between the electrical field applied in the BST and relative permeability of the YIG have been explored and analyzed, which enable the future work to further improve the tunability of the operating frequency range of the antenna.

ACKNOWLEDGMENT

This work was supported by the National Key Scientific Instrument and Equipment Development Projects (Grant No. 2013YQ200503).

REFERENCES

1. Mosallaei, H. and K. Sarabandi, "Design and modeling of patch antenna printed on magneto-dielectric embedded-circuit metasubstrate," *IEEE Trans. Antennas Propag.*, Vol. 55, No. 1, 45–52, Jan. 2007.
2. Ustinov, A. B., G. Srinivasan, and B. A. Kalinikos, "Ferrite-ferroelectric hybrid wave phase shifters," *Applied Physics Letters*, Vol. 90, 031913, 2007.
3. Das, J., Y. Song, N. Mo, P. Krivosik, and C. Patton, "Electric-field-tunable low loss multiferroic ferrimagnetic-ferroelectric heterostructures," *Advanced Materials*, Vol. 21, 1–5, 2009.
4. Mishra, R. K., S. S. Pattnaik, and N. Das, "Tuning of microstrip antenna on ferrite substrate," *IEEE Trans. Antennas Propag.*, Vol. 41, No. 2, 230–233, Feb. 1993.

Compact Triple-band Planar Monopole Antenna with Single Metamaterial Unit

Jian Li, **Guangjun Wen**, **Yongjun Huang**, **Kaimin Wu**, **and Weijian Chen**
Centre for RFIC and System Technology, School of Communication and Information Engineering
University of Electronic Science and Technology of China, Chengdu, China

Abstract— In this paper, we present a novel design for compact triple-band planar monopole antenna by integrating with a single metamaterial unit. The single metamaterial unit (single loop ring resonator which can exhibit three resonances) is set as part of radiation patch. The whole antenna structure including the metamaterial inspired patch and optimized ground plane contribute to an eight-like radiation pattern due to the monopole antenna configuration. Such antenna is first numerical analyzed and optimized by finite element method based simulator (Ansoft HFSS V14), and then the fabricated antenna sample are measured within a commercial near field measurement system (Satimo SG 32). Both numerical and experimental results demonstrate that the designed antenna exhibits three distinct operating frequencies and the eight-like radiation patterns at such three frequency bands are all obtained. At the same time, a compared conventional monopole antenna with the same dimensional sizes is also analyzed. Results show that the metamaterial inspired antenna has more compact size. The proposed novel antenna can be flexibly used for modern wireless communications including both stationary and portable terminal areas.

1. INTRODUCTION

In recent years, due to the breakthrough of modern wireless communications such as the wireless personal communications, near field communication, radio frequency identifications, wireless sensor networks, as well as the internet of things, the developments of compact and multi-band/multi-mode communication components have been the main barriers in such science and engineering area. In particularly, the first component used to send/receive the electromagnetic wave signals is the antenna. To achieve the miniaturization and multi-band/multi-mode requirements, comprehensive researches have focused on the multi-band antennas and/or ultra-wideband antennas. For the virous kinds of reported multi-band antennas, monopole antenna can attract most considerations in recent research progress, because of the compact sizes, flexible configurations, low fabrication costs, and well radiation characteristics. Some of the monopole antenna configurations are, for examples, circular ring patch antenna [1], I-shaped/U-shaped slot defected planar antenna [2], spirograph planar antenna [3], and spiral ring resonators inspired antenna [4]. These multi-band monopole antennas were achieved by designing virous resonator configurations to enhance operating frequencies, improve radiation pattern and at the same time reduce cross-polarization characteristics.

On the other hand, since the first realization of the so called metamaterial in 2000 [5], it has been proposed that the metamaterial can be widely used for designing novel antenna to improve most of the characteristics of conventional antennas [6]. For the monopole antenna integrated with metamaterial, some novel configurations have been reported elsewhere, e.g., the band-notched UWB planar antennas [7] with a modified complementary split-ring resonator, and the metamaterial-inspired dual-band monopole antennas [8]. Taking into deep consideration for the previously mentioned metamaterial-inspired dual-band antenna, two different resonators were integrated as the radiation part to achieve dual-band properties. In this paper, we propose two novel configurations of planar monopole antennas consisting of a single-loop resonator (SLR) as part of the radiation patch and fed with coplanar waveguide (CPW) and microstrip transmission lines, respectively. We also compare the operating frequency band and radiation characteristics with the conventional single band antennas to show the excellence of our proposed antennas. The SLR used in this paper has three distinct resonances states [9], which can be used to achieve the three operating frequency bands in the ranging of 2.4 to 6 GHz. We perform both numerical and experimental method to discuss such antennas. The proposed triple-band antennas possess compact size and exhibit very well eight-like radiation patterns and low cross-polarisations, which have potential applications for wireless communications.

2. ANTENNAS DESIGN AND FABRICATIONS

The schematic geometries of the two proposed metamaterial inspired triple-band antennas and the corresponding conventional single-band monopole antennas are shown in Fig. 1 respectively. The SLR considered as the half part of the radiation patch is placed on the upper side of the whole patch. From previous numerical analysis, there is a huge impedance mismatch between the resonator and the conventional 50-Ω feed line. Therefore, the bottom part of the patch is used to match the impedance between the SLR resonator and the feed line. The whole radiation patch is printed on a 0.8 mm-thick Rogers 4003 substrate (dielectric constant $\epsilon_r = 3.55$ and loss tangent $\tan\delta = 0.0027$) with a dimension of $D \times L = 30\,\text{mm} \times 22\,\text{mm}$. For the first antenna fed by CPW, the ground plane and SLR are printed on the same side of the substrate and the dimensional parameters are optimized as shown follows, by Ansoft HFSS software, $a = 13.1\,\text{mm}$, $b = 13.6\,\text{mm}$, $c = 6.4\,\text{mm}$, $w_1 = 1.9\,\text{mm}$, $w_2 = 0.85\,\text{mm}$, $w_3 = g_3 = g_4 = 0.4\,\text{mm}$, $h = 7.5\,\text{mm}$, $g_1 = 0.2\,\text{mm}$, and $g_2 = 0.3\,\text{mm}$. For the second antenna fed by microscript line, the ground plane is placed on the opposite side of the substrate and its dimensional parameters are the same as the first antenna, except that $w_1 = 1.8\,\text{mm}$ and $w_2 = 1.1\,\text{mm}$ for the impedance match. At the same time, the corresponding conventional signal band monopole antennas for the two kinds of fed lines are also designed with the same radiation patch size and ground plane size as shown in Figs. 1(a) and (c). Finally, through standard printed circuit board fabrication techniques, all of the four antennas are fabricated. In both simulation and measurement procedures, the 50-Ω micro-miniature coaxial connectors (operated from DC to 6 GHz) are used to simulate and test the antennas for reducing the effects of connectors on the antennas.

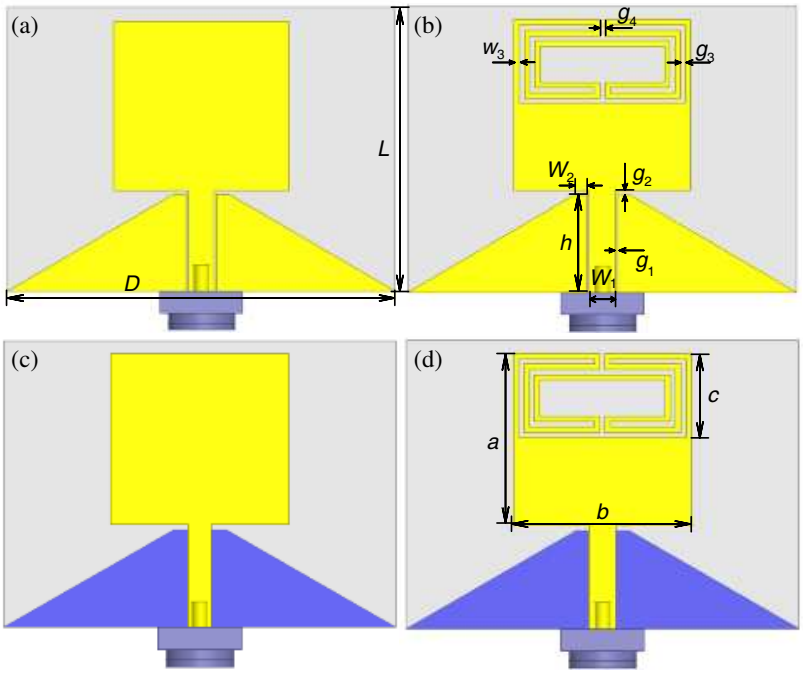

Figure 1: Schematic representations and the geometries of (a) conventional single-band monopole antenna fed by CPW, (b) metamaterial inspired triple-band antenna fed by CPW, (c) conventional single-band monopole antenna fed by microscript line, and (d) metamaterial inspired triple-band antenna fed by microscript lin.

3. SIMULATIONS AND MEASUREMENTS

Firstly, the simulated and measured reflection properties of the four proposed antennas are shown in Fig. 2. It can be known that, for the metamaterial inspired antennas, both the numerical and experimental results show three dips around 2.4, 3.85 and 4.9 GHz for the CPW fed antenna, and 2.4, 3.9 and 5.05 GHz for the microscript fed antenna. The simulated and measured results shown in Figs. 2(a), (c) and (b), (d) imply a good agreement between such two results. In the higher frequency band (4.5–6 GHz), there are slight frequency shifts for both kind of metamaterial inspired antennas. These shifts are mainly resulted from the mutual coupling introduced by connectors and soldering in the experiment at high frequencies. From the measured results, one can obtain three

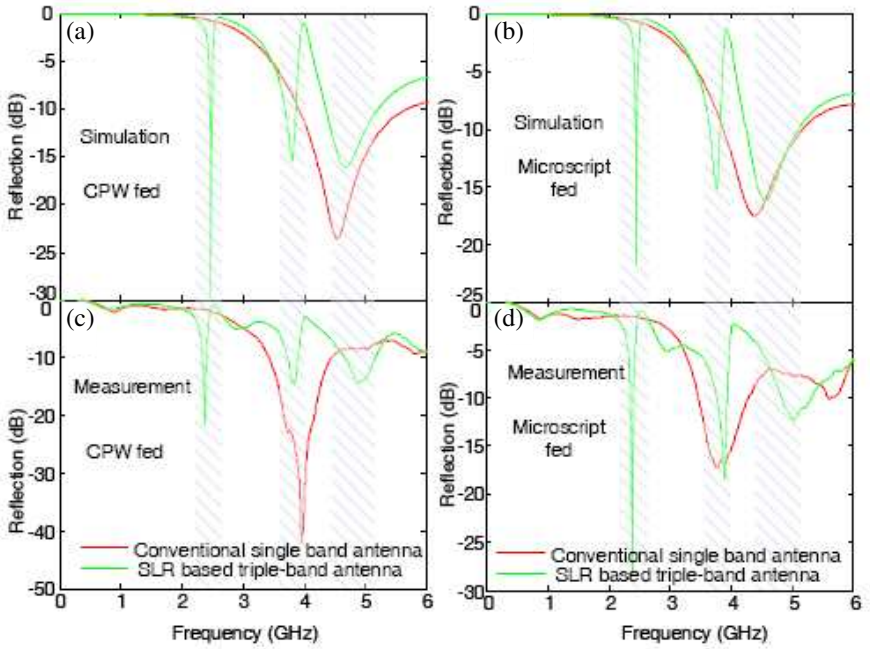

Figure 2: Simulated reflection results for the (a) CPW fed and (b) microscript fed conventional monopole antenna and metamaterial inspired triple-band antenna, and measured reflection results for the (c) CPW fed and (d) microscript fed conventional monopole antenna and metamaterial inspired triple-band antenna. The shadow areas are corresponding to the bandwidth of 10 dB reflection.

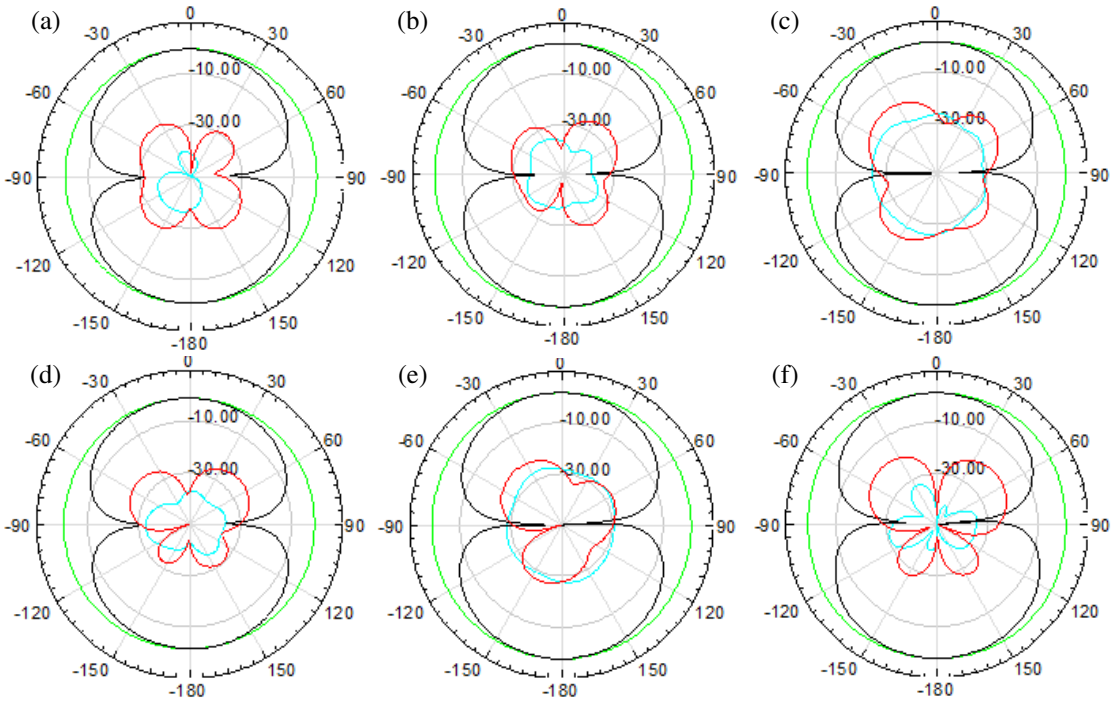

Figure 3: Simulated radiation patterns for the two metamaterial inspired triple-band antennas. (a)–(c) For the CPW fed antenna at corresponding reflection dips. (d)–(f) For the microscript fed antenna at corresponding reflection dips. Black line: co-polarisation E-plane; Blue line: cross-polarisation E-plane; Green line: co-polarisation H-plane; Red line: cross-polarisation H-plane.

distinct operating bands with 10 dB return loss: 2.33–2.42, 3.72–3.9 and 4.65–5.18 GHz for the CPW fed antenna, and 2.33–2.43, 3.75–3.95 and 4.82–5.31 GHz for the microscript fed antenna, respectively. On the other hand, the simulated and measured reflection results for the conventional

monopole antenna show only one transmission dip located in the range of 3.8–5 GHz. It means that our proposed metamaterial inspired antenna can operated a very lower frequency with the same antenna size for the conventional antenna. Therefore the proposed antenna has a compact size property.

Figure 3 shows the simulated co-polarisation and cross-polarisation radiation pattern characteristics for the two metamaterial inspired antennas at three corresponding reflection dips. It can be seen that, at the three frequencies, both the two antennas exhibit typical eight-like radiation patterns in the co-polarisation E-plane, whereas in the co-polarisation H-plane they possess nearly omnidirectional radiation patterns. Moreover, the cross-polarisation radiations of the proposed antennas are very low for all the patterns. For examples, there is a 30 dB below the co-polarisation E-plane over $\pm 45^{\circ}$ range for the first antenna and 25 dB for the second antenna. And there is a 20 dB below the co-polarisation H-plane over the omnidirection for the two antennas, at all the three frequencies. These radiation patterns indicate an excellent polarisation purity and the such patterns are kept very well when integrated with metamaterial unit in the radiation patch. Moreover, it is seen that for both the CPW and microscript fed antennas, they have similar radiation patter at all the three frequencies. Therefore such kind of antenna can be integrated flexibly in to other CPW and/or microscript integration circuits.

To further characterize the designed antennas, we measured the peak gain total and efficiency in a commercial near field measurement system (Satimo SG 32), for the four antennas as comparisons. Table 1 shows the measured Peak gain total and efficiency at the corresponding reflection dips for all the four antennas. It can be seen that all of the antennas at each frequency have the same gain level. However, at higher operating frequency, the efficiency dropped down slightly. This is because the loss at such higher frequency is larger than in the lower frequency. From the above simulated and measured results, we can conclude such metamaterial inspired antenna can be easily used to modern wireless communications.

Table 1: The measured peak gain and efficiency properties for the four antenna samples.

Antenna	CPW fed single band antenna	CPW fed triple band antenna			Microscript fed single band antenna	Microscript fed triple band antenna		
Frequency (GHz)	4.0	2.4	3.85	4.9	3.8	2.4	3.9	5.05
Peak Gain Total (dBic)	3.4	3.7	3.0	3.2	3.5	3.2	3.4	4.2
Efficiency	0.57	0.58	0.45	0.38	0.56	0.53	0.48	0.47

4. CONCLUSION

In this paper, compared with two conventional monopole antennas, two novel metamaterial inspired compact triple-band antennas consisting of a SLR as part of the radiation patch and fed with CPW and microstrip transmission lines, respectively, are discussed through numerical simulations and experimental demonstrations. The proposed two antennas exhibit comparable radiation pattern with the conventional monopole antennas, including very well eight-like radiation patterns and low cross-polarisations, and high peak gain total and efficiency. Such antennas have potential applications for modern wireless communications and can be integrated flexibly in to other CPW and/or microscript integration circuits.

ACKNOWLEDGMENT

This work was partially supported by the National Natural Science Foundation of China (Grant No. 61371047), the Research Fund for the Doctoral Program of Higher Education of China (Grant No. 20110185110014), and the Fundamental Research Funds for the Central Universities (Grant No. E022050205).

REFERENCES

1. Niroo-Jazi, M. and T. A. Denidn, "A new triple-band circular ring patch antenna with monopole-like radiation pattern using a hybrid technique," *IEEE Trans. Antennas Propag.*, Vol. 59, 3512–3517, 2011.
2. Wang, P., G. J. Wen, Y. J. Huang, and Y. H. Sun, "Compact CPW-fed planar monopole antenna with distinct triple bands for WiFi/WiMAX applications," *Electron. Lett.*, Vol. 48, 357–359, 2012.
3. Rayno, J. T. and S. K. Sharma, "Compact spirograph planar monopole antenna covering C-/X-band with invariant radiation pattern characteristics," *IEEE Trans. Antennas Propag.*, Vol. 60, 6002–6007, 2012.
4. Wan, Y. T., D. Yu, F. S. Zhang, and F. Zhang, "Miniature multi-band monopole antenna using spiral ring resonators for radiation pattern characteristics improvement," *Electron. Lett.*, Vol. 49, 382–384, 2013.
5. Smith, D. R., W. Padilla, D. C. Vier, S. C. Nemat-Nasser, and S. Schultz, "Composite medium with simultaneously negative permeability and permittivity," *Phys. Rev. Lett.*, Vol. 84, No. 18, 4184–4187, 2000.
6. Ziolkowski, R. W., P. Jin, and C.-C. Lin, "Metamaterial-inspired engineering of antennas," *Proceedings of the IEEE*, Vol. 99, No. 10, 1720–1731, 2011.
7. Jiang, D., Y. Xu, R. Xu, and W. Lin, "Compact dual-band-notched UWB planar monopole antenna with modified CSRR," *Electron. Lett.*, Vol. 48, 1250–1252, 2012.
8. Si, L. M., W. Zhu, and H. J. Sun, "A compact, planar, and CPW-fed metamaterial-inspired dual-band antenna," *IEEE Antennas Wirel. Propag. Lett.*, Vol. 12, 305–308, 2013.
9. Ekmekci, E. and G. Turhan-Sayan, "Single loop resonator: Dual-band magnetic metamaterial structure," *Electron. Lett.*, Vol. 46, 324–325, 2010.

Discovery and Theory of Small Antenna Near-field Dissipation and Frequency Conversion with Implications for Antenna Efficiency, Beverage Antenna Noise Reduction, Maxwell's Equations and the Chu Criterion

Michael J. Underhill
Underhill Research Ltd., Lingfield, UK

Abstract— The thermal efficiency measured on surface of small antenna conductors is generally found to be much larger than the radiation efficiency measured outside the near-field region. The difference can reach 10 to 20 dB or more at some frequencies. High thermal efficiency means that the surfaces of the antenna conductors do not get excessively hot even with several hundred watts input. Low radiation efficiency with high thermal efficiency means that RF has 'disappeared' in the near-field region. Measurements made so far have discovered that this missing RF in part is converted into low temperature white noise with a flat spectrum up to about twice the carrier frequency. An additional discovery is that part of the 'lost' energy can become attached to any steady modulation sidebands on the transmitted signal so that in the 'dissipative non-linear near-field region' the carrier is more attenuated than some of the sidebands. The additional sideband energy appears to come from reduction of the white noise.

The theory for this 'near-field dissipation and frequency conversion' effect was developed originally to explain measurements made on the 'Wideband Small Loop-monopole HF Transmitting Antenna' announced at PIERS 2013 in Taipei [1]. It is compatible with and based on the 'Physical Model of Electromagnetism' announced at PIERS 2011 in Morocco, [2] and extended in other subsequent papers [3–10].

The discovery of this small antenna 'non-linear' near-field effect would appear to have widespread implications, for example for antenna efficiency, Beverage antenna noise reduction, Maxwell's Equations and the Chu Small Antenna Q Criterion [12]. This effect naturally links to an Electromagnetic Theory of Everything as initiated in [2] and extended in and from [3–10].

1. INTRODUCTION

A small antenna was required to meet the need for a highly portable wideband transmitting antenna for 'anomalous' wave-tilt measurements in the HF band [13]. The novel 'Wideband Small Loop-monopole HF Transmitting Antenna' [1] was invented and crafted to fulfil this requirement. The original example of this loop-monopole concept is shown in Figure 1 and its simple 'wiring' configuration is shown in Figure 2. The original loop-monopole had two turns of coaxial cable, but an increase to three turns gave a small but useful decrease of lowest frequency of operation [1].

Figure 1: Picture of 90 cm loop-monopole with MiniVNApro (Bluetooth connected) vector network analyser at bottom.

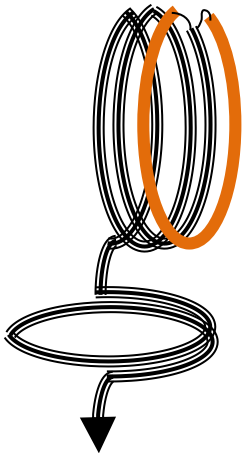

Figure 2: Schematic of loop-monopole seen in Figure 1.

The foldable square loop shown in Figure 3 has three turns of cable. The foldable 'all-coax' loop-monopole of Figure 4 therefore has a total of four turns of cable. All these loop-monopoles exhibit the unprecedented wideband matching performance (2 to 200 MHz) that is characteristic of the loop-monopole antenna.

The total length of the feeder cable was found to be the main parameter determining the lowest frequency of operation of the antenna. The SWR steps down to $\sim 10:1$ when the total coaxial cable length is a quarter wave $\lambda/4$, and steps down to $\sim 6:1$ when the cable length is $\lambda/2$ [1].

2. THE 'MISSING RF' OF AN ANTENNA FOR TRANSMISSION AND RECEPTION?

A very significant discovery for the loop-monopole small antenna at the lower frequencies of operation is the very high measured thermal efficiency $\sim 95\%$ as contrasted with the very poor radiation efficiency $< 1\%$. Thermal efficiency measurements have been with 700 watts input mainly at 3.7 MHz, using non-contact thermometers and a Protek IR thermal camera as noted in [1]. The observed temperature rise of the loop is estimated to correspond with a heat dissipation of ~ 35 watts. The radiation efficiency was estimated by practical measurements of field strength of a transmitted signal of a given power both by 'the two-identical antenna method' and the A/B.

The main question for investigation is what happens to the RF energy that leaves the antenna with 95% efficiency and fails to arrive in the far-field so that the measured radiation efficiency is less than 1%, and the small antenna gain is worse than −20 dB? Is it dissipated as heat or thermal noise energy in the near field space? At what temperature is the heat? What is the heat or thermal energy spectrum for different transmitted frequencies and with different modulation types and spectra? What are the mechanisms of energy conversion? What is the measured formula for (small) antenna efficiency in terms of size and absolute frequency or wavelength? What explanations are there for what is measured? What old or new theory is there for the explanations?

An experiment has been undertaken aimed to detect whether the lost RF energy exerts any measureable reaction force on the loop-monopole antenna structure itself. Figure 4 shows the four turn loop part of the loop-monopole suspended as a pendulum by its own feed cable, with a suspension cable length about 105 cm. The antenna is measured to be directional as a result of the combination of its electric and magnetic radiation modes. With 700 watts of power supplied giving a local magnetic field equivalent to about 4 amps in to 4 turn into a square coil of 70 cm sides, no measureable directional reaction force was detected by the pendulum even when the RF was switched on and off synchronously to excite the pendulum frequency. The limit of delectability was estimated as being < 100 dynes or < 0.1 gram. A null result.

Comparisons of relative antenna gains have also been made of received signal strengths from various distant sources for the loop-monopole compared with full wavelength horizontal loop antennas at 2 m and 15 m heights. The antenna relative gains/efficiencies found by this A/B comparison

Figure 3: 70 cm sided square copper loop foldable loop-monopole with MiniVNApro and battery operated XGA3 DDS signal generator below.

Figure 4: 70 cm square foldable 'all-coax' loop-monopole in plastic conduit, suspended to detect reaction forces. (None seen with 700 w RF input.).

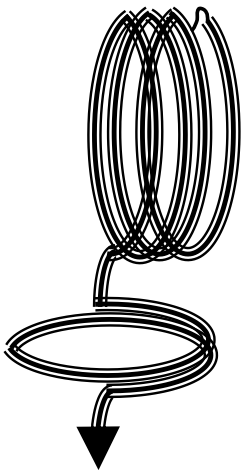

Figure 5: Electrical connection of 'all-coax' loop-monopole. Inner connects to outer of previous turn to make the loop.

reception method are essentially the same as found using the transmission methods. 'Reciprocity' is found to apply.

A further significant discovery is that the received atmospheric noise can be reduced well below thermal noise for the measured antenna impedance provided that low loss coaxial cable is used for the loop monopole construction. Where is the missing RF noise? What is the explanation and theory for this? And how can it be used? What else can it explain?

3. DISCOVERY OF TWO FREQUENCY SPECTRUM CONVERSION PROCESSES IN THE NEAR-FIELD REGION OF (SMALL) ANTENNAS

If the lost RF is not converted into a force or pressure moving the EM ether surrounding the antenna to create a detectable reaction force, then perhaps the lost RF is converted into broadband noise? This is the first assumed conversion process to be investigated. For the assumption that the broadband noise is white and extends only up to twice the carrier frequency f_c, we can calculate the resulting maximum noise level N (in 1 Hz bandwidth at a given frequency f)) relative to the remaining carrier αC) given the proportion α of the carrier power C that has been converted to white noise. This is what can be measured on a spectrum analyser or SDR receiver. Note that it is independent of the pass loss between the two antennas, one of which is the loop monopole. We then have a predicted maximum observable carrier to noise ratio (CNR) of

$$\mathrm{CNR} = N/\alpha C = \alpha/(1-\alpha)2f_c \tag{1}$$

For example at the carrier frequency of 3.5 MHz and assuming 90% of the original carrier power is converted to white noise up to $2 \times 3.5 = 7$ MHz the maximum CNR is $N/\alpha C = 0.9/0.1 \times 7 \times 10^6$ or -59 dBc/Hz. But as yet the measured noise level is usually at least 10 dB lower than this. Not all the lost power has been accounted for.

The second RF energy conversion process that has been discovered is shown in the comparison of Figure 6 with Figure 7. The triple spectrum plots are from WinRadio WR-G31DDC SDR radio receiver. Figure 6 shows the output spectrum of the Elecraft battery operated XGA3 DDS signal generator giving -4 dBm output at 3.52 MHz. The 10 Hz spur sidebands in the top right spectrum are symmetrical about the carrier starting at -63 dBc and falling slowly to about -67 dBc levels.

Figure 7 shows the spectra from the loop monopole antenna when received by a full-sized antenna at a minimum distance of about 15 m, this being the height of this antenna. The received carrier level is -57 dBm and the 10 Hz sidebands as received can be seen to be unsymmetrical and no longer approximate equal in amplitude. The largest sideband at +10 Hz is at -48 dBc. This is some 16 dB higher than its original dBc level. The question is what physical process has made this happen? The modulation level of this component has been increased? Why? It is a very significant discovery.

A clue to what is happening can be seen in the top left 17 second spectrum waterfall of Figure 7. Some of the 10 Hz spaced sidebands are fluctuating randomly with periods between 1 and 2 seconds. This means that energy is being transferred to and from each component in by low level coupling

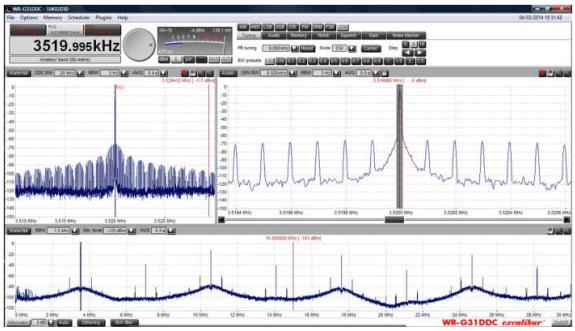

Figure 6: Three direct output spectra of battery operated XGA3 DDS signal generator at 3520 MHz. Clockwise from bottom: 0 to 30 MHz; 60 kHz span; and 120 Hz span showing equal 10 Hz spaced sidebands.

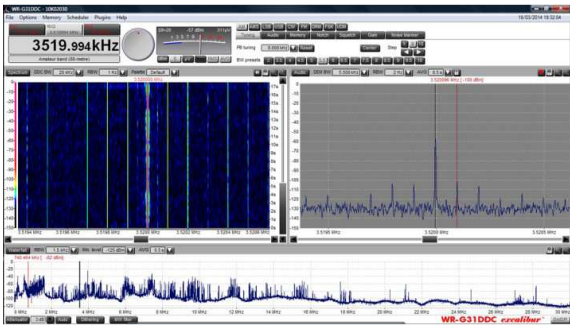

Figure 7: Three spectra of XGA3 at 3520 MHz transmitted from loop-monopole in glass conservatory to outdoor 83 m perimeter loop at 15 m. Clockwise from bottom: 0 to 30 MHz; 120 Hz span upward time 'waterfall'; and 120 Hz span showing time fluctuations of unequal 10 Hz spaced sidebands.

from adjacent noise and spur components. This effect has been found and to some extent explained in LC and crystal oscillator spectra [13, 14].

4. INITIAL THEORY OF SMALL ANTENNA DISSIPATIVE LOSS AND NEAR-FIELD ENERGY FREQUENCY CONVERSION

The near-field loss can be explained by defining radiated power flow as the product of a radially directed (generalised) 'power current density' bi-vector I and a (generalised) 'power potential' vector-scalar Φ in which the power current sits. These I and Φ symbols have previously been defined for use in the 'Generalised Poynting Vector' (GPV) in reference [1].

The power current density and the power potential are assumed to originate at the boundary of the small antenna sphere that contains the small antenna as shown in Figure 8. Local conservation and spherical symmetry requires that I has a $1/r^2$ inverse square law spreading function and Φ has a $1/r$ inverse law spreading function. The total power flux at distance r is $P = I \times \Phi$.

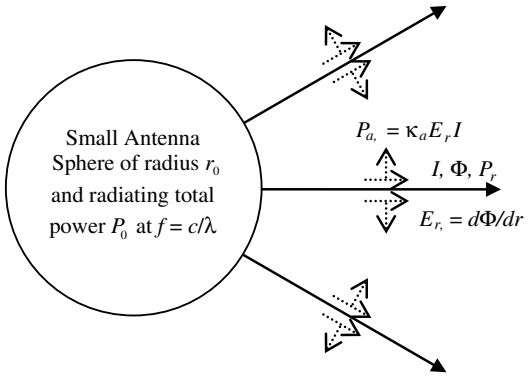

Figure 8: Conversion of lost RF energy to white noise and fluctuating sideband components. Filaments of power beyond the small antenna sphere are progressively attenuated on account of the radial field E_r. The azimuthally radiated power P_a from each radial current filament is opposed by the P_a power from adjacent current filaments. The cancellation of azimuthal power flow appears to cause the attenuation and spectrum conversion of radial power P_r.

But now there is a 'conservation' conflict to be resolved. Classical power conservation states that the total power flux (when in a lossless medium) is constant out to any radial distance. This is the basis of all propagation equations used in sonar, radio, wireless, and optical, communications, radar, and astronomical telescope systems. The classical assumption is that this (inverse square) law extends unchanged down to the sub-wavelength distances of a small antenna. Here we have found by real (not simulated) measurements that this is not so. We need to identify processes that can account for the measured losses of small antennas, and can at least be calibrated to become useful (small) antenna design tools.

Figure 8 shows a process by which the power density from a small antenna is attenuated more than the usual inverse square law spreading function. $E_{r,} = d\Phi/dr$ is the radial field being the gradient of the potential Φ. As in [1] and [2], a radial current I attempts to radiate at right angles proportional to the radial field E_r along each part of the (conical) current filament. κ_a is the coupling constant that determines the radiation proportion per unit (radial) length. The radial potential has the normal inverse distance law so that $\Phi_r = r_0\Phi_{r0}/r$ and $E_r = r_0\Phi_{r0}/r^2$. We then have a (novel) differential equation for the attenuation of the total radiated power P_r with distance, starting at P_0 at r_0, together a solution (of the type originally put forward in [2]):

$$dP_r/P_r = \kappa_a \lambda dr/r^2 \quad \text{having a solution:} \quad P_r = P_0/\{1 - \exp(\kappa_a\lambda/r)\} \tag{2}$$

With $\kappa_a = \kappa_0 = 1/2\pi$ (the limiting value of EM coupling between two parallel filaments) we find a loss $P_r/P_0 = 1 - 1/e = 0.63$ or 2 dB at the classical small antenna boundary radius of $r = \lambda/2\pi$. But small tuned antennas are found to have radiation loss decreased approximately as the square root of antenna Q. A typical small tuned loop of 1 m diameter will have a $Q \sim 250$, giving a $\sqrt{250} = 15.8$ times reduction in the small antenna radiation efficiency radius. For example a 3.75 MHz tuned loop should have a minimum diameter of 1.6 m to have 63% radiation efficiency.

5. CONCLUSIONS

Measurements confirm that the novel small high power wideband loop-monopole emphatically contradicts the Chu small antenna Q criterion as it was originally stated [11]. Measured antenna Q values are typically two to three orders of magnitude lower than those predicted by the Chu Q criterion. At low frequencies the loop-monopole has low gain but with a noise temperature well below ambient temperature.

However the *radiation* efficiencies of small antennas obtained by field strength measurements do fall with frequency at 6 dB per octave below cut-off frequencies f_e that depend on antenna physical size, type, and operating Q. This is more in agreement with the so-called Chu small antenna 'efficiency' criterion (created by Chu supporters and not by Chu himself) [11]. The efficiency criterion assumes that the lost RF energy is dissipated in any antenna conductor loss resistances. Measurements show that this is not so and that in general small antenna *thermal* efficiencies can be made high ($> 95\%$). Early evidence indicates that the cut-off frequency for *radiation* efficiency f_e is inversely proportional to the square root of frequency in agreement with what has been found in practice for the electromagnetic coupling factor [1–5, 7, 9, 10].

Practical measurements indicated that the 'lost' RF energy is frequency converted partly into low white noise at a density and temperature proportional to the transmitter power and partly attaching to and enhancing some of the longer duration modulation sidebands of the transmitter. On reception this process could account for the reported signal-to-noise ratio improvement of the Beverage antenna, in spite of its low antenna gain.

This discovered 'spectrum conversion process' can be said to be 'non-linear' electromagnetic process. It links into, and can be made an intrinsic part of, an Electromagnetic Theory of Everything as initiated in [2] and extended in [3–10].

REFERENCES

1. Underhill, M. J., "Wideband small loop-monopole HF transmitting antenna with implications for Maxwell's equations and the Chu criterion," *PIERS Proceedings*, 764–768, Mar. 25–28, Taipei, 2013.
2. Underhill, M. J., "A physical model of electro-magnetism for a theory of everything," *PIERS Online*, Vol. 7, No. 2, 196–200, 2011.
3. Underhill, M. J., "Maxwell's transfer functions," *PIERS Proceedings*, 1766–1770, Kuala Lumpur, Malaysia, Mar. 27–30, 2012.
4. Underhill, M. J., "A local ether lens path integral model of electromagnetic wave reception by wires," *PIERS Proceedings*, 1005–1008, Moscow, Russia, Aug. 19–23, 2012.
5. Underhill, M. J., "Antenna pattern formation in the near field local ether," *PIERS Proceedings*, 1009–1012, Moscow, Russia, Aug. 19–23, 2012.
6. Underhill, M. J. and M. Harper, "Small antenna input impedances that contradict the Chu-Wheeler Q criterion," *Electronics Letters*, Vol. 39, No. 11, May 23, 2003.
7. Underhill, M. J. and M. Harper, "Simple circuit model of small tuned loop antenna including observable environmental effects," *Electronics Letters*, Vol. 38, No. 18, 1006–1008, 2002.
8. Underhill, M. J. and M. J. Blewett, "Unidirectional tuned loop antennas using combined loop and dipole modes," *8th Int. Conf. on HF Radio Systems and Techniques, 2000*, No. 474, IEE Conf. Publ., 2000.
9. Underhill, M. J., "Novel analytic EM modelling of antennas and fields," *PIERS Proceedings*, 1771–1775, Kuala Lumpur, Malaysia, Mar. 27–30, 2012.
10. Underhill, M. J., "Coupled electromagnetic wave propagation in space and around surfaces and interfaces," *PIERS Proceedings*, 394–398, Stockholm, Aug. 12–15, 2013.
11. Chu, L. J., "Physical limitations of omni-directional antennas," *J. Appl. Phys.*, Vol. 19, 1163–1175, Dec. 1948.
12. Underhill, M. J., "Anomalous ground wave tilt measured over wet ground," *IET Conf. on Ionospheric Radio Systems and Techniques 2012*, Royal York Hotel, York, UK, May 15–17, 2012.
13. Underhill, M. J., "Investigations into spectrum shape fluctuations of oscillators and signal sources," *Proceedings 2013 Joint UFFC, EFTF, and PFM Symposium*, 729–732, Prague, Jul. 21–25, 2013.
14. Underhill, M. J., "Coupling theory for fluctuating spurs in oscillators," *IEEE International Frequency Control Symposium (IFCS)*, May 19–22, 2014.

Analysis of Probability Distribution of Inverse Problem of Nonlinear Model

Xiaolin Tong[1, 2, 3], **Zhenzhan Wang**[2], **and Qingxia Li**[1]

[1]Department of Electronics and Information Engineering
Huazhong University of Science and Technology, Wuhan 430074, China
[2]Key Laboratory of Microwave Remote Sensing, National Space Science Center
Center for Space Science and Applied Research, Chinese Academy of Sciences, Beijing 100190, China
[3]Department of Basic Experiment Teaching Centers, Henan University, Kaifeng 475001, China

Abstract— In the remote sensing field, the SNR is very low and the model is nonlinearity usually. Thus, it is important to analyze the impact of model nonlinearity. Probability distribution can be used to analyze the parameter distribution directly. Some issues involving priors and posteriors were proposed for models with significant nonlinearity and low signal to noise ratio (SNR). Two important issues are as follows: (1) The unimodal probability density function (PDF) of the observation quantity can give rise to a multi-modal PDF of the parameter (parameter). This property could lead to an incorrect maximum a posteriori estimate or a biased mean central estimate. It means that the biased evaluation results could be derived from statistical methods; (2) The rules for assigning non-informative priors in the measurement approach are different from the principle of maximum entropy. The authors point out the distinctions between PDF and probability distribution of non-linear models in the parameter space based on the resolution relationship between the observation space and the parameter space. For models with significant nonlinearity, if the unit grid interval of the observation space is considered regular, then the unit grid interval of the parameter space is considered irregular. The distribution obtained from regular grid is an approximation to the PDF. The probability should be calculated by integrating the PDF in the corresponding irregular grid. The difference between PDF and probability distribution gives rise to the difficulty in reverse problems. Analyzing the properties of the parameter by using the probability distribution instead of the PDF in the parameter space is necessary. The corresponding relationship between the observation and the parameter is researched based on resolution limit analysis. The non-uniform prior PDF was derived from uniform prior probability distribution in accordance with the principle of maximum entropy. Nonlinear analysis of the nature of the probability density distribution is necessary to eliminate bias caused by statistical methods.

1. INTRODUCTION

The methods for solving reverse problems is important in oceanic and atmospheric science. Many papers [1, 2] have applied the observation equation approach and the measurement equation approach to produce the PDF.

We assume that a non-informative prior is obtained, that the model η=ϕ(α, β) represents a smooth response with respect to α, and that $\phi'(\alpha, \beta)$ is continuous. Given an indication ζ, he measurement equation approach determines the PDF $p_{ME}(\alpha, \beta)$ as

$$p_{ME}(\alpha, \beta|\zeta) \propto p(\zeta|\alpha, \beta)\phi'(\alpha, \beta)p(\beta) \tag{1}$$

which involves the likelihood $p(\zeta/\alpha, \beta)$ and the particular prior

$$p(\alpha, \beta) \propto \phi'(\alpha, \beta)p(\beta). \tag{2}$$

Although these recent studies have addressed the effect of the parameter through a nonlinear model, they have not offered an explicit analysis of the relationship between model nonlinearity and the properties of PDF and probability distribution. Several issues have been raised for models with significant nonlinearity [3–6], the two important issues are: 1) The assignment of the non-informative prior (2) is different from the set of rules stated in GUMS1. 2) Explaining some properties of the posterior PDF is difficult. For instance, a unimodal PDF of the observation quantity can give rise to a multi-modal PDF of the parameter in a nonlinear monotonic model. This property could lead to the incorrect maximum a posteriori (MAP) estimate or maximum likelihood estimate in practice if the global maximum is desired.

We take the cubic model $\eta = \alpha^3$ as an example.

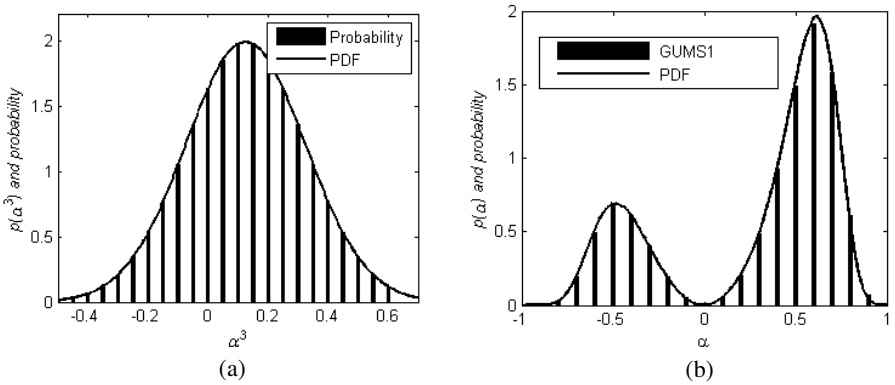

Figure 1: Comparison of PDFs and probability distributions in the observation space and in the parameter space from the model $\eta = \alpha^3$ for the case $\zeta = 0.5^3$ and $\sigma = 0.2$. The bars correspond to the probability distributions from GUMS1, the line corresponds to the result of PDF. (a) The PDF and probability distribution of the observation quantity is normal distribution. (b) The posterior PDF and probability distribution of the parameter is double-modal distribution.

Figure 1 shows the comparison results of the PDFs. The cubic function is a one-to-one correspondence function. The normal PDF of the observation quantity gives rise to a double-modal PDF of the parameter. Thus, this property could lead to an incorrect MAP estimate. A paradox is created with the requirement of parametrization invariance, which states that intrinsic properties of an object do not depend on any particular choice of parameters. In addition, it is difficult to estimate the parameter in non-linear function from the posterior PDF. These issues are fundamental in measurement uncertainty evaluation.

2. ANALYSIS OF THE PROBABILITY DISTRIBUTION

When the instrument resolution is known, defining a discrete and regular grid in the observation space as $\eta = (\eta_{\min}, \ldots, \eta_i, \ldots, \eta_{\max})$ is possible. The observation quantity resolution is denoted by Δd, given that $\Delta d = \text{const}$, so that a displayed reading η_i implies that the actual signal lies the interval $[\eta_i - (\Delta d/2), \eta_i + (\Delta d/2)]$. Within the interval, the relationship of the probability distribution and the PDF in the observation space is as follows:

$$P_{OE}(\eta_i) = \int_{\eta_i - \Delta d/2}^{\eta_i + \Delta d/2} p_{OE}(\eta_i) d\eta. \tag{3}$$

Here, $P_{OE}(\eta_i)$ denotes the probability of i-th observation quantity, and $p_{OE}(\eta_i)$ denotes the PDF in the i-th interval in the observation space.

The parameter is determined by measurement equation $\alpha = \psi(\eta, \beta)$. By this transformation the nonlinear functional dependence of the observation quantities on parameters is mapped. This is equivalent to producing a graph of a function on a coordinate grid. The grid in the measurement space $\alpha = (\alpha_{\min}, \ldots, \alpha_i \ldots, \alpha_{\max})$ is defined as $\Delta\alpha_i$. A indication α_i implies that the actual signal lies the interval $[\psi(\eta_i - \Delta d/2), \psi(\eta_i + \Delta d/2)]$. Owing to the $\Delta d = \text{const}$ and nonlinearity, the unit grid is irregular. The relationship of the probability distribution and the PDF in the parameter space is as follows:

$$P_{ME}(\alpha_i) = \int_{\psi(\eta_i - \Delta d/2)}^{\psi(\eta_i + \Delta d/2)} p_{ME}(\alpha_i) d\alpha \tag{4}$$

where $P_{ME}(\alpha_i)$ denotes the probability of the i-th parameter, and $p_{ME}(\alpha_i)$ denotes the PDF in the ith interval in the parameter space. From (4), we can observe that the distinction appears between the PDF and the probability distribution in the irregular grid parameter space. The properties of the parameter should be analyzed by using the probability distribution instead of the PDF in the parameter space. For a one-to-one function, the mapping relationship of the probability distribution between the two spaces is obtained by combining (3) and (4).

$$P_{ME}(\eta_i) = P_{OE}(\alpha_i) \tag{5}$$

Relationship (5) states that the probability of the observation quantity is equal to the probability of the parameter.

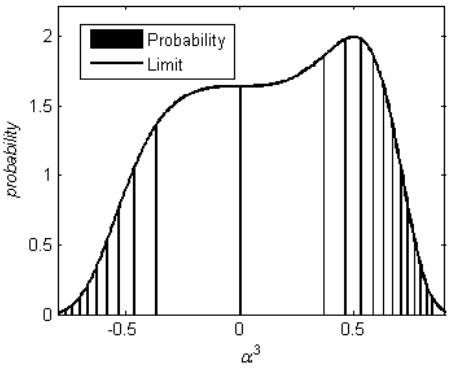

Figure 2: Posterior probability distribution of the parameter obtained by the modified Monte Carlo method for the model $\eta = \alpha^3$ with $\Delta d = 0.05$, $\zeta = 0.5^3$ and $\sigma = 0.2$ corresponding the observation quantity has normal distribution.

Figure 2 shows the probability distribution result of the parameters for the cubic function model. Corresponding to the unimodal probability distribution of the observation quantity, the probability distribution of the parameter is also unimodal. From the Figure 1(a) and Figure 2, we can conclude that the mapping relationship of the probability distribution is invariant between the two spaces. The MAP probability distribution estimate is invariant in both the observation space and in the parameter space.

3. CONCLUSIONS

We pointed out the difference between PDF and probability distribution in the parameter space based on the resolution relationship between the observation space and the parameter space.

Analyzing the properties of the parameter by using the probability distribution instead of the PDF in the parameter space is necessary. The corresponding relationship between the observation and the parameter was obtained based on resolution limit analysis. The non-uniform prior PDF was derived from uniform prior probability distribution in accordance with the rules stated in GUMS1.

Probability distribution can be used to analyze the parameter distribution directly. The method of the MAP probability distribution is useful one to reverse parameter in Inverse Problem.

REFERENCES

1. Weise, K. and W. Woger, "A Bayesian theory of measurement uncertainty," *Measurement Science and Technology*, Vol. 4, 1, 1993.
2. Possolo, A. and B. Toman, "Assessment of measurement uncertainty via observation equations," *Metrologia*, Vol. 44, 464, 2007.
3. Bodnar, O., G. Wübbeler, and C. Elster, "On the application of Supplement 1 to the GUM to non-linear problems," *Metrologia*, Vol. 48, 333, 2011.
4. Forbes, A., "An MCMC algorithm based on GUM Supplement 1 for uncertainty evaluation," *Measurement*, Vol. 45, 1188–1199, 2012.
5. Vukicevic, T. and D. Posselt, "Analysis of the impact of model nonlinearities in inverse problem solving," *Journal of the Atmospheric Sciences*, Vol. 65, 2803–2823, 2008.
6. Attivissimo, F., N. Giaquinto, and M. Savino, "A Bayesian paradox and its impact on the GUM approach to uncertainty," *Measurement*, Vol. 45, 2194–2202, 2012.

Calculation of RFID Antenna Characteristic Parameters under the Condition of Near-field Coupling

Guochun Wan, Dongjie Lu, Jie Zhang, and Meisong Tong
Department of Electronic Science and Technology, Tongji University
4800 Cao'an Road, Shanghai 201804, China

Abstract— Passive near-field coupling antenna is widely used in RFID system. Antenna design is the key part of RFID system. In this paper, we present a fundamental method to design the RFID antenna, in which we mainly focus on some important physical parameters, such as magnetic field intensity, optimal radius of the antenna, turning and estimating inductance of the conductor loop.

1. INTRODUCTION

RFID technology and its three major components have experienced huge progress in these years [1]. This technology has proliferated in almost all sectors of modern society. Healthcare, public transportation, social security is only a small number of the application fields.

Antenna characterization parameters such as gain, radiation pattern, radiation power efficiency and beam width, are normally used in antenna design. So it is important to reinforce those parameters in the mathematical way.

2. MAIN PHYSICAL PARAMETERS UNDER THE CONDITION OF NEAR-FIELD COUPLING

2.1. Calculation of the Magnetic Field Intensity

The distance that a RFID antenna can work effectively is closely related to the magnetic field intensity which is generated by the coil current [2].

The magnetic field intensity of a circular coil can be calculated by

$$H = \frac{I \cdot N \cdot R^2}{2\left(R^2 + x^2\right)^3} \tag{1}$$

in which H is the intensity of magnetic field, I is the intensity of electric current, N is turns of the coil, R is radius of the antenna, x is the distance away from the circular coil.

The magnetic field intensity of a rectangular conductor loop whose side length is ab can be calculated by

$$H = \frac{I \cdot N \cdot ab}{4\pi\sqrt{\left(\frac{a}{2}\right)^2 + \left(\frac{b}{2}\right)^2 + x^2}} \cdot \left[\frac{1}{\left(\frac{a}{2}\right)^2 + x^2} + \frac{1}{\left(\frac{b}{2}\right)^2 + x^2}\right] \tag{2}$$

Conclusions can be made from these two equations, when x is small ($x < R$), H is steady and at a high level, a bigger antenna can still get a high H even x is large in the number ($x > R$) while a smaller one can't.

2.2. The Optimal Radius of the Antenna

Assuming x is a constant and I is unchanged in the coil of antenna, if we change the radius of the antenna, then we can get the maximum H according to the relationship between x and R. As we all know, different x has its own optimal radius of the antenna, to get this R, we can use maximum H to be the solution.

First, derivation for R

$$\frac{d}{dR}H\left(R\right) = \frac{2NR^2}{\sqrt{\left(R^2 + x^2\right)^3}} - \frac{3INR^3}{\left(R^2 + x^2\right) \cdot \sqrt{\left(R^2 + x^2\right)^3}} \tag{3}$$

Then let the equation be 0, we can get

$$R = \pm\sqrt{2}x \tag{4}$$

Discard the negative one, finally we got the optimal radius of the transmitting antenna according to the distance between Reader and Tag.

2.3. Turning

RFID system can be considered as a R-L-R series circuit, in which R is the resistance of coils and L is the inductance of the antenna. In the process of turning, the capacitance of coils can be discarded because of little impact on this process, so another capacitance should be added in order to obtain the maximum electric current for the antenna [3]. The extra capacitance can be determined by

$$f = \frac{1}{2\pi\sqrt{LC}} \tag{5}$$

in which f is the operating frequency.

2.4. Estimating Inductance

If without impedance analyzer, we can use an estimating equation to get the value of L. Assuming the ratio of the diameter d of the conductor to the diameter D of the conductor loop is very small ($d/D < 0.001$), then the inductance of the loop can be determined by [4].

$$L = N^2\mu_0 R \cdot \ln(2R/d) \tag{6}$$

in which N is turns of the coil, R is radius of the antenna, μ_0 is the magnetic permeability of free space.

N can also be estimated by (7), and in practical application, these two equations can be used as a complementary to solve more problems.

$$N = (\text{approx})^{1.9}\sqrt{\frac{L}{2A\ln(A/D)}} \tag{7}$$

in which A is area surrounded by the antenna coil.

The results from these two equations are not extremely accurate, but still can be trustful.

2.5. Quality Factor of the Antenna

As we all know, quality factor Q has an impact on energy transfer efficiency and frequency selection. Although a higher Q can enlarge the transmitting energy from the antenna, the bandpass characteristic of the Reader will be affected. So when adjusting Q, we should consider a compromise. Conventionally, we put a resistance in a R-L-C equivalent circuit to adjust Q, like (8)

$$Q = \omega L/(R + R_1) \tag{8}$$

So if we want to achieve the optimal result, the number of R_1 should be carefully chosen based on the actual demand.

2.6. Near-field Coupling

All the equations mentioned above should be used under the condition of

$$d \ll R \quad \text{and} \quad x < \lambda/2\pi.$$

When not meeting these two conditions, near-field coupling loses its effect and goes to the long-range electromagnetic field. As we all know, the initial magnetic field in a conductor loop begins from the antenna, during the transmission of the electromagnetic field, if x is bigger than $\lambda/2\pi$, then the electromagnetic field will be transmitted like without the antenna, similar to the process of electromagnetic waves going into free space.

3. SIMULATION

It is important to run a simulation of Equation (1) to clearly see the interconnection between distance x and the intensity of magnetic field H.

In order to see the result clearly, we assume I and N are constant numbers.

In Fig. 1, the downward trend is inversely proportional to the size of R.

It is also important to run the simulation of Equations (3) and (4) to see the interconnection between optimal radius of R and distance x like Fig. 2, and we assume I and N are constants.

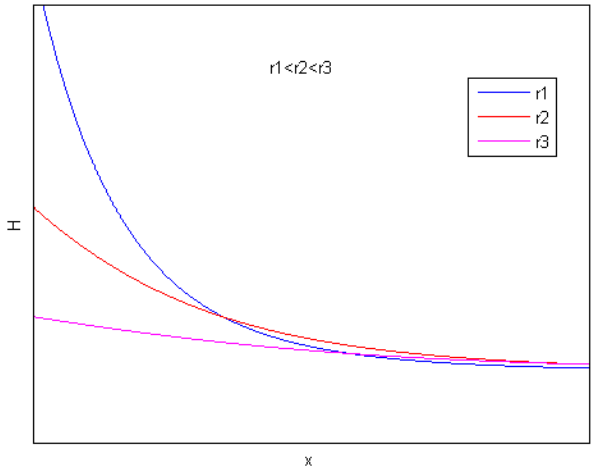

Figure 1: Interconnection between x and H.

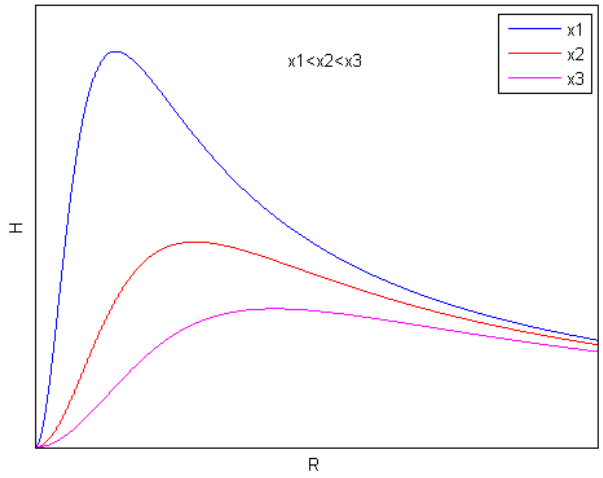

Figure 2: Interconnection between R and H.

4. CONCLUSION

This paper gives a fundamental method to design a RFID antenna which mostly concerns about important physical parameters like magnetic field intensity, optimal radius of the antenna, turning and estimating inductance of the conductor loop in mathematical way.

In the practical designing, more things should be considered based on the materials you have. But the essential still remains the same in this paper.

REFERENCES

1. Maloratsky, L. G., *Passive RF & Microwave Integrated Circuits*, Newnes, 2003.
2. Rao, K. V. S., P. V. Nikitin, and S. F. Lam, "Antenna design for UHF RFID tags: A review and a practical application," *IEEE Transactions on Antennas and Propagation*, Vol. 53. No. 12, 3870–3876, December 2005.
3. Chapman, T. A., R. E. Schumaker, and A. W. Edwards, "RFID tag and printer system," U.S. Patent 7,066,667 B2, June 22, 2006.
4. Dobkin, D. M. and S. M. Weigand, "UHF RFID and tag antenna scattering," *Microwave Journal*, Vol. 49, No. 6, 86–96, June 2006.

A More Practical Patch Used in Microstrip Antenna at Ku-band

Chuanqi Wei, Dawei Liu, Chen Zhu, Jindong Yu, and Jungang Miao
Electromagnetics Laboratory, Beihang University, Beijing 100191, China

Abstract— In this paper, a Ku-band microstrip antenna is analyzed and will be designed. The characteristics of the patch are analyzed and optimized with Ansoft HFSS. A different patch is evolution of the classic rectangular patch. It has a square loop outside the rectangular patch. We can call it window-patch. The construction of the antenna is resulted from considering efficiency of the spillover efficiency (η_s) and the illumination efficiency (η_i).

Once the unit element has been fully characterized and a reflectarray designed, an important aspect in the reflectarray analysis is the computation of the radiation patterns. In this literature, a method of Array Element Factor is used to calculate it. For the reflectarray antenna, the ideal range of phase shift should realize $0 \sim 360°$, but sometimes things go contrary. It would be discussed the effects brought by the lack of the phase shift and electromagnetic wave incident angle.

1. INTRODUCTION

In the last decade, there is an increasing interest in reflectarray antennas for the following advantage: high gain, light weight, low cost, low profile, flexibility, ease of installation and so on.

Due to reflectarray antennas have quasi-periodic structure, infinite periodic unit model is the mainstream approach to analysis the phase shift of patch. In this study, the characteristics of the patch are analyzed and optimized with Ansoft HFSS. It adopts Floquet port and Master-Slave boundary approach. The aperture efficiency (η) is used to design the construction of the reflectarray, which contains the spillover efficiency (η_s) and the illumination efficiency (η_i).

Radiation pattern and Gain is the most important parts of antennas. Array Element Factor is used to calculate the radiation pattern and it would use commercial software FEKO for the analysis of reflectarrays.

2. ELEMENT EFFECTS

The element characterization is the most important part and critical step of the reflectarray design. If the element design is not optimized, the reflectarray will not scatter the signal from the feed effectively to form an efficient far-field beam. Different from conventional waveguide simulation, in order to account for the coupling effect among the elements, infinite periodic unit model is used to mimic an infinite array environment. In this article, the master-slaver conditions and floquet port in HFSS are used to perform the simulation for a single unit as show in Fig. 1.

In this article the antenna works at 12.5 GHz and the side length of the square arrangement lattice is 12 mm. The phase shift is achieved by changing one or more of the geometrical parameter of the patch. Five cases are going to compared, where the substrates of square patch with 0.5 mm, 1 mm, 1.5 mm, 2 mm thickness, the window patch with 3 mm thickness and 2.2 relative permittivity. The results of simulation show in Fig. 2.

As illustrated in Fig. 2(a), the thickness of the substrate has a big impact on the achievable phase range. Generally, the thicker the substrate, the smaller phase range for square patch. The window patch has a larger phase range than the square patch when the substrate thickness is

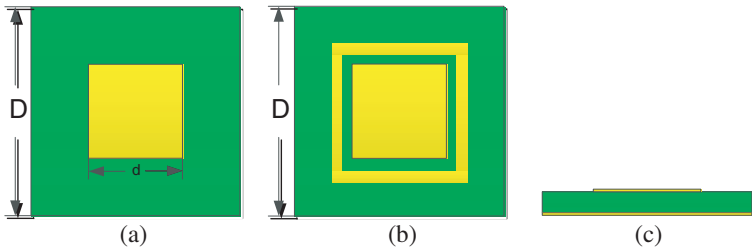

Figure 1: (a) Top view of the square patch. (b) Top view of the window patch. (c) Side view of the patch. The yellow color represents metal patch and the green color for substrate.

greater than 0.5 mm. Fig. 2(b) shows the slope of phase curve, it conclude that the window patch has a smaller slope than the square patch with the substrate thickness smaller than 2 mm except point 3.1 mm. In spite of point 3.1 mm of a larger slope, that is the very thing wants. For the antenna unit periodic changes from the center to the edge, when it reaches $-\pi$, next one is $+\pi$. So the element is not much difference from the former one. The return loss of the window patch has two peaks, the square patch has one peak. An ideal broadband reflectarray element should provide phase curves at different frequencies parallel to each other [1]. From the Fig. 2(d), it knows the reflectarray antenna would have a broadband.

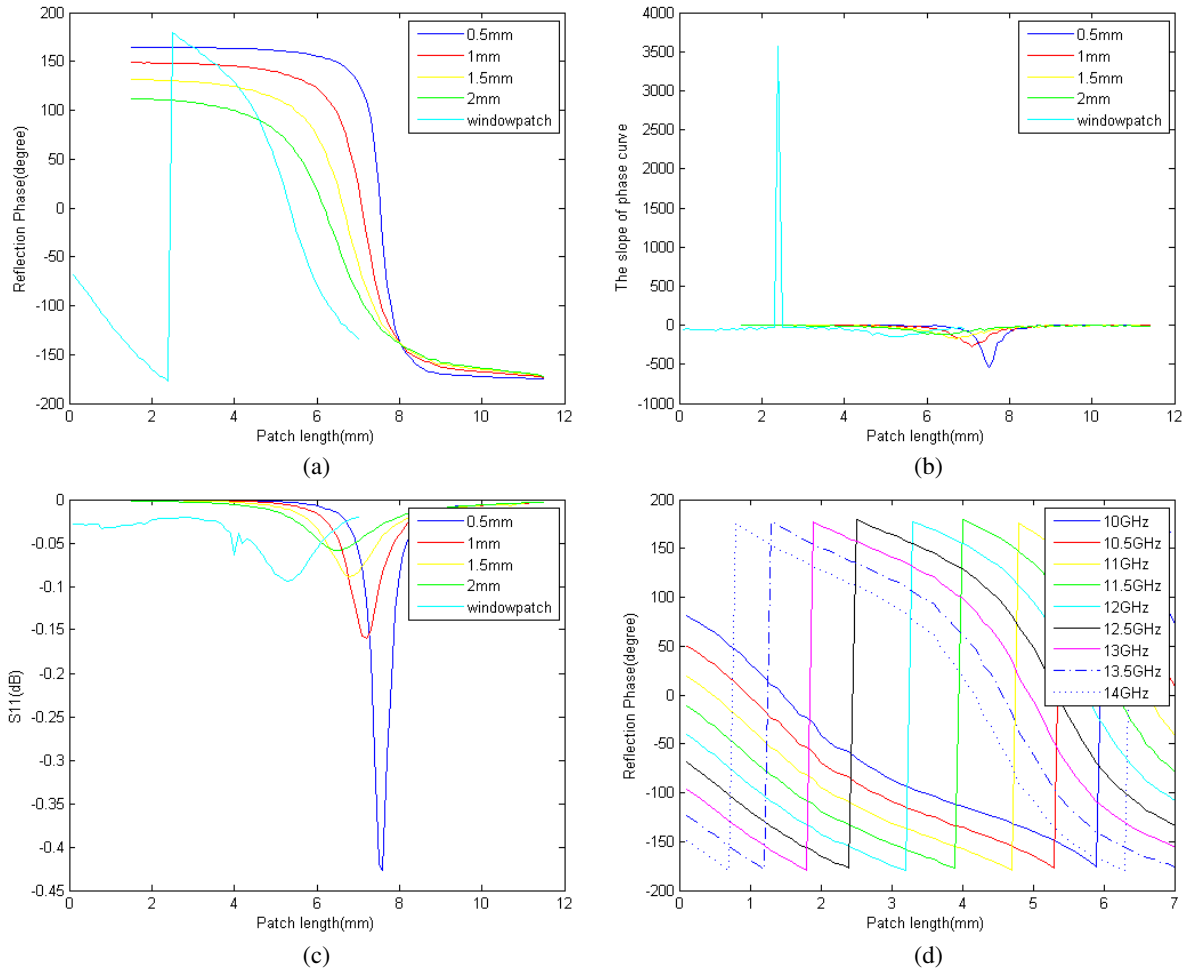

Figure 2: (a) Phase curves obtained with different substrate thickness. (b) The slope of the phase curves. (c) Return loss with different substrate thickness. (d) Phase curves with different frequency.

Table 1: Square patch vs. window patch.

Type of patch	Phase (min)	Phase (max)	slope	S_{11} (dB)
Square patch (0.5 mm)	$-175.3°$	$164.6°$	$-535.3°$/mm	-0.4265
Square patch (1 mm)	$-173.4°$	$148.7°$	$-271.4°$/mm	-0.1604
Square patch (1.5 mm)	$-172.5°$	$131.4°$	$-169.8°$/mm	-0.08926
Square patch (2 mm)	$-172.5°$	$112.1°$	$-119.7°$/mm	-0.05888
Window patch	$-177.5°$	$179.5°$	$-156.6°$/mm (3571)	-0.09358

3. EFFICIENCY AND CONSTRUCTION

The antenna gain is determined by the aperture directivity and the aperture efficiency. In this paper, two major efficiency of the spillover efficiency (η_s) and the illumination efficiency (η_i) are considered, which defined as [2]:

$$\eta_s = \frac{2q+1}{2\pi}\int_0^{2\pi}\int_0^{D/2}\frac{H}{r^3}\left(\frac{r_0^2+r^2-s^2}{2r_0r}\right)^{2q}\rho d\rho d\varphi \tag{1}$$

$$\eta_i = \frac{1}{A_a}\frac{\left|\iint_A I(x,y)dA\right|^2}{\iint_A |I(x,y)|^2 dA} \tag{2}$$

where q is the value of the feed horn, D is the diameter of reflectarray aperture, r_0 is the distance from the feed horn to the center of aperture, r is the distance from the feed horn to the element, s is the distance from the center of aperture to the element. The feed source is located at yoz plane. The efficiency of the reflectarray is shown in Fig. 3.

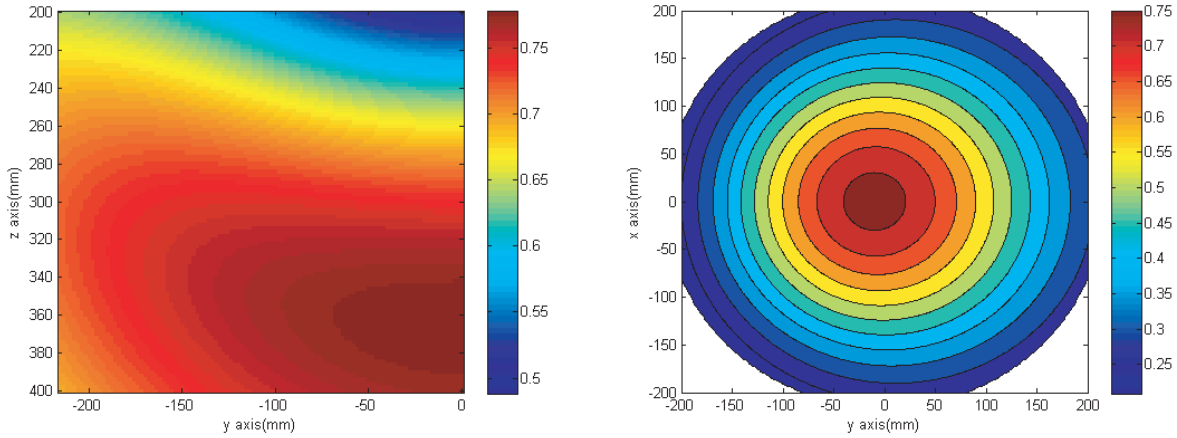

(a) (b)

Figure 3: (a) Efficiency vs. the feed location. (b) Efficiency vs. feed orientation with $q = 7$ and $D = 432$ mm.

4. RADIATION PATTERN AND GAIN

Array Element Factor (AEF) is used to calculate the radiation pattern. Both the feed horn and element pattern are approximated by a cosine q model. The calculation of radiation pattern for each observation point could be simplified as:

$$E(\theta,\varphi) = \cos^{qe}\theta\sum_{n=1}^{N}\sum_{m=1}^{M}\frac{cos^{q_f}\theta_{fmn}(m,n)\cdot\cos^{q_e}\theta_{emn}(m,n)\cdot|\Gamma_{mn}|}{r_{fmn}}\cdot e^{j\Phi_{mn}}\cdot e^{j\beta(\hat{r}\cdot\vec{r}_{mn})} \tag{3}$$

where q_f is the q factor of the feed pattern, q_e is the q factor of the element pattern which is 1 unless otherwise specified, and $|\Gamma_{mn}|$ is the magnitude of reflection coefficient for each element. The antenna directivity is defined though the well-known equation:

$$D_0 = \frac{4\pi|E(\theta_m,\varphi_m)|^2}{\int_0^{2\pi}\int_0^{\pi/2}|E(\theta,\varphi)|^2\sin\theta d\theta d\varphi} \tag{4}$$

When the directivity and efficiency are ensured, the gain is calculated as:

$$G_0 = D_0\times\eta \tag{5}$$

Reflectarray with different thickness of substrate has different phase range as the second part shows. In the Fig. 4, it illuminates four curves of the antenna gain at 0.5 mm, 1 mm, 1.5 mm, 2 mm thickness of the substrate with $D = 432$ mm.

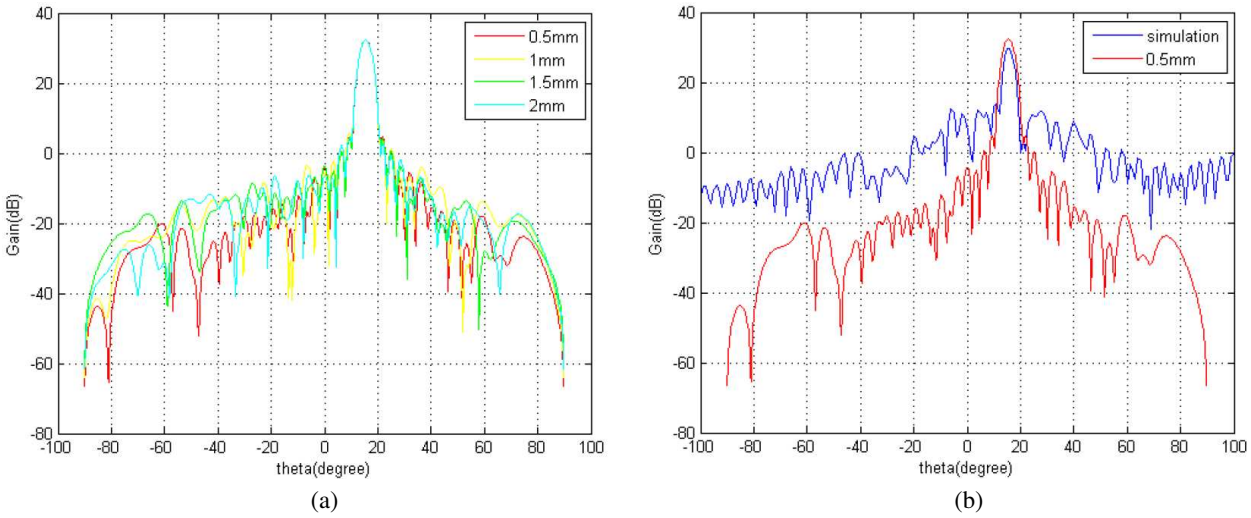

Figure 4: (a) Gain vs. different thickness. (b) Simulation vs. calculate at 0.5 mm thickness.

As shown in Fig. 4(a) the gain values have little change for different thickness. Array Element Factor (AEF) is a good method to calculate the gain as depicted in Fig. 4(b). The red curve is the result of calculating by AEF. The blue one works out by FEKO. They have the same beam direction.

5. CONCLUSION

In this paper, a more practical patch is introduced in detail and the efficiency, the gain of reflectarray is calculated. In the Fig. 4(b) the gain and beam direction of simulation result is very good agreement with the calculation result. The window patch has more advantages against with the square patch: (a) A greater range of phase shift (b) the smaller the slope of phase shift curve (c) the smaller range of the patch change (d) a larger bandwidth as shown in Fig. 2.

REFERENCES

1. Huang, J. and J. A. Encinar, *Reflectarray Antennas*, John Wiley Sons Inc., 2008.
2. Yu, A., F. Yang, A. Z. Elsherbeni, J. Huang, and Y. Rahmat-Samii, "Aperture efficiency analysis of reflectarray antennas," *Microwave and Optical Technology Letters*, Vol. 52, No. 2, February 2010.
3. Pozar, D. M., "Analysis and design of a microstrip reflectarray using patches of variable size," *Antennas and Propagation Society International Symposium*, Vol. 3, AP-S. Digest, 1994.

High-Q Weakly Modulated Nanobeam Cavity Based on a Suspended Silicon Dioxide Waveguide

Senlin Zhang and Sailing He
Centre for Optical and Electromagnetic Research
JORCEP [Sino-Sweden Joint Research Center of Photonics]
State Key Laboratory for Modern Optical Instrumentation, East Building No. 5
Zijingang Campus, Zhejiang University, Hangzhou 310058, China

Abstract— Photonic crystal (PhC) cavities have drawn plenty of attentions during the past several decades for the advantages of ultra-high Q factor and small mode volume. PhC cavities have various applications such as quantum information processing, low threshold lasers, optomechanics, and nonlinear optics. PhC cavities based on silicon material have been heavily investigated due to their compatibility with complementary metal-oxide-semiconductor (CMOS) technology, small feature size and low cost. However, apart from the advantage of high Q factor, silicon based PhC cavities suffer from the drawbacks of high insertion loss because of the mode mismatch with fiber and relatively low sensitivity especially for the sensing application. On the other hand, silicon dioxide (silica) waveguide experience relatively smaller loss and owns a similar refractive index to numerous liquid materials to be detected, which will leads to high sensitivity for a silica based PhC cavity sensor. In this paper, we propose a high Q factor ($Q = 15500$) silica based PhC nanobeam cavity with high sensitivity (the wavelength shift per refractive index unit (RIU) is $S = 338\,\mathrm{nm/RIU}$) at the telecommunication wavelength (1550 nm). Since the refractive index contrast for silica waveguide is low for the realization of the photonic bandgaps, it is essential to utilize a silica waveguide suspended in free space. The PhC nanobeam cavity is then formed by etching a series of elliptical holes, whose dimensions linearly decrease from the center to both ends, directly into the silica waveguide. For the sake of high transmission on-resonance wavelength while maintaining high Q factor, it's important to etch partly into the waveguide, which results in a low-refractive-index perturbation structure. The calculated on-resonance transmission is about 0.26. The novel proposed PhC nanobeam cavity shows a sensitivity 3 times larger than the one based on silicon counterparts and outperforms other low-index-contrast PhC cavities by a higher on-resonance transmission. Such a structure can also be used in spectrally filtering system and nonlinear optics.

1. INTRODUCTION

Silicon photonics have attracted extensive research interests due to the features of low fabrication cost, tiny footprint, low power consumption and the ability to be integrated with various materials. PhC cavities play an important role in the silicon photonics field because they allow for both ultra-high Q factor and small mode volume. Massive applications can be found in optical communications [1], chemical sensing [2], ultrasmall lasers [3], nonlinear optics [4] so on and so forth. Among these examples, silicon material is dominant on account of the relatively large refractive index contrast, which leads to a small feature size. However, drawbacks such as high coupling loss with fiber and low sensitivity for the sensing application also arise from this character.

Materials with lower refractive index such as polymers and silica are able to overcome the high coupling loss problem and realize high sensitive sensors. The main obstacle in implementing PhC cavities with these materials is the low Q factor resulting from the low refractive index contrast. Qimin Quan et al. [5] proposed and demonstrated a polymeric PhC nanobeam cavity with high Q factor ($Q = 36,000$) and sensitivity ($S = 386\,\mathrm{nm/RIU}$). The situation becomes a little different when it comes to the silica material because the refractive index contrast further decreases compared to the polymer used in Ref. [5].

In this paper, we propose a novel PhC nanobeam cavity operating at the telecommunication band (1550 nm). The features of high Q factor ($Q = 15500$) and transmission ($T = 0.26$) enable the structure to be applied in spectrally filtering systems and nonlinear optics. Besides, when used in the sensing realm, the PhC nanobeam cavity shows a high sensitivity ($S = 338\,\mathrm{nm/RIU}$) as a result of the large extension of cavity mode into the background material.

2. DEVICE STRUCTURE

The geometry and mode distribution of the PhC nanobeam cavity are depicted in Figure 1. Figures 1(a) and (b) illustrate the top view and cross section of the schematic structure respectively

and Figure 1(c) shows the mode distribution of the nanobeam cavity. The PhC nanobeam cavity consists of a channel waveguide suspended in the air. There are 100 elliptical holes in total being etched into the waveguide on both sides. The first 50 holes are ellipsis with dimensions linearly decrease from the center to the ends, followed by 50 elliptical holes maintaining the same geometry as the smallest one of the first 50 holes. The detailed parameters of the elliptical holes are designed based on the method proposed by Qimin Quan et al. [6]. The size of the ellipsis is varied from 1186 nm × 172 nm (the major axes multiplied by the minor axes) to 698 nm × 101 nm. In order to obtain a high transmission for the PhC nanobeam cavity, the etching depth is smaller than the height of the waveguide as shown in Figure 1(b).

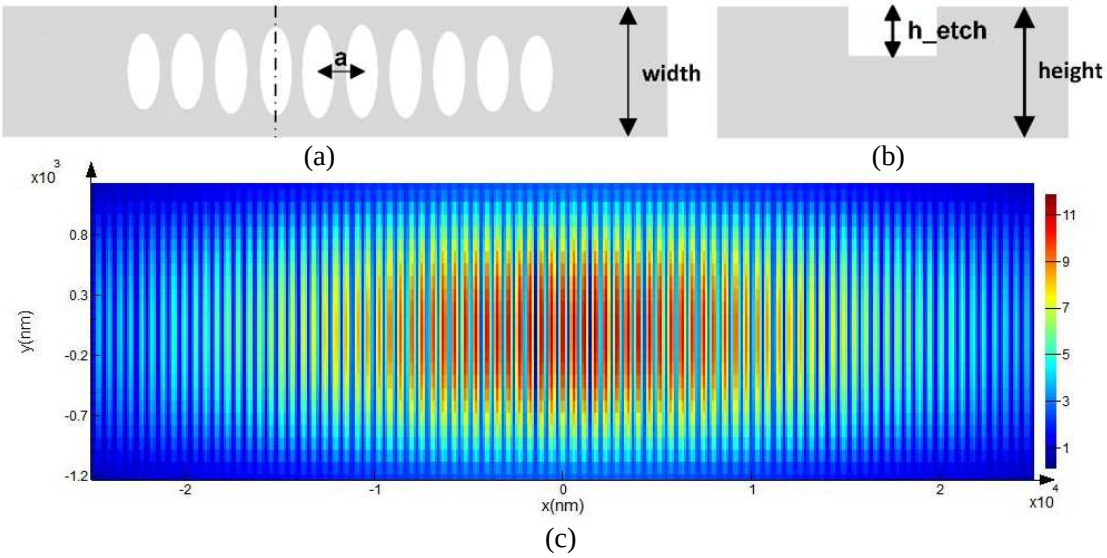

Figure 1: The geometry of the PhC nanobeam cavity and the mode distribution: (a) top view of the structure; (b) cross section of the structure; (c) the cavity mode distribution in the top view.

3. CHARACTERIZATION

The width and height of the waveguide have much impact on the performance of the PhC nanobeam cavity. As indicated in Figure 2, both the width and height of the waveguide have an optimal value in view of a highest Q factor. The phenomenon can be understood intuitively as follows. Larger width of the waveguide leads to a better restriction of the optical field in the channel waveguide and thus reducing the in-plane radiation loss. However, larger beam width will allow for higher order modes, which will results in a decrease in the Q factor. The mechanism of the influence of the height of the waveguide on the Q factor is the same to the above explanation. It is necessary to mention that the relations in Figure 2 are obtained by varying the width and height of the waveguide of a PhC nanobeam cavity consists of 40 full-etching ellipsis in total for convenience. For PhC nanobeam cavity with more elliptical gratings, the relations between Q factor and width or height of the waveguide stay the same.

Another parameter of the waveguide that has crucial impact on the performance of the PhC nanobeam cavity is the etching depth. Larger etching depth leads to higher Q factor and will result in lower transmission in the meanwhile. Thus, we chose to etch the waveguide partly in order to obtain a relatively high Q factor while keeping the transmission high. The eventual parameters of the PhC nanobeam cavity are as follows. The width and height of the waveguide are 2.5 microns and 1.3 microns, respectively. The etching depth is 500 nanometers. To operate at the telecommunication wavelength, the lattice constant is chosen to be 570 nm.

The transmission spectrum and the enlargement of the on-resonance peak of the PhC nanobeam cavity is depicted in Figures 3(a) and (b), respectively. The on-resonance wavelength is 1556 nm and the Q factor can be derived as:

$$Q = \frac{\lambda_{res}}{\Delta\lambda} = \frac{1556\,\text{nm}}{0.1\,\text{nm}} = 15560, \tag{1}$$

where λ_{res} represents the resonant wavelength and $\Delta\lambda$, the Full Width at Half Maximum (FWHM)

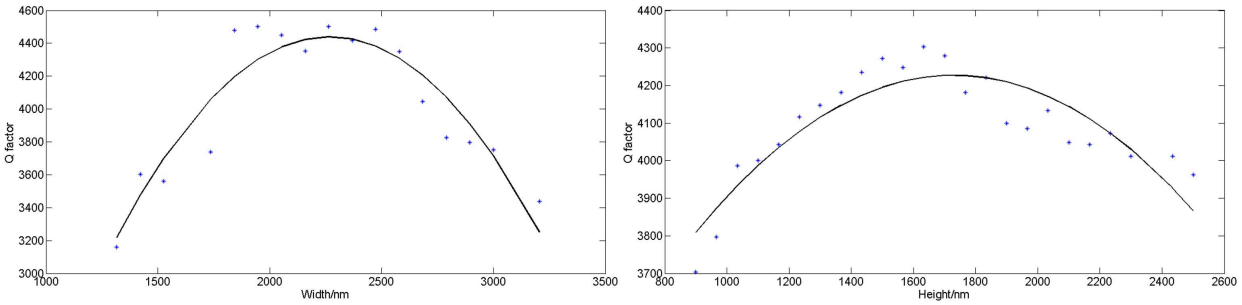

(a) (b)

Figure 2: The impact of (a) the width and (b) height on the Q factor of the PhC nanobeam cavity. The points are simulations results and the solid lines represent the quadratic polynomial fit curve. The calculation accuracy should account for the fluctuations of the Q factor.

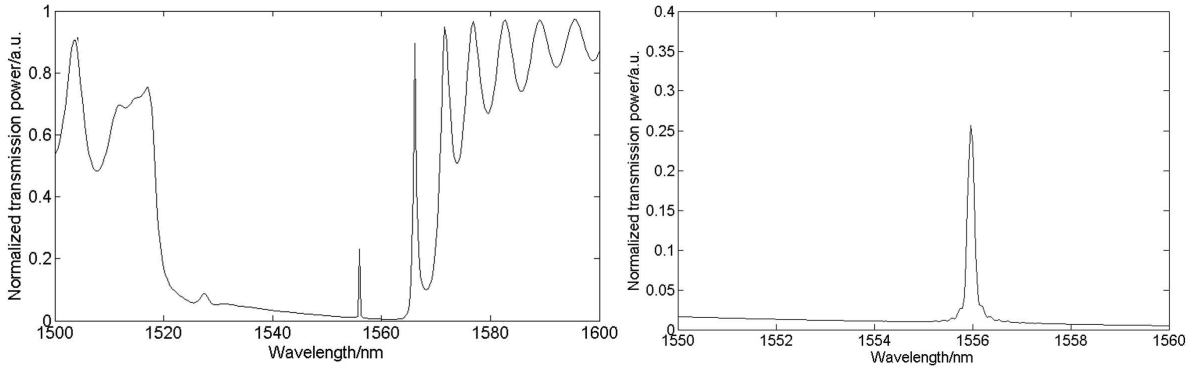

(a) (b)

Figure 3: (a) The transmission spectrum and (b) the enlargement of the on-resonance peak of the PhC nanobeam cavity.

of the extracted transmission peak. As we can see, the cavity mode has an on-resonance transmission 26% with a Q factor about 15500.

As the refractive index of the waveguide is similar to those materials to be detected provided that the PhC nanobeam cavity being used as a sensor, the evanescent field of the silica cavity will extend partly into the background materials. In other words, the background materials have a vital influence on the effective refractive index of the cavity mode, which means that the sensor will show a high sensitivity. The FDTD simulation results agree with this intuitive assumption for the resonant wavelength red shifts 3.38 nm as we increase the background index by 0.01.

4. CONCLUTIONS

We propose a novel weakly modulated PhC nanobeam cavity based on a suspended silica waveguide. The cavity shows a high Q factor ($Q = 15500$), a high on-resonance transmission ($T = 0.26$) and a high sensitivity ($S = 338$/RIU). These features outperform silicon based PhC cavities by a high sensitivity and the high transmission enables the cavity to be used in spectral filtering systems. Also the stucture can be utilized in the nonlinear optics combined with proper materials.

ACKNOWLEDGMENT

This work is partially supported by the National High Technology Research and Development Program (863) of China (No. 2012AA012201).

REFERENCES

1. Foresi, J. S., "Photonic-bandgap microcavities in optical waveguides," *Nature*, Vol. 390, No. 6656, 143–145, 1997.
2. Yao, K. Y. and Y. C. Shi, "High-Q width modulated photonic crystal stack mode-gap cavity

and its application to refractive index sensing," *Opt. Express*, Vol. 20, No. 24, 27039–27044, 2012.

3. Kim, S., B. H. Ahn, J. Y. Kim, K. Y. Jeong, K. S. Kim, and Y. H. Lee, "Nanobeam photonic bandedge lasers," *Opt. Express*, Vol. 19, No. 24, 24055–24060, 2011.
4. Leuthold, J., C. Koos, and W. Freude, "Nonlinear silicon photonics," *Nat. Photonics*, Vol. 4, No. 8, 535–544, 2010.
5. Quan, Q. M., I. B. Burgess, S. K. Y. Tang, D. L. Floyd, and M. Loncar, "High-Q, low index-contrast polymeric photonic crystal nanobeam cavities," *Opt. Express*, Vol. 19, No. 22, 22191–22197, 2011.
6. Quan, Q. M. and M. Loncar, "Deterministic design of wavelength scale, ultra-high Q photonic crystal nanobeam cavities," *Opt. Express*, Vol. 19, No. 19, 18529–18542, 2011.

Design and Analysis of Miniature Fractal Antenna

Ying Suo[1,2], **Jingyu Han**[1], **Wei Li**[1,2], **and Weibo Deng**[1]

[1]School of Electronics and Information Technology
Harbin Institute of Technology, Harbin 150001, China
[2]Electronic Science and Technology Postdoctoral Station
Harbin Institute of Technology, Harbin 150001, China

Abstract— Fractal antenna designs can meet most of the needs in size reduction of antenna design. In this paper, Koch iteration technique is applied to a dipole antenna in order to get a miniaturized radar array element. The dipole antenna with 3rd Koch iteration applied to each of its four segments is designed to operate at a resonant frequency of 500 MHz. The four fractal segments of this antenna spin around the center axis with an angle difference of 90 degrees each, which results to an all-four-direction feature. The overall size of this dipole fractal antenna at the resonant frequency is reduced by around 33% compared with conventional dipole antenna meanwhile retaining its band characters. An improved model is also introduced with a better performance in bandwidth, which can reach more than 12% at 500 MHz.

1. INTRODUCTION

The fractal iteration technique has drawn much attention since its first introduction in 1973 by B. B. Mandelbrot. Among these fractal types, Koch curve has a wide application in the design of miniaturized wire antenna due to its unique self-similarity nature [1]. Under the expanding need of size reduction in antenna design, fractal theory can help provide a great number of solutions for miniaturized antenna [2]. This paper presents the calculation and design of a fractal dipole antenna with an operating frequency of 500 MHz. The creation and optimization of this dipole antenna model using proper fractal dimension is carried out and analyzed according to the effects of miniaturization. The results from simulations and analysis are done in FEKO software environment.

2. ANTENNA DESIGN

2.1. Generation of Koch Fractal Curve

Koch curve as shown in Figure 1 is a simple but effective fractal geometry in the application of wire antenna miniaturization [3]. One of the mathematical approaches that contributes to the modeling of Koch fractal antenna is Iterated Function System (IFS). IFS is in fact an affine transformation cluster which can perfectly match the self-similarity character of fractal patterns [4].

In order to generate a mathematical model of Koch fractal curve, we use IFS method to calculate the exact coordinates of those endpoints on the corresponding curve. Matlab is used in this section of the research to help do iteration calculations and draw the figure. It first determines the trisection points, then make a rotation with a certain angle around those points to make one iteration. Repeat these steps and we can finally get an N-iterated Koch curve, of which the dimension also has a great effect on performance of the antenna [5].

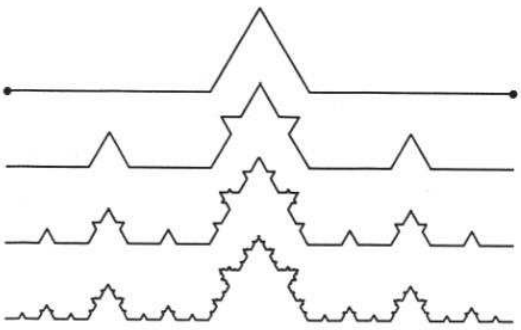

Figure 1: Koch fractal curve.

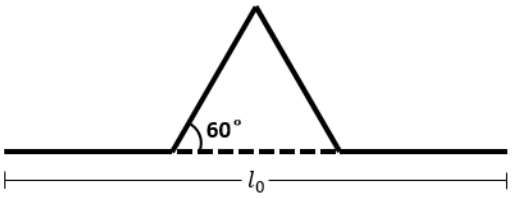

Figure 2: Schematic diagram of single Koch iteration.

2.2. Dimensions of Koch Curve

One of the most significant features of Koch fractal curve is its infinite length. The more iteration applied to the curve, the longer the curve will be. However, when it comes to antenna design, there is always a most suitable dimension of the curve. The relationship between its total length and its initial length is shown below [7].

$$L = (4/3)^n \cdot l_0 \tag{1}$$

L: Total length of the Koch curve.
l_0: Initial length of the Koch curve.
n: Fractal dimension (Iteration times).

This size reduction character of Koch curve helps greatly in the process of antenna miniaturization. According to latest researches, the most ideal iteration times for Koch curve in antenna design is 3rd iteration. When Koch curve is applied iteration three times, it gets a satisfying size reduction feature meanwhile maintain its excellent electrical characteristics [6].

2.3. Antenna Calculation and Modeling

As shown in Figure 3, Koch fractal antenna is composed of two identical wires with pre-designed Koch curve pattern. The feed point is at the connection point between these two parts, which is also the geometric center of the whole antenna.

Considering the unique geometry features of Koch fractal dipole, a transformed Koch dipole antenna is proposed and the diagram is shown in Figure 4.

This Koch fractal dipole antenna design features a four-direction spinning character. The antenna is composed of four identical 3rd iteration Koch curve segments that have a 90 degrees angle between each other, which all spin around the central axis.

The designated resonant frequency of this antenna is 500 MHz. According to equation

$$\lambda = c/f \tag{2}$$

working wave length should be 0.6 m. Then each of the four segments should have an effective length of 0.3 m/4 = 0.075 m = 7.5 cm. Using Equation (1) we can get the initial length of each segment which is calculated and designed to be around 4.96 cm. The total height of this antenna is 19.845 cm.

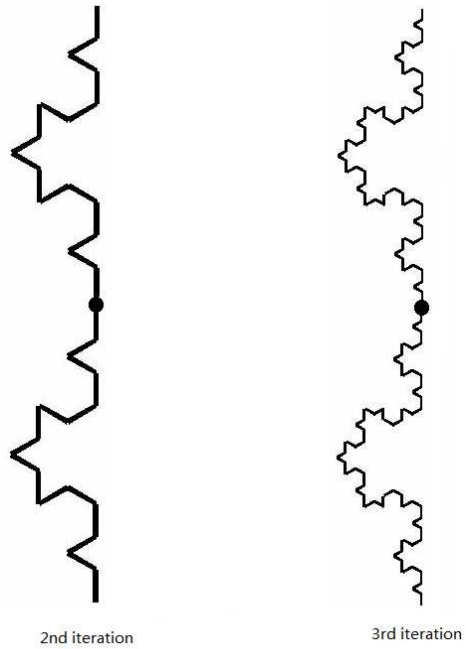

Figure 3: Koch fractal dipole antenna.

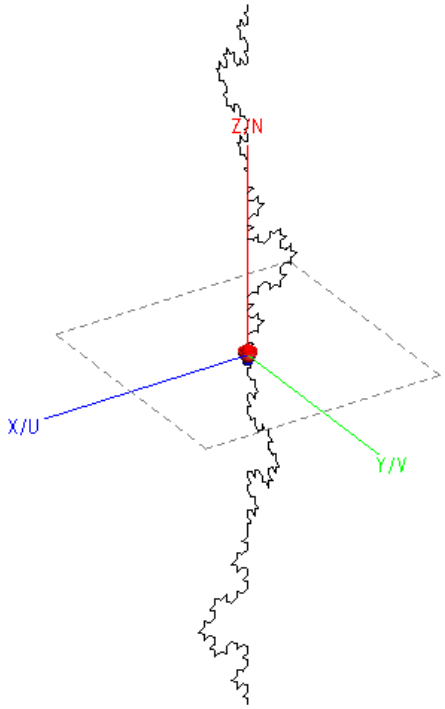

Figure 4: Spinning Koch dipole design.

After the size is decided, the whole antenna model is calculated in MATLAB environment. And the coordinates are imported into FEKO to assemble the wire antenna, after which simulations are done in FEKO environment.

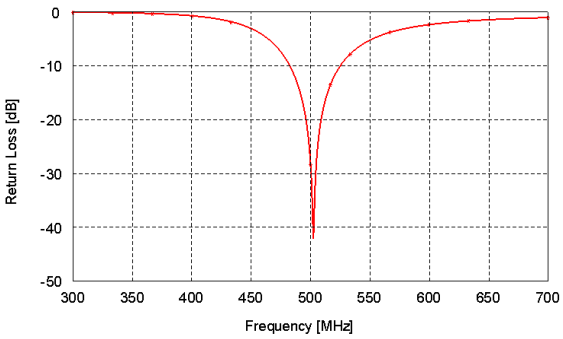

Figure 5: Simulated return loss of designed Koch fractal dipole.

Table 1: Comparison between conventional and Koch dipole.

Antenna	Conventional	Koch Fractal
Length	30 cm	19.845 cm
Resonant Frequency	500 MHz	502 MHz
Return loss	−16 dB	−42 dB
Bandwidth	8%	8.3%
Compactness	-	66.15%

3. RESULTS AND DISCUSSION

3.1. Return Loss

Figure 5 shows the simulation results of return loss for this Koch fractal dipole antenna in the frequency range from 300 MHz to 700 MHz. The measurement at the valley shows that the resonant frequency is at about 502 MHz, where the return loss is at the minimum value of −41.8 dB.

The bandwidth of this antenna is the frequency bandwidth where its return loss is below −10 dB. According to this simulation result, the bandwidth of this antenna is around 8.3%.

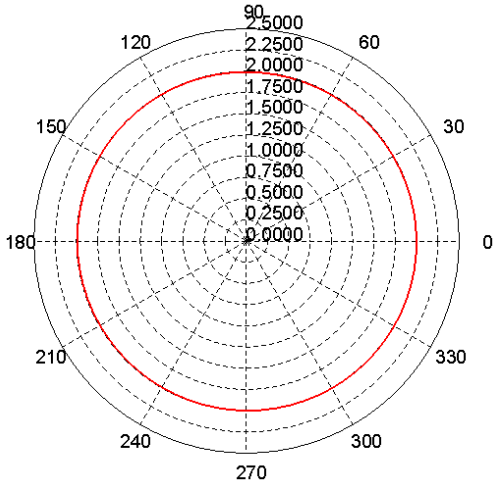

Figure 6: Radiation pattern in Azimuth plane.

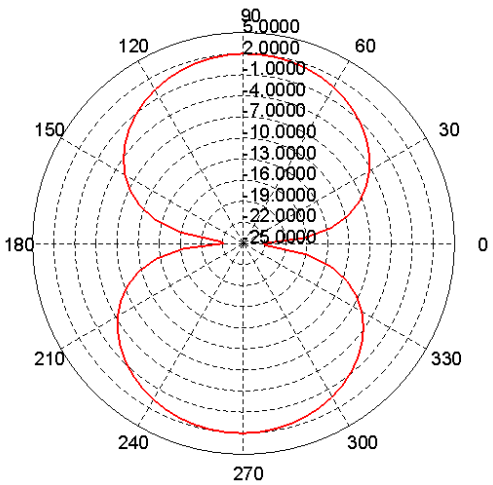

Figure 7: Radiation pattern in Meridian plane.

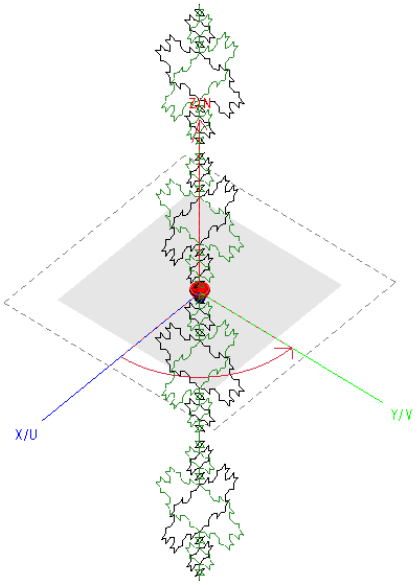

Figure 8: Improved antenna model with better bandwidth.

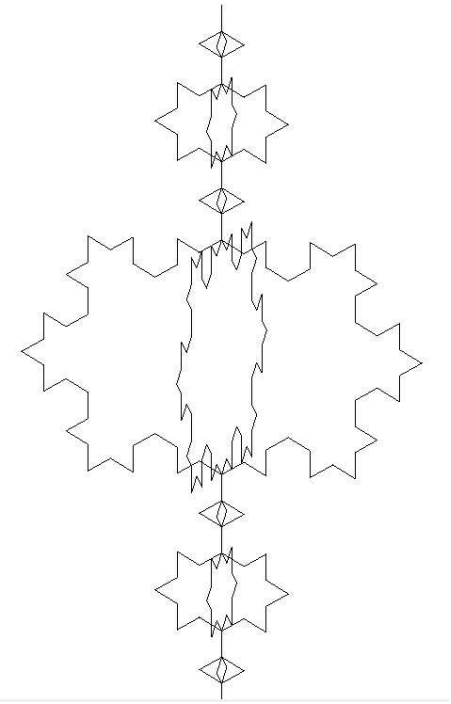

Figure 9: Zoomed structure of improved model.

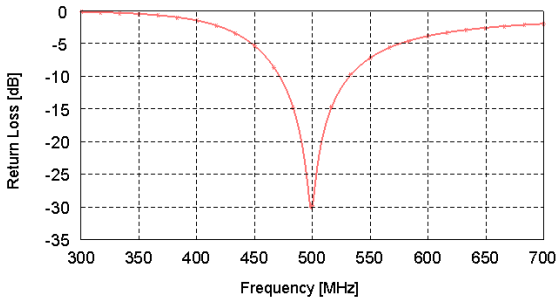

Figure 10: Simulated return loss of improved model.

3.2. Radiation Pattern

Figure 6 describes the radiation pattern of this designed Koch fractal dipole antenna in Azimuth plane. The figure shows a great Omni-directivity character. Directivity of designed Koch fractal antenna is 2 dBi at the resonant frequency of 500 MHz.

Figure 7 provides the radiation pattern of this designed Koch fractal dipole antenna in Meridian plane. It shows a symmetric pattern with the directivity of 2 dBi at the resonant frequency of 500 MHz.

A comparison is also performed between conventional dipole antenna and currently designed Koch fractal antenna. The results are displayed in Table 1.

From the table we can see that the Koch fractal geometry can provide a great miniaturization character. The compactness compared with traditional dipole antenna at 500 MHz can reach 66.15%. That means the size is reduced by 33.85%. The return loss reduces dramatically after Koch fractal is applied. However, the bandwidth only has a slight increase.

4. IMPROVED MODEL

Considering the barely satisfying bandwidth performance of the antenna introduced above, an improved model is proposed and calculated under simulation environment. The diagram of the improved model is shown in Figure 8.

This improved model can be realized by simply rotating and copying the original antenna in-

troduced above three times, making each fractal segment facing all four directions. The zoomed structure of each fractal block is shown in Figure 9.

This improved model shows a great bandwidth boost from the original 8.3% to 12.6%. Simulated return loss is shown in Figure 10.

The radiation patterns show that there is not much differences between the improved and original antenna regarding of radiation patterns.

5. CONCLUSION

Two Koch fractal dipole antennas of 3rd iteration have been designed and simulated successfully in FEKO environment. Antenna size, resonant frequency, return loss and bandwidth are simulated and measured. The antenna's size reduction of 33.85% is the main purpose of this paper. Besides, the rotating shape character of the first antenna can provide better adaptability when it is applied to outdoor or some other certain environments.

ACKNOWLEDGMENT

The authors would like to express their sincere gratitude to funds supported by "the National Natural Science Funds" (Grant No. 61201014), and "the Fundamental Research Funds for the Central Universities" (Grant No. HIT.NSRIF.2014023).

REFERENCES

1. Puente-Baliarda, C., J. Romeu, and A. Cardama, "The Koch monopole: A small fractal antenna," *IEEE Transactions on Antennas and Propagation*, Vol. 48, No. 11, 1773–1781, 2000.
2. Patel, P., et al., "Miniaturized dipole antenna using Koch fractal technique for wearable application," *2013 International Conference on IEEE Communications and Signal Processing (ICCSP)*, 2013.
3. Vinoy, K. J., J. K. Abraham, and V. K. Varadan, "On the relationship between fractal dimension and the performance of multi-resonant dipole antennas using Koch curves," *IEEE Transactions on Antennas and Propagation*, Vol. 51, No. 9, 2296–2303, 2003.
4. Mazel, D. S. and M. H. Hayes, "Using iterated function systems to model discrete sequences," *IEEE Transactions on Signal Processing*, Vol. 40, No. 7, 1724–1734, 1992.
5. Hazdra, P. and M. Capek, "IFS tool for fractal microstrip patch antenna analysis," *14th Conference on IEEE Microwave Techniques, 2008, COMITE 2008*, 2008.
6. Malektaji, S. and W. Kinsner, "Simulation of Koch fractal antennas," *2013 26th Annual IEEE Canadian Conference on IEEE Electrical and Computer Engineering (CCECE)*, 2013.
7. Abbas, S. M., et al., "Radial analysis of fractal Koch curve antenna," *2012 International Conference on IEEE Emerging Technologies (ICET)*, 2012.

An X-band Substrate Integrated Waveguide Vivaldi Array Antenna

Wei Li[1, 2], **Ying Suo**[1, 2], **Jingyu Han**[1], **and Xiaowei Liu**[3]

[1]School of Electronics and Information Engineering
Harbin Institute of Technology, Harbin 150001, China
[2]Electronic Science and Technology Postdoctoral Station
Harbin Institute of Technology, Harbin 150001, China
[3]Department of Microelectronics Science and Technology
Harbin Institute of Technology, Harbin 150001, China

Abstract— In this paper, a kind of compact X-band Vivaldi array antenna printed on a substrate is proposed and designed. The antenna is consisted of 4 Vivaldi structure radiation elements fed by an equal power divider with substrate integrated waveguide technology. The Vivaldi element is antipodal structure composed with an index gradient microstrip line are on both sides of the substrate. The reflection coefficient of the substrate integrated waveguide Vivaldi array antenna is less than −10 dB from 8.9 GHz to 10.06 GHz in X-band. The gain of the array antenna is 14 dB, and the main lobe width is about 17.3° with side lobe level less than −12 dB.

1. INTRODUCTION

The Vivaldi antenna array has been used in many microwave engineering applications for its simple structure, light weight, wideband characteristics, low cross polarization, and highly directive patterns characteristics [1]. An equal power divider is necessary for the antenna array feed network with equal amplitude design. The substrate integrated waveguide (SIW) multi-way microwave power divider attracts a lot of attentions because of its advantages such as high Q-facter, small structural dimension, high integration and low cost [2–5]. A compact Vivaldi antenna array is printed on thick substrate, and it is fed by a SIW binary to significantly minimize the feed structure insertion losses [6]. A compact Vivaldi antenna array fed by a SIW structure is proposed, and four-elements printed Vivaldi array are designed and investigated in [7]. An eight elements antipodal Vivaldi antenna array using SIW technology is researched in [8], and it can reach a 12 dB gain at the center frequency of 10 GHz.

In this paper, a kind of Vivaldi array antenna printed on a substrate operating in X-band is designed and simulated. The antenna is consisted of 4 elements Vivaldi structure radiation fed by an equal SIW power divider. A Vivaldi element is antipodal structure composed with an index gradient microstrip line are on both sides of the substrate, and SIW-microstrip transition structure is designed to satisfy measurement and connection.

2. RADIATION ELEMENT DESIGH

The antipodal Vivaldi radiation element is complementary structure are on both sides of the substrate. The antenna element is consisted of three parts in Figure 1. As shown in Figure 1, the upper part is the antenna radiator, the middle part is the connection structure, and the lower part is microstrip transition. The Vivaldi antenna is directly fed by a microstrip line. Impedance of the microstrip is equal to each export part of equal power divider. A SIW-microstrip transition structure is designed to satisfy measurement and connection. The transition section is taper microstrip line.

The inner part of antenna radiator part is part of an ellipse curve, and the outer is an index gradient curve whose exponential rate r is 1. The shape is determined by the following formula:

$$y = c_1 \times \mathrm{e}^{rz} + c_2 \tag{1}$$

As shown in Figure 1, w_s is an antenna width, L is the antenna length, L_2 set for the length of straight part in SIW microstrip transition, L_1 is the length of the connection part, R is length truncated by elliptic curve. The parameters of the Vivaldi radiation element is shown in Table 1.

The Vivaldi radiation element is simulated by CST MWS software. The reflection coefficient results are shown in Figure 2. It can be seen that the reflection coefficient is less than −12 dB at 8.5 GHz to 10.5 GHz. The pattern of the antipodal Vivaldi antenna is shown in Figure 3, the gain can reach 3.85 dB. The back lobe in H-plane pattern can be greatly improved after cut down part of the antenna radiator. The side lobe level is lower, while the back lobe level reduced 1.1 dB after cut down part of the antenna radiator portion along ellipse.

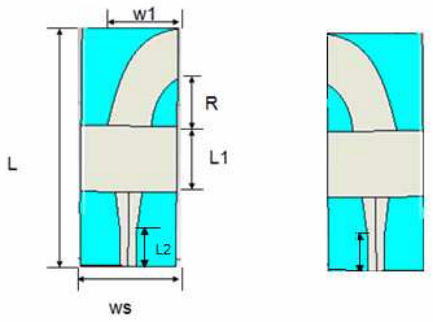

(a) Upper part (b) lower part

Figure 1: Antipodal Vivaldi antenna element.

Table 1: Parameters of the Vivaldi antenna element.

parameters (mm)	w_1	R	L	L_1	L_2	w_S
	8.35	6.2	30.37	8.2	17	11.4

3. FOUR-WAY SIW POWER DIVIDER

A SIW is composed with two column metallized via holes in the dielectric substrate and upper and lower metal layers. A kind of similar rectangular waveguide structure is composed by via hole and two metal layers. The characteristics of electromagnetic wave transmission in SIW is similar with the characteristics in metal waveguide. For integration with coplanar waveguides or microstrip circuits, a transition structure should be designed to satisfy measurement and connection. The electromagnetic field of the microstrip line is similar to the TE_{10} mode of the substrate integrated waveguide. The general SIW-microstrip transition is a section of taper microstrip line in Figure 4. The taper line is able to realize impedance transformation between the $50\,\Omega$ microstrip line and the substrate integrated waveguide.

Ordinary Y-shaped structure can be achieved the power divisions, however its discontinuous structure is able to result in the higher return loss in pass band. The metal pin in SIW can reduce the power reflection. The electric field distribution of the Y-junction is able to be changed by surface current distribution of the metal pin inductance.

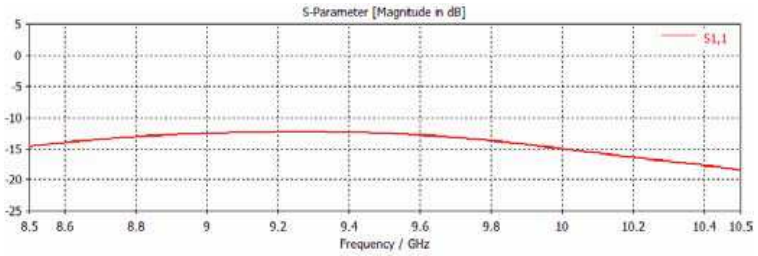

Figure 2: Reflection coefficient of the Vivaldi antenna element.

Table 2: Parameters of the 4-way SIW power divider.

parameters (mm)	a	p	D	h_1	h_2	h_3	D_1
	12	1	0.6	4	17	17	0.5
parameters (mm)	D_2	D_3	D_4	R	L_2	w_s	w_2
	0.5	0.6	0.3	6.2	4.5	11.4	5.5
parameters (mm)	t_2	t_3	t_4	w_4	w	w_1	t_1
	5	5	7	5	2	8.35	4.9

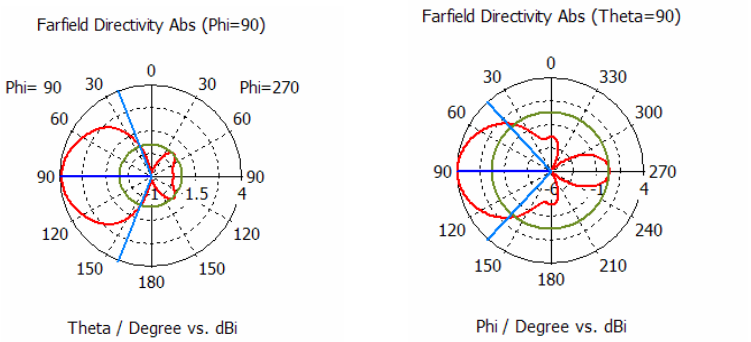

(a) *E*-plane pattern (b) *H*-plane pattern

Figure 3: Pattern of the Vivaldi antenna element.

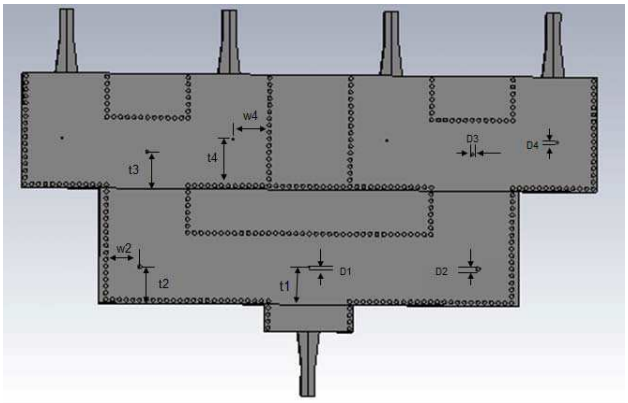

Figure 4: 4-way SIW power divider.

The reflection coefficient can be significantly reduced by adjusting diameter and position of the pin in SIW, which can influence the distribution of the electric field. The parameters of the four way SIW power splitter are shown in Table 2.

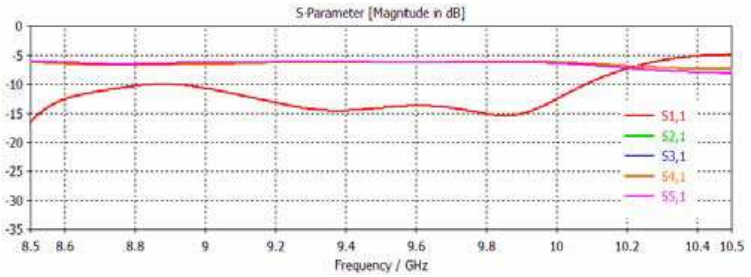

Figure 5: S parameters of the 4-way SIW power divider.

In the Table 2, a is the distance between the antenna, p is the distance between two vias in vias array, D is the diameter of the vias, h_1 is the width of the connection structure, h_2 is the width of the first section of Y-junction structure, h_3 is the width of the second Y-junction structure, Z_1 is the thickness of the medium, Z_2 is the thickness of PEC in simulation.

To be convenient to test by coaxial cable, five SIW micro-strip transitions are needed to connect with SIW power splitter. The 4-way SIW power divider is simulated by CST MWS software. The simulation S parameters results of different ports are shown in Figure 5.

It can be seen that the reflection coefficient is less than -10 dB at 8.5 GHz to 10.5 GHz. The transmission coefficients, such as S_{21}, S_{31}, S_{41}, S_{51} parameters, are almost reach about -6 dB, and they are substantially coincident to achieve the power divisions.

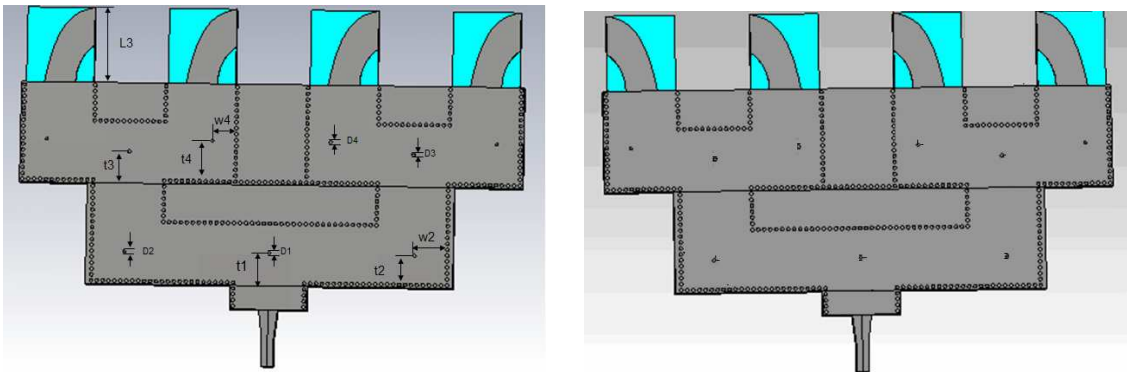

(a) Upper part (b) lower part

Figure 6: Simulation model of the antipodal Vivaldi antenna array.

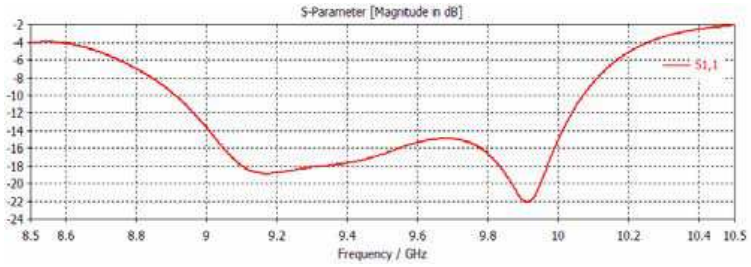

Figure 7: Reflection coefficient of the antipodal Vivaldi antenna array.

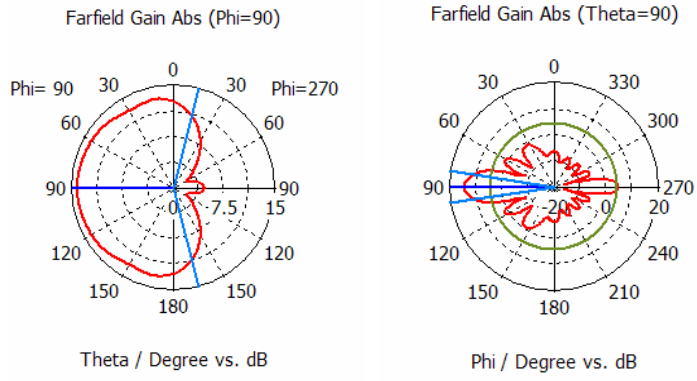

(a) *E*-plane pattern (b) *H*-plane pattern

Figure 8: Pattern of the antipodal Vivaldi antenna array.

4. ANTIPODAL VIVALDI ANTENNA ARRAY

The last simulation model of antipodal Vivaldi antenna based on 4-way SIW power divider is shown in Figure 6. The pin is placed in center of a quarter SIW waveguide wave lengths, then it is optimized to get the best value of r values. Due to the design of the previous step has been made in better results, t_1 need to be tuned, making the minimum point of the reflection is located in the center of the frequency band as should be designed. The length of Vivaldi antenna element is $L_3 = 12.67$. The design of the dielectric substrate using a relative permittivity $\varepsilon_r = 4.5$, dielectric thickness $h = 1.6\,\text{mm}$.

The 4-element antipodal Vivaldi antenna array is simulated by CST MWS software. The simulation results are shown in Figure 7. It is shown that the S_{11} parameter is less than $-10\,\text{dB}$ from 8.9 GHz to 10.07 GHz. The radiation pattern of the antenna array is shown in Figure 8. As shown in Figure 8, the array gain reach 14 dB. And and the main lobe width is about 17.3° with side lobe level less than $-12\,\text{dB}$.

5. CONCLUSION

The planar Y-junction multi-way power distribution with metal pin technology is used in the 4-way SIW equal power divider, and the impedance characteristics and transmission characteristics satisfies the Vivaldi antenna array design. The Vivaldi radiation element is consisted of the antipodal structure. An element is composed with an index gradient microstrip line are on both sides of the substrate. The operating frequency of the SIW Vivaldi array antenna is more than 1.1 GHz in X-band. The gain of the array antenna is 14 dB, and the main lobe width is about 17.3° with side lobe level less than −12 dB.

ACKNOWLEDGMENT

The authors would like to express their sincere gratitude to CST Ltd. Germany, for providing the CST Training Center (Northeast China Region) at our university with a free package of CST MWS software. The authors would like to express their sincere gratitude to funds supported by The authors would like to express their sincere gratitude to funds supported by "The National Natural Science Funds" (Grant No. 61201014), and "Heilongjiang Postdoctoral Financial Assistance" (Grant No. LBH-Z11125).

REFERENCES

1. Langley, J. D. S., P. S. Hall, and P. Newham, "Novel ultrawide-bandwidth Vivaldi antenna and low crosspolarisation," *Electronics Letter,* Vol. 29, No. 23, 2004–2005, 1993.
2. Huang, Y. and K.-L. Wu, "A broadband integrated LTCC laminated waveguide to metallic waveguide transition," *IEEE MTT-S International Microwave Symposium*, 2237–2240, 2003.
3. Song, K., Y. Fan, and Y. Zhang, "Eight-way substrate integrated waveguide power divider with low insertion loss," *IEEE Transactions on Microwave Theory and Techniques*, Vol. 56, No. 6, 1473–1477, 2008.
4. Germain, S., D. Deslandes, and K. Wu, "Development of substrate integrated waveguide power dividers," *IEEE Canadian Electrical and Computer Engineering Proceeding*, 1921–1924, 2003.
5. Hao, Z., W. Hong, H. Li, H. Zhang, and K. Wu, "Multiway broadband substrate integrated waveguide (SIW) for power divider," *IEEE Antennas and Propagation Society International Symposium*, 639–642, 2005.
6. Yang, S., A. Elsherbini, S. Lin, and A. E. Fathy, "A highly efficient Vivaldi antenna array design on thick substrate and fed by SIW structure with integrated GCPW feed," *IEEE Antennas and Propagation Society International Symposium*, 1985–1988, 2007.
7. Li, B., L. Dong, and J.-C. Zhao, "The research of broadband millimeter-wave Vivaldi array antenna using SIW TECHNique," *2010 International Conference on Microwave and Millimeter Wave Technology*, 997–1000, 2010.
8. Kazemi, R., A. E. Fathy, and R. A. Sadeghzadeh, "Ultra-wide band Vivaldi antenna array using low loss SIW power divider and GCPW wide band transition," *2012 IEEE Wireless Symposium,* 39–42, 2012.

An Omni-directional Circularly Polarized Helical Antenna with an Inductive Feed

Yufeng Yu[1], **Xiaoyi He**[1], **Qi Liu**[2], **and Yufeng Wang**[1]

[1]China Jiangnan Electronics Communication Institute, Jiaxing 314000, China
[2]Center for Optical and Electromagnetic Research, Zhejiang University, Hangzhou 310027, China

Abstract— The paper presents an omni-directional circularly polarized (CP) helical antenna with an inductive feeding structure. The antenna is comprised of a printed helix with six arms on a thin rolled substrate and a feeding loop, which acts as the radiator and the feeding structure, respectively. The helix is fed by the feeding loop without physical connection through inductive coupling, which is convenient to achieve impedance matching. The 90° phase difference between the radiated horizontal and vertical electric field components is naturally guaranteed by the helix; therefore, circular polarization is achieved through tuning the height and radius of the helix to ensure equal magnitude of the radiated horizontal and vertical field components. With an electrical size of $0.17\lambda_0 \times 0.17\lambda_0 \times 0.11\lambda_0$, the antenna exhibits a simulated impedance bandwidth ($|S_{11}| \leq -10\,\text{dB}$) of 5.72% and AR bandwidth ($\text{AR} \leq 3\,\text{dB}$) of 27.4%.

1. INTRODUCTION

The omnidirectional circularly polarized (CP) antennas are very attractive in wireless communications. The omnidirectionality allows the antennas cover a large service area while the CP property not only support a free alignment between the receiving and transmitting antennas but also suppress the effects of multi-path reflections of waves caused by the nearby objects.

There are lots of reported works on omnidirectional CP antennas. Some of them utilize two radiators to generate vertical and horizontal polarized components of electric fields (E_θ and E_φ) with 90° phase difference, respectively. The radiator for E_θ can be top-loaded cylindrical monopole [1] or zeroth-order resonance (ZOR) antennas [2] and the radiator for E_φ can be printed arc-shaped dipoles [1] or monopoles [2]. Another design concept is to place several CP elements uniformly on the horizontal plane to form an omnidirectional radiation. In [3], four broadband CP rectangular loops are printed on a thin flexible dielectric substrate and rolled into a hollow cylinder. Fed by a broadband balun, this antenna exhibits a wide bandwidth and good CP property.

Normal mode helical antennas [4] with very small diameters are classical omnidirectional CP antennas. However, the feeding networks are usually needed for impedance mating, which increase the complexity of the antennas and the fabrication costs. A crossed parallel transmission line was proposed to feed a multifilar helical antenna [5] without any feeding network. However, the impedance matching is not good, and each helix needs to be separated and connected to the parallel transmission line, which is still not convenient for fabrication.

The inductively coupled feed using a small loop is an effective feeding technique [6, 7]. In this paper, this technique is utilized to feed a multifilar helical antenna. Compared with the crossed parallel transmission feeding line in [5], the inductively coupled feed can achieve better impedance matching to a 50 Ω feeding line and the tuning procedure is very easy. Additionally, there is no physical connection between the radiating helix and the feeding structure and the two parts can be fabricated respectively and then assembled easily, which eases the fabrication.

2. ANTENNA CONFIGURATION

The configuration of the proposed omni-directional circularly polarized helical antenna is shown in Figure 1(a). The antenna is comprised of a printed helix with six arms and a feeding loop, which acts as the radiator and the feeding structure, respectively.

Figure 1(c) shows the planar layout of the six-arm helix. It is first printed on a thin flexible substrate (Taconic TLY-5) with dielectric constant of 2.2 and thickness of 0.13 mm and then rolled up into a hollow cylinder of radius R_r. Each arm is with the width W_r and pitch angle α. A helical antenna can produce both vertical and horizontal components of the radiated electric fields (E_θ and E_φ) and 90° phase difference between the two components is naturally guaranteed [4, 8]. When α, H and R_r is tuned to ensure equal magnitude of E_θ and E_φ, the antenna can achieve good circular polarization of the radiated waves.

As shown in Figure 1(b), the feeing loop is printed on a Rogers RO4350B substrate with dielectric constant of 3.48 and thickness of 0.508 mm. Note that the loop is composed of two half loops printed on each side of the substrate. Each half loop is connected to the inner and outer conductor of a 50 Ω SMA connector respectively at one end and at the other end they are connected through a shorting pin. A 0.5 pF capacitor is inserted to the loop to add additional capacitance for impedance matching. Detailed dimensions of the antenna shown in Figure 1 are as follows: $R_r = 33.5$ mm, $R_f = 15$ mm, $W_r = 3$ mm, $W_f = 3.5$ mm, $l_e = 8.8$ mm, $\alpha = 17.5°$, $H = 40.4$ mm.

3. SIMULATED RESULTS AND DISCUSSIONS

The proposed antenna is simulated and optimized using HFSS v13. The simulated reflection coefficient is plotted in Figure 2. It is seen that the impedance bandwidth ($|S_{11}| \leq -10$ dB) is 44.4 MHz (from 753.4 MHz to 797.8 MHz), which is approximately 5.72% at the center frequency 775.6 MHz. The average axial ratio (AR) in the azimuth (x-y) plane is also shown in Figure 2. It is noted that the simulated average AR is obtained by averaging the AR results in the azimuth (x-y) plane. It can be seen that the average AR is lower than 3 dB from 630.5 MHz to 831 MHz, which exhibits an AR bandwidth of 200.5 MHz.

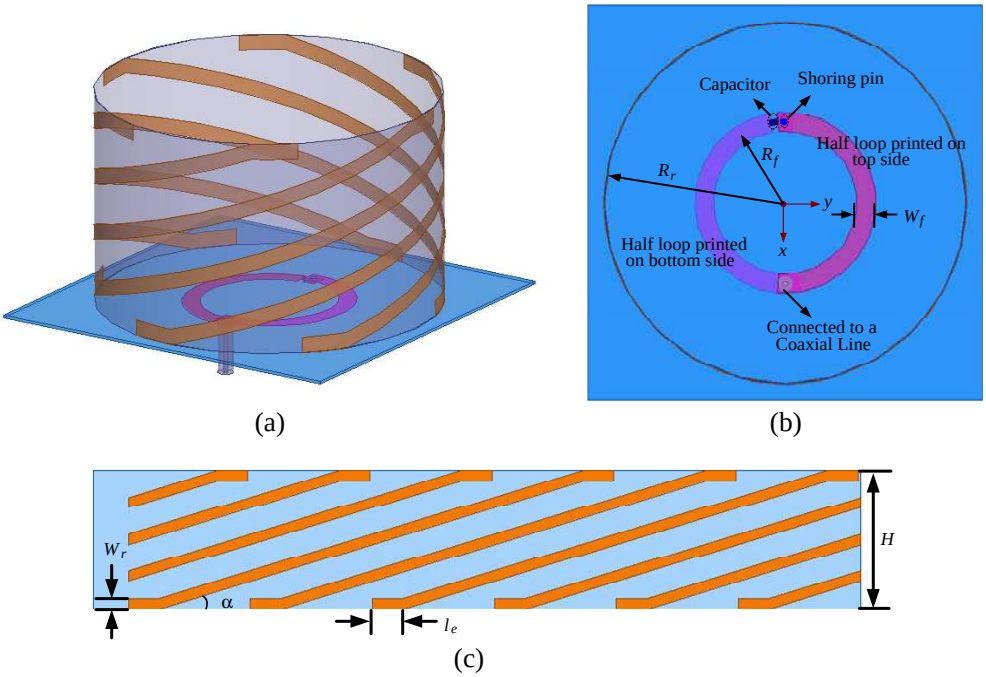

Figure 1: Antenna configuration: (a) 3-D view, (b) top view, and (c) planar layout of the helix.

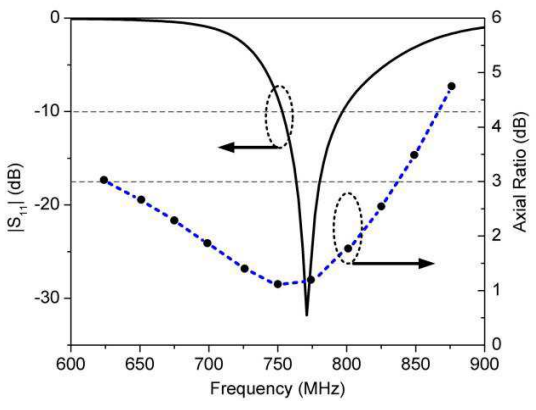

Figure 2: Simulated reflection coefficient and average axial ratio of the proposed antenna.

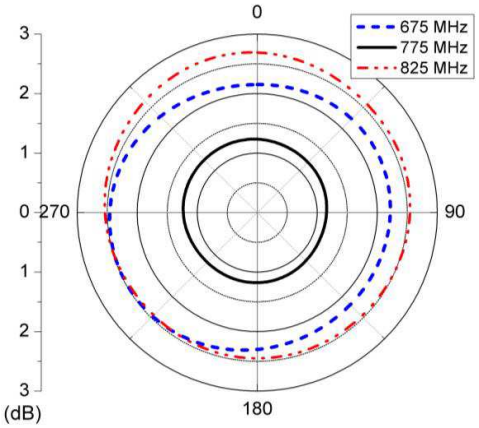

Figure 3: Simulated axial ratio of the proposed antenna in the azimuth plane.

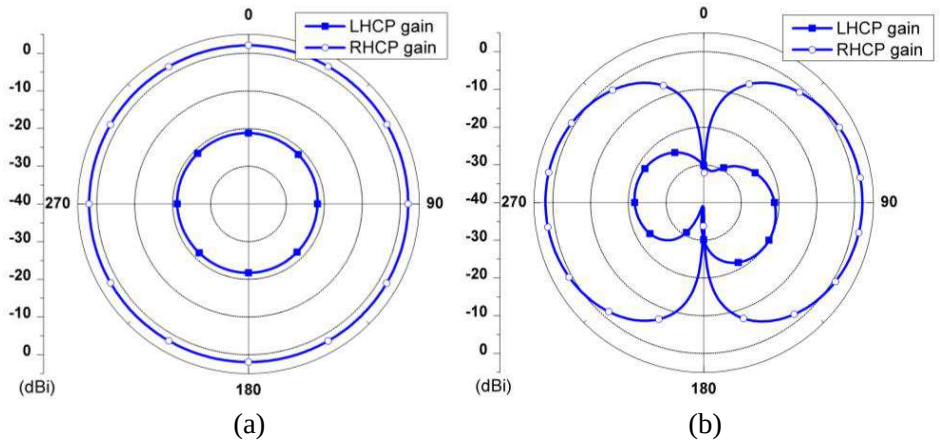

Figure 4: Simulated radiation patterns at 770 MHz. (a) Azimuth (x-y) plane, (b) elevation(x-z) plane.

The simulated axial ratio of the proposed antenna in the azimuth plane at 675 MHz, 775 MHz and 825 MHz are plotted in Figure 3. It is shown that the ripples are 0.33 dB, 0.11 dB and 0.26 dB at the corresponding frequency, which shows good symmetric AR in the azimuth plane.

Simulated radiation patterns at 775 MHz in the azimuth and elevation planes are plotted in Figure 4. The average LHCP gain is 2.02 dBi (1.94 dBi to 2.09 dBi) in the azimuth plane, while the average cross-polarization (RHCP) level is at about −21.50 dBi. It is seen that a very good omni-directional LHCP radiation pattern is achieved in the azimuth plane.

4. CONCLUSION

An omni-directional circularly polarized (CP) helical antenna with an inductive feeding structure is presented in this paper. With a size of 67 mm × 67 mm × 40.9 mm, the antenna exhibits a simulated impedance bandwidth ($|S_{11}| \leq -10$ dB) of 5.72% (753.4 MHz to 797.8 MHz) and AR bandwidth (AR ≤ 3 dB) of 27.4% (630.5 MHz to 831 MHz). The average right-handed CP gain in the azimuth plane is more than 1.4 dBi over the operating band ($|S_{11}| \leq -10$ dB).

REFERENCES

1. Hsiao, F. R. and K. L. Wong, "Low-profile omnidirectional circularly polarized antenna for WLAN access point," *Microw. Opt. Technol. Lett.*, Vol. 46, No. 3, 227–231, Aug. 2005.
2. Park, B. C. and J. H. Lee, "Omnidirectional circularly polarized antenna utilizing zeroth-order resonance of epsilon negative transmission line," *IEEE Trans. Antennas Propag.*, Vol. 59, No. 7, 2717–2720, Jul. 2011.
3. Quan, X., R. L. Li, and M. M. Tentzeris, "A novel broadband omni-directional circularly polarized antenna for mobile communications," *IEEE International Symposium on Antennas and Propagation*, 1777–1779, 2011.
4. Wheeler, H. A., "A helical antenna for circular polarization," *Proc. of the IRE*, Vol. 35, 1484–1488, Dec. 1947.
5. Sakaguchi, K. and N. Hasebe, "A circularly polarized omnidirectional small helical antenna," *International Conference on Antennas and Propagation (ICAP)*, 492–495, 1995.
6. Yu, Y. F., J. Xiong, H. Li, and S. He, "An electrically small frequency reconfigurable antenna with a wide tuning range," *IEEE Antennas and Wireless Propagation Letters*, Vol. 10, 103–107, 2011.
7. Lim, S., R. L. Rogers, and H. Ling, "A tunable electrically small antenna for ground wave transmission," *IEEE Trans. Antennas Propag.*, Vol. 54, No. 2, 417–421, Feb. 2006.
8. Yu, Y., Z. Shen, and S. He, "Compact omni-directional antenna of circular polarization," *IEEE Antennas Wireless Propag. Lett.*, Vol. 11, 1466–1469, 2012.

A Shared Aperture Millimeter Wave Antenna Using 3D SIW Technology

Zeyang Tian, Jun Ouyang, and Yu Long
School of Electronic Engineering, University of Electronic Science and Technology of China
Chengdu, Sichuan 611731, China

Abstract— A shared aperture millimeter wave antenna array based on three-dimensional (3D) substrate integrated waveguide (SIW) technology is designed for millimeter wave wireless communication applications. Dipole and slot antenna are used as elements and the two proposed antenna arrays work at 28 GHz and 75 GHz respectively. Both arrays use SIW H-to-E-plan vertical interconnect to form 3D architecture [1].

1. INTRODUCTION

With the development of wireless communication technology, the lower frequency spectrum is becoming more and more crowded. To solve this problem, millimeter wave wireless communication has been studied for many years, since it has many advantages, such as large capacity of communication, high quality of transmission and high confidentiality

In this paper, a shared aperture antenna using 3D SIW technology is proposed. Because of the narrow spacing between the 75 GHz element, the 28 GHz dipole array is placed in the vertical plane while the 75 GHz slot array is placed in the horizontal plane. A 1/8 and a 1/4 power divider are designed to feed the two arrays respectively. SIW H-to-E-plane interconnect is used to form a 3D power divider structure. Rogers RT/Duroid 5880 $\epsilon_r = 2.2$ with the thickness of 0.254 mm is adopted as substrate material in this design

2. SIW-FED SLOT AND DIPOLE ANTENNA

Figure 1 shows the geometric configuration of the proposed 75 GHz SIW slot antenna A transition structure is designed between the 50 Ω microstrip line and the SIW thus the quasi-TEM mode of the microstrip line can transform into the TE_{10} mode in the SIW by the taper [2]. Considering the element spacing of the 28 GHz dipole, the width of the slot **W** is determined to be at an appropriate value to avoid the grating lobe of the lower frequency array. The diameter **D** of the metallized holes and the spacing **b** between the holes are determined by the rules formulated in [3]. The parameters of the slot antenna are listed in Table 1. Simulated return loss and radiation patterns are shown in Fig. 2. The return loss is better than −10 dB within the bandwidth from 73.2 to 79.6 GHz and the peak gain is 11.7 dB.

SIW-fed dipole antenna is used as the lower frequency element. The design procedures are similar with the quasi-Yagi antenna explain in [4], except that a dipole is chosen instead of the quasi-Yagi in order to reduce the height of the whole array. As shown in Fig. 3, the SIW is transformed to broadside parallel stripline to feed the dipole antenna. The Z axis is perpendicular to the SIW plane and the arm of the dipole lies along the X axis. The optimized parameters of the dipole antenna which operates at 28 GHz are given in Table 2. Fig. 4 presents the simulated return loss and radiation patterns. Multiple simulations shows that the impedance matching is mainly affected by the length of the broadside parallel stripline and the width of $\mathbf{W_{arm}}$. As shown in Fig. 4, the simulated return loss is better than −10 dB from 25.9 to 31.6 GHz and the maximum radiation direction is Z axis with apeak gain of 4.8 dB.

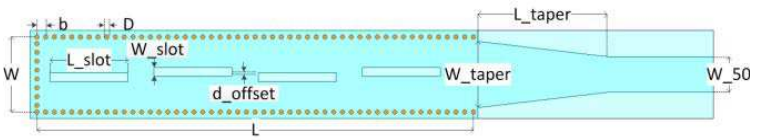

Figure 1: Geometric configuration of the proposed 75 GHz SIW slot antenna.

Table 1: Dimensions of the 75 GHz SIW slot antenna.

Symbol	Quality (mm)	Symbol	Quality (mm)
L	10	W_{slot}	0.1923
W	1.7	d_{offset}	0.0597
b	0.2	L_{taper}	3
D	0.1	W_{taper}	1.5
L_{slot}	1.7897	W_{50}	0.8

Table 2: Dimensions of the 28 GHz dipole antenna.

Symbol	Quality (mm)	Symbol	Quality (mm)
L_1	4.8	W_{50}	0.8
W_1	5.2	L_s	4.1018
b_1	0.4	W_s	1.6499
D_1	0.2	W_2	0.8
$L_{1\ \text{taper}}$	2.2024	L_{arm}	2.7291
$W_{1\ \text{taper}}$	1.818	W_{arm}	0.2147

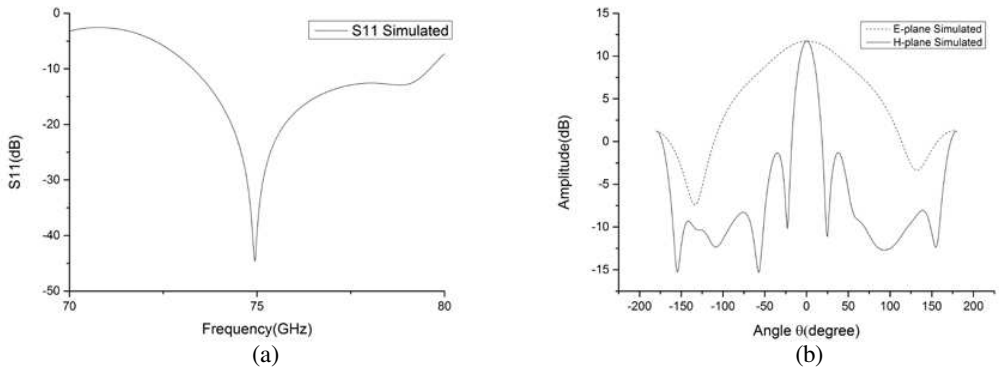

Figure 2: (a) Simulated return loss. (b) Simulated radiation patterns in both E-plane and H-plane at 75 GHz.

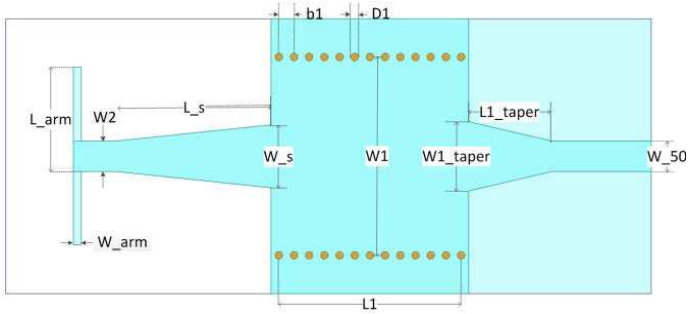

Figure 3: Geometric configuration of the 28 GHz dipole antenna.

3. FEEDING NETWORK

Figure 5 shows the geometric configuration of the 1/8 and 1/4 power dividers. The 1/8 power divider is made up of T-junction power splitters and the 1/4 power divider is made up of one T-junction and one Y-junction [5]. Both Y- and T-junctions are equal power splitters to achieve the same amplitude distribution. The design of the SIW is the same as described above. Fig. 6 depicts the simulated frequency characteristics of the two power dividers, in which the simulated insertion loss is about 1 dB and 0.3 dB respectively.

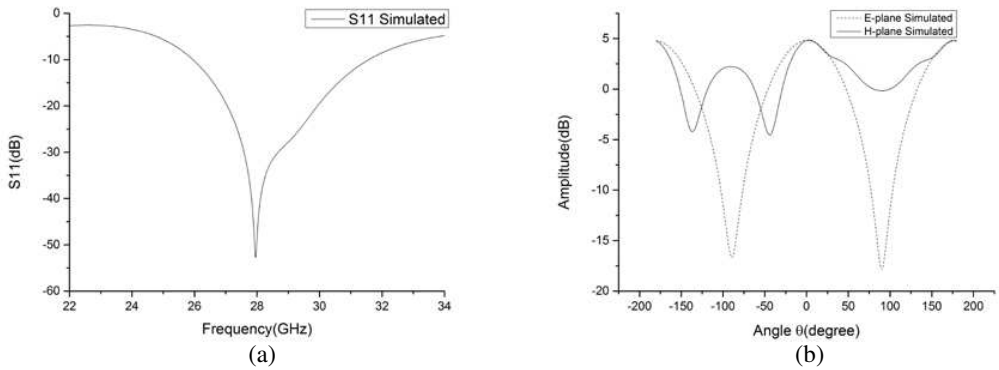

Figure 4: (a) Simulated return loss. (b) Simulated radiation patterns in both E-plane and H-plane at 28 GHz.

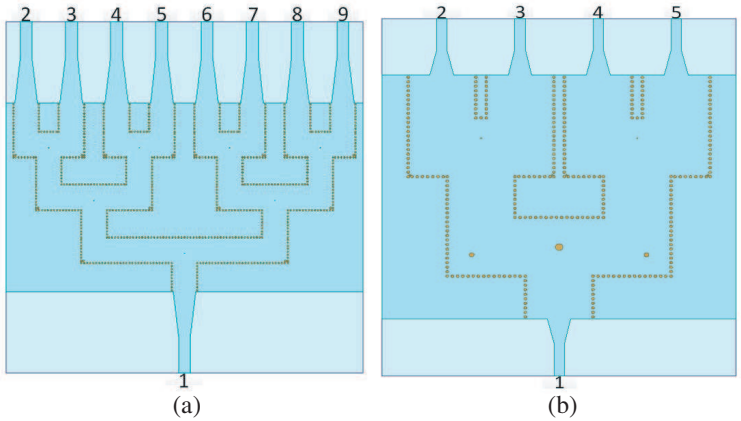

Figure 5: (a) 75 GHz 1/8 power divider, (b) 28 GHz 1/4 power divider.

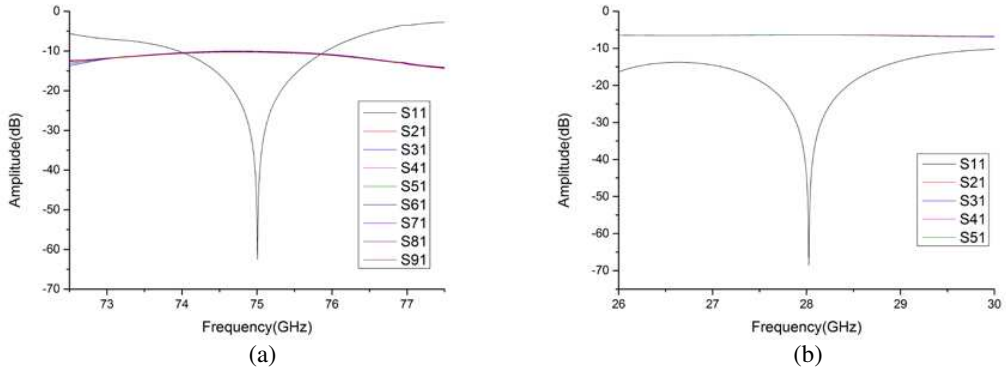

Figure 6: (a) 75 GHz, (b) 28 GHz simulated frequency characteristics of power divider.

4. ARRAY ANTENNA

The overall structure of the proposed shared aperture array antenna is described in Fig. 7. As for the 75 GHz array, the antenna elements are set in the horizontal plane while the power divider is set in the vertical plane. The 28 GHz array is just the other way around. There are two slot antennas between each dipole. Both arrays and their power dividers form 45 degree angle and connect with each other through SIW H-to-E-plane vertical interconnects. The simulated results are shown in Fig. 8. The return loss is better than −10 dB from 74.7 to 75.7 GHz and 26.3 to 29.1 GHz. The peak gain of the two arrays is 18.3 and 11.3 dB. The incision size on the slot array determined the amplitude of the 75G array's back lobe. The value of $\mathbf{L_{cut}}$ is optimized to be 4.5 mm to lower the amplitude of the back lobe to −3.5 dB. In comparison with Fig. 4(b), Fig. 8(d) indicate that the

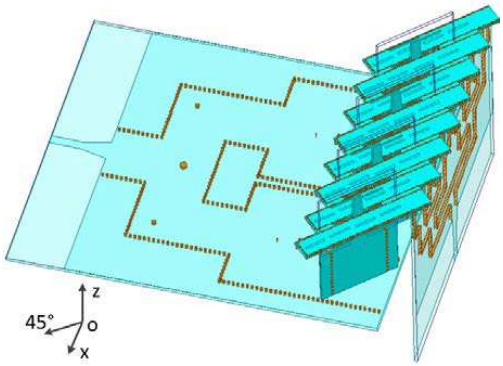

Figure 7: Geometric configuration of the shard aperture antenna.

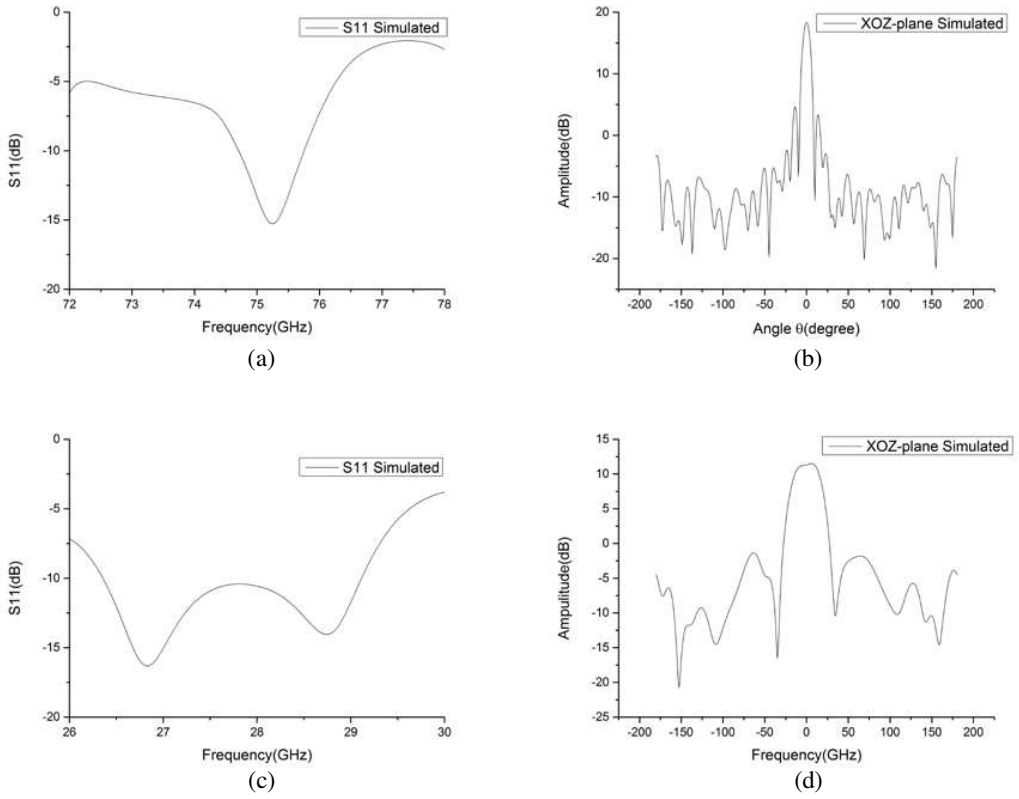

Figure 8: (a) Simulated return loss. (b) Simulated radiation patterns in XOZ-plane at 75 GHz. (c) Simulated return loss. (d) Simulated radiation patterns in XOZ-plane at 28 GHz.

dipole array antenna radiate toward the vertical direction because of the slot array antenna served as a ground. Both arrays can also extend in the 45° direction [6].

5. CONCLUSION

In this paper, a shard Aperture Millimeter Wave Antenna Using 3D SIW Technology is designed and simulated. The slot array antenna works at 75 GHz and has a peak gain of 18.3 dB while the dipole array antenna works at 28 GHz and has a peak gain of 11.3 dB. Simulated results show that both arrays can work properly, thus these arrays can be used to construct a columnar conformal array for millimeter wave communication.

REFERENCES

1. El Khatib, B. Y., T. Djerafi, and K. Wu, "Substrate-integrated wave guide vertical interconnects for 3-d intergrated circuits," *IEEE Trans. Packaging and Manufacturing Tech.*, Vol. 2, No. 9, 1526–1535, 2012.

2. Deslandes, D. and K. Wu, "Integrated microstrip and rectangular waveguide in planar form," *IEEE Microwave and Wireless Components Letters*, Vol. 11, No. 2, 68–70, 2001.
3. Deslandes, D. and K. Wu, "Design considerations and performance analysis of substrate integrated waveguide components," *European Microwave Conference*, 881–884, Milano, Italy, Sept. 2002.
4. Zhang, Z., K. Wu, and N. Yang, "Broadband millimeter-wave quasi-Yagi antenna using Substrate Integrated Waveguide technique," *Radio and Wireless Symposium*, 671–674, Orlando, USA, Jan. 2008.
5. Germain, S., D. Deslandes, and K. Wu, "Development of substrate integrated waveguide power dividers," *Electrical and Computer Engineering*, 1921–1924, Montreal, Canada, May 2003.
6. El Khatib, B. Y., T. Djerafi, and K. Wu, "Three-dimensional architecture of substrate integrated waveguide feeder for fermi tapered slot antenna array applications," *IEEE Trans. Antennas and Propagation*, Vol. 60, No. 10, 4610–4618, 2012.

Target Detection Algorithm for SAR Image Based on Visual Saliency

Huijie Xie, **Tao Tang**, **Deliang Xiang**, **and Yi Su**
College of Electronic Science and Engineering, National University of Defense Technology, China

Abstract— Based on visual saliency theory and local probability density function statistical feature, a target detection algorithm for SAR image is proposed. Local probability density function statistical feature reflects the difference between target and clutter on human vision. According to local probability density function statistical feature, saliency map of SAR image could be calculated by using hypothesis testing theory and Bayes theorem. Then target detection result could be acquired from saliency map by binary segmentation. For different kinds of real SAR images, target detections are implemented by the proposed algorithm and CFAR algorithm. The comparison of the detection results shows that the proposed algorithm detects all size-fixed targets with lower false alarm rate than CFAR algorithm.

1. INTRODUCTION

Synthetic aperture radar (SAR) is an effective instrument to obtain remote sensing information, which is also widely used on civil remote sensing and military reconnaissance. Maneuvering targets, mainly including vehicle, ship and airplane, are interesting targets on civil remote sensing and military reconnaissance. At the present stage, target detection is one of the hotspots and difficulties on SAR image interpretation, which plays an important role in civil and military application.

Constant false alarm rate (CFAR) algorithm [1–3] is a classical target detection algorithm for SAR image. CFAR algorithm is designed based on the fact that the radar cross section (RCS) of the target is larger than the RCS of the clutter. And CFAR algorithm performs efficiently in single clutter background. However, there are rather false alarms if the background is complex with buildings, trees and shadows.

For the moment, the discriminant ability of human vision system (HVS) is far better than target detection algorithm. HVS performs efficiently in image interpretation and extracts interesting target from background rapidly and effectively. For the past few years, salient region detection technique based on visual attention mechanism has been one of the significant techniques on filtrating and analyzing image data. Imitating HVS, several salient region detection algorithms [4–7] have been proposed. Saliency map [4] has been regarded as common measurement for saliency level. The algorithms based on spatial domain calculate saliency map via image features such as intensity, color, orientation, texture, gray level histogram, etc.. The algorithms based on spectrum domain calculate saliency map via the correlation between salient feature and spectrum domain of the image. However, these algorithms are designed for optical image and they should be improved for SAR image.

Considering SAR image, several ship detection algorithms [8, 9] have been proposed based on visual attention mechanism. However, these algorithms are only suitable for ship detection in sea background and they could not be applied to target detection in complex background without any modification.

In this paper, a target detection algorithm based on visual saliency has been proposed for target detection problem in complex background for SAR image. Local probability density function statistical feature is used for the proposed algorithm, which is sensitive to not only the intensity feature but also the shape and size of the target. According to local probability density function statistical feature, saliency map could be calculated by using hypothesis testing theory and Bayes theorem. And then target detection result could be acquired from saliency map by binary segmentation.

2. DESCRIPTION OF THE PROPOSED ALGORITHM

The main process of the proposed algorithm is as following. First of all, the parameter of the proposed algorithm should be determined according to the sizes of the target. And then, local saliency and global saliency of each pixel should be calculated respectively. Furthermore, saliency map could be acquired by combining local saliency map and global saliency map. At last, target detection result could be acquired from saliency map by binary segmentation.

2.1. Local Saliency Measure

In order to estimate the statistical clutter model accurately, most of CFAR algorithms set guard region between target pixel and clutter region in order to avoid the estimation being affected by target pixels. As a reference, sliding square window W of the proposed algorithm has been divided into, from inside to outside, target region, guard region and clutter region, which is shown in Fig. 1. The side length of target region w_T should be less than or equal to the width of the target in order to make sure that most of pixels in target region are target pixel.

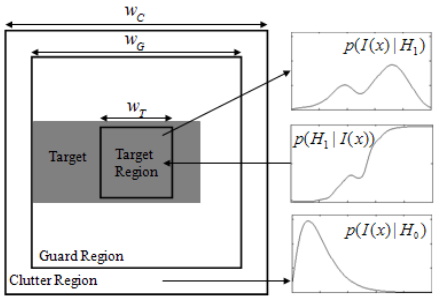

Figure 1: Sketch map of the local saliency measure.

Let $x \in \mathbf{R}^2$ be a pixel in target region and clutter region. And let $I(x)$ to be the intensity value of pixel x. Define two hypotheses as Equation (1).

$$\begin{aligned} &H_0\text{: Pixel } x \text{ is not salient.} \\ &H_1\text{: Pixel } x \text{ is salient.} \end{aligned} \tag{1}$$

And make an initial assumption as Equation (2).

$$\begin{aligned} &H_0\text{: Pixel } x \text{ is not salient.} \quad x \in \text{Clutter Region} \\ &H_1\text{: Pixel } x \text{ is salient.} \quad x \in \text{Target Region} \end{aligned} \tag{2}$$

According to the assumption, conditional probability density function of pixels in target region and clutter region could be estimated.

Based on Bayes theorem $P(A|B) = P(B|A)P(A)/P(B)$, define Equation (3).

$$p(H_1|I(x)) = \frac{p(I(x)|H_1)P(H_1)}{P(I(x))} \tag{3}$$

Since $p(I(x)) = p(I(x)|H_0)P(H_0) + p(I(x)|H_1)P(H_1)$, rewrite Equation (3) to be Equation (4).

$$p(H_1|I(x)) = \frac{p(I(x)|H_1)P(H_1)}{p(I(x)|H_0)P(H_0) + p(I(x)|H_1)P(H_1)} \tag{4}$$

where $P(H_1)$ is the prior probability of assumption H_1 and $P(H_0)$ is the prior probability of assumption H_0. It is obvious that $P(H_0) = 1 - P(H_1)$. Further discussion about H_1 would be shown in Section 3.1. Equation (4) computes the probability of H_1 for each pixel x in target region based on the assumption. Posterior probability $p(H_1|I(x))$ reflects the contrast of the pixels between target region and clutter region. Then define the local saliency measure as Equation (5).

$$S_{local}(x) = p(H_1|I(x)) \tag{5}$$

With the purpose of target detection, rewrite Equation (5) as Equation (6) because of the prior knowledge that target's RCS is larger than clutter's and that target pixel's intensity value is larger than clutter pixel's.

$$S_{local}(x) = \begin{cases} p(H_1|I(x)), & I(x|H_1) \geq \mathrm{E}[I(x|H_0)] \\ \text{Low Value}, & I(x|H_1) < \mathrm{E}[I(x|H_0)] \end{cases} \tag{6}$$

where $\mathrm{E}[I(x|H_0)]$ is the mean value of $I(x)$ in clutter region.

$$\mathrm{E}[I(x|H_0)] = \frac{1}{N}\sum\nolimits_N I(x|H_0) \tag{7}$$

Local saliency measure $S_{local}(x)$ reflects visual saliency of the pixel x in target region in a sliding window. For the target with the length l_{target} and the width w_{target}, the side length of target region w_T would be set as $w_T = w_{target}$ and the side length of guard region w_G would be set as $w_G = 2 \times l_{target} - w_{target}$ in order to assure that there is few target pixels in clutter region.

2.2. Global Saliency Measure

Local saliency measure could be calculated in a sliding window. Then global saliency measure should be calculated in the whole image. Redefine clutter region as the whole image except for target region.

$$\begin{array}{l} H_0\text{: Pixel } x \text{ is not salient.} \quad x \notin \text{Target Region} \\ H_1\text{: Pixel } x \text{ is salient.} \quad x \in \text{Target Region} \end{array} \tag{8}$$

Similar to Section 2.1, global saliency measure could be estimated as Equation (9).

$$S_{global}(x) = \begin{cases} p(H_1|I(x)), \ I(x|H_1) \geq \mathrm{E}[I(x|H_0)] \\ \text{Low Value}, \ I(x|H_1) < \mathrm{E}[I(x|H_0)] \end{cases} \tag{9}$$

where the definitions of $p(H_1|I(x))$ and $\mathrm{E}[I(x|H_0)$are same to Equation (4) and Equation (7). The difference between Equation (6) and Equation (9) is the range of clutter region.

Global saliency measure $S_{global}(x)$ reflects visual saliency of the pixel x in target region in the whole image. For the target with the length l_{target} and the width w_{target}, the side length of target region w_T would be set as $w_T = w_{target}$.

2.3. Saliency Map and Target Detection

Similar to CFAR algorithm, window $W(i)$ would be slid over the whole image with step s_W. Step s_W could be chosen from 1 to w_T. In the proposed algorithm, Step s_W is chosen as $s_W = 0.3 \times w_T$ in order to reduce the amount of calculation and preserve the edge of the target at the same time. Because sliding window $W(i)$ would overlap with each other, saliency measure $S_i(x)$ would be calculated multiple times. As shown in Equation (10), maximum of $S_i(x)$ would be chosen as the saliency measure of pixel x.

$$S(x) = \max_i \{S_i(x) | x \in W(i)\} \tag{10}$$

Using local saliency measure and global saliency measure respectively, local saliency map S_{local} and global saliency map S_{global} could be gained. In both S_{local} and S_{global}, targets possesses higher visual saliency than natural clutter. Therefore, the smaller value of $S_{local}(x)$ and $S_{global}(x)$ would be chosen as the final saliency measure $SaliencyMap(x)$.

$$SaliencyMap(x) = \min(S_{local}(x), S_{global}(x)) \tag{11}$$

In the saliency map, strong scatterer with the same size to target is salient, on the contrary clutter and scatterer with greatly different size of target are not salient. Therefore, target detection result could be easily acquired from saliency map by binary segmentation as shown in Equation (12).

$$Result(x) = \begin{cases} 1, \ SaliencyMap(x) \geq T \\ 0, \ SaliencyMap(x) < T \end{cases} \tag{12}$$

where T is the threshold value that would be discussed about in detail in Section 3.1.

3. EXPERIMENTAL RESULTS AND ANALYSIS

Experimental SAR images are acquired from the moving and stationary target acquisition and recognition (MSTAR) plan and acquired by project term via airborne X-band SAR.

3.1. Parameters Discussion about Prior Probability and Threshold Value

As shown in Equation (4), a positive correlation is obvious between posterior probability $p(H_1|I(x))$ and prior probability $p(H_1)$. Therefore, firstly prior probability $p(H_1)$ should be determined, and then threshold value T would be determined according to $p(H_1)$.

As shown in Fig. 2(a), it is an airborne X-band SAR image with the size of 684×496. There are 6 vehicle targets and a group of corner reflectors locating at twice kinds of low vegetation. The size of targets is about 39×19. And the group of corner reflectors looks like a circle whose diameter is about 9 pixels.

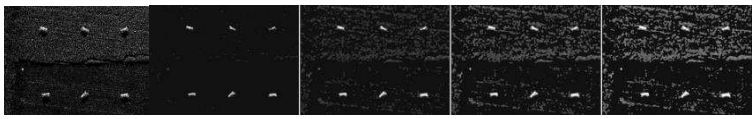

Figure 2: Original SAR image and saliency maps when the prior probability is set as 0.1, 0.2, 0.3, 0.4 respectively. (a) Original SAR image (b) $p(H_1) = 0.1$. (c) $p(H_1) = 0.2$. (d) $p(H_1) = 0.3$. (e) $p(H_1) = 0.4$.

In the experiment, the side length of target region w_T is chosen as 19 pixels. And the prior probability $p(H_1)$ is set as 0.1, 0.2, 0.3, 0.4 respectively. As a result, the saliency maps are shown in Figs. 2(b), (c), (d), (e). It is obvious that targets are more salient when the $p(H_1)$ is smaller. However, when $p(H_1)$ is too small, as shown in Fig. 2(b), the saliency of the target in top right corner has been inhibited because of its slightly incomplete outline. Moreover, the fracture and distortion of the target should be considered in a target detection algorithm for SAR image. According to the discussion as above, the prior probability $p(H_1)$ is chosen as $p(H_1) = 0.2$ in the following experiment.

When $p(H_1)$ is chosen as 0.2, the saliency map is shown in Fig. 2(c). Now the threshold value T is set as 0.6, 0.7, 0.8, 0.9 respectively. As a result, the target detection results are shown in Fig. 3. When $T = 0.6$, all targets have been detected and the group of corner reflectors has been detected as a false alarm. When $T = 0.7$ and $T = 0.8$, there is not false alarm or missing detection. When $T = 0.9$, there are missing detections. Further experiments show that there is not false alarm or missing detection when $T \in [0.64, 0.86]$. This fully shows that targets are far more salient than clutter in the saliency map, and it is easy to detect targets from saliency map by binary segmentation. According to the discussion as above, the threshold value T is chosen as $T = 0.75$ in the following experiment.

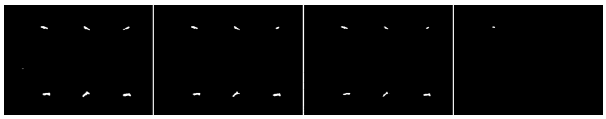

Figure 3: Target detection results when the threshold value is set as 0.6, 0.7, 0.8, 0.9 respectively. (a) $T = 0.6$. (b) $T = 0.7$. (c) $T = 0.8$. (d) $T = 0.9$.

3.2. Experiment with MSTAR Image

As shown in Fig. 4(a), it is a MSTAR image acquired via spotlight X-band SAR with the size of 1472×1784 and the resolution of $0.3\,\mathrm{m} \times 0.3\,\mathrm{m}$. There are 9 vehicle targets marked by circles and 2 unidentified scatterers marked by rectangle locating in the image. The size of targets is about 35×17. The intensity of the unidentified scatterers is almost the same to targets and the sizes of them are quite different to targets. And there are also different kinds of vegetations and shadows in the image.

Experimental parameters are determined according to Section 3.1. Saliency map and target detection result are shown in Fig. 4(b) and Fig. 4(c) respectively. As a result, the proposed algorithm detects all targets without any false alarm or missing detection.

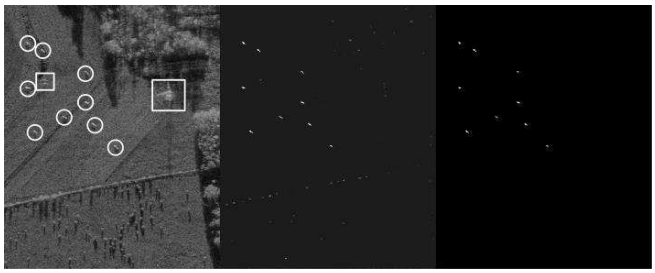

Figure 4: (a) Original MSTAR image. (b) Saliency map. (c) Target detection result.

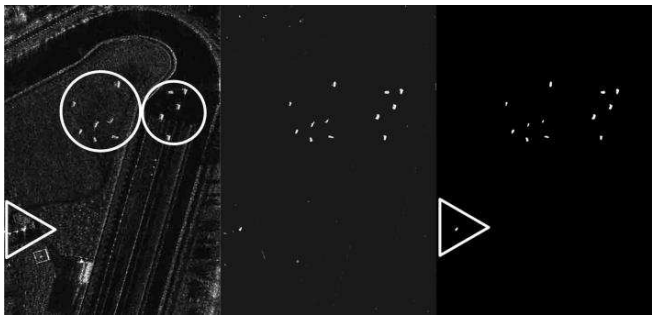

Figure 5: (a) Original airborne SAR image. (b) Saliency map. (c) Target detection result.

3.3. Experiment with Airborne SAR Image

As shown in Fig. 5(a), it is a SAR image acquired via airborne X-band SAR with the size of 587×841 and the resolution of $0.5\,\mathrm{m} \times 0.5\,\mathrm{m}$. There are 12 vehicle targets marked by circles in the image. The size of targets is about 25×11. There are also buildings, corner reflectors, trees, shadows, roadway in the image.

Experimental parameters are determined according to Section 3.1. Saliency map and target detection result are shown in Fig. 5(b) and Fig. 5(c) respectively. The proposed algorithm detects all targets without any missing detection but a false alarm. The false alarm marked by triangle is a strong scatterer with the similar size to the target. However, there is not false alarm caused by clutter.

3.4. Comparison Experiment and Analysis

The CFAR algorithm is implemented for these SAR images and the constant false alarm rate is set as 0.1%. The comparison between the proposed algorithm and CFAR algorithm is shown in Table 1. The comparison shows that the proposed algorithm detects all targets with lower false alarm rate than CFAR algorithm. Since single pixel is judged in CFAR algorithm, mini size strong scatterer, such as corner reflector, must be detected as false alarm. In the proposed algorithm, conditional probability density function $p(I(x)|H_1)$ corresponding to mini size scatterer is comparatively small, so the saliency of mini size scatterer would be inhibited.

The step of sliding window of the proposed algorithm is $s_W = 0.3 \times w_T$, and that of CFAR algorithm is $s_{CFAR} = 1$. The ratio of the proposed algorithm to CAFR algorithm on calculation times is $\eta = (2 \times s_{CFAR}^2)/s_W^2 \approx 22/w_T^2$. As for these SAR images, the proposed algorithm is far more efficient than CFAR algorithm.

Table 1: The comparison between two target detection algorithms.

	Image type	Detection rate	False alarm rate	Computing time/(s)
The proposed algorithm	Simple image	100%	0%	11.4
	MSTAR image	100%	0%	169.7
	Airborne SAR image	100%	8.3%	246.8
CFAR algorithm	Simple image	100%	16.7%	146.1
	MSTAR image	100%	211.1%	1833.1
	Airborne SAR image	100%	125%	921.3

4. CONCLUSION

In this paper, a target detection algorithm for SAR image based on visual saliency has been proposed by connecting visual saliency theory with target detection theory. This algorithm is appropriate for target detection in a SAR image with complex background, and solves the problem of CFAR algorithm that mini size strong scatterer must be detected as false alarm. As for target detection in a high resolution SAR image, the proposed algorithm has advantages such as high detection rate, low false alarm rate and fast computing.

REFERENCES

1. Di Bisceglie, M. and C. Galdi, "CFAR detection of extended objects in high-resolution SAR images," *IEEE Trans. on Geoscience and Remote Sensing,* Vol. 43, No. 4, 833–843, Apr. 2005.
2. Morgan, C. J., L. R. Moyer, and R. S. Wilson, "Optimal radar threshold determination in Weibull clutter and Gaussian noise," *IEEE Aerospace and Electronic Systems Magazines*, Vol. 11, No. 3, 41–43, Mar. 1996.
3. Gao, G., "A parzen-window-kernel-based CFAR algorithm for ship detection in SAR images," *IEEE Geoscience and Remote Sensing Letters*, Vol. 8, No. 3, 557–561, May 2011.
4. Itti, L., C. Koch, and E. Niebur, "A model of saliency-based visual attention for rapid scene analysis," *IEEE Trans. on Pattern Analysis and Machine Intelligence*, Vol. 20, No. 20, 1254–1259, Nov. 1998.
5. Harel, J., C. Koch, and P. Perona, "Graph-based visual saliency," *Advances in Neural Information Processing Systems*, Vol. 19, 545–552, 2007.
6. Hou, X. D. and L. Q. Zhang, "Saliency detection: A spectral residual approach," *IEEE Conference on Computer Vision and Pattern Recognition*, 1–8, Minneapolis, 2007.
7. Rahtu, E. and J. Heikkila, "A simple and effficient saliency detector for background subtraction," *IEEE 12th International Conference on Computer Vision Workshops*, 1137–1144, Kyoto, 2009.
8. Yu, Y., B. Wang, and L. M. Zhang, "Hebbian-based neural networks for bottom-up visual attention and its applications to ship detection in SAR images," *Neurocomputing,* Vol. 74, 2008–2017, 2011.
9. Hou, B., W. Yang, W. Shuang, et al., "SAR image ship detection based on visual attention model," *IEEE International Geoscience and Romote Sensing Symposium*, 2003–2006, Melbourne, 2013.

A New Local Feature Descriptor for SAR Image Matching

Tao Tang, Deliang Xiang, and Yi Su
College of Electronic Science & Engineering, National University of Defense Technology, Changsha, China

Abstract— Because of the weather- and illumination-independent characteristics, Synthetic Aperture Radar (SAR) has been playing a more important role for target recognition. Local stable feature descriptors in SAR image matching have been a interesting field in recent years. A new local feature extraction method like Scale Invariant Feature Transformation (SIFT) is proposed in this presentation, in which Local Gradient Ratio Pattern Histogram (LGRPH) based on SAR image similarity are taken as local feature descriptor from the neighbourhood of key points. Firstly, we extract the keypoints in difference of guassian (DoG) scale pyramid like many modified SAR-SIFT methods. Secondly, in the neighbour of kepoints, the local gradient ratio pattern histogram (LGRPH) is computed individually. Finally, the similarity is obtained by utilizing K-L discrepancy to measure the distance of LGRPH. Experimental results based on synthetic and real SAR images demonstrate that the proposed approach is robust to the speckle noise and local gradient variation in SAR images.

1. INTRODUCTION

It is important to evaluate the similarity of image or targets in remote sensing images acquired by different time or angles or sensors for image registration, change detection and image interpretation. Nowadays, local invariant feature descriptors or local stable feature descriptors has been utilized methods in optical and SAR image due to their robust similarity and repeatness, among which SIFT is the most popular one. SIFT [1] was put forward to be widely used for local feature matching in optical image and is not proper for SAR image which has different imaging mechanism and coherent speckle noise. Thereby many modification of SIFT were introduced, such as SIFT-OCT [2], SIFT+ISEF-OCT [2], SAR-SIFT [3], ISIFT [4], which have obtained good performance in SAR image. Their main contribution is as followed: (1) Abandoning the first octave of DoG pyramids, then starting keypoints detection from the second octave. It equals that SAR image should filtered by Gaussian filter, with image details and speckle smoothed. (2) The Gaussian filter was taken place of with infinite symmetric exponential filter(ISEF) [2] and bilateral filter (BF) [5] to build scale space in SAR image, while decreasing the influence of speckle towards keypoints and maintaining image details. (3) Size of the support region that is the neighbourhood of keypoints is modified from single region of size 16×16 to multiple regions in size 16×16, 24×24, and 32×32. Descriptor computed from multiple support regions could handle the mismatching error better than using only one support region [6]. All these methods should detect keypoints in coarse scale in SAR image avoiding disturbance of keypoint location and descriptor accuracy from coherent speckle, and achieve better performance of matching coherence of local feature in SAR image.

All the presentations mentioned above focus more on overcoming keypoints disturbance of speckle noise, little on local feature descriptors. While dealing with multiple noise in SAR image rather than optical image, the descriptor of SIFT is not robust which is calculated with the image gradient. A novel local feature descriptor method is proposed in this presentation, in which keypoints are located in the second octave like SAR-OCT. Then a new similarity measurement suitable for SAR image named Local Gradient Ratio Pattern Histogram (LGRPH) [7] are taken as feature descriptor for the neighbourhood of key points. Symmetry Kullback-Leibler Divergence (SKLD) [8] is used to measure the similarity of local descriptor. Experiments show that this algorithm is robust against coherent speckle noise and local gradient turbulence in SAR images, which is useful for SAR image matching and registration.

2. LOCAL FEATURE DESCRIPTOR

In SIFT-like methods mentioned above, dominant orientations for constructing local feature descriptor is computed from intensity gradient of neighbourhood around keypoints. It is not inadaptable to SAR image processing because of multiplicative speckle noise. Orientations is sensitive to local image gradient variation, which makes local descriptors invalid in matching the same local blob in different SAR image. Then local gradient ratio is proved to have ability to endurance the speckle [7]. In this paper, local gradient ratio pattern histogram (LGRPH) is proposed for local

feature descriptor for SAR image matching, which takes not only the pixel ratio feature but also the local gradient information into consideration.

In LGRP implementation [7], the Euclidean distance between the neighbour pixel intensity and centre pixel intensity is calculated and regarded as the gradient value of the former. Then the gradient ratio pattern (GRP) of the neighbour pixel is obtained, namely the ratio of the gradient value and the initial intensity of the neighbour pixel, as described in (1). The GRP of the centre pixel is regarded as the average GRPs of the neighbourhoods. After that, the LGRP operator is calculated at the centre pixel by evaluating the binary differences of the GRP values of a small neighbourhood, as described in (2) and (3)

$$G_{ratio}(I_p) = \frac{|I_p - I_c|}{I_p} \tag{1}$$

$$\overline{G_{ratio}(I_c)} = \frac{1}{P}\sum_{p=1}^{P} G_{ratio}(I_p) \tag{2}$$

$$\mathrm{LGRP}_{P,R}(I_c) = \sum_{p=0}^{P-1} s\left(G_{ratio}(I_p) - \overline{G_{ratio}(I_c)}\right) 2^p \tag{3}$$

where I_c is the centre pixel intensity and I_p is the neighbour pixel intensity. P is the number of neighbour pixels, R is the neighbour radius. $G_{ratio}(I_p)$ is the GRP of I_p and $\overline{G_{ratio}(I_c)}$ is the average GRPs of neighbour pixels, i.e., the GRP of I_c. $s(\cdot)$ is a sign function, which is defined as

$$s(x) = \begin{cases} 0 & x < 0 \\ 1 & \text{otherwise} \end{cases} \tag{4}$$

The histogram of the LGRPs is named as LGRPH. For an $N \times M$ image, LGRPH is calculated as

$$\mathrm{LGRPH}(k) = \sum_{i=1}^{N}\sum_{j=1}^{M} f(\mathrm{LGRP}_{P,R}(I_{i,j}), k) \quad k \in [0, K] \tag{5}$$

where

$$f(x, y) = \begin{cases} 1 & x = y \\ 0 & \text{otherwise} \end{cases} \tag{6}$$

K is the maximum LGRP and k is the number of bins.

We have proved that the pixel ratio measurement is robust to multiplicative noise in SAR image. Figure 1 shows how to compute LGRP value. Integrating the measurement into GRP, we can conclude that LGRPH is also insensitive to SAR image speckle. Figure 2 shows LGRPH robust with different local gradient variations, which means that the proposed feature is robust to image gradient variation and can well distinguish the background and target.

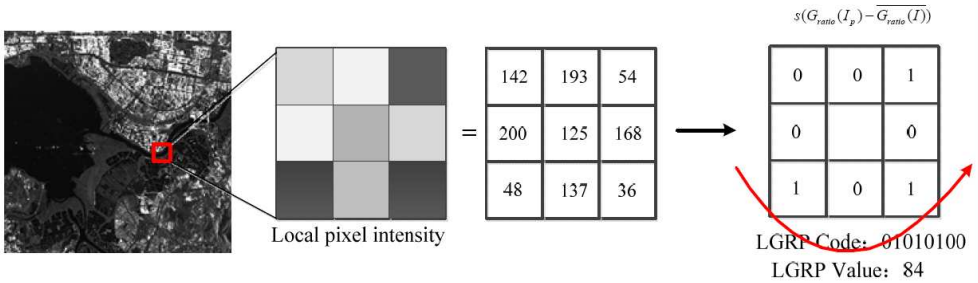

Figure 1: Calculating process of LGRP value. Red: Counter-clockwise coding.

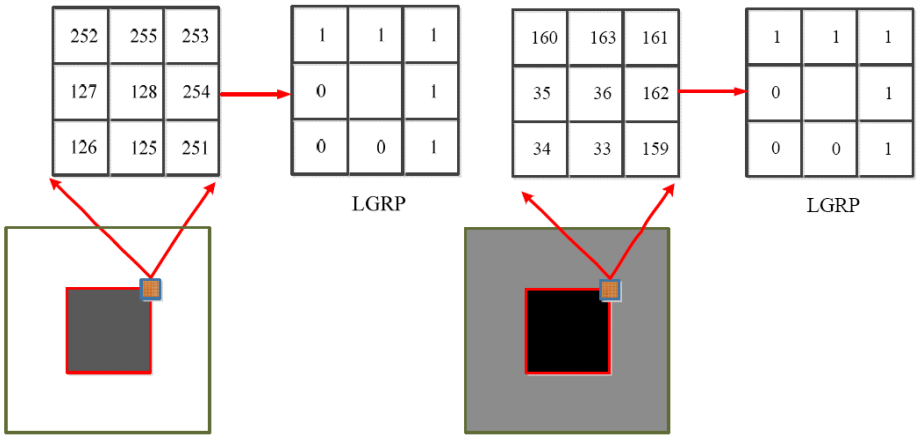

Figure 2: The stability of LGRP on local gradient variation.

3. MATCHING MESUREMENT OF LOCAL DESCRIPTORS

During matching section in SIFT, two sets of local feature descriptor around keypoints could be established correspondence by a matching strategy according to popper descriptor measurements. Similarity measure plays a key role in pattern recognition, the test pattern should be compared with the template pattern and a similarity value is obtained as the recognition criterion. Since we can extract the LGRPH vector from neighbourhood of any keypoint in SAR images, in this paper, Symmetry Kullback-Leibler Divergence (SKLD) is used to measure the similarity of two different sets of LGRPH vector. For two LGRPH vector H and Q, SKLD is defined as

$$\mathrm{SKLD}(H,Q) = \sum_{n=1}^{N} p_n \log\left(\frac{p_n}{q_n}\right) + \sum_{n=1}^{N} q_n \log\left(\frac{q_n}{p_n}\right) \tag{7}$$

where p_n and q_n are the feature vectors of H and Q, N is the feature dimension. Since the similarity ranges from 0 to 1, SKLD should be mapped as a rational normalized relativity. Using Gaussian function, we define the similarity as

$$Similarity = \exp\left(-\frac{[\mathrm{SKLD}(H,Q)]^2}{\sigma^2}\right) \tag{8}$$

where σ is the parameter which controls the width of Gaussian function and the relation between feature divergence and similarity.

After similarity being computed, keypoints matching whose descriptor is named LGPRH is concerned in this paper. Different SAR image matching would turn into different local keypoints sets matching through local feature descriptor and proper correspondence strategy. We choose Random Sample Consensus (RANSAC) to estimated the transformation parameters from established local descriptors correspondence.

4. LOCAL FEATURE EXTRACTION AND MATCHING IN SAR IMAGE

For SAR image matching, this paper proposes a local feature extraction method including three parts like SIFT: (i) keypoints detection and localization; (ii) local feature description; (iii) keypoints matching. In the first step keypoints are detected and located by DoG detector of SIFT skipping the first octave of the scale space pyramid. In the second step LGRPH is used as local descriptor detailed in Section 2. In the last step similarity measurement and correspondence of keypoint sets form reference and test SAR image are computed to realize SAR image matching. Figure 3 shows the whole method processing procedure.

5. EXPERIMENT RESULT

In this section, real SAR image with different imaging direction is used to test performance of the proposed method and SIFT and SIFT-OCT.

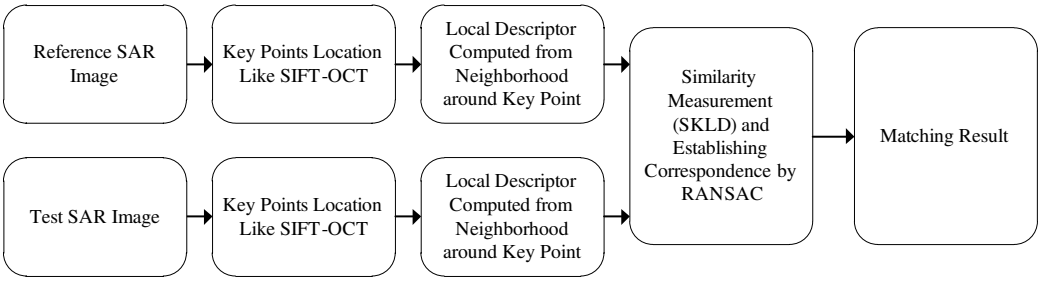

Figure 3: SAR image matching with proposed method.

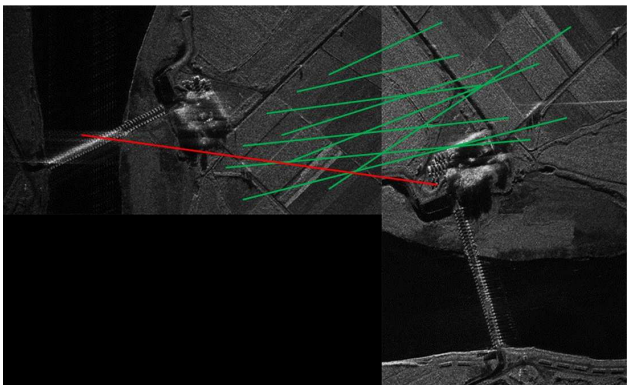

Figure 4: Matching of different SAR image. Green: correct matching. Red: error matching.

The left image and right image were imaged from different directions by airborne SAR in 2013, with the resolution 1 m × 1 m. Table 1 shows the result of experiment using test method and traditional methods.

According to the experiment result, the proposed method can detect correct matching pairs much more than compared methods. It shows that LGRPH is a stable local descriptor and similarity matching strategy is proper. The computation load of proposed method is nearly to SIFT, but more than SIFT-OCT. It is to save computation time that the first octave is skipped in scale space to overcome speckle noise in SIFT-OCT and the proposed method, while computation of LGRPH costs more time than orientation assignment in SIFT.

Table 1: Result of our method and other methods.

Method	**SIFT**	**SIFT-OCT**	**Proposed Method**
Matching pairs/all keypoints num.	**1/338**	**39/64**	**10/64**
Correct matching pairs	0	6	9
Computation time (second)*	11.434	8.653	12.247

The computer is equipped with AMD X2 255 (3.1 GHz CPU) and 2G RAM.

6. CONCLUSION

A new local feature descriptor named LGPRH is introduced for SAR image matching in this paper. Then a SIFT-like method is presented in which LGPRH takes place of the orientation assignment as local descriptor in SIFT. The local image intensity and gradient information are both taken into consideration in this method. Since LGRPH is insensitive to multiplicative speckle noise, LGRPH is adapted to the images with gradient variation which is the common phenomenon in real SAR images and significantly influences matching performance. The experimental results show that the proposed method has a high matching rate. Future work will focus on accuracy of keypoint detection and location and adaptability of this local descriptor on SAR images with various disturb conditions, such as the images with distortion, serious shadow. And more experiments using larger

real data sets will be done for further validation.

REFERENCES

1. Lowe, D., "Distinctive image features from scale-invariant keypoints," *International Journal of Computer Vision*, Vol. 20, 91–110, 2004.
2. Schwind, P., S. Suri, P. Reinartz, and A. Siebert, "Applicability of the SIFT operator to geometric SAR image registration," *Int. J. of Remote Sensing*, Vol. 31, No. 8, 1959–1980, 2010.
3. Dellinger, F., J. Delon, Y. Gousseau, J. Michel, and F. Tupin, "SAR-SIFT: A SIFT-like algorithm for application on SAR images," *Proc. IGRASS 2012*, 3478–3481, Munich, 2012.
4. Ren, S., W. Chang, and X. Liu, "SAR image matching method based on improved SIFT for navigation system," *Progress In Electromagnetics Research M*, Vol. 18, 259–269, 2011.
5. Wang, S.-H., H.-J. You, and K. Fu, "An automatic method for finding matches in SAR images based on coarser scale bilateral filtering SIFT," *Journal of Electronics and Information Technology*, Vol. 34, No. 2, 287–293, 2012.
6. Fan, B., C. Huo, C. Pan, et al., "Registration of optical and SAR satellite images by exploring the spatial relationship of the improved SIFT," *IEEE Geoscience and Remote Sensing Letter*, Vol. 10, No. 4, 657–661, 2013.
7. Yuan, X., T. Tang, D. Xiang, et al., "Target recognition in SAR imagery based on local gradient ratio pattern," *International Journal of Remote Sensing*, Vol. 35, No. 3, 857–870, 2014.
8. Li, L., C. S. Tong, and S. K. Choy, "Texture classification using refined histogram," *IEEE Transactions on Image Processing*, Vol. 19, No. 5, 1371–1378, 2010.

A Dual-band Dual-polarized Antenna and a Switchable Multi-beam Antenna Array

Yu Long, Jun Ouyang, Zeyang Tian, and Yuan Zhang
School of Electronic Engineering, University of Electronic Science and Technology of China
Chengdu, Sichuan 611731, China

Abstract— A dual-band, dual-polarized antenna and a switchable multi-beam antenna array are introduced in this paper. Composed of two orthogonal annular dipoles, the proposed ±45° polarization diversity antenna has two simulated impedance bands: 2.39 GHz ∼ 2.85 GHz and 3.39 GHz ∼ 3.97 GHz, with VSRS < 1.5 and isolation > 28.5 dB. The simulated gain of the antenna is 8.5 dBi at the lower frequency band, and 9.1 dBi at the higher frequency band. In order to compose a $5 * 3$ polarization diversity antenna array, two 3-to-15 feed networks are employed and placed together, one for each polarization. The whole feed network is manufactured using microwave substrate AD255C with thickness of 0.762 mm and dielectric constant of $\varepsilon_r = 2.55$ and its size is limited to 340 mm ∗ 200 mm ∗ 30 mm. The output phase as well as the amplitude of each output port of each network is identical. To realize switchable multi-beam capability in horizontal plane, two microwave switches are used for the array. Connected to 3 out of 6 input ports, one switch has 4 gears and the input phase of the feed network is selected from 4 groups of fixed values. Thus the input phase of the antenna elements can be controlled. In other words, this antenna array can radiate at 4 different angles (within ±30° at 2.6 GHz), yet not simultaneously. Simulated results of the antenna and antenna arrays are presented and discussed. Both the return loss, port isolation and the gain are good enough for civil communication applications.

1. INTRODUCTION

In recent years, the tremendous development of electronic science has greatly pushed wireless communication technology forward to satisfy the increasing demands for various wireless communication services such as cellular networks for 3G/4G mobile phones, WiFi and WiMax. As a key factor of wireless communication, base station antennas are consequently put in the face of challenges for wider bandwidth, higher gain and more channel capacity. Since a dual-polarized (usually ±45° polarized) antenna owes an inherent advantage over a linear one in channel capacity and multi-path effects, it has been widely employed in mobile communication base station applications. Meanwhile, if the space available is limited or greater channel capacity is expected, a dual-band antenna then can be very helpful.

A classical way to obtain a ±45° polarized microstrip antenna is to use two excitation sources on the diagonal lines of the patch [1], but the bandwidth is often limited even if stack patches are brought in to provide extra resonance. Transformed dipole antennas have been proved to have a much wider impedance bandwidth than a regular dipole in previously studies [2–4]. By using a cross-pair of such dipoles it can be down to simultaneously obtain two orthogonal polarizations. None of these studies, however, have looked into antenna arrays yet most realistic base antennas are basically arrays. In this paper, a $5 * 3$ antenna array using the proposed dual-band dual-polarized annular dipole-pair antenna as its element is presented. To make the array produce switchable, multiple beams, a power-dividing phase-shifting microwave switch is used to control the input phase of the feed network, thus the beams is able to cover a certain range in the horizontal plane.

2. DUAL-BAND DUAL-POLARIZED ANNULAR DIPOLE-PAIR ANTENNA

Shown in Fig. 1 is the proposed antenna consisting of two orthogonal annular dipoles for each polarization. Due to mirror image principle, these two dipoles are about 1/4 wavelength away from ground plane with the help of a substrate post made of Teflon with relative permittivity $\varepsilon_r = 2.1$. Each dipole employs a 50 Ω coax as its feed. The outer conduct connects to one arm of the dipole and the inner conduct to the other by using a metal bridge. And a hole is drilled at the center of the post to let the coaxes through.

The S parameters of the antenna are both simulated using Ansoft HFSS and measured with Agilent vector network analyzer. As plotted in Fig. 2, since these two dipoles are not exactly the same (due to excitation matters), simulated S_{11} and S_{22} don't agree very well especially at the higher frequency band, both of them, however, are lower than −14 dB (i.e., VSWR < 1.5)

within frequency bands 2.39 GHz ∼ 2.85 GHz and 3.39 GHz ∼ 3.97 GHz. If VSWR < 2 bandwidth is required instead of VSWR < 1.5, the dual-band dual-polarized antenna becomes a wideband polarization diversity antenna with its frequency band from 2.30 GHz to 4.18 GHz. That's 58% in terms of relative bandwidth. Certainly, this antenna can also be designed to have a wideband other than two spate bands even if VSWR is required to be less than 1.5 [4], but that is not the aim of this paper. As the vertical gap between two bridges inevitably differs from the simulating model because of the narrow space and some practical matter when soldering, the resultant S_{21} also deviate from the simulated one a lot, yet it still remains −20 dB below (not shown in the picture) which is good enough for civil use.

Simulated far field radiation patterns when only one dipole is actually excited are shown in Fig. 3

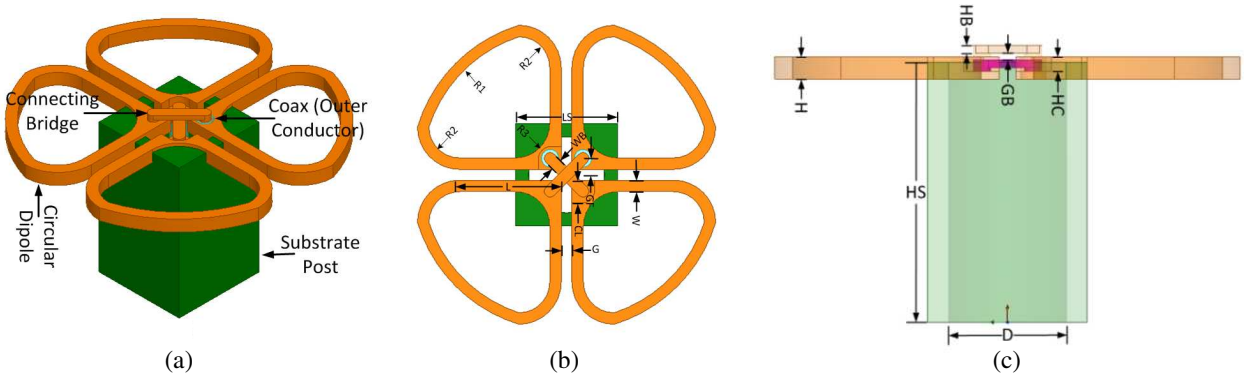

Figure 1: Antenna structure and geometry dimensions. (a) Overall structure. (b) Vertical view. (c) Lateral view. Primary dimension parameters (mm): $L = 10.4$; $W = 1.6$; $WB = 0.8$; $G = 1.5$; $GF = 2.3$; $GB = 0.6$; $R1 = 19.7$; $R2 = 4.3$; $R3 = 4.8$; $H = 2$; $HB = 0.7$; $HC = 1.3$; $HS = 23.2$; $D = 5.3$.

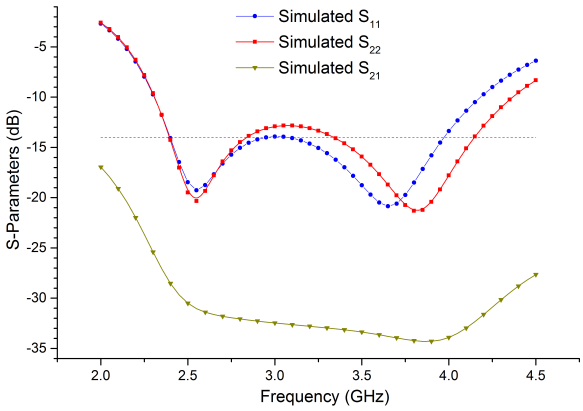

Figure 2: Simulated S parameters.

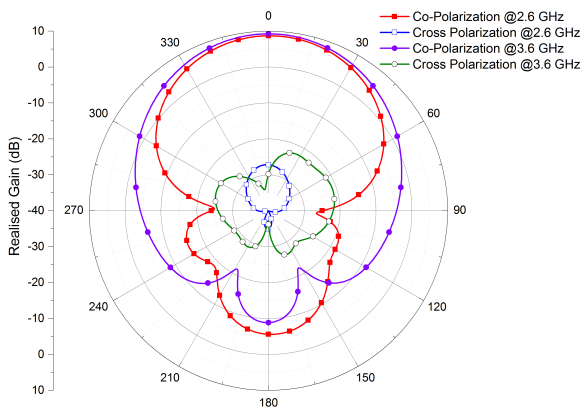

Figure 3: Simulated far field radiation pattern.

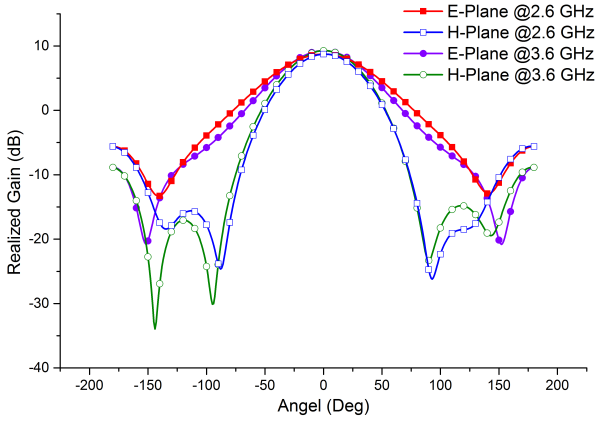

Figure 4: Simulated gain in E-plane and H-plane.

and Fig. 4 at 2.6 GHz and 3.6 GHz. The peak gain is better than 8.5 dB and 9.1 dB respectively. In E-plane, the 3-dB beamwidths at 2.6 GHz and 3.6 GHz are 60.5° and 61.5°, while in H-plane are 83.7° and 67.7°. This dipole also owes a low cross-polarization in both E-plane and H-plane. At 2.6 GHz, it is −25 dB below, and is even better (< −35 dB) at 3.6 GHz.

3. PIMARY DUAL-POLARIZED ANTENNA ARRAY

The primary $5 * 3$ antenna array and the corresponding feed network is shown in Fig. 5. This feed network is designed and manufactured on substrate AD255C with thickness of 0.762 mm and dielectric constant of $\varepsilon_r = 2.55$. It has 3 input ports on both sides and each side feeds one polarization. The input phase of each port of antenna elements is in phase since the feed network is not supposed to produce switchable multiple beams if the switch is not connected. In horizontal plane the power distribution is equal at each port because only 3 antenna elements are placed in this plane, making it very difficult for this specific distribution to come into force.

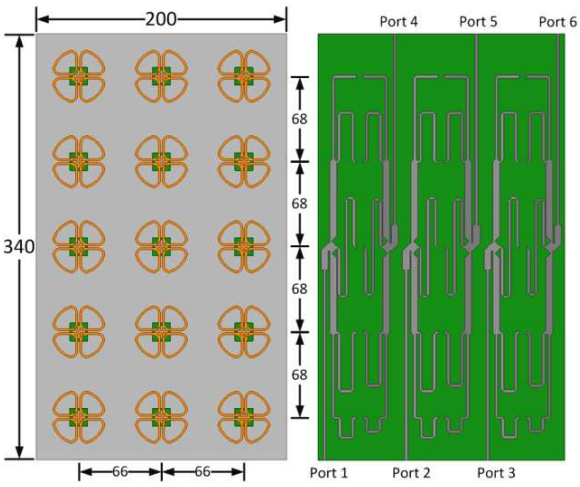

Figure 5: Primary antenna array and feed network. Dimensions are in mm.

4. SWITCHABLE MULTIBEAM DUAL-POLARIZED ANTENNA ARRAY

We designed a switch that has 4 gears and distributes the input power equally to 3 out ports. The gears are controlled by two control level C1 and C0. Once C1 and C0 are determined, the input phase of the feed network is then selected from 4 groups of values to control the input phase of the antenna elements. In other words, this antenna array can radiate at 4 different angles (shown in Table 1) to cover ±30° range in the horizontal plane at 2.6 GHz, yet not simultaneously. As this paper emphasizes on the antenna and antenna array instead of microwave circuits, further details of this switch are omitted here. The whole manufactured antenna array together with the switches connected to the feed network is shown in Fig. 6. Due to our hasty time, we are not able carry out the experiments to get the measured radiation patterns in time, so only simulated far filed results in horizontal plane are presented (see Fig. 7 and Fig. 8). It's clear from these results that the array successfully to obtain gain that is over 16.5 dB within the whole range.

Table 1: The output phase of the switch at 2.6 GHz.

Beam No.	Beam angel (°)	Control level		Output phase (°)	
		C1	C0	Simulated	Measured
Beam 1	21.3	0	0	0/−60/−160	0/−55.4/−159.7
Beam 2	7.6	0	1	0/−60/−60	0/−60.0/−60.2
Beam 3	−8.1	1	0	0/60/60	0/62.7/59.8
Beam 4	−21.2	1	1	0/60/160	0/61.7/161.8

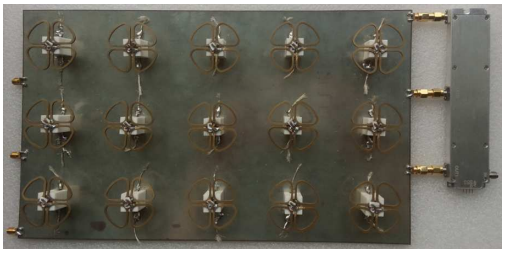

Figure 6: Manufactured antenna array and switch.

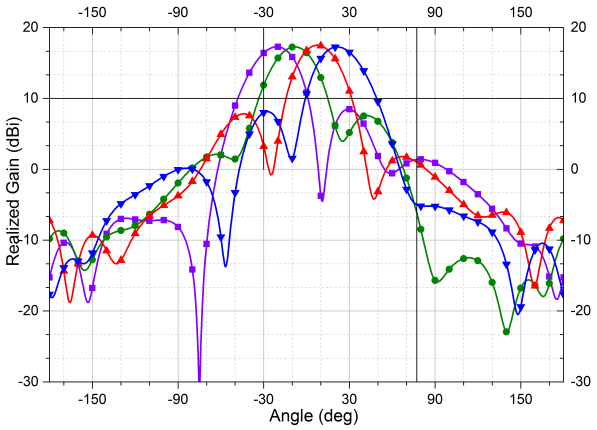

Figure 7: Figure 1 simulated gain of the antenna array.

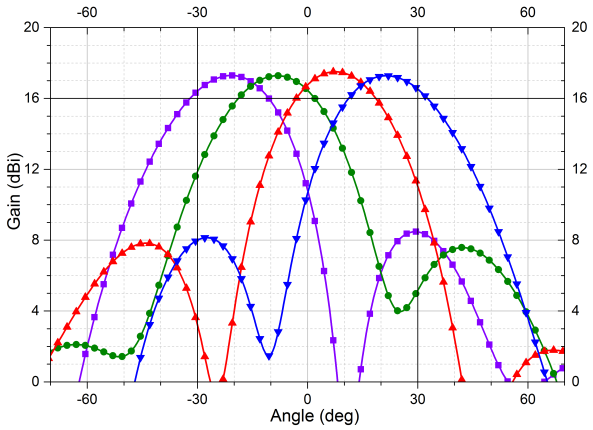

Figure 8: Detailed simulated gain of the antenna array.

5. CONCLUSION

A dual-band dual polarized antenna composed of two orthogonal annular dipoles with high isolation and low cross polarization is presented in this paper. To demonstrate its use in wireless communication base stations, a polarization diversity antenna array is introduced which employs the proposed antenna as its element. Besides, two microwave switches with equal output power and four group of fixed output phase are connected to the feed network in order to make the array produce four selective multiple beams. Simulated results show that these beams manage to cover the $\pm 30^\circ$ range in horizontal plane with gain over 16.5 dB.

REFERENCES

1. Gao, S., L. W. Li, M. S. Leong, and T. S. Yeo, "A broad-band dual-polarized microstrip patch antenna with aperture coupling," *IEEE Transactions on Antennas and Propagation*, Vol. 51, No. 4, 898–900, 2003.
2. Su, D., J. J. Qian, H. Yang, and D. Fu, "A novel broadband polarization diversity antenna using a cross-pair of folded dipoles," *IEEE Antennas and Wireless Propagation Letters*, Vol. 4, 433–435, 2005.
3. Siu, L., H. Wong, and K. Luk, "A dual-polarized magneto-electric dipole with dielectric loading," *IEEE Transactions on Antennas and Propagation*, Vol. 57, No. 3, 616–623, 2009.
4. Bao, Z., Z. Nie, and X. Zong, "A novel broadband dual-polarization antenna with high isolation," *IEEE Antennas and Propagation Society International Symposium (APSURSI)*, 1304–1305, 2013.

Design and Analysis of Planar Phased MIMO Antenna for Radar Applications

Nour El-Din Ismail, Sherif Hanafy Mahmoud, Ahmed Hamed, and Alaa Hafez
Faculty of Engineering, Alexandria University, Alexandria, Egypt

Abstract— Phased-multiple-input multiple-output (phased-MIMO) radar using one-dimensional transmit arrays has been thoroughly investigated in the literature. In this paper, we consider two-dimensional phased-MIMO radar array which is called planar-phased-MIMO radar. This new technique aggregates the advantages of the linear-phased-MIMO radar without sacrificing either the main advantage of the planar-phased-array radar, which is the coherent processing gain, or the main advantage of the planar MIMO array radar, which is the diversity processing gain. The essence of the proposed technique is to partition the planar transmit array into a number of planar subarrays that are allowed to overlap. Then, each subarray is used to coherently transmit a waveform which is orthogonal to the waveforms transmitted by other subarrays. Coherent processing gain can be achieved by designing a weight matrix for each subarray to form a beam towards a certain direction in space. Moreover, the subarrays are combined jointly to form a planar-MIMO radar resulting in higher angular resolution capabilities. Substantial improvements is offered by the proposed planar-phased-MIMO radar technique with respect to the linear-phased-MIMO, planar-MIMO and planar-phased-array radar techniques. The achieved improvements are demonstrated analytically and by simulations through analyzing the corresponding beampatterns, the resultant peak side lobe level, mean side lobe level, and directivity. Both analytical and simulation results validate the effectiveness of the proposed planar-phased-MIMO radar.

1. INTRODUCTION

Phased-array technique have been widely employed in different radars to provide electronic beam steering of radiated or received electromagnetic signals operating at the same frequency [1–3]. Controlling the phase shifts across elements, the beam can be steered to the desired direction. Detecting/tracking weak target echoes and suppressing sidelobe interferences from other directions can be obtained due to its high directional gain. The desire for new more advanced antenna array technologies has been derived by the requirements of many emerging applications [4–8]. Multiple input multiple output (MIMO) radar systems are next-generation radar systems with multiple transmit and receive apertures, equipped with the capability of transmitting arbitrary and differing signals at each transmit aperture. The emerging MIMO radar literature can be broken into two broad areas. The first is characterized by spatially distributed assets that are not phase-coherent on transmitting or receiving, that takes advantage of spatial diversity to gain multiple views of a target and achieves improving in stability of statistical hypothesis tests for target detection. These approaches are often characterized as statistical MIMO. Fishler et al. [9] introduces the statistical MIMO radar concept which provides great improvements over other types of array radars. Haimovich et al. [10] reviews some recent work on MIMO radar with widely separated antennas and it is shown that with noncoherent processing, a target's RCS spatial variations can be exploited to obtain a diversity gain for target detection. Bliss et al. [11], describes the theory behind the improved surveillance radar performance and illustrates this with measurements from experimental MIMO radars. In contrast, there is a MIMO radar literature built around an assumption of colocated assets like one might find with an antenna array or phased-array radar.

Much interesting work has been done in this arena by other researches [12–14] introduce performance advantages of colocated MIMO radars.

A. Hassanien et al. [15] proposes a new technique for MIMO radar with colocated antennas which called linear phased-MIMO radar. This technique enjoys the advantages of the MIMO radar without sacrificing the main advantage of the phased-array radar which is the coherent processing gain at the transmitting side. This paper studies the design of a new technique for partition the planar transmit array into a number of planar subarrays that are allowed to overlap. Each subarray is used to coherently transmit a waveform which is orthogonal to the waveforms transmitted by other subarrays. Then, compares this design with previous techniques through analyzing the corresponding beampatterns, and directivity. Significant improvements offered by the planar-phased-MIMO radar technique.

2. PLANNER PHASED-MIMO MODEL

In this section, the transmit array is divided into multiple $(K \times L)$ subarrays which can be disjoint or overlapped, as shown in Figure 1. Each transmit sub-array can be composed of any number of elements ranging from 1×1 to $M \times N$. However, we will partition the sub-array with different values of $K \times L$ with different numbers of transmitting elements in each sub-array following the rule $M_{KL} = M_K \times N_L$ where $M_K = (M - K + 1)$, $N_L = (N - L + 1)$ and M_{KL} is the number of elements in each sub-array. A beam can be formed by each sub-array towards a certain direction. The beamforming weight vector can be properly designed to maximize the coherent processing gain [16]. At the same time, different waveforms are transmitted by different sub-arrays. Suppose the (k,l)th sub array consists of $M_{KL} < MN$ transmit elements, the equivalent baseband signal model of the (k,l)th sub array can be modeled as,

$$S_{k,l}(t) = \sqrt{\frac{MN}{KL}}\psi_{k,l}(t)\tilde{w}^*_{k,l} \quad k = 1,2,\ldots,K; \quad l = 1,2,\ldots,L \tag{1}$$

where $K \times L$ is the number of sub-arrays, $\tilde{W}_{k,l}$ is the $M \times N$ unit-norm complex matrix which consists of M_{KL} beamforming weights corresponding to the active antennas of the (k,l)th sub-array, that is, the number of nonzero in $\tilde{W}_{k,l}$ equals to M_{KL} and the number of zeros equals to $(M \times N) - M_{KL}$. Note that $\sqrt{MN/KL}$ is used to obtain an identical transmission power constraint for subsequent comparison, which means the transmit energy within one pulse repetition interval (PRI) is given by

$$E_{k,l} = \int_{Tp} S^H_{k,l}(t)S_{k,l}(t)dt = \frac{MN}{KL} \tag{2}$$

This means that the total transmitted energy for the phased-MIMO radar within one radar pulse is equal to MN [17]. The signal reflected by a hypothetical target located at direction in the far-field can be then modeled as

$$\begin{aligned} S_{r(t,\theta,\emptyset)} &= \sqrt{\frac{MN}{KL}}\sigma_s(\theta,\emptyset)\sum\nolimits_{k=1}^{K}\sum\nolimits_{l=1}^{L}\tilde{W}^*_{k,l}\tilde{a}_{k,l}(\theta,\emptyset)\psi_{k,l}(t) \\ &= \sqrt{\frac{MN}{KL}}\sigma_s(\theta,\emptyset)\sum\nolimits_{k=1}^{K}\sum\nolimits_{l=1}^{L}W^*_{k,l}a_{k,l}(\theta,\emptyset)e^{-j\tau_{k,l}(\theta,\emptyset)}\psi_{k,l}(t) \end{aligned} \tag{3}$$

where σ_s is the reflection coefficient of the hypothetical target, $W_{k,l}$ and $a_{k,l}(\theta,\emptyset)$ are the $M_K \times N_L$ beamforming matrix and transmit steering matrix, respectively, which contain only the elements corresponding to the active antennas of the (k,l)th sub-array, $\tau_{k,l}(\theta,\emptyset)$ is the time required for the

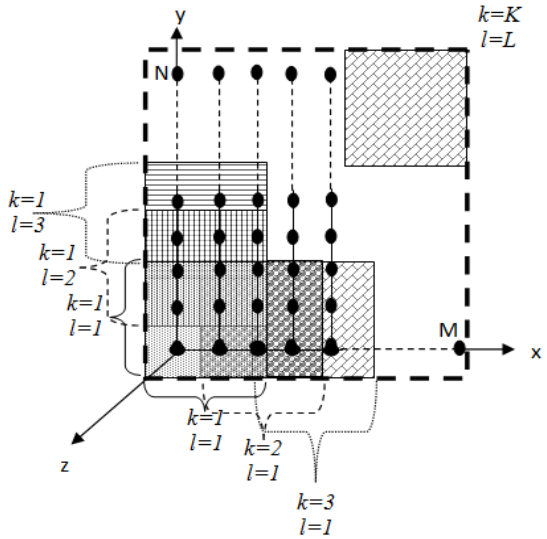

Figure 1: Illustration of the planar phased-MIMO array.

wave to travel across the spatial displacement between the first element of the transmit array and the first element of the (k,l)th sub-array, and stands for the Hadamard (element-wise) product. In (3), we assume that the first element of $a_{k,l}(\theta,\emptyset)$ is taken as a reference element. Let us introduce the $K \times L$ transmit coherent processing matrix.

$$C(\theta,\emptyset) = \begin{bmatrix} \sum_{m_k=1}^{M_K}\sum_{n_l=1}^{N_L} W_{1,1}^{*} a_{1,1}(\theta,\emptyset) & \cdots & \sum_{m_k=1}^{M_K}\sum_{n_l=1}^{N_L} W_{1,L}^{*} a_{1,L}(\theta,\emptyset) \\ \vdots & \ddots & \vdots \\ \sum_{m_k=1}^{M_K}\sum_{n_l=1}^{N_L} W_{K,1}^{*} a_{K,1}(\theta,\emptyset) & \cdots & \sum_{m_k=1}^{M_K}\sum_{n_l=1}^{N_L} W_{K,L}^{*} a_{K,L}(\theta,\emptyset) \end{bmatrix} \tag{4}$$

where $m_k = 1,\ldots,M_K$ and $n_l = 1,\ldots,N_L$ are the orders of elements in each subarray in x-direction and y-direction respectively.

The $K \times L$ waveform diversity matrix is

$$d(\theta,\emptyset) = \begin{bmatrix} e^{-j\tau_{1,1}(\theta,\emptyset)} & \cdots & e^{-j\tau_{1,L}(\theta,\emptyset)} \\ \vdots & \ddots & \vdots \\ e^{-j\tau_{K,1}(\theta,\emptyset)} & \cdots & e^{-j\tau_{K,L}(\theta,\emptyset)} \end{bmatrix} \tag{5}$$

Then, the reflected signal (3) can be rewritten as,

$$S_{r(t,\theta,\emptyset)} = \sqrt{\frac{MN}{KL}}\sigma(\theta,\emptyset)\left(C(\theta,\emptyset)\odot d(\theta,\emptyset)\right)\odot\psi_{k,l}(t) \tag{6}$$

where $\psi_{k,l}(t) = \begin{bmatrix} \psi_{1,1}(t) & \cdots & \psi_{1,L}(t) \\ \vdots & \ddots & \vdots \\ \psi_{K,1}(t) & \cdots & \psi_{K,L}(t) \end{bmatrix}$ is the $K \times L$ matrix of waveforms. Assuming that the target of interest is observed in the background of D interfering targets with reflection coefficient $\{\sigma_i\}_{i=1}^{D}$ and locations $\{\theta_i,\emptyset_i\}_{i=1}^{D}$, the $M_r \times N_r$ received complex matrix of array observations can be written as,

$$X(t) = S_r(t,\theta_s,\emptyset_s)\,b(\theta_s,\emptyset_s) + \sum_{i=1}^{D} S_r(t,\theta_i,\emptyset_i)\,b(\theta_i,\emptyset_i) + n(t) \tag{7}$$

where $S_r(t,\theta_s,\emptyset_s)$ and $S_r(t,\theta_i,\emptyset_i)$ are defined as in (6) and $b(\theta,\emptyset)$ is the receive steering matrix associated at angles $(\theta,\emptyset)$. By matched-filtering $X(t)$ to each of the waveforms $\{\psi_{k,l}\}_{k,l=1,1}^{K,L}$ we can form the $KM_r \times LN_r$ virtual data matrix,

$$y = \begin{bmatrix} X_{1,1} & \cdots & X_{1,L} \\ \vdots & \ddots & \vdots \\ X_{K,1} & \cdots & X_{K,L} \end{bmatrix} = \sqrt{\frac{MN}{KL}}\sigma_s u(\theta_s,\emptyset_s) + \sum\nolimits_{i=1}^{D}\sqrt{\frac{MN}{KL}}\sigma_i u(\theta_i,\emptyset_i) + \tilde{n} \tag{8}$$

where the $KM_r \times LN_r$ matrix

$$u(\theta,\emptyset) = (c(\theta,\emptyset)\odot d(\theta,\emptyset))\otimes b(\theta,\emptyset) \tag{9}$$

is the virtual steering matrix associated with direction $(\theta,\emptyset)$ and $\tilde{n}$ is the $KM_r \times LN_r$ noise term (noise received by $M_r \times N_r$ receivers containing KL matched filters at each receiver) whose covariance is given by $\tilde{R}_n = \sigma_n^2 I_{KM_rLN_r}$ where σ_n^2 is the noise power.

2.1. Planar Phased-MIMO Beamforming

In the case of non-adaptive beamforming, the corresponding conventional beamforming weight matrix is given for the (k,l)th transmitting subarray as [18]:

$$w_{k,l} = \frac{a_{k,l}(\theta_s,\emptyset_s)}{\|a_{k,l}(\theta_s,\emptyset_s)\|_F} = \frac{a_{k,l}(\theta_s,\emptyset s)}{\sqrt{M-k+1}\sqrt{N-l+1}}, \quad k = 1,\ldots,K \quad l = 1,\ldots,L \tag{10}$$

where $\|a_{k,l}(\theta_s,\emptyset_s)\|_F$ is the Frobenius of matrix $a_{k,l}(\theta_s,\emptyset_s)$ and equals to $\sqrt{\sum_{i=1}^{M-k+1}\sum_{j=1}^{N-l+1}\left(a_{i,j}(\theta_s,\emptyset_s)\right)^2}$.

For the receiving array, the conventional beamforming weight matrix is given by:

$$w_d = [c(\theta_s, \emptyset_s) \odot d(\theta_s, \emptyset_s)] \otimes b(\theta_s, \emptyset_s) \tag{11}$$

Let $G(\theta, \emptyset)$ be the normalized beampattern

$$G(\theta,\emptyset) = \frac{\left|\sum_1^{KM_r}\sum_1^{LN_r}\left(w_d^* \odot u(\theta,\emptyset)\right)\right|^2}{\left|\sum_1^{KM_r}\sum_1^{LN_r}\left(w_d^* \odot u(\theta_s,\emptyset_s)\right)\right|^2} = \frac{\left|\sum_1^{KM_r}\sum_1^{LN_r}\left(u^*(\theta_s,\emptyset_s) \odot u(\theta,\emptyset)\right)\right|^2}{\|u(\theta_s,\emptyset_s)\|_F^4} \tag{12}$$

Considering the special case of a uniform planar array (UPA), we have $\sum_1^{M_K}\sum_1^{N_L} a_{1,1}^*(\theta_s,\emptyset_s) \odot a_{1,1}(\theta,\emptyset) = \sum_1^{M_K}\sum_1^{N_L} a_{1,2}^*(\theta_s,\emptyset_s) \odot a_{1,2}(\theta,\emptyset) = \ldots = \sum_1^{M_K}\sum_1^{N_L} a_{2,1}^*(\theta_s,\emptyset_s) \odot a_{2,1}(\theta,\emptyset) = \ldots = \sum_1^{M_K}\sum_1^{N_L} a_{K,L}^*(\theta_s,\emptyset_s) \odot a_{K,L}(\theta,\emptyset)$.

Using (12), the beampattern of the phased-MIMO radar for UPA with partitioning to KL transmit sub-arrays can be written as

$$G_{k,L}(\theta,\emptyset) = \frac{\left|\left(\sum_1^{M_K}\sum_1^{N_L}\left(a_{k,l}^*(\theta_s,\emptyset_s) \odot a_{k,l}(\theta,\emptyset)\right)\right)\left(\sum_1^{KM_r}\sum_1^{LN_r}\left[\left(d(\theta_s,\emptyset_s)\otimes b(\theta_s,\emptyset_s)\right)^* \odot \left(d(\theta,\emptyset)\otimes b(\theta,\emptyset)\right)\right]\right)\right|^2}{\left\|a_{k,l}^*(\theta_s,\emptyset_s)\right\|_F^4 \|d(\theta_s,\emptyset_s)\otimes b(\theta_s,\emptyset_s)\|_F^4} \tag{13}$$

After some algebra and using the facts that $\|a_{K,l}(\theta_s,\emptyset_s)\|_F^2 = (M-K+1)(N-L+1)$, $\|d(\theta_s,\emptyset_s)\|_F^2 = KL$, and $\|b(\theta_s,\emptyset_s)\|_F^2 = M_rN_r$, the beampattern (13) can be rewritten as

$$G_{k,L}(\theta,\emptyset) = C_{k,L}(\theta,\emptyset) D_{k,L}(\theta,\emptyset) \cdot R(\theta,\emptyset) \tag{14}$$

where $C_{k,L}(\theta,\emptyset) \triangleq \frac{|\sum_1^{M_K}\sum_1^{N_L} a_{k,l}^*(\theta_s,\emptyset_s)\odot a_{k,l}(\theta,\emptyset)|^2}{(M-K+1)^2(N-L+1)^2}$ is the transmit beampattern, $D_{k,L}(\theta,\emptyset) \triangleq \frac{|\sum_1^{K}\sum_1^{L} d_{k,l}^*(\theta_s,\emptyset_s)\odot d_{k,l}(\theta,\emptyset)|^2}{K^2L^2}$ is the waveform diversity beampattern, and $R(\theta,\emptyset) \triangleq \frac{|\sum_1^{M_r}\sum_1^{N_r} b^*(\theta_s,\emptyset_s) \odot b(\theta,\emptyset)|^2}{M_r^2N_r^2}$ is the receive beampattern. Therefore, the overall beampattern (14) of the planar phased-MIMO radar with transmitting UPA can be seen as the product of three individual beampatterns.

3. SIMULATION RESULTS

The simulation assumes that the transmitting and receiving antennas are spaced half a wavelength apart from each other at the receiving end. The additive noise is modeled as a complex Gaussian zero-mean spatially and temporally white random sequence that has identical variances in each array sensor. The target of interest is assumed to reflect a plane-wave that impinges on the array from a direction of elevation angle $\theta_s = 30°$ and azimuth angle $\phi_s = 120°$. This simulation examines the received beam pattern of the transmit/receive beamformer for the different cases when the transmit/receive antennas are planar phased-array, planar MIMO, linear phased-MIMO, and also planar phased-MIMO. Figures 2, 3, 4, and 5 show the three-dimensional received beampatterns for the four different techniques, respectively. At Figures 2 and 3, both planar phased-array and planar MIMO have the same beam patterns. This occurs due to the equality of the coherent gain of the planar phased-array and the diversity gain of the planar MIMO.

Figure 4 shows the linear phased-MIMO beam pattern while Figure 5 shows the planar phased-MIMO beam pattern. Using calculation capabilities of Matlab program, average side lobe level can be obtained for planar phased-array and planar MIMO as (-24.5 dB) while it reaches (-29.4 dB) for linear phased-MIMO beam pattern. Moreover, for planar phased-MIMO array it reaches its minimum value at (-37.7 dB).

Figure 6 shows the beam pattern for the four techniques, planar phased-array, planar MIMO, linear phased-MIMO, and planar phased-MIMO in elevation plane (theta-plane). It is worth nothing that peak side lobe level in elevation plane for planar phased-array and planar MIMO radar is (-24 dB) while it reaches (-26.5 dB) for linear phased-MIMO and as lower as (-51.5 dB) for planar phased-MIMO.

Figure 7 shows the beam pattern of the same four techniques in azimuth plane (Phi-plane). Both planar phased-array and planar MIMO beam patterns have the same peak side lobe level

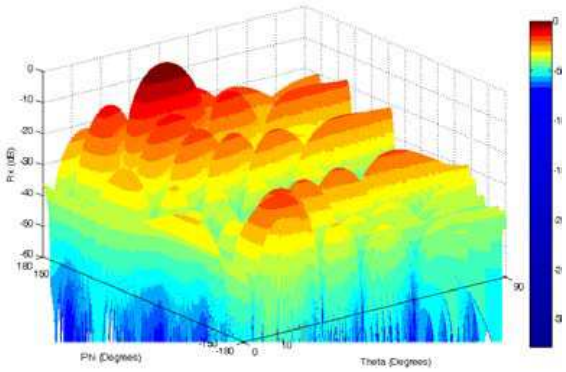

Figure 2: Received beam pattern for planar phased array radar.

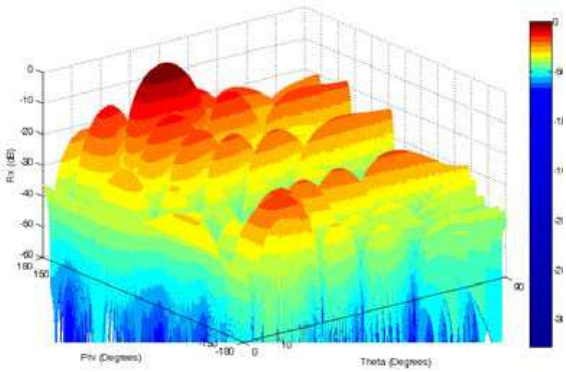

Figure 3: Received beam pattern for planar MIMO radar.

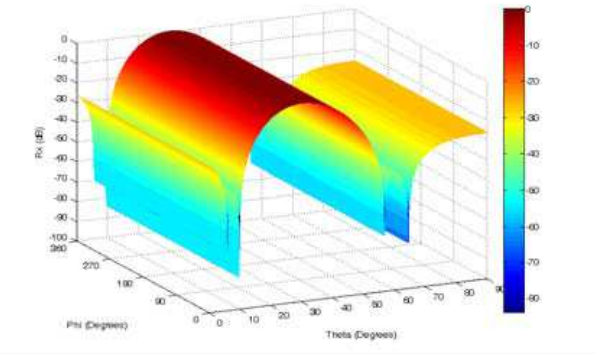

Figure 4: Received beam pattern for linear phased-MIMO radar.

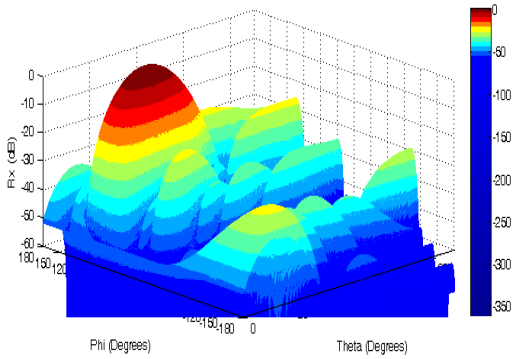

Figure 5: Received beampattern for planar phased-MIMO radar.

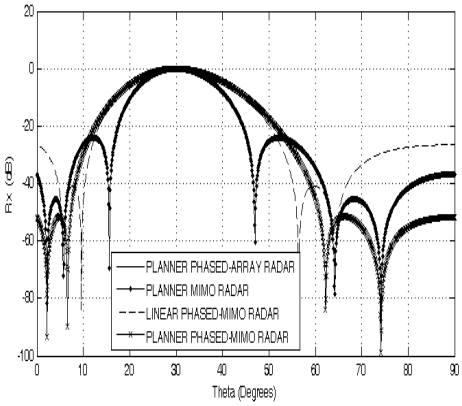

Figure 6: Received beampattern for the four techniques in elevation plane (theta-plane).

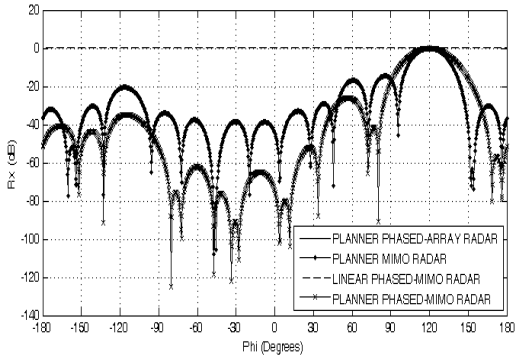

Figure 7: Received beampattern for the four techniques azimuth plane (Phi-plane).

at (−14.5 dB). Planner phased-MIMO beam pattern has a lower side lobe level at (−26 dB) while linear phased-MIMO beam pattern has a symmetrical uniform spatial power distribution at all azimuth angles. Figure 8 shows a spherical representation of linear phased-MIMO array while Figure 9 shows a spherical representation of planar phased-MIMO array. It's clear that while linear phased-MIMO array can steer the beam only along the elevation plane while maintaining symmetrical transmit/receive beam pattern in azimuth plane, planar phased-MIMO array can direct its beam at direction of the target of interest in both elevation and azimuth planes achieving higher directivity.

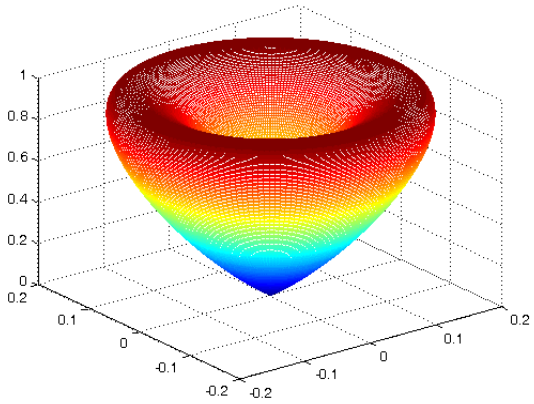

Figure 8: Linear phased-MIMO array directivity.

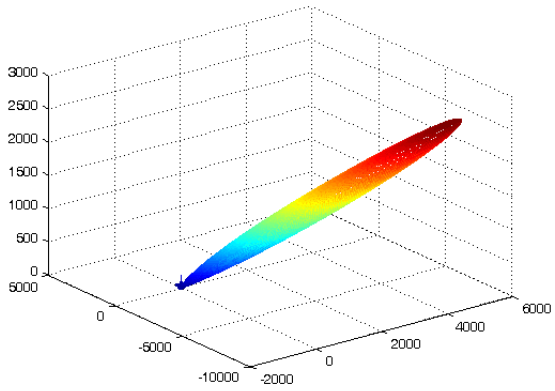

Figure 9: Planner phased-MIMO array directivity.

4. SUMMARY

The paper studies a new technique for partitioning the transmit array into a number of subarrays that are allowed to overlap in planar way. Then, each subarray is used to coherently transmit a waveform which is orthogonal to the waveforms transmitted by other subarrays. Significant improvements in average side lobe level, peak side lobe level and directivity are offered by the planar phased-MIMO radar technique over other techniques.

REFERENCES

1. Wijnholds, S. J. and W. A. van Cappellen, "In situ antenna performance evaluation of the LOFAR phased array radio telescope," *IEEE Transactions on Antennas and Propagation*, Vol. 59, No. 6, 1981–1989, 2011.
2. Zrnic, D. S., G. Zhang, and R. J. Doviak, "Bias correction and Doppler measurement for polarimetric phased-array radar," *IEEE Transactions on Geoscience and Remote Sensing*, Vol. 49, No. 2, 843–853, 2010.
3. Bachmann, M., M. Schwerdt, and B. Bräutigam, "Accurate antenna pattern modeling for phased array antennas in SAR applications demonstration on TerraSAR-X," *International Journal of Antennas and Propagation*, Vol. 2009, 9 pages, Article ID 492505, 2009.
4. Wang, W. Q., "Near-space wide-swath radar imaging with multi-aperture antenna," *IEEE Antennas and Wireless Propagation Letters*, Vol. 8, 461–464, 2009.
5. Younis, M., S. Huber, A. Patyuchenko, F. Bordoni, and G. Krieger, "Performance comparison of reflector- and planar antenna based digital beam-forming SAR," *International Journal of Antennas and Propagation*, Vol. 2009, 13 pages, Article ID 614931, 2009.
6. Wang, W. Q., "Space-time coding MIMO-OFDM SAR for high-resolution remote sensing," *IEEE Transactions on Remote Sensing*, Vol. 49, No. 8, 3094–3104, 2011.
7. Capece, P., "Active SAR antennas: Design, development, and current programs," *International Journal of Antennas and Propagation*, Vol. 2009, 11 pages, Article ID 796064, 2009.
8. Wang, W. Q., *Near-space Remote Sensing: Potential and Challenges*, Springer, New York, NY, USA, 2011.
9. Fishler, E., A. Haimovich, R. Blum, L. Cimini, D. Chizhik, and R. Valenzuela, "Spatial diversity in radars — Models and detection performance," *IEEE Trans. Signal Process.*, Vol. 54, No. 3, 823–838, Mar. 2006.
10. Haimovich, A., R. Blum, and L. Cimini, "MIMO radar with widely separated antennas," *IEEE Signal Process. Mag.*, Vol. 25, No. 1, 116–129, Jan. 2008.
11. Robey, F., S. Coutts, D. Weikle, J. McHarg, and K. Cuomo, "MIMO radar: Theory and experimental results," *Proc. 38th Asilomar Conf. Signals, Syst., Comput.*, Pacific Grove, CA, Nov. 2004.
12. Bliss, D. and K. Forsythe, "Multiple-input multiple-output (MIMO) radar and imaging: Degrees of freedom and resolution," *Proc. 37th Asilomar Conf. Signals, Syst., Comput.*, Pacific Grove, CA, Nov. 2003.

13. Li, J., P. Stoica, and Y. Xie, "On probing signal design for MIMO radar," *IEEE Trans. Signal Process.*, Vol. 55, No. 8, 4151–4161, Aug. 2007.
14. Li, J. and P. Stoica, "MIMO radar with collocated antennas," *IEEE Signal Process. Mag.*, Vol. 24, No. 9, 106–114, Sep. 2007.
15. Hassanien, A. and S. A. Vorobyov, "Phased-MIMO radar: A tradeoff between phased-array and MIMO radars," *IEEE Trans. Signal Process.*, Vol. 58, 3137–3151, Jun. 2010.
16. Browning, J. P., D. R. Fuhrmann, and M. Rangaswamy, "A hybrid MIMO phased-array concept for arbitrary spatial beampattern synthesis," *Proc. IEEE Digital Singal Processing and Signal Processing Education Workshop*, 446–450, Marco Island, FL, Jan. 2009.
17. Fuhrmann, D. R., J. P. Browning, and M. Rangaswamy, "Signaling strategies for the hybrid MIMO phased-array radar," *IEEE J. Select. Topics Signal Processing*, Vol. 4, No. 1, 66-78, Feb. 2010.
18. Hassanien, A. and S. A. Vorobyov, "Transmit/receive beamforming for MIMO radar with colocated antennas," *Proceedings of the IEEE International Conference on Acoustics, Speech, and Signal Processing (ICASSP'09)*, 2089–2092, Taipei, Taiwan, Apr. 2009.

Non Simultaneous-conjugate-match Technique for S-band Low Noise Amplifier Design

Achmad Munir[1] **and Yana Taryana**[1, 2]

[1]Radio Telecommunication and Microwave Laboratory
School of Electrical Engineering and Informatics, Institut Teknologi Bandung, Indonesia
[2]Research Center for Electronics and Telecommunication, Indonesian Institute of Sciences, Indonesia

Abstract— The design of 2-stage low noise amplifier (LNA) working at S-band frequency is proposed by using non simultaneous-conjugate-match technique. Implementation of the technique is motivated by the circumstance that the gain of LNA designed by the familiar technique, i.e. simultaneous-conjugate-match is almost followed by arise of values in noise figure (NF) and voltage standing wave ratio (VSWR). In the design process, the ADS software is applied to determine the desired trade-off value between LNA parameters such as gain and VSWR. The 2-stage LNA which is deployed on an Arlon DiClad527 applies BJT transistors of BFP420. To achieve the impedance matching condition, microstrip lines are employed at the input and output ports. From the experimental characterization, it shows that the prototype of 2-stage LNA produces the gain of 24.32 dB at 3 GHz which is 4.56 dB lower than the simulated result.

1. INTRODUCTION

In wireless communication systems, a front-end amplifier receiver is a very critical block in radio frequency (RF) receivers due to its responsibility to recover the transmitted data out of the weak received signal which is usually accompanied by noise and interference. Thus, a front-end amplifier receiver with high performance capability is an essential device to provide sufficient power gain and low noise figure as well as good input impedance matching within the required operational frequency bands [1–3]. There are a lot of topologies and design methods of RF receiver amplifier including the utilization of RF-CMOS integrated circuit which have been investigated where some achievements in accomplishing specification and aspect of applications have been acquired [4–6]. One of the methods to obtain the match output impedance, as well as better isolation between the input and output ports is by cascading an amplifier in some stages.

In the design of low noise amplifier (LNA), there are many trade-off values involve between noise figure (NF), gain, linearity, impedance matching, and power dissipation [6, 7]. Basically, the main goal of LNA design which is usually carried out by use of a simultaneous-conjugate-match (SCM) technique is to achieve simultaneous noise and input matching at any given amount of power dissipation. The LNA should also provide low noise behavior not only at one frequency but over the whole desired working bandwidth [8]. Beside the mentioned trade-offs above, the stability is the most important thing that has to be paid more attention. To attain the desired stability as well as the stability maintenance, there are few methods that could be implemented including resistive matching, network compensation, negative feedback, balanced circuits, and traveling wave [2, 3]. For some application, however, the resistive matching method can potentially increase the noise figure and simultaneously decrease the gain of LNA, while the method of negative feedback typically produces inferior reflected wave [9, 10]. Moreover, in the LNA design based on SCM technique especially for bilateral and unilateral RF amplifier, due to the influence of reflected waves from the input port to the load and from the output port to the source, it is sometimes very difficult to achieve some condition where the LNA has maximum transducer gain. Thus, it will significantly affect in determining the desired trade-off value between gain and VSWR.

In this paper, the design of LNA is proposed by implementing a technique of non simultaneous-conjugate-match (SCM) where the amplifier will be designed at mismatch condition. The LNA which is intended to be applied for S-band application is powered by 2-stage cascaded RF transistors of BFP420 type to achieve the high gain. Prior to deployment on an Arlon DiClad527, the designed LNA is numerically characterized through the ADS software to determine the desired trade-off value. To compensate impedance mismatch, a method of network compensation is implemented using microstrip lines at the input, interstage and output ports. The dimension of microstrip lines are optimized to achieve the impedance matching condition and optimum performance of LNA with some design parameters such as gain and VSWR are used as performance indicators.

2. OVERVIEW OF NON SCM TECHNIQUE AND CIRCUIT DESIGN

In this work, the employed topology for designing 2-stage LNA powered by RF transistor of BFP420 type is common emitter topology in which the RF input signal is applied to the base of transistor and the RF output is taken from the collector. The topology is chosen in order to obtain good sensitivity and high gain. To achieve a maximum gain in the SCM technique, the reflection coefficients of amplifier at the 1st stage should satisfy the following conditions; $\Gamma_{\text{S-1}} = \Gamma^*_{\text{in-1}}$ and $\Gamma_{\text{L-1}} = \Gamma^*_{\text{out-1}}$, whilst on the 2nd stage; $\Gamma_{\text{S-2}} = \Gamma^*_{\text{in-2}}$ and $\Gamma_{\text{L-2}} = \Gamma^*_{\text{out-2}}$. Those conditions are very difficult to be obtained since according to (1) and (2), $\Gamma_{\text{in-1}}$ is influenced by $\Gamma_{\text{L-1}}$, whereas $\Gamma_{\text{out-1}}$ is influenced by $\Gamma_{\text{S-1}}$. This situation also applies for the 2nd stage of amplifier.

$$\Gamma_{\text{in}} = S_{11} + \frac{S_{12}S_{21}\Gamma_{\text{L}}}{1 - S_{22}\Gamma_{\text{L}}} \tag{1}$$

$$\Gamma_{\text{out}} = S_{22} + \frac{S_{12}S_{21}\Gamma_{\text{S}}}{1 - S_{11}\Gamma_{\text{S}}} \tag{2}$$

Whilst in the non-SCM technique, it is unnecessary to calculate Γ_{in} and Γ_{out} for designing matching impedance network. Therefore, it can simplify the mathematical calculations for gain circles on Smith chart for given value of Z_{L} and Z_{S}. Since the LNA is designed at a condition of mismatch, therefore the impedance mismatch factor (M) expressed in (3) will be used for each stage, i.e., M_1 and M_2 for the 1st and 2nd stage of amplifier respectively, to determine the VSWR of each stage. If the impedance mismatch factor equals 1, as expressed in (4) it means that the VSWR equals 1, too. Or in other words, the RF power signal from the source is fully transferred by the amplifier. In other hand, if the LNA is at a condition of mismatch or mathematically expressed by VSWR > 1 or $M < 1$, it indicates that some of RF power signal is reflected to the source which is important in designing impedance matching network. To obtain the maximum power transfer (G_{T}) so that the LNA has a high gain, it can be calculated by making a relationship between the operating power gain (G_{P}) and the impedance mismatch factor (M), as expressed in (3).

$$G_{\text{T}} = \underbrace{\frac{(1 - |\Gamma_{\text{L}}|^2)|S_{21}|^2}{|1 - S_{22}\Gamma_{\text{L}}|^2(1 - |\Gamma_{\text{in}}|^2)}}_{G_{\text{P}}} \cdot \underbrace{\frac{(1 - |\Gamma_{\text{S}}|^2)(1 - |\Gamma_{\text{in}}|^2)}{|1 - \Gamma_{\text{in}}\Gamma_{\text{S}}|^2)}}_{M} \tag{3}$$

$$\text{VSWR} = \frac{1 + \sqrt{1 - M}}{1 + \sqrt{1 + M}} \tag{4}$$

Based on the common emitter topology, the circuit design of 2-stage LNA equipped with dc bias and dc current block at the input and output ports is shown in Figure 1. The quiescent point (Q) for transistor in both stages is designed at $I_{\text{c}} = 10\,\text{mA}$, $\beta = 100$, $V_{\text{be}} = 0.7\,\text{Volt}$, $V_{\text{ce}} = 2\,\text{Volt}$ and $V_{\text{cc}} = 5\,\text{Volt}$. By using the ADS software, the amplifier confirms to have a good stability

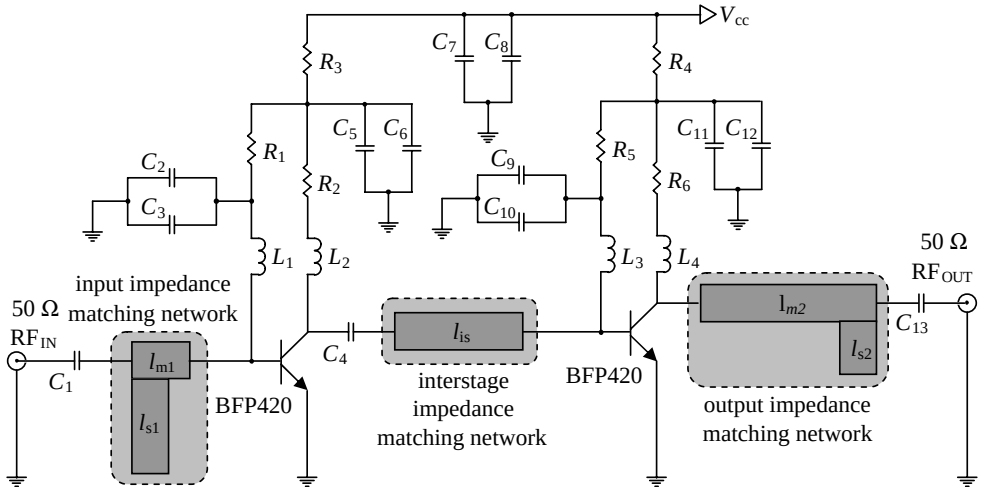

Figure 1: Circuit design of 2-stage low noise amplifier.

with the S-parameter values at frequency of 3 GHz as follows; $S_{11} = 0.540\angle 162.904°$ dB, $S_{12} = 0.075\angle 48.295°$ dB, $S_{21} = 4.240\angle 63.908°$ dB and $S_{22} = 0.151\angle -137.164°$ dB. Furthermore, the values of Z_L and Z_S can also be determined and are $23.95\text{-}j6.65\,\Omega$ and $36.55\text{-}j10.7\,\Omega$, respectively.

Since the input and output ports are set to be 50 Ω, therefore impedance matching networks are required to compensate the impedance mismatch. To minimize parasitic effects which may cause oscillation of amplifier, microstrip lines are applied as the impedance matching network for the input, interstage and output ports of LNA. After conducting some parametrical studies to obtain the optimum dimension of microstrip lines, the length of microstrip line (l_{m1}) and stub (l_{s1}) for the input port is 4.65 mm and 7.56 mm, respectively, and the length of microstrip line for the interstage (l_{is}) is 10.2 mm. Whereas for the output port, the length of microstrip line (l_{m2}) and stub (l_{s2}) is 14.02 mm and 4.2 mm, respectively.

3. REALIZATION AND CHARACTERIZATION

Figure 2 shows the picture of realized 2-stage LNA prototype which is deployed on an Arlon DiClad527 dielectric substrate with SMD (surface-mount device) components for resistors, inductors and capacitors. Two SMA connector types are soldered at the input/output ports of LNA for experimental characterization. The results of experimental characterization for gain, $VSWR_{IN}$ and $VSWR_{OUT}$ are depicted in Figures 3, 4 and 5, respectively. It is noticeable that the measurement of noise figure could not be performed in this work due to the unavailability of noise source instrument. In addition, simulated results of gain, $VSWR_{IN}$ and $VSWR_{OUT}$ are also plotted together in each respected figure as comparison.

From Figure 3, in despite of measured gain is lower than the simulated one, however it has similar tendency for all observed frequency ranges. It shows that the measured gain at frequency of 3 GHz is 24.32 dB, whilst the simulated one is 28.88 dB. The discrepancy is possibly affected by the different parameter of Arlon DiClad527 dielectric substrate, i.e., dielectric loss, used for realizing

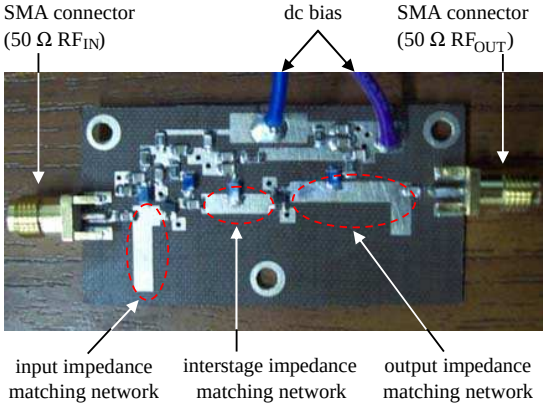

Figure 2: Picture of realized 2-stage low noise amplifier prototype.

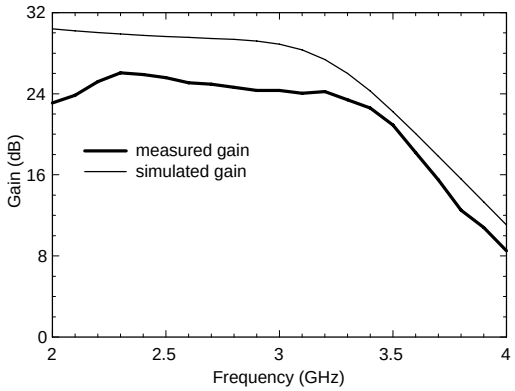

Figure 3: Measured gain of 2-stage LNA prototype with simulated result as comparison.

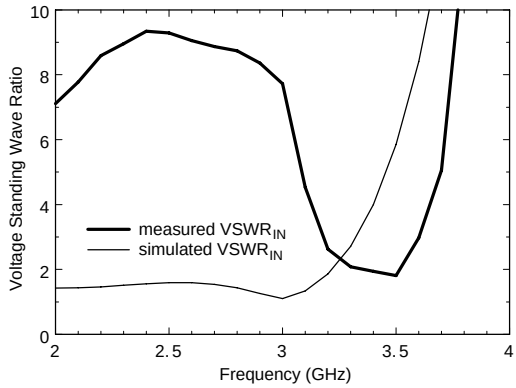

Figure 4: Measured $VSWR_{IN}$ of 2-stage LNA prototype with simulated result as comparison.

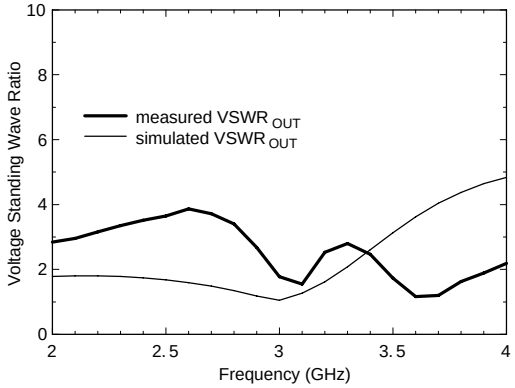

Figure 5: Measured $VSWR_{OUT}$ of 2-stage LNA prototype with simulated result as comparison.

the prototype which has value higher than in the simulation. When the value of dielectric loss is higher, some amount of energy from the input port that should be actually transmitted to the output port is absorbed by the dielectric substrate causing the decrease of measured gain.

The different results of experimental characterization are also found for the value of VSWR at the input and output ports as plotted in Figures 4 and 5, respectively. In general, both VSWR values are shifted to higher frequency range affecting the VSWR values at frequency of 3 GHz. The measured $\mathrm{VSWR_{IN}}$ and $\mathrm{VSWR_{OUT}}$ at frequency of 3 GHz are 7.72 and 1.78, respectively, whilst the simulation is 1.1 and 1.05, respectively. The difference in measured results of VSWR is probably evoked by the different value of relative permittivity of dielectric substrate used in the realization. For the results indicted in Figures 4 and 5, the actual value of relative permittivity seems to be lower than in the simulation. If the actual relative permittivity is lower, thus the impedance of impedance matching networks, i.e., microstrip lines, reacts to move to be bigger resulting the increase of VSWR.

4. CONCLUSION

The design of 2-stage LNA for S-band frequency application has been demonstrated by use of non-SCM technique and realized on an Arlon DiClad527 dielectric substrate for experimental characterization. It has been shown that utilization of non-SCM technique in the design of 2-stage LNA could reduce the flow of design process due to unnecessary to calculate Γ_{in} and Γ_{out} for designing matching impedance network. From characterization results, it has been demonstrated that the realized 2-stage LNA prototype has produced gain of 24.32 dB at frequency of 3 GHz with the values of $\mathrm{VSWR_{IN}}$ and $\mathrm{VSWR_{OUT}}$ of 7.72 and 1.78, respectively. Although the experimental characterization result in some frequencies was worse than the design and has needed to be improved, in general the prototype of 2-stage LNA has shown acceptable performance and similar tendency with the simulated one. It should be noted that parameters of involved materials in the design process should be taken into account to avoid the discrepancies which may occur in the realization. In addition, a further investigation on the performance improvement of 2-stage LNA designed based on non-SCM technique is still underway where the result will be reported later.

REFERENCES

1. Gonzalez, G., *Microwave Transistor Amplifiers Analysis and Design*, Prentice-Hall Inc., New Jersey, 1997.
2. Ludwig, R. and P. Bretchko, *RF Circuit Design: Theory and Applications*, Prentice-Hall Inc., New Jersey, 2000.
3. Misra, D. K., *Radio-frequency and Microwave Communication Circuits: Analysis and Design*, John Wiley & Sons, New York, 2004.
4. Lee, T. H., *The Design of CMOS Radio Frequency Integrated Circuits*, Cambridge University Press, New York, 2003.
5. Razavi, B., *RF Microelectronics*, Prentice-Hall Inc., New Jersey, 2011.
6. Nguyen, T.-K., C.-H. Kim, G.-J. Ihm, M.-S. Yang, and S-G. Lee, "CMOS low-noise amplifier design optimization techniques," *IEEE Trans. Microw. Theory Techn.*, Vol. 52, No. 5, 1433–1442, May 2004.
7. Hamaizia, Z., N. Sengouga, M. C. E. Yagoub, and M. Missous, "S-band low noise amplifier using 1 μm InGaAs/InAlAs/InP pHEMT," *Journal of Semiconductors*, Vol. 33, No. 2, 025001-1–025001-6, Feb. 2012.
8. Kelly, M. I. A., J. P. Starski, N. Wadefalk, and H. Zirath, "48 GHz low noise amplifiers using metamorphic HEMT technology," *Proceeding of the 1st European Microwave Integrated Circuits Conf.*, 118–121, Manchester, UK, Sep. 2006.
9. Othman, A. F. and N. M. Noh, "Wideband LNA design for SDR radio using balanced amplifier topology," *Proceeding of the 4th Asia Symposium on Quality Electronic Design (ASQED)*, 86–90, Penang, Malaysia, Jul. 2012.
10. Ranum, B. T. and A. Munir, "High gain single stage amplifier with wideband characteristic for wireless communication," *Proceeding of the 4th International Conference on Electrical Engineering and Informatics (ICEEI)*, 809–815, Selangor, Malaysia, Jul. 2013.

Characterization of Narrowband Hairpin Bandpass Filter Composed of Fractal Koch Geometry

Achmad Munir[1], **Teguh Praludi**[1, 2], **and Mohammad Ridwan Effendi**[1]

[1]Radio Telecommunication and Microwave Laboratory, School of Electrical Engineering and Informatics
Institut Teknologi Bandung, Indonesia
[2]Research Center for Electronics and Telecommunication, Indonesian Institute of Sciences, Indonesia

Abstract— In this paper, a narrowband hairpin bandpass filter (BPF) composed of fractal Koch geometry is characterized numerically and experimentally. The implementation of fractal Koch geometry aims to minimize the dimension of filter which affects to reduce the need of material. The filter which utilizes the 1st iteration of fractal Koch geometry, later referred as fractal hairpin BPF is established using 7 elements deployed on a Rogers RO4350 dielectric substrate with the thickness of 1.52 mm. Prior to hardware realization, the proposed filter is numerically characterized to deal with the required specification. The filter which is intended for radar application is designed to have center frequency of 3 GHz with the 3 dB minimum working bandwidth of 200 MHz. It is shown that the realized fractal hairpin BPF which has the dimension of 16 mm × 47 mm and is approximately 20% smaller than the dimension of conventional one demonstrates the 3 dB working bandwidth of 260 MHz with the center frequency of 3.01 GHz.

1. INTRODUCTION

In 5 decades ago, the development of filters including bandpass filter (BPF) was usually carried out by employing the concept of electric field and magnetic field interaction. From the concept, the filters were then implemented through lumped elements such as capacitors and inductors [1, 2]. However, along with the growth of technology for communication devices especially in high frequency and microwave regions, some designs of filter have been approached based on distributed elements instead of lumped elements and realized by using dielectric resonator, stripline, and microstrip line [3–5]. Furthermore, BPF with high performance and compact size is primarily required to improve the performance of system, as well as to reduce the cost of fabrication, in microwave communication systems.

During last decade, microstrip-based filter with its advantages such as planarity in structure, insensitivity to fabrication tolerances, and reproducibility has been widely implemented in the RF front end of wireless communication systems [6, 7]. Even so, due to the element of microstrip filter which almost requires $\lambda/2$ resonator, the dimension is essentially considered in which the size is an important issue for the systems. Some solutions have been proposed using hairpin-line filter by applying a structure of folded $\lambda/2$ resonator [8–10]. Although it was some advantage in producing compact structure of filter by adopting the hairpin-line technology, however there was some disadvantage in unavoidable coupling between the elements affecting to the limitation in bandwidth response.

In connection to the size reduction, in this paper, a fractal Koch geometry is applied to design elements of narrowband hairpin bandpass filter (BPF) for the characterization. The fractal Koch geometry which is usually implemented for minimizing the dimension of antenna [11, 12], basically is the repetition of some similar geometry shape. By applying the fractal Koch geometry, the structure of fractal hairpin BPF can be more compact compared to the conventional one so that its dimension can be minimized reducing the need of material. The proposed fractal hairpin BPF which utilizes the 1st iteration of fractal Koch geometry is constructed using 7 elements deployed on a dielectric substrate of Rogers RO4350. The proposed filter is intended for radar application with the center frequency of 3 GHz and 3 dB minimum working bandwidth of 200 MHz. Some basic characteristics of filter such as return loss, insertion loss, and bandwidth are used as the performance indicators. Prior to the characterization, overview of fractal Koch geometry and design of fractal hairpin BPF will be briefly described. Then, the characterization result and its analysis as well as the conclusion will be presented consecutively.

2. OVERVIEW OF FRACTAL KOCH GEOMETRY AND DESIGN OF HAIRPIN BPF

The fractal geometry structure, namely fractal Koch geometry, is implemented by dividing an Euclidian element with 1 unit length, called as the 0th iteration, to be 4 parts in which each of part

has $\frac{1}{4}$ unit length. Then, the second part of divided element is rotated 60 degrees to horizontal following by the third part of divided element which is rotated to the opposite angle to horizontal, i.e., −60 degrees. While the remaining parts are kept parallel to horizontal. Therefore, the total length will be the same as the total length of the Euclidian element, but the length from the starting-point to the end-point of the element will be $\frac{3}{4}$ of the Euclidian element. By using this method, the shorter length from the starting-point to the end-point of the element can be obtained by keeping the same total length of the element, and is called as the 1st iteration. To obtain the 2nd and higher order iteration, it can be carried out by repeating the similar process implemented in the 1st iteration to others. Figure 1 illustrates the fractal Koch geometry for the 0th, 1st, 2nd, and 3rd iteration where one of them, i.e., the 1st iteration, will be implemented in the design of narrowband hairpin BPF.

Figure 2 shows a design of conventional hairpin BPF which is constructed using 7 elements. The construction is deployed on top side of a 1.52 mm thick Rogers RO4350 dielectric substrate with the relative permittivity of 3.48 and the dimension of 56.9 mm × 15.9 mm, while the bottom side is for groundplane. The geometry of filter indicated in Figure 2 is the optimum design for conventional hairpin BPF to work at the center frequency of 3 GHz with 3 dB minimum working bandwidth of 200 MHz where this is obtained by performing intensively parametrical studies for each element filter using a commercial software. The input/output signals for conventional hairpin BPF are obtained from 50 Ω microstrip line ports with the width of each port is the same as of all filter elements, i.e., 1.3 mm. These ports are connected to the SMA connector types for experimental characterization. The thicknesses of lines both for filter elements and input/output ports on the top side of dielectric substrate as well as the ground plane on the bottom side are set to be 0.035 mm. To obtain the accurate design, the dielectric substrate loss and metal copper conductive losses of lines and groundplane are taken into account.

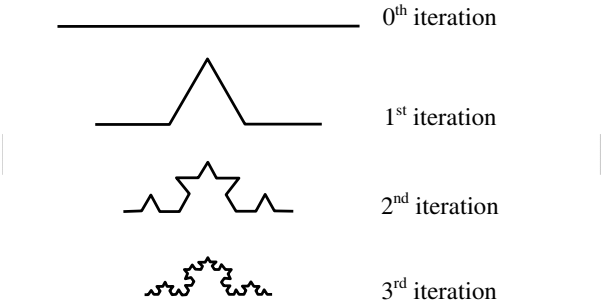

Figure 1: Fractal Koch geometry for the 0th, 1st, 2nd, and 3rd iterations.

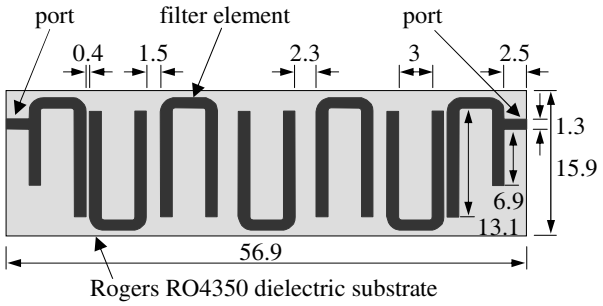

Figure 2: Top view of conventional hairpin band-pass filter (unit in mm).

In order to minimize the dimension of filter, the 1st iteration of fractal Koch geometry illustrated in Figure 1 is applied for conventional hairpin BPF. The hairpin BPF which implements fractal Koch geometry for its elements, namely fractal hairpin BPF, is also deployed on a Rogers RO4350 dielectric substrate with the thickness of 1.52 mm. After performing some parametrical studies for each element filter, the optimum geometry design of proposed fractal hairpin BPF with 7 elements is shown in Figure 3 with the dimension of 42.6 mm × 16.7 mm. The parametrical studies which is carried out by use of a commercial software is conducted not only for acquiring the geometry design but also for obtaining the optimum performance of filter to satisfy the required specifications. Here, parameters used to analyze the performance include center frequency, working bandwidth, return loss and insertion loss.

The performance of both hairpin BPFs as numerical characterization result is plotted in Figure 4. It seems that the characterization result for fractal hairpin BPF has agreed very well with the conventional one for frequency range lower than 3.3 GHz. However, there is some slight difference for frequency range higher than 3.3 GHz where the fractal hairpin BPF has a poor skirt of insertion loss which is possibly affected by unavoidable coupling between elements of filter. From the results, it shows that the maximum insertion loss at passband area is similar each other, that is 2.49 dB at frequency of 2.98 GHz. While the 3 dB working bandwidth for fractal hairpin BPF with center frequency of 3.005 GHz is 230 MHz ranges from 2.89 GHz to 3.12 GHz where this is 10 MHz wider than the conventional one which has 3 dB working bandwidth of 220 MHz ranges from 2.89 GHz to 3.11 GHz with the center frequency of 3 GHz. In addition, it can be inferred that by keeping the

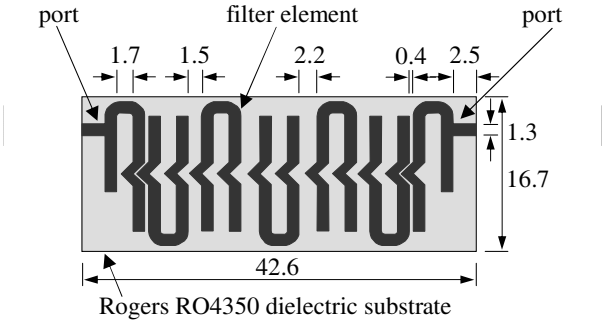

Figure 3: Top view of proposed fractal hairpin bandpass filter (unit in mm).

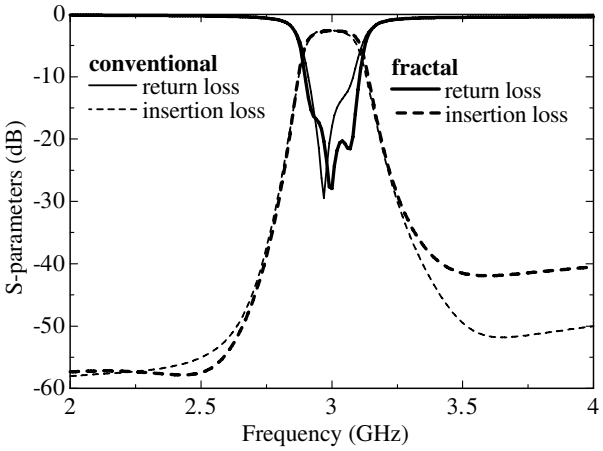

Figure 4: Simulation results for both hairpin bandpass filters.

similarity of performances with some efforts the utilization of fractal Koch geometry for hairpin BPF with 7 elements has reduced the physical dimension up to 20% from the conventional one.

3. HARDWARE REALIZATION AND CHARACTERIZATION

To verify the numerical characterization, the hardware realization is carried out by fabricating both designed hairpin BPFs on Rogers RO4350 dielectric substrates with the thickness of 1.52 mm. Pictures of both realized hairpin BPFs are shown in Figure 5. For experimental characterization purpose, 2 SMA connector types are soldered at the input/output ports of each filter. Figure 6 depicts the measured result of experimental characterization for realized fractal hairpin BPF with the measured result for conventional one plotted together as comparison.

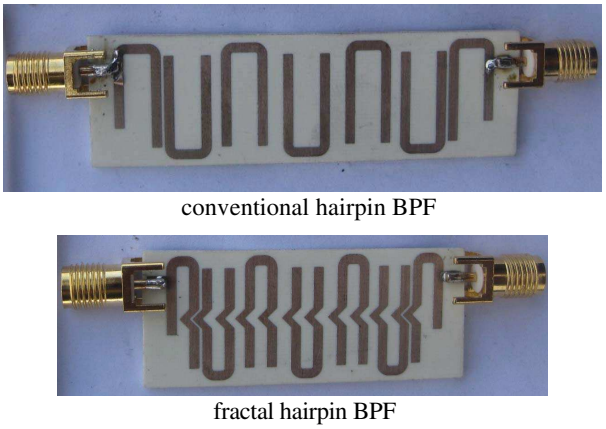

Figure 5: Pictures of both realized hairpin bandpass filters.

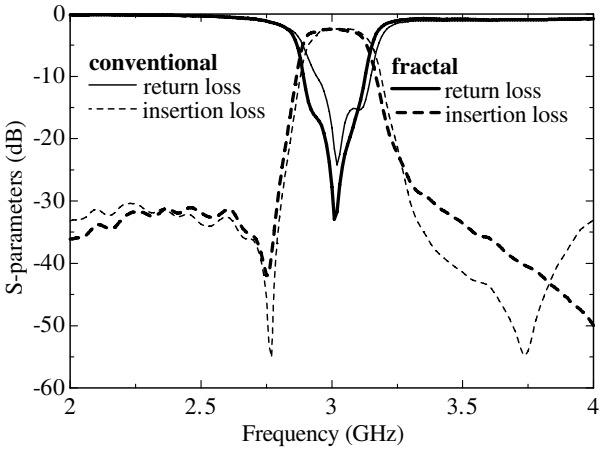

Figure 6: Measurement results for both hairpin bandpass filters.

In general, the characteristic responses for both realized filters as well as their passband characteristics are coincided qualitatively each other. Both results seem to have poor skirt of insertion losses at frequency range lower than 2.75 GHz. This is probably evoked by inappropriateness of RF cables used for the measurement. From the results, although the center frequencies of both realized filters are slightly different, however their 3 dB working bandwidth are similar each other, i.e., 260 MHz, range from 2.88 GHz to 3.14 GHz for fractal hairpin BPF and from 2.9 GHz to 3.16 GHz for convectional one. The center frequency of realized fractal hairpin BPF is at 3.01 GHz which is 5 MHz higher than the simulated result, i.e., 3.005 GHz. Whilst for realized conventional hairpin BPF, the center frequency is at 3.03 GHz which is 30 MHz higher than the simulated one, i.e., 3 GHz. It is noticeable that the insertion loss of measured result in passband area for fractal hairpin BPF shows similar tendency with the conventional one. The maximum insertion loss in passband

area is 2.46 dB and 2.33 dB for realized fractal hairpin at frequency of 2.99 GHz and conventional one at frequency of 3.03 GHz, respectively. It shows that the realized fractal hairpin BPF is worse than the conventional one which is probably caused by inaccurateness of fabrication process. Nevertheless, from the results it can be concluded that the proposed fractal hairpin BPF which has been realized based on microstrip technology has adequate bandwidth response complying with the required bandwidth coverage.

4. CONCLUSION

The characterization of narrowband hairpin BPF composed of fractal Koch geometry has been demonstrated numerically and experimentally. The fractal hairpin BPF which has utilized the 1st iteration of fractal Koch geometry has been implemented using 7 elements deployed on a Rogers RO4350 dielectric substrate. As comparison, a conventional hairpin fractal has also been designed on the same dielectric substrate. From the characterization result, it has been shown that the fractal Koch geometry utilization has reduced the dimension of fractal hairpin BPF up to 20% from the conventional one. It has been demonstrated that the realized fractal hairpin BPF has had narrowband bandwidth response with center frequency of 3.01 GHz and 3 dB working bandwidth of 260 MHz. Whereas the realized conventional hairpin BPF, it has had the center frequency of 3.03 GHz with the similar working bandwidth. It has been confirmand that both realized filters have satisfied and complied with the requirement for desired radar application.

ACKNOWLEDGMENT

This work is partially supported by the Directorate General of Higher Education (DGHE), the Ministry of Education and Culture, the Republic of Indonesia, under the program scheme of decentralization research 2014.

REFERENCES

1. Matthaei, G. L., "Magnetically tunable band-stop filters," *IEEE Trans. on Microw. Theory Techn.*, Vol. 13, No. 2, 203–212, Mar. 1965.
2. Nagumo, J., S. Yoshizawa, and S. Arimoto, "Bistable transmission lines," *IEEE Trans. Circuit Theory*, Vol. 12, No. 3, 400–412, Sep. 1965.
3. Cohn, S. B., "Microwave bandpass filters containing high-Q dielectric resonators," *IEEE Trans. Microw. Theory Techn.*, Vol. 16, No. 4, 218–227, Apr. 1968.
4. Mobbs, C. I. and J. D. Rhodes, "A generalized chebyshev suspended substrate stripline bandpass filter," *IEEE Trans. on Microw. Theory Techn.*, Vol. 31, No. 5, 397–402, May 1983.
5. Munir, A., I. Pradibta, and M. R. Effendi, "Microstrip-based ultra-wideband composite BPF with short-circuited stubs," *Proceeding of ECTI-CON2013*, 1–3, Krabi, Thailand, May 2013.
6. Chang, C. Y. and T. Itoh, "A modified parallel-coupled filter structure that improves the upper stop band rejection and response symmetry," *IEEE Trans. Microw. Theory Techn.*, Vol. 39, No. 2, 310–314, Feb. 1991.
7. Aditomo, W. and A. Munir, "Bandwidth enhancement of ultra-wideband microstrip bandpass filter using defected ground structure," *Proceeding of 13th International Conf. on Quality in Research (QiR) 2013*, 150–154, Yogyakarta, Indonesia, Jun. 2013.
8. Gysel, U. H., "New theory and design for hairpin-line filters," *IEEE Trans. Microw. Theory Techn.*, Vol. 22, No. 5, 523–531, May 1974.
9. Dahlan, S. H. and M. Esa, "Miniaturized internally-coupled hairpin-line bandpass filter," *Proceeding of APACE2005*, 1–4, Johor, Malaysia, Dec. 2013.
10. Hasan, A. and A. E. Nadeem, "Novel microstrip hairpinline narrowband bandpass filter using via ground holes," *Progress In Electromagnetics Research*, Vol. 78, 393–419, 2008.
11. Karim, M. N. A., M. K. A. Rahim, H. A. Majid, O. B. Ayop, M. Abu, and F. Zubir, "Log periodic fractal Koch antenna for UHF band applications," *Progress In Electromagnetics Research*, Vol. 100, 201–218, 2010.
12. Munir, A., D. T. Putranto, and H. Wijanto, "Characterization of series iteration log-periodic fractal Koch printed antenna equipped with balun unit," *Journal of ICT Research and Applications*, Vol. 7, No. 3, 191–204, Dec. 2013.

The Influence of a Magnetic Field on the Behaviour of the Quantum Mechanical Model of Matter

E. Hutova, K. Bartusek, and P. Fiala
Department of Theoretical and Experimental Electrical Engineering
Brno University of Technology, Technická 3082/12, Brno 616 00, Czech Republic

Abstract— The paper presents an experimental measurement of a material inserted in various types of magnetic field. The related model accepts the time component of an electromagnetic field from the perspective of the properties of matter. The relatively moving systems were derived and tested [1], and the influence of the motion on a superposed electromagnetic field was proved to exist already at relative motion speeds. In micro- and nanoscopic objects such as the basic elements of matter, the effect of an external magnetic field on the growth and behaviour of the matter system needs to be evaluated. We tested the model based on electromagnetic field description via Maxwell's equations, and we also extended the monitored quantities to include various flux densities. Experiments were conducted with growth properties of simple biological samples in pre-set external magnetic fields.

1. INTRODUCTION

Similarly as in the first experiment [2], we tested the numerical model and carried out an experimental measurement of material heating speed; also, we designed a method for accurate verification of heating speed changes depending on the external magnetic field.

This paper proposes a very detailed analysis focused on the influence of a magnetic field upon inanimate objects. Experimental measurement of the temperature change of a copper sensor in a stationary homogeneous and gradient magnetic field was performed. Up to 10 times, the sample was cooled down to the nitrogen boiling point ($-195{:}80\pm$C to 77.35 K); the sample was then removed at the pre-selected time and placed in an area where it was heated to the temperature of $-20\pm$C. Using the measuring centre and 4 temperature sensors (2 sensors measuring the temperature of the sample and 2 others for the measurement of the ambient temperature), we recorded the temperature change in the sample and the required heating time. This experiment was repeated with four magnetic fields.

2. MODEL: THE ELECTROMAGNETIC FIELD AND PARTICLES

For a model with distributed parameters of the electromagnetic field, it is possible to use partial differential equations based on the theory of the electromagnetic field to formulate a coupled model with concentrated parameters (in our case, particles) [2]. The details of the model are analyzed in this paper. The forces acting on a moving electric charge in the electromagnetic field can be expressed by means of the formula

$$f_{\mathrm{e}} = \rho\left(\mathbf{E} + \mathbf{v} \times \mathbf{B}\right) \text{ in } \Omega, \tag{1}$$

where $\mathbf{B}$ is the magnetic flux density vector in the space of a moving electrically charged particle with the volume density ρ, $\mathbf{v}$ is the mean velocity of the particle, $\mathbf{v} = \mathrm{d}\mathbf{s}/\mathrm{d}t$, $\mathbf{s}$ is the position vector from the beginning of the coordinate system o, t is the time, $\mathbf{E}$ is the electric intensity vector, and Ω is the definition region of the independent variables and functions. The properties of the area Ω are described by the mutual relationship between the intensities and inductions as defined by

$$\mathrm{rot}\mathbf{E} = -\frac{\partial \mathbf{B}}{\partial t} + \mathrm{rot}\left(\mathbf{v} \times B\right), \quad \mathrm{rot}\mathbf{H} = \mathbf{J} + \frac{\partial \mathbf{D}}{\partial t} + \mathrm{rot}\left(\mathbf{v} \times \mathbf{D}\right) \tag{2}$$

$$\mathrm{div}\,\mathbf{B} = 0, \quad \mathrm{div}\,\mathbf{D} = \rho, \Omega \tag{3}$$

where $\mathbf{H}$ is the magnetic field intensity vector, $\mathbf{J}$ the current density vector, $\mathbf{D}$ the electric flux density vector. The material relations for the macroscopic part of the model are represented by the expressions

$$\mathbf{B} = \mu_0 \mu_r \mathbf{H}, \quad \mathbf{D} = \varepsilon_0 \varepsilon_r E, \tag{4}$$

where the indexes of the quantities of the permeabilities and permittivities r denote the quantity of the relative value and the 0 value of the quantity for vacuum. The relation between the macroscopic

and the microscopic (dynamics of particles in the electromagnetic field) parts of the model is described by the relations of force action on the individual electrically charged particles in the electromagnetic field, and the effect is respected of the movement of electrically charged particles on the surrounding electromagnetic field according to [2]:

$$\mathrm{rot}\mathbf{E} = -\frac{\partial \mathbf{B}}{\partial t} + \mathrm{rot}\left(\mathbf{v}\times\mathbf{B}\right) - \frac{1}{\gamma}\mathrm{rot}\left(\rho\mathbf{v} + \mathrm{j}c\rho\mathbf{u}_t + \mathbf{J} + \frac{\gamma}{q_e}\left(\frac{m_e\mathrm{d}\mathbf{v}}{\mathrm{d}t} + l\mathbf{v} + k\int\limits_t \mathbf{v}\mathrm{d}t\right)\right),$$

$$\mathrm{rot}\mathbf{H} = \gamma\mathbf{E} + \rho\mathbf{v} + \gamma\left(\mathbf{v}\times\mathbf{B}\right) + \frac{\gamma}{q_e}\left(\frac{m_e\mathrm{d}\mathbf{v}}{\mathrm{d}t} + l\mathbf{v} + k\int\limits_t \mathbf{v}\mathrm{d}t\right) + \mathrm{j}c\rho\mathbf{u}_t + \frac{\partial\mathbf{D}}{\partial t} + \mathrm{rot}\left(\mathbf{v}\times\mathbf{D}\right). \quad (5)$$

The coupling of both models is formulated using Equation (5) and the formula

$$q_e\left(\mathbf{E} + \mathbf{v}\times\mathbf{B}\right) + \frac{q_e}{\gamma}\left(\rho\mathbf{v} + jc\rho\mathbf{u}_t - \frac{\partial\left(\varepsilon\mathbf{E}\right)}{\partial t}\right) = \frac{m_e\mathrm{d}\mathbf{v}}{\mathrm{d}t} + l\mathbf{v} + k\int\limits_t \mathbf{v}\mathrm{d}t.$$

The effect of the behaviour of the macroscopic model describing the matter with the quantum mechanical model of elements of the system can be observed using the fluxes of quantities. The known quantities are magnetic flux ϕ, current flux I, and electric flux having the magnitude q:

$$\phi = \iint\limits_\Gamma \mathbf{B}\cdot d\mathbf{S}, \quad I = \iint\limits_\Gamma \mathbf{J}\cdot d\mathbf{S}, \quad q = \iint\limits_\Gamma \mathbf{D}\cdot d\mathbf{S}, \quad (6)$$

where $\mathbf{S}$ is the vector of the oriented boundary (in a 3D model of the plane), and Γ is the boundary of the area Ω, in which the flux is evaluated. If there is a moving element of the system in the model with a scale difference expressed in orders, it is easier to describe the state and effect of the superposed electromagnetic field by expressing the time flux density $\boldsymbol{\tau}$. The time flux can be different or inhomogeneous in parts of the area Ω. It is then possible to write

$$t = \iint\limits_\Gamma \boldsymbol{\tau}\cdot d\mathbf{S}.$$

After expanding the expression with the time flux density for the Cartesian coordinate system o, x, y, z, we have

$$\boldsymbol{\tau} = \frac{1}{v_x\left(t\right)dx}\mathbf{u}_x + \frac{1}{v_y\left(t\right)dy}\mathbf{u}_y + \frac{1}{v_z\left(t\right)dz}\mathbf{u}_z, \quad (7)$$

where $\mathbf{u}_x$, $\mathbf{u}_y$, $\mathbf{u}_z$ are the base vectors of the coordinate system. Time density depends on the instantaneous velocity of the particle motion $\mathbf{v}$ in the quantum mechanical model and on the element of length $d\ell$. Then, for the motion of the electrically charged particle along the element of the closed curve $d\ell$ (according to the microscopic interpretation), it is possible to write

$$\frac{\mathbf{E}}{q_\mathrm{e}}d\ell = \left(\boldsymbol{\tau}^{-1}\times\mathbf{B}\right) \text{ in } \Omega. \quad (8)$$

If an electrically charged particle moves in the magnetic field having a magnetic flux density $\mathbf{B}$, and if the dimensions of the area Ω are multiply larger than the electrically charged particle or groups of particles, it is necessary to consider the question of how the motion of the particle is influenced and what are the observable oscillation changes, namely the time flux density changes in parts of the area Ω. In the quantum-mechanical model of matter, the particles move in a nuclear structure, and their motion dynamics are changed by an external magnetic field. Thus, a simple material heating test can be carried out to demonstrate the influence of an external magnetic field on the elementary model of matter. We tested three basic variants of the state of the macroscopically interpreted distribution of the external magnetic field having a magnetic flux density $\mathbf{B}$ [2] . Using the results obtained from the first experiments [2], we designed an exact technique for measuring the temperature change in the examined copper sample, Fig. 1.

Conditions for the setting of the external magnetic field were taken over from the first experiment, and they were extended with a fourth setup:

Figure 1: The measured Cu sample, $10 \times 10 \times 10$ mm.

1. The external magnetic field exhibits **low values** of magnetic flux density **B**, and its distribution is homogeneous on the microscopic scale. Then we have $B = \min$, $\partial B_x/\partial x = 0$, $\partial B_y/\partial y = 0$, $\partial B_z/\partial z = 0$ in at least one direction of the coordinate system and respecting the curl character of the field.
2. The external magnetic field exhibits **higher values** of magnetic flux density **B**, and its distribution is homogeneous on the microscopic scale. Then we have $B = \max$, $\partial B_x/\partial x = 0$, $\partial B_y/\partial y = 0$, $\partial B_z/\partial z = 0$ in at least one direction of the coordinate system and respecting the curl character of the field.
3. The external magnetic field is **inhomogeneous** on the macroscopic scale. Then we have $\partial B_x/\partial x \neq 0$, $\partial B_y/\partial y \neq 0$, $\partial B_z/\partial z \neq 0$, respecting the curl character of the field.
4. The external magnetic field exhibits **higher values and gradient** on the macroscopic scale. Then we have $B = \max$ $\partial B_x/\partial x \neq 0$, $\partial B_y/\partial y \neq 0$, $\partial B_z/\partial z \neq 0$, respecting the curl character of the field.

3. NUMERICAL MODEL ANALYSIS

In accordance with [2], we used a simple analysis of the FeNdB permanent magnet blocks having the dimensions $15 \times 10 \times 40$ mm, surface magnetic flux density $B_r = 1.2$ T, and intensity $H_{co} = 850$ kA/m. During the experiment, an element evaluating the observed macroscopic behaviour of matter was inserted in the inhomogeneous magnetic field areas.

4. EXPERIMENTS

The verification of the difference in the properties of the microscopic model of matter under the pre-defined condition of the external magnetic field was performed using a copper element having the dimensions $10 \times 10 \times 10$ mm. This element was cooled down to $-193°$C and then heated at the ambient temperature of 20°C. The heating period was measured repeatedly, starting from $-180°$C and proceeding to $-20°$C. These limits had been chosen with respect to suppressing the systematic measurement error in the experiment; the actual experiment is shown in Fig. 2. The aim of the experiment was to repeat the previous measurement [2] and to verify its results.

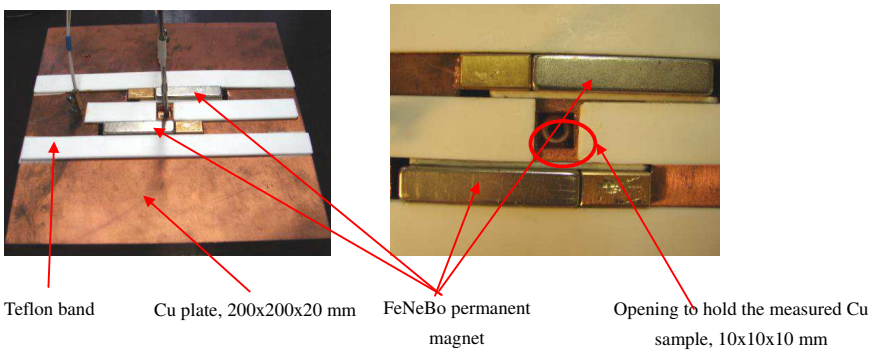

Figure 2: Detailed configuration of the experiment.

Table 1: Measured heating speed values in the examined sample.

Measurement	Time Difference/s			
	1. No Field	2. Gradient Field	3. Homogeneous	4. HomoGrad Field
1	36,64928955	34,48015863	37,71446887	22,82040233
2	38,06576586	36,4855295	41,62355197	28,36592113
3	39,7085593	39,54154481	38,67162785	29,79942564
4	41,18051012	37,88963473	40,20475581	31,49956476
5	42,77172513	38,57823307	38,4903284	33,26028898
6	41,03824944	38,49898872	38,1925093	33,13491397
7	44,16877291	39,23681201	38,91989879	34,11134567
8	45,44665016	38,8054958	37,31208691	33,56003627
9	42,74964147	38,70252762	39,09137363	34,34513303
10	45,26375993	44,30902191	41,99884713	34,38462373
Mean Value	41,70429239	38,65279468	39,22221903	31,21078131
Standard Deviation	2,801316176	2,36366684	1,495505043	3,482702384
Decrease in %	0	−7.317	−5.6	−24.4

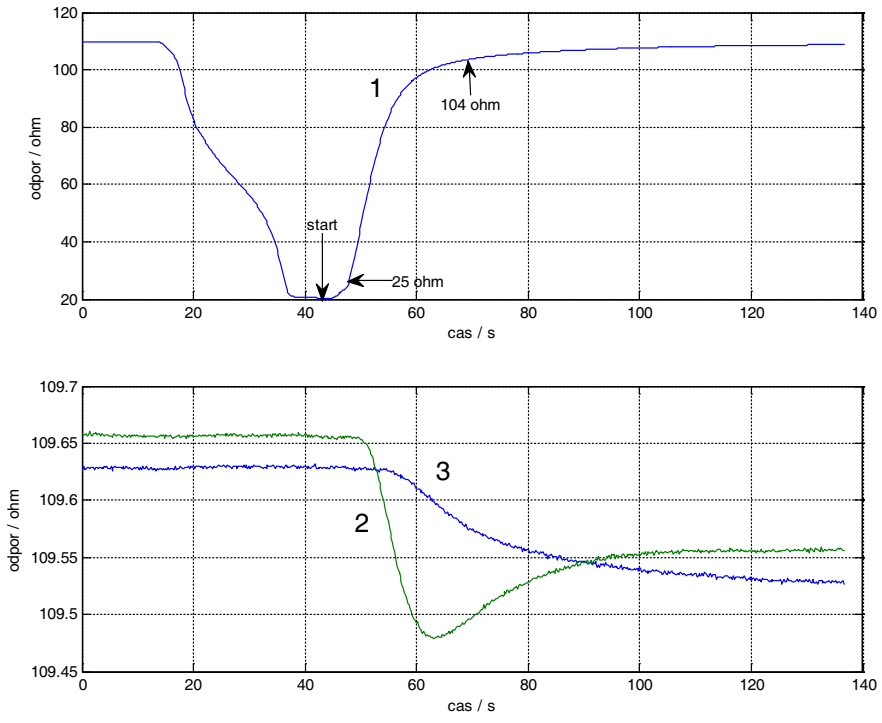

Figure 3: Examples of temperature waveforms during one measurement cycle (the 2nd series of experiments): 1 — Cu cube; 2 — temperature of the Cu block between the magnets at the distance of 60 mm from the centres of the magnets; 3 — temperature of the Cu block at a point located 60 mm (and in a perpendicular direction) from the central section between the magnets.

5. RESULTS OF THE EXPERIMENTS

It follows from the conducted experiments that, in a strong magnetic field with a high gradient character of the magnetic flux density $\mathbf{B}$, $\mathrm{d}B/dx$;200 Tm^{-1} is the lowest density of the time flux τ. A higher value of the time flux density $\boldsymbol{\tau}$ can be found in a magnetic homogeneous field with a low magnetic flux density $\mathbf{B}$, B;2 µT (setting 1, section 2), and the highest value is detected in a homogeneous magnetic field with the magnitude of the Earth's field $-B$;50 µT. (setting 2, section 2). Table 1 contains the values resulting from the tests. The temperature was detected by

a Pt sensor, type PT 100.

The waveforms of the measured temperatures are shown in Fig. 3.

6. CONCLUSION

Repeated measurement has shown that the heating time is shorter than in the first experiments [1]; this condition was achieved via changing the entire measurement task. However, the relative ratio of the heating time is comparable to the previous experiments [2], mainly due to the various magnetic field configurations (1 to 4). Significantly, the HomoGrad configuration (4) exhibits the most distinctive reduction of the time necessary to heat the Cu cube: the total time is only 31.2 ms. All measurements for different settings of the external magnetic field are outside the range of measurement inaccuracy tolerance; thus, it can be proved that the external magnetic field changes the dynamics of the model of matter, and if time density is applied as a quantity, it can be stated that the density of time changes its value in individual cases.

ACKNOWLEDGMENT

The research described in the paper was financially supported by Czech Science Foundation (GA 13-09086S), a project of the BUT science fund, No. FEKT-S-14-2545/2014, and a project from the Education for Competitiveness Operative Programme, No. CZ.1.07.2.3.00.20.0175 (Electro-researcher).

REFERENCES

1. Fiala, P., Z. Szabo, and M. Friedl, "EMHD models respecting relativistic processes of trivial geometries," *PIERS Proceedings*, 95–98, Suzhou, China, September 12–16, 2011.
2. Hutova, E. V., K. Bartusek, and P. Fiala, "The effect of a magnetic field on the speed of temperature change," *PIERS Proceedings*, 915–920, Stockholm, August 12–15, 2013.

Optimized Theoretical Analysis of Antimony Selenide (Sb_2Se_3) Chalcogenide Thin Film

Emmanuel Ifeanyi Ugwu
Department of Industrial Physics, Ebonyi State University, P.M.B 53. Abakaliki, Nigeria

Abstract— Theoretical analysis of the optical and Solid State properties of Antimony Selenide (Sb_2Se_3) thin film using beam propagation technique in which a scalar wave is propagated through the material thin film deposited on a substrate with the assumption that the dielectric medium is section into a homogenous reference dielectric constant term, ε_{ref} and a perturbed dielectric term, $\Delta\varepsilon_p(r)$ representing the deposited thin film medium is presented in this work. These two terms, constitute arbitrary complex dielectric function that describes dielectric perturbation imposed by the medium for the system. This is substituted into a defined scalar wave equation in which the appropriate Green's Function was defined on it and solved using series technique. The field value obtained from Green's Function was used in computation the propagated fields for different wavelength within three windows of electromagnetic wave spectrum during which the influence of the dielectric constants of Sb_2Se_3 thin film on the propagating field was considered. The results obtained from the computation were used in turn to obtain the data that were used in turn to compute the band gaps, solid state and optical properties of the thin film such as reflectance, Transmittance, reflectance and band gap of the thin film.

1. INTRODUCTION

Antimony selenide (Sb_2Se_2) amorphous crystalline thin film (Sato and Miyaoka, 1983) is an alternative material due to its unique switching photovoltaic, thermoelectric, optical and electrical properties [1–3]. Based on this, researchers on material and nona scientists have veraciously applied various techniques to synthesize Sb_2Se_3 thin film. Such methods were single source precursor [4], electro-deposition [4], high temperature evaporation [5] coupled with the use of solution growth technique [7]. In each of these methods, the desire was to discover the one that could be found to enhance optimum efficiency and stabilities in photoelectochemical solar cell configuration as prefigured by [12] that sulfide and selenide of antimony are potential absorber materials in devices for photovoltaic conversion of solar energy As a direct band gap semiconductor whose band gap ranges between 1.10 eV to .60 eV, it is to exhibit photovoltaic and thermoelectric characteristics which endowed the film a good potential in solar selective and a decorative coating, optical and thermoelectric cooling devices. As a matter of fact, with the type of energy band gap possessed by Sb_3Se_3 thin film, it absorbs low energy light in the visible and near infrared regions although this is affected by its deposition composition which often contributes on improving the efficiency and stabilities of its use as solar cell [8]. For instance, some groups have reported that with V-VI composition, the crystal and crystalline Sb_2Se_3 thin film has its band gap energy increased to 1.88 eV [9, 10]. Sze Reported that the conversion efficiency of Sb_2Se_3 thin film in Schottky barrier solar cells of P_t-Sb_2Se_3 [10] and n-Sb_2Se_3IP-Ge [13] structure produced structure with conversion efficiency of 5.55% and 7.3% respectively

This research paper is more oriented towards theoretical concept with regards to quest to probe into study of electromagnetic wave propagation through Antimony selenide. This is due to the fact that it is clear that the application of the thin films generally to harness solar energy and of course even other applications depend on the action of the film on electromagnetic wave propagating through it. Based on this concept, we intend to use computation from beam propagation approach

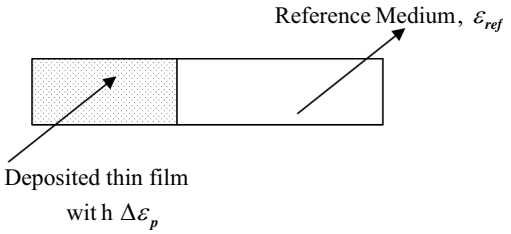

Figure 1: Deposited Sb_2Se_3 thin film model on a glass substrate, where the dielectric function is defined.

to compute the band gap and other solid state properties of Sb_2Se_3 thin film to enable one to ascertain comparatively how the computed result compares to the experimental result.

2. THEORETICAL FRAME WORK OF THE COMPUTATION

In this concept, we start by considering scalar wave equation as given below that defines general expression for wave propagating through an arbitrary medium.

$$\nabla^2\psi(r) + \omega^2\varepsilon_o\mu_o\psi(r) = 0 \quad [14\text{–}16] \tag{1}$$

But however, in this equation we introduce a perturbation that defines dielectric function consisting of reference medium, ε_{ref} representing a space without thin film and a perturbed medium $\Delta\varepsilon_p(r)$ where the thin film is deposited a defined below:

$$\varepsilon_{ref}\varepsilon_p(z) = \varepsilon_{ref} + \Delta\varepsilon(z) \tag{2}$$

where the dielectric function is defined as given below:

$$\varepsilon_p(z) = \varepsilon_{ref} + \Delta\varepsilon(z) \tag{3}$$

$$\psi\left(z, z'\right) = \int_0^{z'} G\left(z, z'\right) V\left(z'\right) \psi\left(z'\right) dz' \tag{4}$$

Given $G\left(z, z'\right)$ the Green's function specified by:

$$G\left(z, z'\right) = \frac{2}{z}\sum_{n=1}^{\infty} \frac{\sin\left(n\pi z'/z\right)}{\gamma^2 - \frac{n^2\pi^2}{z^2}} \tag{5}$$

$$V\left(z\right) = -\gamma^2\Delta\varepsilon_p\left(z\right) = -\gamma^2\left(\varepsilon_p\left(z\right) - \varepsilon_{ref}\right) \tag{6}$$

linearizing $\varepsilon_p\left(z\right)$ as follows:

$$\varepsilon_p\left(z\right) \approx \varepsilon_0 + kz + o\left(z^2\right), \tag{7}$$

We neglect higher order terms as we are dealing with thin film, where ε_0 and k are constants,

$$V\left(z\right) = -\gamma^2\Delta\varepsilon_p\left(z\right) = -\gamma^2\left(\varepsilon_p\left(z\right) - \varepsilon_{ref}\right) = -\gamma^2\left(\varepsilon_0 - \varepsilon_{ref} + kz\right) = -\gamma^2\left(\varepsilon' + kz\right) \tag{8}$$

$\varepsilon' = \varepsilon_0 - \varepsilon_{ref}$ a constant.

Furthermore, we have $\psi\left(z'\right) = \sin\left(\frac{2\pi}{\lambda}z'\right)$, hence the integral becomes:

$$\psi\left(z\right) = \int_0^{z'} \frac{2}{z}\sum_{n=1}^{\infty} \frac{\sin\left(n\pi z'/z\right)}{\gamma^2 - \frac{n^2\pi^2}{z^2}} \left(-\gamma^2\left(\varepsilon' + kz'\right)\right) \sin\left(\frac{2\pi}{\lambda}z'\right) dz' \tag{9}$$

Hence we replaced ε' by ε and write

$$I\left(z, z'\right) = -\gamma^2 \int_0^{z'} \frac{2}{z}\sum_{n=1}^{\infty} \frac{\sin\left(n\pi z'/z\right)}{\gamma^2 - \frac{n^2\pi^2}{z^2}} \left(\varepsilon + kz'\right) \sin\left(\frac{2\pi}{\lambda}z'\right) dz' \tag{10}$$

in which we obtain the integral as

$$\psi\left(z, z'\right) = -\frac{2}{z}\sum_{n=1}^{\infty} \frac{\gamma^2}{\left(\gamma^2 - \frac{n^2\pi^2}{z^2}\right)} \int_0^{z'} \sin\left(n\pi z'/z\right) \left(\varepsilon + kz'\right) \sin\left(\frac{2\pi}{\lambda}z'\right) dz' \tag{11}$$

$$\psi(z,z') = -\frac{2}{z}\sum_{n=1}^{\infty}\frac{\gamma^2}{\left(\gamma^2-\frac{n^2\pi^2}{z^2}\right)}$$
$$\times\left\{\begin{array}{l}\frac{\varepsilon\pi n^3\lambda^3\sin\left[\frac{(2z+n\lambda)\pi z'}{\lambda z}\right]-2\varepsilon\pi n^2\lambda^2 z\sin\left[\frac{(2z+n\lambda)\pi z'}{\lambda z}\right]-4\varepsilon\pi n\lambda z^2\sin\left[\frac{(2z+n\lambda)\pi z'}{\lambda z}\right]}{\pi^2(4z^2-n^2\lambda^2)^2}\\ +\frac{2\varepsilon\pi n^2\lambda^2 z\sin\left[\frac{(2z-n\lambda)\pi z'}{\lambda z}\right]-4k\pi n\lambda z^2\sin\left[\frac{(2z-n\lambda)\pi z'}{\lambda z}\right]-8\varepsilon\pi z^3\sin\left[\frac{(2z-n\lambda)\pi z'}{\lambda z}\right]}{\pi^2(4z^2-n^2\lambda^2)^2}\\ +\frac{8k\pi z^3 z'\sin\left[\frac{(2z+n\lambda)\pi z'}{\lambda z}\right]-8k\pi z^3 z'\sin\left[\frac{(2z-n\lambda)\pi z'}{\lambda z}\right]-4kn\lambda^2 z^2\cos\left[\frac{(2z+n\lambda)\pi z'}{\lambda z}\right]}{\pi^2(4z^2-n^2\lambda^2)^2}\\ +\frac{-4\varepsilon\pi n\lambda z^2\sin\left[\frac{(2z-n\lambda)\pi z'}{\lambda z}\right]+kn^2\lambda^3 z\cos\left[\frac{(2z+n\lambda)\pi z'}{\lambda z}\right]+\varepsilon\pi n^3\lambda^3\sin\left[\frac{(2z-n\lambda)\pi z'}{\lambda z}\right]}{\pi^2(4z^2-n^2\lambda^2)^2}\\ +\frac{k\pi n^3\lambda^3 z'\sin\left[\frac{(2z+n\lambda)\pi z'}{\lambda z}\right]+4kz^3\lambda\cos\left[\frac{(2z+n\lambda)\pi z'}{\lambda z}\right]-2k\pi n^2\lambda^2 z' z\sin\left[\frac{(2z+n\lambda)\pi z'}{\lambda z}\right]}{\pi^2(4z^2-n^2\lambda^2)^2}\\ +\frac{-kn^2\lambda^3 z\cos\left[\frac{(2z-n\lambda)\pi z'}{\lambda z}\right]+8\varepsilon\pi z^3\sin\left[\frac{(2z+n\lambda)\pi z'}{\lambda z}\right]-4kz^2\lambda^2 n\cos\left[\frac{(2z-n\lambda)\pi z'}{\lambda z}\right]}{\pi^2(4z^2-n^2\lambda^2)^2}\\ +\frac{-4kz^3\lambda\cos\left[\frac{(2z-n\lambda)\pi z'}{\lambda z}\right]-4k\pi z^2\lambda n z'\sin\left[\frac{(2z+n\lambda)\pi z'}{\lambda z}\right]-4kn\lambda^3 z^3}{\pi^2(4z^2-n^2\lambda^2)^2}\end{array}\right\}$$

3. RESULTS AND DISCUSSION

Figure 1 is the model of the thin film deposited on a glass side in which we assumed to be the perturbed medium while the portion without thin film represents the reference medium. Fig. 2 shows the optical absorbance of Sb_2Se_3 thin film which appeared is low within the UV region and increased within the optical and near-infrared region. The transmittance within 300 nm and 640 nm seemed higher as when compared to other regions though depicted lower reflectance at the said region. However, both transmittance and reflectance were seen to be high at 640 nm as in Fig. 2 and Fig. 4. The computed band gap of the thin film from the model as in Fig. 3 is 2.56 eV as compared to the experimental value which is 2.430 eV as obtained by Rodrigue-Lazeano et al. in 1999, using chemical bath deposition technique. In another experimental result using the same chemical bath deposition, the band gap was seen to be 1.62 eV while Bajpeyee used the same method and got the band gap to be 1.30 eV [2, 7]. However the prevailing discrepancy in the value of the band gap might have been as a result of the ambient temperature during which the deposition was carried out as it has been noted that annealing and the use of substrate affects the band gap. For instant the same thin film deposited on TiO_2 electrode was to depict band gap of 1.10 eV. On other hand, the discrepancy resulting from the computed band gap could be attributed to the some assumptions and some factors that were neglected during the formulation of the model equation. The behaviour of the spectral absorbance agreed with the report of Rodrigue-Lazeano et al that the thin film absorbs low energy light within visible and near-infrared regions [2]. On the other hand the transmittance and reflectance characteristics within 200 nm–300 nm confirm the observed low energy absorption within UV region. The graphs of the solid state properties were shown in Fig. 4, Fig. 6 and Fig. 7.

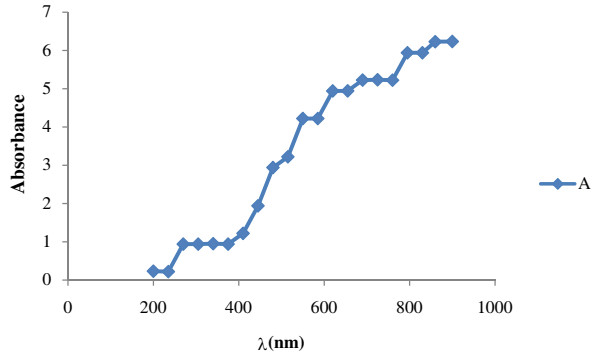

Figure 2: Graph of absorbance as a function of wavelength, λ nm for Antimony Selenide, Sb_2Se_3 thin film.

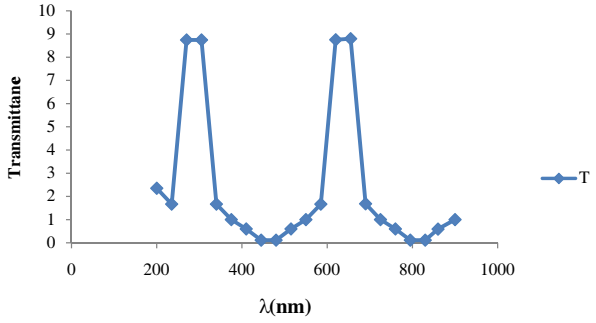

Figure 3: Transmittance vs wavelength, λ nm for Antimony Selenide, Sb_2Se_3 thin film.

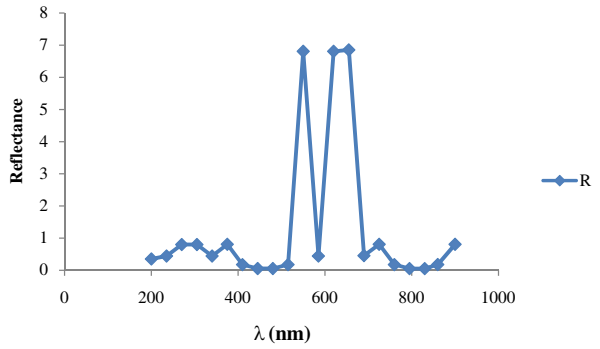

Figure 4: Reflectance vs wavelength, λ nm for Sb_2Se_3 thin film.

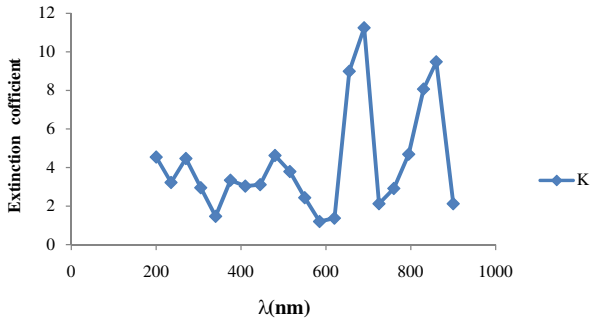

Figure 5: Extinction coefficient as a function of wavelength, λ nm for Antimony Selenide, Sb_2Se_3 thin film.

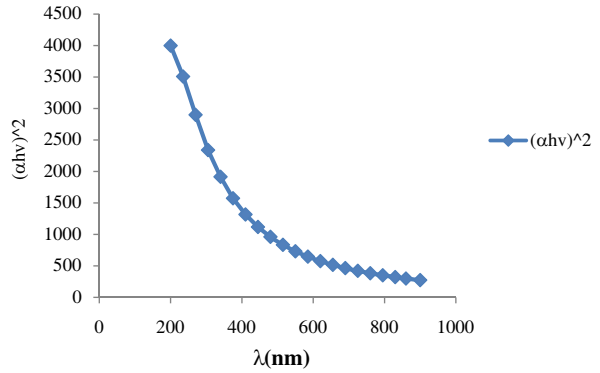

Figure 6: Graph of (αhv)^2 vs wavelength for antimony Selenide, Sb_2Se_3.

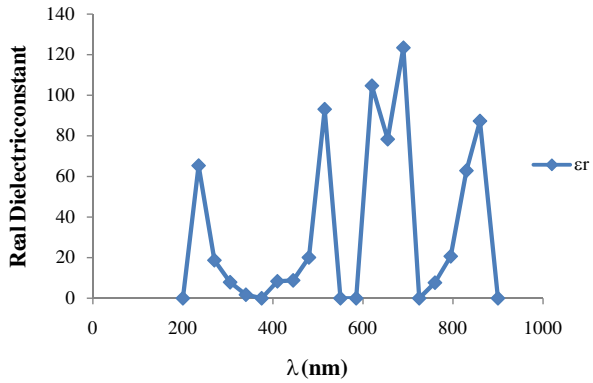

Figure 7: real dielectric constant vs wavelength, λ nm for Antimony Selenide, Sb_2Se_3 thin film.

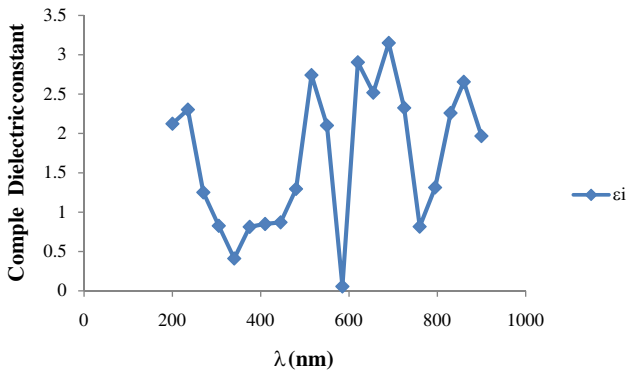

Figure 8: Imaginary dielectric constant vs wavelength, λ nm for Antimony Selenide, Sb_2Se_3 thin film.

4. CONCLUSION

An approach in the form of electromagnetic wave propagation has been employed t optimize the theoretical analysis of the optical and solid state properties of Sb_2Se_3 thin film. A model expression of wave propagating through thin film that was used in the computation was developed from scalar wave equation in conjunction with green's function technique. The data obtained from the model were used in computing the optical, solid state properties and the band gap of the thin film. Comparatively, the computed band gap apart from some approximation and assumption can be compared to the experimentally bath deposited Sb_2Se_3 thin film.

REFERENCES

1. Rajapure, K. Y., C. D Lokhande, and C. H. Bhosele, *Thin Solid Film*, Vol. 311, 114, 1997.
2. Bajpeyee, A. U., *Multilogic Sciences*, Vol. 2, No. 2, 38, 2012.

3. Yang, J., J. H. Zeng, S. H. Yu, L. Yang, Y. H. Zhang, and Y. T. Qiian, *Chem. Meter.*, Vol. 12, 2924, 2002.
4. Bao, J. C., C. Y. Tie, Z. Xu, Z. Y. Suo, Q. F. Zhou, and J. M. Hong, *Adv. Mater.*, Vol. 20, 1483, 2002.
5. Pan, Z. W., Z. R. Dac, and Z. L. Wang, *Science*, 291, Washington, D.C., 2001.
6. Dai, Z. R., D. J. L Gole, J. D. Stout, and Z. L. Wang, *J. Phys. Chem. B*, Vol. 106, 1947, 2002.
7. Owoh, B. and E. I. Ugwu, *JMME*, Vol. 1, No. 1, 38, 2009.
8. Fernandez, A. M. and M. G. Merino, *Thin Solid Films*, Vol. 366, 202–206, 2000.
9. Ritchie, L. and C. W. Kettler, *Proc SPIE*, Vol. 832, 2, 1987.
10. Nair, P. K., M. T. S. Nair, A. Fernandez, and M. Ocampo, *J.Phys. D Appl. Phys.*, Vol. 22, 829, 1989.
11. Rodriguez-Lazeano, Y. and K. N. Watanabe, *Thin Solid Films*, Vol. 493, 77–82, 2005.
12. Rodriguez-Lazeano, Y., L. Gurrero, O. G. Daza, M. T. S. Nair, and P. K. Nair, *Superficies Y Vacio*, Vol. 9, 100–103, 1999.
13. Sze, S. M., *Physics of Semiconductor Devices*, 751, Wiley, New York, 1981. and 849.
14. Dereux, J. F. O. A. and C. Girarad, *J. Opt. Soc. Am.*, Vol. 2, 1073–1081, 1994.
15. Ugwu, E. I., *Int. J. of Multi. Phsics*, Vol. 4, No. 4, 306–315, 2010.
16. Ugwu, E. I. and C. E. Okeke, *Int. J. of Multi. Physics*, Vol. 5, No. 3, 267–274.

Matlab Extension for 3DSlicer: A Robust MR Image Processing Tool

J. Mikulka
Department of Theoretical and Experimental Electrical Engineering
Brno University of Technology, Technická 12, Brno 616 00, Czech Republic

Abstract— Using magnetic resonance tomography to scan biological tissues is currently a very dynamic approach. Based on various image parameters, the method enables us to analyze tissue properties, recognize healthy and pathological tissues, and diagnose the disease or indicate its progression. However, the acquired data must be correctly interpreted and visualized by means of a suitable software tool, such as 3DSlicer (http://www.slicer.org). This well-designed platform provides an interface between the user and the data available in the popular DICOM format, and it facilitates very simple 3D visualization of the MR-based data. One of the main advantages of the open-source software package is undoubtedly its ability to be extended with supplementary modules, for example the Matlab script. The paper describes the open-source environment with a focus on Slicer3D and introduces possible extension of this platform with a module for MR data processing via the three-dimensional, mutiparametric, SVM trainable segmentation method. The module is freely downloadable. The paper also presents a comparison of the processing results with respect to the cycle time and the necessary interactivity. Moreover, the author proposes multiparametric segmentation of a brain tumor edema from T1 and T2-weighted images, and the advantages of the SVM technique are compared with corresponding features of both other fast segmentation methods and the one-parameter approach.

1. INTRODUCTION

In the past, the processing of medical images obtained via magnetic resonance (MR) tomography was reduced to a mere analysis of parameters in a slice [1]. However, the determination of real properties in the examined tissues invariably requires us to produce and process an image via the three-dimensional method, securing the smallest and (if possible) equidistant resolution.

This paper presents a procedure for simple, three-dimensional processing of an MR image of the human brain; the aim of the proposed technique is to facilitate segmentation of the edema in the vicinity of a tumor [2, 3]. Segmentation quality constitutes a very important factor. The boundary accuracy further influences the precision of the time examination of the contrast agent perfusion into the investigated tissue [4, 5]. Moreover, as the perfusion analysis is obviously assumed in the entire volume of the tissue to be analyzed, there follows the necessity of three-dimensional segmentation.

Generally, all segmentation methods can be modified to enable three-dimensional data segmentation. Yet the set of available techniques is very wide, and we therefore need to select the procedure most suitable for the given application. In medical image processing, trainable segmentation methods are frequently used because, as a rule, more images showing the same type of pathological tissue are accessible. Based on such images, it is then possible to set up a model of the investigated tissue, which can be subsequently utilized in the automatic processing of other images [6, 7]. This type of image processing was applied in the described segmentation procedure; here, the conversion of image segmentation to the data classification problem is used. The input data consist in the intensities of the selected pixels/voxels in the regions of the examined tissue and adjacent areas. Each intensity value of the individual pixels is assigned one of the two classifier classes, and the data are further used to train the classifier until suitable coefficients are found. The three-dimensional image processing is carried out in the 3DSlicer environment; this is open-source software for the visualisation and processing of multidimensional tomographic data. The package contains many available plugins, and it can be extended with other tools, such as Matlab scripts. This option is used precisely for the extension with a tool learning multiparametric segmentation. The DICOM format is obviously supported.

2. METHODS

The segmentation method is based on the binary classification of multidimensional data; the processing chain is shown in Fig. 1. First, randomly selected pixels inside and outside the area of

interest are marked with the mouse. The values of intensities at indicated points across all images (T1W, T2W, DWI) constitute the input data for the training of the segmentation model/classifier. In addition to the coordinates of the points, the input to the model comprises also original images and their blurred versions obtained via the application of a Gaussian blurring filter. The output of the model is a grayscale image that has to be thresholded; the threshold level was chosen to be in the middle of the range of intensities. As pointed out above, the actual segmentation is carried out using an SVM classification model. The SVM approach, which finds wide application in the binary classification of data, is based on the search for the optimum hyperplane dividing the data into two groups with minimum error; moreover, there is maximum distance between the hyperplane and the data within both these groups. The training of the model is performed over a set of manually selected points, while the testing is carried out over the set of all image points. Good segmentation results can be achieved if the SVM model parameters are suitably selected; in this context, an important step is the selection of the SVM model kernel. For the purposes of multidimensional data segmentation, the Gaussian radial basis function was chosen to constitute the kernel of the model:

$$K(x,y) = e^{\left(-\frac{\|x-y\|^2}{2\sigma^2}\right)}, \tag{1}$$

where K is the kernel of the function, x is the vector of the classified data, y is the auxiliary vector, and the selection of the parameter σ influences the decision power of the auxiliary vector.

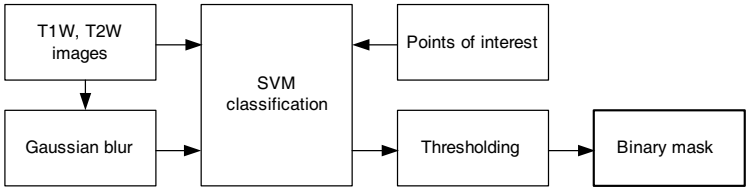

Figure 1: Image processing via the SVM classification model.

3. IMPLEMENTATION

The 3DSlicer application window is shown in Fig. 2. This window comprises several sections: The left part contains a panel enabling the application or the plugins to communicate with the user, and the right portion presents views of the 3D image from several planes. The view planes can be changed arbitrarily; furthermore, it is also possible to display a 3D model, for example after segmentation.

The entire image processing chain is shown in Fig. 3; the indicated processing procedure comprises several stages. First, three-dimensional images weighted by relaxation times T1 (3D-T1) and T2 (3D-T2) and the perfusion coefficient (3D-PR) are read. The images 3D-T1 and 3D-T2 enter the algorithm as structural images, whose intensity distribution provides the basis for biparametric

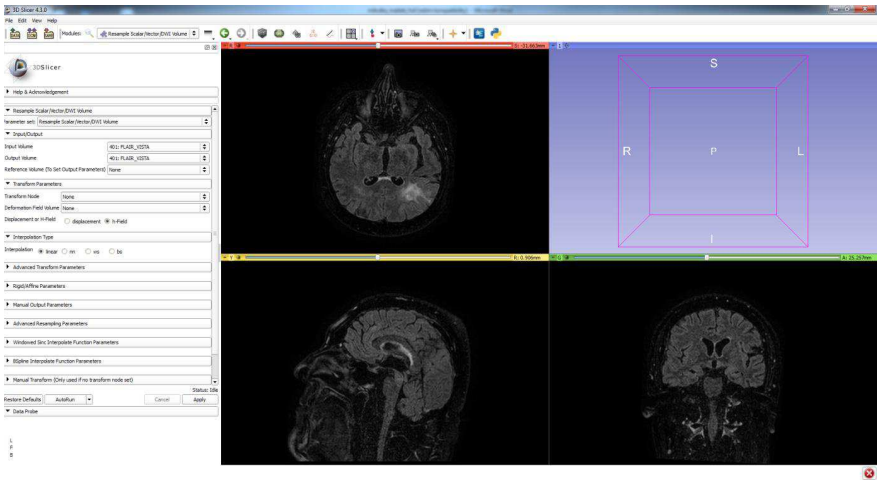

Figure 2: A representative window of the 3DSlicer application.

analysis and segmentation of the examined tissue. The segmentation practice is as follows: During the initial phase, the 3D-T2 image is resampled to the size and number of slices according to the 3D-T1 image. Subsequently, the rigid registration of both images is performed using the marked specific points in the image. Then, in the registered images, the random points are manually selected, and this operation is carried out gradually for both classified groups — inside and outside the classified tissue. The hitherto obtained data (the coordinates of the selected points and their intensities in 3D-T1 and 3D-T2) are sufficient for the classifier learning and segmentation model creation; the setup of the model enables us to segment the complete three-dimensional data and to obtain the binary mask. This 3D mask, in its number of slices and plane, corresponds to the parameters of the original 3D-T1 image and requires further processing. Our objective is to obtain the binary mask of the tissue in the perfusion image; however, due to fast scanning in time, such images exhibit significantly lower resolution than the T1 and T2-weighted images, and their directional vectors may not correspond to one another. The segmented image thus has to be resampled according to the perfusion image parameters. This constitutes the weakest point of the entire algorithm because, ideally, we should also perform registration of the perfusion-weighted images with respect to the T1-weighted images. Such operation is nevertheless almost impossible owing to tissue resolution in perfusion-weighted images; perfusion-weighted images are noise-laden and exhibit very low resolution (in our case, 20 slices with the resolution of 64×64 px). The output of the algorithm therefore consists in a binary image, where the white pixels correspond to points of the examined tissue in the analysed perfusion images; the black pixels then correspond to points in the tissue's environment.

The main advantage of the implementation in 3DSlicer consists in that the software enables the processing of multidimensional tomographic data. The described algorithm utilises the already implemented functions of three-dimensional data resampling, including the change of the image directional vector, rigid or other image registration, and visualisation involving 3D modelling.

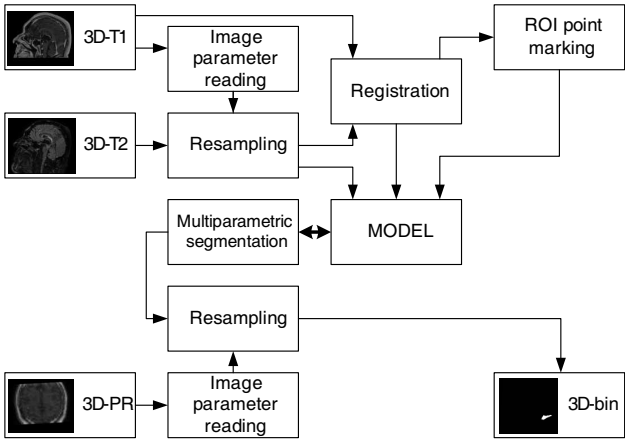

Figure 3: Diagram of the image processing chain in 3Dslicer-based tissue segmentation.

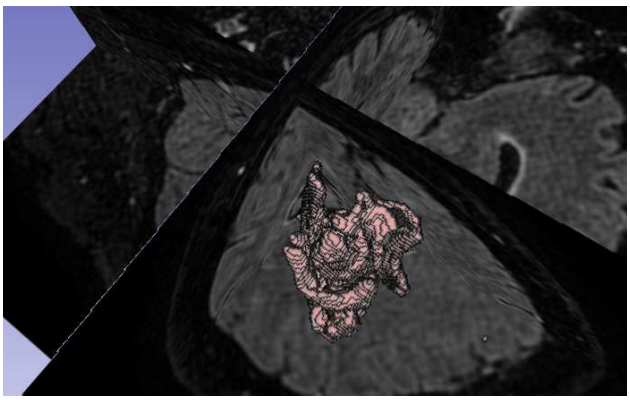

Figure 4: An example of the 3DSlicer-generated output model of the segmented tissue.

4. CONCLUSION

The paper presents and algorithm for the multiparametric segmentation of three-dimensional tomographic images and discusses the 3DSlicer-based implementation of the algorithm carried out using a Matlab plugin. The input data consist in three-dimensional tomographic images representing multiple parameters to increase segmentation efficiency; typically, these data are T1 and T2-weighted images and manually marked points located within the examined tissue. The output of the algorithm is a three-dimensional binary mask resampled to fit perfusion images in the research of perfusion tissue analysis. An example of the output model of the segmented tissue is shown in Fig. 4.

ACKNOWLEDGMENT

This work was supported in part via a grant provided by Czech Science Foundation (GAČR, No. 102/12/1104) and through the project CZ.1.07/2.3.00/30.0039 of Brno University of Technology.

REFERENCES

1. Mikulka, J., E. Gescheidtova, and K. Bartusek, "Soft-tissues image processing: Comparison of traditional segmentation methods with 2D active contour methods," *Measurement Science Review*, Vol. 12, No. 4, 153–161, ISSN: 1335-8871, 2012.
2. Mikulka, J. and E. Gescheidtova, "An improved segmentation of brain tumor, edema and necrosis," *PIERS Proceedings*, 25–28, Taipei, Mar. 25–28, 2013.
3. Mikulka, J., R. Burget, K. Riha, and E. Gescheidtova, "Segmentation of brain tumor parts in magnetic resonance images," *36th International Conference on Telecommunications and Signal Processing*, 565–568, 2013, ISBN: 978-1-4799-0403-7.
4. Cap, M., E. Gescheidtova, and P. Marcon, "Fusion of the T1, T2 weighted and perfusion weighted images for peritumoral region evaluation," *PIERS Proceedings*, 103–105, Suzhou, Sep. 12–16, 2011.
5. Cap, M., E. Gescheidtova, and P. Marcon, "MR perfusion visualization in 3D image," *PIERS Proceedings*, 380–384, Kuala Lumpur, Mar. 27–30, 2012.
6. Mikulka, J., M. Kabrda, E. Gescheidtová, and V. Peřina, "Classification of jawbone cysts via orthopantomogram processing," *TSP Proceedings*, 499–502, Praha, 2012, ISBN: 978-1-4673-1116-8.
7. Marcon, P., K. Bartusek, and M. Cap, "Multiparametric data collection and data processing of animal tissues in MRI images," *PIERS Proceedings*, 358–362, Moscow, Russia, Aug. 19–23, 2012.

Multiparametric Biological Tissue Analysis: A Survey of Image Processing Tools

J. Mikulka
Department of Theoretical and Experimental Electrical Engineering
Brno University of Technology, Technická 12, Brno 616 00, Czech Republic

Abstract— The use of magnetic resonance tomography to scan biological tissues is currently a very dynamic approach. Based on various image parameters, the method enables us to analyze tissue properties, recognize healthy and pathological tissues, and diagnose the disease or indicate its progression. These activities are then necessarily accompanied by the processing of the acquired images. The paper introduces a comparison of statistical tools for the trainable segmentation of multiparametric data obtained through magnetic resonance tomography. In this context, the author briefly compares various available tools (Weka, Slicer3D, and RapidMiner) in view of the input data training and testing, applicability of the classification models, and ability of the input/output data to be extended with other systems for further processing. The paper also describes as a multiparametric task the segmentation of a brain tumor performed with real MR data. The source of the data consists in T1 and T2-weighted images. The proposed segmentation method is carried out within the following phases: data resampling; spatial data coregistration; definition of the training points; training of the SVM classification model; testing of the model and interpretation of the classification results.

1. INTRODUCTION

Magnetic resonance imaging (MRI) is currently one of the most advanced diagnostic techniques, in which the image is generated via the excitation of hydrogen nuclei in the examined tissue and the subsequent sensitive detection of the response. A multitude of imaging sequences is available, and each of them represents different tissue properties. The set of the most common tomograpically acquired parameters includes the relaxation times T1 (spin-lattice) and T2 (spin-spin). In pure water, both the relaxation times are identical. However, they can be suitably applied to recognize biological tissues, respecting that the T2 relaxation time is smaller than T1. The more tissue parameters are known, the higher their recognition rate and the better the possibility of correct pathology diagnosis [1].

2. BRAIN IMAGE PROCESSING

The presented segmentation method is based on the binary classification of multidimensional data [2–4]; the processing chain is shown in Figure 1. First, randomly selected pixels inside and outside the area of interest are marked with the mouse. The values of intensities at indicated points across all images (T1W, T2W, DWI) constitute the input data to train the segmentation model/classifier. In addition to the coordinates of the points, the input to the model comprises also original images and their blurred versions obtained via the application of a Gaussian blurring filter. The output of the model is a grayscale image that has to be thresholded; the threshold level was chosen to be in the middle of the range of intensities. As pointed out above, the actual segmentation is carried out using an SVM classification model. The SVM approach, which finds wide application in the binary classification of data, is based on the search for the optimum hyperplane dividing the data into two groups with minimum error; moreover, there is maximum distance between the hyperplane and the data within both these groups. The training of the model is performed over a set of manually selected points, while the testing is carried out over the set of all image points.

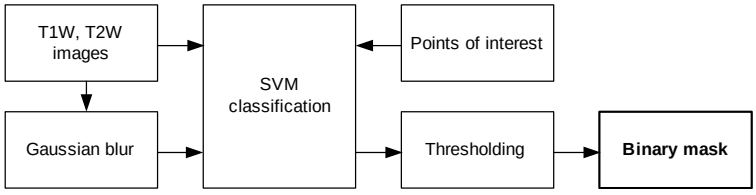

Figure 1: Image processing via the SVM classification model.

Good segmentation results can be achieved if the SVM model parameters are suitably selected; in this context, an important step is the selection of the SVM model kernel. For the purposes of multidimensional data segmentation, the Gaussian radial basis function was chosen to constitute the kernel of the model:

$$K(x,y) = e^{\left(-\frac{\|x-y\|^2}{2\sigma^2}\right)}, \tag{1}$$

where K is the kernel of the function, x is the vector of the classified data, y is the auxiliary vector, and the selection of the parameter σ influences the decision power of the auxiliary vector.

Figure 2 shows the result of brain tumor segmentation described by the multiparametric classification method. This technique has provided very good results in the segmentation of tumor, edema and necrotic tissues; moreover, the robustness of this approach enables us to set up models for the segmentation of concrete types of tumor. The necessity to apply the multiparametric method in the segmentation of MR tomographic data is indicated in Figure 3, which proves that the employed single-parameter classification technique fails to recognize the brain tumor parts. In the described case, the recognition is carried out based on the distribution of the T1 or T2 relaxation time [5–7].

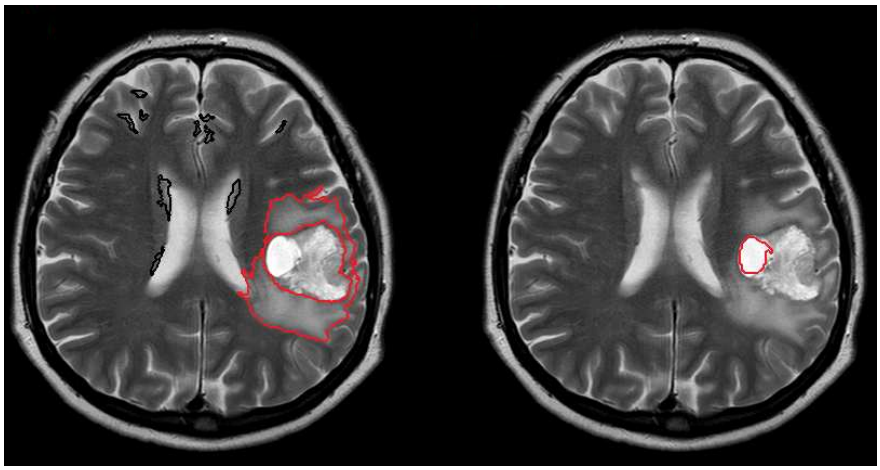

Figure 2: The multiparametric segmentation result for: (a) brain tumor and edema; (b) a necrotic tissue. The examined region is bounded by the red curve.

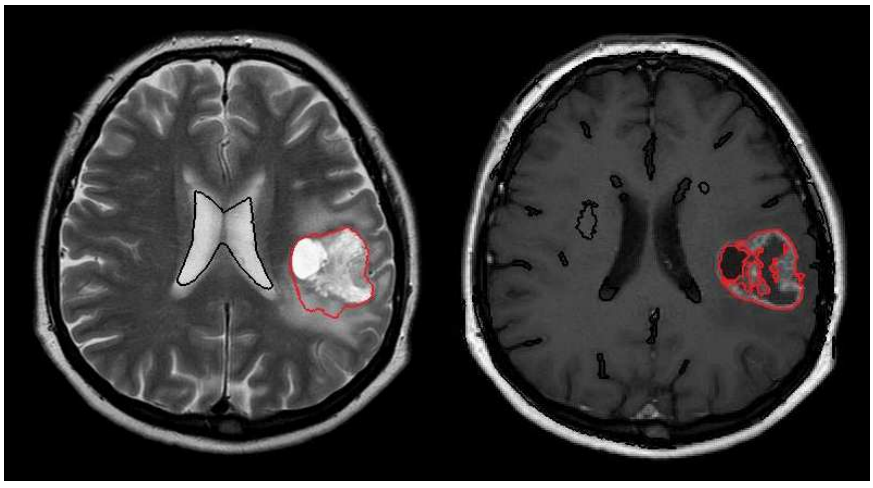

Figure 3: The result for incorrect brain tumor segmentation performed with the single-parametric approach. (a) Tumor segmentation in a T2-weighted image; (b) tumor segmentation in a T1-weighted image.

3. IMAGE PROCESSING TOOLS

Even though a large number of image processing tools are currently available, it is advisable to select software capable of solving the processing chain within the given task completely, without any exception. In practice, however, such choice constitutes the most common difficulty related to the discussed procedure; the individual tools therefore have to be suitably combined. The above-presented multiparametric segmentation of MR tomographic images may serve as a typical example. As is obvious from Figure 1, the entire processing operation involves, first of all, the reading of several three-dimensional images; after this initial stage, the images are resampled to an identical number of slices, and their directional vectors (or scanning levels) are unified. The subsequent phase consists in registering the actual image data, from which the characteristic images suitable for the tissue classification are computed. These feature images constitute the training/testing data that enter the classifier together with the coordinates of the manually selected points representing the regions inside/outside the examined tissue to be segmented. The probability image, which constitutes the output of the classification model, has to be further processed (via techniques such as simple thresholding), and the result of this step already consists in the final binary mask representing the examined tissue region. Table 1 demonstrates the use of selected free access software tools and shows their capabilities within the above-discussed operations.

Table 1: Comparison of software tools for experimental processing of tomographic images.

	3D data support	3D data visualization	advanced data segmentation	data classification	data registration	resampling	manual selection of regions/points
3DSlicer	√ √ √	√ √ √	×	×	√ √ √	√ √ √	√ √ √
ImageJ	√ √	√ √	√**	×	√**	√	√ √ √
RapidMiner	×*	×*	√ √	√ √ √	√	×	√ √
Weka	×	×	×	√ √ √	×	×	×
Matlab	√	√	×	√	√	×	√

* Support for commercial versions only. ** Only with plugins.

4. CONCLUSION

The paper presents and discusses the possibilities of multidimensional tomographic data processing by means of free access software tools. In the described case, the aim of the processing is to carry out multiparametric segmentation of three-dimensional tomographic data. The actual registration is preceded by the resampling of the data, unification of their directional vectors, registration of the image data, and computation of characteristic images. The real segmentation then consists in the selected data classification, in which the classifier model is first set up using the manually selected data; at this initial stage, the data are subdivided into groups inside/outside the examined tissue. As shown in Table 1, it is very difficult to find a tool that would enable us to materialize the entire measuring chain. Considering their individual characteristics, the software tools can be suitably combined, for example in the following manner:

- Preprocessing (resampling; rotation): 3DSlicer.
- Synthesis of the data to be classified (computation of characteristic images): Matlab.
- Data registration: 3DSlicer; Matlab.
- Manual classification and training data preparation: Matlab; ImageJ.
- Classification model setup: Matlab.
- Data visualization; DICOM import and export: 3DSlicer.

The output of the described research consists in both the implementation of the selected algorithms in Matlab and the creation of a Matlab plugin for the 3DSlicer environment. Through combining 3DSlicer and Matlab, it is possible to achieve effective implementation because all the processing chain stages can be carried out only within 3DSlicer; this procedural characteristic markedly simplifies the performance of the tasks and reduces the time necessary for the binary mask to be acquired from the multiparametric analysis of the tomographic data.

ACKNOWLEDGMENT

This work was supported in part via a grant provided by Czech Science Foundation (GAČR, No. 102/12/1104) and through the project CZ.1.07/2.3.00/30.0039 of Brno University of Technology.

REFERENCES

1. Mikulka, J., E. Gescheidtova, and K. Bartusek, "Soft-tissues image processing: Comparison of traditional segmentation methods with 2D active contour methods," *Measurement Science Review*, Vol. 12, No. 4, 153–161, 2012, ISSN: 1335-8871.
2. Mikulka, J. and E. Gescheidtova, "An improved segmentation of brain tumor, edema and necrosis," *PIERS Proceedings*, 25–28, Taipei, Mar. 25–28, 2013.
3. Mikulka, J., R. Burget, K. Riha, and E. Gescheidtova, "Segmentation of brain tumor parts in magnetic resonance images," *36th International Conference on Telecommunications and Signal Processing*, 565–568, 2013, ISBN: 978-1-4799-0403-7.
4. Cap, M., E. Gescheidtova, and P. Marcon, "Fusion of the T1, T2 weighted and perfusion weighted images for peritumoral region evaluation," *PIERS Proceedings*, 103–105, Suzhou, China, Sep. 12–16, 2011.
5. Cap, M., E. Gescheidtova, and P. Marcon, "MR perfusion visualization in 3D image," *PIERS Proceedings*, 380–384, Kuala Lumpur, Malaysia, Mar. 27–30, 2012.
6. Mikulka, J., M. Kabrda, E. Gescheidtová, and V. Peřina, "Classification of jawbone cysts via orthopantomogram processing," *TSP Proceedings*, 499–502, Praha, 2012, ISBN: 978-1-4673-1116-8.
7. Marcon, P., K. Bartusek, and M. Cap, "Multiparametric data collection and data processing of animal tissues in MRI images," *PIERS Proceedings*, 358–362, Moscow, Russia, Aug. 19–23, 2012.

Automatic Segmentation of Multi-contrast MRI Using Statistical Region Merging

P. Dvorak[1, 2], K. Bartusek[2], and E. Gescheidtova[3]

[1]Department of Telecommunications, Faculty of Electrical Engineering and Communication
Brno University of Technology, Technicka 12, Brno 612 00, Czech Republic
[2]Institute of Scientific Instruments of the ASCR, v.v.i., Kralovopolska 147, Brno 612 64, Czech Republic
[3]Department of Theoretical and Experimental Electrical Engineering
Faculty of Electrical Engineering and Communication, Brno University of Technology
Technicka 12, Brno 612 00, Czech Republic

Abstract— Several methods have been developed for segmentation of MR images. Some of them are fully automated and some of them rely on an expert's assistance, such as determination of a starting point etc.. The fully automated methods are usually based on prior knowledge of a given object and can be used only for particular problem. The purpose of the proposed method is a fully automatic segmentation for general MR images independent on the number of tissues present. The proposed method is based on Statistical Region Merging (SRM) algorithm developed by Richard Nock and Frank Nielsen in 2004. The suitable MR contrasts for this algorithm, as it was confirmed during the test phase, are T1, T2 and FLAIR images. The segmentation process divides to image into regions according the properties in the area, but it does not consider the unconnected areas. For this reason, the algorithm is repeated for created segments without a joint border condition. The algorithm was tested on 5000 axial images with resolution 256×256 pixels. In 2256 slices, the tumor was present. Since the proposed method is fully automatic and independent of image intensities, each image of the database can be considered as unique and independent of others. The Dice coefficient for tissue segmentation varies for particular tissues. The best average result was achieved for grey matter, where the dice coefficient reached value 0.84. The results show the suitability of SRM method for multi-contrast MRI segmentation.

1. INTRODUCTION

This paper focuses on automatic segmentation of magnetic resonance images, which belongs to the general problem of image segmentation. Since the MR technique is becoming more popular due to its non-invasive principle, the imaging of biological structures by MR equipments is a routine investigating procedure today [1]. For this reason, the automatic processing of this kind of images is getting more attention and can lead to automatic evaluation of tissue properties [2] or pathology detection [3].

General image segmentation is still an unsolved problem, therefore specific methods have to be applied for particular types of images. General method that could be applied for all kinds of images has not been developed so far and in the near future the situation will probably remain the same. For MR image segmentation, the classic techniques such as thresholding, region growing, active contour, etc. can be used [4]. Another type of segmentation used in MRI is pixel classification into several classes. This can be either supervised using algorithms such as SVM [5] used e.g., in [6], or unsupervised using clustering algorithms. Such algorithms can be based on data space division such as k-means algorithm [7] or they can respect the noise distribution such as Gaussian Mixture Model using the Expectation-Maximization algorithm for determination of model parameters [8].

The method proposed in this paper does not involve any a priori knowledge about the input image, such as reference image, training process or defined number of tissues. Hence, the technique can be labeled as a fully automatic and unsupervised segmentation algorithm of MR brain images.

2. METHODOLOGY

The segmentation process consists of three main steps: Preprocessing, Segmentation and Segment merging. At first, the preprocessing is performed. This step consists of general preprocessing algorithms used in MR processing works. The preprocessing is followed by the segmentation, which is carried out by Statistical Region Merging algorithm, which was developed by Nock and Nielsen in 2004 [9]. When the image is segmented, the regions are merged to detect occurrences of particular tissues in several locations.

2.1. Preprocessing

As in every kind of image processing, the preprocessing is an important step for image analysis. The preprocessing here consists of Region of Interest (ROI) definition, noise reduction, and inhomogeneity compensation. In case of multi-contrast segmentation, the registration of particular images is desired. Since the aim of this work is the segmentation itself, the preprocessing process is described roughly and several techniques are recommended.

Several techniques for ROI definition (Brain extraction) such as the algorithm proposed in [10] have been developed. This step also decreases the run-time since the image can be cut to the smallest necessary size. The noise reduction is carried out by Wiener filter [11], which uses a statistical approach and makes the tissues more compact and reduces the noise with borders preserved, which is the advantage compared to, e.g., widely used Gaussian filter. For the inhomogeneity compensation purpose, the algorithm Histogram matching, which is implemented in 3D Slicer (http://www.slicer.org/) can be used. The multi-contrast registration can be done by algorithm for multi-modal brain images, the new technique described in (bi-modal) is suitable.

Nevertheless, the images of the testing database are already co-registered and skull-stripped. Thus, the aim of this work is the segmentation technique and the registration and skull-stripping are not performed here.

2.2. Segmentation

The segmentation uses the Statistical Region Merging (SRM) algorithm. Here, the method was adapted to multi-contrast MR images, where the algorithm can work with any number of contrasts. The reason has been described above.

The only input of Statistical Region Merging Algorithm, except the image itself, is a parameter Q, which according to [9] "allows quantifying the statistical complexity of the image, the generality of the model, and the statistical hardness of the task." The larger Q, the more smaller segments are created. In our case of MRI segmentation with image size about 200×200 px, this parameter was firmly set to value 256 according to experiments. Since the Segment Merging is carried out afterwards, the slight oversegmentation is appropriate here. Since the SRM is primarily designed to RGB image segmentation, where each channel is represented by 8 bits, the intensities in every MR contrast are normalized into the range $\langle 0; 255 \rangle$.

The SRM algorithm starts with splitting the input image into small segments with the size just of one pixel. In 4-connexity, every pixel creates 4 or less adjacent pairs. The pairs of adjacent pixels are sorted according to the similarity between these two pixels. The neighboring pixels are joined into segments if they meet the similarity condition. The set of adjacent pixels is traversed only once, which makes the algorithm very fast. The detailed information about the SRM algorithm can be found in [9]. The advantage of this method, compared to segmentation techniques based on boundary detection, such as active contours [12], is its performance in areas where no clear border are visible, which is also the case of brain MR images. Another advantage, as already mentioned, is its speed.

2.3. Segment Merging

The segmentation process divides the image into regions according to the properties in the area, but it does not consider the unconnected areas. For this reason, the postprocessing step consisting of segments unification has to be performed.

The unification process is similar to the segmentation algorithm and it is also mentioned in [9]. In SRM, each pixel is considered to be a unique region at the beginning and only adjacent pixels can be merged during this process. Here, each segment created during SRM can be merged with any other segment. In SRM, each pixel creates no more than 4 pairs. Every segment creates $N-1$ pairs, where N denotes the number of regions in segmented image. All of these pairs enter the same computation as pairs in SRM algorithm. According to the experiments, the Q in this process is reduced to value 128 to avoid the repetition of the oversegmentation.

The result of the Segment Merging is a labeled image, where one label does not need to create a connected region, which means that more locations of particular tissue were detected.

3. EXPERIMENTS AND RESULTS

3.1. Datasets

Brain tumor image data used in this work were obtained from the MICCAI 2012 Challenge on Multimodal Brain Tumor Segmentation (http://www.imm.dtu.dk/projects/BRATS2012) organized by

B. Menze, A. Jakab, S. Bauer, M. Reyes, M. Prastawa, and K. Van Leemput. The challenge database contains fully anonymized images from the following institutions: ETH Zurich, University of Bern, University of Debrecen, and University of Utah.

The test database consists of simulated T1, T2, and FLAIR images. From each case, 100 slices in each plane were taken. 25 subjects of high-grade and 25 subjects of low-grade glioma were available, which means that the algorithm was tested on 5000 images with resolution 255×255 px. In 2256 slices, the tumor was present. Since the proposed method is fully automatic and independent of image intensities, each image of the database can be considered as unique and independent of others.

All the simulated images are in BrainWeb space [13]. The information about the simulation method can be found in [14].

3.2. Evaluation Criteria

For the evaluation of region segmentation, Dice Coefficient and Accuracy were used. The Dice Coefficient (DC) (DICE), in some works called Similarity Index, is computed according to the equation

$$\mathrm{DC} = \frac{2\,|A \bigcap B|}{|A| + |B|}, \tag{1}$$

where A and B denotes the ground truth and the result masks of the segmentation, respectively. This criterion compares the intersection of two sets with their union. The range of values of DC is $\langle 0; 1 \rangle$, where the value 1 expresses the perfect segmentation. According to [15], the DC $> 0,7$ indicates an excellent similarity.

Another measure widely employed for segmentation evaluation is Accuracy (A), used e.g., in [6] and defined by the equation:

$$A = \frac{TP + TN}{TP + FP + TN + FN}, \tag{2}$$

where TP, FP, FN and TN stand for "True Positive", "False Positive", "False Negative", and "True Negative", respectively. Both measures are in the same range as DC and the higher value indicates the better performance as well.

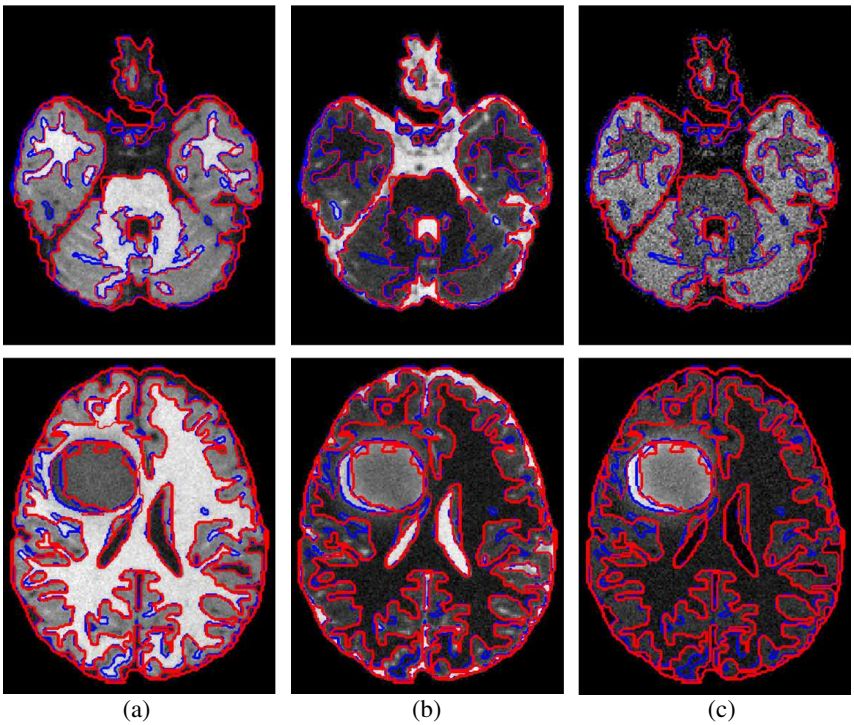

(a) (b) (c)

Figure 1: Results of the segmentation of healthy slices with and without a tumor for different subjects. (a) T1-weighted images. (b) T2-weighted images. (c) FLAIR images, Red: result of segmentation, Blue: ground truth.

Table 1: Segmentation evaluation by dice coefficient and accuracy for both planes.

	Dice		Accuracy	
	Median	Average	Median	Average
WM	0.87	0.84 ± 0.13	0.91	0.91 ± 0.05
GM	0.87	0.85 ± 0.06	0.87	0.86 ± 0.05
CSF	0.81	0.78 ± 0.16	0.95	0.94 ± 0.03
Tumor	0.59	0.47 ± 0.31	0.96	0.92 ± 0.17
Edema	0.56	0.49 ± 0.34	0.97	0.95 ± 0.95

3.3. Results

The summary of the segmentation process results is in Table 1.

In average, the number of detected tissues in images was 1.4 more than the true number. This was due to inaccurate segmentation of small regions. The average size of such redundant region was about 11.8% of the brain size. This was mostly due to unclear border between adjacent tissues and created regions in between.

The results are visualized in Fig. 1, where the ground truth segmentation (blue) is compared with the result of the proposed algorithm (red) on all T1, T2 and FLAIR contrast that were used for the segmentation. The results for healthy brains and brains with tumor are shown.

4. CONCLUSION

The purpose of this work is to show a fully automatic segmentation technique for multi-contrast MRI. This method works also for one-contrast MRI but with less precision, since not all tissues could be well separated according to intensities in one image. The future work will cover an improvement in segment merging process, the automatic tissue determination according to properties, and extension into 3D.

The big advantage compared to other state-of-the-art methods is its independence of the number of segmented tissues. The algorithm can automatically segment both healthy and afflicted brains and could be used also for other parts of the body.

ACKNOWLEDGMENT

The described research is funded by projects SIX CZ.1.05/2.1.00/03.0072, project GACR 102/12/1104, and project COST CZ LD14091.

REFERENCES

1. Gogola, D., A. Krafck, O. Strbak, and I. Frollo, "Magnetic resonance imaging of surgical implants made from weak magnetic materials," *Measurement Science Review*, Vol. 13, No. 4, 165–168, 2013.
2. Mikulka, J., E. Gescheidtova, P. Marcon, K. Bartusek, and A. prlkov, "Evaluation of tissue properties in MR images," *PIERS Proceedings*, 339–342, Moscow, Russia, Aug. 19–23, 2012.
3. Dvorak, P., W. Kropatsch, and K. Bartusek, "Automatic detection of brain tumors in MR images," *36th International Conference on Telecommunications and Signal Processing (TSP)*, 577–580, 2013.
4. Zhang, H., J. E. Fritts, and S. A. Goldman, "Image segmentation evaluation: A survey of unsupervised methods," *Computer Vision and Image Understanding*, Vol. 110, No. 2, 260–280, 2008, [Online] Available: http://www.sciencedirect.com/science/article/pii/S1077314207001294.
5. Cortes, C. and V. Vapnik, "Support-vector networks," *Mach. Learn.*, Vol. 20, No. 3, 273–297, Sep. 1995, [Online] Available: http://dx.doi.org/10.1023/A:1022627411411.
6. Mikulka, J. and E. Gescheidtova, "An improved segmentation of brain tumor, edema and necrosis," *PIERS Proceedings*, 25–28, Taipei, Mar. 25–28, 2013.
7. MacQueen, J. B., "Some methods for classification and analysis of multivariate observations," *Proceedings of 5th Berkeley Symposium on Mathematical Statistics and Probability 1*, 281–297, 1967.
8. McLachlan, G. and D. Peel, *Finite Mixture Models*, John Wiley & Sons, Inc., 2000.
9. Nock, R. and F. Nielsen, "Statistical region merging," *IEEE Transactions on Pattern Analysis and Machine Intelligence*, Vol. 26, No. 11, 1452–1458, 2004.

10. Uher, V., R. Burget, J. Masek, and M. Dutta, "3d brain tissue selection and segmentation from MRI," *36th International Conference on Telecommunications and Signal Processing (TSP)*, 839–842, 2013.
11. Lim, J. S., *Two-dimensional Signal and Image Processing*, Prentice Hall, 1990.
12. Mikulka, J., E. Gescheidtova, and K. Bartusek, "Soft-tissues image processing: Comparison of traditional segmentation methods with 2d active contour methods," *Measurement Science Review*, Vol. 12, No. 4, 153–161, 2012.
13. Prastawa, M., E. Bullitt, and G. Gerig, "Simulation of brain tumors in MR images for evaluation of segmentation efficacy," *Medical Image Analysis*, Vol. 13, No. 2, 297–311, 2009. [Online] Available: http://www.sciencedirect.com/science/article/pii/S1361841508001357.
14. Cocosco, C. A., V. Kollokian, R. K.-S. Kwan, G. B. Pike, and A. C. Evans, "Brainweb: Online interface to a 3d MRI simulated brain database," *NeuroImage*, Vol. 5, 425, 1997.
15. Zijdenbos, A. and B. Dawant, "Brain segmentation and white matter lesion detection in MR images," *Critical Reviews in Biomedical Engineering*, Vol. 22, 401–465, 1994.

The Optical Angular Momentum in a Vector Vortex Optical Field

Rui-Pin Chen
Department of Physics, Zhejiang Sci-Tech University, Hangzhou 310028, China

Abstract— We study the propagation dynamics of vortex vector field with azimuthally locally uniform and inhomogeneous polarization states by using angular spectrum the electromagnetic beam. The evolution of the polarization states in the field cross section is analyzed numerically in detail during propagation by using the Stokes polarization parameters. The results indicate that the polarization states in the field cross section rotate along the propagation axis due to the existence of vortex field. In particular, the interaction between the central phase singular point (i.e., dislocation) and the polarization singular point (i.e., disclination) leads to the creation or annihilation of optical field in the center of optical field, depending on the number of vortex and polarization topological charges. The transverse energy flux distributions and both spin and orbital optical angular momentum of vector vortex optical field with the different states of polarization in the cross-section of the field are computed and analyzed. Our results indicate that the different states of polarization in the cross-section of the optical vector vortex field can influence and reconstruct the transverse Poyting vector (energy flux) and both spin and orbital optical angular momentum flux distribution in the cross-section of the field. These results, therefore, provide useful information on how to spatially manipulate the angular momentum of laser beams by choosing appropriate states of polarization in the cross-section of the field. This work provides further insight into dynamic behaviors of the vector vortex optical field and sheds light on a new approach in manipulating micro-particles.

Light carries angular momentum comprised of both a spin component associated with polarization, and an orbital component arising from the spatial profile of light intensity and the phase [1]. Considerable interest in orbital angular momentum arises from its potential use in multiple applications including quantum information processing, atomic manipulation, micro-manipulation and the biosciences [2–5].

In the coordinate system, the z-axis is taken to be the propagation axis. A cylindrical optical vector field is expressed as [6, 7]

$$E(r,\theta) = A(r,\theta)\left[\cos(m\theta+\theta_0)\mathbf{e_x} + \exp(i\Delta\theta)\sin(m\theta+\theta_0)\mathbf{e}_y\right] \tag{1}$$

where $r = \sqrt{x^2+y^2}$ and $\theta = \arctan(y/x)$ are the polar radius and azimuthal angle in the polar coordinate system, respectively. m is the topological charge, and θ is the initial phase. $\mathbf{e}_x$ and $\mathbf{e}_y$ are the unit vectors in x and y-direction, respectively. In Eq. (1). $\Delta\theta = 0$ implies that the x- and y-components have the same phase. In this case, it is seen from Eq. (1) that the SoP depends only on the azimuthal angle φ. The vector optical field is linearly polarized at any position in the field cross section. When $m = 1$ with $\theta = 0$ and $\pi/2$, the vector fields describe the radially and azimuthally polarized vector fields, respectively. On the other hand, Eq. (1) degenerates to the linearly-polarized fields if $m = 0$.

By using the Fourier transform, the transverse components of the vector angular spectrum $A_x(\rho\cos\theta, \rho\sin\theta)$ and $A_y(\rho\cos\theta, \rho\sin\theta)$ are given by the Fourier transform of the initial field:

$$\begin{pmatrix} A_x(\rho\cos\phi, \rho\sin\phi) \\ A_y(\rho\cos\phi, \rho\sin\phi) \end{pmatrix} = \left(\tfrac{k}{2\pi}\right)^2 \begin{pmatrix} \int_0^\infty\int_0^{2\pi} A(r)\cos(m\theta+\theta_0)\exp\left[-ikr\rho\cos(\theta-\phi)\right] r d\theta dr \\ \int_0^\infty\int_0^{2\pi} A(r)\exp(i\Delta\theta)\sin(m\theta+\theta_0)\exp\left[-ikr\rho\cos(\theta-\phi)\right] r d\theta dr \end{pmatrix} \tag{2}$$

where k is the wavenumber. For the Gaussian distribution with the n-th vortex and an arbitrary polarized electromagnetic field (see Eq. (1)) in the source plane $z = 0$, $A(r,\theta) = \exp(-r^2/w^2)\exp(in\theta)$

where w is beam-width, the angular spectrum is

$$\begin{aligned} A(\rho\cos\phi,\rho\sin\phi) \;=\; & \pi i^{m+n}\left(\frac{k}{2\pi}\right)^2\frac{\sqrt{\pi}kw^3\rho}{8}\exp\left(-k^2w^2\rho^2/8\right) \\ & \times\Big\{P\exp\left[i(m\phi+n\phi+\theta_0)\right](\mathbf{e_x}-i\exp(i\Delta\theta)\mathbf{e}_y) \\ & +T\exp\left[-i(m\phi-n\phi+\theta_0)\right](\mathbf{e_x}+i\exp(i\Delta\theta)\mathbf{e}_y) \\ & -\Big[P\exp\left[i(m\phi+n\phi+\theta_0)\right](\cos\phi-i\exp(i\Delta\theta)\sin\phi) \\ & +T\exp\left[-i(m\phi-n\phi+\theta_0)\right](\cos\phi+i\exp(i\Delta\theta)\sin\phi)\Big]\rho/\gamma\mathbf{e}_z\Big\} \end{aligned} \tag{3}$$

with

$$\begin{aligned} P \;&=\; I_{(m+n-1)/2}\left(k^2w^2\rho^2/8\right)-I_{(m+n+1)/2}\left(k^2w^2\rho^2/8\right) \\ T \;&=\; I_{(m-n-1)/2}\left(k^2w^2\rho^2/8\right)-I_{(m-n+1)/2}\left(k^2w^2\rho^2/8\right) \end{aligned}$$

where $I(\cdot)$ are the Bessel functions of the second kind and $\mathbf{e_z}$ is the unit vector in z direction. The electric field component of the vector cylindrical optical field in z plane can be represented as:

$$\begin{aligned} E(r) \;=\; & (-1)^{m+n}\frac{k^3w^3\sqrt{\pi}}{16}\int_0^\infty e^{-\frac{k^2w^2\rho^2}{8}} \\ & \Big\{PJ_{m+n}(-kr\rho)\exp\left[i(m\theta+n\theta+\theta_0)\right](\mathbf{e_x}-i\exp(i\Delta\theta)\mathbf{e}_y) \\ & +TJ_{m-n}(-kr\rho)\exp\left[-i(m\theta-n\theta+\theta_0)\right](\mathbf{e_x}+i\exp(i\Delta\theta)\mathbf{e}_y) \\ & +\Big[PJ_{m+n+1}(-kr\rho)\exp\left[i(m\theta+n\theta+\theta+\theta_0)\right](1-\exp(i\Delta\theta)) \\ & +PJ_{m+n-1}(-kr\rho)\exp\left[i(m\theta+n\theta-\theta+\theta_0)\right](1+\exp(i\Delta\theta))) \\ & +TJ_{m-n-1}(-kr\rho)\exp\left[-i(m\theta-n\theta-\theta+\theta_0)\right](1+\exp(i\Delta\theta)) \\ & +TJ_{m-n+1}(-kr\rho)\exp\left[-i(m\theta-n\theta+\theta+\theta_0)\right](1-\exp(i\Delta\theta))\Big]i\rho/2\gamma\mathbf{e}_z\Big\} \\ & \times\exp\left(ik\gamma z\right)\rho^2d\rho \end{aligned} \tag{4}$$

Under the paraxial approximation, the transverse energy (TE) flow of the vector cylindrical optical field in z plane can be written in the following forms:

$$\vec{S}=\frac{1}{2}\mathrm{Re}\left[\vec{E}(r)\times\vec{H}^*(r)\right]=\frac{1}{2\mu_0\omega}\mathrm{Im}\left[\vec{E}(r)\times\left(\nabla\times\vec{E}(r)^*\right)\right] \tag{5}$$

where Re[·] and Im[·] denote the real and imaginary parts, respectively, and the asterisk corresponds to its complex conjugation. Therefore, Eq. (7) describes the energy flux distribution at the propagation plane of $z\equiv$ constant. The optical angular momentum flux density is [8]

$$J_z=l_z+s_z=\frac{E^*\cdot(r\times\nabla)E\cdot e_z}{\iint E^*\cdot Edxdy}+\frac{E^*\times E\cdot e_z}{i\iint E^*\cdot Edxdy} \tag{6}$$

where the first and second terms represent the flux density of the orbital angular momentum (OAM) flux density Lz and the spin angular momentum flux density Sz, respectively.

The distribution of the TE flux and the OAM flux are depicted in Fig. 1. It is clearly seen from Fig. 1 that the TE flux and the OAM flux depend on SoP, as expected. The results indicate that the different states of polarization in the cross-section of the optical vector vortex field can influence and reconstruct the transverse Poyting vector (energy flux) and both spin and orbital optical angular momentum flux distribution in the cross-section of the field. The results provide a deeper understand to manipulate the angular momentum of laser beams.

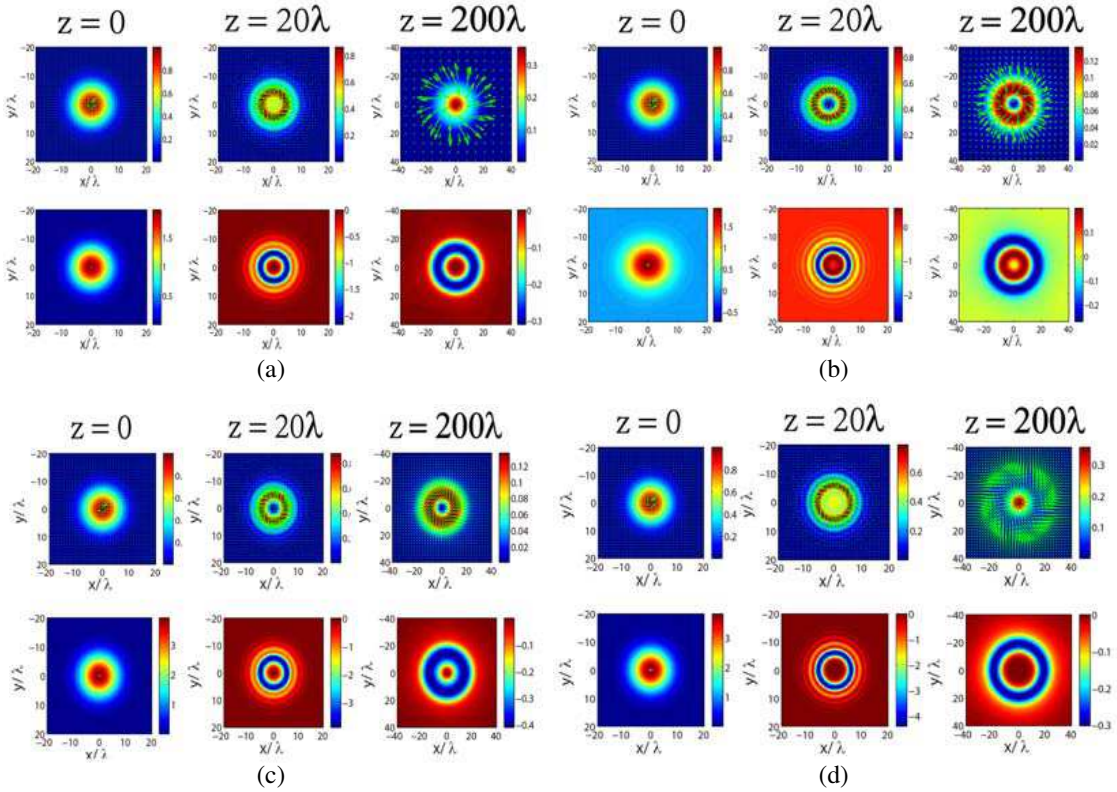

Figure 1: The distribution of TE flows (upper) and OAM flux density (lower) in the cross-section of a local linearly polarized vortex vector optical field ($\Delta\theta = \pi/2$ and $\varphi_0 = 0$) with (a) $n = 1$, $m = 1$; (b) $n = 1$, $m = 2$; (c) $n = 2$, $m = 1$; (d) $n = 2$, $m = 2$ for different propagation distance. Arrows represent the directions of transverse energy flow in the field cross-section.

REFERENCES

1. Allen, L., M. W. Beijersbergen, R. J. C. Spreeuw, and J. P. Woerdman, "Orbital angular momentum of light and the transformation of Laguerre-Gaussian laser modes," *Phys. Rev. A*, Vol. 45, 8185–8189, 1992.
2. Molina-Terriza, G., J. P. Torres, and L. Torner, "Management of the angular momentum of light: Preparation of photons in multidimensional vector states of angular momentum," *Phys. Rev. Lett.*, Vol. 88, 013601, 2002.
3. Chen, R. P., K. H. Chew, and S. He, "Dynamic control of collapse in a vortex airy beam," *Sci. Rep.*, Vol. 3, 1406, 2013.
4. Berkhout, G. C. G., M. P. J. Lavery, J. Courtial, M. W. Beijersbergen, and M. J. Padgett, "Efficient sorting of orbital angular momentum states of light," *Phys. Rev. Lett.*, Vol. 105, 153601, 2010.
5. Wang, X. L., J. Chen, Y. Li, J. Ding, C. S. Guo, and H. T. Wang, "Optical orbital angular momentum from the curl of polarization," *Phys. Rev. Lett.*, Vol. 105, 253602, 2010.
6. Zhan, Q. W., "Cylindrical vector beams: From mathematical concepts to applications," *Adv. Opt. Photon.*, Vol. 1, 1–57, 2009.
7. Wang, X. L., Y. N. Li, J. Chen, C. S. Guo, J. P. Ding, and H. T. Wang, "A new type of vector fields with hybrid states of polarization," *Opt. Express*, Vol. 18, 10786–10795, 2010.
8. Berry, M., "Paraxial beams of spinning light," *Proc. SPIE*, Vol. 3487, 6, 1998.

Improvement on Optical Microfiber Fabrication Control Technique by Monitoring Mode Cutoff Position

Yang Yu, Xueliang Zhang, Zhangqi Song, Jianfei Wang, and Zhou Meng
College of Optoelectronic Science and Engineering
National University of Defense Technology, Changsha 410073, China

Abstract— By monitoring the intermodal interference pattern, we realize online diameter calibration during optical microfiber (OM) tapering process. By a comparison of LP_{02} mode cut-off position between theoretically prediction and the actual monitoring result, we introduce modifications of tapered parameters, and realize an online and precise feedback control in the OM tapered process. Our online feedback control technology provides an effective tool in acquiring high quality OMs by improving the tapered accuracy while maintaining good repeatability, which is essential for applications in scientific research and engineering areas.

1. INTRODUCTION

Optical microfiber (OM) has been concerned for its special characteristics such as large evanescent field, high disperse and strong nonlinearity et al. [1]. Many works had been performed to try to get OM with various fabricating technologies. An OM with conventional optical fiber as pigtails has been paid more attentions for its convenient application. Although the manufacture and application of OM have obtained much development, some problems still exist in aspects such as production process, transmission loss, and uniformity of waveguide structure et al., which may not meet the requirement of engineering and scientific research [2]. For example, in research areas such as atomic trapping [3, 4], sensing technique based on evanescence field [5, 6], the production monitoring technology should be exploited to ensure the characteristics of OMs reliable in practical applications.

The OM fabrication monitoring systems had been studied by many people to ensure well optical transmission properties. The monitoring systems constructed with different devices were used. A combination of white light source and optical spectrum analyzer can be used to get the evolution of the transmitting spectrum of the tapering fiber during the whole tapering process. Another combination of laser source and photo-detector can be used to get the evolution of excited modes based on the intermodal energy transfer [7–10]. In this paper, we want to enhance the interference phenomenon in the tapering fiber during the fabrication process of OM, by choose a high coherent laser as the monitoring light source, and use a power jumping point in the monitoring signal corresponding to the normalized cut-off frequency of the LP_{02} mode to judge the diameter of the fabricated OM. So, by using different online feedback methods to adjust the tapered parameters, the OM tapered accuracy could be improved.

2. ANALYSIS OF INTERMODAL INTERFERENCE CHARACTERISTICS IN OM MANUFACTURE PROCESS

In this paper, the OM tapering device was set up based on a widely used modified flame-brushing technique [11], shown in Figure 1. A telecom fiber (SMF-28, Corning) is clamped onto the two motorized precision translation stages and stretched under the control of computer, while the bare part of the fiber is heated by a micro-heater (CMH-7019, NTT-AT). Both stages and micro-heater are automatically controlled by a computer. One end of the drawn fiber is connected with a high coherent laser source (RIO, 1550 nm, line width 2 kHz). The other end is directly connected to the detector (OE-200). Based on the model in Ref. [12], OMs with different structure and transmission characteristics can be tapered, by precisely control of parameters such as heating zone length, heating temperature, tapered velocity, cone angle et al..

In different stages of tapered process, as the decrease of waist diameter, the fundamental mode in the original core will expand into the clad, shown in Figure 2. The mode will transmit in the new "core", which consists of the original clad layer and the new air clad, that form a "clad-air clad mode". By the normalization equation:

$$V = \frac{2\pi a}{\lambda_0}\sqrt{n_{core}^2 - n_{clad}^2} \tag{1}$$

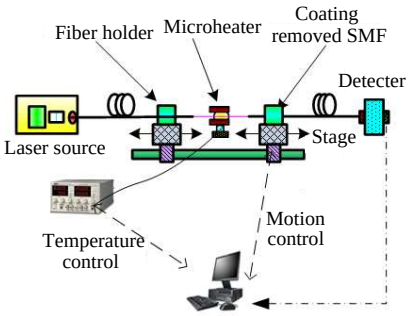

Figure 1: Schematic illustration of the OM fabrication setup.

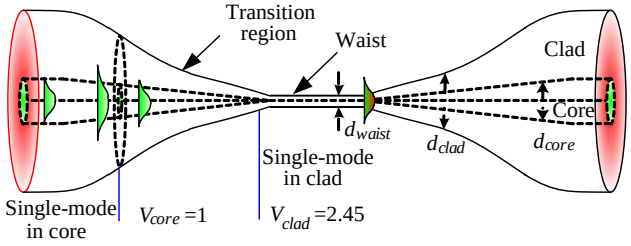

Figure 2: Schematics of typical structure and mode transmission in OMs satisfying adiabatic condition.

We could know that, in the tapered process, the permitted mode numbers in waist region will first increase and then decrease [9, 10]. When the waist diameter decreases to a single mode limited value, only the fundamental mode transmits in the waist.

In tapered process, waist parameters will be affected by factors such as the change of heating temperature, tensile strain et al.. When the waist region permits multimode transmission, higher mode will be excited. Due to different transmission constant, phase differences exist among modes when transmit a distance, and induce intermodal interference. The fundamental mode is rotational symmetrically, when the waveguide symmetry is kept well in tapered process, only LP_{0m} mode could be excited. Ignoring the radiation mode and bending influence, the intermodal interference intensity distribution is described as [13]:

$$I(r,z) = E(r,z)E^*(r,z) = \sum_{m=1}^{M}\sum_{n=1}^{M} c_m c_n^* E(r,z)E^*(r,z)\exp[i(\beta_m - \beta_n)z] \tag{2}$$

where c_m is the coupled coefficient between fundamental mode and LP_{0m} mode, β_m is the transmittance constant of higher mode, z is the transmission distance. Under influence of changed heating temperature and tensile strain, c_m, β_m and z will be modulated, and the interference pattern changes correspondingly that could be detected.

When the waist diameter become smaller to a certain value, higher modes will be cut off, and will result in a change of the intermodal interference pattern. We can see that, when LP_{02} (HE_{12}) mode is cut off, at most LP_{01} (HE_{11}) and LP_{11} (TE_{01}, TM_{01}, HE_{21}) are permitted (in cases of disturbing such as bending). When LP_{02}(HE_{12}) is cut off, the corresponding OM diameter is about 1.8 µm. Now the diameter scale of OMs is mainly in the sun-wavelength range. For example, the most common applied OMs have a diameter range of 0.5∼2 µm [1, 2]. Our experiment also shows that, the tapered device has a relatively larger error when the waist diameter becomes smaller than 4 µm, and we can utilize this featured position (when LP_{02} mode is cut off) to scale the diameter of the tapered fiber, and improve the tapered accuracy.

In order to monitor the intermodal interference during the fabrication process of OM, A high coherent laser (RIO Company) with no less than 2 kHz line width is chosen as the light source. Corresponding parameters were set up in order to fabricate an OM with waist region diameter about 1 µm and waist length about 10 mm. The output light of the tapering fiber was detected with a detector sampled by an A/D converter with 100 Hz sampling frequency.

3. FABRICATION CONTROL TECHNIQUE BASED ON MONITORING INTERMODAL INTERFERENCE

The theoretical analysis results show that, by using high coherent light source to online monitor the OM tapered process, the jump point could be detected when the mode cut off, and the phenomenon be especially obvious when the LP_{02} mode cut off. For this reason, we use this intermodal interference featured point to establish the diameter in the OM tapered process, and add feedback control to adjust the tapered parameters, which may increase the tapered accuracy and stability.

In the tapered process, by set tapered parameters: taper uniform waist length $l_w = 10$ mm; taper waist diameter $d_w = 1$ µm; taper speed $v = 100$ µm/s; liner revise factor $a = 0.1$ [12]. Then we use many methods including compensated control of initial heating width, suppress the circumstance noise, and adjust the temperature, to make the intermodal interference jump point maximally close

to the theoretical LP_{02} mode cut off position, and then detect the acquired OM in the microscope. Figure 3(a) shows the online monitoring of OM sample. It can be seen that the difference between LP_{02} mode's theoretical cut off position and intermodal interference jump point is 1.829 s, by which we could infer that the diameter error between prediction and actual result will in 0.01 μm. The measured the diameter of the sample by microscope is 1.03 μm, see Figure 4. Figure 3(b) is the theoretical diameter in the tapered process. The red line and the three asterisk points respectively represent the theoretical result and the measured values, which are in good agreement. From the monitoring result, we can see that the transmission loss is as low as 1%. The additional loss after tapered process mainly comes from the circumstance pollution, and the pollution sensing could be realized by measuring this additional loss [5, 6].

The above experiment sufficient demonstrated the effectiveness of the diameter establish method by using intermodal interference jump point (LP_{02} cut off), and the OM tapered error is expected to be deceased below 2%.

Additionally, we have made 3D transmission spectrogram of the sample's monitoring result, see Figure 5. We can see that, two main routing evolutions of interference appeared in the tapered process, which means that two higher order modes were excited [7–10, 14]. At about 450 s, the first routing evolution disappeared which represents the cut off of one of the high order mode, and at about 510 s, the second routing evolution disappeared with clear dividing line, which is the LP_{02} cut off point.

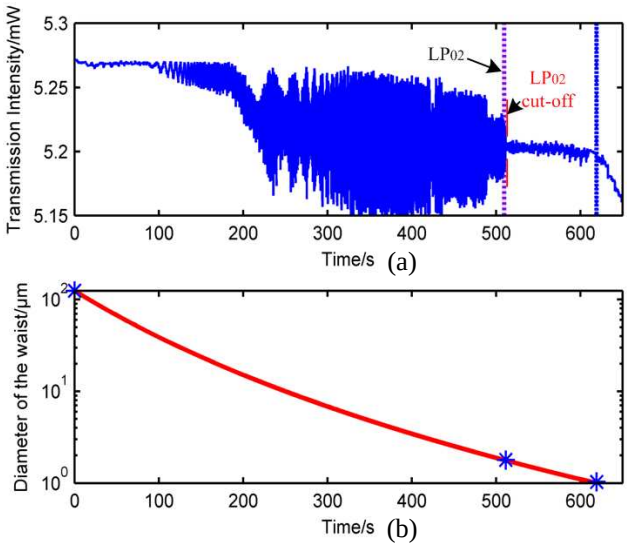

Figure 3: (a) Online detection of OM sample and (b) diameter measurement and theoretical prediction in the tapered process ($l_w = 10$ mm, $d_w = 1$ μm).

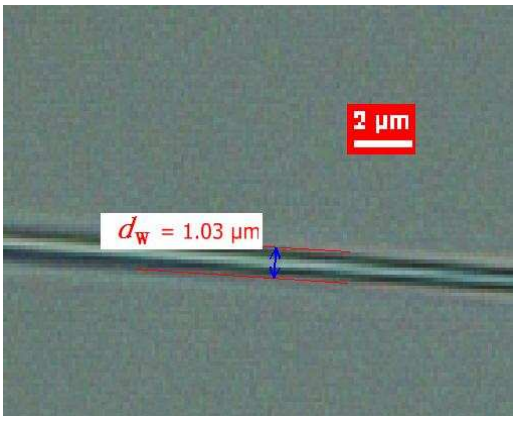

Figure 4: Images of the OM sample-2 in optical microscope ($l_w = 10$ mm, $d_w = 1$ μm).

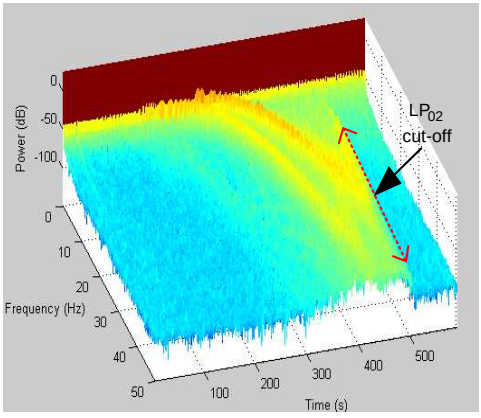

Figure 5: The 3D transmission spectrogram of the sample-2's monitoring result ($l_w = 10$ mm, $d_w = 1$ μm).

In practice, different OMs with different parameters will be required. The diameter of OM is usually estimated according to volume conservation rule. But the estimated diameter value may not be correct due to the different tapering conditions such as environment temperature or the variation of the fabrication devices. Now, we can judge the diameter accuracy just by measuring the time of the jumping points during the fabrication process with the optical monitoring system. According to the last jumping point in the time domain signal, we can deduce the terminal diameter of the OM and modify the parameters so as to ensure a correct diameter monitor for the OM fabrication monitoring system.

Three methods have been used to decrease the errors that mentioned. First, use compensation tapering based on the delay between actual and predicted jump point. Second, due to the fact that the error keeps stable at the same tapered parameters and conditions, we can make one sample to establish the error, and then add proper modifications. For the OM itself, the influence of the length of tapered waist (l_w) on optical characteristics could be ignored, but the diameter influence is obvious (d_w). So we can change the l_w while keeping other parameters unchanged, especially for d_w to decrease the tapered error. So we can decrease the diameter error by just change the single variable l_w. Third, from the mentioned error analysis, we can see that the initial heating width of the tapered volume is an inevitable and important factor to induce tapered error. And we can attribute all the error factors to the heating width error. So we can compensate the initial heating width to realize modification while keeping OM's waveguide structure unchanged. For the three methods mentioned here, repeated experiments demonstrated that the tapered structure error could be controlled below 5%.

Through theoretical analysis and experiment, the last jumping point is corresponding to the time when the LP_{02} mode is cut off in the tapering fiber process. We can calculate the normalized frequency of the tapering OM and deduce the diameter of the tapering OM at that time, and also can obtain the diameter of the OM combining the initial diameter of the taper fiber (usually 125 µm) and the theoretical formula of the estimated diameter of the OM. The jumping point characteristic used for judging the diameter of the tapering OM and even to correct the theoretical diameter of the fabricated OM based on the initial fiber diameter, tapering length, OM terminal diameter and others parameters which could be estimated by person or software online. When the deviation between actual LP_{02} mode jump point and theoretical value is large, we can add software online controlled feedback to adjust the tapered parameters. This technology is benefit for large amount production of qualified OMs.

4. CONCLUSION

In this paper, an OM tapering device based on the modified flame-brushing technique was made systematic error analysis and online measurement. The OM fabrication monitoring system is set up with a high coherent laser so as to enhance the interfere effect in the tapering process. The corresponding spectrograph of the OM tapering process is plotted, which is helpful to analyze the evolution of excited modes. A jumping point is used to judge the correction of the calculated diameter of the OM. The results used for obtaining OMs with accurate structural parameter. So, by using different online feedback methods to adjust the tapered parameters, the OM tapered accuracy could be improved. The intermodal inference based online monitoring method in OM tapered process will improve the technological level of OM production, and make the OMs more qualified in scientific and engineering applications.

REFERENCES

1. Brambilla, G., "Optical fibre nanowires and microwires: A review," *J. Opt.*, Vol. 12, 043001, 2010.
2. Tong, L., F. Zi, X. Guo, and J. Lou, "Optical microfibers and nanofibers: A tutorial," *Optics Communications*, Vol. 285, 4641–4647, 2012.
3. Sagué, G., A. Baade, and A. Rauschenbeutel, "Blue-detuned evanescent field surface traps for neutral atoms based on mode interference in ultrathin optical fibres," *New J. Phys.*, Vol. 10, 113008, 2008.
4. Vetsch, E., D. Reitz, G. Sagué, R. Schmidt, S. T. Dawkins, and A. Rauschenbeutel, "Optical interface created by laser-cooled atoms trapped in the evanescent field surrounding an optical nanofiber," *Phys. Rev. Lett.*, Vol. 104, 203603, 2010.
5. Wei, Z., Z. Song, X. Zhang, and Z. Meng, "Microparticle detection with optical microfibers," *IEEE Photonics Technology Letters*, Vol. 25, No. 6, 568–571, 2013.

6. Wei, Z., Z. Song, X. Zhang, and Z. Meng, "Inline contaminants detection with optical microfiber in high-power laser system," *Proc. of SPIE, ISPDI*, 891104, 2013.
7. Ding, L., C. Belacel, S. Ducci, G. Leo, and I. Favero, "Ultralow loss single-mode silica tapers manufactured by a microheater," *Applied Optics*, Vol. 49, No. 13, 2441–2445, 2010.
8. Frawley, M. C., A. Petcu-Colan, V. G. Truong, and S. N. Chormaic, "Higher order mode propagation in an optical nanofiber," *Optics Communications*, Vol. 285, 4648–4654, 2012.
9. Ravets, S., J. E. Hoffman, L. A. Orozco, S. L. Rolston, G. Beadie, and F. K. fatemi, "A low loss photonic silica nanofiber for higher order modes," *Optics Express*, Vol. 21, No. 15, 191071, 2013.
10. Ravets, S., J. E. Hoffman, P. R. Kordell, J. D. Wong-Campos, S. L. Rolston, and L. A. Orozco, "Intermodal energy transfer in a tapered optical fiber: Optimizing transmission," *Physics Optics*, Vol. 30, No. 11, 2361–2371, 2013.
11. Brambilla, G., F. Xu, and X. Feng, "Fabrication of optical fibre nanowires and their optical and mechanical characterisation," *Electronics Letters*, Vol. 42, No. 9, 517–519, 2006.
12. Birks, T. A. and Y. W. Li, "The shape of fiber tapers," *J. Lightwave Technology*, Vol. 10, No. 4, 432–438, 1992.
13. Salceda-Delgado, G., D. Monzon-Hernandez, A. Martinez-Rios, G. A. Cardenas-Sevilla, and J. Villatoro, "Optical microfiber mode interferometer for temperature-independent refractometric sensing," *Optics Letters*, Vol. 37, No. 11, 1974–1976, 2012.
14. Orucevic, F., V. Lefèvre-Seguin, and J. Hare, "Transmittance and near-field characterization of sub-wavelength tapered optical fibers," *Optics Express*, Vol. 15, 13624–13629, 2007.

The Design of Band-pass Frequency Selective Surface with All Dielectric Metamaterial

Fei Yu, Shaobo Qu, Jiafu Wang, Hao Huang, and Jun Wang
Department of Mathematics and Physics, College of Science
Air Force Engineering University, Xi'an, Shaanxi 710051, China

Abstract— The traditional metamaterial and frequency selective surfacesFSS basically is the mixed structure of the metal and dielectric. However, due to the inherent defects of metal materials, the dielectric metamaterial FSS is necessary. All dielectric metamaterial FSS can be designed, according to the constitutive parameters and dielectric resonator theory based on equivalent. This paper presents the design of dielectric materials FSS, and studies the principles and methods about using high dielectric constant to design dielectric FSS, and the design of the band-pass characteristics of dielectric metamaterial FSS has been proposed. In this paper, the design principle is much important practical significance and guiding significance for the all dielectric metamaterial FSS.

1. INTRODUCTION

The concept of metamaterials is late for thirty years than the frequency selective surfaces (FSS), but periodic structure of the FSS and metamaterials in the design is quite similar. In the traditional sense of the metamaterials and frequency selective surface, periodic structures are made of metal materials. But in the high frequency band (such as millimeter wave field), the metal material is much less practical due to the skin effect of metal surface. And the physical properties of metal material itself brings many limitations [1].

These problems can be well solved by dielectric materials. This article verifies the high dielectric constant of medium also have plasma liquid through the derivation of the Drude model, designs and simulates the one-dimensional grid structure all dielectric metamaterial FSS. At last the transmission characteristic curve is optimized and the simulation results are analyzed [2, 3].

2. THE METAL PROPERTIES OF HIGH DIELECTRIC CONSTANT OF MEDIUM

According to the Pendry's research [3, 6], Infinite array of metal wire can be equivalent to the plasma. Under the action of electromagnetic wave, the equivalent dielectric constant ε_{eff} meet Drude model:

$$\varepsilon_{eff} = 1 - \frac{w_p^2}{w \cdot (w + i \cdot \gamma)}, \quad w_p^2 = \frac{n \cdot e^2}{\varepsilon_0 \cdot m}$$

where, n for the electronic density, m and e for the respectively the electron mass and charge, i for the imaginary unit, ε_0 for the permittivity of free space, ω_p for the plasma frequency of metal. ω for the electromagnetic wave frequency, γ for the attenuation factor.

It can be seen from the formula that the equivalent dielectric constant to be negative, electromagnetic wave frequency must be smaller than the ω metal plasma frequency. Plasma frequency of the metal is generally high, however, the plasma frequency of the metal must be reduced to the scope of what we need to get a negative permittivity metamaterials needed.

The plasma frequency of the metal ω_p can be written as:

$$\omega_p^2 = \frac{ne^2}{\varepsilon_0 m_{eff}}$$

where, m_{eff} for electronic equivalent mass, n for electronic number per unit volume.

According to the formula, as a result of electronic number per unit volume is only related to the metal itself, so that one of the effective methods to reduce increase m_{eff}.

The Drude model of high dielectric constant of medium can be written as:

$$\varepsilon_{eff} = \varepsilon_0 \left(1 - \frac{\omega_p^2}{\omega^2}\right)$$

where, ω_p for the plasma frequency of medium model constructed, ω for the frequency of electromagnetic waves [4, 5].

3. THE DESIGN AND SIMULATION OF ONE-DIMENSIONAL GRATING ALL-DIELECTRIC FSS

According to the analysis in the previous section, the high dielectric constant of the medium is in the nature of metals. Palisade structure can be viewed as long column of high dielectric constant of the medium with air. Two kinds of composite material unit, through the medium, the dielectric constant of air cycle change on the influence of different frequency incident electromagnetic wave transmission coefficient of frequency selection [7–9].

Figure 1 is the simulation of the grating dielectric metamaterial FSS using CST MWS software. Dielectric periodic extension is adopted in the XY plane. Background conditions set in free space, the boundary conditions are set to: X and Y direction are periodic boundary (Unit Cell), Z direction for Open boundary (Open), the electromagnetic wave transmission along the Z direction. Using TE wave vertical incidence (electric field along the X direction), the curve of the S parameters can be calculated as shown in Figure 2.

As you can see from Figure 2, FSS frequency response is the single pass band, pass band is located in the x-band, pole 10.75 GHz band pass is the center frequency. The design of the pass band is in 10.53∼11.05 GHz for all dielectric FSS of 3 dB transmission pass band. The bandwidth is 497 MHz, has largely promoted the medium type of metamaterials pass band bandwidth. Analyzing the characteristics of the S parameters of graphics, pass band belt is more smooth, and the out-of-band grating lobe suppression is quite well.

To verify that the sensitivity of the incident plane wave angle, inspection transmission coefficient of different angles of incidence has been inspected. Figure 3 is for different incidence angles of TE wave feedback wave of S_{21} transmission parameter curves.

The different angle of incidence of S_{21} curve Can be seen in the Figure 3. With the increase of incident angle degree, center frequency does not change. It is proved that the one dimensional all dielectric FSS has good practical value.

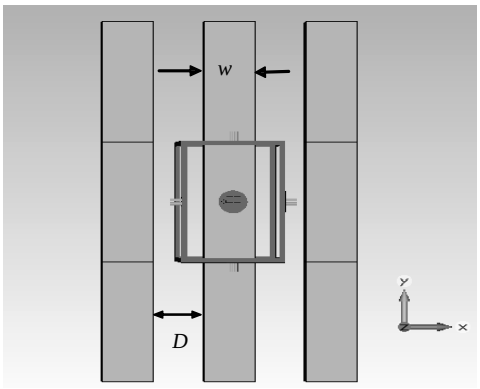

Figure 1: The structure diagram of the grating dielectric metamaterial FSS.

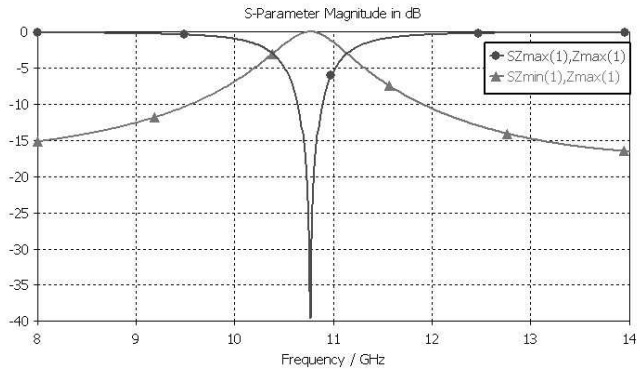

Figure 2: The S parameters of the grating dielectric metamaterial FSS.

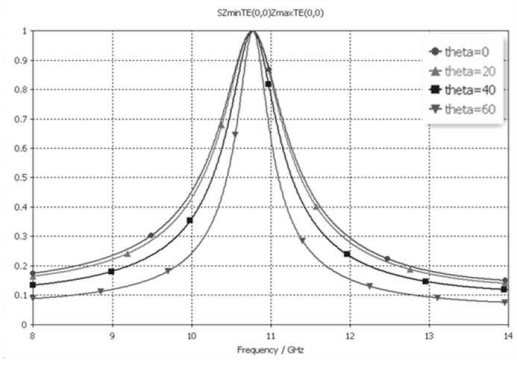

Figure 3: The S parameters of different incidence angles of TE wave feedback wave.

4. CONCLUSION

High dielectric constant of the dielectric materials have plasma liquid property as the metal. On the basis of the theoretical basis, design the one-dimensional grating all dielectric metamaterials FSS with good band pass characteristics.

REFERENCES

1. Munk, B. A., *Frequency Selective Surfaces: Theory and Design,* 1–4, Wiley-Inter science, New York, 2000.
2. Cui, T. J., D. R. Smith, and R. Liu, *Metamaterials Theory, Design, and Applications*, 1–2, Springer, New York, 2009.
3. Pendry, J. B., A. J. Holden, W. J. Stewart, et al., "Extremely low frequency plasmons in metallic mesostructures," *Physical Review Letters*, Vol. 76, 4773–4776, 1996.
4. Shelby, R. A., D. R. Smith, and S. Schultz, "Experimental verification of a negative index of refraction," *Science*, Vol. 292, 77–79, 2001.
5. Veselago, V. G., "The electrodynamics of substances with simultaneously negative values of ε and μ," *Soviet Physics Uspekhi*, Vol. 10, 509–514, 1968.
6. Smith, D. R., J. B. Pendry, and M. C. K. Wiltshire, "Metamaterials and negative refraction index," *Science*, Vol. 305, 788–792, 2004.
7. Anthony, L., C. Caloz, and T. Itoh, "Left-handed metamaterials for microwave engineering applications," *IEEE Microwave Magazine*, Vol. 9, 34, 2004.
8. Yu, F., S. Qu, Z. Xu, and J. Wang, "Investigations on the design of all-dielectric frequency selective surfaces," *PIERS Proceedings*, 472–475, Suzhou, China, Sep. 12–16, 2011.
9. Smith, D. R., S. Schultz, P. Markos, et al., "Determination of effective permittivity and permeability of metamaterials from reflection and transmission coefficients," *Physical Review B*, Vol. 65, 195104, 2002.

The Design of Band-pass Frequency Selective Surface with the Grid Dielectric Metamaterial

Fei Yu, **Shaobo Qu**, **Jiafu Wang**, **Hao Huang**, **and Jun Wang**
Department of Mathematics and Physics, College of Science
Air Force Engineering University, Xi'an, Shaanxi 710051, China

Abstract— Metallic parts are indispensable to traditional frequency selective surfaces. However, for millimeter waves, because of surface wave skin effect, the loss of metal-containing FSS is so large that the performance is badly affected. Besides, metal materials are quite unfavorable for high-temperature resistance and corrosion resistant requirements. The article adopt period dielectric structure to achieve band-pass frequency selective properties. The design principles proposed in this paper are of great practical values in designing all-dielectric metamaterials frequency selective surfaces.

1. INTRODUCTION

Frequency selective surface (FSS), as a kind of spatial filter, is planar or curved surfaces composed of periodically arranged scatter arrays. FSS can exhibit one or more pass-bands or stop-bands. Conventional FSSs are usually two-dimensional structures composed of periodically arranged metallic patches or slits. Metamaterial are artificial composite structures or composite materials that exhibit u-natural physical properties [1–5]. The concept of metamaterial not only gives us a new material form, but only provides us a new material design concept. This brings revolutionary changes to the world view and methodology of human beings [6].

All-dielectric metamaterial are now receiving more and more attentions from the academic world. This kind of metamaterial includes no metallic part and thus has the advantages of low loss, simple structure, better homogeneity and isotropy at high frequencies (millimeter waves, sub-millimeter waves, infrared waves and etc.).

Based on these merits, this thesis introduces all-dielectric metamaterials into the design of FSSs and mainly investigates the principles and methods of designing all-dielectric FSSs using high-permittivity dielectric materials [7, 8].

2. THE ANALYSIS OF THE THEORY BASED ON MIE SCATTERING [9–11]

Mie scattering is the most widely used application and the basic algorithms of the particle scattering than any other theories. There is nothing comparable to this precision in the processing in the wavelength particle scattering problem. Specifically refers to isotropic, particles in a highly dilute medium system, such as air scattering and the particle diameter, the refractive index difference between incident particles to the medium on the theory of the relation between the wavelength of incident light.

Traditional mie scattering thought is as follows.

Plane wave scattering problem of small ball can be calculated strictly by matching the boundary conditions. For isolation of single spherical scatterer, the electromagnetic wave into the background material of the dielectric constant as ε_b, permeability as μ_b, the radius of spherical scatterer as r_0, dielectric constant as $\varepsilon_r = n^2$ (n for the refractive index of the scatterer). The m class of scattering coefficient a_m and coefficient b_m respectively:

$$a_m = \frac{n\Psi_m(nx)\Psi'_m(x) - \Psi_m(x)\Psi'_m(nx)}{n\Psi_m(nx)\xi'_m(x) - \xi_m(x)\Psi'_m(nx)} \quad b_m = \frac{\Psi_m(nx)\Psi'_m(x) - n\Psi_m(x)\Psi'_m(nx)}{\Psi_m(nx)\xi'_m(x) - n\xi_m(x)\Psi'_m(nx)}$$

where, $x = k_0 r_0$, $k_0 = {}^{\omega}/_{c}$ is the wave vector in Vacuum, Ψ_m, ξ_m is Reccati-Bessel Functions.

According to the Clausius-Mossotti Equation, if $\lambda > r_0$,

$$\varepsilon_{eff} = \frac{2(k_0 r_0)^3 + 6if a_1}{2(k_0 r_0)^3 - 3if a_1} \qquad \mu_{eff} = \frac{2(k_0 r_0)^3 + 6if b_1}{2(k_0 r_0)^3 - 3if b_1}$$

where, $f = {}^{4\pi N r_0^3}/_{3}$, N for the number of the unit volume of the spherical scatterer.

According to mie scattering theory,

$$a_1 = j\frac{2}{3}\left(k_0^2\mu_b\varepsilon_b\right)^{3/2}\frac{\varepsilon_b - \varepsilon_r F(\theta)}{2\varepsilon_b + \varepsilon_r F(\theta)}r^3 \tag{1}$$

$$b_1 = j\frac{2}{3}\left(k_0^2\mu_b\varepsilon_b\right)^{3/2}\frac{\mu_b - \mu_r F(\theta)}{2\mu_b + \mu_r F(\theta)}r^3 \tag{2}$$

where,

$$F(\theta) = \frac{2(\sin\theta - \theta\cos\theta)}{(\theta^2-1)\sin\theta + \theta\cos\theta}, \quad \theta = k_0 a\sqrt{\varepsilon_r'\mu_r'}$$

3. THE DESIGN AND SIMULATION OF BAND-PASS FSS WITH THE GRID DIELECTRIC METAMATERIAL

For the symmetry of the grid unit, we should adjust the only parameter length during the optimization. And the sample with grid unit is much easy to implement. Based on these reasons, a kind of grid as the basic unit of the whole medium type FSS is designed.

As can be seen from the Figure 1(b), unit structure is periodic extension in the XY plane. The dielectric grid and the air are the two different kind of material structure. The effect of band-pass may be produced by this structure. As shown in Figure 2 is obtained by frequency domain calculation, S parameters of the curve.

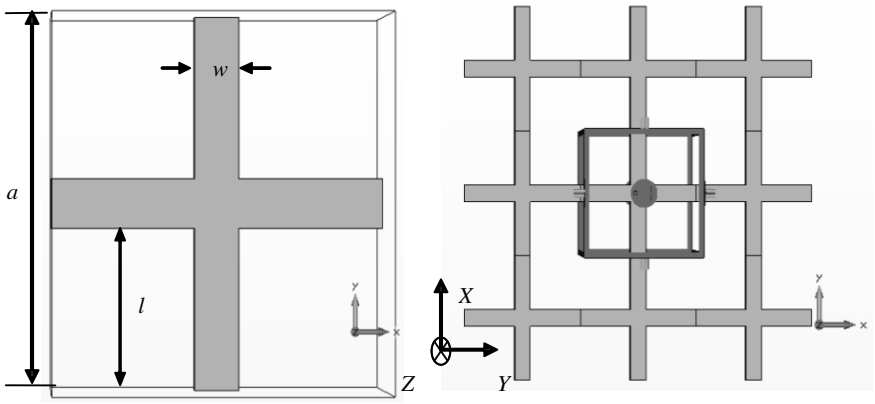

Figure 1: The structure diagram of the grid dielectric metamaterial single band FSS.

Figure 2 for the TE polarized wave is incident when the FSS S_{11} and S_{21} frequency response curve. As can be seen from the graph, the pass band is a single band, the pole is 11.17 GHz, 3 dB work pass band is $1.08 \sim 11.34$ GHz, the bandwidth is 260 MHz, the reflectivity of resonant pole is greater than -40 dB.

However, we found that the pass band result is not very ideal by analysis of transmission characteristics of the corresponding curve, the smooth curve does not appear in the pass band, the

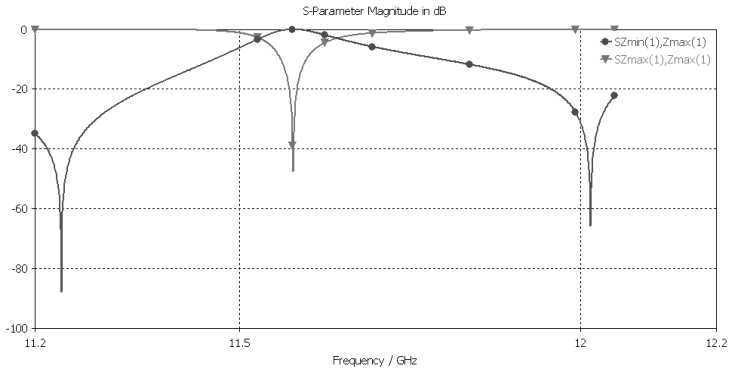

Figure 2: The S parameters of the grid dielectric metamaterial single band FSS.

decrease is not significantly with inside and outside.

Figure 3 for the set in a free space of the double layer grid dielectric metamaterial FSS. Keep the dielectric constant, dielectric loss and the size of unit the same.

From Figure 3 we can find the pass band characteristics can be significantly improved. The optimized FSS has good pass band performance. Contrast can be seen in Figure 2 that transmission pass band center frequency has not changed, the two poles of pass band are 11.13 GHz and 11.24 GHz, 3 dB pass band is $10.07 \sim 11.32$ GHz, the passband bandwidth of 1.23 GHz, reflectivity of two resonant pole are larger than -40 dB.

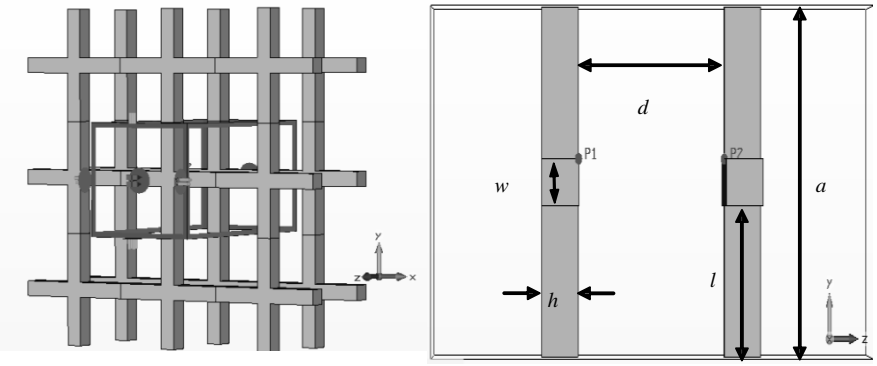

Figure 3: The structure diagram of the double layer grid dielectric metamaterial FSS.

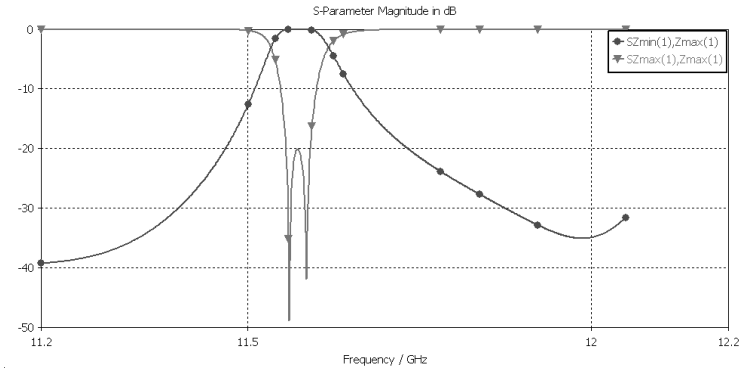

Figure 4: The S parameters of the double layer grid dielectric metamaterial single band FSS.

4. CONCLUSION

This paper uses the method of the combination of the FSS and the metamaterial design, and analyze the mechanism of pass band characteristic by Mie scattering principle. Through the coupling between different layers of pass band bandwidth, designs the grid type all dielectric metamaterials FSS, formed pass band in x-band, 3 dB transmission pass band is $10.07 \sim 11.32$ GHz, pass band bandwidth is 1.23 GHz, in-band insertion loss maximum 0.78 dB. The principle proposed by this paper is important to guide significantly to design the all dielectric metamaterials FSS.

REFERENCES

1. Munk, B. A., *Frequency Selective Surfaces: Theory and Design*, 1–4, Wiley-Inter Science, New York, 2000.
2. Cui, T. J., D. R. Smith, and R. Liu, *Metamaterials Theory, Design, and Applications*, 1–2, Springer, New York, 2009.
3. Veselago, V. G., "The electrodynamics of substances with simultaneously negative values of ε and μ," *Soviet Physics Uspekhi*, Vol. 10, 509–514, 1968.
4. Pendry, J. B., A. J. Holden, W. J. Stewart, et al., "Extremely low frequency plasmons in metallic mesostructures," *Physical Review Letters*, Vol. 76, 4773–4776 1996.

5. Shelby, R. A., D. R. Smith, and S. Schultz, "Experimental verification of a negative index of refraction," *Science*, Vol. 292, 77–79, 2001.
6. Smith, D. R., J. B. Pendry, and M. C. K. Wiltshire, "Metamaterials and negative refraction index," *Science*, Vol. 305, 788–792, 2004.
7. Anthony, L., C. Caloz, and T. Itoh, "Left-handed metamaterials for microwave engineering applications," *IEEE Microwave Magazine*, Vol. 9, 34, 2004.
8. Yu, F., S. Qu, Z. Xu, J. Wang, Y. Yang, X.-H. Wang, H. Zhou, and Y. Li, "Investigations on the design of all-dielectric frequency selective surfaces," *PIERS Proceedings*, 472–475, Suzhou, China, September 12–16, 2011.
9. R. F., 1981.
10. ???, 2002.
11. Smith, D. R., S. Schultz, P. Markos, et al., "Determination of effective permittivity and permeability of metamaterials from reflection and transmission coefficients," *Physical Review B*, Vol. 65, 195104, 2002.

Automatic Extraction of Pathological Area in 2D MR Brain Scan

P. Dvorak[1, 2], K. Bartusek[2], and E. Gescheidtova[3]

[1]Department of Telecommunications, Faculty of Electrical Engineering and Communication
Brno University of Technology, Technicka 12, Brno 612 00, Czech Republic
[2]Institute of Scientific Instruments of the ASCR
v.v.i., Kralovopolska 147, Brno 612 64, Czech Republic
[3]Department of Theoretical and Experimental Electrical Engineering
Faculty of Electrical Engineering and Communication, Brno University of Technology
Technicka 12, Brno 612 00, Czech Republic

Abstract— The aim of this work is to propose the fully automated pathological area extraction. The proposed method is based on multi-resolution symmetry analysis and automatic thresholding. The multi-contrast MRI (T2 and FLAIR images) is used. Since the method is based on symmetry, it works for both axial and coronal planes. In these both planes of healthy brain, the approximate left-right symmetry exists and it is used as the prior knowledge for searching the approximate pathology location. The algorithm was tested on 357 axial and 443 coronal real images from publicly available BRATS databases containing 3D brain volumes afflicted by a brain tumor. The results were evaluated by Dice Coefficient (axial: 0.85 ± 0.11, coronal 0.82 ± 0.18) and by Accuracy (axial: 0.96 ± 0.05, coronal 0.94 ± 0.09).

1. INTRODUCTION

Nowadays, the issue of automatic analysis of brain tumors is of great interest. It is the first step in surgical and therapy planning. And the very first step of the automatic analysis of brain tumor is its detection and subsequent segmentation. The detection of brain tumors is generally a more complex task than the detection of any other image object. Pattern recognition usually relies on the shape of the required objects. Since the tumor shape varies in each case, other properties have to be used. Several different and interesting methods have been developed in recent years. The existing algorithms can be classified into semi- and fully-automatic methods.

The semi-automatic [1, 2] require some user interaction, e.g., to select the starting point lying inside the tumor or to select several points of foreground and several points of background. The automatic [3, 4] methods do not require any interaction and are usually based on prior knowledge of the human brain structure, either tissue atlas or left-right symmetry, or their combination.

2. METHODOLOGY

In this work, for the better performance, the usage of multi-contrast MR is suitable. FLAIR and T2-weighted images are used. In both images, the pathological areas are well visible. Compared to the T1CE images, which is the most common contrast used in tumor segmentation, these contrasts do not require the contrast agent fluid.

The reason for multi-contrast MRI is much better differentiation of particular tissues than in case of using only one contrast image. E.g., the edema reaches similar intensities as CSF (Cerebro-Spinal Fluid) in T2-weighted images, while in FLAIR images, the intensities are absolutely different. On the other hand, the differentiation between necrosis and white matter is much better in T2-weighted images. That method is based on multi resolution symmetry analysis.

The input of the whole process are stand-alone registered 2D T2 and FLAIR magnetic resonance images. No neighbor slices are considered. The reason for these contrast images is the good visibility of this kind of pathology in them.

2.1. Preprocessing

The preprocessing consists of brain extraction, image registration and the symmetry axis detection. None of these parts is the aim of this work, but for this purpose, the existing algorithms described in [5–7] can be used for brain extraction, image registration and symmetry axis detection, respectively. Addition of such methods as a preprocessing step is the aim of future work.

2.2. Symmetry Analysis

The most important part of the presence detection process is the detection of symmetry anomalies, which are usually caused by a brain tumor, whose detection is the main purpose of this article. The first step of this process is dividing the input image into two approximately symmetric halves. Assuming that the head is not rotated and the skull is approximately symmetric, the symmetry axis is parallel to the vertical axis and divides the image of the detected brain into two parts of the same size. Since the method is not pixel-based, the precision of the determined symmetry axis does not have significant influence.

A squared block, with the side length computed as one quarter of the cropped image side length, is created. This size and sizes computed in the following computation are suitable for the detection of both small and large tumors. The algorithm goes through both halves symmetrically by this block. The step size is smaller than the block size to ensure the overlapping of particular areas. These areas are compared with their opposite symmetric part. In this case, the step size of one eighth of the block size was set.

A omparison is done by the Bhattacharya Coefficient [8]. Normalized histograms with the same range are computed from both parts and the Bhattacharya Coefficient (BC) is computed from these histograms as follows [8]:

$$\mathrm{BC} = \sum_{i=1}^{N} \sqrt{l\,(i) \cdot r\,(i)}, \tag{1}$$

where N denotes the number of bins in the histogram, l and r denote histograms of blocks in left and right half, respectively. The range of values of BC is $\langle 0; 1 \rangle$, where the smaller the value, the bigger the difference between histograms. For the next computation, the asymmetry is computed as:

$$A = 1 - B. \tag{2}$$

This asymmetry is computed for all blocks. Since the step size is smaller than the block size, the overlap exists and more values of asymmetry are present for most pixels. To obtain the appropriate asymmetry map, the mean of all values computed for a particular pixel is computed. The computed values of asymmetry create the asymmetry map, which expresses the probability of tumor presence in a particular location. The higher the asymmetry is, the higher is the probability of the tumor presence in a given location.

2.3. Multi-resolution Map

The whole cycle of symmetry checking is repeated four times but with different size of block. Height and width of the block are iteratively reduced to the half of the previous value. So the size of the block is 1/1, 1/4, 1/16, and 1/64 of the initial size, respectively. The purpose of smaller areas is the more precise detection of asymmetry. This approach corresponds to the multi resolution image analysis described in [9]. A block size of 1/256 of the initial size was tested as well, but the results were not improved and the maximum of asymmetry coefficient for this block size was equal to 1 for every image in database.

The output of each cycle is a probabilistic map of anomalies. The product of values corresponding to a particular pixel is computed. The output is the new multi resolution probabilistic map. The example of multi-resolution probabilistic maps are shown in Fig. 1.

2.4. Glioma Extraction

The pathological area extraction is based on the method described in [10], but multi-contrast images, namely T2 and FLAIR, are now involved in this task. In T2-weighted images, glioma and potential edema produce much stronger signal that the white matter, in which they are mostly located. For this reason, the thresholding is employed here. Since the intensities in image can differ from case to case depending on the data acquisition, it has to be computed from the particular image. Moreover, only pixels in the most asymmetric parts have to be involved in the threshold computation. Otherwise, the threshold would be computed incorrectly in case of small tumors. For this purpose, the asymmetry mask is computed. This mask includes the regions, where the asymmetry reached at least 10% of the maximum asymmetry for particular image. Since the result is both-sided mask, healthy and pathological areas are included.

The threshold is determined automatically by Otsu's algorithm [11], but any other automatic method can be used.

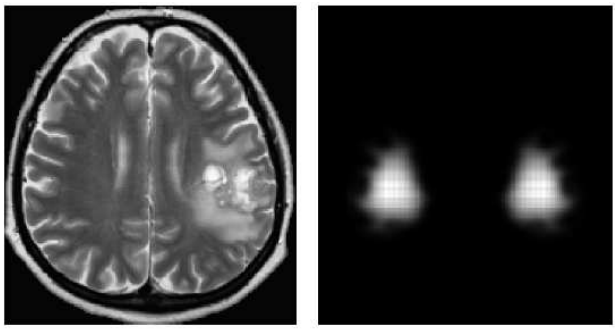

(a) (b)

Figure 1: Asymmetry probabilistic maps for block side length equal to 1/4, 1/8, 1/16, and 1/32 of shorter side of cut image are shown in (a), (b), (c) and (d), respectively. In (e) and (f), input image and total probabilistic map are shown, respectively.

Even though, the threshold is determined only from the image points in the most asymmetric parts, the thresholding process is applied to the whole image. Since some incorrect areas could be extracted, only the regions that have the intersection with the asymmetry mask are labeled as pathological. Regions with the size smaller than 10% of the largest segment are eliminated as well.

Since CSF appears hyper-intense in T2-weighted images as well, the FLAIR volume is employed. In FLAIR the CSF produces much weaker signal than the white matter and the tumor or edema itself. Hence, the areas with the lower intensity than the median intensity (which is most likely the intensity of the white matter) in FLAIR image are eliminated.

3. EXPERIMENTS AND RESULTS

3.1. Datasets

The testing dataset was obtained from the MICCAI 2012 Challenge on Multimodal Brain Tumor Segmentation organized by B. Menze, A. Jakab, S. Bauer, M. Reyes, M. Prastawa, and K. Van Leemput. The challenge database contains fully anonymized images from the following institutions: ETH Zurich, University of Bern, University of Debrecen, and University of Utah.

For each patient, T1, T2, FLAIR, and post-gadolinium T1 MR volumes are available. All volumes are linearly co-registered to the T1 contrast image, skull stripped, and interpolated to 1 mm isotropic resolution.

The data used in algorithm evaluation contains real volumes of 15 high-grade and 7 low-grade glioma subjects. From each case, several slices with pathological area in axial and coronal plane were taken. In total, the extraction algorithm was tested on 357 images with resolution 256×256 pixels in axial plane and on 443 images with resolution 256×181 in coronal plane. Since the proposed method is fully automatic and independent of image intensities, each image of the database can be considered as unique and independent of others. All the simulated images are in BrainWeb space [12]. The information about the simulation method can be found in [13].

3.2. Evaluation Criteria

For the evaluation of region segmentation, Dice Coefficient and Accuracy were used. The Dice Coefficient (DC) (DICE), in some works called Similarity Index, is computed according to the equation

$$\mathrm{DC} = \frac{2\,|A \bigcap B|}{|A| + |B|}, \tag{3}$$

where A and B denotes the ground truth and the result masks of the segmentation, respectively. This criterion compares the intersection of two sets with their union. The range of values of DC is $\langle 0; 1\rangle$, where the value 1 expresses the perfect segmentation. According to [14], the DC $> 0,7$ indicates an excellent similarity.

Another measure widely employed for segmentation evaluation is Accuracy (A), used e.g., in [1] and defined by the equation:

$$A = \frac{TP + TN}{TP + FP + TN + FN}, \tag{4}$$

where TP, FP, FN and TN stand for "True Positive", "False Positive", "False Negative", and "True Negative", respectively. Both measures are in the same range as DC and the higher value indicates the better performance as well.

3.3. Results

This method was tested on 357 axial and 443 coronal images. The summary of the extraction process results is in Table 1. The results are separated according to the tumor type and the slice plane. Slightly better results were achieved for high grade gliomas (HG) than for low grade gliomas (LG).

Table 1: Segmentation evaluation by dice coefficient and accuracy for both planes.

	Axial		Coronal	
	DC	Accuracy	DC	Accuracy
HG	0.86 ± 0.09	0.97 ± 0.03	0.86 ± 0.12	0.96 ± 0.06
LG	0.85 ± 0.12	0.96 ± 0.05	0.79 ± 0.22	0.92 ± 0.12
Overal	0.85 ± 0.11	0.96 ± 0.04	0.82 ± 0.18	0.94 ± 0.10

The worst results were achieved for LG in coronal planes, while in other cases the results are comparable and achieved the value 0.86 for DC and 0.96 for Accuracy. The several results for both planes, both types of glioma and several intervals of resulting DC are shown in Fig. 2.

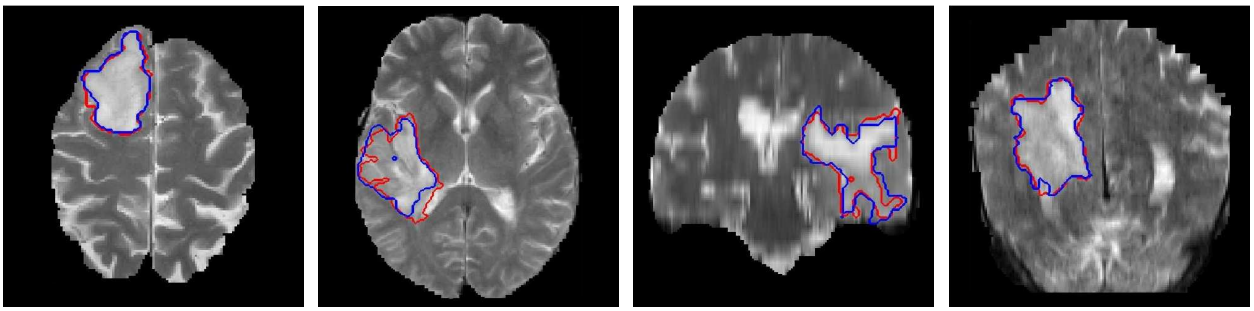

(a) (b) (c) (d)

Figure 2: (a) The average and (b) above-average results for axial slice of low grade glioma and (c) the average and (d) above-average results for coronal slice of high grade glioma. Red: segmentation, Blue: ground truth.

4. CONCLUSION

The aim of this work was an extraction of glioma and edema from 2D MRI images. In axial and coronal plane, the DC coefficient reached value 0.85 ± 0.11 and 0.82 ± 0.18, respectively. Considering the statement that the DC > 0.7 indicates an excellent similarity, the achieved result can be evaluated as very good. Moreover the algorithm considers only information from 2D image and it is fully automated. It is expected that the performance will be improved in future using the neighbor slices information. The accuracy reached values 0.96 ± 0.04 and 0.94 ± 0.10 for axial and coronal plane, respectively. This indicates that in average 95% of pixels were correctly labeled either as pathological or as healthy tissue.

The attention in the future work will also be paid on the relations between neighbor slices and after that, the work will continue with extending the proposed algorithm to 3D. The future work will also consist of implementing the automatic symmetry axis detection, based on literature referred in Section 2, and the separation of the tumor and the edema.

ACKNOWLEDGMENT

The described research is funded by projects SIX CZ.1.05/2.1.00/03.0072, project GACR 102/12/11-04, and project COST CZ LD14091.

REFERENCES

1. Mikulka, J. and E. Gescheidtova, "An improved segmentation of brain tumor, edema and necrosis," *PIERS Proceedings*, 25–28, Taipei, March 25–28, 2013.

2. Wu, Y., W. Yang, J. Jiang, S. Li, Q. Feng, and W. Chen, "Semi-automatic segmentation of brain tumors using population and individual information," *Journal of Digital Imaging*, Vol. 26, No. 4, 786–796, 2013, [Online] Available: http://dx.doi.org/10.1007/s10278-012-9568-1.
3. Pedoia, V., E. Binaghi, S. Balbi, A. De Benedictis, E. Monti, and R. Minotto, "Glial brain tumor detection by using symmetry analysis," *Proc. SPIE*, Vol. 8314, 831445–831445-8, 2012, [Online] Available: http://dx.doi.org/10.1117/12.910172.
4. Zhang, N., S. Ruan, S. Lebonvallet, Q. Liao, and Y. Zhu, "Kernel feature selection to fuse multi-spectral fMRIg images for brain tumor segmentation," *Computer Vision and Image Understanding*, Vol. 115, No. 2, 256–269, 2011, [Online] Available: http://www.sciencedirect.com/science/article/pii/S1077314210002018.
5. Uher, V., R. Burget, J. Masek, and M. Dutta, "3d brain tissue selection and segmentation from mri," *36th International Conference on Telecommunications and Signal Processing (TSP)*, 839–842, 2013.
6. Arce-Santana, E. R. and A. Alba, "Image registration using markov random coefficient and geometric transformation fields," *Pattern Recognition*, Vol. 42, No. 8, 1660–1671, 2009, [Online] Available: http://www.sciencedirect.com/science/article/pii/S0031320308005104.
7. Karuppanagounder, S. and K. Thiruvenkadam, "A novel technique for finding the boundary between the cerebral hemispheres from MR axial head scans," *IICAI*, B. Prasad, P. Lingras, and A. Ram, Eds., 1486–1502, 2009.
8. Bhattacharyya, A., "On a measure of divergence between two statistical populations defined by their probability distribution," *Bulletin of the Calcutta Mathematical Society*, Vol. 35, 99–110, 1943.
9. Kropatsch, W. G., Y. Haxhimusa, and A. Ion, "Multiresolution image segmentations in graph pyramids," *Applied Graph Theory in Computer Vision and Pattern Recognition Studies in Computational Intelligence*, Vol. 52, 3–41, 2007.
10. Dvorak, P., K. Bartusek, and W. G. Kropatsch, "Automated segmentation of brain tumor edema in FLAIR MRI using symmetry and thresholding," *PIERS Proceedings*, 936–939, August 12–15, Stockholm, 2013.
11. Otsu, N., "A threshold selection method from gray-level histograms," *IEEE Transactions on Systems, Man and Cybernetics*, Vol. 9, No. 1, 62–66, 1979, [Online] Available: http://dx.doi.org/10.1109/TSMC.1979.4310076.
12. Prastawa, M., E. Bullitt, and G. Gerig, "Simulation of brain tumors in MR images for evaluation of segmentation efficacy," *Medical Image Analysis*, Vol. 13, No. 2, 297–311, 2009, [Online] Available: http://www.sciencedirect.com/science/article/pii/S1361841508001357.
13. Cocosco, C. A., V. Kollokian, R. K.-S. Kwan, G. B. Pike, and A. C. Evans, "Brainweb: Online interface to a 3d mri simulated brain database," *NeuroImage*, Vol. 5, 425, 1997.
14. Zijdenbos, A. and B. Dawant, "Brain segmentation and white matter lesion detection in mr images," *Critical Reviews in Biomedical Engineering*, Vol. 22, 401–465, 1994.

Numerical Modeling of Electromagnetic Field in the Biological Cell

E. Vlachova Hutova[1], **T. Kriz**[1], **E. Gescheidtova**[1], **and K. Bartusek**[2]

[1]Department of Theoretical and Experimental Electrical Engineering
Brno University of Technology, Technicka 12, Brno 616 00, Czech Republic
[2]Institute of Scientific Instruments, Academy of Sciences of the Czech Republic
Kralovopolska 147, Brno 612 64, Czech Republic

Abstract— This work demonstrates how a stochastic model can be implemented to obtain a realistic description of the interaction of a biological cell with an external magnetic or electrical fields. In our model formulation, the stochasticity is adopted by introducing various levels of forcing intensities in model parameters. The presence of noise in nuclear membrane capacitance has the most significant effect on the current flow through a biological cell. The increasing amount of data reporting on the biological effects of magnetic and electric fields is leading researchers to understanding of how important it is to fully understand the mode of action of magnetic or electric fields to living organisms. Indeed, even if the perturbations of biological systems by magnetic or electric fields are sublethal at shorter times of exposure, these perturbations could, especially at longer times of exposure, evolve into a progressive accumulation of modifications, whose ultimate effects still need to be clarified.

1. INTRODUCTION

The influence of static magnetic fields (SMFs) or modulated magnetic fields (MFs) on biological systems has been a topic of considerable interest for many years [1, 2]. At the current state of knowledge, the biological effects, both in vivo and in vitro, of SMFs have yet to be unequivocally interpreted. Induced electric currents, unlike time-varying (electromagnetic) fields, are not associated with these fields except during activation and deactivation or when there is movement within the field. The increasing production of electric (EMFs) and magnetic fields (MFs) due to the expanding use of electronic devices in normal life, is encouraging studies on the effects of EMFs and MFs on living organisms, with a view to better protecting human health against their probable unfavorable effects [3]. The recent growing interest in the influence of MFs on life process derives from the concern about their possible harmful effects on human health. Although the data reported in the literature are quite heterogeneous in terms of MF intensity (from 10^{-7} to 10 T), type of field (static or oscillatory), and subjects exposed to MFs (from in vitro cultured cells to humans), a link between MFs and tumor genesis has been suggested [4]. Since the cell fate process under the external stimulation involve the interaction of external field with biological cells dispersed in extracellular matrix (ECM) is important to initially understand such interaction for a single cell. Also, the evaluation of the time scale for such fundamental interactions requires careful theoretical analysis, as precise experimental measurements can be difficult. At a much finer scale, one has to consider how the electric current path will be influenced by the electric transport properties of cell membrane, cytoplasm, nuclear membrane, nucleoplasm, etc.. Typically, a biological cell contains various ions such as K^+, Na^+, Cl^-, Ca^{+2}, etc.. All such ions are also present in ECM, however, with different concentration. As ECM and cytoplasm have different chemical composition, the conductivity of the two medium will also different and hence, the mobilities of the ions. A dielectric membrane surrounds the cellular organelles as well as all the inorganic ions and organic compounds. As a potential difference is maintained due to the presence of the ions across the dielectric cell membrane, the interaction of the cellular field with the external electric fields is to be expected. If the membrane potential difference reached in the range of 0.7–1 V in response to externally applied E-field, structural changes in the membrane occur with the transient pore formation across the membrane, a process known as electroporation. Electroporation is important for many cellular processes. The effect of electric field depends on the pulse duration, field strength and cell type [5]. Although the influence of electric field on various biophysical and biochemical process is known or clinically realized, the fundamental understanding of interaction is still missing.

2. MODEL ASSUMPTIONS

In order to develop a model of electrical analog for a biological cell, a number of assumption are made.

Table 1: Basic model parameters for various cell sizes.

Parameters	Standard value	Lower limit	Upper limit	Used
Extracellular conductivity (σ_0, S/m)	1.2	-	-	1.2
Cell membrane conductivity (σ_1, S/m)	3e-7	1.0e-8	1.0e-6	3e-7
Cytoplasmic conductivity (σ_2, S/m)	0.3	0.1	1.0	0.3
Extracellular dielectric permittivity (ε_0, As/Vm)	6.4e-10	-	-	6.4e-10
Cell membrane dielectric permittivity (ε_1, As/Vm)	4.4e-11	1.8e-11	8.8e-11	4.4e-11
Cytoplasmc dielectric permittivity (ε_2, As/Vm)	6.4e-10	3.5e-10	7.0e-10	6.4e-10
Cell radius (R, μm)	10	5	100	20
Cell membrane thickness (D, nm)	5	3	7	5
Magnetic flux density (B_0, Tesla)	2	-	-	2
Electrical voltage (V)	200	-	-	200
Field frequency (f, kHz)	10	2	200	1 k–100 M

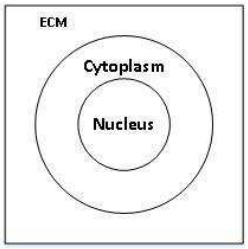

Figure 1: Schematic representation of the cross section of an ideal spherical shaped biological cell embedded in ECM.

3. MODEL DESCRIPTION

The cross section of a spherical cell, embedded in ECM, is shown in Fig. 1. The simple model of the cell is consisted only of the extracellular matrix, the cell cytoplasm and the cell nucleus. Other cellular structures are in this model neglected because their life cycle is very complex and does not exist the easy way to model their behavior. Parameters of the model and used material characteristics are shown in Table 1. The model was developed with the use a rotational symmetry as a two dimensional (2D). Analysis of the electromagnetic field has been divided on the analysis of the magnetic and electric field. For the analysis of the magnetic field has been used element PLANE53 where has been identifying the magnetic vector potential created by the magnetic field of size $B = 2\,\mathrm{T}$. For the analysis of the electric field has been used the element PLANE121. On the top and bottom sites has been specified the electric potential $V = 200\,\mathrm{V}$. In both cases was made a harmonic analysis of which was adjusted by the frequency $f = 1\,\mathrm{kHz}$, 100 kHz, 200 kHz, 400 kHz, 800 kHz, 1 MHz and 100 MHz. The finite element mesh was created by 7778 elements and 23609 nodes.

4. RESULTS OF THE MODELING AND DISCUSSION

The analysis was divided into a few steps. In the first step were analyzed changes in the influence of the magnetic field in the cell and ECM for all frequencies. Material properties that were applied in the magnetic analysis, especially relative permeability which is for all materials differ from one with very small changes, causes changes the magnetic induction ΔB in the ranging $\pm 10\,\mu\mathrm{T}$. To displaying of this small changes were deducted the basic magnetic field of 2 T. To displaying the magnetic field intensity was subtracted value of 1.59 MA/m. The distribution of magnetic flux density and magnetic field intensity is shown in Fig. 2. The changing of the magnetic field are reflected in the cell membrane. The distribution of the magnetic field is not changing with a frequency.

In the next step was analyzed the electric field in the model. There were performed analysis for all of the selected frequencies. In the model were evaluated distribution of the electric potential, the electric field strength, the overall capacity of the model and the capacity of the cell membrane and the ICM. The evaluation of the frequency depending on the capacity is of the Fig. 3. The figure shows that the capacity of ECM is frequency independent and in the entire frequency band takes

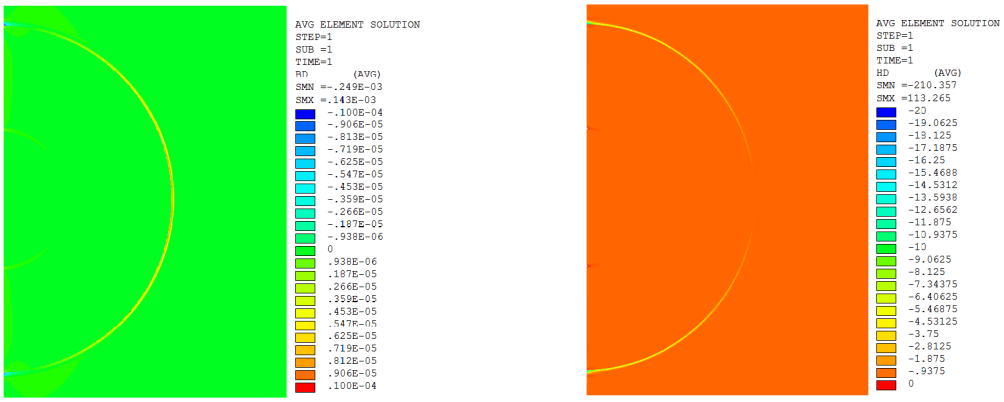

Figure 2: Magnetic flux density **B** and magnetic field intensity **H** distribution in the model.

a value of 11.8 fF. The capacity of the membrane is approximatly constant between values of 1 kHz to 100 kHz. After crossing the frequency $f = 100$ kHz begins the capacity to decline sharply until to frequency $f = 1$ MHz. The capacity drops from 1.61e-13F to 9.8e-18F. After crossing frequency of 1 MHz starts gradual decrease in capacity. The capacity of the membrane contributes of the largest part to the total capacity of the entire model. Due to the decline in the capacity of the membrane start to operate capacities in the ICM. Due this capacity represents the cell membrane a high impedance for frequencies up to 100 kHz and prevents the penetration of the electric field into the ICM. We can say that the membrane behaves as a high-pass filter. In the next step of the modeling we are examined the analysis of the electrostatic field and the change in frequency due to electrostatic field. It was evaluated the overall capacity of the model and other partial capacity of the cell membrane, ICM and ECM. The capacity in the ICM is constant with a value bout 1.18e-14F. The capacity inside the cell varies only little and with increasing of the frequency it increases too. The most interesting result is the change of the capacity of the cell membrane or the reactance. This value decline steeply after crossing the value of frequency 100 kHz to 1 MHz and then is decline finer. The cell membrane has the largest share of the total capacity of the model. The cell membrane can act as a capacitor. It is a high impedance (or resistance) at lower frequencies and at high frequencies is like a little resistance. This property may be likened to a highpass in electrical circuits.

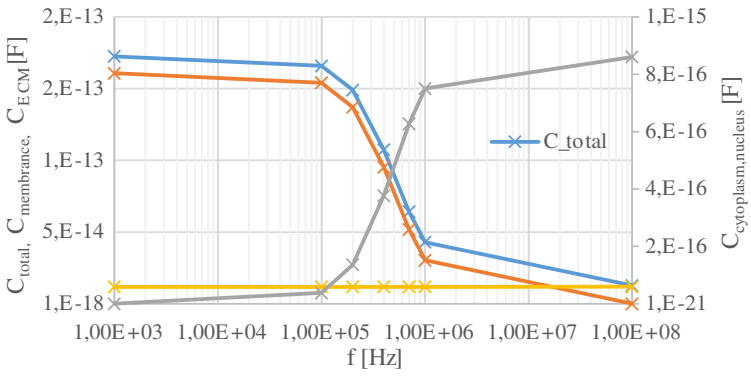

Figure 3: The evaluation of the frequency depending on the capacity.

The following figures (Fig. 5) shows the layout of vectors of electrical potential in the throughout of the model and vectors of electrical field intensity in the cell membrane. For low frequencies is inside the cell only little difference of potentials — A few volts and low intensity electric field (intensity difference-gradient). For a frequency of 100 MHz is the potential distribution such the field appears to be with the absence of the cell (the influence of the cell to the field is only minimally) and is evident the big difference intensity of the electric field (Fig. 4).

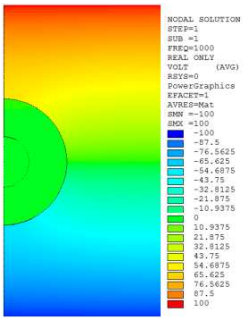

The distribution of electric potential (1kHz)

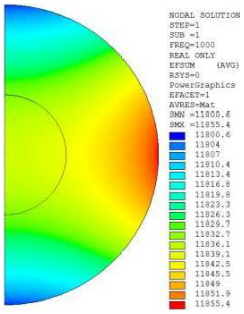

The distribution of **E** (1kHz)

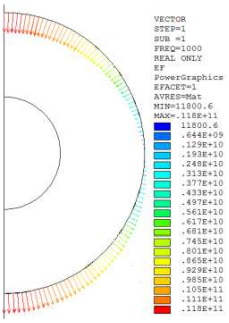

The vector of **E**

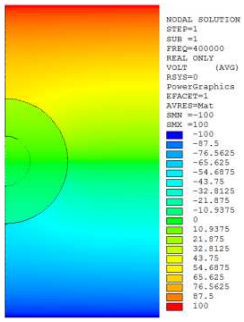

The distribution of electric potential (400kHz)

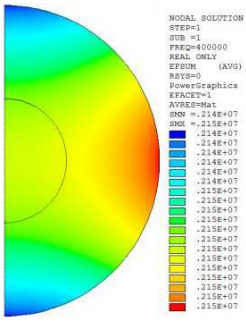

The distribution of **E** (400kHz)

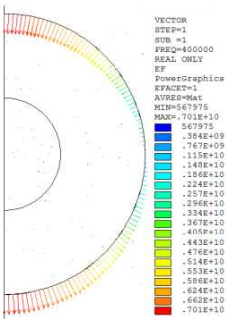

The vector of **E**

Figure 4: The results of the modeling.

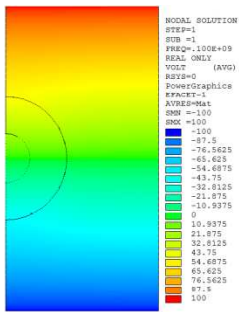

The distribution of electric potential (100MHz)

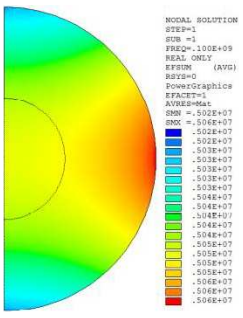

The distribution of **E** (100MHz)

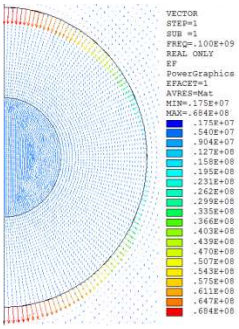

The vector of **E**

Figure 5: The results of the modeling.

5. CONCLUSION

Information on the cellular effects of magnetic and electromagnetic fields is limited. The results obtained in the present study the first description of the behavior of cell structure exposed to different frequency electric and electromagnetic fields. This fields were created using the program ANSYS and thanks to this the living cells not be used in the experiment. This model could not confirm the influence of magnetic field on the cell structure. This effect could occur in other cell organelles, which can be very difficult analyzed in the numerical model. Electrostatic fields can affect the distribution of the cell charge at very small values of the intensity and could result in a change in certain cellular properties, or change the permeability of the cell membrane to the anions and cations. If are changes in membrane seen at small changes in intensity, the further question of research will be how can be the effect to the cell of the electrostatic field with the large difference of intensity.

ACKNOWLEDGMENT

This work was supported within the project of the Grant Agency of the Czech Republic GA 102/12/1104 and project of the BUT Grant Agency FEKT-S-14-2545.

REFERENCES

1. Hong, F. T., "Magnetic field effects on biomolecules, cells, and living organisms," *Biosystems*, Vol. 36, No. 3, 187–229, [online], 1995, DOI: 10.1016/0303-2647(95)01555-Y.
2. Rosen, A. D., "Mechanism of action of moderate-intensity static magnetic fields on biological systems," *Cell Biochemistry and Biophysics*, Vol. 39, No. 2, 163–174, [online], 2003, DOI: 10.1385/CBB:39:2:163.
3. Wartenberg, D., "Residential EMF exposure and childhood leukemia: Meta-analysis and population attributable risk," *Bioelectromagnetics*, Vol. 22, No. S5, 86–104, [online], 2001, DOI: 10.1002/1521-186X(2001)22:5+<::AID-BEM1026>3.0.CO.
4. Mccann J., F. Dietrich, C. Rafferty, and A. O. Martin, "A critical review of the genotoxic potential of electric and magnetic fields: Mutation research/reviews," *Genetic Toxicology*, Vol. 297, No. 1, 61–95, [online], 1993, DOI: 10.1016/0165-1110(93)90008-B.
5. Šimurda, J., *Bioelektrické Jevy*, 1–72, Faculty of Electrical Engineering and Comunication, BUT, Brno, 2007.

The Connection of a Micro-hydropower Plant to an Experimental Electrical Network

P. Marcon[1], **Z. Szabo**[1], **Z. Roubla**[1], **and F. Zezulka**[2]

[1]Department of Theoretical and Experimental Electrical Engineering, FEEC
Brno University of Technology, Technicka 12, Brno, Czech Republic
[2]Department of Control and Instrumentation, FEEC
Brno University of Technology, Technicka 12, Brno, Czech Republic

Abstract— The paper describes the connection of a micro-hydropower plant to a 24 V experimental smart grid. The principle of the proposed design consists in improving the stability of the current grid and enabling maximum exploitation of the electric energy produced by renewable sources (hydroelectric stations, photovoltaics, wind power plants). In this respect, the authors present a very important module to the renewable sources connection and change the current flow direction.

This module, denoted as Control Block, serves both to dispatch the energy to the grid and to charge the smart grid batteries. In order to secure correct operation and functioning of the Control Block, the authors applied a step-up converter and designed a special step-down converter.

1. INTRODUCTION

The authors describe the connection of a micro-hydropower plant to an Experimental Electrical Network (E.E.N.) [1]. The principle of the proposed design consists in improving stabilization of the current grid and enabling maximum exploitation of electric energy produced by renewable sources (hydroelectric stations, photovoltaic, and wind power plants) [2, 3]. In this respect, the authors present a very important block for change the direction of a current flow [4]. It is very useful block for the connection of a micro-hydropower plant to a smart grid, see Chapter 3. This paper presents also the measured characteristics of our micro-hydropower plant, see Chapter 4.

2. EXPERIMENTAL ELECTRICAL NETWORK

Small power plants utilizing renewable energy sources are connected to a grid. Some of these power plants are shown at the Automation Laboratory, Brno University of Technology, where the E.E.N. is located. Firstly, there is a PV panel and small wind power plant which are situated on a roof of the building. The micro-hydropower plant must be placed in other locations from practical reasons. But the performance of micro-hydropower plant is measured and information about power is send to our laboratory via a GPRS data logger. In E.E.N. is this information used for physical model of renewable energy sources (RES). Physically RES is the voltage control current source [1] Produced energy is stored in batteries and in the hydrogen container.

The physical realization of the E.E.N. is presented in the Fig. 1. The figure shows renewable sources (hydroelectric stations, photovoltaic, and wind power plants) connection to the smart grid. While the thick lines represent the material and energy flows, the thin lines indicated communication links. Each power control source communicates with the CompactRIO and LabView control system physically through the input/output circuits available via the wired connections in the laboratory.

The resources supplying energy to the E.E.N. describing in this paper are a water turbine and solar panels. Each of these elements supplies approximately 200–500 W peak to the E.E.N. Given the simplicity of the physical realization, the safety experiments, and the low cost, the E.E.N. works with 24 V DC. Very important part of the E.E.N is the Control Block 1 (CB1).

3. CONTROL BLOCK 1

Control block 1 denoted as CB1 serves both to dispatch energy to the grid and to charge the smart grid batteries. In order to secure correct operation and functioning of the CB1, the authors applied a step-up converter and designed a special step-down converter.

The first mode of CB1 enables to charge the local 12 VDC batteries (whose voltage may range between 11 VDC and 14.5 VDC depending on the battery charge status). The batteries are charged via a DC/DC converter, which behaves like a current source. The 24 VDC smart grid is used as the supporting source. The DC/DC converter is controlled depending on both the current sensed by

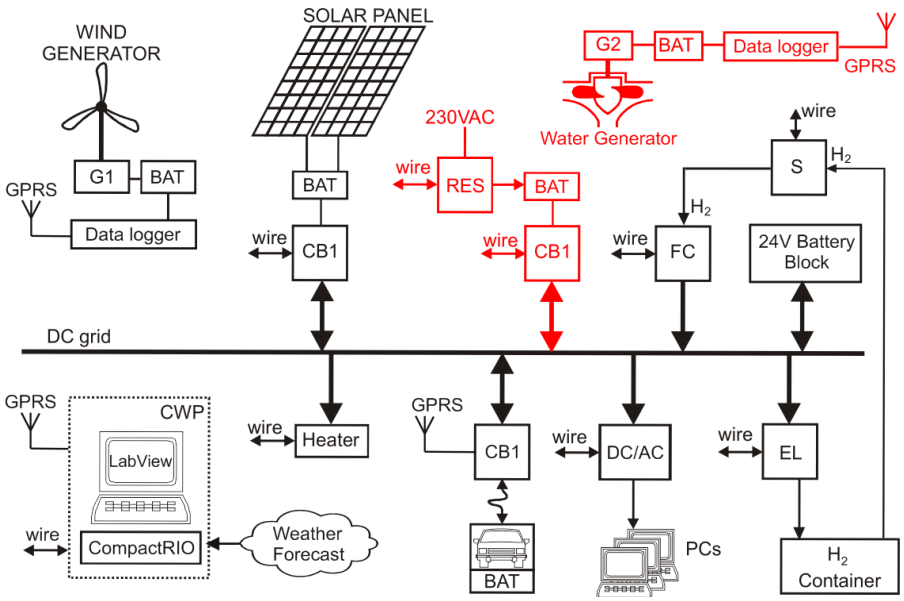

Figure 1: Block diagram of the experimental electrical network: **CB1** — Control Block 1, **BAT** — accumulator of DC energy, **RES** — physical model of remote energy source, **S** — valve to switch and control the hydrogen flow to the fuel cell (FC), **EL** — electrolyzer, **FC** — fuel cell, **G1** — wind turbine generator 24 Vss, 160 W, **G2** — water turbine generator 230 V, 50 Hz, 500 W, **Heat** — electric heater, **Container**: metal-hydride container of hydrogen, **CWP** — control work place.

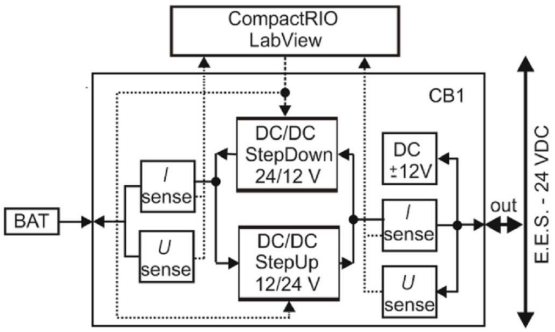

Figure 2: A block diagram of the Control Block 1.

a HY10 sensor and the voltage determined on a divider; the current and the voltage are measured at the CB1 input. The applied DC/DC converter is a special Linear Technology circuit controlled by a D/A converter via the LabView environment.

The second mode of CB1 allows power the 24 VDC smart grid from local 12 VDC batteries. For this purpose, we used a step down DC/DC converter, whose output voltage is controlled via LabView. In general terms, the controlling is performed through a D/A converter in CompactRIO; the output of the converter is connected to the controlling input of the changer. Here, the controlling is also realized depending on the output current and voltage, and sensor types similar to those applied within mode 1 are utilized.

Mutual switching between the two modes is performed using the LabView controlling interface; thus, the activity of only one converter (the step-up or the step-down) at a given moment is secured.

4. MONITORING OF MICRO-HYDROPOWER PLANT

A micro-hydropower plant has also been included in our E.E.N.. The capable of generating the maximum power of 500 W. For modeling of the E.E.N., it is very important to monitor the performance of the hydroelectric plant. The performance depends on the amount of water in the weir; this amount is proportional to the level h in the weir, which is used as the water source for the hydropower plant.

Figure 3 left shows our micro-hydropower plant and the right-hand side Fig. 3 shows a six-hour power recording. The regulator should keep the harmonic network voltage at 230 V and maintains

the frequency of 50 Hz. It is possible to connect any load (and also a charger) to the output of the regulator.

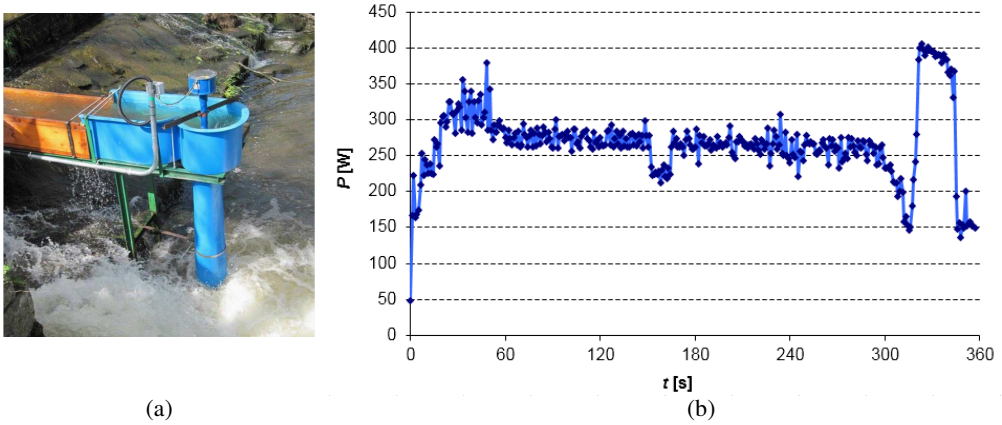

(a) (b)

Figure 3: (a) Micro-hydropower plant, (b) six-hour power recording.

5. CONCLUSIONS

In this paper the connection of a Micro-Hydropower plant to an Experimental Electrical Network was presented. A new module, Control Block 1 — CB1, was designed. Then the paper presents the output power characteristics of our experimentally micro-hydroelectric power plant. This characteristic can be suitably utilized in the modelling of an E.E.N..

As the output power of a micro-hydropower plant markedly depends on the weather, With increasing precipitation, the water level in the weir of the station will rise, thus improving the output power of the turbine. For the six-hour power recording see Fig. 3.

The micro-hydropower plant can be connected directly to the grid loads via a regulator; alternatively, the energy can be stored in batteries. Data-loggers are located in the stations to transmit the measured output power data to an SQL server. In the future, the data could be used to support the entire process of modelling the functions of an E.E.N..

ACKNOWLEDGMENT

This work was supported by the Research and Development for Innovations Operational Programme; the CVVOZE project — Center for Research and Utilization of Renewable Energy Sources, No. CZ.1.05/2.1.00/01.0014; by the programme FEKT-S-14-2545 and Education for Competitiveness Operative Programme CZ.1.07.2.3.00.20.0175 (Electro-researcher).

REFERENCES

1. Marcon, P., Z. Roubal, F. Zezulka, Z. Szabo, and O. Sajdl, "Energy sources for and experimental electrical network: PV panel and micro-hydroelectric power plants," *12th IFAC Conference on Programmable Devices and Embedded Systems*, 449–454, Czech Republic, 2013.
2. Hidayatullah, N. A., B. Stojcevski, and A. Kalam, "Analysis of distributed generation systems, smart grid technologies and future motivators influencing change in the electricity sector," *Smart Grid and Renewable Energy*, Vol. 2, No. 3, 216–229, 2011.
3. Fan, J. and S. Borlase, "The evolution of distribution," *IEEE Power & Energy Magazine*, Vol. 7, No. 2, 63–68, 2009.
4. Zezulka, F., Z. Bradac, O. Sajdl, and J. Sembera, " Experimental smart grid," *Proceedings of 11th IFAC/IEEE International Conference on Programmable Devices and Embedded Systems*, 1–6, Brno, Czech Republic, 2012.

The Statistical Evaluation of Data Obtained via the Manual Segmentation of MRI Images of a Pathological Tissue

P. Marcon[1], **J. Mikulka**[1], **E. Gescheidtova**[1], **K. Bartusek**[2], **and A. Sprlakova**[3]

[1]FEEC, Department of Theoretical and Experimental Electrical Engineering
Brno University of Technology, Technicka 3082/12, Brno 616 00, Czech Republic
[2]Institute of Scientific Instruments of the ASCR
v.v.i, Kralovopolska 147, Brno 612 64, Czech Republic
[3]Radiological Clinic, The University Hospital Brno
Jihlavska 20, Brno 625 00, Czech Republic

Abstract— The authors present a statistical evaluation of the MRI images of bones and soft tissues. MRI imaging of small bones is a problem issue because the measured bone images are loaded with susceptibility artifacts and low signal-to-noise ratio. Therefore, we compare the commonly used MRI contrast and looking for the best contrast to bone marrow imaging. The acquired images are classified in terms of the signal-to-noise ratio, intensity difference and steepness of the edges.

The aim of this research was to statistically evaluate and determine the deviation of MRI images; this step was performed by several experts. These specialists conducted proper segmenting of pathological and healthy tissues, and they also compared the selected areas. In some cases, especially when the boundaries of the area are not clearly visible, the problem is to delimit the bone marrow area. Therefore, it is not possible to use automatic segmentation algorithms, and we focused on the manual evaluation of the statistical data in the area of the patient's bone marrow pathology (e.g., the probability of cyst formation can be determined from abnormal levels of vitamin D and osteocalcin).

1. INTRODUCTION

The research of pathology of human tissues is currently very interesting [1–4]. Development of the magnetic resonance imaging represent very significant step because this technique provides images with excellent soft tissues contrast [5, 6]. We focus on MRI imaging of small bones, it is a problem issue because the measured bone images are loaded with susceptibility artifacts and low signal-to-noise ratio [7–11].

In our research, we focus on a manual segmentation, data processing and a statistical analysis of MRI data [12]. The main task of our research was to compare the number of MRI contrast and determine the appropriate contrast for an imaging of specific tissues. The second task was statistical data comparison. The method of measurement and data processing was tested on the volunteers with pathology in the area of mandibular bone marrow.

2. STATISTICAL ANALYSIS

For our experiment we have to introduce the notion of a box plot. The box plot (a.k.a. box and whisker diagram) is a standardized way of displaying the distribution of data based on the five number summaries: minimum, first quartile, median, third quartile, and maximum. In the simplest box plot the central rectangle spans the first quartile to the third quartile (the *interquartile range* or IQR). A segment inside the rectangle shows the median and "whiskers" above and below the box show the locations of the minimum and maximum [12].

3. EXPERIMENT

In our experiment we used a MR tomograph at the University Hospital Bohunice. The MR tomograph dispose of static field flux density $B_0 = 1.5\,\mathrm{T}$. From the tomograph we obtain images of a mandibular region and of a hip joint region to signal processing. The specialist processed the T_1 Weighted Images without contrast agent — T1W and with Contrast Agent — T1W_ContAgent; T_2 Weighted Images — T2W; Short Tau Inversion Recovery weighted images — STIR and Diffusion Weighted Images — DWI.

The aim of this research was to statistically evaluate and determine the deviation of MRI images; this step was performed by several experts. These ten specialists conducted proper segmenting

of pathological and healthy tissues, and they also compared the selected areas. In some cases, especially when the boundaries of the area are not clearly visible, the problem is to delimit the bone marrow area. Therefore, it is not possible to use automatic segmentation algorithms, and we focused on the manual evaluation of the statistical data in the area of the patient's bone marrow pathology (e.g., the probability of cyst formation can be determined from abnormal levels of vitamin D and osteocalcin).

Therefore, the specialists segmenting pathological and healthy tissues, namely: bone and bone marrow; further muscle, fat, ligament, gray matter, white matter, eye. After that they performed a statistical analysis of segmenting area. On the basis of this statistical data from individual human tissues a new statistics (statistic from statistic) was made. By each statistical evaluation of tissue were calculated following statistical quantities: minimum value, maximum value, mean value, standard deviation (S.D.), skewness and kurtosis. The box plots were created.

4. RESULTS

Figure 1 shows two coronal MRI slices of human head. The specialists focus on the segmentation and statistical analysis of mandibular region.

Figure 2 shows also two MR images of human head. Left figure shows a diffusion weighted image of a transversal slice and right figure shows T_2 weighted image of transversal slide. Figure 3 on the left shows T_1 weighted image of the human hip and the right image shows diffusion weighted image of the human hip. As you can see, the diffusion weighted image is affected by artefacts [13, 14].

In Figure 4 you can see the box plot obtained by statistical analysis of bone marrow. This step was performed by several experts. First, these specialists conducted proper segmenting of pathological bone marrow. Second, these specialist made statistical analysis of selected data. We obtain these data from the ten specialists and we made a new statistic. Ideally, the specialists should evaluate the same data, but really as you can see in Figure 4, the data are different. A scattering of obtained data is represent by box plot.

Figure 5 shows a mean values box plot of individual tissues. These data was obteined form

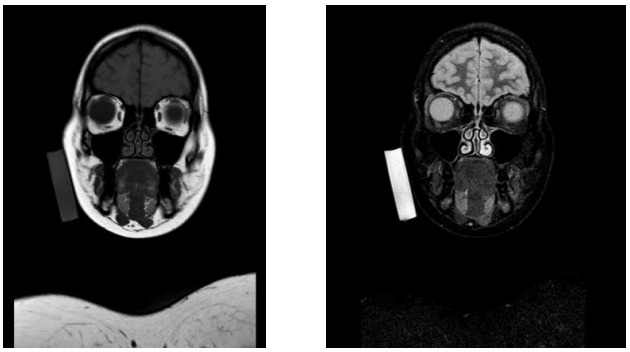

Figure 1: Coronal slices with 2D imaging of the human head. (a) T1W image. (b) STIR weighted image.

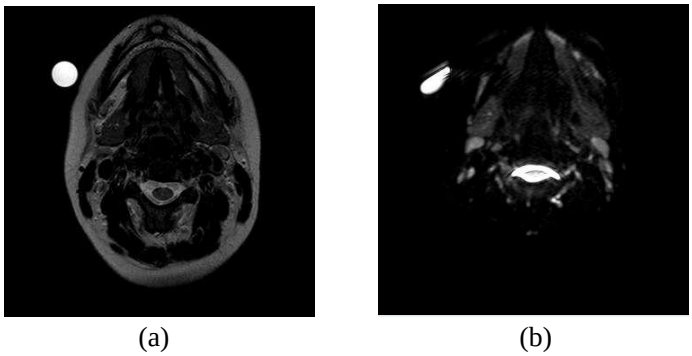

Figure 2: Transversal slices with 2D imaging of the human head. (a) T2W image. (b) Diffusion weighted image.

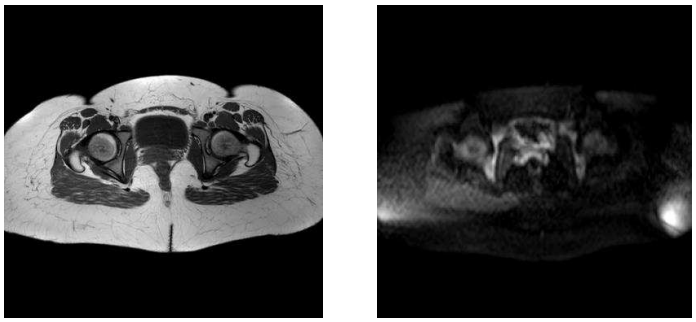

(a) (b)

Figure 3: Transversal slices with 2D imaging of the human hip. (a) T1W image. (b) DWI image.

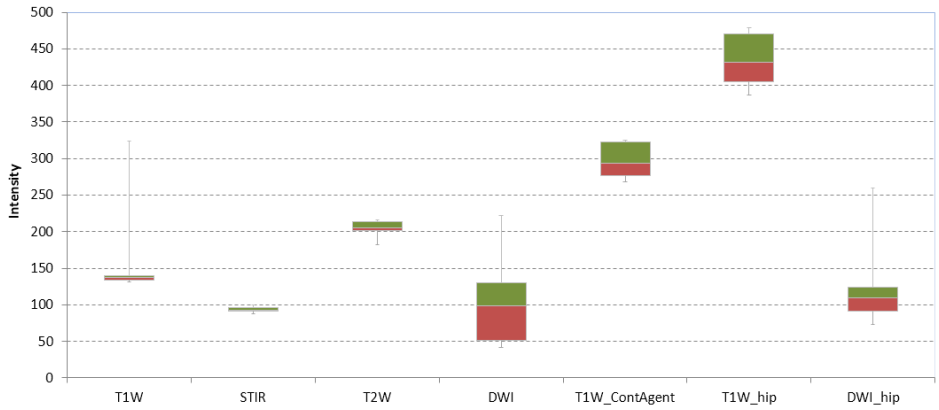

Figure 4: The Box blot obtained by statistical analysis of MR bone marrow data selected and processed by ten specialist.

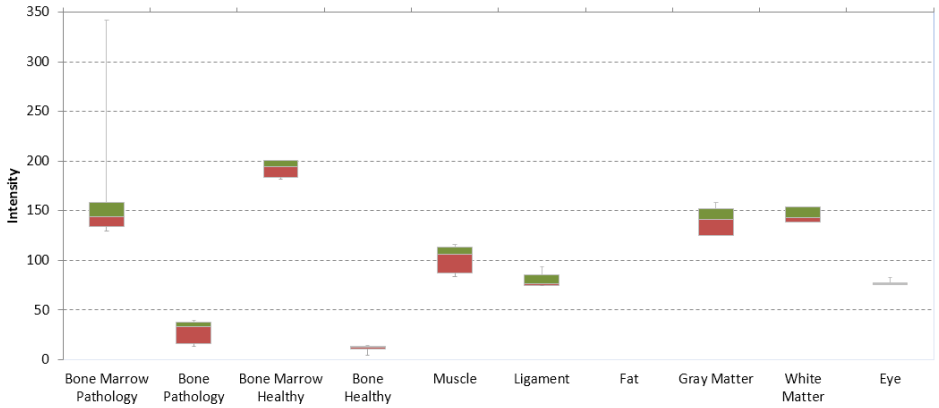

Figure 5: The Box plot of T_1 weighted mean values of individual tissues.

T_1 weighted images of bone marrow, see Figure 1(a). There, the right hand side of mandibula is without bone marrow pathology and left hand side exhibit a bone marrow pathology. The box plot in Figure 5 present differences not only between healthy and pathology bone marrow, but also statistical differences between individual tissues. These data are very useful for programing a automatig segmentation procedure.

5. CONCLUSIONS

We evaluated a statistical analysis of the MR images of bones and soft tissues. Therefore, we compared the commonly used MRI contrast and we found the best contrast to bone marrow imaging, namely T_1 weighted imaging. From the statistical evaluation we created the small database of healthy human tissues: bone, bone marrow, muscle, fat, white matter, gray matter and eye. By

each tissue we evaluated following statistical quantities: mean value, standard deviation, skewness and kurtosis. The box plots and small statistic database were created. The results of the statistics data are presented in the Figure 5. This database is used to identification the unknown tissues.

Further, we evaluated the statistical deviation arising by segmentation and determining healthy or pathology human tissues; this step was performed by several experts. These specialists conducted proper segmenting of pathological and healthy tissues, and they also compared the selected areas. First, these specialists conducted proper segmenting of pathological bone marrow. Second, these specialist made statistical analysis of selected data. We obtain data from the ten specialists and we made a new statistic. Ideally, the specialists should evaluate the same data, but really as you can see in Figure 4, the data are different. A scattering of obtained data is represent by box plot.

ACKNOWLEDGMENT

This work was supported in part by the Grant GACR 102/12/1104 and the programme FEKT-S-14-2545 and Education for Competitiveness Operative Programme CZ.1.07.2.3.00.20.0175 (Electro-researcher).

REFERENCES

1. Andris, P. and I. Frollo, "Measurement of magnetic field with background using a low-field NMR scanner," *Measurement Science Technology*, Vol. 23, 2012.
2. Marcon, P., K. Bartusek, and M. Cap, "Multiparametric data collection and data processing of animal tissues in MRI images," *PIERS Proceedings*, 358–362, Moscow, Russia, Aug. 19–23, 2012.
3. Gogola, D., A. Krafcik, O. Strbak, and I. Frollo, "Magnetic resonance imaging of surgical implants made from weak magnetic materials," *Measurement Science Review*, Vol. 13, No. 4, 165–168, 2013.
4. Mikulka, J., E. Gescheidtova, and K. Bartusek, "Processing of MR slices of human liver for volumetry," *PIERS Proceedings*, 202–204, Xi'an, China, Mar. 22–26, 2010.
5. Bartusek, K., E. Gescheidtova, and J. Mikulka, "Data processing in studying biological tissues, using MR imaging techniques," *33th International Conference on Telecommunications and Signal Processing*, 171–175, Asszisztenda Szervezo, Budapest, 2010.
6. Mikulka, J., E. Gescheidtova, and K. Bartusek, "Soft-tissues image processing: Comparison of traditional segmentation methods with 2D active contour methods," *Measurement Science Review*, Vol. 12, No. 4, 153–161, 2012.
7. Rupp, R. E., N. A. Ebraheim, and R. J. Coombs, "Magnetic resonance imaging differentiation of compression spine fractures or vertebral lesions caused by osteoporosis or tumore," *Spine*, Vol. 20, 2499–2503, 1995.
8. Marcon, P. and K. Bartusek, "Errors in diffusion coefficients measurement," *PIERS Proceedings*, 1035–1039, Cambridge, USA, Jul. 5–8, 2010.
9. Tsai, J. Z., S. J. Peng, Y. W. Chen, K. W. Wang, H. K. Wu, Y. Y. Lin, Y. Y. Lee, C. J. Chen, H. J. Lin, E. E. Smith, P. S. Yeh, and Y. L. Hsin, "Automatic detection and quantification of acute cerebral infarct by fuzzy clustering and histographic characterization on diffusion weighted MR imaging and apparent diffusion coefficient map," *BioMed Research International*, Vol. 2014, 1–6, Hindawi, 2014.
10. Marcon, P., K. Bartusek, R. Korinek, and Z. Dokoupil, "Correction of artifacts in diffusion-weighted MR images," *34th International Conference on Telecommunications and Signal Processing (TSP)*, 391–397, Budapest, 2011.
11. Wapler, M. C., J. Leupold, I. Dragonu, D. Elverfeld, M. Zaitsev, and U. Wallrabe, "Magnetic properties of materials for MR engineering, micro-MR and beyond," *Journal of Magnetic Resonance*, Vol. 242, 233–242, 2014.
12. McGill, R., J. W. Tukey, and W. A. Larsen, "Variations of boxplots, "*The American Statistician*, Vol. 32, No. 1, 12–16, 1978.
13. Marcon, P., K. Bartusek, E. Gescheidtova, and Z. Dokoupil, "Diffusion MRI: Magnetic field inhomogeneities mitigation," *Measurement Science Review*, Vol. 12, No. 5, 205–212, 2012.
14. Marcon, P., K. Bartusek, M. Burdkova, and Z. Dokoupil, "Magnetic susceptibility measurement using 2D magnetic resonance imaging," *Measurement Science and Technology*, Vol. 22, 2001.

Uncertainty Determination in Measurements Using a Gerdien Tube

Z. Roubal, Z. Szabo, and M. Steinbauer
Department of Theoretical and Experimental Electrical Engineering
Brno University of Technology, Technicka 12, Brno 616 00, Czech Republic

Abstract— Light negative air ions demonstrably exhibit positive influence on the human organism. The concentration of these ions can be effectively used as the integral criterion for the evaluation of air purity, and there also exists a multitude of other applications. The presented aspiration method enables us to establish the concentration of air ions in the atmosphere. In a Gerdien tube fitted with a one-piece inner electrode, measurement of the saturation characteristics must be performed to facilitate the determination of the air ion mobility spectrum. This method is very sensitivity to noise and leakage current. In this paper is determination uncertainty of type B in Gerdien tube and electrometric amplifier. This method is very sensitive to noise and leakage current. In this paper, the determination of uncertainty B in a Gerdien tube and an electrometric amplifier is presented. The uncertainty depends on the input bias current and input noise current of the applied operational amplifier. Another significant source of B uncertainty is the temperature and time instability of the Teflon insulator.

1. INTRODUCTION

In industrial zones, where the environment air is often polluted with dust and smog, the concentration of air ions can be regulated or measured only with difficulty. Any thus impaired area shows an inherent deficiency of negative ions and, conversely, an abundance of positive ions complementing the nano and microscopic dust particles. Significantly, the described aspects have a markedly negative effect on the overal degree of fatigue and professional performance of a human being [1, 2]. The impact of environment on a human organism has been analyzed in studies [1, 2]. In the DTEEE laboratories, the methodology supporting the measurement of air ions concentration and mobility spectrum utilizes an aspiration condenser [3–9], this method is dependent upon a suitable approximation of saturation characteristics.

2. GERDIEN TUBE

A Gerdien tube (GT) is an instrument used for the measurement of air ions concentration assuming that the volume of tested air has not been limited or the ions are continuously generated. In the time domain, it is possible to measure by means of an GT only ions of one polarity; then, following a certain interval, ions of the other polarity can be measured. Ionized air is sucked into the GT by a ventilator. The homogeneous electric field is set between the inner and the outer electrode. If an electric ion shows a negative electric charge and the collecting inner electrode has a positive electric potential, the ion is progressively attracted to the inner electrode. Provided that the ion impinges upon the electrode, it will induce an electric current that is measured by the help of a sensitive electrometric picoampermeter [4]. The velocity of the ions motion in the electric field can be described by mobility $k\,[\mathrm{m}^2 \cdot \mathrm{V}^{-1}\,\mathrm{s}^{-1}]$.

It is possible to determine boundary mobility k_m for every GT configuration.

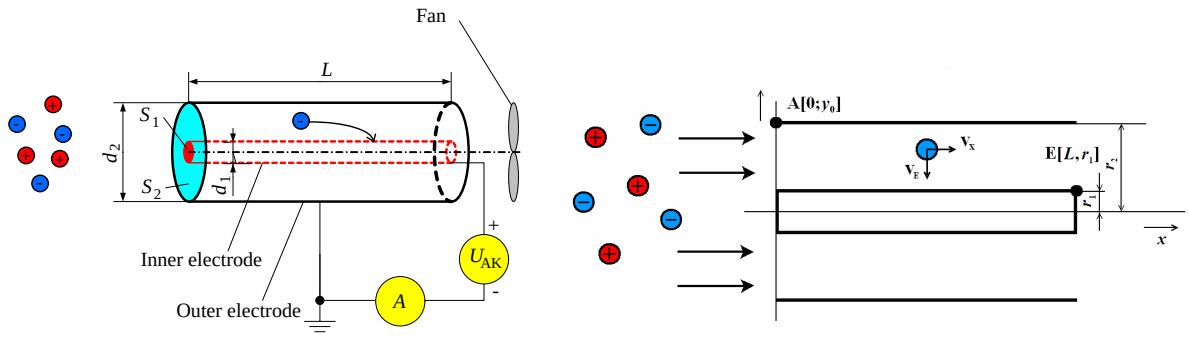

Figure 1: The basic principle of a Gerdien tube.

All ions showing an index of mobility greater than k_m will impinge upon the inner electrode; however, only a proportionate part of them will impinge in ions which mobility is smaller than k_m. Based on the aspiration condenser parameters, the air flow volume rate is defined as

$$M = \left(r_2^2 - r_1^2\right) \cdot \pi \cdot v_x, \tag{1}$$

where M, r_2, r_1, v_x, ... are the air flow volume rate, the outer electrode radius, the inner electrode radius, and the air flow velocity, respectively.

The main parameter applied for the definition of air ions mobility consists in boundary mobility k_m,

$$k_m = \frac{\varepsilon_0 \cdot \varepsilon_r \cdot M}{C_{\mathrm{AK}} \cdot U_{\mathrm{AK}}}, \tag{2}$$

where ε_0, ε_r, C_{AK}, U_{AK}, ... are the vacuum permittivity, the relative permittivity, the GT capacity, and the GT polarization voltage, respectively. Then, for current I measured by the electrometric picoampermeter, we can define

$$I_{k<k_m} = \frac{k}{k_m} \cdot n \cdot q \cdot M, \quad I_{k \geq k_m} = n \cdot q \cdot M, \tag{3}$$

where n, q, ... are the volume concentration of ions and the elementary charge, respectively.

3. THE EQUIVALENT CIRCUIT OF THE MEASUREMENT EQUIPMENT

The measured current I_{IONT} is measured with a high-quality picoampermeter, namely an electrometer. However, we must consider the fact that high-impedance measurement is performed, and therefore the structure and insulation of the component will influence the measured current. The equivalent circuit of the measuring equipment is shown in Fig. 1. At the DTEEE, an older GT manufactured by the Brno Institute of Scientific Instruments (ISI) is used together with a new type designed at the department (DTEEE). By constructing a new electrometric amplifier, we recently modernised the older GT.

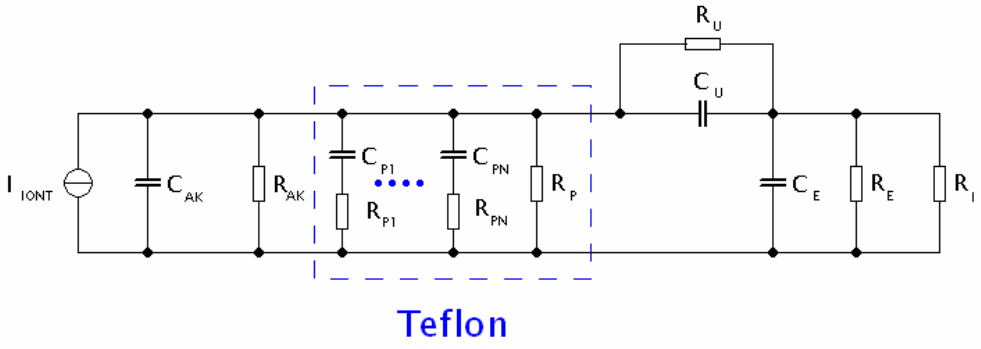

Figure 2: The equivalent circuit of the measuring equipment using the Gerdien tube.

Table 1: The value of elements in the equivalent circuit.

	ISI GT	DTEE GT
C_{AK}	15,06 pF	7,72 pF
$R_{\mathrm{AK}} \parallel R_P$	910 TΩ	5889 TΩ
C_U	1 µF/250 V	1 µF/250 V
R_U	10 TΩ	10 TΩ
C_E	6 pF	3 pF
R_E	100 TΩ	100 TΩ

In both GTs, we measured the insulation resistance R_{AK} in parallel with the R_P and the capacitance C_{AK}. The values of other elements in the equivalent circuit are indicated in Table 1. Here R_{AK}, R_P, C_U, R_U, C_E, R_E, ... are the insulation resistance of the GT, the insulation resistance of the teflon duct, the charge capacitor, the insulation resistance of the charge capacitor, the input capacity of the electrometer, and the input insulation resistance of the electrometer.

The dielectric absorbtion of the Teflon material (represented in the equivalent circuit by the elements R_{P1}, C_{P1}, ..., R_{PN}, C_{PN}) causes leakage current changes during the measurement. Thus, when measuring AV characteristics of the leakage current (from which the parallel values $R_{\mathrm{AK}} \parallel R_P$, are subsequently determined), we need to wait for the end of the transient process. The measurement time dependence of the leakage current is presented in Fig. 3.

From the AV characteristics of the GTs manufactured by both the DTEEE and the ISI, the relevant are determined. After charging the capacitor C_U, it is suitable to observe a delay of approximately 2 minutes, as shown in Fig. 3. Using Pspice, we simulated the equivalent circuit and defined the charging interval of the capacitor C_U. This recharge time interval depends on the air ion concentration n. The result is obvious from Fig. 5. Near strong ion fields, such as those

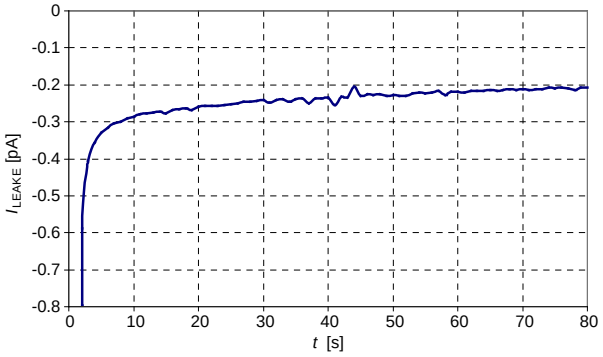

Figure 3: The time dependence of the leakage current after polarisation voltage changes.

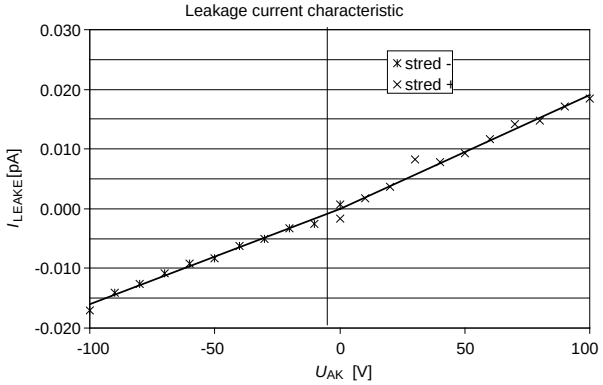

Figure 4: The AV characteristics of the GT by the DTEEE.

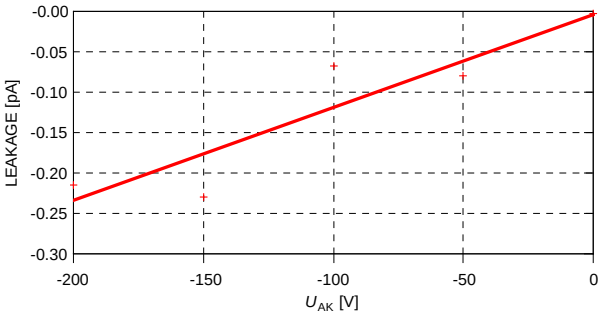

Figure 5: The AV characteristics of the GT by the ISI.

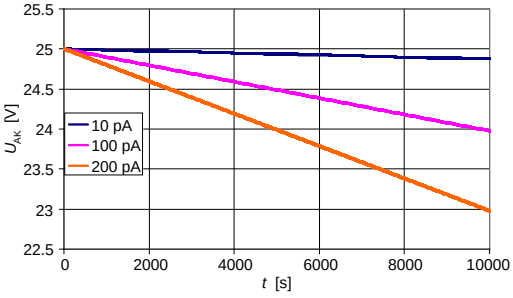

Figure 6: The discharge capacitor C_U.

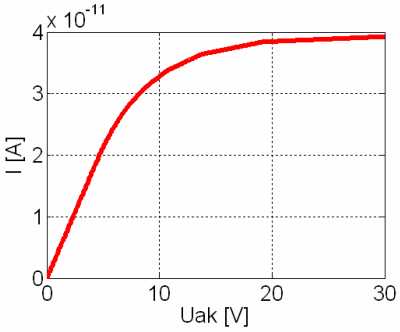

Figure 7: The typical saturation characteristic the GT DTEEE.

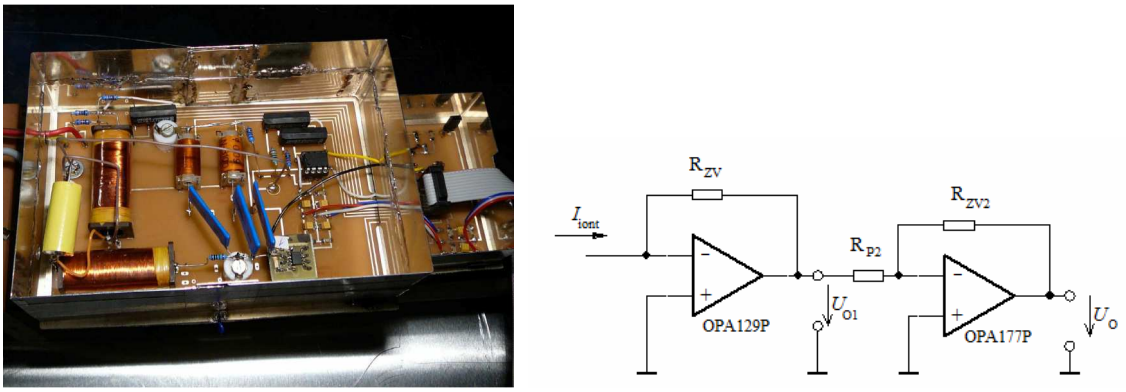

(a) (b)

Figure 8: The new electrometric amplifier for (a) the GT ISI and (b) its simplified circuit.

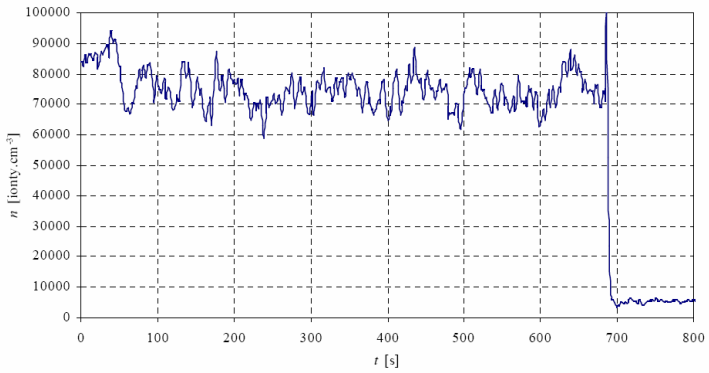

Figure 9: The time dependence of the air ion concentration measured with the new electrometric amplifier near the ioniser BIV-06.

Table 2: The relative uncertainty of type B for several variant electrometric amplifier.

	R_I	uncertainty of type B
ISI GT with electrometric amplifier WSH223	100 GΩ	10%
ISI GT with electrometric amplifier OPA129	10 MΩ	1%
DTEEE GT with electrometric amplifier INA116	10 GΩ	1%
DTEEE GT with electrometric amplifier OPA129	10 MΩ	0.25%

created by an ioniser or a waterfall, it is important to recharge the capacitor C_U. If the saturation characteristic [11] used for the determination of the air ion mobility spectrum is measured, the above-shown decrease in the polarisation voltage U_{AK} causes a rapid increase of the saturation characteristic slope. This results in erroneous estimation of the air ion mobility spectrum.

The measured current is given by the equation

$$I = I_{\mathrm{ions}} \cdot \frac{G_I}{G_I + G_{\mathrm{AK}} + G_P + G_E}. \tag{4}$$

where the conductivities correspond to individual elements in the equivalent circuit, and G_I is the input conductivity of the electrometric amplifier.

4. THE MODERNISATION GT ISI

If we need to minimalise the systematic error of the measurement, it is suitable to decrease the input resistance value of the electrometric amplifier. For this purpose, a feedback ammeter performs better than the shunt amplifier used in electrometers with INA116. When modernising the GT manufactured by the ISI, we designed a new electrometric amplifier with an OPA129 operation amplifier [12]. The result is presented in Fig. 9.

5. CONCLUSION

The GT manufactured by the DTEEE exhibits smaller uncertainty B than the older GT supplied by the ISI. The sensitivity of the former device is nevertheless worse than that of the GT ISI; thus,the team at our department eventually modernisedthe GT ISI. In the measurement configuration, we decreasedthe input resistance of electrometric amplifier, andthis change then improved the features of the GT ISI. During the simulation in Pspice, the recharge interval of the capacitor C_U was determined to be 3 hours. In the course of this time, the polarisation voltage U_{AK} near the ioniser decreases (in the GT UTEEE) to 2,5 V. In the GT ISI, this interval is longer.

ACKNOWLEDGMENT

The research described in the paper was financially supported by a grant of the BUT science fund, No. FEKT-S-14-2545/2014, and the authors also received assistance from projects within the Education for Competitiveness Operative Programme, Nos. CZ.1.07.2.3.00.20.0175 and CZ.1.07/2.3.00/3-0.0005.

REFERENCES

1. Roubal, Z., M. Steinbauer, and Z. Szabó, "Modeling of saturation characteristic of an aspiration condenser," *PIERS Online*, Vol. 6, No. 1, 26–30, 2010.
2. Kondrashova, M. N., E. V. Grigigorreko, A. N. Tikhonov, T. V. Sirota, A. V. Temnov, I. G. Stavrovskaya, N. I. Kosyakova, N. V. Lange, and V. P. Tikonov, "The primary physicochemical mechanism for the beneficia biological/medical effects of negative air ions," *IEEE Trans. Plasma Scien.*, Vol. 28, No. 1, 230–237, 2000.
3. Roubal, Z. and M. Steinbauer, "Design of electrometric amplifier for aspiration condenser measurement," *PIERS Proceedings*, 1430–1434, Xi'an, China, Mar. 22–26, 2010.
4. Szabó, Z., Z. Roubal, and K. Bartušek, "Filtration properties of a system for the measurement of air ions," *PIERS Proceedings*, 154–158, Taipei, Mar. 25–28, 2013.
5. Tammet, H. F., *The Aspiration Method for Determination of Atmosphericion Spectra*, IPST, Jerusalem, 1970.
6. Vojtek, T., T. Skoupil, P. Fiala, and K. Bartušek, "Accuracy of air ion field measurement," *PIERS Proceedings*, 412–415, Cambridge, USA, Mar. 26–29, 2006.
7. Bartušek, K., "Meření spektrálních charakteristik iontových polí," *Elektrorevue*, 2001, Online: http://www.elektrorevue.cz/clanky/01038/index.html.
8. Steinbauer, M., P. Fiala, K. Bartušek, and Z. Szabó, "Experiments with accuracy of air ion field measurement," *PIERS Online*, Vol. 3, No. 8, 1330–1333, 2007.
9. Kadlec, R., P. Fiala, and E. Kroutilová, "Multiple reflection from layered heterogeneous medium," *PIERS Proceedings*, 87–90, Suzhou, China, Sep. 12–16, 2011.
10. Drexler, P., P. Fiala, and R. Kadlec, "Utilization of faraday mirror in fiber optic current sensors and experiments," *PIERS Proceedings*, 142–146, Beijing, China, Mar. 23–27, 2009.
11. Roubal, Z. and P. Křpelka, "Estimation of the air ion mobility spectrum by means of a gerdien tube with a segmented inner electrod," *PIERS Proceedings*, 767–771, Stockholm, Sweden, Aug. 12–15, 2013.
12. Šot, J., "Nízkoúrovňová měření pro zjištění koncentrace vzdušných iontů," Bachelor Thesis, VUT Brno, 2012.

Detector for Nuclear Quadrupole Resonance Spectroscopy

J. Chytil and R. Kubasek
Department of Theoretical and Experimental Electrical Engineering
Brno University of Technology, Technicka 12, Brno 616 00, Czech Republic

Abstract— Nuclear quadrupole resonant spectroscopy is method similar to nuclear magnetic resonant spectroscopy also called zero field NMR [1, 2]. The response signal magnitude is very low and it is immersed in to the noise. There can be used some methods to harvest signal from noise it can be matched receiver [3] or averaging. This authors describe detector for Nuclear quadrupole resonant spectroscopy based on statistic methods and probability of distribution, that allow to measure repetitive signals below noise level. The paper presents the mathematical model and practical solution of the detector, and problems such as the dynamic range and signal distortion based on the signal-to-noise ratio are also analyzed in the given context. If the time of signal occurrence is known, the repetitive signal below the noise level can be harvested out of noise by averaging because of the wanted signal is correlated therefor highlighted by averaging contrast to the noise which is not correlated so it is supressed by averaging. The same principle we can use in domain of digital signal. So the input signal can be converted to the digital representation. There is an comparator with a triggering level immersed in the noise so the comparator is flipping continuously and the probability of output values is affected by input signal. The output digital signal can be processed by FPGA.

1. INTRODUCTION

One of the most significant obstacles in the usage of Nuclear quadrupole resonance spectroscopy is the magnitude of the response signal. This signal is very low and immersed in noise. Thus, increased demands are put not only on the shielding or the quality of the detector but also on the measurement time because of the signal immersion in noise. Out of the methods mentioned in the abstract, only averaging is suitable for spectroscopy. in this context, there then arises the need of a minimal amount of measurements. Generally, the result of the averaging process improves with the growing number of measurement repetitions; at the same time, however, the measurement time becomes longer. The second method outlined herein consists in that a matched reciever can be used to detect the presence of specific substances.

2. MATHEMATICAL MODEL

According to the well-known equation for the averaging of repetitive signals under the noise level, a signal can be harvested out of noise. Noise is not correlated, and thus it is suppressed by averaging; conversely, a signal is correlated and therefore highlighted by averaging (1).

We need to know where the signal begins. Due to known waveform of the excitation pulses and the time of the excitation start, it is not difficult to determine beginning of the response signal.

$$x_{avg}(t) = \frac{1}{n}\sum_{i=1}^{n}(x_i(t)) \tag{1}$$

Generally, we have to use a fast analogue-to-digital converter, which is a rather expensive device. The same principle can be used in the domain of digital signals; thus, we can convert an input signal to the digital form. This procedure is facilitated by a comparator, whose trigger level is immersed in the noise. This means that the comparator flips continuously, and consequently there is digital noise at the output of the comparator.

The probability of output values for a comparator without an input signal (only white noise is present at the input) is, at any time, the same for both output values (in our case, 1 and -1 due to signal centering) (2).

$$\begin{aligned} p(1) &= 0.5 \\ p(-1) &= 0.5 \end{aligned} \tag{2}$$

However, in the case of an input signal $f(t)$, the probability of output values is affected by this signal (3).

$$\begin{aligned} p(1) &= x = 0.5 + kf(t) \\ p(0) &= 1 - x = 0.5 - kf(t) \end{aligned} \tag{3}$$

The magnitude of the signal is proportional to the splitting of the probability of the comparator's output values. But due to the limitation, the proportionality is non-linear and depends on the signal-to-noise ratio. The digital averaging can be described by (4).

$$x_{avg}(t) = \sum_{i=1}^{n} (2 * p(1(f_i(t))) - 1) = \sum_{i=1}^{n} p(1(f_i(t))) - p(-1(f_i(t))) \tag{4}$$

As shown in Fig. 1, the dependence on the SNR markedly influences the sensitivity and linearity of the detector. Signals with a high SNR are easily noticable, but the linearity is not good. The signals immersed deep in noise (signals with a low SNR) exhibit good linearity, but their sensitivity is inferior.

The problem of this mathematical model and also of the circuit analysed below is overdrive. If the signal magnitude is higher than the noise magnitude, then the probability of the occurrence of symbols $+1$ or -1 is close to zero for one of the symbols and close to one for the other.

The averaged output signal is led to the FFT procesor and converted from the time domain to the freguency domain, where we can observe the occurrence of the searched substance (Fig. 2). From the characteristics of the digital NQR detector for different SNRs, the dynamic ratio can be determined. The lowest limit of the detector dynamic ratio is given by sensitivity of the detector;

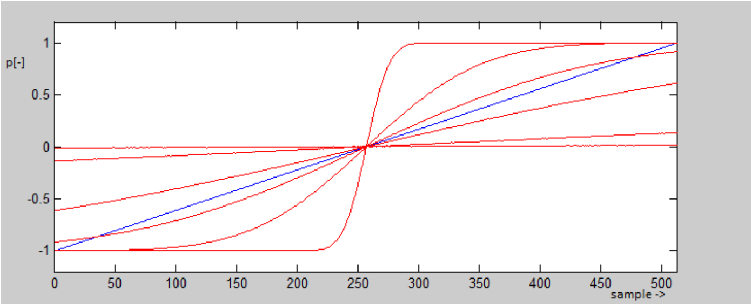

Figure 1: The averaging of 10^7 an input signal with with different SNR levels. The blue line represents the original signal and also the output of analog averaging (regardless of the signal-to-noise ratio). The red curves indicate the results of digital averaging. The steepest curve stands for SNR 20 dB; the gradually flattening one is for 6 dB, 0 dB, -6 dB, -20 dB; and the flattest line represents -40 dB.

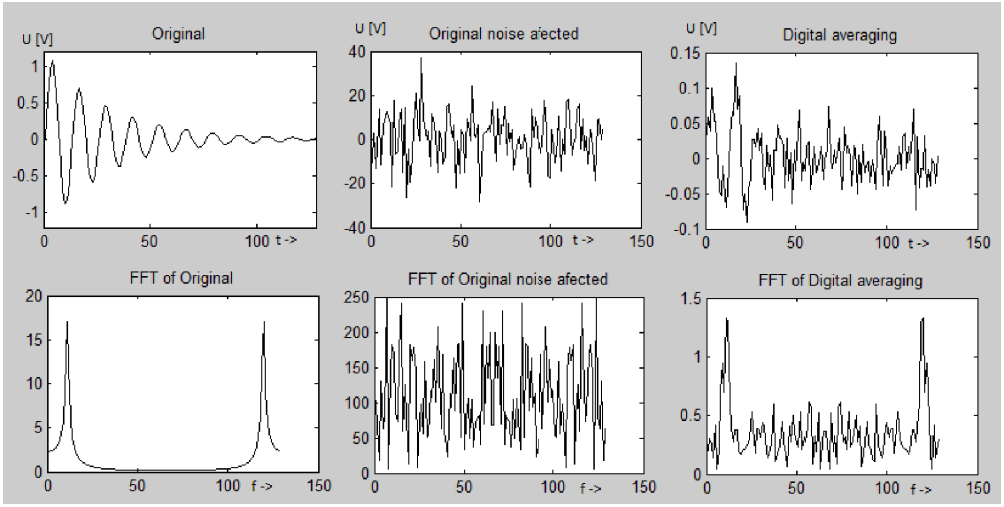

Figure 2: Example of noise-affected and averaged signal. The 1st row is for the signal in the time domain; the 2nd row represents the signal in the spectrum. SNR = -30 dB, 10000 averaging.

the highest limit is then determined by linearity of the output signal. Due to the non-linearities caused by high SNR, the higher harmonic frequencies are produced. These higher freguencies can be detected as foreign substances which, in fact, are not present.

3. PRACTICAL REALISATION

The system for NQR spectroscopy (Fig. 3) consists of an excitation circuit (a radio frequency generator, an amplifier, and a probe). The probe is used both as a part of the excitation circuit and as a component of detector. Furthermore, this probe constitutes an LC resonant circuit (the examined substance is placed into the coil) connected to the excitation circuit and the detector via decoupling circuits. The decoupling circuits protect the detector from damage caused by a high level of the signal from the excitation circuit. The detector is described in more detail within references [4, 5]. In general terms, it is followed by an FPGA for signal processing (averaging and the FFT). The whole spectroscope is regulated by a microcontroller (which can also be implemented in the FPGA) or a PC.

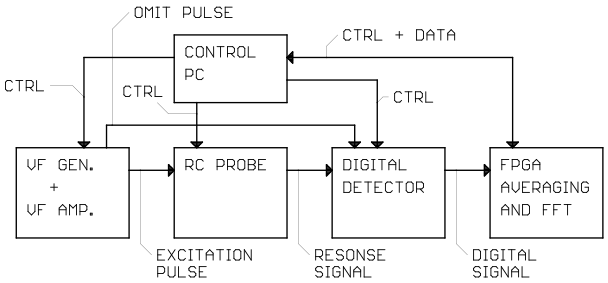

Figure 3: Block scheme *o* NQR spectroscope.

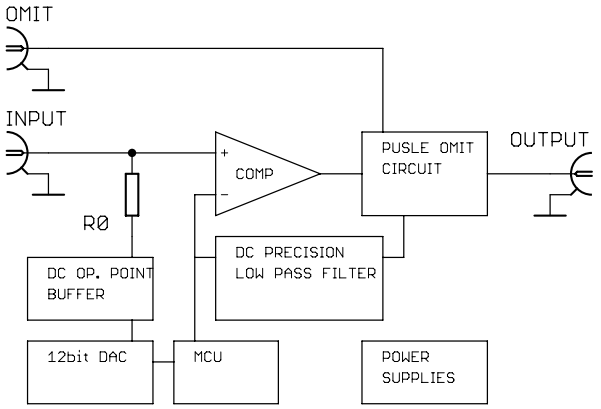

Figure 4: Block scheme NQR detector.

The fabricated digital NQR detector comprises the high speed comparator [6–8] with low-pass feedback circuits designed to pass the DC component of the signal without corruption. The filter can be realised as passive (an RC ladder network) or active; the active variant then utilises DC precision filters (Fig. 5). In both these cases, howeever, it is necessary to use foil condensators with low leakage currents.

Another part of the detector is a DC operating point circuit implemented as a 12-bit DA convertor regulated by a microcontroller (Fig. 6).

The digital part of the cicruit is implemented as an FPGA. The FPGA contains averaging and FFT or averaging and matched recievers. The second solution can be used to search for pre-specified substances (for example, 35Cl or 14N). Thanks to the matched reciever implemented in the FPGA, a large amount of substances can be retrieved.

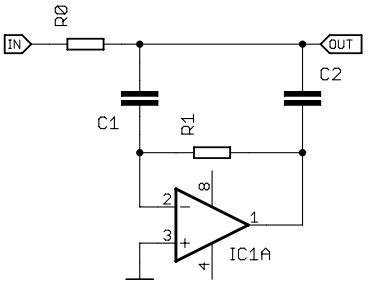

Figure 5: DC precision low-pass filter.

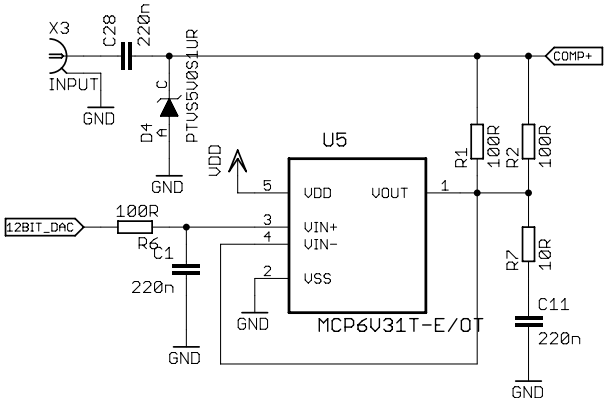

Figure 6: Implementation of the circuit for the DC operating point setting.

4. CONCLUSION

A mathematical model has been developed and tested in MATLAB. Based on this model, the proposed detector was created and measured; the measurement showed the necessity to limit the signal bandwidth by a low-pass filter for better sensitivity. Due to the significant number of measuring cycles required for clear results, the method of averaging detection became rather time-consuming; in this context, the most problematic aspect definitely consists in the presence of the relaxation time. Importantly, as the measurement of one sample can last several minutes, the commercial applicability of averaging-based NQR spectroscopy is limited to a great extent; commercial users would then probably prefer averaging marged with matched recieving. A matched reciever can be easily implemented in an FPGA.

ACKNOWLEDGMENT

The research described in the paper was financially supported by a grant of the BUT science fund, No. FEKT-S-11-5/1012, and the authors also received assistance from projects within the Education for Competitiveness Operative Programme, Nos. CZ.1.07.2.3.00.20.0175.

REFERENCES

1. Garroway, A. N., M. L. Buess, J. B. Miller, B. H. Suits, A. D. Hibbs, G. A. Barrall, R. Matthews, and L. J. Burnett, "Remote sensing by nuclear quadrupole resonance," *Geoscience and Remote Sensing*, Vol. 39, No. 6, 1108–1118, 2001.
2. Motycka, L., "RF detection method of explosives and drugs — NQR," 118, Department of Radio, Faculty of Electrical Engineering and Communication, Brno University of Technology, 2013.
3. Jakobsson, A., M. D. Rowe, J. Smith, N. R. Butt, and K. Althoefer, "Robust detection of stochastic nuclear quadrupole resonance signals" *Signal Processing*, Vol. 56, No. 9, 4221–4229, 2008.
4. Somasundaram, S. D., A. Jakobsson, N. R. Butt, M. D. Rowe, J. A. S. Smith, and K. Althoefer, "Detecting stochastic nuclear quadrupole resonance signals in the presence of strong radio frequency interference," *Acoustics, Speech and Signal Processing*, Vol. 15, 3645–3648, 2008.
5. Somasundaram, S. D., A. Jakobsson, N. R. Butt, M. D. Rowe, J. A. S. Smith, and K. Althoefer, "Detection of stochastic nuclear quadrupole resonance signals," *Digital Signal Processing*, Vol. 15, 367–370, 2007.
6. Williams, J., *A Seven-nanosecond Comparator for Single Supply Operation — Linear Technology AN72*, May 1988.
7. Williams, J., *A High Speed Comparator Techniques — Linear Technology AN13*, April 1985.
8. Williams, J., *Nanovolt Noise Measurement for a Low Noise Voltage Reference — Linear Technology AN124*, April 2009.

Design of Dual Cross Dipole Antennas with Dual Frequencies and Dual Circularly-polarized

Yu-Feng Wang, Lei Chang, and Yu-Feng Yu
No. 36 Research Institute of CETC, China

Abstract— An integrated antennas are presented with dual frequencies and dual circularly-polarized (CP) in a common aperture. The proposed integrated antennas are consisted of dual crossed dipole antennas (CDA) with stacked structure, which used 90° self-phase shifting structures in both CDAs for CP wave achieving by adjusting the proportion of the orthogonal arm lengths for 90° phase difference forming. The upper CDA covers 4.7% relative bandwidth from 1.55 GHz to 1.625 GHz with VSWR less than 2 and axial ratio (AR) less than 3 dB of left-hand CP (LHCP) and the nether CDA covers 3.4% relative bandwidth of 2.44∼2.525 GHz for right-hand CP (RHCP).

1. INTRODUCTION

With the rapid development of satellite communication and navigation technology, CP antennas' requirement has greatly aroused, recently. CDA is a common terminal antenna for satellite communication for its well CP performance and broad beam. Usually, the CP performance of CDA is

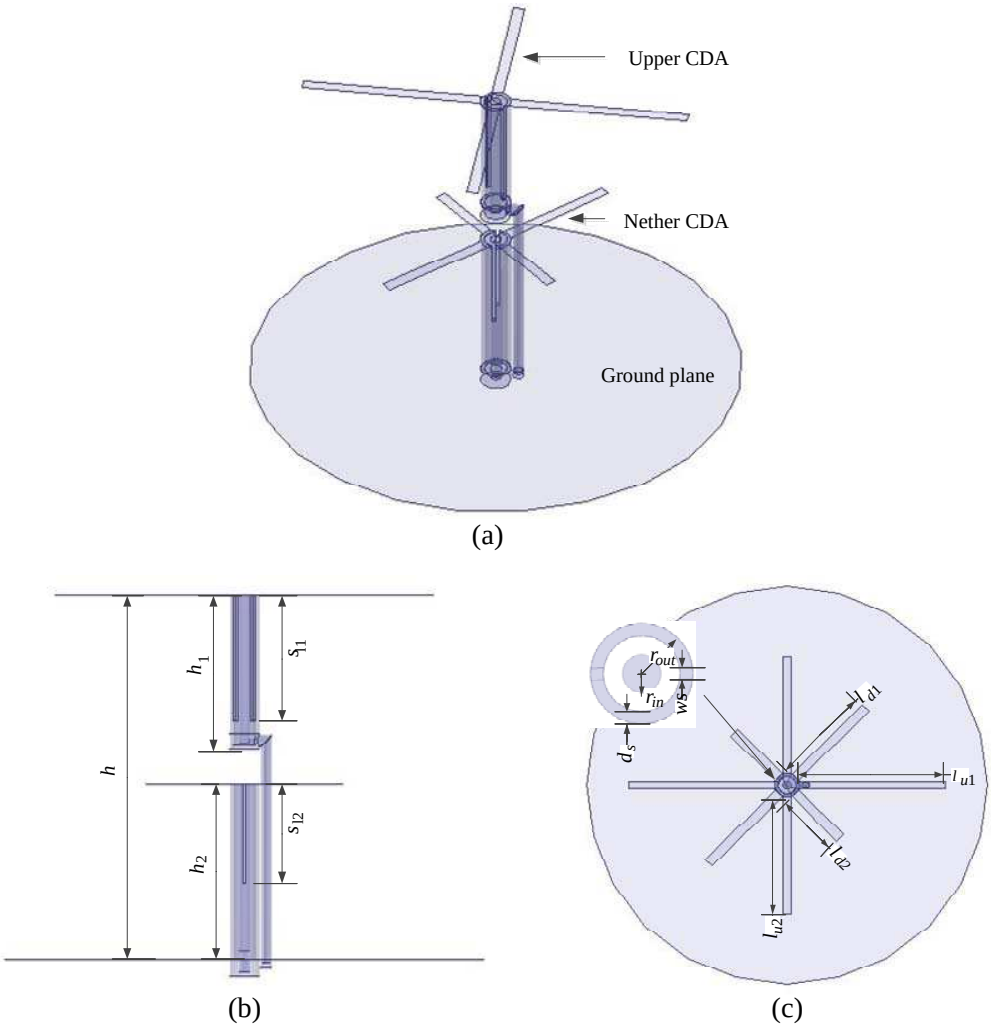

Figure 1: Antenna configuration: (a) 3-D view, (b) side view, and (c) top view.

achieved by orthogonal dipoles with feeding excitations of equal amplitudes and 90° phase difference [1]. However, the feeding excitation is obtained by phase shifting network placing at the back of antenna. CDA can also obtain CP performance using self-phase shifting structure with more simple and reliable structure [2–5]. Several researches are done for frequency band widening, beam broadening and miniature [6–8]. However, designs of CP antennas integrating for multifunction are seldom seen in the published literatures, which is the newest rising requirement for satellite communication and navigation. In Beidou satellite navigation system (BD) application, terminal antenna must radiate dual CP waves at different frequencies for receiving and transmitting. The integrated antennas with dual frequencies for BD satellite navigation's up-link and down-link of LHCP and RHCP radiation patterns.

In this paper, we integrate two CDAs with different CP characteristics in a common three-dimensional aperture. The CDA with lower frequency is at the bottom and the other is at the top. The proposed antenna operates at 1.55∼1.625 GHz with LHCP and 2.44∼2.525 GHz with RHCP.

2. ANTENNA CONFIGURATION

The configuration of the proposed dual-frequencies and dual CP antenna is shown in Figure 1(a). The antenna is comprised of two CDAs with low frequency CDA at the top and the high frequency CDA at the bottom. The upper CDA is fed by a coaxial line expanded to the ground and the nether CDA's feeding port is at the ground too. The detail parameter of the proposed antenna is shown in Figure 1(b) and Figure 1(c). The proposed antenna is designed for low AR and well VSWR at the center frequency at 1.616 GHz and 2.492 GHz, which obtained the parameters as: $h = 87$ mm, $h_1 = 39.5$ mm, $h_2 = 42$ mm, $s_{11} = 30$ mm, $s_{12} = 24$ mm, $l_{u1} = 49.6$ mm, $l_{u2} = 38.4$ mm, $l_{d1} = 28.8$ mm, $l_{d2} = 23.2$ mm, $r_{out} = 4$ mm, $r_{in} = 1.5$ mm, $w_s = 1$ mm, $d_s = 1$ mm.

3. SIMULATED RESULTS AND DISCUSSIONS

The proposed antenna is simulated and optimized using HFSS. The simulated VSWR is plotted in Figure 2 and simulated axial ratio is shown in Figure 3. It is seen that the impedance bandwidth (VSWR ≤ 2) of the antenna is much wider than the AR bandwidth (AR < 3 dB), and so the AR bandwidth is considered as the working bandwidth in this paper. Form Figure 3(a), the upper CDA covers 0.075 GHz bandwidth (from 1.55 GHz to 1.625 GHz), which is approximately 4.7% at

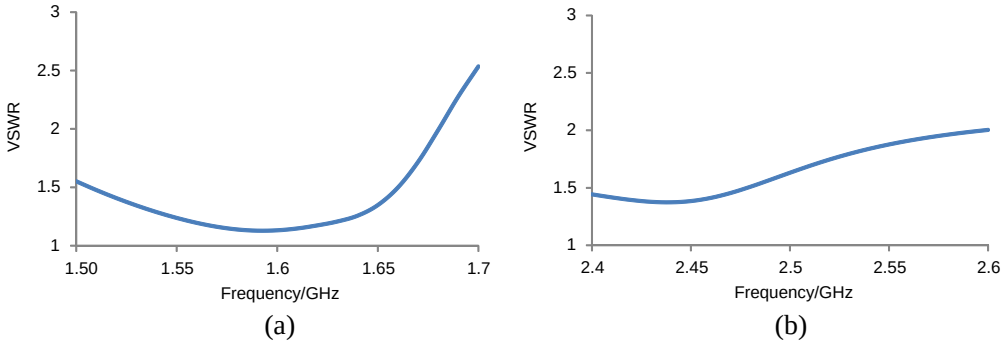

Figure 2: Simulated VSWR of the proposed antenna.

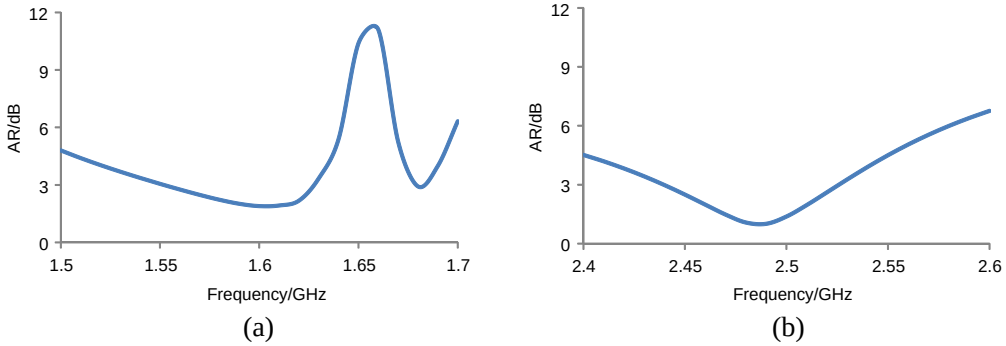

Figure 3: Simulated axial ratio of the proposed antenna.

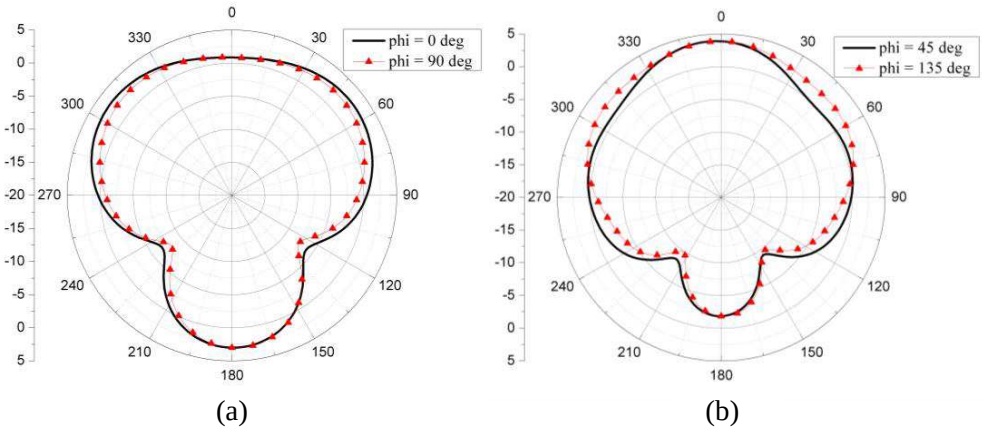

Figure 4: Simulated radiation patterns at (a) 1.616 GHz and (b) 2.492 GHz.

the center frequency 1.5875 GHz. Form Figure 3(b), the nether CDA covers 0.0857 GHz bandwidth (from 2.44 GHz to 2.525 GHz), which is approximately 3.4% at the center frequency 2.4825 GHz. The frequency bands of the presented antenna cover the BD working band of 1.616 GHz ± 0.01 GHz and 2.492 GHz ± 0.01 GHz.

Simulated radiation patterns at 1.616 GHz and 2.492 GHz in the elevation planes of phi = 0 deg and 90 deg are plotted in Figure 4. The gain of 1.616 GHz is larger than −0.5 dBi above the elevation angle of 10 deg, while the two patterns are well consistent. The gain of 2.492 GHz is larger than 0 dBi above the elevation angle of 10 deg, while the two patterns are well consistent.

4. CONCLUSION

An integrated design of two CP antennas in a common aperture has been presented. The operating band with VSWR < 2 and AR < 3 dB is obtained of 1.55–1.625 GHz for LHCP radiation and 2.44–2.525 GHz for RHCP radiation. The proposed antennas exhibit broad beam radiation patterns and appreciable gain above the azimuth angle of 10° at the operating band. These integrated dual frequencies and dual CP antennas are compact in their structures and suit for the BD terminal antennas.

REFERENCES

1. Suh, S.-Y., W. Stutzman, W. Davis, A. Waltho, and J. Schiffer, "A generalized crossed dipole antenna, the Fourtear antenna," *IEEE Antennas and Propagation Society International Symposium*, 2004.
2. Zhang, X., "Design of the imphase feed cross element circular polarized antenna," *Modern Radar*, Vol. 31, No. 2, 67–70, Feb. 2009.
3. Cao, H. L., N. X. Yi, L. S. Yang, and S. Z. Yang, "Design and realization of circular polarized crossed dipole feeds," *Journal of Chongqinguniversit (Natural Science Edition)*, Vol. 28, No. 10, 70–74, Oct. 2005.
4. Baik, J. W., K. J. Lee, W. S. Yoon, T. H. Lee, and Y. S. Kim, "Circularly polarized printed crossed dipole antennas with broadband axial ratio," *Electron. Lett.*, Vol. 44, No. 13, 2008.
5. Yoon, W. S., S. M. Han, J. W. Baik, S. Pyo, K. J. Lee, and Y. S. Kim, "Crossed dipole antenna with switchable circular polarization sense," *Electron. Lett.*, Vol. 45, No. 14, 2008.
6. Caillet, M., M. Clénet, A. Sharaiha, and Y. M. M. Antar, "A broadband folded printed quadrifilar helical antenna employing a novel compact planar feeding circuit," *IEEE Transactions on Antennas and Propagation*, Vol. 58, No. 7, 2203–2209, 2010.
7. Rabemanantsoa, J. and A. Sharaiha, "Size reduced multi-band printed quadrifilar helical antenna," *IEEE Transactions on Antennas and Propagation*, Vol. 59, No. 9, 3138–3143, 2011.
8. Letestu, Y. and A. Sharaiha, "Broadband folded printed quadrifilar helical antenna," *IEEE Transactions on Antennas and Propagation*, Vol. 54, No. 5, 1600–1604, 2006.

Design and Study of Multiband Microstrip Antenna

Lei Chang, Jian-Qiang Zhang, Yu-Feng Wang, and Yu-Feng Yu
No. 36 Research Institute of CETC, Jiaxing, China

Abstract— A multiband antenna which is fed by a SMA coaxial probe is investigated in this paper. The proposed antenna is composed of a circular patch and a loop microstrip line. By introducing a loop microstrip line and three probes feeding for the circular patch, the proposed antenna delivers the multiband impedance matching performance. The simulated result shows that the antenna has three frequency bands covering 1.254–1.404 GHz, 1.653–1.746 GHz and 2.142–10.752 GHz for VSWR < 3. Details of the antenna design and results are presented.

1. INTRODUCTION

With the rapid developments in wireless communication technology, multiband antennas are increasingly demanded in many wireless systems. Many printed multiband antennas can be achieved by microstrip line feed [1–6]. By adding extra resonant elements to the main patch, a microstrip-fed multi-band planar antenna was presented in [1]. In [2], two resonant radiating parts were used for a dual-band antenna. In [3], a dual-band slot antenna was proposed for wireless local area network (WLAN) applications. A multiband antenna consisting of a set of printed frame dipoles was proposed in [4]. A dual-band dipole antenna with an integrated balun feed was given in [5]. In [6], a dual-band planar antenna design using a dual-feed monopole slot was proposed for WLAN applications.

Multiband antennas can also be designed by using a coaxial probe feed [7, 8]. A dual-band antenna was proposed in [7], which consisted of a longer dipole for the lower band and a pair of shorter dipoles for the upper band. In [8], a dual-band patch antenna was achieved by using a double SRR on a grounded dielectric slab.

In this paper, we propose a new simple multiband antenna. The tri-band antenna consists of a circular patch and a loop microstrip line, which is fed by a SMA coaxial probe. The circular patch is fed by three probes connected to the loop microstrip line. The proposed antenna is designed

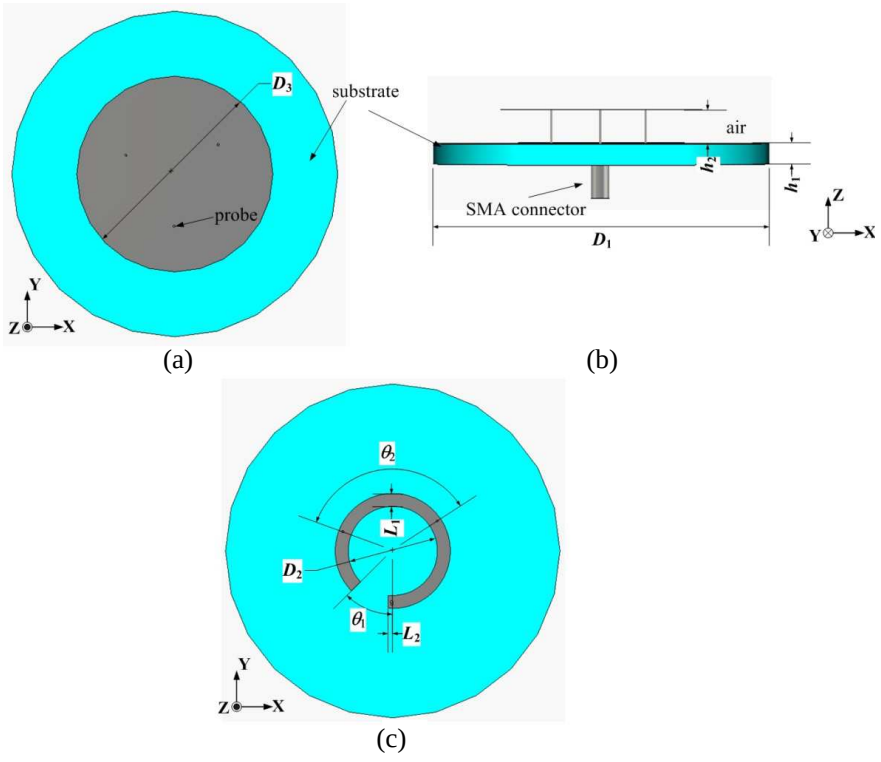

Figure 1: Geometry of the proposed antenna.

to cover three bands of 1.254–1.404 GHz, 1.653–1.746 GHz and 2.142–10.752 GHz with acceptable performance in terms of gain, and impedance matching. Radiation patterns at different frequencies, and the gain across the operating bandwidth are studied.

2. ANTENNA DESIGN

The configuration of the proposed antenna is illustrated in Figure 1. The antenna comprises three layers of conductor, which include a circular radiating patch, a loop microstrip feed line, and a circular ground plane. The loop microstrip line is fabricated on a FR4 substrate with diameter $D_1 = 150\,\text{mm}$, thickness $h_1 = 3\,\text{mm}$, relative permittivity $\varepsilon_r = 4.4$. The inner diameter and width of the loop microstrip line are $D_2 = 40\,\text{mm}$ and $L_1 = 5.8\,\text{mm}$, respectively. The loop microstrip line has a cut with $\theta_1 = 46°$, and is connected with a rectangular metal ($L_1 \times L_2 = 5.8\,\text{mm} \times 2\,\text{mm}$). The antenna is fed by SMA coaxial probe which places at a distance of 22.9 mm away from the center along y-axis, and connected to the loop microstrip line. The circular radiating patch of diameter $D_3 = 90\,\text{mm}$ is placed above the feed line at spacing of $h_2 = 5\,\text{mm}$. The circular radiating patch

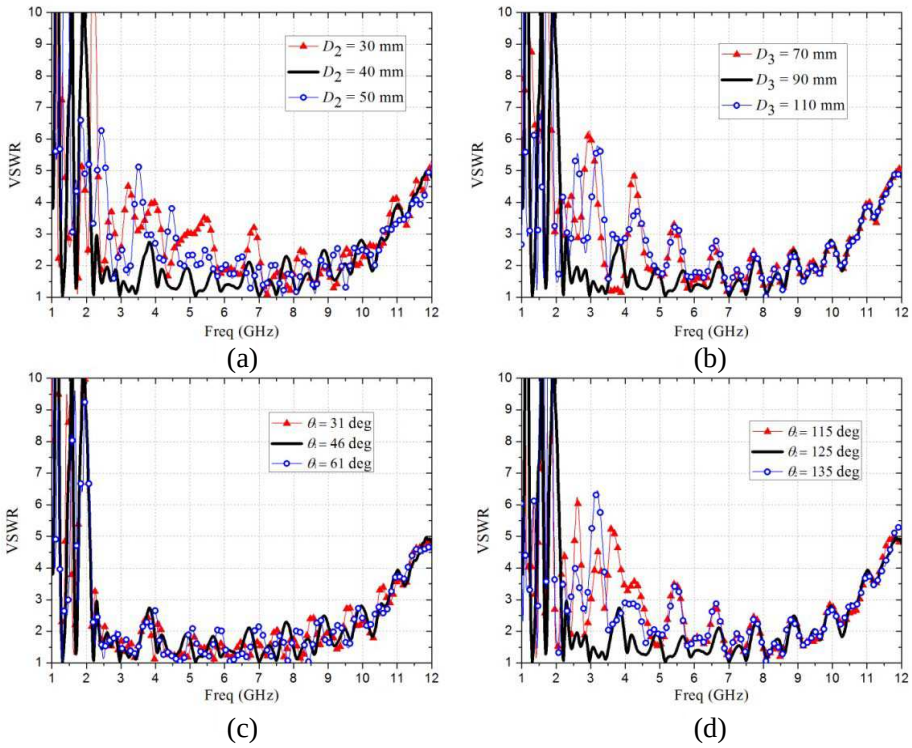

Figure 2: VSWR variation for different (a) D_2, (b) D_3, (c) θ_1, and (d) θ_2.

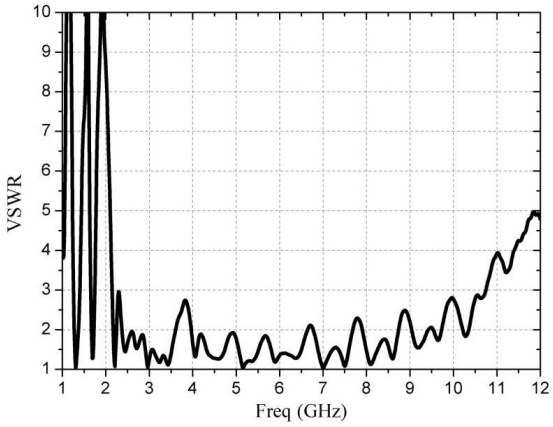

Figure 3: Simulated VSWR of the proposed antenna.

is fed by three probes. The diameter of probes is 1 mm. These three probes are placed along the microstrip feed line with 24 mm away from the center and sequentially rotated 125° (θ_2).

The performance of the proposed antenna is analyzed and optimized by full-wave electromagnetic simulation software based on FITD.

3. RESULTS AND DISCUSSIONS

A series of simulations are conducted in order to provide more detailed information about the antenna design. The diameters of the loop microstrip line and circular radiating patch have effects on impedance matching. From Figures 2(a) and (b), it is observed that the impedance bandwidth greatly depends on D_2 and D_3. Narrowing or increasing these two diameters, respectively, makes the impedance bandwidth reduce. Figure 2(c) shows the effects of the angle θ_1 on the impedance matching. It is shown that the angle θ_1 mainly affect the performance on the low frequency band.

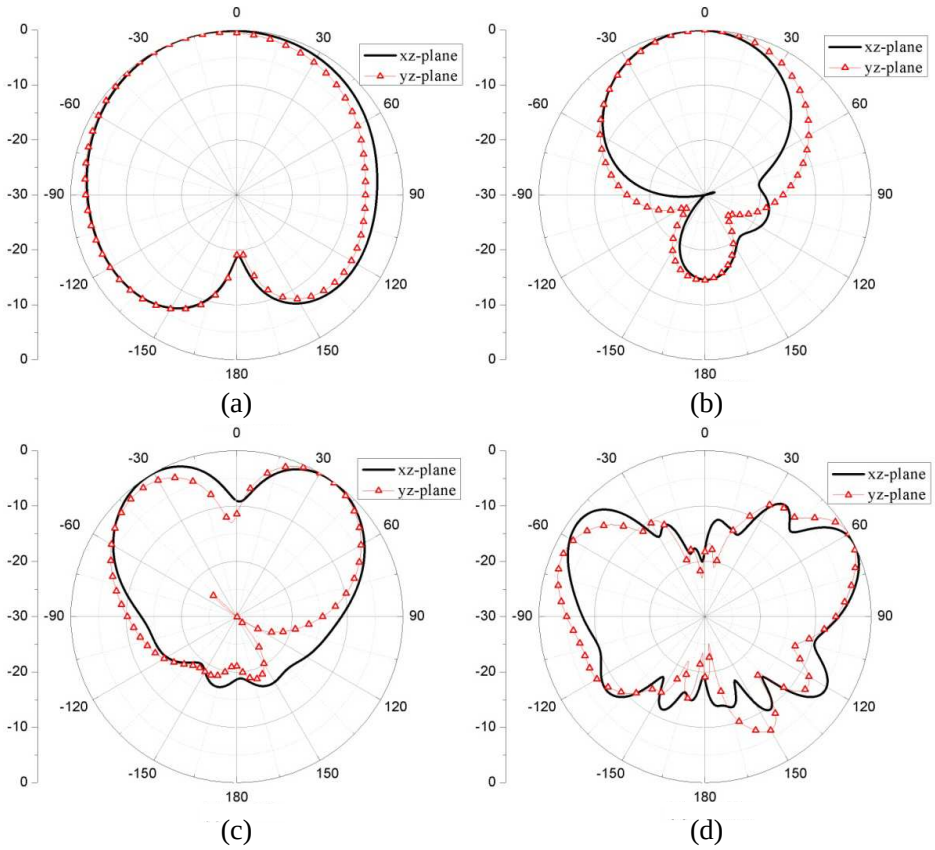

Figure 4: Radiation patterns of the proposed antenna at (a) 1.3 GHz, (b) 1.69 GHz, (c) 2.5 GHz, and (d) 8.5 GHz.

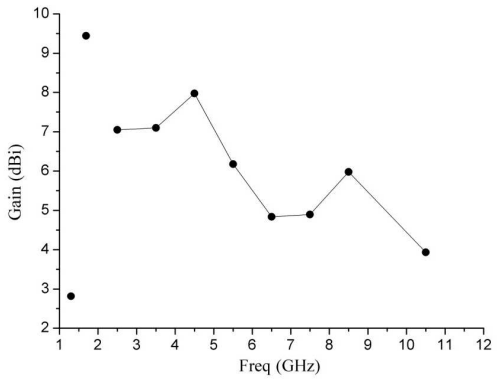

Figure 5: Gain of the proposed antenna.

The effect of the angle θ_2 is also very remarkable, shown in Figure 2(d). The impedance matching can be obtained by tuning angle θ_2. The VSWR based on the optimal parameters are given in Figure 3.

The radiation patterns of the proposed antenna in the two principle planes are shown in Figure 4. It can be seen that the proposed antenna has good directional radiation patterns at 1.3 and 1.69 GHz. However, at 2.5 and 8.5 GHz, the antenna exhibits conical beam patterns. The gains of the proposed multiband antenna are respectively about 2.8 dBi for the 1.3-GHz band, 9.4 dBi for the 1.69-GHz band and 3.9–8.0 dBi for the third band as shown in Figure 5.

4. CONCLUSION

A novel multiband antenna, fed by a SMA coaxial probe, is successfully implemented with good impedance matching characteristic. The diameter and height of the proposed antenna is 150 mm and 8 mm, respectively. The 3 : 1 VSWR bandwidths are ranging from 1.254 to 1.404 GHz, from 1.653 to 1.746 GHz, and from 2.142 to 10.752 GHz. Besides, the antenna exhibits a good and stable radiation performance across the whole band. The proposed antenna is suitable in many wireless systems.

REFERENCES

1. Foudazi, A., H. R. Hassani, and S. M. Ali Nezhad, "Small UWB planar monopole antenna with added GPS/GSM/WLAN bands," *IEEE Trans. Antennas Propag.*, Vol. 60, No. 6, 2987–2992, 2012.
2. Mandal, M. K. and Z. N. Chen, "Compact dual-band and ultrawideband loop antennas," *IEEE Trans. Antennas Propag.*, Vol. 59, No. 8, 2774–2779, 2011.
3. Hsieh, C., T. Chiu, and C. Lai, "Compact dual-band slot antenna at the corner of the ground plane," *IEEE Trans. Antennas Propag.*, Vol. 57, No. 10, 3423–3426, 2009.
4. Wu, P., Z. Kuai, and X. Zhu, "Multiband antennas comprising multiple frame-printed dipoles," *IEEE Trans. Antennas Propag.*, Vol. 57, No. 10, 3313–3316, 2009.
5. He, Q. Q., B. Z. Wang, and J. He, "Wideband and dual-band design of a printed dipole antenna," *IEEE Antennas Wireless Propag. Lett.*, Vol. 7, 1–4, 2008.
6. Hsieh, C. and T. Chiu, "Dual-band antenna design using a dual-feed monopole slot," *IET Microw. Antennas Propag.*, Vol. 5, No. 12, 1502–1507, 2011.
7. Quan, X. L., R. L. Li, Y. H. Cui, and M. M Tentzeris, "Analysis and design of a compact dual-band directional antenna," *IEEE Antennas Wireless Propag. Lett.*, Vol. 11, 547–550, 2012.
8. Quevedo-Teruel, O., M. N. M. Kehn, and E. Rajo-Iglesias, "Dual-band patch antennas based on short-circuited split ring resonators," *IEEE Trans. Antennas Propag.*, Vol. 59, No. 8, 2758–2765, 2011.

A Compact Dual Band Band-pass Filter Using a New Topology of Transmission Line Metamaterial

Akram Boubakri[1], **Fethi Choubani**[1], **Tan Hoa Vuong**[2], **and Jacques David**[2]

[1]Innov'Com Laboratory, Sup'Com, Ariana, Tunisia
[2]Plasma and Energy Conversion Lab, INPT, France

Abstract— In this paper, we introduce a dual-band band pass filter based on a transmission line metamaterial. The unit cell of this metamaterial was loaded with shunt inductor and series capacitor. Once simulated with HFSS, our band pass filter revealed two operational frequencies 5.8 GHz and 8.7 GHz, making it a good candidate for many microwave applications and especially for RADAR.

1. INTRODUCTION

Band pass filters are employed in wireless systems to remove signals from an undesired frequency or channel and we often find it before and after the mixer in many cases as revealed in Figure 1.

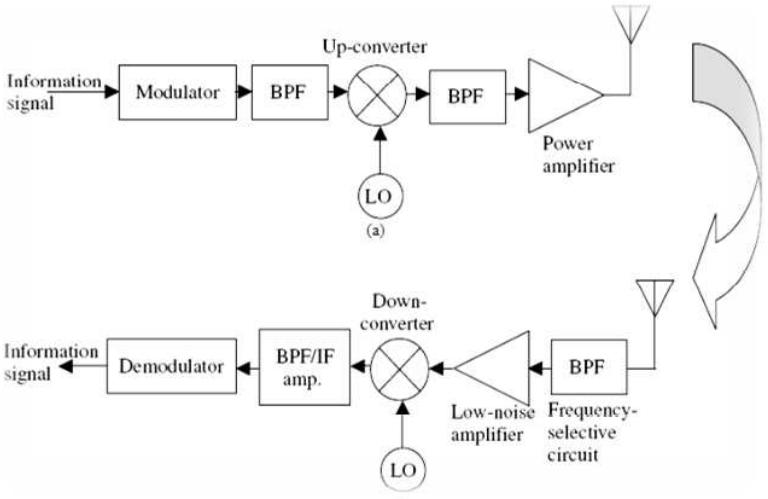

Figure 1: Transmitter/receiver block diagram for microwave communications.

With the rapid development of microwave and millimeter wave communication systems the demand on high performance band-pass filters with compact dimensions, low insertion loss and low cost was greatly stimulated. However, most of conventional band-pass filters are unsuitable for miniaturized realization demand of modern communication and electronic systems. In this study, we developed a novel compact dual band band-pass filter using a new type of transmission line metamaterial as depicted in Figure 2. The aim of using such type of metamaterial is the low cost and the easy achievement using the coupling method to synthesize such a filter.

Multiple studies showed that Metamaterial based on SRR, exhibit LH property only around the resonance frequency and this is called the resonant approach which permits only a narrow band and presents losses due to the requirement of operation near SRR resonance [1–3]. To overcome those drawbacks, we used Transmission Line metamaterial made by loading the conventional transmission line with discrete lumped inductors and capacitors with high quality factors to enable a good control and mitigate losses [5].

2. METAMATERIAL TRANSMISSION LINE UNIT CELL DESIGN

2.1. Unit Cell Design

The loading may be achieved using either discrete lumped elements or printed lumped elements as in the shunt NRI-TL structure. Discrete lumped elements have the advantage of permitting small structures at low frequencies and are easier to model.

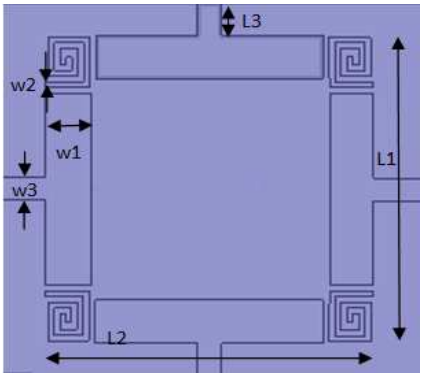

Figure 2: Unit cell of the MTM TL. $L_1 = L_2 = 5.5\,\text{mm}$, $W_1 = 0.788\,\text{mm}$, $W_2 = 0.1\,\text{mm}$, $W_3 = 0.4\,\text{mm}$, $L_3 = 0.5\,\text{mm}$.

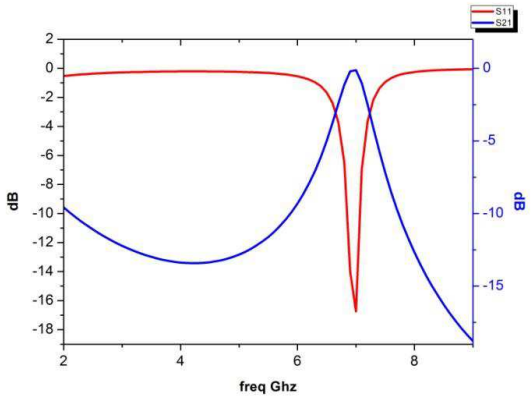

Figure 3: Scattering parameters of the simulated of the array of 3 unit cells.

On the other hand, printed lumped elements allow scalability and can lower the cost of fabrication significantly. In our case, we considered a design employing printed lumped capacitors and inductors rather than discrete elements. For the shunt inductive loading, we employed a strip of width w_3 connecting the coplanar-strip TLs, and, for the series capacitive loading, we propose the use of spiral strip capacitors with finger width w_2 with a distance between turns of about 0.2 mm. The resulting of the complete, printed planar unit cell is shown in Figure 2.

The loaded TL is printed over a Roger O3003 substrate with $\varepsilon = 3$ and at a height of about 1.5 mm. In addition the overall size of the super lens unit cell is a sub-wavelength size $\lambda/3$ which fulfills the condition of loss reducing mentioned before.

In an effort to find out the contribution of each load in the creation of NRI TL, and with analogy to the behavior of SRR and wire studied by Smith [4, 6], we will try to focus on the behavior of series capacitor and shunt inductor in response to electromagnetic excitation. When the TL is loaded with shunt inductors only or when rings are connected via the inductor strip to each other, the propagation is forbidden at low frequencies and this is explained by the fact that the inductive loading creates a continuous path at low frequency which cause the behavior of ground plane. We also noted that the permittivity of the medium is negative, below the effective plasma frequency ω_{ep}. When the host TL is loaded with series capacitors, the dispersion characteristic is similar to that obtained for an array of SRR. Thus we have a forbidden frequency band between resonance frequency ω_0 and magnetic plasma frequency ω_{mp} where the permeability is negative.

Once the host medium is loaded with series capacitors and shunt inductors, a region of left hand propagation is created inside the forbidden frequency band created by the series capacitor load and mentioned above [7].

2.2. Simulation Result

In order to study the behavior of the structure when responding to an electromagnetic excitation, an array of three unit cells with a period $p = 6.5\,\text{mm}$, was simulated with HFSS.

To do that, our structure is excited with an electric field polarized perpendicular to the ring and by a magnetic field lying in the ring plane which would excite the gap between rings and also the ring capacitors [10]. The return loss as depicted in Figure 3 is about $-17\,\text{dB}$ at 7 GHz as well as and the transmission coefficient S_{21} is about 0 dB which means that the incident wave is fully transmitted.

3. DUAL PASS BAND FILTER

Our purpose was to design a band-pass filter and after that we will manage to modify the filter structure so that we got a dual pass band filter. Our structure was printed over a Roger O3003 substrate with $\varepsilon = 3$ and at a height of about 1.5 mm.

The filter was simulated with HFSS and excited using two coupled microstrip lines associated to a taper line which permits to achieve good matching input impedance for the desired band. To modify the bandwidth of the filter we have to adjust the lengths of the H structure. After the

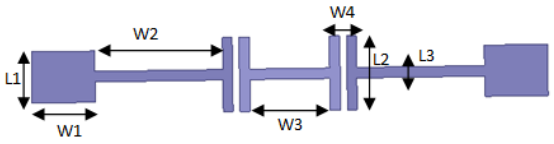

W1	W2	W3	W4	L1	L2	L3
4.7	9.5	5.92	0.5	3.8	5.5	0.788

Figure 4: The bandpass filter structure (dimensions are in mm).

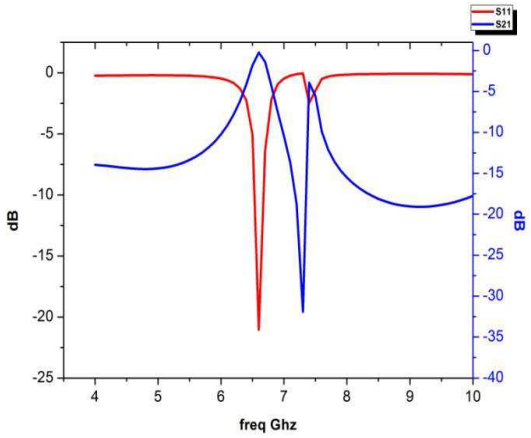

Figure 5: S parameters of the H filter structure.

optimization of this structure we have obtained a band-pass filter centered at 6.8 GHz with an S_{11} of about -21 dB.

After the validation and the simulation of the H filter, we conducted a study to improve the response of the structure and realize a dual band band-pass filter using a new topology of transmission line metamaterial as described in the first section.

As depicted in the above structure, the load is ensured by an array of three unit cell with an overall length of $w = 17.5$ mm. The filter has dimensions of $48.35 \times 24\,\text{mm}^2$.

It's important to note that we have kept the same dimensions of the microstrip lines and the feeder to maintain the impedance mach. The filter was excited by an electromagnetic wave where E is perpendicular to the structure and according to z direction while H is according to x direction. The simulation was made using HFSS and it showed a dual-band band pass filter and the first frequency was 5.8 GHz and the second frequency was 8.7 GHz with a return loss of about -22 dB for the first and -27 dB for the second. Those results are showed in the Figure 7 below.

The Figure 8 presents the current distribution for the two filtered band frequency the first around 5.8 GHz and the second around 8.7 GHz. The exchange of energy between resonators can be concluded from the coupling coefficient, nevertheless the use of sub-wavelength resonators provide a significant reduction in the planar area of microwave filter [8, 9].

The dual band operation is an important issue in band-pass filter design and it answers the demand in conception of band-pass filter in many in many RADAR applications ensuring miniaturization, low cost and fulfill the ISM band (Industrial , Scientific and Medical) thanks to the

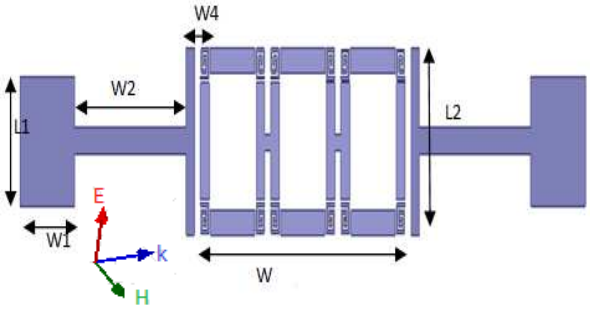

W1	W2	W	W4	L1	L2
4.7 mm	9.5 mm	17.5 mm	0.5 mm	3.8 mm	5.5 mm

Figure 6: The novel band pass filter topology.

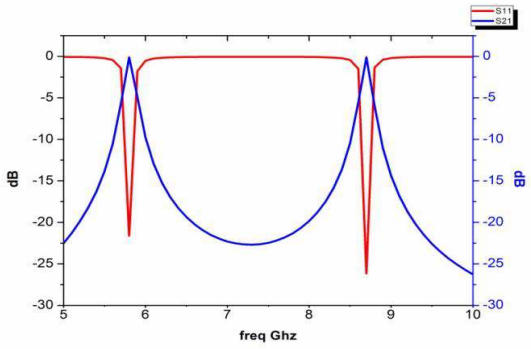

Figure 7: The simulation results of the band pass filter.

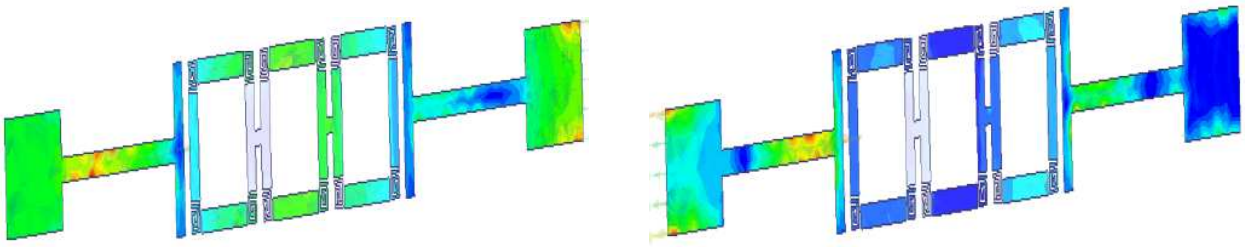

(a) (b)

Figure 8: The current distribution at (a) 5.8 GHz and (b) 8.7 GHz.

planar micro strip technology. Meanwhile we should mention that a dual band band-pass filter with highly selective response in conjunction with lower insertion loss and wide stop band still a challenge in microwave applications. Practically, we can use our filter in Weather RADAR applications operating at 5.8 GHz and in the same time for RADAR applications operating in X band.

4. CONCLUSION

In this study we are proposing a dual pass band filter using a new type of metamaterial transmission line. The structure was compact and low cost thanks to MTM TL and it can be used in many applications related to RADAR.

REFERENCES

1. Veselago, V. G., "The electrodynamics of substances with simultaneously negative value of ε and μ," *Soviet Physics Uspekhi*, Vol. 10, No. 4, Jan. 1968.
2. Pendry, J. B., A. J. Holden, D. J. Robbins, and W. J. Stewart, "Low frequency plasmons in thin-wire structures," *J. Phys. Cond. Matter.*, Vol. 10, 4785–4809, 1998.
3. Pendry, J. B., et al., "Magnetism from conductors and enhanced nonlinear phenomena," *IEEE Transactions on Microwave Theory and Techniques*, Vol. 47, No. 11, Nov. 1999.
4. Shelby, R. A., D. R. Smith, and S. Schultz, "Experimental verification of negative index of refraction," *Science*, Vol. 292, 77–79, May 2001.
5. Eleftheriades, G. V. and R. Islam, "Miniaturized microwave components and antennas using negative-refractive-index transmission-line (NRI-TL) metamaterials," *Metamaterials*, Vol. 1, 53–61, 2007.
6. Smith, D. R., et al., "Composite medium with simultaneously negative permeability and permittivity," *Physical Review Letters*, Vol. 18, 4184–4187, May 2000.
7. Iyer, A. K. and G. V. Eleftheriades, "Volumetric layered transmission-line metamaterial exhibiting a negative refractive index," *J. Opt. Soc.*, Vol. 23, No. 3, Mar. 2006.
8. Baral, R. N. and P. K. Singhal, "Miniaturized microstrip bandpass filter using coupled metamaterial resonators," *International Journal of Microwave and Optical Technology*, Vol. 4, No. 2, Mar. 2009.
9. Benmostefa, N., et al., "Metamaterial tunable filter design," *Journal of Electromagnetic Analysis and Applications*, No. 5, 250–254, 2013.

A Novel Wideband Wide-angle Frequency Selective Surface Composite Structure

Zhan-Bo Lu, Xue-Quan Yan, and Jian-Jian She
AVIC Leihua Electronic Technology Research Institute, WuXi, China

Abstract— A novel wideband FSS composite structure is proposed, Which use modified C-type sandwich cascaded structure and Hexagonal loop element with the characteristics of center symmetry in FSS design resulting in good electrical performance such as high transmission efficiency and stable working frequency band at a wide range of incident angle. The FSS sample is fabricated using low temperature pressing processes and then measured in anechoic chamber, The measured results show relative bandwidth of the FSS composite structure reaches to 45% (Transmission efficiency > 85%) for arbitrary incident angle from 0° to 60° and both polarization. With the increase of the incident angle, the center resonant frequency tends to shift to higher frequency, the maximum offset of which is below 0.5 GHz. Inner envelope relative bandwidth is close to 41% (transmission efficiency > 85%) at a range of 0° ∼ 68° incident angle of vertical polarization wave and 0° ∼ 60° incident angle of horizontal polarization wave.

1. INTRODUCTION

Frequency selective surface (FSS) act as space filters to propagating electromagnetic waves. One of the most important applications of FSS is to design the conformal radome with band-pass characteristics [1]. Airborne active phased array radar has become main developing direction of airborne radar in the future for more agile scan and farther detecting-distance. For meeting the stealth demands of active phased array radar with broad bandwidth and wide scan angle, the FSS composite structure mounted on the front of radar antenna also must have characteristics of wideband and wide scan angle correspondingly. The larger bandwidth and better frequency stability with respect to wide incident angle of the FSS composite structure are to a great degree depended on stratified medium structure, FSS element types, and the whole hybrid structure, and so on [2]. A lot of simulations and experiments have shown that wideband FSS structure must be hybrid structure which consists of multilayer medium, multilayer periodic FSS screens, and multilayer foam, as is similar to the design of ultra wide circuit filters.

A Novel Wideband FSS Composite structure which is modified C-type sandwich hybrid structure is provided, which has some advantages of broad bandwidth, unfluctuating passband and excellently stable resonant frequency at a wide range of 0° ∼ 68° incident angle. As known from the results of experiments about electrical performance of the fabricated FSS sample, it can reduce antenna's RCS greatly on the condition of ensuring the normal work of antenna.

2. DESIGN OF THE FSS COMPOSITE STRUCTURE

The relative bandwidth of the formerly designed C-type sandwich FSS structure (seen in Figure 1) from the reference [3] is around 20% at arbitrary incident angle from 0° to 45°, and that Inner envelope relative bandwidth is about 16% at a range of 0° ∼ 45° incident angle. This FSS structure may be available in the undemanding circumstance of bandwidth or scan angle. With higher and higher demand of antenna's bandwidth and scan angle, the loaded FSS composite structure also must have the characteristics of wideband and large scan angle. Therefor, a modified C-type sandwich structure is designed as seen in Figure 2. As seen from comparison between the two FSS structures, the modified C-type structure is constructed by mounting lower dielectric constant foam on the both sides and swap outer-layer FSS screen and thin dielectric slab of C-type sandwich. In accordance with FSS design theory [2], the passband resonant frequency of the modified C-type structure mainly depend on the electric and physical parameters of the inner two-layer foam (foam $3b$ and $3c$ in Figure 2). In addition, the accessional foam not only improve the stability of resonant frequency with respect to incident angle and polarization [4], not only strengthen the suppressing effect of stopband and mechanical intensity. Swap of the position of outer-layer FSS screen and thin dielectric slab improve inter-layer matching performance resulting in much more wider bandwidth to a certain extent.

Many simulation results have proven that the larger gaps between the elements will leads to the emergence of resonant peak at higher frequency, which greatly influence the suppressing characteristics in stopband. Therefor, It still use hexagonal loop element which is easy to realize more

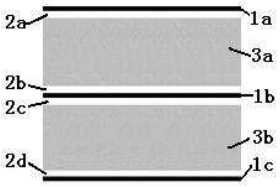

Figure 1: C-type sandwich structure.

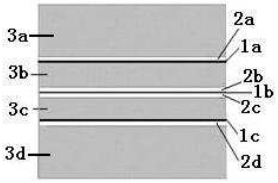

Figure 2: Modified C-type sandwich structure.

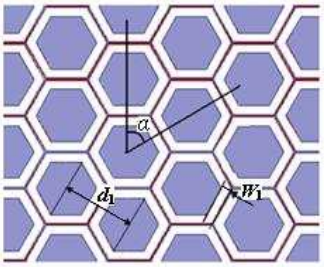

Figure 3: Regular hexagonal loop structure.

compact triangular arrangement resulting in stable and good electrical performance (such as wider bandwidth), with respect to incident angle and polarization.

In Figure 2, 1a, 1b, 1c are FSS screens. 2a and 2d are identical thin dielectric slab, the thickness $h1$ and the dielectric constant ε_{r1} of which are 0.127 mm and 2.2 respectively; 2b and 2c are identical thin dielectric slab, the thickness $h2$ and the dielectric constant ε_{r2} of which are 0.127 mm and 2.5 respectively; foam 3a and 3d are identical materials, the thickness $h3$ and the dielectric constant ε_{r3} of which are 8 mm and 1.05 respectively; foam 3b and 3c are identical materials, the thickness $h4$ and the dielectric constant ε_{r4} of which are 4 mm and 1.25 respectively. All FSS screens are made up of regular hexagonal loop Array as shown in Figure 3. but the designing parameters of FSS screen 1a and 1c are quite identical. For the symmetry of the structure, electrical performance of the designed FSS structure is quite identical regardless of propagating electromagnetic waves from any side of the structure.

As for FSS screen 1a and 1c, the incline angle $\alpha = 60°$, the distance between the center of two adjacent FSS element $d_1 = 8.9$ mm. The width of slot w_1 is close to 1 mm. Design parameters of FSS screen 1b are basically identical to FSS screen 1a and 1c.

3. SIMULATED RESULTS

Based on the aboved design parameters, The transmission efficiency curves of FSS composite structure versus frequency for various angle of incidence and both polarization (vertical and horizontal) wave are shown in Figure 4.

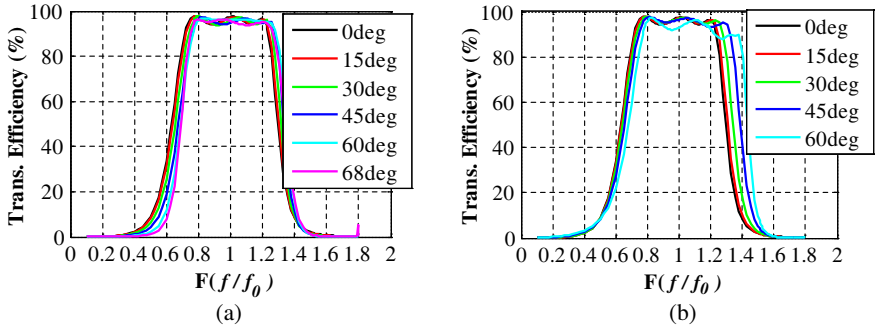

Figure 4: The simulated transmission curves versus frequency for various angle of incidence and both polarization, (a) vertical polarization wave, (b) horizontal polarization wave.

It was seen in Figure 4 that the passband relative bandwidth of the FSS structure exceeds 46% (transmission efficiency $> 93\%$, or transmission coefficient > -0.32 dB) for $0° \sim 68°$ incident angle of vertical polarization wave and $0° \sim 60°$ incident angle of horizontal polarization wave.

Because of passband center frequency's shift with various angle of incidence Inner envelope relative bandwidth reduce to 41% (transmission efficiency $> 93\%$, or transmission coefficient $> -0.32\,\mathrm{dB}$) with $0^\circ \sim 68^\circ$ incident angle of vertical polarization wave and $0^\circ \sim 60^\circ$ incident angle of horizontal polarization wave. In addition, the average transmission efficiency in stopband for vertical polarized wave is less than 10.8% ($-9.67\,\mathrm{dB}$, $0.1f_0 \sim 0.6f_0$) and 7.6% ($-11.9\,\mathrm{dB}$, $1.4f_0 \sim 1.8f_0$); the average transmission efficiency in stopband for horizontal polarized wave is less than 12.4% ($-9\,\mathrm{dB}$, $0.1f_0 \sim 0.6f_0$) and 8.3% ($-8.1\,\mathrm{dB}$, $1.4f_0 \sim 1.8f_0$). Due to the big fall of the transmission efficiency in band at large incident angle of 68° of horizontal polarization wave, its results are not given.

4. MEASURED RESULTS

To demonstrate the accuracy of simulation results, experiment sample is fabricated by photo-etch and low temperature bonding process between various medium layer and FSS screens (shown in Figure 5). The impact of fabricating tolerance on the transmission performance of sample is firstly analyzed to ensure good agreement between measured and simulation results. The results of analysis has shown that when fabricating tolerance of thin dielectric slab and foam are less than 0.005 mm and 0.1 mm respectively, the better approximate results can be obtained. The measured results about transmission curves for various incident angle and both polarization are shown in Figure 6.

It is shown from the measured curves of Figure 6 that inner envelope passband bandwidth with $0^\circ \sim 68^\circ$ angle of incidence for vertical polarized wave is around 40% ($0.8f_0 \sim 1.2f_0$, transmission efficiency $> 90\%$); The inner envelope passband bandwidth with $0^\circ \sim 60^\circ$ angle of incidence for horizontal polarized wave is also around 40% ($0.8f_0 \sim 1.2f_0$, transmission efficiency $> 90\%$). In addition, the average transmission efficiency in stopband for vertical polarized wave is less than 4.17% ($-13.8\,\mathrm{dB}$, $0.1f_0 \sim 0.6f_0$) and 3.86% ($-14.1\,\mathrm{dB}$, $1.4f_0 \sim 1.8f_0$); the average transmission efficiency in stopband for horizontal polarized wave is less than 5.58% ($-12.36\,\mathrm{dB}$, $0.1f_0 \sim 0.6f_0$) and 4.3% ($-13.66\,\mathrm{dB}$, $1.4f_0 \sim 1.8f_0$).

As can be known from comparison of above simulation and measured curves, the measured bandwidth is less than the simulation bandwidth, transmission efficiency in band reduce. The reason is that The simulated FSS composite structure is seen as infinite periodic structure in an ideal environment, however, The fabricated FSS sample is finite size (when the size is greater than 10 wavelengths, It's electric performance close to infinite structure), and the measured results is easy to suffer interference brought by environmental factors. However, stopband suppression performance become better because of the fall of transmission efficiency in the whole frequency band and other factors such as environment, finite size of the FSS structure etc..

In order to validate the effect of the FSS sample on radiation and scattering performance of

Figure 5: FSS composite structure sample.

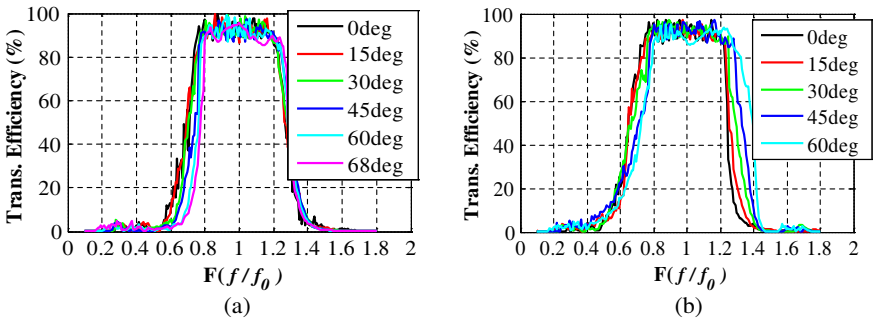

Figure 6: The measured transmission curves versus frequency for various angle of incidence and both polarization, (a) vertical polarization wave, (b) horizontal polarization wave.

antenna, the radiation and scattering experiment on antenna loaded with FSS sample or without is made. The measured results to a certain extent demonstrate the good ability of the newly designed FSS sample on reducing antenna's RCS. For some reasons, the measured results are not provided.

5. CONCLUSION

The FSS composite structure designed in the paper has the advantage of wideband, good transmission efficiency in band, low frequency shift with various angle of incidence and polarization etc.. Many experiments have proven that after it is mounted on the front of the phased array antenna or other types of antenna, the RCS of the corresponding antenna is reduced greatly on the condition of ensuring radiation performance of antenna. The developed FSS sample must will provide technological help for the development of various types of stealth fighter in future.

REFERENCES

1. Wahid, M. and S. B. Morris, "Bandpass radome for reduced RCS," *IEE Colloquium on Antenna Radar Crosssection*, 1991.
2. Munk, B. A., *Frequency Selective Surface: Theory and Design*, Wiley Interscience, New York, 2000.
3. Lu, Z., R. Shen, and X. Yan, "A novel wideband frequency selective surface composite structure," *China-Japan Joint Microwave Conference Proceesings*, 513–515, 2011.
4. Kraus, J. D. and R. J. Marhefka, *Antennas: For All Applications*, 3rd Edition, McGraw-Hill, New York, 2002.

Highly Birefringent Photonic Crystal Fibers with a High-index Doped Rod

Wei-Hsiang Chuang[1], **Che-Wei Yao**[1], **and Jui-Ming Hsu**[1, 2]

[1]Department of Electro-Optical Engineering, National United University, Miaoli 360, Taiwan, R.O.C.
[2]Optoelectronics Research Center, National United University, Miaoli 360, Taiwan, R.O.C.

Abstract— This article designs and theoretically investigates a highly birefringent photonic crystal fiber (HB-PCF) for reducing the effect of polarization-mode dispersion (PMD) in high-speed optical communication system. To achieve a high modal birefringence in the proposed HB-PCF, we designed four types of HB-PCF by adding some birefringence-enhancing factors step by step in sequence. Ultimately, from the simulation results, the numeric value of modal birefringence of the proposed HB-PCF is up to 25.008×10^{-3} at the habitual wavelength $\lambda = 1.55\,\mu$m of optical-fiber communications.

1. INTRODUCTION

Some imperfections of a single mode fiber (SMF) are produced due to variations in geometric shape or impurity-introducing in practical fiber-fabrication processes, and anisotropic stress acting on the fiber due to the fiber-installation in an optical communication system. These imperfections result in an uncontrolled and unpredictable modal birefringence in the SMF and bring about polarization-mode dispersion (PMD). The PMD induces pulse broadening and seriously restricts the data rates in a high-speed optical communication links. The polarization-maintaining fibers (PMF) were used to significantly reduce the governing factor of small random birefringence fluctuations. Conventional PMFs (such as elliptical core fibers, bowtie structured fibers, and PANDA fibers) have a modal birefringence with a value of about 10^{-4} order typically. Recently many articles used photonic crystal fibers (PCF) to realize a highly birefringent photonic crystal fiber (HB-PCF) [1–8]. Modal birefringence of about 10^{-3} order was achieved typically for these HB-PCFs at a wavelength of 1550 nm.

To enlarge the modal birefringence, one can destroy the six-fold symmetry of the fiber to the best of one's ability and strongly split the degenerated doublet pair. The modal birefringence B of a fiber is defined as the difference in effective index of the split modes

$$B = \left| n_{eff}^{x} - n_{eff}^{y} \right|, \tag{1}$$

where n_{eff}^{x} and n_{eff}^{y} are the effective indices of the x- and y-polarization mode, respectively. In this paper, by overlapping some birefringence-enhancing factors step by step, and then the difference between the effective indices of the degenerated fundamental mode is enlarged. According to Eq. (1), a HB-PCF with ultra high birefringence is designed. Ultimately, the numeric results reveal that the value of modal birefringence of the proposed HB-PCF is up to 25.008×10^{-3} at a wavelength of 1.55 μm.

2. SIMULATION MODEL AND PRINCIPLES

The cross-sectional view of a regular index-guiding PCF is shown in Fig. 1(a). The cladding of the PCF consists of a triangular lattice of air-holes, referred to as cladding holes in this paper, each one with a diameter of $D_c = 0.5\,\mu$m and a pitch (center-to-center distance between the holes) Λ of 0.8 μm in a background of undoped silica (refractive index of about $n = 1.444$ at a wavelength of 1.55 μm). The solid core is formed by removing the central air hole.

To destroy the six-fold symmetry of the fiber and split the degenerated doublet pair for enlarging the modal birefringence, the first birefringence-enhancing factor is introduced — two air holes at the innermost layer of the PCF were replaced with larger holes with a diameter of $D_1 = 0.74\,\mu$m. This type of structure is named as Type 1 in this article and indicated in Fig. 1(b). In addition to the two larger holes, the second birefringence-enhancing factor in Type 2 is a removal of two holes in appropriate orientation at the innermost layer of the PCF, which is shown in Fig. 1(c). To enhance the birefringence more, one can confine the splitting degeneration modes in a smaller core region. Therefore, as shown in Fig. 1(d), the third birefringence-enhancing factor is added, Type 3

was designed by inserting a circular Ge-doped rod with a cladding diameter of $D_c = 0.5\,\mu m$ while a higher refractive index of $n_{core} = 1.7$ at a wavelength of 1.55 μm in the center of the core. Ultimately, the fourth birefringence-enhancing factor is that the circular Ge-doped rod was replaced with elliptic one with the same refractive index to even more enlarge the modal birefringence. The lengths of major axis and minor axis of the central elliptic rode are $D_y = 0.755\,\mu m$ and $D_x = 0.54\,\mu m$, respectively. The final structure is named as Type 4 and exhibited in Fig. 1(e).

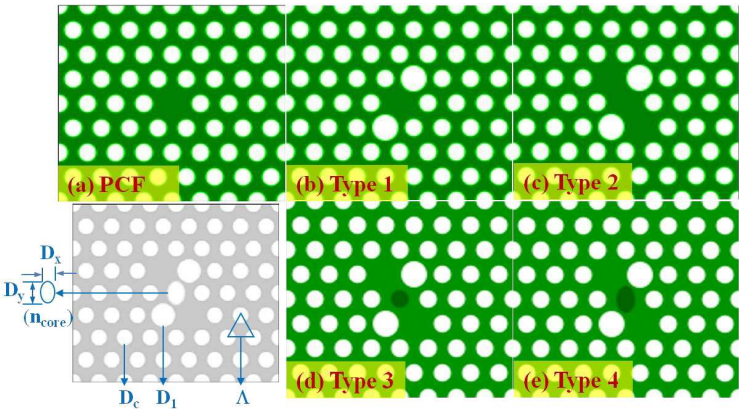

Figure 1: Cross-sectional view of (a) a regular PCF and the HB-PCFs, (b) Type 1, (c) Type 2, (d) Type 3, and (e) Type 4.

3. NUMERICAL RESULTS AND DISCUSSIONS

The refractive indices of the split modes n_{eff}^x and n_{eff}^y were estimated by means of the plane-wave expansion (PWE) method, and then the modal birefringence was deduced by using Eq. (1). Fig. 2 compares the modal birefringence of these four types of HB-PCF. As shown in Fig. 2, the birefringence values increase in sequence for adding the birefringence-enhancing factors as mentioned previously. However, the maximum values of birefringence for the majority of HB-PCF types occurred at a wavelength that is far from the habitual wavelength of optical-fiber communications (1.55 μm). To shift the maximum birefringence wavelength toward a shorter wavelength while still keeping its birefringence at an original maximum value, one can shrink the whole structure with a scale-down factor [7]. On the other hand, one can expend the whole structure to shift the maximum birefringence wavelength toward a longer wavelength. In this work, the birefringence curves (B-curves) of some types of HB-PCF need to red-tune (to be tuned toward a longer wavelength) and the B-curves of some types need to blue-tune toward a shorter wavelength. To shift the maximum birefringence wavelength of all the HB-PCF types toward a wavelength of 1.55 μm, we defined a scale-adjust factor of m. For $m < 1$, the structure is modified by shrinking the whole structure, and the B-curve is blue-tuned. For $m > 1$, on the contrary, the structure is modified by expanding the whole structure, and the B-curve is red-tuned.

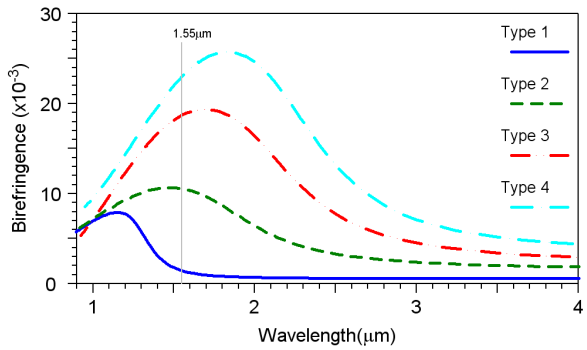

Figure 2: Dependence of birefringence on wavelength for the HB-PCF Type 1 to 4.

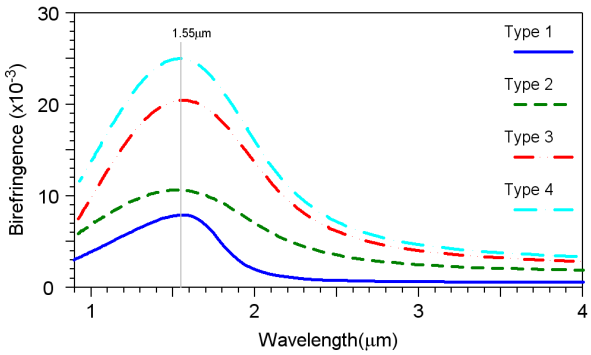

Figure 3: Dependence of birefringence on wavelength for the modified HB-PCF types.

For different types of HB-PCF, according to Fig. 2, the B-curves of Type 1 and 2 need to red-tune and those of Type 3 and 4 need to blue-tune. Particular values of m were designed to be 1.35,

1.03, 0.9 and 0.85 for Type 1 to 4, respectively. Fig. 3 indicates the dependence of birefringence on wavelength for the four types of modified HB-PCF. For the habitual wavelength $\lambda = 1.55\,\mu m$ of optical-fiber communications, for ultimate result, the numeric values of modal birefringence are 7.926×10^{-3}, 10.625×10^{-3}, 20.473×10^{-3}, and 25.008×10^{-3} with respect to Type 1 to Type 4. Table 1 exhibits the designed geometric and optical parameters of the modified HB-PCF Type 1 to 4.

Table 1: Geometric and optical parameters of the modified HB-PCF types.

HB-PCF types	scale-adjust factor m	Λ (μm)	D_1 (μm)	D_c (μm)	D_x (μm)	D_y (μm)	n_{core}
Type 1	1.35	1.08	0.999	0.675	–	–	–
Type 2	1.03	0.824	0.762	0.515	–	–	–
Type 3	0.9	0.72	0.666	0.45	0.45	0.45	1.7
Type 4	0.85	0.68	0.629	0.425	0.459	0.642	1.7

4. CONCLUSIONS

This study systematically designs and theoretically investigates a highly birefringent photonic crystal fiber (HB-PCF) by adding some birefringence-enhancing factors step by step in sequence. The modal birefringence is increased even more whenever a birefringence-enhancing factor is introduced. By adding all the four birefringence-enhancing factors, the modal birefringence of the HB-PCF Type 4 is up to 25.008×10^{-3} at a wavelength of about 1.57 μm. To shift the maximum birefringence wavelength toward the habitual wavelength of optical-fiber communications (1.55 μm), we introduced a scale-adjust factor m. Finally, the proposed HB-PCF with a high-index Ge-doped elliptic rod in the central core was designed. The numeric value of modal birefringence of the proposed HB-PCF is up to 25.008×10^{-3} at the habitual wavelength $\lambda = 1.55\,\mu m$ of optical-fiber communications.

REFERENCES

1. Ortigosa-Blanch, A., J. C. Knight, W. J. Wadsworth, J. Arriaga, B. J. Mangan, T. A. Birks, and P. S. J. P. St. J. Russell, "Highly birefringent photonic crystal fibers," *Opt. Lett.*, Vol. 25, 1325–1327, 2000.
2. Suzuki, K., H. Kubota, S. Kawanishi, M. Tanaka, and M. Fujita, "Optical properties of a low-loss polarization-maintaining photonic crystal fiber," *Opt. Express*, Vol. 9, 676–680, 2001.
3. Hansen, T. P., J. Broeng, S. E. B. Libori, E. Knudsen, A. Bjarklev, J. R. Jensen, and H. R. Simonsen, "Highly birefringent index-guiding photonic crystal fibers," *IEEE Photon. Technol. Lett.*, Vol. 13, 588–590, 2001.
4. Sun, Y. S., Y. F. Chau, H. H. Yeh, L. F. Shen, T. J. Yang, and D. P. Tsai, "High birefringence photonic crystal fiber with a complex unit cell of asymmetric elliptical air hole cladding," *Appl. Opt.*, Vol. 46, 5276–5281, 2007.
5. Nasilowski, T., T. Martynkien, G. Statkiewicz, et al., "Temperature and pressure sensitivities of the highly birefringent photonic crystal fiber with core asymmetry," *Appl. Phys. B*, Vol. 81, 325–331, 2005.
6. Chen, M., S. G. Yang, F. F. Yin, H. W. Chen, and S. Z. Xie, "PMD compensation using birefringence photonic crystal fiber in 40Gbit/s optical communication system," *Optoelectron. Lett.*, Vol. 4, 19–22, 2008.
7. Hsu, J. M., G. S. Ye, and D. L. Ye, "Birefringence and loss consideration for a highly birefringent photonic crystal fiber," *Fiber Integrated Opt.*, Vol. 31, 11–22, 2012.
8. Hsu, J. M., C. L. Lee, J. S. Horng, and J. J. H. Kung, "Polarization-maintaining photonic crystal fiber with rim-touched defect-holes," *Opt. Comm.*, Vol. 298–299, 125–128, 2013.

Nonlinear Optical Loop Mirror-based Linear Cavity Tunable Multi-wavelength Fiber Laser

B. Huang, H. Y. Meng, R. Xiong, Q. Q. Yao, H. H. Wang, Q. H. Wang, C. H. Tan, and X. G. Huang
Laboratory of Nanophotonic Functional Materials and Devices
South China Normal University, Guangzhou, Guangdong 510006, China

Abstract— We propose and experimentally demonstrate a nonlinear optical loop mirror (NOLM)-based linear cavity tunable multi-wavelength fiber laser. The NOLM, providing intensity-dependent transmissivity, can effectively alleviate the mode competition so that the multi-wavelength lasing can be achieved at room temperature. By adjusting the polarization controllers (PCs), the proposed laser can generate multi-wavelength output. Moreover, the number of the lasing wavelength can be adjusted flexibly from 11 to 13 with a wavelength spacing of 0.4 nm.

1. INTRODUCTION

Multi-wavelength fiber lasers have been drawn great interest for their potential applications in wavelength division multiplexing (WDM) transmission systems, optical sensors and optical signal processing and so on. With the characteristics of low threshold broad gain bandwidth and high power conversion efficiency, the multi-wavelength erbium-doped fiber (EDF) lasers have been extensively investigated. However, the fierce mode competition prevents multi-wavelength EDF lasers from attaining stable multi-wavelength lasing at room temperature. The straight method is to cool the EDF in liquid nitrogen to overcome the homogeneous gain broadening effect [1]. Evidently, this technique is impossible for the generally practical applications. Therefore, others methods have been proposed to alleviate the mode competition for instance, adding a frequency shifter [2], inserting a semiconductor optical amplifier [3], using nonlinear gain of cascaded stimulated Brillouin scattering or stimulated Raman scattering [4], providing four-wave-mixing [5] and utilizing nonlinear polarization rotation [6, 7]. But all the above techniques inevitably add the excess complexity and the cost to the multiwavelength lasers. In contrast, the NOLM has the advantages of simple constitution and costless components [8, 9].

In this letter, we propose and experimentally demonstrate a NOLM-based linear cavity tunable multi-wavelength laser. In the proposed laser, the NOLM is used to mitigate the mode competition in the EDF. A polarization maintaining fiber (PMF)-based Sagnac interferometer acts as the comb filter. By adjusting the PCs in loops, the number of the lasing wavelength can be adjusted flexibly from 11 to 13 with a wavelength spacing of 0.4 nm in the wavelength region of 1530 nm at room temperature.

2. EXPERIMENTAL SETUP AND PRINCIPLE

As shown in Figure 1, the proposed laser consists of a pump optical source, a WDM coupler, a segment of EDF, a NOLM and a fiber Sagnac interferometer. The linear lasing cavity is formed by the NOLM and the Sagnac interferometer. The EDF is 10 m which plays a role of the gain medium. The Sagnac interferometer, which includes a 3 dB optical coupler, a polarization controller (PC1) and a segment of PMF, severs as the output port as well. The length and the refractive index difference of the PMF used in the experiment are 10 m and 6.54×10^{-4}, respectively. The comb filter is achieved and the wavelength interval is 0.4 nm. The NOLM, which consists of a 3 dB optical coupler, a polarization controller (PC2) and a 2.1-km long conventional SMF, acts as an amplitude equalizer. It is worth to note that an optimum length of the SMF in the NOLM should be selected to attain the multi-wavelength lasing. In the experiment, 1 km, 2.1 km, 5 km and 10 km SMF have been used in the NOLM, respectively. As a result, the best performance can be gained when the length of the SMF is 2.1 km. The PCs in the loops were used for polarization biasing. The output spectrum characteristics of the laser are monitored by an optical spectrum analyzer (OSA) with a resolution of 0.02 nm.

The principle of the NOLM is analyzed as follows. When the light propagates in the NOLM, the different nonlinear phase shifts will be formed due to the Kerr effect of the SMF. Moreover, the rotation of the polarization state will be accumulated in the SMF and is dependent on the light intensity. The NOLM can work as an amplitude equalizer to mitigate the mode competition

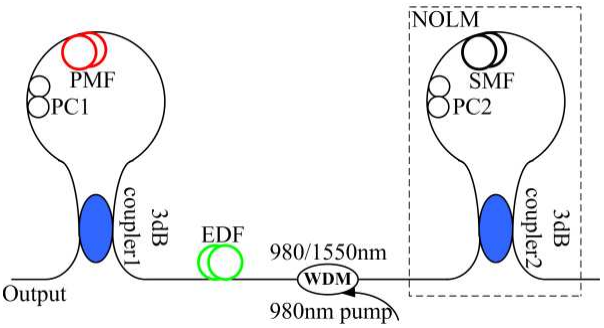

Figure 1: Experimental schematic of the proposed laser.

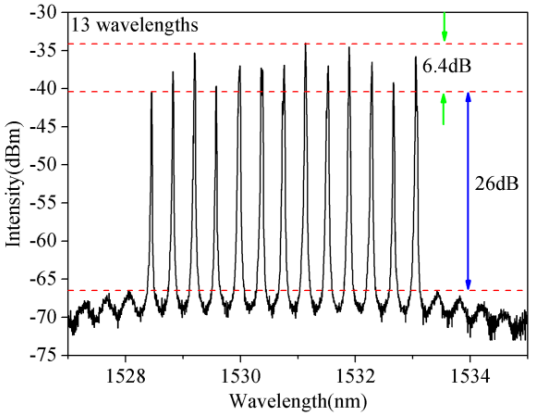

Figure 2: 13-line lasing operation.

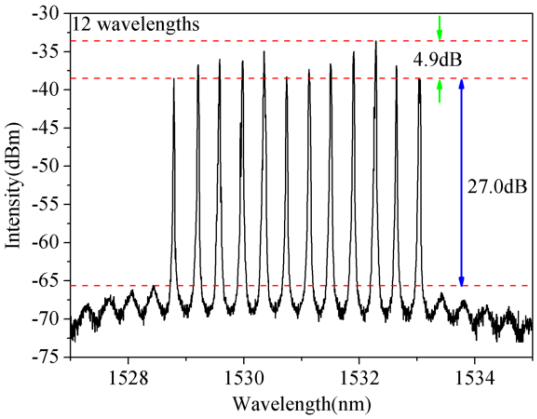

Figure 3: 12-line lasing operation.

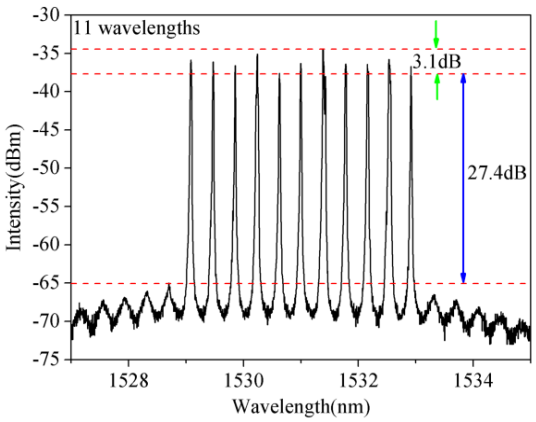

Figure 4: 11-line lasing operation.

when the PC2 is adjusted to the state where the transmissivity decreases with the signal power increasing. Consequently, the multi-wavelength oscillations can be attained when the IDL induced by the NOLM matches with the mode competition in the cavity.

3. RESULTS AND DISCUSSION

In our experiment, a 980 nm laser diodes (LD) and a 980/1550 nm WDM coupler are used. At first, the output power of the LD was increased to 200 mW and fixed. Then the PC1 was rotated to the position where the fiber Sagnac interferometer can get a comb output and fixed. By changing the PC2, the multi-wavelength oscillation can be attained around 1530 nm, as shown in Figure 2. As a result, a 13-line lasing is achieved with the bandwidth of 6.4 dB. The wavelength spacing and the side mode suppression ratios (SMSR) are 0.4 nm and 26 dB, respectively. By appropriately adjusting the PC2, the number of the lasing wavelength decreased, as shown in Figure 3. During the bandwidth of 4.9 dB, the 12-line lasing is gained and the SMSR is 27 dB. With further carefully adjusting the PC2, the evenness of multi-wavelength lasing could be improved, as shown in Figure 4. An 11-line lasing is achieved during the bandwidth of 3.1 dB and the SMSR increases to 27.4 dB. The experimental results indicate that the fluctuation of the lasing wavelength power decreases and the SMSR increases as the number of the lasing line decreasing. As far as we know, this is the first time to report the NOLM-based linear cavity tunable multi-wavelength EDF laser. Compared with our previous work [6], the proposed laser has more lasing wavelengths with 0.4 nm channel spacing and less cost, in which the expensive polarization-dependent isolator and optical circulator is not used.

To verify the stability of the proposed laser, we repeated scanning of the power fluctuation and the wavelength drift of the three channels in the 12-line laser state with 3 minutes interval within 30 minutes, as shown in Figure 5. The results show that the maximum power fluctuation is smaller than 2.2 dB, and the wavelength shift is less than 0.08 nm. In our opinions, the power fluctuation

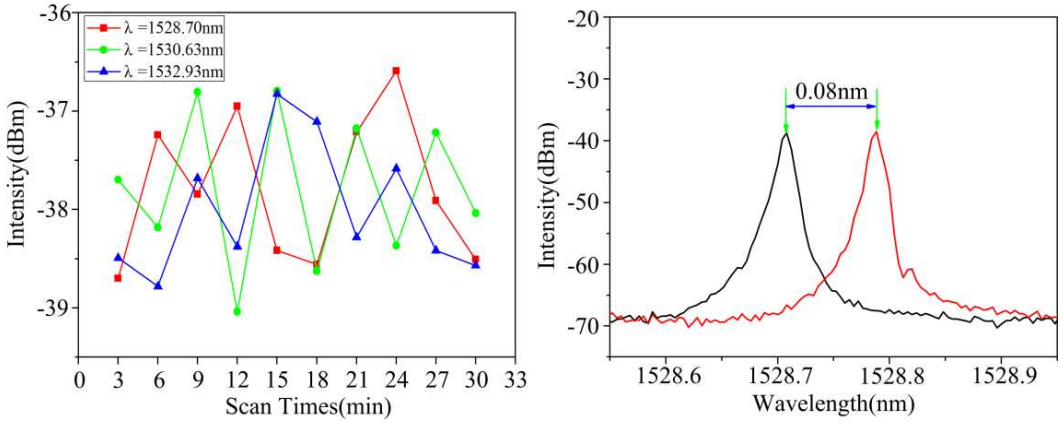

Figure 5: Power variation of three individual channels and the wavelength drift over 30 min.

is mainly caused by the stability of pump optical source's polarization state, the vibration of the experimental platform and the performance of the passive devices. Those factors can affect the polarization states of the fiber laser so that the power of lasing wavelengths and the stability of the proposed laser are fluctuating. By equipping the high performance devices and the package, the stability of the proposed laser can be highly improved.

4. CONCLUSION

In conclusion, we propose and experimentally demonstrate a NOLM-based linear cavity tunable multi-wavelength laser. By rotating the PCs, the multi-wavelength operation can be attained and the number of lasing wavelengths can be changed flexibly form 11 to 13. As a result, 11-line lasing operation within 3.1 dB bandwidth and with a SMSR of 27.4 dB was achieved experimentally. What's more, the experiment results indicate that the proposed laser can stably operate at room temperature.

REFERENCES

1. Park, N. and P. F. Wysocki, "24-line multiwavelength operation of erbium-doped fiber-ring laser," *IEEE Photon. Technol. Lett.*, Vol. 8, 1459–1461, 1996.
2. Zhou, K. J., D. Y. Zhou, F. Z. Dong, and N. Q. Ngo, "Room-temperature multiwavelength erbium-doped fiber ring laser employing sinusoidal phase-modulation feedback," *Opt. Lett.*, Vol. 28, 893–895, 2003.
3. Chen, D., H. Ou, H. Fu, S. Qin, and S. Gao, "Wavelength-spacing tunable multi-wavelength erbium-doped fiber laser incorporating a semiconductor optical amplifier," *Laser Phys. Lett.*, Vol. 4, 287–290, 2007.
4. Zhan, L., J. H. Ji, J. Xia, S. Y. Luo, and Y. X. Xia, "160-line multiwavelength generation of linear-cavity self-seeded Brillouin-erbium fiber laser," *Opt. Exp.*, Vol. 14, 10233–10238, 2006.
5. Harun, S. W., S. D. Emami, F. A. Rahman, S. Z. Muhd-Yassin, M. K. Abd-Rahman, and H. Ahmad, "Multiwavelength Brillouin/erbium-ytterbium fiber laser," *Laser Phys. Lett.*, Vol. 4, 601–603, 2007.
6. Wang, W., H. Y. Meng, X. W. Wu, W. Wang, R. Xiong, H. C. Xue, C. H. Tan, and X. G. Huang, "A nonlinear polarization rotation-based linear cavity waveband switchable multi-wavelength fiber laser," *Laser Phys. Lett.*, Vol. 10, 015104, 2013.
7. Wang, W., H. Y. Meng, X. W. Wu, W. Wang, H. C. Xue, C. H. Tan, and X. G. Huang, "Three channel-spacing switchable multiwavelength fiber laser with two segments of polarization-maintaining fiber," *IEEE Photon. Technol. Lett.*, Vol. 24, 470–472, 2012.
8. Feng, X. H., P. K. A. Wai, C. Lu, H. Y. Tam, J. Li, and B. O. Guan, "Investigation of a multiwavelength erbium-doped fiber laser employing a nonlinear high-birefringence fiber loop mirror," *Opt. Eng.*, Vol. 49, 074202, 2010.
9. Feng, X. H., C. Lu, H. Y. Tam, P. K. A. Wai, D. Y. Tang, and B. O. Guan, "Mechanism for stable, ultra-flat multiwavelength operation in erbium-doped fiber lasers employing intensity-dependent loss," *Opt. Laser Technol.*, Vol. 44, 74–77, 2012.

10. Dong, X. P., S. P. Li, K. S. Chiang, M. N. Ng, and B. C. B. Chu, "Multiwavelength erbium-doped fibre laser based on a high-birefringence fibre loop mirror," *Electron. Lett.*, Vol. 36, 1609–1610, 2000.

A New Uniplanar Compact Photonic-bandgap (UC-PBG) Structure in Transmission Line

Wuqiong Luo and Bo Chen
University of Electronic Science and Technology of China, Chengdu, China

Abstract— Recently, the photonic band-gap (PBG) structure has received much interest in microwave and millimeter-wave domain. Applications of PBG in transmission line, microwave components and antennas have been studied and discussed. Especially the compact PBG structure consisting of small metal pads has been demonstrated to improve the performance of microwave circuits and antenna performance.

In this paper, a new uniplanar compact photonic-bandgap (UC-PBG) structure was presented. The proposed PBG structure unit has a two dimensional structure of a rectangle box with two branches intersecting at center. Then this identical unit was connected as a periodical structure. The periodical structure acting as the ground plane of the microstrip transmission line was studied. The transmission line model with the proposed UC-PBG structure ground (TL-UC-PBG) was then studied. An equivalent circuit model of this TL-UC-PBG was suggested to analyze the characteristics of the transmission line with PBG ground. From our study, it was found that this structure has a nice character of low-pass filter. At high-frequency, it showed a broad stop-band.The proposed TL-UC-PBG structure could be used in compact microwave circuit.

1. INTRODUCTION

Recently, there has been great interest in the application of the structure of the photonic bandgap (PBG) which was developed from optical regime, especially in the microwave devices [1–3]. Such as the application of microstrip antennas, resonant cavities, filters and so on.

Typical PBG structure has periodical elements etched in the conducting plane in a PCB board as the ground plane of microstrip devices. The PCB structure and the microstrip structure constitute the left-handed structure (LH). The LH material was first studied by Vselago in 1960s [1]. A planar slab of material with a negative refractive index (NRI) focusing rays of light emanating from the source to the other side of the slab. After that, the effect of the slab on the image quality has been studied. Eleftheriades el al. [4] proposed the equivalent circuit model of the LH transmission line with the concept of L-C components. The distributed circuit model of the LH transmission line unit was constructed of a series connected capacitor and shunt connected inductor exhibiting a negative refractive index.

In [5], the LH structure was implemented in a two dimensional periodic elements with split ring resonators and long wire strips to model the behaviors of magnetic and electric dipoles respectively. Extended studied was then carried out on various similar structures with the effective electromagnetic parameters were retrieved experimentally and numerically combining the LH structure with the transmission line. Besides, three dimensional LH structure was introduced in [6] with conducting vias connecting ground and metal pads.

In this paper, a new uniplanar compact photonic bandgap (PBG) structure was designed and studied. The construction of the paper was as following. The structure of the proposed UC-PBG structure would be introduced in the first part with the equivalent circuit model presented to analyze the structure. In the second part, the characteristics of the transmission line with the PBG structure would be shown; the effect of the parameters on the TL-UC-PBG model would be discussed. In the third part, the conclusion and future work would be presented.

2. DESIGN AND DISCUSSION

The structure of the proposed PBG structure was shown in Fig. 1. The units were etched on the surface of a PCB periodically in two-dimension. Each of the unit was constructed four parts. The patch at the center was surrounded with a rectangular ring which could also a circular ring. Small parasitic patches were around the patch and the ring. Each of the unit was connected to the neighboring units by four arms which intersect at the center. The patch and the ring introduced the series inductance in the structure, the parasitic patches together with the ring made the series capacitance and the gap between the elements introduced the shunt capacitance.

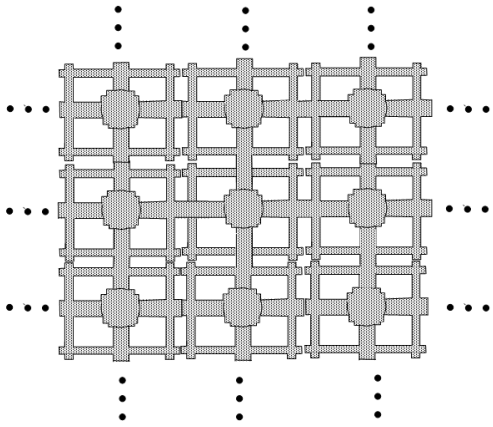

Figure 1: Schematic of the proposed PBG structure.

To find the properties of the PBG structure acting as the ground plane of the transmission line, the model shown in Fig. 2 was studied. The proposed PBG structure was etched on one side of the PCB board with the microstrip line on the other side which constructed the LH transmission line model. When this LH transmission line worked at the stop-band, the qusi-TEM transmission mode would be stopped, so that a deep stop band would be appeared as shown in Fig. 3. In this figure, the curve of the S_{21} was given. At the frequency near to 3 GHz, a stop-band was showed. It was also shown in Fig. 4. The phase also made it obvious that the Braag frequency of our structure is near 3 GHz. Fig. 5 showed the comparison of the group delay between the LH transmission line and the traditional transmission line having conducting ground plane. From this figure, it was showed

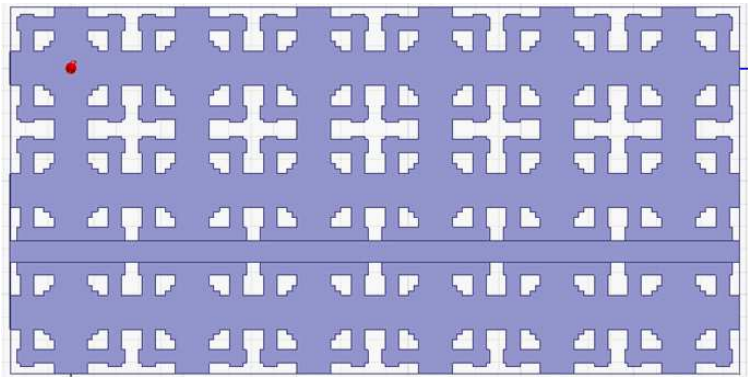

Figure 2: Transmission Line with PBG structure as the ground plane.

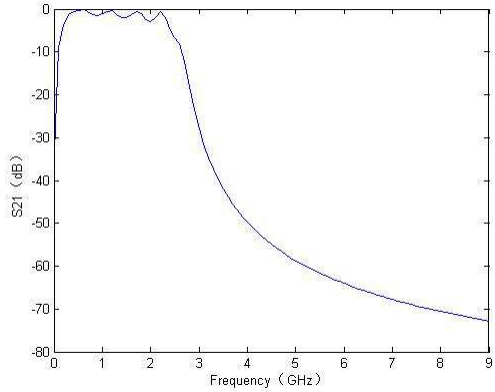

Figure 3: S_{21} of the transmission line with PBG structure as the ground plane.

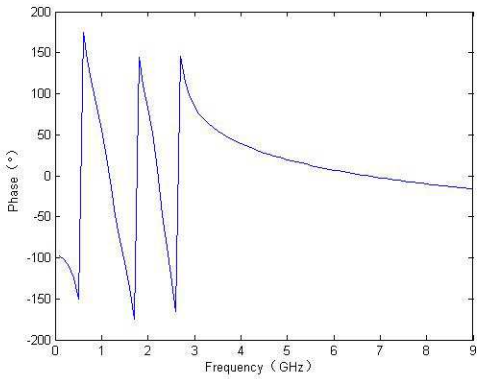

Figure 4: Phase delay of the transmission line with PBG structure as the ground plane.

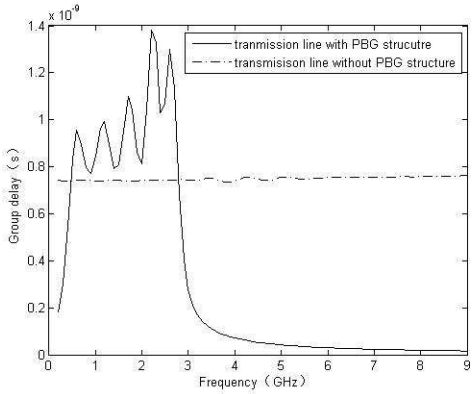

Figure 5: Comparison of the group delay between the transmission line with PBG structure and without PBG structure.

that a slowing factor of 1.5 achieved.

3. CONCLUSION

In this paper, a new uniplanar band-gap structure was proposed. Its application in LH transmission line was studied and discussed. The comparison between the proposed transmission line structure and the traditional RH transmission line was shown. The result showed the proposed structure had the characteristics of slow wave.

REFERENCES

1. Vesslago, V. G., "The electrodynamics of substances with simultaneously negative values of ε and μ," *Soviet Physics Uspekhi*, Vol. 10, No. 4, 509–514, Jan.–Feb. 1968.
2. Qian, Y., V. Radisic, and T. Itoh, "Simulation and experiment of photonic bandgap structures for micorstrip circuits," *IEEE APMC. Symp. Dig.*, 585–588, Hongkong, Dec. 2–5, 1997.
3. Joannopoulos, J. D., R. D. Meade, and J. N. Winn, *Photonic Crystals*, Princeton University Press, Princeton, NY, 1995.
4. Iyer, A. K. and G. V. Eleftheriades, "Negative-refractive-index metamaterials supporting 2-D waves," *IEEE Int. Microwave Symp. Dig.*, 1067–1070, Seattle, WA, Jun. 2–7, 2002.
5. Hirota, T., A. Minakawa, and M. Muraguchi, "Reduced-size branch-line and rat-tace hybrids for uniplanar MMIC's," *IEEE Trans. Microwave Theory Tech.*, Vol. 38, No. 33, 270–275, Mar. 1990.
6. Qian, Y., D. Sievenpiper, V. Radisic, E. Yablonovitch, and T. Itoh, "A novel approach for gain and bandwidth enhancement of patch antenna," *IEEE RAWCON Symp. Dig.*, 221–224, Colorado, Springs, CO, Aug. 9–12, 1998.

Planar Monopole Antenna for WBAN

Ebrahim Sailan Aabidi, **M. R. Kamarudin**, **T. A. Rahman**, **and Mohsen Khalily**
Wireless Communication Centre (WCC), Faculty of Electrical Engineering
Universiti Teknologi Malaysia, UTM Skudai, Johor 81310, Malaysia

Abstract— This paper presents circular-shape monopole antenna for wireless body area network (WBAN) applications at 3.1 to 5.1 GHz and 6.5 to 8 GHz. The design and simulation of proposed antenna for WBAN applications in the free space and close proximity of body surface has been done by using CST Microwave Studio. The proposed antenna was designed on FR4 substrate with dielectric constant (ε_r) of 4.4 and thickness of 1.6 mm. The final optimized design is $50 \times 40\,\text{mm}^2$. The simulated current distribution on the radiating patch for the proposed circular-shaped monopole antenna frequencies of 3.3 and 7.5 GHz in the free space is presented. The size of circular-shape monopole antenna it is suitable for WBAN application.

1. INTRODUCTION

The UWB technology has loaded much attention and experienced considerable growth a few years ago due to its distinctive characteristics. One of the most promising areas of UWB applications is WBAN, where the wireless connectivity between body centric units is provided through the deployment of light weight and compact UWB antennas [1–3]. The Federal Communications Commission (FCC) about one decade ago prescribed the frequency range for UWB to be 3.1–10.6 GHz [4]. The FCC also described in its initial report and order, huge absolute bandwidth to be structures that is more than 500 MHz in bandwidth.

This paper presents Circular-shaped monopole antenna for WBAN application for the lower frequency band from 3.1 to 5.1 GHz and the higher frequency band from 6.5 GHz to 8 GHz of the UWB band. The simulation results of the Circular-shaped monopole antenna in free space and close proximity to body tissues has been presented. The organized of this paper as follows. In Section 2, the antenna geometry and design are described. The results and discussion the antenna performance are explained in Section 3. Finally, some conclusions are given in Section 4.

2. ANTENNA DESIGN

In this paper, Circular-shape monopole antenna operating from 3.1 GHz to 5.1 GHz and 6.5 GHz to 8 GHz frequency band has been presented. The antenna is printed on the FR4 substrate with dielectric constant of 4.4, loss tangent of 0.02 a thickness of 1.6 mm. The optimized dimension of the propose antenna is $50 \times 40 \times 1.6\,\text{mm}^3$. The geometry and dimension of proposed Circular -shaped monopole antenna is shown in Figure 1.

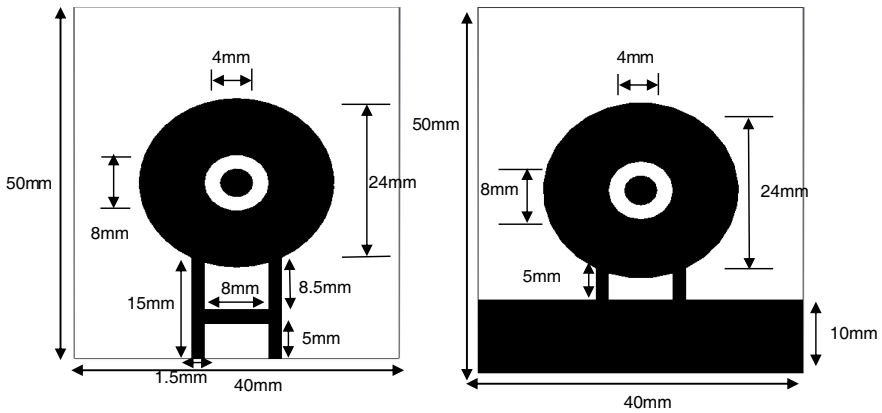

(a) Front view (b) Back view

Figure 1: The geometry of the proposed circular-shaped monopole antenna.

2.1. Surface Current Distribution

Current surface distribution determines how the current flow on the patch of antenna. Hence, the most significantly part of the patch can determine the current flow of the proposed antenna. The simulated current distribution on the radiating patch for the presented Circular-shaped monopole Antenna frequencies of 3.3 and 7.5 GHz in the free space is presented in Figure 2. It can be observed on Figure 2(a) that the current concentrated on the edges of the exterior and interior of the circular-shaped on the radiating patch and circular-shaped element is connected to the ground plane on the back view at 3.3 GHz. The vertical current is most concentrated near the patch edges and Circular-shaped element rather than distributed on the antenna surface at 7.5 GHz and this cause the decrement of the intensity of vertical electrical current on antenna surface. The horizontal current mode occurs on the ground plane on the back view as indicated in the Figure 2.

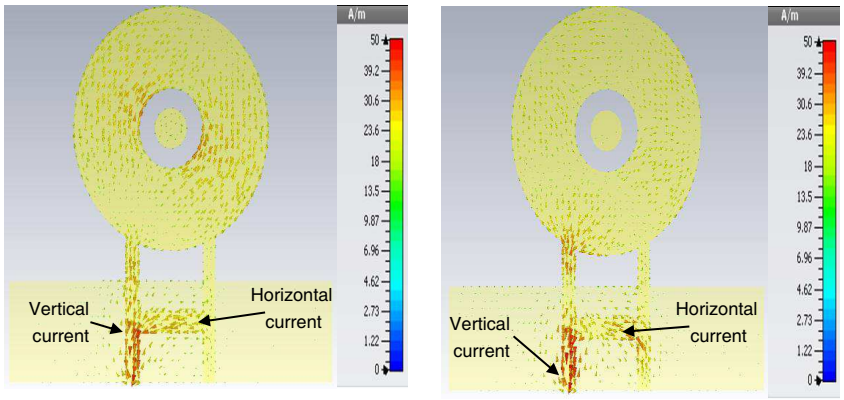

(a) Current distribution at 3.3 GHz (b) Current distribution at 7.5 GHz

Figure 2: Surface current distributions of the proposed antenna.

3. RESULTS AND DISCUSSION

The parametric studies were carried out to investigate different antenna parameters in order to achieve the optimized design. The effect of the slot on the patch has been investigated. The

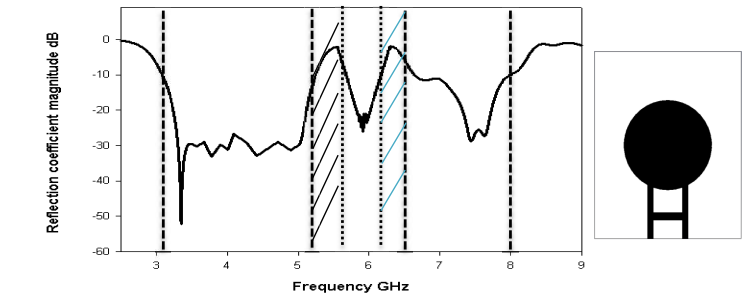

(a) Without slot

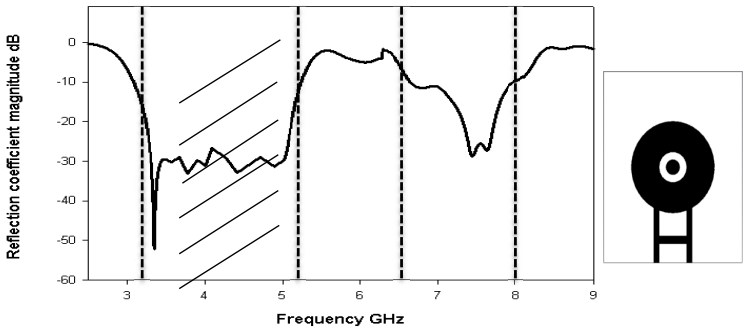

(b) With slot

Figure 3: The reflection coefficient magnitude result of the proposed antenna.

proposed circular-shaped antenna with and without the slot on the radiating element is shown in Figure 3. The simulated reflection coefficient magnitude is operate at (3.1–5.1 GHz), (5.55–6.28 GHz) and (6.5–8 GHz) without the implementation as illustrated in Figure 3(a). While the reflection coefficient magnitude results of the proposed antenna with the slot is (3.1–5.1 GHz) and (6.5–8 GHz) as indicated Figure 3(b). The dimension of the slot on the proposed antenna is 8 mm as shown in Figure 3(a). It can be seen that in section of the slot on the patch of the proposed antenna resulted from 5.55 to 6.28 GHz band rejection. The circular-shaped antenna with slot is introduced that resulted to avoid interference with WLAN at 5.8 GHz.

Figure 4 shows that the E- and H-plane patterns in 3.3 and 7.5 GHz of the proposed antenna in the close to human body tissues. It can be seen that the E-plane and H-plane radiation pattern is affected when the antenna placed close to the body.

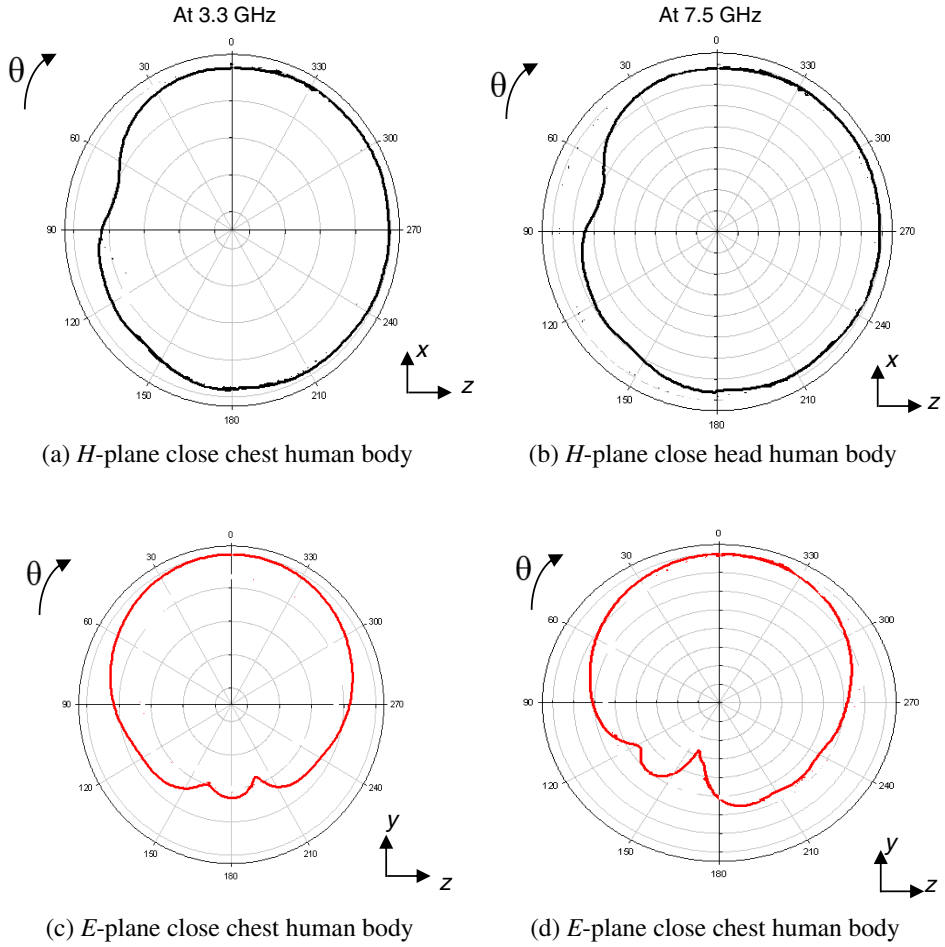

(a) H-plane close chest human body (b) H-plane close head human body

(c) E-plane close chest human body (d) E-plane close chest human body

Figure 4: Simulated radiation pattern of the proposed antenna.

4. CONCLUSION

In this paper, Circular-shaped monopole antenna has been presented investigating the surface current distributions, the slot on the radiating element and radiation patterns in the free space and close proximity of the human body. The Circular-shaped antenna with slot is introduced that resulted to avoid interference with WLAN at 5.8 GHz. The simulated results show that the proposed antenna provides good performance when placed close human body in term of reflection coefficient magnitude and radiation pattern for WBAN applications.

ACKNOWLEDGMENT

The authors would like to thank to Ministry of Higher Education (MOHE) and UTM GUP (vote 01H00 and vote 00G36) for sponsoring this work. Bedsides, thanks to the members of Wireless Communication Center (WCC), UTM for helping and providing resources to enable this work to be completed.

REFERENCES

1. Ali, P., "Connectance and reliability computation of wireless body area networks using signal flow graphs," *Life Science Journal*, Vol. 7, No. 2, 52–56, 2010.
2. Ali, P., "Reliability of wireless body area networks used for ambulatory monitoring and health care," *Life Science Journal*, Vol. 6, No. 4, 5–14, 2010.
3. Kohno, R., K. Hamaguchi, H. B. Li, and K. Takizawa, "R & D and standardization of body area network (BAN) for medical healthcare," *Proc. IEEE Int. Conference on Ultra-wideband, (ICUWB)*, Vol. 3, 5–8, 2008.
4. Chatterjee, I., et al., "Plane-wave spectrum approach for the calculation of electromagnetic absorption under near-field exposure conditions," *Bioelectromagnetics*, Vol. 1, No. 4, 363–377, 1980.

Dynamics of Many-soliton Molecules in Dispersion-managed Optical Fiber

Abdelâali Boudjemâa
Department of Physics, Faculty of Sciences, Hassiba Benbouali University of Chlef
P. O. Box 151, Ouled Fares, Chlef 02000, Algeria

Abstract— We study the stability and the dynamics of many-soliton molecules in dispersion-managed optical fiber with focus on 4- and 5-soliton molecules by analytical and numerical means. We calculate in particular their binding energy, pulse width and their chirp using a variational approach. We found that our variational calculations agreed favorably with the numerical solutions of the nonlinear Schrödinger equation and they well describe the intensity profiles of the experimental molecules.

1. INTRODUCTION

Few years ago, a stable bound state of two DM solitons in opical fibers was realized experimentally [1] and most recently three-soliton molecules in DM optical fibers were also realized by the same group [2, 3]. The main motivation behind creating such molecules is to increase the bit-rate of data transfer in optical fibers. Coding with two or more solitons per clock period increases the alphabet beyond the binary system of a single soliton: logical zero, one (single soliton), two (two-soliton molecule) and three (three-soliton molecule) in time slot. Clock period of commercial systems are now often 25 ps corresponding to 40 GBits/s transmission rate.

The main preoccupation in soliton molecules is their stability against disintegration. Hence, intensive interest in their stability has emerged [4–10]. The existence of a nonzero binding energy in terms of the width of the soliton molecules is an indication on its stability. Indeed, the stability of the many soliton molecule can be problematic since in [2, 3], 3-soliton molecule was found to be less stable than 2-soliton molecule. For many soliton molecules, matters appeared more denser with rising number. Therefore, the stability of such molecules become a difficult task.

The aim of this paper is to study the existence regimes and dynamics of many-soliton molecules in DM optical fibers. Initially we develop a variational approximation to describe the periodic dynamics of a soliton molecule. The obtained system of coupled equations for the pulse width and chirp allows to find the parameters of DM soliton molecules for the given dispersion map and pulse energy. The binding energy and equilibrium separations of the molecules of larger molecules is calculated in the frame of the variational approximation. The predictions of the variational approximation are compared with results of numerical simulations of the nonlinear Schrödinger equation (NLSE) and good agreement is found for both few and many soliton-molecules. All numerical simulations are performed using the parameters of the existing DM fiber setup [2, 3].

2. DISPERSION-MANAGED NONLINEAR SCHRÖDINGER EQUATION

Solitons in dispersion-managed dissipative optical fibers are described by the following NLSE:

$$iE_z - \frac{d(z)}{2}E_{tt} + S(z)|E|^2E = -ig(z)E, \tag{1}$$

where $E(t,z)$ $|E|^2[W]$, $z[m]$ and $t[s]$ are the complex envelope of the electri field, the propagation distance, and the retarded time, respectively. $S(z)[1/\mathrm{W}\cdot\mathrm{m}]$ and $g(z)\,[1/\mathrm{m}]$ represent the nonlinearity and the gain/loss parameters, respestively. $d(z)\,[\mathrm{s}^2/\mathrm{m}]$ corresponds to the dispersion management map defined by

$$d(z) = \begin{cases} d^+, & 0 \le z \le L^+, \\ d^-, & L^+ < z \le L^+ + L^-, \end{cases} \tag{2}$$

where $d^{+,-}$ are constant group velocity dispersions of the fiber segments $L^{+,-}$, respectively.

Using the transformation $E(t,z) = a(z)\,u(t,z)$, $a(z) = a_0 \exp\left(-\int_0^z g(x)\,dx\right)$ where a_0 is dimensionless parameter.

This moves the loss term to the coefficient of the nonlinear term. Thus, Equation (1) reduces to

$$iu_z - \frac{d(z)}{2}u_{tt} + \gamma(z)|u|^2 u = 0, \tag{3}$$

where $\gamma(z) = S(z)a(z)^2$ is the fiber's effective nonlinearity.

In general, for any $\gamma(z) > 0$, we then introduce a new coordinate z' [1/W] defined by $z'(z) = \exp\left(-\int_0^z \gamma(x)\,dx\right)$

$$i\,u_{z'} - \frac{d'(z')}{2}\,u_{tt} + |u|^2\,u = 0, \tag{4}$$

where $d'(z') = d'(z')/\gamma(z')[\mathrm{W}\cdot\mathrm{s}^2]$represents fibers effective dispersion including the variations both of fibers GVD and effective nonlinearity.

Equation (4) permits us to describe the variations of dispersion, nonlinearity, and optical power due to loss or gain by a single variable on the distance which is measured with the accumulation of nonlinearity. For a negative constant, (4) is called the NLSE, can be analytically solved for any initial input by using the inverse scattering transformation, and has soliton solution [11, 12].

For numerical purposes, it is useful to reduce Equation (4) into a dimensionless form. First we introduce $Z = z'/L'$, $T = t/\tau_m$ and $Q(Z,T) = u(z',t)\cdot\sqrt{L'}$ where τ_m is the characteristic time scale equal to the pulse duration of the laser source and $L' = (L^+ + L^-)\gamma$ is the length of the dispersion map period. In terms of these parameters, the dimensionless NLSE takes the form

$$iQ_Z - \frac{D(Z)}{2}Q_{TT} + |Q|^2 Q = 0, \tag{5}$$

where $D = d'L'/\tau_m^2$.

We use the experimental parameters for the DM map corresponding to the setup of [2]. The pulse duration $\tau_m = 0.25\,\mathrm{ps}$, $d^- = -4.259\,\mathrm{ps}^2/\mathrm{km}$, $d^+ = 5.159\,\mathrm{ps}^2/\mathrm{km}$, $\gamma = 1.7\,\mathrm{W}^{-1}\mathrm{km}^{-1}$, $L^+ = 24\,\mathrm{m}$, $L^- = 22\,\mathrm{m}$, $L' = 0.078\mathrm{W}^{-1}$ and $D = 0.521$.

3. VARIATIONAL CALCULATION FOR: SINGLE AND TWO SOLITON-MOLECULES

The variational approach is based on restating the governing equation in terms of a variational problem, where the Lagrangian, generating the original equation, is minimized for a particular trial function. As a result, one obtains a set of coupled ordinary differential equations for parameters of the corresponding ansatz. The technique is proved to be efficient for the analysis of non-integrable soliton bearing equations in different areas of physics [13].

We employ the following trial wavefunction:

$$Q(Z,T) = A\sum_{j=1}^{2}\exp\left[-\frac{(T-\eta_j)^2}{q_j^2} + i\alpha_j T^2 + i\varphi_j\right], \tag{6}$$

where A guarantees the normalization of Q, the number of solitons in the molecule, namely $N = 2$. The variational parameters $q(Z)$, $\varphi(Z)$ and $\eta(Z)$ and $\alpha(Z)$ correspond respectively to the width, the phase, the peak position and the chirp of the soliton. The Lagrangian corresponding to Equation (5) reads

$$L[Q,Q^*] = \int_{-\infty}^{\infty}\frac{i}{2}\left(QQ_Z^* - Q^*Q_Z\right)dT - E. \tag{7}$$

where

$$E = -\int_{-\infty}^{\infty}\left[\frac{D}{2}|Q_T|^2 + \frac{1}{2}|Q|^4\right]dT. \tag{8}$$

is the energy functional.

For the sake of completeness we start with the development of the variational approach for a single DM soliton. The energy of pulse is given by

$$E_s = \int_{-\infty}^{\infty}|Q|^2 dT = A^2 q\sqrt{\pi/2}. \tag{9}$$

In real units, this energy can be expressed as $E[J] = (\tau_m/L')\mathcal{E}$, for the above experimetal parameters $\mathcal{E} = 20\,[\mathrm{pJ}]$.

Equations of motion for the differents variational parameters are then derived from the Euler equations, namely

$$\frac{d}{dZ}\cdot\frac{\partial L}{\partial F_Z}-\frac{\partial L}{\partial F}=0. \tag{10}$$

where F and F_Z denote a variational parameter and its time derivative, respectively.

Taking the corresponding derivatives, the Lagrangian (7) reads

$$L_1=E_s\left\{\frac{1}{4}(q^2+4\eta^2)\alpha_Z+\varphi_Z-\frac{D(Z)}{2}\left[\frac{1}{q^2}+(q^2+4\eta^2)\alpha^2\right]-\frac{E_s}{2\sqrt{\pi}q}\right\}. \tag{11}$$

Using (10), equations of motion for variational parameters take the explicit form:

$$E_Z=0, \tag{12a}$$

$$\alpha_Z-2D(Z)\left(\frac{1}{q^4}+\alpha^2\right)+\frac{E_p}{\sqrt{\pi}q^3}=0, \tag{12b}$$

$$\alpha_Z-2D(Z)\alpha^2=0, \tag{12c}$$

$$qq_Z+4\eta\eta_Z-2D(Z)(q^2+4\eta^2)\alpha=0. \tag{12d}$$

Interestingly, Equation (12a) shows the conservation of the energy. Equations (12b) and (12c), allow us to find the chirp by two ways, all depends on the data that we have. Equation (12d) describes the time evolution of both the width and pick position of the soliton. For fixed η, Equation (12d) reduces to $q_Z-2D(Z)\alpha q=0$.

For two soliton-molecule, the resulting coupled equations of motion, which turn out to be lengthy and hence will not be shown here for convenience, are then solved numerically.

The stationary point of Equations (12b)–(12d) for a given energy E_p determines the width and chirp of a single DM soliton at some point of a DM map and can be found using the numerical technique of Nijhof et al. [14, 15]. Once the width is found, the amplitude of the DM soliton is determined form Equation (9).

Figure 1 shows that the center of mass and the chirp exhibit periodic dynamics, while the DM soliton propagates along the fiber line over 20 map periods. The amplidue of both center of mass and chirp is reduced for two soliton molecules.

In Figure 2, we compare the intensity profile obtained by our variational calculation with our simulation results for both single and two-soliton molecules. Our numerical solution was performed by the split-step fast Fourier transform method, with 2048 Fourier modes and the step size was $dz=5\times10^{-4}$. These figures clearly show the good agreement between the variational calculation on the one hand and the direct numerical solution of the NLSE on the other. Our curves were calculated using the experimental values of [2] apart from the phases where here we have worked with anti-phases solitons.

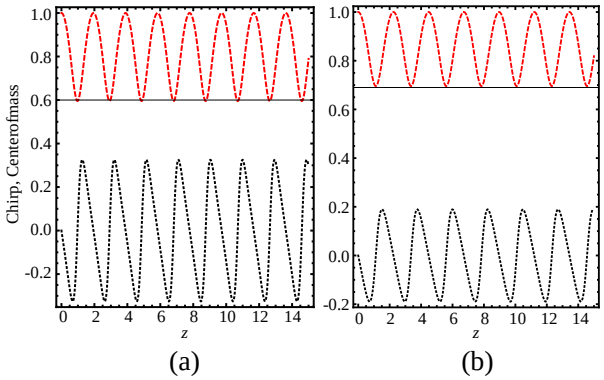

Figure 1: Center of mass and chirp for (a) single soliton and (b) two soliton-molecule with same experimental parameters of Refs. [2, 3].

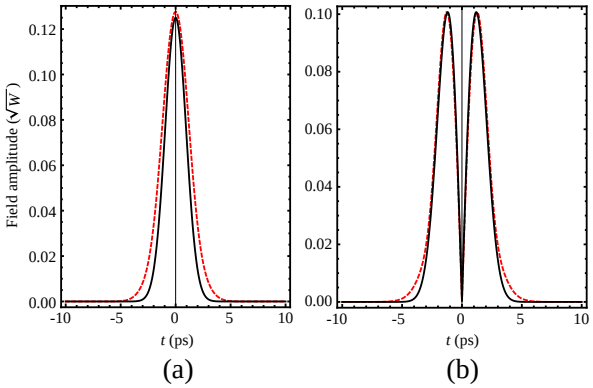

Figure 2: Field amplitude envelopes along dispersion managed fiber of (a) single soliton and (b) two-soliton molecule. Solid line: our variational calculation and Red dashed line: our numerical simulation.

4. MANY-SOLITON MOLECULES

In this section, we investigate the formation and existence of many-soliton molecules in DM optical fiber. We then extend the variational ansatz of the previous section to four and five soliton molecules. To check the validity of our variational calculations for many soliton molecules, we solve again numerically our NLSE.

Figure 3 shows that 5-soliton molecule has indeed nonzero binding energy in terms of the width of solitons. The depth of the minimum gives an estimate to the strength of the bond in the molecule.

Figures 4 depicts the formation and the existence of four-and five-soliton molecules in agreement with our recent theoretical work [16]. It is seen also from the same figure that our numerical simulation coincides with our variational calculation. The stability of 5-soliton molecule during its spatiotemporal evolution is clearly visible in Figure 5.

The existence of four- and five-soliton molecules is indeed an important result because it makes alphabets of five and six different symbols complete: no pulse, single pulse, two pulse molecule, three pulse molecules, four pulse molecules and five pulse molecules in a time slot. We theoretically showed that the same fiber can support all these six symbols. Consequently, a fiber-optic transmission of three bits per clock period is strongly possible. This highly confirms that soliton molecules in DM fiber can be used for enhancing the capacity of the communication system via extension of the coding alphabet.

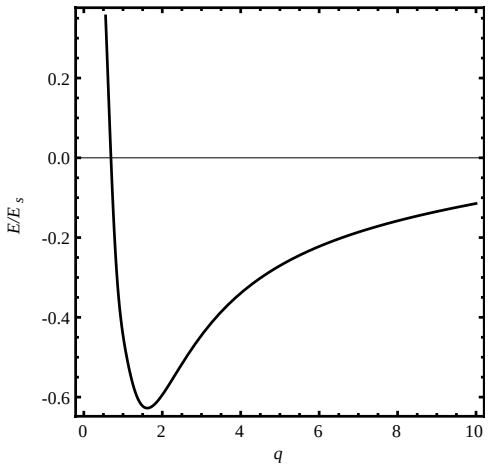

Figure 3: Binding energy of five solitons relative to that of the single-soliton energy E_s as function of the separation of the width q with same experimental parameters of Ref. [3].

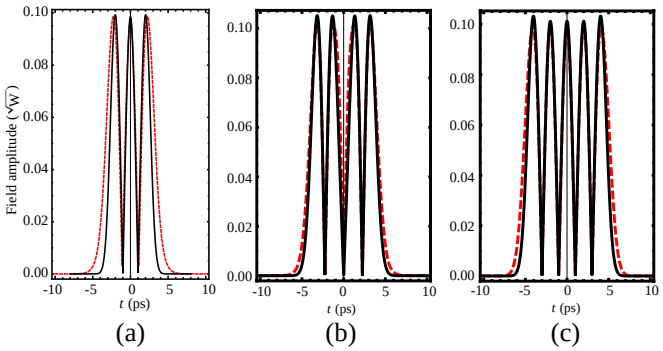

Figure 4: Field amplitude envelopes along dispersion managed fiber of (a) three-soliton molecule, (b) four-soliton molecule and (c) five-soliton molecule. Solide lines: our variational calculation and Red dashed lines our numerical simulation. The parameters are the same as in Figure 2.

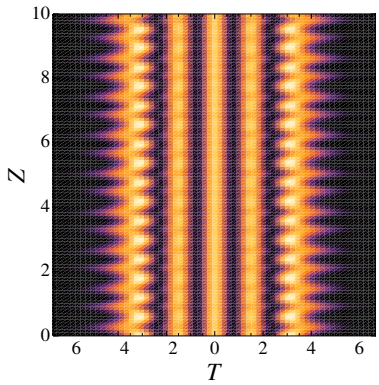

Figure 5: Spatiotemporal evolution of the field amplitude of a 5-soliton molecule. The parameters are the same as in Fig. 2.

5. CONCLUSIONS

In this paper, we have considered many-soliton molecules propagating in DM optical fibers. Using a variational calculation, the binding energy of the 5-soliton molecule was calculated. The coupled system of variational equations for the pulse width and chirp parameter appears to be structurally similar for all considered cases, namely for a single DM soliton, few soliton molecule and many soliton molecule. The difference is seen only in altered numerical coefficient, originating from nonlinearity of the fiber. Furthermore, we have solved numerically the NLSE and verified the stability of the both few-and many-solitons molecules. In addition, the field amplitudes of our trial function agreed favorably with the numerical solution. We theoretically proved that a fiber-optic transmission of beyond two bits per clock period is possible. Therefore, this extended coding alphabet leads to increase the capacity of communication systems.

ACKNOWLEDGMENT

We acknowledge support of Hassiba Benbouali University of Chlef and the Algerian Government research Grant CNEPRU-D00720130045.

REFERENCES

1. Stratmann, M., T. Pagel, F. Mitschke, *Phys. Rev. Lett.*, Vol. 95, 14, 2005.
2. Rohrmann, P., A. Hause, and F. Mitschke, *Sci. Rep.*, Vol. 2, 866, 2012.
3. Rohrmann, P., A. Hause, and F. Mitschke, *Phys. Rev. A*, Vol. 87, 043834, 2013.
4. Malomed, B. A., "Variational methods in nonlinear fiber optics and related fields," *Progress in Optics*, Vol. 43, 69–191, E. Wolf, Ed., North Holland, Amsterdam, 2002.
5. Feng, B. and B. A. Malomed, *Opt. Commun.*, Vol. 229, 173, 2004.
6. Serkin, V. N., A. Hasegawa, and T. L. Belyaeva, *Phys. Rev. Lett.*, Vol. 98, 074102, 2007.
7. Al Khawaja, U. and A. Boudjemâa, *Phys. Rev. E*, Vol. 86, 036606, 2012.
8. Al Khawaja, U., *Phys. Rev. E*, Vol. 81, 056603, 2010.
9. Hause, A., H. Hartwig, and F. Mitschke, *Phys. Rev. A*, Vol. 82, 053833, 2010.
10. Turitsyn, S. K., B. G. Bale, and M. P. Fedoruk, *Phys. Rep.*, Vol. 521, 135203, 2012.
11. Hasegawa, A., Y. Kodama, and A. Maruta, *Optical Fiber Technology*, Vol. 3, 197, 1997.
12. Zakharov, V. E. and A. B. Shabat, *Sov. Phys. JETP*, Vol. 34, 62, 1972.
13. Turitsyn, S. and E. Shapiro, *Opt. Fiber Technol.*, Vol. 4, 151160, 1998.
14. Nijhof, J. H. B., N. J. Doran, W. Forysiak, and F. M. Knox, *Electron. Lett.*, Vol. 33, 1726, 1997.
15. Nijhof, J. H. B., W. Forysiak, and N. J. Doran, *IEEE J. Select. Topics Quantum Electron.*, Vol. 6, 330, 2000.
16. Boudjema, A. and U. Al Khawaja, *Phys. Rev. A*, Vol. 88, 045801, 2013.

Photostimulated Quantum Effects in Quantum Wire with a Parabolic Potential

Hoang Van Ngoc, Nguyen Vu Nhan, and Nguyen Quang Bau
Department of Physics, College of Natural Sciences, Hanoi National University
No. 334, Nguyen Trai Str., Thanh Xuan Dist., Hanoi, Vietnam

Abstract— The quantum theory of the photostimulated effects in quantum wire has been studied based on the quantum kinetic equation for electrons with a parabolic potential $V(z) = \frac{m\omega_0^2 z^2}{2}$. In this case, electrons system in quantum wire is placed in a constant electric field $\vec{E}_0$, an electromagnetic wave $\vec{E}(t) = \vec{E}(e^{-i\omega t} + e^{i\omega t})$ and in the presence of an intense laser field $\vec{F}(t) = \vec{F}\sin\Omega t$. In the presence of laser radiation and polarized electromagnetic wave can influence that current carrier, and do appear an electric field intensity vector $\vec{E}_0$ with open circuit conditions. Hence, the analytic expressions of electric field intensity vector $\vec{E}_0$ **along the coordinate axes has been calculated**. The dependence of the components $\vec{E}_0$ on the frequency Ω of the laser radiation field, the frequency ω of the electromagnetic wave field, the frequency ω_0 of the parabolic potential are shown. From the analytic results, when $\omega_0 \to 0$, the result will turn back to the photostimulated kinetic effects in semiconductors.

1. INTRODUCTION

In recent times, there have been many studies on the influence of intense laser radiation and polarized electromagnetic wave in low dimensional systems. It is known that the presence of intense laser radiation can influence the electrical conductivity and kinetic effects in material [1–4]. A serial of photostimulated kinetic effects such as Nernst-Ettingshausen, Ettingshausen, and Peltier effects, ect. ... have been researched in semiconductors [5, 6, 12]. However, in quantum wire, the photostimulated quantum effects still opens for studying. In this paper, we use the quantum kinetic equation for electrons system is placed in a constant electric field $\vec{E}_0$, an electromagnetic wave $\vec{E}(t) = \vec{E}(e^{-i\omega t}+e^{i\omega t})$ and in the presence of an intense laser field $\vec{F}(t) = \vec{F}\sin\Omega t$, in quantum wire with a parabolic potential. The problem is considered for electron-optical phonon scattering, the analytic expressions of electric field intensity vector $\vec{E}_0$. Numerical calculations are carried out with a specific GaAs/GaAsAl quantum wire. The comparison of the result of quantum wire to semiconductors builk shows that the difference.

2. PHOTOSTIMULATED QUANTUM EFFECTS IN QUANTUM WIRE WITH A PARABOLIC POTENTIAL

2.1. Expressions for the Photostimulated Quantum Effects in Quantum Wire with a Parabolic Potential

We examine the system which is placed in a linearly polarized EMW field ($\vec{E}(t) = \vec{E}(e^{-i\omega t} + e^{i\omega t})$, $\vec{H}(t) = [\vec{n}, \vec{E}(t)]$), in a dc electric field $\vec{E}_0$ and in a strong radiation field $\vec{F}(t) = \vec{F}\sin\Omega t$. The Hamiltonian of the electron-optical phonon system in the quantum wire (QW) in the second quatization representation can be written as [7, 8]

$$\begin{aligned} H =& H_0 + U = \sum_{n,l,\vec{p}_z} \varepsilon_{n,l,\vec{p}_z}\left(\vec{p}_z - \frac{e}{hc}\vec{A}(t)\right)\cdot a^+_{n,l,\vec{p}_z}\cdot a_{n,l,\vec{p}_z} + \sum_{\vec{q}} h\omega_{\vec{q}} b^+_{\vec{q}} b_{\vec{q}} \\ &+ \sum_{n,l,n',l'}\sum_{\vec{p}_z,\vec{q}} C_{n,l,n',l'}(\vec{q})\cdot I_{n,l,n',l'} a^+_{n',l',\vec{p}_s+\vec{q}}\cdot a_{n,l,\vec{p}_z}(b_{\vec{q}} + b^+_{-\vec{q}}) \\ H_0 =& \sum_{n,l,\vec{p}_z} \varepsilon_{n,l,\vec{p}_z}\left(\vec{p}_z - \frac{e}{hc}\vec{A}(t)\right)\cdot a^+_{n,l,\vec{p}_z}\cdot a_{n,l,\vec{p}_z} + \sum_{\vec{q}} h\omega_{\vec{q}} b^+_{\vec{q}} b_{\vec{q}} \\ U =& \sum_{n,l,n',l'}\sum_{\vec{p}_z,\vec{q}} C_{n,l,n',l'}(\vec{q})\cdot I_{n,l,n',l'} a^+_{n',l',\vec{p}_s+\vec{q}}\cdot a_{n,l,\vec{p}_z}\left(b_{\vec{q}} + b^+_{-\vec{q}}\right) \end{aligned} \quad (1)$$

with $f_{n,l,\vec{p}_z}(t) = \langle a^+_{n,l,\vec{p}_z}\cdot a_{n,l,\vec{p}_z}\rangle_t$ is an unknow distribution function perturbed due to the external fields.

In order to establish the quantum kinetic equations for electrons in QW, we use general quantum equations for the particle number operator or electron distribution function

$$ih\frac{\partial f_{n,l,\vec{p}_z}(t)}{\partial t} = \left\langle \left[a^{+}_{n,l,\vec{p}_z} \cdot a_{n,l,\vec{p}_z}, H \right] \right\rangle_t \tag{2}$$

- From Eqs. (1) and (2), we obtain the quantum kinetic equation for electrons in QW:

$$\begin{aligned}
&\frac{\vec{P}_z}{m}\frac{\partial f_{n,l\vec{p}_z}(t)}{\partial t} - \left(e\cdot\vec{E}(t) + e\cdot\vec{E}_0 + \omega_H\left[\vec{p}_z,\vec{h}(t)\right]\right)\frac{1}{h}\frac{\partial f_{n,l,\vec{p}_z}(t)}{\partial \vec{p}_z} + \frac{\partial f_{n,l,\vec{p}_z}(t) - f_0}{\tau} \\
=&\frac{2\pi}{h}\sum_{n',l',\vec{q}}|D_{n,l,n',l'}(q)|^2\cdot\sum_{L=-\infty}^{\infty}J_L^2\left(\frac{\Lambda}{\Omega}\right)\cdot N_q\{\left[f_{n',l',\vec{p}_z+\vec{q}}(t) - f_{n,l,\vec{p}_z}(t)\right]\cdot\delta(\varepsilon_{n',l',\vec{p}_z+\vec{q}_z} - \varepsilon_{n,l\vec{p}_z} - h\omega_{\vec{q}} - Lh\Omega) \\
&+\left[f_{n',l',\vec{p}_z-\vec{q}_z} - f_{n,l,\vec{p}_z}\right]\delta\left(\varepsilon_{n',l',\vec{p}_z-\vec{q}_z} - \varepsilon_{n,l,\vec{p}_z} + h\omega_{\vec{q}} - Lh\Omega\right)\}
\end{aligned} \tag{3}$$

where ω_H is the cyclotron frequency, $\vec{h} = \frac{\vec{H}}{H}$ is the unit vector in the magnetic field direction, $J_L(x)$ is the Bessel function of real argument; $N(q)$ depends on the electron scattering mechanism.

For simplicity, we limit the problem to the case of $l = 0, \pm 1$. We multiply both sides Eq. (3) by $(-e/m)\vec{p}_\perp \cdot \delta(\varepsilon - \varepsilon_{n,\vec{p}_\perp})$ are carry out the summation over n and $\vec{p}_\perp$, we obtain

$$\vec{j}_{tot} = \vec{j}_0 + \vec{j}(t) = \int_0^\infty \left\{\vec{R}_0(\varepsilon) + \left[\vec{R}(\varepsilon)\cdot e^{-i\omega t} + \vec{R}^*(\varepsilon).e^{i\omega t}\right]\right\}\cdot d\varepsilon \tag{4}$$

$$\vec{R}_0(\varepsilon) = \tau(\varepsilon)\left(\vec{Q}_0 + \vec{S}_0\right) + \frac{\omega_H\tau^2(\varepsilon)}{1+\omega_H^2\tau^2(\varepsilon)}\left[\vec{Q},\vec{h}\right] + \omega_H\tau^2(\varepsilon)\mathrm{Re}\left\{\frac{\left[\vec{S},\vec{h}\right]}{1 - i\omega_H\tau\left(\varepsilon\right)}\right\} \tag{5}$$

$$\vec{R}\left(\varepsilon\right) = \frac{\tau\left(\varepsilon\right)}{1 - i\omega_H\tau(\varepsilon)}\left(\vec{Q} + \vec{S}\right) \tag{6}$$

$\tau(\varepsilon)$ is the relaxation time of electrons with energy ε [13]; has meaning of a partial current density transportable with energy ε, this quantity is related to the total current density $\vec{j}_{tot}$ by means of the relationship.

Taking the statistical average over time of the total current density $\vec{j}_{tot}$ and pay attention to open circuit conditions, we find the expressions for electric field intensity vector $\vec{E}_0$ along the coordinate axes:

$$\begin{aligned}
E_{0x} =& -\left\{a + \frac{e^2F^2}{\beta h^4\Omega^4}\cdot b\tau(\varepsilon_F)\right\}^{-1}\times\frac{\omega_H\tau(\varepsilon_F)}{1+\omega_H^2\tau^2(\varepsilon_F)} \\
&\times\left\{a\left[E_yh_z - E_zh_y\right] + \frac{e^2F^2}{\beta h^4\Omega^4}\cdot b\frac{\tau(\varepsilon_F)\left[1-\omega_H^2\tau^2(\varepsilon_F)\right]}{1+\omega_H^2\tau^2(\varepsilon_F)}\times E_yh_z\right\}
\end{aligned} \tag{7}$$

$$\begin{aligned}
E_{0y} =& -\left\{a + \frac{e^2F^2}{\beta h^4\Omega^4}\cdot b\tau(\varepsilon_F)\right\}^{-1}\times\frac{\omega_H\tau(\varepsilon_F)}{1+\omega_H^2\tau^2(\varepsilon_F)} \\
&\times\left\{a\left[E_zh_x - E_xh_z\right] - \frac{e^2F^2}{\beta h^4\Omega^4}\cdot b\frac{\tau(\varepsilon_F)\left[1-\omega_H^2\tau^2(\varepsilon_F)\right]}{1+\omega_H^2\tau^2(\varepsilon_F)}\times E_xh_z\right\}
\end{aligned} \tag{8}$$

$$E_{0z} = -\frac{\omega_H\tau(\varepsilon_F)}{1+\omega_H^2\tau^2\left(\varepsilon_F\right)}\left\{1 + \frac{e^2F^2}{\beta h^4\Omega^4}\frac{b}{a} - \frac{\tau\left(\varepsilon_F\right)\left[1-\omega_H^2\tau^2(\varepsilon_F)\right]}{1+\omega_H^2\tau^2(\varepsilon_F)}\right\}\left(E_xh_y - E_yh_x\right) \tag{9}$$

where

$$a=\frac{n_0^* e^2}{2\pi m h^2}\sqrt{\frac{2m\pi}{\beta}}\sum_{n,l}\exp\left\{-\beta h\omega_0(2n+l+1)\right\} \tag{10}$$

$$b=a(b_1+b_2+b_3+b_4+b_5+b_6);\quad b_1=A\sum_{n,l,n',l'}|I_{n,l,n',l'}(q_\perp)|^2 B_1\exp\left\{\frac{\beta B_1}{2}\right\}K_1\left\{\frac{\beta B_1}{2}\right\} \tag{11}$$

$$b_2=\frac{A}{2}\sum_{n,l,n',l'}|I_{n,l,n',l'}(q_\perp)|^2 B_2\exp\left\{\frac{\beta B_2}{2}\right\}K_1\left\{\frac{\beta B_2}{2}\right\};\quad b_3=\frac{A}{2}\sum_{n,l,n',l'}|I_{n,l,n',l'}(q_\perp)|^2 B_3\exp\left\{\frac{\beta B_3}{2}\right\}K_1\left\{\frac{\beta B_3}{2}\right\} \tag{12}$$

$$b_4=A\sum_{n,l,n',l'}|I_{n,l,n',l'}(q_\perp)|^2 B_4\exp\left\{\frac{\beta B_4}{2}\right\}K_1\left\{\frac{\beta B_4}{2}\right\};\quad b_5=A\sum_{n,l,n',l'}|I_{n,l,n',l'}(q_\perp)|^2 B_5\exp\left\{\frac{\beta B_5}{2}\right\}K_1\left\{\frac{\beta B_5}{2}\right\} \tag{13}$$

$$b_6=A\sum_{n,l,n',l'}|I_{n,l,n',l'}(q_\perp)|^2 B_6\exp\left\{\frac{\beta B_6}{2}\right\}K_1\left\{\frac{\beta B_6}{2}\right\};\quad A=\frac{e^2 h\sqrt{2m\pi\beta}}{m^2\,\epsilon_0}\left(\frac{1}{\chi_\infty}-\frac{1}{\chi_0}\right) \tag{14}$$

$$B_1=h\omega_{L_0}-2h\omega_0(n'-n)-h\omega_0\left(l'-l\right);\quad B_2=B_1+h\Omega;\quad B_3=B_1-h\Omega \tag{15}$$

$$B_4=h\omega_{L_0}+2h\omega_0(n'-n)+h\omega_0\left(l'-l\right);\quad B_5=B_4-h\Omega;\quad B_6=B_4+h\Omega \tag{16}$$

3. NUMERICAL RESULTS AND DISCUSSION

In this section, we will survey, plot and discuss the expressions for E_{0z} for the case of a specific GaAs/GaAsAl quantum wire. The parameters used in the calculations are as follows [7, 8]: $\epsilon_0 = 12,5$; $\chi_\infty = 10.48$; $\chi_0 = 12.90$; $h\omega_{LO} = 36.8\,\text{meV}$; $m = 0.0665m_0$ (m_0 is the mass of free electron); $e = 1.60219\cdot 10^{-19}\,\text{C}$; $\varepsilon_F = 50\,\text{meV}$; and we also choose $\tau(\varepsilon_F)\sim 10^{-11}\,\text{s}^{-1}$; $\tau(\Omega)\sim 10^{-10}\,\text{s}^{-1}$.

In the Fig. 1 and Fig. 2, we show the dependence of E_{0z} (express for the longitudinal radioelectric effect) on the frequency Ω of the intense laser radiation (Fig. 1) and on the frequency ω of the EMW (Fig. 2). From these figures, we can see that the appearance and the nonlinear dependence of E_{0z} on the exterior elements.

From this figure, we can see that the more amplitude F of the intense laser radiation increases, the more the quotient goes up.

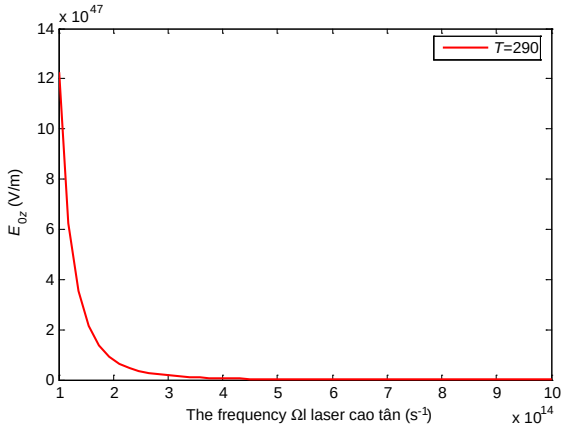

Figure 1: The dependence of E_{0z} on the frequency Ω of the intense laser radiation (in case $\omega = 10^{10}\,\text{Hz}$; $F = 1.2\cdot 10^5\,\text{V/m}$).

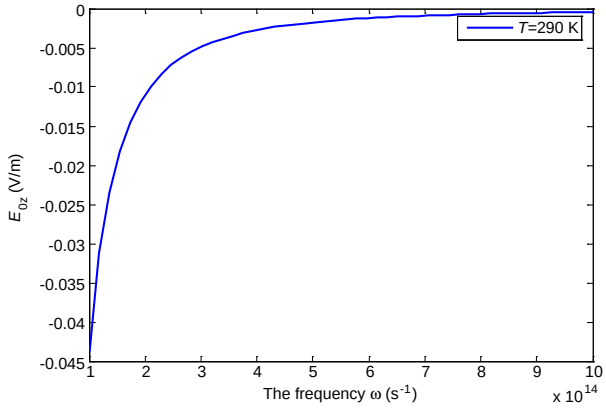

Figure 2: The dependence of E_{0z} on the frequency ω of the EMW (in case $\Omega = 10^{14}\,\text{Hz}$; $F = 1.2\cdot 10^5\,\text{V/m}$).

4. CONCLUSIONS

In this paper, we have studied photostumilated quantum effects in quantum wire with a parabolic potential. In this case, two dimensional electron gas systems is placed in an EMW and a laser radiation at high frequency, and the electron gas is completely degenerate. We obtain the expressions for electric field intensity vector $\vec{E}_0$, in which E_{0x}, E_{0y} express for the longitudinal radioelectric effect and E_{0z} expresses for the horizontal radioelectric effect. And, the expressions of $\vec{E}_0$ show clearly the dependence of $\vec{E}_0$ on the amplitude E_w, on the frequency ω of the EMW and on the

amplitude F, the frequency Ω of the intense laser radiation; and on the basic elements of QW with a parabolic potential. The analytical results are numerically evaluated and plotted for a specific quantum wire, GaAs/AlGaAs. The comparison of the result of quantum wire to semiconductors builk [5, 7, 10] and superlattice [11, 12] shows that the difference.

REFERENCES

1. Shmelev, G. M., L. A. Chaikovskii, and N. Q. Bau, *Sov. Phys. Semicond.*, Vol. 12, 1932, 1978.
2. Bau, N. Q., D. M. Hung, and L. T. Hung, "The influences of confined phonons on the nonlinear absorption coefficient of a strong electromagnetic wave by confined electrons in doping superlattices," *Progress In Electromagnetics Research Letters*, Vol. 15, 175–185, 2010.
3. Bau, N. Q. and D. M. Hung, "Calculation of the nonlinear absorption coefficient of a strong electromagnetic wave by confined electrons in doping superlatices," *Progress In Electromagnetics Research Letters*, Vol. 25, 39–52, 2010.
4. Shmelev, G. M., N. Q. Bau, and N. H. Shon, *Izv. Vyssh. Uch. Zaved. Fiz.*, Vol. 7, 105, 1981.
5. Malevich, V. L. and E. M. Épshtein, *Izv. Vyssh. Uch. Zaved. Fiz.*, Vol. 2, 121, 1976.
6. Malevich, V. L., *Izv. Vyssh. Uch. Zaved. RadioFizika*, Vol. 20, 151, 1977.
7. Shmelev, G. M., G. I. Tsurkan, and E. M. Épshtein, *Physica Status Solidi B*, Vol. 109, 53, 1982.
8. Bau, N. Q. and B. D. Hoi, *J. Korean Phys. Soc.*, Vol. 60, 765, 2012.
9. Bau, N. Q., D. M. Hung, and N. B. Ngoc, *J. Korean Phys. Soc.*, Vol. 54, 765, 2009.
10. Shmelev, G. M., N. H. Shon, and G. I. Tsurkan, *Izv. Vyssh. Uch. Zaved. Fiz.*, Vol. 2, 84, 1985.
11. Kryuchkov, S. V., E. I. Kukhar', and E. S. Sivashova, *Physics of the Solid State*, Vol. 50, 1150, 2008.
12. Milovzorov, D. E., *Technical Physics Letters*, Vol. 22, 896, 1996.

The Influence of the Electromagnetic Wave on the Quantum Acoustomagnetoelectric Field in a Quantum Well with a Parabolic Potential

N. Q. Bau[1] and N. V. Hieu[2]

[1]Faculty of Physics, Hanoi University of Science, Vietnam National University, Hanoi, Vietnam
[2]Faculty of physics, Danang University of Education, Danang, Vietnam

Abstract— The influence of the electromagnetic wave on the quantum acoustomagnetoelectric (QAME) field in a quantum well with a parabolic potential (QWPP) is investigated for an acoustic wave whose wavelength $\lambda = 2\pi/q$ is smaller than the mean free path l of the electrons and in the region $ql \gg 1$ (where q is the acoustic wave number). The dependence of the QAME field E^{QAME} on the frequency of external acoustic wave ω_q, the temperature T, the magnetic field B, the amplitude E_0 and frequency Ω of the electromagnetic wave are obtained by using the quantum kinetic equation. Numerical calculation is done, and the result is discussed for a typical AlAs/GaAs/AlAs QWPP. The computational results show that the dependence of the QAME field E^{QAME} on the external acoustic wave frequency ω_q, the frequency of electromagnetic wave Ω and the magnetic field B is non-monotonic, the cause of appearance peaks attributes the transition between mini-bands $N \to N'$. The quantum theory of the QAME current in a QW is newly developed.

1. INTRODUCTION

The acoustic waves propagate along the stress-free surface of an elastic medium has attracted much attention in the past two decades because of their utilization in acoustoelectronics. Considerable interest in such waves has also been stimulated by the possibility of their use as a powerful tool for studying the electronic properties of the surfaces and thin layers of solids.

It is well known that the propagation of the acoustic wave in conductors is accompanied by the transfer of the energy and momentum to conduction electrons which may give rise to a current usually called the acoustoelectric current, in the case of an open circuit called acoustoelectri field. Presently this effect has been studied in detail both theoretically and experimentally and has been found in wide application in radioelectrionic systems [1–3]. The presence of an external magnetic field applied perpendicularly to the direction of the sound wave propagation in a conductor can induce another field, the so-called AME field. It was predicted by Galperin and Kagan [4] and observed in bismuth by Yamada [5]. Calculations of the AME field in bulk semiconductor [6–9] and the Kane semiconductor [10] in both cases The weak and the quantized magnetic field regions have been investigated. In recent years, the AME field in low-dimensional structures have been extensively studied [11, 12]. However, the calculation of the QAME field E^{QAME} and influence of the electromagnetic wave on QAME field in QWPP by using the quantum kinetic equation method is still open for study. In the present work, we use the quantum kinetic equation method to study the influence of the electromagnetic wave on the QAME field E^{QAME} induced by the electron-external acoustic wave interactions and the present work is different from previous works [13–18] because 1) we use the quantum kinetic equation method, 2) we calculated the influence of an electromagnetic wave on E^{QAME}. Numerical calculations are carried out for a specific quantum well AlAs/GaAs/AlAs to clarify our results. This paper is organized as follows. In Section 2, we find analytic expression for the QAME field in the QWPP, in Section 3 we discuss the results, and in Section 4 we come to a conclusion.

2. ANALYTIC EXPRESSION FOR THE AME FIELD IN THE QWPP

When the magnetic field is applied in the x-direction, in that case the vector potential is chosen as: $A = A_y = -zB$. If the confinement potential is assumed to take the form $V(z) = m\omega^2 z^2/2$ the eigenfunction of an unperturbed electron is expressed as

$$\psi_{N,\vec{p}}(r) = \left(\frac{2}{L_x L_y}\right)^{1/2} \phi_N(z - z_0) \times \exp(ip_x x) \exp(ip_y y), \tag{1}$$

where L_x and L_y are the normalization length in the x and y direction, respectively, $\phi_N(z-z_0)$ is the oscillator wavefunction centred at $z_0 = p_y\Omega_c/[m(\Omega_c^2+\omega^2)]$, m is the effective mass of a conduction electron, ω and Ω_c are the characteristic frequency of the potential and the cyclotron frequency, respectiverly, $N = 0, 1, 2, \ldots$ is the azimuthal quantum number; $\vec{p} = (p_x, p_y, 0)$ is the electron momentum vector. The electron energy spectrum takes the form

$$\varepsilon_N(\vec{p}) = \Omega_0(N+1/2) + \frac{p_x^2}{2m} + \frac{p_y^2}{2m}\left(\frac{\omega}{\Omega_0}\right)^2, \tag{2}$$

with $\Omega_0 = (\Omega_c^2+\omega^2)^{1/2}$ and $\Omega_c = eB/m$.

Let us suppose that the acoustic wave of frequency ω_q is propagated along the z QWPP axis (along the z direction, the energy spectrum of electron is quantizied or the motive direction of electron is limited) and the magnetic field is oriented along the x axis. We consider the most realistic case from the point of view of a low-temperature experiment, when $\omega_q/\eta = c_s|q|/\eta \ll 1$, $ql \gg 1$, where c_s is the velocity of the acoustic wave and q is the modulus of the acoustic wave vector and l is the electron mean free path. The compatibility of these conditions is provided by the smallness of the sound velocity in comparison with the characteristic velocity of the Fermi electrons. The acoustic wave will be considered as a packet of coherent phonons with the delta-like distribution function $N_{\vec{k}} = (2\pi)^3\Phi\delta(\vec{k}-\vec{q})/\omega_q c_s$ in the wavevector $\vec{k}$ space, Φ is the sound flux density. The Hamiltonian describing the interaction of the electron-phonon system in the QWPP, which can be written in the secondary quantization representation as

$$H = \sum_{N,\vec{k}} \varepsilon_N\left(\vec{k} - \frac{e}{c}\vec{A}(t)\right) a^+_{N,\vec{k}} a_{N,\vec{k}} + \sum_{N,\vec{k},N',\vec{q}} C_{\vec{q}} U_{N,N'}(\vec{q}) a^+_{N',\vec{k}} a_{N',\vec{k}+\vec{q}} b_{\vec{q}} \exp(-i\omega_{\vec{q}}t), \tag{3}$$

with $C_{\vec{q}}$ is the electron-phonon interaction factor and takes the form [11]

$$C_{\vec{q}} = i\Lambda c_l^2(\hbar\omega_{\vec{q}}^3/2\rho_0\Xi S)^{1/2}, \qquad \Xi = q\Big[\frac{1+\sigma_l^2}{2\sigma} + \left(\frac{\sigma_l}{\sigma_t} - 2\right)\frac{1+\sigma_t^2}{2\sigma_t}\Big], \tag{4}$$

$$\sigma_l = (1-c_s^2/c_l^2)^{1/2} \qquad \sigma_t = (1-c_s^2/c_t^2)^{1/2}, \tag{5}$$

Λ is the deformation potential constant; $a^+_{N,\vec{k}}$ and $a_{N,\vec{k}}$ are the creation and the annihilation operators of the electron, respectively; $b_{\vec{q}}$ is the annihilation operator of the external phonon. $|N,\vec{k}\rangle$ and $|N',\vec{k}+\vec{q}\rangle$ are electron states before and after interaction, $U_{N,N'}(\vec{q})$ is the matrix element of the operator $U = \exp(iqy - \lambda z)$, $\lambda = (q^2 - \omega_q^2/c_l^2)^{1/2}$ is the spatial attenuation factor of the potential part the displacement field; c_l and c_t are the velocities of the longitudinal and the transverse bulk acoustic wave; ρ_0 is the mass density of the medium and $S = L_xL_y$ is the surface area. $\vec{A}(t)$ is the vector potential of an external electromagnetic wave $\vec{A}(t) = \frac{e}{\Omega}\vec{E}_0\sin(\Omega t)$, Ω is the frequency of electromagnetic wave. The quantum kinetic equation of the problem which is that equation for the distribution function of electrons interacting with external phonons in the presence of an external magnetic fields in QWPP:

$$\begin{aligned}
&-\left(e\vec{E} + \Omega_c[\vec{h},\vec{p}]\right)\frac{\partial f_{N,\vec{p}}}{\partial p} \\
&= -\frac{f_{N,\vec{p}} - f_0}{\tau} + \sum_{N',\vec{k}} |C_{\vec{k}}|^2 |U_{N,N'}|^2 \sum_{l,s} J_l\left(\frac{e\vec{E}_0\vec{k}_\perp}{m\Omega^2}\right) J_{l+s}\left(\frac{e\vec{E}_0\vec{k}_\perp}{m\Omega^2}\right)\exp(-is\Omega t) \\
&\times\Big(\Big[f_{N',\vec{p}+\vec{k}}(N_{\vec{k}}+1) - f_{N,\vec{p}}N_{\vec{k}}\Big]\delta(\varepsilon_{N',\vec{p}+\vec{k}} - \varepsilon_{N,\vec{p}} - \omega_{\vec{k}} - l\Omega) \\
&+[f_{N',\vec{p}-\vec{k}}N_{\vec{k}} - f_{N,\vec{p}}(N_{\vec{k}}+1)]\delta(\varepsilon_{N',\vec{p}-\vec{k}} - \varepsilon_{N,\vec{p}} + \omega_{\vec{k}} - l\Omega)\Big),
\end{aligned} \tag{6}$$

Multiply both sides of Eq. (6) by $(e/m)\vec{p}\delta(\varepsilon - \varepsilon_{N,\vec{p}})$ and carry out the summation over N and $\vec{p}$, we have the equation for the partial current density $\vec{R}_{N,N'}(\varepsilon)$ (the current caused by electrons which have energy of ε):

$$\frac{\vec{R}_{N,N'}(\varepsilon)}{\tau(\varepsilon)} + \Omega_c[\vec{h},\vec{R}_{N,N'}(\varepsilon)] = \vec{Q}_N(\varepsilon) + \vec{S}_{N,N'}(\varepsilon), \tag{7}$$

where

$$\vec{Q}_N(\varepsilon) = -\sum_{N,\vec{p}} e\frac{\vec{p}}{m}\left(\vec{E}, \frac{\partial f_{N',\vec{p}}}{\partial \vec{p}}\right)\delta(\varepsilon - \varepsilon_{N,\vec{p}}),$$

$$\vec{S}_{N,N'}(\varepsilon) = \frac{(2\pi)^3|C_{\vec{q}}|^2\Phi}{\omega_{\vec{q}}c_s}\sum_{N,N',\vec{p},\vec{k}}|U_{N,N'}|^2\sum_{l,s}J_l\left(\frac{e\vec{E}_0\vec{k}_\perp}{m\Omega^2}\right)J_{l+s}\left(\frac{e\vec{E}_0\vec{k}_\perp}{m\Omega^2}\right)\exp(-is\Omega t)\frac{\vec{p}}{m}\delta(\varepsilon-\varepsilon_{N,\vec{p}})$$
$$\times\delta(\vec{k}-\vec{q})\Big((f_{N',\vec{p}+\vec{k}}-f_{N,\vec{p}})\delta(\varepsilon_{N',\vec{p}+\vec{k}}-\varepsilon_{N,\vec{p}}-\omega_{\vec{k}}-l\Omega)+(f_{N',\vec{p}-\vec{k}}-f_{N,\vec{p}})\delta(\varepsilon_{N',\vec{p}-\vec{k}}-\varepsilon_{N,\vec{p}}+\omega_{\vec{k}}-l\Omega)\Big).$$

Solving the Eq. (7), we obtained the partial current $\vec{R}_{N,N'}(\varepsilon)$

$$\begin{aligned}\vec{R}_{N,N'}(\varepsilon) &= \frac{\tau(\varepsilon)}{1+\Omega_c^2\tau^2(\varepsilon)}\Big\{\left(\vec{Q}_N(\varepsilon)+\vec{S}_{N,N'}(\varepsilon)\right)\tau(\varepsilon)\\ &\quad -\Omega_c\tau(\varepsilon)\left([\vec{h},\vec{Q}_N(\varepsilon)]+[\vec{h},\vec{S}_{N,N'}(\varepsilon)]\right)+\Omega_c^2\tau^2(\varepsilon)\left(\vec{Q}_N(\varepsilon)+\vec{S}_{N,N'}(\varepsilon),\vec{h}\right)\vec{h}\Big\}, \quad (8)\end{aligned}$$

the total current density is generally expressed as

$$\vec{j} = \int_0^\infty \vec{R}_{N,N'}(\varepsilon)d\varepsilon, \quad (9)$$

we find the current density

$$j_i = \alpha_{ij}E_j + \beta_{ij}\Phi_j, \quad (10)$$

where α_{ij} and β_{ij} are the electrical conductivity and the acoustic conductivity tensors, respectively

$$\alpha_{ij} = \frac{e^2n_0}{m}\Big\{a_1\delta_{ij}-\Omega_c a_2\epsilon_{ijk}h_k+\Omega_c^2a_3h_ih_j\Big\}; \qquad \beta_{ij} = A\Big\{b_1\delta_{ij}-\Omega_c b_2\epsilon_{ijk}h_k+\Omega_c^2b_3h_ih_j\Big\}, \quad (11)$$

here ϵ_{ijk} is the unit antisymmetric tensor of third order, n_0 is the carrier concentration, and a_x, b_x $(x = 1, 2, 3)$ are given as

$$\begin{aligned}a_x &= \frac{m^2}{\pi n_0}\int_0^\infty\frac{\tau^x(\varepsilon)}{1+\Omega_c^2\tau^2(\varepsilon)}\left(\varepsilon-\Omega_0(N+1/2)\right)\frac{\partial f_0}{\partial\varepsilon}d\varepsilon; \qquad b_x = \int_0^\infty\frac{\tau^x(\varepsilon)}{1+\Omega_c^2\tau^2(\varepsilon)}\frac{\partial f_0}{\partial\varepsilon}d\varepsilon,\\ A &= \frac{8e\pi^3|C_q|^2E_0}{\omega_q c_s\Omega^3}\sum_l\frac{1}{l\Big[(l\Omega\tau)^2+1\Big]}\sum_{N,N'}\frac{4}{(L_yL_x)^2}(2\pi)^4\Big[L_N^0\left(\frac{-\lambda^2}{m\Omega_0}\right)\Big]^2\frac{q}{m(2\pi)^2}\\ &\quad\times\exp\left(-\frac{\lambda^2}{4m\Omega_0}-\frac{2\lambda\Omega_c^2}{m\Omega_0^3}q\right)\Big\{\delta\left((N'-N)\Omega_0-\omega_q-l\Omega\right)-\delta\left((N'-N)\Omega_0+\omega_q-l\Omega\right)\Big\}.\end{aligned}$$

We considered a situation whereby the sound is propagating along the x axis and the magnetic field B is parallel to the z axis and we assume that the sample is opened in all directions, so that $j_i = 0$. Therefore, from Eq. (10) we obtained the expression of the AME field E_{AME}, which appeared along the y axis of the sample

$$\begin{aligned}E_y &= E_{AME} = \frac{\beta_{zz}\alpha_{yz}-\beta_{yz}\alpha_{yy}}{\alpha_{yy}^2+\alpha_{yz}^2}\Phi = \frac{\pi\Omega_cA\tau_0\Phi}{e^2mk_BT}\cdot\Big\{F_{2\nu,2\nu}F_{\nu+1,2\nu}-F_{\nu,2\nu}F_{2\nu+1,2\nu}\Big\}\\ &\quad\times\left\{\left(F_{\nu+1,2\nu}-\frac{\Omega_0(N+1/2)}{k_BT}F_{\nu,2\nu}\right)^2+\Omega_c^2\tau_0^2\left(F_{2\nu+1,2\nu}-\frac{\Omega_0(N+1/2)}{k_BT}F_{2\nu,2\nu}\right)^2\right\}^{-1} \quad (12)\end{aligned}$$

where $F_{\nu,\nu'} = \int_0^\infty\frac{x^\nu}{1+\Omega_c^2\tau_0^2x^{\nu'}}\frac{\partial f_0}{\partial x}dx$. The Eq. (12) is the AME field in the QWPP in the case of the external magnetic field and electromagnetic wave. We can see that the dependence of the AME field on the external magnetic field, the frequency $\omega_{\vec{q}}$ and the frequency of electromagnetic wave is nonlinear. We will carry out further analysis of the Eq. (12) separately for the two limiting cases: the weak magnetic field region and the case of quantized one.

2.1. The Case of Weak Magnetic Field Region

In the case of the weak magnetic field

$$\Omega_c \ll k_B T; \qquad \Omega_c \ll \eta, \tag{13}$$

in this case, the expression of E_{AME} in the Eq. (12) takes the form

$$E_{AME} = \frac{\pi \Omega_c A \tau_0 \Phi}{e^2 m k_B T} \Big\{ F_{2\nu,2\nu} F_{\nu+1,2\nu} - F_{\nu,2\nu} F_{2\nu+1,2\nu} \Big\} \Big\{ F^2_{\nu+1,2\nu} + \Omega_c^2 \tau_0^2 F^2_{2\nu+1,2\nu} \Big\}^{-1}, \tag{14}$$

2.2. The Case of Quantized Magnetic Field Region

In the case of quantized magnetic field region

$$\Omega_c \gg k_B T, \qquad \Omega_c \gg \eta, \tag{15}$$

in this case, the expression of E_{AME} in Eq. (12) takes the form

$$E_{AME} = \frac{\pi \Omega_c A \tau_0 k_B T \Phi}{e^2 m \Omega_0^2 (N + 1/2)^2} \Big\{ F_{2\nu,2\nu} F_{\nu+1,2\nu} - F_{\nu,2\nu} F_{2\nu+1,2\nu} \Big\} \Big\{ F^2_{\nu,2\nu} + \Omega_c^2 \tau_0^2 F^2_{2\nu,2\nu} \Big\}^{-1}, \tag{16}$$

From Eq. (14) and Eq. (16), we see that in both cases, the weak magnetic field and the quantized magnetic field, the dependence of AME field on external magnetic field B is nonlinear.

3. NUMERICAL RESULTS AND DISCUSSIONS

To clarify the results that have been obtained, in this section, we considered the AME field in two limited cases weak magnetic field region and the case of quantized magnetic field region in QWPP. This quantity is considered as a function of an external magnetic field B, the frequency ω_q of ultrasound, the temperature T of system, and the parameters of the AlAs/GaAs/AlAs quantum well. The parameters used in the numerical calculations are as follow: $\tau_0 = 10^{-12}\,\mathrm{s}$, $\Phi = 10^4\,\mathrm{Wm^{-2}}$, $m = 0.067 m_0$, m_0 being the mass of free electron, $\rho_0 = 5320\,\mathrm{kg\ m^{-3}}$, $c_l = 2 \times 10^3\,\mathrm{m\ s^{-1}}$, $c_t = 18 \times 10^2\,\mathrm{m\ s^{-1}}$, $c_s = 8 \times 10^2\,\mathrm{m\ s^{-1}}$, $\Lambda = 13.5\,\mathrm{eV}$, $\omega_q = 10^9\,\mathrm{s^{-1}}$.

Figure 1 present The dependence of the QAME field on the magnetic field at different values of the frequency of electromagnetic wave shows that when magnetic field rises up, the QAME field increases monotonically. However, it reached a maximum value at B is about 0.12 T, and decreased again above 0.12 T. On the other hand, E^{QAME} increases nonlinearly with the magnetic field. This result is different from those for bulk semiconductor [11-14] and the Kane semiconductor [15] under condition $ql \gg 1$, and the weak magnetic field region. Because the QAME field expression E_{AME} in bulk semiconductor [11–14] and the Kane semiconductor [15] is proportional to B. In other words, E^{QAME} increases linearly with the magnetic field. Our result indicates that the dominant mechanism for such a behaviour is attributed to the electron confinement in the QWPP. From Figure 1, we see that the E^{QAME} depends significantly on the frequency of electromagnetic wave, when the frequency of electromagnetic wave increase the position of the peaks change.

Figure 2 investigated the dependence of QAME field on the magnetic field in the quantized magnetic field region which have many distinct maxima. The result showed the different behaviour from results in bulk semiconductor [11–14] and the Kane semiconductor [15]. Different from the bulk semiconductor, these peaks in this case are much sharper. According to the result in the bulk semiconductor [11–14] and the Kane semiconductor [15] in the case of strong magnetic field E^{QAME} which is proportional to $\frac{1}{B}$. There are two reasons for the difference between our result and other results: one is that in the presence of the quantum magnetic field, the electron energy spectrum was affected by quantized magnetic field and the other is the effect of the electrons confinement in the QWPP, that means above $B > 1.8T$ and below 4 K, carriers in the samples satisfy the quantum limit conditions: $\Omega_c \gg k_B T$ and $\Omega_c \tau \gg 1$, and in the QWPP the energy spectrum of electron is quantized. Also, the result is different from those in superlattice [16, 17]. In [16, 17] by using the Boltzmann kinetic equation, QAME field is proportional to B with all regions of temperature. By using the quantum kinetic equation method, our result indicate that it is only linear to B in case of the weak magnetic field and higher temperature, while in case of the strong magnetic field and low temperature QAME field is not proportional to B, but there are many peaks in Figure 2. This is our new development.

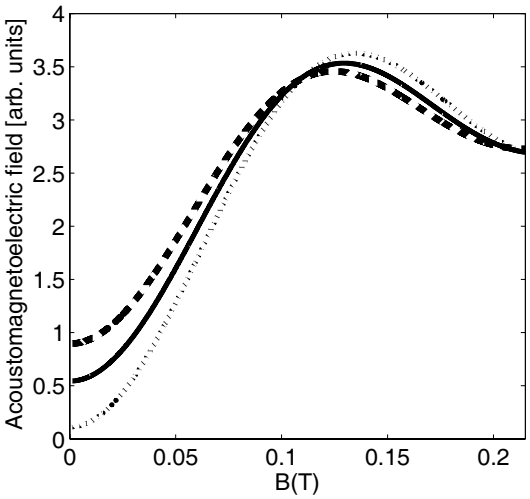

Figure 1: Dependence of the E^{QAME} field QAME on the magnetic field B at different values of the frequency of electromagnetic wave $\Omega = 8 \times 10^{13}\,\mathrm{s}^{-1}$ (dot line), $\Omega = 9 \times 10^{13}\,\mathrm{s}^{-1}$ (solid line), $\Omega = 10 \times 10^{13}\,\mathrm{s}^{-1}$ (dashed line). Here $T = 280\,\mathrm{K}$.

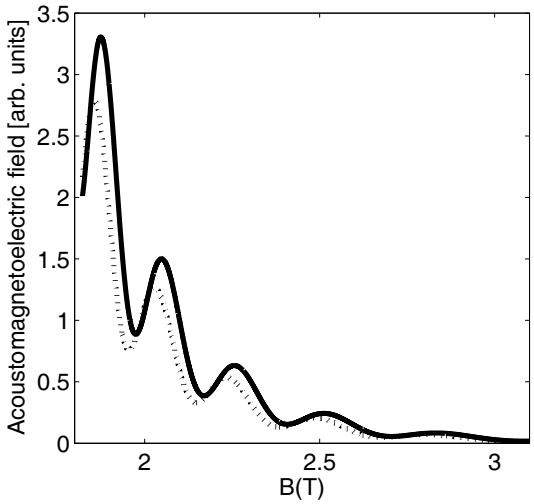

Figure 2: Dependence of the E^{QAME} field QAME on the magnetic field B at different values of the frequency of electromagnetic wave $\Omega = 8 \times 10^{13}\,\mathrm{s}^{-1}$ (solid line), $\Omega = 9 \times 10^{13}\,\mathrm{s}^{-1}$ (dot line). Here $T = 4\,\mathrm{K}$.

4. CONCLUSION

In this paper, we have obtained analytical expressions for the QAME field in presence of the external electromagnetic wave in a QWPP for both the case of quantized magnetic field and the weak magnetic field region. There is a strong dependence of QAME field on the cyclotron frequency Ω_c of the magnetic field, $\omega_{\vec{q}}$ of the acoustic wave, and the temperature T of system. The numerical result obtained for AlAs/GaAs/AlAs QWPP shows that in the quantized magnetic field region, the dependence of QAME field on the magnetic B is nonlinear, and there are many distinct maxima. This dependence has differences in comparison with that in normal bulk semiconductors [12–14] and the Kane semiconductor [15].

ACKNOWLEDGMENT

This work was completed with financial support from the Vietnam National University, Ha Noi (No. QGTD.12.01) and Vietnam NAFOSTED (No. 103.01-2011.18)

REFERENCES

1. Shilton, J. M., D. R. Mace, and V. I. Talyanskii, *J. Phys: Condens. Matter.*, Vol. 8, 337, 1996.
2. Wohlman, O. E., Y. Levinson, and Y. M. Galperin, *Phys. Rev. B*, Vol. 62, 7283, 2000.
3. Zimbovskaya, N. A. and G. Gumbs, *J. Phys: Condens. Matter.*, Vol. 13, 409, 2001.
4. Galperin, Y. M. and B. D. Kagan, *Phys. Stat. Sol.*, Vol. 10, 2037, 1968.
5. Toshiyuki, Y., *J. Phys. Soc. Japan*, Vol. 20, 1424, 1965.
6. Margulis, A. D. and V. A. Margulis, *J. Phys: Condens. Matter.*, Vol. 6, 6139, 1994.
7. Kogami, M. and S. Tanaka, *J. Phys. Soc. Japan*, Vol. 30, 775, 1970.
8. Epshtein, E. M., *JETP Lett.*, Vol. 19, 332, 1974.
9. Shmelev, G. M., G. I. Tsurkan, and N. Q. Anh, *Phys. Stat. Sol.*, Vol. 121, 97, 1984.
10. Anh, N. Q., N. Q. Bau, and N. V. Huong, *J. Phys. Vn.*, Vol. 2, 12, 1990.
11. Mensah, S. Y. and F. K. A. Allotey, *J. Phys: Condens. Matter.*, Vol. 8, 1235, 1996.
12. Bau, N. Q. and N. V. Hieu, "Theory of the acoustomagnetoelectric effect in a superlattice," *PIERS Proceedings*, 342–346, Xi'an, China, March 22–26, 2010.
13. Bau, N. Q., N. V. Hieu, N. T. Thuy, and T. C. Phong, *Coms. Phys. Vn.*, Vol. 3, 249, 2010.
14. Shilton, J. M., D. R. Mace, and V. I. Talyanskii, *J. Phys. Condens.*, Vol. 8, 337, 1996.
15. Wohlman, O. E., Y. Levinson, and Y. M. Galperin, *Phys. Rev. B*, Vol. 62, 7283, 2000.
16. Levinson, Y., O. Entin-Wohlman, and P. Wolfle, *J. Appl. Phys. Lett.*, Vol. 85, 635, 2000.
17. Kokurin, I. A. and V. A. Margulis, *J. Exper. and Theor. Phys.*, Vol. 1, 206, 2007.
18. Cunningham, J., M. Pepper, and V. I. Talyanskii, *J. Appl. Phys. Lett.*, Vol. 86, 152105, 2005.

Small Design for Wireless Antenna Used by Ultra-wideband Systems

Rashid A. Fayadh[1], **F. Malek**[2], **Hilal A. Fadhil**[1], **Farah Salwani Abdullah**[2], **Sameer A. Dawood**[1], **and Ihsan Jabar Hasan**[3]

[1]School of Computer and Communication Engineering
Universiti Malaysia Perlis (UniMAP), Perlis, Malaysia
[2]School of Electrical System Engineering, Universiti Malaysia Perlis (UniMAP), Perlis, Malaysia
[3]Faculty of Electrical Engineering, Universiti Teknikal Malaysia (UTeM), Melaka, Malaysia

Abstract— This work focuses on ultra-wideband (UWB) antenna analysis and design. The proposed design has been undertaken to cover the area of UWB frequency range to be suitable for application of wireless UWB communication systems. UWB of 7.5 GHz is very large spectrum of frequencies which is able to achieve high transmission bit rates. As there are many challenges in indoor and outdoor wireless propagation, high gain and sensitive antenna design plays crucial role in UWB small size systems. The main object of this research is to design and implement small size UWB antenna that satisfy the ultra wide bandwidth technology requirements. The proposed antenna design has been simulated using CST microwave studio software to provide results of return loss, gain, radiation efficiency, surface current distribution, and radiation patterns. These results make the design is very useful for UWB technology applications.

1. INTRODUCTION

The wireless technology is very important in our daily lives and the people around the world use to have this technology especially in cellular phones. The wireless systems give us more free reliable to communicate to each other without position limitations. In 2002 the Federal Communications Commission (FCC) has been licensed the UWB frequency range (3.1 GHz to 10.6 GHz) [1]. Since then, it had a good attention in researches with considering as a promising technology. Because of very low transmission power (-41.3 dBm/MHz), the system elements need to be sensitive in implementation [2]. A train of short time pulses (less than 1 ns) in the transmission and reception scenarios forced us to look for high gain antennas. These antennas are very important elements for UWB systems through private and military applications. Also the lightweight, small size, low cost, high performance, easy to fabricate and integrate with other circuits is required in designing of wireless antennas. To meet the above requirements, microstrip planar antenna is achieved for design to radiate electromagnetic energy [3].

During the literature review, there are several published samples of UWB antennas such as large rectangular patch antennas of 47 mm × 36 mm dimensions [4] use RF-4 substrate material and of 36 mm × 46 mm dimensions using FR-4 epoxy substrate material [5]. A diamond patch shape of $30 \times 26\,\text{mm}^2$ in [6] was simulated and printed on FR4 substrate to cover 95% of UWB starting from 3.39 GHz and has not got omni-directional radiation patterns. Also another antenna scheme of multiple fractal slots was implemented in [7] of 45 mm × 25 mm dimensions with unstable radiation patterns. In addition, a compact microstrip patch antenna was proposed in [8] with total size of $40 \times 35 \times 1.575\,\text{mm}^3$ and from the simulation results, the gain reduces at higher frequencies due to increasing the losses in the feed line.

In this work, small size antenna design with planar ground plane is proposed and curved edges of the patch are fed by microstrip feed line. This design is used to achieve the frequency range of UWB to cover most of its applications. Section 2 shows the parametric study and the dimensions of the design parameters. Sections 3 detailed the simulated results and discussions for return loss. Section 4 presents surface current distribution, and radiation patterns, while Section 5 concentrates with conclusions.

2. TWO SIDED AX-SHAPED PATCH ANTENNA CONFIGURATION AND DESIGN

The UWB digital wireless communication systems operate with narrow pulses that lead to low power and high capacity of bit rate [9]. The antenna was designed to develop the conventional rectangular patch antenna. Fig. 1 shows the design element which is including the antenna parameters and the steps of the proposed design methodology. First, the substrate material was chosen to be Taconic TLY5 with relative dielectric constant (ε_r) of 2.2, loss tangent of 0.0009, and dimensions of $30 \times 28 \times 1.575\,\text{mm}^3$. Second, the radiated shape was selected to be two sided ax-shaped to

extend the operating frequency range that can exhibit the UWB characteristics. Third, microstrip transmission feed line was used to feed the radiating area with dimensions of $12 \times 4.8\,\text{mm}^2$. Forth, the ground plane on the opposite side of the substrate was proposed to be planar plane of 11.25 mm with gap of 0.75 mm between the radiator and ground plane. Next, three parameters were used to optimize the impedance matching bandwidth, feed gap, upper slot width (W_s), and lower slot depth dimension. These parameters were adjusted to show the effects of their dimensions on the impedance bandwidth stability.

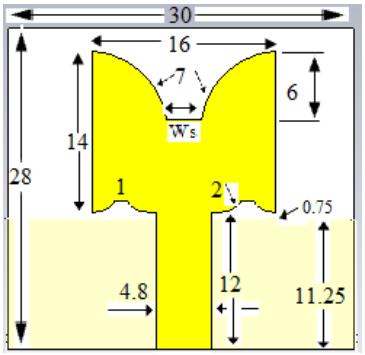

Figure 1: The geometry of the proposed two sided as-shaped patch antenna.

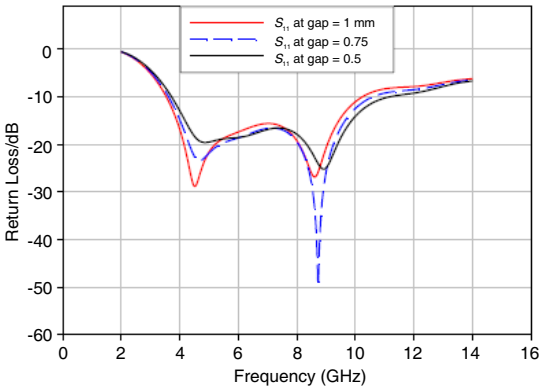

Figure 2: Effects of feed gap on S_{11}.

3. SIMULATION RESULTS AND DISCUSSION

By using the CST microwave studio software, the simulation was run to display the impedance bandwidth across the UWB range. To reduce the conventional overall antenna size, parametric study was carried out to get the optimized dimension for antenna parameters. Essentially, the antenna performance was affected by the geometrical shape and after that three parameters were proposed to achieve the optimal design. Firstly, the feed gap size and its effect is illustrated in Fig. 2 and the wider bandwidth can be shown at gap of 0.5 mm but the best resonance frequency of 8.7 GHz is applied at gap of 0.75 mm. Secondly, the effect of the lower slot depth is shown in Fig. 3 of three different values of the depth to have better matching impedance over the required bandwidth. The studying of this parameter is to present the best depth size for frequency range. The entire band is provided when the lower slot depth in the patch is 1 mm and the band is highly affected when the depth is 2 mm. Next, the effects of upper slot width are shown in Fig. 4 for three values of 3 mm, 4 mm, and 5 mm. Better impedance matching at $W_s = 3$ mm while no change when the width value increases to 4 or 5 mm but getting extended impedance bandwidth to cover most of UWB range. In general all the above parameters introduce the effects on antenna performance in order to optimize the antenna patch shape for wireless UWB applications.

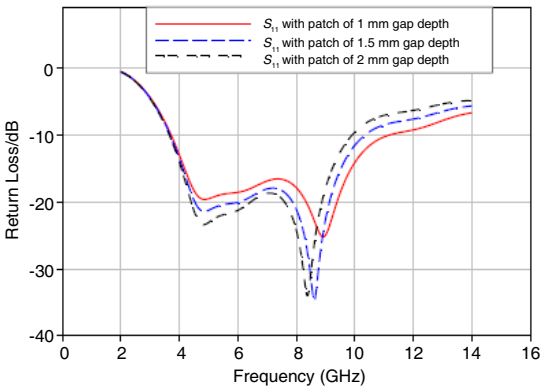

Figure 3: Effects of lower slot depth on S_{11}.

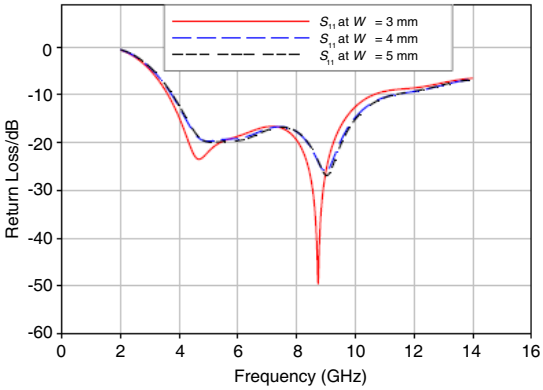

Figure 4: Effects of upper slot width on matching impedance bandwidth.

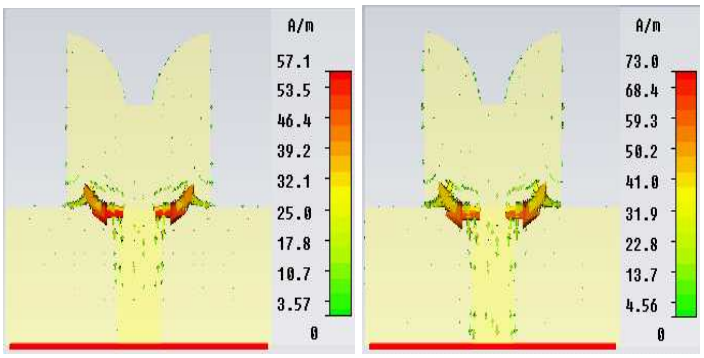

(a) (b)

Figure 5: Surface current distribution at resonance frequencies of (a) 5 GHz and (b) 9 GHz.

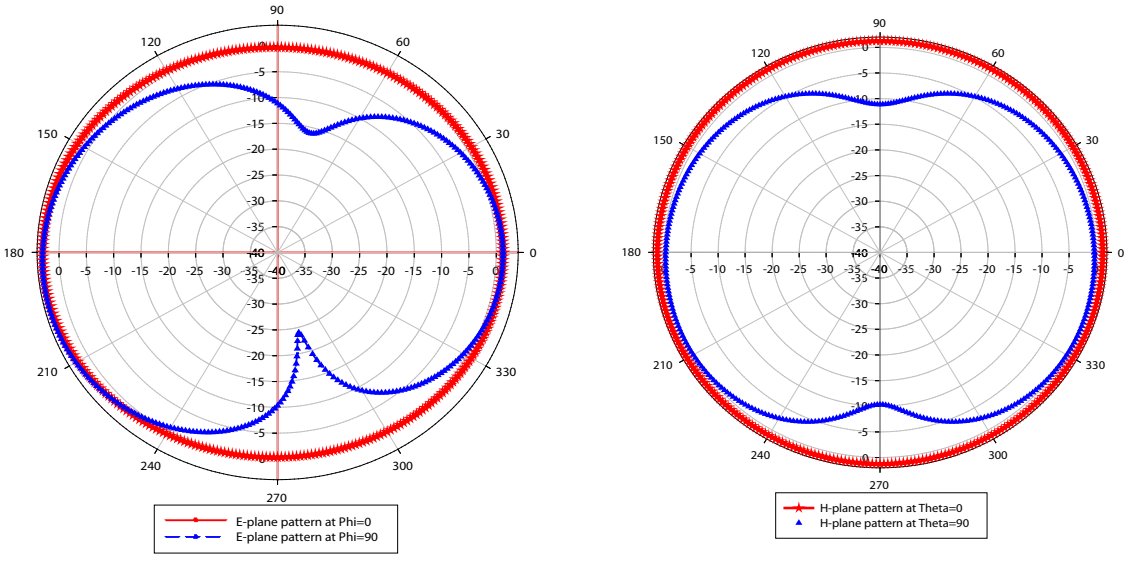

(a) (b)

Figure 6: Simulated radiation patterns for designed antenna at frequency of 5 GHz with Phi and Theta equal to 0° and 90°, (a) E-plane, (b) H-plane.

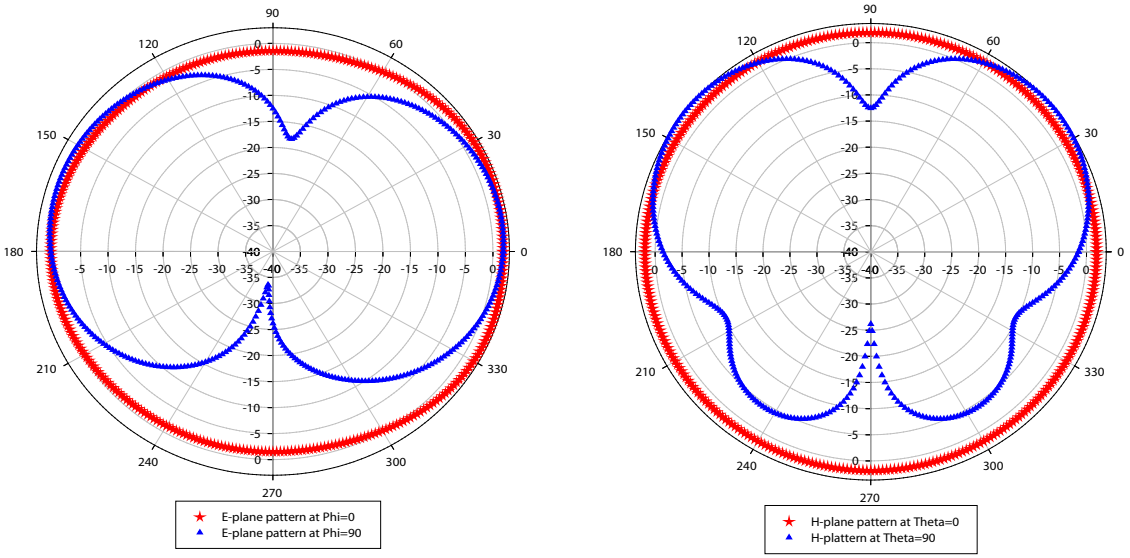

(a) (b)

Figure 7: Simulated radiation patterns for designed antenna at frequency of 9 GHz with Phi and Theta equal to 0° and 90°, (a) E-plane, (b) H-plane.

4. ANTENNA CURRENT DISTRIBUTION AND RADIATION PATTERNS

The simulated surface current distributions are shown in Fig. 5 at resonant frequencies of 5 GHz and 9 GHz. It is absorbed that the most of current field is concentrated near the slots of low patch edge and on the other radiated area; the current is distributed in different densities. The maximum surface current density is 57 A/m at 5 GHz and 73 A/m at 9 GHz which are higher than that in [10] of no more than 10 A/m.

Figure 6(a) shows the two dimensional simulated radiation patterns were taken at resonant frequency of 5 GHz in E-plane when Phi = 0° and Phi = 90°. Fig. 6(b) shows the radiation patterns in H-plane when Theta = 0° and Theta = 90°. Fig. 7 illustrates the simulated H-plane and E-plane radiation patterns at resonant frequency of 9 GHz. However, the analysis of these patterns results shows that the proposed microstrip antenna is characterized by omni-directional radiation patterns in both planes.

5. CONCLUSIONS

In this research, an UWB antenna design of small dimensions was implemented using low cost and lightweight substrate material. The design was improved by using three parameter techniques to enhance the impedance bandwidth. These parameters are feed gap, upper patch slot, and lower patch slot depth. From the simulation results, the design is covering the UWB frequency range to be more suitable for wireless system applications. Radiation patterns are provided omni-directional patterns in E-plane and H-plane over the required band.

REFERENCES

1. Federal Communications Commission (FCC), "Revision of Part 15 of the Commission's rules regarding ultra-wideband transmission systems," First Report and Order, FCC 02-48, 2002.
2. Bellofiore, S., J. Foutz, C. A. Balanis, and A. S. Spanias, "Smart antenna system for mobile communication networks, Part II: Performing and network throughput," *IEEE Antennas Propagat. Mag.*, Vol. 5, Aug. 2002.
3. Liang, J., "Antenna study and design for ultra-wideband communication applications," Ph.D. Thesis, Queen Mary, University of London, 2006.
4. Gupta, B., S. Nakhate, and M. Shandilya, "A compact UWB microstrip antenna with modified ground plane for bandwidth enhancement," *International Journal of Computer Applications (0975-8887)*, Vol. 49, No. 19, Jul. 2012.
5. Lu, J., S. Lin, Y. Tian, L. Jing, M.-Q. Liu, and Z. Zhao, "The simulation and experiment of a UWB printed dipole antenna," *Progress In Electromagnetics Research Letters*, Vol. 36, 21–30, 2013.
6. Djalal, Z. K. and M. S. Mouhamed, "New diamond antenna for ultra wideband applications," *IJCSI International Journal of Computer Science Issues*, Vol. 9, No. 4, 387–390, 2012.
7. Karmarkar, A., S. Verma, M. Pal, and R. Ghatak, "An ultra wideband monopole antenna with multiple fractal slots with dual band rejection characteristics," *Progress In Electromagnetics Research C*, Vol. 31, 185–197, 2012.
8. Kasi, B. and C. K. Chakrabarty, "Ultra-wideband antenna array design for target detection," *Progress In Electromagnetics Research C*, Vol. 25, 67–79, 2012.
9. Sarkar, T., M. C. Wichs, M. Salazar-Plama, and R. J. Bonnean, *Smart Antennas*, John Wiley, IEEE Press, 2003.
10. Srifi, M. N., "Ultra wideband communications: Novel trends — Antennas and propagation," *Ultra-wideband Printed Antennas Design*, Chapter 10, 196–215, InTechOpen, ISBN: 978-953-307-452-8, 2011.

Improve the Performance of Multi-users MC-CDMA Based on Critically Sampling Multi-wavelet Transform over Wireless Propagation Channel

Sameer A. Dawood[1], **F. Malek**[2], **M. S. Anuar**[1], **Rashid A. Fayadh**[1], **Farah Salwani Abdullah**[2], **and Mohd Hariz Mohd Fakri**[2]

[1]School of Computer and Communication Engineering
University Malaysia Perlis (UniMAP), Pauh Putra, Arau, Perlis 02000, Malaysia
[2]School of Electrical System Engineering
University Malaysia Perlis (UniMAP), Pauh Putra, Arau, Perlis 02000, Malaysia

Abstract— In this paper, Critically Sampling Inverse Discrete Multi-Wavelet Transform (CSID-MWT) are proposed as a modulator technique instead of Inverse Fast Fourier Transform (IFFT) in the realization of the Multi-Carrier Code Division Multiple Access (MC-CDMA) system. The proposed structure improved the bandwidth efficiency through the elimination of the cyclic prefix (CP) due to the good orthogonality and time-frequency localization properties of the Multi-Wavelet transform. The proposed system was simulated using MATLAB to allow various parameters of the system to be varied and tested. Simulation results showed that the proposed system outperforms conventional MC-CDMA system, and its performance is superior to that of the conventional MC-CDMA with CP.

1. INTRODUCTION

Recently, Multi-carrier Code Division Multiple Access (MC-CDMA) technique based on the combination of orthogonal frequency division multiplexing (OFDM) and conventional CDMA has received much attention among researchers, it is one of the most promising techniques for the future wireless mobile communication systems beyond *3G* [1].

A MC-CDMA system basically applies the OFDM type of transmission to a Direct Sequence (DS)-CDMA signal. In conventional DS-CDMA each user symbol is transmitted in the form of sequential chips, each of which is narrow in time and hence wide in bandwidth. In contrast to this, in MC-CDMA due to the fast Fourier transform (FFT) along with OFDM the chips are longer in time duration and hence narrow in bandwidth. The multiple chips for a data symbols are not sequential but instead transmitted in parallel over many subcarriers. An interesting feature of MC-CDMA is that modulation and demodulation can be easily implemented using simple inverse fast Fourier transform (IFFT) and FFT operators. This transform however has the drawback that it uses a rectangular window, which creates rather high side lobes. Moreover, the pulse shaping function used to modulate each subcarrier extends to infinity in the frequency domain this leads to high interference and lower performance levels [2].

Many researchers replaced the FFT with another transforms to improve the BER performance for the MC-CDMA system. In [3] the FFT was replaced by an orthonormal wavelets in order to reduce the level of interference. It is found that MC-CDMA based on discrete wavelet transform (DWT) are capable of reducing the inter symbol interference ISI and inter carrier interference ICI, which are caused by the loss in orthogonality between the carriers.

In this paper the FFT in MC-CDMA will be replaced with another transform called Multi-wavelet that based on multi-filters. It has two or more low-pass and high-pass filters. The purpose of this multiplicity is to achieve more properties which cannot be combined in other transforms (Fourier and Wavelet).

A very important multi-wavelets filter is the GHM filter proposed by Geronimo, Hardian, and Massopust. In multi-wavelets setting, GHM multi-scaling and multi-wavelets functions coefficients are 2×2 matrices, and during transformation step they must multiply vectors (instead of scalars). This means that multi-filter bank need 2 input rows, where this can be done by preprocessing the input signal of length N to a sequence of length-2 vectors in order to start the analysis algorithm. If the preprocessing produces N length-2 vectors it is said to be an oversampling scheme, while if it produces $N/2$ length-2 vectors the result is a critical sampling will be used in this paper [4, 5].

In the proposed MC-CDMA systems, there is no need for using Cyclic Prefix (CP), which subsequently reduces the system complexity, increases the transmission rate because it decreases the number of symbol per frame, and increases spectral efficiency.

The rest of the paper is organized as follows: Section 2 introduces the proposed system for MC-CDMA Based on multi-wavelet. Performance results are shown in Section 3 and conclusions are given in Section 4.

2. PROPOSED SYSTEM FOR MC-CDMA BASED ON MULTI-WAVELET

The block diagram of the proposed system for MC-CDMA is depicted in Fig. 1 and Fig. 2, where Fig. 1 is the structure of the transmitter of the kth user, and Fig. 2 is the structure of receiver of the kth user. The OFDM modulator and demodulator based on multi-wavelet that used here are shown in the Fig. 3.

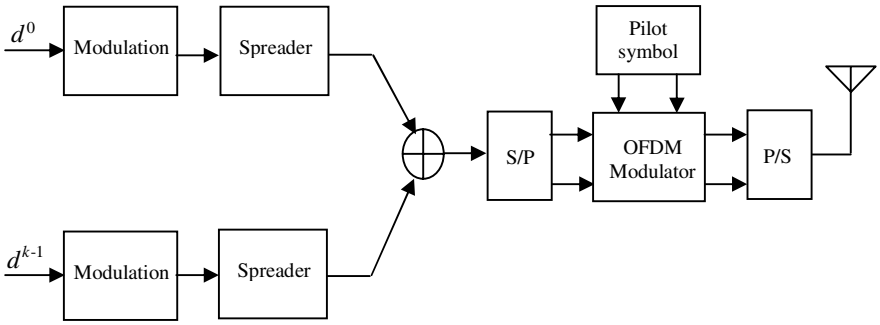

Figure 1: MC-CDMA transmitter model.

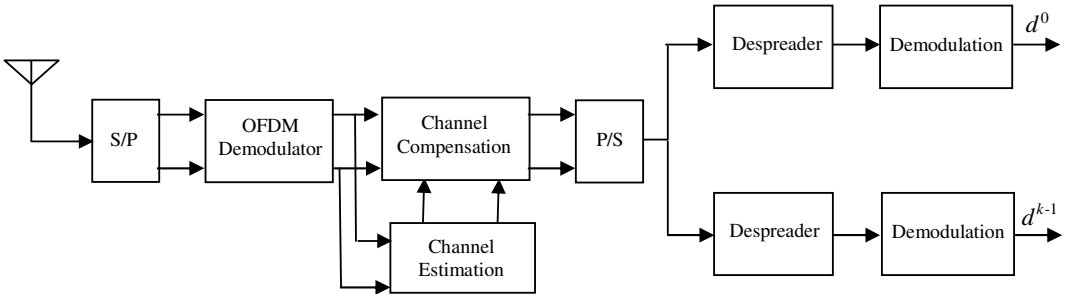

Figure 2: MC-CDMA receiver model.

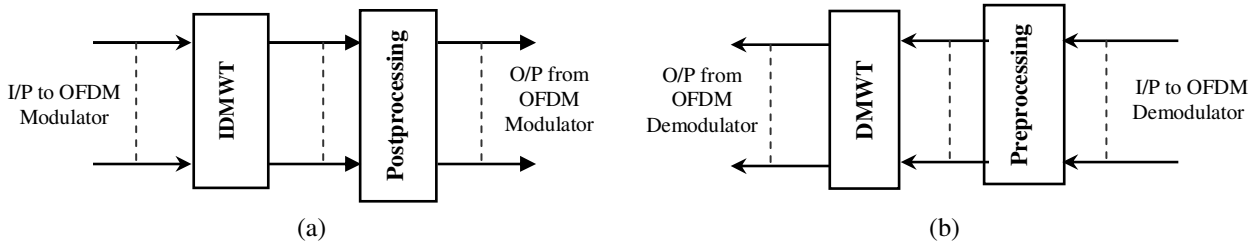

Figure 3: DMWT-OFDM, (a) DMWT-OFDM modulator, (b) DMWT-OFDM demodulator.

At the transmitter, the complex valued data of the user k is multiplied with the user specific spreading code. The coded signals of k active users are added to each other and then serial to parallel converted. The training sequence (pilot sub-carriers) will be inserted and sent prior to information frame. This pilot symbol will been used to make channel estimation that's used to compensate the channel effects on the signal. After that the inverse discrete multi-wavelet transform (IDMWT) with post-processing will be applied to the signal. Now parallel to serial converter (P/S) converts parallel data into serial data stream and transmit over channel.

At the receiver, first S/P converts the data to parallel version. After that the preprocessing and DMWT will be done. Also the channel estimation, channel compensation, despreadingand demodulation the users signal.

To compute a single-level 1-D discrete multi-wavelet transform, the next steps should be followed:

1. Checking input dimensions: input vector should be of length N, where N must be power of 2.
2. Constructing a transformation matrix: Using an $N/2 * N/2$ transformation matrix should be constructed using GHM low- and high-pass filters matrices given in Equations (1) and (2) respectively [6]. After substituting GHM matrix filter coefficients values, an $N * N$ transformation matrix results given in Equation (3).

$$H_0 = \begin{bmatrix} \frac{3}{5\sqrt{2}} & \frac{4}{5} \\ -\frac{1}{20} & -\frac{3}{10\sqrt{2}} \end{bmatrix},\ H_1 = \begin{bmatrix} \frac{3}{5\sqrt{2}} & 0 \\ \frac{9}{20} & \frac{1}{\sqrt{2}} \end{bmatrix},\ H_2 = \begin{bmatrix} 0 & 0 \\ \frac{9}{20} & -\frac{3}{10\sqrt{2}} \end{bmatrix},\ H_3 = \begin{bmatrix} 0 & 0 \\ -\frac{1}{20} & 0 \end{bmatrix} \tag{1}$$

$$G_0 = \begin{bmatrix} -\frac{1}{20} & -\frac{3}{10\sqrt{2}} \\ \frac{1}{10\sqrt{2}} & \frac{3}{10} \end{bmatrix},\ G_1 = \begin{bmatrix} \frac{9}{20} & -\frac{1}{\sqrt{2}} \\ -\frac{9}{10\sqrt{2}} & 0 \end{bmatrix},\ G_2 = \begin{bmatrix} \frac{9}{20} & -\frac{3}{10\sqrt{2}} \\ \frac{9}{10\sqrt{2}} & -\frac{3}{10} \end{bmatrix},\ G_3 = \begin{bmatrix} -\frac{1}{20} & 0 \\ -\frac{1}{10\sqrt{2}} & 0 \end{bmatrix} \tag{2}$$

$$W = \begin{bmatrix} H_0 & H_1 & H_2 & H_3 & 0 & 0 & \dots & 0 & 0 & 0 & 0 \\ 0 & 0 & H_0 & H_1 & H_2 & H_3 & \dots & 0 & 0 & 0 & 0 \\ \vdots & \vdots & \vdots & \vdots & \vdots & \vdots & \dots & \vdots & \vdots & \vdots & \vdots \\ H_2 & H_3 & 0 & 0 & 0 & 0 & \dots & 0 & 0 & H_0 & H_1 \\ G_0 & G_1 & G_2 & G_3 & \vdots & \vdots & \dots & 0 & 0 & 0 & 0 \\ 0 & 0 & G_0 & G_1 & G_2 & G_3 & \dots & 0 & 0 & 0 & 0 \\ \vdots & \vdots & \vdots & \vdots & \vdots & \vdots & \dots & \vdots & \vdots & \vdots & \vdots \\ 0 & 0 & 0 & 0 & 0 & 0 & \dots & G_0 & G_1 & G_2 & G_3 \\ G_2 & G_3 & 0 & 0 & 0 & 0 & \dots & 0 & 0 & G_0 & G_1 \end{bmatrix} \tag{3}$$

3. Preprocessing rows: critically sampling preprocessing can be computed by applying Equations (4) and (5) to the odd- and even-rows of the input vector respectively [7].

a) For any odd row

$$\begin{aligned} \text{new odd row} = &\left(10/8\sqrt{2}\right)[\text{same odd row}] \\ &+ \left(3/8\sqrt{8}\right)[\text{next even row}] + \left(3/8\sqrt{2}\right)[\text{previous even row}] \end{aligned} \tag{4}$$

b) For any even-row

$$\text{new even row} = [\text{same even row}] \tag{5}$$

4. Transformation of input vector which can be done by applying matrix multiplication to the $N/2 * N/2$ constructed transformation matrix by the $N * 1$ preprocessing input vector.

3. SIMULATION RESULTS

The proposed MC-CDMA system described in the previous section is simulated for various numbers of active users and its bit error rate (BER) performance is compared with the conventional standard MC-CDMA system based on FFT and MC-CDMA based on DWT using Daubechies wavelet (4 dB). These systems have been examined in different channel models, which is additive white Gaussian noise (AWGN) channel, flat fading channel, and frequency selective fading channel. This system was implemented using MATLAB software (version 7.8). Table 1 shows the parameters of the system that used in the simulation.

Figure 4, shows the BER performance of MC-CDMA in AWGN channel. It is found that the MC-CDMA based on DMWT is better and more significant than the two other systems based on the FFT and DWT. In case of two active users, the BER = 10^{-3} at signal-to-noise ratio (SNR) is about 6.8 dB for DMWT model while it's about 7.5 dB for DWT model and 17.5 dB for FFT model. With increasing the number of users, the bit error rate is increased also, this is due to multiple access interference (MAI).

The BER performance of the MC-CDMA system in the flat fading channel is presented in Fig. 5. From this figure, it can be seen that the DMWT-MCCDMA is close to DWT-MCCDMA and both of them are much better than the FFT-MCCDMA in case of two users, while in case of four users the DMWT-MCCDMA is better than the two other systems, the BER = 10^{-3} at SNR is about 22 dB for DMWT model while it's about 24 dB for DWT model and 33.5 dB for FFT model.

Table 1: Simulation parameters.

Parameter	Value
System BW	5 MHz
Modulation types	QPSK
Spreading code	Walsh-Hadamard code
Spreading factor	16
Number of users	2, 4
Number of sub-carriers	64
Number of cyclic prefix	16
Channel model	Rayleigh fading channel, Jakes model
Doppler Frequency	10 Hz

Figure 6, gives the BER performance of DMWT-MCCDMA in frequency selective fading channel. A 3-rays Rayleigh-distributed multi-path fading channel is assumed here, where the parameters of the channel in this case corresponding to multipath are (0 dB, −4 dB, −8 dB) paths gain and the paths delay are set to (0, 2-sample, 3-sample). It is clearly shown from this figure that the DMWT-MCCDMA needs SNR more than 19 dB to reach 10^{-3} BER, while DWT-MCCDMA needs SNR around 23 dB to reach 10^{-3} BER, and FFT-MCCDMA needs SNR more than 27 dB to reach 10^{-3} BER, in case of two users.

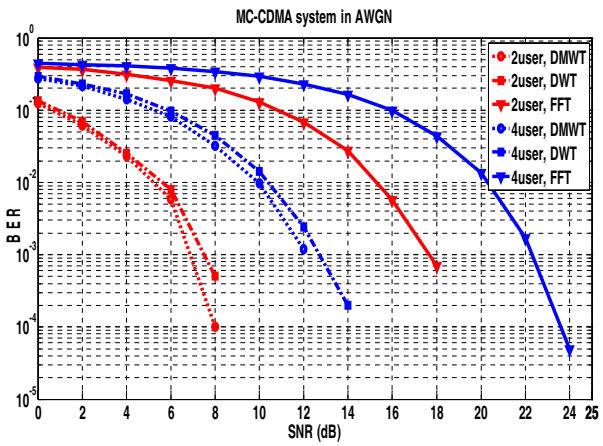

Figure 4: Performance of MC-CDMA in AWGN channel.

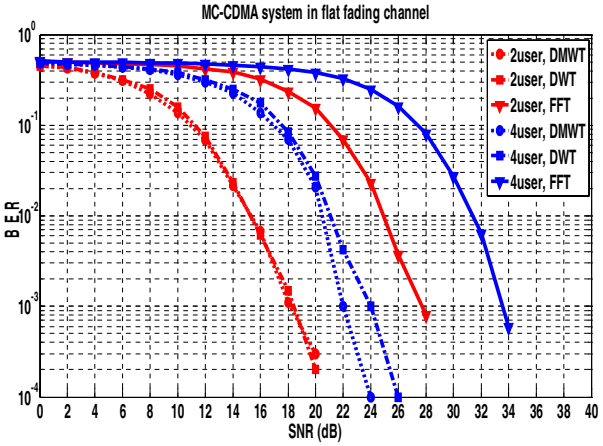

Figure 5: Performance of MC-CDMA in flat fading channel.

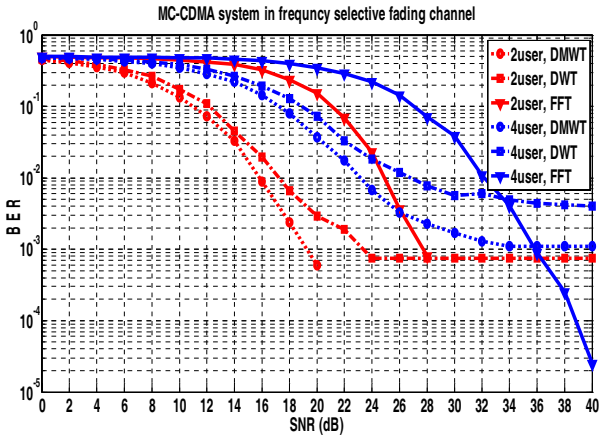

Figure 6: Performance of MC-CDMA in frequency-selective fading channel.

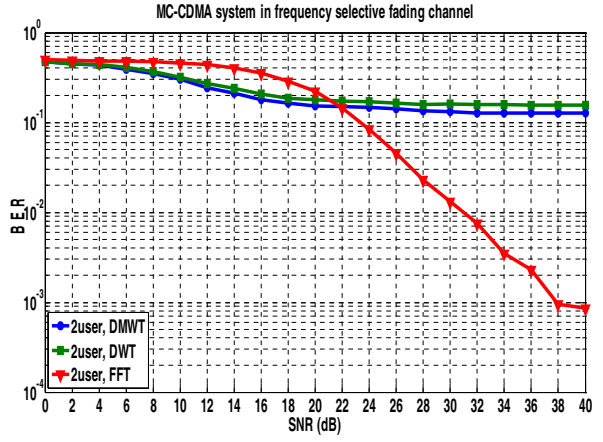

Figure 7: Performance of MC-CDMA in frequency-selective fading channel with Fd = 200 Hz.

Figure 7, shows the effect of Doppler frequency on performance of DMWT-MCCDMA in the frequency selective fading channel where Doppler frequency equal to 200 Hz (fast fading). In fast fading channel, the bit error rate increases for all schemes. From this figure, it is clear that the DMWT-MCCDMA and DWT-MCCDMA have better performance than FFT-MCCDMA up to about SNR = 20 dB, after this value the FFT-MCCDMA became better than the both other systems.

4. CONCLUSIONS

In this paper, the MC-CDMA based on Critically Sampling Multi-wavelet was proposed and compared with the MC-CDMA based on wavelet and MC-CDMA based on FFT in three types of channels. It can be concluded that this structure achieves much lower bit error rates than traditional models based on FFT and wavelet transform. Therefore this structure can be considered as an alternative to the conventional MC-CDMA.

REFERENCES

1. Yu, X., "Performance of turbo-coded MC-CDMA system based on complex wavelet packet in Rayleigh fading channel," *International Conference on Communications, Circuits and Systems, 2004, ICCCAS 2004*, 52–56, 2004.
2. Nathan, Y., J.-P. M. Linnartz, and G. Fettweis, "Multi-carrier CDMA in indoor wireless radio networks," *IEICE Transactions on Communications*, Vol. 77, 900–904, 1994.
3. Negash, B. and H. Nikookar, "Wavelet-based multicarrier transmission over multipath wireless channels," *Electronics Letters*, Vol. 36, 1787–1788, 2000.
4. Geronimo, J. S., D. P. Hardin, and P. R. Massopust, "Fractal functions and wavelet expansions based on several scaling functions," *Journal of Approximation Theory*, Vol. 78, 373–401, 1994.
5. Strela, V., "Multiwavelets: Theory and application," Ph.D. Thesis, MIT, Jun. 1996.
6. Strela, V. and A. T. Walden, "Orthogonal and biorthogonal multiwavelets for signal denoising and image compression," *Aerospace/Defense Sensing and Controls*, 96–107, 1998.
7. Mohammed, Z. J., "VIDEO image COMPRESSION based on multiwavelets transform," Ph.D. Thesis, University of Baghdad, 2004.

Novel Design of H-plane Bandpass Waveguide Filters Using Complementary Split Ring Resonators

S. Stefanovski[1], **D. Mirković**[1, 2], **M. Potrebić**[1], **and D. Tošić**[1]

[1]School of Electrical Engineering, University of Belgrade
P. O. Box 35-54, Belgrade 11120, Serbia
[2]National Severe Storm Laboratory (NOAA), CIMMS, University of Oklahoma
120 David L. Boren Blvd, Norman, OK 73072, USA

Abstract— In this paper, a novel design of bandpass waveguide filters, using complementary split ring resonators is proposed. Resonators are implemented as inserts in a form of metal plates, with properly shaped slots, in the transverse planes of the rectangular waveguide. Filter response has been investigated for various parameters of the resonator and its position. Simple design of dual-band filter is introduced, using resonators attached to the top and bottom waveguide wall. Also, second-order dual-band filter is proposed.

1. INTRODUCTION

In communication systems where high-power structures with small losses need to be implemented, waveguide filters are of particular interest. These filters are usually implemented by inserting discontinuities of various shapes and positions in the waveguide. These discontinuities operate as resonators, thus by setting their parameters and positions, central frequency and bandwidth of the filter can be controlled. For bandpass waveguide filter design, complementary split ring resonators (CSRR) have wide implementation, either as single-mode or multi-mode. In previous publications, various design methods for filters with a single frequency band, using CSRRs, are proposed: implementation in the microstrip technology with defected ground structure as in [1, 2], using substrate integrated waveguide [3] or using rectangular waveguide [4–6]. Multi-band filter design is particularly attractive these days, so this topic calls for closer attention. Therefore, dual-mode resonators can be applied by properly combining single-mode resonators and dual-band filters are developed in this manner. One of the main characteristics of dual-mode resonators used for the filter design is that the resonators can be independently tuned [7], hence each frequency band can be independently controlled, as presented in [8].

Herein, we propose novel design of the X-band bandpass waveguide filter using the CSRRs. Resonators are implemented as inserts in a form of metal plates, having properly shaped slots, in the transverse planes of the standard WR90 rectangular waveguide, in order to obtain H-plane bandpass waveguide filters. Solutions presented in this paper assume that the resonators are attached to the top and bottom waveguide walls. It is noticed that the resonators implemented in such a manner provide the same resonant frequencies as the ones not attached to the waveguide walls, but they are more compact in terms of dimensions. Filter response is investigated for various parameters of the resonators and their positions. For the filter design and analysis, WIPL-D software [9] is used, as powerful three-dimensional electromagnetic (3D EM) solver capable to perform full-wave simulations.

Proposed design using CSRRs is recognized as scalable solution, applicable for multi-band waveguide filter design. Relatively simple implementation of dual-band filter is introduced, along with the model of the second-order dual-band filter.

2. BANDPASS WAVEGUIDE FILTER USING ONE CSRR

Design starts from the model using insert in a form of flat metal plate with a resonator attached to the top waveguide wall. The three-dimensional electromagnetic model of the filter is depicted in Fig. 1. The parameters of the CSRR are tuned in order to obtain resonant frequency of 11 GHz. According to Fig. 1(a), for the resonator with $f_0 = 11$ GHz dimensions of the CSRR are as follows: $d_1 = 2.8$ mm, $d_2 = 2.1$ mm, $c_1 = 1.5$ mm, $c_2 = 0.25$ mm, $p = 0.8$ mm.

For the filter design, the standard WR90 rectangular waveguide of width $a = 22.86$ mm and height $b = 10.16$ mm is used. Considered waveguide filters are excited by means of properly modeled ports with quarter-wave probes. It is assumed that the dominant mode of propagation is the transverse electric TE_{10} mode. Discontinuities inside the waveguide are implemented using metal

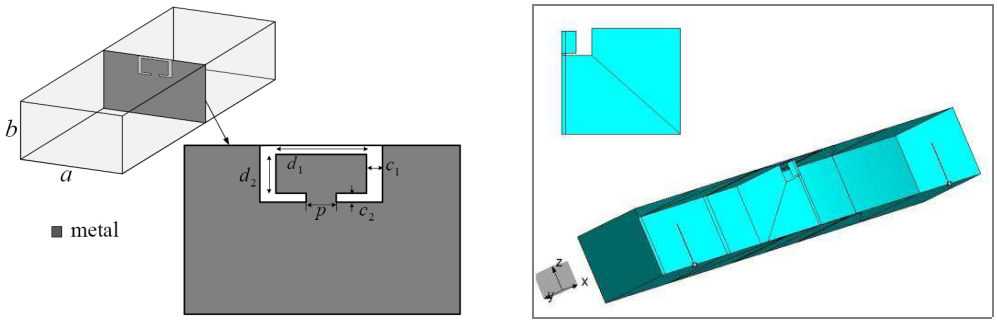

(a) (b)

Figure 1: (a) 3D EM model of the bandpass waveguide filter using one CSRR. (b) WIPL-D model of the bandpass waveguide filter using one CSRR (symmetry applied).

plates, either as flat or folded, with properly shaped slots. These plates are placed in the transverse planes of the described rectangular waveguide. The WIPL-D model of the waveguide filter with one CSRR is shown in Fig. 1(b). The symmetry is used for the filter modeling in WIPL-D software in order to speed up the full-wave simulations. This property significantly reduces the number of unknowns and the CPU time needed to perform the simulation [9].

The frequency response is analyzed for various parameters of the resonator. Comparison of frequency responses, when only one dimension of the CSRR varies, while the others remain unchanged, is shown in Fig. 2. According to the obtained results, it is noticed that the resonator length (e.g., parameter d_1 in Fig. 1(a)) primarily influences the resonant frequency (f_0) while the bandwidth ($B_{3\,\mathrm{dB}}$) is preserved (Fig. 2(a)). On the other hand, variation of resonator width (e.g., parameter c_1 in Fig. 1(a)) introduces the change of both resonant frequency and bandwidth: by decreasing c_1, resonant frequency shifts toward higher values, while the bandwidth becomes narrower (Fig. 2(b)).

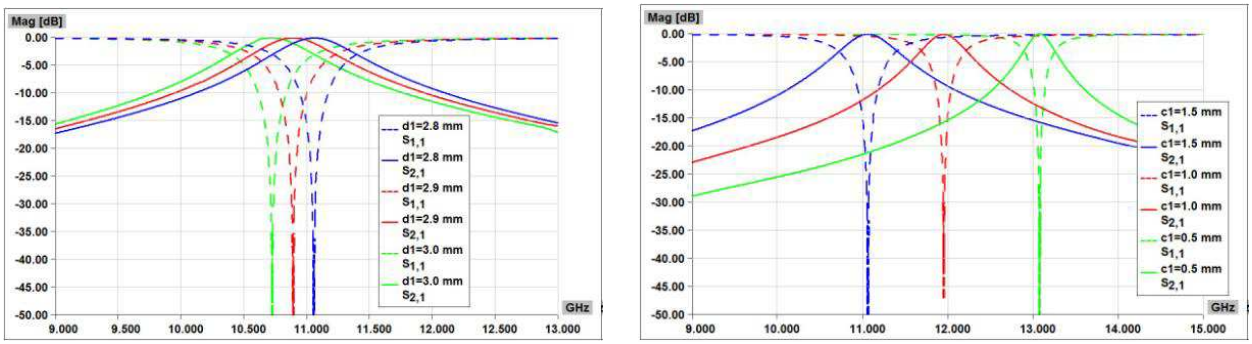

(a) (b)

Figure 2: Comparison of filter responses: (a) d_1 varies, $d_2 = 2.1\,\mathrm{mm}$, $c_1 = 1.5\,\mathrm{mm}$, $c_2 = 0.25\,\mathrm{mm}$, $p = 0.8\,\mathrm{mm}$; (b) $d_1 = 2.8\,\mathrm{mm}$, $d_2 = 2.1\,\mathrm{mm}$, c_1 varies, $c_2 = 0.25\,\mathrm{mm}$, $p = 0.8\,\mathrm{mm}$.

Furthermore, the frequency response is analyzed for various positions of the resonator on the metal plate. If the resonator is moved away from the central position, i.e., it is moved to the left or right for the same distance, the response changes similarly: the increase of the distance from the central position results in the narrower bandwidth, while the frequency remains unchanged (Fig. 3).

Finally, the filter response is also investigated when the resonator is attached to the bottom waveguide wall. The obtained result shows no significant change in terms of the resonant frequency and bandwidth, as can be seen in Fig. 4 for the considered example with $f_0 = 11\,\mathrm{GHz}$. To be more precise, the deviation introduced by the change of position is 0.6% for the resonant frequency and 3.2% for the bandwidth, compared to the reference values adopted for the model with CSRR attached to the top wall ($f_0 = 11.069\,\mathrm{GHz}$, $B_{3\,\mathrm{dB}} = 683\,\mathrm{MHz}$).

It should be emphasized that the proposed design of the inserts in the form of metal plates with CSRRs attached to the top and bottom waveguide wall, provides the possibility to have the same resonant frequencies as for the models with CSRRs not attached to the waveguide walls, but

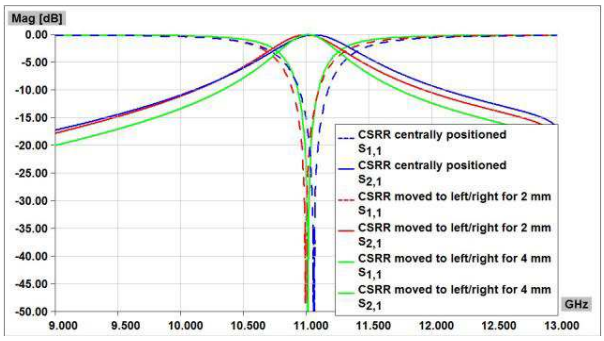

Figure 3: Comparison of filter responses when the resonator is moved away from the central position.

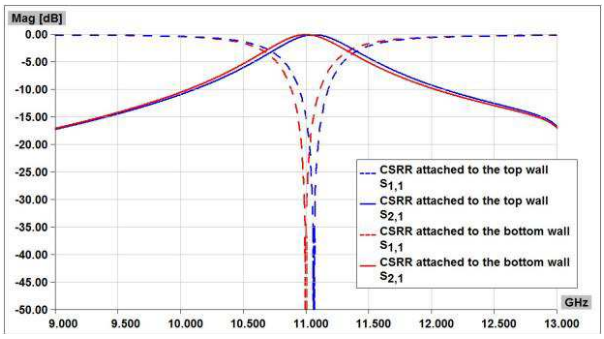

Figure 4: Comparison of filter responses when the resonator is attached to the top and bottom waveguide wall.

with more compact resonators in terms of dimensions. As an example, resonator with $f_0 = 9\,\text{GHz}$ is considered. In case when the resonator is not attached to the waveguide wall, its dimensions are as follows (according to the labels in Fig. 1(a)): $d_1 = 6.0\,\text{mm}$, $d_2 = 23\,\text{mm}$, $c_1 = 1.5\,\text{mm}$, $c_2 = 0.25\,\text{mm}$, $p = 0.8\,\text{mm}$. Therefore, the occupied area can be reduced up to 20% when the resonator is attached to the waveguide wall. Since the resonators occupy less space on the metal insert, it turns out that this approach can be applied for the design of multi-band filters without mutual coupling of the resonators.

3. DUAL-BAND BANDPASS WAVEGUIDE FILTER

As an example of the multi-band filter design using proposed metal inserts, dual-band filter is developed. Considered filter has two central frequencies, $f_{01} = 9\,\text{GHz}$ and $f_{02} = 11\,\text{GHz}$. In order to obtain two frequency bands, flat metal insert is implemented with two CSRRs, one is attached to the top waveguide wall ($f_{01} = 9\,\text{GHz}$) and the other one to the bottom wall ($f_{02} = 11\,\text{GHz}$), as depicted in Fig. 5(a). Dimensions of the resonators, according to Fig. 5(a), are given in Table 1. The same WR90 standard rectangular waveguide is used, as for the model with one CSRR. WIPL-D model of the dual-band filter is shown in Fig. 5(b). The filter response is given in Fig. 6.

As can be seen, relatively simple design provides acceptable solution for dual-band bandpass filter. Since there is no mutual coupling between the resonators on the same plate, each frequency band can be independently controlled by tuning only the corresponding resonator.

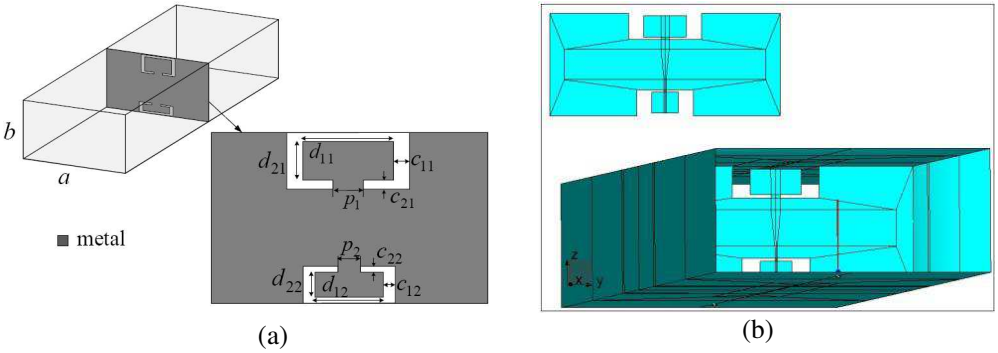

Figure 5: (a) 3D EM model of the dual-band bandpass waveguide filter. (b) WIPL-D model of the dual-band bandpass waveguide filter.

Table 1: Dimensions of the CSRRs used for dual-band filter design.

Dimension	d_{1i} [mm]	d_{2i} [mm]	c_{1i} [mm]	c_{2i} [mm]	p_i [mm]
1st resonator ($i = 1$)	4.25	2.10	1.50	0.25	0.80
2nd resonator ($i = 2$)	2.65	2.10	1.50	0.25	0.20

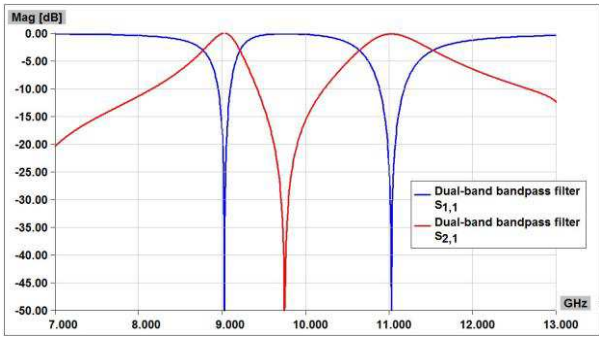

Figure 6: Frequency response of the dual-band bandpass waveguide filter.

4. SECOND-ORDER DUAL-BAND BANDPASS WAVEGUIDE FILTER

Starting from the previously proposed dual-band filter design, second-order bandpass filter is also developed. In this case, folded metal inserts with CSRRs are used in order to implement inverters between the resonators as $\lambda_g/4$ waveguide sections, for each central frequency ($f_{01} = 9\,\text{GHz}$, $f_{02} = 11\,\text{GHz}$). The 3D EM model of the proposed second-order dual-band filter is depicted in Fig. 7(a). Dimensions of the resonators are given in Table 1. According to Fig. 7(a), $l_{pl} = (\lambda_{g9} - \lambda_{g11})/8 = 1.84\,\text{mm}$, $a_{pl} = a = 22.86\,\text{mm}$, $b_{pl} = b/=5.082\,\text{mm}$. The second-order dual-band filter model made in software WIPL-D is shown in Fig. 7(b). The obtained filter response is given in Fig. 8.

In order to obtain better matching, i.e., to have lower value for the return loss, proposed model is slightly modified. To be more precise, the plate connecting parts of the folded metal insert with resonators is designed to be narrow, as depicted in Fig. 9(a). All dimensions correspond to those given in Fig. 7(a), except that the width of the plate is set to $w_{pl} = 2\,\text{mm}$. WIPL-D model of the modified filter is shown in Fig. 9(b). The obtained filter response is given in Fig. 10. According to the filter response, the return loss is slightly improved for the second frequency band ($f_{02} = 11\,\text{GHz}$), though at the expense of wider bandwidth. However, the required bandwidth can be obtained by additional modification of the corresponding resonator.

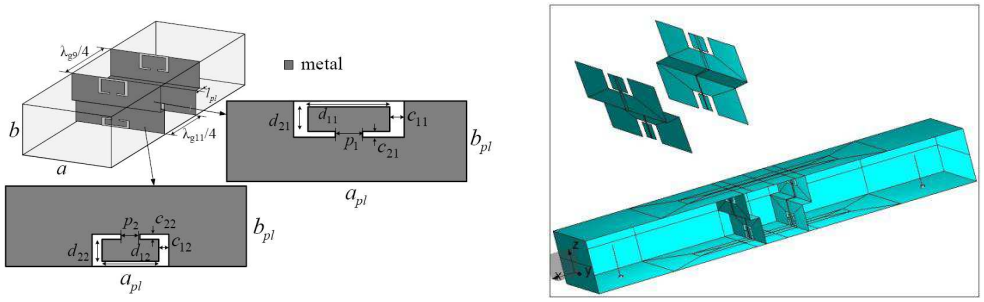

Figure 7: (a) 3D EM model of the second-order dual-band bandpass waveguide filter. (b) WIPL-D model of the second-order dual-band bandpass waveguide filter.

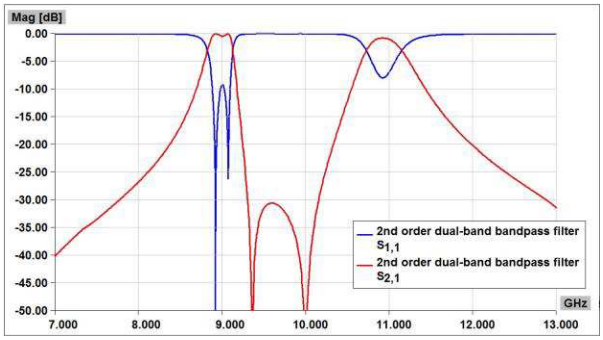

Figure 8: Frequency response of the second-order dual-band bandpass waveguide filter.

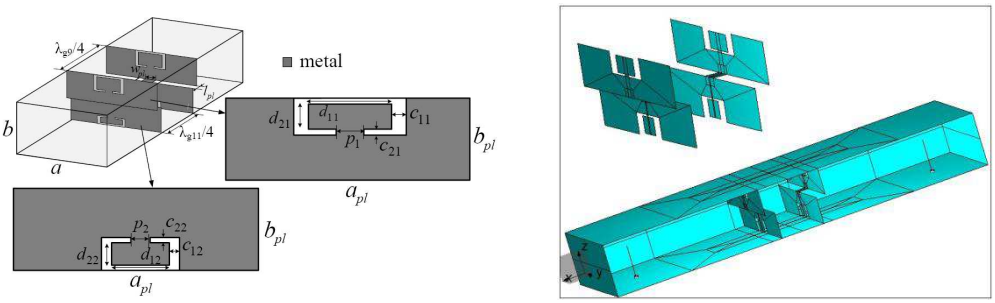

Figure 9: (a) 3D EM model of the modified second-order dual-band bandpass waveguide filter. (b) WIPL-D model of the modified second-order dual-band bandpass waveguide filter.

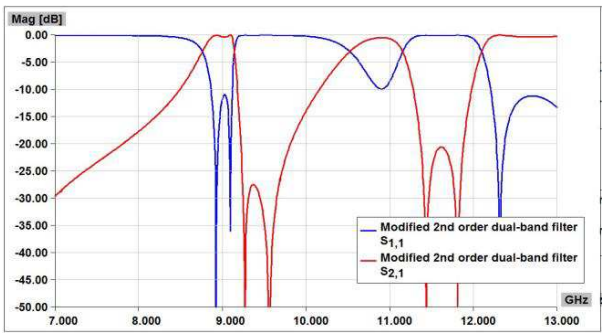

Figure 10: Frequency response of the modified second-order dual-band bandpass waveguide filter.

5. CONCLUSION

Novel design of the H-plane bandpass waveguide filters using CSRRs is proposed. Resonators are implemented as metal inserts with properly shaped slots in the transverse planes of the standard rectangular waveguide. The filter response is investigated for various parameters of the resonators and their positions. The proposed solution with the resonators attached to the waveguide walls provides the same resonant frequencies as the models with resonators not attached to the waveguide walls, but the implementation according to the novel design results in more compact solution (the occupied area on the plate for the resonator can be reduced up to 20%). Also, there is no mutual coupling between the resonators on the same plate. These are important properties for the multi-band filter design. As an example, dual-band bandpass filter is proposed, followed by the second-order dual-band filter. Possible solution for improving the return loss for the second-order dual-band filter is introduced, by slightly modifying the metal inserts without changing the resonators' dimensions. The most important characteristics of the proposed design are simplicity and applicability for multi-band filters, allowing for the higher order filters to be easily developed, as verified in the presented research.

ACKNOWLEDGMENT

This work was supported by the Ministry of Education, Science and Technological Development of the Republic of Serbia under Grant TR32005.

REFERENCES

1. Bonache, J., F. Martin, F. Falcone, J. D. Baena, T. Lopetegi, J. Garcia-Garcia, M. A. G. Laso, I. Gil, A. Marcotegui, R. Marques, and M. Sorolla, "Application of complementary split-ring resonators to the design of compact narrow band-pass structures in microstrip technology," *Microw. Opt. Techn. Lett.*, Vol. 46, No. 5, 508–512, 2005.
2. Bonache, J., F. Martin, I. Gil, J. Garcia-Garcia, R. Marques, and M. Sorolla, "Microstrip bandpass filters with wide bandwidth and compact dimensions," *Microw. Opt. Techn. Lett.*, Vol. 46, No. 5, 343–346, 2005.
3. Zhang, X. C., Z. Y. Yu, and J. Xu, "Novel band-pass substrate integrated waveguide (SIW)

filter based on complementary split ring resonators (CSRRs)," *Progress In Electromagnetics Research*, Vol. 72, 39–46, 2007.

4. Ortiz, N., J. D. Baena, M. Beruete, F. Falcone, M. A. G. Laso, T. Lopetegi, R. Marques, F. Martin, J. Garcia-Garcia, and M. Sorolla, "Complementary split-ring resonator for compact waveguide filter design," *Microw. Opt. Techn. Lett.*, Vol. 46, No. 1, 88–92, 2005.
5. Bahrami, H. and M. Hakkak, "Analysis and design of highly compact bandpass waveguide filter utilizing complementary split ring resonators (CSRR)," *Progress In Electromagnetics Research*, Vol. 80, 107–122, 2008.
6. Potrebić, M. M., D. V. Tošić, Z. Ž. Cvetković, and N. Radosavljević, "WIPL-D modeling and results for waveguide filters with printed-circuit inserts," *Proceedings of 28th International Conference on Microelectronics*, 309–312, Niš, Serbia, May 2012.
7. Hong, J. S., *Microstrip Filters for RF/Microwave Applications*, Wiley, New York, 2011.
8. Stefanovski, S. L., M. M. Potrebić, and D. V. Tošić, "Design and analysis of bandpass waveguide filters using novel complementary split ring resonators," *Proceedings of 11th International Conference on Telecommunications in Modern Satellite, Cable and Broadcasting Services*, 257–260, Niš, Serbia, Oct. 2013.
9. WIPL-D Pro 11.0, 3D Electromagnetic Solver, WIPLD d.o.o., Belgrade, Serbia, 2013.

Indoor Transparent Antenna for Television Reception

S. N. H. Sa'don, **M. R. Kamarudin**, **and M. Khalily**
Wireless Communication Centre (WCC), Universiti Teknologi Malaysia, UTM Skudai 81310, Malaysia

Abstract— The characteristics of indoor transparent antenna are investigated. The purpose of the antenna is applied for television signal reception which is operating at Ultra High Frequency band. The antenna was made from silver coated polyester film (AgHT-4), the transparent conductive material and it is attached on a layer of glass substrate. The antenna size has width and length of 120 mm × 150 mm. It was fed by a co-planar waveguide due to the opportunity of low radiation loss and to reduce reflection of the antenna. The frequency range of 500 MHz to 800 MHz is chosen as it is the UHF television reception band and allocated by Federal Communications Commission. Due to the television station provided in Malaysia, each station have different channel with its own specification frequencies. The channels also are based on the transmitter base station location. Since the proposed project launches at Universiti Teknologi Malaysia, Skudai, Johor, Malaysia so all the channel is following the frequency from GunungPulai, Johor transmitter base station. The channel utilizations are Channel 55 (742–750 MHz): TV1, Channel 26 (510–518 MHz): TV3, Channel 42 (638–646 MHz): NTV7, Channel 44 (654–662 MHz): TV9 and Channel 46 (670–678 MHz): 8TV. Then, the proposed antenna was designed by using Computer Simulation Software (CST) Microwave Studio to obtain the simulation result. The simulated bandwidth of the antenna obtained is 448 MHz (502 MHz to 950 MHz) with bandwidth of 61.71%. It has a potential to be realized for TV reception because of the omni-directional radiation pattern and gain is more than 2.0 dBi.

1. INTRODUCTION

In recent years, the invention of antenna for television reception is increasing rapidly in order to fulfill demand and improve their performance suitable to the latest application technology. For this application, the frequency band allocated by Federal Communication Commission (FCC) is Ultra High Frequency (470–806 MHz) [1]. There are several commercial applications for UHF band, such as Digital Television (DTV, 470–806 MHz) [2–7], Digital Video Broadcasting-Terrestrial (DVB-T, 870–862 MHz) [8] and Digital Video Broadcasting-Handheld (DVB-H, 470–862 MHz) [9] and also some research works on UHF/VHF antennas as reported in [10, 11]. Looking to Malaysia situation, the television station provides the variety of station with their specification channel. Thus, the channels are based on the frequency of transmitter base station location. Since the proposed antenna was investigated at Universiti Teknologi Malaysia (UTM), Skudai, that is therefore all the channels need to use the frequency of GunungPulai transmitter base station [12, 13]. Table 1 briefs the channel utilization in GunungPulai transmitter base station, Malaysia.

Table 1: Channel utilization in Malaysia (GunungPulai transmitter base station).

Station	TV1	TV3	NTV7	TV9	8TV
Channel	55	26	42	44	46
Frequency (MHz)	742–750	510–518	638–646	654–662	670–678

From the previous research, a lot of television reception antennas have been designed and improved. One of the techniques investigated is the conductor material and substrate used. Most researchers used FR-4 substrate [2–4], but at some case or study, they used flexible Copper Clad Laminate (FCCL) film [5], Nora conductive textile and felt substrate [6, 7] and aluminum material [14]. However, this paper proposed indoor transparent antenna for television reception replacing the conventional antenna.

The transparent conductive film currently has been researched on by a decade ago. Some of the proposed applications has been done used transparent antenna are photovoltaic solar-panel integration and RF energy harvesting [15], radio frequency identification (RFID) [16], inter-vehicle communication [17], wireless local area network (WLAN) [18, 19], worldwide interoperability for microwave access (WiMAX) [20], wide-band code-division multiple-access (WCDMA) [19] and CubeSat [21]. In addition, the transparent conductive film is the best candidate to be mounted on the glass or window [20], attracts great interest, light weight, thin volume [18], limpidity and flexibility [19]

and for security [22]. The transparent conductive films so called transparent conducting oxides (TCO) [15, 23] can be as indium thin oxide (ITO) [16], fluorine-doped thin oxide (FTO) [24] and silver coated polyester film (AgHT) [15, 17, 25]. It is challenges but AgHT-4 is chosen because of lower surface resistance. Lower surface resistance is more conductive. The AgHT-4 is commercially used as a sun-shielding film to cut down heat and conserve energy in homes and buildings [15].

2. ANTENNA DESIGN

The indoor transparent antenna for television reception is designed using AgHT-4. It is fed by 50 Ω co-planar waveguide (CPW) and mount on a piece of glass, with thickness of 2 mm and dielectric constant of 7. The AgHT-4 is 0.175 mm thick and has a surface resistance of 4 Ω-Sq. The conductivity is 2×10^5 S/m. The AgHT-4 consists of ITO which is coated at the polyethylene terephthalate (PET) substrate with relative permittivity, ε_r of 3.24. Figure 1(a) shows the geometry of the antenna and Figure 1(b) shows the thickness of the antenna. All the antenna parameters are summarized in Table 2.

The proposed antenna is overall length, l and width, w at 150 mm and 120 mm, respectively. It is fed by 50 Ω co-planar waveguide (CPW) antenna. A portion of transparent film has been cut at the left side. So the left sidelength, l_1 is 35 mm. The feed line width, w_s is 3 mm and feed gap, g is 0.3 mm. Therefore the length of CPW ground, l_{CPW} is 9.9 mm. The CPW is fed to the antenna because of it has much benefit such as no soldering point, easy fabrication [3] and a simplified configuration with a single conductive layer. Therefore in terms of art, the CPW design will offer satisfactory impedance matching over a wide frequency range and the ability to maintain nearly omnidirectional radiation pattern.

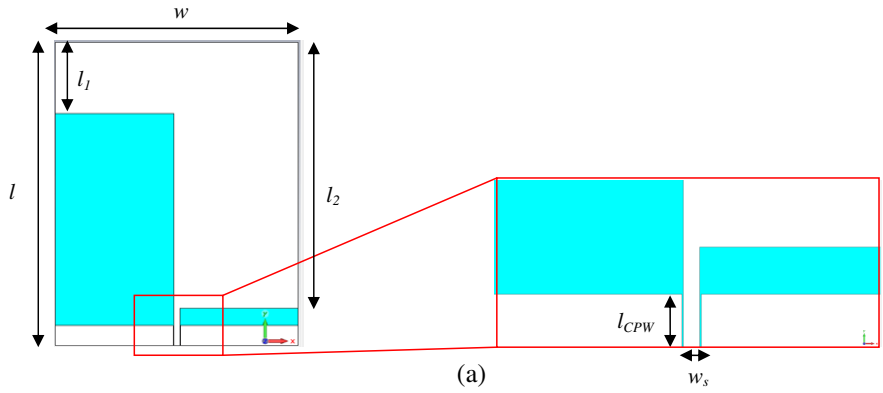

(a)

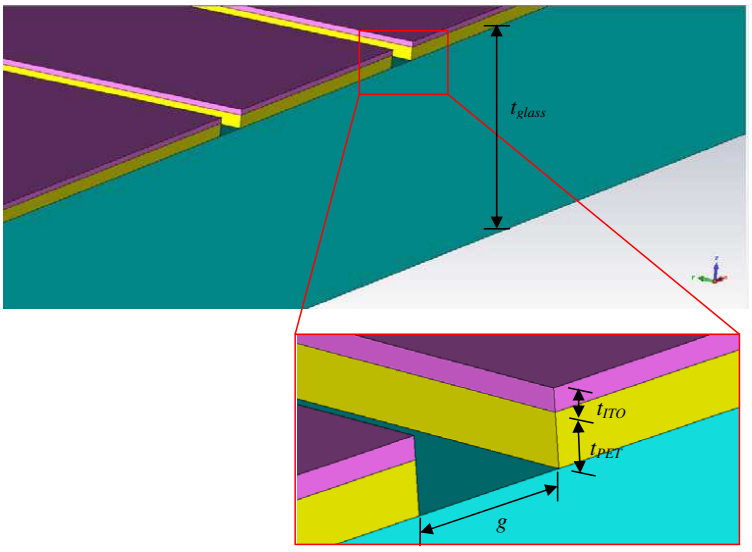

(b)

Figure 1: (a) Geometry of the proposed antenna. (b) Thickness of the antenna.

Table 2: Summary of the antenna parameters.

Description	Parameter	Length (mm)	Description	Parameter	Length (mm)
Length of glass	l	150	Length of CPW ground	l_{CPW}	9.9
Width of glass	w	120	Thickness of glass	t_{glass}	2
Left side length of transparent film	l_1	35	Thickness of PET	t_{PET}	0.1225
Right side length of transparent film	l_2	131.5	Thickness of ITO	t_{ITO}	0.0525
Feed gap	g	0.3	Feed line width	w_s	3

3. SIMULATED RESULT AND DISCUSSIONS

The performance of this transparent antenna is very sensitive to many parameters. The parameters can be as the size of the radiation element, the size of the ground plane, and the gap between the plane and the ground [17]. Since the frequency range should be at least 500 MHz to 800 MHz to receive all the stations. So a parametric study has been done to achieve the frequency range. Figure 2 shows the variation of reflection coefficient magnitude (dB) by changing the left side length, l_1. The simulated reflection coefficient magnitude covers from 500 to 800 MHz is at length of 25 mm to 60.5 mm. At 96 mm, the bandwidth becomes smaller and there is no radiation at 131.5 mm length. Table 3 has shown the bandwidth of the left side length changes. It can be concluded that the longer the left side length, the lower the bandwidth.

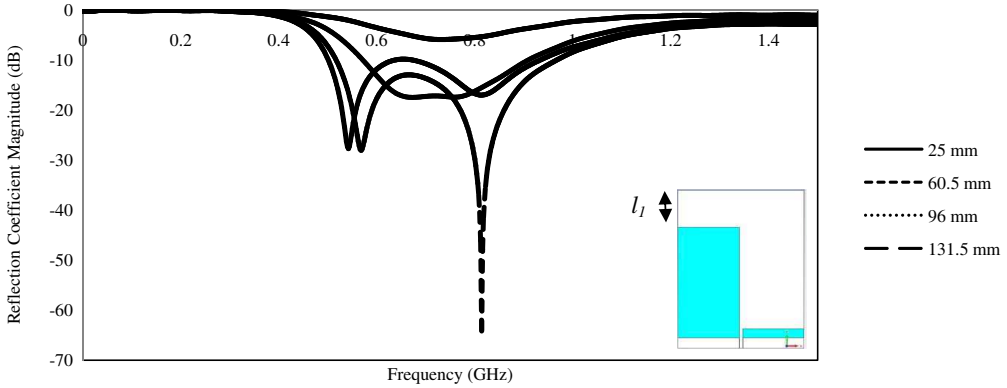

Figure 2: The variation of reflection coefficient magnitude at different left side length.

Figure 3 shows the simulated result that completely covered frequency range of 500 MHz to 800 MHz at the left side length, l_1 of 35 mm. The frequency range is 502 MHz to 950 MHz. It completely covers the frequency at GunungPulai transmitter base station. The bandwidth obtained is 448 MHz or 61.71% of the fractional BW. The minimum value of reflection coefficient magnitude obtained is −32.68 dB.

Figure 4 shows the simulated radiation pattern at 514 MHz, 629 MHz, 642 MHz, 658 MHz, 674 MHz and 743.25 MHz, respectively. All the radiation patterns are omnidirectional. The omnidirectional radiation is acceptable for indoor TV reception. Due to such pattern form, low gain are

Table 3: The bandwidth of left side length.

Left side length, l_1 (mm)	Frequency range (MHz)	Bandwidth (MHz)
25	502–934	432
60.5	516–968	452
96	572–910	338
131.5	No, higher than −10 dB	-

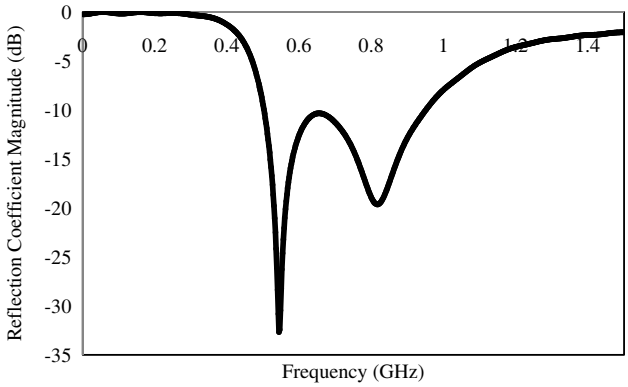

Figure 3: The simulated return loss at 35 mm left side length, l_1.

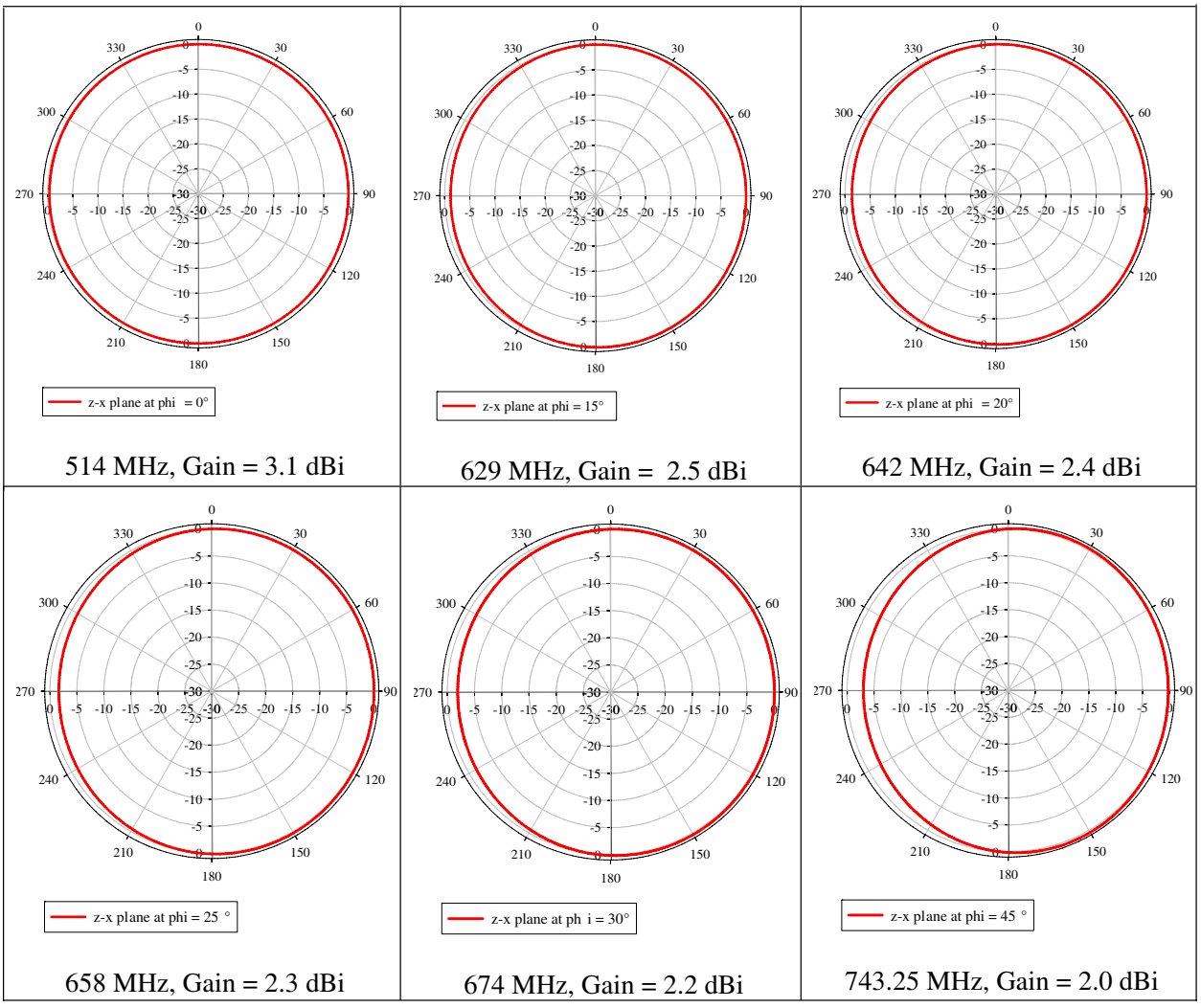

Figure 4: The simulated radiation pattern at frequency of 514 MHz, 629 MHz, 542 MHz, 658 MHz, 674 MHz and 743.25 MHz.

achieved as it varies from 2.0 dBi to 3.1 dBi at the specific channel frequency shown in Figure 4.

4. CONCLUSION

The proposed indoor transparent antenna has been presented. The transparent conductive film implemented by the antenna shows that the coverage frequency fulfilled the requirement of television signal reception. The simulated frequency range successfully covers the frequency from 502 MHz to

950 MHz which including the necessary frequency band for TV broadcasting; 510 MHz to 750 MHz. Therefore, the bandwidth achieved was 448 MHz (or 61.71 %) with gain is at least 2.0 dBi. By having an omnidirectional pattern in all frequency channels, such antenna could become a good candidate for indoor TV reception.

ACKNOWLEDGMENT

The authors wish to thank Ministry of Higher Education (MOE) and Universiti Teknologi Malaysia (UTM) for providing some funding through GUP (Vote 00G36, Vote 00M21, Vote 00M22, Vote 05H34 and Vote 04H36) to enable this work to be completed.

REFERENCES

1. "Unlicensed operation in the TV broadcast bands," *Third Memorandum Opinion and Order*, 104–186, Apr. 2012.
2. Zhou, S., et al., "Broadband dual frequency sleeve monopole antenna for DTV/GSM applications," *Electronics Letters*, Vol. 45, 766–768, 2009.
3. Chen, O. T. C. and T. Chih-Yu, "CPW-fed wideband printed dipole antenna for digital TV applications," *IEEE Transactions on Antennas and Propagation*, Vol. 59, 4826–4830, 2011.
4. Lin, D.-B., et al., "Spiral and multimode antenna miniaturization for DTV signal receptions," *IEEE Antennas and Wireless Propagation Letters*, Vol. 9, 902–905, 2010.
5. Chen, H.-Y., et al., "A miniaturized built-in antenna for USB digital television (DTV) tuners," *2010 IEEE Antennas and Propagation Society International Symposium (APSURSI)*, 1–4, 2010.
6. Paul, D. L., et al., "A low-profile textile antenna for reception of digital television and wireless communications," *2012 IEEE Radio and Wireless Symposium (RWS)*, 51–54, 2012.
7. Paul, D. L., et al., "Conformability of a textile antenna for reception of digital television," *2010 Loughborough Antennas and Propagation Conference (LAPC)*, 225–228, 2010.
8. Caso, R., et al., "An integrated dual-band PIFA for DVB-T and WiMAX applications," *IEEE Antennas and Wireless Propagation Letters*, Vol. 10, 1027–1030, 2011.
9. Luyi, L., et al., "Tunable multiband handset antenna operating at VHF and UHF bands," *IEEE Transactions on Antennas and Propagation*, Vol. 61, 3790–3796, 2013.
10. Jusoh, M., M. F. Jamlos, M. R. Kamarudin, Z. A. Ahmad, M. A. Romli, and N. Sabri, "A dual bevel compact planar monopole antenna for UHF application," *PIERS Proceedings*, 1506–1509, Kuala Lumpur, Malaysia, Mar. 27–30, 2012.
11. Jusoh, M., et al., "A compact dual bevel planar monopole antenna with lumped element for ultra high frequency/very high frequency application," *Microwave and Optical Technology Letters*, Vol. 54, 156–160, 2012.
12. Elshafie, H. E. A., et al., "Spectrum utilization in Malaysia," *3th International Graduate Conference on Engineering, Science and Humanities (IGCESH)*, 1–3, 2010.
13. Elshafie, H., et al., "Measurement of UHF signal propagation loss under different altitude in hilly environment," *Applied Mechanics and Materials*, Vol. 311, 37–42, 2013.
14. Palantei, E., et al., "Internal antennas for digital TV receiver," *2011 IEEE International Symposium on Antennas and Propagation (APSURSI)*, 817–820, 2011.
15. Peter, T., et al., "A novel transparent UWB antenna for photovoltaic solar panel integration and rf energy harvesting," *IEEE Transactions on Antennas and Propagation*, Vol. 62, 1844–1853, 2014.
16. Serra, C. C., et al., "Mirror-integrated transparent antenna for RFID application," *IEEE Antennas and Wireless Propagation Letters*, Vol. 10, 776–779, 2011.
17. Katsounaros, A., et al., "Optically transparent ultra-wideband antenna," *Electronics Letters*, Vol. 45, 722–723, 2009.
18. Peter, T., et al., "Miniature transparent UWB antenna with tunable notch for green wireless applications," *2011 International Workshop on Antenna Technology (iWAT)*, 259–262, 2011.
19. Lee, C.-T., et al., "The transparent monopole antenna for WCDMA and WLAN," *IEEE Annual Wireless and Microwave Technology Conference, WAMICON'06*, 1–3, 2006.
20. Azini, A. S., M. R. Kamarudin, T. A. Rahman, H. U. Iddi, A. Y. Abdulrahman, and M. F. B. Jamlos, "Transparent antenna design for WiMAX application," *Progress In Electromagnetics Research*, Vol. 138, 133–141, 2013.

21. Neveu, N., et al., "Transparent microstrip antennas for CubeSat applications," *2013 IEEE International Conference on Wireless for Space and Extreme Environments (WiSEE)*, 1–4, 2013.
22. Yasin, T., et al., "A comparative study on two types of transparent patch antennas," *2011 XXXth URSI General Assembly and Scientific Symposium*, 1–4, 2011.
23. Saberin, J. R. and C. Furse, "Challenges with optically transparent patch antennas," *IEEE Antennas and Propagation Magazine*, Vol. 54, 10–16, 2012.
24. Jae, S. H., et al., "A method for improving the efficiency of transparent film antennas," *IEEE Antennas and Wireless Propagation Letters*, Vol. 7, 753–756, 2008.
25. Peter, T., et al., "A novel technique and soldering method to improve performance of transparent polymer antennas," *IEEE Antennas and Wireless Propagation Letters*, Vol. 9, 918–921, 2010.

Electrical Characterization of GaN

Nazir A. Naz[1], **M. Suleman**[2], **and Akbar Ali**[1, 2]

[1]Department of Applied Physics
Federal Urdu University of Arts, Science and Technology Islamabad, Pakistan
[2]Department of Basic Sciences, Riphah International University, Islamabad, Pakistan

Abstract— GaN based blue light emitting diodes were characterized, using deep level transient spectroscopy technique. Nine defects having ionization energies: 0.06, 0.08, 0.09, 0.14, 0.10 , 0.14, 0.14, 0.16 and 0.65 eV and corresponding capture cross-sections (σ_∞)4.0×10^{-14}, 1.3×10^{-13}, 7.6×10^{-14}, 6.95×10^{-13}, 3.53×10^{-14}, 1.6×10^{-13}, 8.0×10^{-14}, 7.34×10^{-14} and 1.8×10^{-5} cm^2 were identified. Respective concentrations were found to be 8.81×10^{13}, 8.56×10^{13}, 8.90×10^{13}, 8.68×10^{13}, 8.62×10^{13}, 8.56×10^{13}, 8.66×10^{13}, 8.57×10^{13}, 8.54×10^{13}, 8.68×10^{14}, and 8.46×10^{14} cm^{-3}.

1. INTRODUCTION

GaN and associated alloys (III-N compounds) have been focus of research for more than three decades [1–4] due to their wide verity of applications in opto-electronic devices. Tunable band gap of these materials (0.7 to 6.1 eV) makes their use versatile in the fields of ultra-high frequency (RF) components [1, 5, 6]. The realization of hetero-structures out of these materials opened a new era in the field of telecommunication. High electronic mobility transistors (HEMT's) based on these materials, can support power densities ten times higher than those accessible with silicon and gallium arsenide [1, 7]. These materials are famous for their excellent optical properties such as laser diodes (LDs), high performance light emitting diodes (LEDs), and solar cells [8–12]. Laser diodes are used in high density optical processing systems like digital versatile disk random access memory (DVD-Ram, and DVDR) [13–16]. Deep level defects in these materials may act as non radiative recombination or trapping centers, which significantly decrease the radiative efficiency and increase the thresh hold current density, thus deteriorate device performance [13, 17, 18]. To improve the performance of such devices and, particularly, to increase the light intensity, it is, therefore, important to optimize growth conditions of each layer of the diodes by defect engineering [13, 19]. The knowledge of deep level defects is of primary importance for the improvement of performance of devices based on III-N compounds. The deep levels can be easily identified by deep level transient spectroscopy (DLTS), a powerful and well established technique for the investigation of electronic properties of deep level defects in semiconductors [20]. In this report we present a study of defects in GaN material by DLTS technique.

2. EXPERIMENTAL

High bright blue GaN based light emitting diodes imported from Hebei I.T, China [21] were used as our samples. The samples are single blue color emitting devices which have high bright output, low power consumption, high reliability and long life.

Capacitance-voltage characteristics of GaN based LEDs were measured to determine the quality of diodes using capacitance meter Boonton 7200. Typical capacitance-voltage characteristics have been shown in Fig. 1. The data points in plot, $1/C^2$ Vs applied voltage v, are found approximately fit on a straight line, indicating junction as a step junction [22]. However, a careful examination shows that two different straight lines can be fit in the voltage range 0–4 and 6–10 volts. The least square fitting show that shallow level concentration on p- and n-sides of the junction are nearly equal [23].

For DLTS [20] measurements, a deep level transient spectrometer DLS-83D, manufactured by Semi trap, Hungary was used. The spectrometer provides a quiescent reverse bias and filling pulse with a repetition rate from 0.1 Hz to 1 kHz and temperature accuracy of better than 1 K. Output of the sensor and spectrometer is fed to CPU through a data bus. Shielded cables were used to provide connections from the samples to the spectrometer. Sample is mounted in a sample holder of the cryostat with the help of two spring-loaded pins for this purpose.

Temperature of the sample is lowered to 77 K by slowly lowering the sample holder into liquid nitrogen container and raised to room temperature or above, by gradually lifting the sample holder or by increasing the current through a heater embedded inside the sample holder. The rate of

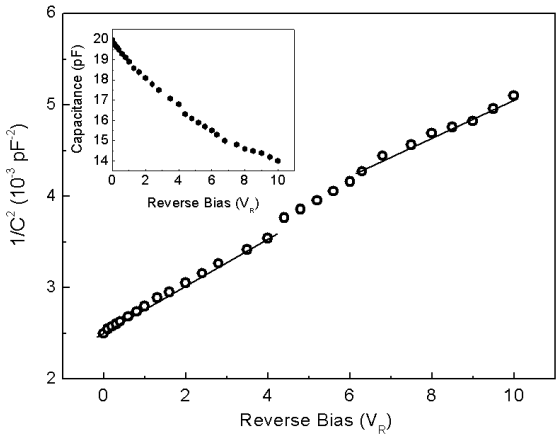

Figure 1: Typical $1/C^2$ verses reverse bias plot of GaN diodes, inset shows capacitance verses voltage graph.

emission of the charge carriers from deep levels is monitored by measuring change in capacitance of the diode under quiescent reverse bias using the above setup. Output of the spectrometer gives a scan. For maximum emission rate of a defect, scan shows a peak at a fixed temperature. DLTS scan exhibits different peaks for different defects. The DLTS scans were repeated at different emission-rate windows to obtain a data for estimating the energy-position of the traps in the band gap. Emission rates were plotted against the temperature (K) on the semi-logarithmic scale using the equation,

$$\ln\left(\frac{e_n}{T^2}\right) = \ln A + [-\Delta E/k_B T]$$

The slope of the best fit line of the Arrhenius plot, $\ln[e_n/T^2]$ Vs $1000/T$ gives activation energy of the deep levels [20]. The activation energies of different defects were obtained from such best-fit lines. Capture cross sections (σ_∞) for the corresponding levels were calculated from the y-intercept of $\ln[e_n/T^2]$ Vs $1000/T$ at $T = \infty$.

3. RESULTS AND DISCUSSION

A typical DLTS scan is shown in Fig. 2. At least fourteen peaks, $P1$–$P14$, have been noticed in the scans. Emission rate data for peaks $P1$, $P2$, and $P12$–$P14$ were not sufficient to get a reliable energy, therefore, not reported. Measured activation energies of the defects assigned to peaks $P3$–$P11$ are 0.06, 0.08, 0.09, 0.14, 0.10, 0.14, 0.14, 0.16 and 0.65 eV and corresponding capture cross-sections (σ_∞) are 4.0×10^{-14}, 1.3×10^{-13}, 7.6×10^{-14}, 6.95×10^{-13}, 3.53×10^{-14}, 1.6×10^{-13}, 8.0×10^{-14}, 7.34×10^{-14} and 1.8×10^{-5} cm^2. Respective concentrations are found to be 8.81×10^{13}, 8.56×10^{13}, 8.90×10^{13}, 8.68×10^{13}, 8.62×10^{13}, 8.56×10^{13}, 8.66×10^{13}, 8.57×10^{13}, 8.54×10^{13}, 8.68×10^{14}, and 8.46×10^{14} cm^{-3}. The data is also listed in Table 1.

Although, in literature [24–26], deep levels in this material have been studied, however, most of the investigations limited to electron trapping centers related to doping impurities such as Si and Se. Both electron and hole emitting deep levels need to be examined quantitatively to study the defects responsible for reduction of radiative efficiency. We performed DLTS measurements to study electron and hole emitting centers. It is reported in literature that inherent threading dislocation density in this material is of the order of 10^9–10^{10} cm^{-2} [27, 28]. Such a high dislocation density could be attributed to the large difference in lattice constants and thermal expansion coefficient between the substrate and epitaxial GaN films. Characteristics of the devices could be strongly influenced by the high dislocation density and limit the performance by affecting life time, mobility and the quantum efficiency of radiative recombination.

Recent theoretical studies on native point defects in III–V nitrides [29, 30] show that nitrogen vacancies have the lowest formation energy in p-type GaN and can be produced in a significant concentration during the growth. We can, thus, speculate that defects reported in this work are nitrogen-vacancy related defects. Ionization energy, 0.65 eV, of a trap observed in this study is comparable to that reported by Dyba et al. [18] for trap E (0.63). This trap was identified with single vacancy or V_{Ga}-O complex [18, 31}. As DLTS signal from both sides is possible as a majority signal we are, therefore, of the opinion that energy state (0.65 eV) is due to vacancy or V_{Ga}-O complex [18, 31].

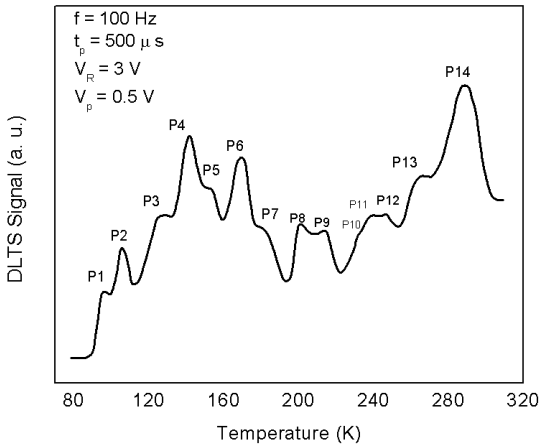

Figure 2: A typical DLTS scan of GaN-LEDs.

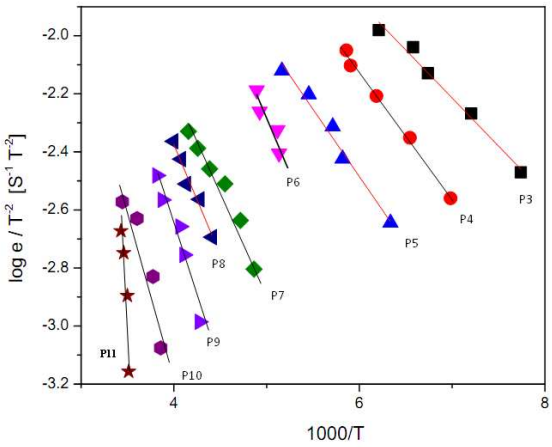

Figure 3: Emission rate data of defects corresponding to peaks $P3$ to $P11$.

Table 1: Characteristics of defects related to different peaks.

Peaks	**Activation Energy (eV)**	**Capture Cross-section (σ_∞) (cm^2)**
$P3$	0.059	4.0×10^{-14}
$P4$	0.083	1.3×10^{-13}
$P5$	0.087	7.6×10^{-14}
$P6$	0.107	6.94×10^{-13}
$P7$	0.124	3.53×10^{-14}
$P8$	0.142	1.6×10^{-13}
$P9$	0.141	8.04×10^{-14}
$P10$	0.155	7.34×10^{-14}
$P11$	0.648	1.8×10^{-5}

REFERENCES

1. Charfeddine, M., M. Gassoumi, H. Mosbahi, C. Gaquiére, M. A. Zaidi, and H. Maaref, *Journal of Modern Physics*, Vol. 2, 1229–1234, 2011.
2. Khan, M. A., A. Bhattarai, J. N. Kuznia, and D. T. Olson, "High electron mobility transistor based on a GaN-AlX, Ga1-XN heterojunction," *Applied Physics Letters*, Vol. 63, 1214–1215, 1993.
3. Omling, P., E. R. Weber, L. Montelius, H. Alexander, and J. Michel, *Physical Review B*, Vol. 32, 6571–6581, 1985.
4. Kim, H., S. J. Park, and H. Hwang, "Design and fabrication of highly efficient ganbased light-emitting diodes," *IEEE*, Vol. 49, 1715–1721, 2002.
5. Semra, L., A. Teliaa, and A. Soltani, *Surface and Interface Analysis*, Vol. 42, 799–802, 2010.
6. Dumka, D. C., C. Lee, H. Q. Tserng, P. Saunier, and M. Kumar, *Electronics Letters*, Vol. 40, 1023–1024, 2004.
7. Dupuis, R. D., *Journal of Crystal Growth*, Vol. 178, 56–73, 1997.
8. Chu, M.-T., W. Y. Liao, R.-H. Horng, T.-Y. Tsau, T.-B. Wu, S.-P. Liu, M.-H. Wu, and R.-M. Lin, Vol. 32, 922–924, 2011.
9. Horng, R. H., Y. A. Lu, and D. S. Wuu, *IEEE Photon. Technol. Lett.*, Vol. 23, 54–56, 2011.
10. Hansen, M., J. Piprek, P. M. Pattision, J. S. Spech, S. Nakamura, and S. P. Den Baars, *Applied Physics Letters*, Vol. 81, 4275–4277, 2002.
11. Horng, R. H., M. T. Chu, H. R. Chen, W. Y. Liao, and D. S. Wuu, *IEEE Electron Device Letters*, Vol. 31, No. 6, 585–587, 2010.
12. Dahal, R., B. Pantha, J. Li, J. Y. Lin, and H. X. Jiang, *Applied Physics Letters*, Vol. 94, 063505, 2009.

13. Kima, D. S., K. C. Kima, Y. C. Shina, D. H. Kang, B. J. Kim, Y. M. Kim, Y. Park, and T. G. Kim, *Physica B*, Vol. 376–377, 610–613, 2006.
14. Yagi, T., H. Nishiguchi, Y. Yoshida, M. Miyashita, M. Sasaki, Y. Sakamoto, K. I. Ono, and Y. Mitsui, *IEEE J. Sel. Top. Quantum Electron.*, Vol. 9, 1260, 2003.
15. Shima, A., H. Tada, K. Ono, M. Fujiwara, T. Utakoji, T. Kimura, M. Takemi, and H. Higuchi, *IEEE Photon. Technol. Lett.*, Vol. 9, 413, 1997.
16. Xi, Y. and E. F. Schubert, *Applied Physics Letters*, Vol. 85, 2163–2165, 2004.
17. Domen, K., K. Sugiura, C. Anayama, M. Kondo, M. Sugawara, T. Tanahashi, and K. Nakajima, *J. Cryst. Growth*, Vol. 115, 529, 1991.
18. Dyba, P., E. Placzek-Popko, E. Zielony, Z. Gumienny, S. Grzanka, R. Czernecki, and T. Suski, *ACTA Physica Polonica*, Vol. 119, 2011.
19. Kaniewska, M., D. Krynska, and M. Wesolowski, *Opt. Mater.*, Vol. 17, 283, 2001.
20. Lang, D. V., *J. Appl. Phys.*, Vol. 58, 3023, 1974.
21. Data sheet Hebei I.T, China, LED, specification.
22. Neamen, D., *Semiconductor Physics and Devices*, 3rd Edition, University of Mexico, 2011.
23. Tsarova, T., T. Wosinski, A. M. Kosa, C. Skierbiszewski, I. Grzegory, and P. Perlin, *Acta Physica Polonica A*, Vol. 112, 331, 2007.
24. Nojima, S., H. Tanaka, and H. Asahi, *J. Appl. Phys.*, Vol. 59, 3489, 1986.
25. Watanabe, M. O. and Y. Ohba, *J. Appl. Phys.*, Vol. 60, 1032, 1986.
26. Sugiura, K., K. Domen, M. Sugawara, C. Anayama, M. Kondo, T. Tanahashi, and K. Nakajima, *JAP*, Vol. 70, No. 9, 4946–4949, 1991.
27. Elsner, J., R. Jones, P. K. Sitch, V. D. Porezag, M. Elstner, T. Frauenheim, M. I. Heggie, S. Oberg, and P. R. Briddon, *Phys. Rev. Lett.*, Vol. 79, 3672–3675, 1997.
28. Chu, M.-T. and W. Y. Liao, *IEEE Electron Device Letters*, Vol. 32, 922–924, 2011.
29. Tsarova, T., T. Wosinski, A. M. Kosa, C. Skierbiszewski, I. Grzegory, and P. Perlin, Vol. 112, 331–337, Institute of High Pressure Physics "unipress", Polish Academy of Sciences, 2007.
30. Van de Walle, C. G. and J. Neugebauer, *Appl. Phys.*, Vol. 95, 3851, 2004.
31. Ashgar, M., P. Muret, B. Beaumont, and P. Gibart, *Mater. Sci. Eng. B*, Vol. 113, 248, 2004.

Study of p-type Porous Silicon

Nazir A. Naz, M. Jamil, and Akbar Ali
Federal Urdu University of Arts, Science and Technology, Islamabad G-7/1, Pakistan

Abstract— Porous silicon fabricated by electrochemical etching was studied using Scanning Electron Microscope and Elemental Differential X ray Analyzer. The etched samples were found to emit red luminescence when exposed to ultraviolet light of wavelength 254 nm. Micrographs of the samples obtained by Scanning Electron Microscope showed a porous layer at the surface. Elemental Differential X ray Analysis provided the evidence of oxidation of a porous layer. Red luminescence emitted from the surface may be attributed to confinement of holes in the oxidized layer.

1. INTRODUCTION

Porous silicon (PS) has received considerable attention due to its photo- and electro-luminescence emission in the visible range. Surface-pore morphology of etched silicon plays an important role in emission process [1], which is controlled by parameters governing the etching reaction [2, 3]. A shift in the photoluminescence spectra to longer or shorter wavelength also depends upon etching conditions [4–6]. Though a lot of work has been done on porous silicon yet a comprehensive picture to understand the mechanism that produces luminescence in the visible range is still not clear [3]. Surface reaction follows different paths under different etching conditions. In an earlier study [1], Fluorine concentration (Si-F) was found on the etched surface after a reaction with concentrated HF. In another report by R. L. Smith et al. [2], HF treated silicon surface showed a high concentration of hydride species with a predominance of monohydride on the etched surface. Such discrepancies suggest that more work is required to understand the role of porous silicon in photo- and electro-luminescence emission [1]. We report here a study on oxidized surface of HF-pretreated silicon using Scanning Electron Microscope (SEM) and Elemental Differential X ray Analyzer (EDX).

2. EXPERIMENTAL

One side polished p-type silicon wafers have been used in electrochemical etching. 1–20 Ω cm resistive wafers were grown along (100)-direction by Czochralski (CZ) technique. 40% HF and 95% ethanol solution (1 : 1 by volume) was used as an electrolyte. Sample and platinum wire, 0.5 cm apart, were used as an anode and cathode, respectively. Approximately, 80% area of the samples ($50 \times 30\,\mathrm{mm}^2$) was immersed into the electrolyte. A constant current of $32\,\mathrm{mA/cm}^2$ was maintained for two hours across the electrodes. Etching setup is shown in Fig. 1.

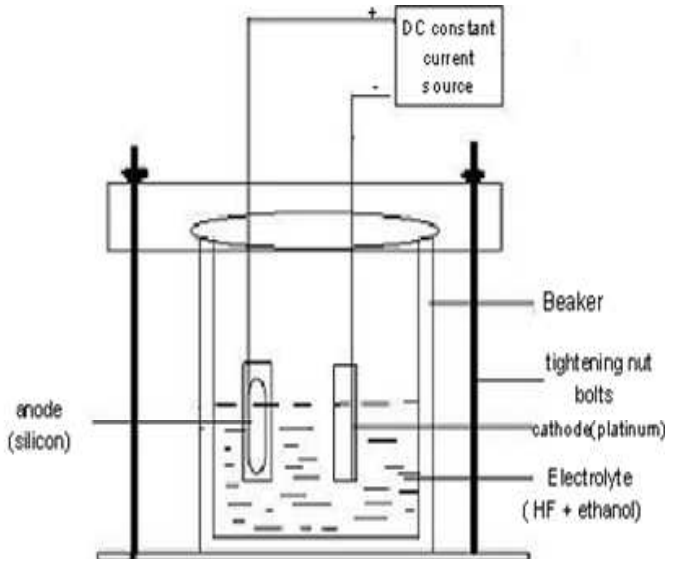

Figure 1: Anodic etching setup.

3. MEASUREMENTS

Immediately after anodic etching, the samples were taken out from the solution and rinsed with de-ionized water and then dried in laboratory air. Samples were exposed to 254 nm ultraviolet (UV) light, red luminescence was found to emit from selective parts of the samples, but within $\sim$ 24 hours the luminescence intensity increased to maximum and whole etched part of the wafer started to emit red luminescence. Further characterization of the as-grown (named A) and etched (named B) samples was carried out using Scanning Electron Microscope (SEM), model JSM-5910 JEOL and Elemental Differential X ray Analyzer (EDX), model INCA 200. SEM micrographs, taken at 500 and 1000 magnification with 20 kV accelerating voltage, are shown in Fig. 2, respectively.

SEM micrographs (a) and (b) of as-grown samples taken at 500 and 1000 magnification, respectively, depict a regular arrangement of rectangle-like grains (high lighted in the figure) with sharp boundaries. Dimensions of grains are roughly less than 10 µm. After etching, micrographs (c) and (d) recorded at 500 and 1000 magnifications are shown in Fig. 2. Porous layer, formed on the surface can be seen in the images. Etching appears to proceed in all direction around the

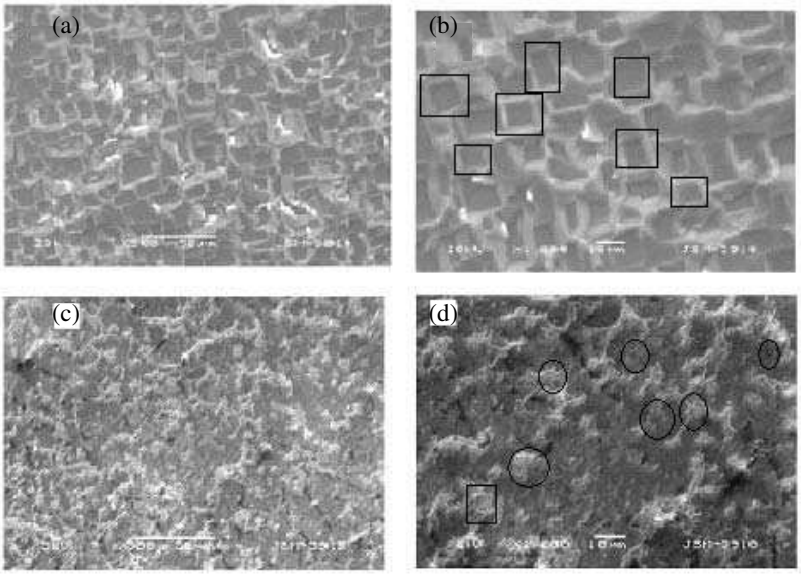

Figure 2: Micrographs of reference and etched samples.

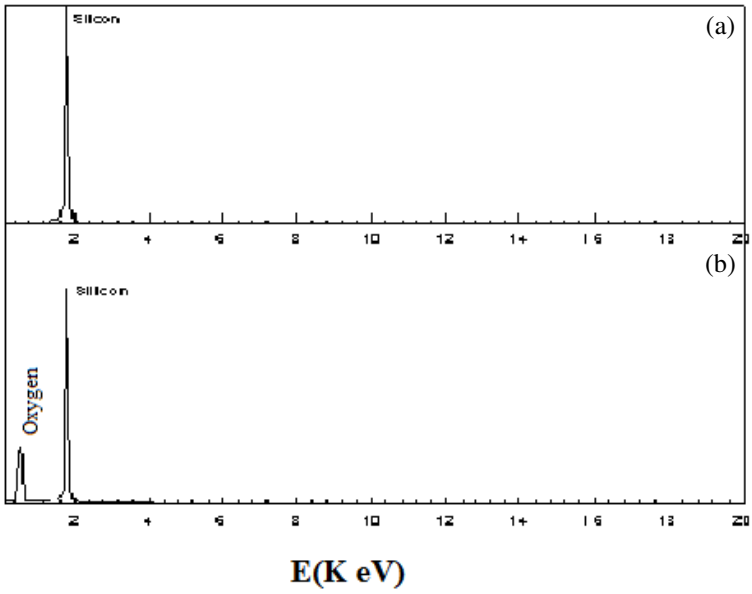

Figure 3: EDX spectra for (a) as-grown (b) etched, samples.

first attacking point, following channel like paths in different directions, as shown by circles in the Fig. (d). Etching on some places proceeds to follow screw like paths as highlighted with a rectangle. After etching grain boundaries disappeared and a new morphology, full of pores, appeared on the surface. Samples were stored in laboratory air. It is noted that luminescence increases with the passage of time, may be due to oxidation. Elemental analyses of the samples have been performed with Elemental Differential X ray Analyzer to check the formation of porous layer on the surface of etched surface. EDX measurements of the samples A and B are shown in Figs. 3(a) and (b), respectively.

Only a single peak corresponding to pure silicon is seen in the spectrum (a). The scan clearly indicates that sample A is 100% pure silicon because no trace of any other element has been found. On the other hand EDX spectrum of etched sample B, shown in Fig. 3(b), reveals an additional small peak along with large peak of silicon. Presence of small peak clearly indicates the formation of oxidized layer.

Weight and atomic percentages of elements measured by EDX are given in Table 1.

Table 1: Weight and atomic percentage of oxygen and silicon in etched samples.

Elements	weight %	Atomic %
Oxygen	27	40
Silicon	73	60

4. RESULTS AND DISCUSSION

The scanning electron micrograph (a) of Fig. 1, recorded at 500 magnification for as grown sample (A) shows a uniformly distributed regular pattern of rectangular shaped grains of (100) silicon. In the Fig. (a), grain boundaries clearly reflect the orientation of the crystal. The same observation is demonstrated in Fig. (b) taken at 1000 magnification. The scanning electron micrograph of etched sample, B, obtained at 500 magnification is shown in Fig. 2 (c). This micrograph shows that regular pattern of rectangular shaped grains has vanished away and instead a porous growth appeared on the surface. The same surface has also been examined using 1000 magnifications, as shown in Fig. 2(d). In both, (c) and (d), figures micro pours are found to distribute uniformly all over the surface.

Weight and Atomic percentage of oxygen and silicon, measured by Elemental Differential X-ray Analyzer (EDX), given in Table 1, indicate the oxidation of the surface in air after etching. Several studies [6–9] have been performed to understand the reaction of silicon surface pretreated in a concentrated HF solution. It was found that fluorine is rapidly replaced by oxygen containing species, when such surface after rinsing with water is placed in air. The exchange reaction is shown by the following equation [1],

$$\text{Si-F} + \text{H}_2\text{O} \rightarrow \text{Si-OH} + \text{HF}$$

It is thought that OH-group on the surface become polarized and destabilized the Si-Si bonding. The weakened bond is attached with polar H_2O molecule making possible for oxygen atom to form Si-O-Si bonding. Since the Si-O bond in silica has some ionic character [1], oxygen insertion gives rise to a positive charge on an adjacent Si surface atom there by facilitating OH^- to attack on that Si atom followed by oxidation of the Si-H bond. The remaining Si-O-Si bonds can be oxidized in a similar fashion. It is clear that Si-O-Si group dominates on the etched surface and Si-H group eliminates with time. It can be assumed that in the beginning, immediately after taking out the sample from the cell, other species like hydrides, fluorides and hydroxides are present on the surface, disappear with time and oxidation of the surface increases.

Our results obtained from scanning electron microscope and Elemental Differential X-ray Analyzer (EDX) gives the direct evidence of growth of oxide at the surface of silicon. The porous oxidized surface appears to be responsible for the emission of red color when illuminated by Ultra Violet light. Kebbi et al. [8] and Aria et al. [9] pointed out that passivated surface and quantum confinement of charge carriers are responsible for red luminescence. We propose that oxidized layer of the pores or quantum dots formed on the surface due to etching is of the order of nm or comparable to Bohr radius. This very thin layer of atomic dimension is assumed to be responsible for quantum confinement.

5. CONCLUSIONS

Investigation of the etched silicon has been carried out by SEM and EDX. Oxidized porous layer was found on the surface of etched silicon. Hole confinement of oxidized surface of pores was assumed to be responsible for red luminescence.

REFERENCES

1. Boonekamp, E. P. and J. J. Kelly, *J. Appl. Phys.*, Vol. 75, 8121, 1994.
2. Smith, R. L. and S. D. Collins, *J. Appl. Phys.*, Vol. 71, R_1, 1992.
3. Salonen, J., V. P. Lehto, and E. Laine, *J. Applied Surface Science*, Vol. 120, 191, 1997.
4. Prokes, S. M., *J. Appl. Phys. Lett.*, Vol. 62, 3244, 1993.
5. Mruyama, T. and S. Ohtani, *J. Appl. Phys. Lett.*, Vol. 65, 1346, 1994.
6. Kontkiewicz, A. J., A. M. Kontkiewiez, J. Siejka, S. Sen, G. Novak, A. M. Hoff, P. Sakthivel, K. Ahmed, P. Mukherjee, S. Witanachehi, and J. Lagowski, *Appl. Phys. Lett.*, Vol. 65, 1436, 1994.
7. Zhao, Y., et al., *Applied Surface Science*, Vol. 252, 1065–1069, 2005.
8. Kabbi, H., N. Miliki, M. Cheynet, W. Saikalay, D. Gibbert, B. Bassïs, B. Yangui, and A. Charï, *Crystal Res. Tech.*, Vol. 41, 154–162, 2006.
9. Arita, Y., K. Kuranari, and Y. Sunohara, *Journal of Applied Physics*, Vol. 15, 1655–1664, 1976.

Wideband Antenna for Microwave Imaging

R. Yahya[1, 2], **M. R. Kamarudin**[2], **and N. Seman**[2]

[1]Faculty of Electrical and Electronic Engineering, Universiti Tun Hussein Onn Malaysia (UTHM)
Parit Raja, Batu Pahat, Johor 86400, Malaysia
[2]Wireless Communication Center (WCC), Universiti Teknologi Malaysia (UTM)
Skudai, Johor Bahru, Johor 81310, Malaysia

Abstract— A robust antenna which designed on fully textile material is presented. A denim jean textile is used as the dielectric substrate while the radiating elements are using conductive shieldit super textile. The simulated operating bandwidth of the antenna is 4540 MHz with maximum −10 dB reflection coefficient magnitudes of 1.46–6 GHz. The antenna has bi-directional radiation pattern and provides simulated gain values that fluctuate between 1.5 to 7 dBi at the entire frequency range. This antenna which operates in the mentioned wideband frequency is highly acceptable for microwave imaging application. In addition, the capability of the textile material to be formed into flexible shape such as bending will be an advantage of its use in flexible microwave imaging purpose.

1. INTRODUCTION

Microwave imaging is a sensing technique that recently proven its use in providing diagnostic capabilities in several areas including body imaging [1]. Several antennas have been reported for microwave imaging application. Antennas in [2–4] are purposely designed for breast microwave imaging. The antennas are made of FR4 based material. Moreover, antennas in [5–8] are introduced for brain microwave imaging and also for body communication. The respective antennas are made of either FR4 or Rogers microstrip. However, all kinds of the mentioned antennas have limitation on flexible feature such as to be bent on various shape of human body. Therefore, fully textile antenna is seen to be the best option that has flexible feature. The flexibility allows the antenna to be used for various part of human body, not only breast and head. Therefore, a wideband textile antenna is proposed in this study.

2. ANTENNA GEOMETRY

A denim jean textile is used as the dielectric substrate while the radiating elements are using conductive shieldit super textile. The thickness of the substrate is 0.7 mm while the conductive textile is 0.17 mm. The conductive textile has surface resistivity value less than 0.5 Ohm/sq. The antenna that fed by coplanar waveguide (CPW) technique consists of radiating patch and ground that attached on the substrate with the dimension of 80 mm × 77.5 mm as presented in Figure 1. The grounding element that comprises of slots and blending edges produce a wideband impedance

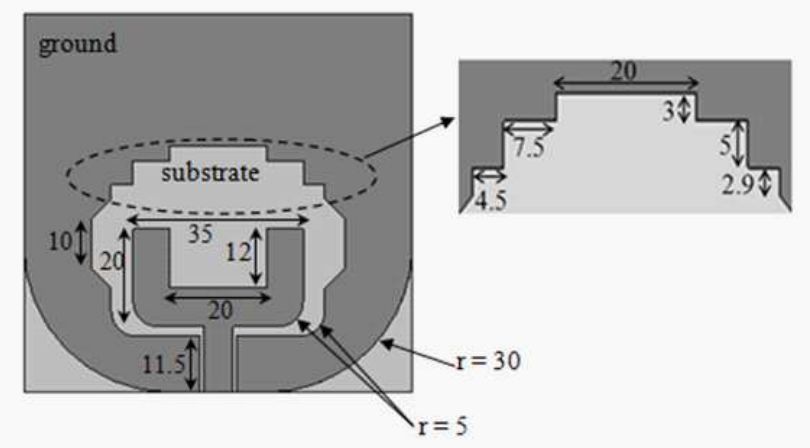

Figure 1: Wideband antenna dimension.

bandwidth. Figure 2 shows the effects of the slots and blending edge on the ground plane towards the reflection coefficients.

According to Figure 2, the initial coplanar waveguide (CPW) ground plane without any slot gives some band rejections. However, while the two symmetrical slots at the side of the ground plane are added, there is improvement of reflection coefficients for the frequency lower than 4 GHz. Furthermore, with the addition of slots at the top side of the ground plane, this enhances the bandwidth for the entire frequency from 1.57 GHz up to 6 GHz. Even though there is slight improvement by having the blending ground plane, it is however improve the reflection coefficient to the lower values and helps the antenna to operate from 1.46 GHz to 6 GHz.

3. RESULT AND DISCUSSION

The antenna is observed on its reflection coefficient and gain. Based on the previous section, it has been determined that the antenna may operates from 1.46 GHz to 6 GHz which covers 4540 MHz bandwidth. The gain of the antenna increases with the frequency from 1.5 to 7 dBi, except at 4 GHz as presented in Figure 3. However, the gain of the antenna is acceptable for microwave imaging purpose.

In addition, radiation patterns of the wideband textile antenna have been simulated and the results are shown in Figure 4. The simulated radiation patterns at phi = 90 (E-plane) and phi = 0 (H-plane) for 2, 4, and 6 GHz are presented. All the results show bi-directional radiation patterns

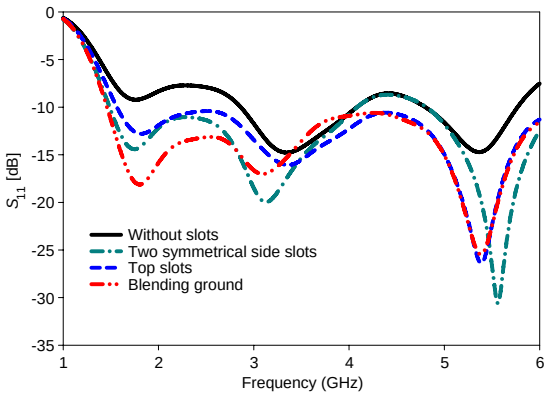

Figure 2: The implementation effects of slots and blending edges on the ground plane.

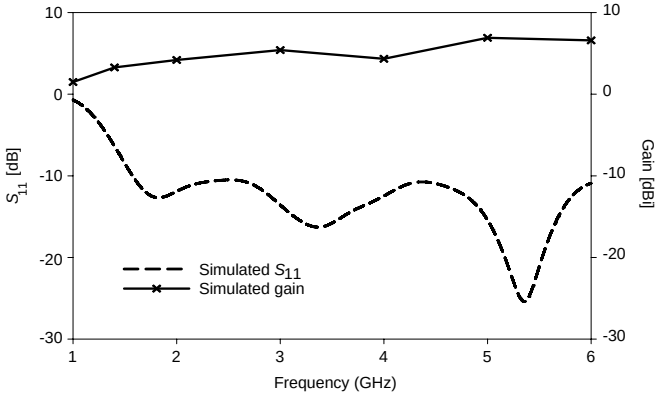

Figure 3: Simulated gain and reflection coefficient magnitudes of the wideband antenna.

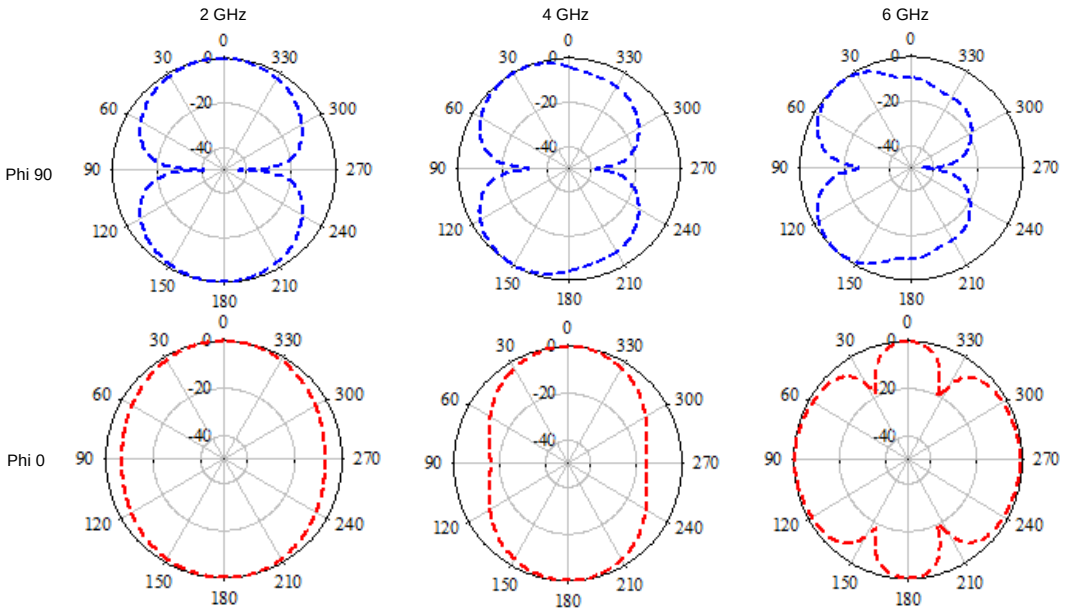

Figure 4: Simulated radiation patterns of the wideband antenna.

at Phi = 90, while it shows nearly omni-directional at phi = 0 at 2 GHz. At the frequency of 4 GHz and 6 GHz, the radiation patterns are different as shown in Figure 4. Moreover, the efficiencies of the antenna changes between 73% and 90% throughout the frequencies.

4. CONCLUSION

Antenna which based on textile material is proposed for microwave imaging. The antenna may operate from as low as 1.46 GHz to 6 GHz, provided with the acceptable gain values. The antenna which is textile based material provides flexibility features of microwave imaging. This will benefit to various shapes and parts of human body microwave imaging application.

ACKNOWLEDGMENT

The authors would like to thank the Ministry of Science, Technology An Innovation (MOSTI) under Science Fund (Vote 4S056: Development of Head Monitoring System Using Array Transceiver for Microwave Imaging Application), Minister of Higher Education (MOHE) and Universiti Teknologi Malaysia for funding this project under GUP Grant (Vote 00M21, Vote 00M22, Vote 04H36 and Vote 05H34). Besides, thanks to the members of Wireless Communication Center (WCC), UTM for helping and providing resources to enable this work to be completed. Authors also would like to thanks to Universiti Tun Hussein Onn Malaysia for the sponsor.

REFERENCES

1. Pastorino, M., *Microwave Imaging,* John Wiley & Sons, 2010.
2. Mahalakshmi, N., N. Indira, and P. Vasikaran, "Design and development of stacked patch antenna for breast cancer detection," *Int. Conf. Work. Emerg. Trends Technol. (ICWET 2011)*, 1150–1152, 2011.
3. Yu, J., M. Yuan, and Q. H. Liu, "A wideband half oval patch antenna for breast imaging," *Progress In Electromagnetics Research*, Vol. 98, 1–13, 2009.
4. Yang, F. and A. Mohan, "Microwave imaging for breast cancer detection using Vivaldi antenna array," *2012 International Symposium on Antennas and Propagation (ISAP)*, 479–482, 2012.
5. Zhang, H. and A. El-Rayis, "A smart antenna array for brain cancer detection," *2011 Loughborough Antennas and Propagation Conference (LAPC)*, 1–4, Nov. 2011.
6. Zhang, H. and B. Flynn, "Microwave imaging for brain tumour detection using an UWB Vivaldi antenna array," *2012 Loughborough Antennas and Propagation Conference (LAPC)*, 1–4, Nov. 2012.
7. Mohammed, B. and A. Abbosh, "Wideband antenna for microwave imaging of brain," *International Conference Series on Intelligent Sensors, Sensor Networks and Information Processing (ISSNIP)*, 17–20, 2011.
8. Kamarudin, M. R., Y. I. Nechayev, and P. S. Hall, "Onbody diversity and angle of arrival using a pattern switching antenna," *IEEE Transactions on Antenna and Propagation*, Vol. 57, No. 4, 964–971, Apr. 2009.

Projection Method for Solving Scalar Problem of Diffraction of a Plane Wave on a System of Two- and Three-dimensional Obstacles

M. Yu. Medvedik, Yu. G. Smirnov, A. A. Tsupak, and D. V. Valovik
Penza State University, Russia

Abstract— We investigate scalar problem of diffraction of a plane wave on a system of obstacles consisting of disjoint smooth screens Ω_i and volume inhomogeneous bodies Q_j. The original boundary value problem leads to a system of weakly singular integral equations on two- and three-dimensional manifolds. We obtain important results on smoothness of the solution to the system of the integral equations in the interior points of the screens, on the equivalence of the integral equations to the original boundary value problem. Finally we prove the invertibility of the integral operator. We propose Galerkin method for numerical solving of the integral equations. We prove the approximation property for the piecewise constant basis functions as well as the statement of Galerkin method convergence.

1. INTRODUCTION

The scalar problems of diffraction by two- or three-dimensional obstacles only are well known.

For example, in monograph [1] and papers [2–4] one can find detailed description and investigation of acoustic diffraction by volume obstacles. In [5], integral equation of Lippmann-Schwinger type is investigated. The problem of diffraction by acoustically soft (or hard) screens is investigated in [6] — Here the boundary value problem is reduced do integral equation which is treated as pseudodifferential equation in Sobolev spaces.

In this paper, we investigate new problem of diffraction by a compound scatterer consisting of both two- and three-dimensional obstacles. Following [6] we reduce boundary value problem for Helmholtz equation to weakly singular integral equations and prove the invertibility of the integral operator. For numerical solving of the problem we propose Galerkin method.

2. STATEMENT OF THE PROBLEM

Let $\Omega = \bigcup\limits_j \Omega_j$, $(\bar{\Omega}_{j_1} \bigcap \bar{\Omega}_{j_2} = \varnothing,\ j_1 \neq j_2)$ be a union of oriented screens (two-dimensional C^∞-manifolds) with C^∞-smooth boundary $\partial\Omega = \bar{\Omega} \setminus \Omega$. We define δ-neighbourhood of $\partial\Omega_\delta$ as follows: $\partial\Omega_\delta = \{x \in \mathbb{R}^3 : dist(x, \partial\Omega) < \delta\}$.

Let $Q = \bigcup\limits_i Q_i$, $(\bar{Q}_{i_1} \bigcap \bar{Q}_{i_2} = \varnothing,\ i_1 \neq i_2)$ be a union of bounded volume bodies with piecewise smooth boundary ∂Q. Assume also that $\bar{Q} \cap \bar{\Omega} = \varnothing$. The body Q is inhomogeneous

$$k(x) = \begin{cases} k_e, & x \in \left(\bar{Q} \cup \bar{\Omega}\right)^c \\ k_i(x), & x \in \bar{Q}_i, \end{cases}$$

where $k_i(x) \in C^\infty(\bar{Q}_i)$ and $M^c = \mathbb{R}^3 \setminus M$. The media outside obstacles is homogeneous – $k_e = \text{const}$. The conditions $\Re k(x) > 0$ and $\Im k(x) \geqslant 0$ hold everywhere in $\bar{\Omega}^c$. The incident field is $u_0(x) = e^{ik_e(\alpha x_1 + \beta x_2 + \gamma x_3)}$, $x \in \mathbb{R}^3$.

We find the solution

$$u \in C^2\left((\partial Q \cup \bar{\Omega})^c\right) \bigcap C^1\left(\bar{Q}^c \setminus \bar{\Omega}\right) \bigcap C^1(\bar{Q}) \bigcap_{\delta>0} C((\partial\Omega_\delta)^c), \tag{1}$$

to the Helmholtz equation

$$\Delta u(x) + k^2(x) u = 0, \quad x \in \left(\partial Q \cup \bar{\Omega}\right)^c, \tag{2}$$

which satisfies transmission conditions, Dirichlet condition on the screen

$$[u]|_{\partial Q} = 0, \quad \left[\frac{\partial u}{\partial \mathbf{n}}\right]\Big|_{\partial Q} = 0, \quad u\,|_\Omega = 0, \tag{3}$$

as well as the condition of finite energy [6]

$$u \in H^1_{loc}\left(\mathbb{R}^3\right). \tag{4}$$

The scattered field $u_s = u - u_0$ should satisfy Sommerfeld conditions at the infinity:

$$\frac{\partial u_s}{\partial r} = ik_e u_s + o\left(r^{-1}\right),\ (\Im k_e = 0);\ u_s(r) = O\left(r^{-2}\right),\ (\Im k_e > 0);\ r := |x| \to \infty. \tag{5}$$

Definition. Solution $u(x)$ to (2)–(5) is called *quasiclassical* if it satisfies (1) (compare with [7]).
Statement 1. [9] For $\Im k(x) \geq 0$ there is at most one solution to (2)–(5).

3. THE SYSTEM OF INTEGRAL EQUATIONS

We represent the solution to the problem via composition

$$u = u_0 + u_1 + u_2, \tag{6}$$

where u_0 is the incident field; u_1 is the field scattered by the screens only:

$$u_1(x) = \int\limits_{\Omega} G(x,y)\varphi(y)ds_y,$$

here $G(x,y) = \frac{1}{4\pi} \cdot \frac{e^{ik_e|x-y|}}{|x-y|}$, and φ is unknown.

Using methods of potential theory, taking (6) and Dirichlet conditions into account we obtain the following system of integral equations:

$$\begin{cases} (I-A)u + K_1\varphi = u_0|_Q \\ K_2 u + S\varphi = u_0|_\Omega \end{cases}. \tag{7}$$

Here

$$Au = \int\limits_{Q} \left(k^2(y) - k_e^2\right) G(x,y)u(y)dy, \qquad K_1\varphi = -\int\limits_{\Omega} G(x,y)\varphi(y)ds_y,\ x \in Q;$$

$$K_2 u = -\int\limits_{Q} \left(k^2(y) - k_e^2\right) G(x,y)u(y)dy, \quad S\varphi = -\int\limits_{\Omega} G(x,y)\varphi(y)ds_y,\ x \in \Omega.$$

Let us define matrix operator of the system (7):

$$\hat{L} = \hat{L}_1 + \hat{L}_2 = \begin{pmatrix} I & 0 \\ 0 & S \end{pmatrix} + \begin{pmatrix} -A & K_1 \\ K_2 & 0 \end{pmatrix} \tag{8}$$

and treat it as a pseudodifferential operator in Sobolev spaces (see [8]):

$$\hat{L} : L_2(Q) \times \tilde{H}^{-1/2}\left(\bar{\Omega}\right) \to L_2(Q) \times H^{1/2}\left(\Omega\right). \tag{9}$$

As the operator S is a Fredholm with zero index [6] we can prove
Statement 2. [9] $\hat{L}$ is a Fredholm operator with zero index.
For the solution of (7) the following statements hold (see [9]):
Statement 3. If $u_0 \in C^\infty(\mathbb{R}^3)$ and pair $(u,\varphi) \in L_2(Q) \times \tilde{H}^{-1/2}(\bar{\Omega})$ is a solution to the system (7) then $\varphi \in C^\infty(\Omega)$, and u satisfies (1).
Statement 4. Let $u_0 \in C^\infty(\mathbb{R}^3)$. Then the BVP (2)–(5) is equivalent to (7).
Taking into account the aforementioned statements we obtain the main result on the solvability of the problem under consideration:
Statement 5. The matrix operator $\hat{L}$ is continuously invertible.

4. GALERKIN METHOD

We consider Galerkin method for equation $Af = g$, where A is invertible operator that maps Hilbert space H_1 onto its anti-dual H_2. The approximate solution is sought as follows: $f_N = \sum\limits_{i=1}^{N} c^i w_i$; basis functions w_i satisfy the *approximation condition*:

$$\forall f \in H_1 \quad \lim_{N\to\infty} \inf_{f_N \in H_{1,N}} \|f - f_N\| = 0, \tag{10}$$

the coefficients c^i satisfy the system of linear equations

$$\sum_{j=1}^{N} c^j (Aw_j, w_i) = (g, w_i), \quad i = 1, \ldots, N; \tag{11}$$

here $(\cdot,\cdot)$ denotes natural antiduality between H_1 and H_2.

Let us define the approximate solution $f_N = (u_n, \varphi_m)$ to the system (7) as follows:

$$u_n(x) = \sum_{i=1}^{n} c_u^i v_i(x),\ x \in Q; \qquad \varphi_m(x) = \sum_{i=1}^{m} c_\varphi^i \psi_i(x),\ x \in \Omega.$$

Here $v_i(x)$, $\psi_i(x)$ are basis functions. First, we define functions v_i in Q.

Let $\Pi = \{x : a_1 < x_1 < a_2,\ b_1 < x_2 < b_2,\ c_1 < x_3 < c_2\}$ be a parallelepiped: $Q \subset \Pi$. Then

$$v_i(x) = v_{i_1 i_2 i_3}(x) := \begin{cases} 1, & x \in Q \cap \bar{\Pi}_{i_1 i_2 i_3} \\ 0, & x \notin Q \cap \bar{\Pi}_{i_1 i_2 i_3} \end{cases} \tag{12}$$

where $\Pi_{i_1 i_2 i_3} = \{x : x_{1,i_1} < x_1 < x_{1,i_1+1},\ x_{2,i_2} < x_2 < x_{2,i_2+1},\ x_{3,i_3} < x_3 < x_{3,-i_3}\}$, $x_{1,i_1} = a_1 + \frac{a_2-a_1}{n_1} i_1$, $x_{2,i_2} = b_1 + \frac{b_2-b_1}{n_2} i_2$, $x_{3,i_3} = c_1 + \frac{c_2-c_1}{n_3} i_3$; $i_k = 0, \ldots, n_k - 1$, $n = n_1 n_2 n_3$.

Let Ω be a *plane* screen; then basis functions $\psi_i = \psi_{i_1,i_2}$ $(i_k = 0, \ldots, m_k - 1)$ can be defined in the same way.

Let Ω be a *not plane* screen with parametrization $x = x(t_1, t_2)$, $(t_1, t_2) \in D \subset \mathbb{R}^2$, where D – is a compact (e.g., a rectangle). Then $\psi_i = \psi_{i_1 i_2}$ are finite functions with support $supp(\psi_i) = x(\Pi_{i_1,i_2}) \subset \Omega$. If $\lim\limits_{m\to\infty} \max\limits_{i_1,i_2} \mu_D(\Pi_{i_1,i_2}) = 0$; then owing to smoothness of the screen we obtain $\lim\limits_{m\to\infty} \max\limits_{i} \mu_\Omega(supp(\psi_i)) = 0$.

Statement 6. [9] The approximation condition holds for basis functions (v_i, ψ_j) in $H_1 = L_2(Q) \times \tilde{H}^{-1/2}(\bar{\Omega})$.

As S is a coercive operator (see. [6], p.245) the following statement holds

Statement 7. Galerkin method (11) is convergent for $\hat{L}$.

Galerkin method leads to a system of linear equations $[\hat{L}][\mathbf{u}] = [\mathbf{u_0}]$; the augmented matrix can be represented in block form as follows:

$$\left[\hat{L}\right] = \left[\begin{array}{c|c|c} [A] & [K_1] & [u_{0,1}] \\ \hline [K_2] & [S] & [u_{0,2}] \end{array}\right] \tag{13}$$

where

$$[A]_{ij} = vol(\Pi_i)\delta_{ij} - \int\limits_{\Pi_i}\int\limits_{\Pi_j} (k^2(y) - k_e^2) G(x,y) dy dx$$

$$[K_1]_{ij} = -\int\limits_{\Pi_i}\int\limits_{\omega_j} G(x,y) ds_y dx, \quad [K_1]_{ij} = -\int\limits_{\omega_i}\int\limits_{\Pi_j} \left(k^2(y) - k_e^2\right) G(x,y) dy ds_x,$$

$$[S]_{ij} = -\int\limits_{\omega_i}\int\limits_{\omega_j} G(x,y) ds_y ds_x, \quad [u_{0,1}]_i = \int\limits_{\Pi_i} u_0(x) dx, \quad [u_{0,2}]_i = \int\limits_{\omega_i} u_0(x) ds_x.$$

To obtain good precision of the approximate solution we must use a sufficient number of basis functions — at least 10 per wavelength for each dimension of the scatterers. For this reason we get dense matrices $[A]$ of order $N \sim 10^3$ and more. As the kernels of integral operators depend on $|x-y|$, the matrices $[A]$ under consideration are block-Toeplitz. This allows to accelerate Galerkin procedure and perform calculations in reasonable time.

We represent below some results of numerical tests.

Consider a cube $Q = \{x \in \mathbb{R}^3 : x_i \in [0; 0.5]\}$ and a rectangle screen $\Omega = \{x \in \mathbb{R}^3 : x_1, x_2 \in [0; 0.5],\ x_3 = 1\}$; let $k_e = 2\pi$, and $u_0 = e^{ik_e x_3}$; $n_i = m_k = 12$.

Figure 1 represents the absolute values $|\varphi(x)|$ of the solution $\varphi(x)$ in Ω and $|u(x)|$ in three cross-sections of the cube (given $x_3 = 0.5$, $x_3 = 0.25$, $x_3 = 0.$)

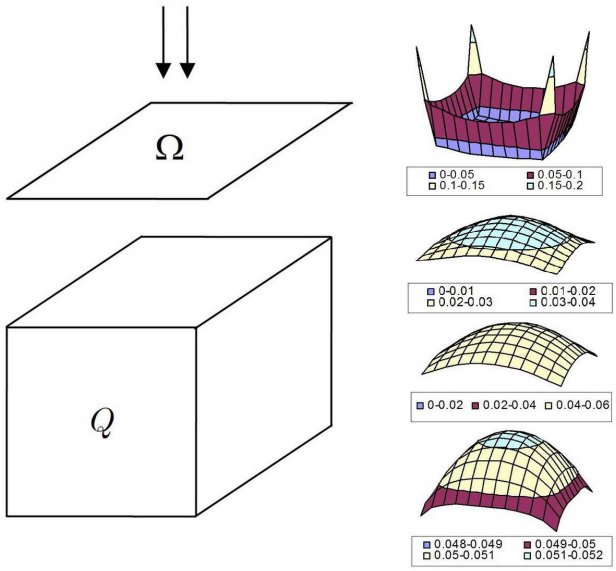

Figure 1.

Excluding blocks K_i (and $[A]$) allows to solve simultaneously the problems of diffraction on a volume body and a screen (on the screen only).

5. CONCLUSION

The scalar problem of diffraction of a plane wave on a system of bodies and screens is investigated. The system of integral equations is obtained and is proved to be uniquely solvable. The convergence of Galerkin method is proved, several numerical results are presented.

ACKNOWLEDGMENT

This work was supported by the Russian Science Foundation (grant 14-11-00344).

REFERENCES

1. Colton, D. and R. Kress, *Integral Equation Methods in Scattering Theory*, Wiley-Interscience, New York, 1983.
2. Durand, M., "Layer potentials and boundary value problems for the Helmholz equation in the complement of a thin obstacle," *Mathematical Methods in the Applied Sciences*, No. 5, 389–421, 1983.
3. Costabel, M. and E. Stephan, "A direct boundary integral equation method for transmission problems," *Journal of Mathematical Analysis and Applications*, No. 106, 367–413, 1985.
4. Costabel, M., "Boundary integral operators on Lipschitz domains: Elementary results," *SIAM Journal of Mathematical Analysis*, Vol. 19, No. 3, 613–626, 1988.
5. Kirsch, A. and A. Lechleiter, "The operator equations of Lippmann-Schwinger type for acoustic and electromagnetic scattering problems in L_2," *Applicable Analysis*, No. 88, 807–830, 2010.
6. Stephan, E. P., "Boundary integral equations for screen problems in $\mathbb{R}^3$," *Integral Equations and Potential Theory*, Vol. 10, No. 10, 236–257, 1987.

7. Ilinskii, A. S. and Yu. G. Smirnov, *Electromagnetic Wave Diffraction by Conducting Screens: Pseudodifferential Operators in Diffraction*, VSP, Utrecht, 1998.
8. Rempel, S. and B.-W. Schulze, *Index Theory of Elliptic Boundary Problems*, Akademie-Verlag, Berlin, 1982.
9. Medvedik, M. Yu., Yu. G. Smirnov, and A. A. Tsupak, "Scalar problem of diffraction of a plane wave on a system of disjoint screens and inhomogeneous bodies," *Computational Mathematics and Mathematical Physics*, No. 8, 2014 (in print).

Propagation of Electromagnetic Waves along a Nonlinear Inhomogeneous Cylindrical Waveguide

Yu. G. Smirnov and D. V. Valovik
Department of Mathematics and Supercomputing, Penza State University, Russian Federation

Abstract— Electromagnetic TE waves propagating in an inhomogeneous nonlinear cylindrical waveguide are considered. The permittivity inside the waveguide is described by the Kerr law. Inhomogeneity of the waveguide is modeled by a nonconstant term in the Kerr law. Physical problem is reduced to a nonlinear eigenvalue problem for an ordinary differential equation. Theorem of existence of propagation constants and their localization is formulated. Conditions of k waves existence are found.

1. INTRODUCTION

We investigate guided waves in a nonlinear dielectric inhomogeneous cylindrical waveguide filled with Kerr medium. The waveguide is placed in cylindrical coordinate system $O\rho\varphi z$, where axis z coincides with axis of the waveguide. The permittivity inside the waveguide is $\varepsilon = \varepsilon_2(\rho) + \alpha|\mathbf{E}|^2$, where $\varepsilon_2(\rho)$ is the inhomogeneity, $\alpha > 0$ is a real constant, and $\mathbf{E}$ is the complex amplitude of an electromagnetic field.

This problem and similar ones lead to nonlinear transmission eigenvalue problems for ordinary differential equations (a short review of the problems and results see in [1]). Eigenvalues in these problems correspond to propagation constants of the waveguides. In these problems differential equations depend nonlinearly either on sought-for functions and the spectral parameter. The transmission conditions depend nonlinearly on the spectral parameter. The main goal is to prove existence of eigenvalues and determine their localization. Existence and localization can be derived from the dispersion equation (DE). The DE is an equation with respect to the spectral parameter. There are two ways to obtain the DE. The first one is to integrate the differential equations and obtain, using the transmission conditions, the DE. This way is of very limited applicability, as it is very rarely possible to find explicit solutions of nonlinear differential equations. The second one is a very general approach based on a reduction of the differential equations to integral equations using the Green function. Here we consider this very method. In spite of the fact that by this method the DE is found in an implicit form, it is possible to prove existence of eigenvalues and find their localization.

Two circumstances are important for the following analysis. First, in the case of a homogeneous waveguide ($\varepsilon_2(\rho) \equiv$ const) this Green function can be found explicitly. Second, the DE of the nonlinear homogeneous case can be written as $\mathrm{DE}_{\mathrm{lin}} + \mathrm{T}_{\mathrm{nonlin}} = 0$, where $\mathrm{DE}_{\mathrm{lin}}$ is a linear problem term and $\mathrm{T}_{\mathrm{nonlin}}$ is an extra nonlinear term. Here the linear problem term is written in an explicit form. Moreover, the equation $\mathrm{DE}_{\mathrm{lin}} = 0$ is well known and examined. Its roots are also known. All this allows proving the existence of the nonlinear problem solutions at least near to the linear problem solutions. The nonconstant term $\varepsilon_2(\rho)$ dramatically changes the situation. In this case we cannot find the necessary Green function explicitly, so we investigate it in an implicit form. The DE of the nonlinear inhomogeneous case can also be written as $\mathrm{DE}_{\mathrm{lin}} + \mathrm{T}_{\mathrm{nonlin}} = 0$. However, in this case the term $\mathrm{DE}_{\mathrm{lin}}$ is found in an implicit form and roots of the equation $\mathrm{DE}_{\mathrm{lin}} = 0$ are unknown. In spite of the fact that the method here looks similar to the method in [2, 3] we solve a radically different problem.

2. STATEMENT OF THE PROBLEM

Let us consider three-dimensional space $\mathbb{R}^3$ with cylindrical coordinate system $O\rho\varphi z$. The space is filled by isotropic medium with constant permittivity $\varepsilon_1 \geqslant \varepsilon_0 > 0$, where ε_0 is the permittivity of free space. In this medium a cylindrical waveguide is placed. The waveguide is filled by isotropic nonmagnetic medium and has cross section $W := \{(\rho, \varphi) : \rho \leqslant R, 0 \leqslant \varphi < 2\pi\}$ and its generating line (the waveguide axis) is parallel to the axis Oz. We shall consider electromagnetic waves propagating along the waveguide axis. Everywhere below $\mu = \mu_0$ is the permeability of free space.

We use Maxwell's equations in the following form [4]

$$\operatorname{rot} \tilde{\mathbf{H}} = \partial_t \tilde{\mathbf{D}}, \quad \operatorname{rot} \tilde{\mathbf{E}} = -\partial_t \tilde{\mathbf{B}}, \tag{1}$$

where $\tilde{\mathbf{D}} = \varepsilon\tilde{\mathbf{E}}$, $\tilde{\mathbf{B}} = \mu\tilde{\mathbf{H}}$ and $\partial_t = \partial/\partial t$. Field $(\tilde{\mathbf{E}}, \tilde{\mathbf{H}})$ is the total field.

Real monochromatic field $(\tilde{\mathbf{E}}, \tilde{\mathbf{H}})$ in the medium can be written in the following form

$$\begin{aligned}\tilde{\mathbf{E}}(\rho,\varphi,z,t) &= \mathbf{E}^+(\rho,\varphi,z)\cos\omega t + \mathbf{E}^-(\rho,\varphi,z)\sin\omega t;\\ \tilde{\mathbf{H}}(\rho,\varphi,z,t) &= \mathbf{H}^+(\rho,\varphi,z)\cos\omega t + \mathbf{H}^-(\rho,\varphi,z)\sin\omega t,\end{aligned} \tag{2}$$

where ω is the circular frequency; $\mathbf{E}^+$, $\mathbf{E}^-$, $\mathbf{H}^+$, $\mathbf{H}^-$ are real required vectors.

Let us form complex amplitudes $\mathbf{E}$, $\mathbf{H}$:

$$\mathbf{E} = \mathbf{E}^+ + i\mathbf{E}^-, \quad \mathbf{H} = \mathbf{H}^+ + i\mathbf{H}^-. \tag{3}$$

It is clear that $\tilde{\mathbf{E}} = \mathrm{Re}\{\mathbf{E}e^{-i\omega t}\}$ and $\tilde{\mathbf{H}} = \mathrm{Re}\{\mathbf{H}e^{-i\omega t}\}$, where $\mathbf{E} = (E_\rho, E_\varphi, E_z)^T$ and $\mathbf{H} = (H_\rho, H_\varphi, H_z)^T$, and the components depend on three spatial variables.

It is known (see, e.g., [5–7]) that the Kerr law in isotropic medium for a monochromatic wave $\mathbf{E}e^{-i\omega t}$ has the form $\varepsilon = \varepsilon_2 + a|\mathbf{E}|^2$, where $\mathbf{E}$ is complex amplitude, a is the coefficient of the nonlinearity. Thus, for a monochromatic wave $(\mathbf{E}, \mathbf{H})e^{-i\omega t}$ the complex amplitudes satisfy stationary Maxwell's equations

$$\mathrm{rot}\,\mathbf{E} = i\omega\mu\mathbf{H}, \quad \mathrm{rot}\,\mathbf{H} = -i\omega\varepsilon\mathbf{E}, \tag{4}$$

the continuity condition for the tangential components on the media interfaces (on the boundary of the waveguide) and the radiation condition at infinity: the electromagnetic field decays as $O(\rho^{-1})$ when $\rho \to \infty$.

Inside the waveguide the permittivity has the form $\varepsilon = \varepsilon_2(\rho) + a\,|\mathbf{E}|^2$, where where a is a real positive value, $\varepsilon_2(\rho)$ is a real continuous function. Here $\varepsilon_2(\rho)$ is a linear part of the permittivity.

Thereby, passing from time dependent Equation (1) to time independent Equation (4) is grounded on the previous consideration.

The solutions to Maxwell's equations are sought in the entire space.

Geometry of the problem is shown in Fig. 1. The waveguide is infinite along axis Oz.

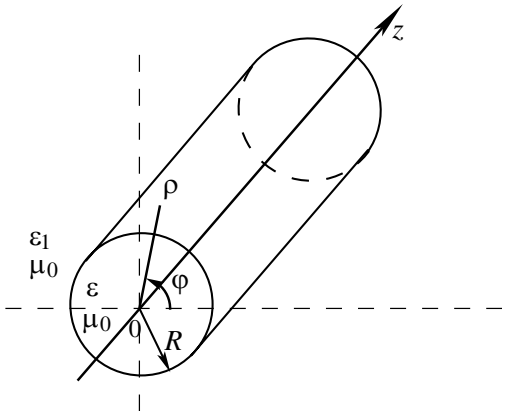

Figure 1: Geometry of the problem.

Consider the TE waves with harmonical dependence on time

$$\mathbf{E}e^{-i\omega t} = e^{-i\omega t}(0, E_\varphi, 0)^T, \quad \mathbf{H}e^{-i\omega t} = e^{-i\omega t}(H_\rho, 0, H_z)^T,$$

where $\mathbf{E}$, $\mathbf{H}$ are the complex amplitudes.

Substituting the complex amplitudes into Maxwell's Equation (4), we obtain that they do not depend on φ.

Waves propagating along waveguide axis Oz depend harmonically on z. This means that the fields components have the form

$$E_\varphi = \mathrm{E}_\varphi(\rho)e^{i\gamma z}, \quad H_\rho = \mathrm{H}_\rho(\rho)e^{i\gamma z}, \quad H_z = \mathrm{H}_z(\rho)e^{i\gamma z},$$

where γ is the unknown real spectral parameter of the problem (propagation constant). Substituting these components into Maxwell's Equation (4) and introducing notation $u(\rho) := \mathrm{E}_\varphi(\rho)$, $k_0^2 = \omega^2\mu\varepsilon_0$ we obtain

$$\rho u'' + u' - \rho^{-1}u + \rho\left(k_0^2\tilde{\varepsilon} - \gamma^2\right)u = 0, \tag{5}$$

where $\tilde{\varepsilon} = \begin{cases} \varepsilon_1, & \rho > R, \\ \varepsilon_2(\rho) + au^2, & \rho \leqslant R. \end{cases}$

Also we assume that function u is sufficiently smooth

$$u(\rho) \in C[0,+\infty) \cap C^1[0,+\infty) \cap C^2(0,R) \cap C^2(R,+\infty).$$

We will seek γ under conditions $k_0^2\varepsilon_1 < \gamma^2$.

In the domain $\rho > R$ we have $\tilde{\varepsilon} = \varepsilon_1$. From (5) we obtain the equation

$$u'' + \rho^{-1}u' - \rho^{-2}u + k_1^2 u = 0, \tag{6}$$

where $k_1^2 = k_0^2\varepsilon_1 - \gamma^2$. It is the Bessel equation. In accordance with the radiation condition its solution is

$$u(\rho) = \tilde{b}K_1(|k_1|\rho), \quad \rho > R, \tag{7}$$

where $K_1(z)$ is the Macdonald function, $\tilde{b}$ is a constant of integration. The radiation condition is fulfilled since $K_1(|k_1|\rho) \to 0$ as $\rho \to \infty$.

In the domain $\rho < R$ we have $\tilde{\varepsilon} = \varepsilon_2(\rho) + au^2$. From (5), we obtain the equation

$$(\rho u')' + \left(k^2(\rho)\rho - \rho^{-1}\right) u + \alpha\rho u^3 = 0, \tag{8}$$

where $k^2(\rho) = k_2^2(\rho) - \gamma^2$, $k_2^2(\rho) = k_0^2\varepsilon_2(\rho)$, and $\alpha = ak_0^2$.

Tangential components of electromagnetic field are known to be continuous at media interfaces. Hence, we obtain $E_\varphi(R+0) = E_\varphi(R-0)$, $H_z(R+0) = H_z(R-0)$. These conditions imply the transmission conditions for the functions $u(\rho)$ and $u'(\rho)$

$$[u]|_{\rho=R} = 0, \ [u']\big|_{\rho=R} = 0, \tag{9}$$

where $[f]|_{x=x_0} = \lim\limits_{x\to x_0-0} f(x) - \lim\limits_{x\to x_0+0} f(x)$.

The problem P is to prove existence of eigenvalues γ for which a nontrivial solution $u(\rho;\gamma)$ to (6), (8), which is called an eigenfunctions, exists; this solution must satisfy transmission conditions (9) and the radiation condition at infinity: each eigenfunction decay as $O(\rho^{-1})$ when $\rho \to \infty$.

3. NONLINEAR INTEGRAL EQUATION AND DISPERSION EQUATION

Suppose that the Green function $G_k(\rho,\rho_0;\lambda)$ exists for the following boundary value problem

$$L_kG_k = -\delta(\rho-\rho_0), \quad G\,|_{\rho=0} = G'\,|_{\rho=R} = 0 \quad (0 < \rho_0 < R)\,,$$

where $L_k := \frac{d}{d\rho}(\rho\frac{d}{d\rho}) + (k^2(\rho)\rho - \frac{1}{\rho})$; here we place index k in order to stress that the operator and the Green function depend on $k(\rho)$.

In this case the Green function has the representation (see, for example, [8])

$$G_k(\rho,\rho_0;\lambda) = -\frac{v_i(\rho)v_i(\rho_0)}{\lambda-\lambda_i} + G_1(\rho,\rho_0;\lambda) \tag{10}$$

in the vicinity of eigenvalue λ_i. Here $\lambda := \gamma^2$ and $G_1(\rho,\rho_0;\lambda)$ is regular w.r.t. λ in the vicinity of λ_i; λ_n, $v_n(\rho)$ are complete (real) eigenvalues and orthonormal eigenfunctions systems of the boundary eigenvalue problem

$$(\rho v_n')' + \left(k_2^2(\rho)\rho - \rho^{-1}\right) v_n = \lambda_n\rho v_n; \ \ v_n\,|_{\rho=0} = v_n'\,|_{\rho=R} = 0\,. \tag{11}$$

The Green function exists if $\lambda \neq \lambda_i$.

For $\varepsilon_2 \equiv$ const explicit form of the Green function is given in [2].

Let us write Equation (8) in the operator form

$$L_ku + \alpha B(u) = 0, \quad B(u) = \rho u^3(\rho). \tag{12}$$

Using the second Green formula [9] and Equation (12) we obtain the nonlinear integral representation of solution $u(\rho_0)$ of Equation (8) on the segment $[0,R]$

$$u(\rho_0) = \alpha\int\limits_0^R G_k(\rho,\rho_0)\rho u^3(\rho)d\rho + Ru'(R-0)G_k(R,\rho_0), \quad 0 \leqslant \rho_0 \leqslant R. \tag{13}$$

Using the transmission condition $u'(R-0) = u'(R+0)$ we can rewrite Equation (13)

$$u(\rho_0) = \alpha \int\limits_0^R G_k(\rho, \rho_0)\rho u^3(\rho)d\rho + Ru'(R+0)G_k(R, \rho_0), \quad 0 \leqslant \rho_0 \leqslant R. \tag{14}$$

Using Equation (14) and the transmission condition $u(R-0) = u(R+0)$ we obtain the DE w.r.t. the propagation constant

$$u(R+0) = \alpha \int\limits_0^R G_k(\rho, R)\rho u^3(\rho)d\rho + Ru'(R+0)G(R, R). \tag{15}$$

4. EXISTENCE AND LOCALIZATION OF EIGENVALUES

Taking into account formula (7), DE (15) can be represented in the form

$$K_1(|k_1|R) - |k_1|RK_1'(|k_1|R)\, G_k(R, R; \lambda) = \frac{\alpha}{\tilde{b}} \int\limits_0^R G_k(\rho, R; \lambda)\rho u^3(\rho)d\rho. \tag{16}$$

It is clear that DE (16) depends on $\tilde{b}$. Here $\tilde{b}$ is an initial condition. This is a peculiarity of nonlinear eigenvalue problems. For the linear problem (if $\alpha = 0$) we obtain, as it is expected, the DE, which does not depend on the initial condition.

DE (16) can be rewritten in the following form

$$g(\lambda) = \alpha F(\lambda),$$

where

$$g(\lambda) = K_1(|k_1|R) + (|k_1|RK_0(|k_1|R) + K_1(|k_1|R))\, G_k(R, R; \lambda),$$

and

$$F(\lambda) = \int\limits_0^R G_k(\rho, R; \lambda)\rho u^3(\rho)d\rho.$$

The zeros of the function $\Phi(\lambda) \equiv g(\lambda) - \alpha F(\lambda)$ are eigenvalues of the problem P.

At first, consider the linear problem $g(\lambda) = 0$. This equation can be rewritten in the form

$$G_k(R, R; \lambda) = -\frac{K_1(|k_1|R)}{|k_1|RK_0(|k_1|R) + K_1(|k_1|R)}.$$

From the expression $G_k(R, R; \lambda) = -\frac{v_i^2(R)}{\lambda - \lambda_i} + G_1(R, R; \lambda)$, it follows that $G_k(R, R; \lambda)$ continuously varies from $-\infty$ to $+\infty$ when λ varies from λ_i to λ_{i+1}.

As value $\frac{K_1(|k_1|R)}{(|k_1|RK_0(|k_1|R)+K_1(|k_1|R))}$ is bounded, then there is at least one root of the equation $g(\lambda) = 0$ and this root lies between λ_i and λ_{i+1}.

Finally, it is necessary to prove that the term $v_i(R)$ does not vanish in expression $G_k(R, R; \lambda)$. Prove this from the contrary. Let $v_i(R) = 0$. Consider the Cauchy problem for the equation $\rho v_i'' + v_i' + \left(k_2^2(\rho)\rho - \rho^{-1}\right) v_i = \lambda_i \rho v_i$, $\rho \in [\delta, R]$, where $\delta > 0$, with initial conditions $v_i|_{\rho=R} = v_i'|_{\rho=R} = 0$. From the general theory of ordinary differential equations (see, for example, [10]) it is known that solution $v_i(\rho)$ of considered Cauchy problem exists and is unique for all $\rho \in [\delta, R]$. In this case, this solution coincides with function $v_i(R)$ for all $\rho \in [\delta, R]$. Function $v_i(R)$ is the function, which is contained in Green's function representation (10). On the other hand, the solution of the Cauchy problem for a linear equation with zero initial condition is the trivial solution. This contradicts to representation (10) of Green's function $G_k(\rho, \rho_0; \lambda)$ in the vicinity of $\lambda = \lambda_i$.

The following statement is the main result of this paper.

Statement 1. *Let $\varepsilon_1 \geqslant \varepsilon_0 > 0$, $\alpha > 0$ be real constants, and problem (11) have k eigenvalues λ_i such that the following inequalities $k_0^2\varepsilon_1 < \lambda_k < \lambda_{k-1} < \ldots < \lambda_2 < \lambda_1$ hold, where $k \geqslant 2$ be an*

integer. Then there is a value $\alpha_0 > 0$ *such that for any* $\alpha \leqslant \alpha_0$ *the problem* P *has at least* $k-1$ *solutions* $\gamma_i \in (\sqrt{\lambda_{i+1}} + \delta_{i+1}, \sqrt{\lambda_i} - \delta_i)$, $i = \overline{1, k-1}$, *where* δ_i *are positive constants.*

Sketch of the proof. Let inequalities

$$k_0^2 \varepsilon_1 < \lambda_k < \lambda_{k-1} < \ldots < \lambda_2 < \lambda_1$$

hold, where $k \geqslant 2$, λ_i are solutions to (11).

We can choose sufficiently small $\delta_i > 0$ such that the Green function $G_k(\rho, \rho_0; \lambda)$ exists and is continuous on $\Gamma := \bigcup_{i=1}^{k-1} \Gamma_i$, where $\Gamma_i := [\sqrt{\lambda_{i+1}} + \delta_{i+1}, \sqrt{\lambda_i} - \delta_i]$, $i = \overline{1, k-1}$ and the following inequality $g(\sqrt{\lambda_{i+1}} + \delta_{i+1}) \cdot g(\sqrt{\lambda_i} - \delta_i) < 0$ takes place.

It follows from the choice of δ_i that $F(\lambda)$ is bounded. Moreover, product $\alpha F(\lambda)$ can be made sufficiently small by choosing appropriate α. Consider the DE $\Phi(\lambda) = 0$. As it is shown before the function $g(\lambda)$ is continuous and reverses its sign when λ varies from $\lambda_{i+1} + \delta_{i+1}$ to $\lambda_i - \delta_i$. As the function $F(\lambda)$ is bounded then it is clear that the equation $\Phi(\lambda) = 0$ has at least $k-1$ roots $\tilde{\lambda}_i$, $i = \overline{1, k-1}$, if we choose appropriate α. Here $\tilde{\lambda}_i \in (\lambda_{i+1} + \delta_{i+1}, \lambda_i - \delta_i)$, $i = \overline{1, k-1}$.

From Statement 1 it follows that, under the above assumptions, there exist axially symmetrical propagating TE waves in cylindrical dielectric waveguides of circular cross-section filled with a nonmagnetic isotropic inhomogeneous medium with Kerr nonlinearity. This result generalizes the well-known similar statement for dielectric waveguides of circular cross-section filled with a linear medium ($\alpha = 0$).

It should be noticed that the value α_0 can be effectively estimated [1].

ACKNOWLEDGMENT

The work is partly supported by the Russian Federation President Grant (No. MK-90.2014.1), RFBR (No. 12-07-97010-r-A), and The Ministry of Education and Science of the Russian Federation (Goszadanie No. 2.1102.2014K).

REFERENCES

1. Smirnov, Y. G. and D. V. Valovik, "On the problem of electromagnetic waves propagating along a nonlinear inhomogeneous cylindrical waveguide," *ISRN Math. Phys.*, Vol. 2013, 1–7, 2013, http://dx.doi.org/10.1155/2013/184325.
2. Schürmann, H.-W., Y. G. Smirnov, and Y. V. Shestopalov, "Propagation of te-waves in cylindrical nonlinear dielectric waveguides," *Phys. Rev. E*, Vol. 71, No. 1, 016614-1–10, 2005.
3. Smirnov, Y. G. and S. N. Kupriyanova, "Propagation of electromagnetic waves in cylindrical dielectric waveguides filled with a nonlinear medium," *Comp. Maths. Math. Phys.*, Vol. 44, No. 10, 1850–1860, 2004.
4. Stretton, J. A., *Electromagnetic Theory*, McGraw Hill, New york, 1941.
5. Akhmediev, N. N. and A. Ankevich, *Solitons, Nonlinear Pulses and Beams*, Chapman and Hall, London, 1997.
6. Eleonskii, P. N., L. .G. Oganesyants, and V. P. Silin, "Cylindrical nonlinear waveguides," *Soviet Physics JETP*, Vol. 35, No. 1, 44–47, 1972.
7. Landau, L. D., E. M. Lifshitz, and L. P. Pitaevskii, *Course of Theoretical Physics (Vol. 8). Electrodynamics of Continuous Media*, Butterworth-Heinemann, Oxford, 1993.
8. Naimark, M. A., *Linear Differential Operators, Part I: Elementary Theory of Linear Differential Operators. Part II: Linear Differential Operators in Hilbert Space*, Frederick Ungar Publishing Co., New York, 1967, 1968.
9. Stakgold, I., *Greens Functions and Boundary Value Problems*, Wiley, New York, 1979.
10. Lizorkin, P. I., *Course of Differential and Integral Equations with Supplementary Chapters of Calculus*, Nauka, Moscow, 1981 (in Russian).

Preliminary Study of Embedded Structural Anomalies in Architectural Structures by Microwave Subsurface Tomography

S. Beni[1], **R. Olmi**[1, 2], **F. Micheletti**[2], **and C. Riminesi**[1, 3]

[1]ELab Scientific Srl, Firenze, Italy
[2]Institute for Applied Physics, National Research Council, Firenze, Italy
[3]Institute for the Conservation and Valorization of Cultural Heritage
National Research Council, Firenze, Italy

Abstract— A non-destructive technique (NDT) based on microwave reflectometry has been applied to perform subsurface tomography images. The localization in depth of anomalies in architectural structures such as, for example, inhomogeneity in the masonry texture (cavity of air, metals, and humidity) or on timber structure by means of NDT approach is crucial not only in the diagnostics of the Cultural Heritage, but in general for all civil industry. The target of our research is the development of a robust and user-friendly system to investigate the materials used in architecture until 20 cm in depth, with a resolution less than 1 cm. The system consists by a vector network analyzer and an wide band antenna (ridged antenna) operating in the range 1.5–6 GHz. The measurement of the reflection coefficient variation (amplitude and phase) due to the dielectric dis-homogeneity into the materials under investigation is acquired. The equivalent time-domain response is reconstructed using an Inverse Fourier Transform of the baseband signal and by a simple model based on TEM approach is determined the constrains on the size of the anomaly (maximum resolution) and on its position into the host medium (maximum non unambiguous range).

The material can be investigated by scanning — step by step — the surface by the probe antenna. For each step is obtained the reflection coefficient in the frequency range, and subsequently transformed in the time-domain by out-line processing.

Thanks to the penetration of the used microwave radiation, it is possible to sectioning the material under test in slices transversal to the surface up to 20 cm in depth. The interdistance between two consecutive slices is related to the distance between the two corresponding scanning lines.

The performance of the proposed technique together with its resolution limits are discussed as regards with other approach proposed in literature. The results on architectural structure are presented. The potentiality of the system as diagnostic tool based on NDT approach for the framework of Cultural Heritage will be discussed together with its limits.

1. INTRODUCTION

Non-destructive testing (NDT) and evaluation techniques for to extract information about the internal structures of the material are of crucial importance in the Cultural Heritage framework [1–3]. The reason for this interest is the possibility to determine and to locate anomalies in architectural structures such as, for example, inhomogeneity in timber structures or in mural structure such as cavity of air, metals and humidity. Thanks to these facilities can be improved the strategies of the restoration and maintenance procedures.

In the past, several approaches to solve these tasks have been suggested for example ultrasound techniques and also microwave techniques ([4–7]). The object of our research is to develop a robust and user friendly system to diagnose the architectural structures until 20 cm in depth, with a resolution less than 1 cm such as a possible alternative to the aforementioned methods. The aim is achieved by a microwave reflectometer system operating in the time domain.

The choice of the probe is important for two reasons: (1) must be able to ensure a good matching with the material to be investigated; (2) the frequency band must be sufficiently larger to allow the detection of interfaces slab embedded in the host medium until 2 cm from $z = 0$.

The paper is organized in sections. The theoretical background is described in Section 2, where by a simple model, an air slab hosted in a medium with low dielectric constant — it is the case of air cavity in a wood on wall in quite-dry condition — will be evaluated the constrains of the technique. In Section 3 is presented the microwave reflectometer measurement system and the approach used to interpret the data collected in the frequency domain. The Section 4 is devoted to present the results obtained on case study: a large vaulted with frescoed ceiling.

2. THEORETICAL BACKGROUND

The issue of detection of anomalies within an architectural structure, in particular an air slab hosted into a homogenous medium, can be mathematically approximated such as the problem concerning the localization of the interface of the air slab embedded in a half-space of dielectric with loss simulating masonry support with approximation of plane wave. We consider a plan wave of unitary amplitude $E_{inc}(z,\omega) = \exp(-j\beta_0 z)$, being β_0 the free space wavenumber that impinge from the first interface stratified medium at the different frequency $f \in [f_{\min}, f_{\max}] = B$.

In Fig. 1 is sketch a possible measurement configuration with the probe no-contacting the surface of the masonry support. In historical building the walls are often frescoed and it is not possible put in contact the probe with the painted surface, so a small gap (0.5 cm) is left from the surface. Known the size and the dielectric characteristics of the first layer the positioning of the interface of the slab 2 and 3 (z_2 and z_3), and the respective size (d_2 and d_3) can be determined. The permittivity of the first layer of the masonry can be determined by truncated coaxial method implemented from the author in [8] when there are no artistic and architectural constraints.

Being β_g the gap free space wavenumber, β_w the host medium wavenumber and β_d the dielectric slab wavenumber, the expression of the reflection coefficient for the considered problem, at the section $z = 0$, is given by the following relation [9]:

$$\Gamma(0,\omega) = \frac{\begin{array}{c}\Gamma_0 + \Gamma_1 e^{-2\mathrm{j}\,\beta_g d_1} + \Gamma_0\Gamma_1\Gamma_2 e^{-2\mathrm{j}\,\beta_w d_2} + \Gamma_2 e^{-2\mathrm{j}\beta_g d_1} e^{-2\mathrm{j}\,\beta_w d_2} \\ +\Gamma_3 e^{-2\mathrm{j}\,\beta_g d_1} e^{-2\mathrm{j}\,\beta_w d_2} e^{-2\mathrm{j}\,\beta_d d_3} + \Gamma_0\Gamma_1\Gamma_2\Gamma_3 e^{-2\mathrm{j}\,\beta_d d_3}\end{array}}{\begin{array}{c}1 + \Gamma_0\Gamma_1 e^{-2\mathrm{j}\beta_g d_1} + \Gamma_1\Gamma_2 e^{-2\mathrm{j}\beta_w d_2} + \Gamma_0\Gamma_2 e^{-2\mathrm{j}\beta_g d_1} e^{-2\mathrm{j}\beta_w d_2} \\ +\Gamma_0\Gamma_2 e^{-2\mathrm{j}\,\beta_g d_1} e^{-2\mathrm{j}\,\beta_w d_2} e^{-2\mathrm{j}\,\beta_d d_3} + \Gamma_1\Gamma_3 e^{-2\mathrm{j}\,\beta_d d_3} e^{-2\mathrm{j}\,\beta_w d_2} + \Gamma_2\Gamma_3 e^{-2\mathrm{j}\,\beta_d d_3}\end{array}} \tag{1}$$

where:

$$\Gamma_i = \frac{\zeta_i - \zeta_{i-1}}{\zeta_i + \zeta_{i-1}} \quad i = 1, \ldots, n \tag{2}$$

is the reflection coefficient at the interfaces located in $z = z_i$, ζ_i is the characteristic impedance of medium, and ζ_0 is the characteristic impedance of the free space. This very simplified model is useful to understand the limits of the approach in terms of maximum resolution and maximum non unambiguous range.

In the proposed method the reflection coefficient is represented by N complex values corresponding to N discrete frequencies separated by Δf. As well know the Fourier Transform of a periodic signal give one discrete spectrum in the frequency domain, equivalently, a periodic signal can be expressed in time domain by the Fourier series where the coefficient of the series are the spectral line (amplitude and phase) in the frequency domain, so the reflection coefficient in the time domain

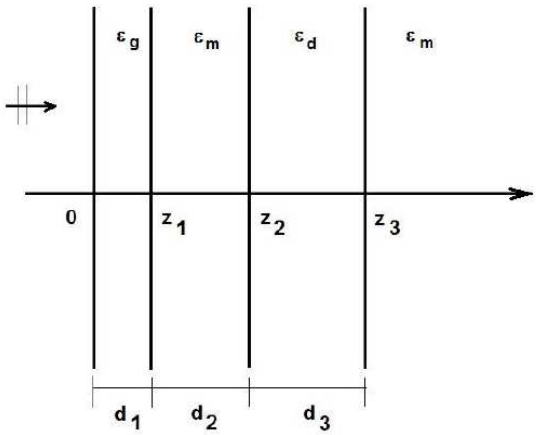

Figure 1: Geometry of the problem. The air gap (d_1, ε_g) and slab (d_3, ε_d) embedded in a homogeneous half-space medium (ε_m).

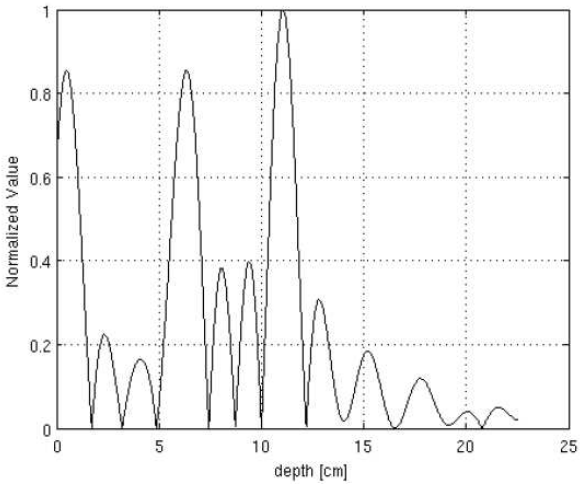

Figure 2: Normalized reflected signal from a host medium ($\varepsilon_m = 2.5 + j0.02$) with embedded a free-space slab at $z_2 = 4.5$ cm and with a thickness of $d_3 = 5$ cm.

can be determined by the following relation:

$$\Gamma(0,\omega) = \Sigma_{n=1}^{N} 2\left|\Gamma(0,\omega_n)\right| \cos\left(\omega_n t + \arg\left(\Gamma(0,\omega_n)\right)\right) \operatorname{sinc}\left[\pi B \frac{(t - \arg\left(\Gamma(0,B/2)\right))}{2\pi B/2}\right] \tag{3}$$

Let us to define, by the Nyquist sampling criterion, the maximum unambiguous distance:

$$R_{\max} = \frac{c_0}{4\Delta f\sqrt{\varepsilon}} \tag{4}$$

moreover we define, by the Rayleigh's criterion, the maximum resolution distance, i.e., the minimum distance between two interface for their unique positioning:

$$R_{\min} = \frac{c_0}{2B\sqrt{\varepsilon}} \tag{5}$$

Let us consider the dielectric permittivity of the dielectric slab more large then the host medium. In this case the propagation velocity of the electromagnetic wave in the host medium is more great then the velocity inside the slab, consequently we have an in-depth delocalization of the second interface of the dielectric slab and this make more easy the discrimination the interfaces. Otherwise, when the dielectric permittivity of the host medium is more large then the slab is more difficult discriminate the presence of the second interface in fact, we have a reconstructed peak located backwards respect at actual location of the second interface and this make difficult to discriminate the second interface.

For evaluation of the ability of the model let us consider, in addition to the free-space gap $\varepsilon_0 = 1$, an anomaly in the masonry support consisting on a free-space slab with $\varepsilon_d = 1$ embedded in host media with $\varepsilon_m = 2.5 + j0.02$ (this can be the case of masonry quite near dry condition [4]), and the frequency ranging from $f_{\min} = 1.5\,\text{GHz}$ to $f_{\max} = 6\,\text{GHz}$. The anomaly have the first interface located at $z_2 = 4.5\,\text{cm}$ and thickness 5 cm ($d_3 = 5\,\text{cm}$). The Fig. 2 shows the normalized reflected signal resulting from the proposed model. The x-axis labelled with "depth" explains the penetration profile of the electromagnetic wave this distance is normalized to the permittivity of the host medium (ε_m). The first peak in Fig. 2 refers to the interface air/medium (air gap), the second and the third refer to the interface slab/host medium.

3. EXPERIMENTAL RESULTS

The microwave reflectometer system consist of a portable vector network analyser (VNA Anritsu S331E Site Master), a double ridged antenna with unimodal waveguide propagation in the 1.5–6 GHz band, and a notebook with dedicated software to remote control of the instrument and data acquisition. The data are elaborated offline by a Matlab code implementing the IFFT algorithm and the graphical elaboration of data.

The double ridged antenna (DRG) is the best commercial solution as antenna probe, because it has a width band for unimodal propagation more large than other commercial rectangular waveguide such as, for example, the type WR430 or WR229. Furthermore, the double ridge antenna shows a better matching with the impedance of the material constituting the masonry. In Fig. 3 are plotted the waveguide impedance, for double ridged waveguide and for rectangular waveguide (WR229), respect to the typical impedance of a plaster.

The investigation of the material is performed by a step frequency continuous-wave in the 2–6 GHz band with step $\Delta f = 50\,\text{MHz}$. The sub-surface investigation is possible thanks to ability of the electromagnetic wave to penetrating dielectric materials. The penetration depth depends on the electromagnetic characteristics of the material under test, mainly it affected from moisture content and in second order from the field polarization if the medium is anisotropic (this issue must be well considered on timber structures because wood is an anisotropic dielectric [10]).

The investigation of the surface is performed with scans step by step in order to obtain a vector with N elements (complex value of the reflection coefficient) corresponding to N frequencies for each step (M total number of steps). The overall data are collected in $N \times M$ matrix for each scanning line. Each vector of reflection coefficient is replaced in the time-domain by Equation (3).

In Fig. 5 are presented the results obtained from scans along the principle axes on a vaulted ceiling frescoed in a historic building (Fig. 4). In both tomograms the deep red color indicates an hard discontinuity in the masonry structure due to the detachment of the first layer of the plaster. The deeper anomalies (at about 4–5 cm) are due to the interface brick/air on the top of the vault.

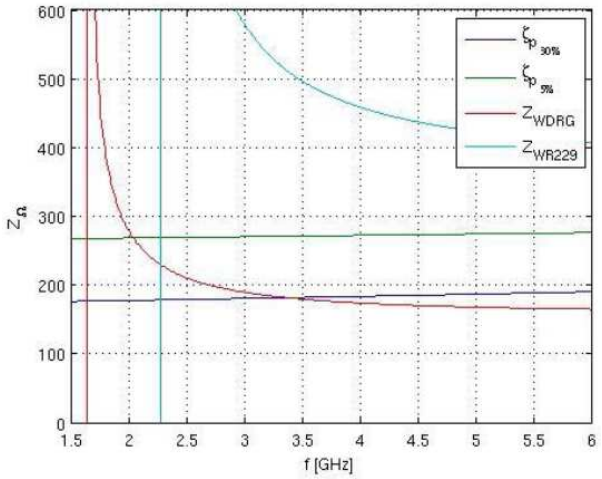

Figure 3: Impedance comparison between characteristics impedance of plaster at different moisture content (5% and 30%), and waveguide impedance for WR229 and DRG.

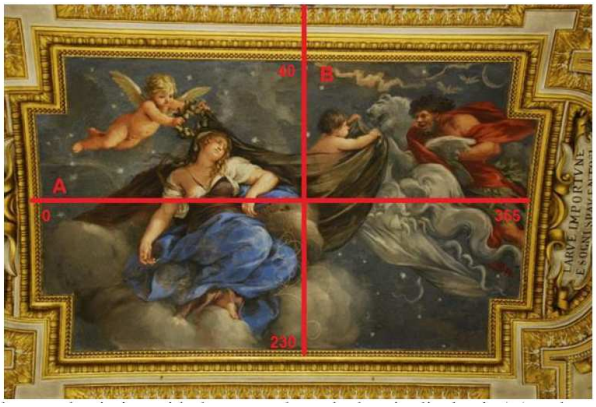

Figure 4: Photo of the mural painting with the scans along the longitudinal axis (A) and transversal axis (B).

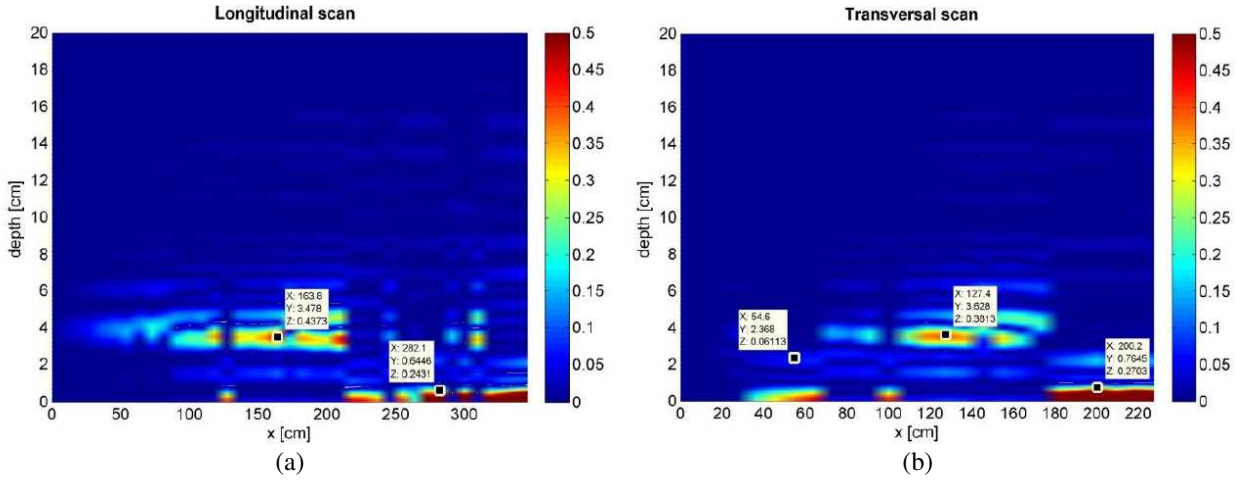

Figure 5: (a) Tomogram of the longitudinal scan; (b) tomogram of the transversal scan.

It is correct to underline that where are located the detachment the discontinuity due the interface brick/air is masked.

4. CONCLUSION

The proposed system based on microwave reflectometric method allows to perform tomography by non-contacting way until to 20 cm in depth with a resolution no more than 1 cm. The system is fully portable and robust and it has been tested on a vaulted ceiling to highlight anomalies in the masonry structure (detachment and air cavity). These preliminary results can be considered promising; the future research activities will be focused on the identification of operative limits in terms of maximum resolution and maximum unambiguous distance respect to the characteristic of the material under test.

ACKNOWLEDGMENT

The research activity has been partially supported by Tuscany Region, Italy (POR CReO FESR 2007-2013 Intervention sector 1.5a 1 1.6) within the PRIMARTE project (Italian acronym "ApProccio integrato di Rete per l'Innovazione nelle Metodologie di diAgnostica e inteRvento sul paTrimonio artistico e architEttonico").

REFERENCES

1. Bucur, V., "Techniques for high resolution imaging of wood structure: A review," *Meas. Sci. Technol.*, Vol. 14, 91–98, 2003.
2. Olmi, R., et al., "Innovative techniques for sub-surface investigations," *Materials Evaluation*, Vol. 69, No. 1, 89–96, 2011.
3. Capineri, L., P. Falorni, C. Frosinini, M. Mannucci, N. Macchioni, R. Olmi, S. Palanti, S. Penoni, S. Pieri, S. Priori, C. Riminesi, A. Santacesaria, and C. Todaro, "Microwave reflectometry for the diagnostic of cultural heritage assets," *PIERS Proceedings*, 778–781, Kuala Lumpur, Malaysia, Mar. 27–30, 2012.
4. Binda, L. and A. Saisi, "Application of NDTs to the diagnosis of historic structures," *Non-Destructive Testing in Civil Engineering Nantes, NDTCE'09*, France, 2009.
5. Capineri, L., G. Castellini, L. Masotti, and S. Rocchi, "Three dimensional lesion reconstruction by ultrasound," K. H. Labs, K. A. Jager, D. E. FitzGerald, J. P. Woodcock, and D. Neuerberg Heusler, *Diagnostic Vascular Ultrasound*, 300–311, Edward Arnold Ltd, London, 1992.
6. Daniels, D., *Ground Penetrating Radar*, 2nd Edition, IEE Press, London, U.K., 2004.
7. Brandelik, A. and C. Huebner, *Subsurface Sensing, Subsurface Aquametry*, Vol. 1, No. 4, 365–376, 2000.
8. Olmi, R., M. Bini, A. Ignesti, and C. Riminesi, "Non-destructive permittivity measurement of solid materials," *Measurement Science and Technology*, Vol. 11, No. 11, 1623–1629, 2000.
9. Collin, R. E., *Foundations for Microwave Engineering*, 2nd Edition, IEEE Press, Piscataway, NJ, 1992.
10. Torgovnikov, G. I., *Dielectric Properties of Wood and Wood-based Materials*, Springer-Verlag, Berlin, 1993.

Optimization of Nonlinear Coefficient Map in Back-propagation

Yanru Cao and Junhe Zhou
Department of Electronics Science and Engineering, Tongji University, Shanghai 200092, China

Abstract— In this paper, an optimized back-propagation algorithm for nonlinear compensation is proposed. Two parameters are proposed to control the nonlinear phase shift in BP algorithm. The parameters alter the nonlinear phase shift linearly with respect to the span number and are optimized in different dispersion maps.

1. INTRODUCTION

In optical communication systems, chromatic dispersion (CD) and fiber nonlinearities are the main effects that limit the system performance. Compensation of these effects is essential to realize high speed and ultra-long distance fiber transmission.

Back-propagation (BP) algorithm is one of the most extensively used methods which can jointly compensate the chromatic dispersion and the fiber nonlinearities. The algorithm can virtually inverse the fiber transmission by adopting the digital signal processing (DSP) technique. During the application of the algorithm, the dispersion and nonlinearity interplay with each other. The amount of the dispersion should be exactly compensated, while the nonlinearity should be partially compensated [1]. The nonlinear coefficient used in the BP algorithm should be between 0 and the actual fiber nonlinear coefficient. It was further proposed in [2] that the nonlinear parameter used in the simulation can be optimized with respect to the fiber locations in the span, and this optimal nonlinear compensation map should change with respect to dispersion. However, no systematic approaches have been proposed to optimize the nonlinear compensation map in the BP algorithm.

In this paper, we propose to use two parameters to control the value of the nonlinear coefficient map. The nonlinear coefficient in the BP algorithm changes linearly with respect to the span number and is evaluated as $an + b$, where a and b are two constants to be optimized, n the span number. Numerical simulation shows that by adopting this optimized BP algorithm, the BER performance can be greatly improved.

2. BACK-PROPAGATION THEORY

The evolution of the signal envelope in the optic fiber link is described by the well-known nonlinear Schrodinger equation (NLSE) [3]:

$$\frac{\partial A}{\partial z} = \left(\hat{D} + \hat{N}\right) A \tag{1}$$

$$\hat{D} = -\frac{i\beta_2}{2}\frac{\partial^2}{\partial T^2} + \frac{\beta_3}{6}\frac{\partial^3}{\partial T^3} - \frac{\alpha}{2}, \quad \hat{N} = i\gamma\left|A\right|^2 \tag{2}$$

where $\hat{D}$ is the linear operator which accounts for the fiber dispersion and attenuation, $\hat{N}$is the nonlinear operator which represents the effect of fiber nonlinearities. α,β_2, β_3 and γ are the fiber attenuation coefficient, group velocity dispersion coefficient, dispersion slope, and nonlinear coefficient, respectively.

Based on the theory of BP, the inverse process of fiber transmission is realized by solving the inversed-NLSE [1]

$$\frac{\partial A}{\partial z} = \left(-\hat{D} - \hat{N}\right) A \tag{3}$$

This equation can be numerically solved by using the split step Fourier method (SSFM) which divides the whole fiber length into a large number of segments and calculates the signal envelope step by step [3, 4]

$$A_{BP}(z,t) \approx \exp\left(-h\hat{D}\right)\exp(-hN(z+h))A_{BP}(z+h,t) \tag{4}$$

where h is the step size. While in the presence of noise, the optical signal can't be exactly recovered. It has been demonstrated that by partially compensate the nonlinear section, the system performance can be improved [1]. The equation above thus can be modified as

$$A_{BP}(z,t) \approx \exp(-h\hat{D})\exp(-h\xi N(z+h))A_{BP}(z+h,t) \tag{5}$$

where $0 \leq \xi \leq 1$ is the nonlinear compensation coefficient which represents the fraction of the nonlinearity compensated.

The length of the step size can be altered according to the computational capacity. In the case of the real time applications, the step size h is usually set to be the span length of the transmission system.

3. OPTIMIZED BACK-PROPAGATION ALGORITHM

During the fiber transmission, chromatic dispersion and fiber nonlinearities interact with each other. As the dispersion accumulates along the optic fiber link, the influence of the dispersion on fiber nonlinearity will vary along the fiber link accordingly. So the nonlinear coefficient map should be optimized with respect to the dispersion map and the fiber location. For the receiver side BP, the accuracy of the signal reduces as it traces back to the transmitter, so ξ should be larger for the spans nearer to the receiver and be smaller for the spans further away [2]. Without loss of generality, we consider the case that ξ changes linearly with the back-propagation span number n $(1 \leq n \leq N)$

$$\xi = an + b \tag{6}$$

where a and b are two constants to be optimized. Since ξ is preferred to be located between 0 and 1, in order to control the range of ξ during the simulation, we use the value of ξ at the starting point ξ_1 and the ending point ξ_N of the transmission link to control the variation of ξ

$$\frac{\xi - \xi_1}{\xi_N - \xi_1} = \frac{n-1}{N-1} \tag{7}$$

$$a = \frac{\xi_N - \xi_1}{N-1}, \quad b = \xi_1 - \frac{\xi_N - \xi_1}{N-1} \tag{8}$$

where ξ_1 and ξ_N are the values of ξ at span 1 and span N respectively, and satisfy the condition $\min(\xi_1, \xi_N) \leq \xi \leq \max(\xi_1, \xi_N)$.

4. NUMERICAL SIMULATION

In this section we compare the performance of the BP algorithm with constant nonlinear coefficient and the proposed optimized BP algorithm with linearly changed nonlinear coefficient for the optical transmission system shown in Fig. 1.

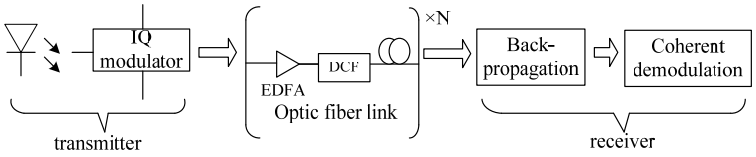

Figure 1: Block diagram of optical transmission system with BP.

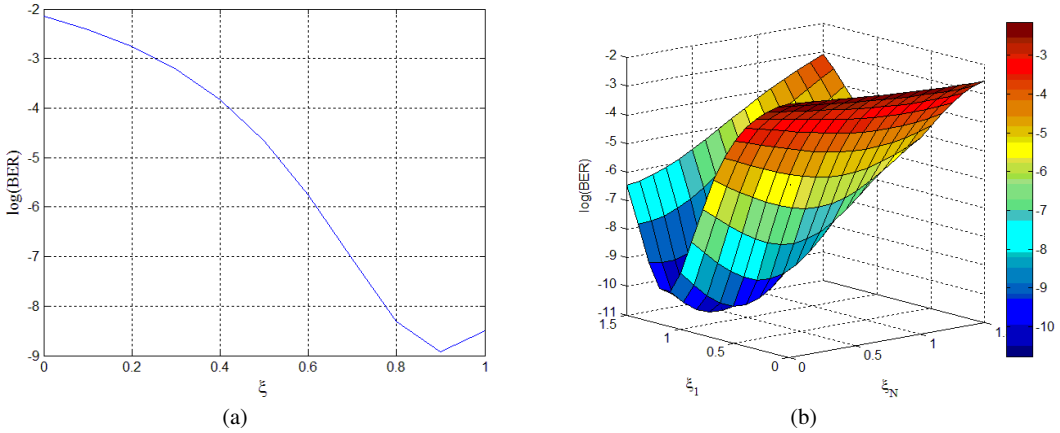

Figure 2: (a) BER vs. ξ obtained in BP algorithm with constant phase shift parameters and (b) BER vs. ξ_1 and ξ_N obtained in BP algorithm with linearly varying phase shift parameters.

In the simulation, 20 Gb/s QPSK signals are transmitted through 20 fiber spans. The fiber is the standard single mode fiber (SMF) whose α, β_2 and γ are 0.2 dB/km, $-20\,\mathrm{ps}^2/\mathrm{km}$ and $2 \times 10^{-3}\,\mathrm{km}^{-1} \cdot \mathrm{W}^{-1}$ respectively. The span length is 100 km. In each fiber span, attenuation is fully compensated by an erbium doped fiber amplifier (EDFA), CD is 90% undercompensated by the dispersion compensation fiber (DCF) and the residual dispersion is 10%. At the receiver side BP algorithm is applied to compensate the nonlinearity and the residual CD. The signals after compensation are demodulated by the coherent QPSK detector. The bit error rate (BER) is calculated depending on the eye pattern of the received signal. The BER performance of the BP algorithm versus the nonlinear phase shift parameters is shown in Fig. 2.

In the BP with constant phase shift parameters, the optimal ξ is 0.9 and the minimum BER is 1.18×10^{-9}. While in BP algorithm with linearly varying phase shift parameters, the minimum BER obtained is 1.70×10^{-11} with the optimal ξ_1 and ξ_N to be 1.1 and 0.4. The BER has been reduced about 18 dB as compared to the BP algorithm with constant phase shift parameter. The constellation diagrams of the received signals without and with the nonlinear compensation are shown in Fig. 3. The comparison of the constellations demonstrates that by using the optimized BP algorithm, the system performance is greatly improved.

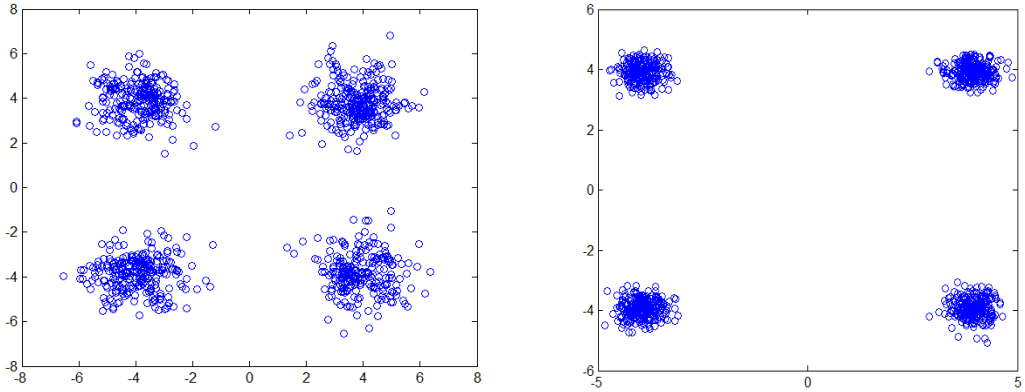

Figure 3: (a) Constellation obtained without nonlinear compensation and (b) constellation obtained with optimized BP algorithm when $\xi_1 = 1.1$, $\xi_N = 0.4$.

The performance of the systems with different values of dispersion compensation map is shown in Table 1 and Table 2.

The results show that the optimal nonlinear coefficient map strongly depends on the dispersion

Table 1: The performance of the system using BP algorithm with constant phase shift parameters.

Residual CD per span	Optimal ξ	BER
100%	0.5	3.02×10^{-6}
80%	0.5	1.65×10^{-6}
60%	0.5	1.49×10^{-6}
40%	0.6	5.98×10^{-7}
20%	0.8	7.13×10^{-9}

Table 2: The performance of the system using BP algorithm with linearly varying phase shift parameters.

Residual CD per span	Optimal ξ_1	Optimal ξ_N	BER
100%	0.7	0.3	1.74×10^{-6}
80%	0.7	0.3	9.69×10^{-7}
60%	0.7	0.3	6.83×10^{-7}
40%	0.8	0.3	2.46×10^{-7}
20%	1	0.4	1.13×10^{-9}

map. The comparison of Table 1 and Table 2 demonstrates that for all different dispersion maps, the proposed BP algorithm with linearly varying phase shift parameters is superior to the BP algorithm with constant phase shift parameters.

5. CONCLUSION

This paper propose to optimize the nonlinear coefficient map in BP by using two parameters to control the value of the nonlinear coefficient and make it change linearly with respect to the span number. The simulation results show that the BER performances of the systems with different dispersion maps have all been improved by using the BP algorithm with linearly varying phase shift parameters, and when the residual CD is 10%, the BER of the system can reduce about 18dB as compared to the system using BP algorithm with constant phase shift parameters.

ACKNOWLEDGMENT

This work is supported in part by the National science foundation of China (Grant No. 61201068).

REFERENCES

1. Ip, E. and J. M. Kahn, "Compensation of dispersion and nonlinear impairments using digital backpropagation," *IEEE Journal of Lightwave Technology*, Vol. 26, 3416–3425, 2008.
2. Ip, E. and J. M. Kahn, "Nonlinear impairment compensation using backpropagation," *Optical Fiber New Developments*, Intech, 2009.
3. Agrawal, G. P., *Nonlinear Fiber Optics*, 3rd Edition, Academic, London, U.K., 2001.
4. Binh, L. N., "Matlab simulink simulation platform for photonic transmission systems," *I.J. Communications, Network and System Sciences*, Vol. 2, 91–168, 2009.

Generic InP-based Integration Technology: RF Crosstalk in High-capacity Optical Transmitter PICs

W. Yao[1], **G. Gilardi**[1], **M. K. Smit**[1], **and M. J. Wale**[1, 2]

[1]COBRA Institute, Photonic Integration Group, University of Technology Eindhoven, The Netherlands
[2]Oclaro Technology Ltd., Caswell, Towcester, Northamptonshire, NN12 8EQ, UK

(*Invited Paper*)

Abstract— This paper reviews the basic ideas behind generic photonic integration and outlines how high-capacity integrated optical transmitters can benefit from this approach. Measurements of electrical coupling effects in a packaged transmitter chip are given, showing 2 dB power penalty due to RF crosstalk. A suitable simulation method for analyzing coupling effects on the integrated chip is presented and used to investigate the crosstalk originating from on-chip electrical routing lines and electro-optical phase shifters.

1. INTRODUCTION

Photonics is regarded by many as an enabling technology of the 21st century and it is been applied in many application areas such as in telecommunications, sensing and in the healthcare field. Similar to electronic integrated circuits, optical components and functionalities can also be combined together on one single, small form-factor chip, leading to a photonic integrated circuit (PIC). In the photonics industry, PIC based solutions are gaining popularity due to their small size, low cost and added functionality and value. However, development of the necessary integration technology is costly and time-consuming, as it is usually specifically tailored to the desired application and not easily transferable to others. This also restricts the access to photonic integration technology to a small group of preferential users. The recent emergence of generic photonic integration based on a foundry model approach aims at solving this issue by providing a few integration technologies that can realize a broad range of functionalities and by offering its access to a wide user range at low cost [1]. One of the traditional drivers of PIC development lies in the field of optical communications, where high-capacity wavelength-division multiplex (WDM) transmitters and receivers are needed to keep up with the increasing bandwidth demand. High-performance and large-scale photonic integrated circuits (LSPIC) coming from optimized integration processes has been the state-of-the-art solutions up until now [2], but could be replaced by lower-cost PICs in future created using generic integration technology. To maintain a high performance and its competitiveness and at the same time keep costs low, generic integration technology has to address certain challenges in transmitter and receiver PIC design. Owing to the high integration density of those PICs, interactions between components on the same chip in form of crosstalk, especially radio-frequency (RF) coupling, pose serious limitations and is the focus of this paper. At first, the generic foundry model is introduced in more detail and example designs of WDM transmitter chips are given. Afterwards, RF crosstalk issues are introduced and studied in experiment and simulation.

2. GENERIC PHOTONIC INTEGRATION

2.1. Generic Foundry Model

Although photonic integration density and complexity increased greatly through the years after its first emergence in the 1970s, its development did not experience such a fast pace as in case of microelectronics. The main reasons lies in the different methodologies followed in photonic and electronic integration. In photonics, most integration technologies are developed and optimized for one specific application, so that with time, the number of different technologies increased. Many of them are very similar to each other but still differ so much, that they cannot be easily transferred from one fab to the other. This lead to a fragmentation of integration processes, where no standard was available and each user had to spend effort and resources into application specific technology development first before having access to PICs. This is not the case in electronics, where a few standard processes are available (i.e., CMOS) that can serve a wide application and user group. Standard building-blocks (BBs) such as RLC-components, interconnects, diodes and transistors are defined with known performances from which complex circuits can be built up that suit the

desired application. This approach can be also adopted for photonic integration because usually most of the PICs are made from a composition of basic BBs such as optical amplifiers, phase shifters, waveguides and couplers. From the basic BBs more complex composite BBs can be built to realized the different required functionalities in a PIC, leading to the definition of a generic photonic integration process.

The practical implementation of the generic integration processes is performed by fabs acting as foundries that offer multi-project wafer runs. Because the process is the same for all users and their applications, different designs can be collected on the same wafer and fabricated in the same run, allowing cost sharing by the users and a further reduction of chip cost. A process design kit (PDK) is provided by the foundries that facilitate the PIC design procedure through appropriate mask layout and simulation software. Essentially, the users of the foundry do not need to know about the process details but interact only with the PDK. This way, the generic foundry model to photonic integration can make low-cost PICs available to a broad range of users and has been adopted already by several industrial partners [3]. Readers are referred here to the literature for a more detailed treatment of this topic [4, 5].

2.2. WDM Transceiver PICs

Historically, PIC development has been driven by the demand for high-speed optical transmitter and receiver chips for telecommunications. Long-haul optical transport systems require high-quality lasers and high-speed modulators and detectors. By using integrated solutions instead of discrete components the transmission capacity and channel count could be easily scaled up, keeping a small footprint at the same time. The underlying costs of PIC development and fabrication were covered because they were destined for a high-performance market which tolerates expensive components. However, as optical technologies gain more attention in short-reach applications such as in access networks or for interconnects in data centers, low-cost devices are desired that can be produced in very large quantities and are widely accessible. Generic photonic integration plays a key role here, because it meets those requirements and can lead to circuits with very high performance. Some examples of WDM transmitter PICs are shown in Figure 1, all of which were fabricated from generic photonic integration processes. Figure 1(a) depicts a DBR-laser based PIC with an array of 8 lasers and 4 Mach-Zehnder modulators (MZM) operating above 10 Gbps from the Oclaro foundry [6]. Figure 1(b) shows an 8-channel reflective modulator chip from the same foundry based on Michelson interferometers for short-reach applications [7]. A 10-channel transmitter chip based on an AWG-laser and designed for aggregated 100 Gbps is shown in Figure 1(c) from the COBRA generic integration process.

As integration density and PIC complexity increases, many challenges emerge during the design of WDM transmitters. Due to the close spacing of components on the chip, undesired coupling effects in form of thermal, RF and optical crosstalk can occur in laser or modulator arrays. In particular, electric and magnetic field coupling between high-speed modulator electrodes is undesired and can lead to signal integrity issues. Furthermore, high-capacity transmitters have many electrical inputs and outputs that need to be addressed with a suitable packaging solution. All those issues and their impact on the chip performance need to be properly understood when scaling-out transmitter PIC complexity. Here, we focus on RF crosstalk effects in transmitter PICs.

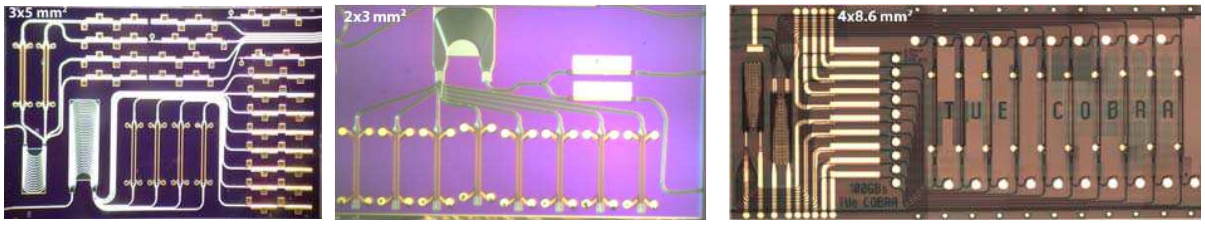

(a) (b) (c)

Figure 1: (a) DBR based 4-channel WDM transmitter chip with Mach-Zehnder modulators [6]. (b) 8-channel WDM reflective transmitter chip based on Michelson modulators [7]. (c) AWG-laser based 10-channel transmitter.

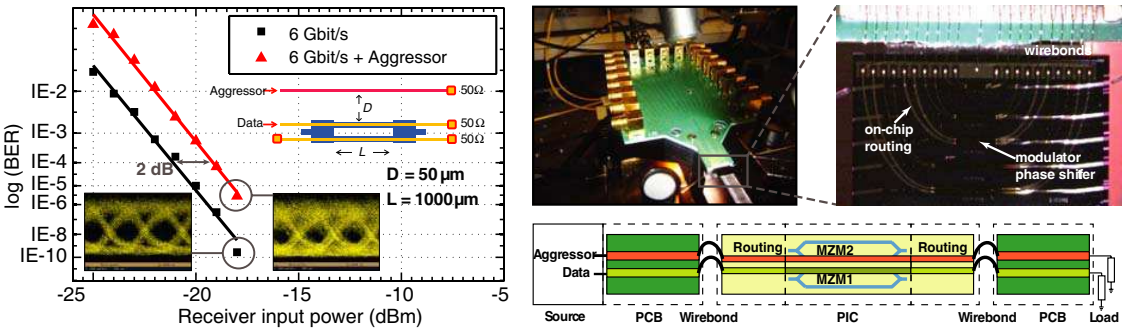

Figure 2: (a) Effect of RF crosstalk on BER curves measured on an assembly of modulator chip and high-speed PCB. (b) Several crosstalk sources contribute to the overall RF coupling in the assembly.

3. RF CROSSTALK IN PICS

3.1. Impact on System Performance

An example analysis of the impact of RF crosstalk on transmit system performance is presented to illustrate its importance. We have fabricated a test chip with closely spaced MZMs and on-chip electrical routing lines in the COBRA generic process as shown in Figure 2(b). The routing lines connect the travelling-wave phase shifters of the MZMs to bond-pads at the edge of the chip. A high-speed PCB is then connected to the chip through short wire-bonds for system-level measurements. To investigate any degrading effect of RF crosstalk, one channel is operated in single-drive mode with 50 Ω termination whereas a neighbour channel acts as an aggressor line. Overall crosstalk is then a combination of PCB, wire-bond, on-chip routing line and phase shifter crosstalk. Measured bit-error-rate curves with and without aggressor line are presented in Figure 2(a). It is evident that a 2 dB power penalty is introduced here due to the effects of RF crosstalk. Noise caused by the aggressor degrades the optical eye diagram at 6 Gbps visibly which leads to the observed power penalty.

The results indicate that RF crosstalk can have a significant effect on PIC system performance. However, it is very difficult to relate the effect of crosstalk specifically to one of its many possible sources. Usually, crosstalk in electronic packages such as in PCBs can be controlled properly with given effort and techniques in PCB design. This is more difficult for wire-bond interfaces to the PIC but crosstalk could be essentially reduced using alternative technologies such as flip-chip bonding. However, RF coupling on the PIC itself has not been investigated much so far as it only recently became important with high channel-count PICs with close channel spacing and high integration density emerged. One possibe way to analyze RF crosstalk within the PIC is presented in the following.

3.2. Crosstalk Simulations

To continue the example above, crosstalk between on-chip routing lines and electro-optical phase shifters from the COBRA generic integration process is analyzed using the commercial 3D field solver CST MWS. It has been shown in the literature that FEM and FDTD based field solvers are able to accurately simulate the microwave behaviour of electro-optical phase shifters [9, 10]. The method has been used before to model electrical properties of single phase shifters from the COBRA integration process [11] and is extended here to account for crosstalk effects of two coupled phase shifters and routing lines.

Figures 3(a) and 3(b) show the layer build-up of the phase shifter and routing line respectively which are both metal-insulator-semiconductor transmission lines. When two transmission lines are coupled together, we distinguish between near-end (NEXT) and far-end crosstalk (FEXT) as illustrated in Figure 3(c). In the first approximation, FEXT is more important for the modulation process, as it co-propagates with the optical signal, and accordingly we can restrict ourselves to FEXT in the following. To have a better understanding of the coupling process, electric field plots of two closely spaced phase shifters and routing lines are given in Figures 4(a) and 4(c). We can make out distinct differences between the two with respect to field concentration and coupling. In the former, the field is concentrated close to the depletion area of the optical waveguide, because the top metal is electrically connected to the doped semiconductor underneath through a highly

doped contact layer. In the latter case, the field takes the form of a typical microstrip line, localized within the passivation layer directly below the top metal. This leads to different coupling of the electric field. For the phase shifters, most of the evanescent field is kept within the trench region, because the semiconductor stack in the middle between the two phase shifters acts as a shield, so that only a small amount couples from the aggressor to the victim line through air. For the routing lines however, no such trench exists and coupling occurs through the passivation layer and air, not shielded by the semiconductor stack below, and more field arrives at the victim line. Magnetic field coupling (not shown here) is not affected by the trench and also contributes to the overall FEXT. Figures 4(b) and 4(d) show the overall FEXT for varying coupling distances and lengths at 10 GHz in case of phase shifters and feeding lines respectively. In general, reducing the separation distance or increasing the coupling length will increase FEXT. The dependence on the coupling length starts

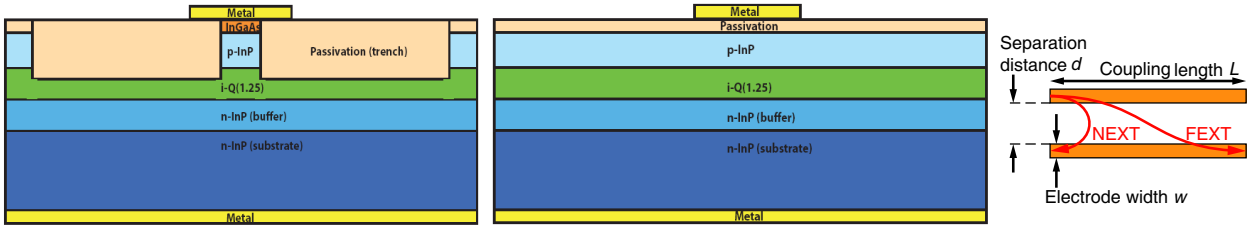

(a) (b) (c)

Figure 3: (a) Cross-section of high-speed electro-optical phase shifter and (b) cross-section of on-chip RF routing line from the COBRA generic integration process. (c) Illustration of two coupled lines.

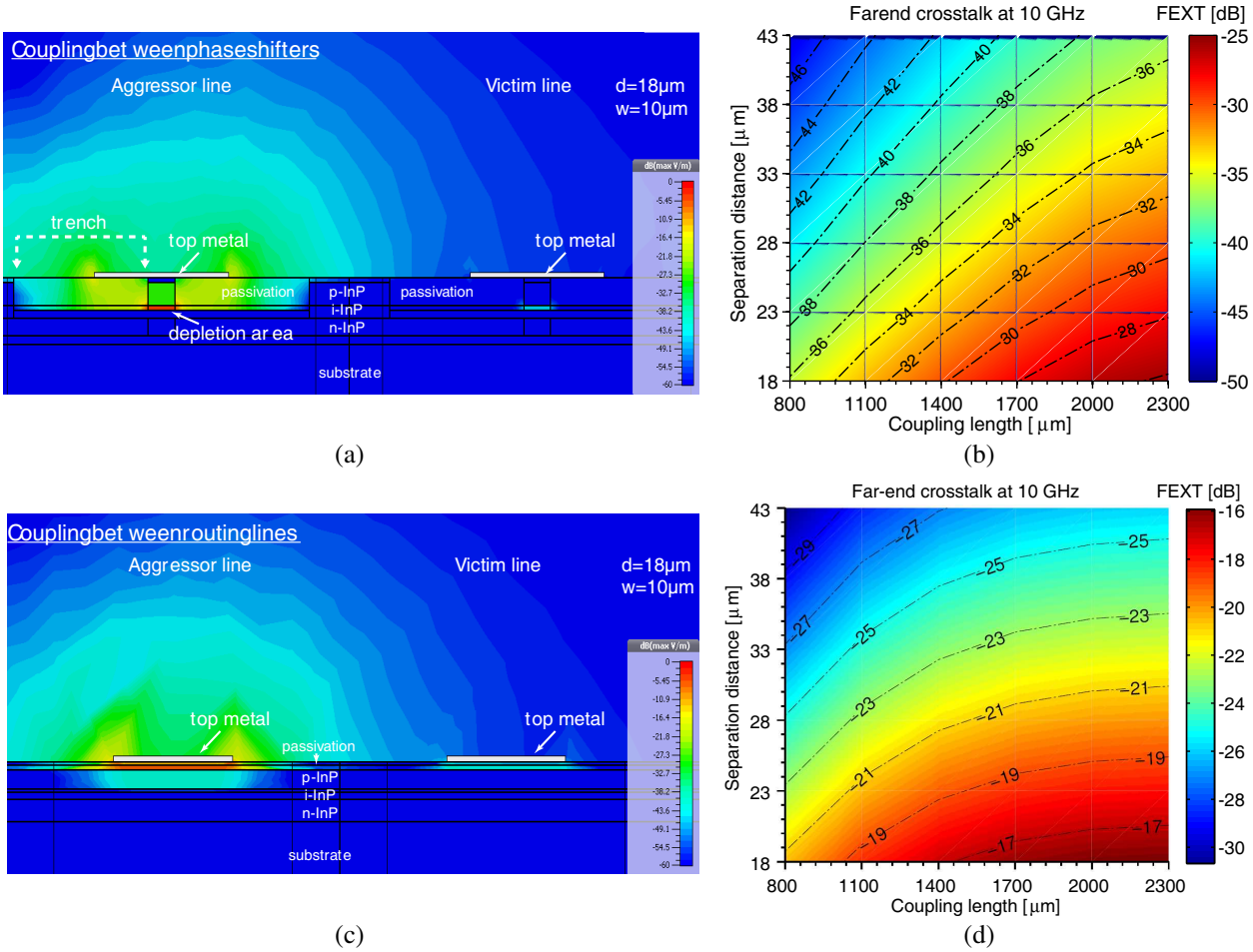

(a) (b)

(c) (d)

Figure 4: (a) Electric field coupling between MZM phase shifters ($w = 10\,\mu\text{m}$, $f = 14\,\text{GHz}$) and their FEXT variation (b) depending on coupling distance d and length L. (c) Electric field coupling between on-chip routing lines ($w = 10\,\mu\text{m}$, $f = 14\,\text{GHz}$) and their FEXT dependence on coupling geometry.

to saturate after a certain value because the coupling mechanism resembles that of a directional coupler and shows periodicity in frequency and coupling length. When comparing Figures 4(b) with 4(d), coupled routing lines experience more than 10 dB higher FEXT than coupled phase shifters for the same geometry, which can be attributed to the effect of the trenches mentioned earlier. Crosstalk can be kept below −30 dB for usual modulator length of 1.5 mm when placing phase shifters more than 20 µm away from each other, whereas 1 mm long routing lines need at least 40 µm spacing to achieve comparable low crosstalk levels.

It has been shown through simulations that routing lines contribute more to crosstalk effects on the PIC than modulator phase shifters, which is a useful insight for PIC design. Furthermore, using this methodology, design rules can be defined for determining minimum distances between components to avoid excessive crosstalk. Additionally, 4-port matrix representations can be extracted and used in circuit level analysis and simulation.

4. CONCLUSION

This paper has reviewed the basic ideas of generic photonic integration and outlined how it can speed up PIC complexity development and reduce its costs. Examples of WDM transmitter PICs based on this approach were given and in a test chip from the COBRA process, RF crosstalk, leading to 2 dB power penalty, has been identified as a major impairment for such systems. A 3D-solver based simulation model has shown that on-chip routing lines generate higher crosstalk than modulator phase shifters. The presented simulation methodology can be used to introduce design rules for crosstalk minimization and used together with circuit-level based simulations for RF design in transmitter PICs. Further experimental verification and estimation of the amount of tolerable crosstalk level need to be performed in future.

REFERENCES

1. Smit, M., et al., "Generic foundry model for InP-based photonics," *IET Optoelectron.*, Vol. 5, No. 5, 187–194, 2011.
2. Kish, F. A., et al., "Current status of large-scale InP photonic integrated circuits," *IEEE J. Sel. Top. Quant.*, Vol. 17, No. 6, 1470–1489, 2011.
3. The InP-based platform JePPIX: www.JePPIX.eu.
4. Gilardi, G. and M. K. Smit, "Generic InP-based integration technology: Present and prospects," *Progress In Electromagnetics Research*, Vol. 147, 23–35, 2014.
5. Smit, M., et al., "An introduction to InP-based generic integration technology," *Semicond. Sci. Technol.*, 2014 accepted for pub..
6. Ławniczuk, K., et al., "InP-based photonic multiwavelength transmitter with DBR laser array," *IEEE Photonics Technology Letters*, Vol. 25, No. 4, 352–354, 2013.
7. Stopinski, S., et al., "Monolithically integrated 8-channel WDM reflective modulator," *Optical Fiber Communication Conference (OFC/NFOEC)*, 1–3, Anaheim, USA, 2013.
8. CST Microwave Studio: www.cst.com.
9. Koshiba, M., Y. Tsuji, and M. Nishio, "Finite-element modeling of broad-band traveling-wave optical modulators," *IEEE Trans. Microw. Theory Techn.*, Vol. 47, No. 9, 1627–1633, 1999.
10. Lewen, R., S. Irmscher, and U. Eriksson, "Microwave CAD circuit modeling of a traveling-wave electroabsorption modulator," *IEEE Trans. Microw. Theory Techn.*, Vol. 51, No. 4, 1117–1128, 2003.
11. Yao, W., et al., "Microwave modeling and analysis of an InP based phase shifter from a generic foundry process," *Proceedings of the 18th Annual Symposium of the IEEE Photonics Society Benelux Chapter*, 151–154, Eindhoven, The Netherlands, 2013.

Design of an Efficient and a Compact Optical Pulse Compressor Using a Tapered Photonic Crystal Fiber

A. Manimegalai[1, 2], D. R. Divya[2], Abdosllam M. Abobaker[3], K. Senthilnathan[1], S. Sivabalan[4], K. Nakkeeran[5], and P. Ramesh Babu[1]

[1]Photonics, Nuclear and Medical Physics Division, School of Advanced Sciences
VIT University, Vellore 632 014, India
[2]Department of Electronics and Communication Engineering
Ganadipathy Tulsi's Jain Engineering College, Vellore 632 102, India
[3]Department of Communications Engineering, College of Electronic Technology, Bani Walid, Libya
[4]School of Electrical Engineering, VIT University, Vellore 632 014, India
[5]School of Engineering, University of Aberdeen, Aberdeen AB24 3UE, UK

Abstract— Ultrashort pulses (USPs) at wavelengths down to the communication window with a high repetition frequency range (GHz-THz) have found wide applications, especially, in bio-photonic sensors, optical coherence tomography, materials processing, etc.. There are some desirable features that USPs need to satisfy such as being pedestal-free and transform-limited for their suitability in communication as well as non-communication based applications. However, it is very difficult to meet out these desirable characteristicseven with carefully configured laser system. Hence, pulse-compression techniques have been the ultimate solution for generating USPs, in recent times.

Having realized the importance of generating USPs through pulse compression, we aim at designing a novel practicable pulse compressor using a tapered photonic crystal fiber (PCF) operating down to ultraviolet regime. The pulse propagation in a tapered PCF is governed by the nonlinear Schrdinger (NLS) type equation. We adopt the self-similar scaling analysis for generating USPs. Based on the analytical results, we model a tapered PCF such that the dispersion decreases exponentially while the nonlinearity increases exponentially along the propagation direction. Here, the required tapering is achieved by exponentially decreasing the diameter of the air hole as well as its pitch. We envisage that the proposed pulse compressor would turn out to be an excellent tool for generating high quality USPs down to ultraviolet regime, which, in turn, might be very much useful in bio-photonic related applications.

1. INTRODUCTION

There has been remarkable progress over the past two decades in the generation of USPs using photonic crystal fibers because of their wide applications in the fields of medicine, science, engineering and technology. Although there are several techniques in vogue for generating USPs, pulse compression technique stands unique for several reasons [1]. Pulse compression in fiber was first investigated by Mollenauer et al. [2]. Generally, optical pulse compression is categorized into two types, namely, linear compression and nonlinear compression. Using a dispersive fiber delay line or grating pairs, linear compression of chirped pulses has been demonstrated [1, 3]. Recently, several nonlinear pulse compression techniques, namely, adiabatic pulse compression, soliton pulse compression and self-similar techniques have evolved and these techniques generally rely on the interplay between the self-phase modulation (SPM) and group velocity dispersion (GVD) [1].

Photonic crystal fibers are ideal media for generation of USPs owing to the design flexibility in controlling the mode propagation properties [4]. PCF consists of a central defect region surrounded by periodic air holes. Controlling the dispersion becomes an important issue in the case of practical optical communication systems [5]. It is obvious that, in PCFs, one can easily control the dispersion by appropriately choosing the designing parameters such as the air hole spacing Λ and the air hole diameter d [6]. By varying the arrangement and size of the air holes, the fiber dispersion can be tailored in broad ranges. Recently, Travers et al. have demonstrated the adiabatic pulse compression at 1.06 µm in a dispersion and nonlinearity varying PCF [10]. It has been demonstrated that the dispersion and nonlinear profiles could be engineered through the tapering process which has been achieved by simultaneously stretching and heating to post-process the fiber [8, 9]. In general, the tapering is done by reducing the pitch and diameter. Fiber tapering provides a convenient way to reduce the mode-field diameter (MFD) of fibers, thereby allowing for a better

pulse compression [10–12]. We, thus, emphasize that the tapered PCFs are very much suitable for effective pulse compression studies when compared to conventional PCFs.

In this paper, we investigate the variations in optical properties, namely, the group velocity dispersion (GVD) and non-linearity along the propagation direction. Recently, the efficient pedestal-free pulse compression has been demonstrated using a PCF with an exponentially decreasing dispersion and increasing non-linearity profiles [10, 11].

2. DESIGNING TAPERED PCF

In the proposed geometric tapered structure,there are 4 sections containing 5 rings of air holes. Tapered PCF can be designed by simultaneous reduction of its geometrical parameters, namely, diameter d, and pitch (Λ). In this work, the physical parameter $d/(\Lambda)$ (air filling fraction) is varied exponentially from 0.2796 to 0.2910 and pitch is varied from 4 to 3.5 µm. While tapering the PCF, we decrease the diameter of air hole as well as the pitch. Fig. 1 illustrates the schematic view of the tapered PCF that is designed using finite element method (FEM) [12]. Fig. 2 shows the exponentially decreasing $d/(\Lambda)$ and (Λ) along the fiber length.

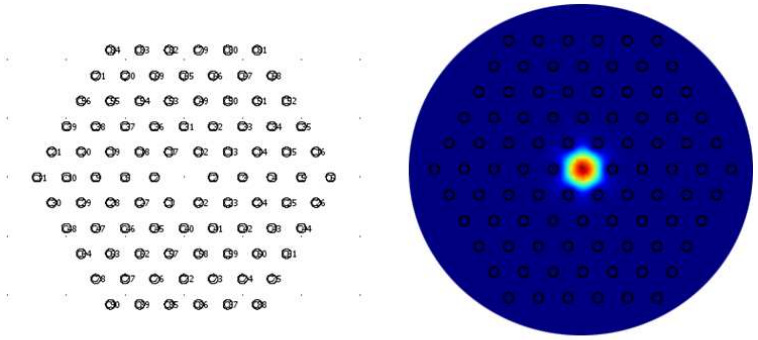

(a) (b)

Figure 1: (a) Geometrical structure and (b) mode field distribution of the proposed tapered PCF with $d/(\Lambda)0.2796$ and $(\Lambda)4$ µm.

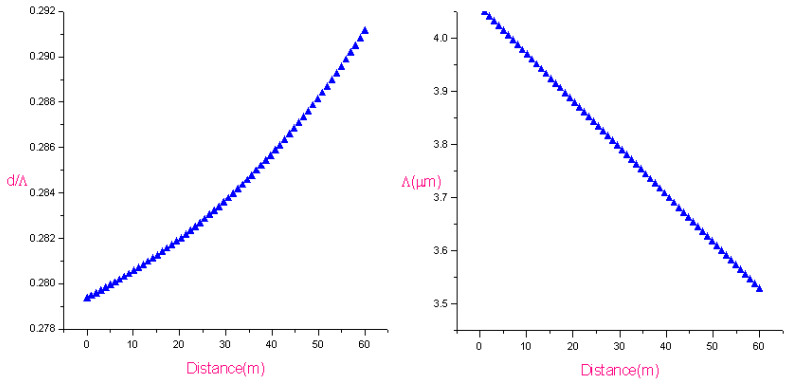

(a) (b)

Figure 2: (a) The variation of PCF parameter d/Λ along the propagation distance and (b) the physical parameter profile for tapered PCF with Λ along the propagation distance.

3. STUDY OF OPTICAL PROPERTIES

3.1. Dispersion

In this section, we delineate the important linear effect called group velocity dispersion. It is known that the dispersion does depend on both operating wavelength and the physical parameters such as core diameter and pitch. The dispersion parameter, D is determined from the second derivative of the computed n_{eff} value using finite element method. Fig. 3 depicts the variation of calculated dispersion with respect to distance. From Fig. 3, it is clear that the proposed tapered PCF exhibits anomalous dispersion which decreases exponentially from 75.3 to 5.9 ps/nmkm. The values of core

diameter and pitch affect the GVD [13]. The dispersion value of the tapered fiber is calculated by using equation $D = \frac{\lambda}{c}\frac{d^2n}{d\lambda^2}$. Fig. 3 depicts the variation of calculated dispersion with respect to distance.

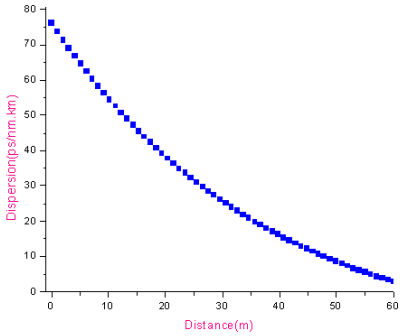

Figure 3: Variation of dispersion with respect to propagation distance.

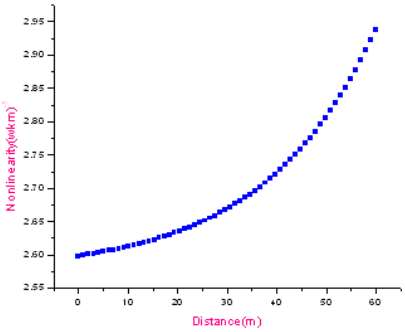

Figure 4: Variation of effective nonlinearity of the tapered PCF.

3.2. Nonlinear Property

By utilizing the A_{eff} value through FEM for different four PCF structures, the nonlinearity coefficient of the tapered fiber is computed using eqn $\gamma = \frac{2\pi n_2}{\lambda A_{eff}}$ where n_2 value is $2.3 \times 10^{-20}\,\mathrm{m}^2/\mathrm{W}$, which can be calculated using various nonlinear method [1]. The effective mode area of the fundamental mode is calculated using finite element method and the initial value of A_{eff} is found to be $0.3602\,\mu\mathrm{m}^2$ and its final value is $0.3169\,\mu\mathrm{m}^2$. The decrease in effective area leads to significant enhancement in the nonlinear effect and consequently the intensity of the compressed pulses goes high. In Fig. 4, it is very clear that the non-linearity increases exponentially along the propagation distance. Increasing nonlinearity does result in high intensity of pulses. Nonlinearity is increased exponentially from 2.587 to $2.940\,\mathrm{W}^{-1}\mathrm{m}^{-1}$).

4. DESIGNING TAPERED PCF THROUGH SELF SIMILAR ANALYSIS

The nonlinear pulse propagation in a tapered PCF is described by the following modified NLS equation with the varying dispersion and the nonlinearity [14, 15].

$$\frac{\partial U}{\partial z} + i\frac{\beta_2(z)}{2}\frac{\partial^2 U}{\partial t^2} - i\gamma(z)|U|^2 U = 0, \tag{1}$$

where U is the slowly varying envelope of the wave, z is the longitudinal coordinate, and t is the time in the moving reference frame. The parameters β_2 and γ are the second order dispersion coefficient and Kerr nonlinearity, respectively. We assume that the self-similar solution of above equation is given by

$$U(z,t) = \frac{1}{\sqrt{1-\alpha_{20}D(z)}} R\left[\frac{t-T_c}{1-\alpha_{20}D(z)}\right] \exp\left[i\alpha_1(z) + i\frac{\alpha_2(z)}{2}(t-T_c)^2\right] \tag{2}$$

The self-similar solution is possible if and only if the following conditions are satisfied [16]:

$$\beta_2(z) = \beta_{20}\exp(-\sigma z) \tag{3}$$

$$\sigma = \alpha_{20}\beta_{20} \tag{4}$$

$$\gamma(z) = \gamma_0 \exp(\rho z) \tag{5}$$

where β_{20}, γ_0, σ and ρ are the initial dispersion, nonlinearity, decay rate and growth rate, respectively. Based on the analytical results, we model a tapered PCF such that the dispersion decreases exponentially while the nonlinearity increases exponentially along the propagation direction. Here, the required tapering is achieved by exponentially decreasing the diameter of the air hole as well as its pitch. We point out that the results pertaining to the generation of USPs will be published elsewhere.

5. CONCLUSION

In conclusion, we have successfully designed a tapered PCF at 1550 nm by increasing the air filling fraction $d/(\Lambda)$ and decreasing pitch (Λ) along propagation direction. In this tapering, dispersion is exponentially decreased and nonlinearity is exponentially increased along the fiber length. The generation of ultrashort pulses at 1550 nm can be used in telecommunications applications, ultrahigh optical data rate systems and used in bio-photonic related applications.

ACKNOWLEDGMENT

KSN wishes to thank CSIR [No. 03(1264)/12/EMR-II] and DST [No. SR/FTP/PS-66/2009], Government of India, for the financial support through the sponsored projects. SS wishes to thank DST [No. SR/S2/LOP-0014/2012], Government of India, for the financial support through the sponsored project.

REFERENCES

1. Agrawal, G. P., *Nonlinear Fiber Optics*, 4th Edition, Academic Press, New York, 1989.
2. Mollenauer, L. F., R. H. Stolen, and J. P. Gordon, "Experimental observation of picosecond pulse narrowing and solitons in optical fibers," *Phys. Rev. Lett.*, Vol. 45, 1095–1098, Sep. 1980.
3. Li, Q., K. Senthilnathan, K. Nakkeeran, and P. K. A. Wai, "Nearly chirp and pedestal-free pulse compression in nonlinear fiber Bragg gratings," *J. Opt. Soc. Am. B*, Vol. 26, No. 3, 432–443, 2009.
4. Poli, F., A. Cucinotta, and S. Sellari, *Photonic Crystal Fiber Properties and Applications*, Springer, 2007.
5. Russell, P. S. J., "Photonic crystal fibers," *Science*, Vol. 299, 358–362, 2003.
6. Knight, J. C., T. A. Birks, P. S. J. Russell, and D. M. Martin, "All silica single mode optical fiber with photonic crystal cladding," *Opt. Lett.*, Vol. 21, 1547–1459, 1996.
7. Tse, M. L. V., P. Horak, F. Poletti, and D. J. Richardson, "Designing tapered holey fibers for soliton compression," *IEEE J. Quantum Electron.*, Vol. 44, No. 2, 192–198, Feb. 2008.
8. Travers, J. C., J. M. Stone, A. B. Rulkov, B. A. Cumberland, A. K. George, S. V. Popov, J. C. Knight, and J. R. Taylor, "Optical pulse compression in dispersion decreasing photonic crystal fiber," *Opt. Express*, Vol. 15, No. 20, 13203–13211, 2007.
9. Dudley, J. M. and J. Roy Taylor, "Ten years of nonlinear optics in photonic crystal fibre," *Nat. Photon.*, Vol. 3, No. 2, 85–90, 2009.
10. Nguyen, H. C., B. T. Kuhlmey, E. C. Magi, M. J. Steel, P. Domachuk, C. L. Smith, and B. J. Eggleton, "Tapered photonic crystal fibers: Properties, characterization and applications," *Appl. Phys. B*, Vol. 81, Nos. 2–3, 377–387, Jul. 2005.
11. Tse, M. L. V., P. Horak, F. Poletti, and D. J. Richardson, "Designing tapered holey fibers for solitoncompression," *IEEE J. Quantum Electron.*, Vol. 44, No. 2, 192–198, Feb. 2008.
12. Salem, A. B., R. Cherif, and M. Zghal, "Sub-two-cycle soliton self-compression in a tapered tellurite photonic crystal fiber," *Proc. of SPIE*, Vol. 8434, 84340B, 2003.
13. Raja, V. J., K. Senthilnathan, K. Porsezian, and K. Nakkeeran, "Efficient pulse compression using tapered photonic crystal fiber at 850 nm," *IEEE J. Quantum Electronics*, Vol. 46, No. 12, 1795–1802, Dec. 2010.
14. Abobaker, A. M., S. Olupitan, S. S. Aphale, K. Nakkeeran, K. Senthilnathan, and P. Ramesh Babu, "Dynamics of 850 nm optical pulses upon compression in a tapered photonic crystalfiber," *SIECPC*, 1–4, 2011.
15. Saitoh, K. and M. Koshiba, "Full-vectorial imaginary-distance beam propagation method based on a finite element scheme: Application to photonic crystal fibers," *IEEE J. Quant. Elect.*, Vol. 38, 927, 2002.
16. Dudley, J. M., C. Finot, D. J. Richardson, and G. Milot, "Self-similarity in ultrafast nonlinear optics," *Nat. Phys.*, Vol. 3, No. 9, 597–603, 2007.
17. Moores, J. D., "Nonlinear compression of chirped solitary waves with and without phase modulation," *Opt. Lett.*, Vol. 21, No. 8, 555–557, 1996.
18. Kruglov, V. I., A. C. Peacock, and J. D. Harvey, "Exact self-similar solutions of the generalized nonlinear Schrdinger equation with distributed coefficients," *Phys. Rev. Lett.*, Vol. 90, No. 11, 113902, 2003.

Regulating Carriers and Excitons in Simplified Hybrid WOLEDs by Using a Bipolar Interlayer Switch

Baiquan Liu[1], **Jianhua Zou**[1], **Miao Xu**[1], **Lei Wang**[1], **Hong Tao**[1], **Yueju Su**[2], **Dongyu Gao**[2], **Linfeng Lan**[1], **and Junbiao Peng**[1]

[1]Institute of Polymer Optoelectronic Materials and Devices
State Key Laboratory of Luminescent Materials and Devices
South China University of Technology, Guangzhou 510640, China
[2]New Vision Opto-Electronic Technology Co., Ltd, Guangzhou 510530, China

Abstract— As phosphorescent (P) emitters allows for a conversion of up to 100% of injected charges into emitted photons, resulting in a theoretical internal quantum efficiency of unity, P materials are usually imperative to boost the efficiency of white organic light-emitting diodes (WOLEDs). Unfortunately, there is still no proper blue P material in terms of operational lifetime and color-stability until now, limiting the development of all-phosphor devices. To solve the above conflicts, the hybrid WOLEDs, combining blue flourescent (F) emitters with P green-red/orange emitters, are considered to be an effective way due to their merits, such as high efficiency, stable color and long lifetime. A key feature of designing HWOLEDs is utilizing an appropriate interlayer, which locates between the F emitter and the P emitter. Herein, by mixing 4,4-N,N-dicarbazolebiphenyl (CBP) with bis[2-(2-hydroxyphenyl)-pyridine] beryllium ($Bepp_2$) as the interlayer, a simple hybrid with dual-emitting-layer a realized. The device with the bipolar interlayer shows higher performance than the device with CBP, $Bepp_2$interlayer and the device without interlayer. The reasons can be attributed to the bipolar interlayer which not only regulating the carriers in the device, but also eliminate the both the non-radiative Dexter energy Förster energy transfer between the two layers. The resulting device exhibits a total current efficiency of 23.6 cd/A and power efficiency of 16.2 lm/W at the illumination-relevant luminance of 1000 cd/m^2, respectively. Besides, a Commission Internationale de L'Eclairage (CIExy) variation of (0.31, 0.41) and a high color rendering index of 85 at 1000 cd/m^2 can be obtained. Moreover, the lifetime of the device is also discussed.

1. INTRODUCTION

White organic light-emitting diodes (WOLEDs) are now entering mainstream display markets and also being explored for next-generation lighting applications owing to their high efficiency, light weight and low cost [1]. Generally, WOLEDs are classified into three kinds according to the used emissive materials, including all-phosphorescent WOLEDs, all-flourescent WOLEDs and hybrid WOLEDs (HWOLEDs) which are based on hybrid (flourescent (F) and phosphorescent (P)) emissive materials [2–4] Among them, the utilizition of P emitters is desirable because P emitters are able to harvest both singlet and triplet excitons. Therefore, devices with internal quantum efficiencies up to 100% have been demonstrated. However, there is no perfect blue P material in terms of lifetime and color-stability untill now, limiting the development of P devices. In recent years, several publications have been devoted to address the conflict by creating HWOLEDs [2–4], which combine stable F blue emitters with P green-red/orange emitters. Sun et al. took the first step to realize HWOLEDs with high efficiency by using the combination of stacked F-interlayer (IL)-P-P-IL-F emitters, achieving a maximum total power efficiency (PE) of 37.6 lm/W and 23.8 lm/W at 500 cd/m^2 [2]. Since then, a large number of attentions have been paid to HWOLEDs. A key feature of designing HWOLEDa is utilizing an appropriate IL, which locates between the F emitter and the P emitter. Playing the crucial role in HWOLEDs, ILs can not only prevent Förster energy transfer (ET) from the F blue emitters to the red-green/orange P emitters, but also eliminate the non-radiative Dexter ET between the two layers [2]. Furthermore, emission color can also be tuned by changing the IL thickness. Therefore, by using a thin IL, both singlet and triplet excitons can be effectively managed. So far, 4,4-N,N-dicarbazolebiphenyl (CBP) is the most popular and efficient spacer owing to its high triplet energy (2.6 eV) and bipolar conducting properties [5]. However, it is found that its hole mobility of CBP is 10^{-3} cm^2/V s, much higher than its electron mobility (10^{-4} cm^2/V s) [5], leading to unbalanced carriers in this spacer. Hence, CBP can not be considered as an ideal spacer. In order to solve the issue, it is wise to mix an appropriate n-type material with CBP as the spacer, however, reports about it are scarce. On the other hand, it is easily noted that

the HWOLED created by Sun et al. shows complicated structure and the efficiency roll-off is serious To simplify structures, an alternative way is the utilization of stacked P-IL-F emitters to realize HWOLEDs. In fact, tremendous efforts have been devoted to the pursuit of this simple approach. For example, Ho et al. constructed a two-element HWOLED with the P-IL-F structure by utilizing a heteroleptic orange Ir-complex, obtaining a maximum total PE of 23 lm/W and 13.2 lm/W at 1000 cd/m^2 [3]. Yang et al. fabricated the P-IL-F device by applying a naphthalenebenzofuran compound as the deep-blue F emitter, achieving a maximum efficiency of 25 lm/W and 7.0 lm/W at 500 cd/m^2 [4]. From these facts, it is noted that the P-IL-F structure is simplified and the efficiency of these devices has experienced step-bystep increase in the last few years. However, the efficiency roll-off is still being a big obstacle. Moreover, the color rendering index (CRI) of this kind devices, which is important for the lighting applications [6], is paid negligible attention. As a result, the CRI of these simple devices is usually below 75. Therefore, there is an urgent need to simultaneously realize high efficiency, low efficiency roll-off and high CRI WOLEDs with the simplified P-IL-F structures.

In this paper, the device performance is greatly improved via an effective IL. The optimized device exhibits a maximum total current efficiency (CE) and PE of 24.7 cd/A and 16.2 lm/W during a large range of luminance, respectively. And the device exhibits a total CE of 23.6 cd/A and PE of 16.2 lm/W at 1000 cd/m^2, respectively. Besides, a high CRI of 85 is obtained, which is the highest value in the WOLEDs with P-IL-F structures, to the best of our knowledge. Moreover, the device shows rather low efficiency roll-off. Such presented results demonstrate that high efficiency, low efficiency roll-off and high CRI can be simultaneously realized in simple WOLEDs.

2. EXPERIMENTAL

As depicted in Figure 1, the configuration of the resultant device ($W4$) is ITO/MeO-TPD: F4-TCNQ (100 nm, 4%)/NPB (15 nm)/TCTA (5 nm)/MADN: DSA-ph(9 nm, 1%)/CBP: $Bepp_2$ (8.5:1.5, 5 nm)
/$Bepp_2$: $Ir(ppy)_3$: $Ir(piq)_3$ (1: 0.06: 0.01, 25 nm, 5%)/$Bepp_2$ (25 nm)/LiF (1 nm)/Al (200 nm), where ITO is indium tin oxide, MeO-TPD is N, N, N′,N′- tetrakis(4-methoxyphenyl)-benzidine F4-TCNQ is tetrafluoro-tetracyanoqino dimethane, NPB is N,N'-di(naphthalene-1-yl)-N,N'-diphenyl-benzidine, TCTA is 4,4',4"-tri(9-carbazoyl) triphenylamine, $Ir(ppy)_3$ is tris(2-phenylpyridinne)iridium(III), $Ir(piq)_3$ is tris(1-phenylisoquinolinolato-C^2, N) iridium(III), DSA-ph is p-bis(p-N,N-diphenyl-aminostyryl) benzene, MADN is 2-methyl-9,10-di(2-naphthyl)anthracene, $Bepp_2$ is bis[2-(2-hydroxyphenyl)-pyridine] beryllium. The detailed fabrication and measurement of devices followed well-established processes and as reported elsewhere [7].

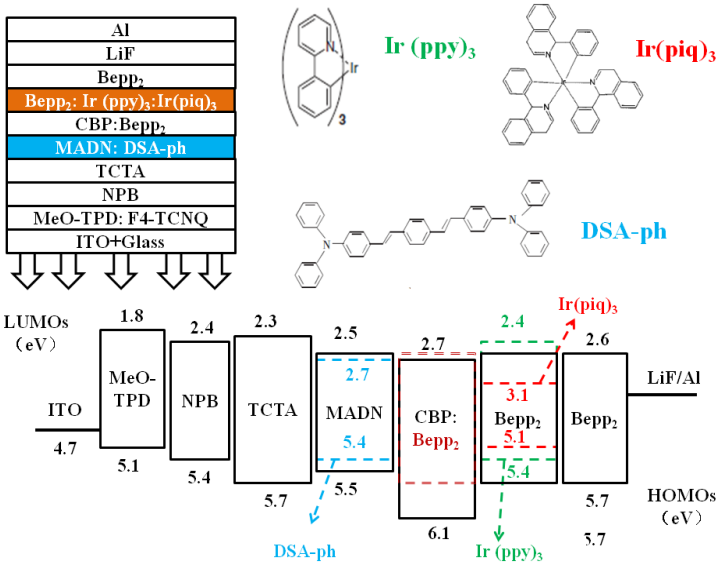

Figure 1: Top: Schematic layer structure of the WOLED and the chemical structure of emissive dopants. Bottom: Proposed energy-level diagram.

3. DISCUSSION AND RESULTS

Since improvement of both efficiency and stability in WOLEDs can be expected by rational design of the structure several strategies are employed to achieve high efficiency, low efficiency roll-off together with high CRI for our HWOLED with P-IL-F structure

First, to lower manufacturing cost, device architectures should be simple. Thus, we utilized double emitting layer to furnish white emission, surprisingly, performances of the simple device are very impressive. Second, to maximize exciton formation and emission in WOLEDs, it is necessary to optimize the concentration in the host-guest doped system. Therefore, monochromatic devices with various concentrations of dopant were tested to determine the best concentrations, as shown in Section 2. Third, emission peaks at 512 nm and 615 nm originating from $Ir(ppy)_3$ and $Ir(piq)_3$ ensure that P-EML exhibits broad emission spectra covering about three fourth of the visible spectrum. The F-EML is formed by doping DSA-ph into MADN (emission peak at 463 nm), greatly overcoming the color-stability limitations found for P WOLEDs. Consequently, high CRI and stable color are expected. Next, the p-doped hole injection layer improves holes injection from ITO anode into NPB hole transporting layer and prevents pinhole defects [7]. Moreover, the $Bepp_2$ electron transport layer exhibits high electron mobility [$10^{-4}\,cm^2/(Vs)$], giving effective electrons injection and thus an improved carrier balance [8]. Additionally $Bepp_2$ blocks holes and confines excitons in the EML because of its deep HOMO (5.7 eV) and high triplet energy (2.6 eV) [8]. Therefore, a carrier- and exciton-confining structure is formed via the combination of TCTA and $Bepp_2$, boosting efficiencies [7]. Finally, since the Dexter energy transfer can only occur within 1–2 nm and the Förster radius is around 3 nm, by introducing the 5 nm IL between P and F regions, both singlet and triplet excitons are confined efficiently, whereas the charge carriers still flexibly transport across this thin spacer bridge [2]. Based on these considerations, we put forward a simple HWOLED, simultaneously achieving high efficiency, low efficiency and high CRI

As shown in Figure 2, by using different ILs, the electroluminescent (EL) spectra of devices are significantly affected. At the illumination-relevant luminance of $1000\,cd/m^2$ the CIE coordinates of device $W1$ (without IL), $W2$ (with $Bepp_2$ IL), $W3$ (with CBP IL), and $W4$ (with CBP: $Bepp_2$ IL) are (0.18, 0.29), (0.19, 0.29), (0.31, 0.45) and (0.31, 0.41), respectively. In fact, we can not classify $W1$ and $W2$ into WOLEDs because they are far away from the white equivalent-energy point of (0.33, 0.33). Although the color of $W3$ is located in the white region, the CRI is only 71, which is not satisfied the demand of lighting applications. By using the more balanced IL, $W4$ shows a high CRI of 85. Moreover, the combination of high CRI, correlated color temperature (CCT), which is better located between 2500 and 6500 K, and the special CRI R9, which quantifies the color reproduction of saturated red and should be positive, is very interesting for commercial applications. $W4$ shows a CCT of 6245 K and a R9 of 63 at $1000\,cd/m^2$.

The reasons for this phenomenon are explained as follows. Since the triplet energy of $Bepp_2$ and $Ir(ppy)_3$ are much higher than that of DSA-ph and MADN, $W1$ without IL can not effectively eliminate the influence of Dexter ET between the F emitter and the P emitter, leading to no green and red intensity and hence we can not obtain a balanced white color For $W2$, holes are difficult to pass through the 5 nm $Bepp_2$ IL since $Bepp_2$ is an n-type material, leading to no white color. In the case of $W3$, although CBP is a bipolar material, its hole mobility is greater than electron mobility. Namely, elecrons will be more difficult than holes passing through the CBP bridge, implying few electrons can reach the blue emissive layer to recombine with the holes injected from the anode, which leads to weak blue intensity and hence we can not get a reasonable white light. On the other hand, by slightly codoped $Bepp_2$ with CBP as the IL, a more balanced carrier is achieved, leading to more balanced color.

The CE and PE of $W4$ in dependence of the luminance are shown in Figure 3. At the typical luminance of $1000\,cd/m^2$, the forward-viewing CE and PE are 13.9 cd/A and 9.5 lm/W, respectively. Since illumination sources are typically characterized by their total emitted power [2], $W4$ exhibits a total CE of 23.6 cd/A and PE of 16.2 lm/W at $1000\,cd/m^2$, respectively. Obviously, it is noted that the efficiency of this simplified device is higher than that of previous HWOLEDs at the practical luminance of $1000\,cd/m^2$ [2–4]. And much higher efficiency can be expected if we replaced the ETL with an n-doped layer to form a pin structure or utilized out-coupling techniques to increase the light extraction

More remarkably, $W4$ shows rather low efficiency roll-off. For example, a maximum forward-viewing CE of 14.5 cd/A is obtained at $2200\,cd/m^2$, which remains unchanged to a rather high brightness of 4700 cd/m^2, and even at an ultra high brightness of $10000\,cd/m^2$, the CE rolls off slightly to 13.6 cd/A. A maximum forward-viewing PE of 9.5 lm/W is obtained at $600\,cd/m^2$,

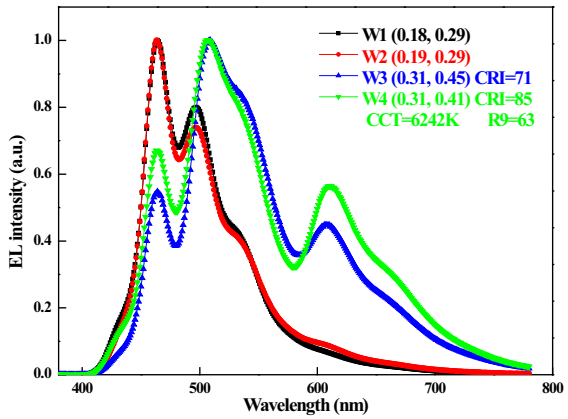

Figure 2: EL spectra of devices at a luminance of 1000 cd/m^2.

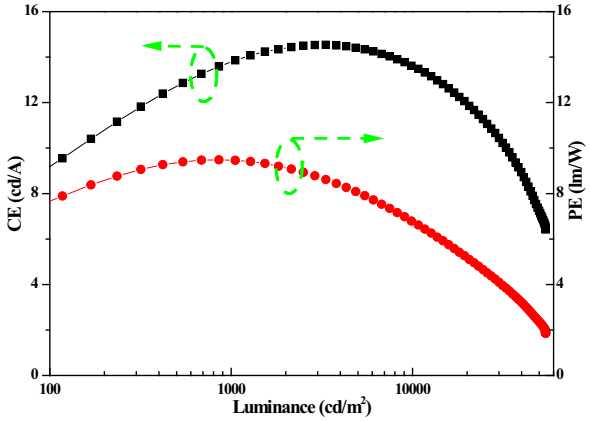

Figure 3: Power and current efficiencies as a function of luminance.

which remains unchanged to a high brightness of 1100 cd/m^2, and even at an high brightness of 5000 cd/m^2, the PE rolls off slightly to 8.1 lm/W. Apparently, the efficiency roll-off is much lower than previous HWOLEDs [2–4]. In fact, this is one of the lowest efficiency roll-off in WOLEDs in the literature so far, to our knowledge.

Finally, it is deserved to discuss the lifetime of $W4$, although there is no report has been documented on the lifetime of HWOLEDs in the revealed literature so far, which may be attributed to the lifetime of HWOLEDs is still poor nowadays. The lifetime of $W4$ at an initial illumination of 1000 cd/m^2 is only $\sim$ 1 hour. The poor lifetime can be attributed to the poor lifetime of CBP and TCTA. More stable charge transport materials and state-of-the-art emitters are expected to prolong lifetime.

4. CONCLUSIONS

In conclusion, we have successfully demonstrated a three-color hybrid WOLED with the P-IL-F structure. By using an effective IL, the device performance is dramatically boosted. The optimized device exhibits a maximum total CE and PE of 24.7 cd/A and 16.2 lm/W during a large range of luminance, respectively. Besides, a high CRI of 85 and rather low efficiency roll-off are achieved. We believe such presented results would provide an instructive guide for the rational design of ultra high-performance HWOLEDs, which will be very advantageous for the realization of next-generation solid-state indoor lighting sources in the future.

REFERENCES

1. Sasabe, H. and J. Kido, "Development of high performance OLEDs for general lighting," *J. Mater. Chem. C*, 1, 1699, 2013.
2. Sun, Y., et al., "Management of singlet and triplet excitons for efficient white organic light-emitting devices" *Nature*, Vol. 440, 908, 2006.
3. Ho, C. L., et al., "A multifunctional Iridium-Carbazolyl orange phosphor for high-performance two-element WOLED exploiting exciton-managed fluorescence/phosphorescence," *Adv. Funct. Mater.*, Vol. 18, 928, 2008.
4. Yang, X. H., et al., "Fluorescent deep-blue and hybrid white emitting devices based on a naphthalene-benzofuran compound," *Org. Electron.* Vol. 14, 2023, 2013.
5. Zhang, D., et al., "Extremely low driving voltage electrophosphorescent green organic light-emitting diodes based on a host material with small singlet–triplet exchange energy without p- or n-doping layer," *Org. Electron.*, Vol. 14, 260, 2013.
6. Jou, J., et al. "Efficient very-high color rendering index organic light-emitting diode," *Org. Electron.*, Vol. 12, 865, 2011.
7. Liu, B., et al., "Investigation and optimization of each organic layer: A simple but effective approach towards achieving high-efficiency hybrid white organic light-emitting diodes," *Org. Electron.*, Vol. 15, 926, 2014.
8. Zhao, F., et al., "A hybrid white organic light-emitting diode with stable color and reduced efficiency roll-off by using a bipolar charge carrier switch," *Org. Electron.*, Vol. 13, 1049, 2012.

Formation of Internal Micro-lens-like Structure for Organic Light-emitting Diodes

C. M. Hsu, Y. X. Zeng, B. T. Lin, W. M. Lin, and W. T. Wu
Department of Electro-Optical Engineering, Southern Taiwan University of Science and Technology
1, Nan-Tai St., Yung-Kang District, Tainan City 710, Taiwan, R.O.C.

Abstract— Micro-lens-like structures fabricated on indium tin oxide were employed to promote light extraction efficiency of an organic light-emitting diode (OLED). Four array patterns with coverage ratios of 7.9%, 14.1%, 20.9% and 27.7% were examined. The current efficiency of OLED was enhanced by 26.5% for the 14.1% recessed device (4.8 cd/A) compared with the planar device (3.8 cd/A). The improved current efficiency was attributed to the additional light-emitting area generated on the recess wall as well as the light scattering/deflection effects on the recessed surfaces. The current efficiency was found coverage-ratio independent suggesting that the light extraction is limited by the arrangement of the recesses.

1. INTRODUCTION

It is well known that the emitted light from the active layers of an organic light-emitting diode (OLED) is largely constrained in the refractive-index-mismatched structure, leading to low external quantum efficiency [1–3]. Two optical total reflections are responsible for light confinement in the refractive-index-mismatched structure. The total reflection at glass/air interface is called glass mode total reflection and that at indium tin oxide (ITO)/glass interface is called waveguide mode total reflection. Reduction of these two total reflections and thus to enhance light extraction efficiency of OLEDs has become a major research topic in recent years, particularly for lighting applications.

Reduction of glass mode total reflection by an external micro-lens film on glass has been demonstrated, and with which light extraction efficiency improved up to 70% has been reported [4, 5]. Attaching a porous film outside the glass can provide centers for light scattering and is also able to reduce glass mode total reflection [6]. On the other hand, surface-patterned structures such as photonic crystals and optical gratings have been introduced at glass/ITO or ITO/organic interfaces to minimize waveguide mode total reflection [7, 8]. The same effect can be achieved by internally embedding a scattering layer in a stacked OLED structure [9]. These approaches indeed have brought OLED lighting to become a practical stage.

This study reports the fabrication of micro-lens-like structure on ITO films and their application for OLED devices to enhance the external light extraction efficiency. Four arrays of recesses with various coverage ratios are created on an ITO film to form micro-lens-like internal structures in the OLED. The light extraction efficiency is expected to be enhanced by side wall effects of the recesses. These effects are discussed in detail.

2. EXPERIMENTAL DETAILS

To fabricate circular micro-lens-like internal structures, commercially available ITO films with a thickness of 250 nm deposited on glass were cleaned, patterned and etched to a depth of 200 nm. The circular patterns were designed to have two diameters of 4 μm and 6 μm with various pitches, yielding the recessed area a coverage ratio of 7.9%, 14.1%, 20.9% and 27.7%, as shown in Fig. 1(a). Morphology, optical, and electrical characteristics of the recessed ITO films were examined using atomic force microscope, ultraviolet-visible spectrophotometry, and 4-point prober, respectively.

Fabrication of OLED devices on the recessed ITO started with sequentially coating an organic hole transportation layer (PT-04, Lumitech Corp.), a light-emitting layer (PT-01/PT-86) and an electron transportation layer (PT-74) using thermal evaporation. Lithium fluoride (LiF) and aluminum (Al) cathode layers were then thermally evaporated. The complete OLED device comprised a glass/ITO(250 nm)/PT-04(30 nm)/PT-05+0.7%PT-01+2%PT-86(15 nm)/PT-74(20 nm)/LiF(0.5 nm)/Al(100 nm) structure, as shown in Fig. 1(b). The luminance-voltage (L-V) and current-voltage (I-V) characteristics of the OLED devices were measured using an I-V meter (model 237, Keithly Instruments Inc.) and an optical spectrometer (PR-650, PhotoResearch). The effects of recesses on light extraction are discussed.

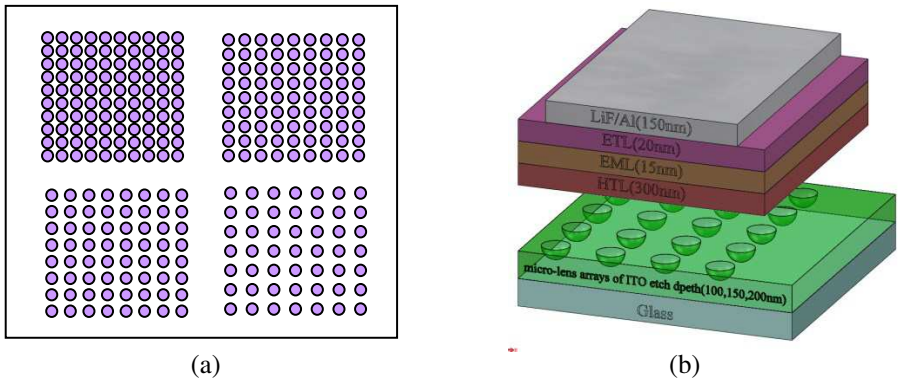

Figure 1: (a) The four array patterns designed to generate various coverage ratios of the recesses. (b) The complete OLED structure with recessed ITO anodes.

3. RESULTS AND DISCUSSIONS

Figures 2(a) and (b) show the AFM surface profiles of the planar and recessed ITO films, respectively. The recess surface roughness (Ra) at depth of 200 nm was measured to be 53 nm, much rougher than that of the initial ITO film (Ra = 0.6 nm). A rough surface can cause a higher degree of light scattering and thus minimize the amount of light conducting total reflections at a refractive-index-mismatched interface. Fig. 3 shows the optical and electrical properties of 200-nm recessed ITO at various coverage ratios. The optical transmittance (averaged from 380–800 nm) dropped from 90.7% for the initial ITO to slightly below 90% for recessed ITO films. The haze ratio dramatically increases from 0.6% for the initial ITO to 6.7% and 21.4% for 7.9% and 14.1% recess ITO films, respectively. Haze ratio does not increase further for ITO with recess coverage ratio higher than 14.1%. This suggests that the scattering or deflection was more serious with increasing coverage ratio but limited by the recess wall density. The scattering and deflection at recesses causes the emitted light propagating differently from that in a planar OLED device, and this explains why the optical transmittance is low for recessed ITO films. The electrical sheet resistivity of ITO films linearly increases with recess coverage ratio. The ITO sheet resistivity is $1.4 \times 10^{-4}\,\Omega$cm/□ with no recess and increases slightly to $39 \times 10^{-4}\,\Omega$cm/□ for the 27.7% recessed ITO film. This is reasonable because interfacial carrier scattering is more serious and carrier concentration is less for ITO films with denser recesses. The increase in resistivity of an ITO anode would generally lead to a degraded I-V characteristics of an OLED. However, this was not observed in this study.

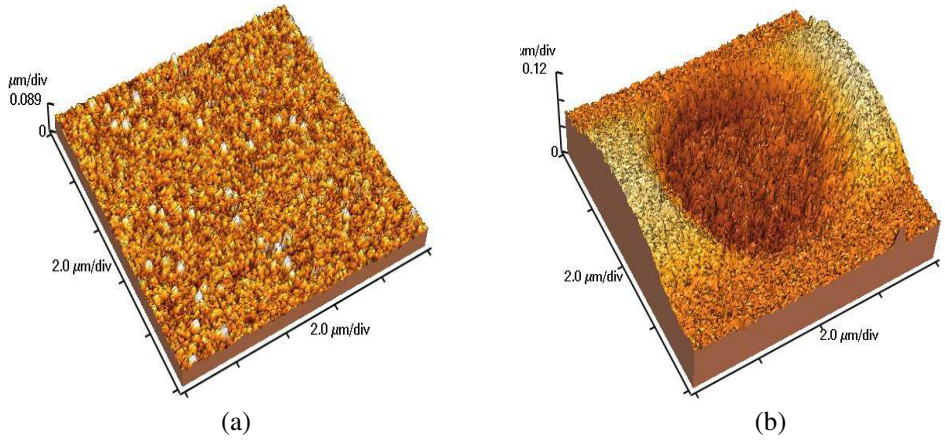

Figure 2: (a) AFM images of planar and (b) recessed ITO surfaces.

Figure 4(a) shows the I-V characteristics of OLEDs. It can be seen that the current density of the planar device was higher than that of the recessed devices. The threshold voltage defined at $10\,\text{mA/cm}^2$ was however almost the same at ~ 3.4 V for all the devices. The higher current density for the planar device reflects that the electrical resistance of the planar ITO film is lower than

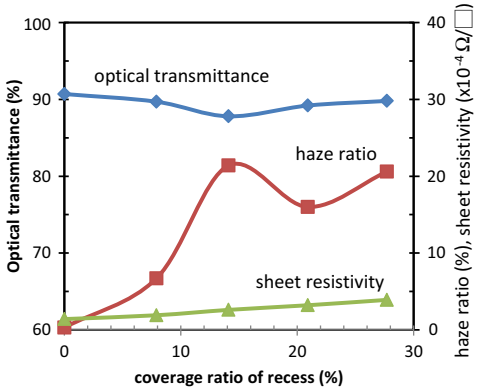

Figure 3: Optical transmittance, haze ratio and sheet resistivity of ITO films as a function of recess coverage ratio.

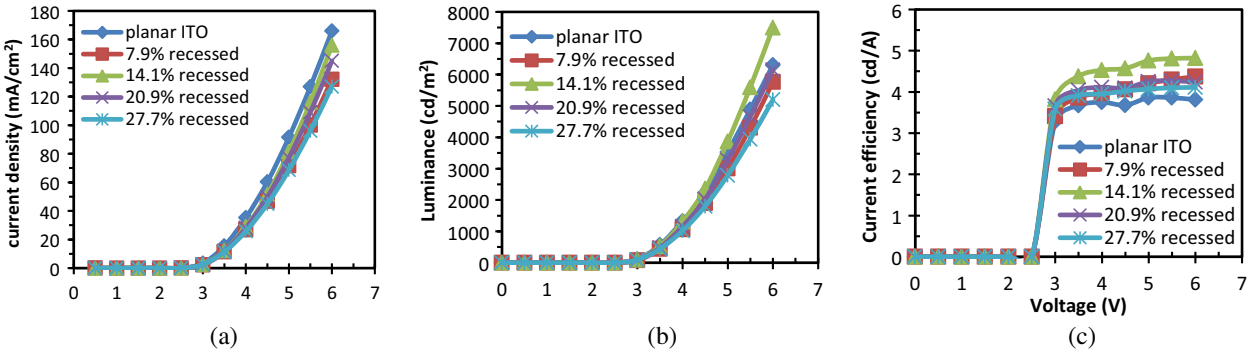

Figure 4: (a) I-V, (b) L-V, (c) η-V of OLEDs with various recess coverage ratios.

that of the recessed ITO film. Fig. 4(b) reveals the L-V characteristics of OLED devices. OLED with 14.1% recessed ITO anode apparently has better L-V characteristic than the planar device. Further examining the voltage dependent current efficiency (η) as shown in Fig. 4(c), one can see all recessed OLEDs performed improved current efficiency over the planar device. The 14.1% recessed device had the highest current efficiency of 4.8 cd/A at 6 V, which was 26.5% higher than that of the planar device (3.8 cd/A). The possible reasons are (1) the emitted light that generally trapped in a planar device now has a chance to reflect at the recess wall. The reflected light has a high possibility of escaping from the glass when moving in a direction almost normal to the glass; (2) the emitted light at recess bottom travels to a rougher ITO/organic interface and scatters more seriously. Part of the scattered light may be redirected in the normal direction of the glass and contribute to the total output optical density; (3) the emitted light in the recess wall area is an extra light source and has a large chance of escaping from the glass when moving upwards and downwards.

The degree of improvement in current efficiency is found not coverage-ratio dependent. The 14.1% recessed device has the highest, followed by the 7.9%, 20.9% and 27.7% recessed devices with current efficiency of 4.37, 4.24, and 4.11 cd/A at 6 V, respectively. The reasons for that are complicated since the light out-coupling involves the possible routes mentioned above. The recess covered area, the recess wall area and the pitches all can change the way the emitted light propagates in the recessed and stacked structure. In addition, the deteriorated electrical and optical properties of the recessed ITO anode are among other factors for this observation.

4. CONCLUSIONS

OLED devices with ITO anodes having circular micro-lens-like structures have been demonstrated to perform improved external current efficiency by up to 26.5%. The deflection effect at the recess wall and the scattering effect at the recess bottom enhanced out-coupling efficiency and led to the improved external current efficiency. The current efficiency is found coverage-ratio independent due to mixed optical and electrical effects at various recess patterns.

ACKNOWLEDGMENT

The authors would like to thank the National Science Council for financially supporting this work under contract grant NSC-101-2221-E218-042.

REFERENCES

1. Lin, C. L., T. Y. Cho, C. H. Chang, and C. C. Wu, "Enhancing light outcoupling of organic light-emitting devices by locating emitters around the second antinode of the reflective metal electrode," *Appl. Phys. Lett.*, Vol. 88, No. 8, 81114, 2006.
2. Meerheim, R., M. Furno, S. Hofmann, B. Lussem, and K. Leo, "Quantification of energy loss mechanisms in organic light-emitting diodes," *Appl. Phys. Lett.*, Vol. 97, No. 25, 253305, 2010.
3. Mladenovski, S., S. Hofmann, S. Reineke, L. Penninck, T. Verschueren, and K. Neyts, "Integrated optical model for organic light-emitting devices," *J. Appl. Phys.*, Vol. 109, No. 8, 083114, 2011.
4. Madigan, C., M. H. Lu, and J. Sturm, "Improvement of output coupling efficiency of organic light-emitting diodes by backside substrate modification," *Appl. Phys. Lett.*, Vol. 76, No. 13, 1650–1652, 2000.
5. Moller, S. and S. Forrest, "Improved light out-coupling in organic light emitting diodes employing ordered microlens arrays," *J. Appl. Phys.*, Vol. 91, No. 5, 3324–3327, 2002.
6. Peng, H. J., Y. L. Ho, X. J. Yu, and H. S. Kwok, "Enhanced coupling of light from organic light emitting diodes using nanoporous films," *J. Appl. Phys.*, Vol. 96, No. 3, 1649–1654, 2004.
7. Lee, Y., J. S. H. Kim, and J. Huh, "A high-extraction-efficiency nanopatterned organic light-emitting diode," *Appl. Phys. Lett.*, Vol. 82, No. 21, 3779–3781, 2003.
8. Do, Y. R., Y. C. Kim, and Y. M. Song, "Enhanced light extraction from organic light-emitting diodes with 2D SiO_2/SiNx photonic crystals," *Adv. Mat.*, Vol. 15, No. 14, 1214–1218, 2003.
9. Chang, H. W., J. H. Lee, S. Hofmann, Y. H. Kim, L. Muller-Meskamp, B. Lussem, C. C. Wu, K. Leo, and M. Gather, "Nano-particle based scattering layers for optical efficiency enhancement of organic light-emitting diodes and organic solar cells," *J. Appl. Phys.*, Vol. 113, No. 20, 204502, 2013.

Optical Properties of Graphene on Quartz and Polyethylene Substrates in Terahertz Frequency Range

A. K. Denisultanov, **S. E. Azbite**, **N. S. Balbekin**, **S. I. Gusev**, **and M. K. Khodzitsky**
Department of Photonics and Optoinformatics, ITMO University
Kronverkskiy pr. 49, Saint-Petersburg 197101, Russia

Abstract— We report measurements of the real and imaginary part of the optical properties of graphene (refractive index, permittivity, conductivity, penetration depth) in the far-infrared region from 0.1 to 1.2 THz at the temperature of 300 K.

1. INTRODUCTION

Last years graphene increasingly attracts attention of scientists by unusual properties such as high electric and thermal conductivity etc. [1]. Also terahertz (THz) radiation has tremendous potential for applications in imaging, medical diagnosis, health monitoring, environmental control, chemical & biological identification, security infrastructure, military industry. So to use graphene in terahertz optics it would be useful to know dispersion of graphene optical properties, such as refractive index $n(\omega)$, optical conductivity $\sigma(\omega)$ etc.. The purpose of this paper is to experimentally obtain optical properties of graphene in the frequency range of 0.1–1.2 THz.

2. SUBJECT OF RESEARCH

In this research we used dielectric substrates (polyethylene terephthalate (PET), quartz) that are transparent for terahertz radiation, have low absorption coefficient in terahertz frequency range [2, 3]. Also it is possible to transfer the graphene layer on these substrates surface. PET substrate thickness is $d_p = 175\,\mu$m; the quartz substrate thickness is $d_q = 500\,\mu$m. The theoretical thickness of graphene is $d_g = 0.345$ nm, the grain size is up to 10 µm (Graphenea company). The bare substrates and graphene layer on these substrates are used in the experiment. The sample holder is demonstrated in Figure 1.

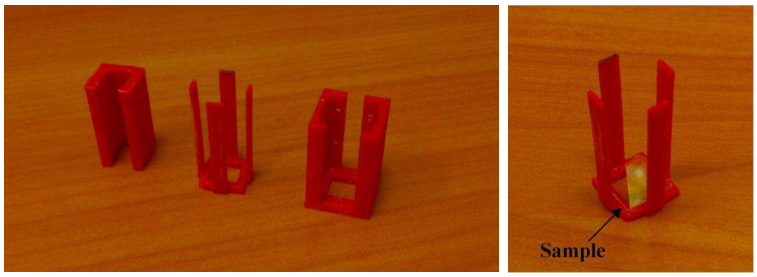

Figure 1: Sample holder.

3. EXPERIMENTAL SETUP

FL-1 — laser of femtosecond pulses, M — mirrors, BS — beam splitter, DL – optical delay line, G — generator of THz radiation based on the crystal InAs, PM — parabolic mirrors, TL — lenses for THz radiation, f — filter of infrared (IR) radiation, TP — translucent silicon plate, Ch — chopper, EOC — electro optical crystal of CdTe, W — Wollaston prism, BP — balanced photodiodes, LA — lock-in amplifier, ADC — analog-to-digital converter, PC — personal computer.

The scheme of THz spectrometer is shown in Figure 2. The laser beam is splitted by two ones in the ratio of 10% to 90%. 10% energy is probe beam, 90% one is pump beam. The pump beam optical path is controlled by optical delay line. The pump beam is modulated by chopper at the frequency of 667 Hz. The generator of THz radiation is based on the crystal InAs in the magnetic system. After passing through IR radiation filter THz beam incidents on the sample. Then, THz radiation induces birefringence in electro-optical crystal. Wollaston prism splits the probe IR beam on two ones with orthogonal polarization, which are detected by balanced photodiodes. Parameters of THz spectrometer: the pump pulse power of 1 W, the pump pulse duration of 200 fs,

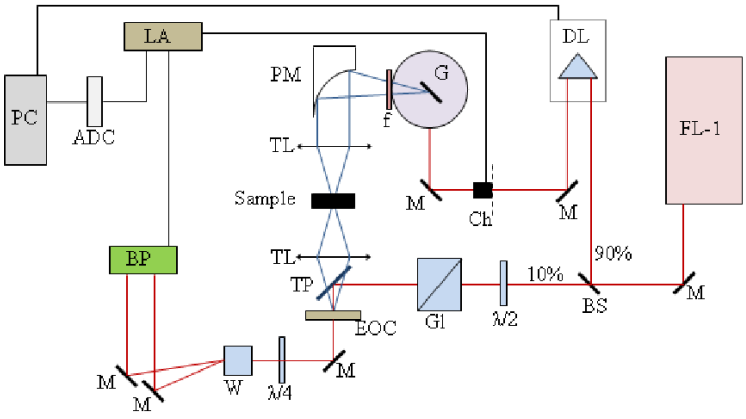

Figure 2: Scheme of the time-domain THz spectrometer in transmission mode.

the frequency range of 0.1–1.2 THz, the average THz radiation power of 30 μW. Photo of the setup and the typical time-domain waveforms are shown in Figure 3.

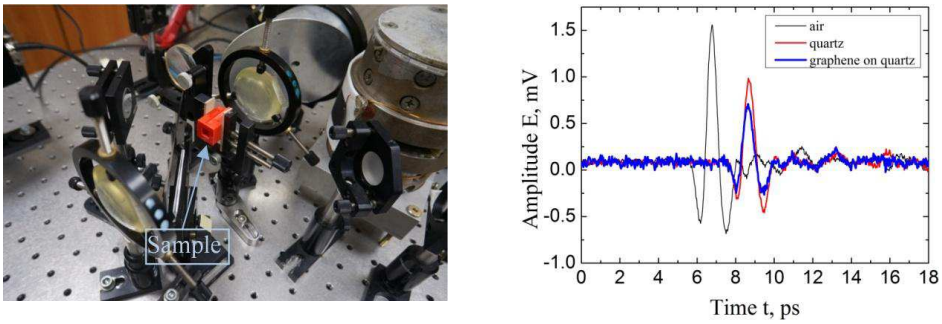

(a) (b)

Figure 3: (a) Photo of time-domain THz spectrometer in transmission mode and (b) typical waveforms of THz pulses.

4. EXPERIMENT RESULTS

The dispersion of substrates complex refractive indices were extracted by comparing the signal spectrum with the reference spectrum using the transmission method described in [4]. The complex refractive indices of PET and quartz for the frequency range of 0.1–1.2 THz were shown in Figure 4.

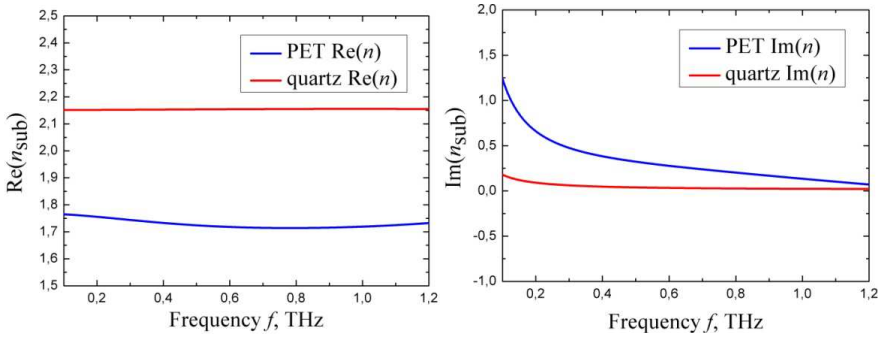

Figure 4: Complex refractive index $\hat{n}_{sub}(\omega)$ of substrates.

The graphene monolayer complex conductivity $\hat{\sigma}(\omega)$ was calculated from the equation [5]:

$$\hat{\sigma}(\omega) = \frac{\left[\frac{(\hat{n}_{sub}(\omega)+1)\hat{E}_0(\omega)}{\hat{E}(\omega)} - \hat{n}_{sub}(\omega) - 1\right]}{Z_0}, \tag{1}$$

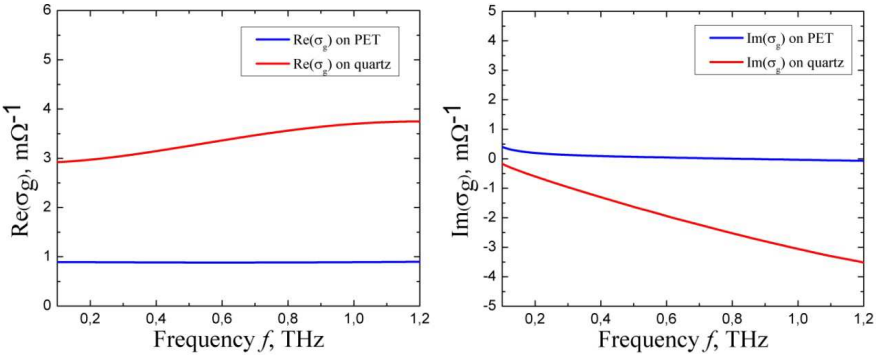

Figure 5: Graphene monolayer complex conductivity $\hat{\sigma}_g(\omega)$.

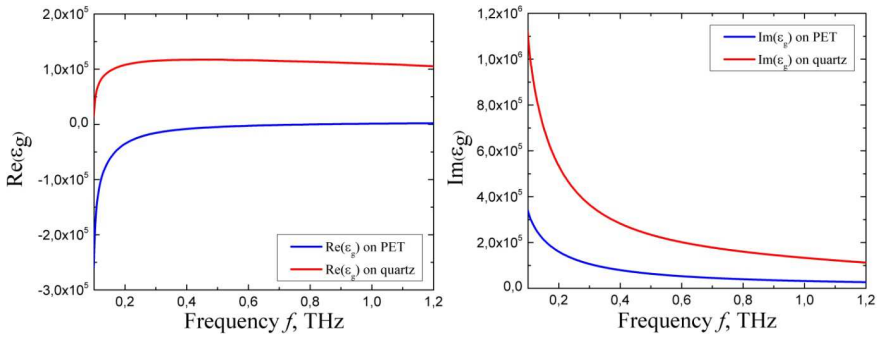

Figure 6: Graphene complex permittivity $\hat{\varepsilon}_g(\omega)$.

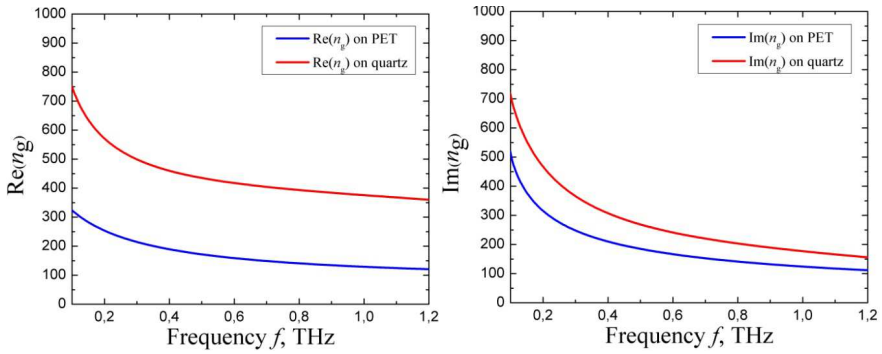

Figure 7: Graphene complex refractive index $\hat{n}_g(\omega)$.

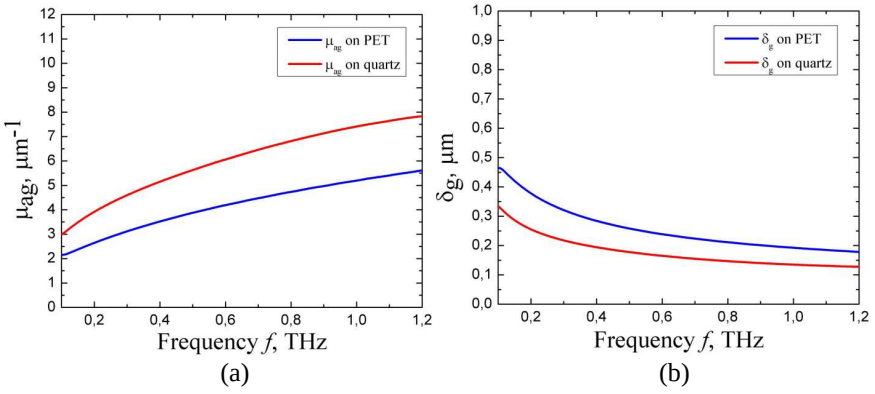

Figure 8: Graphene (a) absorption coefficient $\mu_{ag}(\omega)$ and (b) penetration depth $\delta_g(\omega)$.

where $\hat{E}_0(\omega) = E_0(\omega) * e^{i\varphi(\omega)}$ is the complex electric field amplitude of THz wave transmitted through the bare substrate; $E(\omega)$ is the complex electric field amplitude of THz wave transmitted through the substrate with the graphene monolayer; $\hat{n}_{sub}$ is the complex substrate refractive index; $Z_0 = 377\,\Omega$ is the impedance of free space. $E_0(\omega)$ and $E(\omega)$ were obtained by Fourier transformation of the time-domain waveforms of THz pulses.

Using the Equation (1) and the substrates complex refractive indices data we can obtain the complex conductivity $\hat{\sigma}_g(\omega)$ of the graphene monolayer for the frequency range of 0.1–1.2 THz (Figure 5).

Then, the graphene complex permittivity $\hat{\varepsilon}_g(\omega)$ can be obtained from the following equation [6]:

$$\hat{\varepsilon}_g(\omega) = 1 - i\frac{\hat{\sigma}_g(\omega)}{\omega\varepsilon_0 t_g}, \tag{2}$$

where ε_0 is dielectric constant; $t_g \approx 0.345$ nm is the graphene monolayer thickness. The calculation results are shown in Figure 6.

The Equation (2) and the measured complex conductivity $\hat{\sigma}_g(\omega)$ allows to obtain several optical graphene properties, such as the complex refractive index $\hat{n}_g(\omega)$, the absorption coefficient $\mu_{ag}(\omega)$ and the penetration depth $\delta_g(\omega)$. The complex refractive index $\hat{n}_g(\omega)$ is shown in Figure 7 for various substrates.

The imaginary part of $\hat{n}_g(\omega)$ allows to calculate the graphene monolayer absorption coefficient $\mu_{ag}(\omega)$ by the next formula:

$$\mu_{ag}(\omega) = \frac{4\pi n''_g(\omega)}{\lambda}, \tag{3}$$

where $n''_g(\omega)$ is the imaginary part of $\hat{n}_g(\omega)$, λ is the wavelength of THz radiation.

The penetration depth $\delta_g(\omega)$ was calculated as $1/\mu_{ag}(\omega)$.

5. CONCLUSION

In this paper, experimentally graphene monolayer general optical parameters for the frequency range 0.1–1.2 THz (the complex conductivity $\sigma_g(\omega)$, the complex permittivity $\varepsilon_g(\omega)$, the complex refractive index $n_g(\omega)$, the absorption coefficient $\mu_{ag}(\omega)$ and the penetration depth $\delta_g(\omega)$) were obtained. This experimental data may be used in practical purposes, that are respective to graphene application.

ACKNOWLEDGMENT

This work was financially supported by Government of Russian Federation, Grant 074-U01.

REFERENCES

1. Warner, J. H., *Graphene. Fundamentals and Emergent Applications*, Elsevier, Amsterdam, 2013.
2. Grischkowsky, D., S. Keiding, M. van Exter, and C. Fattinger, "Far-infrared time-domain spectroscopy with terahertz beams of dielectrics and semiconductors," *J. Opt. Soc. Am. B*, Vol. 7, No. 10, 2006–2015, 1990.
3. Jin, Y.-S., G.-J. Kim, and S.-G. Jeon, "Terahertz dielectric properties of polymers," *J. Korean Phys. Soc.*, Vol. 49, 51–517, 2006.
4. Zhang, X.-C. and J. Xu, *Introduction to THz Wave Photonics*, Springer, New York, 2010.
5. Jnawali, G., Y. Rao, H. Yan, and T. F. Heinz, "Observation of a transient decrease in terahertz conductivity of single-layer graphene induced by ultrafast optical excitation," *Nano Lett.*, Vol. 13, No. 2, 524–530, 2013.
6. Choon, H. G., "Analysis of surface plasmon excitation at terahertz frequencies with highly-doped graphene sheets via attenuated total reflection," *Appl. Phys. Lett.*, Vol. 101, No. 11, 111609, 2012.

Recent Developments in Graphene-based Optical Modulators

Ran Hao, J. M. Jin, and E. P. Li
Department of Information Science and Electronics Engineering
Zhejiang University, Hangzhou 310027, China
(*Invited Paper*)

Abstract— Graphene has shown promising perspectives in optical active components due to the large active-control of its permittivity-function. This paper systematically reviews the recent developments of graphene-based optical modulators, including material property, single-layer, multi-layer, few-layer graphene-based modulator and corresponding figure-of-merits. The results showed graphene is an excellent material for enhancing silicon's weak modulation capability after it is integrated into the silicon platform, showing significant influence on optical interconnects in future integrated optoelectronic circuits.

1. INTRODUCTION

Optical modulator is a device which is used to modulate (alter) the properties of a light such as amplitude, phase or polarization by electro-refraction (ER) or electro-absorption (EA) modulation. The electric effects that traditionally cause either ER or EA are Pockels effect, Kerr effect, Franz-Keldysh effect and plasma dispersion effect [1]. However, these effects are too weak in pure silicon material at the communication wavelengths so that it usually needs an extremely large arm length which results in large footprint as well as high drive voltage to reach the required modulation [9]. In addition, the side-effect introduced to the pass-band and stability after applying some enhancement methods is still challenging. Even with the doping of silicon, the modulation speed is limited due to the low carrier mobility in silicon, e.g., the best reported modulation speed is up to 50 Gbit/s and difficult to be further improved [2]. To overcome these fundamental bottlenecks, novel materials need to be explored so that they can provide better modulation capability and CMOS compatibility simultaneously. Graphene has attracted lots of interest due to its remarkable mechanical, electric, magnetic thermal and optical properties [6]. The unique properties of graphene such as strong coupling with light, high-speed operation, and gate-variable optical conductivity make it a very promising material for optical modulators [1]. When the imaginary part of graphene conductivity is negative, graphene supports the transverse magnetic mode noted as surface plasmon polaritons (SPP) [4], displaying potential applications for highly tunable SPP modulator applications [5]. This is why a large amount of research attention has been focused on the graphene-based optical modulator [11].

In this paper, we systematically reviewed the mechanism and recent developments for various graphene-based electro-refraction (ER) modulators.

2. OPTICAL MATERIAL PROPERTIES OF SINGLE-LAYER GRAPHENE

Figure 1 shows the 3D graphene permittivity introduced by Vakil and Engheta, and the conductivity of an infinite graphene sheet with a thickness of 0.7 nm at the wavelength $\lambda = 1550$ nm which is computed from the Kubo formula [4, 7]. It can be seen that there is a dip in the curve of permittivity magnitude, and the epsilon-near-zero (ENZ) point is obtained at the chemical potential $\mu_{c0} = 0.513$ eV where the absolute value of epsilon is approaching zero. When the chemical potential $\mu_c < \mu_{c0}$, both the real and imaginary part of the permittivity ($\mathrm{Re}(\varepsilon_{//})$ and $\mathrm{Im}(\varepsilon_{//})$) have the positive sign so that the graphene layer behaves like a dielectric material. When the chemical potential is gradually increased, the "dielectric graphene" is gradually transforming into "metallic graphene" at the transition chemical potential $\mu_{c0} = 0.513$ eV. There exists a range where in which both $\mathrm{Re}(\varepsilon_{//})$ and $\mathrm{Im}(\varepsilon_{//})$ are very close to zero called ENZ point. When $\mu_c > 0.52$ eV, $\mathrm{Re}(\varepsilon_{//})$ becomes negative and $\mathrm{Im}(\varepsilon_{//})$ is approaching zero which means the graphene layer acts like a metallic layer, and the graphene layer is then fabulous to transfer surface plasmon polaritons (SPP) [10], displaying much more potential for future optoelectronic devices.

3. SINGLE-LAYER GRAPHENE-BASED MODULATOR

The effective modal refractive index (n_{eff}) of the graphene-embedded silicon waveguide (GESW, as depicted in Fig. 2(a)) is the critical parameter that determines the overall GESW properties. The

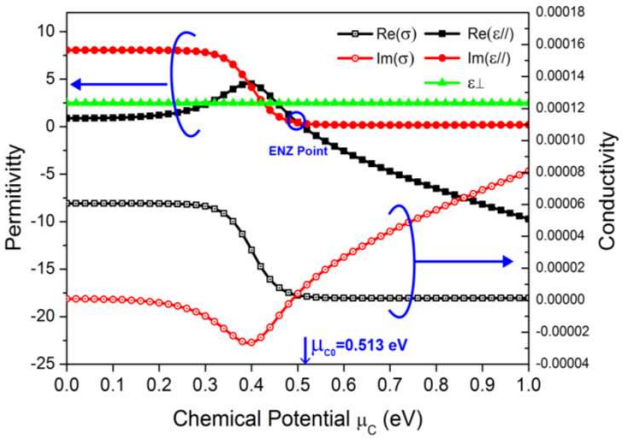

Figure 1: Conductivity and permittivity of an infinite graphene sheet (the wavelength is fixed at 1550 nm) (reprinted from Ref. [5]).

real part of the index ($\mathrm{Re}(n_{\mathrm{eff}})$) is linear to mode's phase information via: $\varphi = k_0 \mathrm{Re}(n_{\mathrm{eff}})L$, where k_0 is the wave number in vacuum and L is the propagation distance. The imaginary part of the index ($\mathrm{Im}(n_{\mathrm{eff}})$) is related to the propagation loss α through $\alpha = 8.68 k_0 \mathrm{Im}(n_{\mathrm{eff}})$ [5]. Therefore, the configuration of an optical modulator can be implement by changing either the $\mathrm{Re}(n_{\mathrm{eff}})$ or $\mathrm{Im}(n_{\mathrm{eff}})$: the former one is typically the phase modulator, while the later one is amplitude modulator. The calculated $\mathrm{Re}(n_{\mathrm{eff}})$ and the $\mathrm{Im}(n_{\mathrm{eff}})$ for the proposed GESW under the chemical potential from 0 to 1 eV is shown as Fig. 2(b). According to the modal theory, the n_{eff} is then calculated from

$$n_{\mathrm{eff}} = \frac{\zeta}{k_0} = \frac{\beta}{k_0} + i\frac{\delta_z}{k_0}, \tag{1}$$

where ζ is the eigenvalue of the system, β is the propagation constant, and δ_z is the attenuation constant. In Fig. 2(b), the n_{eff} of the proposed waveguide is lower than silicon's refractive index (3.45) at all chemical potentials. An inflection point is observed in the $\mathrm{Re}(n_{\mathrm{eff}})$ curve at $\mu_c = 0.4$ eV, where n_{eff} changes intensively near the inflection point. If comparing Fig. 2(b) with Fig. 1, a similarity between the n_{eff} curve and graphene's $\varepsilon_{//}$ curve can be found. It is thus inferred that n_{eff} is proportional with $\varepsilon_{//}$, and one could control n_{eff} to the desired value in terms of simply changing n_{eff}.

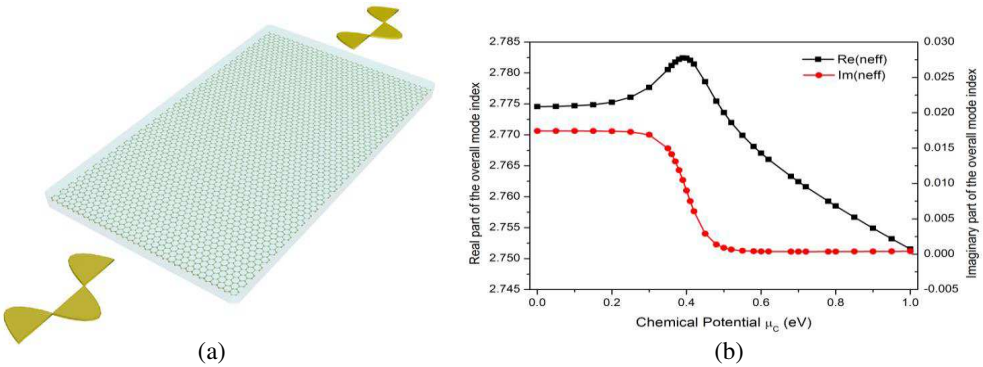

Figure 2: (a) 3D view of GESW; (b) real and imaginary parts of effective modal index variation under different chemical potentials for GESW (reprinted from Ref. [5]).

The impressive large value of Δn_{eff} is great appreciated for the modulator designs based on ER effect, such as MZ modulator, as shown in the schematic picture of Fig. 3(a). Let us first fix one chemical potential at $\mu_{c1} = 1$ eV. With μ_{c2} changing, the corresponding Δn_{eff} will be modified, thus the required arm length L_π to reach the π phase shift is modified. The propagation loss can be evaluated in terms of the maximum allowed length $L_{\max}$ as shown in the red curve in Fig. 3(b), indicating the length where the energy at the output decays to $1/e$ of its original value. We would

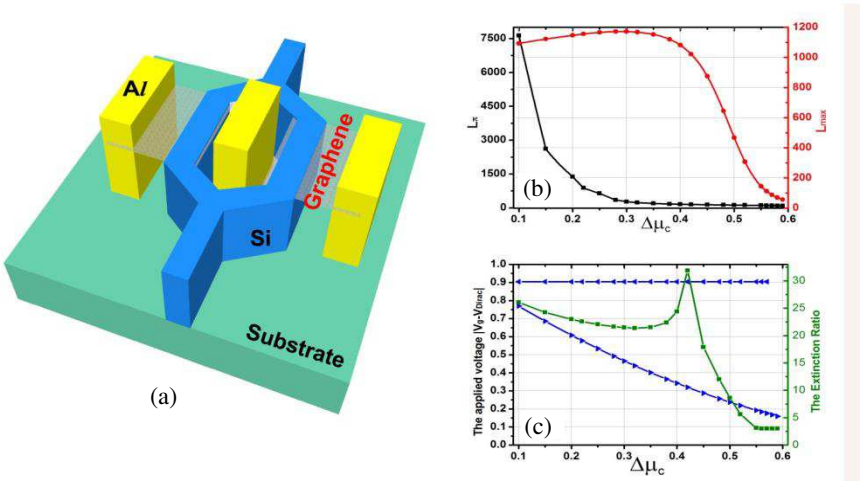

Figure 3: (a) Schematic pictures for top view of the MZ modulator configuration; (b) relationship between $L_\pi/L_{\max}$ and μ_c; (c) relationship between the applied votages/extinction ratio and μ_c.

focus our attention on the condition that $L_\pi < L_{\max}$ in which case the waveguide has enough power at the output [5]. When $\Delta\mu_c = 0.3\,\text{eV}$, L_π is 120 μm, which is one order of magnitude smaller than the present reported value [3]. If the width of the modulation arm is 450 nm and the distance between the two arms is 1.7 μm. Taking into account of the electrode width of 1 μm on each arm side, the overall width of the device is 5 μm. thus the footprint of our proposed modulator is only 120 μm × 5 μm [5]. This small size as well as the CMOS compactable structure indicates its valuable capability to be integrated into photonic circuits in a single chip.

Another important parameter for the MZ modulator is the applied voltage V_g. The blue curves in Fig. 3(c) have shown the difference between V_{g1} (for signal "1" of the reference arm) and V_{g2} (for signal "0" of the modulated arm) is called π shift voltage V_π. As expected. Since L_π decreases much faster than the increase speed of V_π, the minimum modulation efficiency $V_\pi L_\pi$ would be achieved at $55\,\text{V}\cdot\mu\text{m}$ where L_π is smallest at 120 μm. One significant advantage for MZ modulator is that the extinction ratio is high if compared with EA modulators. Fig. 3(c) shows the extinction ratio and applied voltage V_g variations with μ_c, where a maximum extinction ratio of 34 dB has been observed at $\Delta\mu_c = 0.42\,\text{eV}$.

4. MULTI-LAYER GRAPHENE-BASED MODULATOR

4.1. Multi-layer Graphene-based Modulator

Multi-layer graphene based devices have also been studied for the modulator application. Based on the above monolayer graphene-embedded modulator, it is straightforward to embed the multi-layer graphene sheets inside silicon waveguide. An eight-layer graphene embedded MZ modulator [5] is shown in Fig. 4(a). The corresponding electric field distribution in one of the arm of modulator is shown in Fig. 4(b). As demonstrated previously, the field profile displays a Gaussian-like distribution. It has been theoretically demonstrated that by embedding multi-layer graphene in the silicon waveguide, the Δn_{eff} has been increased significantly under the same chemical potential change compared with the monolayer graphene. Therefore, the L_π has been reduced to 27.57 μm which means a much smaller arm length is needed to acquire the π phase shift, as shown in Fig. 4(c). The overall footprint is then estimated as 5 μm × 30 μm. Moreover, the proposed graphene embedded modulator is highly tunable whose overall modal index is in linear relationship with the in-plane permittivity of graphene. The high modulation efficiency is further optimized to $20\,\text{V}\cdot\mu\text{m}$, which is 6 times better than the monolayer case. In Fig. 4(d), The extinction ratio is 35 dB at smaller arm length compared with Fig. 3.

4.2. Few-layer Graphene-based Modulator

Previous discussion on multi-layer graphene relies on the fact that graphene sheets are inserted into the silicon waveguide individually, separated with a distance between the adjacent sheets. However, this scheme adds the difficulties in fabrication and the modulation efficiency. There is an alternative way to embed an N-layer thick graphene sheet in the silicon waveguide. Particularly, when the number of layer $N < 5$, it is called few-layer graphene that exhibits even better performance than

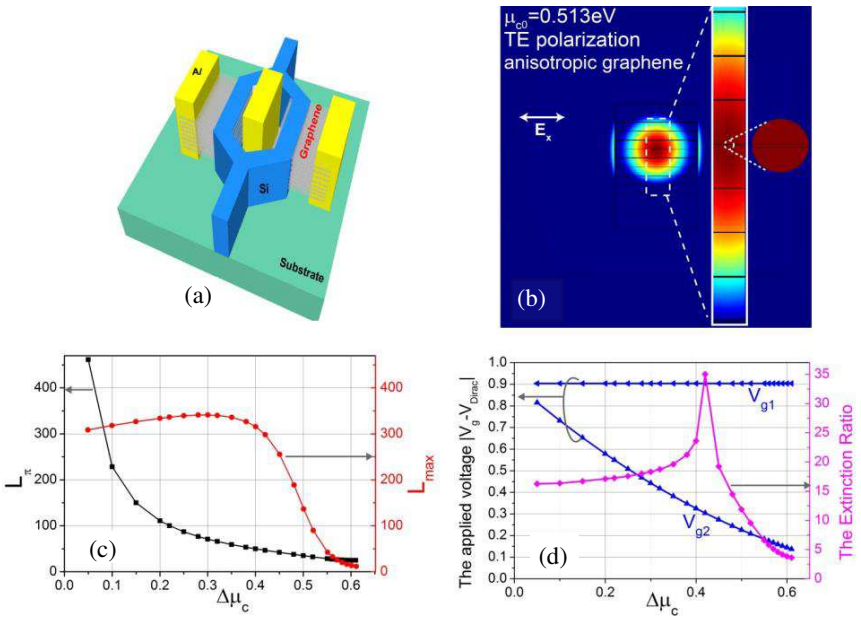

Figure 4: (a) Schematic pictures for eight-layer graphene embedded MZ modulator configuration; (b) corresponding electric field distribution in one of the arm; (c) relationship between $L_\pi L_{\max}$ and $\Delta\mu_c$; (d) relationship between the applied votages/extinction ratio and $\Delta\mu_c$ (reprinted from Ref. [5]).

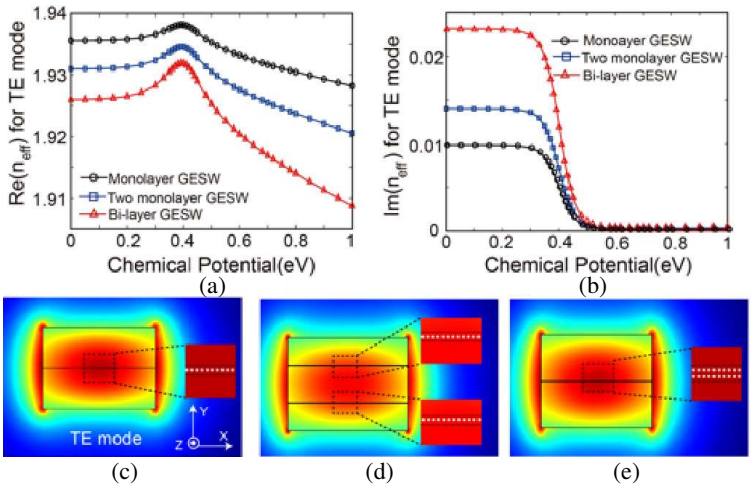

Figure 5: (a) Re(neff) with chemical potential variation for monolayer, two separated monolayer, and bi-layer GESW; (b) Im(neff) with chemical potential variation for monolayer, two separated monolayer, and bi-layer GESW; (c) (d) and (e) represent the electric field distribution for TE polarization mode of monolayer, two separated monolayer, and bi-layer GESW under chemical potential of 0 eV, respectively.

the monolayer graphene.

The effective mode index curves for monolayer GESW, two separated monolayer GESW, and bi-layer GESW are plotted in Figs. 5(a) and 5(b). First, the variation of $\mathrm{Re}(n_{\mathrm{eff}})$ for the bi-layer GESW is roughly two times of the monolayer GESW as expected. However, the variation of $\mathrm{Re}(n_{\mathrm{eff}})$ for the bi-layer GESW is much larger than that of the two separated monolayer GESW, which implies the light-matter interaction between light and bi-layer graphene is much more pronounced compared to that of the two separated monolayer graphene. Secondly, these three curves have basically the same variation trend, namely, it first increases to a maximum value (around the chemical potential of 0.4 eV) and then decreases to the minimum value (at the chemical potential of 1 eV). Therefore, a large Δn_{eff} can be obtained when chemical potential is between 0.4 and 1 eV. To show the difference, the typical electric field modal profiles for monolayer, two separated monolayer, and bi-layer GESW under chemical potential of 0 eV are plotted in Figs. 5(c)–5(e), respectively.

5. CONCLUSION

In conclusion, we reviewed recent progress in graphene-based electro-refraction (ER) modulators. By embedding the graphene sheet into the silicon waveguide, the light-matter interaction has been significantly enhanced: the overall mode index, $\mathrm{Re}(n_{\mathrm{eff}})$ and $\mathrm{Im}(n_{\mathrm{eff}})$, are linked to the in-plane permittivity of the embedded graphene and the n_{eff} variation of GESW can be orders of magnitude larger than silicon waveguide. The modulators based on single-layer graphene, bi-layer graphene, eight-layer graphene, and few-layer graphene were investigated and categorized. It can be concluded that graphene is a very promising material for enhancing the modulation effect in silicon, and has great potentials for future CMOS compatible high efficiency optical modulator, showing significant influence for optical interconnects in future integrated optoelectronic systems.

REFERENCES

1. Liu, M., X. Yin, E. Ulin-Avila, B. Geng, T. Zentgraf, L. Ju, F. Wang, and X. Zhang, "A graphene-based broadband optical modulator," *Nature*, Vol. 474, No. 7349, 64–67, 2011.
2. Tu, X., T. Y. Liow, J. Song, X. Luo, Q. Fang, M. Yu, and G. Q. Lo, "50-Gb/s silicon optical modulator with traveling-wave electrodes," *Optics Express*, Vol. 21, No. 10, 12776–12782, 2013.
3. Thomson, D., F. Y. Gardes, J. M. Fedeli, S. Zlatanovic, Y. Hu, B. P. P. Kuo, E. Myslivets, N. Alic, S. Radic, G. Z. Mashanovich, and G. T. Reed, "50-Gb/s silicon optical modulator," *IEEE Photonics Technology Letters*, Vol. 24, No. 4, 234–236, 2012.
4. Vakil, A. and N. Engheta, "Transformation optics using graphene," *Science*, Vol. 332, No. 6035, 1291–1294, 2011.
5. Hao, R., W. Du, H. Chen, X. Jin, L. Yang, and E. Li, "Ultra-compact optical modulator by graphene induced electro-refraction effect," *Applied Physics Letters*, Vol. 103, No. 6, 061116, 2013.
6. Ju, L., B. Geng, J. Horng, C. Girit, M. Martin, Z. Hao, H. A. Bechtel, X. Liang, A. Zettl, Y. R. Shen, and F. Wang, "Graphene plasmonics for tunable terahertz metamaterials," *Nature Nanotechnology*, Vol. 6, No. 10, 630–634, 2011.
7. Gusynin, V. P., S. G. Sharapov, and J. P. Carbotte, "Magneto-optical conductivity in graphene," *Journal of Physics: Condensed Matter*, Vol. 19, No. 2, 026222, 2007.
8. Du, W., R. Hao, and E. P. Li, "The study of few-layer graphene based Mach-Zehnder modulator," *Optics Communications*, Vol. 323, 49–53, 2014.
9. Hao, R., E. Li, and X. Wei, "Two-dimensional light confinement in cross-index-modulation plasmonic waveguides," *Optics Letters*, Vol. 37, No. 14, 2934–2936, 2012.
10. Lee, C. C., S. Suzuki, W. Xie, and T. R. Schibli, "Broadband graphene electro-optic modulators with sub-wavelength thickness," *Optics Express*, Vol. 20, No. 5, 5264–5269, 2012.
11. Barnes, W. L., A. Dereux, and T. W. Ebbesen, "Surface plasmon subwavelength optics," *Nature*, Vol. 424, No. 6950, 824–830, 2003.

Anisotropy and Non-reciprocity in Boundary Conditions: Generalized PEMC Surface

A. Sihvola, H. Wallén, P. Ylä-Oijala, and S. Kiminki
Department of Radio Science and Engineering
Aalto University School of Electrical Engineering, Espoo, Finland

Abstract— Boundary conditions play an important role in electromagnetics, and not the least in connection with metamaterials and metasurfaces. In this paper we present a generalization of the PEMC (perfect electromagnetic conductor) boundary. The generalization extends the isotropic and non-reciprocal character of the PEMC boundary into anisotropic and reciprocal dimensions. The effect of the generalized boundary on the polarization of incident waves is analyzed.

1. INTRODUCTION

The perfect electromagnetic conductor (PEMC) boundary [1] is a lossless boundary defined with the following conditions for the tangential components of the electric and magnetic fields:

$$\begin{pmatrix} E_x \\ E_y \end{pmatrix} = -\begin{pmatrix} 1/M & 0 \\ 0 & 1/M \end{pmatrix} \begin{pmatrix} H_x \\ H_y \end{pmatrix} \tag{1}$$

where it is assumed that the boundary is locally perpendicular to the z-axis ($\mathbf{u}_z$ pointing into the domain), and M is the admittance-type PEMC parameter. These boundary conditions are non-reciprocal, and appear on the surface of a so-called axion medium [2]. As is known, the PEMC (axion) medium, defined by the conditions $\mathbf{D} = M\mathbf{B}$, $\mathbf{H} = -M\mathbf{E}$, contains both the perfect electric conductor (PEC) and perfect magnetic conductor (PMC) as special cases ($1/M = 0$ and $M = 0$, respectively).

The particular character of the condition (1) becomes clear when it is paralleled with the (isotropic) impedance boundary condition (IBC) [3]

$$\mathbf{n} \times \mathbf{E} = Z_s \mathbf{n} \times (\mathbf{n} \times \mathbf{H}) \tag{2}$$

where $\mathbf{n}$ is the unit normal, in the present case $\mathbf{n} = \mathbf{u}_z$. Writing this in matrix form, the non-diagonality and antisymmetry of (2) contrasts strongly with (1):

$$\begin{pmatrix} E_x \\ E_y \end{pmatrix} = \begin{pmatrix} 0 & Z_s \\ -Z_s & 0 \end{pmatrix} \begin{pmatrix} H_x \\ H_y \end{pmatrix} \tag{3}$$

Let us set the PEMC condition in a broader setting of boundary conditions. In terms of the classification of boundary conditions with the four elementary dyadics $\overline{\overline{\mathrm{I}}}$, $\overline{\overline{\mathrm{J}}}$, $\overline{\overline{\mathrm{K}}}$, $\overline{\overline{\mathrm{L}}}$ [4], the general surface impedance dyadic $\overline{\overline{\mathrm{Z}}}_s$ in

$$\mathbf{n} \times \mathbf{E} = \overline{\overline{\mathrm{Z}}}_s \cdot \mathbf{n} \times (\mathbf{n} \times \mathbf{H}) \tag{4}$$

reads

$$\overline{\overline{\mathrm{Z}}}_s = Z_I \begin{pmatrix} +1 & 0 \\ 0 & +1 \end{pmatrix} + Z_J \begin{pmatrix} 0 & -1 \\ +1 & 0 \end{pmatrix} + Z_K \begin{pmatrix} +1 & 0 \\ 0 & -1 \end{pmatrix} + Z_L \begin{pmatrix} 0 & +1 \\ +1 & 0 \end{pmatrix} \tag{5}$$

where Z_I equals Z_s in (3) and $Z_J = 1/M$ in (1). For the boundary to be lossless, the following needs to apply [4]: $\overline{\overline{\mathrm{Z}}}_s^T = -\overline{\overline{\mathrm{Z}}}^*$, the star denoting the complex conjugate. This means that for lossless boundary conditions the following is required:

$$\mathrm{Re}\{Z_I\} = 0, \quad \mathrm{Re}\{Z_K\} = 0, \quad \mathrm{Re}\{Z_L\} = 0, \quad \mathrm{Im}\{Z_J\} = 0 \tag{6}$$

Furthermore, the reciprocity condition means symmetry: $\overline{\overline{\mathrm{Z}}}_s^T = -\overline{\overline{\mathrm{Z}}}_s$, in other words $Z_J = 0$ with no restriction on Z_I, Z_K, Z_L.

2. GENERALIZED PEMC BOUNDARY

One possibility to generalize the PEMC boundary condition (1) is to allow the two diagonal "admittances" to be different, while still keeping it complementary to the IBC. This means allowing the parameter Z_L to be nonzero. For a lossless boundary, (6) requires that Z_L has to be purely imaginary.

This leads to the following boundary condition:

$$\begin{pmatrix} E_x \\ E_y \end{pmatrix} = -\begin{pmatrix} P & 0 \\ 0 & P^* \end{pmatrix} \begin{pmatrix} \eta H_x \\ \eta H_y \end{pmatrix} \tag{7}$$

where the characteristic impedance η has been included to reduce dimensions from the complex boundary parameter P. Note that if P is real, the boundary distills down to the classical PEMC (1) with $\eta MP = 1$.

Of course other generalizations of (1) can be envisioned. However, (7) is the only one which retains the diagonal character of the relation between the tangential fields. This choice extends the PEMC condition into anisotropic domain [5] and also adds a reciprocal part into the purely non-reciprocal condition (1).

3. REFLECTION WITH NORMAL INCIDENCE

Assume that an incident plane wave $\mathbf{E}^i$ with polarization $\mathbf{E} = \mathbf{u}_x E_x + \mathbf{u}_y E_y$ hits the generalized PEMC boundary (7) with normal incidence. Then the reflected field $\mathbf{E}^r = \overline{\overline{\mathrm{R}}} \cdot \mathbf{E}^i$ can be calculated from the reflection matrix

$$\overline{\overline{\mathrm{R}}} = \frac{1}{|P|^2+1} \begin{pmatrix} |P|^2-1 & -2P \\ 2P^* & |P|^2-1 \end{pmatrix} \tag{8}$$

The eigenvectors in reflection (those polarizations that keep their polarization in the reflection) are

$$P\,\mathbf{u}_x \pm \mathrm{j}|P|\mathbf{u}_y \tag{9}$$

with eigenvalues

$$\frac{|P|^2 - 1 \mp 2\mathrm{j}|P|}{|P|^2+1} = \frac{(|P| \mp \mathrm{j})^2}{|P|^2+1} \tag{10}$$

From this it can be seen that the reflection is always 100% in amplitude (both eigenvalues have unity absolute value). Also, the eigenpolarizations are circular if P is real (classical PEMC), and otherwise elliptical. The other limiting case is purely imaginary P, which leads to linear eigenpolarizations.

4. RENORMALIZATION OF PARAMETERS

Let us express the generalized PEMC surface impedance P with two angular parameters in the following way

$$P = \tan\beta\, \exp(\mathrm{j}\varphi) \tag{11}$$

with $\varphi = 0$ for PEMC, $\beta = 0$ for PEC, and $\beta = \pi/2$ for PMC.

Then the reflection matrix looks like

$$\overline{\overline{\mathrm{R}}} = \begin{pmatrix} -\cos(2\beta) & -\sin(2\beta)\exp(\mathrm{j}\varphi) \\ \sin(2\beta)\exp(-\mathrm{j}\varphi) & -\cos(2\beta) \end{pmatrix} \tag{12}$$

with eigenvectors as

$$\exp(\mathrm{j}\varphi)\mathbf{u}_x \pm \mathrm{j}\mathbf{u}_y \tag{13}$$

and the eigenvalues are

$$-\exp(\pm\mathrm{j}2\beta) \tag{14}$$

5. BEHAVIOR OF THE POLARIZATION

The polarization vector **p** describes the polarization state (character of a complex vector) of a complex vector **a**. It is defined as [4]

$$\mathbf{p}(\mathbf{a}) = \frac{\mathbf{a} \times \mathbf{a}^*}{\mathrm{j}\mathbf{a} \cdot \mathbf{a}^*} \tag{15}$$

The handedness of the vector is positive when looked into the direction of the vector. The magnitude $|\mathbf{p}| = 2b/(1+b^2)$ gives information about the ellipticity of the vector (b is the axis ratio of the ellipse).

The polarization vector for the eigenpolarizations can be seen to be simple:

$$\mathbf{p} = \mp\frac{\Re\{P\}}{|P|}\mathbf{u}_z = \mp\cos\varphi\,\mathbf{u}_z \tag{16}$$

In other words, the polarizations are of opposite handedness but have the same elliptical shape. In addition, the polarization does not depend at all on the parameter β. Figure 1 shows the axis ratio of the eigenpolarization depending on φ. We can see the monotonous change from the circularly polarized PEMC case to the linear polarization for the fully anisotropic surface.

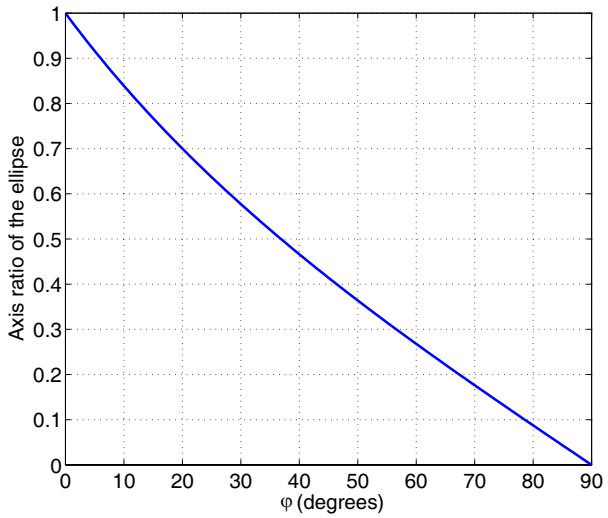

Figure 1: The axis ratio of the eigenpolarizations in normal-incidence reflection from the generalized PEMC boundary, as function of the φ parameter. The case $\varphi = 0$ corresponds to the pure PEMC surface.

6. CONCLUSION

A generalization of the fully non-reciprocal PEMC boundary condition in the form (7) retains the non-diagonal character of the PEMC impedance dyadic (5) but extends the isotropy of a pure PEMC case into anisotropic boundaries. In addition, the modification introduces a reciprocal component into the boundary. The boundary is lossless, in other words all incident fields are reflected with reflection coefficient $|R| = 1$. As is known, a PEMC boundary rotates the polarization plane of a linearly polarized incident field in reflection, and hence the additional parameteric dimension that the generalized PEMC boundary offers gives interesting potential for polarization control of electromagnetic waves.

Promising progress toward practical realizations of PEMC-metasurfaces has been documented [6]. The materialization of generalized PEMC surfaces of the type that was outlined above is certainly conceivable due to the fact that the additional parameters correspond to anisotropic but reciprocal effects.

REFERENCES

1. Lindell, I. V. and A. H. Sihvola, "Realization of the PEMC boundary," *IEEE Transactions on Antennas and Propagation*, Vol. 53, No, 9, 3012–3018, September 2005.
2. Hehl, F. W. and Yu. N. Obukhov, *Foundations of Classical Electrodynamics*, Birkhäuser, Boston, 2003.

3. Lindell, I. V. and A. H. Sihvola, "Realization of the impedance boundary," *IEEE Transactions on Antennas and Propagation*, Vol. 54, No, 12, 3669–3676, December 2006.
4. Lindell, I. V., *Methods for Electromagnetic Field Analysis*, Oxford University Press and IEEE Press, Oxford, 1992, 1995.
5. Lindell, I. V., A. H. Sihvola, and I. Hänninen, "Perfectly anisotropic impedance boundary," *IET Microwaves, Antennas Propagation*, Vol. 1, No, 3, 561–566, June 2007.
6. Shahvarpour, A., T. Kodera, A. Parsa, and C. Caloz, "Arbitrary electromagnetic conductor boundaries using Faraday rotation in a grounded ferrite slab," *IEEE Transactions on Microwave Theory and Techniques*, Vol. 58, No, 11, 2781–2793, November 2010.

The Growth and Magneto-optical Properties of Large Size Single-crystal Thick TmBiIG Films from Lead-free Flux by LPE Technology

Bing Mei, Huai-Wu Zhang, Qing-Hui Yang,
Shu-Chen Jin, Xiao-Jie Tian, and Ying-Heng Rao
State Key Laboratory of Electronic Films and Integrated Devices
University of Electronic Science and Technology, Chengdu 610054, China

(*Invited Paper*)

Abstract— In this paper, we prepared the 3-inch magneto-optical (MO) single crystal garnet film with the composition of $(TmBi)_3(FeGa)_5O_{12}$ by Liquid phase epitaxy (LPE) from lead-free flux. The MOgarnet films are grown on $Gd_3Ga_5O_{12}$ (GGG (111)) substrate because of the good lattice match between the film and the substrate. In our experiment, we choose the Bi_2O_3 as the fluxing agent not frequently-used PbO because the latter is poisonous and brings negative impact to the growth film. The good films with low defects, mirror surface, high Faraday Rotation angle(FR) and big thickness have been obtained by optimizing the flux ratio and LPE technological parameters. The thickness of the film can reach about 50–60 micrometers in 3-inch GGG substrate. The optimal growth rate is 0.85 ... 0.95 μm/min, and mismatch between TmBiIG film and GGG substrate gets its smallest and good magnetic and MO properties have been obtained with this growth rated. The biggest FR is 0.54 degree/ μm as the external magnetic field is as small as 25 Oe. The Ms and Hc of TmBiIG film reaches its biggest and smallest value as the growth rate is 0.92 μm/min, respectively, and the value is 50 emu/cm^3 and 5 Oe.

1. INTRODUCTION

Garnet films have been shown to be good material for MO application in high performance optical communication devices due to their high FR and low propagation loss [1–4]. A wide range of techniques have been applied to fabricate MO garnet films including liquid phase epitaxy (LPE), pulsed laser deposition (PLD) and radio frequency (RF) magnetron sputtering. In order to obtain the 45°FR in optical communication device, the thickness of single-crystal garnet film should be more than dozens of micrometers. However, it is very difficult to grow so thick film with PLD or RF sputtering because of the non-equilibrium growth mode, so the LPE is the only feasible method to grow the thick film. Generally, the pure $Y_3Fe_5O_{12}$ (YIG) film is not desirable for MO devices because of its small FR and the bismuth (Bi^{3+}) substitute garnet film (Bi: YIG) is the best choice. In Bi: YIG film, Bi^{3+} ions substituted the part of Y^{3+} ions on dodecahedron sites, and FR increases with the increase of bismuth content, since Bi^{3+} can increase the multiple split of energy level that excited by Fe^{3+} sub-lattice. However, the diameter of Bi^{3+} is bigger than Y^{3+} and leading to the lattice expound of the film and mismatch between the film and GGG substrate, and results in the failure epitaxy. There are two ways to solve this problem, one is growing the film on substitute GGG substrate which with the bigger lattice constant; This has been investigated by some groups, G. Y. Kima [5] and the researchers of Korean [6] Ceramic Society have reduced the mismatch of the film and the substrate by changing the characteristics of the substrate and grown MO garnet film on SGGG substrate; Another way is introducing the ions with small diameter to compensate the lattice expound because of Bi^{3+} ions, Lu^{3+}, Ga^{3+}, Yb^{3+}, Ho^{3+} et al., are the normal choice. LuBiIG [7–11], Bi: YIG [12], Bi: YbIG [13] and $(HoYb)_{3-x-y}CexBiyFe_5O_{12}$ [14] have been prepared by LPE on GGG substrate. But both of them can't epitaxial thick film more than tens of micrometers, and the maximum FR is corresponding to a huge magnetic field.

The main work of this paper is finding the best technology of preparing the $(TmBi)_3(FeGa)_5O_{12}$ more than 50 μm with big FR with the external magnetic field less than 75 Oe. Non-magnetic Bi^{3+}, Tm^{3+}, Ga^{3+} and Fe^{3+} ions were incorporated into the garnet matrix for the purposes of improving the lattice match between the film and the GGG substrate to guarantee the single crystal garnet film can be prepared by liquid phase epitaxy (LPE) method, and lead-free flux has been applied in order to decrease the absorption and increase the FR. Finally, high quality garnet films were successfully fabricated on GGG (111) substrate by LPE method with Bi_2O_3 as the melting agent by optimizing the growth conditions. The crystal structure, microstructure, magnetic and MO

properties were investigated in detail. Our results indicate that the thick garnet film has a perfect micro-structure,mirror surface and good MO and magnetic properties.

2. EXPERIMENT

In our experiment, the non-magnetic GGG (111) single crystal substrate was applied due to its good match to the garnet film in both lattice constant (12.383 Å) and thermal expansion coefficient (9.2×10^{-6}/°C). The oxides of Bi_2O_3, Ga_2O_3, Tm_2O_3 and Fe_2O_3 with high purity (99.999%) were mixed completely and then melted in a platinum crucible at 1000 ... 1050°C for 24 h. The solution was homogenized by stirring with a platinum paddle for another 12 h at 1000°C, and then cooled to the growth temperature. The substrate was mounted on a platinum holder with a small slant angle to the liquid surface. During the growth, the substrate was rotated at a rate of 60 ... 100 rpm/min, and the rotation direction was reversed with a fixed period. The growth rate of the film can be controlled by the growth temperature and the rotation speed. When the film growth was finished, the substrate was lifted from the flux, and hovered above the flux surface for 10 ... 60 min to drop out the appendiculate flux. Finally, the film/substrate was withdrawn from the furnace slowly to avoid the formation of micro-cracks due to surface shrinking (thermal expansion), and then cleaned in a hot nitric acid to eliminate the residual flux. By this method, three-inch $Tm_{2.28}Bi_{0.72}Fe_{4.3}Ga_{0.7}O_{12}$(TmBiIG) films were successfully fabricated on GGG substrates.

Table 1: Parameters for growing TmBiIG film by LPE method from lead-free flux (T_s is saturation temperature, T_g is growth temperature, V_R is rotation speed in growth process.

Flux Composition	T_s	T_g	V_R	Interval of rotation reversion
$Tm_{2.28}Bi_{0.72}Fe_{4.3}Ga_{0.7}O_{12}$	928°C	880 ... 920°C	60 rpm/min	5 s

A typical growth condition applied in our experiments is listed in Table 1. It is noted that the furnace temperature profile in the grown zone is strictly controlled with a variation less than 0.1°C, and a rotation that changes direction every 5 s during the growth is used to obtain a uniform film. The growth rate of the film is calculated from growth temperature and rotation speed to be 0.45 ... 1.45 μm/min. The growth time is about 40 ... 130 min, thus a thickness of about 50 ... 60 μm on each side of GGG substrate is expected for our epitaxial TmBiIG thick film.

The crystal graphic and surface morphology of the film were examined by a Bede D1 x-ray diffractometer (XRD) with Cu Kα radiation, a SEIKO SPA-300HV atomic force microscope (AFM) respectively. The magnetic characteristics were measured using VSMVT-800 vibrating sample magnetometer (VSM), and the MO characteristic was determined with Faraday loop tracer.

3. RESULTS AND DISCUSSION

The growth temperature of $(TmBi)_3(FeGa)_5O_{12}$ film is broad which is about 880 ... 920°C. Growth rate of the film decreases with the increasing growth temperature and can be changed from 1.45 ... 0.45 μm/min. As shown in Fig. 1, the growth rate decrease of 0.035 μm/min when the growth temperature increase of 1°C from point A to point B, and that value increases as the increasing temperature, it is 0.0468 μm/min from point B to C. In our experiment, the very thick film were grown and the garnet content in flux is decreasing distinctly during the growing process and leading

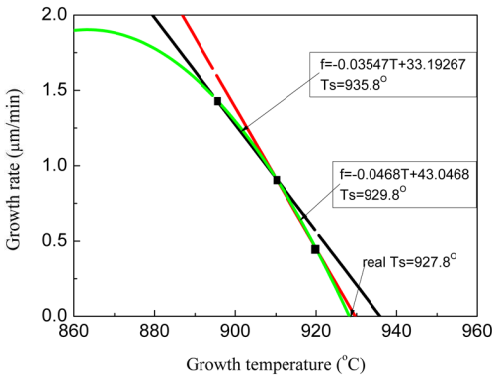

Figure 1: The growth rate depends on growth temperature.

to decreasing growth rate, so we should decreasing the growth temperature to compensate that. For example, it is about 3.2 g garnet is extracted from the flux for growing 3-inch 50 μm thick film, the growth temperature is decreased from 926 ... 922°C during the growth process.

In our experiment, the Bi_2O_3 replaced the PbO as the flux agent, and it acts as both the flux agent and composition of the film and does not bring other impurities to the film. But the flux is with high viscosity and can't be removed from the substrate after growth. The traditional method of removing the flux is rotating the film with high speed, but it not suitable for $(TmBi)_3(FeGa)_5O_{12}$, because its growth mechanism is different with the pure YIG. So we have to find another way to solve this problem. The "buffer method" is applied in our experiment which hovering the film just above the melt at the growth temperature for a long time to wait the flux flow along the declining substrate, and the time is decided by the thickness and the size of the film, it is usually from 10 ... 60 min.

Figure 2(a) shows 3-inch thick TmBiIG film sample, the thickness of film is 60.04 μm, and it is obvious that the sample surface is mirror, the film is clean and flat, and no micro-cracks and residual flux droplets are observed. The RMS surface roughness, estimated from the AFM image shown in Fig. 2(b), is as small as about 2 nm.

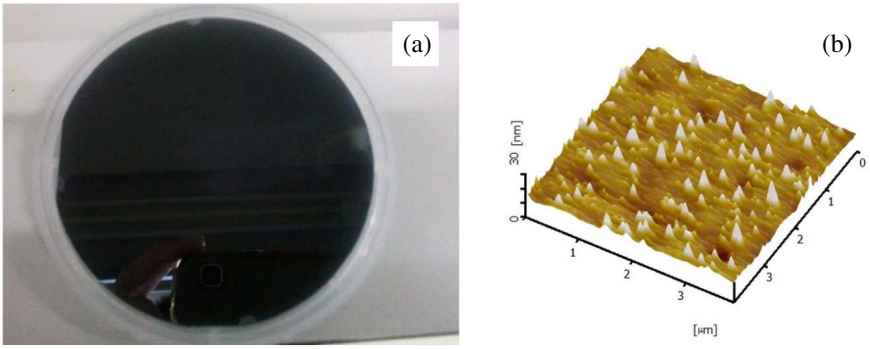

Figure 2: (a) The 3-inch thick TmBiIG film sample, (b) AFM picture of the TmBiIG film. Thickness of sample is 60.04 μm. Growth rate is 0.71 μm/min. Growth temperature is 905 ... 900°C.

The lattice constant match between the film and substrate is very important to grow the large size thick film, because the stress will increase obviously with increasing of film thickness and size and leading to the crack of the film. The composition of garnet film is $Tm_{2.28}Bi_{0.72}Fe_{4.3}Ga_{0.7}O_{12}$, only the lattice constant of garnet film with this composition will matched the lattice constant of GGG substrate and the film can be grown by LPE method. Fig. 3 shows the XRD patterns of $(TmBi)_3(FeGa)_5O_{12}$ film on GGG (111) substrate. It can be seen that the TmBiIG film exhibits a perfect crystalline structure with (444) diffraction peak, indicating that the film is a single garnet phase. The lattice constant of the film is 12.445 Å, and the lattice mismatch between the film and the substrate is as small as 0.05%. Such a small mismatch is due to the ionic radius compensation of Bi^{3+} and Tm^{3+} ions in the film. As we know, Bi^{3+} has a larger ionic diameter than Y^{3+} and

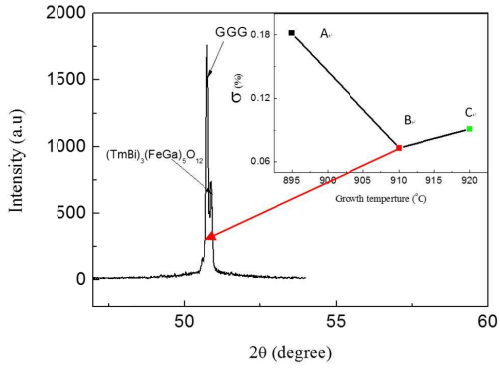

Figure 3: Figure 3 shows the XRD patterns of $(TmBi)_3(FeGa)_5O_{12}$ film on GGG (111) substrate. Thickness of sample A is 14.53 μm. Growth rate is 1.45 μm/min. Growth temperature is 895°C. Thickness of sample B is 9.18 μm. Growth rate is 0.92 μm/min. Growth temperature is 910°C. Thickness of sample C is 9.02 μm. Growth rate is 0.45 μm/min. Growth temperature is 920°C.

Fe^{3+} ions. Therefore, for the Bi^{3+}-doped garnet film the lattice constant solely increases with the Bi^{3+} concentration. Tm^{3+} ions, with smaller ion diameter, can balance out the lattice mismatch that occurs with Bi^{3+}-doped garnet film.

The Mismatch between the film and substrate can be expressed by,

$$\sigma = \frac{d_e - d_s}{d_s}$$

d_e is the spacing (444) of epitaxial films, d_s for substrate, σ is the mismatch. The lattice constant of epitaxial film can be modified by growth temperature and growth rate, so the mismatch σ can be adjusted to near zero to grow thick film. It is impossible to grow thick film when the lattice mismatch is bigger than 0.05%, just like point A and point C in the top right corner of Fig. 3, the films cracked when the thickness were more than 10 μm.

Figure 4(a) shows the magnetic hysteresis loop of $(TmBi)_3(FeGa)_5O_{12}$ film were measured under the condition of room temperature along in-plane and perpendicular-plane. The saturation magnetization (Ms) and coercive force (Hc) depends on growth rate is shown in Fig. 4(b) it can be seen that the easy axis of TmBiIG film is along the perpendicular because of the growth anisotropy by Bi^{3+} [15].

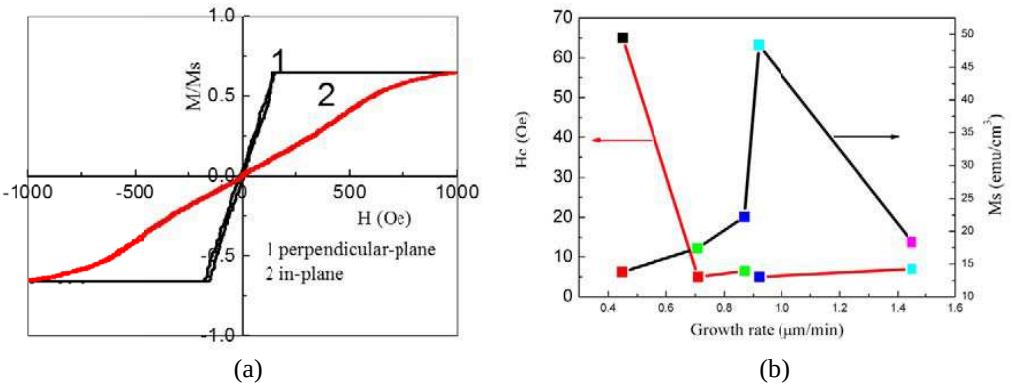

Figure 4: (a) The magnetic hysteresis loop of $(TmBi)_3(FeGa)_5O_{12}$ film were measured under the condition of room temperature along in-plane and perpendicular-plane directions. (b) The Ms and Hc depend on growth rate.

Figure 4(b) shows the Ms and Hc of the TmBiIG films depends on the growth rate. In general, Ms is determined bythe Fe^{3+} magnetic ion content in the tetrahedral and octahedral sites. Ga^{3+} is non-magnetic ions, when it is incorporated into the garnet crystal lattice, it will substitute the Fe^{3+} ion in tetrahedron and octahedral sites, and result the decreasing of Ms of the film. The content of Ga^{3+} ions which incorporate into the garnet film is various slightly as the growth rate is different, so the Ms of the film changes with the growth rate slightly. In YIG crystal, a unit of each formula have $2Fe^{3+}$ (a) and $3Fe^{3+}$(d), their magnetic moment against each other in parallel, the total magnetic moment is equal to the net magnetic moment of $1Fe^{3+}$. The total magnetic moment of the lattice for Fe^{3+} will be reduced due to the non-magnetic Ga^{3+} ions occupy the position of Fe^{3+} (d). So Ms is much lower than YIG garnet material. The Ms and Hc of TmBiIG film reaches its biggest and smallest value as the growth rate is 0.92 μm/min, respectively, and the value is 50 emu/cm^3 and 5 Oe.

The FR of $(TmBi)_3(FeGa)_5O_{12}$ film were measured at the wavelength of 633 nm along the perpendicular-plane. The Fig. 5 shows the relationship between FR of TmBiIG film at different growth rate and external magnetic field. We can see that the FR all reach their maximum value as the external magnetic field is smaller than 75 Oe, it is a desirable value for the MO film applied in devices, means that the MO component can be driven by flat magnetic field, it is beneficial to reduce the volume and weight of the devices. Additionally, the Faraday loop traces are different as the growth rate because the composition of the film changed slightly with the growth rate. We can see that the FR reaches 0.54 degree/μm when the growth rate is 0.87 μm/min. It is because that the film has more Bi^{3+} in the composition of the film.

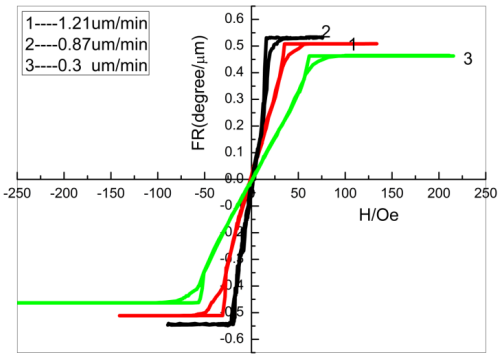

Figure 5: The relationship between FR and external magnetic field.

4. CONCLUSION

In this paper, 3-inch MOTmBiIGthick film was synthesized by LPE method. The Bi_2O_3 was applied as flux agent replaces the normal PbO flux. The effects of the growth rate on the structure, magnetic and MO properties were studied experimentally. Results show that the MO and magnetic properties of the TmBiIG film can be modified by growth rate. We can grow the TmBiIG film with thickness of 50–60 μm as the growth rate between 0.8 to 0.9 μm/min, the mismatch between the film and substrate can be near zero. The FR reach its biggest value 0.54 μm/min, this is due to the slightly increase of Bi^{3+} in the film composition and leading to the splitting of excited energy lever caused by bismuth ion substitution.

ACKNOWLEDGMENT

This work was supported by the National Natural Science Foundation of China (NSFC) under Grants 61021061, 51272036 and 51002021, 61131005, International cooperation project 2012DFR 10730, 2013HH0003 and 2012CB933104, 111project No. B13042.

REFERENCES

1. Pritchard, J., M. Mina, R. J. Weber, and S. Kemmet, "Low power field generation for magneto-optic fiber-based interferometric switches," *J. Appl. Phys.*, Vol. 111, No. 7, 07A941-1–07A941-3, 2012.
2. Xu, Q., B. Schmidt, S. Pradhan, and M. Lipson, "Micrometre-scale silicon electro-optic modulator," *Nature*, Vol. 435, No. 7040, 325–327, 2005.
3. Vlasov, Y., W. M. J. Green, and F. Xia, "High-throughput silicon Nan photonic wavelength-insensitive switch for on-chip optical networks," *Nat. Photon.*, Vol. 2, No. 4, 242–246, 2008.
4. Ghosh, S., S. Keyvaninia, W. Van Roy, T. Mizumoto, G. Roelkens, and R. Baets, "Ce: YIG/SOI optical isolator realized by BCB bonding," *Proc. 8th IEEE Int. Conf. GFP*, 196–198, 2011.
5. The Korean Ceramic Society, "Growth of Bi: YIG thick films by change of PO/Bi_2O_3 molar ratio," *Journal of the Korean Ceramic Society*, Vol. 39, No. 6, 589–593, 2002.
6. Kima, G. Y., S. G. Yoona, I. S. Chungb, S. B. Parkb, S. J. Suha, and D. H. Yoona, "Growth and magnetic properties of LPE-grown $(EuTbBi)_3(FeAlGa)_5O_{12}$ garnet films," *Thin Solid Films*, Vol. 475, Nos. 1–2, 246–250, Mar. 22, 2005.
7. Syvorotka, I. I., I. M. Syvorotka, and S. B. Ubizskii, "Growth peculiarities and magnetic properties of $(LuBi)_3Fe_5O_{12}$ films by LPE method," *Solid State Phenomena*, I. I. Syvorotka et al., Vol. 200, 256, 2013.
8. Keszei, B., Z. Vértesy, and G. Vértesy, "Growth of Bi and Ga substituted YIG and LuIG layers by LPE method," *Crystal Research and Technology*, Vol. 36, Nos. 8–10, 953–959, Oct. 2001.
9. Kono, T., T. Machi, N. Chikumoto, K. Nakao, N. Koshizuka, N. Adachi, and T. Okuda, "LPE growth of bismuth substituted iron garnet films with in-plane magnetization," *Journal of the Magnetics Society of Japan*, Vol. 30, No. 6_2, 600–603, 2006.
10. Görnert, P., T. Aichele, A. Lorenz, R. Hergt, and J. Taubert, "Liquid phase epitaxy (LPE) grown Bi, Ga, Al substituted iron garnets with huge Faraday rotation for magneto-optic applications," *Physical Status Solidi (A)*, Vol. 201, No. 7, 1398–1402, May 2004.

11. Huang, M. and Z.-C. Xub, "Liquid phase epitaxy growth of bismuth-substituted yttrium iron garnet thin films for magneto-optical applications," *Thin Solid Films*, Vol. 450, No. 2, 324–328, Mar. 1, 2004.
12. Xu, W., X. W. Xu, T. C. Chong, Y. S. Tay, G. Y. Zhang, M. H. Li, and B. Freeman, "Magneto-optical properties of Ce and Bi co-substituted iron garnets grown by the Bi_2O_3 self-flux technique," *Applied Physics A*, Vol. 81, No. 3, 565–568, Aug. 2005.
13. Kim, T., S. Nasu, and M. Shima, "Growth and magnetic behavior of bismuth substituted yttrium iron garnet nanoparticles," *Journal of Nanoparticle Research*, Vol. 9, No. 5, 737–743, Oct. 2007.
14. Zhuang, N., W. Chen, L. Shi, J. Nie, X. Hu, B. Zhao, S. Lin, and J. Chen, "A new technique to grow incongruent melting Ga:YIG crystals: The edge-defined film-fed growth method," *Journal of Applied Crystallography*, Vol. 46, No. 3, 746–751, Jun. 2013.
15. Kahl, S., V. Popov, and A. M. Grishin, "Optical transmission and Faraday rotation spectra of a bismuth iron garnet film," *J. Appl. Phys.*, Vol. 94, 5688, 2003.

Finite Airy Beam Based on Polymer-stabilized Blue Phase Liquid Crystal

D. Luo and X. W. Sun
Department of Electrical & Electronic Engineering
South University of Science and Technology of China
Xueyuan Road 1088, Shenzhen, Guangdong 518055, China

Abstract— Polymer-stabilized blue phase liquid crystal was used to generate polarization-independent finite energy Airy beam. The intensity of output Airy beam was unchanged while rotating the linear polarization direction of illumination laser. This device also exhibited advantages of simplified fabrication process, and fast opto-electro response time.

1. TECHNICAL SUMMARY

1.1. Objective and Background

Blue phases (BPs) are special phase between the isotropic and chiral nematic phase of liquid crystal. The applications of BPs are limited due to its narrow temperature of around 2 K, which can be improved by adding a small concentration of polymer to form polymer-stabilized blue phase liquid crystal (PS-BPLC) [1]. Because of its intrinsic features, e.g., sub-micro second response time, PS-BPLC is thought to be a good choice for next generation display [2–5]. The blue phase liquid crystal is useful for fabricating tunable polarization-independent photonic devices, due to the Kerr effect-induced birefringence under external electric field [6, 7].

Airy beam is a kind of beam with acceleration and non-diffraction during propagation [8, 9]. It has been widely used in optical manipulation, plasma channel generation and optical vortex generation [10–12]. Different kinds of ways have been used to generate finite Airy beam, such as spatial light modulator, phase mask [11], or liquid crystal/polymer [13, 14]. However, in all of mentioned ways, polarized light source is required for phase difference generation, thus a great part of energy is wasted before it meets the Airy beam generator. Therefore, photonic device with non-polarization incident light is highly desirable. In this letter, a PS-BPLC Airy beam cell with binary-phase is demonstrated in vertical filed driven (VFD) mode. It has advantages of polarization independence, electrically tunable property, wide working temperature range, fast response time, and easy fabrication.

The finite energy Airy beams is generated through multiplying an exponential aperture function by the Airy function, and in initial condition we have [8]:

$$\phi(s, \xi = 0) = Ai(s) \exp(as) \tag{1}$$

where φ represents the electric field envelope, $s = x/x_0$ is a dimensionless transverse coordinate, where x_0 is an arbitrary transverse scale, $\xi = z/kx_0^2$ is the normalized propagation distance, where k is the wavenumber of the optical wave, and a is a positive parameter.

When $a \ll 1$, the finite energy Airy beams will closely resemble the Airy functions and could be expressed by [9]:

$$\phi(\xi, s) = Ai[s - (\xi/2)^2 + ia\xi] \exp[as - (a\xi^2/2) - i(\xi^3/12) + i(a^2\xi/2) + i(s\xi/2)] \tag{2}$$

The Fourier transform of finite energy Airy beam, $\Phi_0(k) \propto \exp(-ak^2) \exp(ik^3/3)$, which can be treated as a Gaussian function modulated by a cubic phase. For two-dimensional (2D) case, we have $\Phi_0(k_x, k_y) \propto \exp[-a(k_x^2 + k_y^2)] \exp[i(k_x^3 + k_y^3)/3]$, where k_x and k_y are Fourier spectrum coordinates.

2. RESULTS

A two-dimensional (2D) binary-phase pattern of Airy wave packet with cubic phase modulation was generated from a continuous phase pattern, varying from $-11.5\pi \sim 11.5\pi$ in 0.43 cm, by choosing the phase value delay between $0 \sim \pi$ as 0 and $\pi \sim 2\pi$ as π, respectively. An indium-tin-oxide (ITO)-coated glass substrate was recorded the phase pattern through a photomask by photolithographic method. A cell was formed by assemble the patterned ITO glass with another blank ITO glass. The cell gap was $d = 8\,\mu$m controlled by spacers. Here, no rubbing process was needed. The

cross section of cell and enlarged electrode pattern are shown in Figure 1. The optical property of PS-BPLC depends on external electric field. The PS-BPLC is optically isotropic without electric field. The refractive index of PS-BPLC could be approximated to $n_i = (2n_e + n_o)/3$. When electric field applies, the LC director tends to be parallel to the electric field. Due to Kerr effect, the PS-BPLC is optically anisotropic. The index ellipsoid thus becomes ellipsoidal, with its optic axis (n_z) parallel to the electric field, as shown in Figure 1.

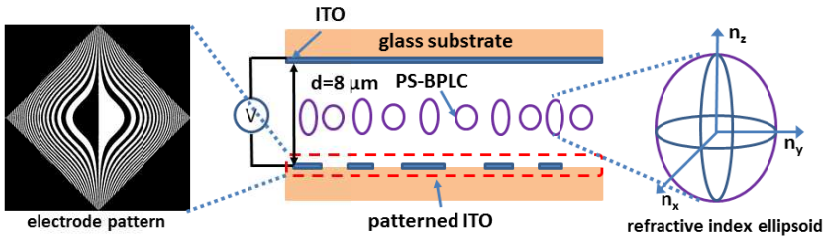

Figure 1: PS-BPLC in glass cell with patterned ITO and refractive index ellipsoid change of PS-BPLC under applied electric field.

The induced ordinary refractive index of BPLC $n_o(E)$ varies with the strength of electric field. Therefore, the phase difference between regions with and without electrode is expressed by: $\Gamma = \frac{2\pi}{\lambda}[n_o(E) - n_i]d$, where λ is the wavelength.

The LC/monomer mixture consists of 59.55 wt% nematic LC host MLC-2142 (Merck), 30.18 wt% chiral dopants (22.49 wt% CB15 and 7.69 wt% R-1011, Beijing Ba Yi Space), 9.27 wt% monomers (5.72 wt% RM257, Merck, and 3.55 wt% TMPTA, Sigma-Aldrich), and 1 wt% photoinitiator Darocur 1173 (Sigma-Aldrich). The mixture was heated up to an isotropic phase of liquid crystal and filled into the cell. Then, the sample was cooled down at a rate of 0.1°C/min. The blue phase showed within range of 39.4°C to 32.0°C. To generate the finite Airy beam, an expanded and collimated He-Ne laser beam (633 nm) was used to illuminate the PS-BPLC cell. A neutral density (ND) filter was used to adjust intensity of laser. Two polarizer and one quarter wave plate were used to control and monitor the polarization status of light. The polarization of light from the first polarizer was set to have angle 45° to the fast and slow axis of quarter-wave plate to generate circular polarized light, the second polarizer was used to control the polarization of output light. A spherical lens, with focal length of $f = 20$ cm, was located after the sample at distance of focal length for Fourier transform. The Fourier transform or Airy beam was obtained behind the lens and collected by a screen behind. Without external voltage, the phase difference Γ was zero. When external voltage applied, the electric field induced Kerr effect started to change the refractive index of PS-BPLC in the region with electrode, thus changed the phase difference between those two regions. Figures 2(a)–2(c) show the PS-BPLC image obtained by optical microscopy at different voltages of 10, 35, and 45 V, respectively.

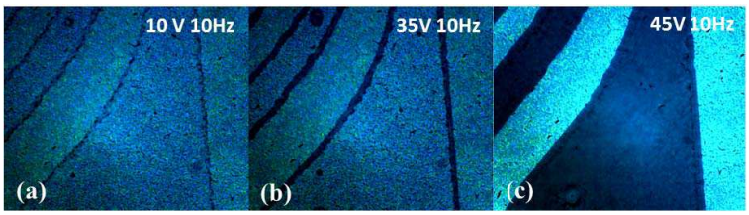

Figure 2: Image of PS-BPLC cell at different voltages, (a) 10 V, (b) 36 V, (c) 45 V, the frequency is 10 Hz.

The images of simulated and actually generated finite Airy beam are shown in Figures 3(a)–3(b) respectively. The generated finite Airy beam was consisted with the simulated one. It is noticed that, the changing input polarization of light didn't influence the output finite Airy beam profile, which meant that this kind of photonic devices, based on PS-PBLC, had no specially requirement on the polarization of input light, thus polarization independent. The PS-BPLC cell had a fast opto-electro response time. The PS-BPLC sample was measured to have rise time of $\tau_{rise} = 526$ μs and decay time of $\tau_{decay} = 678$ μs, respectively, where the rise and decay times were defined as 10%–90% transmittance change of main lope of generated Airy beam.

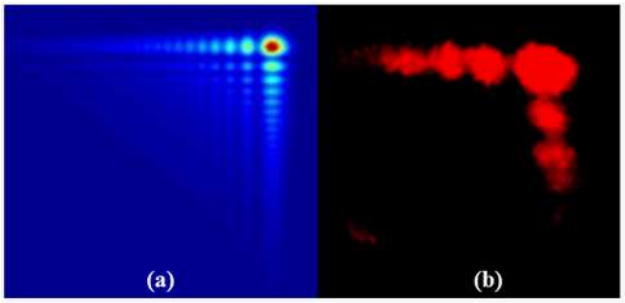

Figure 3: (a) Simulated and (b) experimentally generated finite Airy beam.

3. IMPACT

In summary, we demonstrated a PS-BPLC based finite Airy beam. The PS-BPLC Airy beam cell has simplified fabrication process, wide working temperature range, polarization independence, electrically tunable property, and fast opto-electro response time. The intrinsic features of PS-BPLCs also make it useful for application in other tunable binary-phase diffractive optical elements and photonic devices.

REFERENCES

1. Kikuchi, H., M. Yokota, Y. Hisakado, H. Yang, and T. Kajiyama, "Polymer-stabilized liquid crystal blue phases," *Nature Mater.*, Vol. 1, 64–68, 2002.
2. Hisakado, Y., H. Kikuchi, T. Nagomura, and T. Kajiyama, "Large electro-optic Kerr effect in polymer-stabilized liquid-crystalline blue phases," *Adv. Mater.*, Vol. 17, 96–98, 2005.
3. Yan, J. and S. T. Wu, "Polymer-stabilized blue phase liquid crystals: A tutorial [Invited]," *Opt. Mater. Express*, Vol. 1, 1527–1535, 2011.
4. Ge, Z., S. Gauza, M. Jiao, H. Xiangyu, and S. T. Wu, "Electro-optics of polymer-stabilized blue phase liquid crystal displays," *Appl. Phys. Lett.*, Vol. 94, 101104, 2009.
5. Rao, L., Z. Ge, S. Gauza, K. M. Chen, and S. T. Wu, "Emerging liquid crystal displays based on the Kerr effect," *Mol. Cryst. Liq. Cryst.*, Vol. 527, 30–42, 2010.
6. Rao, L., Z. Ge, and S. T. Wu, "Viewing angle controllable displays with a blue-phase liquid crystal cell," *Opt. Express*, Vol. 18, 3143–3148, 2010.
7. Lin, C. H., Y. Y. Wang, and C. W. Hsieh, "Polarization-independent and high-diffraction-efficiency Fresnel lenses based on blue phase liquid crystals," *Opt. Lett.*, Vol. 36, 502–504, 2011.
8. Siviloglou, G. A. and D. N. Christodoulides, "Accelerating finite energy Airy beams," *Opt. Lett.*, Vol. 32, 979–981, 2007.
9. Siviloglou, G., A. J. Broky, A. Dogariu, and D. N. Christodoulides, "Observation of accelerating Airy beams," *Phys. Rev. Lett.*, Vol. 99, 213901, 2007.
10. Baumgartl, J., M. Mazilu, and K. Dholakia, "Optically mediated particle clearing using Airy wavepackets," *Nature Photonics*, Vol. 2, 675–678, 2008.
11. Polynkin, P., M. Kolesik, J. V. Moloney, G. A. Siviloglou, and D. N. Christodoulides, "Curved plasma channel generation using ultraintensen Airy beams," *Science*, Vol. 324, 229–232, 2009.
12. Dai, H. T., Y. J. Liu, D. Luo, and X. W. Sun, "Propagation dynamics of an optical vortex imposed on an Airy beam," *Opt. Lett.*, Vol. 35, 4075–4077, 2010.
13. Dai, H. T., X. W. Sun , D. Luo, and Y. J. Liu, "Airy beams generated by a binary phase element made of polymer-dispersed liquid crystals," *Opt. Express*, Vol. 17, 19365–19370, 2009.
14. Luo, D., H. T. Dai, X. W. Sun, and H. V. Demir, "Electrically switchable finite energy Airy beams generated by a liquid crystal cell with patterned electrode," *Opt. Commun.*, Vol. 283, 3846–3849, 2010.
15. Coles, H. J. and M. N. Pivnenko, "Liquid crystal 'blue phases' with a wide temperature range," *Nature*, Vol. 436, 997–1000, 2005.

Resonant Properties of Subwavelength Voids in Anisotropic Metamaterials

A. V. Vozianova[1], **P. B. Ginzburg**[2], **and A. N. Poddubny**[1, 3]

[1]ITMO University, St. Petersburg, Russia
[2]Department of Physics, Kings College London, Strand, London WC2R 2LS, United Kingdom
[3]Ioffe Physical Technical Institute of the Russian Academy of Sciences, St. Petersburg, Russia

Abstract— Resonant properties of subwavelength voids in strongly anisotropic (hyperbolic) metamaterials were investigated by means of spherical harmonics expansion. These harmonics, being eigen resonances in isotropic environment, are nontrivially coupled by strong anisotropy and corresponding boundary conditions. Eigen resonances of the void are linked to the local field corrections for spontaneous emission rates inside metamaterial environment.

1. INTRODUCTION

Spontaneous emission processes are efficiently manipulated by nano-structured environment, which could almost on demand control both rates and coherence of quantum emitters [1]. Local density of states, being the key characteristic of electromagnetic space, could be dramatically enhanced by so-called hyperbolic metamaterials — strongly anisotropic artificial composites [2, 3]. However, radiating sources, situated inside a material, strongly interact with their surrounding by inducing additional local polarizations of the matter. One of the well-established approaches, enabling to address this issue, is the Clausius-Mosotti theory, which introduces a virtual cavity around an emitter [4]. This virtual void, being non-resonant for transparent dielectric environment, has nontrivial eigen resonances in the case of hyperbolic metamaterial. Investigation of the nature of these resonances and their impact on the local field correction for emission processes will be studied here.

2. QUASISTATIC MODEL FOR SPHERICAL VOID INSIDE ANISOTROPIC UNIAXIAL MEDIUM

We consider a subwavelength spherical void with radius R and dielectric constant ε_{in} situated inside anisotropic uniaxial medium with the dielectric tensor $\varepsilon_{out} = \mathrm{diag}(\varepsilon_{\parallel}, \varepsilon_{\parallel}, \varepsilon_{\perp})$.

The problem of eigen modes of the system was solved in the quasistatic limit by adopting Laplace equation for electric potential u:

$$\begin{cases} \frac{\partial^2 u}{\partial x^2} + \frac{\partial^2 u}{\partial y^2} + \frac{\partial^2 u}{\partial z^2} = 0, & r \le R \\ \varepsilon_{\parallel}\frac{\partial^2 u}{\partial x^2} + \varepsilon_{\parallel}\frac{\partial^2 u}{\partial y^2} + \varepsilon_{\perp}\frac{\partial^2 u}{\partial z^2} = 0, & r > R \end{cases} \tag{1}$$

The appropriate boundary conditions for normal field components are following:

$$D_n^{in}\big|_{R-0} = D_n^{out}\big|_{R+0}\,. \tag{2}$$

In the case of isotropic embedding medium the resonances (material must have negative permittivity in order to support a one) have well-defined sequence — dipole, quadrupole, and higher-poles, defined by spherical harmonic decomposition. However, in the case of anisotropic medium all spherical harmonics are non-trivially coupled via boundary conditions.

The well-known solution of the first equation in (1) may be written in spherical coordinates [5]:

$$u_{in} = \sum_{n=1}^{\infty} A_{nm} P_n^m(\cos\theta)\, R^{n+1}(\cos m\phi + \sin m\phi) \tag{3}$$

But the potential u_{out} outside the sphere can be obtained by using scale transformation theory [5] in a more complex form

$$u_{out} = \sum_{n=1}^{\infty} F_{nm} P_n^m\left(\frac{\cos\theta}{q}\right)\left(\frac{\sqrt{\varepsilon_{\perp}}}{Rq}\right)^{n+1}(\cos m\phi + \sin m\phi) \tag{4}$$

where denominator $q = \sqrt{k\sin^2\theta + \cos^2\theta}$, coefficient $k = \frac{\varepsilon_\perp}{\varepsilon_\parallel}$, P_n^m — associated Legendre polynomial, A_{nm}, F_{nm} — indeterminate coefficients. In this work we consider the case of azimuthally uniform oscillations to coordinate ($m = 0$).

We substituted solutions (3) and (4) in the boundary condition (2), and further we multiplied the resulting expression by $P_n(\cos\theta)$ and integrated over spatial angle we obtain the linear system of equations for the indeterminate coefficients:

$$\begin{aligned}\varepsilon_{in}R^{k-1}A_k \;=\; & -\varepsilon_\parallel\sum_{n=1}^{\infty}\frac{F_n(n+1)}{R^{n+2}}\int_0^\pi P_n\left(\frac{\cos\theta}{q}\right)\left(\frac{\sqrt{\varepsilon_\perp}}{q}\right)^{n+1}P_n(\cos\theta)\sin\theta d\theta \\ & +\left(\varepsilon_\parallel-\varepsilon_\perp\right)\sum_{n=1}^{\infty}\frac{F_n(n+1)}{R^{n+2}}\int_0^\pi P_n\left(\frac{\cos\theta}{q}\right)\left(\frac{\sqrt{\varepsilon_\perp}}{q}\right)^{n+1}P_n(\cos\theta)\cos^2\theta\sin\theta d\theta \\ & -\left(\varepsilon_\parallel-\varepsilon_\perp\right)\sum_{n=1}^{\infty}\frac{F_n(n+1)}{R^{n+2}}\int_0^\pi P_n\left(\frac{\cos\theta}{q}\right)\left(\frac{\sqrt{\varepsilon_\perp}}{q}\right)^{n+1}P_n(\cos\theta)\cos\theta\sin^2\theta d\theta d\theta \quad (5)\end{aligned}$$

In this system Legendre polynomial with different arguments are not orthogonal as the result, causes the coupling between harmonics.

3. RESULTS AND DISCUSSION

Uniaxial material, having well-defined crystallographic axis in its natural Cartesian coordinate system, was transformed into full 3×3 tensor in the spherical system, appropriated for solution of the spherical cavity.

$$\overline{\varepsilon}_{out} = \begin{bmatrix}\varepsilon_\parallel-\left(\varepsilon_\parallel-\varepsilon_\perp\right)\cos^2\theta & \left(\varepsilon_\parallel-\varepsilon_\perp\right)\cos\theta\sin\theta & 0\\ 0 & \varepsilon_\parallel-\left(\varepsilon_\parallel-\varepsilon_\perp\right)\cos^2\theta & 0\\ 0 & 0 & \varepsilon_\parallel\end{bmatrix} \quad (6)$$

The presence of off-diagonal terms, calculated with the help of scale transformation theory [5], breaks the natural rotation a symmetry of the problem. Consequently, eigen resonances of the void are described now by infinite series of spherical harmonics. The convergence of these series is strongly dependent on the strength of anisotropy. In the case of extreme anisotropy — hyperbolic metamaterial (ordinary and extraordinary permitivities have different sign) [2] the convergence is enabled solely by introduction of Joule losses. In order to address the impact of anisotropy on the radiation pattern, the boundary problem with the dipolar extrication was solved. While the classical dipole pattern appears at the classic isotropic case (Fig. 2), the strongly anisotropic regime manifests itself in multiple harmonic generations outside the void (Fig. 2–Fig. 4). The impact of these harmonics on the radiation will be addressed.

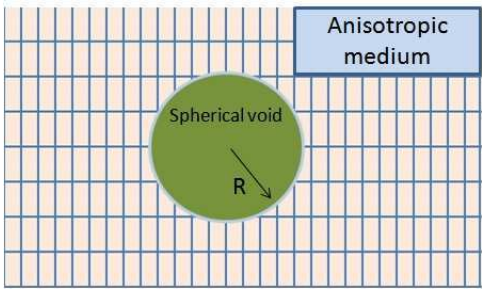

Figure 1: Geometry of problem.

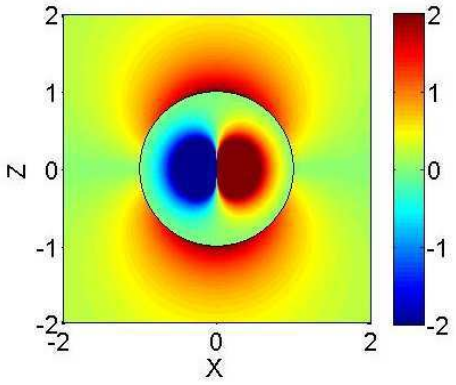

Figure 2: Radial components of electric field, excited by point vertically polarized dipole, situated in spherical void situated inside an isotropic medium ($\varepsilon_{in} = 1$, $\varepsilon_{out} = 3$).

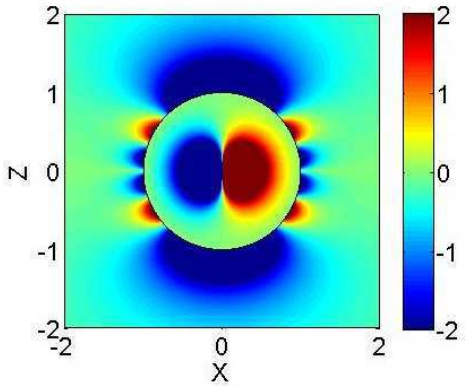

Figure 3: Radial components of electric field, excited by point vertically polarized dipole, situated in spherical void situated inside an anisotropic (elliptic) medium ($\varepsilon_{in} = 1$, $\varepsilon_{out} = \mathrm{diag}(2, 2, 3)$).

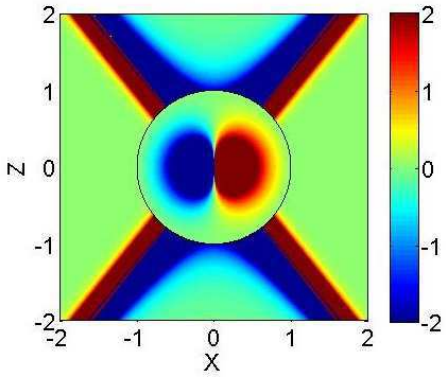

Figure 4: Radial components of electric field, excited by point vertically polarized dipole, situated in spherical void situated inside an anisotropic (hyperbolic) medium ($\varepsilon_{in} = 1$, $\varepsilon_{out} = \mathrm{diag}(2, 2, -3+0.1i)$).

In this paper we have used the scale transformation theory to consider the electric fields inside and outside subwavelength spherical void and have investigated the resonant properties of subwavelength voids in anisotropic (elliptic, hyperbolic) metamaterials by means of spherical harmonics expansion. These harmonics are nontrivially coupled by strong anisotropy and corresponding boundary conditions. Also we have solved the boundary problem with the dipolar extrication.

ACKNOWLEDGMENT

This work was financially supported by Government of Russian Federation, Grant 074-U01.

REFERENCES

1. Poddubny, A. N., et al., "Spontaneous radiation of a finite-size dipole emitter in hyperbolic media," *Physical Review A*, Vol. 84, No. 2, 023807, 2011.
2. Poddubny, A. N., et al., "Hyperbolic metamaterials," *Nature Photonics*, Vol. 7, 948–957, 2013.
3. Barnett, S. M., et al., "Spontaneous emission in absorbing dielectric media," *Phys. Rev. Lett.*, Vol. 68, 2012.
4. Poddubny, A. N., et al., "Hyperbolic metamaterials," *Nature Photonics*, Vol. 7, 948–957, 2013.
5. Li, Y.-L. and J.-Y. Huang, "The scale-transformation of electromagnetic theory and its applications," *Chinese Physics*, Vol. 14, No. 4, 0646-10, 2005.

THz Waveguides, Devices and Hybrid Polymer-chalcogenide Photonic Crystal Fibers

Hualong Bao[1], **Christos Markos**[1], **Kristian Nielsen**[1], **Henrik K. Rasmussen**[2], **Peter Uhd Jepsen**[1], **and Ole Bang**[1]

[1]DTU Fotonik — Department of Photonics Engineering
Technical University of Denmark, Kongens Lyngby Dk-2800, Denmark
[2]DTU Mekanik — Department of Mechnical Engineering
Technical University of Denmark, Kongens Lyngby Dk-2800, Denmark

Abstract— In this contribution, we review our recent activities in the design, fabrication and characterization of polymer THz waveguides. Besides the THz waveguides, we finally will also briefly show some of our initial results on a novel hybrid polymer photonic crystal fiber with integrated chalcogenide glass layers.

1. INTRODUCTION

Waveguides and functional devices in the Terahertz range have attracted considerable interest in recent years because they can offer the opportunity to develop compact, reliable and flexible THz systems

In this paper, we will first present a novel polymer (TOPAS) solid-core Photonic Crystal Fiber (PCF) with ultra-wide bandwidth, which is bendable and has low loss and unique dispersion properties. Then we demonstrate both numerically and experimentally a novel band-gap THz fiber design, which consists of a honeycomb cladding structure with a porous core. This structure uses Photonic Bandgap (PBG) guidance, while keeping the loss at low levels due to its special porous-core. Last but not least, we will also demonstrate a special design of a broadband THz directional coupler, which uses mechanical down-doping of the two cores. We show how this provides a broad bandwidth with relative low device loss and we performe a detailed optimization of the coupler design to maximize bandwidth and minimize loss.

Besides THz waveguides and devices, we also demonstrate a novel way to develop hybrid polymer photonic crystal fiber with integrated chalcogenide glass layers based on a solution-processed method. The proposed integration method allows the deposition of nanofilms with a wide range of nonlinear glasses and potentially offers the possibility for multi-layer deposition of different glasses inside the holes of the polymer PCF.

2. SOLID-CORE PCFS

We fabricated THz fibers based on the structure of solid-core PCFs [1], which guides by total internal reflection. The fibers were fabricated by using drill-and-draw technology and made of the cyclic olefin co-polymer TOPAS. The reason for using TOPAS is because it has very low loss and flat dispersion in the THz range. The images of the fabricated fibers with two different hole diameter (d) to pitch (Λ) ratios are shown in Figs. 1(a) and 1(b).

The fiber loss, measured using the cutback method, is shown in Fig. 1(c). The results show that the fiber can have propagation losses lower than the bulk material loss of TOPAS (gray line in Fig. 1(c)).

The spectrograms in Figs. 1(d) and (e) show a short time FFT of the THz pulse after propagation through a 26 mm Small-Mode Area (SMA) fiber and through a 29 mm Large-mode area (LMA) fiber, respectively. Overlaid on the spectrograms are the time traces of the electric field of the THz pulses. The results show the strong dispersion of the SMA fiber and small dispersion of the LMA fiber, which agree well with the calculated dispersion profiles shown in Figs. 1(f) and 1(g). Due to the strong confinement of the field in the solid core the fibers can be bent without significant increase in loss [1], which indicates that the proposed fibers are tolerant towards sharp bends of the fiber.

3. POROUS-CORE PBG TYPE FIBERS

Although some polymer materials such as TOPAS [1] and Zeonex [2], have relative low loss in the THz region compared to other polymer materials such as PMMA, their loss levels are still high.

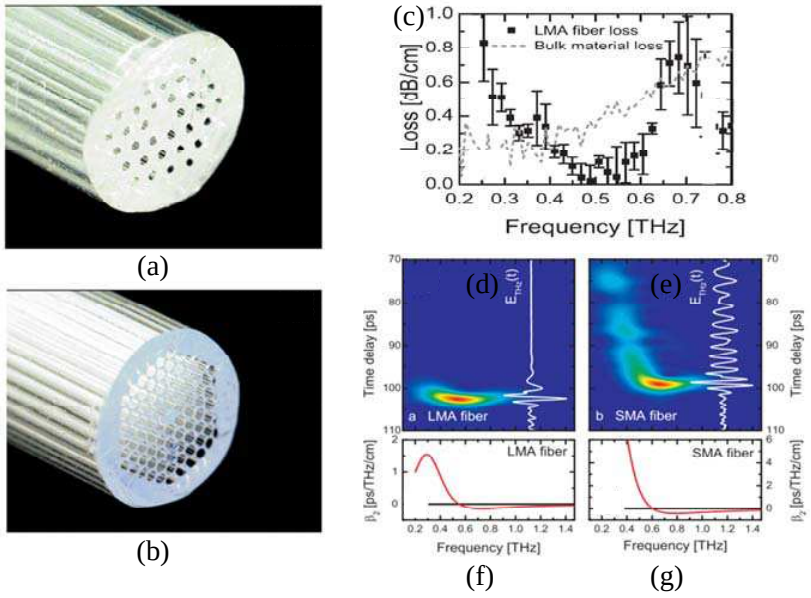

Figure 1: (a) Image of the LMA and (b) SMA fibers, respectively. (c) Frequency dependant loss of the LMA fiber. Spectrogram and temporal profile of the THz pulse after propagation through (d) 26 mm SMA fiber and (e) 29 mm LMA fiber. Calculated dispersion for (f) SMA and (g) LMA fiber.

Dry air is transparent in the THz region and thus an effective approach to lower the propagation loss of a THz waveguide is to maximize the fraction of the power propagating in air, while still being confined to a waveguide. Towards this point, hollow-core PBG fibers are good candidates due to the fact that they can confine most power in the air-core as well as have flexibility in the design of critical parameters such as center frequency, bandwidth, and dispersion. However, good-quality hollow-core PBG THz fibers have so far been difficult to draw, mainly due to the different expansion ratios of holes with different diameter during the drawing process.

To overcome the fabrication problems of differently sized holes in the hollow core THz fiber, a novel porous-core honeycomb bandgap design was numerically and experimentally investigated [3, 4]. Basically it consists of a hollow-core PBG THz fiber cladding structure (honeycomb) with a porous core (the same size as cladding hole) inserted into the hollow core. This allows PBG guidance, while still keeping the loss low due to the porous core. Due to the increased effective index of the core, the cladding PBG structure is a honeycomb structure, which from optical fibers is known to more easily allow broad bandgaps.

The fact that all air-holes are of the same size results in a fiber that can be drawn with much higher precision and reproducibility than a corresponding air-core fiber. Figs. 2(a) and 2(b) show an idealized structure and a microscope image of the end facet of the proposed porous-core honeycomb

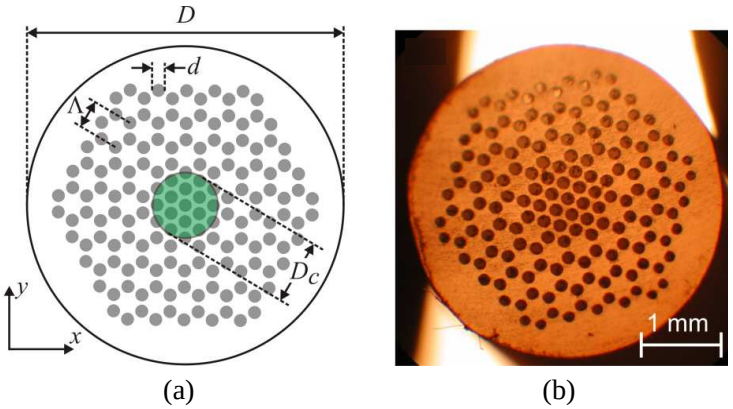

Figure 2: (a) Idealized structure used in the simulation ($d = 165\,\mu m$, $\Lambda = 360\,\mu m$). (b) Microscope image of the actual fiber.

bandgap THz fiber, respectively. The high-precision hole structure provides very clear bandgap guidance and the location of the two measured bandgaps agree well with simulations based on finite-element modeling (not shown here). Moreover, it was shown in Figs. 3(a)–(d) that cladding mode can be effectively stripped away by adding an absorptive water layer around the fiber. Fiber loss measurement results shown in Figs. 3(e)–(g) reveal the frequency-dependent coupling loss and propagation loss, and the fact that the fiber propagation loss can be significantly lower than the bulk material loss (dash line in Fig. 3(g)) within the first band gap between 0.75 and 1.05 THz.

4. 3-dB THz FIBER DIRECTIONAL COUPLERS

Due to the progress in THz fibers and waveguides, it has now become possible to develop THz devices. THz directional couplers are particularly interesting due to their controllable directional power transfer between fiber cores. However, most of the reported THz couplers have in common that they only have a constant coupling length over a narrow bandwidth. For removing the bandwidth limitation, very recently, one kind of broadband THz directional fiber coupler working in the THz region was proposed [5, 6]. Broad transmission was achieved by using down-doping in two cores of a dual-core PCF. Instead of normal chemical down-doping a mechanical down-doping was implemented by using a triangular array of air holes, which can be easily achieved by drill-and-draw technology [1]. The cross section of the proposed coupler, together with an enlarged view of the doped core is shown in Fig. 4(a). The downdoped cores experience mode-field diameter minima

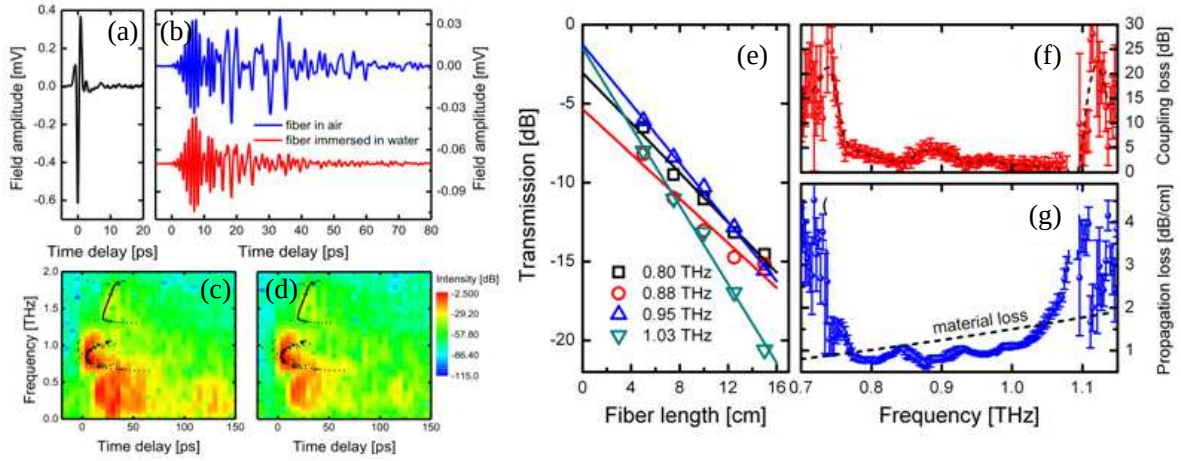

Figure 3: Measured THz pulse for (a) reference signal and (b) transmitted pulse through a 5 cm long honeycomb fiber with water (red curve) and air (blue curve) around the surface. Short-time Fourier transforms of the transmitted waveforms in (b) are shown in (c) and (d), respectively, with simulated group velocity arrival times of the spectral components overlaid. (e) Relative transmission of the fiber with different lengths. (f) Coupling loss (red symbols), (g) Frequency dependent propagation loss of the fiber (blue data markers) and material loss of TOPAS (dashed line).

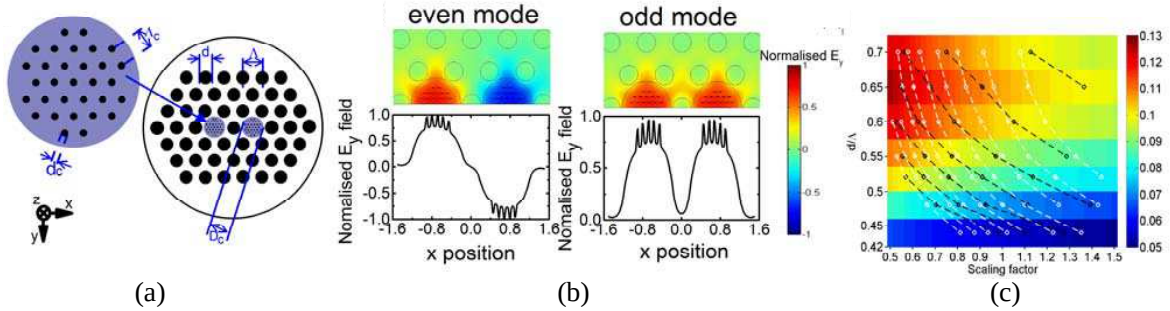

Figure 4: (a) Cross section of the air-doped dual-core coupler. (b) Electric field profiles at 0.9 THz (y polarization) of even and odd super-modes. (c) Optimum FOM ($\Lambda = 682.5\,\mu$m and $\Lambda_c = 102.375\,\mu$m at $m = 1$) versus d/Λ and scaling factor m. Black dashed lines have fixed center frequency from 0.6 to 1.4 THz with a step of 0.1 THz. White dashed lines have fixed 3-dB bandwidth from 0.15 to 0.4 THz with a step of 0.05 THz (right to left).

(corresponding to maximum coupling length), at which the first derivative of the coupling length vanished, which results in a bandwidth broadening.

Due to the existence of a huge parameter space (d, Λ, d_c, Λ_c), further work was done by a thorough numerical design optimization of the structure parameters. Optimizations were performed by using a figure of merit (FOM), which takes both the 3-dB bandwidth and device loss into account [5, 6]. Fig. 4(c) shows the optimum FOM of the coupler for different d/Λ as a function of a scaling factor, which scales, or multiplies, all geometrical parameters of the coupler. Note here that the optimum FOM without scaling is obtained by fixing $\Lambda = 682.5\,\mu$m. Simulation results show that at a center frequency of 1 THz a structure with suitable parameters can have a large bandwidth of 0.25 THz and relative low device loss of 9.2 dB [6]. In the work, single-mode guidance within the desired working region was also verified for the optimum coupler (not shown here).

5. HYBRID POLYMER-CHALCOGENIDE PCFS

A novel hybrid polymer PCF with integrated chalcogenide glass layers was fabricated using a solution-based method [7]. Fig. 5(a) shows a SEM image of the initial fabricated PMMA PCF and Fig. 5(b) shows the SEM image after the deposition of the chalcogenide films inside the cladding holes of the fiber (using a concentration of ∼400 mg As_2S_3 in 1 mL of n-butylamine). After the solvent evaporation, energy dispersive X-ray (EDX) analysis was used to verify the existence of As (arsenic) and S (sulfide) lines as can be seen from Fig. 5(c). Fig. 5(d) shows the normalized transmission (black line) of a 4-cm long hybrid fiber and how the transmission edge shifts after the increase of the power (red line). This is because the ultra-high Kerr nonlinearity of the chalcogenide glass makes the polymer PCF nonlinear and consequently red-shifts the long wavelength band edge as the power increases. The proposed fabrication technique constitutes a new highway towards all-fiber nonlinear tunable devices based on polymer PCFs.

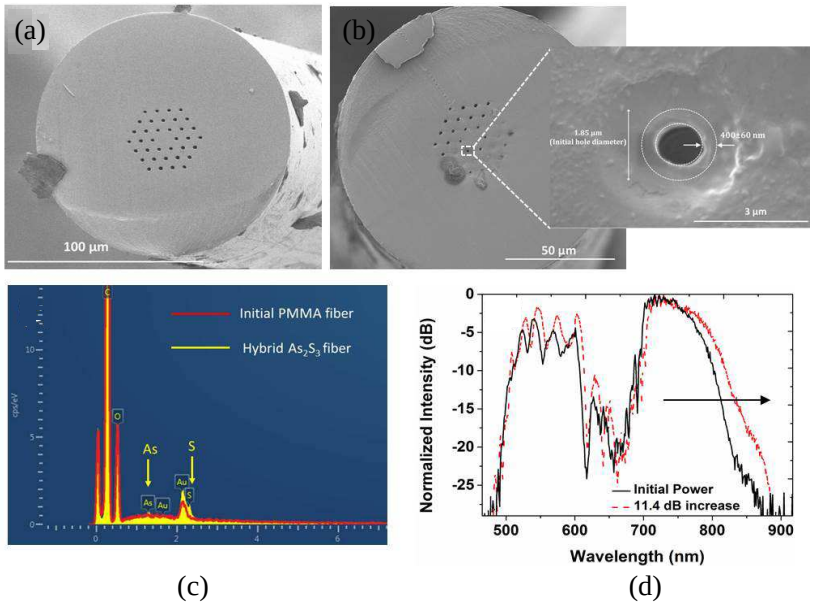

Figure 5: SEM image of the (a) fabricated PMMA PCF and (b) the hybrid chalcogenide/PMMA PCF. Inset is magnified single hole showing the thickness of the chalcogenide film to be ∼400 nm. (c) Energy dispersive X-ray spectroscopy verifying the existence of the Arsenic and Sulfide elements on the inner wall of the air-holes. (d) Normalized transmission spectrum of the hybrid fiber at two different power levels.

REFERENCES

1. Nielsen, K., H. K. Rasmussen, A. J. Adam, P. C. Planken, O. Bang, and P. U. Jepsen, "Bendable, low-loss Topas fibers for the terahertz frequency range," *Optics Express*, Vol. 17, No. 10, 8592–8601, 2009.
2. Anthony, J., R. Leonhardt, A. Argyros, and M. C. Large, "Characterization of a microstructured Zeonex terahertz fiber," *JOSA B*, Vol. 28, No. 5, 1013–1018, 2011.
3. Nielsen, K., H. K. Rasmussen, P. U. Jepsen, and O. Bang, "Porous-core honeycomb bandgap THz fiber," *Optics Letters*, Vol. 36, No. 5, 666–668, 2011.

4. Bao, H., K. Nielsen, H. K. Rasmussen, P. U. Jepsen, and O. Bang, "Fabrication and characterization of porous-core honeycomb bandgap THz fibers," *Optics Express*, Vol. 20, 29507–29517, 2012.
5. Nielsen, K., H. K. Rasmussen, P. U. Jepsen, and O. Bang, "Broadband terahertz fiber directional coupler," *Optics Letters*, Vol. 35, No. 17, 2879–2881, 2010.
6. Bao, H., K. Nielsen, H. K. Rasmussen, P. U. Jepsen, and O. Bang, "Design and optimization of mechanically down-doped terahertz fiber directional couplers," *Optics Express*, Vol. 20, 9486–9497, 2014.
7. Markos, C., S. N. Yannopoulos, and K. Vlachos, "Chalcogenide glass layers in silica photonic crystal fibers," *Optics Express*, Vol. 20, 14814–14824, 2012.

The Study on Equivalent Models of Finite-size Carbon Fiber Composite Materials

Y. Liao, Y. Zhang, and K. Cai
Shanghai Key Laboratory of Electromagnetic Environmental Effects for Aerospace Vehicle
846 Minjing RD, Yangpu District, Shanghai 200438, China

Abstract— The purpose of this paper is to investigate the use of equivalent-layer models for the analysis of finite-size carbon-fiber composite materials. A macroscopically equivalent model based on the homogenization technique, which is a more efficient method for analyzing fiber composite is investigated. Finite size composite slabs, consist of loose carbon fibers mixed with resins, are used to validate the equivalent models. Different thicknesses and sizes of the slabs, as well as relative volume of carbon fibers are considered. It is found that the breakdown frequencies of equivalent models vary significantly with the various geometries. It is important to validate the equivalent models of each finite-size composite block before simplifying them in the whole large structure model.

1. INTRODUCTION

Carbon fiber reinforced composites (CFRC) are being used more widely in the aerospace and automotive industries as replacement for metals due to the good strength and weight properties [1]. They are realized by a matrix of resin in which high strength carbon fibers are embedded and aligned along a preferred direction of reinforcement. Despite the many mechanical advantages, composite materials are not as electrically conductive as metals such as aluminum and titanium. It has an electrical conductivity that is nearly 1000 times lower than that of most metals [2]. Therefore, Carbon composite materials usually have poor performance of shielding effectiveness which may leads to electromagnetic interference (EMI) problems under EM hazards [3].

Full numerical approaches are often used to analyze the influence of composite electrical properties on the electromagnetic performance. However, prohibitive computational time and computer memory may be required when thin panels and fibers of composite materials are spatially resolved. Thus, approximate formulas for the effective material properties are very useful. Previous work shows that equivalent models with effective electromagnetic parameters are usually proposed for the analysis of periodic carbon fiber composite materials when the period of the structure is small compared to the wavelength [4]. Basically, finite-size CFRCs are often constructed as parts of the large structure system such as aircraft in practical cases. The authors' interest stems from an analysis of aircraft structure model with many finite-size CFRC slabs. The applicable frequency range of equivalent models for finite-size CFRC may vary with different geometries.

In this paper, we firstly review close-form expressions available in the literature for approximating the effective permittivity and permeability of composite materials. A macroscopically equivalent model based on the homogenization technique, which is a more efficient method for analyzing fiber composite is investigated. Several carbon fiber composite slabs are used to validate the equivalent models. Different thicknesses and sizes of the slab, as well as relative volumes of carbon fiber are considered. It is found that the breakdown frequencies of equivalent models vary significantly with the geometries of the composite materials. It is of prime importance to validate the equivalent models of each finite-size composite block before simplifying them in the whole large structure model.

2. REVIEW OF KNOWN APPROXIMATIONS FOR EFFECTIVE PARAMETERS

In the earlier past, there has been a great deal of attention toward determining the effective properties of composite regions based on effective medium theory. Famous formulas from the historical point of view include Maxwell-Garnett, Bruggeman, and QCA-CP equations in terms of the volume fractions and properties of the constituting phases [5]. However, these formulas are oftern used to determine the effective permittivity and permeability of homogeneous and isotropic multiphase materials, such as a dispersion of dielectric spheres in a homogeneous matrix and particle medium mixtures.

The present paper consider exclusively with two-phase media. Figure 1(a) shows the geometrical structure of periodic fiber composite slab and its coordinate system. The composite layer is realized

by carbon fibers with circular cross-section, having conductivity σ_f and permittivity ε_f, embedded in a matrix resin of conductivity σ_m and permittivity ε_m. The cross-section of xy-plane is shown in Figure 1(b). P is the distance between the carbon fibers, D the fiber diameter and L the overall thickness of the layer. In this paper, we only consider the two-phase dielectric materials (i.e., the permeability is assumed to be μ_0) with the appropriate invariance in the z direction.

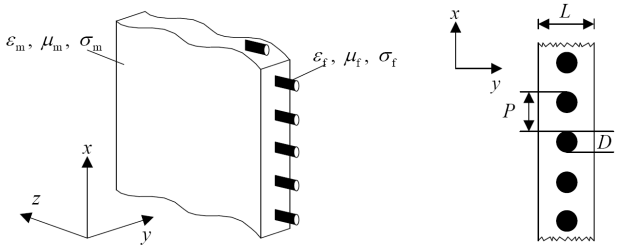

(a) Composite structure (b) Cross section

Figure 1: Carbon fiber composite structure and coordinate system.

As to the inhomogeneous and anisotropic composite materials, an efficient method known as homogenization has been used to solve problems of this periodic type in reasonable low frequency ranges. Homogenization technique allows the separation of the average field from the microstructure. If the period of a periodic structure is small compared to a wavelength, the EM waves see the composite as an effective anisotropic homogeneous region with tensor permittivity $[\varepsilon^h]$ given by [4]

$$\left[\varepsilon^h\right] = \begin{bmatrix} \varepsilon_x & 0 & 0 \\ 0 & \varepsilon_y & 0 \\ 0 & 0 & \varepsilon_z \end{bmatrix}. \tag{1}$$

Among many approximation techniques, the most widely known were the Hashin-Shtrikman (HS) upper and lower bounds, which were derived in terms of the material parameters and the volume fraction [6]. They limit ε_x and ε_y to a region between two bounds defined as

$$\varepsilon_{HS}^L = \varepsilon_m \frac{(1+g)\varepsilon_f + (1-g)\varepsilon_m}{(1-g)\varepsilon_f + (1+g)\varepsilon_m}, \tag{2}$$

$$\varepsilon_{HS}^U = \varepsilon_f \frac{(2-g)\varepsilon_m + g\varepsilon_f}{g\varepsilon_m + (2-g)\varepsilon_f}, \tag{3}$$

where g is the relative volume of space occupied by the material with carbon fibers,

$$g = \pi D^2/(4PL) \tag{4}$$

Another approximation technique is the Lichtenecker (Li) bounds depend on the specific geometry of the unit cell and can be written as

$$\varepsilon_{Li}^L = \int_0^P \frac{dy}{\int_0^P \frac{dx}{\varepsilon(x,y)}}, \tag{5}$$

$$\varepsilon_{Li}^U = \frac{1}{\int_0^P \frac{dx}{\int_0^P \varepsilon(x,y)dy}}. \tag{6}$$

Previous work has shown that, in general, the HS lower bound is a good approximation for the effective properties when ε_f is larger than ε_m [4]. Similarly, HS upper bound is better when resin is a denser medium. For more complicated composites, Li bounds are more accurate. However, these bounds are recommended to be used for composite material with real permittivity. Besides these bounds, [7] has proposed formulas for the components in (1).

$$\varepsilon_x^{-1} = (1-g)\varepsilon_m^{-1} + g\varepsilon_f^{-1}, \tag{7}$$

$$\varepsilon_y = \varepsilon_z = (1-g)\varepsilon_m + g\varepsilon_f. \tag{8}$$

This approximation approach is a better estimate for single-panel carbon fiber composite materials. In general, this homogenous model can be accurate for periods as large as half wavelength [8]. Once either the frequency of operation or the material of the structures becomes too highly conductive the homogenization technique begins to break down. Meanwhile, different from infinite periodic structures, the size of composite materials would influence the applicable frequency range of the equivalent model. Actually, finite-size composite models are often built for large structures on analysis of the interaction of EM field in practical cases.

3. DISCUSSION OF EQUIVALENT MODEL FOR FINITE-SIZE COMPOSITE SLABS

In this section, an equivalent model based on approximated formulas (7) and (8) is investigated. Four configurations with different geometrical parameters of carbon fiber composite slabs are used for validating the equivalent model. The EM parameters are: $\varepsilon_m = 5\varepsilon_0$, $\varepsilon_f = 2\varepsilon_0$, $\sigma_f = 70000\,\mathrm{S/m}$, $\sigma_m = 0\,\mathrm{S/m}$. The geometrical parameters of the slabs are given in Table 1. They are illuminated by an incident plane wave ($+y$ direction) with electric field parallel to z direction, as shown in Figure 2(a). The magnitude of E-field of plane wave is 1 V/m. An observation point (0 cm, 2 cm, 0 cm) is set to get the transmitted electric field strength on the other side of the slabs. By using the formulas (7) and (8), effective permittivity $[\varepsilon^h]$ can be calculated and an equivalent homogenous anisotropic model is given in Figure 2(b).

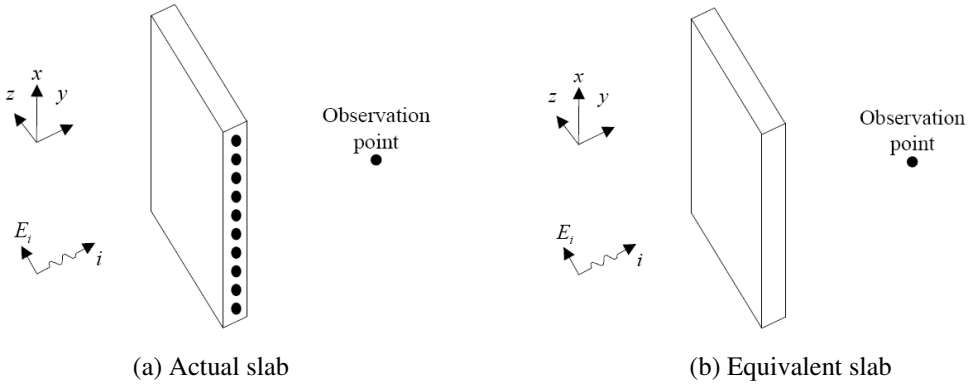

(a) Actual slab (b) Equivalent slab

Figure 2: Setup of finite size slab models.

Table 1: Geometric structures of finite-size carbon fiber composites.

No.	Geometry
1	Dimension: 10 cm × 10 cm×2 cm, $P = 2$ cm, $D = 1$ cm, $L = 2$ cm
2	Dimension: 20 cm × 20 cm×2 cm, $P = 2$ cm, $D = 1$ cm, $L = 2$ cm
3	Dimension: 20 cm × 20 cm×3 cm, $P = 2$ cm, $D = 1$ cm, $L = 3$ cm
4	Dimension: 20 cm × 20 cm×2 cm, $P = 1.25$ cm, $D = 1$ cm, $L = 2$ cm

The evaluation of breakdown frequency of equivalent model is carried out by computing the relative differences in the E-field strength at the observation point. The error is defined as the ratio of E-field strength different over the E-field strength of actual carbon fiber composite model. The equation for the error is indicated below:

$$Error = \frac{|E_{act} - E_{eff}|}{E_{act}} \times 100\%, \tag{9}$$

where E_{act} is the E-field strength at the observation point for actual composite model. E_{eff} is for equivalent anisotropic model. The equivalent model fails when the error is larger than 25%.

Numerical results are obtained with a full-wave tool (HFSS) for these four finite-size composite slabs. The results are shown Figure 3 and Figure 4. It can be seen that the E-field results of equivalent model agree well with that of actual composite model in the low frequency. When frequency of operation becomes too high, the equivalent model begins to break down. The breakdown frequency is 2.9 GHz in Geometry 1 (i.e., the error is larger than 25% after 2.9 GHz). Similarly,

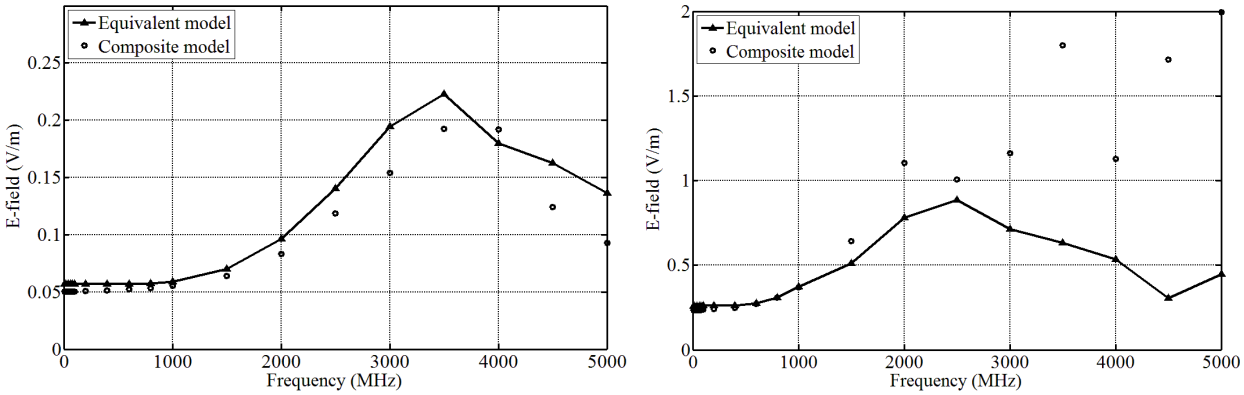

(a) Geometry 1 (b) Geometry 2

Figure 3: *E*-field strength at observation point in Geometry 1 and Geometry 2.

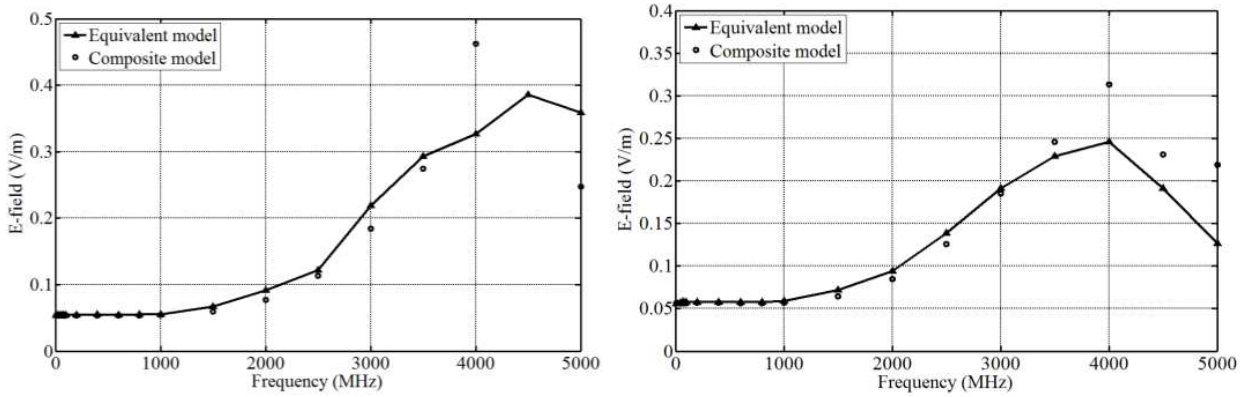

(a) Geometry 3 (b) Geometry 4

Figure 4: *E*-field strength at observation point in Geometry 3 and Geometry 4.

the breakdown frequencies are 1.8 GHz in Geometry 2, 3.9 GHz in Geometry 3, 4.6 GHz in Geometry 4. Different configurations of finite-size composite slabs results in different frequency limits for equivalent models.

4. CONCLUSION

Equivalent model based on homogenization technique can be used efficiently to analyze the interaction of EM field with carbon fiber composite structures. A macroscopically equivalent model derived under the assumption of infinite periodic structures is investigated for analysis of finite-size structure. Several carbon fiber composite slabs are used to validate the equivalent models. Different thicknesses and sizes of the slab, as well as relative volume of carbon fiber are considered. The breakdown frequencies of equivalent models vary significantly with the geometries of the composite materials. It is of prime importance to validate the equivalent models of each finite-size composite block before simplifying them in the whole large structure model.

ACKNOWLEDGMENT

This work was supported in part by the National Natural Science Foundation of China (No. 61302036).

REFERENCES

1. Chu, H. C., S. K. Jeng, and C. H. Chen, "Reflection and transmission characteristics of lossy periodic composite structures," *IEEE Trans. Antennas Propag.*, Vol. 44, No. 3, 580–587, 1996.
2. Evans, R. W., "Design guidelines for shielding effectiveness, current carrying capability, and

the enhancement of conductivity of composite materials," *NASA Contractor Report*, No. 4784, 1997.
3. D'Amore, M. and M. S. Sarto, "Theoretical and experimental characterization of the EMP-interaction with composite-metallic enclosures," *IEEE Trans. Electromagn. Compat.*, Vol. 42, 152–163, 2000.
4. Johansson, M., C. L. Holloway, and E. F. Kuester, "Effective electromagnetic properties of honeycomb composites, and hollow-pyramidal and alternating-wedge absorbers," *IEEE Trans. Antennas Propag.*, Vol. 53, No. 2, 728–736, 2005.
5. Wu, M., H. Zhang, X. Yao, and L. Zhang, "Microwave characterization of ferrite particles," *Journal of Physics D: Applied Physics*, Vol. 34, 889–895, 2001.
6. Hashin, Z. and S. Shtrikman, "A variational approach to the theory of the effective magnetic permeability of multiphase materials," *Journal of Applied Physics*, Vol. 33, No. 10, 3125–3131, 1962.
7. Kuester, E. F. and C. L. Holloway, "A low-frequency model for wedge or pyramid absorber arrays — I: Theory," *IEEE Trans. Electromagn. Compat.*, Vol. 36, No. 4, 300–306, 1994.
8. Holloway, C. L., M. S. Sarto, and M. Johansson, "Analyzing carbon-fiber composite materials with equivalent-layer models," *IEEE Trans. Electromagn. Compat.*, Vol. 47, No. 4, 833–844, 2005.

Wavelength-tunable Dual-concentric-core Photonic Crystal Fibers

Che-Wei Yao[1], **Wei-Hsiang Chuang**[1], **and Jui-Ming Hsu**[1, 2]

[1]Department of Electro-Optical Engineering, National United University, Miaoli 360, Taiwan, R.O.C.
[2]Optoelectronics Research Center, National United University, Miaoli 360, Taiwan, R.O.C.

Abstract— A wavelength-tunable and strongly dispersion-compensating photonic crystal fiber based on a hybrid structure of dual-concentric-core photonic crystal fiber (DCC-PCF) structure and depressed-clad photonic crystal fiber (DeC-PCF) is proposed. To enhance the dispersion compensation effect, we used a hybrid structure of DCC-PCF and DeC-PCF as a basic structure. In the central core of the hybrid fiber, different kinds of liquid with various refractive indices are filled into the air hole with appropriate diameter. The numeric results show that the operation wavelength is determined by the refractive index of the liquid.

1. INTRODUCTION

Chromatic dispersion in transmission fibers induces temporal optical pulse broadening, resulting in serious restrictions in transmission data rates in optical fiber communication systems. Currently, dispersion-compensating fibers (DCFs) are extensively used to minimize the negative effects of chromatic dispersion. The absolute dispersion value of conventional MCVD DCFs was approximately −250 ps/km-nm [1]. J. L. Auguste et al. reported another design of DCF based on a dual-concentric core fiber (DCCF) structure with a high dispersion coefficient of −1800 ps/km-nm [2]. Additional dispersion-compensation research involved altering the air hole size of a specific layer of photonic crystal fiber (PCF) to design dual-concentric core PCFs (DCC-PCFs) [3–7]. We had proposed a liquid-filled hybrid structure of DCC-PCF and depressed clad photonic crystal fiber (DeC-PCF) with an ultra-large dispersion coefficient of −40400 ps/km-nm at a wavelength of around 1.55 μm [7]. The design of this hybrid structure can avoid the restriction of "mutual involvement" between two supermodes, significantly increasing the index slope difference between two supermodes and thereby enlarging the dispersion coefficient.

In this study, we present a wavelength-tunable dispersion-compensating photonic crystal fiber (WT-DCPCF) with large dispersion coefficient based on a hybrid structure of DCC-PCF and DeC-PCF due to an ultra-large dispersion coefficient of this structure as mentioned above. Furthermore, to achieve a wavelength-tunable capability, different kinds of liquid with various refractive indices were selected to fill into the air hole with appropriate diameter in the central core of the hybrid fiber. Ultimately, the numeric results indicated that the proposed WT-DCPCF with chromatic dispersion coefficients of −32352 ps/km-nm to −41575 ps/km-nm at a wavelength range between 1472 nm to 1617 nm.

In general, a single-wavelength dispersion compensation photonic crystal fiber (DC-PCF) has a value of dispersion coefficient considerably larger than that of a broadband DC-PCF [8–11]; however it is just suitable for using at a fixed wavelength. In addition to with a high dispersion coefficient close to a single-wavelength DCC-PCF, the proposed WT-DCPCF is even more having an advantage of flexible wavelength-variation fabrication.

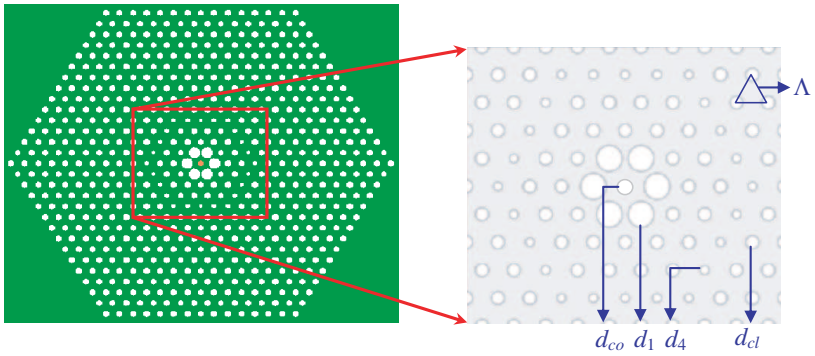

Figure 1: Cross-sectional view of the proposed WT-DCPCF.

2. SIMULATION MODEL AND PRINCIPLES

The Cross-sectional view of the proposed WT-DCPCF structure is shown in Figure 1. The cladding of the proposed WT-DCPCF consists of a triangular lattice of air holes with a diameter of $d_{cl} = 1.40\,\mu m$ and a pitch (center-to-center distance between the holes) of $\Lambda = 2.50\,\mu m$ in a background of undoped silica, whose refractive index can be estimated using the Sellmeier equation [12]:

$$n(\lambda) = \left[1 + \frac{0.6961663\lambda^2}{\lambda^2 - (0.0684043)^2} + \frac{0.4079426\lambda^2}{\lambda^2 - (0.1162414)^2} + \frac{0.8974794\lambda^2}{\lambda^2 - (9.896161)^2}\right]^{1/2}. \quad (1)$$

where λ represents the operating wavelength.

To enhance the dispersion compensation effect, a hybrid structure of DCC-PCF and DeC-PCF was used [7], that is to say, we enlarged the size of holes at first layer ($d_1 = 2.00\,\mu m$). The outer ring core with smaller-diameter air holes ($d_4 = 0.68\,\mu m$), which is designed to locate at fourth layer of the WT-DCPCF, separates the cladding region into inner and outer cladding. The mode-couple between inner and outer modes then results in a negative dispersion of the fiber at the phase-matching wavelength. In the inner core, different kinds of the Cargille® optical liquid with various refractive indices (n_{co}), which is colored in orange in the figure, are filled into the central air hole with appropriate diameter of $d_{co} = 1.00\,\mu m$. The refractive index of $n_{co}(\lambda)$ is defined by the Cauchy equation as

$$n_{co}(\lambda) = A + \frac{B}{\lambda^2} + \frac{C}{\lambda^4}. \quad (2)$$

Here, the Cauchy coefficients A, B and C, which are provided by Cargille Laboratories, are different for various liquids. The numeric results show that the operation wavelength is determined by the refractive index of the liquid.

The chromatic dispersion coefficient D is used to quantify the amount of chromatic dispersion. $D(\lambda)$ is defined as

$$D(\lambda) = \frac{-\lambda}{c}\frac{d^2 n_{eff}}{d\lambda^2}, \quad (3)$$

where c is the speed of light in a vacuum, and n_{eff} is the effective indices of the fundamental guided modes on a fiber at various wavelengths.

In this work, the effective refractive index (n_{eff}) of the fundamental mode is first estimated using the plane-wave expansion (PWE) method. The dispersion coefficient $D(\lambda)$ is then evaluated by substituting n_{eff} into Equation (3).

3. NUMERICAL RESULTS AND DISCUSSIONS

Figure 2 indicates the dependence of the chromatic dispersion coefficients on wavelength for various indices of the liquids filled in the central hole. Here the denoted refractive index n_D values of the

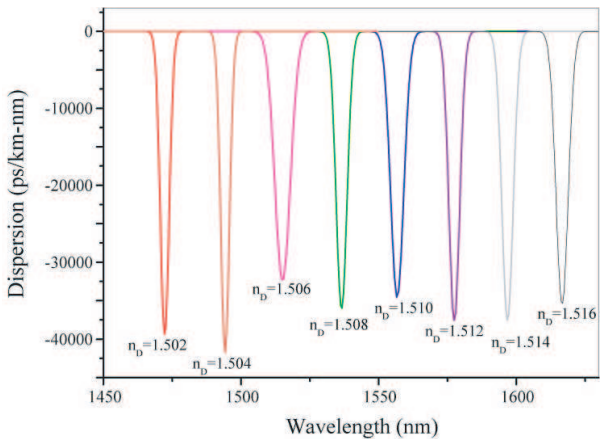

Figure 2: Dependence of the chromatic dispersion on wavelength for various indices of the liquids.

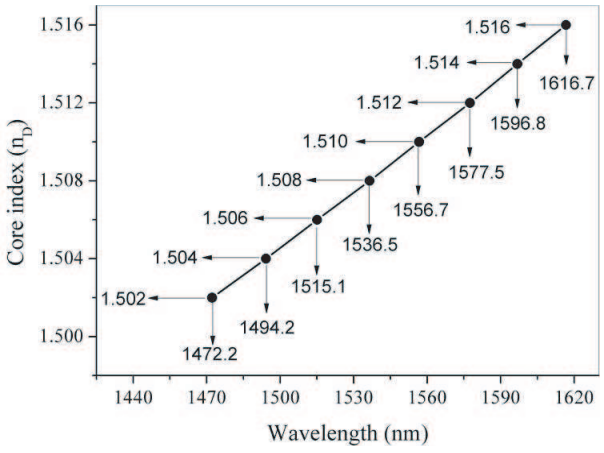

Figure 3: Relationship between the n_D of the filled liquid and the minimum-dispersion wavelength for the proposed WT-DCPCF.

used Cargille optical liquid are measured at 25°C, Sodium D Line ($\lambda = 589.3$ nm). As shown in the figure, the refractive index of the liquid determines the operation wavelength. The numeric results indicate that the proposed WT-DCPCF with chromatic dispersion coefficients of -32352 ps/km-nm to -41575 ps/km-nm at a wavelength range between 1472 nm to 1617 nm.

To realize what the filled liquid is needed for a specific operating wavelength in an optical communication system, Figure 3 indicates the relationship between the wavelengths of the minimum dispersions shown in Figure 2 and the n_D of the filled Cargille optical liquid. The precise values of the minimum-dispersion wavelengths and the n_D's are denoted in the figure. As shown in the figure, the relation curve of these two parameters is quite linear. Therefore, by using interpolation or extrapolation in Figure 3, it is helpful for designing a WT-DCPCF with an operating wavelength excluded from the numerical results of this work.

4. CONCLUSIONS

This study proposes a wavelength-tunable dispersion compensating photonic crystal fiber (WT-DCPCF) with an ultra-large negative dispersion coefficient. The operating wavelength is determined by the refractive index of the Cargille optical liquid filled in the central hole of the core. The numeric results show that the proposed WT-DCPCF with chromatic dispersion coefficients of -32352 ps/km-nm to -41575 ps/km-nm at a wavelength range between 1472 nm to 1617 nm while filled liquids with n_D's of 1.502 to 1.516. The wavelength range covers the whole C band and great parts of L and S bands. Furthermore, the relationship between the n_D of the filled liquid and the operating wavelength is quite linear. Therefore, it can be predicted that the tunable range of wavelengths can be more widely extended by filling liquid with an n_D beyond the investigated range of 1.502 to 1.516.

REFERENCES

1. Vengsarkar, A. M. and W. A. Reed, "Dispersion-compensating single-mode fibers: Efficient designs for first- and second-order compensation," *Opt. Lett.*, Vol. 18, 924–926, 1993.
2. Auguste, J. L., J.-M. Blondy, J. Maury, B. Dussardier, G. Monnom, R. Jindal, K. Thyagarajan, and B. P. Pal, "Conception, realization, and characterization of a very high negative chromatic dispersion fiber," *Opt. Fiber Technol.*, Vol. 8, 89–105, 2002.
3. Gerome, F., J.-L. Auguste, and J.-M. Blondy, "Design of dispersion compensating fibers based on a dual-concentric-core photonic crystal fiber," *Opt. Lett.*, Vol. 29, 2725–2727, 2004.
4. Zhao, X., G. Zhou, S. Li, Z. Liu, D. Wei, Z. Hou, and L. Hou, "Photonic crystal fiber for dispersion compensation," *Appl. Opt.*, Vol. 47, 5190–5196, 2008.
5. Yang, S., Y. Zhang, X. Peng, Y. Lu, S. Xie, J. Li, W. Chen, Z. Jiang, J. Peng, and H. Li, "Theoretical study and experimental fabrication of high negative dispersion photonic crystal fiber with large area mode field," *Opt. Express*, Vol. 14, 3015–3023, 2006.
6. Yu, C. P., J. H. Liou, S. S. Huang, and H. C. Chang, "Tunable dual-core liquid-filled photonic crystal fibers for dispersion compensation," *Opt. Express*, Vol. 16, 4443–4451, 2008.
7. Hsu, J. M. and G. S. Ye, "Dispersion ultra-strong compensating fiber based on a liquid-filled hybrid structure of dual-concentric core and depressed clad photonic crystal fiber," *J. Opt. Soc. Am. B*, Vol. 29, 2021–2028, 2012.
8. Fujisawa, T., K. Saitoh, K. Wada, and M. Koshiba, "Chromatic dispersion profile optimization of dual-concentric-core photonic crystal fibers for broadband dispersion compensation," *Opt. Express*, Vol. 14, 893–900, 2006.
9. Varshney, S. K., T, Fujisawa, K, Saitoh, and M, Koshiba, "Design and analysis of a broadband dispersion compensating photonic crystal fiber Raman amplifier operating in S-band," *Opt. Express*, Vol. 14, 3528–3540, 2006.
10. Begum, F., Y. Namihira, S. M. A. Razzak, S. Kaijage, N. H. Hai, T. Kinjo, K. Miyagi, and N. Zou, "Novel broadband dispersion compensating photonic crystal fibers: Applications in high-speed transmission systems," *Opt. Laser Technol.*, Vol. 41, 679–686, 2009.
11. Beltrán-Mejía, F., C. M. B. Cordeiro, P. Andrés, and E. Silvestre, "Broadband dispersion compensation using inner cladding modes in photonic crystal fibers," *Opt. Express*, Vol. 20, 3467–3472, 2012.
12. Malitson, I. H., "Interspecimen comparison of the refractive index of fused silica," *J. Opt. Soc. Am.*, Vol. 55, 1205–1209, 1965.

Multi-channel RZ to NRZ Format Conversion Based on a Single Fiber Bragg Grating

Hui Cao[1], **Javid Atai**[2], **Yu Yu**[3], **Qian Dong**[1], **Jun Zuo**[1], **Guo Jie Chen**[1], **and Xuewen Shu**[3]

[1]School of Electronics and Information Engineering, Foshan University, Foshan 528000, China
[2]School of Electrical and Information Engineering, The University of Sydney, NSW, 2006, Australia
[3]Wuhan National Laboratory for Optoelectronics & School of Optoelectronic Science and Engineering
Huazhong University of Science and Technology, Wuhan 430074, China

Abstract— A multi-channel RZ-to-NRZ conversion scheme based on a single custom-designed FBG is proposed. This customized FBG is a comb filter characterized by the multi-channel reflectivity spectra. The spectral response of each channel is customized according to the optical spectra algebraic difference between the NRZ signals and the RZ signals. Simulation results show that four 200 GHz-spaced 40 Gbits/s RZ channels can be converted into NRZ signals with high Q-factor.

1. INTRODUCTION

All-optical RZ to NRZ format conversion schemes fall into two categories, namely time-domain waveform processing and frequency-domain signal spectrum tailoring [1–5]. Generally, the spectrum tailoring based converter is all-passive and very attractive compared with active-operation device [6, 7]. This is due to the advantages such as the simplicity of the structure and stable performance. However, a drawback of these devices is that they need two filters making their structure more complex [7–10].

In this work, we propose a multi-channel RZ-to-NRZ conversion scheme based on a single custom-designed FBG. This customized FBG is a comb filter characterized by the multi-channel reflectivity spectra. The only difference between the channels is their central wavelengths.

2. FBG DESIGN

The spectral response of each channel is customized according to the algebraic difference between the NRZ signals and the RZ signals. This process is described below.

As is well known, the FBG based filtering is a linear process. Thus, it's convenient to analyze the FBG based RZ to NRZ format converter with the theory of linear time-invariant system. Then, the complicated problem of converting random RZ stream to NRZ stream can be reduced to constructing an appropriate transfer function for the FBG filter based on the input spectra of RZ and the output spectra of NRZ.

In Fig. 1, we plot the spectra of RZ, the spectra of NRZ, and their algebraic difference. An interesting feature of Fig. 1 is that, although the optical spectra of the NRZ signals and the RZ signals are not smooth, their algebraic difference is quite smooth and independent of the data carried. This indicates that one can construct a transfer function based on the optical spectra algebraic difference. Since most of the NRZ signal powers are swarmed in the main lobe of the spectra (bandwidth of $|\lambda - \lambda_c| \leq \lambda_c^2/c{\cdot}T_p$) [6–11], it is reasonable to set a uniform attenuation (say, 25-dB) for out of main lobe components, and construct a band-pass filter as the spectral response of each channel. Such a well-designed single-channel spectral response is then shifted and superposed linearly to form the multi-channel reflectivity spectra. Assuming that the FBG is operated in reflection mode, mathematically, the multi-channel reflectivity spectra are written as follows:

$$r_{\mathrm{FBG,dB}}(\lambda) = \sum_{i=1}^{m} r_{i,\mathrm{dB}}(\lambda - \lambda_{c,i}),$$

$$r_{\mathrm{i,dB}}(\lambda - \lambda_{c,i}) = \begin{cases} \max\left(n \cdot \left(\mathrm{FFT}_{\mathrm{dB}}(E_{\mathrm{NRZ}}(t, \lambda_{c,i})) - \mathrm{FFT}_{\mathrm{dB}}(E_{\mathrm{RZ}}(t, \lambda_{c,i}))\right), -25\right), & |\lambda - \lambda_{c,i}| \leq \dfrac{\lambda_{c,i}^2}{c \cdot T_p}, \\ -25, \ |\lambda - \lambda_{c,i}| > \dfrac{\lambda_{c,i}^2}{c \cdot T_p} \end{cases} \quad (1)$$

where $r_{\mathrm{FBG,dB}}(\lambda)$ is the FBG multi-channel reflectivity spectra, $\lambda_{c,i}$ is the ith-channel carrier wavelength, $r_{i,\mathrm{dB}}(\lambda - \lambda_{c,i})$ is the ith-channel reflectivity spectra, m is the channel number of the FBG,

$E_{\mathrm{RZ}}(t, \lambda_{c,i})$ and $E_{\mathrm{NRZ}}(t, \lambda_{c,i})$ are the electric field of the ith-channel RZ signals and NRZ signals, respectively, 25-dB is the inter-channel isolation, T_p is the interval between pulses, c is the velocity of light in vacuum, function $\max(a, b)$ returns the largest component, FFT denotes the fast Fourier transform, and n is the filter order to be optimized according to the Q-factor of the output NRZ signals.

It should be mentioned here that the channel spacing should be chosen according to the signal bit rate. For instance, for the input RZ signals at 40-Gbit/s per channel, the channel spacing should be no less than 80 GHz. Taking into account the crosstalk between adjacent channels as well as the ITU WDM grid, we choose 200 GHz-spaced 4 channels (1546.92 nm, 1548.51 nm, 1550.12 nm, and 1551.72 nm) for the simulations. At the same time, the filter order n is optimized according to the Q-factor of the output NRZ signals, as a results, $n = 2.07$. By properly matching the FBG multi-channel reflection spectra with the spectra of the input multi-channel RZ signals, the customized FBG is well designed and synthesized using discrete layer-peeling algorithm [12].

3. SIMULATION RESULTS AND DISCUSSION

Given the 200 GHz-spaced 4 channels each operating at bit rate of 40-Gbit/s, we simulate the operation of customized FBG based optical filter for multi-channel RZ to NRZ format conversion for a pseudo-random binary sequence (PRBS) of length $2^{31} - 1$ bits. The spectra transformation is shown in Figs. 2(a) and (b). Fig. 2(a) plots the spectra of the input RZ signals before filtering, while Fig. 2(b) presents the spectra of the output NRZ signal after filtering. It is clear that the carriers which are around with strong and periodic spikes in the input RZ spectra can finely pass the FBG, while the sidebands around carriers are suppressed by the FBG. Thus the corresponding NRZ spectra are obtained via the comb filtering introduced by the proposed single FBG. In Fig. 3

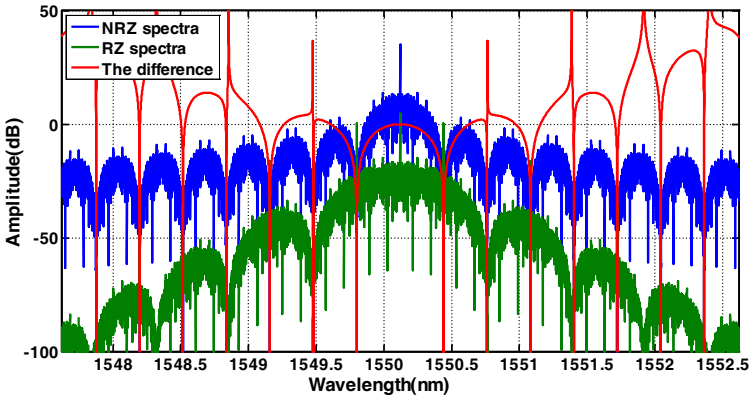

Figure 1: The spectra of the RZ signals with 50% duty cycle (the green line), the NRZ signals with $T_p = 25$ ps, the wavelength of the carrier $\lambda_c = 1550.12$ nm, and $\beta = 0.2$ (the blue line), and their algebraic difference (the ideal transfer function of the first-order filter, the red line).

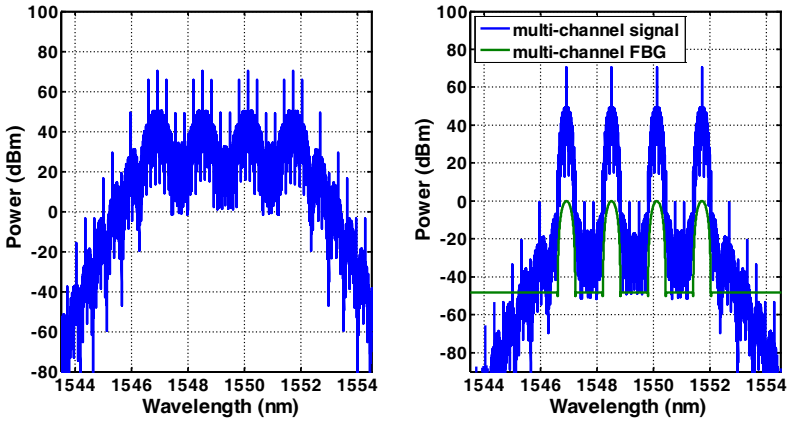

Figure 2: The spectra of (a) the 4-channel, 200 GHz-spaced input RZ signal and (b) the corresponding NRZ output.

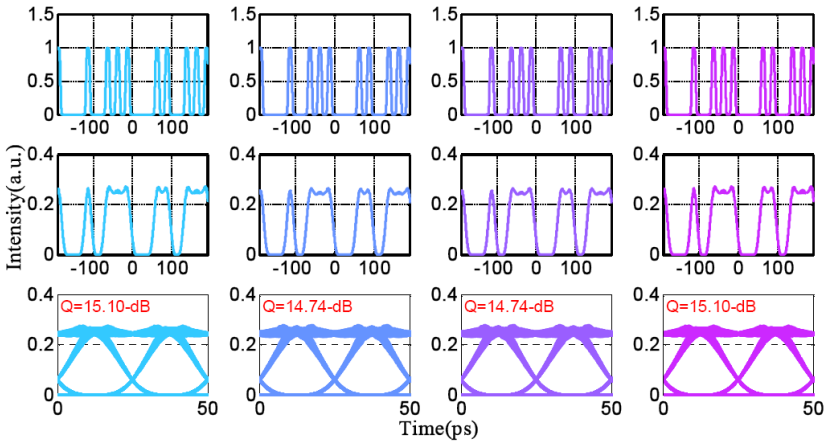

Figure 3: The input RZ waveform (the first row), the waveform and the eye diagrams for the output NRZ signals (the second row and the third row). The first column to the fourth column correspond to the carrier wavelength of 1546.92 nm, 1548.51 nm, 1550.12 nm, and 1551.72 nm, respectively (from left to right).

we plot the input RZ waveform, the waveform and the eye diagrams for the output NRZ signals. From left to right, the columns correspond to channels one to four, respectively. In the third row, the clean and open eye diagrams show that the input 4-channel RZ signals are converted to NRZ signal simultaneously with high Q-factor thanks to the all-passive scheme that introduces hardly any additional noise. The tiny decreasing of Q-factor ($<$ 0.4-dB) in the middle channels is attributed to the residual crosstalk.

4. CONCLUSION

A single FBG based multi-channel RZ to NRZ format conversion has been proposed and simulated. Simulation results show that the customized FBG can convert 4-channel RZ signals to NRZ signals simultaneously with high Q-factor. The proposed single FBG scheme does not require any active components. It is free from any interferometric instability and ASE noise.

ACKNOWLEDGMENT

This research was supported by the National Natural Science Foundation of China (grant 61178030), the Natural Science Foundation of Guangdong Province, China (grant S201101000122), and the Fundamental Research Funds for the Central Universities, China (HUST2013TS047).

REFERENCES

1. Silveira, T., A. Teixeira, G. T. Beleffi, D. Forin, P. Monteiro, H. Furukawa, et al., "All-optical conversion from RZ to NRZ using gain-clamped SOA," *IEEE Photonics Technology Letters*, Vol. 19, 357–359, 2007.
2. Yi, A.-L., L.-S. Yan, B. Luo, W. Pan, J. Ye, Z.-Y. Chen, et al., "Simultaneous all-optical RZ-to-NRZ format conversion for two tributaries in PDM signal using a single section of highly nonlinear fiber," *Optics Express*, Vol. 20, 9890–9896, 2012.
3. Du, J., Y. Dai, G. K. Lei, H. Wei, and C. Shu, "RZ-to-NRZ and NRZ-to-PRZ format conversions using a photonic crystal fiber based Mach-Zehnder interferometer," *Conference on Optical Fiber Communication (OFC), Collocated National Fiber Optic Engineers Conference, (OFC/NFOEC)*, 1–3, 2010.
4. Tang, W., M. Fok, and C. Shu, "20 Gb/s all-optical RZ to NRZ format conversion using frequency-doubling polarization-maintaining fiber loop mirror filter," *Pacific Rim Conference on Lasers and Electro-Optics, CLEO/Pacific Rim*, 1577–1578, 2005.
5. Wang, L., Y. Dai, G. K. Lei, J. Du, and C. Shu, "All-optical RZ-to-NRZ and NRZ-to-PRZ format conversions based on delay-asymmetric nonlinear loop mirror," *IEEE Photonics Technology Letters*, Vol. 23, 368–370, 2011.
6. Xiang, L., D. Gao, B. Zou, S. Hu, and X. Zhang, "Simultaneous multi-channel RZ-OOK/DPSK to NRZ-OOK/DPSK format conversion based on integrated delay interferometers and arrayed-waveguide grating," *Science China Technological Sciences*, Vol. 56, 558–562, 2013.

7. Xiong, M., O. Ozolins, Y. Ding, B. Huang, Y. An, H. Ou, et al., "Simultaneous RZ-OOK to NRZ-OOK and RZ-DPSK to NRZ-DPSK format conversion in a silicon microring resonator," *Optics Express*, Vol. 20, 27263–27272, 2012.
8. Yu, Y., Z. Xinliang, D. Huang, L. Lijun, and F. Wei, "20-Gb/s all-optical format conversions from RZ signals with different duty cycles to NRZ signals," *IEEE Photonics Technology Letters*, Vol. 19, 1027–1029, 2007.
9. Wang, F., E. Xu, Y. Yu, and Y. Zhang, "All-optical 40 Gbit/s data format conversion between RZ and NRZ using a fiber delay interferometer and a single SOA," *SPIE/OSA/IEEE Asia Communications and Photonics*, 83080E-83080E-6, 2011.
10. Yu, Y., X. Zhang, and D. Huang, "Simultaneous all-optical multi-channel RZ and CSRZ to NRZ format conversion," *Optics Communications*, Vol. 284, 129–135, 2011.
11. Ip, E. and J. M. Kahn, "Power spectra of return-to-zero optical signals," *Journal of Lightwave Technology*, Vol. 24, 1610, 2006.
12. Cao, H., J. Atai, X. Shu, and G. Chen, "Direct design of high channel-count fiber Bragg grating filters with low index modulation," *Optics Express*, Vol. 20, 12095–12110, May 21, 2012.

Classification of Chaotic Codes Using Discriminant Analysis Classifiers and Higher Order Statistical Features

Hend A. Elsayed[1] **and Said E. El-Khamy**[2]

[1]Department of Communication and Computer Engineering, Faculty of Engineering
Delta University for Science and Technology, Mansoura, Egypt
[2]Department of Electrical Engineering, Faculty of Engineering
Alexandria University, Alexandria 21544, Egypt

Abstract— This paper investigates the classification of a new type of Pseudo-Random (PN) codes which are generated using noise-like chaotic signals. The classification is made using different discriminant analysis classifiers such as linear, diagonal linear, quadratic, diagonal quadratic, and mahalanobis discriminant analysis classifiers. These classifiers are compared with other classifiers such as neural networks, support vector machines, k-nearest neighbor, and maximum likelihood classifiers. Higher order statistical (HOS) moments and cumulants of the eighth order are used as features. Simulation results illustrates the dependence of the proposed classification method on the type of the used classifier, the type of chaotic map and the initial values used for generating the chaotic code. Two types of one dimensional chaotic maps are considered in this work, namely, the logistic map and the Bended up down map. The performance, considered as the probability of correct decision, is shown to differ according to the type of the used classifier and is dependent on the signal-to-noise ratio. The results show that the quadratic discriminant analysis classifier outperforms the other discriminant analysis classifiers. Also, the performance of two codes generated from one logistic map with two different initial values outperforms the performance of two codes generated from one Bended up down map with two different initial values, two codes generated from logistic map with initial value and Bended up down map with the same initial value, and two codes generated from logistic map with one initial value and Bended up down map with another initial value.

1. INTRODUCTION

Chaotic signals have several properties which make them attractive candidate for communications. They have wideband spectrum, they do not accurately repeat themselves, they have a random-like appearance, and they are relatively simple to be implemented [1]. The mathematical definition of chaos is an unpredictable long time behavior arising in a deterministic dynamical system because of the sensitivity to initial conditions. So, these signals are very sensitive to initial conditions and hence one can generate a large number of codes using the same chaotic map. Chaotic codes are used in a variety of applications in communications such as code-division multiple-access (CDMA).

The discrete chaotic signal is generated by a chaotic map $M(x)$ which is a nonlinear function describing the relation between the previous states and the next state. The general form of m-dimensional chaotic map is defined by Equation (1). where x_n and x_{n+1} are successive iterations of the output x and M is the forward transformation mapping function.

$$x_{n+1} = M(x_n, x_{n-1}, \ldots, x_{n-m}) \tag{1}$$

One dimensional chaotic maps are the simplest form of chaotic maps and the commonly used in communication applications are logistic map, bended up down map, chebyshev map. The general form of the logistic map and bended up down map are defined by Equation (2) in Figure 1 and (3) in Figure 2 respectively.

$$x_{n+1} = \mu x_n(1 - x_n), \quad 0 < x_n < 1 \quad \text{and} \quad 0 < \mu < 4 \tag{2}$$

$$x_{n+1} = \begin{cases} \frac{9x_n}{2x_n+3} & \text{for } 0 \le x_n < \frac{1}{3} \\ \frac{13x_n-3}{3x_n+3} & \text{for } \frac{1}{3} \le x_n < \frac{3}{5} \\ \frac{29x_n-15}{7x_n+3} & \text{for } \frac{3}{5} \le x_n < \frac{9}{11} \\ \frac{99x_n-81}{25x_n-3} & \text{else} \end{cases} \tag{3}$$

The output of chaotic map is quantized to convert to a stream of ones and zeros using threshold level. The optimum threshold is suggested to be the median of the invariant probability density

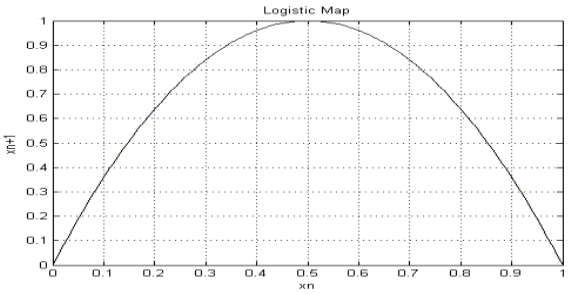

Figure 1: Logistic map.

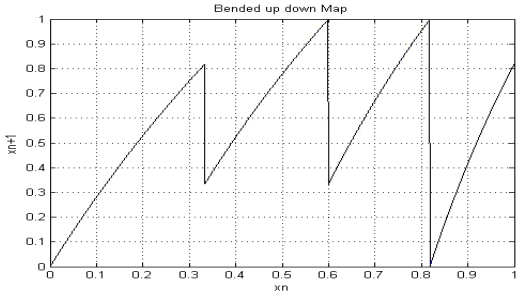

Figure 2: Bended up down map.

function (pdf) of the used chaotic map; the invariant pdf is the histogram of the long generated sequence using any initial conditions, where the invariant pdf is independent of the used initial conditions and hence independent of the generated sequence. Then the threshold of the logistic map and bended up down map is 0.5 and 0.639 respectively [2].

Classification using higher order statistics and linear discriminant analysis classifiers was considered in [3] to classify mental tasks from EEG signals, in [4] to classify digital modulated signals and in [5] to classify electrical power quality signals. Quadratic discriminant analysis classifiers were used to classify electrical power quality signals in [6].

The paper is organized as follows. Section 2 describes features extraction and Section 3 describes the discriminant analysis classifiers. Section 4 shows simulation results. Finally, Section 5 concludes the paper.

2. FEATURES EXTRACTION

In this paper, we used two features for classification and compare its performance with the cases of only two features and only four features are used. These features are the eighth order moment and cumulant of the higher order statistics. Even order moments and cumulants expressions up to eighth order are found in the appendix of [7]. The used features are those which show significant differences between the different chaotic codes.

3. DISCRIMINANT ANALYSIS CLASSIFIERS

We use five discriminant analysis classifiers such as linear discriminant analysis classifier, diagonal linear discriminant analysis classifier, quadratic discriminant analysis classifier, diagonal quadratic discriminant analysis classifier, and mahalanobis discriminant analysis classifier [8] and compare the results with the classifiers used in [7] such as maximum likelihood classifier, k-nearest neighbor classifier, multilayer perceptron neural networks, and support vector machine classifiers.

4. SIMULATION RESULTS

In this section, we evaluate the performance of classification of two codes of chaotic maps using different types of discriminant analysis classifiers and higher order statistics for features extraction. We used four groups of two different codes generated using four chaotic signals. The two codes of the first group are generated using different types of chaotic maps and using the same phase or initial value 0.3, the second two codes are generated using the same one type of chaotic map and using different initial values 0.3 and 0.45, the third two codes are generated using the other type of chaotic map and using different initial values 0.3 and 0.45, and the fourth two codes are generated using two different types of chaotic maps and two different initial values 0.3 and 0.45. The four chaotic signals used in generating these codes are shown in Figure 3. Each signal is

Table 1: The eighth order features for Logistic map with different phase codes.

	Logistic map with 0.3 phase	**Logistic map with 0.45 phase**	**Bended up down map with 0.3 phase**	**Bended up down map with 0.45 phase**
M8	−243.8503	−243.4009	−243.2175	−243.9946
C8	1.0025	1.0101	1.0132	1.0001

chosen to have 150 realizations and 4096 samples (1 second). They are then divided into 100 realizations for training and 50 realizations for testing data sets. White Gaussian noise is added to these signals and features are extracted using eight order moment and cumulant using equations in [7]. The two features used are M8 and C8 and are shown in Table 1 under the constraints of zero mean, unit variance and noise free. This method is compared with classifiers in [7]. The performance considered is the probability of correct decision. using Figure 4, Figure 5, Figure 6, and Figure 7 show the performance using maximum likelihood classifier, nearest neighbor classifier for $k = 3$, multilayer perceptron neural network with MSE is taken to be 10-6, and support vector machine classifier. Figure 8, Figure 9, Figure 10, Figure 11, and Figure 12 show the performance using linear discriminant analysis classifier, diagonal linear discriminant analysis classifier, quadratic discriminant analysis classifier, diagonal quadratic discriminant analysis classifier, and mahalanobis discriminant analysis classifier. The comparison between different discriminant analysis classifiers are shown in Figure 13. From Figure 13, we note the performance of quadratic discriminant analysis classifier is the best and compare the performance of this with the classifiers used in [7] as shown in Figure 14.

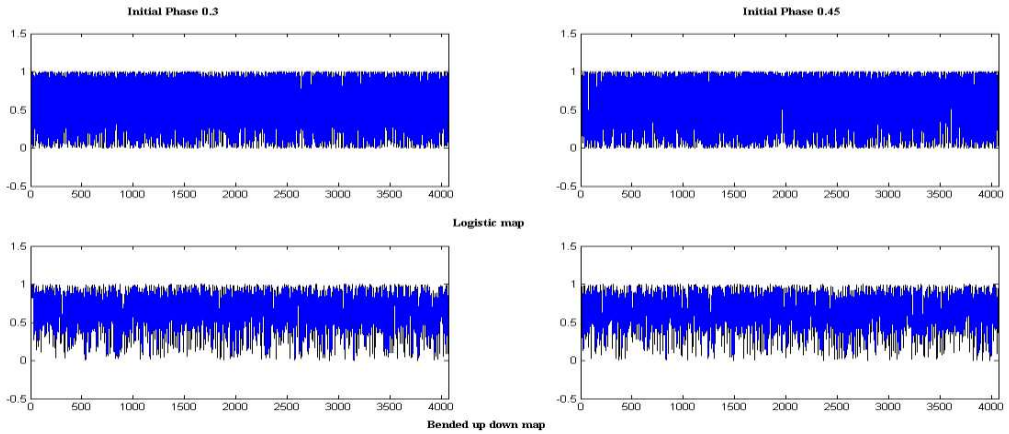

Figure 3: The considered four chaotic signals.

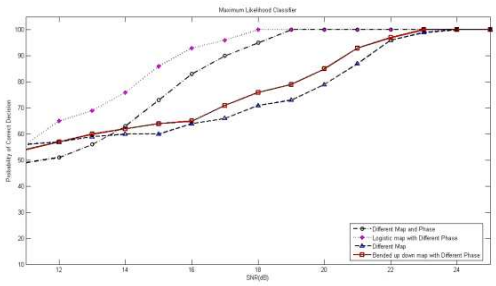

Figure 4: The Performance using ML classifier.

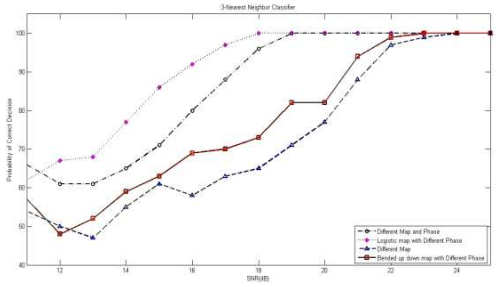

Figure 5: The Performance using 3NN classifier.

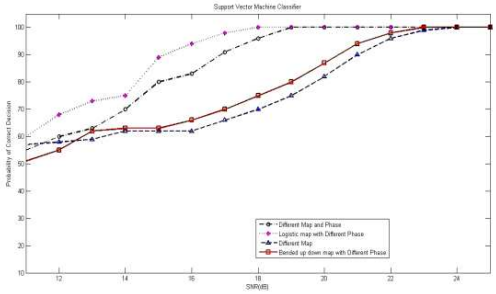

Figure 6: The Performance using NN classifier.

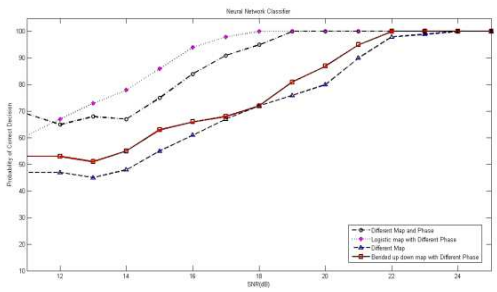

Figure 7: The Performance using SVM classifier.

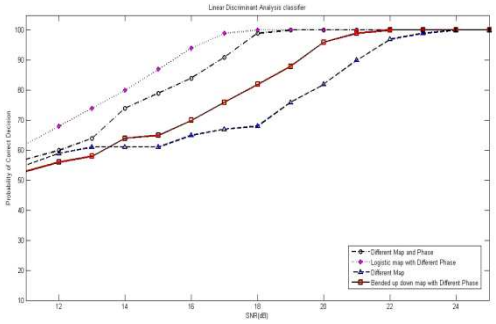

Figure 8: The Performance using LDA classifier.

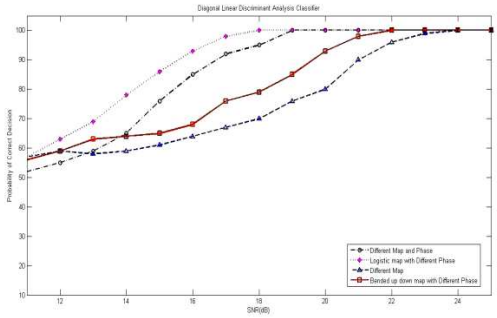

Figure 9: The Performance using diagonal LDA classifier.

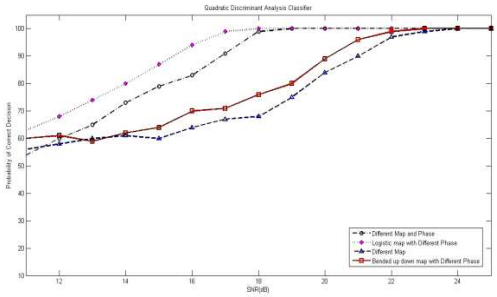

Figure 10: The Performance using QDA classifier.

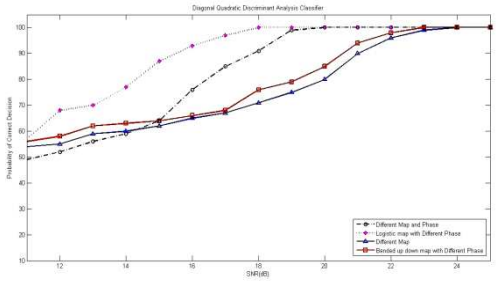

Figure 11: The Performance using diagonal QDA classifier.

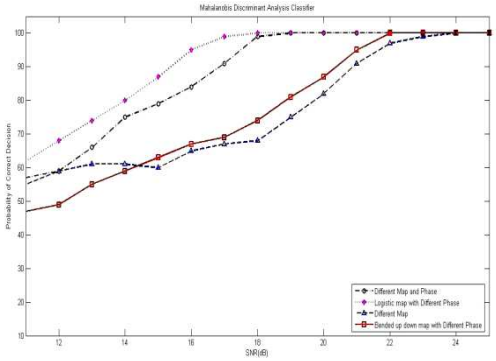

Figure 12: The Performance using Mahalanobis DA classifier.

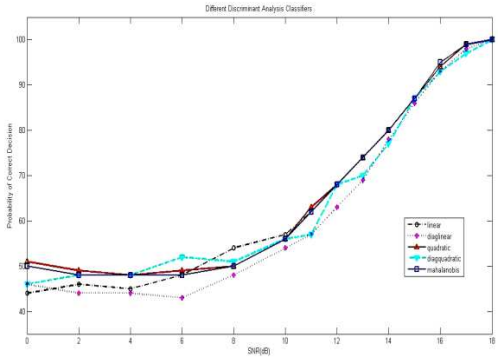

Figure 13: The Performance using different DA classifier.

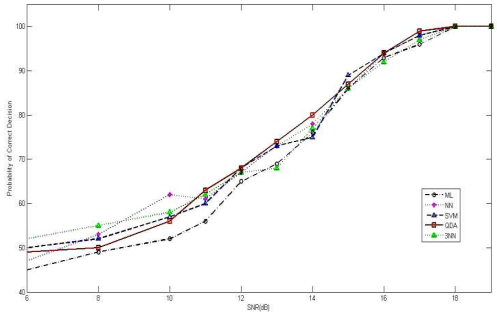

Figure 14: The Performance using different classifiers.

5. CONCLUSION

In this paper, we presented classification of chaotic codes using different classifiers and using eighth orders moment and cumulant as features. We have shown the dependence of the performance on the type of the used classifier, the type of the discriminant analysis classifiers, the type of chaotic maps, the initial values used for generating the chaotic code, and the signal-to-noise ratio.

REFERENCES

1. El-Khamy, S. E., "New trends in wireless multimedia communications based on chaos and fractals," *Proceedings of the 21st National Radio Science Conference, NRSC'2005*, Cairo, Egypt, 2004.
2. Gad, M. M., "Optimization of chaotic spreading codes for spread spectrum cdma communication systems," Master Thesis, Supervised by S. E. El-Khamy and S. E. Shaaban, Faculty of Engineering, Alexandria University, Egypt, 2005.
3. Zhou, S. M., J. Q. Gan, and F. Sepulveda, "Classifying mental tasks based on features of higher-order statistics from EEG signals in brain–computer interface," *Information Sciences*, 178, 1629–1640, 2008.
4. Ghauri, S. A. and I. M. Qureshi "Automatic classification of digital modulated signals using linear discriminant analysis on AWGN channel," *1st International Conference on Information and Communication Technology Trends (ICICTT)*, 2–5, Sep. 2013.
5. Palomares-Salas, J. C., J. J. G. De la Rosa, A. A. Perez, and A. M. Munoz, "Intelligent methods for characterization of electrical power quality signals using higher order statistical features," *Przeglad Elektrotechniczny (Electrical Review)*, ISSN 0033-2097, R. 88 NR 8, 2012.
6. Gerek, O. N. and D. G. Ece, "Power-quality event analysis using higher order cumulants and quadratic classifiers," *IEEE Transactions on Power Delivery*, Vol. 21, No. 2, 883–889, 2006.
7. El-Khamy, S. E., H. A. Elsayed, and M. R. Rizk, "Classification of multi-user chirp modulation signals using higher order cumulant features and four types of classifiers," *28th National Radio Conference (NRSC'2011)*, Cairo, Egypt, Apr. 26–28, 2011.
8. McLachlan, G. J., *Discriminant Analysis and Statistical Pattern Recognition*, John Wiley and Sons, New York, 1992.

Novel Optical Fast Random Number Generators Based on Integer Domain Chaotic Iterations

Qianxue Wang[1], **Simin Yu**[1], **and Xiaole Fang**[2]

[1]College of Automation, Guangdong University of Technology, China
[2]Land and Resources Technology Center of Guangdong Province, China

Abstract— For cryptography and secure communications, it is very prerequisite that the random number generator (RNG) is based on non-deterministic physical mechanisms, extremely fast generator and robustness to noise are required. In this work, we present novel fast optoelectronic architecture RNGs based on integer domain chaotic iteration (IDCI), with a chaotic semiconductor laser, having time-delayed self-feedback. The solution stems from some well-defined discrete chaotic iterations that satisfy the reputed Devaney's definition of chaos, namely the integer domain chaotic iterations technique, improve the statistical properties of this RNG. Using standard criteria named NIST and DieHARD (famous batteries of tests), the randomness of the output sequences is verified.

1. INTRODUCTION

Due to the rapid development of the Internet in recent years, the discovery of fast random number generator (RNG) with a strong level of security is thus becoming a hot topic, because numerous cryptosystems and data hiding schemes are directly dependent on the quality of these generators. Considerable improvements for the rate of chaotic random bits generator have been however reached by using a semi-conductor laser in the presence of external feedback [11], a well known setup in chaotic optical systems.

However, according to the analysis of [7], correct sampling method and using Most Significant Bits (MSB) is a key factor to preserve the deterministic origin in the generator of random streams using optoelectronic chaotic lasers. However if the sequence keeps the most large part of information on the signal, its statistical performance might be not good. Integer domain chaotic iteration has been proved not only to assign discrete chaotic properties to the output streams (if the input source is truly unpredictable random), but also to improve the statistical properties of various defectives PRNGs [2]. Thus we think interesting to regard weather this approach can work too for chaotic laser based pseudorandom generator.

In this paper, the study of using broadband optical signal to generate random binary sequence according to the method proposed in [7], is going to be deepen. We propose to apply the same method on the chaotic waveform generated by broadband photonic oscillations with or without integer domain chaotic iterations, and to analyze the differences.

2. SETUP FOR THE CHAOTIC LASER

Indeed, as shown in Fig. 1, the chaotic laser signal considered in this paper is similar to the one described in [7], except that there is no output signal for photonic noise. This physical source of entropy presents a very strong determinism. The output chaos signal is generated by a nonlinear dual delay differential equation implemented in an optoelectronic and electro-optic feedback loop.

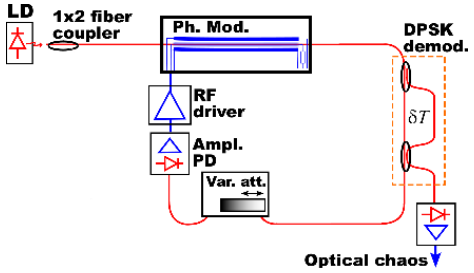

Figure 1: Chaotic laser signal setup.

3. XOR IDCI

In this section, we first introduce the basic concept of IDCI. Let $N \in \{1, 2, \ldots\}$ be a positive integer, $\mathbb{B} = \{1, 0\}$ denotes the set of binary numbers, while $\mathbb{B}^N$ is the set of binary vectors of size N. The integer $x^n \in \{0, 1, 2, \ldots, 2^N - 1\}$, $n = 0, 1, 2, \ldots$ is represented using N bits in base-2: $x^0 = (x^0_{N-1} x^0_{N-2} \ldots x^0_0) \in \mathbb{B}^N$ is the initial condition, while $x^{n-1} = (x^{n-1}_{N-1} x^{n-1}_{N-2} \ldots x^{n-1}_0) \in \mathbb{B}^N$ and $x^n = (x^n_{N-1} x^n_{N-2} \ldots x^n_0) \in \mathbb{B}^N$ denote the $n-1$-th and n-th iteration respectively. In IDCI systems, the iterative equation is defined as follows:

$$x^n_i = \begin{cases} x^{n-1}_i & \text{if} \quad i \neq s^n \\ (f(x^{n-1}))_i & \text{if} \quad i = s^n, \end{cases} \tag{1}$$

where $i = 0, 1, 2, \ldots, N-1$, $n = 1, 2, \ldots$, and $s = (s^1 s^2 \ldots s^n \ldots)$ is an one-sided infinite sequence of integers bounded by $N-1$: $\forall n \in \mathbb{N}^*$, $s^n \in \{0, 1, 2, \ldots, N-1\}$. Additionally, the iterate function f is usually the vectorial Boolean negation, given by $f(x^{n-1}) = (\overline{x^{n-1}_{N-1}} \overline{x^{n-1}_{N-2}} \ldots \overline{x^{n-1}_i} \ldots \overline{x^{n-1}_0})$, and the following notation is used: $(f(x^{n-1}))_{i=s^n} = (\overline{x^{n-1}_{N-1}}\ \overline{x^{n-1}_{N-2}} \ldots \overline{x^{n-1}_i} \ldots \overline{x^{n-1}_0})_{i=s^n} = \overline{x^{n-1}_{i=s^n}}$, that is, $(f(x^{n-1}))_{i=s^n}$ is the i-th component of $f(x^{n-1})$. Let us finally remark that, in IDCI, the one-sided infinite sequence of integers $s = (s^1 s^2 \ldots s^n \ldots)$ is usually named a chaotic strategy.

Secondly, XOR IDCI is one of the IDCIs, instead of updating only one component at each iteration a subset of components are updated together, which is introduced in [1]. Comparing with the other IDCIs, XOR IDCI is much more compatible in physical design. Here the updating function is chosen as the vectorial negation, the iterative equation can be rewritten as:

$$x^n = x^{n-1} \oplus s^n \tag{2}$$

where x^n and x^{n-1} are integers, which are represented in binary form as $x^n = (x^n_{N-1} x^n_{N-2} \ldots x^n_0) \in \mathbb{B}^N$ and $x^{n-1} = (x^{n-1}_{N-1} x^{n-1}_{N-2} \ldots x^{n-1}_0) \in \mathbb{B}^N$ and $s = (s^1 s^2 \ldots s^n \ldots)$ is an one-sided infinite sequence of integers bounded by $N-1$: $\forall n \in \mathbb{N}^*$, $s^n \in \{0, 1, 2, \ldots, N-1\}$.

Select $N = 4$, chaotic waveforms obtained by simulation as shown in Fig. 2(a). Fig. 2(b) shows the intensity map for $N = 4$. In order to appear random, the histogram should be uniformly distributed in all areas. It can be observed that a uniform histogram and a flat color intensity map are obtained when using XOR IDCI.

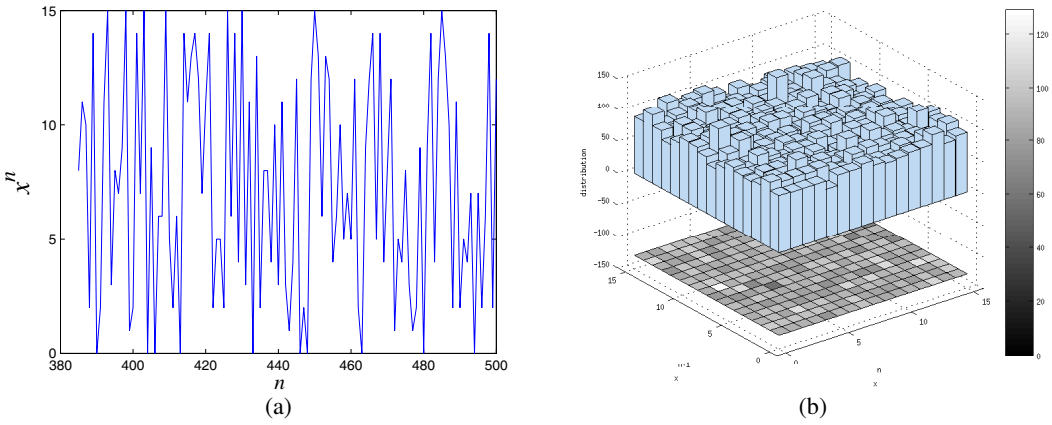

Figure 2: Chaotic waveforms and histogram of XOR IDCI for $N = 4$. (a) Chaotic waveforms. (b) Histogram.

The single basic component presented in Equation (2) is of ordinary use as a good elementary brick in various PRNGs, it corresponds to the discrete dynamical system in chaotic iterations.

4. RNG APPROACHES BY APPLYING IDCI METHOD TO CHAOTIC LASER

4.1. Devaney's Chaos Property

Generally speaking, the quality of a RNG depends, to a large extent, on the following criteria: randomness, uniformity, independence, storage efficiency. A chaotic sequence may satisfy these requirements and also other chaotic properties, as ergodicity, entropy, and expansivity. A chaotic

sequence is extremely sensitive to the initial conditions. That is, even a minute difference in the initial state of the system can lead to enormous differences in the final state, even over fairly small timescales. Therefore, chaotic sequence fits the requirements of (or pseudo-)random sequence well. However, despite a large number of papers published in the field of chaos-based generators, the impact of this research is rather marginal. This is due to the following reasons: almost all PRNG/RNG algorithms using chaos are based on dynamical systems defined on continuous sets (e.g., the set of real numbers). So these generators are usually slow, requiring considerably more storage space, and lose their chaotic properties during computations as mentioned earlier in this paper. These major problems restrict their use as generators [8]. For RNG approaches by applying IDCI method to chaotic laser, we do not simply integrate chaotic maps hoping that the implemented algorithm remains chaotic. Indeed, the IDCI method we used here is just discrete chaotic iterations and have been proven in [1] that these iterations produce a topological chaos as defined by Devaney: they are regular, transitive, and sensitive to initial conditions. This famous definition of a chaotic behavior for a dynamical system implies unpredictability, mixture, sensitivity, and uniform repartition. Moreover, as only integers are manipulated in discrete chaotic iterations, the chaotic behavior of the system is preserved during computations, and these computations are fast. For the approaches listed in this section, XOR IDCI method is applied because of its easy adoptable algorithm.

4.2. Approach 1: Improve the Performance of Randomness via IDCI

To improve the optical RNGs, as shown in Fig. 3. XOR IDCI is used.

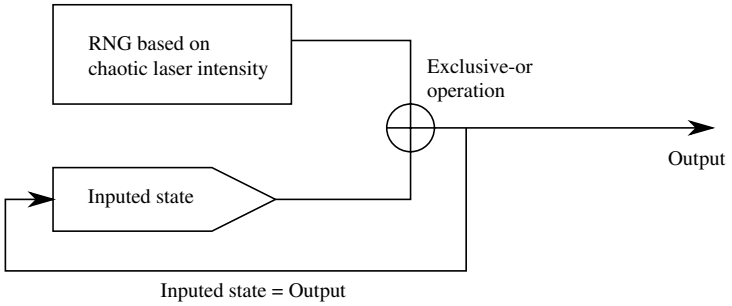

Figure 3: The XOR IDCI scheme applied to optical RNG.

Here, RNG introduced in [3, 4] is used to demonstrated. Firstly, our chaotic laser intensity is undersampled at rate clock 2.5 GHz; Then three times difference of nearest neighbor points (in [3, 4], it is named "derivative") are computed for all obtained values; At last, the 8 LSBs of each difference value are collected to build as a random sequence. To apply the XOR IDCI, the initial state will be randomly set as an 8-bits value, every 8 LSBs built out from the generator are then exclusive-or with the state value as Fig. 3, its output is appended as random sequence and also feedback as new state value.

For verifying the improvement of XOR IDCI, the output sequence (10^8 bits) with and without XOR IDCI are tested by NIST and DieHARD battery suite, which are famous statistical standard tests for RNGs [6, 9]. After XOR IDCI merged, the NIST suite are successfully passed all, and passing rate of DieHARD suite are improved from 11/18 to 15/18.

4.3. Approach 2: Chaotic Laser Sample Data with Multiple IDCI

In this section, firstly, the RNG with IDCI methods stratifies the Devaney's chaos property, a brief description is given; Then the method that XOR IDCI used to improve the RNGs based on chaotic laser is introduced; At last a new scheme based on XOR IDCI to generate random numbers with chaotic laser intensity is depicted, which is able to reach 320 GHz generator speed and very good robustness to external perturbations.

Table 1: The passing rate for different n of IDCIORNG in NIST and DieHARD tests.

Tests \ n	1	10	20	30	40
NIST suite	0/15	14/15	15/15	15/15	15/15
DieHARD suite	1/18	11/18	14/18	18/18	18/18

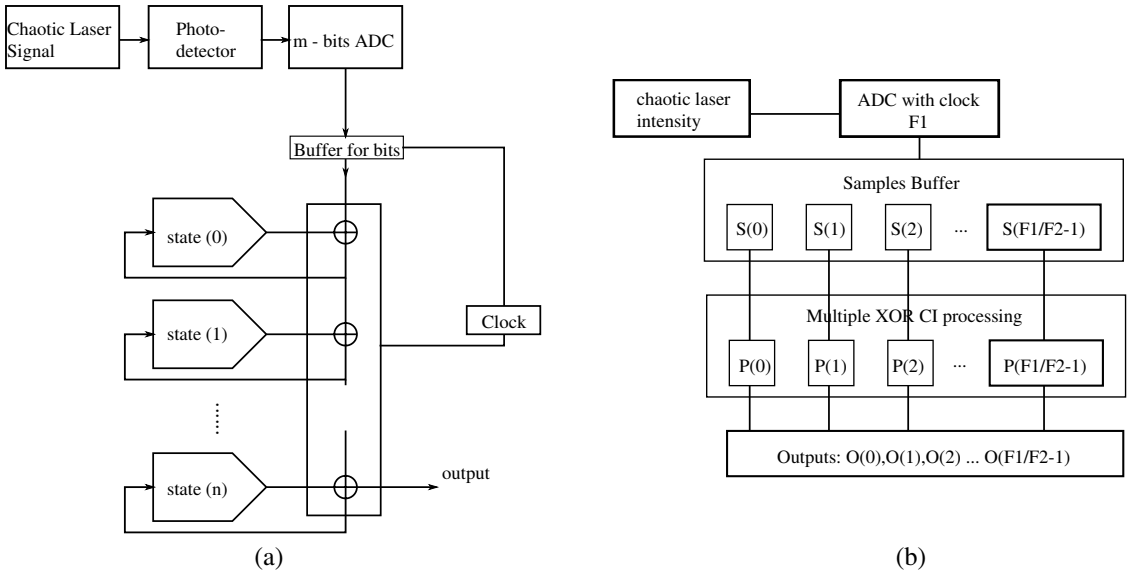

Figure 4: Experimental setup of the optical system used to generated signal as physical random sources for random bit sequences. (a) Multiple XOR IDCI. (b) Parallel processing to IDCIRNG.

For achieve good randomness, a multiple mode of XOR IDCI is used, as shown in Fig. 4(a), n state values and XOR IDCI iteration have been used, every state value will be randomly initialed as an m-bits integer for respective to the buffer. In our experiments, the chaos laser intensity are undersampled at 8-bit 40 GHz rate, and initial state are set as 8-bit, hence the undersampling frequency 40 GHz $\times$ 8 bits = 320 Gbitps is achieved. Here we named such generator IDCIORNG (chaotic iteration optical random number generator).

To test the randomness of the IDCIORNG, 10^8 bits output sequence are tested by NIST and DieHARD test suite, $n = 1, 10, 20, 30$, and 40 are used for IDCIORNG in tests to make a comparison. The passing rates of the test results are shown in Table 1, it is not difficult to find out increasing the n, the XOR IDCI processing, can improve the statistical performance. When $n \geq 30$, all test suited are able to be successfully passed.

4.4. Approach 3: Parallel Processing to IDCIRNG Based on Chaotic Laser

In Approach 2, random stream generator might be related to two elements: Firstly, in 40 GHz sampling frequency, the correlations between neighbor sampled values are very small; Secondly, the chaotic iterations are rearranging the distribution of the sample values. If we increase the sampling frequency, the correlation between two adjacent samples are correspondingly increased, and that leads random number generator impossible. To solving this problem, a parallel architecture would be applied.

Firstly assuming that the chaotic laser signal with bandwidth F_0 has been sampled by very huge frequency F_1, which $F_1 \gg 2 \times F_0$, that means such sample are designed to follow the classical Shannon sampling theorem (The Shannon sampling theorem indeed states that a limited bandwidth signal can be digitized without loss of information, when the sampling frequency is at least twice the maximum signal frequency); Secondly, frequency F_2 is known to be small enough to break the correlations between nearest samples, we divided the samples into F_1/F_2 parts and F_1/F_2 multiple XOR IDCI processes are prepared, the first F_1/F_2 samples are arranged as $S_0, S_1, S_2, \ldots, S_{(F_1/F_2)-1}$ then put into their corresponding processes, then $S_{F_1/F_2}, S_{(F_1/F_2)+1}, \ldots, S_{2(F_1/F_2)-1}$ for the second ones and so on; At last, the output from the processes are collected as random sequence. The procedure is shown in Fig. 4(b), the speed of such generator is extremely fast, we define in ADC we use n-bit sampling length, then the produce rate can reach $n/timeF_1$ in theory.

The standard statistical tests: NIST and DieHARD suites are applied here to verify the approach 3. An chaotic laser signal data are stimulated in computer with the method from [5], its frequency is $F_1 = 4000$ GHz, and corresponding parameters is listed as:

- **Time delay**: Set as 60 ns;
- **High Frequency Cut-off**: 13 ps;
- **Ratio between high and low frequency cut-off**: 5×10^{-5};

- **Type of nonlinear transformation**: square of Sine;
- **Highest complexity chaotic regime**: 5.

Here the states in XOR IDCI processing are set as 32-bits words, which are generated from XOR-shift, which are designed by George Marsaglia [10], and each process provide 30 times iterations. Then three random sequence are generated by:

- **Sequence1**: By approach 2, every data are quantized by 8-bits, it can achieve $8 \times 4000 = 3.2/times10^4$ GHz;
- **Sequence2**: By approach 3, every data are quantized by 8-bits, $F_2 = 40$ GHz, then there are $4000/40 = 100$ XOR IDCI processes, it can achieve $8 \times 4000 = 3.2 \times 10^4$ GHz;
- **Sequence3**: By approach 3, every data are quantized by 1-bits, $F_2 = 40$ GHz, it can achieve 4000 GHz.

And the passing rate of the tests are shown in Table 2, Sequence1 generated by approach 2 are really bad in randomness as we predict. For NIST, the Sequence2 and Sequence3 are both fluently pass them all, but for DieHARD, Sequence2 is able to pass, and Sequence 3 fail 3 subjects.

Table 2: The passing rate of NIST and DieHARD.

Sequence / **Tests**	Sequence1	Sequence2	Sequence3
NIST suite	1/15	15/15	15/15
DieHARD suite	3/18	18/18	15/18

5. CONCLUSION

Three examples of mixing IDCI and MSB of optoelectronic chaotic signal are given, the results of NIST and DieHARD test suite show the improvements of randomness, in future, the practical implementation is looking forwarded.

ACKNOWLEDGMENT

This work was supported by the National Natural Science Foundation of China under Grant 61172023; by the Specialized Research Foundation of Doctoral Subjects of Chinese Education Ministry under Grant 20114420110003; and by China Postdoctoral Science Foundation No. 2014M552175.

REFERENCES

1. Bahi, J., R. Couturier, C. Guyeux, and P.-C. Héam, "Efficient and cryptographically secure generation of chaotic pseudorandom numbers on gpu," *CoRR*, abs/1112.5239, 2011.
2. Bahi, J., X. L. Fang, C. Guyeux, and Q. X. Wang, "Suitability of chaotic iterations schemes using xorshift for security applications," *Journal of Network and Computer Applications*, Vol. 37, 282–292, 2014.
3. Kanter I., et al., "An optical ultrafast random bit generator," *Nature Photonics*, Vol. 4, No. 1, 58–61, 2010.
4. Reidler, I., et al., "Ultrahigh-speed random nuber generation based on a chaotic semiconductor laser," *Physical Review Letters*, Vol. 103, No. 2, 24–28, Jul. 2009.
5. Michael, P., et al., "Routes to chaos and multiple time scale dynamics in broadband bandpass nonlinear delay electro-optic oscillators," *Phys. Rev. E*, Vol. 79, 026208, Feb. 2009.
6. Andrew, R., et al., "A statistical test suite for random and pseudorandom number generators for cryptographic applications," 2001.
7. Fang, X. L., et al., "Noise and chaos contributions in fast random bit sequence generated from broadband optoelectronic entropy sources," *IEEE Trans. Circ. Syst. I*, Vol. 61, No. 3, 888–901, Mar. 2014.
8. Kocarev, L., "Chaos-based cryptography: A brief overview," *IEEE Trans. Circ. Syst. Mag.*, Vol. 7, 6–21, 2001.
9. Marsaglia, G., "Diehard battery of tests of randomness," Florida State University, 1995.
10. Marsaglia, G., "Xorshift rngs," *Journal of Statistical Software*, Vol. 8, No. 14, 1–6, 2003.
11. Mukai, T. and K. Otsuka, "New route to optical chaos: Successive-subharmonic-oscil-lation cascade in a semiconductor laser coupled to an external cavity," *Physical Review Letters*, Vol. 55, No. 17, 17–11, 1985.

Modification of Simplified Modal Method for Subwavelength Triangular Grating with Very High Efficiency

Bin Wang[1, 2], **Yihui Wu**[1], **Peng Hao**[1], **and Wenchao Zhou**[1, 2]

[1]State Key Laboratory of Applied Optics, Changchun Institute of Optics, Fine Mechanics and Physics
Chinese Academy of Sciences, Changchun 130033, China
[2]University of Chinese Academy of Sciences, Beijing 100039, China

Abstract— A modification of simplified modal method (MSMM) is presented to calculate the transmission efficiencies of subwavelength fused-silica grating. In order to consider the reflection of grating, which is neglected in simplified modal method (SMM). Then the grating region is divided into N thin planer grating slabs and regarded as multilayer films. Then the reflectance is characterized by the effective admittances of air and grating which are complete characteristic of multilayer films. This proposes a manner of reducing the reflection loss of dielectric grating. By analyzing the effective index and admittance of grating, we designed a triangular fused-silica grating with more than 99.9% diffraction efficiency for both TE and TM-polarization. This method offers a clear physical insight of diffraction characteristic: a deep-etched grating would get a high efficiency when the average difference of its mode indices is odd times of π and the admittance of the grating is approximate to that of air. Due to tiny deviation between this method and RCWA, MSMM can be used to design and optimize fused-silica gratings directly. It is better than SMM which only gives starting value of grating parameters. Contrast to RCWA, the starting parameters values of subwavelength dielectric grating can be predicted by the formulas in MSMM when the transmission efficiency is known. However, the starting values are got by cut-and-try procedure in RCWA.

1. INTRODUCTION

Dielectric gratings with high damage threshold are important elements in the pulse compressors in high power laser systems [1, 2]. In these devices, a high efficiency for the dispersive -1st order is usually required. Calculated by rigorous coupled wave analysis (RCWA) [3–5], a triangular dielectric grating can get efficiency 99% for TE polarization [3]. But we can't know the physical mechanism that a dielectric grating with designated parameters can get a high efficiency when grating was designed by RCWA. Recently, Clausnitzer et al. introduced the simplified modal method (SMM) [6, 7], which analyzes the transmission efficiency by the phase shift of different modes, to explain the diffraction in deep-etched dielectric grating. This provides a new method for designing highly-efficient grating. But the reflection is neglected in SMM, thus the diffraction efficiency of a real grating is always less than the predicted result. Fresnel reflection at interfaces is introduced into SMM by a symmetrical embedded grating and a 99.9% efficient grating was designed for TE polarization [8]. Sun et al. proposed multireflection modal method (MRMM) [9] by introducing multiple Fresnel reflection into SMM. An enhanced simplified modal method (ESMM), considering the reflection of modes, was presented by Jing et al. [10]. But these methods only discussed the TE-polarized illumination. Actually, TM-polarized light is different with TE-polarized light. It is impossible to deflect both TE and TM-polarized light to -1st order with 100%-efficiency for a rectangular grating [8].

In this paper, a modification of simplified modal method (MSMM) is presented to calculate the transmission efficiencies of subwavelength dielectric grating. The total reflection of a grating is characterized by the effective admittances of air and grating. The admittance of triangular grating is analyzed to decide when a triangular grating with some particular parameters will get a low reflection. Together with the average difference of mode indices fulfilling a certain condition, a grating with efficiency more than 99.9% for both TE and TM-polarized light is designed.

2. MODIFICATION OF SIMPLIFIED MODAL METHOD

For a rectangular grating, the effective index n_{eff}^m is given by the dispersion equation [11]:

$$\cos(\alpha d) = \cos(\beta b)\cos(\gamma g) - \frac{\beta^2 + \tau^2\gamma^2}{2\tau\beta\gamma}\sin(\beta b)\sin(\gamma g) \tag{1}$$

where $\alpha = k_0 \sin\theta_{in}$, $\beta = k_0\sqrt{n_b^2 - n_{eff}^2}$, $\gamma = k_0\sqrt{n_g^2 - n_{eff}^2}$, $\tau = n_b^2$ for TM polarization or 1 for TE polarization, b and g are the width of the grating ridge and groove respectively, n_b and n_g are the corresponding refractive indices. For a dielectric grating with depth h, approximated by a stack of lamellar gratings and neglecting the reflection, the -1st and 0th transmission efficiencies could be approximated as [12]:

$$\eta_{-1T} = \sin^2\left(\frac{k_0 h \Delta\overline{n}_{eff}}{2}\right) \tag{2a}$$

$$\eta_{0T} = \cos^2\left(\frac{k_0 h \Delta\overline{n}_{eff}}{2}\right) \tag{2b}$$

where $\Delta\overline{n}_{eff} = \sum_m (n_{0eff}^m - n_{0eff}^m)h_m/h$ is the average difference of mode effective indices, h_m is the depth of mth layer, n_{0eff}^m and n_{1eff}^m are the corresponding effective indices of mode 0 and mode 1.

For neglecting reflection of the grating, there exit deviations between the efficiencies calculated by RCWA and those calculated by Eq. (2). Now we consider a grating with period p and wavelength λ. And the incidence angle is the first Bragg angle $\theta = \arcsin[\lambda/(2n_g p)]$. In the next analysis, the grating region is divided into N thin planer grating slabs as shown in Fig. 1(a).

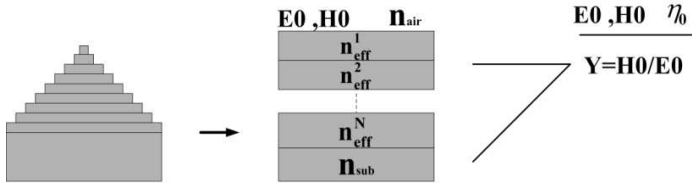

Figure 1: (a) The division of triangular grating; (b) slabs are regarded as multilayer films; (c) equivalent interface of the multilayer films.

Based on the optical thin film theory [13], the characteristic matrix of this N layer structure is:

$$\begin{bmatrix} B \\ C \end{bmatrix} = \left\{ \prod_{m=1}^{N} \begin{bmatrix} \cos\delta_m & \frac{i}{\eta_m}\sin\delta_m \\ i\eta_m \sin\delta_m & \cos\delta_m \end{bmatrix} \right\} \begin{bmatrix} 1 \\ \eta_{sub} \end{bmatrix} \tag{3}$$

where $\delta_m = 2\pi h n_{eff}^m/(N\lambda)$ is the phase shift of mth layer, $\eta_0 = n_g \cos\theta$, $\eta_m = n_{eff}^m$, $\eta_{sub} = n_{sub}$ for TE-polarization and $\eta_0 = n_g/\cos\theta$, $\eta_m = [(n_{eff}^m)^2 + n_g^2 \sin^2\theta]/n_{eff}^m$, $\eta_{sub} = n_b^2/n_{sub}$ for TM-polarization, $n_{sub} = (n_b^2 - n_g^2 \sin^2\theta)^{1/2}$ is the effective index of the substrate. Then the optical admittance of the grating is $Y = H_0/E_0 = C/B$, and the reflectance can be calculated by:

$$R = \left(\frac{\eta_0 - Y}{\eta_0 + Y}\right)\left(\frac{\eta_0 - Y}{\eta_0 + Y}\right)^* \tag{4}$$

If the grating period fulfills the condition $\lambda/2 < p < 3\lambda/(2n_b)$ and the incidence is first Bragg angle, there are only two transmitted modes in grating region and each of them carries nearly half of the energy of the incident wave [14]. Thus the -1st and 0th transmission efficiency formulas could be modified as:

$$\eta_{-1T} = \left(1 - \frac{R_0}{2} - \frac{R_1}{2}\right)\sin^2\left(\frac{k_0 h \Delta\overline{n}_{eff}}{2}\right) \tag{5a}$$

$$\eta_{0T} = \left(1 - \frac{R_0}{2} - \frac{R_1}{2}\right)\cos^2\left(\frac{k_0 h \Delta\overline{n}_{eff}}{2}\right) \tag{5b}$$

where R_0 and R_1 are the corresponding transmission of mode 0 and mode 1.

To illustrate the accuracy of this modification of simplified modal method (MSMM), the transmission efficiencies of -1st and 0th orders are plotted versus the triangular depth in Fig. 2. we assume that $n_b = 1.45$, $n_g = 1$ and the incidence is first Bragg angle.

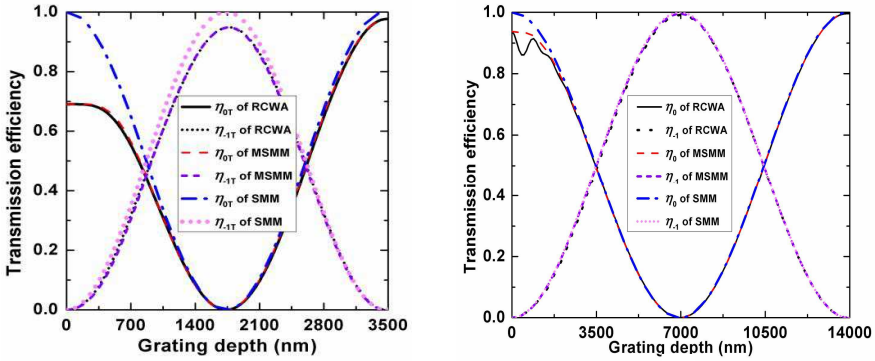

Figure 2: Transmission efficiencies of a triangular grating calculated by MSMM, SMM and RCWA respectively versus the grating depth, with the period $p = 560\,\text{nm}$ and the incident wavelength $\lambda = 1064\,\text{nm}$. (a) TE-polarization; (b) TM-polarization.

According to Fig. 2, we can conlude that MSMM makes a better result than SMM. The biggest deviation between MSMM and RCWA are 2% for TE-polarization and 5% for TM-polarization. The fine approximation is in that the admittance Y is a complete characteristic of multilayer films, which includes all information of grating layer and the substrate. The little deviation may be due to the evanescent modes and little difference of energy between mode 0 and mode 1 which is considered equal in Eq. (5).

3. DESIGN OF HIGHLY-EFFICIENT GRATING

The guideline for design of a subwavelength highly-efficient grating for both TE and TM-polarization [15] is:

$$\Delta\overline{n}_{eff\_TE}/\Delta\overline{n}_{eff\_TM} = (2l-1)/(2m-1) \tag{6}$$

where l and m are integers. Fig. 3 shows the average difference of mode effective indices as defined in Eq. (2). The triangular grating is divided into a stack of 100 layers with equal depth. As in shown, for $\lambda = 1064\,\text{nm}$ and $n_b = 1.45$, the period $p = 546\,\text{nm}$ fulfills Eq. (6) with $l = 2$, $m = -1$ and period $p = 747\,\text{nm}$ with $l = 2$ and $m = 1$.

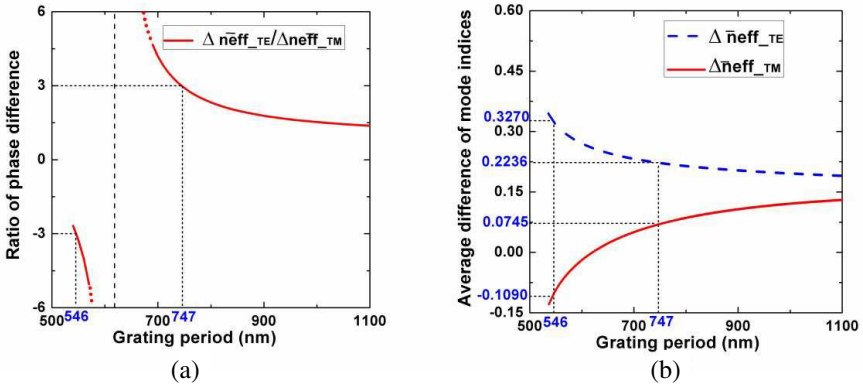

Figure 3: Ratio of accumulated phase difference for TE-polarization to that for TM-polarization and average difference of mode indices as a function of triangular gratings' period.

Using Eqs. (2) and (6), the grating can get a high efficiency for both TE and TM-polarization when $p = 546\,\text{nm}$ wit $h = \lambda/(2\Delta\overline{n}_{eff\_TM}) = 4480\,\text{nm}$ and $p = 747\,\text{nm}$ with $h = 7137\,\text{nm}$. SMM can not tell us which one could get a higher efficiency because of neglecting reflection. Now, from Eq. (4), the reflection will vanish while the admittance of grating Y is close to that of air η_0 (Fig. 4(c)). Correspondingly, the transmission efficiency is almost 100% (Fig. 5(b)) due to $T = 1 - R$.

Thus if we want to design a high efficiency grating for incident wavelength $\lambda = 1064\,\text{nm}$, the period should be chosen as $p = 747\,\text{nm}$, and depth $h = 7137\,\text{nm}$. The data in Table 1 exhibits this accurate conclusion.

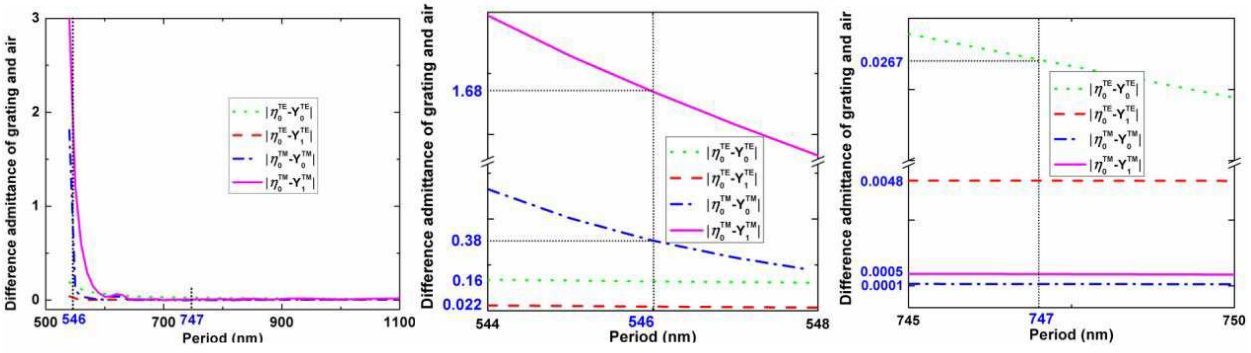

Figure 4: Difference admittance of grating and air versus the period. Y_0 and Y_1 are admittances of mode 0 and mode 1 respectively. (b) and (c) are magnifications of (a).

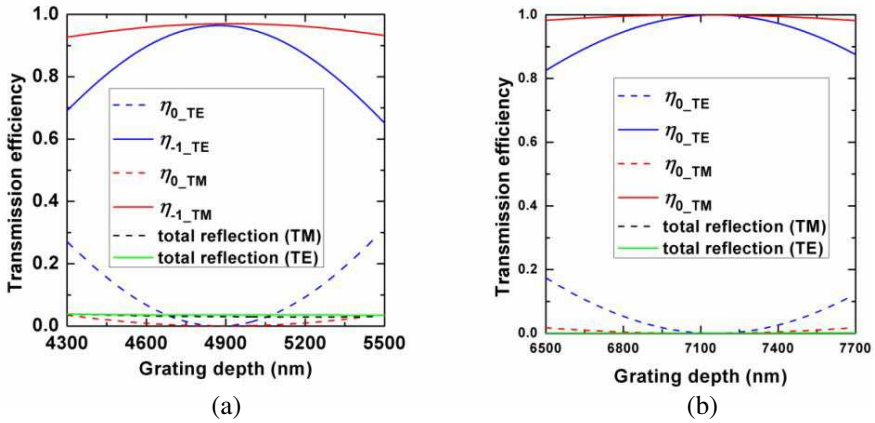

Figure 5: The efficiency versus the grating depth. (a) $p = 546\,\text{nm}$; (b) $p = 747\,\text{nm}$. Total reflection could not see clearly in (b) because they are less than 0.0005.

Table 1: Diffractive efficiencies of the triangular gratings at wavelength $\lambda = 1064\,\text{nm}$ and first Bragg angle for high efficiency at the -1st order by using RCWA.

Period (nm)	Height (nm)	η_{0_TE}	η_{-1_TE}	(TE) total reflection	η_{0_TM}	η_{-1_TM}	(TM) total reflection
546	4880	0.044%	95.666%	4.290%	0.052%	96.006%	3.942%
747	7137	0.005%	99.977%	0.018%	0.040%	99.958%	0.002%

4. DISCUSSION AND CONCLUSION

The simplified modal method (MSMM) was modified by regarding the grating as multilayer thin films. The grating region is divided into N thin rectangular grating slabs and regarded as multilayer films. Then the reflectance is characterized by effective admittances of air and grating. The calculation by MSMM is a very good approximation for RCWA. According to MSMM, a grating can get a high efficiency when its parameters fulfill two conditions: firstly, the average difference of mode indices is odd times of π and secondly the admittance of the grating is approximate to that of air. At last, a grating with more than 99.9% for both TE and TM-polarized light was designed..

ACKNOWLEDGMENT

The work was funded by the National Natural Science Foundation of China (Nos. 61102023 and 11034007), the development plan project of Jilin province science and technology (20120329), and the project supported by the National High Technology Research and Development Program of China (Grant No. 2012AA040503)

REFERENCES

1. Clausnitzer, T., J. Limpert, K. Zöllner, H. Zellmer, H. Fuchs, E. Kley, A. Tünnermann, M. Jupé, and D. Ristau, *Appl. Opt.*, Vol. 42, 6934–6938, 2003.
2. Wu, T., C. Zhou, J. Zheng, J. Feng, H. Cao, L. Zhu, and W. Jia, *Appl. Opt.*, Vol. 49, 4506–4513, 2010.
3. Moharam, M. G. and T. K. Gaylord, *J. Opt. Soc. Am.*, Vol. 72, 1385–1392, 1982.
4. Moharam, M. G. and T. K. Gaylord, *J. Opt. Soc. Am. A*, Vol. 3, 1780–1787, 1986.
5. Moharam, M. G., D. A. Pommet, E. B. Grann, and T. K. Gaylord, *J. Opt. Soc. Am. A*, Vol. 12, 1077–1086, 1995.
6. Clausnitzer, T., T. Kämpfe, E.-B. Kley, A. Tünnermann, U. Peschel, A. V. Tishchenko, and O. Parriaux, *Opt. Express*, Vol. 13, 10448–10456, 2005.
7. Clausnitzer, T., T. Kämpfe, E.-B. Kley, A. Tünnermann, A. Tishchenko, and O. Parriaux, *Appl. Opt.*, Vol. 46, 819–826, 2007.
8. Clausnitzer, T., T. Kämpfe, E.-B. Kley, A. Tünnermann, A. V. Tishchenko, and O. Parriaux, *Opt. Express*, Vol. 16, 5577–5584, 2008.
9. Sun, W., P. Lv, C. Zhou, H. Cao, and J. Wu, *Appl. Opt.*, Vol. 52, 2800–2807, 2013.
10. Jing, X., S. Jin, J. Zhang, Y. Tian, P. Liang, H. Shu, L. Wang, and Q. Dong, *Opt. Lett.*, Vol. 38, 10–12, 2013.
11. Sheng, P., R. S. Stepleman, and P. N. Sanda, *Phys. Rev. B*, Vol. 26, 2907–2917, 1982.
12. Zheng, J., C. Zhou, J. Feng, and B. Wang, *Opt. Lett.*, Vol. 33, No. 14, 1554–1556, 2008.
13. Macleod, H. A., *Thin Film Optical Filters*, Institute of Physics Publishing, 41, 2001.
14. Tishchenko, A. V., *Opt. Quantum Electron.*, Vol. 37, 309–330, 2005.
15. Zhou, C., *Proc. of SPIE*, Vol. 8564, 856412-1–11, 2013.

Broadband Measurement of Complex Permittivity for Liquids Using the Open-ended Cut-off Circular Waveguide Reflection Method

Kouji Shibata
Department of Electrical and Electric Systems, Hachinohe Institute of Technology
88-1, Aza-oubiraki, Ouaza-myou, Hachinohe, Aomori 031-8501, Japan

Abstract— Various studies on specific absorption rates (SARs) have been carried out with liquid phantoms representing human body tissues in the field of electromagnetic compatibility (EMC) research. As a faithful representation of human body tissue is needed to establish an accurate SAR for measurement, knowledge regarding the precise measurement of sample materials with high permittivity and high loss is very important. In this study, the complex permittivity of a liquid phantom material was measured using the open-ended cut-off circular waveguide reflection method. The effectiveness of the proposed approach for measuring a liquid phantom with high permittivity and high loss was also confirmed by comparing the measurement results with those obtained using the TM_{010} circular cavity resonator method.

1. INTRODUCTION

In response to recent health concerns regarding the application of electromagnetic waves to the human body, the effects of such waves and methods for measuring complex permittivity in relation to liquids used for humanoid phantoms have been studied [1].

Meanwhile, the development of techniques for creating new chemical materials based on exposure to electromagnetic waves has accelerated. In research on such microwave chemistry applications, liquids are generally used as solvents for the synthesis of new chemical materials. Accordingly, knowledge of exact material constants for objects to be heated in the frequency band of electromagnetic wave exposure is very important.

In general, reflection constant determination method using a coaxial probe is a popular technique for measuring the complex permittivity of liquids [2]. Although this method readily supports broadband estimation of material constants for liquids, a large amount of water is needed to avoid the influence of reflective waves from the vessel bottom. The cavity resonator method can also be used for high-precision measurement [3–5]. A transmission constant determination technique involving the insertion of a liquid sample into a Teflon tube with a waveguide can be used for measurement at a continuous frequency [6]. A cross-shaped coaxial probe can be used for simple measurement of complex permittivity, but material constant data on a known material is required as a standard with this approach [8]. A transmission constant determination method involving the insertion of sample materials into a coaxial line [7] and a reflection constant determination method involving the insertion of sample materials into a cylindrical cavity [9] can be adopted for broadband measurement.

In this study, the complex permittivity of tap water, methanol, ethanol (99.5) and isopropanol with high permittivity and high loss was measured via the reflection method using a coaxial feed open-ended cut-off circular waveguide [10] to reduce the effects of liquid spillage at the time of sample material insertion. The effectiveness of the proposed method was then evaluated by comparing its results with those of the TM_{010} cylindrical cavity resonator method [4]. Next, the complex permittivity of the liquids was measured at frequencies ranging from 50 MHz to 3.0 GHz using the procedure outlined above. In this case, the measurement limit was set at a very low frequency.

2. MEASUREMENT PROCEDURE

The liquid phantom was measured using the method outlined here.

1. Calibration of S_{11} (input impedance) is performed at the tip of a coaxial line before mounting on the measurement jig.
2. The jig is attached to a measurement cable connected to a network analyzer (see Figs. 1 and 2).
3. Complex permittivity is measured at the front of the sample material when it is inserted into the network analyzer.

4. The complex permittivity of the sample material is estimated based on an inverse problem to coincide with the calculated input impedance and the result of input impedance measurement.

The measurement jig for liquid insertion is made from a cut piece of worked brass and an SMA connector. S_{11} calibration must be performed under a condition in which the measurement jig is not mounted when input impedance is measured using a network analyzer. The reference plane is then moved using a VNA electrical delay function so that the input impedance is $\infty\Omega$ on the Smith chart when the measurement jig is attached. When actual measurement is made, a coaxial line attenuator (6 dB) is connected to the front of the measurement jig to reduce the influence of reflection waves on the measurement results with this setup (Figure 2). In addition, the complex permittivity of the inserted sample material must be estimated from the measured input impedance as an inverse problem. This work is performed using the 2D Newton-Raphson method.

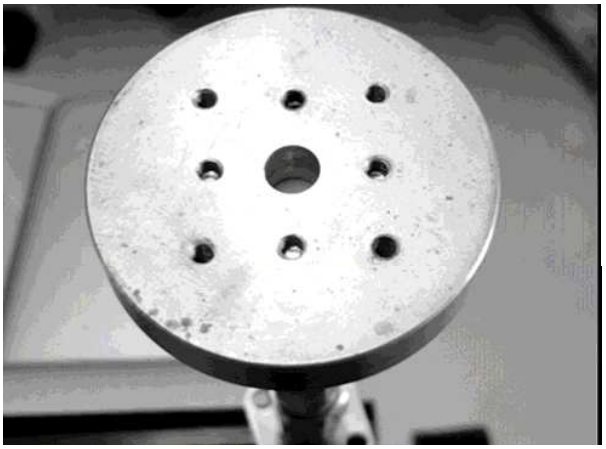

Figure 1: Measurement jig.

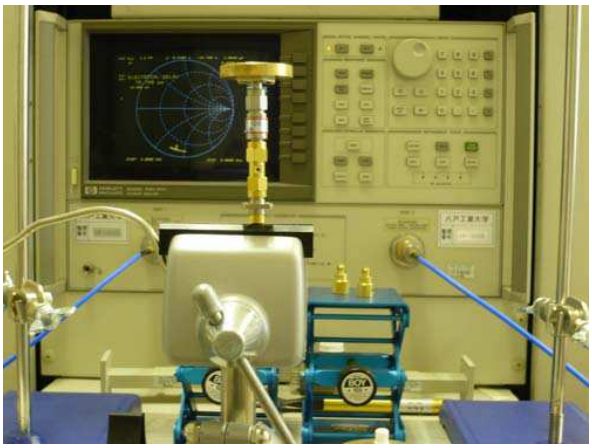

Figure 2: Measurement setup.

3. CALCULATION OF INPUT IMPEDANCE

In the proposed method, input impedance at the reference plane (as seen from the right-hand side in Figure 3) is measured with the sample insertion slot in a patulous state. However, it is impractical to assume an open condition for this slot when the analytical model for estimating complex permittivity is computed due to the large analytical area and computational resources needed. However, the proposed method does not require computation for the region outside the aperture plane as explained below. Electromagnetic wavelengths are longer at low measurement frequencies. Therefore, electromagnetic waves are cut off because they cannot propagate into the cylindrical waveguide of a sample insertion space with a sufficiently small diameter. Accordingly, the value of electromagnetic waves at the aperture area for liquid sample insertion (based on the propagation of a sample insertion hole excited from an SMA connector) appears very low because such waves decay exponentially with distance when the sample insertion length is above a certain value. The termination condition of the cut-off cylindrical waveguide is therefore assumed to be the perfect magnetic condition (PMC), which differs from the open condition in input impedance computation. On the assumption that the boundary condition of the sample insertion space's aperture area is the PMC, the mode-matching method [10, 11] can be applied to the analytical model shown in Figure 3 for calculation of the input admittance at the reference plane as seen from

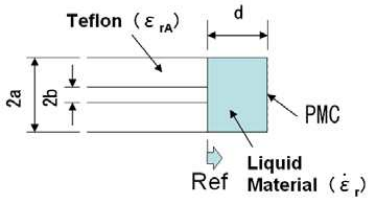

Figure 3: Analytical model.

the right-hand side using Equation (1).

$$\dot{y}_m = j \cdot \frac{2k_0 a \cdot \dot{\varepsilon}_r}{\sqrt{\varepsilon_{rA}} \cdot \ln\left(\frac{a}{b}\right)} \left(y_0 - \sum_{q=1}^{\infty} y_q \cdot x_q \right) \tag{1}$$

Here, y_m is the complex admittance (a combination of real and imaginary parts), and its inverse is the complex impedance. The complex permittivity of the inserted sample material is also uniquely decided from the measured complex permittivity. To calculate y_m, matrix elements such as y_q and x_q are first computed for convergence of the computational result with a sufficiently large q value for each change in measurement frequency.

4. FUNDAMENTAL STUDY

First, complex permittivity was estimated as an inverse problem by measuring the input impedance with tap water at a frequency of 2.49806 GHz with values of $2a = 4.1$ mm, $2b = 1.3$ mm, $d = 5.0$ mm and $\varepsilon_{rA} = 2.05$. Table 1 summarizes the means of the measurement results obtained using the proposed method along with those obtained using the TM_{010} cylindrical cavity resonator method [4] and the open-ended coaxial line method [14, 15]. In this case, the measurement jig was filled with the liquid again and the dielectric constant was measured five times each using the proposed method and the cylindrical cavity resonator method. The mean value obtained with the proposed method was $73.02 \pm 0.4 - j8.38 \pm 0.3$, which was close to the cavity resonator method result of $73.20 \pm 0.4 - j7.45 \pm 0.8$ at a frequency of 2.49806 GHz.

Room temperature was 22.4°C for input impedance measurement with the proposed method and 20.2°C for measurement with the cavity resonator method. Next, methanol, ethanol and isopropanol (IPA) samples were inserted into the jig, their input impedances were measured three times, and complex permittivity was estimated from each value. Tables 2 to 4 show the estimation results obtained with the proposed method, the measurement results obtained with the TM_{010} cylindrical cavity resonator method [4, 5], and those obtained with the open-ended coaxial line method [14, 15]. The measurement frequency value for input impedance using the proposed method is the same as that for measurement using the cavity resonator method. The outcomes show that measurement results obtained with the proposed method closely match those of the cavity resonator method.

Table 1: Measurement results for tap water.

Complex permittivity (proposed method)	Complex permittivity (Refs. [14, 15])	Complex permittivity (cavity resonator method [4])
73.55 ± 0.93	73.57 ± 0.93	73.20 ± 0.40
$-j8.49 \pm 0.41$	$-j8.44 \pm 0.40$	$-j8.28 \pm 1.50$

Table 2: Measurement results for methanol (2.5314 GHz).

Complex permittivity (proposed method)	Complex permittivity (Refs. [14] and [15])	Complex permittivity (cavity method [4])
21.33 ± 0.50	20.56 ± 0.09	22.1 ± 1.30
$-j13.77 \pm 0.10$	$-j12.41 \pm 0.07$	$-j11.4 \pm 2.10$

5. INFLUENCE OF MATERIAL FILLING SPACE DEPTH

In this study, termination was assumed to occur in the perfect magnetic condition (PMC). However, this differs from the termination condition of jigs that can be used in practice. Accordingly, input impedance variations were studied by calculating values with different sample insertion lengths when the termination condition was selected as PMC or PEC.

The results, which are detailed in reference [10], indicate little change in calculated input impedance values with insertion length variations of $d = 3$ to 5 mm. However, the calculated input impedance values shown in Figures 4 to 5 for a low measurement frequency of $f = 50$ MHz

Table 3: Measurement results for ethanol (2.5395 GHz).

Complex permittivity (proposed method)	Complex permittivity (Refs. [14] and [15])	Complex permittivity (cavity method [4])
6.26 ± 0.18	6.05 ± 0.19	6.30 ± 0.30
$-j7.13 \pm 0.18$	$-j6.76 \pm 0.26$	$-j6.80 \pm 0.30$

Table 4: Measurement results for IPA (2.5415 GHz).

Complex permittivity (proposed method)	Complex permittivity (Refs. [14] and [15])	Complex permittivity (cavity method [4])
3.04 ± 0.25	3.24 ± 0.19	3.50 ± 0.50
$-j3.23 \pm 0.05$	$-j3.04 \pm 0.05$	$-j3.00 \pm 0.10$

in relation to tap water and methanol, respectively, also indicate little change in calculated input impedance at low frequency (50 MHz) with insertion length variations of $d = 3$ to 5 mm in common with the 500 MHz and 2 GHz bands. These results can be explained by the fact that most electromagnetic waves were reflected at the discontinuity plane between the coaxial line and the cut-off waveguide because the propagation mode is the cut-off mode at the measurement frequency with the jig used here.

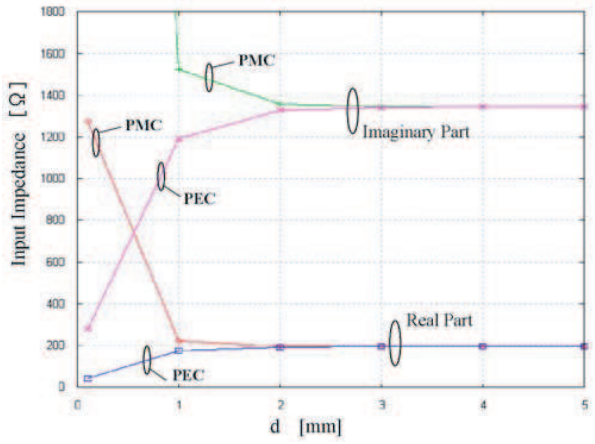

Figure 4: Results of input impedance calculation with various d-dimension values (for tap water at 50 MHz, $\varepsilon_r = 82.0 - j12.0$).

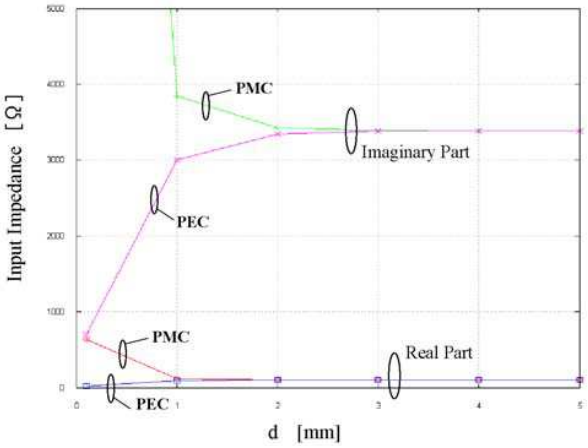

Figure 5: Results of input impedance calculation with various d-dimension values (for methanol at 50 MHz, $\varepsilon_r = 33.0 - j1.0$).

Reflected electromagnetic waves in the cut-off waveguide also attenuate within the waveguide because the inserted liquid is a high-loss material. As a result, reflected waves do not reach the reference plane. Based on these observations, it was concluded that the complex permittivity of a high-loss liquid can be estimated using the proposed method if the tip of the measurement jig is open-ended. The suitability of measurement can also be judged by checking the convergence of calculated results for input impedance with variation of the d-dimension for unknown materials.

6. FREQUENCY CHARACTERISTICS OF COMPLEX PERMITTIVITY IN CERTAIN LIQUID TYPES

The results of the study confirmed the proposed method's applicability to the measurement of complex permittivity for high-loss liquids. The complex permittivity of certain liquid types was subsequently measured under the conditions of $2a = 4.1$ mm, $2b = 1.3$ mm, $d = 5.0$ mm and $\varepsilon_{rA} = 2.0$ at frequencies ranging from 50 MHz to 3.0 GHz. The measurement results, which are shown in Figs. 6 to 9, indicate that the real and imaginary parts of the complex permittivity of tap water were 82.0 to 72.0 and 3.0 to 9.0, respectively. The corresponding figures for methanol were 34.0 to 21.0 and 1.0 to 14.0, those for ethanol (99.5) were 20.0 to 6.0 and 9.0 to 2.0, and those for

IPA were 17.0 to 3.0 and 7.0 to 3.0.

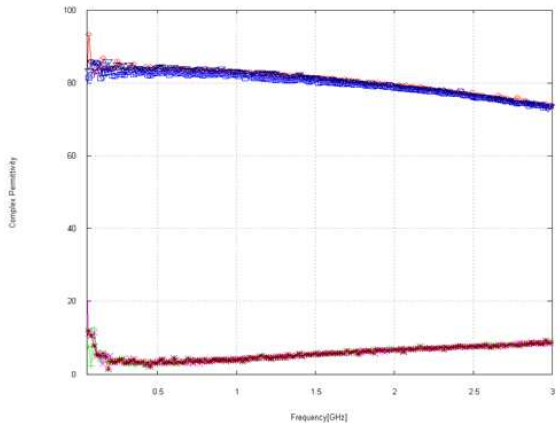

Figure 6: Frequency characteristics of complex permittivity (tap water).

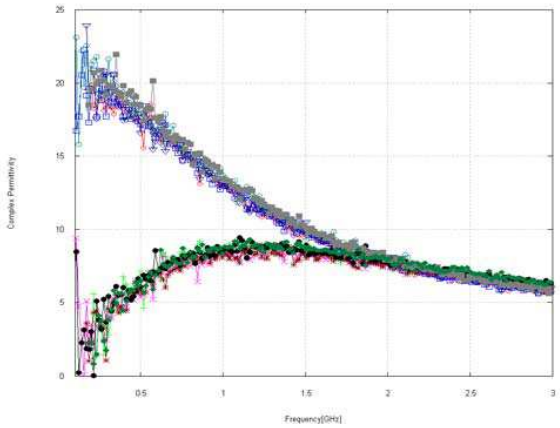

Figure 7: Frequency characteristics of complex permittivity (ethanol 99.5).

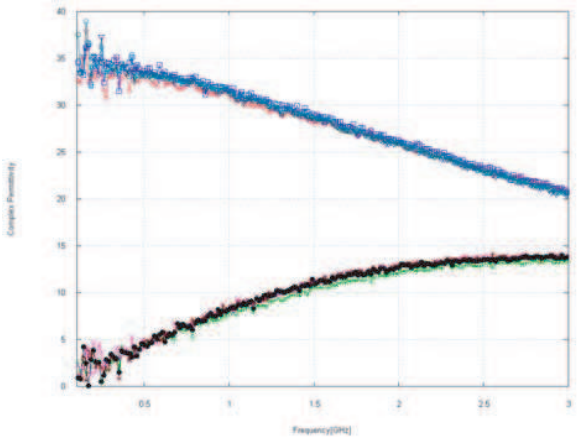

Figure 8: Frequency characteristics of complex permittivity (methanol).

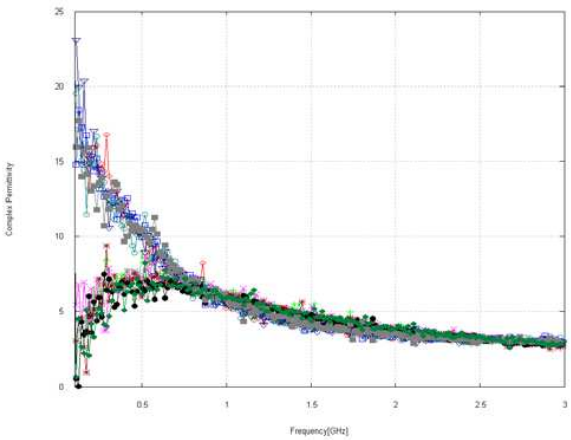

Figure 9: Frequency characteristics of complex permittivity (IPA).

The results highlighted the frequency characteristics of complex permittivity with different liquids. However, as input impedance was found to be mostly open in the ultra-low frequency band, it can be inferred that measurement precision deteriorates significantly due to large variation in the results of complex permittivity estimation. Possible methods of improving measurement precision include increasing the diameter of the coaxial tube and inserting the liquid into the coaxial region of the SMA connector. These are issues for future study.

7. CONCLUSION

This study involved verification for a proposed method of broadband measurement to determine the complex permittivity of liquids using the reflection method with an open-ended cut-off waveguide as a coaxial feed. The complex permittivity of tap water, methanol, ethanol and IPA was actually estimated from the measured input impedance. Next, measurement results and outcomes obtained using the cylindrical cavity resonator method were compared to evaluate the effectiveness of the proposed technique. The extent to which different insertion lengths and the termination conditions influence measurement results was also evaluated. Based on the outcomes, the frequency characteristics of the complex permittivity of certain types of high-loss liquids were confirmed at frequencies ranging from 50 MHz to 3.0 GHz on the basis of the measurement procedure outlined above. As complex permittivity was measured with the nose section open, the effects of liquid spillage were reduced. The method is therefore considered applicable for small amounts of liquid for cost-effective measurement in a broad frequency range. In future work, the temperature dependence of these

liquids will be studied using the proposed method. However, as this method is characterized by problems in the low-frequency band, jig improvement with a particular coaxial tube diameter and material insertion space is required. Highly accurate numerical analysis for the open-ended section is also needed to deal with low-loss materials. Research to extend the method to the measurement of liquids in the millimeter band is also required.

REFERENCES

1. Fukunaga, K., S. Watanabe, K. Wake, and Y. Yamanaka, "Time dependence of tissue-equivalent dielectric liquid materials and its effect on SAR," *Intl. Symp. on Electromagn. Compat.*, 763–767, Sorrento, Sep. 2002.
2. Mosig, J. R. and J. C. Ebesson, "Reflection of an open- ended coaxial line and application to nondestructive measurement of materials," *IEEE Trans. on Instru. and Meas.*, Vol. 30, No. 1, 46–51, Mar. 1981.
3. Li, S. and R. G. Bosisio, "Composite hole conditions on complex permittivity measurements using microwave cavity perturbation," *IEEE Trans. Microw. Theory Tech.*, Vol. 30, No. 1, 100–104, Jan. 1982.
4. Maslenikov, A. B. and A. S. Omar, "Accurate microwave resonant method for complex permittivity measurements of liquids," *IEEE Trans. Microw. Theory Tech.*, Vol. 48, No. 11, 2159–2164, Nov. 2000.
5. Kawabata, H., H. Tanpo, and Y. Kobayashi, "Analysis and experiments of a TM_{010} mode cylindrical cavity to measure accurate complex permittivity of liquid," *IEICE Trans. Electron.*, Vol. E87-C, No. 5, 694–699, May 2004.
6. Nishikata, A., Y. Kuriyama, N. Ueda, K. Fukunaga, S. Watanabe, and Y. Yamanaka, "Complex permittivity measurement of a liquid phantom material using a dielectric tube piercing a rectangular waveguide," *IEICE Tokyo Japan, Tech. Rep.*, Vol. EMCJ 2002-55, MW2002-85, 27–33, Oct. 2002 (in Japanese).
7. Shibata, K., K. Tani, O. Hashimoto, and K. Wada, "Measurement of complex permittivity for liquid phantom by transmission line method using coaxial line," *IEICE Trans. Electron.*, Vol. E87-C, No. 5, 689–693, May 2004.
8. Michiyama, T., E. Tanabe, and Y. Nikawa, "Measurement of complex permittivity of lossy materials using an obliquely cut open-ended coaxial probe," *IEICE Trans. Electron.*, Vol. J89-C, No. 12, 1082–1084, Dec. 2006 (in Japanese).
9. Kushizaki, E., J. Chakarothai, Q. Chen, K. Sawaya, and M. Suzuki, "A study on measurement of permittivity of liquid using a cylindrical cavity," *IEICE Tokyo Japan, Tech. Rep.*, Vol. 108, No. 132, EMCJ 2008-37, 67–70, Jul. 2008 (in Japanese).
10. Shibata, K., "Measurement of complex permittivity for liquid materials using the open-ended cut-off waveguide reflection method," *IEICE Trans. Electron.*, Vol. E93-C, No. 11, 1621–1629, Nov. 2010.
11. Belhadj-Tahar, N.-E. and F.-L. Arlette, "Broad-band analysis of a coaxial discontinuity used for dielectric measurements," *IEEE Trans. Microw. Theory Tech.*, Vol. 34, No. 3, 346–349, Mar. 1986.
12. Press, W. H., S. A. Teukolsky, W. T. Vetterling, and B. P. Flannery, *Numerical Recipes in Fortran 77*, 2nd Edition, 372–375, Cambridge University Press, 1992.
13. Ypma, T. J., "Historical development of the Newton-Raphson method," *SIAM Review*, Vol. 37, No. 4, 531–551, 1995.
14. Jarvis, J. B., M. D. Janezic, and C. A. Jones, "Shielded open-circuited sample holder for dielectric measurements of solids and liquids," *IEEE Trans. Instru. and Meas.*, Vol. 47, No. 2, 338–344, Apr. 1998.
15. Shibata, K. and J. Kamiyama, "Fundamental study on measurement of complex permittivity for liquid materials using the open-ended coaxial waveguide reflection method," *IEICE Tokyo Japan, Tech. Rep.*, Vol. EMCJ 2009-57, MW 2009-106, 75–80, Oct. 2009 (in Japanese).

Electromagnetic Surface Wave Scattering with Microwaves

M. Chamtouri[1], **O. Merchiers**[1], **M. Francoeur**[3],
H. Tortel[2], **J.-M. Geffrin**[2], **and R. Vaillon**[1]

[1]Université de Lyon, CNRS, INSA-Lyon, UCBL, CETHIL UMR 5008, F-69621 Villeurbanne, France
[2]Aix Marseille Université, CNRS, Centrale Marseille
Institut Fresnel UMR 7249, 13013 Marseille, France
[3]Department of Mechanical Engineering, University of Utah, Salt Lake City, UT 84112, USA

Abstract— We present a microwave analog experiment for evanescent surface wave scattering by dielectric objects. The instrument provides the amplitude and the phase of the scattered fields in both the near- and far-field regions. We compare the experimental results against numerical simulations, which take into account particle-substrate interaction. This not only allows assessing the validity of the numerical methods but also offers a better understanding of surface wave scattering.

1. INTRODUCTION

Microwave-analog-to-light-scattering (MALS) is a powerful method to analyze electromagnetic scattering properties of systems, which are difficult to manipulate and hence to study in the optical domain. Furthermore, modern detection techniques give direct experimental access to the field value (amplitude and phase), which is much more difficult for optical frequencies. The linearity of Maxwell's equations is the physical principle underlying the method. It allows rescaling wavelength together with object size, keeping field distributions invariant. These properties make it suitable as a proof of concept tool (near-field optical microscopy, metamaterials, cloaking, Kerker conditions), but also as an experimental validation tool of numerical methods [1–3].

MALS has been applied extensively to the study of free space electromagnetic wave scattering by single particles [4] and complex aggregates [5]. In some cases it has also been applied to surface geometries [6]. On the other hand, the case of simple and complex-shaped objects deposited on a surface has received little attention despite numerous applications in nanoscience such as biological detection and surface contamination. To fill in this gap, we present a new device in which evanescent waves are generated on top of a dielectric substrate. This allows studying the behavior of the electromagnetic fields scattered by objects placed on the substrate, in both the near- and far-field regions. Over the past few years, numerical methods capable of handling correctly particle-surface interactions started to emerge [7–12]. These methods are, however, still in a process of development and require experimental validation. Our set-up offers ideal conditions to perform such tests.

After a presentation of the experimental set-up, we will provide some experimental and numerical results.

2. EXPERIMENTAL SET-UP

To measure electromagnetic surface wave scattering by macroscopic objects (object sizes between few millimeters to few centimeters), experiments were performed in an anechoic chamber of Institut Fresnel in Marseille using a device specially designed for this purpose called Surface Wave Scattering-Microwave Scanner (SWS-MS) (see Figure 1) [13]. It consists of a polyamide (PA6) semi-circular prism ($\varepsilon = 2.9 + i0.05$) and emitting and receiving antennas operating in the [4–8 GHz] frequency range. The set-up allows two types of illuminations: a propagating illumination (PI) and an evanescent illumination (EI). The PI consists in placing both emitter and receiver on top of the substrate. Hence, the object is excited with a propagating wave. For the EI, the emitter is placed against the cylinder wall and sends the beam through the prism with an angle of incidence θ_{inc} larger than the critical angle θ_{cri}, thus generating an evanescent wave at the air-prism interface. In this work we will focus on this EI configuration.

Evanescent waves are very sensitive to the presence of any object placed near the surface (at a distance of the order of the penetration depth) since it induces scattering of the evanescent wave, which can be detected in near- or far-field. In the latter case, the receiver is placed on an arm with translation and rotation capabilities. In the near-field region, the electric field is measured using a probe.

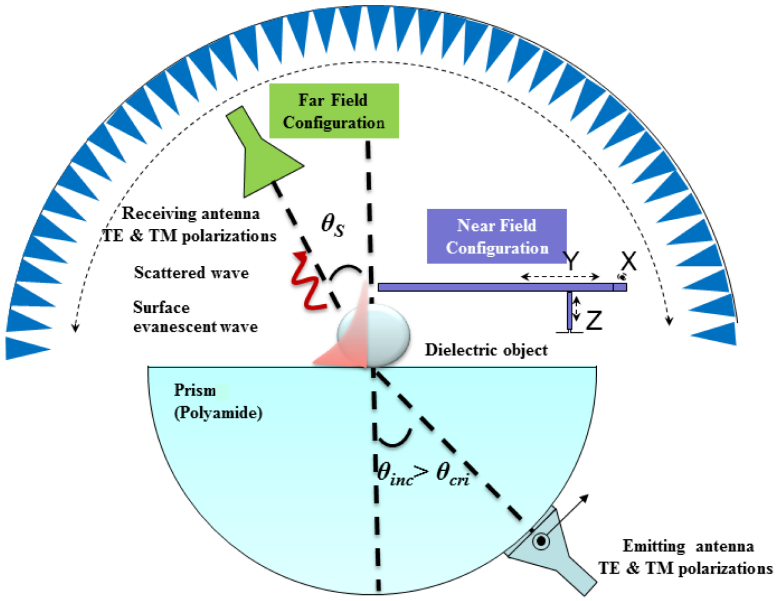

Figure 1: SWS-MS device. The emitting antenna produces a beam with an angle of incidence θ_{inc} and generates an evanescent wave at the top surface of the semicircular prism. Objects placed on or near the interface scatter the evanescent field and create propagating modes that can be detected in both the far- and near-field.

3. RESULTS

We report scattering measurements for two types of spheres: the first one is a quasi-lossless sphere (PA6), with a permittivity of $2.9 + i0.05$ (refractive index of $1.7 + i0.02$) and a diameter of 30 mm ($\lambda/1.92$), and the second is an absorbing sphere, with a permittivity of $1.4 + i0.3$ (refractive index of $1.19 + i0.13$) and a diameter of 69 mm ($\lambda/0.87$).

The first sphere is placed on the top surface of the prism and illuminated by a TE polarized plane wave at a frequency of 5.2 GHz, with an incident angle for the EI illumination of $\theta_{inc} = 36°$.

The results show the measured electric fields amplitude scattered by the particle located on the substrate. The amplitude is plotted in logarithmic scale as a function of the scattering angle θ_S (Figure 2(a)). The measurements are used to assess numerical simulations, carried out by two open source codes based on the Discrete Dipole Approximation taking into account particle-surface interaction: DDA-SI [14] and ADDA [9]. For both DDA-SI and ADDA calculations, the sphere was modeled using 512 cubical sub-volumes. To compare with a different numerical approach we also

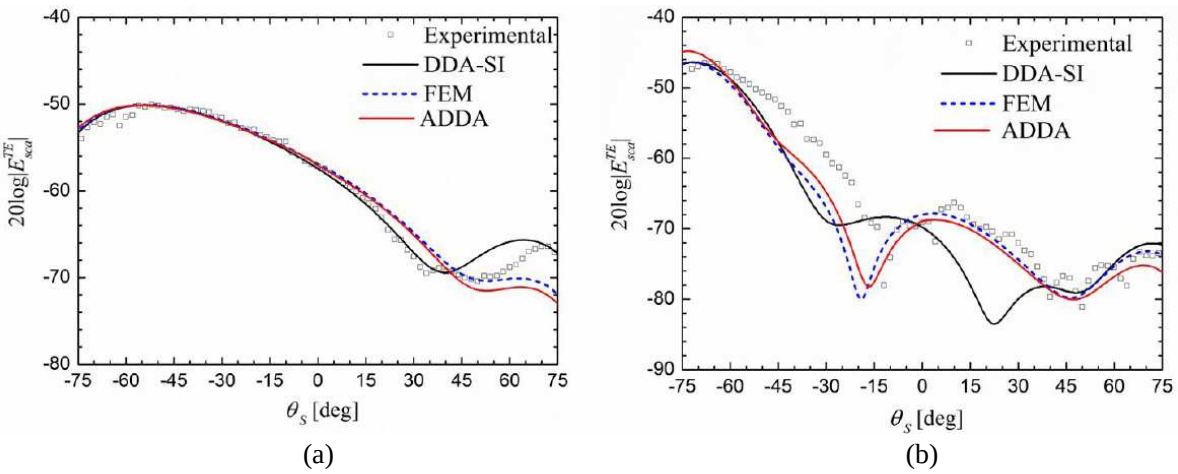

Figure 2: TE-polarized electric field scattered in the far zone by (a) quasi-lossless sphere illuminated at a frequency of 5.2 GHz, (b) absorbing sphere illuminated at a frequency of 5 GHz.

used a "home implementation" of the Finite Element Method (FEM) using an adaptive triangular mesh with adequate high mesh density.

Despite slight differences in the positions of the minima, measurements and simulations by ADDA and FEM are generally in good agreement. This agreement is excellent between 0° and −75°, but important differences appear in the range [0°–75°] for the three methods, especially for DDA-SI. Part of the observed differences is likely to be due to spurious reflections at the interfaces and due to the fact that the beam is slightly diverging. Both phenomena introduce propagating modes in the evanescent wave. In the future, we will use new antennas with better collimation to avoid the generation of non-evanescent modes.

In Figure 2(b), the large absorbing sphere is illuminated by an evanescent wave generated by a TE-polarized plane wave at an angle of incidence of 36° with a frequency of 5 GHz. Here, the sphere was modeled using 1472 cubical sub-volumes. Compared to the quasi-lossless sphere, the differences between numerical predictions and experimental results are more pronounced. We observe again that FEM and ADDA reproduce the experiments better than DDA-SI. This indicates that DDA-SI suffers from numerical inaccuracies more apparent in the case of higher losses. We think that the most probable cause for these problems is the numerical evaluation of the Sommerfeld integrals.

4. CONCLUSION

We have presented experimental results and numerical simulations for far-field scattering of evanescent waves by two types of dielectric spheres. The experimental results are found to be in reasonable agreement with the numerical simulations obtained with the FEM and ADDA including surface interactions. Our set-up offers the possibility to researchers to evaluate the accuracy of their codes. Experimental work is ongoing to demonstrate the set-up capabilities for both near- and far-field in terms of detection sensitivity, object size resolution and object separation resolution.

ACKNOWLEDGMENT

The authors are indebted to Institut Carnot Ingénierie@Lyon (I@L) and Institut Carnot STAR for their support and funding of the project SPLM.

REFERENCES

1. Greenberg, J. M., N. E. Pedersen, and J. C. Pedersen, "Microwave analog to the scattering of light by nonspherical particles," *Journal of Applied Physics*, Vol. 32, 233–242, 1961.
2. Gustafson, B. A. S., "Microwave analog to light scattering measurements: A modern implementation of a proven method to achieve precise control," *Journal of Quantitative Spectroscopy and Radiative Transfer*, Vol. 55, 663–672, 1996.
3. Vaillon, R., J.-M. Geffrin, C. Eyraud, O. Merchiers, P. Sabouroux, and B. Lacroix, "A new implementation of a microwave analog to light scattering measurement device," *Journal of Quantitative Spectroscopy and Radiative Transfer*, Vol. 112, 1753–1760, 2011.
4. Geffrin, J.-M., B. García-Cámara, R. Gómez-Medina, P. Albella, L. S. Froufe-Pérez, C. Eyraud, A. Litman, R. Vaillon, F. González, M. Nieto-Vesperinas, J. J. Sáenz, and F. Moreno, "Magnetic and electric coherence in forward- and back-scattered electromagnetic waves by a single dielectric subwavelength sphere," *Nat. Commun.*, Vol. 3, 1171, 2012.
5. Merchiers, O., C. Eyraud, J.-M. Geffrin, R. Vaillon, B. Stout, P. Sabouroux, and B. Lacroix, "Microwave measurements of the full amplitude scattering matrix of acomplex aggregate: A database for the assessment of light scattering codes," *Optics Express*, Vol. 18, 2056–2075, 2010.
6. Hibbins, A. P., B. R. Evans, and J. R. Sambles, "Experimental verification of designer surface plasmons," *Science*, Vol. 308, 670–672, 2005.
7. Loke, V. L. Y. and M. P. Mengüç, "Surface waves and atomic force microscope probe-particle near-field coupling: Discrete dipole approximation with surface interaction," *J. Opt. Soc. Am. A*, Vol. 27, 2293–2303, 2010.
8. Short, M. R., J.-M. Geffrin, R. Vaillon, H. Tortel, B. Lacroix, and M. Francoeur, "Evanescent wave scattering by particles on a surface: Validation of the discrete dipole approximation with surface interaction against microwave analog experiments," *Journal of Quantitative Spectroscopy and Radiative Transfer*, Vol. 146, 452–458, 2014.
9. Yurkin, M. A. and A. G. Hoekstra, "The discrete-dipole-approximation code ADDA: Capabilities and known limitations," *Journal of Quantitative Spectroscopy and Radiative Transfer*, Vol. 112, 2234–2247, 2011.

10. Schmehl, R., B. M. Nebeker, and E. D. Hirleman, "Discrete-dipole approximation for scattering by features on surfaces by means of a two-dimensional fast Fourier transform technique," *J. Opt. Soc. Am. A*, Vol. 14, 3026–3036, 1997.
11. Nebeker, B. M., J. L. de la Peña, and E. D. Hirleman, "Comparisons of the discrete-dipole approximation and modified double interaction model methods to predict light scattering from small features on surfaces," *Journal of Quantitative Spectroscopy and Radiative Transfer*, Vol. 70, 749–759, 2001.
12. Nebeker, B. M., "Modeling of light scattering from features above and below surfaces using the discrete-dipole approximation," Ph.D. Dissertation, Arizona State University, 1998.
13. Vaillon, R. and J.-M. Geffrin, "Recent advances in microwave analog to light scattering experiments," *Journal of Quantitative Spectroscopy and Radiative Transfer*, Vol. 146, 100–105, 2014.
14. Loke, V. L. Y., M. Pinar Mengüç, and T. A. Nieminen, "Discrete-dipole approximation with surface interaction: Computational toolbox for MATLAB," *Journal of Quantitative Spectroscopy and Radiative Transfer*, Vol. 112, 1711–1725, 2011.

On Capacity Performance of 2×2 Satellite-earth Link at 30 GHz in Rain Environment

Jing Yang, Xiaowei Xue, and Shuhong Gong
School of Physics Optoelectronic Engineering, Xidian University, China

Abstract— Give the equivalent model of STBC, VBLAST sche mes for analyzing their channel capacity. The channel capacity performances of SISO, 2×2 STBC and 2×2 VBLAST schemes in 20 mm/h rain environment are simulated and discussed based on an assumed 2×2 satellite-earth link at 30 GHz in circular polarization as an example.

1. INTRODUCTION

In comparison with traditional Single-Input Single-Output (SISO) communication technology, MIMO communication technology shows great advantages, such as higher transmission rate, spectrum utilization ratio and power efficiency. Therefore, MIMO communication technology represents a breakthrough in the modern communication field [1–3].

Many reports about MIMO communication have been focused on the frequencies below 10 GHz [1]. In contrast, the research on the MIMO communication above 10 GHz, such as Ku and Ka bands or higher frequencies, is still in its infancy, although the communication technology at those frequencies has many advantages [1]. Available publications only explored some particular aspects for the MIMO communication above 10 GHz, for example the references of [4–8]. The most those publications concern terrestrial MIMO systems or indoor environment, where the multipaths induced by terrain and the objects around the receiver are present. Though earth-station receiving diversity is exploited for mitigating the fading caused by tropospheric scattering effect on Ka band satellite signal in [9], the MIMO communication is not straightforward on satellite communication. Fortunately, attention has been paid to the application of the MIMO technology above 10 GHz in satellite communication system in recent years in [2] and [10–12] which just specifically analyze the effect of rain-induced attenuation on the channel characteristics.

This paper focuses on the capacity performance of 2×2 satellite-earth link at 30 GHz in rain environment. the equivalent model of STBC, VBLAST schemes for analyzing their channel capacity are given. The channel capacity performances of SISO, 2×2 STBC and 2×2 VBLAST schemes in 20 mm/h rain environment are simulated and discussed based on an assumed 2×2 satellite-earth link at 30 GHz in circular polarization as an example. The equivalent model given in this paper is valid for the single-polarization MIMO satellite-earth link at other bands above 10 GHz.

2. THE EQUIVALENT MODEL FOR MIMO SYSTEM CAPACITY

For a MIMO system with variance is m_T transmitting antennas and m_R receiving antennas, the relationship between the transmitted signal vector $\mathbf{x}(t)$ and the received signal vector $\mathbf{y}(t)$ can be given as

$$\mathbf{y}(t) = \mathbf{H}\mathbf{x}(t) + \mathbf{n}(t) \tag{1}$$

In (1), $\mathbf{H}$ expresses channel matrix, whose element $h_{i,j}(i = 1, 2, \ldots, m_R;\ j = 1, 2, \ldots, m_T)$ represents the random channel parameter from the jth transmitting antenna to the ith receiving antenna. In fact, a complete model for $h_{i,j}$ should include all the propagation and scattering effects except for noise and all filters, such as attenuation, multipath fading and receiver filter etc.. The propagation and scattering impacts are considered in this paper. For convenience, $h_{i,j}$ is also written as $h_{i,j} = h_{1\_i,j}h_{2\_i,j}$. Where, $h_{1\_i,j}$ represents path loss, which is a constant for a given specific link and specific propagation environment parameters. $h_{1\_i,j}$ mainly determines the average energy of received signals. $h_{2\_i,j}$ is a complex random variable, which indicates the randomly fading coefficient induced by random multipath propagation or the combination of the incoherent scattering in the troposphere. the incoherent scattering effect is similar to the multipath effect on mobile communications but their physical nature is not the same.

If the channel is unknown to the transmitter, then the vector $\mathbf{x}(t)$ is statistically independent, This implies that the signals are independent and the power is equally divided among the transmit antennas. The capacity in such a case is presented as

$$C = \log_2 \det\left(\mathrm{I}_{m_R} + E_s/m_T N_0 \mathbf{H}\mathbf{H}^{\mathrm{H}}\right) \tag{2}$$

where, E_s is the total energy of a transmitted symbol in J, N_0 is noise power spectrum density in J, the superscript H denotes Hermitian Transpose operation. If $m_T = m_R = 1$, (2) simplified as

$$C = \log_2\left(1 + E_s/N_0\,|H|^2\right) \tag{3}$$

For 2×2 STBC scheme using Maximal Ration Combing, the equivalent model of capacity can be given as

$$C = \log_2\left[1 + E_s'/N_0\left(|h_{2\_1,1}|^2 + |h_{2\_1,2}|^2 + |h_{2\_2,1}|^2 + |h_{2\_2,2}|^2\right)\right] \tag{4}$$

For 2×2 VBLAST scheme using Maximal Ration Combing, the equivalent model of capacity can be given as

$$C = \log_2\left[1 + E_s'/N_0\left(|h_{2\_1,1}|^2 + |h_{2\_2,1}|^2\right)\right] + \log_2\left[1 + \frac{E_s'}{N_0}\left(|h_{2\_2,1}|^2 + |h_{2\_2,2}|^2\right)\right] \tag{5}$$

E_s' in (4) and (5) signifies the symbol energy from the transmitting antenna j to the receiving antenna i after taking path loss into account, is presented as

$$E'_{s\_i,j} = E_s/m_T h^2_{1\_i,j} \tag{6}$$

N_0 can be given by

$$N_0 = 1.38 \times 10^{-23} T_{sys}/2 \tag{7}$$

where

$$T_{sys} = T_{clear} + T_m\left(1 - 10^{-\frac{L_{atm}}{10}}\right) \tag{8}$$

In (8), T_{clear} is a given constant, L_{atm} signifies all atmosphere-induced attenuation.

The fading coefficient in rain can be given as

$$h_{2\,rain\_i,j} = \alpha_{i,j} \cdot \exp\left[-j(\varphi_{0\_i,j} + \varphi_{f\_i,j})\right] \tag{9}$$

where, $\alpha_{i,j}$ and $\phi_{f\_i,j}$ are the random number respectively following

$$p(\alpha) = 2K\alpha \exp[-K(\alpha^2 + 1)] I_0(2K\alpha) \tag{10}$$

$$p(\varphi_f) = 1/2\pi \tag{11}$$

And, φ_0 can be calculated by $\varphi_0 = L_{eff} \cdot 57.296 \times 10^3 \frac{2\pi}{k^2} \int_{D_{\min}}^{D_{\max}} \mathrm{Im}(S(0)) N(D) dD$ [1].

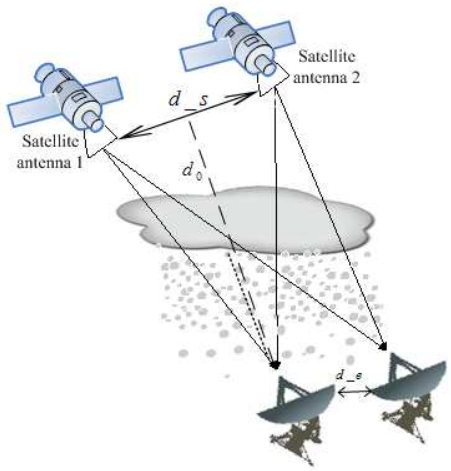

Figure 1: The sketch of the assumed satellite-earth MIMO communication link.

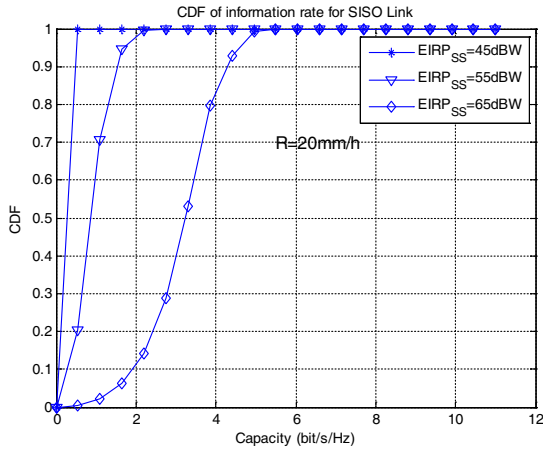

Figure 2: CDF of capacity for SISO link in rain.

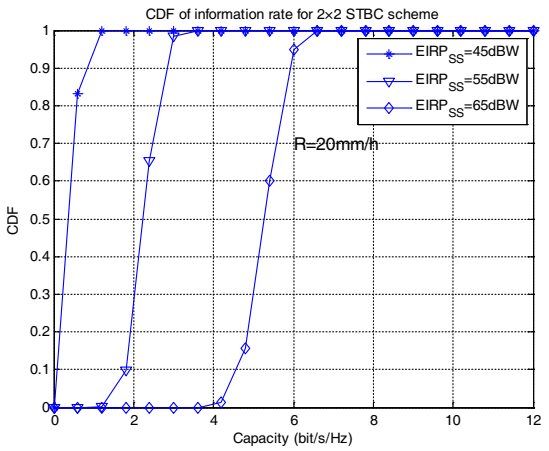

Figure 3: CDF of capacity for 2×2 STBC scheme in rian.

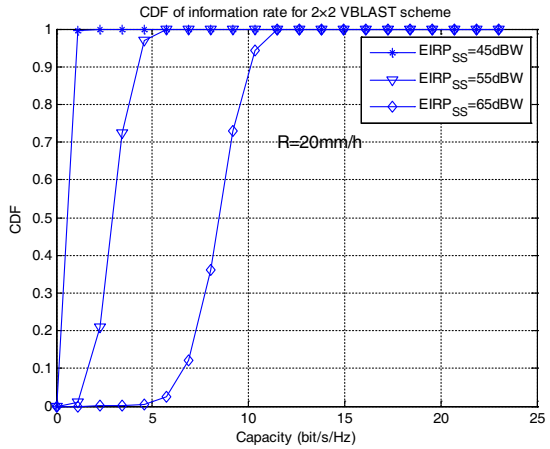

Figure 4: CDF of capacity for 2×2 VBLAST scheme in rain.

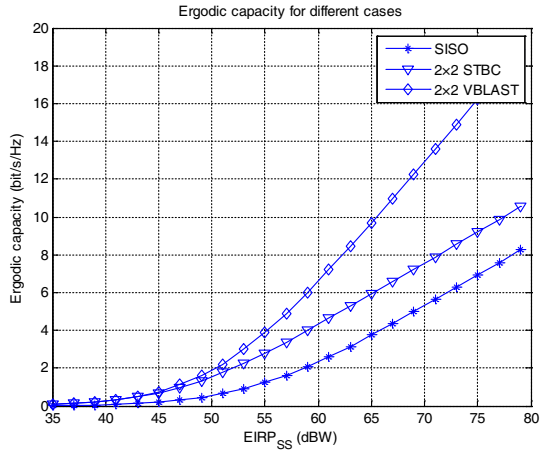

Figure 5: Ergodic capacity for SISO, 2×2 STBC and 2×2 VBLAST schemes in rain.

Table 1: The parameters of the link illustrated in Figure 1.

The parameters of earth station			Satellite Parameters	
The parameters of earth station		108.95°E; 34.26°N	Location of the subsatellite point	100°E 0°
Receiving frequency		30.0 GHz	Transmitting frequency	30.0 GHz
T_{clear_i}		95.09 K	Orbit altitude	15000 km
Antenna parameter I	type	Parabolic	IPB_o	3.83 dB
	aperture	1 m		
	gain	48 dB		
	Half-power beamwidth	0.7°		
	Elevation angle	40.7°		
Antenna parameter II	type	reflector	Polarization state	Circular polarization
	aperture	27 m		
	gain	76 dB		
	Half-power beamwidth	0.3°		
	Elevation angle	40.7°		

In (10), K in rain environment is estimated by (13) [1]

$$K = \exp(-\gamma \cdot L_{eff})/2\pi \int_{D_{\min}}^{D_{\max}} \int_{0}^{\theta_A} \sin\Theta N(D) g(\gamma \cdot L_{eff}, \Theta) |f(\Theta, D)|^2 / \gamma \mathrm{d}\Theta \mathrm{d}D \tag{12}$$

And, the model for calculating atmosphere-induced attenuation can find in [1].

3. SIMULATION AND DISCUSSION

An assumed link parameters are listed in Table 1, and link configuration is illustrated in Figure 1. The simulation results in 20 mm/h rain environment are given in the figures of Figure 2–Figure 5.

Note that the performance of a MIMO is critically de *d_s d_e* pendent on the availability of an independent and identically distributed channel fading matrix. It is well known that channel correlation will downgrade the performance of a MIMO system. Therefore, it is assumed that and are great enough to ensure the fading matrix being independent and identically distributed.

It is obvious that channel capacity can be improved by adopting MIMO technology in satellite communication system. It is natural that VBLAST scheme is the best scheme to improve channel capacity, however it is at the cost of bit error rate. STBC should be the ideal scheme because of its potential merit of both capacity and bit error rate. We will give more comprehensive and deeper investigation in future.

ACKNOWLEDGMENT

This work has been supported by "the National Natural Science Foundation of China (61001065)" and "the Fundamental Research Funds for the Central Universities". And, thank all teachers and students, who do many contributions for measuring.

REFERENCES

1. Gong, S. H., "Study on some problems for radio wave propagating and scattering through troposphere," Ph.D. Dissertation, Dept. Science, Xidian Univ., 2008.
2. Arapoglou, P. D., K. Liolis, M. Bertinelli, A. Panagopoulos, P. Cottis, and R. D. Gaudenzi, "MIMO over satellite, a review," *IEEE Communications Surveys & Tutorials First Quarter,* Vol. 13, No. 1, 27–51, May 2011.
3. Paulraj, A. J., D. A. Gore, R. U. Nabar, and H. Bolcskei, "An overview of MIMO communications — A key to gigabit wireless," *Proc. IEEE,* Vol. 92, No. 2, 198–218, Nov. 2004.
4. Huang, K. C. and Z. C. Wang, "Millimeter wave MIMO," *Millimeter Wave Communication Systems*, Vol. 29, 133–159, Wiley-IEEE, CA, 2011.
5. Pi, Z. Y. and F. Khan, "A millimeter-wave massive MIMO system for next generation mobile broadband," *Signals, Systems and Computers*, 693–698, ASILOMAR, Pacific Grove, CA, 2012.
6. Suzuki, S., T. Nakagawa, H. Furuta, and T. Ikeda, "Evaluation of millimeter-wave MIMO-OFDM transmission performance in a TV studio," *APMC Asia-Pacific*, 843–846, Yokohama, Japan, 2006.
7. Madhow, U., "Multi gigabit millimeter wave communication: System concepts and challenges," *Proc. Information Theory and Applications Workshop*, 193–196, San Diego, CA, 2008.
8. Moraitis, N. and P. Constantinou, "Indoor channel capacity evaluation utilizing ULA and URA antennas in the millimeter wave band," *The 18th Annual IEEE International Symposium on PIMRC*, 1–5, Athens, Greece, 2007.
9. Enserink, S. W., "Analysis and mitigation of troposphere effects on Ka band satellite signals and estimation of ergodic capacity and outage probability for terrestrial links," Ph.D. Dissertation, Dept. Electrical Engineering, University of California-Los Angeles, 2012.
10. Oh, C. I., S. H. Choi, D. I. Chang, and D. G. Oh, "Analysis of the rain fading channel and the system applying MIMO," *ISCIT 2006*, 507–510, Bangkok, Thailand, 2006.
11. Schwarz, R. T., A. Knopp, and B. Lankl, "The channel capacity of MIMO satellite links in a fading environment: A probabilistic analysis," *IWSSC*, 78–82, Tuscany, Italy, 2009.
12. Liolis, K. P., A. D. Panagopoulos, and P. G. Cottis, "Multi-satellite MIMO communications at Ku-band and above: Investigations on spatial multiplexing for capacity improvement and selection diversity for interference mitigation," *EURASIP Journal on Wireless Communications and Networking*, Vol. 2007, 1–11, Jul. 2007.

Error in Phase Verification Results for Vector Network Analyzer Measurements in Coaxial Line System

Masahiro Horibe and Ryoko Kishikwa
National Metrology Institute of Japan, Japan

Abstract— This paper presents error analysis of a simple method for verifying the phase of transmission measurements — for example, as made using instruments such as Vector Network Analyzers (VNAs). Phase verification method by using air line as a phase standard has been published by N. Ridler and M. Horibe. Examples are given that show the method being used at millimeter wavelengths (i.e., at frequencies up to 33 GHz) in the 3.5 mm coaxial line size. It is trusted that the method will be suitable for use by calibration laboratories seeking verified and/or accredited measurements in VNAs. An air dielectric coaxial line (air line) is commonly used as the reference impedance and absolute phase standard in a VNA measurement. In the method, phase measurement accuracy is verified by comparing between dimensional length and electrical length, analyzed by measured value of transmission phase, of air line. However, reflection characteristics of air line at connection interfaces affects to error of analytical results of electrical length.

1. INTRODUCTION

Precision coaxial unsupported air lines are used as reference standards of impedance at RF and microwave frequencies [1–3]. In this paper, we use the air lines as phase standards against which the phase of transmission measurements can be verified in a vector network analyser (VNA) measurements. In advance, the air lines are characterised by their measured mechanical dimensions and measured insertion loss. The electrical length of the air line is calculated from the phase values of the transmission measurements made by the VNA being verified and this is then corrected to take into account the measured insertion loss. Subsequently, the calculated electrical length of the air lines is compared with the measured mechanical length of the air line. If the electrically derived length agrees with the mechanically measured length, then verification process of the phase measurements in VNA is passed.

The above method has previously been proposed elsewhere (see, for example [4–6]). However, in this paper, we extend this work by analysing the error in the calculation of electrical length from the S-parameter measurement results.

2. CALCULATION OF ELECTRICAL LENGTH

At first, the characteristic impedance, Z_a, of the air line should be verified by using dimensional measurements of the radii of the center conductor, a, and outer conductor, b, using:

$$Z_a \approx 59.939\ 045 \times \ln\left(\frac{b}{a}\right) \tag{1}$$

And, the physical length of the air line, l_m, should be determined by using dimensional measurements with traceability back to the SI base unit of length, the metre.

Then, the complex-valued S-parameters of the air line, at a range of frequencies, are obtained by the VNA measurement system that is to be verified. Note that, the measured reflection coefficient magnitudes, $|S_{11}|$ and $|S_{22}|$, should be sufficiently small to approximate the match condition for the line at all measured frequencies in the VNA measurement.

Using measured values of magnitude and phase of S_{21} and S_{12}, the resistivity, ρ, and electrical length for the air line, l_e are determined by the method presented in Ref. [6].

3. ANALYSIS OF PHASE VERIFICATION IN VNA

When ideal air lines having no reflection characteristics, $|S_{11}| = |S_{22}| = 0$, is used, transmission magnitude and phase characteristics are only depends on length and resistivity of conductivity of the air lines.

$$S_{21} = S_{12} = e^{-(\alpha + j\beta)l_e} \tag{2}$$

However, usual air lines have some mismatch effect at the connector interface, then $|S_{11}|$ and $|S_{22}|$ are non-zero values, i.e., $Z_a = 50\,\Omega$.

$$S_{21} = S_{12} = \frac{2\left(\cosh^2(\alpha + j\beta) - \sinh^2(\alpha + j\beta)\right)}{2\cosh(\alpha + j\beta) + \left(\frac{Z_0}{Z_a} + \frac{Z_a}{Z_0}\right)\sinh(\alpha + j\beta)} \tag{3}$$

Here, Z_0 is system impedance of VNA, i.e., $50\,\Omega$.

In the case of S_{11} and S_{22} being not small, There is no longer simple equation shown in Eq. (3) compared to Eq. (2).

In the next section, this paper presents the VNA phase verification result compering to physical length of the air lines, and then investigate and discussion the relationship between phase verification errors and S_{ii} of the air lines.

4. RESULT AND DISCUSSION

Four air lines with 50 mm long length and 3.5 mm connectors at the both ends were used in the VNA phase verification. Length difference between electrical and physical is drawn in Figure 1. The electrical lengths of three lines, A, C and D, has less than 10 µm difference from physical length of air lines. However, electrical length is approximately 30 µm longer than physical length for line B. According to Ref. [6], uncertainty of this type of comparison is approximately 10 µm when use of typical air lines, i.e., low reflection loss at the connector interface. Then electrical lengths of the lines, A, C and D are good agreement with their physical lengths. However, line B has large error in the phase verification result.

In order to understanding the difference between electrical and physical lengths, reflection characteristics were obtained and drawn in Figure 2. Three air lines, A, C and D, show small reflection characteristics, S_{ii}, within 0.02. Line B has larger reflection characteristics, i.e., maximum value of

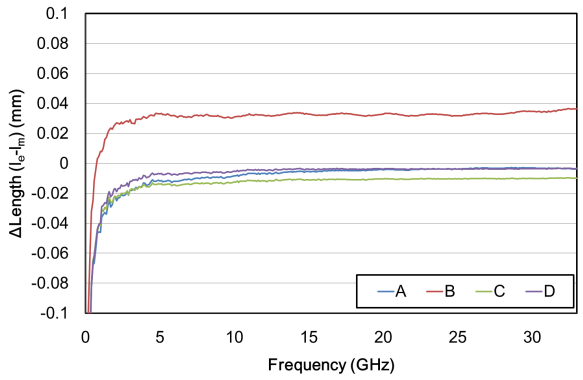

Figure 1: Difference between electrical and physical lengths of the 50 mm air lines.

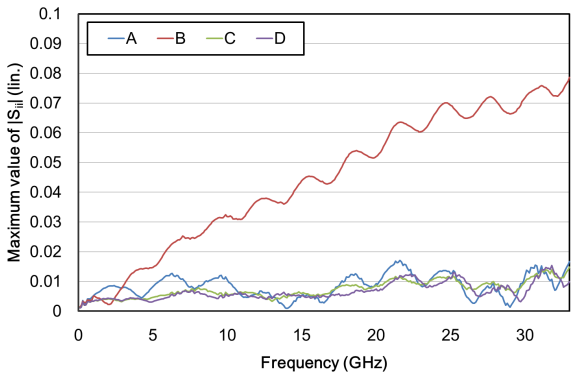

Figure 2: Maximum values of measured $|S_{11}|$ or $|S_{22}|$ for the air lines.

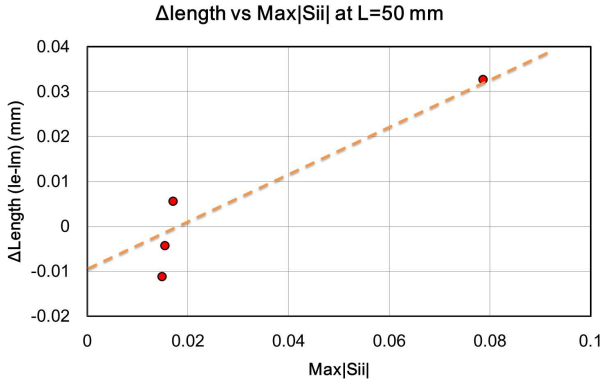

Figure 3: Dependence of length difference on reflection characteristics of the air lines.

0.08. As the results, length difference depends on reflection characteristics. Figure 3 shows plots of relationship between length difference and maximum $|S_{ii}|$. This graph indicates one of major error source in VNA phase verification is measured reflection characteristics of the air lines.

This means that the air line should have a small reflection characteristics in the VNA phase verification.

5. SUMMARY

This paper has described an error source in the VNA phase verification of transmission coefficients, based on determining the electrical length of precision beadless air lines. The method is good way to verify the phase measurement accuracy, but the result strongly depends on reflection characteristics of air lines.

REFERENCES

1. Weinschel, B. O., "Air-filled coaxial lines as absolute impedance standards," *Microwave Journal*, 47–50, Apr. 1964.
2. Harris, I. A. and R. E. Spinney, "The realization of high-frequency impedance standards using air spaced coaxial lines," *IEEE Trans. Instrum. Meas.*, Vol. 13, 265–272, 1964.
3. Wong, K. H., "Using precision coaxial air dielectric transmission lines as calibration and verification standards," *Microwave Journal*, 83–92, Dec. 1998.
4. De Vreede, J. P. M. and N. M. Ridler, "Beadless air lines as phase standards," *2006 Conference on Precision Electromagnetic Measurements (CPEM)*, 286–287, Torino, Italy, Jul. 9–14, 2006.
5. Eio, C. P., S. J. Protheroe, and N. M. Ridler, "Characterising beadless air lines as reference artefacts for S-parameter measurements at RF and microwave frequencies," *IEE Proc. — Sci. Meas. Technol.*, Vol. 153, No. 6, 229–234, Nov. 2006.
6. Horibe, M. and N. Ridler, "Verifying transmission phase measurements at millimeter wavelengths using beadless air lines," *74th ARFTG Microwave Measurement Conference Digest*, 65–71, 2009.

Dielectric Loss at Millimeter Range and Temperatures 300–950 K, and Electrophysical Properties in Diamonds Grown by the Arc Plasma Jet Technology

B. M. Garin[1], V. I. Polyakov[1], A. I. Rukovishnikov[1], A. V. Khomich[1], V. V. Parshin[2], E. A. Serov[2], Ch. Ch. Jia[3], F. X. Lu[3], and W. Z. Tang[3]

[1]Kotelnikov Institute of Radio Engineering and Electronics of Russian Academy of Sciences
Fryazino Branch, 1, Vvedensky Sq., Fryazino, Moscow Region 141190, Russia
[2]Institute of Applied Physics of Russian Academy of Sciences
46, Ulianov Str., Nizhny Novgorod 603950, Russia
[3]Beijing University of Science and Technology, 30, Cellege Str., Beijing 100083, China

Abstract— The results of study of the dielectric loss at millimeter (MM) wavelengths range and temperatures 300–950 K in two different diamonds grown by the arc plasma jet (APJ) technology are presented. The electrophysical properties and parameters of point defects are also investigated. A comparison of results was made for these samples with the diamonds which have been grown by the technology of microwave plasma chemical vapor deposition (MPCVD).

It is revealed that both frequency and temperature loss dependences as well as the electrophysical properties and parameters of point defects in the APJ diamonds essentially differ from the MPCVD diamonds properties.

Also these properties in the studied APJ diamonds also essentially differ.

The dielectric loss mechanisms are discussed.

1. INTRODUCTION

Diamond films are a new kind of high quality dielectric material because they possess a combination of novel properties, i.e., low dielectric loss, extremely high thermal conductivity, high dielectric strength, etc..

Conventionally, high quality diamond films are prepared by using microwave plasma chemical vapor deposition (MPCVD) technique [1]. The dielectric and other properties of such diamonds were presented in [2–4]. However the deposition rate of high-quality diamond films by this technique is rather low (2–3 mkm/hour). Such material is rather expensive and its application is restricted.

During the last decade, a high power DC arc plasma jet (APJ) technique has been developed [5] which shows the advantages of higher deposition rate and lower material cost. Until now, there has been little report on dielectric properties of diamond films prepared by the APJ technique.

The first results on dielectric properties at MM range at the first time for the APJ diamonds were presented in [6] for one sample (K1). In [7] also the first data on electrophysical properties and parameters of point defects are investigated also by the charge-based deep level transient spectroscopy (Q-DLTS) technique. The metal (Ag) contacts were fabricated on diamond surface. However the Ag contacts provided only a qualitative data.

In this paper the results of investigation of the dielectric properties in two different APJ diamond samples are presented. The dielectric loss temperature dependences at the range $T = 300$–950 K are measured at the first time for the APJ diamonds. Also electrophysical properties and parameters of point defects are studied. A "strict" Ni and Ti contacts have been used that allowed to obtain quantitative data at the first time for the APJ diamonds.

A comparison with the MPCVD diamonds was made.

2. RESULTS AND DISCUSSION

In the present work the results of study of two APJ diamond samples are presented and discussed. The first sample "K1" is the disk of 18.2 mm in diameter and with the thick of 0.316 mm (the dielectric properties in it were studied earlier only at room temperature [6]. The second sample "K2" is the disk of 63 mm in diameter and with the thick of 0.401 mm. The samples were presented by the Beijing University of Science and Technology (BUST).

Earlier the dielectric loss tangent $\tan\delta$ was measured in the sample K1 at millimeter (MM) wavelengths range and room temperature [6]. At long MM range the measuring technique at the

base of cylindrical cavity resonator was used. At short MM range the measuring technique at the base of high-Q open resonator was used [6]. It was found that $\tan\delta{\sim}2\cdot10^{-4}$ at frequency $f = 35\,\mathrm{GHz}$, and $\tan\delta{\sim}3\cdot10^{-3}$ at $f = 201\,\mathrm{GHz}$. The later measurement was made on "resonant" frequency of a disk at which the optical thickness of a disk is equal to a half wave ($t\cdot n = \lambda/2$) where t is the geometrical thickness of the sample, n is the refractive index of material, λ is the length of wave in vacuum. The refractive index in the sample K1 has been found on the specified resonant frequency. Its value $n = 2.354$ (±0.002) essentially less than refractive index $n = 2.380$ (±0.001) found in our previous measurements in various MPCVD diamonds in which the given value is close to the value for monocrystal diamond. The smaller value of the refractive index in the sample K1 in comparison with other diamonds means, that the given sample has smaller density.

From a comparison of the measurements data on different frequencies described above it follows, that in the APJ sample K1 an essential increase $\tan\delta$ with frequency ($\tan\delta{\sim}f$) in the MM a range is observed. It essentially differs from the frequency dependence of loss in other diamonds, in particular in MPCVD diamonds, where reduction of loss with frequency ($\tan\delta{\sim}1/f$) in the given range was observed at $f < 200\,\mathrm{GHz}$. In the MPCVD diamonds it caused by electric conductance in the intercrystalline (intergranular) areas [2, 8, 9].

From observable increase of loss with frequency in the investigated APJ diamond K1 follows, that the mechanism of loss in it is another compared to the MPCVD diamonds. As theoretical interpretation of the loss in the sample K1, the mechanism of the lattice loss induced by the lattice disorder can beoffered because it corresponds to dependence $\tan\delta{\sim}f$ [10]. It agrees also with smallerdensity (in comparison with MPCVD diamonds), corresponding to smaller value of the measured refractive index.

In the present work the dielectric loss and refraction index at the MM range was measured at another APJ diamond: sample K2.

The dielectric loss was measured at various temperatures $T = 300$–$950\,\mathrm{K}$ (at the first time for the APJ diamonds). The temperature dependences were measured on two frequencies, 157 and 313 GHz. The results are presented in the Figure 1.

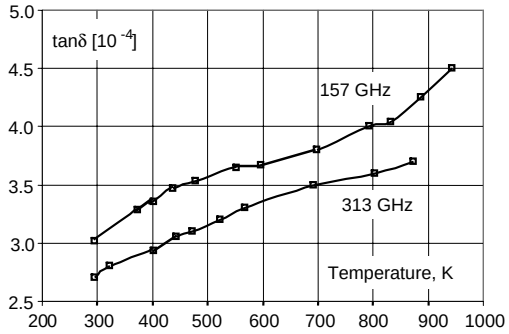

Figure 1. Temperature dependences of the dielectric loss tangent $\tan\delta$ in the APJ diamond sample K2 on two frequencies, 157 and 313 GHz.

The APJ sample K2 essentially differs on the loss temperature and frequency dependences from the MPCVD diamonds. In particular, the loss weakly depends on temperature not only at the "low" temperatures ($T{\sim}300\,\mathrm{K}$), but also at the "high" temperatures ($T{\sim}900\,\mathrm{K}$). Whereas in the MPCVD diamonds a sharp increase of loss is observed at $T{\sim}500$–$900\,\mathrm{K}$ [2, 3]. The decrease of loss at the increase of frequency in the sample K2 is observed as well as in the MPCVD diamonds. However it is much weaker compared to the dependence $\tan\delta{\sim}1/f$ that is observed in the MPCVD diamonds at $f < 300\,\mathrm{GHz}$ [2, 3] and is due to the electric conductance in the intercrystalline areas [2, 8, 9].

The APJ sample K2 also essentially differs on the loss frequency dependence from the APJ sample K1. In the sample K2 a decrease of loss with frequency is observed. Whereas in the sample K1 an increase with frequency is observed [6, 7]. It is possible to explain these frequency and temperature dependences in the sample K2 by the combination of contributions of two loss mechanisms: a) lattice loss induced by the lattice disorder which do not depend on temperature [10] (and can predominate at rather low temperatures; b) the loss caused by electric conductance in the intercrystalline areas [2, 8, 9]. The received results, including much lower losses in the sample 2 show, that in this sample the concentration of lattice disorder much low, than in the APJ diamond K1.

As it had shown in the previous our researches, the defects of various nature are characteristic for artificial diamond materials. And they can render essential influence on value of dielectric loss. However the mechanisms and character of influence of defects, in particular point defects, are not sufficiently studied.

In the present work the electric conductivity σ and its activation energy of E_a were obtained for the samples K1 and K2 from the volt-ampere characteristics measured at various temperatures (290–520 K).

The defect concentrations N_t, were determined by the Charge-based Deep Level Transient Spectroscopy [8]. The Q-DLTS spectrum is the charge $\Delta Q = Q(t_2) - Q(t_1)$, which is measured as a function of the "time of rate window" $\tau_m = (t_2 - t_1)/\ln(t_2/t_1)$, where t_1 and t_2 are the times from the beginning of the defect discharge, upon applying a voltage pulse to the sample. The ratio $t_2/t_1 = 2$ was kept constant while the Q-DLTS spectra were obtained. The amplitudes of ΔQ peaks (which are directly proportional to the defect concentration) are used to determine the N_t values as described in [8].

The results were compared with the data for typical MPCVD diamond sample "D1" that we researched earlier.

In the Table 1 some data obtained are presented: electric conductivities σ (at $T = 520$ K), its activation energies E_a, and point defect concentrations N_t.

Table 1.

Sample	σ , $\mathrm{Ohm}^{-1} \cdot \mathrm{cm}^{-1}$	E_a, eV	N_t, cm^{-3}
D1	$3.8 \cdot 10^{12}$	1.43	$\sim 4 \cdot 10^{10}$
K1	10^{12}	0.33 at $T < 450$ K 0.89 at $T > 480$ K	$\sim 8 \cdot 10^{10}$
K2	$6 \cdot 10^{12}$	0.63	$\sim 7 \cdot 10^{10}$

In the sample K1 two different activation energies are observed: 0.33 eV at $T < 450$ K and 0.89 eV at $T > 480$ K. It indicates that there are two deep levels in the forbidden gap. Their contributions dominate in the thermal excitation of the free char carries and in the electric conductivities at $T < 450$ K and $T > 480$ K respectively. The activation energy of levels corresponding to the room temperatures is the most in the sample D1 (1.43 eV) and the least in the sample K1 (0.33 eV). So at the room temperatures the dielectric loss in the sample D1 is significantly lower compared to the sample K2, and in the sample K1 it is significantly above.

3. CONCLUSION

The studied samples of APJ diamonds essentially differ from the MPCVD diamonds studied earlier. In particular:

1. The observed both frequency and temperature dependences of dielectric loss essentially differ from the dependences in the MPCVD diamonds. Also the frequency dependences in the studied samples of APJ diamonds essentially differ.
2. It follows from the results obtained that the loss natures in these three diamonds are different among all them.
3. The dielectric loss at the short MM wavelengths region in the subsequent APJ sample K2 is significantly lower compared to the sample K1. So a progress in the further reduction of loss in the APJ diamonds can be proposed.

The APJ diamonds are perspective material in applications for the flats and layers in the high power electronics at MM and THz ranges as a material combining very low dielectric loss, extremely high thermal conductivity (5 times higher compared to the copper), electric insulating properties, high dielectric strength, and rather low cost (compared to the MPCVD diamonds).

ACKNOWLEDGMENT

The work was supported by the Russian Foundation for Basic Research (projects No. 11-02-91179 and No. 14-02-90458) and the Chinese Foundation for Natural Sciences (project No. 51010204).

REFERENCES

1. *Handbook of Industrial Diamonds and Diamond Films,* M. Prelas, et al., Eds., Marcel Dekker, NY, 1997.
2. Garin, M., V. V. Parshin, S. E. Myasnikova, and V. G. Ralchenko, *Diamond and Related Materials*, Vol. 12, 1755, 2003.
3. Parshin, V., B. Garin, S. Myasnikova, and A. Orlenekov, *Radiophysics and Quantum Electronics*, Vol. 47, 974, 2004.
4. Bertolotti, M., G. L. Liakhou, A. Ferrari, V. G. Ralchenko, A. A. Smolin, E. Braztsova, K. G. Korotoushenko, S. M. Pimenov, and V. I. Konov, *J. Appl. Phys.*, Vol. 75, 7795, 1994.
5. Lu, F. X., W. Z. Tang, T. B. Huang, et al., *Diamond and Related Materials*, Vol. 10, 1551, 2001.
6. Garin, B. M., V. V. Parshin, E. A. Serov, C. C. Jia, W. Z. Tang, and F. X. Lu, "Electromagnetic properties at millimeter wavelength range of diamond films grown by DC arc plasma jet technique," *PIERS Proceedings*, 455–457, Suzhou, China, Sep. 12–16, 2011.
7. Garin, B. M., V. V. Parshin, V. I. Polyakov, et al., "Recent advances in broadband dielectric spectroscopy," *NATO Science for Peace and Security Series B: Physics and Biophysics*, Chapter 6, Y. P. Kalmykov, Ed., © Springer Science + Business Media, Dordrecht, Netherlands, 2012.
8. Garin, B. M., *Sov. Phys. Solid State*, Vol. 32, 1917, 1990.
9. Polyakov, V. I., A. I. Rukovishnikov, B. M. Garin, et al., *Diamond and Related Materials*, Vol. 14, 604, 2005.
10. Garin, B. M., V. I. Polyakov, A. I. Rukovishnikov, L. A. Avdeeva, V. N. Derkach, V. V. Parshin, and V. G. Ralchenko, *Diamond and Related Materials*, Vol. 15, 1917, 2006.

Coupled Line 180° Hybrids with Modified Trans-directional Couplers

Hongmei Liu, Shaojun Fang, and Zhongbao Wang
Information Science and Technology Institute, Dalian Maritime University, Liaoning 116026, China

Abstract— A novel coupled line 180° hybrid comprises of two modified trans-directional (TRD) couplers and one half-wave transmission line is proposed. The two identical TRD couplers are perpendicular connected to each other at two end points with one directly and the other through a $\lambda/2$ line section. The proposed hybrid can be easily realized on a single-layer substrate by using general printed circuit board (PCB) technology with a low cost. Modified TRD couplers with arbitrary coupling are presented in the paper to construct the hybrid with simple structure, easy fabrication, and wide range of coupling values. Theoretical analysis of the modified TRD coupler and detailed design procedures of the hybrid is given. To validate the structure, experimental circuit with a 3 dB coupling value was also designed and fabricated. Simulation results are compared with the measurements, and a good agreement is observed.

1. INTRODUCTION

Hybrid couplers are essential component used extensively in various microwave circuits, such as balanced amplifiers, balanced mixers, phase shifters, and feed networks in antenna arrays. Consider the phase differences between the two output ports, hybrid couplers can be classified into two categories: 9° and 180°. For 90° hybrids, parallel couple-line and branch-line couplers are well known examples [1]. For certain applications, namely, mixers and phase shifters, the 180° hybrids are preferred since the isolation between the two input ports may be independent of the value of two balanced-impedance loads [2]. Regarding the signal split ratio, the most commonly used is the equal power split hybrid.

The rat race is a widely used 180° hybrid [3]. It consists of a $3\lambda/2$ perimeter microstrip ring at the operating frequency with four ports connected along the ring. Numerous publications have been reported for the improvements of this type of hybrid mainly dealing with size reduction [4, 5], simultaneous size reduction and suppression of the harmonic response [6], increasing the bandwidth [7, 8], dual band operation [9], and arbitrary power divisions [10].

In [11], an alternative realization of a 180° hybrid is proposed based on a cascade connection of the two identical parallel coupled line couplers. Figure 1 shows the electrical schematic of such a coupled line hybrid. The parallel coupled lines are connected at two end points with one directly and the other through a $\lambda/2$ line section. It features the characteristics of simple structure, easy fabrication, and wide range of coupling values. However, the coupling levels of the parallel coupled line couplers are smaller due to fabrication constraints on the spacing of the coupled lines. Thus, it is hard to realize a tight coupling 180° hybrid on a substrate with arbitrary height and permittivity.

Based on the structure, coupled line 180° hybrids with non-TEM directional couplers [12] and Near-TEM Lange couplers [13] are presented. However, single frequency of equal power division or symmetrical over-coupling is not possible if non-TEM directional couplers are used, since the even and odd mode velocities of the coupled lines are different. Though the near-TEM Lange couplers tends to compensate for the unequal even and odd mode phase velocities, the closed narrow lines and the necessary bonding wires across the lines are difficult to fabricate using PCB technology.

In the paper, modified TRD couplers with arbitrary coupling are presented to construct the coupled line 180° hybrid. An experimental microstrip prototype with a 3-dB coupling has been fabricated on a PCB substrate ($\varepsilon = 3.5$, $h = 1.5$) with a low cost. The consistency with the simulated and measured results validates the proposed circuit structure.

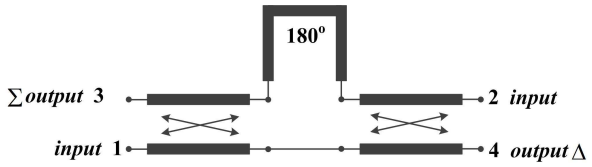

Figure 1: Electrical schematic of the coupled line 180° hybrid.

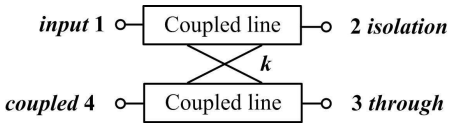

Figure 2: Schematic of the TRD coupler.

2. PROPOSED MODIFIED TRD COUPLER

From the port numbers of Figure 1, three types of directional couplers can be described according to the relative location of the isolation port to the input port. If port 3 is the isolation port, then co-directional coupler can be formed, while if port 4 is the isolation port, contra-directional coupler is constituted. The isolation port of port 2 is corresponding to the TRD coupler.

In [14], a realization of the TRD coupler is reported with the coupling level limited to less than 4.8 dB. However, the coupling values of the two couplers are 7.67 dB [11] for constructing the 3-dB 180° hybrid. Thus, the structure is needed to be modified for large range of coupling. Though TRD couplers for weak coupling are presented [15], the equations are complicated and the realizations are complex with the inductance (L) added to the four ports of the TRD coupler.

Figure 3 shows the schematic of the modified TRD coupler. It consists of three cells of capacitor-loaded coupled lines. The parameters of cell_1 are the same with cell_3. The even (odd) mode characteristic impedances of the cell_2 are equal with $\text{cell}_{1,3}$, except the shunt capacitors.

A convenient method for analyzing the proposed TRD coupler involves the derivation of an ABCD matrix for each of the constituent cell. The circuit is decomposed into three cells, described by $M_{1(e,o)}$, $M_{2(e,o)}$ and $M_{3(e,o)}$. The $ABCD$ matrices of the three cells are

$$M_{1(e,o)} = \begin{bmatrix} a_{1(e,o)} & b_{1(e,o)} \\ c_{1(e,o)} & d_{1(e,o)} \end{bmatrix} \tag{1}$$

$$M_{2(e,o)} = \begin{bmatrix} a_{2(e,o)} & b_{2(e,o)} \\ c_{2(e,o)} & d_{2(e,o)} \end{bmatrix} \tag{2}$$

$$M_{3(e,o)} = M_{1(e,o)} \tag{3}$$

where

$$a_{1,2(e,o)} = d_{1,2(e,o)} = \cos\theta_1 - \frac{b_{1,2(e,o)}}{2}\sin\theta_1 \tag{4}$$

$$b_{1,2(e,o)} = jZ_{1(e,o)}\left(\sin\theta_1 - \frac{b_{1,2(e,o)}}{2} + \frac{b_{1,2(e,o)}}{2}\cos\theta_1\right) \tag{5}$$

$$c_{1,2(e,o)} = \frac{j}{Z_{1(e,o)}}\left(\sin\theta_1 + \frac{b_{1,2(e,o)}}{2} + \frac{b_{1,2(e,o)}}{2}\cos\theta_1\right) \tag{6}$$

$$b_{1,2(e)} = 0 \tag{7}$$

$$b_{1,2(o)} = 2\omega C_{1,2} Z_{1o} \tag{8}$$

$$\omega = 2\pi f \tag{9}$$

The equivalent $ABCD$ matrix of the TRD coupler is

$$M_{\text{all}(e,o)} = \begin{bmatrix} \cos\theta_{e,o} & jZ_{0(e,o)}\sin\theta_{e,o} \\ \frac{jZ_{0(e,o)}}{\sin\theta_{e,o}} & \cos\theta_{e,o} \end{bmatrix} \tag{10}$$

where

$$Z_{0e} = Z_0\sqrt{\frac{1+k}{1-k}} \tag{11}$$

$$Z_{0o} = Z_0\sqrt{\frac{1-k}{1+k}} \tag{12}$$

In the above equations, f is the frequency, θ_1 is the electrical length of each cell, and $Z_{1(e,o)}$ are the even and odd mode characteristic impedance of the coupled lines. $\theta_{(e,o)}$ and $Z_{0(e,o)}$ are the electrical length and equivalent characteristic impedance of the even and odd mode transmission line. Z_0 is the equivalent port impedance (50 Ω) and k is the coupling coefficient of the coupler. Matrix multiplication gives the equation listed as follows.

$$M_{\text{all}(e,o)} = M_{1(e,o)} \cdot M_{2(e,o)} \cdot M_{3(e,o)} \tag{13}$$

Then we have

$$Z_{1e} = Z_{0e} \tag{14}$$

$$b_{2o} = \frac{2\left[m_1 \cdot \cos\theta_1 - (m_2 + m_3) \cdot \sin\theta_1 - \cos\theta_o\right]}{m_1 \cdot \sin\theta_1 + m_2 \cdot (1 + \cos\theta_1) + m_3 \cdot (\cos\theta_1 - 1)} \tag{15}$$

$$Z'_{0o} = \frac{Z_{0o}}{\sqrt{\frac{p_1 \cdot (2\sin\theta_1 + b_{1o}\cos\theta_1 - b_{1o}) - p_2 + p_3}{p_1 \cdot (2\sin\theta_1 + b_{1o}\cos\theta_1 + b_{1o}) - p_4 + p_5}}} \tag{16}$$

where

$$m_1 = \cos 2\theta_1 - b_{1o} \cdot \sin 2\theta_1 - \frac{b_{1o}^2 \cdot (\cos 2\theta_1 - 1)}{4} \tag{17}$$

$$m_2 = \left(\cos\theta_1 - \frac{b_{1o} \cdot \sin\theta_1}{2}\right) \cdot \left[\sin\theta_1 + \frac{b_{1o}\,(\cos\theta_1 - 1)}{2}\right] \tag{18}$$

$$m_3 = \left(\cos\theta_1 - \frac{b_{1o} \cdot \sin\theta_1}{2}\right) \cdot \left[\sin\theta_1 + \frac{b_{1o}\,(\cos\theta_1 + 1)}{2}\right] \tag{19}$$

$$p_1 = \left(\cos\theta_1 - \frac{b_{1o} \cdot \sin\theta_1}{2}\right) \cdot \left(\cos\theta_1 - \frac{b_{2o} \cdot \sin\theta_1}{2}\right) \tag{20}$$

$$p_2 = \left[\sin\theta_1 + \frac{b_{1o} \cdot (\cos\theta_1 - 1)}{2}\right]^2 \cdot \left[\sin\theta_1 + \frac{b_{2o} \cdot (\cos\theta_1 + 1)}{2}\right] \tag{21}$$

$$p_3 = \left[\cos\theta_1 - \frac{b_{1o} \cdot \sin\theta_1}{2}\right]^2 \cdot \left[\sin\theta_1 + \frac{b_{2o} \cdot (\cos\theta_1 - 1)}{2}\right] \tag{22}$$

$$p_4 = \left[\sin\theta_1 + \frac{b_{1o} \cdot (\cos\theta_1 + 1)}{2}\right]^2 \cdot \left[\sin\theta_1 + \frac{b_{2o} \cdot (\cos\theta_1 - 1)}{2}\right] \tag{23}$$

$$p_5 = \left[\cos\theta_1 - \frac{b_{1o} \cdot \sin\theta_1}{2}\right]^2 \cdot \left[\sin\theta_1 + \frac{b_{2o} \cdot (\cos\theta_1 + 1)}{2}\right] \tag{24}$$

For simplification, the phase coupling of the transmission lines is ignored, $\theta_e = \pi/2$, $\theta_o = 3\pi/2$, and $\theta_1 = \pi/6$. For certain coupling value, $Z_{0(e,o)}$ are calculated using Equations (11) and (12), and functional dependency of Z_{1o} to the value of b_{1o} can be plotted according to Equation (16). Thus, proper values of Z_{1o} can be chosen, and all the other parameters of the TRD coupler are obtained.

3. 180° HYBRID DESIGN

As a first step in the design of a 3-dB 180° hybrid, the 7.67-dB TRD coupler operating at 3 GHz is designed. From Equations (11) and (12), for 7.67 dB coupling, $Z_{0e} = 77.6\,\Omega$ and $Z_{0o} = 32.2\,\Omega$.

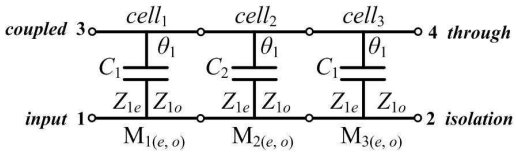

Figure 3: Schematic of the proposed TRD coupler.

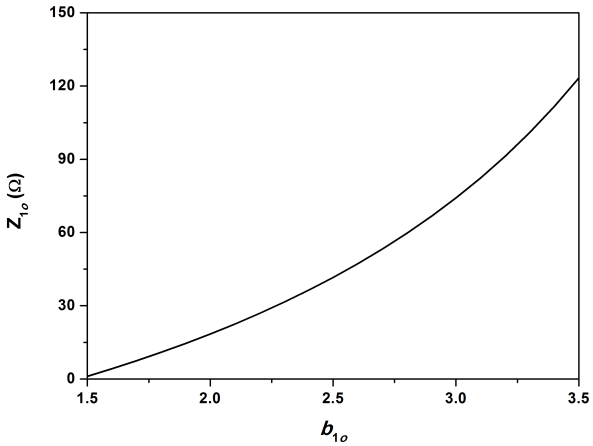

Figure 4: Z_{1o} curve as a function of b_{1o}.

The Z_{1o} curve as a function of b_{1o} with 7.67 dB coupling value is plotted, as illustrated in Figure 4. It can be seen that with the increase of b_{1o}, the value of Z_{1o} increases, and when b_{1o} is more than 3.03, the value of Z_{1o} exceeds 77.6 Ω (more than Z_{1e}). Thus, considering the coupling value of the coupled lines, $Z_{1o} = 66.6\,\Omega$ and $b_{1o} = 2.9$ is chosen. The coupling value of the coupled line is 18 dB. Finally, with Equations (8) and (15), $C_1 = 1.15$ pF and $C_2 = 1.86$ pF.

After optimizing using Ansoft HFSS, the suitable coupling value of 7.5 dB has been obtained with a line width of 1.6 mm, a separation gap of 0.9 mm $C_1 = 1.0$ pF and $C_2 = 1.8$ pF. The length of the coupler was 16 mm.

In the next step, models of the 180° hybrid comprises of the two TRD couplers and a 180° transmission line were constructed, as shown in Figure 5. Optimizations have been carried out to obtain a 3-dB 180° hybrid. The final dimensions are $w_1 = 3.3$ mm, $w_2 = 1.6$ mm, $s_1 = 0.9$ mm, $l_1 = 15.4$ mm, $l_2 = 14.0$ mm, $l_3 = 4.0$ mm, $l_4 = 6.7$ mm, $l_5 = 5.7$ mm, $l_6 = 7.4$ mm, $l_7 = 6.5$ mm, $l_8 = 6.6$ mm, $C_1 = 1.0$ pF and $C_2 = 1.8$ pF.

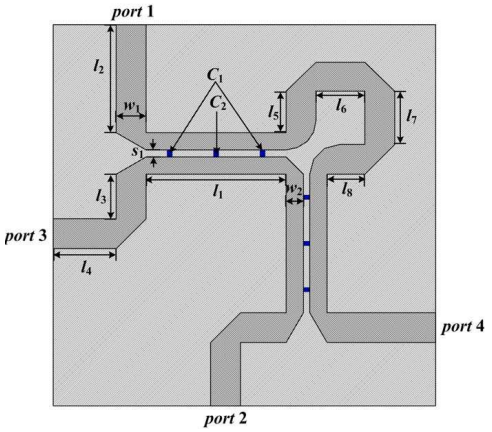

Figure 5: The layout of the proposed 180° hybrid.

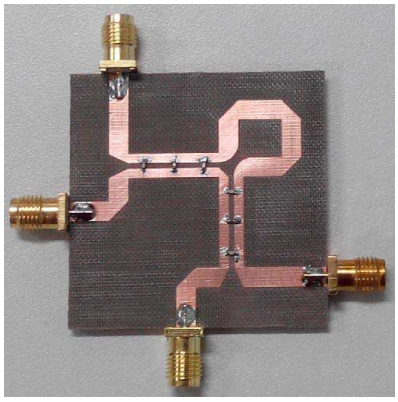

Figure 6: The photograph of the proposed 180° hybrid.

4. SIMULATED AND MEASURED RESULTS

The fabricated sample with optimization dimensions was manufactured on an FB4 substrate with a dielectric constant of 3.5, a loss tangent of 0.003, and a thickness of 1.5 mm. The photograph of the prototype is shown in Figure 6.

Figures 7(a) and (b) display the measured results with the comparison of the simulated results when input at port 1. The amplitude bandwidth defined by 4.1 ± 1.0 dB between ports 3 and 4 is from 2.75 to 3.20 GHz, and their phase bandwidth, defined by $180° \pm 10°$ is in the range of 2.68–3.22 GHz. Meanwhile, the isolation is more than 20 dB throughout the frequency band of

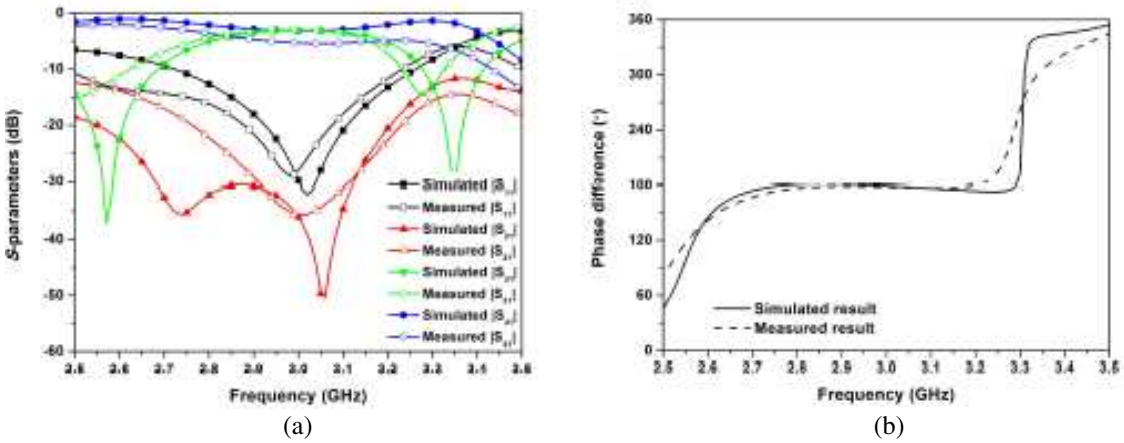

(a) (b)

Figure 7: Measured and simulated results when input at port 1. (a) S-parameters. (b) Phase difference.

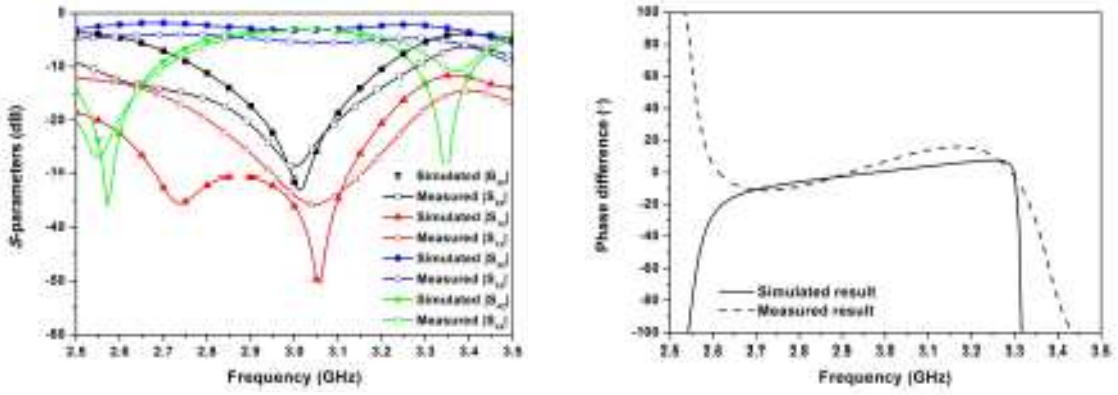

(a) (b)

Figure 8: Measured and simulated results when input at port 2. (a) S-parameters. (b) Phase difference.

2.75–3.22 GHz, and the return loss is larger than 15 dB from 2.74 GHz to 3.13 GHz.

Figures 8(a) and (b) show the case of input at port 2 of the hybrid. From 2.70 to 3.10 GHz, the insertion loss is 4.2 ± 1.0 dB and the phase difference is $0° \pm 10°$. The isolation is more than 20 dB in the range of 2.76–3.22 GHz, and a return loss of larger than 15 dB is obtained from 2.88 to 3.13 GHz. The measured results are in good agreement with the simulated results. The slight discrepancies between the simulated and the measured results are believed to be due to the losses introduced by the connectors and the substrate.

5. CONCLUSIONS

A coupled line 180° hybrid comprises of modified TRD couplers and one half-wave transmission line has been presented. To demonstrate the structure, a 3-dB 180° hybrid has been designed and fabricated. Results show that the proposed 180° hybrid has simple structure, and is easy to fabricate on planar PCB circuits with a low cost. Therefore, the proposed 180° hybrid can be a suitable candidate for microwave applications.

ACKNOWLEDGMENT

This work was supported jointly by the Scientific Research Project of the Department of Education of Liaoning Province (Nos. L2013196 and L2012171), the Fundamental Research Funds for the Central Universities (No. 3132013053), the National Natural Science Foundation of China (No. 61231006), the National Excellent Doctoral Dissertation cultivate Fund (No. 2014YB05), and the National Key Technologies R&D Program of China (No. 2012BAH36B01).

REFERENCES

1. Pozar, D. M., *Microwave Engineering*, 2nd Edition, Wiley, New York, 1998.
2. Wang, T. and K. Wu, "Size-reduction and band-broadening design technique of uniplanar hybrid ring coupler using phase inverter for M(H)MIC's," *IEEE Trans. Microw. Theory Tech.*, Vol. 47, No. 2, 198–206, Feb. 1999.
3. March, S., "A wideband stripline hybrid ring," *IEEE Trans. Microw. Theory Tech.*, Vol. 16, No. 6, 361, Jun. 1968.
4. Eccleston, K. W. and S. H. M. Ong, "Compact planar microstripline branch-line and rat-race couplers," *IEEE Trans. Microw. Theory Tech.*, Vol. 51, No. 10, 2119–2125, Oct. 2003.
5. Lin, C.-K. and S.-J. Chung, "A compact filtering 180 hybrid," *IEEE Trans. Microw. Theory Tech.*, Vol. 59, No. 12, 3030–3036, Dec. 2011.
6. Kuo, J.-T., J.-S. Wu, and Y.-C. Chiou, "Miniaturizad rat race coupler with suppression of spurious passband," *IEEE Microw. Wireless Compon. Lett.*, Vol. 17, No. 1, 46–48, Jan. 2007.
7. Mo, T. T., Q. Xue, and C. H. Chan, "A broadband compact microstrip rat-race hybrid using a novel CPW inverter," *IEEE Trans. Microw. Theory Tech.*, Vol. 55, No. 1, 161–167, Jan. 2007.
8. Kim, T.-G. and B. Lee, "Metamaterial-based wideband rat-race hybrid coupler using slow wave lines," *IET Microw. Antennas Propag.*, Vol. 4, No. 6, 717–721, Jun. 2009.
9. Zhang, H. and K. J. Chen, "Design of dual-band rat-race couplers," *IET Microw. Antennas Propag.*, Vol. 3, No. 3, 514–521, Apr. 2009.

10. Cheng, K.-K. M. and S. Yeung, "A novel rat-race coupler with tunable power dividing ratio, ideal port isolation, and return loss performance," *IEEE Trans. Microw. Theory Tech.*, Vol. 61, No. 1, 55–60, Jan. 2013.
11. Park, M. J. and L. Byungje, "Coupled line 180 hybrid coupler," *Microw. Opt. Technol. Lett.*, Vol. 45, No. 2, 173–176, Apr. 2005.
12. Napijalo, V. and B. Kearns, "Multilayer 180 hybrid coupler," *IEEE Trans. Microw. Theory Tech.*, Vol. 56, No. 11, 2525–2535, Nov. 2008.
13. Napijalo, V., "Coupled line 180 hybrids with Lange couplers," *IEEE Trans. Microw. Theory Tech.*, Vol. 60, No. 12, 3674–3682, Dec. 2012.
14. Shie, C.-I., J.-C. Cheng, S.-C. Chou, and Y.-C. Chiang, "Transdirectional coupled-line couplers implemented by periodical shunt capacitors," *IEEE Trans. Microw. Theory Tech.*, Vol. 57, No. 12, 2981–1988, 2009.
15. Liu, H. M., Z. B. Wang, and S. J. Fang, "Trans-directional coupler with capacitor-shunted ground-defected coupled CPWs and inductor-loaded ACPWs for weak coupling applications," *Journal of Electromagnetic Waves and Applications*, Vol. 27, No. 1, 104–116, 2013.